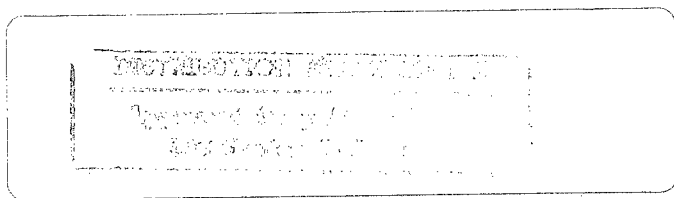


STRUCTURAL DYNAMICS RECENT ADVANCES



**PROCEEDINGS OF THE
6TH INTERNATIONAL
CONFERENCE**

**EDITED BY:
N. S. FERGUSON
H. F. WOLFE
C. MEI**

STRUCTURAL DYNAMICS: RECENT ADVANCES

Proceedings of the 6th International Conference

Volume I

Proceedings of the Sixth International Conference on Recent Advances in Structural Dynamics, held at the Institute of Sound and Vibration Research, University of Southampton, England, from 14th to 17th July, 1997, co-sponsored by the US Airforce European Office of Aerospace Research and Development and the Wright Laboratories, Wright Patterson Air Force Base.

Edited by

N.S. FERGUSON

*Institute of Sound and Vibration Research,
University of Southampton, Southampton, UK.*

H.F. WOLFE

*Wright Laboratory,
Wright Patterson Air Force Base, Ohio, USA.*

and

C. MEI

*Department of Aerospace Engineering,
Old Dominion University, Norfolk, Virginia, USA.*

© The Institute of Sound and Vibration Research, University of Southampton, UK.
ISBN no. 0-85432-6375

19970814 054

PERIODICAL DEPARTMENT

PREFACE

The papers contained herein were presented at the Sixth International Conference on Recent Advances in Structural Dynamics held at the Institute of Sound and Vibration Research, University of Southampton, England in July 1997. The conference was organised and sponsored by the Institute of Sound and Vibration Research and co-sponsored by the Wright Laboratories, Wright Patterson Air Force Base. We wish to also thank the following for their contribution to the success of the conference: the United States Air Force European Office of Aerospace Research and Development. The conference follows equally successful conferences on the same topic held at Southampton in 1980, 1984, 1988, 1991 and 1994.

There are over one hundred papers written by authors from approximately 20 different countries, making it a truly international forum. Many authors have attended more than one conference in the series whilst others attended for the first time.

It is interesting to note the change in emphasis of the topics covered. Analytical and numerical methods have featured strongly in all the conferences. This time, system identification and power flow techniques are covered by even more papers than previously. Also, there are many contributions in the field of passive and active vibration control. Papers dealing with nonlinear aspects of vibration continue to increase. These observations seem to reflect the trend in current research in structural dynamics. We therefore hope that the present series of International Conferences will play a part in disseminating knowledge in this area.

We would like to thank the authors, paper reviewers and session chairmen for the part they played in making it a successful conference.

My personal thanks go to the following individuals who willingly and enthusiastically contributed to the organisation of the event:

Dr. H.F. Wolfe	Wright Laboratories, WPAFB, USA
Dr. C. Mei	Old Dominion University, USA
Mrs. M.Z. Strickland	ISVR, University of Southampton, UK

Grateful thanks are also due to many other members of ISVR who contributed to the success of the event.

N.S. Ferguson

**Sixth International Conference on
Recent Advances in Structural Dynamics**

Volume I

Contents

Page No.

INVITED PAPERS

D.J. INMAN and M.J. LAM Active constrained layer damping treatments	1
P. SAS and W. DEHANDSCHUTTER Design of active structural and acoustic control systems for the reduction of road noise in a passenger car	21
J.N. REDDY A review of theories and computational models of laminated composite structures	45

ANALYTICAL METHODS I

1. S. CHAKRAVERTY and M. PETYT Transverse vibration of orthotropic elliptic plates using orthogonal polynomials in the Rayleigh-Ritz method	67
2. A.V. SINGH A unified approach for the free vibration analysis of circular plates and shells of revolution	81
3. S. KARUNAMOORTHY and G. REGULEZ A study on aerofoil section flutter with two dimensional finite-state aerodynamics	97
4. YU.A. ROSSIKHIN and M.V. SHITIKOVA A nonstationary Rayleigh wave of the 'diverging circle' type on the heat-insulated surface of a thermoelastic sphere	113
5. R. SHEN and H. ZHU Theoretical and experimental investigation of multistage vibration isolation system	129

PASSIVE AND ACTIVE CONTROL I

- | | | |
|-----|---|-----|
| 6. | M.J. BRENNAN
Design of a wideband vibration neutraliser | 145 |
| 7. | A.K. BELYAEV
On the tuned vibration absorber for the suppression of a parametric resonance | 161 |
| 8. | S.O. OYADIJI, K.T. FERROZ and G.R. TOMLINSON
Characteristics of viscoelastically-damped mechanical filters | 173 |
| 9. | S.O. OYADIJI
Passive control of the vibrational response characteristics of hollow beams using viscoelastic spheres | 187 |
| 10. | P. CLARK and R.G. WHITE
Measurement and control of low frequency vibrational power transmission in pipeline structures | 199 |

FINITE ELEMENT METHODS I

- | | | |
|-----|--|-----|
| 11. | L.J. WEST, N.S. BARDELL, J.M. DUNSDON and P.M. LOASBY
Some limitations associated with the use of k -orthogonal polynomials in hierarchical versions of the Finite Element method | 217 |
| 12. | N.S. BARDELL, R.S. LANGLEY, J.M. DUNSDON and K.N. KHATRI
On the free vibration of completely free, open, thin, conically curved panels | 233 |
| 13. | A.A. LAKIS and A. SELMANE
Vibration analysis of circumferentially non-uniform cylindrical shells subjected to a flowing fluid | 249 |
| 14. | U. LEE and J. LEE
Dynamic analysis of one and two-dimensional structures using spectral element method | 263 |
| 15. | B.A. BILODEAU and J.F. DOYLE
Spectral elements for acoustic wave propagation through thin-walled complex structures | 279 |
| 16. | G.I. LVOV and V.V. OVCHARENKO
Finite Element analysis of adaptive laminated shell vibration | 295 |

NUMERICAL METHODS I

17. E.P. PETROV
Analysis of influence of technological and design distortions
of rotationally periodic symmetry on forced response
characteristics and stress scattering of bladed disks 309
18. E.P. PETROV
Essentially nonlinear forced vibrations of mistuned turbine
blade packets 325
19. Y.F. HWANG and L. LOUIE
A component mode synthesis method for substructures
connected by elastic joints 339
20. G. OLIVETO, I. CALIO and A. SANTINI
Complex eigensolutions for frequency dependent soil-
structure interacting systems 353
21. P. RUGE
Eigenvalue evaluation for nonlinear matrix polynomials in
structural dynamics in original space of DOF 369

SYSTEM IDENTIFICATION I

22. M.I. FRISWELL, S.D. GARVEY and J.E.T. PENNY
Parameter subset selection in damage location 383
23. S.W. DOEBLING, C.R. FARRAR and P.J. CORNWELL
DIAMOND: A graphical interface toolbox for comparative
modal analysis and damage identification 399
24. W.J. STASZEWSKI
Fault detection in machinery using orthogonal wavelet
decomposition 413
25. M.H. SADEGHI and S.D. FASSOIS
Information-based reduced-dimensionality geometric
approach to fault identification in stochastic structural
systems 427
26. B. BENCHEKCHOU and N.S. FERGUSON
Fatigue behaviour of carbon fibre reinforced plates with
embedded optical fibres 443
27. D.H. KIM and P.R. WHITE
Parametric system identification using higher-order
statistics 457

PASSIVE AND ACTIVE CONTROL II

28. C.Y. WU, R.R. HAYMANALI, E.C. DE METER and M.W. TRETHEWEY
Static and dynamic structural evaluation of workpiece/fixtures systems for machining operations 471
29. M. ABE
Variable gain control for structures with closely spaced natural frequencies 487
30. P. GARDONIO, S.J. ELLIOTT and R.J. PINNINGTON
Mobility model for active isolators 501
31. M. ZHU and C. ZHAO
An application of an artificial neural network method to nonlinear vibration control systems 521
32. M. ZHU, C. ZHAO and F. WANG
A stability analysis of a rotor system with electromagnetic control forces 531
33. M. AHMADIAN and X. SONG
Effect of system delays on semiactive suspension performance 541

POWER FLOW TECHNIQUES I

34. R.Y.Y. LEE and C.F. NG
Insertion loss of stiffened enclosures 553
35. C.H. RIEDEL and C.A. TAN
Free response and wave propagation in constrained strings and beams on partial elastic foundations 563
36. S.H. LIU and R.J. PINNINGTON
The measurement of in-plane wave power flow in plates 583
37. B.A.T. PETERSSON
Vibration transmission at large interfaces 597
38. S. FINNVEDEN
Vibration energy transmission in fluid-filled pipes connected with flanges 613
39. R.S. LANGLEY, J.R.D. SMITH and F.J. FAHY
Statistical Energy Analysis of periodically stiffened damped plate structures 629

EXPERIMENTAL METHODS I

- | | | |
|-----|---|-----|
| 40. | M.A. CATCHINS and M.L. TINKER
Boundary influences in dynamic testing | 645 |
| 41. | D. RAVI and K.M. LIEW
Effect of elastic constraints introduced by microcracks on
mode shapes in aluminum 6061 sheet | 661 |
| 42. | M. BOLTEZAR, B. STRANCAR and A. KUHELJ
Assessing the transverse crack location in flexural
vibrations of straight uniform beams | 671 |
| 43. | S.O. OYADIJI and M. SOLOOK
Use of PVDF for distributed sensing of vibrations of a
beam | 681 |

NONLINEAR VIBRATION I

- | | | |
|-----|--|-----|
| 44. | M.S. PASRICHA and A.Y. HASSAN
Effects of damping on secondary resonances in torsional
vibrations of a two-degree-of-freedom system - a variable
inertia aspect in reciprocating engines | 693 |
| 45. | S. CAFFERTY, J. GIACOMIN AND K. WORDEN
Simple nonlinear models for automotive shock absorbers | 709 |
| 46. | K. WORDEN
Energy transmission through nonlinear suspension
systems | 725 |
| 47. | D.M. SANTEE and P.B. GONÇALVES
Non-linear vibrations and instabilities of structural systems
liable to asymmetric bifurcation | 743 |
| 48. | N. POPPLEWELL, M. LIAO and A. SHAH
Gallopings of twin-bundled conductors | 757 |
| 49. | J-Y LEE and J.K. HAMMOND
Safe design of impacting systems | 773 |
| 50. | FENG QI
Chaotic stochastic vibration on Duffing system with
friction | 785 |

NONLINEAR VIBRATION II

- | | | |
|-----|---|-----|
| 51. | J.A. BRANDON, E. BENOIT and L. JEZEQUEL
The dynamics of a modally complex structure with a
clearance nonlinearity | 801 |
|-----|---|-----|

52.	M. KISA and J.A. BRANDON A numerical study of the dynamics of a cracked beam	811
53.	G.T. ZHENG and A.Y.T. LEUNG The stability study of cracked rotor systems by virtual oil-film bearings	823
54.	Z. ZHENG, Z. HOU and A.Y.T. LEUNG Stability of unclassically damped gyroscopic systems with parametric excitation	833
55.	S. AOKI and T. WATANABE Forced vibration analysis of a beam with a nonlinear support	847
56.	F. PELLICANO and F. VESTRONI Free nonlinear vibrations of an axially moving beam	863
57.	I. YILDIRIM, M.Ö. AKBAL and H.T. BELEK Transient contact response of a hermetic reciprocating compressor valve	873

INVITED PAPERS

ACTIVE CONSTRAINED LAYER DAMPING TREATMENTS

Daniel J. Inman and Margaretha J. Lam
Department of Engineering Science and Mechanics
Virginia Polytechnic Institute and State University
Blacksburg, VA 24061-0219 USA

ABSTRACT

This work examines the use of piezoceramic devices combined with viscoelastic material as a damping treatment to suppress unwanted vibrations in structural elements. This is an extension of the mature technology of passive constrained layer damping (PCLD) treatments which have been so successful in the past. In applying viscoelastic damping treatments it is thought that the best design is one that increases shear in the viscoelastic layer (VEM). This led to the use of constraining layers to form sandwiches consisting of the host structure, viscoelastic treatment and cover layer. Recently, piezoceramics layers have been applied to structures as actuators and sensors to provide active vibration suppression. It was thus natural to replace the cover plate in passive designs with a piezoceramic material to produce a layer that could actively increase the shear in the viscoelastic layer. This approach, called active constrained layer damping (ACL D) and its variations form the topic of this presentation. Here the previous work in ACL D for vibration suppression is reviewed, modeling and control issues are identified and design considerations are discussed. Some new configurations and results are also presented.

INTRODUCTION

Passive constrained layer damping treatments have been, and are, a successful means of suppressing unwanted vibrations in various structural components [1], [2], [3]. A natural extension of PCLD treatments is to combine them with the fast growing area of smart structures [4]. Smart structures technology covers a wide variety of electrically active materials [5], the most common of which are materials that exhibit the piezoelectric effect. One such material, piezoceramics (such as PZT: lead zirconate titanate), produce a voltage (or current) when they are strained making them useful as sensors, and produce a strain or bending moment when a voltage is applied across them rendering them useful as actuators. Another common material used for sensing and sometimes as an actuator is a piezo film (PVFD: polyvinylidene flourides). These materials allow the construction of unobtrusive sensors and actuators fully integrated into a structural system. The combining of the use of piezoelectric materials with



Free layer damping



Segmented treatment of constraining layer (active or passive)



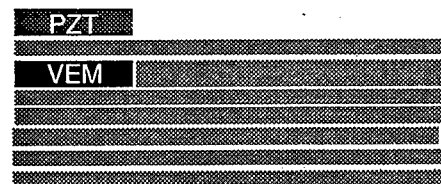
Passive constrained layer damping (PCLD)



ACLD configuration used by Van Norstrand, et al.



Active treatment



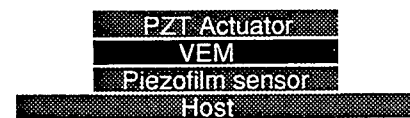
Embedded, layered configuration used by Saunders, et al.



Standard configuration of active constrained layer damping (ACLD)



Edge effect configuration by Wang



ACLD configuration used by BAZ



Configuration used by Tomlinson

Figure 1: Various configurations of viscoelastic materials (VEM), constraining layer (CL), sensors and piezoceramic actuators (PZT) used for vibration suppression.

viscoelastic damping treatments is called ACLD and the use of active damping and passive damping together is called hybrid damping. The various designs and configurations studied are based on trying to take advantage of the best properties of passive damping (PCLD, in particular) and of active damping and actuation provided by smart structures. Various configurations of sensors, actuators and damping methods are illustrated in figure 1.

One line of thought has been that the viscoelastic material will have enhanced damping capabilities if the cover plate (made of PZT) can be used to actively increase the shear in the VEM causing it to dissipate more energy resulting in improved vibration suppression. A second line of thought is that the VEM will provide a passive high frequency vibration suppression and that the piezoelectric element will be used to enhance low frequency vibration suppression. Put another way, the combination of PZT and VEM could provide broader band vibration suppression than either of the two treatments used separately. These thoughts have encouraged several researchers to pursue various designs combining the two technologies and to investigate the related mechanics and control issues.

A counter point of view in combining VEM and PZT is that if the PZT is mounted on top of a VEM layer to increase the shear in the viscoelastic, the configuration also decreases the effect of the PZT as an actuator because it must act through the rubbery viscoelastic material. Thus the issue of why not just use active control and not use the viscoelastic treatment at all arises. Such questions are addressed in the following along with providing some alternative configurations and alternate modeling methods.

PREVIOUS WORK

The use of piezoelectric materials combined with closed loop control laws provides a very effective means of suppressing unwanted vibration. Agnes and Napolitano [6] and Baz [7] suggested combining these two technologies to create an even more effective means of suppressing vibration. Baz [8] provides a survey of the first two years of research in this new technology and provides an excellent overview. Shen [9] addressed the issue of stability and controllability of ACLD while the optimal placement and size of the ACLD treatment was studied in [8]. Baz [8] and Liao and Wang [10] compared the performance of the ACLD to the performance of passive constrained layer damping (PCLD), and to that of the purely active case (PZT), as has Tomlinson [11]. Huang et. al. [12] showed that ACLD offers improved performance when compared with purely active or purely passive treatments if the thickness and feedback gain are limited. Saunders

[13] provided a pole-zero analysis and experiments of an embedded ACLD configuration.

Several different configurations and arrangements of PZT and VEM have been suggested and examined by various researchers as displayed in figure 1. The most common approach is to simply replace the constraining layer with PZT to enhance the shear in the viscoelastic layer. Baz [7,8] uses a film sensor between the viscoelastic layer and the host structure and a piezoceramic material as the constraining layer. Tomlinson [11,14] advocates using a tip accelerometer for the sensing and has suggested placing the piezoceramic layer between the host structure and the viscoelastic. The motivation to consider placing the PZT next to the host beam is that the control action of the piezoceramic is reduced by having to act through the viscoelastic. Shen's group [9,15] has used a point sensor and has recently examined using a distributed self sensing actuation approach [16]. Lesieutre [17] and Kawiecki [18,19] have proposed examining a fully covered but segmented treatment motivated by the success in passive constrained layer treatments when segmented to handle long wave length vibrations. Liao and Wang [20] configured the piezoceramic constraining layer to run past the VEM layer and created a load path for the PZT directly to the host at the edges of the treatment in an attempt to increase the authority of the actuator. Here we examine completely separating the passive and active treatments. Motivation for doing this is to retain the control authority of having the PZT bonded directly to the structure and the other is to provide as thin as possible treatment.

The modeling used here for the piezoceramics is a standard bending "moment model" [21] although several more advanced models are available [4]. The modeling used for the viscoelastic layer by previous researchers has largely followed the work of Mead and Marcus [22] for sandwiched layers and uses a complex modulus approach to capture the damping effects of the viscoelastic layer. The current work departs from both of these standard approaches with the goal of providing a more accurate model.

The use of the complex modulus approach for modeling the viscous damping effects restricts the analysis to a single frequency, steady state analysis. This of course is unsettling for use in transient vibration analysis. Thus, a more advanced modeling technique accounting for the frequency dependence of the viscoelastic is used here following Lam, [23]. This approach was later incorporated in [10] and is experimentally verified by Lam [24]. The second departure from standard modeling approaches for ACLD materials is an examination of the Mead and Marcus based modeling which is flawed because it does not allow the VEM layer to collapse to zero. This was simultaneously examined by Huang [12] and

by Liao and Wang [20]. Both groups provided modified models which allow the damping treatment layer thickness to go to zero. This is important because in many applications, the total damping treatment thickness is restricted, so that a usable model must be able to treat thin layers.

The recent article by Lesieutre and Lee [17] points out that the various research efforts on combining passive and active treatments focus on configuration, modeling assumptions, choice of control, choice of approximation and optimization. Most of the work in ACLD models the viscoelastic damping using the complex modulus approach [7,8]. The exceptions have been Inman and his students [23,24,25,26], Wang and his students [10,20] and Lesieutre who use various time domain models of the viscoelastic material as nicely summarized by Lesieutre and Lee [17]. Here the time domain model developed by Hughes and his students [27] is used (called GHM) to model the viscoelastic property. In addition to using a more accurate modeling approach, the work here also presents a new configuration for combining active and passive damping treatments. Liao and Wang [10] also applied the GHM method and showed the required control effort is less for ACLD than PZT, and in some cases gives better performance. One rationale for using ACLD is in the event the active element fails, the treatment will act as a PCLD treatment and still damp vibration. This paper proposes the use of an active element (PZT) along with a PCLD element to damp vibration. The active element is separate from the PCLD, so that the active element can actuate effectively. The PCLD hybrid treatment will improve robustness and reliability of the system and reduce vibration at the higher modes. It is shown through optimization of performance and control effort that the separate application of the PZT and PCLD give better performance than either the active, PCLD, or ACLD treatments. While the active model proposed in this paper has not yet been experimentally verified, experimental evidence is provided to verify the GHM modeling.

The basic modeling issues addressed here are to provide a model of the viscoelastic layer that is useful in transient analysis and consistent across a broad range of frequencies, and to provide a model that allows thin treatments to be considered. Two models are examined here. The first is that derived by Huang [12] which allows the treatment of thin layers. The second is that of Lam [23,24] which accounts for the frequency dependence in the viscoelastic and hence is useable in transient analysis.

THE MATHEMATICAL MODEL

A cantilever beam of length ℓ with constrained layer damping treatment, covered from positions x_1 to x_2 . The kinematic relations

between the three layers are given by [22]:

$$\epsilon_b = \frac{\partial u_b}{\partial x} - z \frac{\partial^2 w}{\partial x^2} \quad (1)$$

$$\epsilon_x = \frac{\partial u_c}{\partial x} - z \frac{\partial^2 w}{\partial x^2} \quad (2)$$

$$\gamma = \frac{d}{h_v} \frac{\partial w}{\partial x} + \frac{u_x - u_b}{h_v} \quad (3)$$

where $\partial/\partial x$ denotes the partial derivative with respect to x , and u and w , respectively, denote the longitudinal and transverse displacements. The variable x is measured along the beam's axis, and h_v denotes the VEM thickness. Subscripts b , c , and v refer to the host beam, constraining layer, and viscoelastic material respectively. The shear strain of the VEM is denoted by γ , ϵ denotes the strain, z denotes the orthogonal z -direction, and d denotes the distance between the neutral axes of the host beam and constraining layer.

Next an energy approach is used to derive the equations of motion. The VEM is assumed to be in pure shear throughout, and the inertia forces in the x -direction are neglected for all layers. The strain energies (U) and kinetic energies (T) of the layers are then

$$U_b = \frac{1}{2} \int_0^L E_b I_b \left(\frac{\partial^2 w}{\partial x^2} \right)^2 dx + \frac{1}{2} \int_0^L E_b A_b \left(\frac{\partial u_b}{\partial x} \right)^2 dx \quad (4)$$

$$T_b = \frac{1}{2} \int_0^L \rho_b A_b \left(\frac{\partial w}{\partial t} \right)^2 dx \quad (5)$$

$$U_c = \frac{1}{2} \int_{x_1}^{x_2} E_c I_c \left(\frac{\partial^2 w}{\partial x^2} \right)^2 dx + \frac{1}{2} \int_{x_1}^{x_2} E_c A_c \left(\frac{\partial u_c}{\partial x} \right)^2 dx \quad (6)$$

$$T_c = \frac{1}{2} \int_{x_1}^{x_2} \rho_c A_c \left(\frac{\partial w}{\partial t} \right)^2 dx \quad (7)$$

$$U_v = \frac{1}{2} \int_{x_1}^{x_2} G A_v \left(\frac{d}{h_v} \frac{\partial w}{\partial x} + \frac{u_c - u_b}{h_v} \right)^2 dx \quad (8)$$

$$T_v = \frac{1}{2} \int_{x_1}^{x_2} \rho_v A_v \left(\frac{\partial w}{\partial t} \right)^2 dx \quad (9)$$

where ρ is the density, G the shear modulus, E the Young's modulus, A the cross-sectional area, I the area moment of inertia, and $\partial/\partial t$ denotes the partial derivative with respect to time. Again the subscripts b , c , and v refer to the base, constraining layer and VEM, respectively.

Before applying Lagrange's equations, the displacements are first approximated by a modal expansion. There are better approximations [4] but none that are as simple to implement. Since a cantilever beam is the main structure of the system, it is reasonable to choose the modes of a clamped-free beam in bending for the expansion of the transverse displacements, and the longitudinal modes of a fixed-free bar for the axial displacements. Using these modes, the displacements can be written as

$$w(x, t) = \sum_{i=1}^n \eta_i(t) W_i(x) = \mathbf{w}^T \boldsymbol{\eta} \quad (10)$$

$$u_b(x, t) = \sum_{r=1}^m \xi_r(t) U_r(x) = \mathbf{u}^T \boldsymbol{\xi} \quad (11)$$

where η and ξ are the generalized coordinates. The functions $W_i(x)$ and $U_r(x)$ are the transverse longitudinal mode shapes of the cantilevered beam and as such they satisfy the following set of conditions:

$$\int_0^L \rho_b A_b W_i(x) W_j(x) dx = \delta_{ij} \quad (12)$$

$$\int_0^L E_b I_b \frac{\partial^2 W_i(x)}{\partial x^2} \frac{\partial^2 W_j(x)}{\partial x^2} dx = \omega_i^2 \delta_{ij} \quad (13)$$

$$\int_0^L \rho_b A_b U_r(x) U_s(x) dx = \delta_{rs} \quad (14)$$

$$\int_0^L E_b A_b \frac{\partial U_r(x)}{\partial x} \frac{\partial U_s(x)}{\partial x} dx = \bar{\omega}_r^2 \delta_{rs} \quad (15)$$

where ω_i and $\bar{\omega}_r$ respectively, denote the i th bending the the r th axial natural frequencies of the beam, and δ_{ij} is the usual Kronecker delta.

Because the axial inertia effects have been neglected, each layer should be in equilibrium in the x -direction. Thus examining a cut piece of the structure and enforcing the equilibrium of the beam section in the x -direction yields

$$u_c = u_b - c_b \frac{\partial^2 u_b}{\partial x^2} - d \frac{\partial w}{\partial x} \quad (16)$$

where $c_b = E_b h_b / (G / h_v)$, and $d = h_v + (h_b + h_c) / 2$ is the distance from the base beam's neutral axis to the constraining layer's central axis. Likewise, equilibrium of the constraining layer yields

$$c_c \frac{\partial^2 u_c}{\partial x^2} - u_c + u_b - d \frac{\partial w}{\partial x} = 0 \quad (17)$$

where $c_c = E_c h_c / (G / h_v)$. Substituting equations (10), (11), (16) and (17) into the energy expressions and applying Lagrange's equation, one obtains the equations of motion for the sandwich beam as

$$M\ddot{\eta} + K\eta = Q \quad (18)$$

where M and K denote the $n \times n$ generalized mass and stiffness matrices and Q denotes the $n \times 1$ generalized force vector. The entries of the mass matrix given by

$$M_{ij} = \delta_{ij}(\rho_c A_c + \rho_v A_v) \int_{x_1}^{x_2} \mathbf{W}_i(x) \mathbf{W}_j(x) dx \quad (19)$$

and the stiffness matrix is

$$K = K^b - K^{cT} K^a^{-1} K^c \quad (20)$$

where $K_{m \times m}^a$, $K_{n \times n}^b$ and $K_{m \times n}^c$ represent axial, bending, and axial-bending-coupled stiffness matrices, respectively. The entries of these matrices are

$$K_{ij}^b = \omega_i^2 \delta_{ij} + (E_c I_c + E_c A_c d^2) \int_{x_1}^{x_2} W_i'' W_j'' dx + E_c A_c c_c d^2 \int_{x_1}^{x_2} W_i''' W_j''' dx \quad i, j = 1, 2, \dots \quad (21)$$

$$K_{rs}^a = \bar{\omega}_r^2 \delta_{rs} + E_c A_c \left(1 + \frac{c_b \rho_b \bar{\omega}_r^2}{E_b} \right) \left(1 + \frac{c_b \rho_b \bar{\omega}_s^2}{E_b} \right) \times \left[\int_{x_1}^{x_2} U_r' U_s' dx + c_c \left(\frac{\rho_b \bar{\omega}_r \bar{\omega}_s}{E_b} \right)^2 \int_{x_2}^{x_2} U_r U_s dx \right] \quad (22)$$

$$r, s = 1, 2, \dots, m$$

$$K_{rj}^c = E_c A_c d \left(1 + \frac{c_b \rho_b \bar{\omega}_r^2}{E_b} \right) \left[\int_{x_1}^{x_2} U_r' W_j'' dx - c_c \left(\frac{\rho_b \bar{\omega}_r^2}{E_b} \right) \int_{x_1}^{x_2} U_r W_j''' dx \right] \quad (23)$$

$$r = 1, 2, \dots, m \quad j = 1, 1, \dots, n.$$

It is noted that the matrix K varies with VEM thickness, constraining layer (CL) properties, and the treatment length ($x_2 - x_1$). It is therefore expected that there must be 'optimal' selection of those parameters to yield the best damping effect.

Equation (18) gives the equations of motion for a PCLD treatment. Active damping (ACLD) can be achieved by either replacing the CL with

an active element, e.g., a piezoceramic (PZT), or adding an active layer on top of the CL. Here the CL is replaced with a piezoceramic-based self-sensing actuator to provide both the active layer for ACLD and to provide the active control (AC) case with $h_v \rightarrow 0$. With this implementation, the sensor voltage output, V_s , according to Dosch et al. [20] is

$$V_s = -\frac{d_{31}}{\epsilon} \frac{E_c h_c}{L_c} s^T \eta. \quad (24)$$

Here d_{31} is the piezo-constant, ϵ is the permittivity, L_c is the length of the CL, and s is the $1 \times n$ feedback sensor vector taken to be

$$s^T = -\left(1 + \frac{c_b \rho_b \bar{\omega}_r^2}{E_b}\right) U_r|_{x_1}^{x_2^T} T + dW_i'|_{x_1}^{x_2^T}. \quad (25)$$

Here $T_{m \times n}$ is the constraint matrix relating ξ and η , i.e.,

$$\eta = T\xi = K^a{}^{-1} K^c \eta. \quad (26)$$

Note that the first term of the sensor equation (25) comes from beam's axial motion, and the second term is attributed to its transverse motion.

The intentions here are to show that ACLD improves the PCLD and to compare the differences between ACLD and pure active control (AC) treatment. Therefore, simple velocity feedback control law is applied in the first case, though it is well known that much better performance can be obtained with compensation or other control laws. Using velocity feedback, equation (18) is augmented for ACLD to become

$$M\ddot{\eta} + E_c A_c K_d \text{diag}[s] \dot{\eta} + K\eta = Q \quad (27)$$

where $\text{diag}[s]$ is a diagonal matrix with elements taken from the vector s and K_d is the derivative feedback gain including the piezoelectric constants.

Assuming a unit harmonic point load applied at the center of the tip ($x = L$), the frequency response function $H(\omega)$ of the tip is calculated for PCLD to be

$$H(\omega) = W_i(L)^T (-\omega^2 M + K)^{-1} W_i(L) \quad (28)$$

and for ACLD to be

$$H(\omega) = W_i(L)^T (-\omega^2 M + i\omega E_c A_c K_d \text{diag}[s] + K)^{-1} W_i(L). \quad (29)$$

A complex shear modulus of the VEM has been assumed in calculating $H(\omega)$. The viscoelastic material property, is taken to be [12]

$$G(\omega) = 0.142(\omega/2\pi)^{0.494} (1 + 1.46i) \text{ MPa}. \quad (30)$$

Thus the matrix K is complex, representing the complex damping properties of the VEM. This commonly used complex modulus model represents an additional approximation avoided in the second half of the paper.

Equation (27) and (29) are referred to here as “model I” which will be used to discuss the design of ACLD system versus those of pure active or pure passive damping treatments. This model differs from previous models as the thickness of the VEM does not appear in the denominator and hence you approach zero allowing the treatment of this (or no) layer. Next a second model is presented, based on the first model but deliberately treating the frequency dependence of the VEM. In this case, the modeling of the piezoceramic and viscoelastic layers is similar to that of Model I, however the viscoelastic material damping is modeled using the GHM method and the system is analyzed in the time domain. Then the entire system is approximated using a Ritz-Galerkin approach to obtain discretized equations of motion.

The Golla-Hughes-McTavish modeling approach models hysteretic damping by adding additional “dissipation coordinates” to the system to achieve a linear non hysteretic model providing the same damping values over a wide range of frequencies. The dissipation coordinates are used with the discretized equations of motion (27). Linear matrix-second-order form is maintained as well as symmetry and definiteness of the augmented system matrices. The time domain stress relaxation is modeled by a modulus function in the Laplace domain.

This complex modulus can be written in Laplace domain as

$$G^*(s) = G_0(1 + h(s)) = G_0 \left(1 + \sum_{n=1}^k \hat{\alpha}_n \frac{s^2 + 2\hat{\zeta}_n \hat{\omega}_n s}{s^2 + s\hat{\zeta}_n \hat{\omega}_n s + \hat{\omega}_n^2} \right) \quad (31)$$

where G_0 is the equilibrium value of the modulus, i.e. the final value of the relaxation function $G(t)$, and s is the Laplace domain operator. The hatted terms are obtained from a curve fit to the complex modulus data for a particular VEM. The expansion of $h(s)$ represents the material modulus as a series of second order equations [27]. The number of terms kept in the expansion will be determined by the high or low frequency dependence of the complex modulus.

The equation of motion (27) in the Laplace domain is

$$Ms^2 q(s) + K(s)q(s) = F(s) \quad (32)$$

where M is the mass matrix, K the complex stiffness matrix, F the forcing function, and $q(s)$ the transform of the generalized coordinate.

The complex stiffness matrix can be written as the summation of the contributions of the n complex moduli to the stiffness matrix such that

$$K(s) = (G_1^*(s)\bar{K}_1 + G_2^*(s)\bar{K}_2 \dots G_n(s)\bar{K}_n) \quad (33)$$

where $G_n^*(s)$ refers to the n th complex modulus and \bar{K}_n to the contribution of the n th modulus to the stiffness matrix. For simplicity, assume a complex modulus model with a single expansion term and zero initial conditions, so equation (33) can be written as

$$M_s^2 q(s) + G_0 \left(1 + \hat{\alpha} \frac{s^2 + 2\hat{\zeta}\hat{\omega}s}{s^2 + 2\hat{\zeta}\hat{\omega}_2 + \hat{\omega}^2} \right) Kq(s) = F(s) \quad (34)$$

The coefficient of equation (34) is determined by the frequency dependent loss factor curves for a particular VEM (determined experimentally or from manufacturer's data). This coefficient in the Laplace Domain contains dynamics that are now associated with a psuedo coordinate $z(s)$ which is essentially a state estimation compensating for the frequency dependence of the VEM. The comparison (see [28] for a short derivation) and subsequent inverse transform yields a linear viscously damped system of the form

$$M\ddot{x} + C\dot{x} + Kx = f \quad (35)$$

where $x(t)$ is now an expanded coordinate $x(t) = [q^T(t) z^T(t)]^T$ containing the additional coordinate $z(t)$. The matrices M , C , and K are all real valued, symmetric and positive (semi) definite and the viscoelastic nature of the system is captured in the viscous damping matrix C combined with a new expanded version of the generalized coordinates $x(t)$. The coefficient matrices M , C and K now take the expanded form

$$M = \begin{bmatrix} M & 0 \\ 0 & \frac{\hat{\alpha}}{\hat{\omega}^2} G_0 I \end{bmatrix}, \quad C = \begin{bmatrix} \Omega & 0 \\ 0 & \frac{2\hat{\alpha}\hat{\zeta}}{\hat{\omega}} G_0 I \end{bmatrix}, \quad K = \begin{bmatrix} (1 + \hat{\alpha})G_0\bar{K} & -\hat{\alpha}G_0\bar{K} \\ -\hat{\alpha}G_0\bar{K} & \hat{\alpha}G_0\bar{K} \end{bmatrix} \quad (36)$$

where Ω is a diagonal matrix of model damping from the natural damping of the beam.

In order to model the behavior of the VEM which partially covers a beam, the stiffness and mass matrices for the covered area are first assembled. This procedure, outlined in Lam [24] requires the use of heavyside step functions to locate the various components. The effects of the dissipation modes on the system are calculated. The full mass and stiffness matrices for the whole beam are assembled, using the mass and stiffness matrices obtained from equation (36) to model the effects of the VEM on the whole structure. The order of the system increases as the number of terms in the expansion are kept, which increases the accuracy

for modeling the damping effects. An experimental verification is given in figure 2.

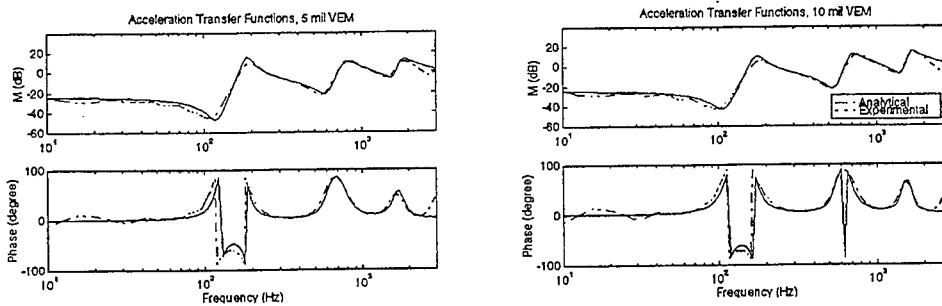


Figure 2. A comparison of analytical and experimental transfer functions for a constrained layer beam, verifying the GHM approach used here to model the VEM.

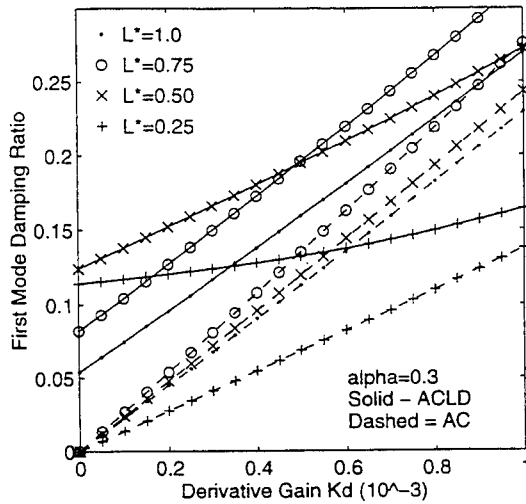


Figure 3. First mode damping ratio as a function of feedback gain for a variety of treatment coverage lengths (L^*). Here the thickness constraint is $h_c + h_v \leq 0.3h_b$ and the gain is limited.

DESIGN CONSIDERATIONS

As in model I, it can be shown that for gain and treatment thickness limited applications that ACLD has advantage over just passive or just active treatments. It is conclusive that both AC and ACLD out-perform traditional PCLD treatment. A comparison of AC and ACLD, however, is not as straightforward. First consider the case where there is no restriction on the total thickness of the damping treatment. In this case, the AC with no limit on applied gain can be made to out-perform ACLD. However, if the gain is limited, as is usual in practice, the ACLD treatments can provide better vibration suppression as measured by a decrease in first-

mode amplitude, and an increase in first-mode damping ratio as plotted in figure 3 for a variety of coverage lengths. As expected, the AC response amplitude and ACLD response amplitude approach each other as the gain increases. Furthermore the smaller the coverage (L^*), the greater the improvement offered by ACLD over AC in the low-gain region ($k_d < 0.4 \times 10^{-3}$). However, as gains increase and hence the AC response approaches the ACLD response, the VEM thickness does not go to zero. Thus in cases where higher gain values are available and AC and ACLD amplitude reduction is similar, it is probably better to use ACLD because of the control robustness provided by the VEM damping [31].

Next consider the case where both the total treatment thickness and the gains are restricted. Here the effect of adding an active layer is to reduce the optimal VEM thickness as the gain increases. Furthermore, for lower gains, ACLD always out-performs the strictly active treatment. However, for some thickness restrictions damping ratio versus gain curves for various coverage lengths cross. This makes it possible to compare design strategies for a given desired performance. For example for $\alpha = 0.3$ and a desired performance of say $\zeta = 0.2$, there are six possible designs for a gain greater than about 0.5×10^{-3} . For instance a 75%-coverage ACLD could be used with a gain of 0.5×10^{-3} , or a 50% coverage of piezoceramic could be used with a gain of 0.8×10^{-3} to active the same modal damping. Thus considering total thickness, gain, length of coverage, and robustness factors, ACLD may offer the best solution for a damping treatment in many applications.

OPTIMAL PLACEMENT AND SIZING

In this section the hybrid model, model II, is used to examine the placing and size of the passive constrained layer and the piezoelectric patch using two optimization routines. For the passive case, the energy of the states was minimized. The optimal placement and size for the active case was determined using LQR. The cost function for the passive case is

$$J_P = \int_0^\infty (x^T Q_1 x) dt \quad (37)$$

where x is the state vector, and Q_1 is a semi positive-definite weighting matrix. Equation (37) is minimized as the length and placement of the PCLD treatment is varied such that

$$J_{\min} = x_0^T P_1 x_0. \quad (38)$$

where x_0^T is a vector of initial states and P_1 is the unique positive definite solution to the Ricatti type equation

$$P_1 X + A^T P_1 = -Q_1. \quad (39)$$

The cost function for the active case is

$$J_a = \int_0^\infty (y^T Q y + u^T R u) dt \quad (40)$$

where y is the output vector, u the input, and Q and R are semi and positive definite weighting functions respectively. A higher value on Q means more vibration suppression, while a higher value on R signifies greater limit on the control effort. The minimum of this cost function is defined as

$$J_{\min} = x_0^T P x_0 \quad (41)$$

where the length and placement of the PZT patch is varied. P satisfies the Ricatti equation

$$P A + A^T P - P B R^{-1} B^T P = -Q \quad (42)$$

The corresponding control law (full state feedback) is given as

$$u = -R^{-1} B^T P x. \quad (43)$$

The new hybrid application will be compared with the purely passive, purely active and standard ACLD treatments. An aluminum cantilevered beam was considered and the VEM was assumed to be ISD 112. The dimensions for the PZT, VEM, cover plate and beam were chosen based on easily available materials. The constraining layer was assumed to be aluminum with the same thickness as the beam in order to maximize passive damping [2]. The minimal length for any treatment was set at 1 cm. Since neither the PCLD nor PZT can be clamped, the constraint on its placement was 1 mm from the base. In the hybrid case, there was assumed to be at least a 1 mm space between treatments. The equations of motion were discretized using a five term expansion. The excitation force was assumed to be a unit impulse function, applied at 0.9L.

The transverse displacement was measured at the tip. The weighting function, R , was assumed to be 1. To find the minimum passive cost function, equations (37)-(39) were used, where the weighting matrix is such that only the transverse modes were penalized. Since LQR optimization was used, the control was heavily penalized thereby making the optimization passive.

L	15 in (0.381 m)	t_p	0.02 in (0.5 mm)	p_s	100 kg/m ³
b	1.5 in (0.038 m)	p_p	7600 kg/m ³	E_s	14 × 10 ⁶ Pa
t_b	1/8 in (0.0032 m)	E_p	6.3 × 10 ¹⁰	G_0	5 × 10 ⁴
p_b	2710 kg/m ³	d_{31}	-109 × 10 ¹²	$\hat{\alpha}$	[9.6 99.1 26.2]
E_b	70 × 10 ⁹ Pa	t_s	5 mil (0.13 mm)	$\hat{\zeta}$	[73.4 1.1 3.28]
				$\hat{\omega}$	[1 5 0.5] × 10 ⁴

Table 1. System parameters.

	$L_{\text{pcld}}(\text{m})$	start PCLD (m)	$L_{\text{pzt}}(\text{m})$	start PZT (m)	$J_{\text{min},p}$	$J_{\text{min},a}$
PCLD	0.27	0.001			591	
PZT			0.277	0.001		8.8534
ACLD-passive	0.267	0.001	0.267	0.001	8.758e4	
ACLD-active	0.267	0.001	0.267	0.001		5450
hybrid-passive	0.262	0.012	0.10	0.001	7203	
hybrid-active	0.262	0.012	0.01	0.001		449

Table 2. Optimal lengths and placements for different treatments and the minimum cost functions.

The time responses for tip displacement in the transverse direction of a clamped aluminum beam with different treatments. The optimal lengths and placements of those treatments, as well as the minimal cost functions can be found in table 2. The optimal length for PCLD was found to be 27 cm, with the treatment starting 1 mm from the base of the beam. The optimal length for a PZT was found to be 27.7 cm applied 1 mm from the base. Two different (passive and active) optimizations were applied for both the ACLD and hybrid treatment. For passive and active optimization, the optimal length of the ACLD was found to be 26.7 cm, applied at the base of the beam. For the hybrid treatment, the optimal length for the PZT for either optimization scheme was found to be 1 cm, applied at the root, and the optimal length of the PCLD was 26.2 cm. Note from table 2 that the PCLD patch gives the smallest passive cost function. This corresponds with finding in [2] since the constraining layer for the passive case is the same thickness as the beam and the placement of the patch is at the area of greatest strain, the base of the beam. While ACLD is also at the root, the PZT does not add enough stiffness to the system. The hybrid treatment places the PZT at the root, since this is the place of greatest strain. Therefore, the effectiveness of the PCLD treatment is reduced, as can be seen in the higher passive cost function. The addition of constrained layer damping to the beam lowers the active cost function, with the hybrid treatment being the most effective. The time response of a clamped aluminum beam without any treatment is shown in figure (4a). The optimal placement and size of a PCLD patch was investigated and its response is given in Figure (4b). The time response of the purely active case is shown in figure (4c). The response of PZT patch can be improved by increasing the weighting function on vibration suppression, which will increase the control effort. The response for ACLD is given in figure (4d) for the passive case and (4e) for the active case. The beam with ACLD performs better than a PZT patch, since the control effort is reduced. Note that in figure (4e) the scale on the y -axis is reduced to show that there is little response to an impulse function. The main advantage of using ACLD over a PZT is that the active cost function is an order of magnitude lower and in case failure, there still is passive damping available.

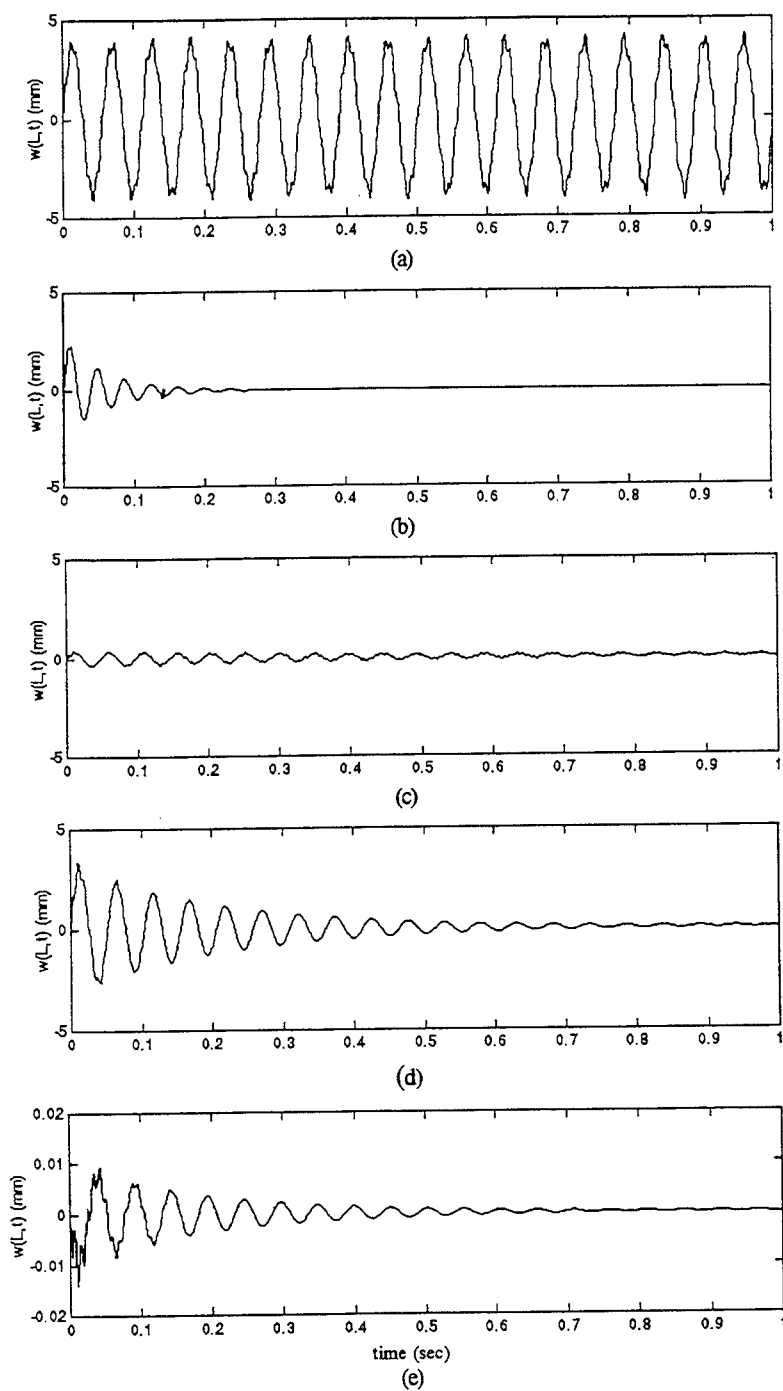


Figure 4. Time responses for optimal configurations of (a) untreated beam, (b) PCLD treated beam, (c) active beam, (d) ACLD treatment with control off and (e) ACLD treatment with control on.

The time responses for the new hybrid combination of an active element separate from a passive element illustrate that the active element in conjunction with the passive element is able to damp the vibration almost immediately. When looking at the passive cost functions, the optimal case is for PCLD on the beam. There is an increase in the cost function for the hybrid case due to the placement of the PCLD away from the root, but the advantage is the added effect of the active element. The cost function for the active optimization for the hybrid is the lowest, since it takes advantage of the inherent damping available with the PCLD by allowing the length of the PCLD vary separate from the PZT. While ACLD allows the length of the treatment to vary, the length of the passive treatment is dictaged by the length of the PZT applied and visa versa. There is a significant reduction in actual cost for the hybrid case, since the PZT is only a fraction of the length when compared to ACLD.

The required control effort for the PZT, ACLD and hybrid treatment also illustrates that it is more advantageous to use ACLD treatment. However, when comparing both results to the new hybrid treatment, the hybrid requires about an order of magnitude less control effort than the ACLD. It is therefore more advantageous to use the new hybrid treatment than PCLD, PZT, or ACLD.

SUMMARY

The area of active constrained layer damping treatments has been briefly reviewed and summarized. This area of research combines the use piezoelectric and viscoelastic materials to provide damping treatments for suppressing unwanted vibrations. A variety of configurations have been proposed and these are summarized in figure 1. Research in this area is focused on the choice of configuration, the modeling of the viscoelastic behavior, the mechanics of the various layers and segments, the control laws and comparisons with other methods of suppressing vibration. Here, an improved model of the viscoelastic behavior of such systems was presented and a comparison of passive, active and combined passive and active responses was made in the presence of a thickness constraints and limitations on the control gain. The various comparisons made here and in the literature have been some what inconclusive in answering the question of which configuration is best. The answer to the question of which treatment works the best depends entirely on circumstances and on design constraints. Most of the treatments discussed so far are external add on systems and thus subject to weight and size constraints. In this situation it is clear that combining active and passive treatments can out perform either treatment taken by itself. It is also clear that passive treatments are a lot less trouble then active treatments, and hence passive solutions are more desirable and should be used when possible.

Layered combinations of VEM and PZT have not been examined, (with the exception of [8,13] as much as add on treatments have and may offer different results when comparing passive versus active. There is little doubt however, that the active cases have the potential for resulting in improved performance. The question of when to use active or hybrid systems then becomes centered on deciding if the complexity warranted. As was shown in figure xx, certain performance requirements may demand that active or hybrid systems be incorporated. For instance if high damping is needed and a thickness limitation prevents the passive solution from being implemented then the an active solution must be used. If the electronic power requirements limit the control can to a lower value then is called for by the performance specification then the ACLD solution must be used.

In the preceding it was shown that the GHM modeling approach can yield an analytical model which agrees with experimental evidence and provides a way around the frequency dependence of VEM. These models as well as those proposed by Lesieutre [17] and used by Inman [23,24,25,26], allow ACLD treatments to be treated in the transient case where broad band response is important. Further research is encouraged in the areas of modeling and configuration in order to provide the broadest possible design selection to the engineering community.

ACKNOWLEDGMENTS

This work was supported in part by the Air Force Office of Scientific Research grant number F49620-93-1-0280, and in part by Army Research Office grant number DAAL 03-92-G-0180 for which the author is grateful.

REFERENCES

1. Johnson, C. D., Design of passive damping systems, *ASME 50th Anniversary of the Design Engineering Division; J. Mech. Design and J. Vib. Acoust.*, 1995, B 117, 171-7 (special combined issue).
2. Nashif, A., Jones, D. I. G., and Henderson, J. *Vibration Damping*, John Wiley and Sons, New York, 1985
3. Sun, C. T., and Lu, Y. P., *Vibration Damping of Structural Elements*, (Englewood Cliffs, NJ: Prentice-Hall), 1995.
4. Banks, H. T., Smith, R. C. and Wang, Y., *Smart Material Structures: Modeling, Estimation and Control*, Research in Applied Mathematics Series, Wiley, 1996.
5. Giurgirtiu, V., Chaudhry, Z., and Rogers, C. A., Energy-based comparison of solid-state actuators, CIMSS Report No. 95-101
6. Agnes, G. and Napolitano, K., Active constrained layer viscoelastic damping, Proceedings 3rd SDM Conference, AIAA 1993, pp. 3499-3506.

7. Baz, A. and Ro. J., Partial treatment of flexible beams with active constrained layer damping, *Proceedings Society of Engineering Science*, 1993, Vol. 167, pp. 61-80.
8. A. Baz and J. Ro, Optimum design and control of active constrained layer damping, *ASME Special 50th Anniversary Design Issue*, 1995, 117, pp. 135-144.
9. Shen, I. Y., Hybrid damping through intelligent constrained layer treatments, *ASME J. of Vibration and Acoustics*, 1994, Vol. 116, pp. 341-349.
10. Liao, W. H. and Wang, K. W., On the active-passive vibration control actions of structures with active constrained layer treatments,"1995, ASME Design Engineering Technical Conferences, 84-3, pp. 125-141.
11. Azvine, B., Tomlinson, G. R., and Wynne, R. J., Use of active constrained-layer damping for controlling resonant vibration, *Smart Materials and Structures*, 1995, Vol 4, pp. 1-6.
12. Huang, S. C., Inman, D. J. and Austin, E. M., Some design considerations for active and passive constrained layer damping treatments, *Smart Materials and Structures*, 1996, Vol. 5, pp. 301-313.
13. Saunders, W. R., Inman, D. J., and Robertshaw, H. H., Pole-zero modeling for smart viscoelastic structures, pp. 1044-1054.
14. Rongong, J. A., Wright, J. R., Wynne, R. J. and Tomlinson, G. R., Modelling of a hybrid constrained layer/piezoceramic approach to active damping, *ASME Journal of Vibration and Acoustics*, 1997, Vol. 119, No 4, pp. 120-130.
15. Shen, I. Y., Bending vibration control of composite and isotropic plates through intelligent constrained layer treatments, *Smart Materials and Structures*, 1994, Vol. 3, pp. 59-70.
16. Yellin, J. M., and Shen, I. Y., Comparision of experimental measurements and theoretical predictions of a self-sensing active constrained layer Treatment, *Passive Damping and Isolation*, 1997, ed. L. P. Davis, SPIE, Vol. 3045, paper No 34.
17. Lesieutre, G. A., and Lee, U., A finite element for beams having segmented active constrained layers with frequency-dependent viscoelastics, *Smart Materials and Structures*, 1996, Vol. 5, pp. 615-627.
18. Kawiecki, G., Low frequency vibration attenuation using segmented active constrained layer damping treatments, *Proceedings of the First European Conference on Structural Control*, 1996, Barcelona, Spain, May 29-31.
19. Kapadua, R. K. and Kawiecki, G., Experimental evaluation of segmented active constrained layer damping treatments, *Journal of Intelligent Material Systems and Structures*, to appear
20. Liao, W. H., and Wang, K. W., A new active constrained layer

- configuration with enhanced boundary actions, *Smart Materials and Structures*, 1996, Vol. 5, pp. 638-648.
21. Crawley, E. F. and J. deLuis, Use of piezoelectric actuators as elements of intelligent structures, *AIAA Journal*, 1987, Vol. 25(10), pp. 1373-1385.
 22. Mead, D. J. and Markus, S., The forced vibration of a three-layer damped sandwich beam with arbitrary boundary conditions, *J. Sound Vib.*, 1969, 10, 163-75.
 23. Lam, M. J., Saunders, W. R., and Inman, D. J., Modeling active constrained layer damping using Golla-Hughes-McTavish approach, *Passive Damping*, 1995, 1995 North American Conference on Smart Structures and Materials, Ed. C. D. Johnson and L. C. Rogers, 2445, pp. 86-97.
 24. Lam, M. J., Inman, D. J. and Saunders, W. R., Vibration control through passive constrained layer damping and active control, *Passive Damping and Isolation*, 1997, ed. C. P. Davis, SPIE Paper No. 3045-11.
 25. Van Norstrand, W. C., Knowles, G. and Inman, D. J., Active constrained-layer damping for micro-satellites, Proceedings 2nd International Conference on Dynamics and Control of Structures in Space, 1993, ed. C. L. Kirk and P. C. Hughes, pp. 667-81.
 26. Van Norstrand, W. C., Knowles, G. and Inman, D. J., Finite element model for active constrained-layer damping, *Passive Damping*, 1995, ed. C. D. Johnson, SPIE Vol. 2445, pp. 98-109.
 27. McTavish, D. J. and Hughes, P. C., Modeling of linear viscoelastic space structures, *Journal of Vibration and Acoustics*, 1993, 115, pp. 103-110.
 28. Smith, C. B. and Wereley, N. M., Active-passive constrained layer damping of composite rotating flexbeams, AIAA paper no 96-1290-CP, Proceedings 1996 Adaptive Structures Conference, April 1996, pp. 207-216.
 29. Inman, D. J., On vibration analysis of viscoelastic beams by separation of variables, *Mechanics Research Communications*, 1989, Vol. 16, No. 3-4, pp. 213-218.
 30. Dosch, J. J., Inman, D. J. and Garcia, E., A self-sensing piezoelectric actuator for collocated control, *J. Intell. Mater. Syst. Struct.*, 1992, 3, 167-85.
 31. Banks, H. T. and Inman, D. J., On the significance of modeling internal damping in the control of structures, *AIAA J. Guidance, Control Dyn.*, 1992, 15, 1509-12.

DESIGN OF ACTIVE STRUCTURAL AND ACOUSTIC CONTROL SYSTEMS FOR THE REDUCTION OF ROAD NOISE IN A PASSENGER CAR

Paul Sas, Wouter Dehandschutter

Mechanical Engineering Department, Division PMA
Katholieke Universiteit Leuven,
Celestijnenlaan 300 B, B-3001 Leuven, Belgium

Abstract

Within the Brite-Euram Project "Anrava" several active control systems have been evaluated in order to reduce the road noise generated inside the cabin of a mid size station wagon during driving condition on different road surfaces. Different control strategies (feedforward with local and global control, pure feedback) and different approaches (active structural acoustic control and active noise control) have been tested on the car in laboratory conditions and the control performances have been evaluated.

The final control strategies, that have been selected based on the results of this study, are based on an adaptive feedforward control algorithm: six accelerometers provide the reference signals and 4 microphones placed inside the cabin give the error feedbacks. Two control configurations, each using a different kind of control sources, have been retained : a structural acoustic control system which works with 6 inertial shakers positioned at the main vibration transmission paths of the car suspension, an anti-noise system with 4 loudspeakers inside the cabin.

The paper describes the approaches utilised to design the different control systems and presents the results obtained during laboratory and road tests comparing them with the performances predicted by numerical simulations.

1. Introduction

One of the main sources of interior noise in modern passenger cars is the noise generated by the rolling of the wheels over the road surface (structure borne road noise). Especially at higher speeds or on rough road surfaces the contribution of the structure borne road noise is dominant and determinant for the comfort of the passengers. Since in modern cars engine noise is well under

control, considerable effort is nowadays spent on the reduction of the structure borne road noise.

Current techniques for structure borne road noise reduction rely mainly on the use of rubber bushings at the connection of the wheel suspensions with the chassis. The isolation capabilities of these connections are however compromised because of the need for high stiffness at lower frequencies, as required for road handling purposes. Neither passive noise reduction techniques using absorbing or damping material give full satisfaction since they are only effective in the higher frequency range (above 400 Hz).

Moreover the frequency band below 400 Hz is critical in car acoustics due to the presence of pronounced acoustic cavity resonances in the range 100 to 200 Hz and below. The aim of the work presented here is to reduce the structure borne noise level by using active control systems and to compare the efficiency of different control strategies and different approaches for the actuation schemes. Acoustical actuator (loudspeaker) systems, placed in the car cavity, can be used in order to generate a sound field reducing the original sound field. This solution is known as Active Noise Control (ANC). Vibration actuation systems can be placed on the body of the vehicle in order to reduce the interior noise level by modifying the vibration behaviour of the radiating structure or by blocking some vibration transfer paths. This is the so called Active Structural Acoustic Control (ASAC). From the control side adaptive control based on a feedforward scheme combined with acoustical or vibrational feedback can be utilised.

Active control of road noise using acoustic control sources has been discussed previously by Sutton et al. (study of control performance, [1], results of road tests, [2]), Ferren and Bernhard (laboratory study, [3]), Heatwhole et al. (optimisation of control parameters, [4] [5]). Signal processing issues are dealt with by Freymann et al. [6], an alternative (RLS) controller is suggested by Bronzel [7] and Sano [8], both including simulation studies but without road tests. The system presented by Sutton et al. [2] uses two loudspeakers located in the front door of a Citroen AX. For the experiments, the car was driven at 60 km/h on a coarse surface. Reductions of about 7 dB are apparent at the major peaks of interest in the range 100-200 Hz. No experiments involving vibration actuators have been reported in literature.

This paper presents the control performance achieved with various control configurations installed on a demonstrator car (mid size station wagon). The practical realisation of the ANC and ASAC schemes for road noise control is illustrated in figures 1 and 2. The actual design of these schemes will be discussed in detail in this paper. Results obtained during laboratory tests as well as final validation by means of road tests are presented.

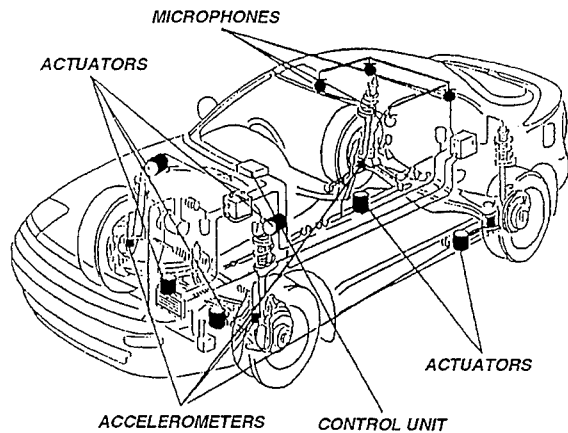


Figure 1. ASAC system..

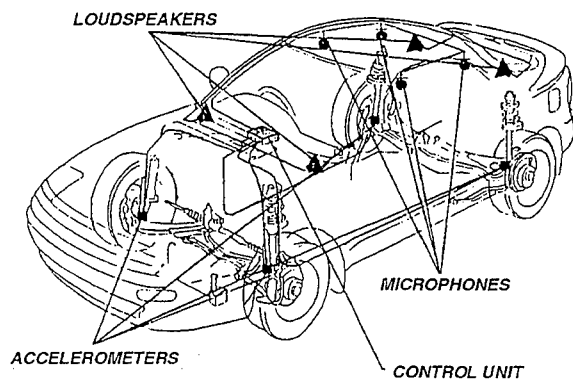


Figure 2. ANC system.

2. Design of the control configuration

2.1 Control strategies

Feedback and feedforward schemes are the two categories of strategies for active control of sound. Feedback schemes have been successfully applied in systems in which the secondary source is close to the sensor measuring the residual noise (such as active headsets). In these cases the phase lag, introduced due to the acoustic delay, doesn't determine the instability of the system in the frequency range of interest. In these cases a priori knowledge of the primary noise is not required.

A feedforward controller generates the control signal by feeding a reference signal (e.g. the wheel hub acceleration), which carries information on the perturbation that is to be controlled, through a control filter. The control filter is updated taking into account information coming from an error sensor (measuring the residual sound pressure). Feedforward control only cancels the partial sound pressure correlated with the reference signal and thus it does not interfere with other sound sources (e.g. car hi-fi). As a corollary, this solution requires a good correlation between the reference and the error signals in order to yield satisfactory control performance. On the other hand, feedforward control leaves more freedom in positioning of control actuators and sensors because it is not so sensitive to instability problems.

The feedforward control scheme has been selected for this application after verification on the demonstrator car which showed that the feedback strategy is not feasible due to instability of the control loop.

In order to determine the number and location of the control actuators, the nature of the noise source is taken into account. Structure-borne noise generation involves three elements : a noise source (or the primary disturbance), a transfer path and a receiver system. Though it is often not possible to remove the noise source without changing the functionality of the system (road-tire contact cannot be avoided), the transfer path or the receiver system can be controlled actively. The number of actuators, used to realise this, must be minimised (due to weight and controller design constraints), but a maximal possible noise reduction must be envisaged. Therefore it is important to understand which energy transmission paths from the suspension elements to the car interior acoustics are the most important with respect to the total noise level in the cabin. This study was done based upon the transmission path analysis technique [9]. For structure-borne road noise, the transfer paths are locations in which the suspension elements are connected to the car body by means of "bushings". The transmission path analysis technique is based upon combining estimates of the operational forces in each of the transmission paths with in laboratory measured frequency response functions (pressure or acceleration to force applied in each of the transmission paths). The determination of the operational forces can be based upon the complex dynamic stiffness method, which combines measurements of the complex dynamic stiffness of the bushings, with relative operational displacements over the mounts. An alternative but less well established methodology is based upon the inversion of a matrix of frequency response functions between acceleration responses on the car body and force applied at the different transmission paths. This matrix is combined with operational accelerations on the car body, in order to obtain estimates of the operational forces on the body.

In total 30 transmission paths have been considered from the suspension into the car body : 10 connection points (rear axle, rear shock absorbers, 2 front suspension connection locations, front shock absorbers), in 3 translational directions (rotational degrees of freedom have not been

considered). Six main transmission paths have thus been identified. In order to actively control the transmission of vibration, vibration actuators have been mounted in parallel with the bushings (figure 3), connecting them to the car body and working against an inertia mass.

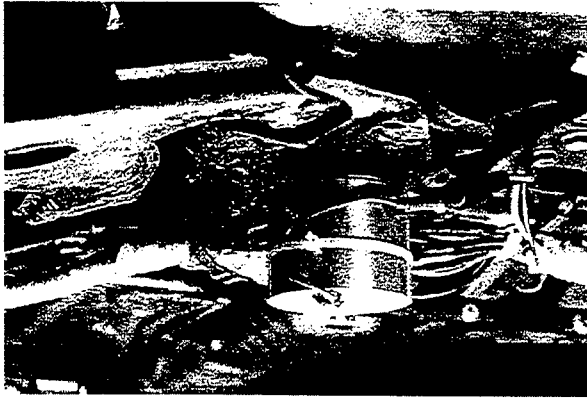


Figure 3. Actuator mounted at the transmission path.

2.2 The control algorithm

Most multichannel adaptive feedforward controllers in Active Noise Control are based on the LMS (least mean square) algorithm of Widrow and Hoff [10] which is a gradient search algorithm optimising the control filters in order to minimise the sum of the squared error signals. The algorithm used here (figure 4) is an alternative form of the conventional LMS algorithm in order to ensure convergence of the algorithm in the presence of secondary paths (the transfer function from the controller output to the error sensor). It is referred to as Filtered-X LMS. The single-channel Filtered-X LMS algorithm was independently derived by Widrow in the context of adaptive control and Burgess [11] for ANC applications. The multiple error Filtered-X LMS algorithm for ANC applications was introduced by Elliott et al. [12].

Extensive treatment of the algorithm is provided in literature, e.g. by Kuo and Morgan [13], some basic equations are recapitulated here. Assuming a control system with N control sources, M error sensors and P reference sensors, the sound pressure measured at M error sensors is expressed in vector notation as :

$$\mathbf{e}(k) = \mathbf{d}(k) + \mathbf{X}^f(k)^T \mathbf{w}(k) \quad (1)$$

where $\mathbf{e}(k) = [e_1(k) \ e_2(k) \ \dots \ e_M(k)]^T$,

$\mathbf{d}(k) = [d_1(k) \ d_2(k) \ \dots \ d_M(k)]^T$ is the contribution of the primary noise source,

$$\mathbf{X}^f(k) = [\mathbf{x}^{f1}(k) \ \mathbf{x}^{f2}(k) \ \dots \ \mathbf{x}^{fM}(k)],$$

with $\mathbf{x}^{fm}(k) = [\mathbf{x}^{fm1}(k)^T \mathbf{x}^{fm2}(k)^T \dots \mathbf{x}^{fmN}(k)^T]^T$,
 $\mathbf{x}^{fmn}(k) = [\mathbf{x}_1^{fmn}(k)^T \mathbf{x}_2^{fmn}(k)^T \dots \mathbf{x}_p^{fmn}(k)^T]^T$, and
 $x_p^{fmn}(k) = \sum_{i=0}^{L_{sp}-1} h_{mni} x_p(k-l-i)$,

$\mathbf{w}(k) = [\mathbf{w}_1(k)^T \mathbf{w}_2(k)^T \dots \mathbf{w}_N(k)^T]^T$ is the adaptive FIR control filter,
 with $\mathbf{w}_n(k) = [\mathbf{w}_{n1}(k)^T \mathbf{w}_{n2}(k)^T \dots \mathbf{w}_{nP}(k)^T]^T$.

The FIR control filter $\mathbf{w}_{np}(k)$ and the time vector $\mathbf{x}^{fmn}(k)$ have length L_{cf} . $\mathbf{X}^f(k)$ is the *filtered-x* reference signal vector, $x_p(k)$ is the p -th reference signal and h_{mni} is the i -th coefficient of the FIR filter (length L_{sp}) that models the secondary path between the n -th control actuator and the m -th error sensor. Secondary path modelling is performed in parallel with control as shown in figure 4 and can be implemented both off-line or on-line.

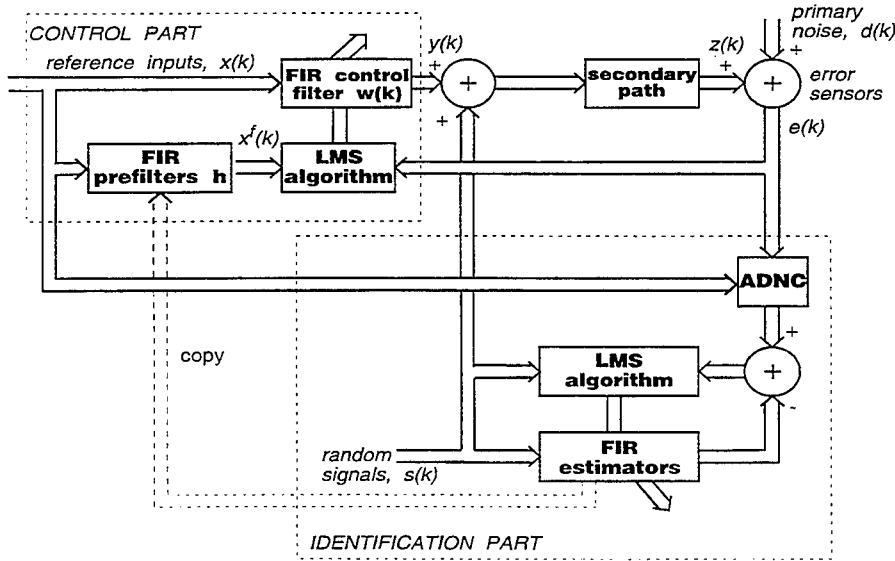


Figure 4. Block diagram of the control algorithm.

The control filters $\mathbf{w}(k)$ are updated inversely directional to the gradient of $E\{\mathbf{e}(k)^T \mathbf{e}(k)\}$. An instantaneous estimate for the gradient is used, resulting in the update rule :

$$\mathbf{w}(k+1) = \mathbf{w}(k) - \mu \mathbf{X}^f(k) \mathbf{e}(k) \quad (2)$$

in which the *convergence coefficient* μ sets the step size of the update.

The choice of an appropriate set of references is of fundamental importance to the final controller performance. First of all a high multiple

coherence between reference and error signals is required. This is necessary because the information in the reference signals must be representative for the noise at the error sensors. Secondly the causality constraint has to be satisfied.

By a proper choice of the convergence coefficient, also *adaptivity rate*, fast tracking of time varying disturbances (large μ) or accuracy (small μ) of the algorithm can be given priority. However, an upper limit for μ must be imposed to ensure stable convergence : as the gradient is not determined recursively, but estimated per time sample, the expected value of the control filter weights will only converge to the optimal solution in a statistical sense (therefore this is a so-called stochastic gradient algorithm). Because of these considerations, it is important to understand and to quantify the conditions for convergence to the optimal solution.

Convergence analysis of adaptive systems generally involves complicated mathematics and can only be accomplished under the assumption of certain boundary conditions. Consequently, though the convergence behaviour is one of the most important aspects for any adaptive algorithm, a convergence analysis for the Filtered-X LMS algorithm only exists for some special cases (Frequency domain analysis for MIMO systems [14] ; Time domain analysis for SISO systems [12], MIMO but limited to very slow adaptation rate [15], Bao deals with MIMO but secondary paths are pure delays [16]).

The analysis shows that the maximum step size is limited by maximum eigenvalue of covariance matrix $E\{\mathbf{X}'(k)\mathbf{X}'(k)^T\}$ on the one hand, but may be further reduced by the eigenvalue structure of the secondary path transfer function matrix and the delays caused by their physical separation of control sources and error sensors on the other hand. These criteria cannot always directly be quantified. Therefore, as a practical rule of thumb, it is often suggested to increase μ until the algorithm becomes unstable (if circumstances allow this), and then to use half of this value for the final implementation.

One final remark pertains to the type of control filters and secondary path model filters that are used in the algorithm. Theoretically, the algorithm derived here might as well be implemented using IIR (Infinite Impulse Response filters or recursive) filters. Though the LMS algorithm is more complex for recursive filters than in case of FIR filters, some benefit may result from the fact that lightly damped systems can be modelled to the same accuracy using shorter filter lengths which would in turn reduce the number of calculations per sample period. On the other hand, the Wiener optimal solution is not unique for this kind of filters and moreover, IIR filters may become unstable if some of the poles lie outside the unit circle (which may always occur because the update rule (2) does not check this). The extension of the Filtered-X LMS algorithm for IIR filters may thus very easily become more complex and more computationally demanding than in case of FIR filters and above all, the performance may depend very much on how well local minima

are checked and avoided. It has been shown by Bernhard [17] that especially for this reason, IIR filters are not suitable for the application in mind.

2.3 Control hard- and software

A specific actuator, based on the moving coil inertial mass principle, has been designed in order to satisfy the determined requirements of force, bandwidth and size, and generate 40 N peak force (weight 1.1 kg, dimensions $\varnothing 80 \times 76$ mm). The loudspeakers utilised in the ANC system have been selected considering the power spectra of the error microphones during road measurements and their locations have been determined with the constraint of causality.

A state of the art DSP-processor is used for the implementation of the control algorithm. Control and identification programs have been implemented in C-code and run on a DSP Board (Loughborough Sound Images) which is hosted in an industrial PC. The DSP board hosts 4 Texas Instruments TIM TMS320C40 DSP modules. Three DSPs run in parallel for the execution of the control routines, the fourth communicates with the PC, e.g. for data exchange purposes. Additionally an I/O board able to manage up to 16 inputs and 8 outputs is linked to the DSP board.

A classic configuration of anti-aliasing filters at the inputs (cut-off frequency smaller than Nyquist frequency) and reconstruction filters at the outputs (control signals sent to shakers or loudspeakers), to avoid high frequency quantisation noise, is used.

More importantly, all inputs signals are also filtered with high pass filters in order to reduce the influence of low frequency components that otherwise would saturate the outputs, which would cause distortions in the actuator responses. Moreover, since the human ear is not sensitive to these frequencies, it makes no sense to try and control at these frequencies. Low pass filters have been set at 320 Hz directly on the I/O board, while the high pass filters cut off at 60 Hz.

All these filters introduce considerable time delays due to their phase lags and it is of prime importance to fine-tune the system in order to reduce all delays introduced in the control loop such that the control performance is not compromised. In the case of road noise, a random disturbance signal is picked up by the reference sensors and since this signal is of stochastic nature it is impossible to predict the time history of the disturbance signal. Obviously, the control action should reach the error microphone at the same time as the primary disturbance. In other words, the sum of the electrical time delay (the time delay between the measurement of the reference signal and the control action) and the secondary time delay (the time required for the control action to reach the error microphones) should not be longer than the time required for the primary disturbance to travel from the reference signal locations to the error microphones (physical time delay). Theoretically, in cases where this time constraint is not satisfied, the optimal controller would have to be non-

causal. However a non-causal control filter cannot be implemented in practice and hence, any causal control filter that is used under these circumstances will converge to a suboptimal solution.

The electrical time delay from reference to actuator can be estimated taking into account the phase lag of the single signal processing elements (such as filters, DSP etc...). It is mainly determined by the sample frequency at which the control algorithm runs. The time delay for the secondary paths is measured from the actuator locations to the error microphones and can be derived from the secondary path model. The physical time delay of the primary disturbance has been measured on the demonstrator car [18] for all possible delay paths (i.e. from possible reference locations to potential actuator locations). A range of time delays from 0.3 ms to 1.7 ms have been measured.

2.4 Experimental systems implemented

An ASAC system (figure 1) has been realised with 6 references (accelerometers at wheel hubs), 6 actuators (shakers along the principal vibration transmission paths) and 4 feedback errors. Two different kinds of error signals have been considered:

- Feedforward with local feedback (accelerometers placed close to the vibration actuators);
- Feedforward with global feedback (microphones at the car roof).

An ANC system (figure 2) has been implemented with 6 references, 4 actuators (loudspeakers at the car doors) and 4 feedback errors (microphones at the car roof).

Two different kind of references have been considered:

- Accelerometers at wheel hubs;
- Accelerometers at the car body along the principal vibration transmission paths.

For the accelerometers at the wheel hubs (ASAC and ANC) a multiple coherence analysis has been carried out considering the 12 signals coming from 4 triaxial accelerometers (one each wheel) and the 4 signals of the error microphones at the car roof. The selection of the best 6 references has been made under the principle of the highest multiple coherence.

The accelerometers at the car body (ANC) have been placed along the 6 main vibration transmission paths. This is not applicable in the case of ASAC since the control input would then be measured through the references which would destabilise the controller.

The references were selected taking into account the timing constraints imposed by each control configuration used.

Figure 5 presents a view on the hardware installation in the test car.

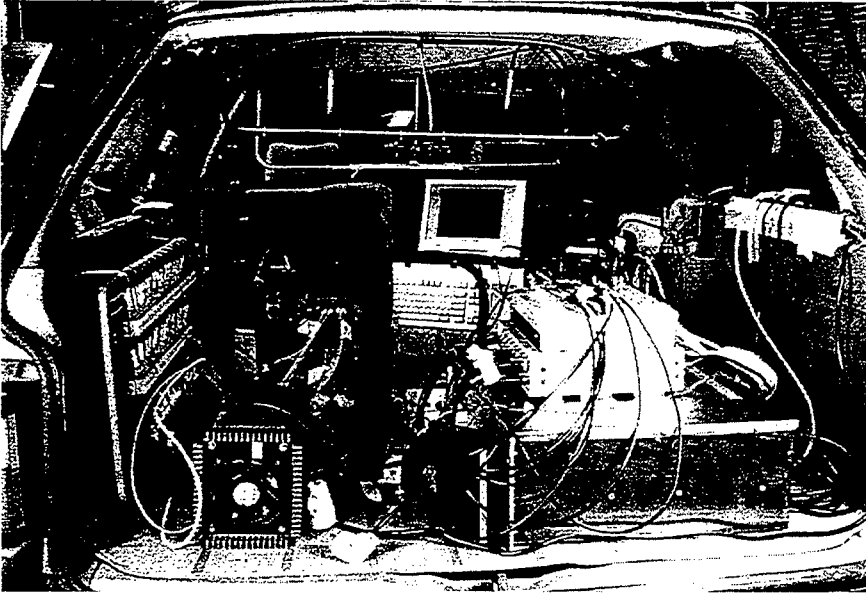


Figure 5. Installation of the controller hardware in the test car

4. Optimisation of the control configuration by means of numerical simulations

The control performance of different control configurations for a car driven on rough asphalt has been simulated with numerical models in order to determine the optimal control configuration and corresponding controller parameters to be implemented for the road tests.

Simulations have been performed in the frequency domain, as well as in the time domain. The main difference between the time and the frequency domain lies in the fact that in the frequency domain only steady state behaviour can be analysed. In the time domain, on the other hand, transient effects can be simulated as well. Thus, in the time domain, it is possible to take into account the behaviour of the adaptive control algorithm. The frequency domain simulations have been used to determine the optimal control configuration in terms of the optimal number and location of control actuators and feedback sensors.

4.1 Frequency domain simulations

These simulations have been carried out using experimentally acquired data (operational data taken on the road, i.e. acoustical and vibrational measurements) as well as in-laboratory acquired frequency response functions in order to compare the achievable performance of local and global control in ASAC systems. Using the original (primary) sound field, and the pseudo-inverse of the relevant FRF matrix (viz. the transfer matrix between applied

actuator forces and the secondary sound field), a set of control forces can be calculated per frequency line such that the superposition of primary and secondary sound field is minimised in a least squares sense. Once the optimal control forces are determined, the residual sound field (and thus the achieved reduction) can be determined by superposition of the primary sound field and the secondary sound field obtained by applying the optimal control forces to the FRF matrix.

By these simulations it was understood that using microphones as feedback sensors is more efficient in terms of interior noise reduction compared to feedback of the vibration levels at the actuator locations, even if the controller would be able to significantly suppress these vibration levels (figures 6-7). As a consequence, local feedback was not retained.

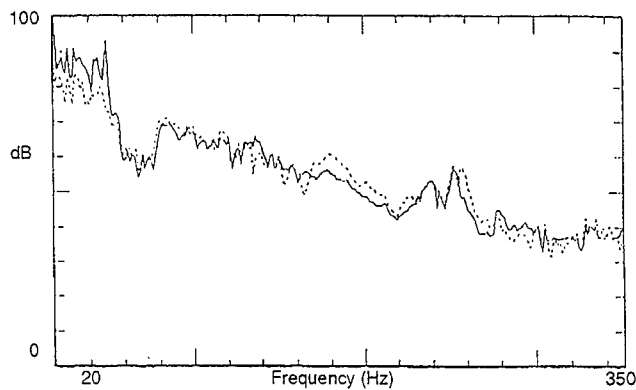


Figure 6. Vibration feedback ;
dotted : with control, solid : without control.

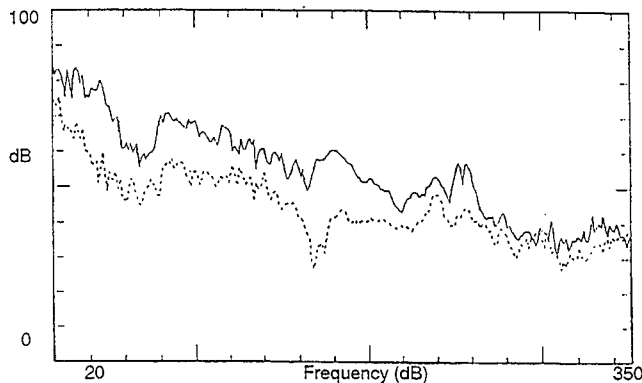


Figure 7. Microphone feedback ;
dotted : with control, solid : without control.

Frequency domain simulations lack the constraint of causality and assume stationarity. Furthermore, the effect of coherence between references and error signals is not included, such that the selection of the appropriate

reference signals is not taken into account. Frequency domain simulations may indicate limits of performance for various control actuator configurations but they do not exactly predict the control performance nor do they yield information on the transient behaviour of the controller. For these reasons, a time domain simulation tool has been developed, which is discussed below.

4.2 Time domain simulations

The basic principle of the time domain simulations is depicted in figure 8. The idea is to "feed" the (simulated) adaptive controller with time domain test data, measured during road tests, and to calculate the noise level at the error microphone by superposition of the control action and the primary noise.

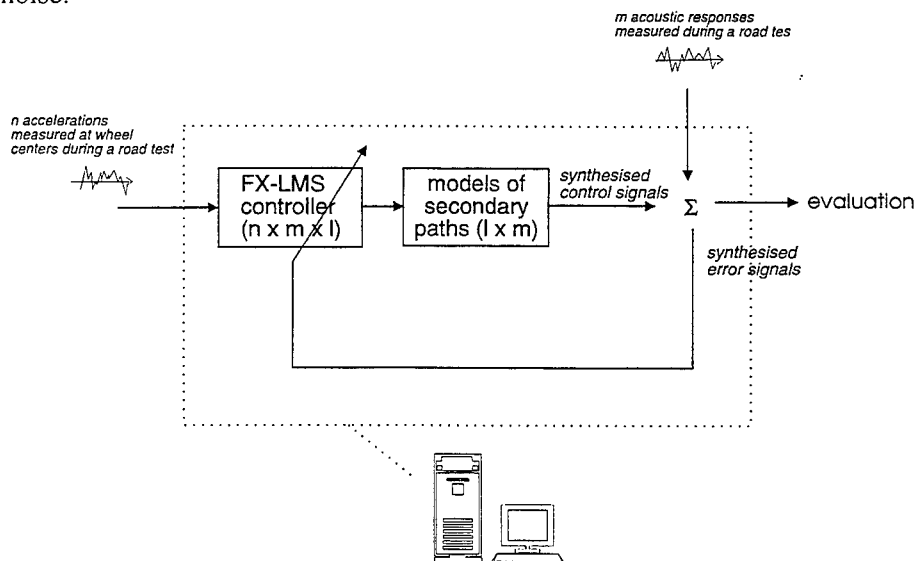


Figure 8. Time domain simulation

An FRF model of the complete car (a 30 by 4 FRF matrix for 30 possible actuator positions and 4 possible error microphone positions) has been composed to represent the physical secondary paths. The control actuators can thus be "connected" to any of the excitation points by selecting the appropriate FRF in the simulations. The operational data are the wheel centre vibrations and the sound pressure levels inside the car cabin, measured during road tests performed on rough asphalt. A selection of wheel centre vibrations is used as a reference set for the feedforward controller, which in turn drives models of the secondary paths (impulse response functions, derived from the FRFs) instead of physical secondary paths. The output of the secondary path models (synthesised secondary sound pressures) is delayed one sample period, to account for computational delay introduced by the DSP,

after which it is added to the primary sound pressure measured at the error microphones during road tests. This provides the error signal to be used in the adaptive loop of the control algorithm.

These simulations have been performed in order to further optimise the efficiency of the feedforward control and to compare the performances of ASAC and ANC implementations. Figures 9 and 10 present the sound power measured at the rear left error microphone for the optimised ASAC and ANC control configurations.

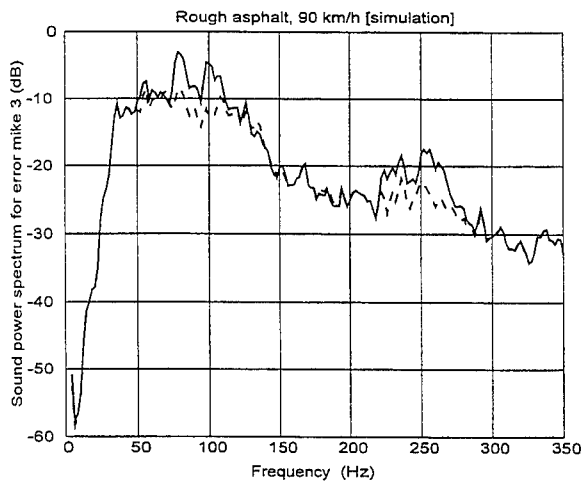


Figure 9. Result of simulation of ASAC (6x6x4).

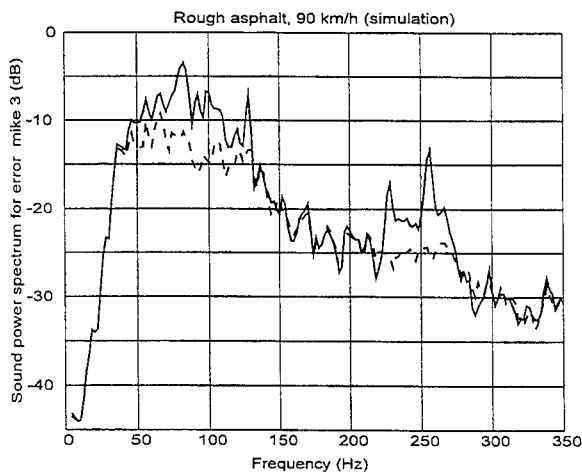


Figure 10. Result of simulation of ANC (6x4x4).

The results have been achieved after a time domain simulation that has been run until the control filters had completely converged (data set of 120,000 data samples). The control systems achieve an average noise reduction of 7 dB (for ASAC) and 7.5 dB respectively (for ANC) in the frequency range from 75 to

105 Hz. Secondly, at the tire resonance (from 225 Hz to 280 Hz), 5.5 dB noise reduction is achieved with the ASAC system and 5.8 dB noise reduction is achieved with the ANC system.

5. Laboratory tests

5.1 *The experimental set-up*

To experimentally validate the control approach, tests have been performed on a demonstrator car (a mid-size station wagon). An electrodynamic shaker (the primary disturbance) excites one rear wheel of the demonstrator car to simulate a random road input to the car suspension (Figure 11). Band-limited white noise is used as an input to the disturbance shaker, to reproduce the wheel centre vibrations for normal operating conditions (measured during road tests) in terms of frequency content and amplitude.

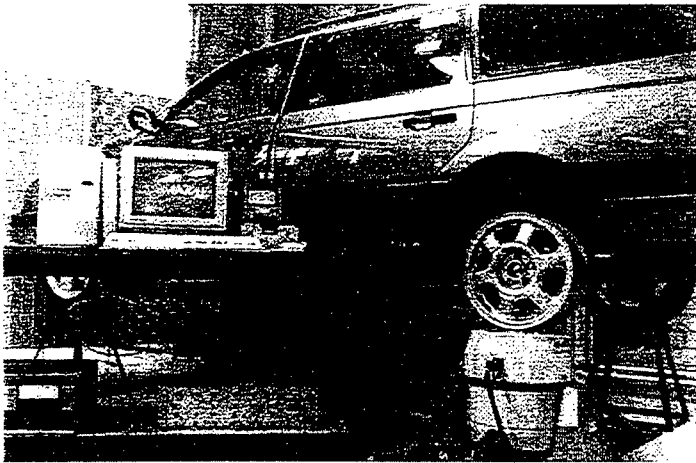


Figure 11. Laboratory set-up.

5.2 *Single channel control*

A single channel controller (one control actuator and one error microphone) was used in a first series of experiments to demonstrate the effect of causality. Figure 12 presents the coherence for three different reference sensor positions (position (a) corresponds to the wheel hub, (b), and (c) are locations on the suspension and closer to the car body). The overall values indicate that the coherence increases for position (b) and (c), although this effect is very limited because the measurements have been performed in laboratory conditions and thus the effect of non-linearities and other non-coherent noise sources is well under control. Figure 13 presents the noise levels inside the car cabin when one error microphone and one control actuator are used to control the structure-borne noise level, for each of the reference sensor positions. Although the coherence is slightly better, the overall

reduction decreases for positions (b) and (c), indicating that the corresponding control configuration does not meet the time constraints any more. The best performance is achieved when the reference sensor is located at the wheel hub : 7.13 dB overall noise reduction from 50 to 200 Hz, and over 10 dB in the frequency range from 110 to 160 Hz.

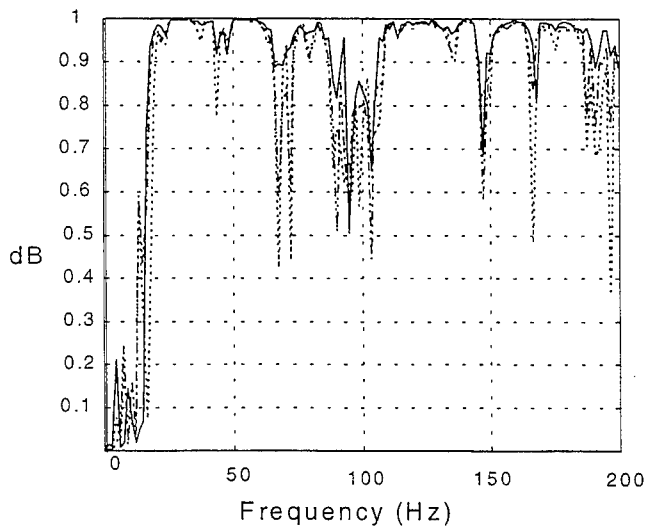


Figure 12. Coherence of the reference signal with the error sensor signal for three different reference sensor positions. Overall values : position (a) : 0.91, position (b) : 0.92, position (c) : 0.94.

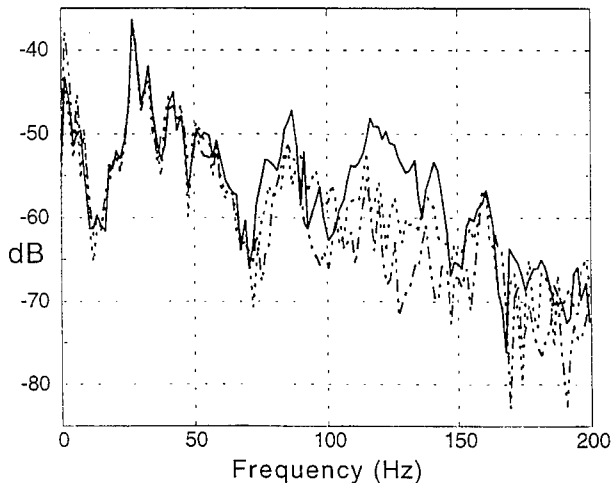


Figure 13. Controlled noise level in the error microphone using one control actuator and three different reference sensor positions. Overall reduction for reference sensor in : position (a) : 7.13 dB, position (b) : 5.44 dB, position (c) : 2.6 dB.

5.3 Multiple references

In order to simulate road excitation by multiple uncorrelated forces, an additional primary disturbance shaker was connected to the second rear wheel of the demonstrator car. The primary disturbance shakers were driven with uncorrelated white noise signals.

The maximum achievable reduction drops drastically when only one reference signal is used under these circumstances. This is mainly due to the fact that an individual reference sensor does not pick up all necessary information to control both uncorrelated sources. This is clearly indicated by the ordinary coherence of a single reference sensor with respect to the sound pressure at the error microphone, in the case where two uncorrelated primary sources are exciting the demonstrator car (figure 14). The reference sensors were located on the left and right rear wheel hub (figure 14a and 14b, respectively). Note that both reference signals are complementary, which indicates the need for two references to detect both primary disturbances.

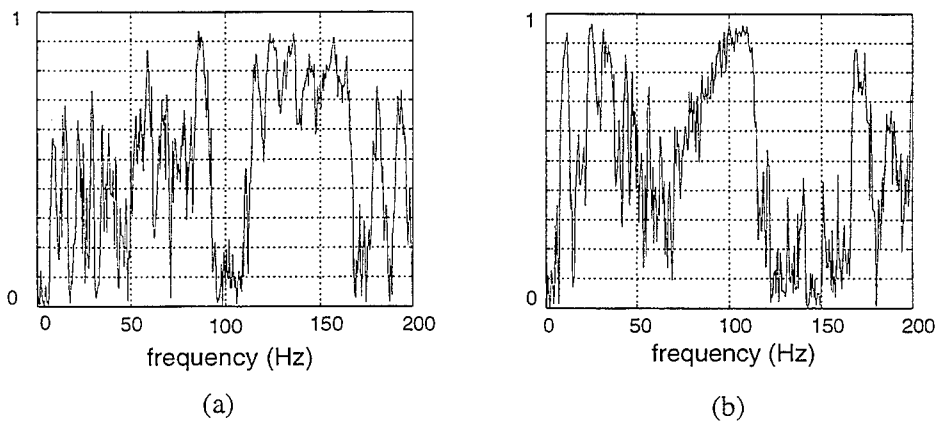


Figure 14. Ordinary coherence of the sound pressure at the error microphone with respect to each of the reference signals in the case of two uncorrelated primary sources.

The control result for the case where only one reference signal (corresponding to figure 14a) is used in the presence of two primary disturbances, is shown in figure 15. Two control actuators have been used to reduce the sound pressure at two error microphones inside the car cabin. The sound pressure at the error microphone is only effectively reduced in the range where the ordinary coherence is considerably high (cf. figure 14a). The maximum achievable reduction is 3.83 dB in the frequency range from 70 to 150 Hz.

Using both reference signals (located on the left and right rear wheel hub), two control actuators and two error microphones, the overall reduction in

the frequency range from 50 to 160 Hz has been increased to 7.8 dB (Figure 16).

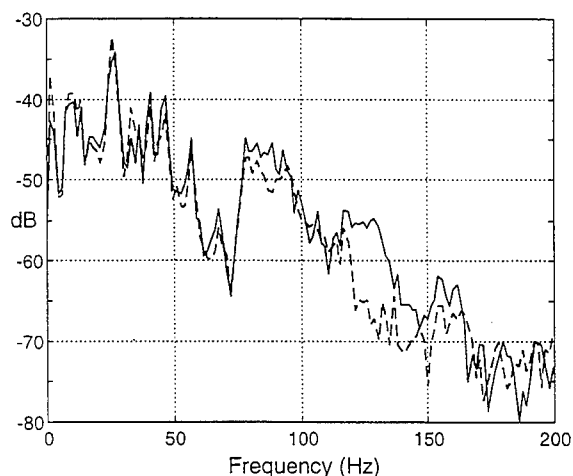


Figure 15. Sound power spectrum of the error microphone for two uncorrelated primary disturbances when only one reference signal is used (solid : without control, dashed : with control).

Overall reduction in the band from 70-150 Hz is 3.8 dB.

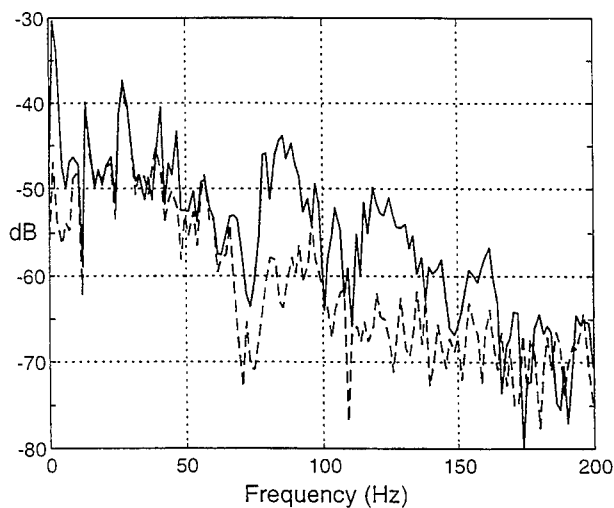


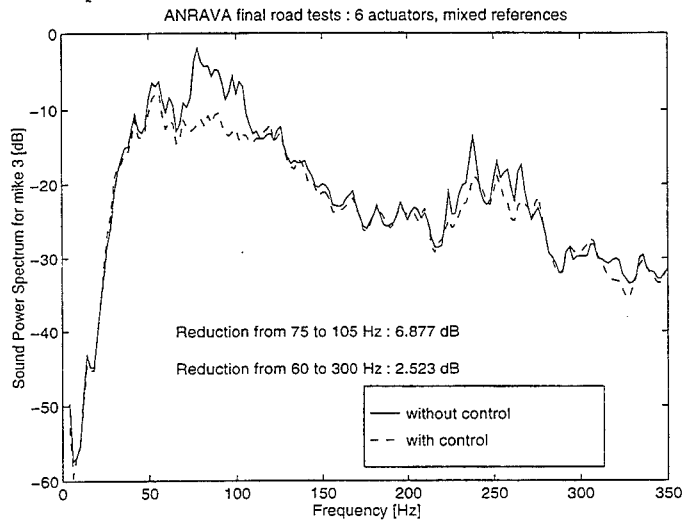
Figure 16. Sound power spectrum of the error microphone for two uncorrelated primary disturbances (solid : no control, dashed : with control).

Overall reduction in the frequency band from 50-160 Hz is 7.8 dB.

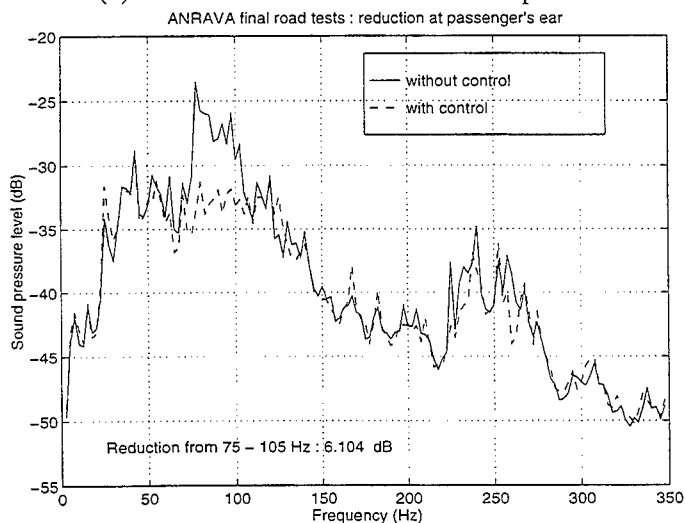
6. Road tests

6.1 ASAC system

Road tests with the full system (6 references, 6 actuators, 4 error microphones) have been performed at a constant speed of 90 km/h. Special care was taken to prevent output saturation, which easily occurs in overdetermined control systems (more control actuators than error sensors). Figure 17 presents the attenuation obtained with the ASAC system (non-calibrated sound pressure levels are shown for reasons of confidentiality).



(a) Reduction at rear left error microphone



(b) Reduction at the passenger's ear at rear left seat

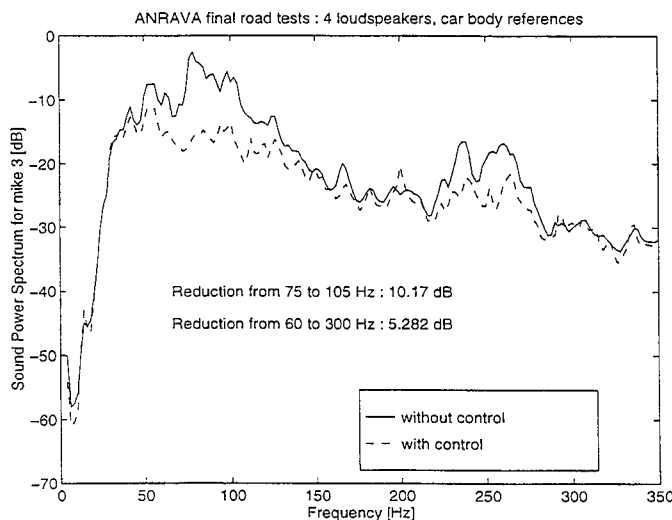
Figure 17. Results of the road tests with the ASAC system.

The reduction is sensible in particular frequency ranges (60-120, 225-280 Hz) that correspond to booms of the car cavity and to the tire resonance respectively. An average noise reduction of 6.9 dB reduction has been achieved in the range from 75 - 105 Hz at the error microphone. This yields 6.1 dB reduction at the passenger's ear in the same frequency range.

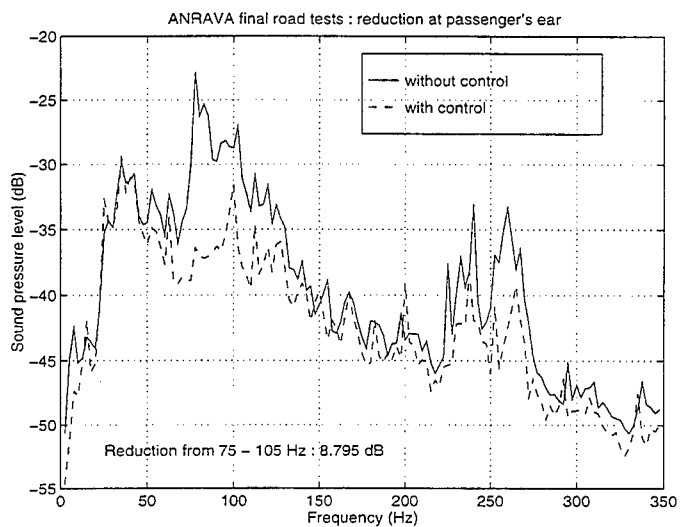
6.2 ANC system

Comparative road tests with the ANC system have been carried out. The number of loudspeakers used for this control system was limited to 4 for practical reasons. The results presented in figure 18 have been achieved using car body references. As in the case of ASAC, the noise reduction is sensible in particular frequency ranges (60-120, 225-280 Hz). A maximum reduction of 10.2 dB was achieved in the range from 75 - 105 Hz at the error microphone. At the passenger's ear, this yields 8.8 dB reduction.

The reason why the loudspeaker system achieves better performance than the actuator system is twofold. First of all, when using loudspeakers instead of actuators, it is possible to locate the reference sensors on the main transfer paths and thus to achieve relatively high multiple coherence. Secondly, the sound levels that are to be generated to control the sound field inside the car cabin are within the dynamic range of the loudspeakers while the control forces that are to be generated by the vibration actuators are very close to the maximum force that can be generated by the vibration actuators.



(a) Reduction at rear left error microphone



(b) Reduction at the passenger's ear at rear left seat

Figure 18. Results of the road tests with the ANC system.

7. Conclusions

The paper demonstrates the feasibility of active structural and acoustic control of structure borne rolling noise in a passenger car. A full vibro-acoustical analysis of the demonstrator vehicle was carried out, in order to fully characterise the on-road behaviour (coherence analysis, operational force analysis and transfer path analysis), as well as to derive the necessary input/output models. The results of these analyses have been used as input for the actuator design, the control configuration determination (reference signals, actuator number and location, feedback signal determination).

Different control configurations have been investigated and tested by means of numerical simulations and laboratory tests.

A broadband control system based on an adaptive feedforward control system using 6 reference signals, 6/4 actuators (ASAC/ANC) and 4 error signals has been implemented in the demonstrator car. A new inertial actuator based on moving coil work principle has been designed and realised.

With the ANC configuration the largest reductions have been obtained. This is primarily due to the fact that with reference sensor configuration of the ANC system a higher multiple coherence is obtained. Also the dynamic output range of the actuators seems to be a limiting factor for the control performance of the ASAC system.

Though the absolute reduction at the error microphones as well as at the monitor microphone are larger than with the ASAC system, the sound field outside the error microphones gets relatively heavily distorted. Because the loudspeakers act much more as point sources, this effect is easily recognisable

when the observer is moving closer to the loudspeakers (although the reduction measured at the passenger's ear, presented in Fig. 14, is considerable). Therefore, there is less sensation of acoustic comfort with the ANC system, compared to the ASAC system which achieves a more uniform reduction in the entire car cabin.

ACKNOWLEDGEMENT

The work reported herein was related to the EC Brite/Euram Research Project ANRAVA (under contract BRE2-CT92-0327). The project is supported by the Directorate-General for Science; Research and Development of the CEC. Partners in this project were : Elesa (I), KULeuven (B), University of Manchester (UK), LMS International (B), Monroe Belgium (B), University of Patras (Gr), Metzeler Gimetall (G), and Volkswagen (G). This text presents parts of the research results of the Belgian programme on Interuniversity Poles of Attraction initiated by the Belgian State, Prime Minister's Office, Science Policy Programming.

REFERENCES

1. Sutton, T. J., Elliott, S. J., and Moore, I., 1991, "Use of nonlinear controllers in the active attenuation of road noise inside cars", *Proc. Recent Advances in Active Control of Sound and Vibration*, VA, USA, April, 1991, pp. 682-690.
2. Sutton, T., Elliot, S., Malcom McDonald, A., "Active Control of Road Noise inside Vehicles", *Noise Control Eng. J.*, 42(4), 1994
3. Ferren, W. Brent, Bernhard, R.J., "Active Control of Simulated Road Noise," Purdue University, 1991
4. Heatwole, C.M., Dian, X., and Bernhard, R.J., 1993, "Parameter Studies of Active Control of Road Noise in Automobiles", *Proc. of Second Conf. on Recent Advances in Active Control of Sound and Vibration*, Blacksburg, Virginia, 28-30 April 1993, pp. 813-825.
5. Heatwole, C.M., and Bernhard, R.J., 1994, "Prediction of Multiple-Input Active Control of Road Noise in Automobile Interiors", *Proc. of Noise-Con 94*, Ft. Lauderdale, Florida, 1-4 May 1994, pp. 367-372.
6. Freymann, R. et al., 1995, "Vorrichtung zur aktiven akustischen Schallkompensation in Hohlräumen eines Kraftfahrzeuges," European Patent Appl. No. 0649129 A2. Prior. (D) : Oct. 13, 1993. Pbl. : April 19, 1995.
7. Bronzel, M., 1993, "Aktive Beeinflussung nicht-stationärer Schallfelder mit adaptiven Digitalfiltern," (in German) Ph.D. Dissertation, Drittes Physikalisches Institut, University of Göttingen.

8. Sano, H., Adachi, S., and Kasuya, H., 1995, "Active Noise Control based on the RLS algorithm for an automobile," *Proc. of ACTIVE 95*, Newport Beach, CA, 1995 July 06 - 08, pp. 891 - 898.
9. Wyckaert, K., Hendricx, W., 1994, "Transmission path analysis in view of active cancellation of road induced noise in automotive vehicles", *Proceedings of Inter-Noise 94*, August 29-31, 1994, Yokohama, Japan, pp. 653-656.
10. Widrow, B., and Stearns, S.D., 1985, "Adaptive Signal Processing," Prentice - Hall, Inc., Englewood Cliffs.
11. Burgess, J.C., 1981, "Active adaptive sound control in a duct : A computer simulation," *J. Acoustic Soc. Am.*, Vol. 70, pp. 715-726.
12. Elliott, S.J., Stothers, I.M., and Nelson, P.A., 1987, "A Multiple Error LMS Algorithm and Its Application to the Active Control of Sound and Vibration," *IEEE Transactions on Acoustics, Speech, and Signal Processing*, Vol. ASSP-35, No. 10, October 1987, pp.1423 - 1434.
13. Kuo, S.M., and Morgan, D.R., 1996, "Active Noise Control Systems," John Wiley & Sons, Inc., New York.
14. Elliott, S.J., Boucher, C.C., and Nelson, P.A., 1992, "The behavior of a multiple channel active control system", *IEEE Trans. on Signal Processing* **40**, No. 5, May 1992, pp. 1423-1434.
15. Snyder, S.D., and Hansen, C.H., 1992, "Design consideration for active noise control systems implementing the multiple input, multiple output LMS algorithm", *Journal of Sound and Vibration*, Vol. 159, No. 1, pp. 157 - 174.
16. Bao, C., 1994, "Adaptive algorithms for active noise control and their applications", Ph.D. thesis, K.U.Leuven, Fac. Eng., Dept. Mechanical Eng.
17. Bernhard, R.J., 1995, "Active Control of Road Noise inside Automobiles," *Proc. of ACTIVE 95*, Newport Beach, CA, 1995 July 06 - 08, pp. 21 - 33.
18. Vermersch, F., Veys, P., "Active Control of road noise in cars: aspects of implementation", *Thesis 94ep03*, Dept. of Mech. Eng., KULeuven, Belgium, 1994
19. Burdisso, Vipperman, Fuller, "Causality constraints of feedforward controlled systems with broadband inputs", *J. Acoust. Soc. Am.* 94 (1), pp.234-242, July 1993
20. Dehandschutter, W., Sas, P., Banfo, G.-L., 1996, "Active control of rolling noise in a passenger car through structural and acoustic control," *Proc. of ISMA 21*, 18-20 Sept., Leuven, Belgium, pp. 401 - 412.
21. Dehandschutter, W., Van Cauter, R., and Sas, P., 1995a, "Active Control of Simulated Structure Borne Road Noise using Force Actuators", *Proc. of SAE Conference on Noise and Vibration*, Detroit, May 1 - 3, pp. 737 - 745.

22. Dehandschutter, W., Van Cauter, R., and Sas, P., 1995b, "Active Structural Acoustic Control of Structure Borne Road Noise : Theory, Simulations, and Experiments", *Proc. of ACTIVE 95*, Newport Beach, CA, USA, 1995 July 06 - 08, pp. 735 - 746.
23. Dehandschutter, W., Van Herbruggen, J., 1996, "Active control of road noise, validation of the controller developed in the ANRAVA project (road tests)", *Internal Report 96R06*.
24. Wyckaert, K., Dehandschutter, W., and Banfo, G-L., 1995, "Active vibration control of rolling noise in a passenger car : performance evaluation of actuator and feedback sensor configuration", *Proc. of Active 95*, Newport Beach, California, 6-9 July 1995.

**A REVIEW OF THEORIES AND COMPUTATIONAL MODELS
OF LAMINATED COMPOSITE STRUCTURES**

J. N. Reddy

Department of Mechanical Engineering
Texas A & M University
College Station, Texas 77843-3123

Paper presented at
**Sixth International Conference on
Recent Advances in Structural Dynamics**
The Institute of Sound and Vibration Research
University of Southampton
Southampton, England
14-17 July 1997

A REVIEW OF THEORIES AND COMPUTATIONAL MODELS OF LAMINATED COMPOSITE STRUCTURES

J. N. Reddy

Oscar S. Wyatt Chair in Engineering
Department of Mechanical Engineering
Texas A & M University
College Station, Texas 77843-3123

ABSTRACT

The equivalent single layer theories, layerwise theories, and variable kinematic theories of laminated composite plates and shells are reviewed and their computational models are discussed. Examples of applications of single layer theories for global response, layerwise theories for local response, and variable kinematic theories for global local analysis of laminated plates and shells are presented to illustrate their usefulness. In particular, postbuckling and failures of laminated panels in compression, postbuckling of stiffened cross-ply cylindrical shells, and free edge stress fields in laminates in extension and bending are studied.

1. INTRODUCTION

The use of composite materials in defense structures has led to many important developments in the analysis, design, and manufacturing of structures made of such materials. In recent years, composite materials are used in all types of civilian structures, *e.g.*, automotive parts, medical prosthetic devices, electronic circuit boards, and sports equipment. This in turn generated interest in developing new composite material systems, theories and analysis methods.

Composite laminates are formed by stacking layers of different composite materials and/or fiber orientation. By construction, composite laminates have their planar/surface dimensions one to two orders of magnitude larger than their thickness. Often laminates are used in applications that require inplane and bending strengths. Therefore, composite laminates are treated as plate or shell structural elements.

The analyses of composite structures are based on one of the following theories [1]: (2) models based on 3D or quasi-3D elasticity theories [11-17], and (3) multiple models [18-22]. The equivalent single layer (ESL) theories are derived from the 3D elasticity theory by assuming the form of the displacement field or the stress field through the thickness of the laminate. These assumptions allow the reduction of a 3D problem to a 2D problem. In the 3D and quasi 3D theories, each layer is modeled as a 3D solid. In a multiple model method, a combination of single layer and 3D elasticity theories are combined to achieve the level of accuracy needed in different regions of the same problem. Such approaches are called global local analyses. Each of these approaches are appropriate for certain class of problems. For example, the ESL theories are adequate for global response predictions, 3D theories are required for the determination of 3D stress states, and the multiple model approaches are suitable problems that have regions of both 2D and 3D stress states.

In this paper a review of the three classes of theories is presented and a typical application of each of the three classes of theories is discussed. These include: (1) postbuckling and progressive failure analysis of laminated panels in compression using an ESL theory, (2) postbuckling analysis of stiffened cross-ply cylindrical shells using the layerwise theory, and (3) a study of free edge stress fields in laminates subjected to extension and bending, using the variable kinematic finite element (VKFE) model.

2. THEORIES OF LAMINATED STRUCTURES

2.1 Equivalent Single Layer Theories

The simplest ESL laminate theory is the *classical laminated plate theory* (or CLPT) [1,2], which is an extension of the Kirchhoff (classical) plate theory to laminated composite plates. It is based on the displacement field

$$\begin{aligned} u(x, y, z, t) &= u_0(x, y, t) - z \frac{\partial w_0}{\partial x} \\ v(x, y, z, t) &= v_0(x, y, t) - z \frac{\partial w_0}{\partial y} \\ w(x, y, z, t) &= w_0(x, y, t) \end{aligned} \quad (2.1)$$

where (u_0, v_0, w_0) are the displacement components along the (x, y, z) coordinate directions, respectively, of a point on the midplane (*i.e.*, $z = 0$). The displacement field (2.1) implies that straight lines normal to the xy -plane before deformation remain straight and normal to the midsurface after deformation. The Kirchhoff assumption amounts to neglecting both transverse shear and transverse normal effects, *i.e.*, deformation is due entirely to bending and inplane stretching.

The next theory in the hierarchy of ESL laminate theories is the *first order shear deformation theory* (or FSDT) [1,6-8], which is based on the displacement field

$$\begin{aligned} u(x, y, z, t) &= u_0(x, y, t) + z\phi_x(x, y, t) \\ v(x, y, z, t) &= v_0(x, y, t) + z\phi_y(x, y, t) \\ w(x, y, z, t) &= w_0(x, y, t) \end{aligned} \quad (2.2)$$

where ϕ_x and $-\phi_y$ denote rotations about the y and x axes, respectively. The FSDT extends the kinematics of the CLPT by including a gross transverse shear deformation in its kinematic assumptions, *i.e.*, the transverse shear strain is assumed to be constant with respect to the thickness coordinate. Inclusion of this rudimentary form of shear deformation allows the normality restriction of the classical laminate theory to be relaxed. The first order shear deformation theory requires shear correction factors, which are difficult to determine for arbitrarily laminated composite plate structures. The shear correction factors depend not only on the lamination and geometric parameters, but also on the loading and boundary conditions.

Second and higher order ESL laminated plate theories use higher order polynomials in the expansion of the displacement components through the thickness of the laminate (see [23-28], among many others). The higher order theories introduce additional unknowns that are often difficult to interpret in physical terms. For example, the

third order laminate theory of Reddy [24,28] with transverse inextensibility is based on the displacement field

$$\begin{aligned} u(x, y, z, t) &= u_0(x, y, t) + z\phi_x(x, y, t) + z^3 \left(-\frac{4}{3h^2} \right) \left(\phi_x + \frac{\partial w_0}{\partial x} \right) \\ v(x, y, z, t) &= v_0(x, y, t) + z\phi_y(x, y, t) + z^3 \left(-\frac{4}{3h^2} \right) \left(\phi_y + \frac{\partial w_0}{\partial y} \right) \\ w(x, y, z, t) &= w_0(x, y, t) \end{aligned} \quad (2.3)$$

The displacement field accommodates quadratic variation of transverse shear strains (and hence stresses) and vanishing of transverse shear stresses on the top and bottom of a general laminate composed of monoclinic layers. Thus there is no need to use shear correction factors in a third order theory. The theory was generalized in [28]. The third order theories provide a slight increase in accuracy relative to the FSDT solution, at the expense of a significant increase in computational effort. Further, finite element models of third order theories that satisfy the vanishing of transverse shear stresses on the bounding planes require continuity of the transverse deflection and its derivatives between elements. Complete derivations of the governing equations of the third order theories and their finite element models are presented in Chapter 11 of [1].

In addition to their inherent simplicity and low computational cost, the ESL models often provide sufficiently accurate description of global response for thin to moderately thick laminates, *e.g.*, gross deflections, critical buckling loads, and fundamental vibration frequencies and associated mode shapes. Of the ESL theories, the FSDT with transverse extensibility appears to provide the best compromise of solution accuracy, economy, and simplicity. However, the ESL models have limitations that prevent them from being used to solve the whole spectrum of composite laminate problems. First, the accuracy of the global response predicted by the ESL models deteriorates as the laminate becomes thicker. Second, the ESL models are often incapable of accurately describing the state of stress and strain at the ply level near geometric and material discontinuities or near regions of intense loading – the areas where accurate stresses are needed most. In such cases, 3D theories or multiple model approaches are required.

2.2 Layerwise Theories

In all equivalent single layer laminate theories based on assumed displacement fields, it is assumed that the displacements are continuous functions of the thickness coordinate. This in turn results in continuous transverse strains and discontinuous inplane strains. Hence, all stresses in equivalent single layer theories are discontinuous at layer interfaces. More importantly, the transverse stresses at the interface of two layers, called *interlaminar stresses*, are discontinuous. For thin laminates the error introduced due to discontinuous interlaminar stresses can be negligible. However, for thick laminates, the ESL theories can give erroneous results for all stresses, requiring use of layerwise theories.

In contrast to the ESL theories, the layerwise theories are developed by assuming that the displacement field exhibits only C^0 -continuity through the laminate thickness. Thus the displacement components are continuous through the laminate thickness but the transverse derivatives of the displacements may be discontinuous at various points through the thickness, thereby allowing for the possibility of continuous transverse stresses at interfaces separating dissimilar materials. Layerwise displacement fields

provide a much more kinematically correct representation of the moderate to severe cross sectional warping associated with the deformation of thick laminates.

The displacement based layerwise theories can be subdivided into two classes: (1) the *partial layerwise theories* that use layerwise expansions for the inplane displacement components but not the transverse displacement component, and (2) the *full layerwise theories* that use layerwise expansions for all three displacement components. Compared to the ESL theories, the partial layerwise theories provide a more realistic description of the kinematics of composite laminates by introducing discrete layer transverse shear effects into the assumed displacement field. The full layerwise theories go one step further by adding both discrete layer transverse shear effects and discrete layer transverse normal effects.

A more direct method of achieving a layerwise displacement field was proposed by Reddy [15], who represented the transverse variation of the displacement components in terms of one dimensional Lagrangian finite elements. The total displacement field of the laminate is written as (see Robbins and Reddy [16])

$$\begin{aligned} u(x, y, z, t) &= \sum_{I=1}^N U_I(x, y, t) \Phi^I(z) \\ v(x, y, z, t) &= \sum_{I=1}^N V_I(x, y, t) \Phi^I(z) \\ w(x, y, z, t) &= \sum_{I=1}^M W_I(x, y, t) \Psi^I(z) \end{aligned} \quad (2.4)$$

where (U_I, V_I, W_I) denote the nodal values of (u, v, w) , N is the number of nodes and Φ^I are the *global* interpolation functions for the discretization of the inplane displacements through thickness, and M is the number of nodes and Ψ^I are the global interpolation functions for discretization of the transverse displacement through thickness. The governing equations of motion for the present layerwise theory can be derived using the principle of virtual displacements.

The resulting strain field is kinematically correct in that the inplane strains are continuous through the thickness while the transverse strains are discontinuous through the thickness, thereby allowing for the possibility of continuous transverse stresses as the number of layers is increased. The layerwise field proposed by Reddy is very general in that any desired number of layers, distribution of layers, and order of interpolation can be achieved simply by specifying a particular mesh of one dimensional finite elements through the thickness.

2.3 Multiple Model Methods

To accurately capture the localized 3D stress fields in practical laminated composite structures, it is usually necessary to resort to a simultaneous multiple model approach [18–22] in which different subregions of the problem domain are modeled using appropriate kinematic structural theories. The objective of a simultaneous multiple model analysis is to match the most appropriate structural theory with each subregion based on the physical characteristics, applied loading, expected behavior, and level of solution accuracy desired within each subregion. Thus solution economy is maximized without sacrificing solution accuracy.

To overcome the difficulties encountered in the conventional global local analysis of practical composite laminates, a hierarchical finite element model is developed by the author and his colleagues [20–22]. The hierarchical, variable kinematic finite element (VKFE) is developed using a multiple assumed displacement field approach, *i.e.*, by superimposing two or more different types of assumed displacement fields in the same finite element domain. In general, the multiple assumed displacement field can be expressed as

$$u_i(x, y, z) = u_i^{ESL}(x, y, z) + u_i^{LWT}(x, y, z) \quad (2.5)$$

where $i=1,2,3$, and $u_1 = u, u_2 = v$, and $u_3 = w$ are the displacement components in the x, y , and z directions, respectively. The reference plane of the plate coincides with the xy -plane. The underlying foundation of the displacement field is provided by u_i^{ESL} , which represents the assumed displacement field for any desired equivalent single layer theory. The second term u_i^{LWT} represents the assumed displacement field for any desired full layerwise theory. The layerwise displacement field is included as an optional, incremental enhancement to the basic ESL displacement field, so that the element can have full 3D modeling capability when needed. Depending on the desired level of accuracy, the element may use none, part, or all of the layerwise field to create a series of different elements having a wide range of kinematic complexity. Discrete layer transverse normal effects can be added to the element by including u_3^{LWT} . Displacement continuity is maintained between these different types of elements by simply enforcing homogeneous essential boundary conditions on the incremental layerwise variables, thus eliminating the need for multipoint constraints, penalty function methods or special transition elements. It should be noted that a conventional 3D finite element displacement field could be used instead of the full layerwise field in equation (2.4); however, the 2D data structure of the full layerwise finite elements permits much easier coupling with the 2D ESL field.

3. POSTBUCKLING AND FAILURE ANALYSES USING FSDT

3.1 Preliminary Comments

Because of low moduli and strengths in transverse directions compared to that of in-plane directions, composite laminates may fail due to transverse stresses. Indeed, it is found that (see [1,29,30]) composite laminates loaded in compression fail due to high interlaminar stresses. Therefore, shear deformable plate and shell elements are needed to provide information regarding the through-thickness strength of composite structures. Insight gained by using these elements may aid in the characterization of failure modes of composite panels. Here we discuss a study by Engelstad, Reddy, and Knight [30] of the postbuckling response of several graphite–epoxy panels loaded in axial compression. The study makes comparisons between the experimentally obtained and analytically determined postbuckling response of composite panels.

3.2 Experimental Study

The postbuckling and failure characteristics of flat, rectangular graphite–epoxy panels, with and without holes, and loaded in axial compression have been examined in an experimental study by Starnes and Rouse [29]. The panels were fabricated from commercially available unidirectional Thornel 300 graphite–fiber tapes preimpregnated with 450°K cure Narmco 5208 thermosetting epoxy resin. Typical lamina properties for this

graphite-epoxy system are

$$E_1 = 131.0 \text{ GPa (19,000 ksi)}, \quad E_2 = 13.0 \text{ GPa (1,890 ksi)}$$

$$G_{12} = 6.4 \text{ GPa (930 ksi)}, \quad \nu_{12} = 0.38, \quad h_k = 0.14 \text{ mm (0.0055 in.)} \quad (3.1)$$

where h_k denotes ply thickness. Each panel was loaded in axial compression using a 1.33 MN (300 kips) capacity hydraulic testing machine. The loaded ends of the panels were clamped by fixtures during testing and the unloaded edges were simply supported by knife-edge restraints to prevent the panels from buckling as wide columns. Most panels exhibited postbuckling strength and failed along a nodal line of the buckling mode in a transverse shear failure mode (see [29]). However, a different failure mode was observed for some of the 24-ply panels with holes. These panels failed along a transverse line passing through the hole, and failed soon after buckling.

Here we discuss the results of the panel without a hole, denoted C4 in Reference 29. Panel C4 is 50.8 cm by 17.8 cm (20.0 in. long and 7.0 in. wide), 24-ply laminate, $[\pm 45/0_2/\pm 45/0_2/\pm 45/0/90]_s$ (orthotropic). Panel C4 was observed in the test to buckle into two longitudinal half-waves and one transverse half-wave.

3.3 Finite Element Model

Finite element models of these panels were developed in Reference 30 using nine-node quadratic shell elements of Chao and Reddy [31], which are based on continuum formulation of a laminated 3D shell element, denoted 9CR. The incremental equations of a continuous medium are formulated using the principle of virtual displacements and the total Lagrangian description. The continuum shell element is obtained from the three-dimensional solid element by imposing the same two constraints as in FSDT. The nonlinear formulation admits large displacements and rotations of the shell element and small strains, since the thickness does not change and the normal does not distort. The final incremental equations of equilibrium for an element are of the form

$$([K_L] + [K_{NL}])\{\delta\Delta\} = \{R\} - \{F\} \quad (3.2)$$

where $\{\delta\Delta\}$ is the vector of incremental nodal displacements, $([K_L], [K_{NL}])$ are the linear and nonlinear parts of the stiffness matrix, and $\{F\}$ is the force vector.

The finite element model of Panel C4 consists of 12 nine-node quadrilateral elements along the panel length and six along the width. In order to proceed beyond the critical buckling point in the analysis of each panel, an initial geometric imperfection, typically the same shape as the first linear buckling mode, was assumed in the finite element analysis. The amplitude of each mode was selected to be 1-5% of the total laminate thickness. This allows efficient progress past the critical buckling point, but does not affect the results in the postbuckling range.

3.4 Failure Analysis

The laminate failure occurs due to propagation of damage as the load is increased. To model this effect, a progressive failure approach is used in the nonlinear finite element analysis. At each load step, Gauss point stresses are used in the selected failure criterion. If failure occurred at a Gauss point, a modification of the lamina properties was made at that Gauss point, which results in reduced stiffnesses $[A]$, $[B]$, and $[D]$ of the laminate. For example, for the maximum stress criterion, if the σ_1 stress exceeds the longitudinal

tensile strength X_T , then the longitudinal modulus E_1 at that point is reduced to zero. For the Tsai–Wu criterion, if failure occurs, then the following expressions are used to determine the failure mode:

$$\begin{aligned} H_1 &= F_1\sigma_1 + F_{11}\sigma_1^2, & H_2 &= F_2\sigma_2 + F_{22}\sigma_2^2 \\ H_4 &= F_{44}\sigma_4^2, & H_5 &= F_{55}\sigma_5^2, & H_6 &= F_{66}\sigma_6^2 \end{aligned} \quad (3.3)$$

The largest H_i term is selected as the dominant failure mode and the corresponding modulus is reduced to zero. Thus H_1 corresponds to the modulus E_1 , H_2 to E_2 , H_4 to G_{23} , H_5 to G_{13} , and H_6 to G_{23} . As a consequence of this reduction, engineering material properties are updated as failure progresses. An outline of the steps used in the analysis is given below.

1. After the displacement convergence is achieved, calculate stresses in the global (x, y, z) coordinates at the middle of each layer at each Gauss point.
2. Transform the stresses to the principal material coordinates.
3. Compute the failure index, \mathcal{F} .
4. If failure occurs (*i.e.*, $\mathcal{F} \geq 1$), (a) identify the maximum H_i , (b) reduce the appropriate lamina moduli at that Gauss point, and (c) recompute laminate stiffnesses and restart the nonlinear analysis at the same load step (*i.e.*, return to Step 1).
5. If no failure occurs, proceed to the next load step.

The end shortening of the panel is monitored as in a compression test. The failure load is defined to be that load for which the panel undergoes large end shortening for small increments of load.

3.5 Discussion of the Results

Comparison between test results from Reference 29 and finite element results from Reference 30 for Panel C4 are shown in Figure 3.1, where end shortening u_0 , normalized by the analytical end shortening u_{cr} at buckling (Figure 3.1a) and out-of-plane deflection w_0 near a point of maximum deflection, normalized by the panel thickness h (Figure 3.1b) are plotted as a function of the load P , normalized by the theoretical buckling load P_{cr} . The circles in the figure represent test data, and the curves denote the results of the nonlinear finite element analyses. These experimental and finite element results agree well up to failure of the panel. The postbuckling response exhibits large out-of-plane deflections (nearly three times the panel thickness; see Figure 3.1b) and high longitudinal strains from front and back surfaces (not shown here).

Figure 3.2a contains the distribution of the axial stress σ_{xx} in the third layer of the laminate (a 0° ply) at panel midlength for three values of the applied load. At the buckling load, the axial stress is nearly uniform across the panel. Although the axial stress is large, the values are well below the material allowable values in tension $X_T = 1400$ MPa (203 ksi) and compression $X_C = 1138$ MPa (165 ksi). The contour plot of axial stress σ_{xx} over the entire panel in this 0° ply for an applied load of $2.1P_{cr}$ indicates (not shown here) that high compressive axial stresses occur along the longitudinal edges of the panel.

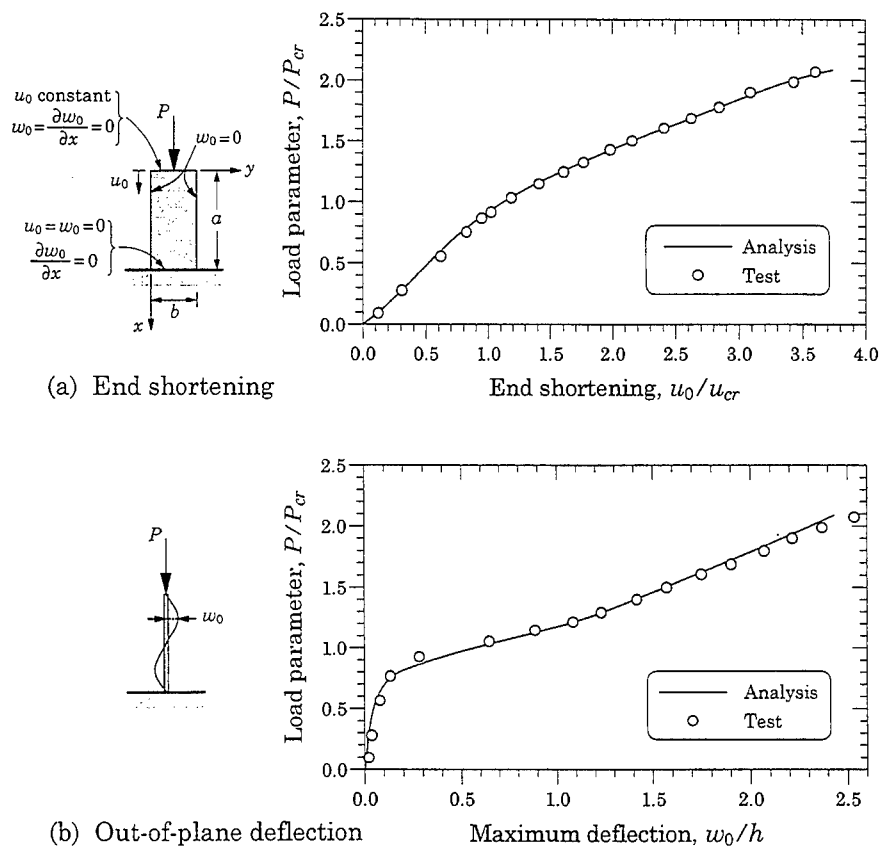


Figure 3.1: Postbuckling response characteristics of panel C4.

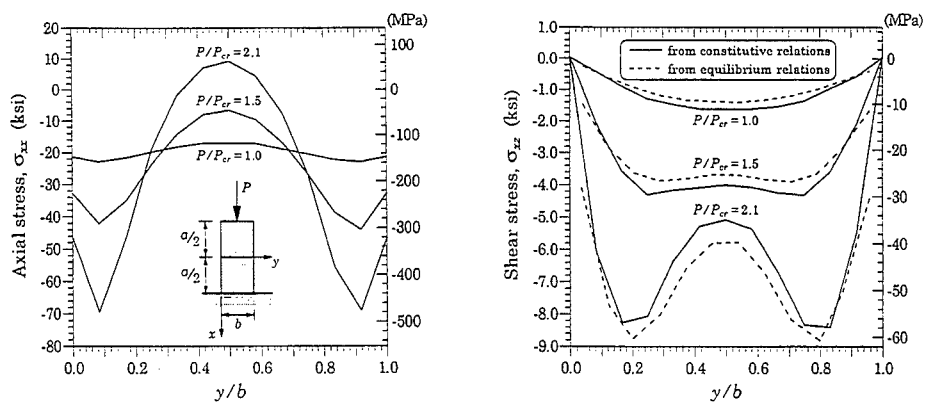


Figure 3.2: (a) Axial stress σ_{xx} and (b) transverse shear stress σ_{xz} distributions in the third layer from the surface (0° ply) of panel C4.

Figure 3.2b shows the distribution of the transverse shear stress in the third layer of the laminate (a 0° ply) at panel midlength for three values of the applied load. The solid curves represent the transverse shear stress distributions obtained using the constitutive relations, and the dashed curves denote the transverse shearing stress distributions obtained from the equilibrium equations. Both methods give very similar results. At the buckling load, the peak transverse shear stress occurs near the center of the panel. After buckling, the transverse shear stresses σ_{xz} redistribute towards the edges of the panel. The peak values of the transverse shear stress σ_{xz} approach the material allowable value of $S = T = 62$ MPa (9 ksi) for $P = 2.1P_{cr}$, indicating the panel failure due to transverse shear stress.

Figures 3.3a and 3.3b contain the progressive failure results for Panel C4, using the maximum stress and Tsai-Wu failure criteria, respectively. In addition to the strengths already mentioned, the other allowables used are transverse tensile strength, $X_T = 80.9$ MPa (11.7 ksi); transverse compressive strength, $X_C = 189.0$ MPa (27.4 ksi); and in-plane shear strength, $T = 69.0$ MPa (10.0 ksi). At some point in the analysis a dramatic change in slope indicates an inability of the panel to support additional load. This location is identified as the failure load. Figures 3.3a and 3.3b show that the Tsai-Wu criterion estimates the experimental failure more closely than the maximum stress criterion. This is attributed to the presence of stress interaction terms in the Tsai-Wu criterion failure index.

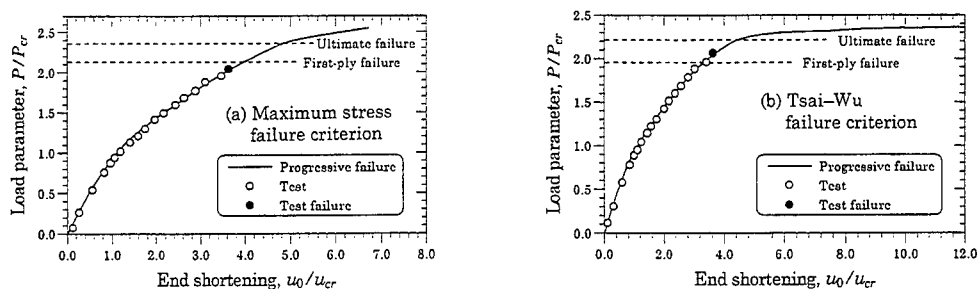


Figure 3.3: Progressive failure results of panel C4.

4. POSTBUCKLING OF STIFFENED CYLINDERS USING LWT

4.1 Introduction

It is generally accepted that the reduced load-carrying capacity of axially loaded cylinders is strictly related to the presence of simultaneous or nearly simultaneous modes. Reddy and Savoia [32] have shown that thin isotropic cylinders of finite length usually have more than hundred modes characterized by a buckling load about 10% higher than the minimum buckling load. In this case, a buckling mode superposition analysis needs a very large number of terms to achieve good estimates of the load-carrying capacity of thin isotropic cylinders. For fiber-reinforced laminated cylinders, the buckling maps are substantially different from those of isotropic cylinders, and usually very few modes are nearly the same. Here we discuss the results of Savoia and Reddy [33] on the postbuckling behavior of stiffened, cross-ply laminated circular cylindrical shells.

4.2 Formulation

In the layerwise theory of Reddy [34] the displacements (u_i, v_i, w_i) and the radial imperfection \hat{w}_i of the cylinder are expressed as

$$[u_1, u_2, u_3, \hat{u}_3](x, y, z) = \sum_{i=1}^{N+1} [u_i, v_i, w_i, \hat{w}_i](x, y) \Phi^i(z) \quad (4.1)$$

where N is the number of numerical layers, (u_i, v_i, w_i) and \hat{w}_i are interface displacements and imperfections, respectively, and $\Phi^i(z)$ are layerwise continuous functions of the thickness coordinate. In the present study, linear (finite element) interpolation functions are used for Φ^i . Here (x, y, z) denotes an orthogonal reference frame, where x is taken along the axis (a) of the cylinder and y along the circumferential (c) direction. The 'smeared stiffener' approach of Hutchinson and Amazigo [36] is adopted for the stiffeners. This approach is very effective when the stiffeners have identical cross section and their spacing is small when compared to the buckling wave length. In the framework of a stability analysis this means that no skin wrinkling before general instability is assumed to take place. The kinematic description of the stiffeners is based on the Euler-Bernoulli beam theory. Axial and ring stiffeners are assumed to deform in the $x-z$ and the $y-z$ planes, respectively.

The total potential energy functional of the stiffened shell can be expressed in terms of the functions u_i, v_i and w_i (see Reddy and Savoia [32,33]). The nonlinear problem derived from the principle of minimum potential energy is solved by means of the Rayleigh-Ritz method for simply-supported edge conditions at $x = 0, L$, where L denotes the length of the cylinder.

4.3 Numerical Results

A three-layer, cross-ply laminated cylindrical shell subjected to axial compression is chosen to study the effect of axial and/or circumferential stiffeners on the postbuckling behavior. The cylinder has the following geometric parameters: length, $L = 300\text{cm}$, radius, $R = L/\pi = 95.49\text{cm}$ and total thickness, $h = 1\text{cm}$. The individual layers have equal thicknesses $h_i = h/3$, and the elastic coefficients are those typical of a high-modulus graphite-epoxy composite:

$$E_1 = 150\text{GPa}, \quad E_2 = 7\text{GPa}, \quad G_{12} = 3.5\text{GPa}, \quad G_{23} = 1.4\text{GPa}, \quad \nu_{12} = \nu_{23} = 0.3$$

The lamination scheme used is: $[0/90/0]$. Since the extensional modulus in the fiber direction E_1 is large with respect to that in the transverse direction E_2 , the cylinder turns out to be reinforced in the axial direction. Moreover, equally-spaced outside stiffeners are considered. The geometric and material characteristics of the I-shaped steel stiffeners adopted here are:

$$E_a = E_c = 210 \text{ GPa}, \quad G_a = G_c = 80.8 \text{ GPa}$$

$$A_a = A_c = 1.2 \text{ cm}^2, \quad \bar{I}_a = \bar{I}_c = 7.2 \text{ cm}^4, \quad J_a = J_c = 0.004 \text{ cm}^4, \quad \bar{z}_a = \bar{z}_c = 3.5 \text{ cm}$$

where a and c refer to axial and circumferential directions. Uniformly distributed axial loads are used here.

The full nonlinear postbuckling analysis has been performed for the cylinder in order to evaluate the influence of stiffening on the reduced load-carrying capacity due to geometrical imperfections, as well as on the minimum postbuckling load. The nonlinear system of equations has been solved by making use of the Riks–Wempner incremental iterative method. The linearized eigenvalue analysis was performed in order to select the modes that dominate the prebuckling state and those having smallest buckling loads. Up to twelve buckling modes have been included in the multimode analysis. In all the cases examined here, the addition of more terms did not change significantly the results obtained. Note that the maximum load can be reached for very small geometric imperfections only.

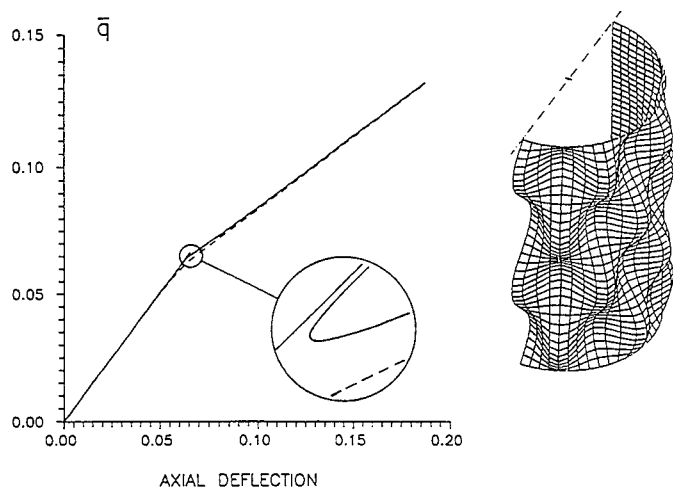


Figure 4.1: Plot of applied axial load vs. axial deflection (at $x = L/2, y = 0, z = -h/2$) for unstiffened cylinder, for different values of the mode imperfection (— : $\hat{w}_i^{mn} = 10^{-5}$ cm; - - - : $\hat{w}_i^{mn} = 10^{-2}$ cm).

For the unstiffened cylinder (see Figure 4.1), the maximum buckling load q_{max} and the minimum postbuckling load q_{mpb} are almost coincident, and are approximately 60% of the linear buckling load q_b obtained through eigenvalue analysis. The postbuckling path is related to the coupling of modes (4,7) and (4,8), and its stiffness in the axial direction is approximately one-half of the membrane stiffness. For the axially stiffened cylinder (figure not included here) the reduction in the load-carrying capacity due to the smaller geometrical imperfection is found to be only 20%. But unlike the previous case, q_{mpb} is found to be considerably lower than q_{max} , and the postbuckling branch is characterized by a stiffness which is comparable to that of the prebuckling path; this is essentially due to the very high bending rigidity of the shapes involved during buckling (*i.e.*, modes (1,4),(1,5),(1,6)). The ring stiffened cylinder (results not shown here) showed the highest reduction of the load-carrying capacity, namely, 44% of the buckling load. Moreover, its deformed shape is almost axisymmetric, with a high number of axial waves (modes (14,1), (14,2) and (14,3)); in this case, no minimum postbuckling load is reached. Higher values of the maximum load have been obtained for very small values of the geometrical imperfections $\hat{w}_i^{mn} < 10^{-7}$ cm. Then, in this case the linearized buckling

analysis cannot yield any information about the real load-carrying capacity of the cylinder. Moreover, even the b-factor initial postbuckling analyses (Koiter [35]) are valid in the neighborhood of the maximum load for small values of geometrical imperfections only, so that they cannot be used to predict this decreasing behavior. When axial and ring stiffeners are used (see Figure 4.2), not only the buckling load is rapidly increased, but also a low imperfection-sensitivity occurs, and the reduction in the load-carrying capacity is approximately 20%.

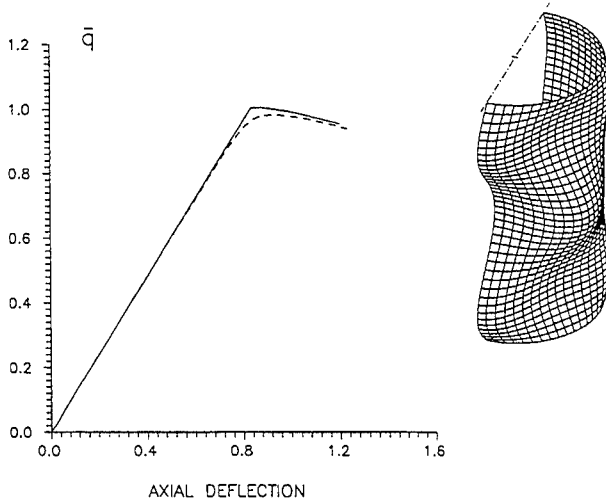


Figure 4.2: Plot of applied axial load vs. axial deflection (at $x = L/2, y = 0, z = -h/2$) for stiffened cylinder with 20 ring and 40 axial stiffeners, for different values of the mode imperfection (— : $\hat{w}_i^{mn} = 10^{-5}$ cm; - - - : $\hat{w}_i^{mn} = 10^{-2}$ cm).

5. ANALYSIS OF THE FREE EDGE PROBLEM USING VKFE

5.1 Introduction

The problem of determining the free edge stress fields in laminates subjected to inplane extension or bending is used to illustrate the variable kinematic finite element (VKFE) model methodology. The free edge problem is ideally suited for global local analysis, because the 3D stress field exists only in a boundary region (*i.e.*, free edge) of the laminate and elsewhere only a 2D stress state exists. Thus, the LWT2 elements can be used in the free edge (local) region and ESL elements can be used everywhere else (global region) to capture the stress fields accurately.

To demonstrate the accuracy and economy afforded by the variable kinematic finite elements, a global local analysis is performed to determine the nature of the free edge stress field in three different laminates subjected to axial extension: $(45/-45)_s$, $(45/0/-45/90)_s$, and $(45/0/-45/90/90/-45/0/45)_s$. The three laminates have length $2a$, width $2b$, and thickness $2h$. Each of the three laminates has a length-to-width ratio of 10 (*i.e.*, $a/b = 10$). The material plies in each laminate are of equal thickness h_k . The following geometric differences exist among the three laminates:

$$\begin{aligned}
(45/-45)_s \text{ laminate: } & \frac{b}{h} = 4, \quad h = 2h_k, \quad \frac{b}{h_k} = 8 \\
(45/0/-45/90)_s \text{ laminate: } & \frac{b}{h} = 15, \quad h = 4h_k, \quad \frac{b}{h_k} = 60 \\
(45/0/-45/90)_{2s} \text{ laminate: } & \frac{b}{h} = 15, \quad h = 8h_k, \quad \frac{b}{h_k} = 120
\end{aligned} \tag{5.1}$$

Each of the material plies in the three laminates is idealized as a homogeneous, orthotropic material; the material properties (expressed in the principal material coordinate system) are defined below.

Material plies in the four-layer laminate:

$$\begin{aligned}
E_1 &= 20 \times 10^6 \text{ psi}, \quad E_2 = E_3 = 2.1 \times 10^6 \text{ psi} \\
G_{12} = G_{23} = G_{13} &= 0.85 \times 10^6 \text{ psi}, \quad \nu_{12} = \nu_{23} = \nu_{13} = 0.21
\end{aligned} \tag{5.2a}$$

Material plies in the eight- and sixteen-layer laminates:

$$\begin{aligned}
E_1 &= 19.5 \times 10^6 \text{ psi}, \quad E_2 = E_3 = 1.48 \times 10^6 \text{ psi} \\
G_{12} = G_{23} = G_{13} &= 0.8 \times 10^6 \text{ psi}, \quad \nu_{12} = \nu_{23} = \nu_{13} = 0.3
\end{aligned} \tag{5.2b}$$

The origin of the global coordinate system coincides with the centroid of each of the 3D composite laminates. The x -coordinate is taken along the length, the y -coordinate is taken across the width, and the z -coordinate is taken through the thickness of the laminate. Since the laminate is symmetric about the xy -plane, only the upper half of each laminate is modeled. Thus the computational domain is defined by $(-a < x < a, -b < y < b, 0 < z < h)$. The displacement boundary conditions for all three laminates are:

$$u_1(a, y, z) = u_0, \quad u_1(-a, y, z) = u_2(-a, 0, 0) = u_2(a, 0, 0) = u_3(x, y, 0) = 0 \tag{5.3}$$

The slight differences in geometry and material properties among the three laminates allow comparison with solutions published in the literature. For the $(45/-45)_s$ laminate, Wang and Choi [12] have developed a quasi-3D elasticity solution. For the $(45/0/-45/90)_s$ and $(45/0/-45/90/90/-45/0/45)_s$ laminates, Whitcomb and Raju [13] obtained quasi-3D finite element solution using a highly refined mesh.

The variable kinematic finite elements are used in a simultaneous multiple model analysis (global-local analysis) of these three laminates in order to accurately yet efficiently determine the free edge stresses near the middle of one of the two free edges. The global region is modeled using first order shear deformable elements (FSDT); the local region, where accurate 3-D stresses are desired, is modeled with LWT2 elements.

First the $(45/-45)_s$ laminate will be used to assess the effects of subregion compatibility type (SSC or RSC) and size of the local LWT2 subregion on the accuracy of the computed transverse stresses near the free edge. For this purpose, five different finite element meshes are created. The 2-D, in-plane discretization for all five meshes is exactly the same, consisting of a 5×11 mesh of eight-node, quadratic, 2-D, quadrilateral finite elements (see Figure 5.1a). All elements have the same length $(2a/5)$; however, the width of the elements decreases as the free edge at (x, b, z) is approached. The

widths of the eleven rows of elements, as one moves away from the refined free edge, are $h_k/16, h_k/16, h_k/8, h_k/4, h_k/2, h_k, h_k, 2h_k, 3h_k, 3h_k$, and $5h_k$ (h_k =ply thickness). The five meshes differ only in the width of the local region where LWT2 elements are used. The LWT2 elements used in the local region employ eight quadratic layers through the laminate thickness (four per material layer) as shown in Figure 5.1b. The thickness of the numerical layers decreases as the $+45^\circ/-45^\circ$ interface is approached. From bottom to top, the layer thicknesses are $0.533h_k, 0.267h_k, 0.133h_k, 0.083h_k, 0.083h_k, 0.133h_k, 0.267h_k$, and $0.533h_k$.

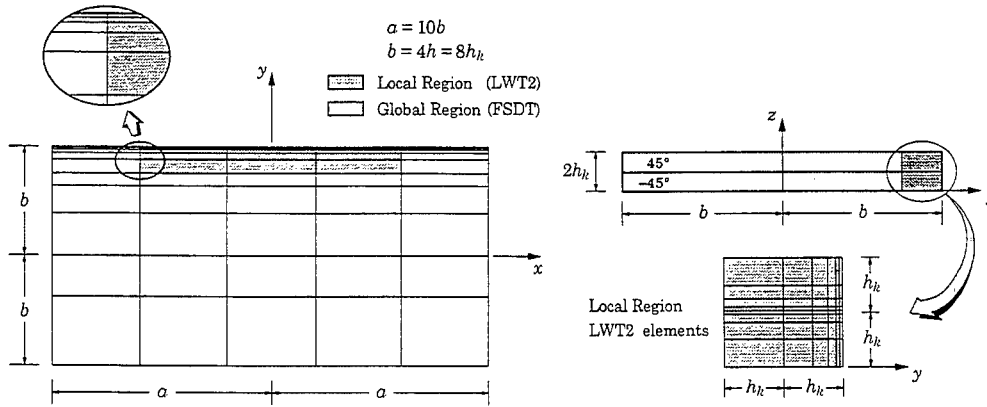


Figure 5.1: (a) The 2-D mesh of variable kinematic finite elements used to model a $(45^\circ/-45^\circ)_s$ laminate under axial extension. All elements are eight-node quadrilaterals. (b) Discretization within the local LWT2 region, on the yz -plane. The eight-node LWT2 elements in the local region use quadratic layers.

Table 5.1: The global local meshes used for the $(45^\circ/-45^\circ)_s$ laminate under axial extension.

Remarks	Mesh 1	Mesh 2	Mesh 3	Mesh 4	Mesh 5
Number of Elements in Local LWT2 Region	3×4	3×5	3×6	3×7	5×11
Width of Local Region	$\frac{1}{2}h_k$	h_k	$2h_k$	$3h_k$	$16h_k$
Length of Local Region	$\frac{6}{5}a$	$\frac{6}{5}a$	$\frac{6}{5}a$	$\frac{6}{5}a$	$2a$
Total Number of Active D.O.F. in VKFE Mesh (Strict Compatibility)	1,986	2,400	2,814	3,228	9,116
Total Number of Active D.O.F. in VKFE Mesh (Relaxed Compatibility)	2,354	2,800	3,246	3,690	9,116

h_k = thickness of a single material ply. All five VKFE meshes have the exact same inplane discretization (5×11).

Table 5.1 summarizes the five meshes used for the $(45/-45)_s$ laminate. Note that mesh 5 is not a global-local mesh. Mesh 5 uses LWT2 elements throughout the entire computational domain, thus serving as a control mesh for judging the accuracy of the four global-local meshes. In meshes 1 through 4, the local region (LWT2 elements) is adjacent to the free edge (x, b, z) and is centered about the plane $(0, y, z)$. In meshes 1 through 4, the length of the local region spans three fifths of the total length of the laminate; however, the width of the local region differs in each mesh ranging from $h_k/2$ to $3h_k$. Two runs are made with each of the four global-local meshes, the first using strict subregion compatibility along the FSDT-LWT2 boundary, and the second using relaxed subregion compatibility along the FSDT-LWT2 boundary.

The stresses are computed via the constitutive relations at the reduced Gauss points within the individual layers of each LWT2 element. All stresses are nondimensionalized as follows:

$$\bar{\sigma}_{ij} = \frac{20\sigma_{ij}}{\varepsilon_0 E_1} \quad (5.4)$$

where ε_0 is the nominal applied axial strain of $u_0/(2a)$.

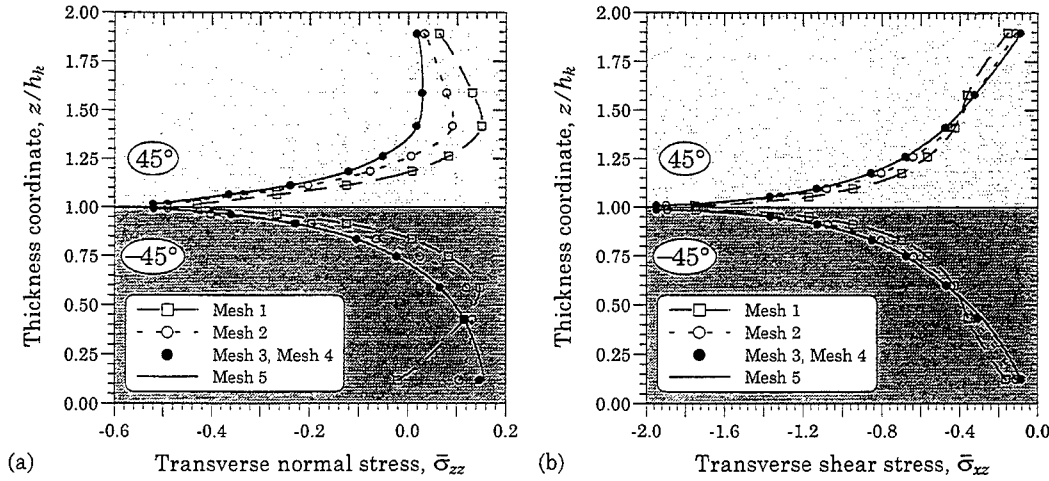


Figure 5.2: Interlaminar stress distribution through thickness of the $(45/-45)_s$ laminate near free edge. Results computed for meshes 1 through 5 with relaxed subregion compatibility.

Figures 5.2a and 5.2b show the distribution of the interlaminar stresses σ_{zz} and σ_{xz} near the free edge. The stress distributions were generated by computing the nondimensionalized stresses at a series of adjacent reduced Gauss points near the middle of the refined free edge, *i.e.*, along the line $(-0.115a, 0.998b, z)$, and then connecting these points with straight lines. The relaxed subregion compatibility conditions were used. All four of the global local meshes are successful in identifying the spikes in σ_{zz} and σ_{xz} that occur at the $45/-45$ interface. The results of meshes 3 and 4 are graphically indistinguishable

from the results of the control mesh, Mesh 5. While meshes 1 and 2 exhibit some error, they do capture the qualitative nature of the transverse stress distributions near the free edge. In meshes 1 and 2, the transverse shear stress are predicted more accurately than the transverse normal stress. The results also indicate that the boundary layer thickness (or the width of the local region) should be at least $2h_k$ to capture both interlaminar stresses accurately.

To illustrate the accuracy of the variable kinematic elements in determining the free edge stress field for more complex laminates, a simultaneous multiple model analysis (global-local analysis) is performed on an eight-ply $(45/0/-45/90)_s$ laminate, and a sixteen-ply $(45/0/-45/90/90/-45/0/45)_s$ laminate. Both of these laminates are subjected to axial extension similar to the previously examined $(45/-45)_s$ laminate. The in-plane discretization consists of a 5×11 2-D mesh of eight-node quadrilateral elements as shown previously in Figure 5.1. The local region is discretized with a 3×6 mesh of LWT2 elements. For the $(45/0/-45/90)_s$ laminate, the LWT2 elements contain 12 quadratic layers (three per material ply). Within each material ply the three quadratic layers have thicknesses of $0.25h_k$, $0.5h_k$, and $0.25h_k$ from bottom to top. For the $(45/0/-45/90/90/-45/0/45)_s$ laminate, the LWT2 elements contain 16 quadratic layers (two per material ply). Within each material ply both of the quadratic layers have thicknesses of $0.5h_k$. The $(45/0/-45/90)_s$ model contains 4,382 active degrees of freedom while the $(45/0/-45/90/90/-45/0/45)_s$ model contains 5,638 active degrees of freedom.

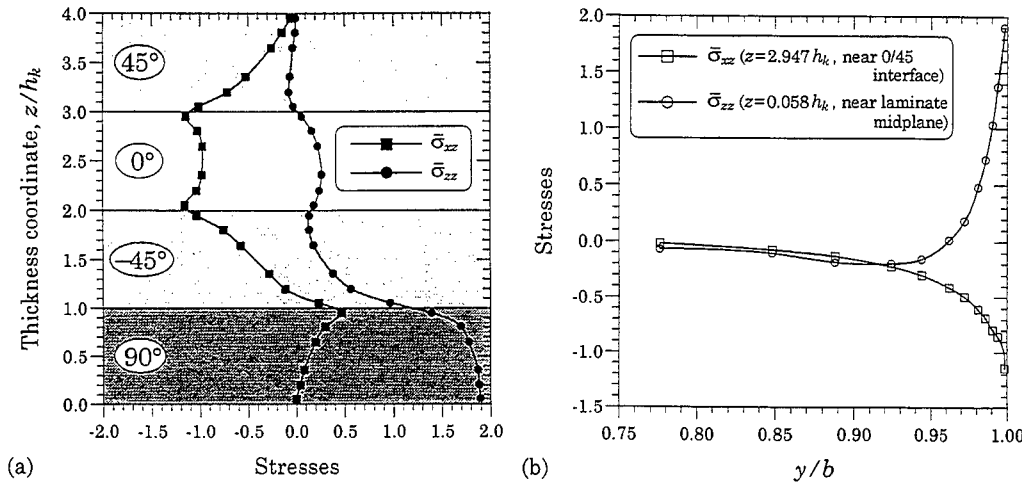


Figure 5.3: Interlaminar stress distributions in $(45/0/-45/90)_s$ laminate under axial extension. (a) Through the thickness near the free edge ($x = -0.115a, y = 0.998b$). (b) Across the width ($x = -0.115a$).

The computed transverse shear stress and transverse normal stress distributions for these two laminates are shown in Figures 5.3 and 5.4. For both laminates the maximum transverse normal stress occurs at the intersection of the $90/90$ interface and the free edge, while the maximum transverse shear stress occurs at the intersection of the $45/0$ and $0/-45$ interfaces with the free edge.

Both of these laminates have enough distinct material plies to make a full 3-D analysis prohibitively expensive, thus a sequential or simultaneous multiple model analysis is the only reasonable alternative. Many laminates have a very large number of distinct material plies, thus even with a multiple model analysis, the investigator may have to resort to using the sublaminate approach (*i.e.*, ply grouping) within the local LWT2 region. In this case the investigator would identify a target group of adjacent material plies that would receive one or more numerical layers each, while the remaining plies are grouped into one or more numerical layers and effectively homogenized. By performing several of these analyses, the investigator can gradually piece together a picture of the 3-D stress state through the laminate thickness within the local LWT2 region.

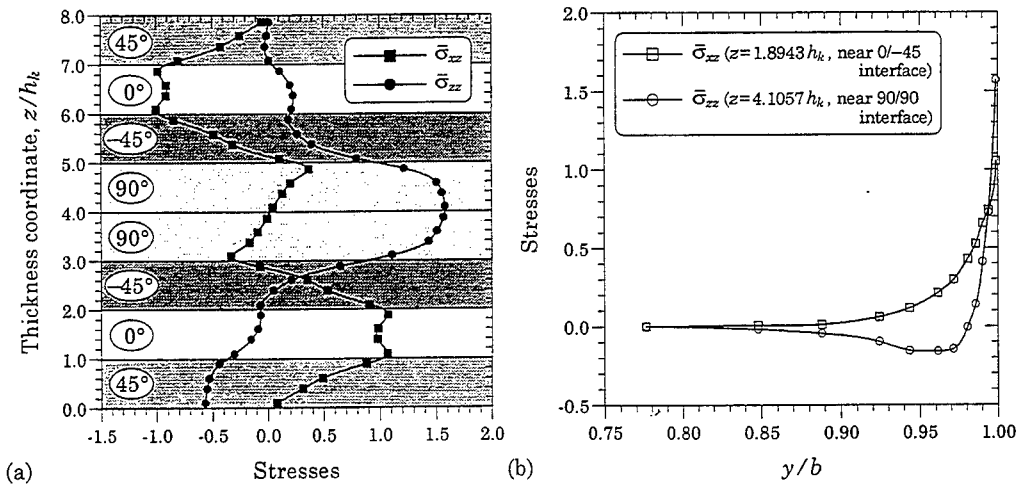


Figure 5.4: Interlaminar stress distributions in $(45/0/-45/90/90/-45/0/45)_s$ laminate under axial extension. (a) Through the thickness near the free edge ($x = -0.115a, y = 0.998b$). (b) Across the width ($x = -0.115a$).

All of the previous examples of this section were concerned with the determination of free edge stress fields in laminates subjected to axial tension. To demonstrate the effectiveness of the variable kinematic finite elements for determining free edge stresses in laminates subjected to bending, consider a simply supported $(45/-45)_s$ laminate subjected to a uniform transverse load. The physical dimensions and material properties of the $(45/-45)_s$ laminate will be the same as in the axial extension example, with the exception that the origin of the coordinate system will be placed at the bottom center of one of the ends of the laminated strip. Thus the laminate occupies the domain $(0 < x < 2a, -b < y < b, 0 < z < 2h)$ where $a = 10b = 40h = 80h_k$ and h_k is the thickness of a material ply. The displacement boundary conditions are

$$u_1(a, -b, 0) = u_2(0, y, z) = u_2(2a, y, z) = u_3(0, y, 0) = 0$$

The uniform transverse load q_0 is applied to the upper surface of the laminate and acts in the negative z direction. Note that there are no planes of symmetry in this problem, thus the computational domain consists of the entire laminate.

To accurately yet efficiently capture the free edge stresses, a global-local analysis is performed using a 2-D mesh of variable kinematic finite elements, where FSDT elements make up the majority of the computational domain and a small patch of LWT2 elements is used to resolve the free edge stress field within a localized region of interest, which is one of the free edges. To investigate the effect of reducing the length of the LWT2 subregion, four different global-local meshes are created. Each mesh has a total in-plane discretization of 9×11 elements (9 elements along the laminate length, 11 elements across the laminate width). As in the previous analyses of the $(45/-45)_s$ laminate under axial extension, the in-plane mesh is highly refined over one of the free edges and is coarse over the other free edge. Note that the collective length of the central three rows of equal length elements is denoted as a_0 . The remaining six rows of elements are of equal length $(2a - a_0)/6$. The in-plane discretization of the five meshes differ in the value of a_0 ; specifically $a_0 = 2h, 4h, 8h$, and $16h$ for meshes 1 through 4, respectively. Each of the four in-plane meshes is used with both a 3×6 LWT2 subregion and 5×6 LWT2 subregion (*i.e.*, three or five LWT2 elements in the x direction and six LWT2 elements in the y direction). The width of the LWT2 subregion is h in each case. Each of the LWT2 elements employs eleven quadratic layers through the laminate thickness: three layers in the bottom $+45^\circ$ ply, five layers in the two collective middle $-45/-45$ plies, and three layers in the top $+45^\circ$ ply. From bottom to top, the layer thicknesses are $0.6h_k, 0.3h_k, 0.1h_k, 0.1h_k, 0.3h_k, 1.2h_k, 0.3h_k, 0.1h_k, 0.1h_k, 0.3h_k$, and $0.6h_k$. By comparing the results of the 3×6 and 5×6 LWT2 subregions for each of the four meshes, the effect of LWT2 subregion length on solution accuracy can be established. Each of the global-local meshes uses relaxed subregion compatibility. Due to space limitations, only results obtained with Mesh 2 are presented here.

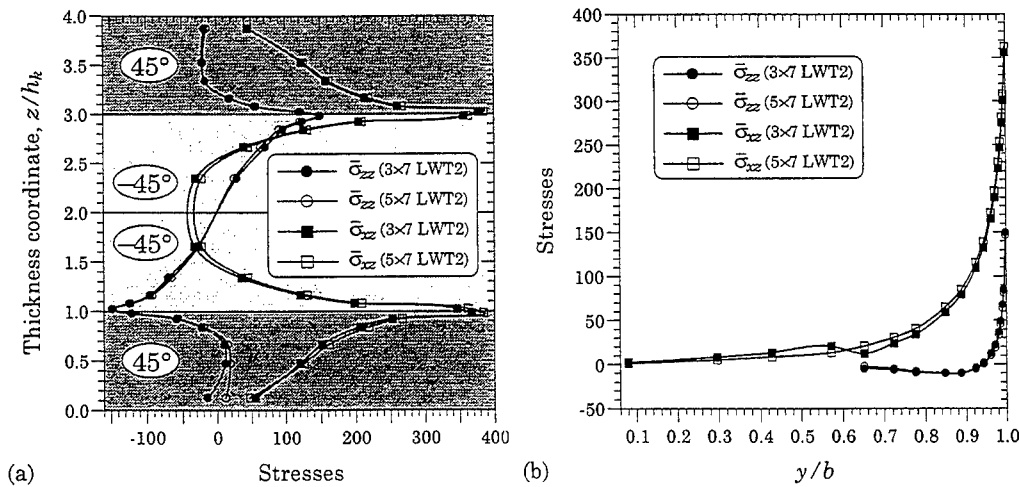


Figure 5.5: Interlaminar stress distributions in $(45/-45)_s$ laminate in bending (Mesh 2). (a) Through the thickness near the free edge at $x = a$ and $y = b$. (b) Across the width of laminate, near the upper $45/-45$ interface.

Figures 5.5a,b show the transverse stress distributions for mesh 2 where $a_0 = 4h$ and the width of the LWT2 subregion is $1.5h$, and meshes of 3×7 and 5×7 were used. The quantitative difference between the 3×7 and 5×7 results is small. In Figure 5.5b, the disruption in the transverse shear stress distribution at the FSDT/LWT2 interface is barely detectable. Further, the increased widths of the LWT2 subregions are adequate to show the complete decay of σ_{zz} .

6. SUMMARY

In this paper an overview of the author's recent research in the theoretical modeling of composite plates and shells is presented and applications of various theories to post-buckling, progressive failures, and free edge stresses in composite panels and shells are discussed. The layerwise theory of Reddy [15] is based on assumed displacement field, in which the thickness variation is represented using one-dimensional finite elements and thereby reducing the 3D continuum to a 2D problem. The procedure has the advantage of using independent approximation of thickness variations from inplane discretizations. Otherwise, the layerwise theory is indeed the same as the traditional 3-D displacement finite element model. Applications of the layerwise theory to stability and vibration of cylindrical shells and high velocity impact, and delamination in composites can be found in [36–40].

The underlying foundation of the variable kinematic element's composite displacement field is provided by a two-dimensional equivalent single layer plate theory (*e.g.*, the first order shear deformation theory). The layerwise displacement field of Reddy [15] is included as an optional, incremental enhancement to the displacement field of the two dimensional plate theory, so that the element can have full three dimensional modeling capability when needed. Discrete layer transverse shear effects and discrete layer transverse normal effects can be independently added to the element by including appropriate terms from the layerwise field. The variable kinematic model provides a robust computational approach for the analysis of real-world problems.

Acknowledgements The author is pleased to acknowledge the contributions of his colleagues, Drs. S. P. Engelstad, D. H. Robbins, Jr., and M. Savoia to the theories and numerical results presented in this paper. The research reported herein was carried out while the author was being supported by the Army Research Office (ARO) and the Air Force Office of Scientific Research (AFOSR). The support is gratefully acknowledged.

REFERENCES

1. Reddy, J. N., *Mechanics of Laminated Composite Plates*, CRC Press, Boca Raton, FL (1997).
2. Kirchhoff, G., "Über das Gleichgewicht und die Bewegung einer Elastischen Scheibe," *J. Angew. Math.*, **40**, 51–88 (1850).
3. Basset, A. B., "On the Extension and Flexure of Cylindrical and Spherical Thin Elastic Shells," *Phil. Trans. Royal Soc.*, (London) Ser. A, **181** (6), 433–480 (1890).
4. Reissner, E., "The Effect of Transverse Shear Deformation on the Bending of Elastic Plates," *Journal of Applied Mechanics*, **12**, 69–77 (1945).
5. Bollé, E., "Contribution au Probleme Lineaire de Flexion d'une Plaque Elastique," *Bull. Tech. Suisse. Romande.*, **73**, 281–285 and 293–298 (1947).

6. Hencky, H., "Über die Berücksichtigung der Schubverzerrung in ebenen Platten," *Ing. Arch.*, **16**, 72-76 (1947).
7. Hildebrand, F. B., Reissner, E., and Thomas, G. B., "Notes on the Foundations of the Theory of Small Displacements of Orthotropic Shells," NACA TN-1833, Washington, D. C. (1949).
8. Mindlin, R. D., "Influence of Rotatory Inertia and Shear on Flexural Motions of Isotropic, Elastic Plates," *Journal of Applied Mechanics, Transactions of ASME*, **18**, 31-38 (1951).
9. Vlasov, B. F., "Ob uravneniyakh teorii isgiba plastinok (On the Equations of the Theory of Bending of Plates)," *Izv. Akd. Nauk SSR, OTN*, **4**, 102-109 (1958).
10. Reissner, E., "Reflections on the Theory of Elastic Plates," *Applied Mechanics Reviews*, **38**(11), 1453-1464 (1985).
11. Pagano, N. J., "Exact Solutions for Rectangular Bidirectional Composites and Sandwich Plates," *Journal of Composite Materials*, **4**, 20-34 (1970).
12. Wang, S. S. and Choi, I., "Boundary-Layer Effects in Composite Laminates, Part I: Free Edge Stress Singularities, and Part II: Free Edge Stress Solutions and Basic Characteristics," *Journal of Applied Mechanics*, **49**, 541-560 (1982).
13. Whitcomb, J. D., and Raju, I. S., "Analysis of Interlaminar Stresses in Thick Composite Laminates With and Without Edge Delamination," *Delamination and Debonding of Materials*, ASTM STP 876, W. S. Johnson(ed.), American Society for Testing and Materials, Philadelphia, pp. 69-94, 1985.
14. Wittrick, W. H., "Analytical Three-Dimensional Elasticity Solutions to Some Plate Problems and Some Observations on Mindlin's Plate Theory," *International Journal of Solids and Structures*, **23**, 441-464 (1987).
15. Reddy, J. N., "A Generalization of Two-Dimensional Theories of Laminated Composite Plates," *Communications in Applied Numerical Methods*, **3**, 173-180 (1987).
16. Robbins, D. H. and Reddy, J. N., "Modeling of Thick Composites Using a Layerwise Laminate Theory," *International Journal for Numerical Methods In Engineering*, **36**, 655-677 (1993).
17. Savoia, M. and Reddy, J. N., "A Variational Approach to Three-Dimensional Elasticity Solutions of Laminated Composite Plates," *Journal of Applied Mechanics*, **59**, S166-S175 (1992).
18. Mote, C. D., "Global-Local Finite Element," *International Journal for Numerical Methods in Engineering*, **3**, 565-574 (1971).
19. Dong, S. B., "Global-Local Finite Element Methods," *State-of-the-Art Surveys on Finite Element Technology*, A. K. Noor and W. D. Pilkey (eds.), ASME, 451-474 (1983).
20. Reddy, J. N., and Robbins, D. H., "Analysis of Composite Laminates Using Variable Kinematic Finite Elements," *RBCM-Journal of the Brazilian Society of Mechanical Sciences*, **14**(4), 299-326 (1992).
21. Reddy, J. N., and Robbins, D. H., "A Simultaneous Multiple Model Approach for the Analysis of Composite Laminates," *Journal of the Aeronautical Society of India*, **45**, 157-177 (1993).
22. Robbins, D. H. and Reddy, J. N., "Variable Kinematic Modeling of Laminated Composite Plates," *International Journal for Numerical Methods in Engineering*, **39**, 2283-2317 (1996).

23. Krishna Murty, A. V., "Higher Order Theory for Vibration of Thick Plates," *AIAA Journal*, **15**(12), 1823-1824 (1977).
24. Reddy, J. N., "A Simple Higher-Order Theory for Laminated Composite Plates," *Journal of Applied Mechanics*, **51**, 745-752 (1984).
25. Di Sciuva, M., "A Refined Transverse Shear Deformation Theory for Multilayered Anisotropic Plates," *Atti della Accademia delle Scienze di Torino*, **118**, 269-295 (1984).
26. Phan, N. D., and Reddy, J. N., "Analysis of Laminated Composite Plates Using a Higher-Order Shear Deformation Theory," *International Journal for Numerical Methods in Engineering*, **21**, 2201-2219 (1985).
27. Di Sciuva, M., "An Improved Shear-Deformation Theory for Moderately Thick Multilayered Anisotropic Shells and Plates," *Journal of Applied Mechanics*, **54**(3), 589-596 (1987).
28. Reddy, J. N., "A General Non-Linear Third-Order Theory of Plates with Moderate Thickness," *International Journal of Non-Linear Mechanics*, **25**(6), 677-686 (1990).
29. Starnes, J. H., Jr. and Rouse, M., "Postbuckling and Failure Characteristics of Selected Flat Rectangular Graphite-Epoxy Plates Loaded in Compression," AIAA Paper No. 81-0543 (1981).
30. Engelstad, S. P., Reddy, J. N., and Knight, N. F., Jr., "Postbuckling Response and Failure Prediction of Graphite-Epoxy Plates Loaded in Compression," *AIAA Journal*, **30**(8), 2106-2113 (1992).
31. Chao, W. C. and Reddy, J. N., "Analysis of Laminated Composite Shells Using a Degenerated 3-D Element," *International Journal for Numerical Methods in Engineering*, **20**, 1991-2007 (1984).
32. Reddy, J. N. and Savoia, M., "The Layer-Wise Shell Theory for Postbuckling of Laminated Circular Cylindrical Shells," *AIAA Journal*, **30**(8), 2148-2154 (1992).
33. Savoia, M. and Reddy, J. N., "Post-Buckling Behavior of Stiffened Cross-Ply Cylindrical Shells," *J. Appl. Mechanics*, **61**, 998-1000 (1994).
34. Barbero, E. J., Reddy, J. N., and Teply, J. L., "General Two-Dimensional Theory of Laminated Cylindrical Shells," *AIAA Journal*, **28**(3), 544-553 (1990).
35. Koiter, W. T., "On the stability of elastic equilibrium," Thesis, Delft (1945); Engl. Transl. issued as NASA TT-F10833, 1967.
36. Hutchinson, J. W. and Amazigo, J. C., "Imperfection-Sensitivity of Eccentrically Stiffened Cylindrical Shells," *AIAA Journal*, **5**, 392-401 (1967).
37. Barbero, E. J. and Reddy, J. N., "Modeling of Delamination in Composite Laminates Using a Layer-Wise Plate Theory," *International Journal of Solids and Structures*, **28**(3), 373-388 (1991).
38. Nosier, A., Kapania, R. K., and Reddy, J. N., "Free Vibration Analysis of Laminated Plates Using a Layerwise Theory," *AIAA Journal*, **31**(12), 2335-2346 (1993).
39. Nosier, A., Kapania, R. K., and Reddy, J. N., "Low-Velocity Impact of Laminated Composites Using a Layerwise Theory," *Computational Mechanics*, **13** (5), 360-379 (1994).
40. Robbins, D. H. and Reddy, J. N., "The Effects of Kinematic Assumptions on Computed Strain Energy Release Rates for Delaminated Composite Plates," *Mathematical Modelling and Scientific Computing*, **1**, 50-66 (1993).

ANALYTICAL METHODS I

TRANSVERSE VIBRATION OF ORTHOTROPIC ELLIPTIC PLATES USING ORTHOGONAL POLYNOMIALS IN THE RAYLEIGH-RITZ METHOD

S. Chakraverty* and M. Petyt

Institute of Sound and Vibration Research, University of Southampton
Southampton, SO17 1BJ U.K.

Abstract - Two dimensional boundary characteristic orthogonal polynomials in the Rayleigh-Ritz method have been used to study the transverse doubly symmetric vibration of orthotropic elliptic and circular plates. The first four natural frequencies are reported here for various values of aspect ratio of the ellipse. Results are given for various boundary conditions at the edges i.e. the boundary may be any of clamped, simply-supported or free. Numerical results are presented here for several orthotropic material properties. Most of the results for elliptical plate reported here are entirely new and are not found elsewhere except a very few results for only the fundamental frequency for a clamped boundary and few for a free boundary.

INTRODUCTION

Application of composite materials in engineering structures require information about the vibration characteristics of anisotropic materials. The free vibration of orthotropic plates is an important area of such behaviour. Orthotropic materials have extensive application in modern technology such as in modern missiles, space crafts, nuclear reactors etc. A vast amount of work has been done for vibration of orthotropic skew, triangular, circular, annular and polygonal plates as mentioned by Bert [1-6] and Leissa [18-21]. But the authors have found very little work on the vibration of elliptic and circular plates with rectangular orthotropy.

For a circular plate with rectangular orthotropy, only a few results are available in the existing literature, namely Dong and Lopez [14], Leissa [18], Narita [25], Rajappa [27], Sakata [28], and also some of the references mentioned therein. For elliptic plates with rectangular orthotropy even less work has been carried out. The only two references known to the authors are Sakata [28] and Narita [26]. Sakata [28] deals with only the fundamental frequency for a clamped elliptic plate. A Ritz method analysis is carried out by taking a complete power series as a trial function by Narita [26] to obtain the first few natural frequencies for an orthotropic elliptical plate with a free boundary. Numerical results are illustrated there by two figures only, for two types of orthotropic material properties.

The present study deals with the use of two dimensional boundary characteristic orthogonal polynomials in the Rayleigh-Ritz method. Recently orthogonal polynomials have been used extensively to find the vibration characteristics of different types of plate geometries with various boundary conditions at the edges. Some of the

* Present address : Central Building Research Institute, Roorkee-247 667, U.P., India.

references in this connection are Bhat [7,8], Dickinson and Blasio [13], Kim and Dickinson [15,16], Laura et al. [17], Liew and Lam [22] and Liew et al. [23]. Chakraverty [9] and Singh and Chakraverty [29-35] have already applied this method to free vibration of isotropic circular, elliptic, annular, skew and triangular plates and also elliptic plates with variable thickness and have obtained excellent results. They have also reported the orthogonal polynomials generated over all the above mentioned domains in a recent paper [36]. Chakraverty and Chakrabarti [11] and Chakraverty [10] have also applied this method to the determination of the static deflection of circular and elliptic plates. In a more recent paper the authors [12] use this method for nonhomogeneous elliptic plates, viz. when the modulus of elasticity and the density of the material are nonhomogeneous. Here the same orthogonal polynomials generated by Chakraverty [9] and Singh and Chakraverty [29-31, 36] have been used to determine the transverse vibration of elliptic and circular plates with rectangular orthotropy having clamped, simply-supported or free boundary at the edges.

METHOD OF SOLUTION

Let us take the domain occupied by the elliptic plate be

$$S = \{ (x,y), x^2/a^2 + y^2/b^2 \leq 1, x,y \in \mathbb{R} \}, \quad (1)$$

where a and b are the semi major and minor axes of the ellipse respectively.

The maximum strain energy V_{\max} of the deformed orthotropic plate is given by Timoshenko and Woinowsky [37] as

$$V_{\max} = (1/2) \iint_R [D_x W_{xx}^2 + 2\nu_x D_y W_{xx} W_{yy} + D_y W_{yy}^2 + 4D_{xy} W_{xy}^2] dydx, \quad (2)$$

where $W(x,y)$ is the deflection of the plate, W_{xx} is the second derivative of W with respect to x . The D coefficients are bending rigidities defined by,

$$\left. \begin{aligned} D_x &= E_x h^3 / (12(1 - \nu_x \nu_y)) \\ D_y &= E_y h^3 / (12(1 - \nu_y \nu_x)) \\ D_y \nu_x &= D_x \nu_y \\ \text{and } D_{xy} &= G_{xy} h^3 / 12 \end{aligned} \right\}, \quad (3)$$

where E_x, E_y are Young's moduli and ν_x, ν_y are Poisson's ratios in the x, y directions, G_{xy} is shear modulus and h is the uniform thickness.

The maximum kinetic energy is given by,

$$T_{\max} = (1/2) \rho h \omega^2 \iint_R W^2 dydx, \quad (4)$$

where ρ is the mass density per unit volume and ω is the radian natural frequency of the plate. Now equating the maximum strain and kinetic energies we have the Rayleigh quotient as,

$$\omega^2 = \frac{\iint_R [D_x W_{xx}^2 + 2\nu_x D_y W_{xx} W_{yy} + D_y W_{yy}^2 + 4D_{xy} W_{xy}^2] dydx}{h\rho \iint_R W^2 dydx}. \quad (5)$$

Substituting the N -term approximation

$$W(x,y) = \sum_{j=1}^N c_j \phi_j(x,y), \quad (6)$$

and minimizing ω^2 as a function of the coefficients c_j 's we have,

$$\sum_{j=1}^N (a_{ij} - \lambda^2 b_{ij}) c_j = 0, i = 1, 2, \dots, N, \quad (7)$$

where, $a_{ij} = \iint_{R'} [(D_x/H) \phi_i^{XX} \phi_j^{XX} + (D_y/H) \phi_i^{YY} \phi_j^{YY} + v_x (D_y/H) (\phi_i^{XX} \phi_j^{YY} + \phi_i^{YY} \phi_j^{XX})$

$$+ 2(1 - v_x (D_y/H)) \phi_i^{XY} \phi_j^{XY}] dY dX, \quad (8)$$

$$b_{ij} = \iint_{R'} \phi_i \phi_j dY dX, \quad (9)$$

$$\lambda^2 = a^4 \rho h \omega^2 / H, \quad (10)$$

$$\text{and } H = D_y v_x + 2D_{xy}, \quad (11)$$

where ϕ_i 's are orthogonal polynomials and are generated as described in Chakraverty [9] and Singh and Chakraverty [29-31, 36]. ϕ_i^{XX} is the second derivative of ϕ_i with respect to X and the new domain R' is defined by

$$R' = \{ (X, Y), X^2 + Y^2 / m^2 \leq 1, X, Y \in R \},$$

where, $X = x/a$, $Y = y/a$ and $m = b/a$.

When the ϕ_i 's are orthonormal, equation (7) reduces to

$$\sum_{j=1}^N (a_{ij} - \lambda^2 \delta_{ij}) c_j = 0, i = 1, 2, \dots, N, \quad (12)$$

where, $\delta_{ij} = 0$, if $i \neq j$,
 $= 1$, if $i = j$.

The three parameters D_x/H , D_y/H and v_x define the orthotropic property of the material under consideration. It is to be noted here that for an isotropic plate these parameters reduce to $D_x/H = D_y/H = 1$ and $v_x = v_y = v$. Equation (12) is a standard eigenvalue problem and can be solved for the vibration characteristics.

To generate the orthogonal polynomials we start with a linearly independent set

$$F_i(X, Y) = f(X, Y) \{ f_i(X, Y) \}, i = 1, 2, \dots, N. \quad (13)$$

where $f(X, Y)$ satisfies the essential boundary conditions and $f_i(X, Y)$ are taken as the combinations of terms of the form $X^{m_i} Y^{n_i}$ where m_i and n_i are nonnegative even integers. The function f is defined by,

$$f(X, Y) = (1 - X^2 - Y^2 / m^2)^p, \quad (14)$$

p takes the value of 0, 1 or 2 according as the boundary of the elliptic (or circular) plate is free, simply-supported or clamped. From $F_i(X, Y)$, we generate an orthogonal set by the well-known Gram-Schmidt process as mentioned in [9, 29-31, 36].

4. NUMERICAL WORK AND DISCUSSIONS

There are five parameters viz., D_x/H , D_y/H , v_x , p and m , and it is not possible here to give the results for all possible combinations of the parameters. We have reported here results for five types of material properties which we have denoted by M1 to M5 as follows :

- i) M1 : Glass-epoxy ($E_x/E_y = 4.67$, $G_{xy}/E_y = 0.50$, $v_x = 0.26$),
- ii) M2 : Boron-epoxy ($E_x/E_y = 11.03$, $G_{xy}/E_y = 0.30$, $v_x = 0.23$),
- iii) M3 : Kevlar ($E_x = E_y = 27.579 \times 10^9 \text{ N/m}^2$, $G_{xy} = 3.447 \times 10^9 \text{ N/m}^2$, $v_x = 0.14$),

iv) M4 : $D_x/H = 2, D_y/H = 0.5, \nu_x = 0.3,$

v) M5 : $D_x/H = 0.5, D_y/H = 2, \nu_x = 0.075.$

For the materials M1, M2 and M3 the values of D_x/H and D_y/H can be found easily by applying the relations (3) and (11). In the following subsections we will discuss the results for different boundary conditions at the edges of the elliptic and circular plates with rectangular orthotropy.

Clamped boundary :

In Tables 1 to 5, the first four natural frequencies for doubly symmetric modes are reported for various values of $m = 0.2, 0.4, 0.5, 0.6, 0.8$ and 1.0 for the materials M1 to M5 respectively. The first row denoted by 'C' in these tables for each m gives the results for clamped boundary. All the results except for the fundamental mode for an elliptic plate (i.e. when $m \neq 1.0$) with a clamped boundary are new and are not found elsewhere. So, comparison can be made for an elliptic plate for the fundamental frequencies only. Few results are available for a clamped circular plate which are also compared here.

Sakata [28] has given a formula for finding the fundamental frequency for a clamped elliptic plate as

$$(\text{natural frequency})^2 = \omega_s^2 = \frac{41.52}{\rho h a^4} \{D_x + \frac{2}{3}(a/b)^2 H + (a/b)^4 D_y\}. \quad (15)$$

As mentioned by him, Rajappa [27] indicates that an accurate value of the numerical coefficient in equation (15) should be 40.0. He also reported that the coefficient is 39.22, according to McNitt's solution [24], for the isotropic clamped elliptical plate which is obtained by the use of Galerkin's method. Finally he mentioned that upon taking the deflection function used in each analysis and the resultant solution into consideration, one should assume that the more accurate coefficient of equation (15) is 39.22.

As per the above discussions by taking the numerical coefficient of (15) as 41.52 due to Sakata [28], 40.0 due to Rajappa [27] and 39.22 due to McNitt [24], we have computed the fundamental frequencies for M1 to M5 for various values of m and report them in Table 6. In this table λ_s, λ_R and λ_M denote the frequencies computed by the numerical coefficients given by Sakata, Rajappa and McNitt in (15) respectively and the last column is our results computed by the present method. It is clear from the Table 6 that by using the coefficient of McNitt the results are more closer to the present results.

Narita [25] has reported a few results for a clamped circular plate. We have compared our results with his in Tables 4 and 5 for $m=1.0$ and found them to be in good agreement. Comparison of the present results with that of Dong and Lopez [14], who have reported the results for a Kevlar (material M3) clamped circular plate has been given in Table 3 for $m=1.0$. They have given a table for a factor K in the frequency formula

$$\omega = K \frac{1}{a^2} \sqrt{\frac{D_x}{\rho h}}. \quad (16)$$

Our present frequency parameter is given by (10). In order to compare with Dong and Lopez [14] the conversion

$$\lambda = K\sqrt{D_x/H}.$$

has been used. We have found that the results compared show good agreement.

Simply-supported boundary :

Again in Tables 1 to 5, the first four natural frequencies for doubly symmetric modes are presented for various values of m for the mentioned material properties. The second row denoted by 'S' in these tables for each m gives the results for a simply-supported boundary. The authors have found no results in the existing literature for this boundary condition except one for the fundamental frequency of a circular plate with material M4 given by Rajappa [27]. This has been reported in Table 4 for $m = 1.0$.

Free boundary :

The third row denoted by 'F' in each of the Tables 1 to 5 (for M1 to M5) for each m gives the first four natural frequencies for doubly symmetric modes for a free boundary. Only one reference by Narita [26] is known to the authors for this boundary conditions, who has illustrated the results by two figures for materials M4 and M5. The authors have found approximate results from the graphs given by Narita for $m = 0.5$ and 1.0 . These are included in Tables 4 and 5 showing good agreement with ours. All other results are entirely new and not found in the open literature.

Special case (isotropic plate) :

As mentioned in earlier sections, the present problem reduces to that of an isotropic plate if $D_x/H = D_y/H = 1$ and $\nu_x = \nu_y = \nu$, for which results are already reported by Chakraverty [9] and Singh and Chakraverty [29-31], where they have already made comparison with all the existing results for the isotropic case. Using the present computer program taking $D_x/H = D_y/H = 1$ and $\nu_x = \nu_y = 0.3$, we have again computed the results for various values of m which are given in Table 7. These are found to be exactly the same as reported in earlier papers (Chakraverty [9] and Singh and Chakraverty [29-31]). Although it is to be noted here that the present study gives only the doubly symmetric modes. So comparison can be made with [9,29-31] for this special type of mode.

Discussion of the results :

It is seen from Tables 1 to 5 (for materials M1 to M5), that for any boundary conditions i.e. for clamped, simply-supported or free, the frequencies decrease as m is increased. For a clamped boundary the frequencies are maximum and for a free boundary these are minimum for each m for all the materials considered here.

As mentioned by Narita [26] for a free boundary, the frequencies for $m=1.0$ in cases M4 and M5 are identical, since one case is just that of a 90 degree rotation of the other. This is true for all the boundary conditions (clamped, simply-supported and free)

as seen from Tables 4 and 5 for $m = 1.0$. Also rightly mentioned by him that as m is decreased, both cases show different variations.

To fix the number of approximations N needed, calculations were carried out for different values of N until the first five significant digits had converged. It was found that the results converged to five significant digits in about 12 to 15 approximations. To get a feel of the convergence, that is how fast the results converge, Table 8 gives results for the first two frequencies for free, simply-supported and clamped (i.e. $p=0, 1$ and 2 respectively) boundary and increasing N from 2 to 15. The results of Table 8 were obtained for the material M4 and taking the aspect ratio of the ellipse to be 0.5.

CONCLUDING REMARKS

Although this approach has been extensively used in isotropic plate vibration problems, it has been applied successfully in this study for the first time to the present problem of an orthotropic plate with a curved boundary (especially for elliptical). The use of two dimensional boundary characteristic orthogonal polynomials in the Rayleigh-Ritz method makes the problem a computationally efficient and simple numerical technique for finding vibration characteristics.

Acknowledgements - The first author wishes to thank the Department of Science and Technology, Government of India for the financial support under the BOYSCAST scheme which permitted this work to be carried out. The same author wishes to extend his thanks to Professor Bani Singh, Department of Mathematics, University of Roorkee, India for helpful discussions.

REFERENCES

1. C.W. Bert 1976 Shock Vibration Digest **8**, 37-48, 15-24. Dynamics of composite and sandwich panels-parts I and II.
2. C.W. Bert 1979 Shock Vibration Digest **11**, 13-23. Recent research in composite and sandwich plate dynamics.
3. C.W. Bert 1980 Recent Advances in Structural Dynamics, Vol.2 (Edited by M. Petyt), pp. 693-712, Southampton, England. Vibration of composite structures.
4. C.W. Bert 1982 Shock Vibration Digest **14**, 17-34. Research on dynamics of composite and sandwich plates, 1979-1981.
5. C.W. Bert 1985 Shock Vibration Digest **17**, 3-15. Research on dynamic behavior of composite and sandwich plates-IV.
6. C.W. Bert 1991 Shock Vibration Digest **23**, 3-14. Research on dynamic behavior of composite and sandwich plates-V:part I.
7. R.B. Bhat 1985 J. Sound Vib. **102**, 493-499. Natural frequencies of rectangular plates using characteristic orthogonal polynomials in Rayleigh-Ritz method.
8. R.B. Bhat 1987 J. Sound Vib. **114**, 65-71. Flexural vibration of polygonal plates using characteristic orthogonal polynomials in two variables.
9. S. Chakraverty 1992 Ph. D. Thesis, University of Roorkee, India. Numerical solution of vibration of plates.
10. S. Chakraverty 1996 J. Inst. Engrs. (India), **77**, 7-11. An efficient method for finding deflection of circular and elliptic plates.

11. S. Chakraverty and S.C. Chakrabarti 1993 ISIAM Conference, Univ. of Roorkee, India. Deflection of circular plate using orthogonal polynomials.
12. S.Chakraverty and M. Petyt 1996 Communicated. Vibration of nonhomogeneous elliptic plates using orthogonal polynomials in two dimensions.
13. S.M. Dickinson and A.DI. Blasio 1986 J. Sound Vib. **108**, 51-62. On the use of orthogonal polynomials in Rayleigh-Ritz method for the study of the flexural vibration and buckling of isotropic and orthotropic rectangular plates.
14. S.B. Dong and A.E. Lopez 1985 Int. J. Solids Struc. **21**, 515-526. Natural vibrations of a clamped circular plate with rectilinear orthotropy by least-squares collocation.
15. C.S. Kim and S.M. Dickinson 1987 J. Sound Vib.**117**, 249-261. The flexural vibration of rectangular plates with point supports.
16. C.S. Kim and S.M. Dickinson 1989 J. Sound Vib. **130**,363-377. On the lateral vibration of thin annular and circular composite plates subject to certain complicating effects.
17. P.A.A. Laura, R.H. Gutierrez and R.B. Bhat 1989 AIAA J. **27**, 921-922. Transverse vibration of a trapezoidal cantilever plate of variable thickness.
18. A.W. Leissa 1969 NASA SP 160. U.S. Government Printing Office, Washington, D.C. Vibration of Plates.
19. A.W. Leissa 1978 Shock Vibration Digest **10**, 21-35. Recent research in plate vibrations : 1973-76 : complicating effects.
20. A.W. Leissa 1981 Shock Vibration Digest **13**, 19-36. Plate vibration research, 1976-80 : complicating effects.
21. A.W. Leissa 1987 Shock Vibration Digest **19**, 10-24. Recent studies in plate vibrations : 1981-85 Part II. complicating effects.
22. K.M. Liew and K.Y. Lam 1990 J. Sound Vib. **139**, 241-252. Application of two dimensional plate functions to flexural vibrations of skew plates.
23. K.M. Liew, K.Y. Lam and S.T. Chow 1990 Comput. Struct. **34**, 79-85. Free vibration analysis of rectangular plates using orthogonal plate functions.
24. R.P. McNitt 1962 J. Aero. Sci. **29**, 1124-1125. Free vibration of a clamped elliptical plate.
25. Y. Narita 1983 J. Appl. Mech. Trans. ASME **50**, 691-692. Flexural vibrations of clamped polygonal and circular plates having rectangular orthotropy.
26. Y. Narita 1985 J. Sound Vib. **100**, 83-89. Natural frequencies of free, orthotropic elliptical plates.
27. N.R. Rajappa 1963 AIAA J. **1**, 1194-1195. Free vibration of rectangular and circular orthotropic plates.
28. T. Sakata 1976 J. Sound Vib. **48**, 405-412. A reduction method for problems of vibration of orthotropic plates.
29. B. Singh and S. Chakraverty 1991 Int. J. Mech. Sci. **33**, 741-751. Transverse vibration of completely free elliptic and circular plates using orthogonal polynomials in Rayleigh-Ritz method.
30. B. Singh and S. Chakraverty 1992 Comput. Struc. **43**, 439-443. On the use of orthogonal polynomials in Rayleigh-Ritz method for the study of transverse vibration of elliptic plates.
31. B. Singh and S. Chakraverty 1992 J. Sound Vibr. **152**, 149-155. Transverse vibration of simply-supported elliptic and circular plates using orthogonal polynomials in two variables.

32. B. Singh and S. Chakraverty 1992 Int. J. Mech. Sci. **34**, 947-955. Transverse vibration of triangular plates using characteristic orthogonal polynomials in two variables.
33. B. Singh and S. Chakraverty 1993 J. Sound Vib. **162**, 537-546. Transverse vibration of annular circular and elliptic plates using characteristic orthogonal polynomials in two dimensions.
34. B. Singh and S. Chakraverty 1994 J. Sound Vib. **173**, 157-178. Flexural vibration of skew plates using orthogonal polynomials in two variables.
35. B. Singh and S. Chakraverty 1994 J. Sound Vib. **173**, 289-299. Use of characteristic orthogonal polynomials in two dimensions for transverse vibrations of elliptic and circular plates with variable thickness.
36. B. Singh and S. Chakraverty 1994 Communications Num. Methods Engg. **10**, 1027-1043. Boundary characteristic orthogonal polynomials in numerical approximation.
37. S. Timoshenko and S. Woinowsky-Krieger 1953 New York : McGraw-Hill Book Co. Theory of Plates and Shells.

TABLE 1. First four frequencies for M1 (Glass-epoxy)

m	B.C.	λ_1	λ_2	λ_3	λ_4
0.2	C	136.51	196.95	291.55	466.41
	S	64.107	117.60	206.17	409.55
	F	13.630	65.255	140.94	173.93
0.4	C	38.849	88.032	175.06	184.52
	S	18.605	61.498	137.37	142.19
	F	13.390	38.493	60.220	89.774
0.5	C	27.376	76.667	121.46	161.41
	S	13.072	55.477	90.674	132.26
	F	13.073	25.723	53.370	75.552
0.6	C	21.476	70.761	87.569	143.23
	S	10.229	52.034	65.331	116.75
	F	12.414	18.980	45.614	70.261
0.8	C	16.242	51.940	67.479	106.96
	S	7.7392	38.107	50.355	87.232
	F	9.1133	14.525	34.126	51.391
1.0	C	14.225	36.986	64.880	76.886
	S	6.8010	26.488	48.426	62.934
	F	6.1159	13.667	26.022	36.673

TABLE 2. First four frequencies for M2 (Boron-epoxy)

m	B.C.	λ_1	λ_2	λ_3	λ_4
0.2	C	168.53	259.89	417.53	696.00
	S	79.662	159.90	309.73	638.62
	F	25.786	121.82	171.30	265.60
0.4	C	50.152	138.17	226.22	296.88
	S	24.296	100.48	168.95	244.19
	F	24.892	46.821	94.403	131.82
0.5	C	37.181	127.35	150.14	246.18
	S	18.022	94.475	112.24	200.19
	F	23.421	32.225	75.029	124.36
0.6	C	30.966	106.38	124.77	205.10
	S	15.009	78.933	93.283	166.79
	F	19.551	26.810	62.517	103.92
0.8	C	25.907	66.946	119.38	142.61
	S	12.545	48.243	89.098	117.49
	F	11.800	24.569	47.020	63.564
1.0	C	24.057	49.722	97.930	117.13
	S	11.606	34.186	79.308	87.263
	F	7.6796	23.623	34.689	48.005

TABLE 3. First four frequencies for M3 (Kevlar plate)

m	B.C.	λ_1	λ_2	λ_3	λ_4
0.2	C	236.43	295.66	395.79	614.13
	S	108.59	159.70	248.31	483.99
	F	11.327	54.504	147.44	334.94
0.4	C	63.077	104.17	175.08	297.10
	S	30.141	66.453	133.80	237.03
	F	11.268	52.720	64.491	108.49
0.5	C	42.043	81.320	152.46	207.00
	S	20.323	54.991	121.91	154.17
	F	11.195	41.805	51.783	82.099
0.6	C	30.666	69.813	141.28	146.10
	S	14.915	49.238	108.72	115.79
	F	11.077	30.031	48.282	68.153
0.8	C	19.726	59.825	85.039	126.11
	S	9.6424	43.998	63.624	103.10
	F	10.611	18.074	38.472	58.262
1.0	C	15.142	53.990	58.822	101.64
	C [14]	15.211	53.877	57.243	100.80
	S	7.4094	40.097	44.034	82.883

TABLE 4. First four frequencies for M4 ($D_x/H = 2.$, $D_y/H = 0.5$, $\nu_x = 0.3$)

m	B.C.	λ_1	λ_2	λ_3	λ_4
0.2	C	109.24	161.12	237.51	378.39
	S	51.430	97.665	168.77	328.25
	F	9.9167	47.656	114.02	128.42
0.4	C	31.435	70.860	136.290	148.33
	S	14.789	48.970	109.09	110.56
	F	9.7549	31.230	45.286	77.013
0.5	C	22.195	60.510	98.269	123.94
	S	10.325	43.171	73.196	100.77
	F	9.5450	20.771	42.340	61.740
	F [26]	9.5	20.89	-	-
0.6	C	17.358	54.865	71.309	113.27
	S	8.0119	39.805	53.012	92.290
	F	9.1259	15.208	37.888	54.813
0.8	C	12.910	41.976	52.078	85.964
	S	5.9520	30.525	38.698	70.016
	F	7.0020	11.160	28.646	41.995
1.0	C	11.097	30.255	49.134	61.971
	C [25]	11.05	30.20	48.75	-
	S	5.1628	21.585	36.598	50.388
	S [27]	5.3591	-	-	-
	F	4.7725	10.385	21.170	30.870
	F [26]	4.7	10.9	21.4	-

TABLE 5. First four frequencies for M5 ($D_x/H = 0.5, D_y/H = 2., \nu_x = 0.075$)

m	B.C.	λ_1	λ_2	λ_3	λ_4
0.2	C	207.23	252.19	330.19	510.78
	S	95.060	134.10	198.58	374.13
	F	4.9659	23.959	65.277	213.88
0.4	C	54.622	80.560	118.75	189.19
	S	25.715	48.832	84.387	164.12
	F	4.9583	23.828	57.010	64.212
0.5	C	36.017	58.970	94.062	154.58
	S	17.060	37.324	70.030	135.22
	F	4.9483	23.665	37.499	62.950
	F [26]	5.0	24.0	38.5	-
0.6	C	25.847	47.096	80.878	127.99
	S	12.256	30.877	62.271	95.300
	F	4.9325	23.414	26.687	54.861
0.8	C	15.717	35.430	68.145	74.168
	S	7.3947	24.485	54.548	55.281
	F	4.8774	15.615	22.643	38.506
1.0	C	11.097	30.255	49.134	61.971
	C [25]	11.05	30.20	48.75	
	S	5.1628	21.585	36.598	50.388
	F	4.7725	10.385	21.170	30.870
	F [26]	4.7	10.9	21.4	-

Table 6. Comparison of fundamental frequencies for clamped boundary with Sakata[28], Rajappa [27] and McNitt [24]

MAT.	m	λ_S	λ_R	λ_M	λ
M1	0.2	147.24	144.52	143.11	136.51
	0.4	40.383	39.637	39.249	38.849
	0.5	28.280	27.757	27.485	27.376
	0.6	22.131	21.722	21.509	21.476
	0.8	16.742	16.433	16.272	16.242
	1.0	14.720	14.448	14.306	14.225
M2	0.2	180.60	177.27	175.53	168.53
	0.4	51.841	50.883	50.385	50.152
	0.5	38.308	37.601	37.232	37.181
	0.6	31.904	31.315	31.008	30.966
	0.8	26.823	26.327	26.069	25.907
	1.0	25.130	24.666	24.424	24.057
M3	0.2	261.08	256.26	253.75	236.43
	0.4	67.016	65.778	65.133	63.077
	0.5	44.080	43.266	42.842	42.043
	0.6	31.880	31.291	30.984	30.666
	0.8	20.351	19.975	19.779	19.726
	1.0	15.596	15.308	15.158	15.142
M4	0.2	117.26	115.09	113.96	109.24
	0.4	32.664	32.061	31.747	31.435
	0.5	22.932	22.509	22.288	22.195
	0.6	17.891	17.561	17.389	17.358
	0.8	13.303	13.057	12.929	12.910
	1.0	11.466	11.254	11.144	11.097
M5	0.2	229.37	225.13	222.93	207.23
	0.4	58.630	57.547	56.983	54.622
	0.5	38.211	37.505	37.138	36.017
	0.6	27.173	26.671	26.409	25.847
	0.8	16.332	16.030	15.873	15.717
	1.0	11.466	11.254	11.144	11.097

Table 7. First five frequencies for isotropic case

m	B.C.	λ_1	λ_2	λ_3	λ_4
0.2	C	149.66	198.55	266.25	414.22
	S	69.684	112.92	174.94	330.50
	F	6.7778	32.817	89.171	154.72
0.4	C	40.646	71.414	119.63	200.63
	S	19.514	46.823	89.356	151.01
	F	6.7321	32.287	41.937	82.041
0.5	C	27.377	55.985	102.79	132.35
	S	13.213	38.354	81.705	98.790
	F	6.6705	27.768	31.538	61.919
0.6	C	20.195	47.820	93.804	93.969
	S	9.7629	33.777	70.210	75.938
	F	6.5712	19.921	30.355	50.481
0.8	C	13.229	39.972	55.781	82.921
	S	6.3935	29.139	41.677	67.826
	F	6.1861	12.128	26.454	40.045
1.0	C	10.216	34.878	39.773	69.675
	S	4.9351	25.613	29.720	56.910
	F	5.3583	9.0031	21.835	35.319

Table 8. Convergence for M4 ($D_x/H = 2.$, $D_y/H = 0.5$, $\nu_x = 0.3$, $m = 0.5$)

N	p=0		p=1		p=2	
	λ_1	λ_2	λ_1	λ_2	λ_1	λ_2
2	11.313	-	11.037	-	22.267	-
3	10.650	25.206	10.339	60.963	22.199	64.689
4	9.6378	24.828	10.331	45.820	22.196	60.815
5	9.6195	23.693	10.329	44.120	22.196	60.717
6	9.5982	21.029	10.325	43.992	22.195	60.699
7	9.5572	21.020	10.325	43.358	22.195	60.530
8	9.5483	20.993	10.325	43.211	22.195	60.514
9	9.5462	20.941	10.325	43.190	22.195	60.513
10	9.5451	20.772	10.325	43.186	22.195	60.512
11	9.5450	20.771	10.325	43.175	22.195	60.510
12	9.5450	20.771	10.325	43.172	22.195	60.510
13	9.5450	20.771	10.325	43.171	22.195	60.510
14	9.5450	20.771	10.325	43.171	22.195	60.510
15	9.5450	20.771	10.325	43.171	22.195	60.510

A Unified Approach for the Free Vibration Analysis of Circular Plates and Shells of Revolution

Anand V. Singh
Department of Mechanical &
Materials Engineering
The University of Western Ontario
London, Ontario, N6A 5B9, Canada

SUMMARY

Simplified Ritz approach for the free vibration analysis of a class of geometrically axisymmetric problems is presented. In particular, it is demonstrated that a single numerical scheme handles successfully the problems of circular plates, cylindrical shells and conical shells. Energy functions are derived from the equations of the theory of elasticity. They are tailored such that the governing equations representing thin to moderately thick plates and shells come out very conveniently. The shear deformation and rotary inertia are parts of the formulation. The investigation includes: comparison of the numerical results with those obtained by finite element methods and the exact solutions from the classical techniques. Numerical results for the natural frequencies and associated three dimensional mode shapes for annular plate are presented. Symmetric and asymmetric modes of vibration of cylindrical and conical shells are discussed in this paper.

INTRODUCTION

Approximate numerical methods to solve problems in elasticity have been proposed by many over a century. Using the variational principles and through the minimization of certain energy functions, it is possible to deduce equations of static or dynamic equilibrium of elastic bodies and obtain state-of-stress as well as the natural frequencies. Lord Rayleigh and W. Ritz independently proposed energy methods to find the natural frequencies of vibrating systems. Their method was later extended by such prominent mathematicians as R. Courant, K. Friedrichs, B. G. Galerkin, L. V. Kantorovich and others. For proper citation of the publications by these well known researchers, reference can be made of the work by Timoshenko and Woinowsky-Krieger [1]. In 1950, D. Young [2] solved the vibration problem of rectangular plates using the Ritz method. Functions defining the normal modes of vibration of a uniform beam were chosen to represent the deflected shape of the plate. Since the late fifties, development of approximate numerical methods picked up momentum and prospered leaps and bounds. Engineers and mathematicians used digital computers to solve complicated problems of interests to the aerospace industries. Finite elements methods were developed, solution techniques were automated, and now-a-days engineers routinely use large scale commercially available FE codes for stress and vibration analysis of structures. The use of finite element methods does not appear to be slowing down and very rapidly growing computer

technology is providing speed and accuracy to this method. However, the size of the FE model of a structure can grow very fast and sometimes become very difficult to manage. During the last twenty five years, Rayleigh-Ritz method has been used very effectively for the free vibration analysis of plates and shallow shells, by researchers like: A. W. Leissa et. al [3], S. M. Dickinson [4] and others. Rayleigh-Ritz method provides very accurate results for problems with only a few unknowns.

Presented in this paper is a simplified Ritz approach for the free vibration analysis of geometrically axisymmetric plates and shells. Governing equations are derived from the basic elasticity equations in spherical coordinate system. Equations are solved using the method of separating variables. Simple algebraic polynomials define the displacement fields and the boundary conditions are enforced by manipulating the coefficients in the polynomials. Validity and the effectiveness of the present solution scheme are examined by comparing with exact results from the classical techniques and finite element methods. Both symmetric and asymmetric modes of vibration of annular plates, conical shells and cylindrical shells are studied in detail.

BASIC EQUATIONS FROM THE THEORY OF ELASTICITY

In this section just the essential equations from the theory of elasticity in spherical coordinate system (ϕ, θ, r) are presented. Here, ϕ = angular coordinate along the meridian, θ = angular coordinate along the tangent to the horizontal circles and r = distance measured radially outward. The displacement components are defined by $u', v',$ and w' along $\phi, \theta,$ and r respectively at any arbitrary point in the body of the shell. Also, r_1 and r_2 are the radii of curvature of a surface containing the arbitrary point along ϕ and θ directions respectively. Strain-displacement relations are (Sokolnikoff [4])

$$\begin{aligned}\epsilon_{\phi}' &= (\partial u' / \partial \phi + w') / r_1 \\ \epsilon_{\theta}' &= (\partial v' / \partial \theta + u' \cos \phi) / (r_2 \sin \phi) + w' / r_2 \\ \epsilon_{\phi\theta}' &= (\partial u' / \partial \theta - v' \cos \phi) / (r_2 \sin \phi) + (1/r_1) \partial v' / \partial \phi \\ \epsilon_{r\phi}' &= \partial u' / \partial r - u' / r_1 + (1/r_1) \partial w' / \partial \phi \\ \epsilon_{r\theta}' &= \partial v' / \partial r - v' / r_2 + (1/r_2 \sin \phi) \partial w' / \partial \theta\end{aligned}\quad (1)$$

Define strain and stress vectors by $\{\epsilon\}^T = \{\epsilon_{\phi}', \epsilon_{\theta}', \epsilon_{\phi\theta}', \epsilon_{r\phi}', \epsilon_{r\theta}'\}$ and $\{\sigma\}^T = \{\sigma_{\phi}', \sigma_{\theta}', \sigma_{\phi\theta}', \sigma_{r\phi}', \sigma_{r\theta}'\}$ respectively. Also, introduce the energy expressions which are integral parts of the Ritz method. The strain-energy and kinetic energy expressions are given by

$$U = (1/2) \int_{\text{vol.}} \{\sigma\}^T \{\epsilon\} dV \quad (2)$$

$$\text{and } K = (1/2) \int_{\text{vol.}} \rho \{\partial \Delta' / \partial t\}^T \{\partial \Delta' / \partial t\} dV \quad (3)$$

where, ρ = mass density of the material, and $\{\Delta'\}^T = \{u', v', w'\}$.

EQUATIONS WITH REFERENCE TO THE SURFACE OF REVOLUTION

In this section, shell equations are derived by considering its middle surface as the reference. The formulation is divided into parts which basically comprise working in the three directions ϕ , θ and r one by one. The first part deals with integration over the thickness of the shell. By doing this, the three dimensional system is transformed into a two dimensional one defined along the reference surface. The radii of curvature can be written as $r_1 = R_1 + \zeta$ and $r_2 = R_2 + \zeta$, where ζ represents the distance measured radially outward from the middle surface and R_1 and R_2 are the principal radii of curvatures. Also, now it is appropriate to express u' , v' , and w' in terms of their counterparts u , v , and w at the middle surface and the components β_1 and β_2 of rotation of the normal to the middle surface.

$$u' = u + \zeta \beta_1 \quad v' = v + \zeta \beta_2 \quad w' = w \quad (4)$$

Theory developed using the above variation is known as the first-order-shear-deformation-theory of shells (Reissner [6] and Nagdhi [7]). For higher order, one can consider more terms with additional parameters in equation (4), e.g. $u' = u + \zeta \beta_1 + \zeta^2 \psi_1 + \zeta^3 \varphi_1 + \dots$. Substitute equation (4) into equation (1) to obtain the strain components in terms of strains and curvatures on the middle surface.

$$\begin{aligned} (1 + \zeta/R_1) \epsilon_\phi' &= \epsilon_\phi + \zeta \kappa_\phi \\ (1 + \zeta/R_2) \epsilon_\theta' &= \epsilon_\theta + \zeta \kappa_\theta \\ (1 + \zeta/R_1)(1 + \zeta/R_2) \epsilon_{\phi\theta}' &= (1 + \zeta/R_1)(\gamma_1 + \zeta \delta_1) + (1 + \zeta/R_2)(\gamma_2 + \zeta \delta_2) \quad (5) \\ (1 + \zeta/R_1) \epsilon_{r\phi}' &= \gamma_{r\phi} \\ (1 + \zeta/R_2) \epsilon_{r\theta}' &= \gamma_{r\theta} \end{aligned}$$

$$\begin{aligned} \text{where, } \epsilon_\phi &= (\partial u / \partial \phi + w) / R_1 \\ \epsilon_\theta &= (\partial v / \partial \theta + u \cos \phi) / (R_2 \sin \phi) + w / R_2 \\ \gamma_1 &= (\partial u / \partial \theta - v \cos \phi) / (R_2 \sin \phi) ; \gamma_2 = (1/R_1) \partial v / \partial \phi \\ \gamma_{r\phi} &= \beta_1 - u / R_1 + (1/R_1) \partial w / \partial \phi \\ \gamma_{r\theta} &= \beta_2 - v / R_2 + (1/R_2 \sin \phi) \partial w / \partial \theta \\ \kappa_\phi &= (1/R_1) \partial \beta_1 / \partial \phi \\ \kappa_\theta &= (\partial \beta_2 / \partial \theta + \beta_1 \cos \phi) / (R_2 \sin \phi) \\ \delta_1 &= (\partial \beta_1 / \partial \theta - \beta_2 \cos \phi) / (R_2 \sin \phi) \\ \delta_2 &= (1/R_1) \partial \beta_2 / \partial \phi \end{aligned} \quad (6)$$

Terms like (u'/R_1) and (v'/R_2) in $\epsilon_{r\phi}'$ and $\epsilon_{r\theta}'$ respectively are of minor significance in the overall picture. Therefore, the second terms of $(1 + \zeta/R_1)$ and $(1 + \zeta/R_2)$ are dropped.

The matrix form of the strain-stress relation is

$$\{\sigma\} = [E]\{\epsilon\}. \quad (7)$$

For orthotropic materials, the non-zero terms of the fifth order matrix $[E]$ are : $E_{11} = E_{\phi\phi}$, $E_{12} = E_{21} = E_{\phi\theta}$, $E_{22} = E_{\theta\theta}$, $E_{33} = G_{\phi\theta}$, $E_{44} = k_s G_{\phi\zeta}$, $E_{55} = k_s G_{\theta\zeta}$. Here, E 's and G 's are the elastic and shear moduli respectively. The shear correction factor k_s is used here to retain the effects due to the parabolic distribution of the transverse shear stresses. Its value is: $k_s = 5/6$ (E. Reissner) or $\pi^2/12$ (R. D. Mindlin).

Substitution of equations (5), (6) and (7) into the strain energy equation (2) yields

$$\begin{aligned} U = (1/2) \int_{vol} [& E_{11} (a_0 \epsilon_\phi \epsilon_\phi + 2a_1 \epsilon_\phi \kappa_\phi + a_2 \kappa_\phi \kappa_\phi) + 2E_{12} \{ c_0 \epsilon_\phi \epsilon_\theta \\ & + c_1 (\epsilon_\phi \kappa_\theta + \epsilon_\theta \kappa_\phi) + c_2 \kappa_\phi \kappa_\theta \} + E_{22} (b_0 \epsilon_\theta \epsilon_\theta + 2b_1 \epsilon_\theta \kappa_\theta + b_2 \kappa_\theta \kappa_\theta) \\ & + E_{33} (b_0 \gamma_1 \gamma_1 + 2b_1 \gamma_1 \delta_1 + b_2 \delta_1 \delta_1 + a_0 \gamma_2 \gamma_2 + 2a_1 \gamma_2 \delta_2 + a_2 \delta_2 \delta_2) \\ & + E_{44} a_0 \gamma_{r\phi} \gamma_{r\phi} + E_{55} b_0 \gamma_{r\theta} \gamma_{r\theta}] R_1 R_2 \sin \phi d\phi d\theta \end{aligned} \quad (8)$$

where, $dV = (1 + \zeta/R_1)(1 + \zeta/R_2) R_1 R_2 \sin \phi d\phi d\theta d\zeta$ and parameters for $m = 0, 1, 2, \dots$ etc. are

$$\begin{aligned} a_m &= \int \zeta^m (1 + \zeta/R_1)^{-1} (1 + \zeta/R_2) d\zeta; \\ b_m &= \int \zeta^m (1 + \zeta/R_1)(1 + \zeta/R_2)^{-1} d\zeta; \\ c_m &= \int \zeta^m d\zeta; \quad d_m = \int \zeta^m (1 + \zeta/R_1)^{-1} (1 + \zeta/R_2)^{-1} d\zeta; \end{aligned} \quad (9)$$

Now define the mid-surface strain components as a vector

$$\{\chi\}^T = \{\epsilon_\phi \quad \epsilon_\theta \quad \gamma_1 \quad \gamma_2 \quad \gamma_{r\phi} \quad \gamma_{r\theta} \quad \kappa_\phi \quad \kappa_\theta \quad \delta_1 \quad \delta_2\} \quad (10)$$

so that the strain energy expression can be written in the following simple form.

$$U = (1/2) \int (\{\chi\}^T [D_0] \{\chi\} dA) \quad (11)$$

Matrix $[D_0]$ having the order of 10 in the above equation is

$$\begin{bmatrix}
a_0 E_{11} & c_0 E_{12} & 0 & 0 & 0 & 0 & a_1 E_{11} & c_1 E_{12} & 0 & 0 \\
c_0 E_{12} & b_0 E_{22} & 0 & 0 & 0 & 0 & c_1 E_{12} & b_1 E_{22} & 0 & 0 \\
0 & 0 & b_0 E_{33} & c_0 E_{33} & 0 & 0 & 0 & 0 & b_1 E_{33} & c_1 E_{33} \\
0 & 0 & c_0 E_{33} & a_0 E_{33} & 0 & 0 & 0 & 0 & c_1 E_{33} & a_1 E_{33} \\
0 & 0 & 0 & 0 & a_0 E_{44} & 0 & 0 & 0 & 0 & 0 \\
0 & 0 & 0 & 0 & 0 & b_0 E_{55} & 0 & 0 & 0 & 0 \\
a_1 E_{11} & c_1 E_{12} & 0 & 0 & 0 & 0 & a_2 E_{11} & c_2 E_{12} & 0 & 0 \\
c_1 E_{12} & b_1 E_{22} & 0 & 0 & 0 & 0 & c_2 E_{12} & b_2 E_{22} & 0 & 0 \\
0 & 0 & b_1 E_{33} & c_1 E_{33} & 0 & 0 & 0 & 0 & b_2 E_{33} & c_2 E_{33} \\
0 & 0 & c_1 E_{33} & a_1 E_{33} & 0 & 0 & 0 & 0 & c_2 E_{33} & a_2 E_{33}
\end{bmatrix} \quad (12)$$

Similarly, the kinetic energy for the shell under consideration is given by

$$K = (1/2) \int \{\partial \Delta / \partial t\}^T [Z_0]^T [Z_0] \{\partial \Delta / \partial t\} (1 + \zeta/R_1)(1 + \zeta/R_2) R_1 R_2 \sin \phi \, d\phi \, d\theta \quad (13)$$

Here, $\{\Delta\}^T = \{u \, v \, w \, \beta_1 \, \beta_2\}$ and

$$[Z_0] = \begin{bmatrix} 1 & 0 & 0 & \zeta & 0 \\ 0 & 1 & 0 & 0 & \zeta \\ 0 & 0 & 1 & 0 & 0 \end{bmatrix} \quad (14)$$

By integrating the kinetic energy expression over the thickness of the shell, equation (13) is reduced to

$$K = (1/2) \int \{\partial \Delta / \partial t\}^T [C_0] \{\partial \Delta / \partial t\} R_1 R_2 \sin \phi \, d\phi \, d\theta \quad (15)$$

$$\text{where, } [C_0] = \begin{bmatrix} r_0 & 0 & 0 & r_1 & 0 \\ 0 & r_0 & 0 & 0 & r_1 \\ 0 & 0 & r_0 & 0 & 0 \\ r_1 & 0 & 0 & r_2 & 0 \\ 0 & r_1 & 0 & 0 & r_2 \end{bmatrix} \quad (16)$$

and $r_m = \int \zeta^m (1 + \zeta/R_1)(1 + \zeta/R_2) \, d\zeta$ for $m = 0, 1, 2, \dots$ etc.

The above derivation, very typical to a text book approach, is quite general for the analysis of shells of revolution. Any shell of revolution can be analyzed using the above, as long as the middle surface is defined properly by its principal radii of curvature. Common

shells like spherical, conical, and cylindrical can be dealt with without any difficulty. In the present study, a conical shell is considered in detail because of the reason that equations and solution procedure derived for the analysis of the conical shell can be used directly to study the behaviour of circular cylindrical shells and circular plates. For example: a circular cylinder of finite length is a special case of frustum of a cone with zero cone-angle. Similarly, if the cone angle is made equal to $\pi/2$, equations and corresponding solutions are good for solid as well as annular circular plates.

ANALYSIS OF CONICAL SHELL

Assume that a conical shell shown in Figure 1 is defined by the following parameters.

- a = radius of the large opening; b = radius of the small opening; ℓ = length of the cone along its axis; $R_1 = \infty$, $r = R_2 \sin \phi_0$; $ds = R_1 d\phi$. Angle ϕ_0 can be obtained from $\cot \phi_0 = (a - b)/\ell$. Similarly, $r = s \cos \phi_0$, $R_2 = s \cot \phi_0$, s = distance measured from the apex (vertex) of the cone and h = thickness.

Using the above, the strain components in equation (6) become

$$\begin{aligned}
 \epsilon_s &= \partial u / \partial s & \epsilon_\theta &= (u \cos \phi_0 + \partial v / \partial \theta) / r + w / R_2 \\
 \gamma_1 &= (\partial u / \partial \theta - v \cos \phi_0) / r & \gamma_2 &= \partial v / \partial s \\
 \gamma_{r\phi} &= \partial w / \partial s + \beta_1 & \gamma_{r\theta} &= -v / R_2 + (1/r) \partial w / \partial \theta + \beta_2 \\
 \kappa_\phi &= \partial \beta_1 / \partial s & \kappa_\theta &= (\beta_1 \cos \phi_0 + \partial \beta_2 / \partial \theta) / r \\
 \delta_1 &= (\partial \beta_1 / \partial \theta - \beta_2 \cos \phi_0) / r & \delta_2 &= \partial \beta_2 / \partial s
 \end{aligned} \tag{17}$$

The solution procedure started with the process of separating variables. First, the radial parameter ζ was taken care of. Next is the turn of the coordinate θ which is isolated by means of the Fourier harmonic functions $\cos(n\theta)$ and $\sin(n\theta)$ as follows.

$$\begin{aligned}
 u &= U(s) \cos n\theta & v &= V(s) \sin n\theta & w &= W(s) \cos n\theta \\
 \beta_1 &= B_1(s) \cos n\theta & \beta_2 &= B_2(s) \sin n\theta
 \end{aligned} \tag{18}$$

Substitute equation (18) into (17) to get

$$\{\chi(s, \theta)\} = [H(\theta)] \{\Gamma(s)\} \tag{19}$$

Here, $[H(\theta)]$ is a diagonal matrix of order 10 having the following terms.

$$\begin{aligned}
 H_1 &= H_2 = H_5 = H_7 = H_8 = \cos n\theta & \text{and} \\
 H_3 &= H_4 = H_6 = H_9 = H_{10} = \sin n\theta.
 \end{aligned} \tag{20}$$

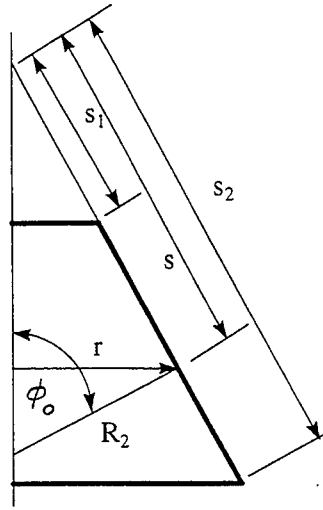


Figure 1. Profile of a Conical Shell with Dimensions.

Components of the strain vector $\{\Gamma(s)\}$ are given by:

$$\begin{aligned}
 \Gamma_1 &= \partial U / \partial s & \Gamma_2 &= (U \cos \phi_0 + nV) / r + W / R_2 \\
 \Gamma_3 &= (-nU - V \cos \phi_0) / r & \Gamma_4 &= \partial V / \partial s \\
 \Gamma_5 &= \partial W / \partial s + B_1 & \Gamma_6 &= -V / R_2 - (n/r)W + B_2 \\
 \Gamma_7 &= \partial B_1 / \partial s & \Gamma_8 &= (B_1 \cos \phi_0 + nB_2) / r \\
 \Gamma_9 &= (-nB_1 - B_2 \cos \phi_0) / r & \Gamma_{10} &= \partial B_2 / \partial s
 \end{aligned} \tag{21}$$

It is seen that the strain-components given by equation (21) contains only one variable (i.e. s). To work on this variable, a dimensionless parameter ξ is introduced such that

$$s = \frac{1}{2}(s_2 + s_1) + \frac{1}{2}(s_2 - s_1)\xi \tag{22}$$

The solution for displacement components $U(s)$, $V(s)$, ...etc. in equation (18) is assumed in algebraic polynomial form. Therefore, the polynomial for $U(s)$ or $U(\xi)$ is assumed to be

$$U(\xi) = [a_0(1 - \xi)^p + a_1(1 - \xi)^{p-1}(1 + \xi) + a_2(1 - \xi)^{p-2}(1 + \xi)^2 + \dots + a_{p-1}(1 + \xi)^p] \quad (23)$$

Similarly, other displacement components and rotation of the normal to the middle surface can be expressed by the same functional form as above with different sets of coefficients, viz. b_i , c_i , d_i and e_i for $V(\xi)$, $w(\xi)$, $B_1(\xi)$ and $B_2(\xi)$ respectively. Coefficients a_i , b_i , c_i , d_i and e_i for $i = 0, 1, 2, 3, \dots, p-1$, are unknown quantities at this stage and to be determined later. If p is the number of terms in each of the above expressions, then in all there are $5p$ unknowns.

Selection of this particular form of the polynomials, in the opinion of the author, has some distinct advantages. Firstly, the above polynomial is complete. Therefore, adding sufficiently large number of terms to the solution polynomials will result in the exact solution of the problem. Secondly, the boundary conditions at the two ends of the shell can be enforced by simply manipulating these unknown coefficients. For example: by letting $a_0 = a_1 = 0$, the condition of $U(\xi) = \partial U(\xi)/\partial \xi = 0$ at $\xi = -1$ is met. The same condition can be obtained at the other end corresponding to $\xi = +1$, by letting $a_{p-1} = a_{p-2} = 0$. Just for simple displacement to be zero at the both ends, set the first and last coefficients of the polynomial to zero.

By substituting equation(23) into equation(21), one can write

$$\{\Gamma\} = [B]\{Q\} \quad (24)$$

where, $[B]$ = matrix of size $10 \times (5p)$ and $\{Q\}^T = \{a_i, b_i, c_i, d_i, e_i\}$ for $i = 0, 1, 2, \dots, p-1$. Substitute $\{\Gamma\}$ from equation(24) into the strain-energy function to get:

$$U = (1/2) \{Q\}^T \left(\int [B]^T \int [H]^T [D_0] [H] r d\theta [B] ds \right) \{Q\} \\ = (1/2) \{Q\}^T [k] \{Q\} \quad (25)$$

where, $\int [H]^T [D_0] [H] d\theta = \alpha [D_0]$ and $[k] = \frac{1}{2}(s_2 - s_1) \alpha \int [B]^T [D_0] [B] r(\xi) d\xi$. The integration limits are: from 0 to 2π for θ and -1 to +1 for ξ .

The infinitesimal area on the middle surface $dA = (R_2 \sin \phi_0 d\theta)(R_1 d\phi) = r d\theta ds$. It can be easily shown that $\alpha = \pi$ for asymmetric case and 2π for symmetric case (i.e. $n = 0$).

Now, proceed to obtain the mass matrix of the shell by following the same procedure as above. Substitute equations (18) into the displacement vector $\{\Delta\}$ of equation (13) to get: $\{\Delta\} = [H(\theta)] [A(\xi)] \{Q\}$ and the kinetic energy expression

$$K = (1/2) \{\partial Q / \partial t\}^T \int [A(\xi)]^T [H(\theta)]^T [C_0] [H(\theta)] [A(\xi)]^T dA \{\partial Q / \partial t\}$$

Using $\int [H(\theta)]^T [C_0] [H(\theta)] d\theta = \alpha [C_0]$, the above equation reduces to

$$K = (1/2) \{ \partial Q / \partial t \}^T [m] \{ \partial Q / \partial t \} \quad (26)$$

where, $[m] = \frac{1}{2}(s_2 - s_1)\alpha \int [A(\xi)]^T [C_0] [A(\xi)]^T r(\xi) d\xi$.

Matrices $[C_0]$ and $[D_0]$ have already been obtained for a shell of revolution. Factors a_0, a_1, a_2, b_0 , etc. for the conical shell are deduced and given below.

$$\begin{aligned} a_0 = b_0 = c_0 = r_0 = h; \quad a_1 = -b_1 = r_1 = (1/12) h^3/(aR_2) \text{ and } c_1 = 0; \\ a_2 = b_2 = c_2 = r_2 = (1/12) (h^3/a^2) \end{aligned} \quad (27)$$

The strain and kinetic energy expressions have been derived in terms of the geometric and material properties of the conical shell. Also they are quadratic functions of the unknown coefficients a_i, b_i, c_i, d_i , and e_i for $i = 0, 1, 2, \dots, p-1$. Applying the variational principles to the potential energy $\Pi = U - K$, one can easily come up with the matrix equation: $([k] - \Omega^2[m]) \{Q\} = 0$, for the free vibration analysis of the conical shell.

NUMERICAL EXAMPLES.

Numerical computations are performed for the symmetric and asymmetric free vibration analysis of circular plates, cylindrical shells and conical shells. These cases are discussed separately in the following. Only one program based on the method discussed in this paper is used to obtain results. To run the computer program, one has to assign the following geometric parameters.

Circular Annular Plate: $a/R_1 = a/R_2 = 0.0, r = s, \phi_0 = 90^\circ$.

Circular Cylindrical Shell: $a/R_1 = 0.0, a/R_2 = 1.0, r = R_2, \phi_0 = 0^\circ$. (28)

Conical Shell: $a/r_1 = 0.0, a/r_2 = a/(s \cot \phi_0), r = s \cos \phi_0$.

Number of terms used in the series given by equation (23) for all of the following numerical results is only eight. Hence, there are $8 \times 5 = 40$ unknown coefficients to be determined. These are numbered from 1 to 40. For example: coefficients 1 to 8 are associated with $U(\xi)$, 9 to 16 with $V(\xi)$, and so on. The boundary conditions are enforced by setting the appropriate coefficients to zero. If the edges are freely supported, then the boundary conditions are: $V(\xi) = W(\xi) = 0$, for $s = s_1$ (or $\xi = -1$) and $s = s_2$ (or $\xi = +1$). This condition is achieved by setting coefficients 9 and 16 (for U) and 17 and 24 (for W) to zero. Similarly, the clamped condition at $s = s_1$ is achieved by setting coefficients 1, 9, 17, 18, 25, and 33 to zero. It is to be noted here that to get $W = \partial W / \partial s = 0$ at $s = s_1$, one has to equate coefficients 17 and 18 to zero. The Poisson's ratio ν is taken to be 0.3. The frequency is obtained in the nondimensional form defined by $\Omega^2 = \rho \omega^2 a^2 / E$.

I. Uniform Annular Plate. Irie et. al [8] published the correct dimensionless natural frequencies of uniform annular plates under nine combinations of boundary conditions. Their analysis is based on the Mindlin plate theory and solution of the differential equations of motion using

Bessels functions of the first and second kinds. For comparison purposes, the case of a clamped-free annular plate, for which the numerical results are presented in Table 1, is selected. Numerical results include both axisymmetric ($n = 0$) and asymmetric ($n = 1$ and 2) modes of vibration. The thickness to outer radius ratio (h/a) are: 0.10, 0.20 and 0.30. The present results are obtained only with eighth order polynomials. Results from the two sources (i.e. the present and ref.[8]) are generally in good agreement. Agreement is very good for the case of $h/a = 0.10$ and not so good for $h/a = 0.20$ and 0.30 . Better agreement is possible, if more terms in the series and high precision in the digital computer are used. The case with thickness parameter $h/a = 0.20$ or 0.30 is really a very thick plate. It is appropriate to use higher order plate theory than the one by Mindlin. Shown in Figure 2 are the three dimensional plots of the mode shapes for an annular plate clamped at the inside radius and free at the outside. The first two natural modes are shown both symmetric ($n = 0$) and asymmetric ($n = 1$) cases.

II. Uniform Circular Cylindrical Shell of Finite Length. For this example, a cylindrical shell clamped at one edge and free at the other is considered. The various parameters taken are: $\nu = 0.30$, $s_1/a = 0$, $s_2/a = 1.0$, $\phi_0 = 90^\circ$, and $h/a = 0.05$. Natural frequencies Ω are calculated using the Ritz and finite element methods for the sake of comparison. Ten geometrically axisymmetric shell elements, each with straight section and two nodes, are used in the model. With each node having 10 d.o.f. namely; $U, U_s, V, V_s, W, W_s, B_1, B_{1,s}, B_2$ and $B_{2,s}$ and eleven nodes in all, the size of the global matrix is 110. In the Ritz method, the matrix size is only 40 with eight terms in the series for each displacement and rotation components. The comparison of results turns out to be very good. For $n = 0$, the first five values of the natural frequency Ω are:

0.99008, 1.0196, 1.2647, 1.6761, and 1.9351	(Ritz Method)
0.98780, 1.0197, 1.2643, 1.6749, and 1.8744	(FE Method)

Similarly, for $n = 1$, the values of the frequencies are:

0.58860, 0.98941, 1.2599, 1.5794, and 1.6765	(Ritz Method)
0.58858, 0.98935, 1.2594, 1.5798, and 1.6760	(FE Method)

Shown in Figure 3 are the results for the same conditions as above plotted against (h/a) to study the effects of thickness on the natural frequencies of the clamped-free cylindrical shell.

III. Uniform Conical Shell Freely Supported at Both Edges. Initially, numerical results are calculated and compared with those of ref. [9]. Good agreement has been found. The results are not included in this paper. However, some results in the form of the variation of the natural frequencies (up to the first five modes for $n = 0$ and 1) with the thickness of the plate (h/a) are shown in Figure 4 for this problem. Various parameters taken are: $\nu = 0.30$, $s_1/a = 1.2797$, $s_2/a = 2.9238$, $\phi_0 = 70^\circ$, and the cone angle $\alpha = 20^\circ$.

The effect of thickness on the first two natural modes does not appear to be pronounced for the case of both the symmetric and asymmetric modes. However, frequencies do increase with the thickness of the shell. Considerable effect of the thickness on the natural frequencies is seen only for modes higher than 2.

CONCLUDING REMARKS

A simple numerical approach based on the Ritz method is presented in this paper for the free vibration analysis of a class of geometrically axisymmetric plates and shells. The formulation is valid for both symmetric and asymmetric natural modes of vibration. The method, though very simple and straight forward, is capable of yielding very accurate results with only few terms in the series which is used to represent the displacement fields.

Computer programs are written to solve for the natural frequencies and associated mode shapes of conical shells, cylindrical shells and circular plates. Only one algorithm is used with some minor changes in the input data file to accommodate different shell and plate configurations. Numerical results show very good agreement with those obtained by means of the analytical solutions for the circular plate and conical shell problems. Using the case of cylindrical shell, it is shown that both the Ritz and FE methods yield basically the same results for the frequencies. Variation of the natural frequencies with the thickness of the shell is also examined presented in this paper. Different combinations of the boundary conditions can be applied very conveniently simply by manipulating the coefficients of the polynomials.

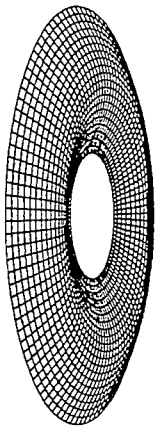
Numerical values of the natural frequencies are calculated using first order shear-deformation-theory of shells. The procedure can be very conveniently extended to deal with the higher order shell theory equivalent to the three dimensional elasticity solution for thick-walled shells.

REFERENCES

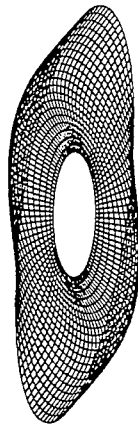
1. S. Timoshenko and S. Woinowsky-Krieger, 1959, *Theory of Plates and Shells*, Second Edition, McGraw-Hill Book Company, New York.
2. D. Young, 1950, "Vibration of Rectangular Plates by the Ritz Method", *J. Applied Mechanics*, vol. 17, p. 448-453.
3. A. W. Leissa, J. K. Lee, and A. J. Wang, 1981, "Vibrations of Cantilevered Shallow Cylindrical Shells of Rectangular Planform", *J. Sound and Vibration*, vol.78(3), p.311-328.
4. S. M. Dickinson and A. Di Blasio, 1986, "On the Use of Orthogonal Polynomials in the Rayleigh-Ritz Method for the Study of the Flexural Vibration and Buckling of Isotropic and Orthotropic Rectangular Plates", *J. Sound and Vibration*, vol. 108(1), p.51-62.
5. I. S. Sokolnikoff, 1954, *Mathematical Theory of Elasticity*, Second Edition, McGraw Hill Publication.
6. E. Reissner, 1952, "Stress Strain Relations in the Theory of Thin Elastic Shells", *J. of Mathematical Physics*, vol. 31, p. 109-119.
7. P. M. Nagdhi, 1957, "On the Theory of Thin Elastic Shells", *Quarterly of Applied Mathematics*, vol. 14(04), p. 369-380.
8. T. Irie, G. Yamada and K. Takagi, "Natural Frequencies of Thick Annular Plates", *J. of Applied Mechanics*, vol.49, p. 633-638.
9. T. Irie, G. Yamada and Y. Keneko, 1982, "Free Vibration of a Conical Shell with Variable Thickness", *J. Sound and Vibration*, vol. 82(1), p. 83-94.

TABLE 1. Non-dimensional Natural Frequency [$\Omega = \omega a \sqrt{\rho/E}$]
of a Clamped- Free Annular Plate

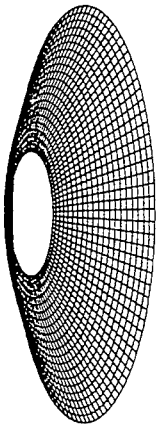
		h/a = 0.10		h/a = 0.20		h/a = 0.30	
		b/a = 0.10					
	Mode	Irie et. al [8]	Present	Irie et. al [8]	Present	Irie et. al [8]	Present
n = 0	1	0.12558	0.12597	0.23725	0.23942	0.326823	0.33332
	2	0.69964	0.70873	1.15296	1.19110	1.407150	1.47220
n = 1	1	0.09744	0.09920	0.17188	0.17672	0.22878	0.23633
	2	0.76259	0.77290	1.28974	1.31840	1.63230	1.67160
n = 2	1	0.16462	0.16542	0.31593	0.31711	0.45210	0.45303
	2	1.02737	1.03350	1.76302	1.77330	2.23150	2.24450
		b/a = 0.30					
n = 0	1	0.19730	0.19745	0.37161	0.37324	0.51202	0.51646
	2	1.14660	1.15640	1.80115	1.84110	2.11254	2.17660
n = 1	1	0.19095	0.19159	0.35043	0.35325	0.47298	0.47844
	1	1.19653	1.20680	1.88830	1.92670	2.23600	2.29500
n = 2	1	0.22847	0.22942	0.41700	0.42006	0.57012	0.57527
	2	1.35661	1.36760	2.15945	2.19270	2.59188	2.63780



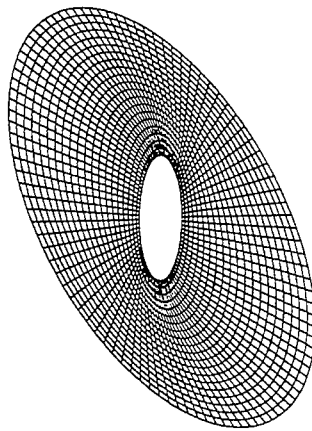
AXISYMMETRIC CASE: $n = 0$, Mode = 2,
 $h/a = 0.05$, $\Omega = 0.62584$



ASYMMETRIC CASE: $n = 1$, Mode = 2,
 $h/a = 0.05$, $\Omega = 0.65432$



AXISYMMETRIC CASE: $n = 0$, Mode = 1,
 $h/a = 0.05$, $\Omega = 0.10025$



ASYMMETRIC CASE: $n = 1$, Mode = 1,
 $h/a = 0.05$, $\Omega = 0.09822$

Figure 2. Three dimensional mode shapes for a clamped-free annular plate.

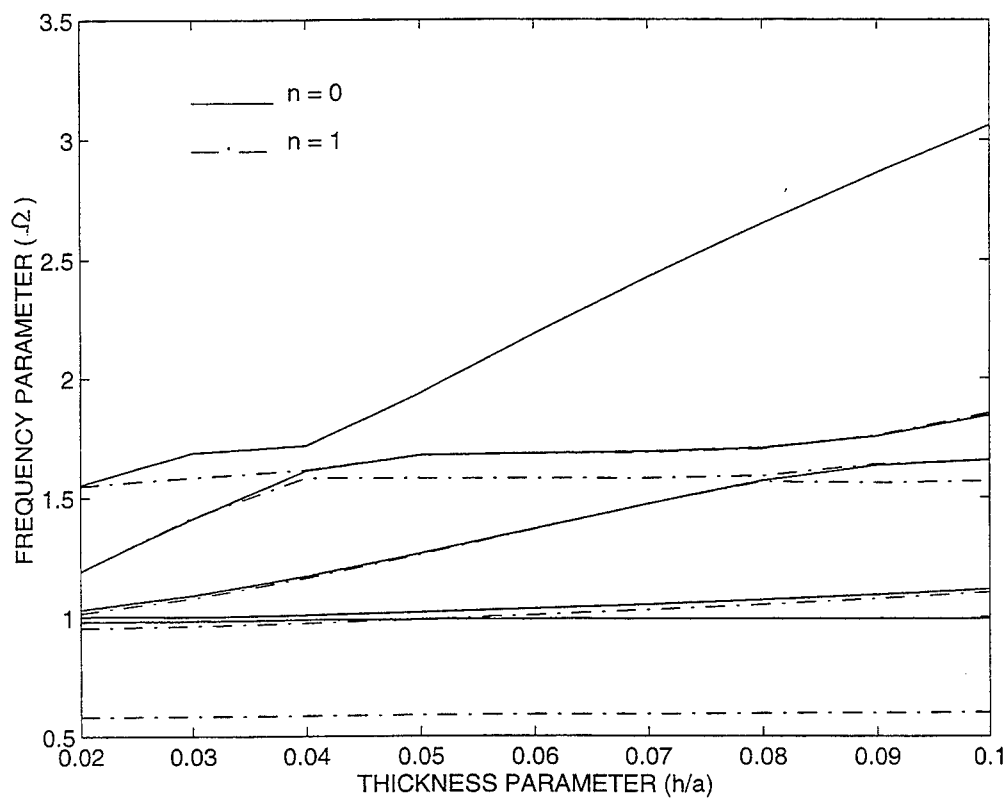


Figure 3. Variation of the non-dimensional frequency Ω with the thickness to radius ratio (h/a) for a cylindrical shell having clamped-free boundary conditions.

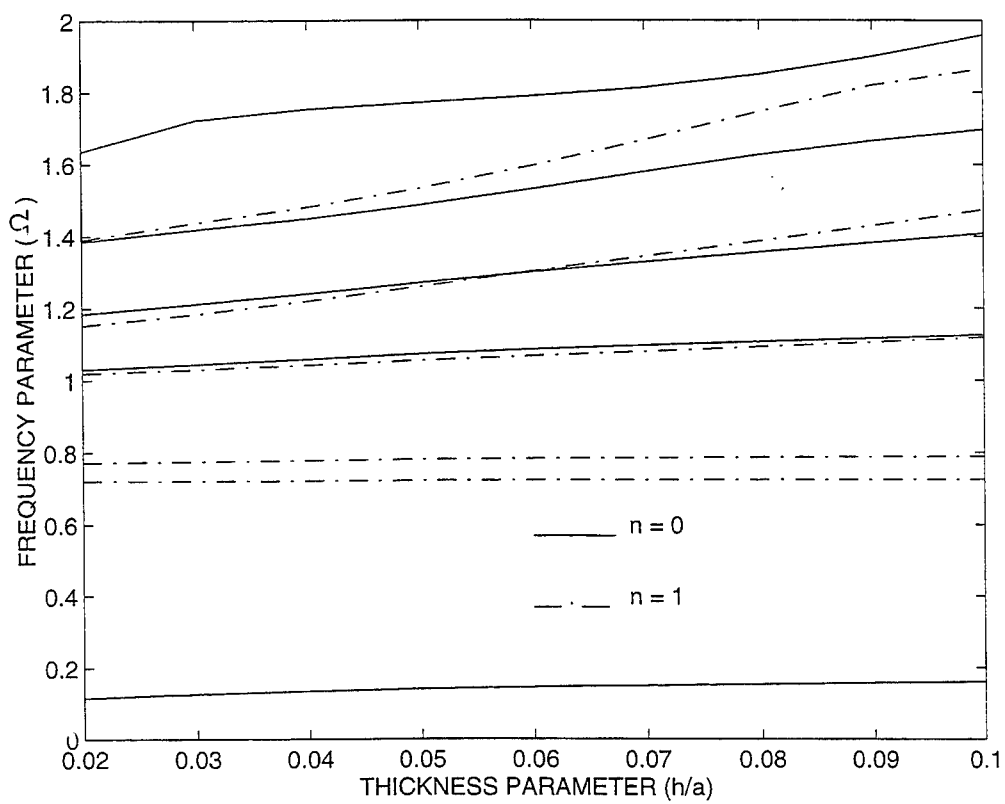


Figure 4. Variation of the non-dimensional frequency Ω with the thickness to radius ratio (h/a) for a conical shell freely supported at both ends.

A STUDY ON AEROFOIL SECTION FLUTTER WITH TWO DIMENSIONAL FINITE-STATE AERODYNAMICS

Swami Karunamoorthy¹, Guillermo Regulez²
Department of Aerospace & Mechanical Engineering
Saint Louis University, Saint Louis, USA

and

David A. Peters³
Department of Mechanical Engineering
Washington University, Saint Louis, USA

Abstract

The structural dynamics of an elastic body with unsteady aerodynamic forces leads to the classical dynamic aeroelastic instability of flutter. The unsteady aerodynamic forces are expressed as differential equations in state variable form, where the induced flow expansion coefficients are used as aerodynamic states. Although the application of three dimensional finite state aerodynamic theory to flutter analysis of fixed wings has been found in the literature, the two dimensional finite state aerodynamic theory is applied for the first time to flutter analysis of a typical aerofoil section. The resulting nondimensional flutter equations for both bending and torsion are hierarchical, and their solution does not require any iterative procedures. The results from the present method (called the p - f method) are in excellent agreement with classical v - g and p - k methods. However, the p - f method is computationally more efficient in predicting flutter boundaries and also it is more accurate away from the flutter boundary compared to existing methods. This method provides an alternate and viable computational tool for aeroelastic analysis of wing sections.

¹ Associate Professor and Director of Mechanical Engineering

² Graduate Student

³ Professor and Director of Center for Computational Mechanics

Introduction

In general, a system with two or more degrees of freedom can be unstable when the individual degrees of freedom interact causing divergent oscillations for certain phase differences. A typical example of a two degree of freedom system is wing bending-torsion flutter. However, a wing section with a single degree of freedom in torsion may also lead to such instability. Flutter is generally defined as a dynamic instability that occurs at a critical speed, namely the flutter speed. At this speed, the structural system would experience catastrophic failure. It is important to identify the flutter speed in the design of an aerospace structure and to optimize the design such that this speed is outside the flight envelope of aircraft.

Investigation of flutter on a typical aerofoil section eliminates the complexity in modeling of a three dimensional wing structure and enhances the understanding of the physics of the phenomenon. The dynamic equilibrium of an aerofoil section with two degrees of freedom leads to two coupled bending - torsion equations of motion [1]. These are second- order, linear differential equations. The forcing functions on the right hand side are due to unsteady aerodynamic forces. Developing a paradigm for these forces in finite-state (differential equation) form has always been a challenge to the aeroelastician. Analytical representation of unsteady flow in differential equation form as a function of aerodynamic state variables is both desirable and compatible with the structural model. Two- dimensional, finite-state aerodynamic theory for thin aerofoils [2] provides such a paradigm; and hence, the classical flutter problem of a typical wing section is revisited in this paper.

An emphasis is given in this paper , (i) to nondimensionalize the flexural-torsional equations of flutter, (ii) to model the unsteady lift and pitching moment with two dimensional finite-state aerodynamics, (iii) to compare the results with v - g and p - k methods, and (iv) to validate the finite state aerodynamic model by comparing with Theodorsen aerodynamics [3].

Flutter Model

A rigid two dimensional wing section is suspended in an airstream with a linear spring and rotational spring for flexural and torsional stiffnesses respectively, as shown in Figure 1. The aerodynamic center is located at one half of a semi chord from the leading edge. The elastic center (shear center) is at a distance of 'e' from the aerodynamic center or at a distance of 'ba' behind the mid-chord, where 'b' is the semi chord. The inertia center (center of gravity) is at a distance of 'x_{c.g.}' from elastic center. The plunge (h) and pitch (α) are the two degrees of freedom used in this flutter model. In nondimensional form, the flutter equations can be written as,

$$(\bar{h})^{**} + x_{\alpha}(\alpha)^{**} + \left(\frac{R}{\bar{U}}\right)^2 \bar{h} + \bar{L} = 0 \quad (1)$$

$$x_{\alpha} (\bar{h})^{**} + r_{\alpha}^2 (\alpha)^{**} + \left(\frac{r_{\alpha}}{\bar{U}}\right)^2 \alpha - \bar{M} = 0 \quad (2)$$

where $\bar{h} = (h/b)$, $x_{\alpha} = \frac{s_{\alpha}}{mb} = \frac{x_{c.g.}}{b}$, $R = \frac{\omega_h}{\omega_{\alpha}}$, $\bar{U} = \frac{U}{b\omega_{\alpha}}$, $r_{\alpha}^2 = \frac{I_{\alpha}}{mb^2}$,

$$\bar{L} = \frac{L}{mb\bar{U}^2\omega_{\alpha}^2}, \quad \bar{M} = \frac{M}{mb^2(\bar{U})^2\omega_{\alpha}^2}, \quad \tau = \frac{Ut}{b} = (\bar{U}\omega_{\alpha})t, \quad (\dot{}) = \frac{d}{dt}, \quad (\dot{})^* = \frac{d}{d\tau}$$

$$(\dot{}) = \bar{U}\omega_{\alpha}(\dot{})^*, \quad (\dot{}) = (\bar{U}\omega_{\alpha})^2(\dot{})^{**}$$

Forcing Functions

The nondimensional lift (\bar{L}) and pitching moment (\bar{M}) are the forcing functions to be derived for flutter equations. The unsteady flow can be modeled in several ways. One category is defined as k-type aerodynamics which assumes simple harmonic motion for the flow. For example, Theodorsen aerodynamics [3], [4] represents the influence of wake circulation as a complex function $C(k)$, where 'k' is the reduced frequency and is a measure of unsteadiness in the flow.

$$C(k) = \frac{H_1^{(2)}(k)}{H_1^{(2)}(k) + i H_0^{(2)}(k)}; \quad H_n^{(2)} = J_n - i Y_n \quad (3)$$

where ' H_n ' are Hankel functions, and ' J_n & Y_n ' are Bessel functions. When the reduced frequency is zero, the lift deficiency function $C(k)$ is equal to unity, which gives quasi-steady aerodynamics in which the influence of wake vortices are neglected. As ' k ' increases from zero to infinity, the real part of $C(k)$ decreases from one to one-half.

Two classical solution methods have been developed based on k-type aerodynamics. One method assumes a simple harmonic (k-type) solution for both the structures and the aerodynamics. It is referred to as the v - g (or k - k) method. It is a simple method and efficient in predicting the critical flutter speed where the structural damping is zero. Away from the flutter point, the results are considered to be unreliable because an artificial structural damping ' g ' is added to the system to ensure the undamped motion. A second method assumes exponentially damped harmonic solution (p-type) for the structure while the aerodynamics remains as k-type. This hybrid method is referred to as the 'p-k' method, and it provides accurate results if the damping is not too high. However, this method requires many iterations on the assumed reduced frequency to converge.

The second category of aerodynamics is based on p-type or Laplace domain aerodynamics in which the flow undergoes exponentially damped harmonic motion. A flutter method based on p-type solutions to both the structure and the aerodynamics is defined as a 'p-p' method. In such methods, an iteration on ' p ' (a complex eigenvalue) is performed for every eigenvalue of interest. However, this method is not considered as viable for flutter analysis due to its complexity in application and numerical computation.

The third category of unsteady flow models is indicial, in which a Green's function is used with a convolution integral to give arbitrary motion response. With this method, one must time march and look for instability to find the flutter boundary. A comparison of v - g , p- k , and indicial methods is given in References [5] and [6]. In principle, k-type, p-type, and indicial aerodynamics can be derived from one to another through Laplace or Fourier Transforms [2], [7].

The fourth category of unsteady flow model is based on a finite-state representation. Classical methods, such as vortex-lattice and

computational fluid dynamics (CFD) models may be described as finite state because the number of states may be interpreted as number of lattice nodes or CFD grid points. However, these methods require large number of states which is not viable for aeroelastic analysis. The Reduced Order Model (ROM) technique [8] describes a method to minimize the number of nodes based on eigen-analysis of unsteady flow. The disadvantage of this technique is that the computation of the eigenvalues is cumbersome.

Another type of finite state model has been developed [2], [9] based on potential flow equations. In these models, the states represent induced flow expansion fields rather than velocities at discrete nodes as found in CFD or vortex lattice methods. As a result, the states are hierarchical and the number of states required is significantly reduced compared to other methods. Based on this new finite state model [2] one can do either: (i) a 'v-g' analysis with assumed simple harmonic motion; (ii) an eigen-value (p-p) analysis by the use of Laplace transform, or (iii) time march as with indicial methods. With finite state models, an assumed complex frequency (analogous to Laplace transform) makes the aero-dynamics p-type, and hence there is no need for p-k iterations. However, unlike the p-p method no iterations on the complex eigenvalues are required. In order to distinguish it from classical p-p method, this finite state approach will be called the "p-f" method.

Finite-State Paradigm

The finite state paradigm is found in the literature as early as 1945, in which Jones [10] uses a two state approximation to the Theodorsen function. Single state models are also available in references [11] and [12]. Later, these models were replaced by a hierarchical finite state inflow models for helicopter rotors [13]. Application of the three dimensional inflow model to fixed wing flutter analysis is found in References [14] and [15]. A true 'p-f' formulation for the flutter of a typical aerofoil section with two dimensional inflow model is presented here.

The differential equation for the induced flow (λ), at a point "x" along the aerofoil ($-b < x < b$) can be written as [16];

$$\frac{\partial \lambda}{\partial t} + U \frac{\partial \lambda}{\partial x} = \frac{1}{2\pi} \frac{d\Gamma/dt}{(b-x)} \quad (4)$$

where Γ is the total bound vorticity on the aerofoil and λ includes the velocity due to shed wake and gusts. The induced flow (λ) can be expressed in terms of expansion coefficients (λ_n) as,

$$\lambda = \sum_{n=0}^{\infty} \lambda_n \cos(n\phi) \quad (5)$$

where ' ϕ ' is the Glauert variable ($x = b \cos \phi$). A set of differential equations for the induced flow expansion coefficients (λ_n) can be derived from equations (4) and (5), and they can be written in non-dimensional form as,

$$(\bar{\lambda})_0^* - \frac{1}{2}(\bar{\lambda})_2^* + (\bar{\lambda})_1 = \frac{(\bar{\Gamma})^*}{\pi} \quad (6)$$

$$\frac{1}{2n} [(\bar{\lambda})_{n-1}^* - (\bar{\lambda})_{n+1}^*] + \bar{\lambda}_n = \frac{(\bar{\Gamma})^*}{n\pi}; \quad n > 1 \quad (7)$$

where,

$$\bar{\lambda}_n = \frac{\lambda_n}{b\omega_\alpha}; \quad \bar{\Gamma} = \frac{\Gamma}{b^2\omega_\alpha}$$

Reference [2] shows that, for a flat wake, an additional constraint must hold on λ_0 :

$$\bar{\lambda}_0 = \frac{1}{2} \sum_{n=1}^N b_n \bar{\lambda}_n$$

$$b_n = (-1)^{n+1} \frac{(N+n-1)!}{(N-n-1)!(n!)^2}; \quad 1 < n < (N-1); \quad b_N = (-1)^{N+1}$$

The nondimensional circulation, $\bar{\Gamma}$ can be expressed in terms of aerofoil motions as,

$$\bar{\Gamma} = 2\pi \left[\bar{U} \bar{h}^* + \bar{U}_\alpha - \left(\bar{\epsilon} - \frac{1}{2} \right) \bar{U}_\alpha^* - \bar{\lambda}_0 + \frac{1}{2} (\bar{U}_\alpha^* - \bar{\lambda}_1) \right] \quad (8)$$

Therefore, equations (6) and (7) can be expressed as,

$$\left[4\bar{U}(\bar{h})^{**} + 4\bar{U}(1-\bar{e})(\alpha)^{**} + 4\bar{U}(\alpha)^* - 3 \sum_{n=1}^N b_n (\bar{\lambda})_n^* - 2(\bar{\lambda})_1^* + (\bar{\lambda})_2^* - 2(\bar{\lambda})_1^* \right] = 0 \quad (9)$$

$$\left[4\bar{U}(\bar{h})^{**} + 4\bar{U}(1-\bar{e})(\alpha)^{**} + 4\bar{U}(\alpha)^* - 2 \sum_{n=1}^N b_n (\bar{\lambda})_n^* - (\bar{\lambda})_{n-1}^* + (\bar{\lambda})_{n+1}^* - 2(\bar{\lambda})_1^* - 2n(\bar{\lambda})_n^* \right] = 0 \quad (10)$$

These induced flow equations in terms of aerodynamic states $(\bar{\lambda}_n)$, represent the unsteady flow in finite state (differential equations) form. These equations are hierarchical, and the number of equations required corresponds to the number of states chosen.

The total nondimensional lift and pitching moment relations can be expressed as a function of aerofoil generalized coordinates (h, α) as [16],

$$\bar{L} = \frac{\bar{m}}{2} \left[(\bar{h})^{**} + \left(\frac{1}{2} - \bar{e} \right) (\alpha)^{**} + (\alpha)^* \right] + \bar{m} \left[(\bar{h})^* + (1-\bar{e})(\alpha)^* + \alpha - \frac{(\bar{\lambda})_0}{\bar{U}} \right] \quad (11)$$

$$\bar{M} = \frac{\bar{m}}{2} \left[\left(\bar{e} - \frac{1}{2} \right) (\bar{h})^{**} - \left(\bar{e}^2 - \bar{e} + \frac{3}{8} \right) (\alpha)^{**} + 2\bar{e}(\bar{h})^* - (2\bar{e}^2 - 3\bar{e} + 1)(\alpha)^* + 2\bar{e}\alpha - 2\bar{e} \frac{(\bar{\lambda})_0}{\bar{U}} \right] \quad (12)$$

where, $\bar{e} = \frac{e}{b}$, $\bar{m} = \frac{\rho s a b}{2m}$, $\bar{\lambda}_0 = \frac{\lambda_0}{b\omega_\alpha}$

These generalized forces reduce to the quasi-steady case for the condition, $\bar{\lambda}_0 = 0$. The unsteady aerodynamic forces in equations (1) and (2) can be replaced by equations (11) and (12). The resulting flexural and torsional flutter equations can be simplified as given below:

$$\left(1 + \frac{\bar{m}}{2} \right) (\bar{h})^{**} + \left\{ \chi_\alpha + \frac{\bar{m}}{2} \left(\frac{1}{2} - \bar{e} \right) \right\} (\alpha)^{**} + (\bar{m})(\bar{h})^* + \bar{m} \left(\frac{3}{2} - \bar{e} \right) (\alpha)^* + \left(\frac{R}{\bar{U}} \right)^2 \bar{h} + \bar{m}\alpha - \left(\frac{\bar{m}}{2\bar{U}} \right) \sum_{n=1}^N b_n (\bar{\lambda})_n^* = 0 \quad (13)$$

$$\left\{ \chi_\alpha + \frac{\bar{m}}{2} \left(\frac{1}{2} - \bar{e} \right) \right\} (\bar{h})^{**} + \left\{ r_\alpha^2 + \frac{\bar{m}}{2} \left(\bar{e}^2 - \bar{e} + \frac{3}{8} \right) \right\} (\alpha)^{**} - (\bar{m}\bar{e})(\bar{h})^* + \left\{ \frac{\bar{m}}{2} (2\bar{e}^2 - 3\bar{e} + 1) \right\} (\alpha)^* + \left\{ \left(\frac{r_\alpha}{\bar{U}} \right)^2 - \bar{m}\bar{e} \right\} \alpha + \left(\frac{\bar{m}\bar{e}}{2\bar{U}} \right) \sum_{n=1}^N b_n (\bar{\lambda})_n^* = 0 \quad (14)$$

The flutter equations (13) and (14), combined with the inflow equations (9) and (10), provide a complete set of hierarchical equations to solve for flutter boundaries. These nondimensional equations are first expressed in state variable form and then solved for the eigenvalues.

The structural states can be defined as,

$$y_1 = \bar{h}, y_2 = \alpha, y_3 = (\bar{h})^* = y_1^*, y_4 = \alpha^* = y_2^*$$

The aerodynamic states are given by the inflow expansion coefficients, λ_n . All these equations can be expressed as functions of state variables in matrix form as [17],

$$[A] \begin{Bmatrix} y_i \\ \lambda_i \end{Bmatrix} + [B] \begin{Bmatrix} y_i \\ \lambda_i \end{Bmatrix} = 0 \quad (15)$$

where,

$$[A]_{n \times n} = \begin{bmatrix} [I]_{n1 \times n1} & [0]_{n1 \times n2} \\ [0]_{n2 \times n1} & [M]_{n2 \times n2} \end{bmatrix}$$

$$[B]_{n \times n} = \begin{bmatrix} [0]_{n1 \times n1} & [-I]_{n1 \times n2} \\ [K]_{n2 \times n1} & [C]_{n2 \times n2} \end{bmatrix}$$

$n = n1 + n2$; $n1 = \frac{n_s}{2}$; $n2 = n1 + n_a$; where ' n_s ' represent the number of structural states, and ' n_a ' represent the number of aerodynamic states.

Results and Discussions

The flutter equations with various aerodynamic models are solved and the results are presented here. The non-dimensional input parameters for the computation of flutter boundaries in Reference [18] are given below;

frequency ratio, $R=0.3$

dimensionless mass, $\bar{m}=0.1$

dimensionless radius of gyration, $r_\alpha=0.5$

location of center of gravity from elastic axis, $x_\alpha=0.2$

location of elastic axis from the aerodynamic axis, $\bar{e}=0.4$

Reference [2] shows that eight inflow states are the optimum number of aerodynamic states to predict the flutter boundary. The damping and frequency plots for this case are given in Figures 2 and 3. The flutter boundary is the point at which the damping becomes negative. A comparison of flutter boundary with other methods is given in Table 1. Damping and frequency comparisons are given in Figures 4 and 5. The percentage error is calculated based on the results given in Reference [18]. The flutter speed predicted by p-f method is in excellent agreement with that found in the Reduced Order Model method [18]. In the v-g and p-k methods, the Bessel functions to compute Theodorsen's lift deficiency function are approximated by a series, which may be the cause of the 5% numerical error in flutter speed. With a consistent numerical model, it is anticipated that all the methods would give the same flutter speed. However, v-g results are reliable only at the flutter point where damping is zero.

Table 1. Comparison of Flutter Speed

METHOD	FLUTTER SPEED (non-dimensional)	ERROR
v-g	1.92	5 %
p-k	1.92	5 %
p-f ; n=8 (Finite State)	2.07	0 %

In comparison of the computational effort, the classical v-g and p-k models have a smaller matrix size; however the solution procedure requires several iterations. In the finite state (p-f) model, no iterations are required; but the computational matrix size is large due to additional aerodynamic states. It has been observed that the computational time required for p-f analysis is relatively less compared to other models.

A parametric study also has been carried out to study the effect of different parameters on flutter control. The parameters are varied one at a time. In practice, the wing is designed such that the flutter speed is beyond the operating flight envelope which will prevent the flutter during various flight operations. For flutter control, the following classical solutions are observed as practical:

- (i) add or redistribute the mass such that x_α is minimum or even negative if possible;
- (ii) increase torsional stiffness (decrease 'R') and hence ω_α ;
- (iii) decrease \bar{e} ;
- (iv) increase r_α ;
- (v) decrease \bar{m} .

As there is no unique solution to prevent flutter, each of the above methods can be used for possible control of flutter phenomenon. The finite state model provides an efficient procedure to choose the aerodynamic states in a hierarchical manner.

Conclusions

The flexural and torsional flutter equations for a typical aerofoil section are nondimensionalized in both space, and time. The well documented hierarchical set of equations with two dimensional finite state aerodynamic model provide an alternate and viable method to predict the flutter boundaries. Comparison with v-g and p-k methods shows that the present (p-f) method is fast, accurate, and does not require iteration. Two dimensional finite state representation of unsteady forces on a wing section provides an excellent paradigm for aeroelastic flutter analysis. The parametric study reaffirms the classical conclusion that flutter can be controlled when the aerofoil section is mass balanced.

Appendix

Comparison with Theodorsen Aerodynamics:

The lift force can be expressed as a sum of circulatory (L_c), and non-circulatory (L_{nc}) components;

$$L = L_c + L_{nc} \quad (A1)$$

In Theodorsen model the circulatory lift, $L_c = C(k)L_Q$ where, L_Q is the quasi-steady part of the circulatory lift. For a typical aerofoil section, Theodorsen lift (L_T) is expressed as a function of aerofoil motions as given below:

$$L_T = C(k) \pi \rho S U \left[\dot{h} + U \alpha + \left(\frac{b}{2} - ba \right) \dot{\alpha} \right] + \frac{\pi \rho S b}{2} [\ddot{h} + U \dot{\alpha} - ba \ddot{\alpha}] \quad (A2)$$

$$= C(k) L_Q + L_{nc} \quad (A3)$$

In finite-state model, the lift (L_F) is expressed as a function of downwash velocity expansion coefficients (w_n), and induced flow expansion coefficient (λ_0):

$$L_F = \pi \rho S U \left[w_0 + \frac{w_1}{2} - \lambda_0 \right] + \frac{\pi \rho S b}{2} [(\dot{w})_0] \quad (A4)$$

$$\text{where, } w_0 = \dot{h} + U \alpha - (ba) \dot{\alpha}, \quad w_1 = b \dot{\alpha}, \quad \lambda_0 = \left(w_0 + \frac{w_1}{2} \right) \{1 - C(k)\}$$

With these transformations, it can be easily verified that, $L_F = L_T$. Similarly, the moment equation is expressed as,

$$M = \left(\frac{b}{2} + ba \right) L + M_{QC} \quad (A5)$$

In Theodorsen model, $L = L_T$; and the moment about quarter chord (M_{QC});

$$M_{QC} = - \frac{\pi \rho S b^2}{4} \left[\ddot{h} + \left(\frac{b}{4} - ba \right) \ddot{\alpha} + 2U \dot{\alpha} \right] \quad (A6)$$

In finite-state model, $L = L_F$, and the quarter chord moment

$$M_{QC} = - \frac{\pi \rho S b^2}{4} \left[(\dot{w})_0 + \frac{U}{b} w_1 + \frac{(\dot{w})_1}{4} \right] \quad (A7)$$

The moment about quarter chord is identical for either of the models with the application of transformation parameters. Since the lift is same for both models, the resulting moment relations are also equivalent. When $\lambda_0=0$, the finite state aerodynamic forces reduce to quasi-steady forces which are equivalent to Theodorsen quasi-steady [$C(k) = 1$] aerodynamic forces.

Non-Dimensional Flutter Equations for "v-g" and "p-k" analysis:

$$[M] \begin{Bmatrix} \bar{h} \\ \alpha \end{Bmatrix}^{**} + [C] \begin{Bmatrix} \bar{h} \\ \alpha \end{Bmatrix}^* + [K] \begin{Bmatrix} \bar{h} \\ \alpha \end{Bmatrix} = 0 \quad (A8)$$

where,

$$[M] = \begin{bmatrix} \left\{ 1 + \frac{\overline{m}}{2} \right\} & \left\{ x_\alpha + \frac{\overline{m}}{2} \left(\frac{1}{2} - \overline{e} \right) \right\} \\ \left\{ x_\alpha + \frac{\overline{m}}{2} \left(\frac{1}{2} - \overline{e} \right) \right\} & \left\{ r_\alpha^2 + \frac{\overline{m}}{2} \left(\overline{e}^2 - \overline{e} + \frac{3}{8} \right) \right\} \end{bmatrix}$$

$$[C] = \begin{bmatrix} \{ \overline{m} C(k) \} & \overline{m} \left\{ \left(\frac{1}{2} + (1 - \overline{e}) C(k) \right) \right\} \\ \{ -\overline{e} \overline{m} C(k) \} & \overline{m} (1 - \overline{e}) \left\{ \frac{1}{2} - \overline{e} C(k) \right\} \end{bmatrix}$$

$$[K] = \begin{bmatrix} \left\{ \left(\frac{R}{U} \right)^2 \right\} & \{ \overline{m} C(k) \} \\ \{ 0 \} & \left\{ \left(\frac{r_\alpha}{U} \right)^2 - \overline{e} \overline{m} C(k) \right\} \end{bmatrix}$$

Acknowledgement

Dr. D.A. Peters' part of this work was funded by the National Rotorcraft Technology Center Program, administered by NASA Ames Research Center. The efforts of Dr. Marty Ferman is greatly acknowledged for reviewing the work of Mr. G. Regulez, as his thesis committee member.

References

1. Bisplinghoff, R.L., Ashley, H., and Halfman, R.L., *Aeroelasticity*, Addison Wesley Publishing Co., 1957, pp. 279-293.
2. Peters, D.A., Karunamoorthy, S., and Cao, W.M., "Finite-State Induced Flow Models, Part I: Two Dimensional Thin Airfoil," *Journal of Aircraft*, Vol. 32, No. 2, 1995, pp. 313-322.
3. Theodorsen, T., "General Theory of Aerodynamic Instability and the Mechanism of Flutter," *NACA Report 496*, 1935, pp.413-433.
4. Theodorsen, T., and Garrick, I.E., "Mechanism of Flutter, A Theoretical and Experimental Investigation of the Flutter Problem," *NACA Report 685*, 1940, pp.101-146.

5. Hassig, H.J., "An Approximate True Damping Solution of the Flutter Equation by Determinant Iteration," *Journal of Aircraft*, Vol. 8, No. 11, 1971, pp. 885-889.
6. Laurence, A.J., and Jackson, P., "Comparison of Different Methods of Assessing the Free Oscillatory Characteristics of Aeroelastic Systems," R.A.E. C.P. No. 1084, 1968.
7. Dowell, E.H., *A Modern Course in Aeroelasticity*, Sijthoff and Noordhoff International Publisher, 1980, pp. 193-227.
8. Dowell, E.H., "Eigenmode Analysis in Unsteady Aerodynamics: Reduced Order Models," *AIAA Journal*, Vol. 34, No. 8, August 1996, pp. 1578-1583.
9. Peters, D.A., and He, C.J., "Finite State Induced Flow Models, Part II: Three Dimensional Rotor Disk," *Journal of Aircraft*, Vol. 32, No. 2, 1995, pp. 323-333.
10. Jones, W.P., "Aerodynamic Forces on Wings in Non-Uniform Motion," *British ARC, R&M 2117*, August 1945.
11. Tran, C.T., and Petot, D., "Some Empirical Model for Dynamic Stall of Airfoils in View of the Application to the Calculation of Response of a Helicopter Blade in Forward Flight," *Sixth European Rotorcraft and Powered Lift Forum*, Bristol, England, U.K., 1980.
12. Peters, D.A., "Toward a Unified Lift Model for Use in Rotor Blade Stability Analysis," *Journal of the American Helicopter Society*, Vol. 30, No. 3, 1985, pp. 32-42.
13. Peters, D.A., and Su, A., "An Integrated Airloads - Inflow Models for Use in Rotor Aeroelasticity and Control Analysis," *Mathematical and Computer Modeling*, Vol. 19, No. 3/4, 1994, pp. 109-123.
14. Nibbelink, B.D., and Peters, D.A., "Flutter Calculation for a Fixed and Rotary Wings with State Space Inflow Dynamics," *AIAA/ASME/ASCE/AHS/ASC Structures, Structural Dynamics, and Materials Conference*, La Jolla, California, 1993, Paper No. 93-1300.

15. Stettner, M., Schrage, D.P., and Peters, D.A., "Application of a State Space Wake Model to Tiltrotor Wing Unsteady Aerodynamics," *American Helicopter Society Aeromechanics Specialist Conference*, San Francisco, Jan 19-21, 1994, paper No. 6.6.
16. Peters, D.A., and Johnson, M.J., "Finite State Airloads for Deformable Airfoils on Fixed and Rotating Wings," *Aeroelasticity, and Fluid Structure Interaction Problems, ASME Winter Annual Meeting*, Chicago, Nov. 6-11, 1994, AD-Vol.44, pp. 1-28.
17. Regulez, G., "Flutter Phenomenon on a Typical Airfoil Section with Two Dimensional Finite State Aerodynamics," *Master of Science (Research) Thesis*, Parks College of Engineering and Aviation, Saint Louis University, 1996.
18. Hall, K.C., "Eigenanalysis of Unsteady Flow about Airfoils, Cascades, and Wings," *AIAA Journal*, Vol. 32, No. 12, 1994, pp. 2426-2432.

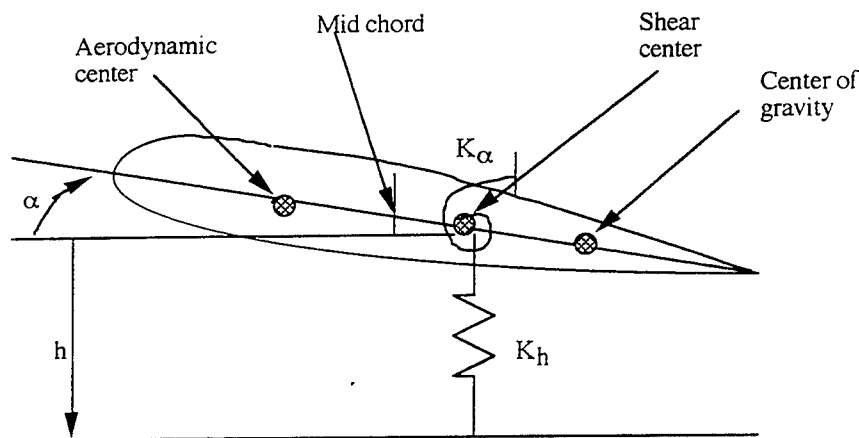


Figure 1. A Typical Section of Two Dimensional Aerofoil

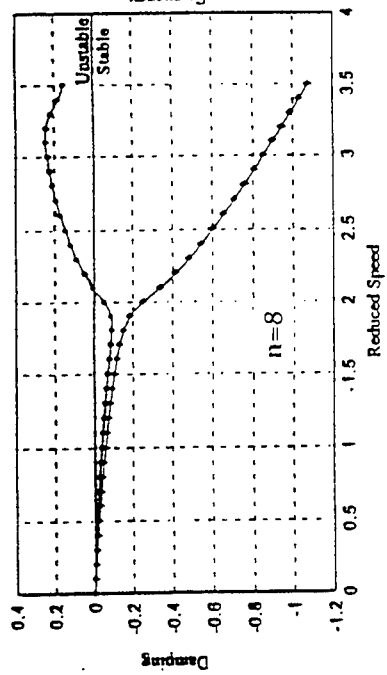


Figure 2. Damping by Finite-State method.

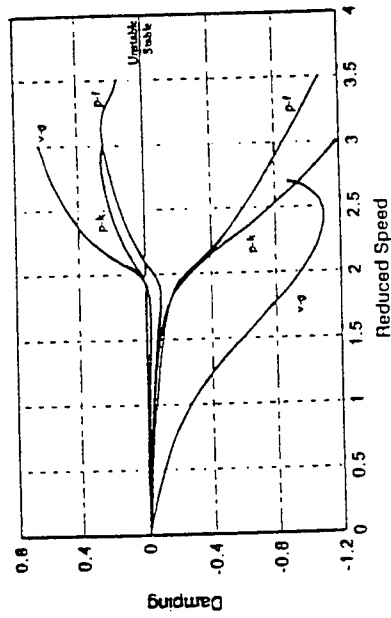


Figure 4. Comparison of Damping.

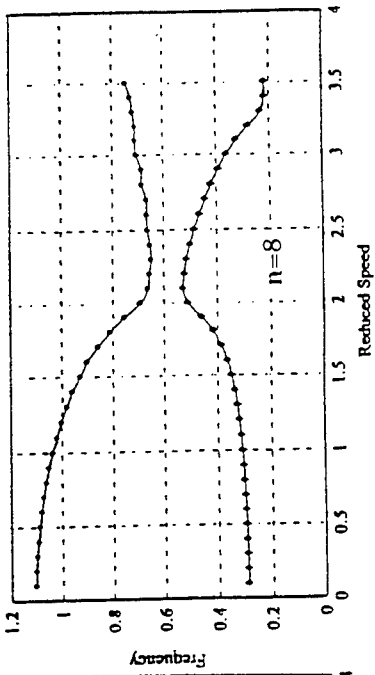


Figure 3. Frequency by Finite-State method.

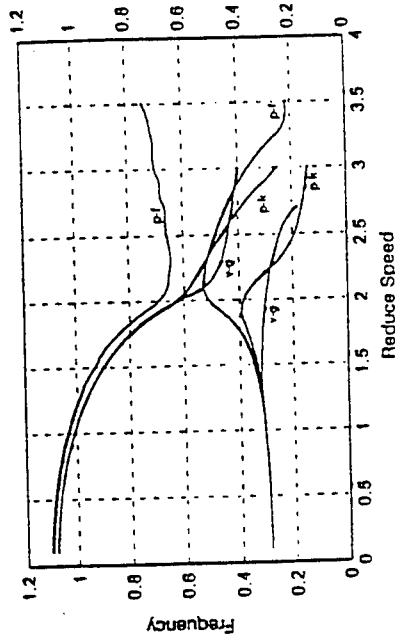


Figure 5. Comparison of Frequency.

A nonstationary Rayleigh wave of the 'diverging circle' type on the heat-insulated surface of a thermoelastic sphere

Yu. A. Rossikhin and M. V. Shitikova

*Department of Theoretical Mechanics,
Voronezh State Academy of Construction and Architecture,
ul.Kirova 3-75, Voronezh 394018, Russia*

Abstract

The influence of heat conduction and thermal relaxation on the propagation of the surface wave polarized in the sagittal plane along the heat-insulated surface of a thermoelastic sphere is investigated. The modified Maxwell law is used as the law of heat conduction, what allows one take a finite speed of heat propagation into account. The nonstationary surface wave is interpreted as the line (a diverging or converging circumference) on which temperature and the components of the stress and strain tensors experience a discontinuity. The discontinuity line propagates with a constant normal velocity across the free from stresses and heat-insulated surface of the sphere along the line of curvature and is obtained by the exit onto the sphere's surface of the three strong discontinuity complex wave surfaces intersecting along this line: quasi-thermal, quasi-longitudinal and quasi-transverse volume waves. Applying the theory of discontinuities, the velocities and the intensities of the surface wave have been found. It has been shown that attenuation of the surface wave intensity is determined by the two factors: a consideration of the related strain and temperature fields and the change in curvature of the surface wave with time.

INTRODUCTION

Nayfeh and Nemmat-Nasser [1] pioneered considering the problem of the propagation of a harmonic Rayleigh wave along the boundary of an isotropic thermoelastic half-space with allowance made for thermal relaxation. The half-space boundary was perceived to be free from stresses and thermally

insulated. The equations for determining the Rayleigh wave velocity and its coefficients of attenuation both with depth and in the direction of propagation were obtained.

The harmonic and nonstationary Rayleigh waves propagating along the free, from stresses, surface of an elastic sphere were studied by Petrashen [2] and Rossikhin [3], respectively, without regard for thermal effects. The Sobolev method [4] suggested by the author for harmonic waves was used in [3] for investigating the nonstationary wave. This method lies in the fact that the nonstationary surface wave is interpreted as a line of strong or weak discontinuity, which is obtained as a result of the exit onto the free, from stresses, sphere's surface of two complex wave surfaces of strong or weak discontinuity (quasi-longitudinal and quasi-transverse volume waves) intersecting with each other and simultaneously with the surface. This approach allows one to use the technique of the theory of discontinuous functions (Thomas, 1961) whereby both the velocity of the surface wave and its intensity are calculated.

In the present paper, this approach is used for the investigation of the nonstationary Rayleigh waves propagating along the free and heat-insulated surface of a thermoelastic sphere.

PROBLEM FORMULATION

Assume that the surface wave polarized in the sagittal plane propagates in the form of the line of strong discontinuity (the line on which the components of the stress and strain tensors change abruptly, in the given case it is a diverging or converging circumference) across the free and heat-insulated surface of a sphere along the geodesic line (Fig.1).

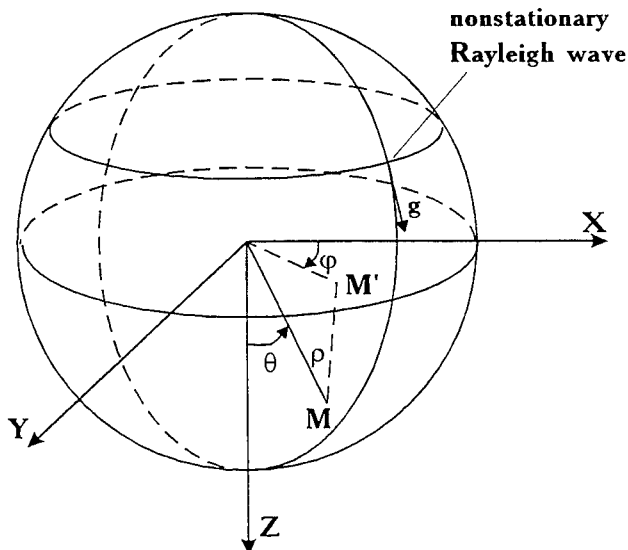


Fig.1. A scheme of a sphere

The dynamic behaviour of a linear thermoelastic material, from which

the sphere is made, in the curvilinear systems of coordinates is described by the following set of equations:

$$q_{,i}^i + c_\epsilon \dot{\Theta} + T_0 \gamma v_{,i}^i = 0 \quad (1)$$

$$q_i = -\lambda_0 \Theta_{,i} - \tau_0 \dot{q}_i \quad (2)$$

$$\sigma_{,j}^{ij} = \rho \dot{v}^i \quad (3)$$

$$\dot{\sigma}_{ij} = \mu(v_{i,j} + v_{j,i}) + \lambda v_{,l}^l g_{ij} - \gamma \dot{\Theta} g_{ij} \quad (4)$$

where σ^{ij} and σ_{ij} are the contravariant and covariant components of the stress tensor, respectively, v^i and v_i are the contravariant and covariant components of the displacement velocity vector, respectively, q^i and q_i are the contravariant and covariant components of the heat flow vector, respectively, g_{ij} are the covariant components of the metric tensor of the space, $\Theta = T - T_0$ is the relative temperature of the body, T_0 is the body's temperature at the natural state, ρ is the density, λ and μ are Lamé's elastic constants, δ_{ij} is the Kronecker's symbol, c_ϵ is the specific heat at constant strain, $\gamma = (3\lambda + 2\mu)\alpha_t$, α_t is the thermal linear expansion coefficient, λ_0 is the thermal conductivity, τ_0 is the thermal relaxation time, a Latin index after a comma denotes a covariant derivative with respect to the corresponding spherical coordinate $x^1 = \rho$, $x^2 = \theta$ or $x^3 = \varphi$ (see Fig.1), an overdot indicates a partial derivative with respect to time t , and Latin indices take on the values 1, 2, and 3.

The boundary conditions

$$\sigma_{11} = 0, \quad \sigma_{12} = 0 \quad (5)$$

$$q_1 = 0 \quad (6)$$

should be added to the set of Eqs.(1)-(4), where σ_{11} and σ_{12} , ($\sigma_{13} = 0$ due to the symmetry of the problem under consideration) are the components of the stress tensor on the boundary surface of the sphere, since the coordinate $x^1 = \rho$ is perpendicular to the boundary surface at each of its points (see Fig.1), and q_1 is the projection of the heat flow vector on the normal to the boundary surface.

PROPAGATION AND ATTENUATION OF NONSTATIONARY VOLUME WAVES OF STRONG DISCONTINUITY

In the subsequent discussion, we shall interpret the nonstationary volume wave of strong discontinuity Σ as a limiting layer of the thickness h at $h \rightarrow 0$, which surrounds the geometric surface Σ and within which the values σ_{ij} , σ^{ij} , v_i , v^i , q_i , q^i , and Θ change monotonically and continuously from the magnitudes σ_{ij}^+ , σ^{ij+} , v_i^+ , v^{i+} , q_i^+ , q^{i+} , and Θ^+ to the magnitudes

$\sigma_{ij}^-, \sigma_{ij}^+, v_i^-, v_i^+, q_i^-, q_i^+$ and Θ^- on the front and back boundaries of the wave layer, respectively.

Within the wave layer the following relationships are fulfilled for a certain function $Z(x^i, t)$:

$$Z_{,i} = \frac{dZ}{dn} \nu_i + g^{\alpha\beta} g_{ij} Z_{,\alpha} x_{,\beta}^j, \quad \dot{Z} = -G \frac{dZ}{dn} + \frac{DZ}{Dt} \quad (7)$$

where $dZ/dn = Z_{,i} \nu^i$ is the derivative with respect to the normal to Σ , ν_i are the covariant components of the unit normal vector, $g^{\alpha\beta}$ are the contravariant components of the metric tensor of the wave surface, $x_{,\beta}^j = \partial x^j / \partial u^\beta$, u^1 and u^2 are the curvilinear coordinates on the wave surface, Greek indices take on the values 1 and 2, a Greek index after a comma denotes a covariant derivative with respect to the corresponding surface coordinate, G is the normal velocity of the propagation of the surface Σ , D/Dt is the invariant derivative with respect to time [5] which for the covariant and contravariant components of the unit normal vector to the wave layer has the form

$$\frac{D\nu_i}{Dt} = \frac{\delta\nu_i}{\delta t} - G\nu_m \Gamma_{in}^m \nu^n, \quad \frac{D\nu^i}{Dt} = \frac{\delta\nu^i}{\delta t} + G\nu^m \Gamma_{mn}^i \nu^n \quad (8)$$

where $\delta/\delta t$ is the Thomas-derivative [5], and Γ_{mn}^i are the Christoffel symbols in the space.

Noting that at $h \rightarrow 0$ the second terms in (7) may be neglected as compared with the first ones, from Eqs.(1-4) we obtain

$$\begin{aligned} \frac{dq^i}{dn} \nu_i - Gc_c \frac{d\Theta}{dn} + T_0 \gamma \frac{dv^i}{dn} \nu_i &= 0, \quad q_i = -\lambda_0 \frac{d\Theta}{dn} \nu_i + \tau_0 G \frac{dq_i}{dn}, \\ \frac{d\sigma^{ij}}{dn} \nu_j &= -\rho G \frac{dv^i}{dn}, \\ -G \frac{d\sigma_{ij}}{dn} &= \lambda \frac{dv^l}{dn} \nu_l g_{ij} + \mu \left(\frac{dv_i}{dn} \nu_j + \frac{dv_j}{dn} \nu_i \right) + \gamma G \frac{d\Theta}{dn} g_{ij} \end{aligned} \quad (9)$$

Integrating relationships (9) with respect to n from $-h/2$ to $h/2$ and going to the limit at $h \rightarrow 0$, we find that the following relationships should take place on Σ :

$$[q^i] \nu_i - Gc_c [\Theta] + T_0 \gamma [v_i] \nu^i = 0, \quad 0 = -\lambda_0 [\Theta] \nu_i + \tau_0 G [q_i],$$

$$[\sigma_{ij}] \nu^j = -\rho G [v_i], \quad -G [\sigma_{ij}] = \lambda [v_l] \nu^l g_{ij} + \mu ([v_i] \nu_j + [v_j] \nu_i) + \gamma G [\Theta] g_{ij}, \quad (10)$$

where $[Z] = Z^+ - Z^-$.

Considering that

$$[v_i] = \omega \nu_i + g_{ij} W^\gamma x_{,\gamma}^j, \quad [v^i] = \omega \nu^i + W^\gamma x_{,\gamma}^i, \quad \omega = [v_i] \nu^i, \quad W_\gamma = [v_i] x_{,\gamma}^i$$

from Eqs.(10) we obtain at $\omega \neq 0$

$$(G^2 - a^2)(G^2 - G_1^2) - G^2 \gamma^2 T_0 (\rho c_c)^{-1} = 0, \quad (11)$$

$$\begin{cases} [\sigma_{ij}] = -G^{-1} \{2\mu\nu_i\nu_j + \lambda q_{ij} + \rho(G^2 - G_1^2)g_{ij}\} \omega \\ [v_i] = \omega\nu_i, \quad W^\gamma = 0, \quad [\Theta] = (\gamma G)^{-1} \rho(G^2 - G_1^2)\omega \\ [q_i] = \lambda_0(\tau_0\gamma G^2)^{-1} \rho(G^2 - G_1^2)\omega\nu_i \end{cases} \quad (12)$$

where $a^2 = \lambda_0(\tau_0 c_\epsilon)^{-1}$, and $\rho G_1^2 = \lambda + 2\mu$,
and at $\omega = 0$

$$\rho G^2 = \rho G_2^2 = \mu, \quad (13)$$

$$\begin{cases} [\sigma_{ij}] = -G^{-1} \mu(x_{,1}^i \nu_j g_{ij} + x_{,1}^j \nu_i g_{ji}) W^1, & [v_i] = g_{ij} x_{,1}^j W^1 \\ W^2 = [q_i] = [\Theta] = 0 \end{cases} \quad (14)$$

Equation (11) defines the velocities $G^{(1)}$ and $G^{(2)}$ of two types of the volume waves of strong discontinuity: quasi-transverse Σ_1 and quasi-longitudinal Σ_2 , formulas (12) determine the relationships which are fulfilled on these waves. Equation (13) governs the velocity $G^{(3)}$ of the quasi-transverse wave of strong discontinuity, and formulas (14) are responsible for the relationships which are valid on this wave. Hereafter an upper index in brackets denotes an ordinal number of the wave.

To determine changes in the intensities of the three waves during their propagation, we write Eqs.(1)-(4) on the different sides of the each wave surface and take the difference of the corresponding equations written ahead of and behind the wave front. Having regard for the conditions of compatibility for discontinuities in the first-order derivatives [5] in arbitrary coordinates

$$[Z_{,i}] = [Z_{,i}] \nu^i + g^{\alpha\beta} g_{ij} [Z]_{,\alpha} x_{,\beta}^j, \quad [\dot{Z}] = -G[Z_{,i}] \nu^i + D[Z]/Dt \quad (15)$$

as a result we obtain

$$Q_i \nu^i + g^{\alpha\beta} g_{ij} [q^i]_{,\alpha} x_{,\beta}^j - c_\epsilon G h + c_\epsilon \frac{D[\Theta]}{Dt} + T_0 \gamma (L_i \nu^i + g^{\alpha\beta} g_{ij} [v^i]_{,\alpha} x_{,\beta}^j) = 0 \quad (16)$$

$$[q_i] = -\lambda_0 h \nu_i - \lambda_0 g^{\alpha\beta} g_{ij} [\Theta]_{,\alpha} x_{,\beta}^j + \tau_0 G Q_i - \tau_0 \frac{D[q_i]}{Dt} \quad (17)$$

$$S^{ij} \nu_j + g^{\alpha\beta} g_{ij} [\sigma^{ij}]_{,\alpha} x_{,\beta}^l = -\rho G L^i + \rho \frac{D[v^i]}{Dt} \quad (18)$$

$$\begin{aligned} -G S_{ij} + \frac{D[\sigma_{ij}]}{Dt} &= \lambda g_{ij} (L_l \nu^l + g^{\alpha\beta} g_{lk} [v^l]_{,\alpha} x_{,\beta}^k) \\ &+ \mu (L_i \nu_j + L_j \nu_i + g^{\alpha\beta} g_{jl} [v_i]_{,\alpha} x_{,\beta}^l + g^{\alpha\beta} g_{il} [v_j]_{,\alpha} x_{,\beta}^l) + \gamma g_{ij} \left(Gh - \frac{D\Theta}{Dt} \right), \end{aligned} \quad (19)$$

where

$$\begin{aligned} S_{ij} &= [\sigma_{ij,l}] \nu^l, \quad S^{ij} = [\sigma_{,l}^{ij}] \nu^l, \quad L_i = [v_{i,l}] \nu^l, \\ L^i &= [v_{,l}^i] \nu^l, \quad h = [\Theta_{,l}] \nu^l, \quad Q_i = [q_{i,l}] \nu^l \end{aligned}$$

Eliminating the values Q_i from Eqs.(16) and (17) and the values S_{ij} from Eqs.(18) and (19) and taking formulas (11)-(14), and the relationships

$$D\nu_i/Dt = D\nu^i/Dt = 0 \quad (20a)$$

$$\nu_{,\alpha}^i = -g^{\sigma\gamma} b_{\sigma\alpha} x_{,\gamma}^i \quad (20b)$$

into account yields

for the two quasi-longitudinal waves ($\omega \neq 0$)

$$\frac{D\omega}{Dt} = -\alpha\omega + G\Omega\omega, \quad \alpha = \frac{a^2(G^2 - G_1^2)}{2\tau_0(G^4 - a^2G_1^2)} \quad (21a)$$

$$L_i x_{,\gamma}^i = \omega_{,\gamma} \quad (21b)$$

$$h = \frac{\rho(G^2 - G_1^2)}{G\gamma} L_i \nu^i - \frac{\rho(G^2 + G_1^2)}{\gamma G^2} \frac{D\omega}{Dt} + \frac{2\rho G_1^2}{\gamma G} \Omega\omega \quad (21c)$$

and for the quasi-transverse wave wave ($\omega = 0$)

$$\frac{DW}{Dt} = G\Omega W, \quad W^2 = W_\gamma W^\gamma \quad (22a)$$

$$\frac{DW^\gamma}{Dt} = G\Omega W^\gamma + G W^\alpha b_{\alpha}^\gamma, \quad \frac{DW_\gamma}{Dt} = G\Omega W_\gamma - G W_\alpha b_\gamma^\alpha \quad (22b)$$

$$L_i \nu^i = -W_{,\alpha}^\alpha \quad (22c)$$

$$h = 0 \quad (22d)$$

where Ω is the mean curvature of each wave surface, $b_{\sigma\alpha}$ are the coefficients of the second quadratic form of these surfaces, and $b_\gamma^\alpha = b_{\gamma\sigma} g^{\sigma\alpha}$.

EQUATIONS OF STRONG DISCONTINUITY WAVE SURFACES AND THEIR GEOMETRIC CHARACTERISTICS

The velocities of the three volume waves and equations describing changes in their intensities during propagation were obtained in the preceding section in arbitrary spatial and surface coordinate systems. However further investigation of the Rayleigh waves calls for specific definition of the spatial and surface curvilinear systems of coordinates. To obtain the equations of these surfaces in the spherical coordinate system, it is necessary to take into account that the volume waves $\Sigma^{(1)}$, $\Sigma^{(2)}$, and $\Sigma^{(3)}$ cropping out at the free and heat-insulated surface of a sphere and crossing there each other generate the line of strong discontinuity L , i.e., the surface wave propagating along the line of curvature (in our case this line is the circle of the radius R) with the constant velocity g ; in so doing the normal velocities of the volume waves $G^{(1)}$, $G^{(2)}$, and $G^{(3)}$ are greater than the velocity g . The equations of the volume waves, due to the symmetry of the problem, lack the variable $x^3 = \varphi$, but depend only on the coordinates $x^1 = \rho$ and $x^2 = \theta$ (Fig.1).

Let us deduce the equations of the line, which represents the envelope of the volume waves; the wave surface is obtained when the generator rotates

around the sphere. For this purpose, we invoke formulas (8) and (20a). As a result we have

$$\frac{\delta \nu_i}{\delta t} = G \Gamma_{in}^m \nu^n \nu_m \quad (23a)$$

$$\frac{\delta \nu^i}{\delta t} = -G \Gamma_{mn}^i \nu^m \nu^n \quad (23b)$$

The index denoting the ordinal number of the volume wave is omitted in the following.

To formulas (23) must be added the relationship [5]

$$\frac{\delta x^i}{\delta t} = G \nu^i \quad (24)$$

Considering that for the spherical coordinate system $\nu^3 = 0$, $g_{11} = 1$, $g_{22} = \rho^2$, $\Gamma_{22}^1 = -\rho$, and $\Gamma_{12}^2 = \Gamma_{21}^2 = \rho^{-1}$ (other Christoffel symbols involving only the indices 1 and 2 are equal to zero), from Eq.(23b) at $i=2$ we find

$$\frac{\delta \nu^2}{\delta t} = -2G \nu^1 \nu^2 \rho^{-1} \quad (25)$$

Adding Eq.(24) at $i=1$

$$\frac{\delta \rho}{\delta t} = G \nu^1 \quad (26)$$

to formula (25), and eliminating the value ν^1 from Eqs.(25) and (26), we have

$$(\nu^2)^{-1} d\nu^2 = -2\rho^{-1} d\rho \quad (27)$$

Integrating Eq.(27) yields

$$\nu^2 = c\rho^{-2} \quad (28a)$$

$$\nu_2 = c \quad (28b)$$

where c is an arbitrary constant which can be put equal to $Gg^{-1}R$. As it would be seen from the following discussion, such a choice of the value c causes the velocity of the surface wave on the thermal-insulated and free from stresses surfaces of the sphere to be in line with the Rayleigh wave velocity on the free and heat insulated boundary of a thermoelastic half-space.

Further we use the relationship (23a) at $i=1$

$$\frac{\delta \nu_1}{\delta t} = \rho^{-1} G \nu^2 \nu_2 \quad (29)$$

Substituting (28) into (29) and considering that

$$\frac{\delta \nu_1}{\delta t} = \frac{d\nu_1}{d\rho} \frac{\delta \rho}{\delta t} = \frac{d\nu_1}{d\rho} \nu_1 G = \frac{1}{2} G \frac{d(\nu_1)^2}{d\rho}$$

after integration we obtain

$$\nu_1 = \sqrt{c_1 - c^2 \rho^{-2}}$$

where c_1 is an arbitrary constant which we put equal to unit in order to fulfill the identity $\nu_i \nu^i = 1$.

Thus,

$$\nu_1 = \rho^{-1} \sqrt{\rho^2 - c^2} \quad (30)$$

i.e., the value ν_1 is the imaginary value, and hence the wave surfaces, which generate the real line (surface wave) at intersections, are found to be complex surfaces.

If now we substitute (30) into Eq.(26) and integrate the resulted equation, then as a result we shall have

$$x^1 = \rho = \sqrt{c^2 + (c_2 + Gt)^2} \quad (31)$$

where c_2 is an arbitrary constant which we denote as $u^1 \Delta^{-1}$. ($\Delta = -gG^{-1} \nu_1^0$, $\nu_1^0 = \nu_1 \Big|_{\rho=R} = \sqrt{1 - G^2 g^{-2}}$). The value u^1 will be taken as one of the surface coordinates (this coordinate is measured along the generatrix), the other surface coordinate coincides with the curvilinear coordinate x^3 . The constant value Δ^{-1} is introduced in Eq.(31) only for the modulus of the vector $k\{x_{,1}^1, x_{,1}^2\}$ detected tangentially to the volume wave generator to be equal to unit.

Note at once that the surface coordinates u^1 and u^2 chosen in such a manner remain constant along the normal trajectories to the wave surfaces (along the lines at every point of which the tangent unit vector coincides with the normal unit vector to the wave surface), i.e., $\delta u^1 / \delta t = \delta u^2 / \delta t = 0$.

Thus,

$$x^1 = \rho = \sqrt{G^2 g^{-2} R^2 + (u^1 \Delta^{-1} + Gt)^2} \quad (32)$$

Since on the surface S of the sphere $\rho=R$, then, as it follows from (32), the following condition is fulfilled on S

$$u^1 = (-Gt + R\nu_1^0) \Delta \quad (33)$$

Putting $i=2$ in (24), substituting (28a) in the resulted expression, and in doing so having regard for (32), we are led to the equation

$$\frac{\delta \theta}{\delta t} = \frac{Gc}{c^2 + (u^1 \Delta^{-1} + Gt)^2} \quad (34)$$

Integrating (34) yields

$$x^2 = \theta = \arctan \left(\frac{u^1 \Delta^{-1} + Gt}{c} \right) + c_3$$

where c_3 is an arbitrary constant which is decided such that on the sphere's surface S the condition

$$\dot{s} = R \dot{\theta} = g \quad (35)$$

is fulfilled.

Thus,

$$x^2 = \theta = \arctan \left[\frac{(u^1 \Delta^{-1} + GT)g}{GR} \right] + \frac{u^1}{\nu_1^0 R} \quad (36)$$

The fulfillment of the condition (35) is easily verified if one substitutes formula (33) into Eq.(36) and then integrates the resulted expression with respect to time.

Hence the equations of the wave surfaces (32) and (36) meet all requirements for the complex waves generating the surface wave at their exit onto the surface of a body.

Based on the formulas presented, one can obtain the main relationships of the theory of moving surfaces which are in use in the subsequent discussion.

Having regard in the spherical coordinate system for the expressions for the spatial components of the metric tensor $g_{11} = 1$, $g_{22} = \rho^2$, $g_{33} = \rho^2 \sin^2 \theta$ and the nonzero spatial Christoffel symbols

$$\Gamma_{22}^1 = -\rho, \quad \Gamma_{33}^1 = -\rho \sin^2 \theta, \quad \Gamma_{33}^2 = -\frac{1}{2} \sin 2\theta$$

$$\Gamma_{21}^2 = \frac{1}{\rho}, \quad \Gamma_{32}^3 = \cot \theta, \quad \Gamma_{31}^3 = \frac{1}{\rho}$$

as well as formulas (32) and (36), we arrive at the following relationships for the complex wave surfaces generating the Rayleigh wave on the surface of a sphere:

$$\begin{aligned} x_{,1}^1 &= -\frac{\nu_1 \nu_2}{\nu_1^0 R}, & x_{,1}^2 &= \frac{\nu_1^2}{\nu_1^0 R}, & x_{,2}^3 &= 1, \\ g_{11} &= \frac{(\nu_1 \rho)^2}{(\nu_1^0)^2}, & g_{22} &= \rho^2 \sin^2 \theta, & \Gamma_{11}^1 &= -\frac{\nu_2}{\rho \nu_1 \nu_1^0 R}, \\ \Gamma_{22}^1 &= \frac{1}{2} \nu_2 \nu_1^0 R (\rho \nu_1)^{-1} (2 \sin^2 \theta - \nu_1 \rho \nu_2^{-1} \sin 2\theta), \\ \Gamma_{12}^2 &= -\frac{\nu_2}{\nu_1^0 R} \nu_1 \rho^{-1} (1 - \rho \nu_1 \nu_2^{-1} \cot \theta), \\ \nu_{,1}^1 &= -\frac{\nu_2}{\rho \nu_1^0 R}, & \nu_{,1}^2 &= \frac{\nu_1}{\rho \nu_1^0 R}, & \nu_{,2}^3 &= \nu_2 \rho^{-2} \cot \theta + \rho^{-1} \nu_1, \\ b_{11} &= -\frac{\rho \nu_1}{(\nu_1^0 R)^2}, & b_{22} &= -\frac{1}{2} \nu_2 \sin 2\theta - \rho \nu_1 \sin^2 \theta, \\ 2\Omega &= -\frac{1}{\rho \nu_1} - \frac{\nu_1}{\rho} - \frac{\nu_2}{\rho^2} \cot \theta, \end{aligned} \quad (37)$$

$$\begin{aligned}
x_{,11}^1 &= -\frac{\rho\nu_1^2}{(\nu_1^0 R)^2}, & x_{,11}^2 &= -\frac{\nu_1\nu_2}{\rho(\nu_1^0 R)^2}, \\
x_{,22}^1 &= -\rho\nu_1^2 \sin^2 \theta - \frac{1}{2}\nu_1\nu_2 \sin 2\theta, & x_{,22}^2 &= -\nu_1\nu_2\rho^{-1} \sin^2 \theta - \frac{1}{2}\nu_2^2\rho^{-2} \sin 2\theta, \\
\frac{Dx_{,1}^1}{Dt} &= -G\frac{\nu_2}{\rho\nu_1^0 R}, & \frac{Dx_{,1}^2}{Dt} &= G\frac{\nu_1}{\rho\nu_1^0 R}, & \frac{Dx_{,2}^3}{Dt} &= G(\nu_2\rho^{-2} \cot \theta + \nu_1\rho^{-1}).
\end{aligned}$$

Note that only nonzero values are presented in (37).

RAYLEIGH WAVES

The following discussion resulting in the investigation of the surface wave characteristics is associated with the boundary conditions (5) and (6). Since the volume waves cropping out at the free thermal-insulated sphere's surface cross each other generating a surface wave, then the stress tensor and heat flow vector components of each of the three volume waves should be added together on the surface wave. As a result from the conditions (5) and (6) on the surface wave can be written as

$$\sum_{i=1}^3 [\sigma_{11}]^{(i)} = 0, \quad \sum_{i=1}^3 [\sigma_{12}]^{(i)} = 0, \quad (38)$$

$$\sum_{i=1}^3 [q_1]^{(i)} = 0. \quad (39)$$

Considering Eqs.(11)-(14) and formulas (28), (30), and (37) at $\rho = R$, from the conditions (38) and (39) we have

$$\begin{aligned}
G^{(1)-1} \left[2\mu \left(1 - \frac{G^{(1)2}}{g^2} \right) + \rho(G^{(1)2} - 2G_2^2) \right] \omega^{(1)} + G^{(2)-1} \left[2\mu \left(1 - \frac{G^{(2)2}}{g^2} \right) \right. \\
\left. + \rho(G^{(2)2} - 2G_2^2) \right] \omega^{(2)} - g^{-1} 2\mu \sqrt{1 - \frac{G_2^2}{g^2}} W^{1(3)} = 0, \quad (40)
\end{aligned}$$

$$2g^{-1} \left(\sqrt{1 - \frac{G^{(1)2}}{g^2}} \omega^{(1)} + \sqrt{1 - \frac{G^{(2)2}}{g^2}} \omega^{(2)} \right) + G_2^{-1} \left(1 - 2\frac{G_2^2}{g^2} \right) W^{1(3)} = 0, \quad (41)$$

$$\omega^{(1)} \frac{G^{(1)2} - G_1^2}{G^{(1)2}} \sqrt{1 - \frac{G^{(1)2}}{g^2}} + \omega^{(2)} \frac{G^{(2)2} - G_1^2}{G^{(2)2}} \sqrt{1 - \frac{G^{(2)2}}{g^2}} = 0. \quad (42)$$

From Eq.(42) we find the connection between $\omega^{(1)}$ and $\omega^{(2)}$

$$\omega^{(2)} = \chi \omega^{(1)} \quad \chi = -\frac{G^{(2)2}(G^{(1)2} - G_1^2)\sqrt{1 - G^{(1)2}g^{-2}}}{G^{(1)2}(G^{(2)2} - G_1^2)\sqrt{1 - G^{(2)2}g^{-2}}}. \quad (43)$$

Substituting formula (43) in Eqs.(41) and (42) yields

$$G_2^{-2}(G^{(1)} + \chi G^{(2)})(1 - 2G_2^2 g^{-2})\omega^{(1)} - 2g^{-1}W^{1(3)}\sqrt{1 - G_2^2 g^{-2}} = 0 \quad (44a)$$

$$2g^{-1} \left(\sqrt{1 - G^{(1)2} g^{-2}} + \chi \sqrt{1 - G^{(2)2} g^{-2}} \right) \omega^{(1)} + G_2^{-1}(1 - 2G_2^2 g^{-2})W^{1(3)} = 0 \quad (44b)$$

Equating the determinant of the set of homogeneous Eqs.(44) to zero, we arrive at the relationship [1]

$$G_2^{-3}(1 - 2G_2^2 g^{-2})^2 (G^{(1)} + \chi G^{(2)}) + 4g^{-2} \left(\sqrt{1 - G^{(1)2} g^{-2}} + \chi \sqrt{1 - G^{(2)2} g^{-2}} \right) \sqrt{1 - G_2^2 g^{-2}} = 0 \quad (45)$$

When $\chi = 0$, and $G^{(1)} = G_1$, i.e., when heat conduction is absent, Eq.(45) goes over into the classic Rayleigh equation.

Since Eqs.(44) subjected to the condition (45) are linear dependent, then dropping one of them, the second as an example, yields

$$W^{1(3)} = \psi \omega^{(1)}, \quad \psi = \frac{(G^{(1)} + \chi G^{(2)})(1 - 2G_2^2 g^{-2})g}{2G_2^2 \sqrt{1 - G_2^2 g^{-2}}}. \quad (46)$$

To determine the differential equation describing the change in the strong discontinuity surface wave intensity during its propagation, we proceed from the boundary conditions (5) and (6) differentiated with respect to time, which take the following form on the Rayleigh waves

$$\sum_{i=1}^3 [\dot{\sigma}_{11}]^{(i)} = 0, \quad \sum_{i=1}^3 [\dot{\sigma}_{12}]^{(i)} = 0, \quad (47)$$

$$\sum_{i=1}^3 [\dot{q}_1]^{(i)} = 0. \quad (48)$$

Based on the compatibility condition (15) and considering Eqs.(21b), (21c), and (22c), as well as the geometric characteristics (37), we find from (47) and (48) that

$$\begin{aligned} & \sum_{\alpha=1}^2 \left\{ \rho \left(1 - 2 \frac{G_2^2}{g^2} \right) G^{(\alpha)2} L_l^{(\alpha)} \nu_l^{(\alpha)} - 4\mu \frac{G^{(\alpha)}}{g} \nu_1^{(\alpha)0} \omega_{,1}^{(\alpha)} \right. \\ & + 2\mu \left(\frac{G^{(\alpha)2}}{g^2 \nu_1^{(\alpha)0} R} + 2\Omega^{(\alpha)} \right) \omega^{(\alpha)} - 2\rho G^{(\alpha)} \frac{D\omega^{(\alpha)}}{Dt} \left. \right\} - 2\mu L_l^{(3)} x_{,1}^{l(3)} \frac{G_2}{g} \nu_1^{(3)0} \\ & + 2\mu \left[\frac{G_2^2}{g^2} W_{,1}^{1(3)} - (\nu_1^{(3)0})^2 W_{,\alpha}^{(3)} \right] + 2\mu \frac{G_2}{gR} W^{1(3)} = 0, \quad (49) \\ & \sum_{\alpha=1}^2 \left\{ 2L_l^{(\alpha)} \nu_l^{(\alpha)} \nu_1^{(\alpha)0} \frac{G^{(\alpha)}}{g} R + 2 \left(1 - 2 \frac{G^{(\alpha)2}}{g^2} \right) R \omega_{,1}^{(\alpha)} - 2 \frac{G^{(\alpha)}}{g} \omega^{(\alpha)} \right\} \end{aligned}$$

$$+ \left(1 - 2\frac{G_2^2}{g^2}\right) R L_l^{(3)} x_{,1}^{l(3)} - 2R \frac{G_2}{g} \nu_1^{(3)0} (W_{,\alpha}^{(3)} + W_{,1}^{1(3)}) - \frac{1}{\nu_1^{0(3)}} \left(1 - 2\frac{G_2^2}{g^2}\right) W^{1(3)} = 0, \quad (50)$$

$$L_l^{(2)} \nu^{l(2)} = \frac{G^{(1)}}{G^{(2)}} \chi L_l^{(1)} \nu^{l(1)} + \sum_{\alpha=1}^2 \left\{ a_{\alpha} \frac{D\omega^{(\alpha)}}{Dt} + b_{\alpha} \omega_{,1}^{(\alpha)} - 2\Omega^{(\alpha)} d_{\alpha} \omega^{(\alpha)} \right\}, \quad (51)$$

where $L_i = L_k \nu^k \nu_i + g_{ij} L_l x_{,\delta}^l g^{\delta\gamma} x_{,\gamma}^j$, an index after a comma denotes that the corresponding value is calculated on the sphere's surface, i.e., at $\rho = R$,

$$a_{\alpha} = \frac{(G^{(\alpha)2} + G_1^2) \nu_1^{(\alpha)0} G^{(2)}}{(G^{(2)2} - G_1^2) \nu_1^{(2)0} G^{(\alpha)2}}, \quad b_{\alpha} = \frac{(G^{(\alpha)2} - G_1^2) G^{(2)}}{(G^{(2)2} - G_1^2) g \nu_1^{(2)0}},$$

$$d_{\alpha} = \frac{G^{(2)} G_1^2 \nu_1^{(\alpha)0}}{(G^{(2)2} - G_1^2) G^{(\alpha)} \nu_1^{(2)0}}.$$

Substituting Eq.(51) into Eqs.(49) and (50) with allowance made for formula (21c) yields

$$\rho G^{(1)} (1 - 2G_2^2 g^{-2}) (G^{(1)} + \chi G^{(2)}) L_k^{(1)0} \nu^{k(1)0} - 2\mu G_2 g^{-1} \nu_1^{(3)0} L_k^{(3)0} (x_{,1}^{k(3)})^0 = F_1, \quad (52)$$

$$2G^{(1)} g^{-1} R (\nu_1^{(1)0} + \chi \nu_1^{(2)0}) L_k^{(1)0} \nu^{k(1)0} + (1 - 2G_2^2 g^{-2}) R L_k^{(3)0} (x_{,1}^{k(3)})^0 = F_2, \quad (53)$$

where

$$F_1 = \sum_{\alpha=1}^2 \left\{ \left[4\mu G^{(\alpha)} g^{-1} \nu_1^{(\alpha)0} - \rho(1 - 2G_2^2 g^{-2}) G^{(2)2} b_{\alpha} \right] (\omega_{,1}^{(\alpha)})^0 + \left[2\rho G^{(\alpha)} - \rho(1 - 2G_2^2 g^{-2}) G^{(2)2} a_{\alpha} \right] (D\omega^{(\alpha)}/Dt)^0 - \left[2\mu (G^{(\alpha)2} g^{-2} R^{-1} (\nu_1^{(\alpha)0})^{-1} + 2\Omega^{(\alpha)}) - 2\rho(1 - 2G_2^2 g^{-2}) G^{(2)2} \Omega^{(\alpha)} d_{\alpha} \right] \omega^{(\alpha)0} \right\} - 2\mu G_2 (gR)^{-1} W^{1(3)0} - 2\mu \left[G_2^2 g^{-2} (W_{,1}^{1(3)})^0 - (\nu_1^{(3)0})^2 (W_{,\gamma}^{\gamma(3)})^0 \right]$$

$$F_2 = \sum_{\alpha=1}^2 \left\{ -2R \left[(1 - 2G^{(\alpha)2} g^{-2}) + G^{(2)} g^{-1} \nu_1^{(2)0} b_{\alpha} \right] (\omega_{,1}^{(\alpha)})^0 - 2G^{(2)} g^{-1} R \nu_1^{(2)0} a_{\alpha} (D\omega^{(\alpha)}/Dt)^0 + 2 (G^{(\alpha)} g^{-1} + 2G^{(2)} g^{-1} \nu_1^{(2)0} \Omega^{(\alpha)0} R d_{\alpha}) \omega^{(\alpha)0} \right\} + (\nu_1^{(3)0})^{-1} (1 - 2G_2^2 g^{-2}) W^{1(3)0} + 2G_2 g^{-1} R \nu_1^{(3)0} \left[(W_{,\gamma}^{\gamma(3)})^0 + (W_{,1}^{1(3)})^0 \right].$$

Multiplying Eq.(52) by $R(1 - 2G_2^2 g^{-2})$ and Eq.(53) by $2\mu G_2 g^{-1} \nu_1^{(3)0}$, adding them and having regard for Eq.(45) yields

$$F_1 R (1 - 2G_2^2 g^{-2}) + 2\mu F_2 G_2 g^{-1} \nu_1^{(3)0} = 0. \quad (54)$$

From the relationship (54) one can obtain the equation for determining the intensities of the Rayleigh waves during their propagation along the free and heat-insulated surface of the thermoelastic sphere. For this purpose we substitute the derivatives $D\omega/Dt$ and DW^γ/Dt for ω and W^γ by the formulas (21a) and (22b), respectively, express $\omega^{(2)}$ and $W^{1(3)}$ in terms of $\omega^{(1)}$ by formulas (43) and (46), introduce the derivative in the direction of the tangent to the line of curvature on the body's surface

$$\frac{d}{ds} = \frac{\delta}{\delta t} \frac{1}{g} + \nu_1^0 \frac{\partial}{\partial u^1}, \quad (55)$$

and take the relationship

$$W_{,\beta}^\alpha = \frac{\partial W^\alpha}{\partial u^\beta} + \Gamma_{\beta\gamma}^\alpha W^\gamma \quad (56)$$

into account.

As a result we obtain

$$\frac{d\omega^{(1)}}{ds} + \alpha\omega^{(1)} + \frac{1}{R}\gamma\omega^{(1)} + \delta\omega^{(1)} = 0, \quad \alpha = \frac{\gamma_1}{\gamma_0}, \quad \gamma = \frac{\gamma_2}{\gamma_0}, \quad \delta = \frac{\gamma_3}{\gamma_0}, \quad (57)$$

where $\gamma_0, \gamma_1, \gamma_2, \gamma_3, l_\alpha$, and β are the coefficients depending on the geometric characteristics and the wave velocities, and an upper "zero" index denotes that the given value is calculated on the surface of the body, i.e., at $\rho = R$.

The analysis of the expressions for α, γ , and δ shows that α is a real value, γ is an imaginary value, and δ is a complex value. With allowance made for the aforesaid, the solution to Eq.(57) has the form

$$\omega^{(1)} = C \exp -\alpha s \exp (-i\gamma^* \frac{1}{R}s) \exp \left(-\int_0^s \delta(s) ds \right), \quad (58)$$

where C is an arbitrary complex constant, and $\gamma^* = -i\gamma$.

Reference to Eq.(58) shows that the connectedness of the strain and temperature fields (the value α characterize the connectivity of the fields) results in the exponential attenuation of the nonstationary Rayleigh wave intensity, the curvature of the sphere's surface R^{-1} along which the surface wave propagates governs the oscillatory character of the behaviour of its intensity (at $R \rightarrow \infty$ the oscillation is disappears), but the function of the Rayleigh wave curvature of the distance s measured along the line of curvature (this dependence is contained in $\delta(s)$) can involve the attenuation and oscillation of its intensity at a time (as it would be shown later, the attenuation has not an exponential but a power nature).

Using expression (58), having regard for formulas (37), and putting $s = R\theta$, we obtain the relations for the Rayleigh wave intensities propagating along the free and heat-insulated surface of the thermoelastic sphere:

$$\omega^{(1)} = C \exp(-\alpha R\theta) \exp[-i\theta(\gamma^* + \kappa_1^* + \kappa_2^*)] |\sin \theta|^{-\kappa_3}, \quad (59)$$

where

$$\kappa_1^* = -i\kappa_1, \quad \kappa_2^* = -i\kappa_2,$$

$$\begin{aligned} \kappa_1 &= \left\{ - \left[l_1 - 4\mu \left(1 - 2 \frac{G_2^2}{g^2} \right) + 2\beta d_1 \right] \frac{1}{\nu_1^{(1)0}} \right. \\ &\quad \left. - \chi \left[l_2 - 4\mu \left(1 - 2 \frac{G_2^2}{g^2} \right) + 2\beta d_2 \right] \frac{1}{\nu_1^{(2)0}} + 2\mu \frac{G_2}{g} \psi \left(\nu_1^{(3)0} \right)^{-2} \right\} \frac{1}{\gamma_0}, \\ \kappa_2 &= \left\{ - \left[l_1 - 4\mu \left(1 - 2 \frac{G_2^2}{g^2} \right) + 2\beta d_1 \right] \nu_1^{(1)0} \right. \\ &\quad \left. - \chi \left[l_2 - 4\mu \left(1 - 2 \frac{G_2^2}{g^2} \right) + 2\beta d_2 \right] \nu_1^{(2)0} + 2\mu \frac{G_2}{g} \psi - 2\mu \psi \frac{G_2^3}{g^3} \right\} \frac{1}{\gamma_0}, \\ \kappa_3 &= \left\{ - \left[l_1 - 4\mu \left(1 - 2 \frac{G_2^2}{g^2} \right) + 2\beta d_1 \right] \frac{G^{(1)}}{g} \right. \\ &\quad \left. - \chi \left[l_2 - 4\mu \left(1 - 2 \frac{G_2^2}{g^2} \right) + 2\beta d_2 \right] \frac{G^{(2)}}{g} + 2\mu \frac{\psi}{\nu_1^{(3)0}} \frac{G_2^4}{g^4} \right\} \frac{1}{\gamma_0}. \end{aligned}$$

Knowing the value $\omega^{(1)}$, all characteristics of the nonstationary Rayleigh wave can be determined, and the discontinuity in temperature on this wave among other factors. Having regard for formulas (12), (43), and (59), for $[\Theta]$ we find

$$\begin{aligned} [\Theta] &= A \exp(-\alpha R\theta) |\sin \theta|^{-\kappa_3} [C' \cos \theta(\gamma^* + \kappa_1^* + \kappa_2^*) \\ &\quad + C'' \sin \theta(\gamma^* + \kappa_1^* + \kappa_2^*)], \end{aligned} \quad (60)$$

where $A = (\gamma G^{(1)})^{-1} \rho(G^{(1)2} - G_1^2) + (\gamma G^{(2)})^{-1} \rho(G^{(2)2} - G_1^2) \chi$, $C' = \Re C$, and $C'' = \Im C$.

The angle θ ($\pi/2 \leq \theta < \pi$) dependence of the value $\Theta_* = [\Theta]/[\Theta]_0$ ($[\Theta]_0 = [\Theta]|_{\theta=\pi/2}$) is presented in Fig.2 for a polycrystalline copper sphere at $C' = C'' = 1$. Reference to Fig.2 shows that the generation of the temperature discontinuity at the equator results in the nonstationary Rayleigh waves converging to the poles, on which the initial jump of temperature increases without bounds as the waves approach the poles. This involves warming up of the material surrounding the poles and its transition into a plasma condition.

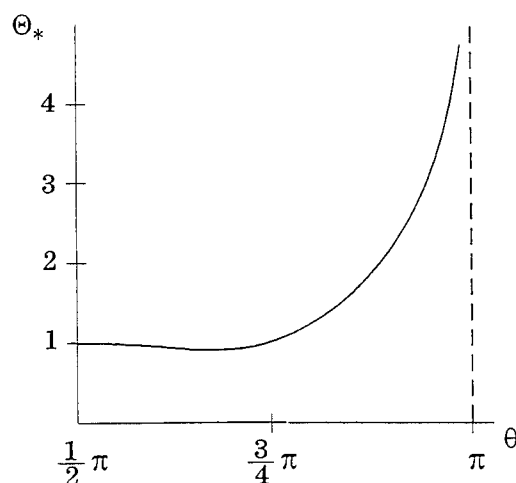


Fig.2. The angle θ dependence of the value Θ_* .

CONCLUSIONS

The investigations carried out show that during the propagation of non-stationary Rayleigh wave (line of discontinuity) across the free and heat-insulated surface of a thermoelastic sphere along the line of curvature the intensity of the wave attenuates by exponential and power laws at a time; in so doing the exponential attenuation occurs due to the connectedness of the strain and temperature fields, but the attenuation by the power law is caused by the presence of the time-dependent curvature of the surface wave. Besides the attenuation, the surface wave intensity oscillates with the time, in so doing the oscillation connects only with the curvature of the thermoelastic body surface.

References

1. Nayfeh, A. and Nemmat-Nasser, S., Thermoelastic waves in solids with thermal relaxation. *Acta Mechanica*, 1971, **12**, 53-69.
2. Petrashen, G.I., Rayleigh problem for surface waves in sphere case (in Russian), *Dokl. Akad. Nauk SSSR*, 1946, **52**, 763-766.
3. Rossikhin, Yu.A., Impact of a rigid sphere onto an elastic half-space. *Sov. Appl. Mech.*, 1986, **22**, 403-409.
4. Sobolev, S.L., Application of the plane wave theory to the Lamb problem" (in Russian). *Trans. Seismol. Inst. Akad. Nauk SSSR*, 1932, N 18, 1-14.
5. Thomas, T.Y., *Plastic Flow and Fracture in Solids*, Academic Press, New York, 1961.

Theoretical and Experimental Investigation of Multistage Vibration Isolation System

Shen Rongying

Institute of Vibration, Shock & Noise Research
Shanghai Jiao Tong University, Shanghai, 200030, P.R.China

Zhu Hua

Shanghai Marine Equipment Research Institute
China State Shipbuilding Corporation, Shanghai, 200031, P.R.China

Abstract

Multistage resilient mounting system of machinery is an effective measure to attenuate unwanted vibration and structureborne sound transmission. In the present paper, the approach of mechanical impedance synthesis under modal coordinates has been developed. The basic idea of the approach is to use modal coordinates instead of physical ones, and physical parameters are represented in terms of modal coordinates. The whole impedance matrix of the system can be obtained by superposition of that of each composed component and isolator. This approach is available to calculate the dynamic characteristics and vibrational power flow transmission of the multistage vibration isolation system with nonrigid subframe and nonrigid foundation. The experimental test results agree favorably with the predicted analytical value.

1. Introduction

Resilient mounting system of machinery is an effective measure to attenuate unwanted vibration and structureborne sound transmission. It is widely accepted and adopted for many engineering installations. With the advent of increasingly requirement for the reduction of vibration transmission from the machinery to the seating structures, the technique and measure of the multistage vibration isolation system have been successfully applied to some engineering practices. For the past decades the theoretical and experimental study on its dynamic characteristics has been intensively pursued by a number of workers, in which the subframe and the foundation were generally considered as rigid bodies and, the purpose was concentrated upon analysis of natural frequencies and vibration transmission of system in order to avoid resonance that would seriously impair its isolation performance and to assess its isolation effectiveness^[1-3]. The advantage of above analytical and

calculation models gives practical, economical and convenient means of obtaining solutions and is suitable for many engineering practices.

In some cases however, it is not always true to treat the subframe and the foundation as the rigid bodies, especially in transport vehicle and on board ships. For this situation, a considerably more precise and detailed form of analysis is required in order to predict the isolation afforded by the mounting. The problem of vibration isolation system with a nonrigid subframe and a nonrigid foundation has been investigated by many other workers and various methods have been developed. These methods can be probably divided into several kinds. For the sake of simplicity, three main methods are reviewed briefly below.

The first one was transfer matrix method based on four pole parameters according to the analysis method of Soliman and Hallam who derived an equation governing the response of nonrigid machine mounted by any number of isolators on a nonrigid foundation and excited by any number of input forces[4]. Applying this method to analysis of isolation system, the machine, the subframe and the foundation were considered as multi-input and multi-output components whose dynamic characteristics can be represented by mobility equation of the component respectively. The isolators can also be represented by their mobility equation derived from its four pole parameters equation. Then according to the condition for force equilibrium and motion compatibility at the junction, the relationship of force and response of the whole system can be given out. However, the method was valid to single stage vibration isolation system, and was available for multistage isolation system while both of the number of points of input and output for each subframe were the same only.

The second was the dynamic stiffness coupling technique proposed by Sainsbury and Ewins[5] that can be used to analyze a complex mechanical structure. That method was based on building block approach to structural dynamics developed by Klosterman et al[6], whose basic idea was to consider the structure as an assembly of connected components and to perform a detailed analysis of each component individually. In [5] a theoretical dynamic analysis of a machinery vibration isolation system with damped subframe that consists of damped sandwich beams was described in detail. That method was basically also feasible for complex multistage isolation system. The key problem was to obtain mechanical impedance data of each component of system. In some cases it was not easy to get that data because its calculation or measurement had to satisfy a certain constraint condition. In

addition, that method just gave out vibration response of the junctions between components only.

The third was a finite element method that has gradually been applied to analysis and calculation of machinery isolation system. Masao and Miyoshi gave out a detailed solution of two stage vibration isolation system of a diesel generator set using finite element method^[7-8]. However, it relies upon the computer capacity and calculating technique.

It is the purpose of this paper to develop a new approach that is referred to as the approach of mechanical impedance synthesis under modal coordinates. The basic idea of the approach is to use modal coordinates instead of physical ones, and physical parameters are represented in terms of modal coordinates. The whole impedance matrix of the system can be obtained by superposition of that of each composed component and isolator. This approach can be used to calculate the natural frequencies and, vibration responses of an arbitrary point of the system as well as vibrational power flow transmission of the multistage vibration isolation system with nonrigid subframes and nonrigid foundation. The experimental test is carried out, consisting of two steel plates mounted upon a thin steel plate via four vibration isolators respectively, which in turn resiliently mounted upon two simply supported beams. The objective of the test is to verify the analysis method. The experimental test results agree favorably with the predicted analytical value.

2. Analysis Method

In general the multistage vibration isolation system consists of several rigid (or nonrigid) machines, nonrigid subframes and rigid (or nonrigid) foundation that are connected together by vibration isolators at different link points respectively. The most general case of a multistage isolation system is schematically shown in figure 1.

2.1. The basic theory of impedance synthesis

According to the modal theory, there is a principle that at any frequency the mechanical impedance of a structure composed of two components connected together can be obtained by adding the mechanical impedance of each component at the connection point. Therefore the mechanical impedance of properties of the assembled structure may be expressed in terms of the corresponding properties of the individual components. This basic principle can be explained with the aid of the specific example in figure 2.

In figure 2, the subsystem A has n points and F_i and U_i denote the input force and the response at point i , and the subsystem B has m points and f_j and V_j denote the input force and the response at point j . Two components are rigidly connected at point n of A and point l of B.

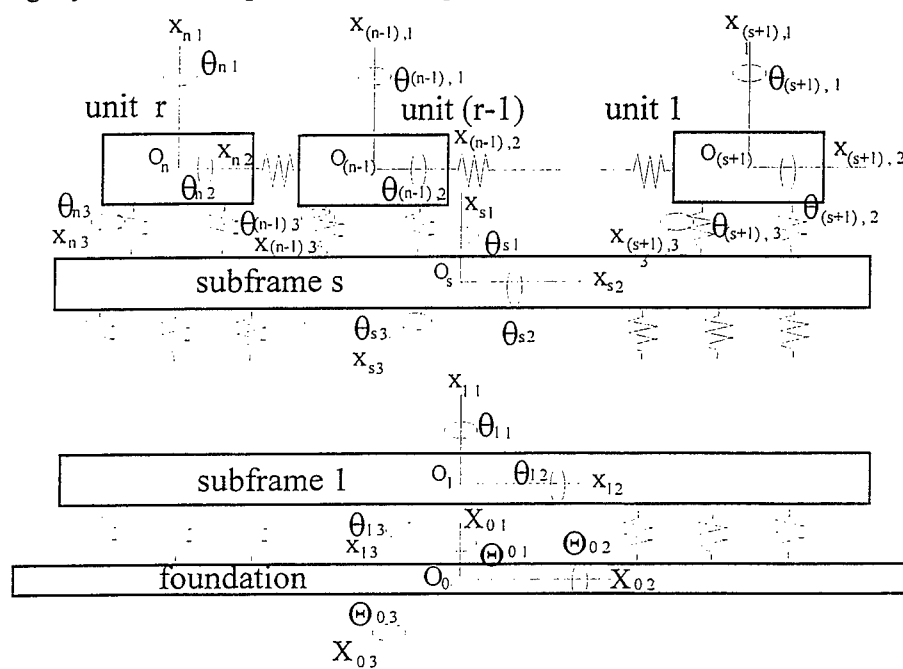


Fig. 1 Diagram of multistage resilient mounting system

The motion equation governing the subsystem A can be expressed as

$$F = ZU \quad (1)$$

in which Z is a $n \times n$ square impedance matrix, U and F are column vectors of the response (displacements and angular displacements) and force (forces and moments) acting on each pole of system A respectively. The equation (1) can further be rewritten in the following form

$$\begin{bmatrix} F_l \\ F_n \end{bmatrix} = \begin{bmatrix} Z_{ll} & Z_{ln} \\ Z_{nl} & Z_{nn} \end{bmatrix} \begin{bmatrix} U_l \\ U_n \end{bmatrix} \quad (2)$$

in which Z_{ll} is a $(n-1) \times (n-1)$ square impedance matrix, Z_{ln} and Z_{nl} are $(n-1) \times 1$ and $1 \times (n-1)$ impedance column respectively. F_l and U_l are 1 to $(n-1)$ column vectors, representing the input force and response of 1 to $(n-1)$ poles in system A. Similarly the motion equation governing the sub-system B is as the same as equation (2), i.e.

$$\begin{bmatrix} f_1 \\ f_m \end{bmatrix} = \begin{bmatrix} z_{11} & z_{1m} \\ z_{m1} & z_{mm} \end{bmatrix} \begin{bmatrix} V_1 \\ V_m \end{bmatrix} \quad (3)$$

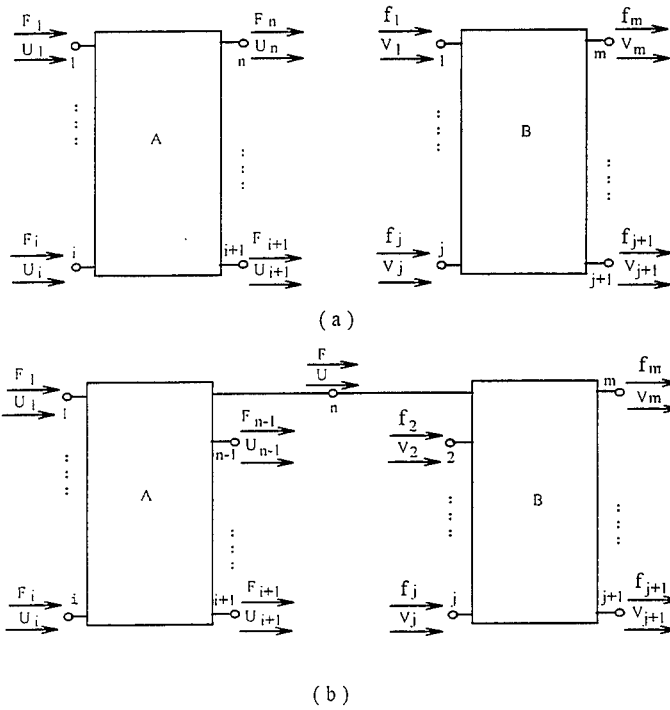


Fig. 2 Typical system consisted of subsystems A and B

where z_{mm} is a $(m-1) \times (m-1)$ square impedance matrix, z_{m1} and z_{1m} are $(m-1) \times 1$ and $1 \times (m-1)$ impedance column respectively. f_m and V_m are 1 to $(m-1)$ column vectors representing the input force and response of 2 to m poles in system B.

Combining equations (2) and (3) gives out

$$\begin{bmatrix} F_1 \\ F_n \\ f_1 \\ f_m \end{bmatrix} = \begin{bmatrix} Z_{11} & Z_{1n} & & \\ Z_{n1} & Z_{nn} & & \\ & & z_{11} & z_{1m} \\ & & z_{m1} & z_{mm} \end{bmatrix} \begin{bmatrix} U_1 \\ U_n \\ V_1 \\ V_m \end{bmatrix} \quad (4)$$

According to impedance equations of subsystems A and B, the dynamic performance of the whole system, in the case of rigid connection at pole n of

A with pole 1 of B, can be described from the conditions for force equilibrium and motion compatibility as follows

$$\begin{cases} \mathbf{F} = \mathbf{F}_n + \mathbf{f}_1 \\ \mathbf{U}_n = \mathbf{V}_1 = \mathbf{U} \end{cases} \quad (5)$$

Thus it can be expressed in the form of matrix equation as

$$\begin{bmatrix} \mathbf{F}_1 \\ \mathbf{F} \\ \mathbf{f}_m \end{bmatrix} = \begin{bmatrix} \mathbf{I}_1 & & \\ & 1 & 1 \\ & & \mathbf{I}_m \end{bmatrix} \begin{bmatrix} \mathbf{F}_n \\ \mathbf{F}_n \\ \mathbf{f}_1 \\ \mathbf{f}_m \end{bmatrix} \quad (6)$$

and

$$\begin{bmatrix} \mathbf{U}_1 \\ \mathbf{U}_n \\ \mathbf{V}_1 \\ \mathbf{V}_m \end{bmatrix} = \begin{bmatrix} \mathbf{I}_1 & & \\ & 1 & \\ & & 1 \\ & & & \mathbf{I}_m \end{bmatrix} \begin{bmatrix} \mathbf{U}_1 \\ \mathbf{U} \\ \mathbf{U} \\ \mathbf{V}_m \end{bmatrix} \quad (7)$$

where \mathbf{I}_1 and \mathbf{I}_m are $(n-1) \times (n-1)$ and $(m-1) \times (m-1)$ unit matrices respectively.

Substituting these conditions into equation (4), the equation of the whole system can be obtained

$$\begin{bmatrix} \mathbf{F}_1 \\ \mathbf{F} \\ \mathbf{f}_m \end{bmatrix} = \begin{bmatrix} \mathbf{Z}_{11} & \mathbf{Z}_{1n} & \\ \mathbf{Z}_{n1} & \mathbf{Z}_{nn} + \mathbf{Z}_{11} & \mathbf{Z}_{1m} \\ & \mathbf{Z}_{m1} & \mathbf{Z}_{mm} \end{bmatrix} \begin{bmatrix} \mathbf{U}_1 \\ \mathbf{U} \\ \mathbf{V}_m \end{bmatrix} \quad (8)$$

2.2. The approach of mechanical impedance synthesis under modal coordinate

The basic idea of this new approach is to use modal coordinates instead of physical ones, and physical parameters are represented in terms of modal coordinates. It is very common that the multistage vibration isolation system consists of several components, including nonrigid subframes and nonrigid foundation, which are connected together by isolators at different link points respectively. The performance of these components can be represented by

their modal impedance matrixes according to modal analysis, and the impedance matrix of each isolator can be derived using modal parameters of the junction. Then the whole modal impedance matrix of the system can be obtained by superposition of that of components and isolators. The analysis procedure is described in detail below.

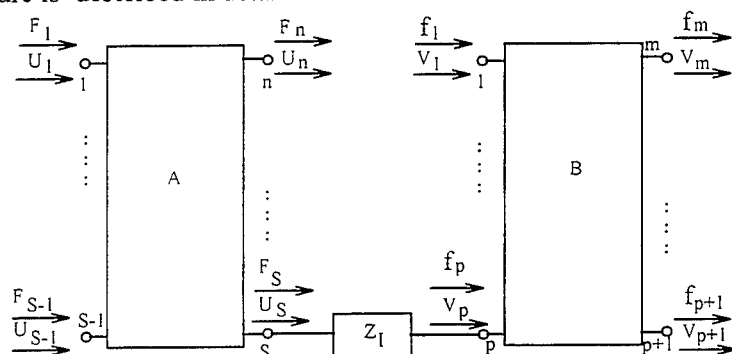


Fig. 3 A coupled system

Figure 3 shows a coupled system consisting of two components A and B that are connected by isolator I at point s of A and point p of B. The modal coordinates of two components A and B are $q_1, q_2 \dots q_N$ and $q'_1, q'_2 \dots q'_M$, the eigenvector columns are $\psi_1, \psi_2 \dots \psi_N$ and $\psi'_1, \psi'_2 \dots \psi'_M$, the modal forces of A and B are $f_1, f_2 \dots f_N$ and $f'_1, f'_2 \dots f'_M$, and the modal stiffness, modal masses and modal damping of two components are $K_1, K_2 \dots K_N, M_1, M_2 \dots M_N, C_1, C_2 \dots C_N$ and $K'_1, K'_2 \dots K'_M, M'_1, M'_2 \dots M'_M, C'_1, C'_2 \dots C'_M$ respectively. N and M are the selected modal numbers of two components. Therefore the performance of component A can be specified by N modal impedance equations, i.e.

$$f_i = Z_i q_i \quad (i=1, 2 \dots N) \quad (9)$$

in which $Z_i = K_i - \omega^2 M_i + j \omega C_i$.

Equation (9) can also be written in terms of matrix form

$$\begin{bmatrix} f_1 \\ f_2 \\ \vdots \\ f_N \end{bmatrix} = \begin{bmatrix} K_1 - \omega^2 M_1 + j C_1 & & \\ & K_2 - \omega^2 M_2 + j C_2 & \\ & & \ddots \\ & & & K_N - \omega^2 M_N + j C_N \end{bmatrix} \begin{bmatrix} q_1 \\ q_2 \\ \vdots \\ q_N \end{bmatrix} \quad (10)$$

The modal impedance matrix of A is the diagonal one. Similarly, that of B has the same form of

$$\begin{bmatrix} f_1' \\ f_2' \\ \vdots \\ f_M' \end{bmatrix} = \begin{bmatrix} K_1' - \omega^2 M_1' + jC_1' & & & \\ & K_2' - \omega^2 M_2' + jC_2' & & \\ & & \ddots & \\ & & & K_M' - \omega^2 M_M' + jC_M' \end{bmatrix} \begin{bmatrix} q_1' \\ q_2' \\ \vdots \\ q_M' \end{bmatrix} \quad (11)$$

Now the problem is how to derive the impedance matrix of isolator I under modal coordinates. For isolator I, its two ends s and p are connected with subsystem A and B respectively, seeing figure 3, the impedance equation of isolator I at point s can be written as

$$F_s = Z_I (U_s - V_p) \quad (12)$$

where Z_I is the impedance data of the isolator that is given by manufactures or from measurement. According to modal superposition theory, there exists following relation

$$\begin{cases} U_s = \sum_{j=1}^N \psi_{sj} q_j \\ V_p = \sum_{j=1}^M \psi_{sj}' q_j' \end{cases} \quad (13)$$

In order to further deduce, a set of equivalent modal force of isolator, that means all each modal force acting on components A to be equivalently acting on point s, could be defined as follows

$$F_i = f_i / \psi_{si} \quad (i=1,2,\dots,N) \quad (14)$$

Substituting equations (14) and (13) to equation (12) N set of impedance equations in terms of modal parameters of components of A and B can be obtained

$$f_i = Z_I \left(\sum_{j=1}^N \psi_{sj} \psi_{si} q_j - \sum_{j=1}^M \psi_{sj}' \psi_{si}' q_j' \right) \quad (i=1,2,\dots,N) \quad (15)$$

Similarly, at point p, there exist M set of impedance equations under similar circumstances

$$f_i' = Z_I \left(\sum_{j=1}^M \psi_{pj}' \psi_{pi}' q_j' - \sum_{j=1}^N \psi_{pj} \psi_{pi} q_j \right) \quad (i=1,2,\dots,M) \quad (16)$$

Combining equations (15) and (16), the impedance equation of isolator I under modal coordinates of its connected components can be obtained

$$\{f_i\} = [Z] \{q_i\} \quad (17)$$

in which $\{f_i\} = [f_1 \ f_2 \ \dots \ f_N \ f_1' \ f_2' \ \dots \ f_M']^T$

$$\{q_i\} = [q_1 \ q_2 \ \dots \ q_N \ q_1' \ q_2' \ \dots \ q_M']^T$$

$$[Z] = Z_I = \begin{bmatrix} \psi_{s1} \psi_{s1} & \psi_{s1} \psi_{s2} & \dots & \psi_{s1} \psi_{sN} & -\psi_{s1} \psi_{p1}' & -\psi_{s1} \psi_{p2}' & \dots & -\psi_{s1} \psi_{pM}' \\ \psi_{s2} \psi_{s1} & \psi_{s2} \psi_{s2} & \dots & \psi_{s2} \psi_{sN} & -\psi_{s2} \psi_{p1}' & -\psi_{s2} \psi_{p2}' & \dots & -\psi_{s2} \psi_{pM}' \\ \vdots & \vdots & \ddots & \vdots & \vdots & \vdots & \ddots & \vdots \\ \psi_{sN} \psi_{s1} & \psi_{sN} \psi_{s2} & \dots & \psi_{sN} \psi_{sN} & -\psi_{sN} \psi_{p1}' & -\psi_{sN} \psi_{p2}' & \dots & -\psi_{sN} \psi_{pM}' \\ -\psi_{s1} \psi_{p1}' & -\psi_{s2} \psi_{p1}' & \dots & -\psi_{sN} \psi_{p1}' & \psi_{p1}' \psi_{p1}' & \psi_{p1}' \psi_{p2}' & \dots & \psi_{p1}' \psi_{pM}' \\ -\psi_{s1} \psi_{p2}' & -\psi_{s2} \psi_{p2}' & \dots & -\psi_{sN} \psi_{p2}' & \psi_{p2}' \psi_{p1}' & \psi_{p2}' \psi_{p2}' & \dots & \psi_{p2}' \psi_{pM}' \\ \vdots & \vdots & \ddots & \vdots & \vdots & \vdots & \ddots & \vdots \\ -\psi_{s1} \psi_{pM}' & -\psi_{s2} \psi_{pM}' & \dots & -\psi_{sN} \psi_{pM}' & \psi_{pM}' \psi_{p1}' & \psi_{pM}' \psi_{p2}' & \dots & \psi_{pM}' \psi_{pM}' \end{bmatrix}$$

$[Z]$ is the impedance matrix of the isolator I under modal coordinates of its connected components, and a symmetric one.

From impedance equations of each component, i.e. equations (10), (11) and (17), using the principle of "dynamic stiffness coupling technique" mentioned above, we can synthesize the impedance matrix equation of the whole system

$$\{f\} = [Z_T] \{q\} \quad (18)$$

in which $\{f\} = [f_1 \ f_2 \ \dots \ f_N \ f_1' \ f_2' \ \dots \ f_M']^T$

$$\{q\} = [q_1 \ q_2 \ \dots \ q_N \ q_1' \ q_2' \ \dots \ q_M']^T$$

$[Z_T]$ is superposition of impedance matrix of each component.

It will be seen from above analysis that the approach of mechanical impedance synthesis under modal coordinates considers the modal coordinates of each composed component as unknown parameters, and the motion equation of system is derived by using impedance synthesis. Here the modal coordinates denote local one, i.e., the modal parameters of component vibrating alone. After getting the modal coordinates solution by using equation (18), the response at any arbitrary point of component should superpose result

of corresponding modal coordinates. For inherent frequency solution, we decompose the impedance matrix into a diagonal mass matrix and a symmetrical stiffness matrix, then solve eigenvalue problem easily. Therefore, the dynamic characteristics analysis of multistage vibration isolation system can easily be executed by using above approach. This approach can be used to calculate the natural frequencies and, vibration responses of an arbitrary point of the system as well as vibrational power flow transmission of the multistage vibration isolation system with nonrigid subframes and nonrigid foundation.

3. Experimental verification of the theory

3.1 Experimental rig

The experimental work is carried out to measure the natural frequency, transfer function and power flow of two stage vibration isolation system in the laboratory in order to verify the preceding analysis of the characteristics of the multistage isolation system.

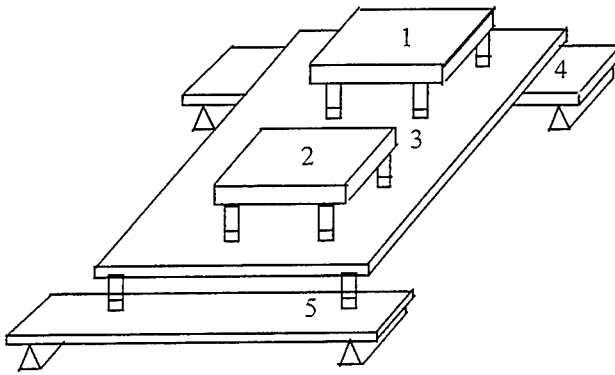


Fig. 4 Experimental rig

Experimental rig was shown in figure 4, which comprises five components: a pair of small size steel plates (designated by 1 and 2), a large steel plate (3) and a pair of steel beams (4 and 5). The size of two plates 1 and 2 is 150×232 mm and thickness 8 mm, representing two machinery sets. The plate 3, representing nonrigid subframe, has width 524 mm and length 624 mm with 5 mm thickness. Two identical steel beams 4 and 5 of width 59 mm and thickness 6 mm with 1000 mm length are simply supported at both ends of the beam representing nonrigid foundation. Here each machinery set was resiliently mounted via four JZN-15 rubber isolators on a subframe which, in

turn, was supported by four BL-2 elastic elements on the beams. Therefore, the measurement system can be considered as two stage isolation system with nonrigid subframe and nonrigid foundation. Table 1 lists the stiffness of isolators.

Table 1. Stiffness of isolator (kN/m)

Type	Vertical	Longitudinal	Lateral
JZN - 15	20.0	17.0	17.0
BL - 2	7.74	12.1	12.1

3.2 Experimental instrumentation

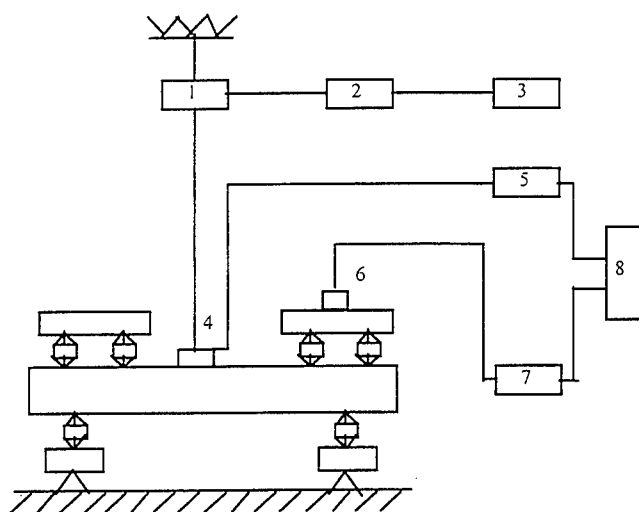


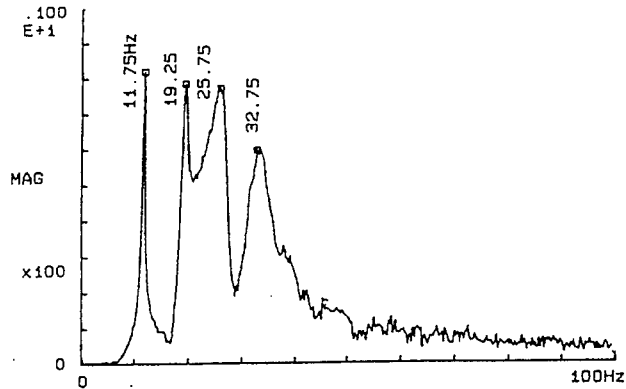
Fig. 5 Block diagram of instrumentation

- 1 electric shaker, 2 power amplifier, 3 signal source, 4 force transducer
- 5 electric charge amplifier, 6 accelerometer, 7 electric charge amplifier
- 8 CF-350 dual channel FFT analyzer

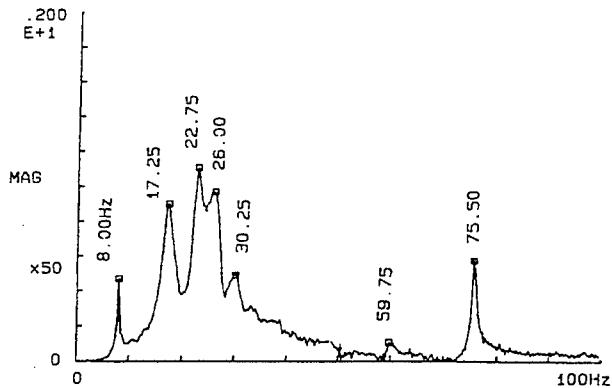
Figure 5 shows the instrumentation used to measure the inherent characteristics of the system. The subframe is excited by a shaker via force transducer that is placed at the center point of subframe. The signals of white noise excitation and acceleration response are measured simultaneously by a dual channel FFT analyzer. Changing exciting and receiving points, the natural frequencies of the system at different directions can be measured in the same way respectively.

3.3 Experimental results and comparison

Figures 6 (a-b) show two representative measured frequency response functions.



(a)



(b)

Fig 6. Measured frequency response curve

The pictures clearly show that the system has natural frequencies of 8, 11.75 and 17.25 Hz etc. Summing up all measured value, we get first eighteen natural frequencies. In order to compare measured value with predicted one, table 2 list as follows

In calculation procedure of experimental rig, the mechanical impedance parameters of plate 3 and beams 4 (5) are obtained by using finite element method, and thirty natural frequencies are calculated. In table 2 we just list

first eighteen natural frequencies. From table 2, it can be seen that measured results agree basically with the predicted one.

Table 2
Comparison of natural frequency between measured and predicted value(Hz)

Order	Predicted	Measured	error(%)
1	7.52	8.0	6.0
2	9.78	10.25	4.6
3	10.84	11.75	7.7
4	12.57	13.25	5.1
5	17.81	17.25	-3.2
6	18.58	19.25	3.5
7	20.36	21.25	4.2
8	22.14	22.50	1.6
9	23.32	22.75	-2.5
10	25.54	24.75	-3.2
11	26.59	25.25	-5.3
12	27.41	26.00	-5.4
13	27.92	29.00	3.7
14	28.16	30.25	6.9
15	29.62	31.75	6.7
16	30.69	32.75	6.3
17	35.42	35.00	-1.2
18	36.88	38.25	3.6

In order to estimate the isolation effectiveness of multistage isolation system, the vibrational power flow transmitted by the isolator is calculated and measured respectively. The power flow measurement is made by using the method developed by Pinnington[9]. Figure 7 shows four curves of the vibrational power flow from machinery (plate 1) to subframe (plate 3) through upper two isolators, in which --- and — lines denote predicted and measured value via isolator 1 respectively, -- and ...lines denote predicted and measured value via isolator 2 respectively. In same way figure 8 displays the power flow from subframe to foundation (beam 4) through lower two isolators. From both figures, it can be seen that transmitted power between predicted and measured is agreement, there by confirming the fesibility of above approach.

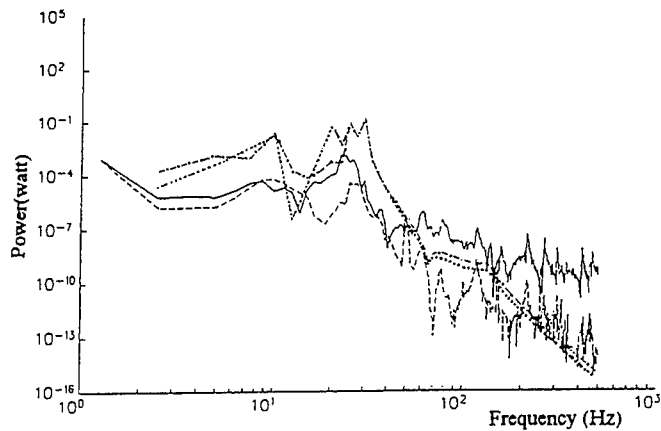


Fig. 7 Vibrational power flow from machinery to subframe

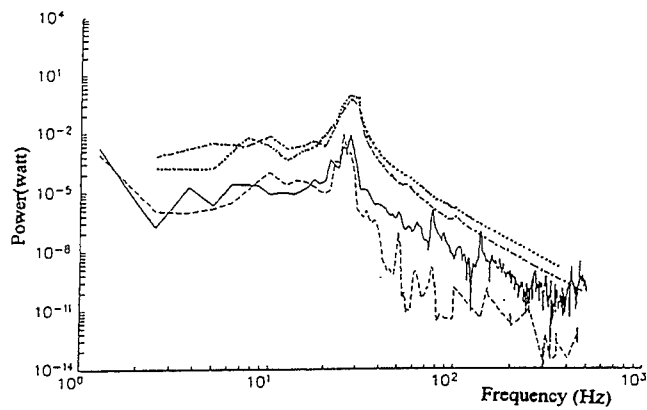


Fig. 8 Vibrational power flow from subframe to fondation

4. Conclusions

An approach of mechanical impedance synthesis under modal coordinates has been developed. The approach incorporates finite element method to obtain the inherent behaviour and the dynamic characteristics of multistage vibration isolation system with nonrigid subframe and nonrigid foundation.

An experimental investigation of a double stage vibration isolation system has been performed which provided favorable agreement between measured and predicted results. This experiment demonstrates that the proposed approach

is available for predicting accurately the dynamic behaviour of multistage isolation system.

Acknowledgements

The authors gratefully acknowledge the support provided for this work by State Shipbuilding Corporation Contract.

References

1. Gorman, R.G., Design and advantage of a two stage mounting system for major machine in ships' engine room. Shock and Vibration bulleting, 1966, 35,5.
2. Snowdon, J.C., Vibration isolation use and characterization. Journal of Acoustical Society of America, 1979, Vol.66.
3. Schult, K.F., The propulsion machinery installation of the type F-122 frigate, Maritime Defence, Sept. 1979, 9(4), 226-231.
4. Soliman, J.I., and Hallam, M.G., Vibration isolation between non-rigid machines and non-rigid foundations. JSV 1968,8(2), 329-351.
5. Sainsbury, M.G., and Ewins, D.J., Vibration analysis of a damped machinery foundation structure using the dynamic stiffness coupling technique. Transactions of the ASME, Aug.,1974, 1000-1005.
6. Klosterman, A.L., and Lemon, J.R., Building block approach to structural dynamics. ASME, Annual Vibration Conference Paper, 69-VIBR-30.
7. Masao and Miyoshi, Main propulsion diesel generators sets with acoustic enclosure and double resilient mounting for low noise application ship board acoustics. ISBN, 1986.
8. Masao and Miyoshi, Vibration characteristics of main propulsion diesel generator sets with double resilient mounting. Transaction of WJSNA, Aug. 1989.
9. Pinnington, R.J., Vibrational power transmission to a seating of a vibration isolation motor. JSV 1987,118(3), 515-530.

PASSIVE AND ACTIVE CONTROL I

DESIGN OF A WIDEBAND VIBRATION NEUTRALISER

M.J. BRENNAN

Institute of Sound and Vibration Research, University of Southampton,
Southampton, Hampshire, SO17 1BJ, UK.

1. INTRODUCTION

Since its inception by Ormondroyd and Den Hartog in 1928 [1], the vibration absorber has been used in many applications. It is usually employed in one of two ways; either to suppress a troublesome natural frequency of the host structure or to reduce vibration at a problematic excitation frequency. It is the latter that is of concern in this paper and to distinguish it from the former it is called a vibration neutraliser [2]. This device has a narrow bandwidth and acts like a notch filter, reducing the vibration of the host structure over a restricted frequency range. Its effectiveness depends upon two parameters, namely its mass and internal damping. If the damping is small then it is more effective, but its bandwidth is also small. At frequencies outside the narrow bandwidth of the neutraliser the vibration of the host structure can be amplified due to the presence of the neutraliser. Although many machines operate nominally at a single speed (frequency), they generally drift around this speed. Thus a narrow bandwidth neutraliser can be inappropriate as the neutraliser may increase the motion of the machine. To overcome this problem tunable neutralisers have been designed, for example [3][4], which can operate effectively when fitted to a machine whose speed fluctuates with time. However, such devices need a control system and are thus much more complicated than a simple passive device. The neutraliser discussed in this paper offers a way of increasing the bandwidth by grouping several neutralisers together in parallel with each device having a slightly different natural frequency than its adjacent partners. This device, which is called a wideband neutraliser, is studied analytically and its performance is compared with a single neutraliser. By making some approximations, several simple formulae that describe the important characteristics of the device are derived. Experimental results are also presented to validate the theoretical model. It should be noted that other investigators have studied similar devices for the attenuation of flexural waves on a plate [5] and the addition of damping to a structure [6].

2. CHARACTERISTICS OF A VIBRATION NEUTRALISER

Before discussing a wideband vibration neutraliser it is necessary to recall the characteristics of a single neutraliser. Consider first the system shown in

Figure 1, which depicts a machine with a neutraliser fitted which has a mass m_a and a complex stiffness $k^* = k(1 + j\eta)$. The frequency domain equations describing the system are:

$$f_1 = z_{11}\dot{x}_1 + z_{12}\dot{x}_2 \quad (1a)$$

$$f_2 = z_{21}\dot{x}_1 + z_{22}\dot{x}_2 \quad (1b)$$

$$f_a = z_a\dot{x}_a \quad (1c)$$

where all the variables are complex functions of frequency. The z 's are mechanical impedances [6].

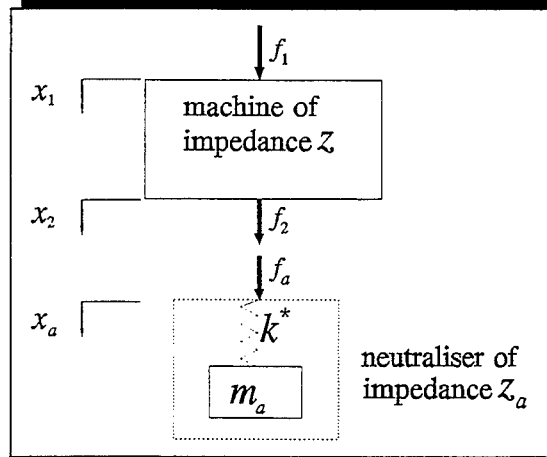


Figure 1 A machine of impedance z with a neutraliser fitted

If we first consider the machine alone in the absence of the neutraliser, then f_2 can be set to zero in equation (1b), and noting that $\dot{x} = j\omega x$ we get:

$$\frac{x_{2(free)}}{x_1} = -\frac{z_{21}}{z_{22}} \quad (2)$$

where the subscript 'free' denotes that the neutraliser is not fitted. When the neutraliser is fitted it applies a force to the machine, and the conditions at the interface between the machine and the neutraliser are $f_2 = -f_a$ and $x_2 = x_a$ because of force equilibrium and continuity of motion. In this case equations (1b) and (1c) combine to give:

$$\frac{x_{2(fitted)}}{x_1} = -\frac{z_{21}}{z_{22} + z_a} \quad (3)$$

where the subscript 'fitted' denotes that the neutraliser fitted. Equations (2) and (3) combine to give the ratio of the machine displacement at the neutraliser attachment position, with and without the neutraliser fitted:

$$\frac{x_{2(fitted)}}{x_{2(free)}} = \frac{1}{1 + \frac{z_a}{z_{22}}} \quad (4)$$

Equation (4) shows that the displacement of the machine can only be substantially reduced if the impedance of the neutraliser z_a is much greater than the impedance of the machine z_{22} . The impedance of a neutraliser is frequency dependent and is given by [7]:

$$z_a = \frac{j \omega m_a (1 + j \eta)}{1 - \Omega^2 + j \eta} \quad (5)$$

where η is the loss factor and $\Omega = \omega/\omega_t$, where ω_t is the tuned (natural) frequency of the neutraliser. The neutraliser's impedance becomes very large when its natural frequency is the same as the forcing frequency, i.e., $\Omega=1$. If we impose this condition and assume that $\eta \ll 1$, then equation (5) becomes:

$$z_{a(\text{tuned})} \approx \frac{\omega_t m_a}{\eta} \quad (6)$$

It can be seen that the neutraliser is more effective if its internal damping is low, if its mass is large or if the tuned frequency is high. To visualise the effect of such a neutraliser, we assume that the machine shown in **Figure 1** is working in a mass dominated region and has a neutraliser fitted. The resulting *change in displacement* due to the neutraliser is shown in **Figure 2**. It can be seen that the displacement of the machine is only substantially reduced over a small frequency range. Above this there is a resonance, and the displacement of the machine at frequencies close to this resonance is increased by the presence of the neutraliser.

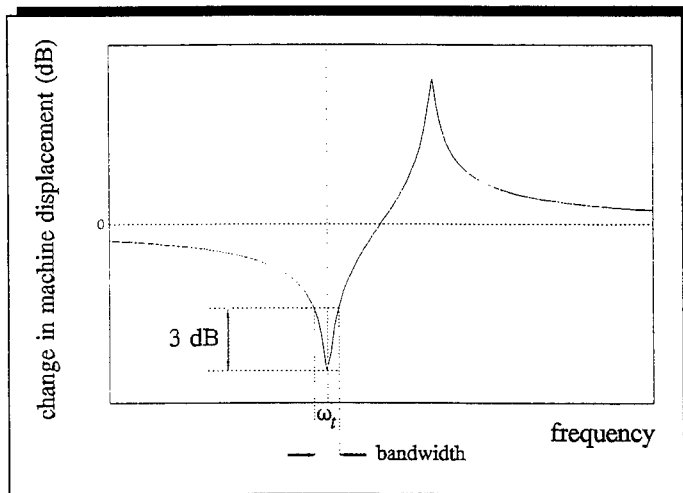


Figure 2 Change in the displacement of a machine operating in the mass-controlled region and fitted with a neutraliser

It is convenient to define an operational bandwidth $\Delta\omega$, of the neutraliser, which is the frequency range over which the neutraliser's impedance is within 3 dB of the maximum. In this frequency range the resulting displacement of the machine to which the neutraliser is attached is a minimum, and this can be seen in **Figure 2**. The bandwidth is related to the neutraliser's loss factor and the tuned frequency by the following expression [4]:

$$\Delta \omega = \eta \omega_r \quad (7)$$

It is clear from the above discussion that, for a given tuned frequency, a wideband neutraliser must have a large loss factor. If this is so then the maximum impedance will be small as can be seen by examining equation (6). The only way of increasing the neutraliser's maximum impedance and hence its effectiveness, but without reducing the bandwidth, is to increase the mass of the neutraliser. If the tuned frequency is to remain invariant then this will also require a proportionate increase in the neutraliser's stiffness.

3. CHARACTERISTICS OF A WIDEBAND VIBRATION NEUTRALISER

As shown in equation (4), if the impedance of a neutraliser is known in addition to that of the host structure then the vibration of the host structure can be predicted when a neutraliser is fitted. Thus we can characterise the dynamic behaviour of a wideband neutraliser by the single complex quantity of input mechanical impedance (input force/velocity), and it is this quantity that is discussed in this paper specifically for wideband neutralisers.

Consider the array of N neutralisers shown in **Figure 3** that make up the wideband neutraliser. The impedance $z = f/\dot{x}$, of the device is the sum of the impedances of the individual neutralisers, and is given by:

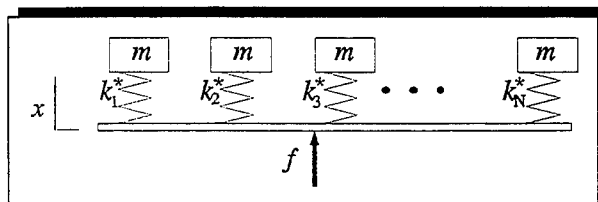


Figure 3 A wideband neutraliser consisting of an array of N neutralisers

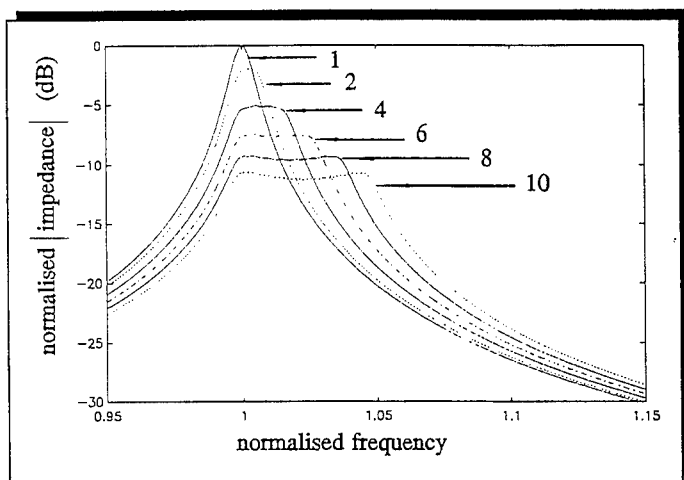
$$z = \sum_{n=1}^N \left(\frac{j \omega m (1 + j \eta)}{1 - (\Omega - \alpha(n-1))^2 + j \eta} \right) \quad (9)$$

where α is the spacing between the natural frequencies of the neutralisers. The normalised modulus of the impedance of the wideband neutraliser is plotted in **Figures 4a** and **b** for arrays of different numbers of neutralisers with $\alpha = \eta/2$ and $\alpha = \eta$. The normalising factor is the maximum impedance of a single neutraliser given by equation (6). In order that a comparison can be made between wideband neutralisers which contain a different number of neutralisers, the total mass of each wideband neutraliser is kept constant, i.e., $m = m_0/N$. A number of observations can be made with regards to **Figure 4**.

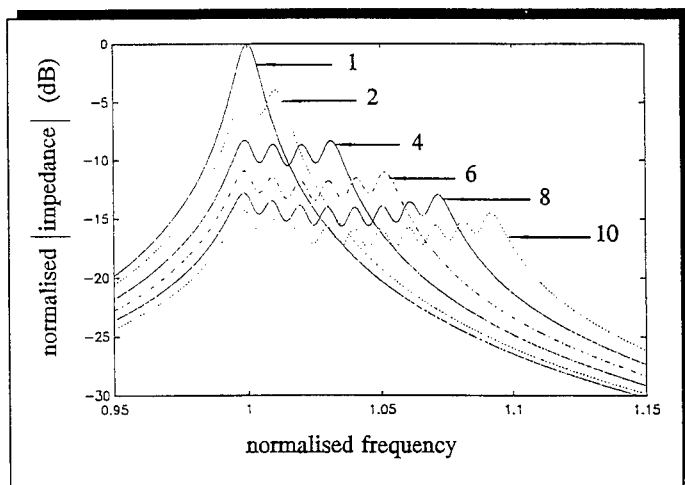
- At the lowest natural frequency of the neutraliser array, the impedance is approximately the maximum.
- Because the total mass is kept constant the normalised maximum

impedance reduces with an increasing number of neutralisers.

- (c) The bandwidth of the device increases with the number of neutralisers.
- (d) As the spacing between the individual neutraliser natural frequencies is increased the ripple in the impedance increases. It appears that a frequency spacing greater than η will result in a ripple which is greater than 3 dB, and this will probably be unacceptable.



(a) The normalised natural frequencies of adjacent neutralisers differ by $\eta/2$



(b) The normalised natural frequencies of adjacent neutralisers differ by η

Figure 4 Normalised modulus of the impedance of a wideband neutraliser consisting of an array of 1-10 neutralisers for different spacing of the neutraliser natural frequencies

The approximate maximum value of the impedance can be determined by evaluating equation (9) at $\Omega=1$. If $\eta \ll 1$, if products of small quantities are neglected and the total mass of the system is kept constant we get:

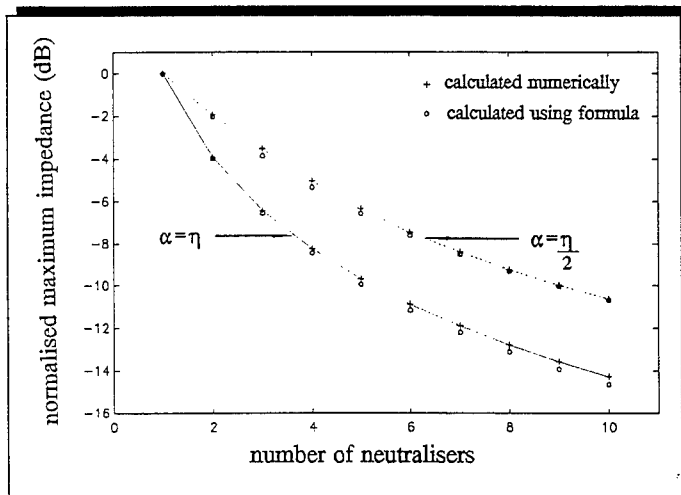
$$z_{\max} \approx \frac{j \omega_t m_a}{N} \sum_{n=1}^N \left(\frac{1}{2(n-1)\alpha + j\eta} \right) \quad (10)$$

The modulus of equation (10) normalised by the tuned impedance of a single neutraliser given in equation (6) can be written as:

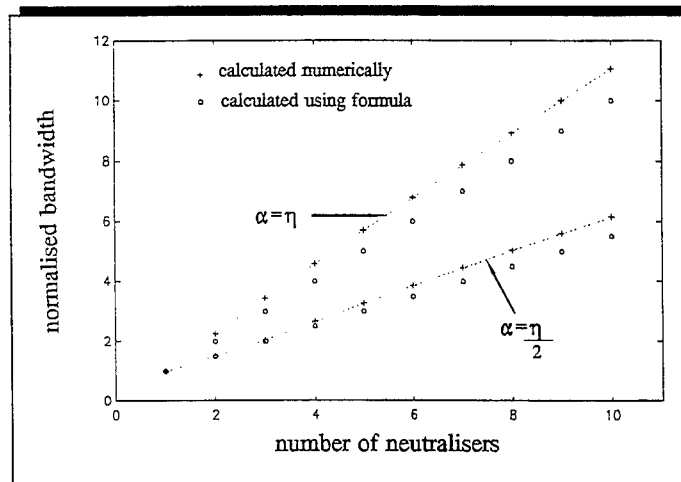
$$|z_{\max(\text{norm})}| \approx \frac{1}{N} \left| \sum_{n=1}^N \left(\frac{1}{1 - j \frac{2\alpha}{\eta} (n-1)} \right) \right| \quad (11)$$

To check the validity of the approximations made in the derivation of equation (11), it is plotted in **Figure 5a** for an array of 1 to 10 neutralisers with $\alpha=\eta/2$ and $\alpha=\eta$, together with the maximum impedance calculated numerically using equation (9) with a normalised frequency increment of 0.00001.

It can be seen that equation (11) gives a reasonable estimate of the maximum impedance of a wideband neutraliser. This graph also shows quite clearly that there is a penalty of a reduction in the maximum impedance when an array of neutralisers is used to increase the bandwidth of the vibration control device. For example if ten neutralisers are used in the array with the same total mass as the single neutraliser, and with a frequency spacing of $\eta/2$, then the maximum impedance is reduced by about 10 dB. If the frequency spacing is η then the maximum impedance is reduced by about 14 dB.



(a) Normalised maximum impedance of the array of neutralisers with natural frequency spacings of η and $\eta/2$.



(b) Normalised bandwidth of the array of neutralisers with natural frequency spacings of η and $\eta/2$.

Figure 5 Comparison of the maximum impedance and bandwidth of a wideband neutraliser consisting of an array of tuned neutralisers

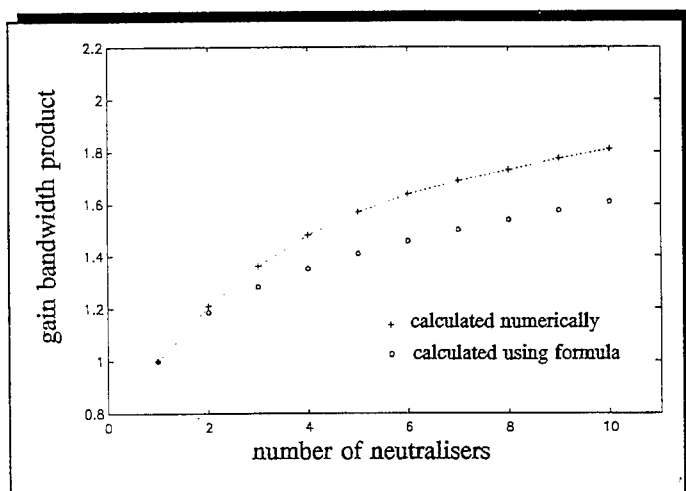
The approximate bandwidth of an array of N neutralisers normalised to the bandwidth η of a single neutraliser can be determined by simply summing the bandwidths of the individual neutralisers and correcting for the overlap between adjacent neutraliser bandwidths. This is given by:

$$\frac{\Delta \omega}{\omega_1} \approx 1 + \frac{\alpha}{\eta} (N - 1) \quad (12)$$

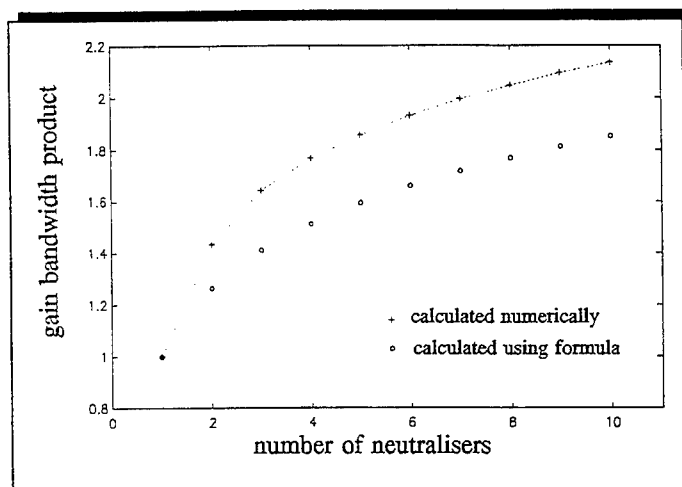
where ω_1 is the lowest natural frequency of the neutraliser array. The 3 dB

bandwidth is also calculated numerically using equation (9) with a normalised frequency interval of 0.00001, and is plotted in **Figure 5b** together with equation (12) for 1 to 10 neutralisers when $\alpha=\eta/2$ and η . It can be seen that equation (12) provides a reasonable estimate of the actual bandwidth.

The quantity that combines the properties of maximum impedance and bandwidth discussed above is the maximum impedance-bandwidth product. For a single neutraliser this is obtained by multiplying equation (6) by equation (7) and is simply $\omega_p m_a$. This shows, that at a given frequency, the only way of increasing the effectiveness of a single neutraliser whilst maintaining its bandwidth is to increase its mass. For the wideband neutraliser, the approximate maximum impedance-bandwidth product can be calculated by multiplying equation (11) by equation (12). To see how this compares with a single neutraliser it is normalised to the maximum impedance-bandwidth product for a single neutraliser. This is plotted in **Figures 6a** and **b** together with maximum impedance-bandwidth product calculated numerically. It can be seen that the errors in this approximation are larger than in previous cases. This is because the errors in approximations of (11) and (12) are compounded. Nonetheless the approximations are considered to be reasonable estimates and are attractive because they are much simpler to calculate. Examination of **Figures 6a** and **b** shows that the normalised maximum impedance-bandwidth product are greater than unity when more than one neutraliser is used in the array. This means that if the bandwidth of a single neutraliser is too small, then to increase it, it is more beneficial to use an array of neutralisers configured to form a wideband neutraliser as shown in **Figure 3**, than it is to either add mass or increase the damping in a single neutraliser.



(a) The normalised natural frequencies of adjacent neutralisers differ by $\eta/2$



(b) The normalised natural frequencies of adjacent neutralisers differ by η

Figure 6 Gain-bandwidth product for a wideband neutraliser consisting of an array of tuned neutralisers

If we compare **Figure 4a** with **Figure 4b**, we can see that the ripple in the impedance increases as the normalised frequency spacing between the individual neutralisers in the array is increased. In the same way as an approximate expression for the maximum impedance was derived, it is possible to derive an expression that gives the approximate size of the ripple. The ripple in dB is given by:

$$\text{ripple(dB)} = 20 \cdot \log_{10} |z_{\max(\text{norm})}| - 20 \cdot \log_{10} |z_{\min(\text{norm})}| \quad (13)$$

As the normalised maximum impedance $|z_{\max(\text{norm})}|$, has already been calculated in equation (11) it remains to calculate the normalised local minimum $|z_{\min(\text{norm})}|$ that occurs within the 3 dB bandwidth of the wideband neutraliser. If there is an **even number** of neutralisers in the array then the minimum occurs approximately when:

$$\Omega = 1 + \frac{(N - 1)}{2} \alpha \quad (14)$$

If we set Ω to this value in equation (9) and assuming that $\eta \ll 1$ and neglecting products of small quantities we get:

$$z_{\min} \approx \frac{j \omega_t m_a}{N} \sum_{n=1}^N \left(\frac{1}{(2n - 1 - N) \alpha + j \eta} \right) \quad (15)$$

The modulus of equation (15) normalised by the tuned impedance of a single neutraliser given in equation (6) can be written as:

$$|z_{\min(\text{norm})}|_{\text{even}} \approx \frac{1}{N} \left| \sum_{n=1}^N \left(\frac{1}{1 - j \frac{\alpha}{\eta} (2n - 1 - N)} \right) \right| \quad (16)$$

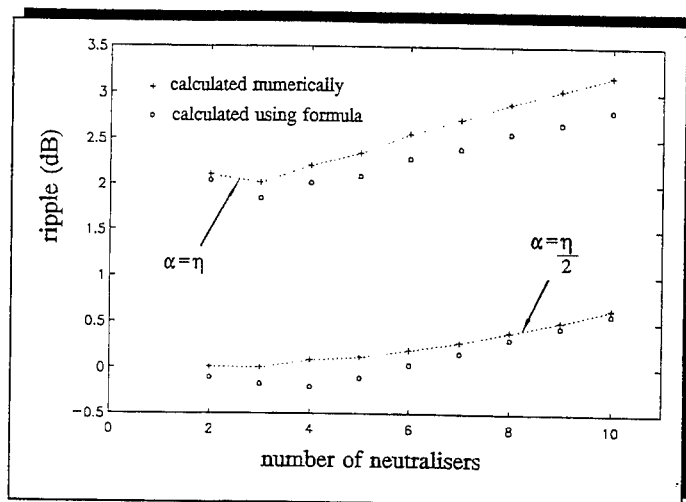
If there is an **odd number** of neutralisers in the array then the local minimum within the 3 dB bandwidth occurs approximately when:

$$\Omega = 1 + \frac{(N - 2)}{2} \alpha \quad (17)$$

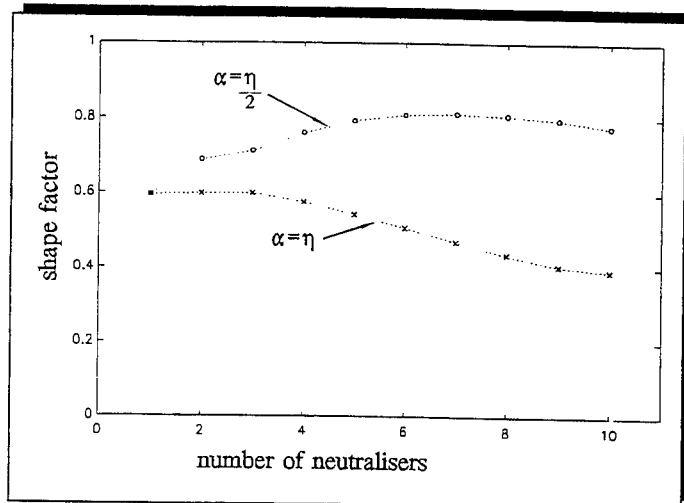
This can be substituted into equation (9) to give the minimum impedance and this can be written in an approximate form similar to equation (16) to give

$$|z_{\min(\text{norm})}|_{\text{odd}} \approx \frac{1}{N} \left| \sum_{n=1}^N \left(\frac{1}{1 - j \frac{\alpha}{\eta} (2n - N)} \right) \right| \quad (18)$$

Thus, equations (11) and (16) or (18) can be substituted into equation (13) to give the ripple. This is plotted in **Figure 7a** together with the numerically calculated ripple for $\alpha = \eta/2$ and $\alpha = \eta$.



(a) Ripple



(b) Shape factor

Figure 7 Comparison of some characteristics of wideband neutralisers consisting of an array of tuned neutralisers

It can be seen that the ripple is dependent primarily upon the frequency spacing between the neutralisers, and there is also a dependency upon the number of neutralisers used in the array. It increases as the frequency spacing increases and as the number of neutralisers in the array increases. For up to 10 neutralisers the ripple is less than 1 dB for $\alpha = \eta/2$ and less than 3.5 dB for $\alpha = \eta$.

One final characteristic of the wideband neutraliser that is worthy of consideration is the "shape factor". The neutraliser can be thought of as a

filter of certain bandwidth and gain (maximum impedance). The ideal characteristic for such a filter is that it should have a rectangular shape, bounded by the 3 dB bandwidth cut-off frequencies. To calculate the shape factor we determine the area under the curve between the cut-off frequencies and divide it by the area of the ideal filter. Thus a shape factor of one would denote a perfect filter. The shape factors have only been calculated numerically as no simple formulae could be derived, and they are shown for $\alpha=\eta/2$ and η in Figure 7b. It can be seen that when $\alpha=\eta$ the shape of the filter is generally worse than when a single neutraliser is used, but when $\alpha=\eta/2$ then the shape factor is improved. In the latter case it appears to peak when there are seven neutralisers in the array.

4. EXPERIMENTAL WORK

To validate the theory discussed in the previous section and to test the feasibility of making a wideband neutraliser using an array of neutralisers, experimental work was conducted. A wideband neutraliser was designed that could accommodate 1 to 10 neutralisers. It consisted of a central bolt to which up to ten thin aluminium beams were attached as shown in Figure 8. Each beam was 20 mm wide and 2 mm thick and differed in length from adjacent beams by 1 mm. The longest beam was 220 mm long and the shortest 211 mm. A 25 mm strip of thin damping tape was fixed close to the root of each beam as shown in Figure 8. Each beam acted as a double cantilever, and it was calculated that the natural frequency of the longest beam (100 mm active length) would be about 164 Hz. The natural frequency of the shortest beam (95.5 mm active length) was calculated to be 180 Hz. The normalised spacing between the natural frequencies of adjacent neutralisers in the array is given by:

$$\alpha = 1 - \left(\frac{l_{n+1}}{l_n} \right)^2 \quad (19)$$

where l is the active length of the individual neutralisers and the index commences with the largest beam (smallest natural frequency). Because the natural frequency of a beam is proportional to l^2 , α is not constant; it ranges from 0.01 to 0.0104 in the array

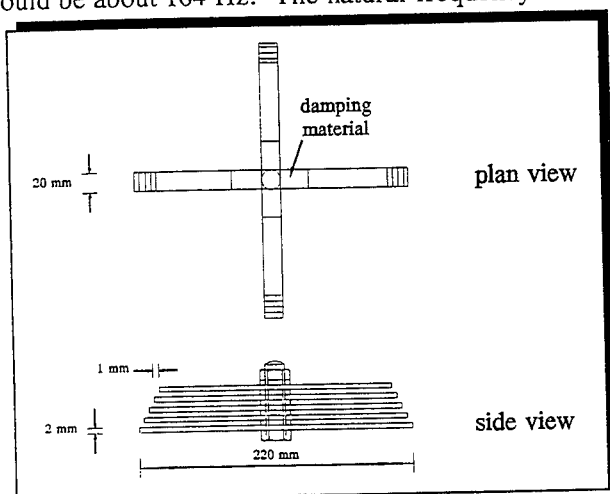


Figure 8 Diagram showing the neutraliser array used in the experimental work

with 10 neutralisers. The loss factor was calculated using the half power point method on the longest beam and was found to be 0.0217, therefore $\alpha \approx \eta/2$.

The wideband neutraliser was fitted to a Derritron type VP4 shaker and was instrumented with a B & K type 4393 accelerometer and type 8200 force gauge as shown in Figure 9.

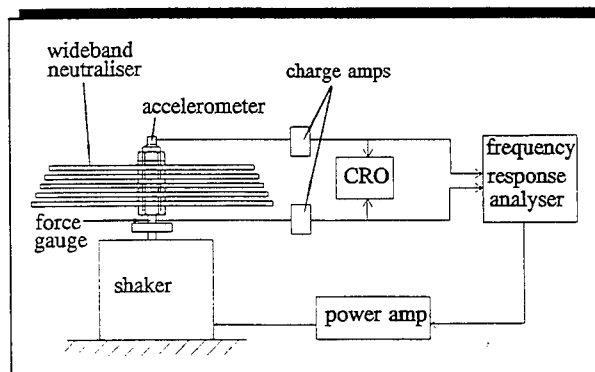


Figure 9 Experimental set up to measure the impedance of a wideband neutraliser

A Hewlett Packard frequency response analyser type 3566A was used to generate a band limited random signal between 126 and 226 Hz which was used to drive the shaker. The frequency response function of force divided by velocity (impedance) was computed by using a 1600 line FFT giving a frequency resolution of 0.0625 Hz. The experiment was repeated for 1 to 10 beams used in the wideband neutraliser.

Because the measured impedance was effectively a mass-spring-mass system rather than a spring-mass system because of the central bolt, washers and constrained section of beam in the vicinity of the bolt, the measured impedance had to be post-processed to remove the effects of this mass. This involved subtracting the impedance of the attached mass (which was 0.0944 kg for the bolt and 0.0017 kg for the constrained section for each beam). The measurements were also normalised to the maximum impedance of the single neutraliser with the lowest natural frequency. The experimental results are plotted in Figure 10 for a selected number of neutralisers in the array. This figure should be compared with Figure 4 where it can be seen that experimental results follow the general trends predicted by the theoretical model.

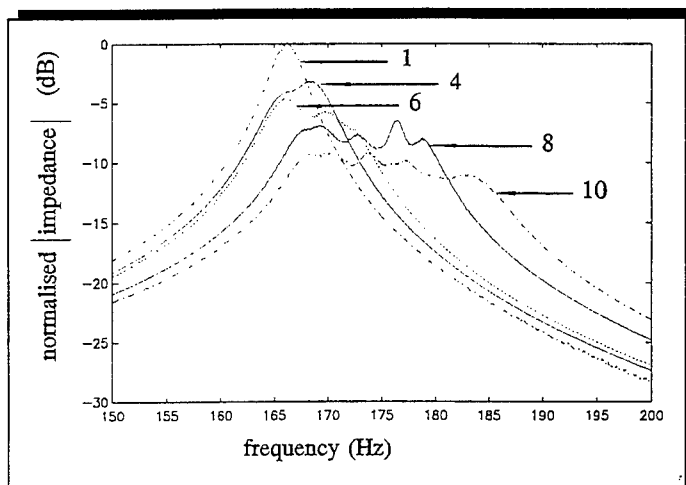


Figure 10 Experimental results

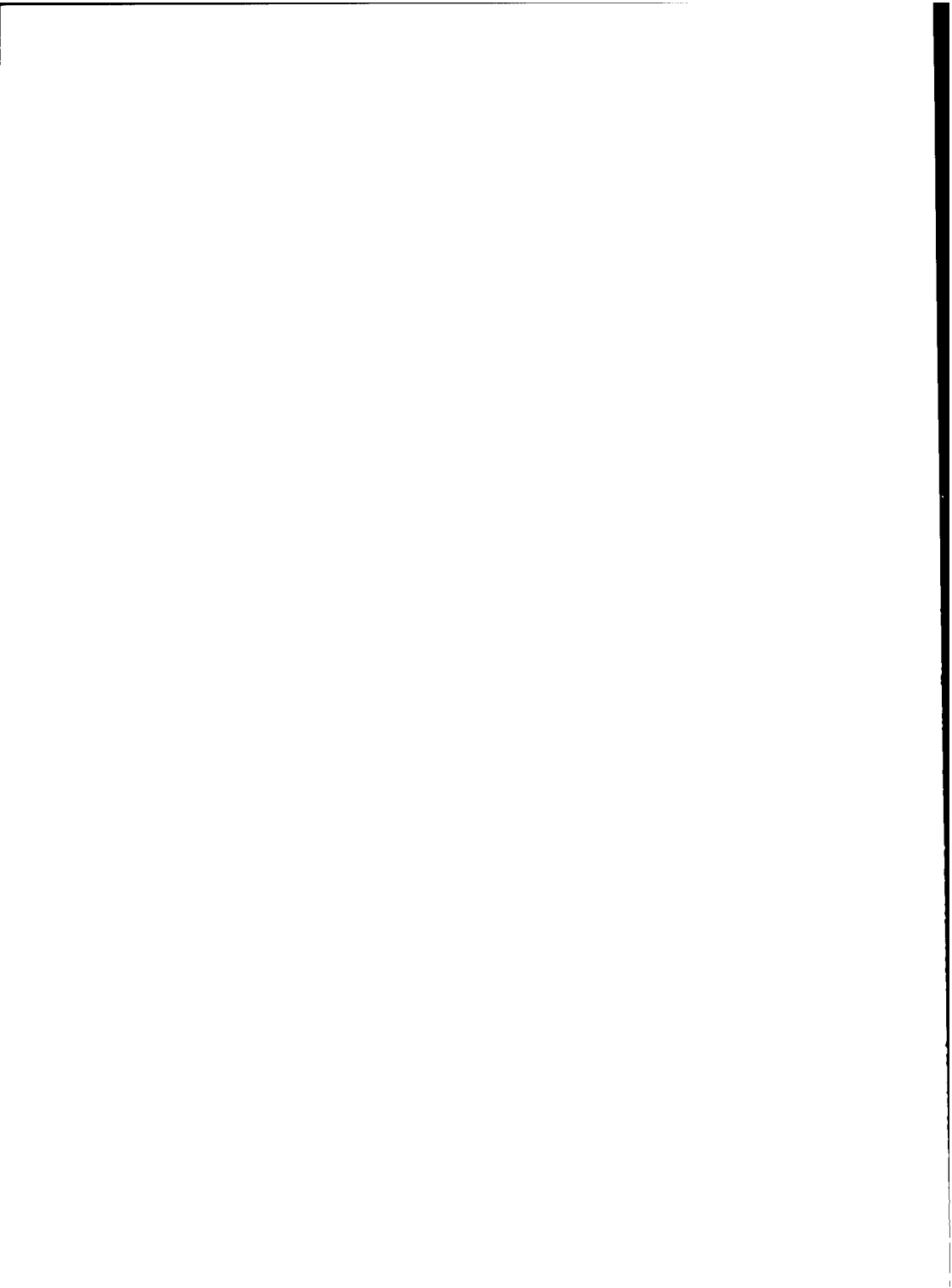
5. CONCLUSIONS

This paper has described a wideband neutraliser which consists of an array of neutralisers that are all tuned to slightly different natural frequencies. This has the effect in the frequency domain of smearing the impedance of a single neutraliser. However, if the total mass of the neutralisers in the array remains constant, then although the bandwidth increases the maximum impedance decreases. It is shown that it is possible for the product of these two quantities to be increased in comparison with a single neutraliser, and this is considered to be the main advantage of the device. Simple expressions have been derived for the maximum impedance and bandwidth of the wideband neutraliser when some simplifying assumptions were made, and the approximate solutions have been compared with numerical simulations. Finally some experiments have been conducted to validate the theoretical model of the wideband neutraliser and to investigate the practical difficulties in fabricating such a device.

REFERENCES

1. J. ORMONDROYD AND J.P. DEN HARTOG 1928. *Transactions of the American Society of Mechanical Engineers*, **50**, 9-22. Theory of the dynamic vibration absorber.
2. D.J. MEAD 1982. *Vibration Control* (in Noise and Vibration ed. by R.G. WHITE and J.G. WALKER), Ellis Horwood Ltd.

3. A.H. VON FLOTOW, A.BEARD and D. BAILEY 1994. *Proceedings of Noise-Con 1994*, 437-454, held in Ft Lauderdale Florida, USA. Adaptive tuned vibration absorbers: tuning laws, tracking agility, sizing and physical implementations.
4. M.J. BRENNAN 1995. *ISVR Technical Report No 244*, Tunable vibration absorbers - key design parameters.
5. T.L. SMITH, K.A.RAO and I. DYER 1986. *Noise Control Engineering Journal* **26**, 56-60. Attenuation of plate flexural waves by a layer of dynamic absorbers.
6. M. STRASBURG and D. FEIT 1996. *Journal of the Acoustical Society of America* **99** (1). Vibration damping of large structures induced by attached small resonant structures.
7. E.L. HIXSON 1987. *Mechanical Impedance* (Ch 10 in Shock and Vibration Handbook ed. C.M. Harris), 3rd edition, McGraw-Hill, London.



ON THE TUNED VIBRATION ABSORBER FOR THE SUPPRESSION OF A PARAMETRIC RESONANCE

A.K. Belyaev

Institute of Technical Mechanics, Johannes Kepler University of
Linz, Altenbergerstr. 69, A-4040, Linz, Austria

Abstract: A tuned vibration absorber which suppresses a parametric resonance in mechanical systems is addressed. The principal domain of the parametric instability is shown to be markedly shifted by a proper choice of the absorber's parameters.

1. INTRODUCTION

Tuned vibration absorber (TVA), also known as tuned mass damper and dynamic vibration absorber, is an important engineering tool for vibration suppression. This simple mechanical device which usually consists of a mass, a spring element and a dashpot has proven very effective for reducing severe vibrations of machinery and many other mechanical systems with relatively low cost. Over the years, many TVA design configurations have been developed. Numerous examples of passive, active, semi-active and adaptive TVAs in civil and mechanical engineering can be found in a detailed survey of the recent developments and applications of the linear TVAs [1] wherein some hundred papers are cited. The operating conditions and the mechanical properties of the controlled systems and the attached TVAs often change with time, that is the linear TVAs lose effectiveness and may even increase the systems' vibration. One of the successful applications of nonlinear TVA is nonlinear centrifugal pendulum TVA, cf. [2].

In what follows we offer an idea of the tuned vibration absorption of the parametric instability in the column. To the best of the author's knowledge, paper [3] remains the only application of TVA to suppression of the parametric instability. It is known that pipelines conveying pulsatile fluids experience parametric instability. In [3] a pinned-pinned pipe is considered and the TVA which consists of a mass, a spring and a dashpot is attached at the midspan and acts in the lateral direction.

The main intent of the present study is twofold: (i) to reveal the regions of dynamical stability of a potentially unstable beam with an attached TVA and (ii) to show how the parameters of an optimum TVA can be chosen, for a given range of the excitation magnitude and frequency.

2. CONCEPT OF THE TVA FOR SUPPRESSION OF PARAMETRIC INSTABILITY AND THE GOVERNING EQUATIONS

Conceptually, a TVA for suppression of parametric resonance consists of a bar attached to a potentially unstable beam, cf. Figure 1.

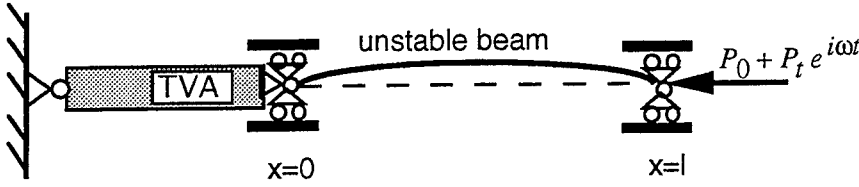


Figure 1. Schematic of a tuned vibration absorber for unstable beam.

We model a potentially unstable member by a simply supported Bernoulli-Euler beam $0 < x < l$ on which a periodic force $P(t) = P_0 + P_t e^{i\omega t}$ is imposed at the end $x=l$. The beam is attached to the TVA at the end $x=0$. TVA is assumed to be dynamically stable, i.e. it does not exhibit any lateral instability.

The nonlinear partial integro-differential equations for the beam vibrations are given as follows (for details see [4])

$$EA \left(1 + \beta \frac{\partial}{\partial t} \right) \frac{\partial^2 u}{\partial x^2} - \rho A \frac{\partial^2 u}{\partial t^2} = \rho A \int_0^x \left[\frac{\partial w}{\partial \xi} \frac{\partial^3 w}{\partial \xi \partial t^2} + \left(\frac{\partial^2 w}{\partial \xi \partial t} \right)^2 \right] d\xi, \quad 0 < x < l \quad (1)$$

$$EI \left(1 + \beta \frac{\partial}{\partial t} \right) \frac{\partial^4 w}{\partial x^4} + \frac{\partial}{\partial x} \left[\frac{\partial w}{\partial x} EA \left(1 + \beta \frac{\partial}{\partial t} \right) \frac{\partial u}{\partial x} \right] + \rho A \frac{\partial^2 w}{\partial t^2} = 0, \quad 0 < x < l \quad (2)$$

Here EI and EA are the flexural and axial rigidities, respectively, u and w are the axial and lateral deflections, respectively, ρ is the mass density and A is the cross-sectional area. To account for material damping in the beam, a viscosity is introduced by means of an operator $\beta \frac{\partial}{\partial t}$. Equation (1) describes the axial vibration of the

beam while eqn (2) describes the bending vibration.

In order to find the boundaries of the instability zones, one can neglect the non-linear terms in the right-hand side of eqn (1), cf. [4], to have

$$\left(1 + \beta \frac{\partial}{\partial t} \right) \frac{\partial^2 u}{\partial x^2} - \frac{1}{c^2} \frac{\partial^2 u}{\partial t^2} = 0, \quad c = \sqrt{\frac{E}{\rho}} \quad (3)$$

where c is the velocity of sound. The absorber is assumed to be

undamped so its longitudinal vibration is governed by the following differential equation

$$\frac{\partial^2 u_a}{\partial x_a^2} - \frac{1}{c_a^2} \frac{\partial^2 u_a}{\partial t^2} = 0, \quad 0 < x_a < l_a, \quad c_a = \sqrt{\frac{E_a}{\rho_a}} \quad (4)$$

where u_a is the axial displacement of the absorber, and c_a is the velocity of sound. Sub-index a is referred to the absorber. Boundary conditions and the conditions of the beam-absorber interaction are given by

$$x_a = 0, \quad u_a = 0; \quad x = l, \quad EA \left(1 + \beta \frac{\partial}{\partial t} \right) \frac{\partial u}{\partial x} = P_o + P_t e^{i\omega t} \quad (5)$$

$$x = 0, \quad x_a = l_a, \quad u(0) = u_a(l_a), \quad EA \left(1 + \beta \frac{\partial}{\partial t} \right) \frac{\partial u}{\partial x} = E_a A_a \frac{\partial u_a}{\partial x_a} \quad (6)$$

Solution of the boundary value problem, eqs (3)-(6), is given by

$$u_a(x_a, t) = H \frac{\sin \lambda_a x_a}{\sin \lambda_a l_a} e^{i\omega t} + \frac{P_o}{E_a A_a} x_a; \quad \lambda_a = \frac{\omega}{c_a} \quad (7)$$

$$u(x, t) = (H \cos \lambda x + Q \sin \lambda x) e^{i\omega t} + \frac{P_o}{EA} x + \frac{P_o}{E_a A_a} l_a; \quad \lambda = \frac{\omega}{c \sqrt{1 + i\beta\omega}}$$

where λ and λ_a are the wave numbers of the beam and the absorber, respectively. Besides,

$$H = \frac{\frac{1}{\omega} P_t \tan \lambda_a l_a}{R_a \cos \lambda l - R \sqrt{1 + i\beta\omega} \tan \lambda_a l_a \sin \lambda l} \quad (8)$$

$$Q = \frac{\frac{1}{\omega} P_t \frac{R_a}{R \sqrt{1 + i\beta\omega}}}{R_a \cos \lambda l - R \sqrt{1 + i\beta\omega} \tan \lambda_a l_a \sin \lambda l}$$

where $R = \rho c A$ and $R_a = \rho_a c_a A_a$ are the impedances of the beam and the absorber, respectively. Substituting eqn (7) into eqn (2) yields

$$EI \left(1 + \beta \frac{\partial}{\partial t} \right) \frac{\partial^4 w}{\partial x^4} + P_o \frac{\partial^2 w}{\partial x^2} +$$

$$EA \lambda (1 + i\beta\omega) \frac{\partial}{\partial x} \left((Q \cos \lambda x - H \sin \lambda x) \frac{\partial w}{\partial x} \right) e^{i\omega t} + \rho A \frac{\partial^2 w}{\partial t^2} = 0 \quad (9)$$

3. THE PRINCIPAL INSTABILITY ZONE OF THE BEAM WITH AND WITHOUT TVA

In order to define the principal zone of instability we assume $w(x,t) = \phi(x) q(t)$ where the fundamental function $\phi(x) = \sin \frac{\pi x}{l}$ is the first vibration mode and the static buckling form of the beam alone. We multiply eqn (9) by $\phi(\omega)$ and integrate along the length of the beam. The result is the following ordinary differential equation for the generalised coordinate $q(t)$

$$\frac{d^2 q}{dt^2} + 2\varepsilon \frac{dq}{dt} + \Omega^2 [1 - 2\mu |\Phi(\omega)| e^{i(\omega t + \arg \Phi(\omega))}] q = 0 \quad (10)$$

Here the natural frequency of the bending vibration of the axially compressed beam Ω , the first critical load P_c , generalised damping ε and dimensionless magnitude of the external force μ are given by

$$\Omega^2 = \left(\frac{\pi}{l}\right)^2 \frac{P_c - P_o}{\rho A}; \quad P_c = EI \frac{\pi^2}{l^2}; \quad \varepsilon = \frac{EI\beta}{2\rho A} \left(\frac{\pi}{l}\right)^4; \quad \mu = \frac{P_t}{2(P_c - P_o)} \quad (11)$$

Function $\Phi(\omega)$ is

$$\Phi(\omega) = \frac{2}{l} \int_0^l \frac{R_a \cos \lambda x - R \sqrt{1 + i\beta\omega} \tan \lambda_a l_a \sin \lambda x}{R_a \cos \lambda l - R \sqrt{1 + i\beta\omega} \tan \lambda_a l_a \sin \lambda l} \cos 2 \frac{\pi x}{l} dx \quad (12)$$

which after the evaluation of the integral takes the following form

$$\Phi(\omega) = \frac{4 \sin \frac{\lambda l}{2}}{\lambda l} \frac{\lambda^2 l^2 - 2\pi^2}{\lambda^2 l^2 - 4\pi^2} \frac{R_a \cos \frac{\lambda l}{2} - R \sqrt{1 + i\beta\omega} \tan \lambda_a l_a \sin \frac{\lambda l}{2}}{R_a \cos \lambda l - R \sqrt{1 + i\beta\omega} \tan \lambda_a l_a \sin \lambda l} \quad (13)$$

We intend to analyse the conditions under which the dynamic buckling of the beam occurs and obtain the boundaries of the principal zone of instability. The first approximation to the boundaries is known to be determined by means of the following substitution, cf. [4], [5]

$$q(t) = a \sin \frac{\omega t + \arg \Phi(\omega)}{2} + b \cos \frac{\omega t + \arg \Phi(\omega)}{2} \quad (14)$$

which leads to the following linear equations for a and b

$$\begin{aligned} \left[-\left(\frac{\omega}{2}\right)^2 + \Omega^2(1 + \mu |\Phi(\omega)|) \right] a - \varepsilon \omega b &= 0 \\ \varepsilon \omega a + \left[-\left(\frac{\omega}{2}\right)^2 + \Omega^2(1 - \mu |\Phi(\omega)|) \right] b &= 0 \end{aligned} \quad (15)$$

The vanishing of the determinant expresses a certain dependence between the frequency and the magnitude of the external axial force. This dependence is known to be the boundary of the principal zone of instability, cf. [4], [5]

$$\left[-\left(\frac{\omega}{2}\right)^2 + \Omega^2 \right]^2 + \varepsilon^2 \omega^2 - \Omega^4 \mu^2 |\Phi(\omega)|^2 = 0 \quad (16)$$

From the latter equation we can see that the case $|\Phi(\omega)| = 1$ corresponds to the boundary of the conventional principal instability zone of the Mathieu equation, cf. [4], [5]. In particular, substituting $\varepsilon = 0$ into eqn (16) yields the following equation for the principal zone of instability of the beam without TVA

$$\omega = 2\Omega\sqrt{1 \pm \mu} \quad (17)$$

The principal zone of instability of the undamped beam emanates from the point $\mu = 0, \omega = 2\Omega$, as shown in Fig. 2.

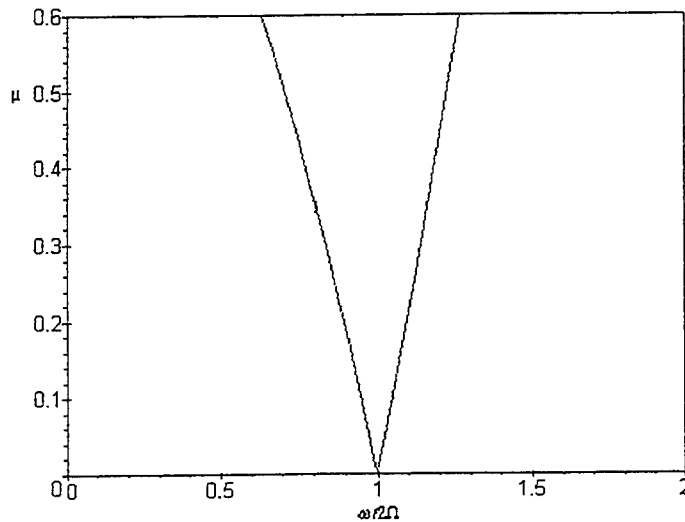


Figure 2. Principal zone of instability for the undamped beam without TVA

The objective of the present study is to choose such TVA parameters that beam in the instability zone of Fig. 2 can be rendered stable by attaching the TVA. This strategy can be easily realized. Equation (16) delivers a stability chart that differs from that of the beam alone since the correction factor $|\Phi(\omega)|$ depends on the frequency ω . Longitudinal vibration can increase or decrease the instability zone.

In the case $|\Phi(\omega)| > 1$, especially at the longitudinal resonances, an enlarged zone of instability is expected. Contrary to this, the antiresonance is expected to diminish the instability zone. Therefore, the parameters of the tuned absorber might be chosen in such a way that the longitudinal vibration of the beam with TVA might have an antiresonance at $\omega = 2\Omega$ or at least might reach a minimum in the vicinity of the frequency $\omega = 2\Omega$. The dependence $|\Phi(\omega)|$ versus frequency is depicted in Fig. 3 for the following tuning parameters: ratio of the impedances $R_* = R_a/R = 0.7$, length ratio $l_* = l_a/l = 0.35$, ratio of the velocities of sound $c_* = c_a/c = 1$. The latter relation says that the beam and TVA are made of the same material. For this particular example we take the following dimensionless material damping $\beta_* = 2\Omega\beta = 0.01$.

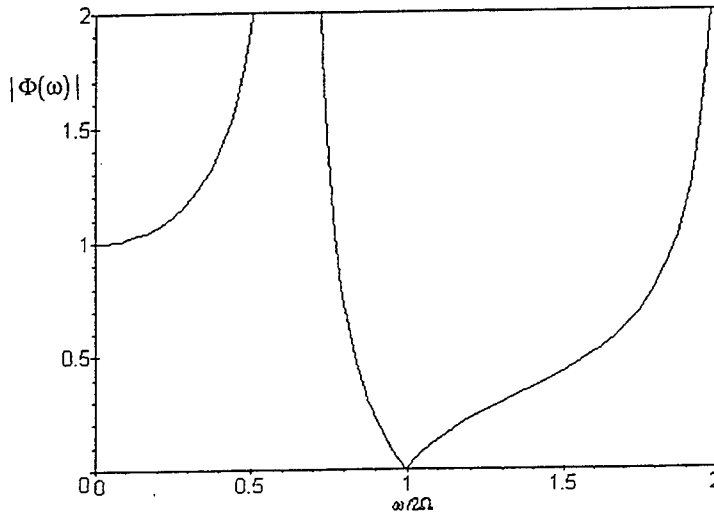


Figure 3. The correction factor $|\Phi(\omega)|$ for the above tuning of TVA

The principal instability zones of the beam with and without the above TVA tuning are shown in Fig. 4. The tuning proposed may be considered an optimal one since it results in considerable shifting and reducing the principal instability zone of the beam. An optimal selection procedure for selecting the optimal parameters of the TVA can be easily elaborated. In fact, the optimal tuning requires the antiresonance region emanating from $\omega = 2\Omega$ to be as broad as possible, cf. Fig. 3.

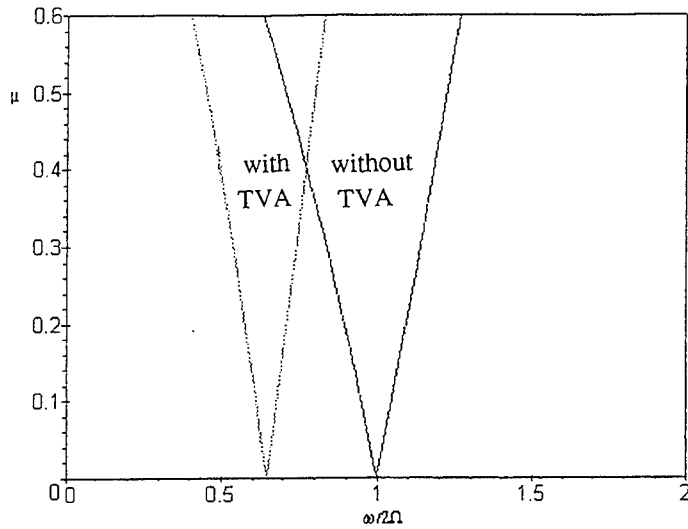


Figure 4. Principal instability zone of the beam with and without the optimal TVA

4. THE SECOND AND THIRD INSTABILITY ZONES

The boundaries of the second instability zone are known to be obtained by substituting

$$q(t) = b_0 + a_2 \sin [\omega t + \arg \Phi(\omega)] + b_2 \cos [\omega t + \arg \Phi(\omega)] \quad (18)$$

into eqn (10), see [4] and [5]. We obtain in this way three homogeneous linear equations in b_0, a_2 and b_2 . The vanishing of the determinant

$$\begin{vmatrix} 1 - \frac{\omega^2}{\Omega^2} & 0 & -\frac{\varepsilon}{2\Omega} \\ 0 & 1 & -\mu |\Phi(\omega)| \\ \frac{\varepsilon}{2\Omega} & -2\mu |\Phi(\omega)| & 1 - \frac{\omega^2}{\Omega^2} \end{vmatrix} = 0$$

delivers the following equation

$$(-\omega^2 + \Omega^2)^2 + 4\varepsilon^2 \omega^2 - 2\Omega^2 \mu^2 (-\omega^2 + \Omega^2) |\Phi(\omega)|^2 = 0 \quad (19)$$

which is the boundary of the second instability zone, cf. [4] and [5].

The second zone of instability for the beam with and without attached TVA is shown in Figure 5. This figure shows that the second zone of instability is reduced after attaching TVA.

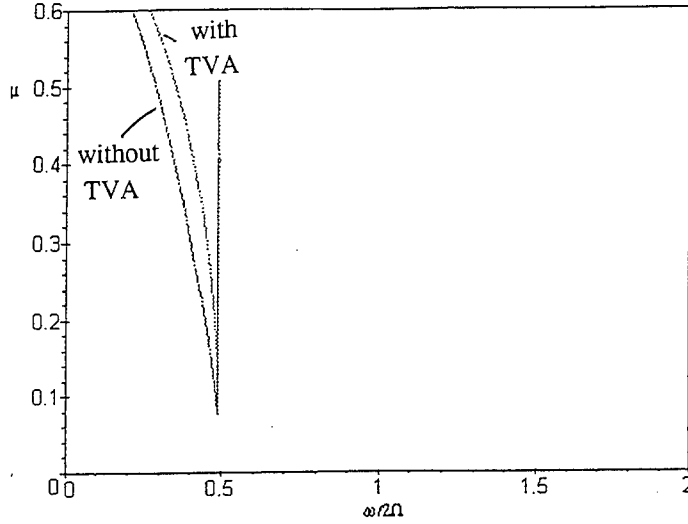


Figure 5. The second instability zone of the beam with and without optimum TVA.

Similarly to the second instability zone, we obtain the boundaries of the third instability zone from the following equation

$$\begin{vmatrix} 1 - \frac{9\omega^2}{4\Omega^2} & -\mu|\Phi(\omega)| & 0 & \frac{2\varepsilon}{\Omega} \\ 0 & \frac{8}{9} + \mu|\Phi(\omega)| & -\frac{2\varepsilon}{3\Omega} & 0 \\ 0 & \frac{2\varepsilon}{3\Omega} & \frac{8}{9} - \mu|\Phi(\omega)| & -\mu|\Phi(\omega)| \\ \frac{2\varepsilon}{\Omega} & 0 & -\mu|\Phi(\omega)| & 1 - \frac{9\omega^2}{4\Omega^2} \end{vmatrix} = 0 \quad (20)$$

A negligible increasing of the third zone of instability is observed after attaching TVA, as Figure 6 shows. However it is worth mentioning that the third zone of instability has no practical significance since value $\mu=0.2$ corresponds to the case where the magnitude of the external harmonic force reaches 40% of the static critical loads.

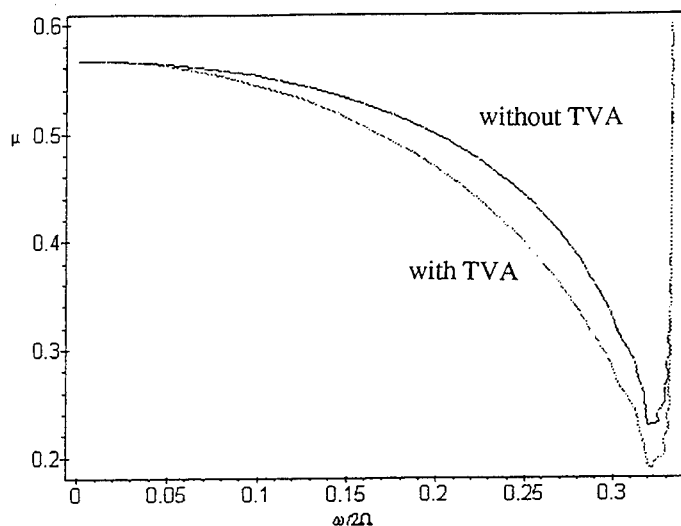


Figure 6. The third instability zone of the beam with and without optimum TVA.

5. STABILITY OF THE TVA

Previous analysis has been performed under the assumption that the TVA does not lose stability. In other words, TVA should be so designed that its stability charts after attaching TVA to the beam should not overlap the instability zones of the beam with and without TVA. The above derivations can be used for the computations of parametric instability zones of TVA. In particular, the equations for the longitudinal vibrations, eqs (3) and (4) remain valid. The governing equation for the bending vibration of the TVA is easily obtained from eqn (2) by substituting u_a , eqn (7), and is given by

$$E_a I_a \frac{\partial^4 w_a}{\partial x_a^4} + P_o \frac{\partial^2 w_a}{\partial x_a^2} + \frac{E_a A_a \lambda_a H}{\sin \lambda_a l_a} \frac{\partial}{\partial x_a} \left(\cos \lambda_a x_a \frac{\partial w_a}{\partial x_a} \right) e^{i\omega t} + \rho_a A_a \frac{\partial^2 w_a}{\partial t^2} = 0 \quad (21)$$

Substituting $w_a(x, t) = \sin \frac{\pi x}{l_a} q_a(t)$ in eqn (21) and applying the Galerkin approach we obtain the following equation for q

$$\frac{d^2 q_a}{dt^2} + \Omega_a^2 [1 - 2\mu_a |\Phi_a(\omega)| e^{i(\omega t + \arg \Phi_a(\omega))}] q = 0 \quad (22)$$

where

$$\Omega_a^2 = \left(\frac{\pi}{l_a}\right)^2 \frac{P_{ca} - P_o}{\rho_a A_a}; \quad P_{ca} = E_a I_a \frac{\pi^2}{l_a^2}; \quad \mu_a = \frac{P_t}{2(P_{ca} - P_o)} \quad (23)$$

and

$$\Phi_a(\omega) = \frac{2}{l_a} \frac{R_a \int_0^{l_a} \cos \lambda_a x_a \cos^2 \frac{\pi x_a}{l_a} dx_a}{R_a \cos \lambda l \cos \lambda_a l_a - R \sqrt{1 + i\beta \omega} \sin \lambda_a l_a \sin \lambda l} \quad (24)$$

Evaluation of the integral in eqn (24) yields

$$\Phi_a(\omega) = \frac{\sin \lambda_a l_a}{\lambda_a l_a} \frac{\lambda_a^2 l_a^2 - 2\pi^2}{\lambda_a^2 l_a^2 - 4\pi^2} \frac{R_a}{R_a \cos \lambda l \cos \lambda_a l_a - R \sqrt{1 + i\beta \omega} \sin \lambda_a l_a \sin \lambda l}$$

The boundaries of the principal zone of instability for the absorber can be computed as follows

$$\omega = 2\Omega_a \sqrt{1 \pm \mu_a |\Phi_a(\omega)|} \quad (25)$$

The absorber should be designed so that for given range of frequency and excitation magnitude no instability occurs. However, there is no need to compute the instability zones of the TVA. Since the optimum TVA is three times shorter than the beam, it is sufficient to admit that the beam and the absorber have the same flexural rigidity. In this case, as eqs (11) and (23) indicate, the eigenfrequency and the critical force of the TVA are much higher than those of the beam, so the TVA remains stable while suppressing the parametric instability of the beam.

CONCLUSIONS

The concept of a tuned vibration absorber which suppresses a parametric resonance in mechanical systems is explored. The principal domain of the parametric instability is shown to be markedly shifted by a proper choice of the absorber's parameters. The second instability domain is slightly reduced in its size while the third one is negligibly increased. This fact should not be considered as a shortcoming since the second and the third domains present no danger in practice.

REFERENCES

1. Sun, J.S., Jolly, M.R. and Norris, M.A., Passive, adaptive and active tuned vibration absorbers - A Survey. In *Transaction of the ASME, Special 50th Anniversary Design Issue*, **117(B)**, pp. 234-42, 1995.
2. Shaw, S.W. and Lee, C.T. On the nonlinear dynamics of centrifugal pendulum vibration absorbers. In *Smart Structure, Nonlinear Vibration, and Control*, eds. A. Guran and D.J. Inman, Prentice Hall, New Jersey, 1995, pp. 247-309.
3. Singh, K. and Mallik, A.K., Use of dynamic absorbers to control parametric instabilities of a pipe. *ASME J. Appl. Mech.*, 1978, **45**, 949-51.
4. Bolotin, V.V., *The Dynamic Stability of Elastic Systems*, Holden-Day, San-Francisco, 1964.
5. Roseau, M., *Vibrations in Mechanical Systems*, Springer-Verlag, Berlin, 1987.

CHARACTERISTICS OF VISCOELASTICALLY-DAMPED MECHANICAL FILTERS

S.O. Oyadiji, K.T. Feroz
Dynamics and Control Research Group,
Division of Mechanical Engineering,
Manchester School of Engineering,
University of Manchester, Manchester M13 9PL

and

G.R. Tomlinson
Dynamics Research Group,
Department of Mechanical Engineering,
University of Sheffield, Sheffield, S1 3JD

ABSTRACT

Predicted transient response characteristics of mechanical filters, each of which comprises of a metallic housing and a viscoelastic isolator, are presented. These filters are to be used for the protection of shock measurement accelerometers from the high frequency components of input shock spectra which often cause irreversible damage to these transducers. The predictions are carried out in the time domain by means of the finite element method. The theoretical transient response characteristics of the mechanical filters designed using various viscoelastic materials are examined. The procedures for the transformation of the frequency domain complex Young's modulus data to the time domain extensional relaxation function using the Fourier transform technique, and for the derivation of the Prony series coefficients from the time data using collocation method are presented. The Prony series coefficients are used to represent the time data in the finite element analysis code. It is shown that the design of optimal mechanical filters depends on the use of viscoelastic materials of optimal properties.

1. INTRODUCTION

Mechanical filters are used for the protection of shock measurement accelerometers from the high frequency components of input shock spectra which often impair correct and accurate operation and

sometimes cause irreversible damage to these transducers. This is particularly true for piezoresistive and piezoelectric shock accelerometers whose sensing elements are relatively brittle materials, in comparison to their stainless steel housings, and are therefore sensitive to very high frequency shock inputs. The resonance frequencies of shock accelerometers are usually designed to be much greater than the highest frequency of their operating range.

Most piezoresistive and piezoelectric shock accelerometers have resonance frequencies in the range of 10 kHz to 200 kHz which are factors of between 5 and 20 greater than the highest operating frequency.

In general, the smaller the size of the accelerometer, the higher the value of its resonance frequency. It is not unusual, however, for input shock waveforms to contain components whose frequencies are up to 1.0 MHz.

This is particularly the case for shock waveforms of very short duration whose shape approach that of the classical Dirac delta function. Hence, there exists the need for optimal mechanical filters for isolating shock accelerometers from the damaging effects of high frequency spectral components of input shock spectra.

There are some commercially-available designs of mechanical filters each of which consists of a metal housing and an elastomeric isolator [1,2]. Because the stiffness of these mechanical filters are relatively high while their damping levels are rather low, many of these commercially-available mechanical filters are not very effective in suppressing high frequency spectral components. Thus there exists the need to improve the design of mechanical filters with particular emphasis on the choice of the elastomeric material, whose properties are frequency or time and temperature dependent, and on the optimisation of the geometry of the metal housing.

In a previous paper, the design of a simple mechanical filter comprising of a viscoelastic disc sandwiched between two steel discs was examined using the finite element method [3]. It was shown that the use of a viscoelastic material designated by the letter N provides the most satisfactory performance of the simple mechanical filter design. In this paper, the design of mechanical filters, each of which comprises of a viscoelastic element which totally encapsulates the shock accelerometer and is, in turn, encapsulated inside a steel housing, is analysed by the finite element technique. Five mechanical filters, which are designated as V, S, U, E and N and are made from viscoelastic materials V, S, U, E and N are analysed. The base polymers of these materials are isoprene, urethane and monothane.

Since the transient response analysis is carried out in the time domain, it is necessary to use the time domain dynamic properties of the viscoelastic element in the finite element computations. This necessitates the transformation of available the frequency domain complex Young's moduli properties of the viscoelastic materials into the time domain using a numerical Fast Fourier Transform procedure. Also, it is necessary to fit a Prony series model to the derived time domain extensional relaxation modulus data in order to obtain the Prony series coefficients which are used to input the viscoelastic properties of the isolator materials into the finite element analysis code. It is shown that the use of the viscoelastic material designated as "M" provides an optimal performance for mechanical filters of the encapsulated design.

2. DERIVATION OF EXTENSIONAL RELAXATION MODULUS

The time domain extensional relaxation moduli of the viscoelastic materials were derived from their frequency domain complex Young's moduli $E^*(\omega)$ which can be expressed as

$$E^*(\omega) = E'(\omega) + jE''(\omega) = E'(\omega) [1 + j\eta(\omega)] \quad (1)$$

where $E'(\omega)$ and $E''(\omega)$ are the real and imaginary parts respectively, $\eta(\omega)$ is the loss factor, ω is the angular frequency and j is the imaginary unit defined as $j = \sqrt{-1}$. The magnitude of the complex Young's modulus is given by

$$E(\omega) = |E^*(\omega)| = E'(\omega) \sqrt{1 + \eta(\omega)^2} \quad (2)$$

The time domain relaxation modulus $E(t)$ is related to the real and imaginary parts of $E^*(\omega)$ by the Fourier transform as [4]

$$E^*(t) = \int_{-\infty}^{+\infty} \left(\frac{E'(\omega) + jE''(\omega)}{j\omega} \right) e^{j\omega t} d\omega \quad (3)$$

From the master curves of the magnitude $E(\omega)$ and loss factor $\eta(\omega)$, the values of $E'(\omega)$ and $E''(\omega)$ are derived over a limited frequency range. Using these values, the integration in Eq. (3) is carried out numerically by means of the inverse Fourier transform procedures of the MATLAB [5] programming environment. Using these procedures, the frequency

domain master curves of complex Young's moduli of the viscoelastic materials are transformed into the time domain. The resulting master curve of extensional relaxation modulus obtained for one of the materials is shown by the solid curves of Figure 1. The saw-tooth form of the curves at very short times (less than 5×10^{-4} s) is due to the size of the frequency steps used in the analysis. The master curves of the extensional relaxation modulus of the five viscoelastic materials investigated are quite similar.

A Prony series expression will now be curve-fitted to the derived time domain extensional relaxation modulus data. By the Wiechert-Kelvin model of viscoelasticity, the extensional relaxation modulus is given by

$$E(t) = E_c + \sum_k E_k \exp(-t/\tau_k) \quad (4)$$

Applying this model to the time domain data and rewriting the equation to include the instantaneous modulus, which is the modulus at time $t=0$ or when $k=0$, gives

$$E_j = E(t_j) = E_g - \sum_k E_k + \sum_k E_k \cdot \exp(-t/\tau_k) \quad (5)$$

which can be simplified to

$$E_j = E_g \left(1 - \sum_k e_k [1 - \exp(-t/\tau_k)] \right) \quad (6)$$

where

$$e_k = E_k / E_g ; \quad k = 0, 1, 2, \dots, N ; \quad j = 1, 2, 3, \dots, k \quad (7)$$

Table 1 : Prony series parameters obtained using Collocation Method

k	e_k	t_k
0	0.661686	1.443E-6
1	0.167211	1.443E-5
2	0.110797	1.443E-4
3	0.328080	1.443E-3
4	0.012251	1.443E-2
5	-0.000180	1.443E-1

E_i 's are the derived relaxation moduli, E_k 's are the relative relaxation moduli, E_e is the equilibrium or long term modulus, E_g is the glassy or instantaneous modulus, e_k is modulus ratio, t_k is the relaxation time constant and t is time.

Equation (6) is known as the Prony series and the parameters e_k and t_k are the Prony series coefficients. These parameters are determined by curve fitting the set of derived time domain extensional relaxation modulus data E_i using Eq. (6) in conjunction with the collocation method [6]. The procedures for implementing this method are described elsewhere [6,7].

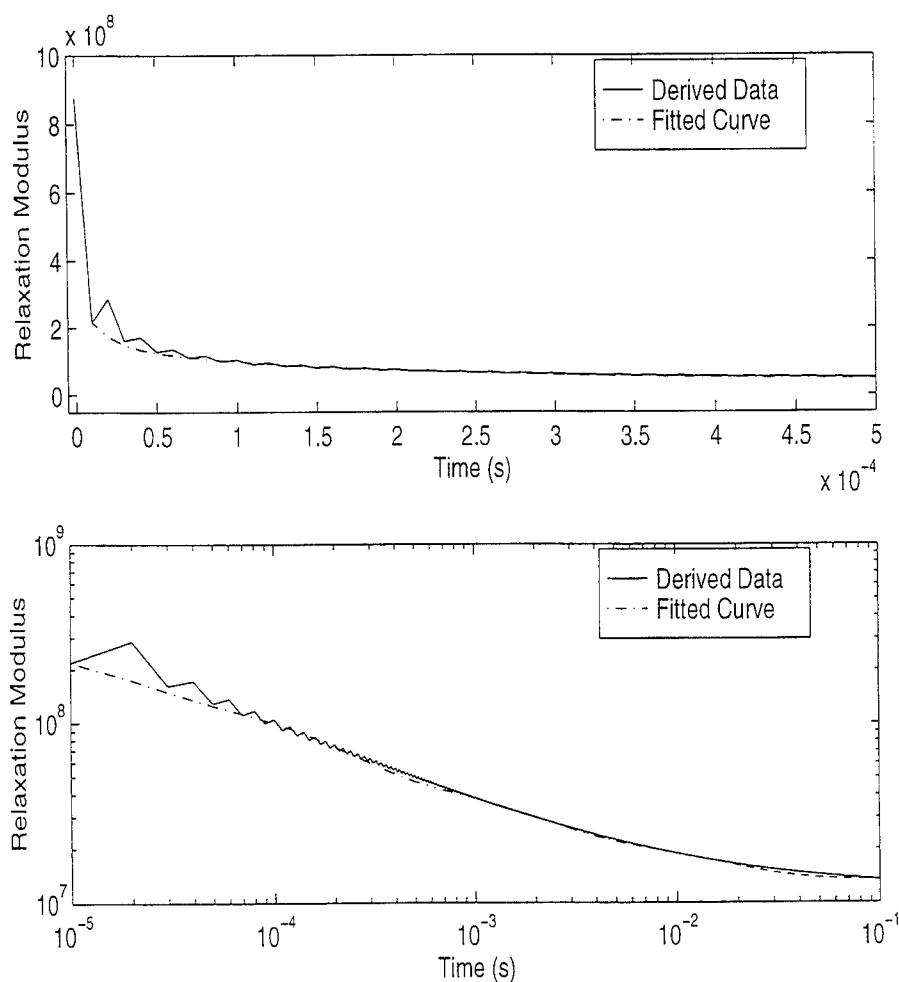


Figure 1 : Extensional Relaxation Modulus of Viscoelastic Material M

For the time domain master curve data depicted by the solid curves of Figure 1, assuming that six terms of the Prony series are sufficient to represent the data, the coefficients e_k and t_k obtained from the derived data by the collocation method are shown in Table 1. Based on these coefficients, the Prony series representation of the time domain data was generated and overlaid on the original derived time data as shown by the dotted curves in Figure 1. It can be seen that the Prony series curve adequately represents the derived time data.

3. FINITE ELEMENT MODELLING

The design of the mechanical filter analysed in the present work is shown by Figure 2. It consists of an inner and an outer steel housings which are separated from each other by four viscoelastic rings as shown in Figure 2. The inner casing houses the shock measurement accelerometer. The figure also shows the corresponding finite element mesh of half of the filter. Because the filter is axisymmetric, it was modelled using axisymmetric finite elements. Also, for the viscoelastic rings, axisymmetric elements which are formulated for incompressible and nearly-incompressible material behaviour were used. The formulation of this so-called hybrid elements is described in the theory manual of the FEA code [8].

A half sine acceleration pulse of 10^4 m/s^2 peak amplitude and of 10^{-4} s duration was applied to all the bottom (input) nodes of the mechanical filter as shown in Figure 2. The time domain extensional relaxation modulus data of the viscoelastic isolators was supplied to the finite element model as a Prony series defined by the parameters e_k and t_k . The finite element analysis of the model was carried out in the time domain using a time stepping procedure and a time step of 10^{-5} s .

The transient responses of the mechanical filter were determined at nodes 43 and 145 which corresponded to the centres of the top and bottom of the inner steel housings, respectively. These nodes represented the output points of the filter. The finite element analysis was repeated for five viscoelastic materials which are designated as materials V, S, U, E and M. From the predicted transient response characteristics of the filters, their frequency response characteristics were computed by means of the fast Fourier transform procedure.

4. DISCUSSION OF RESULTS

In the following discussion, the mechanical filters will be identified by the letter codes of the viscoelastic materials of which they are composed. Thus, mechanical filters V, S, U, E and M are the filters comprising of the viscoelastic materials V, S, U, E and M respectively. The predicted responses of these filters at node 43 are shown in the time and frequency domains. It was found that the predicted responses at node 145 of the filters were identical to those at node 43.

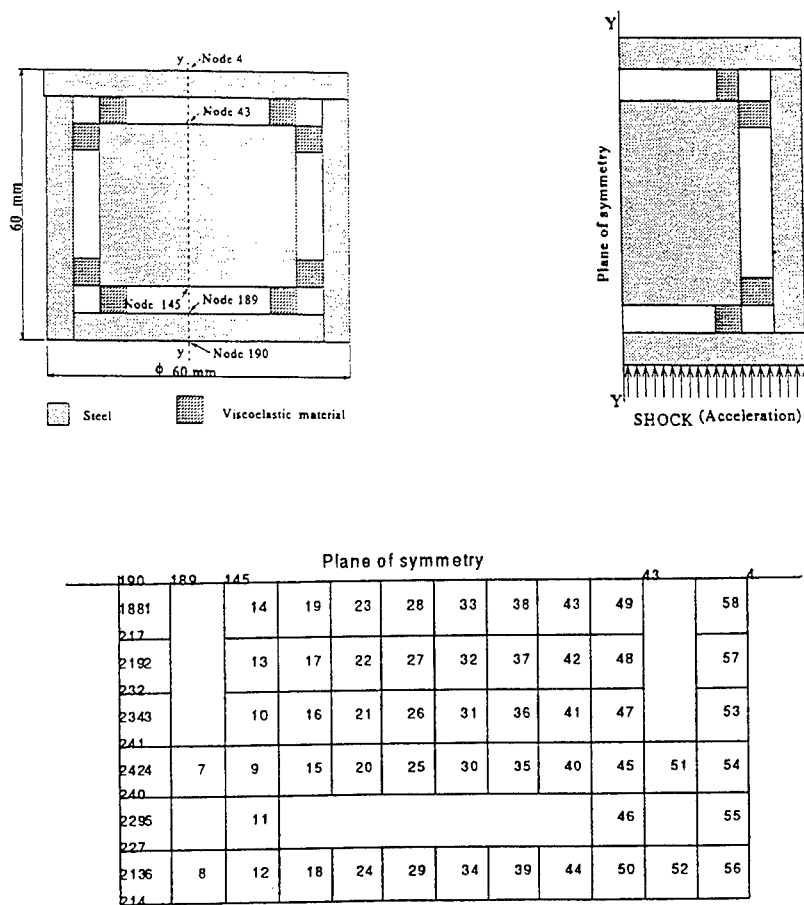


Figure 2 : Design and Finite Element Mesh of the Mechanical Filter

The transient response characteristics of mechanical filter V is shown in Figure 3. The time domain response indicates that the filter is exhibiting the response characteristics of a lightly damped single degree of freedom system. Similarly, the frequency domain response shows that the filter has predominantly a fundamental mode at a frequency of about 300 Hz. A second mode of a rather insignificant amplitude occurs at about 900 Hz. Above 1.0 kHz, it is seen that the response of the filter is practically zero. Since the input half-sine wave shock excitation applied to the input nodes of the filter contains spectral components of frequencies higher than the fundamental frequency of the filter, it is seen that the filter has effectively suppressed these spectral components. However, because

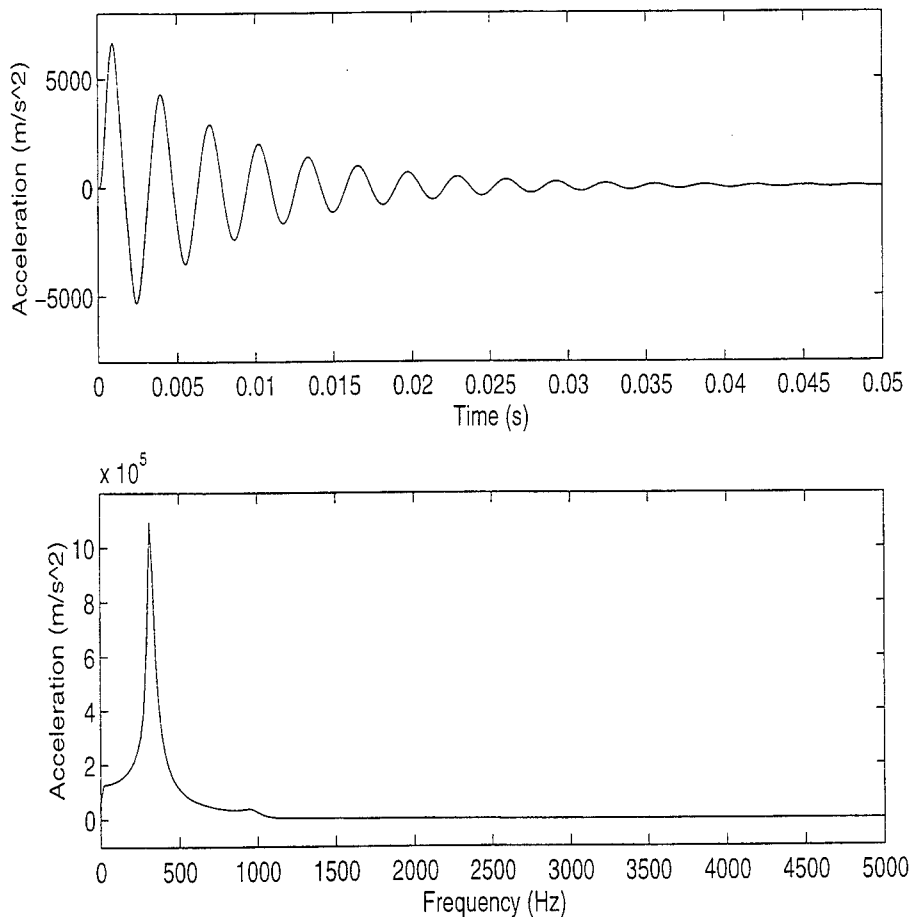


Figure 3 : Transient Response of Mechanical Filter V

of the amplitude magnification that is evident around the fundamental resonance frequency, it is reasonable to assume that the characteristics of the filter will be impaired around this resonance frequency since it will magnify any spectral components whose frequencies occur around this frequency. Nevertheless, above a frequency of about 1.0 kHz, the filter is seen to be very effective.

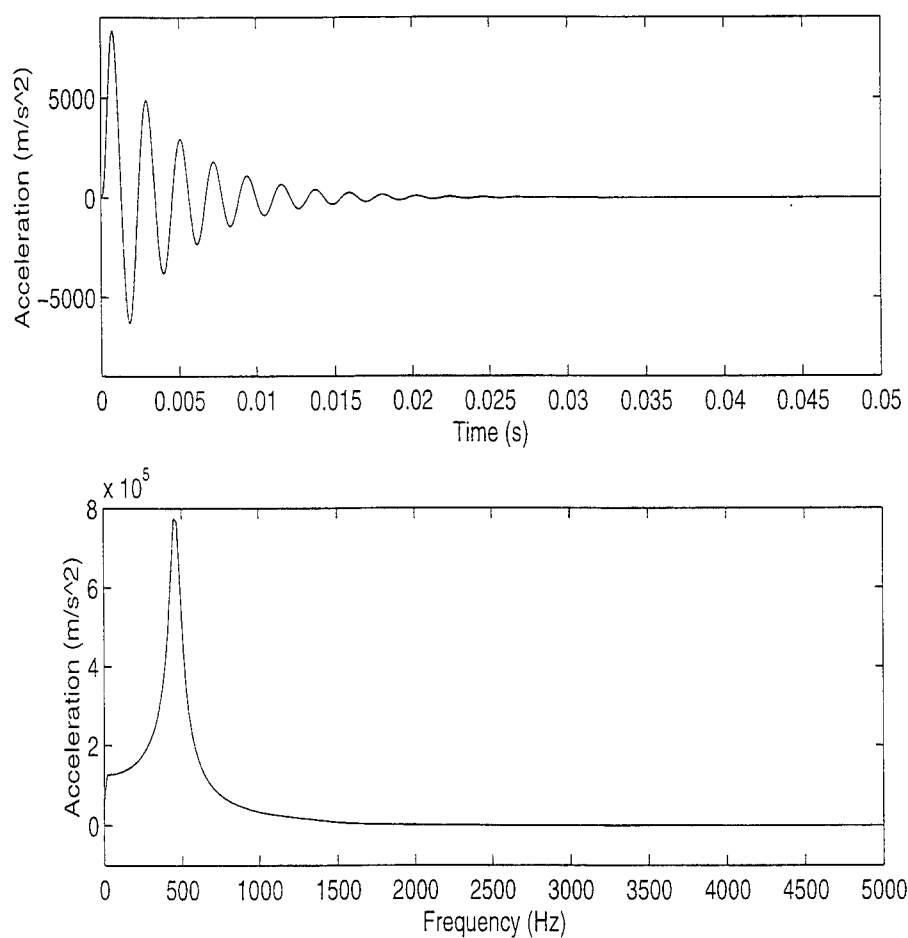


Figure 4 : Transient Response of Mechanical Filter S

Similarly, Figures 4 and 5 show the time and frequency domain response characteristics of the mechanical filters S and U respectively. It is seen that the filters also exhibit the transient response and frequency response

characteristics of a lightly damped single degree of freedom system. The figures also show that the fundamental resonance frequencies of filters S and U are approximately 450 Hz and 900 Hz respectively. For frequencies greater than 1.0 kHz for mechanical filter S and for frequencies greater than 1.5 kHz for mechanical filter U, the frequency response of both filters are practically zero. Thus, like mechanical filter V, both mechanical filters S and U isolate the high frequency spectral components of the input half-sine waveform. Also, filters S and U will isolate the effects of spectral components of input shock waveforms of frequencies greater than 1.0 kHz and 1.5 kHz respectively. However, the

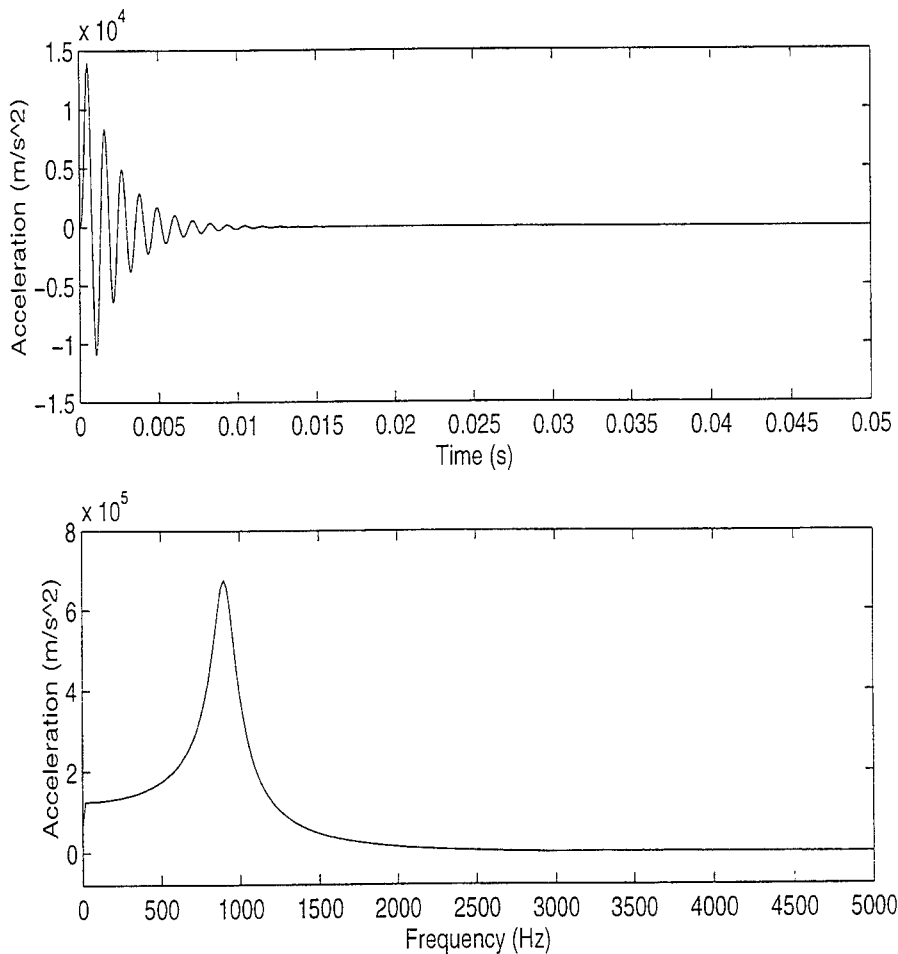


Figure 5 : Transient Response of Mechanical Filter U

filters will magnify the amplitudes of any spectral components whose frequencies are in the neighbourhood of their fundamental resonance frequencies.

The transient and frequency response characteristics of mechanical filter E are shown in Figure 6. These characteristics indicate that the filter is responding as a highly damped single degree of freedom system. It is seen that the fundamental resonance frequency is not clearly defined. However, the fundamental resonance frequency of the filter is estimated

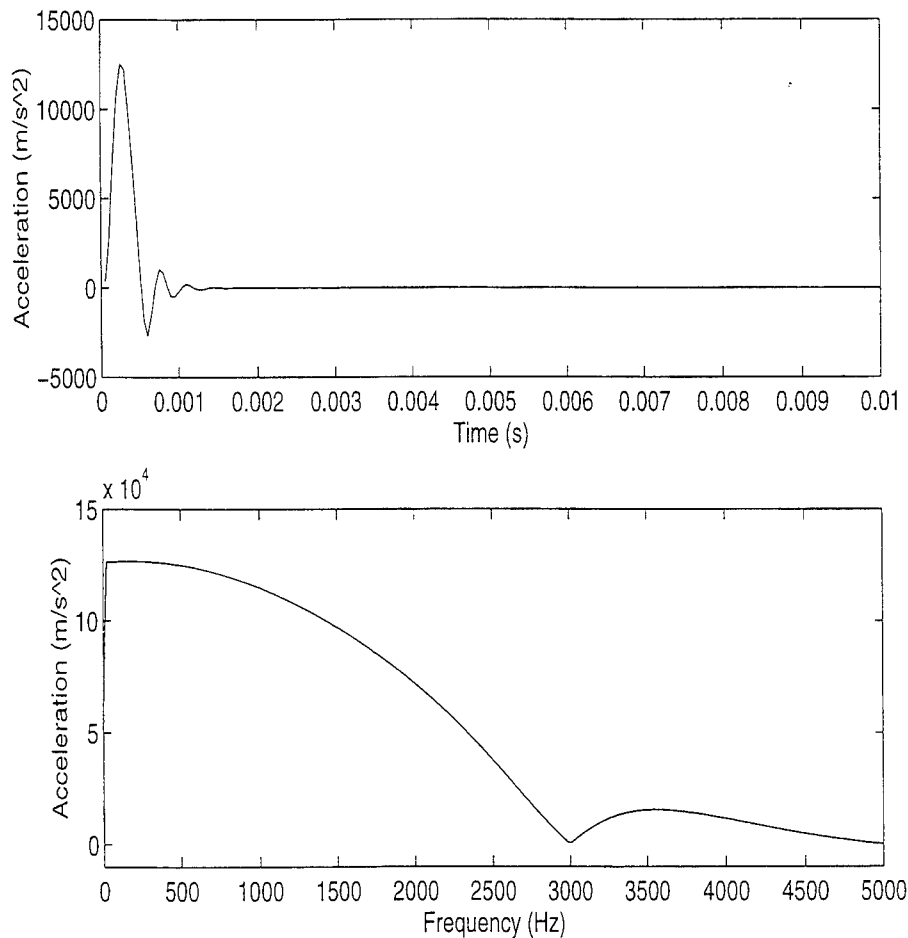


Figure 6 : Transient Response of Mechanical Filter E

approximately as 1.5 kHz. Also, since the filter does not possess a sharp cut-off frequency, its frequency response characteristics roll off from about 1 kHz to 3 kHz. Above 3.0 kHz, some high frequency spectral components of the input shock waveform are transmitted through the filter as shown by the "hump" in the frequency response characteristics.

Figure 7 shows the shock response characteristics of mechanical filter M. The transient and frequency response characteristics of the filter suggest that the filter is responding as a highly damped single degree of freedom system. The fundamental resonance frequency of the filter is seen to be

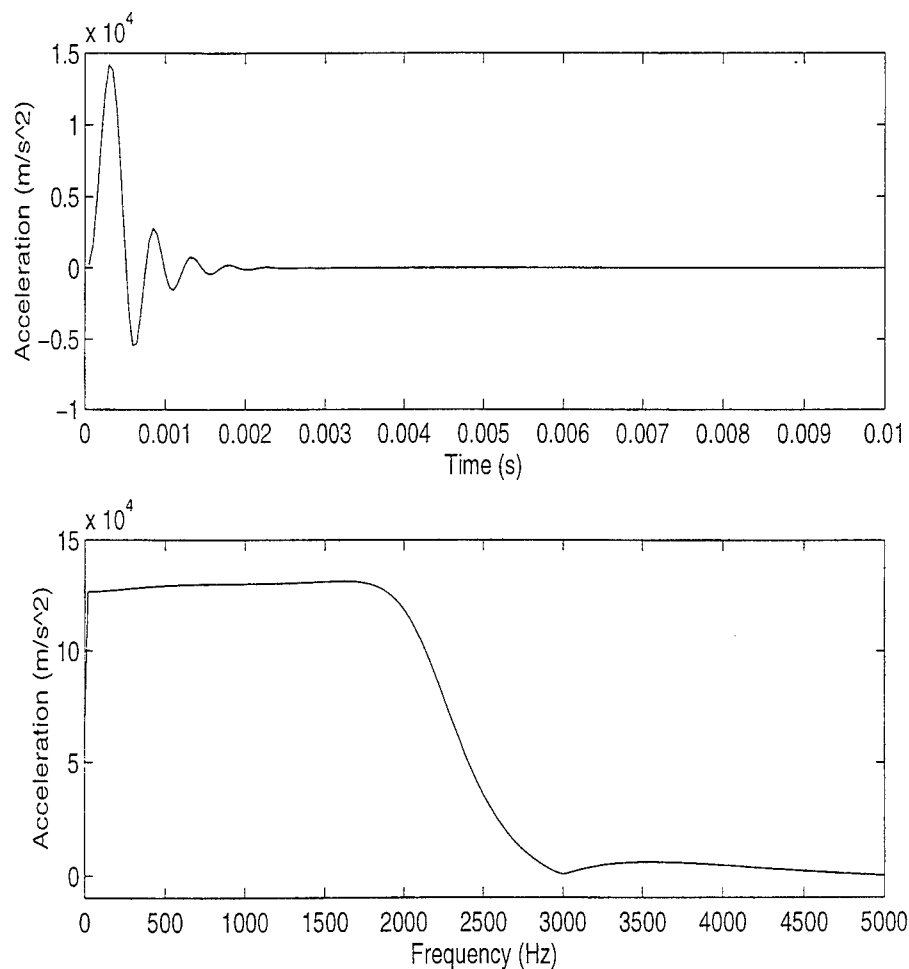


Figure 7 : Transient Response of Mechanical Filter M

about 1.7 kHz while the amplitude of the frequency response of the filter is fairly constant up to its fundamental resonance frequency. Above this frequency, the amplitude decreases rapidly to a value of about zero at 3.0 kHz. Beyond 3.0 kHz, the amplitude remains approximately at a value of zero.

Comparing Figure 7 with Figures 3 to 6, it is seen that the level of damping in filter M is greater than the levels of damping in filters V, S and U but less than the level of damping in filter E. Also, filter M has a wider frequency band over which it isolates the high frequency spectral components of the input shock waveform. Furthermore, the shock isolation characteristics of filter M are not impaired by high amplitude magnification at its fundamental resonance frequency. Thus, of the five mechanical filters analysed, mechanical filter M has the optimum shock isolation performance.

5. CONCLUSIONS

The finite element method has been used to predict the shock response characteristics of five viscoelastically-damped mechanical filters which are designated by the letter codes V, S, U, E and M. These filters were subjected to a half sine pulse input excitation. The Prony series representations of the time domain extensional relaxation moduli data sets required by the finite element code for the time domain analysis were successfully obtained by the collocation method. These extensional relaxation moduli data sets were derived from the frequency domain master curves of the complex Young's moduli of the viscoelastic materials by the application of a fast Fourier transform procedure implemented under the MATLAB programming environment. The results show that mechanical filter M, which is comprised of viscoelastic material M, has the optimum shock isolation performance.

6. ACKNOWLEDGEMENTS

This work is being supported by the Defence Research Agency, Dunfermline, Scotland, U.K. The technical support provided by Dr Bob Haxton and Mr Lindsay Morris of the DRA, who are also in charge of the programme, is gratefully acknowledged.

7. REFERENCES

1. Chu, A.S., "Built-in Mechanical Filter in a Shock Accelerometer", *Proceedings of the 59th Shock and Vibration Symposium*, vol. 1, pp 251-269, Albuquerque, New Mexico, October 1988.
2. Serridge, M. and Licht, T.R., *Piezoelectric Accelerometers and Vibration Preamplifiers: Theory and Application Handbook*, pp 105-107, Bruel & Kjaer, November 1987.
3. Oyadiji, S.O., Feroz, K.T. and Tomlinson, G.R., "Design of Polymer-Based Mechanical Filters for Shock Measurement Accelerometers", in *Smart Structures and Materials 1996: Passive Damping and Isolation*, C. D. Johnson, Editor, Proc. SPIE 2720, pp 305-316, 1996.
4. Bracewell, R.N., *The Fourier Transform and its Applications*, 2nd Edition, McGraw-Hill Book Company, New York, 1978.
5. MATLAB Users' Manual, The MathWorks Inc., 1991.
6. Tschoegl, N.W., *The Phenomenological Theory of Linear Viscoelastic Behaviour: An Introduction*, Springer-Verlag, Berlin, 1989.
7. Feroz, K.T., Oyadiji, S.O. and Tomlinson, G.R., "Analysis of Mechanical Filters", *Technical Report*, TR95/DRA/No. 3 (for DRA Dunfermline), Manchester School of Engineering, July 1995.
8. ABAQUS Theory Manual, Hibbitt, Karlson & Sorensen, Inc, 1992.

PASSIVE CONTROL OF THE VIBRATIONAL RESPONSE CHARACTERISTICS OF HOLLOW BEAMS USING VISCOELASTIC SPHERES

S.O. Oyadiji
Dynamics and Control Research Group
Division of Mechanical Engineering
Manchester School of Engineering
University of Manchester
Manchester M13 9PL, U.K.

ABSTRACT

Viscoelastic spheres of diameters 9 mm, 15 mm and 18 mm and of relatively low, medium and high densities were used for passive damping control of the vibrations of square-section and rectangular-section hollow steel beams. The beams were supported in their vertical and horizontal orientations under free-free boundary conditions and were subjected to random excitation. The transfer inertance frequency response functions of the beams were measured when they were empty and when they were filled with the viscoelastic spheres. A nonlinear least squares modal curve fitting algorithm was used to extract the modal frequencies and loss factors of the composite viscoelastic sphere-filled beams from the measured transfer inertance frequency response functions. The results indicate that the modal loss factors of the hollow steel beams could be increased by factors of up to 32, 40 and 44 by filling them with the high density, medium density and low density viscoelastic spheres, respectively.

1. INTRODUCTION

There are a number of techniques for the passive damping of vibrations of structures containing structural cavities. One of the common techniques is the use of a solid viscoelastic material. The viscoelastic material is compounded in liquid form using the raw ingredients; the liquid is poured into the cavity and left to solidify and cure. This technique is easy and quick to execute and significant levels of damping are usually achieved. However, the viscoelastic material is permanently bonded to the cavity and cannot be easily changed. Also, there is no longer any access through the cavity.

A very common technique for the passive damping of structural vibrations is the constrained layer damping (CLD) treatment method [1]. This technique, which is used generally for the damping of structural vibrations, involves the application of a thin layer of a viscoelastic material with a thin metallic backing to the surface of the structure. This technique has been used successfully to damp the vibrations of beams, plates, shells and panels. However, it is rather awkward to apply to irregular shaped cavities. In addition, CLD treatment is not often very effective in damping the fundamental modes of vibration of structures.

Granular materials and particle dampers have also been used to control the vibrations of structural cavities [2-4]. This involves the filling of the structural cavities with these materials which are generally metallic oxide powder or small-size particles. Using this technique, composite structural loss factors of up to 12.5% have been achieved with metal beams whose intrinsic structural loss factors are of the order of 0.5% or less. This technique has a further advantage of allowing access through the structural cavity. However, the granular material and particular damping technique has the disadvantage that the metal powder/particles are rather very expensive. Furthermore, for large structural cavities, the use of metallic oxide powder or small-size particles can be rather cumbersome.

Another technique for damping the vibrations of structural cavities is the use of solid viscoelastic spheres for filling the structural cavities. This technique combines the damping mechanisms of the particle and impact dampers with the high intrinsic loss factors associated with the high energy dissipation of a wide range of viscoelastic materials operating close to their rubber-to-glass transition temperatures. In an earlier paper [5], the results of experimental vibration tests on hollow steel beams filled with low density viscoelastic spheres of diameters ranging from 9 mm to 18 mm were presented.

In this paper, further results of the measured damping characteristics of the hollow steel beams filled with low density, medium density and high density viscoelastic spheres are presented. It is shown that the use of the low density viscoelastic spheres provides the highest levels of composite damping whereas the use of the high density spheres provides the least levels of composite damping. Specifically, the results indicate that the modal loss factors of the hollow beams could be increased by factors of up to 32, 40 and 44 by filling them with high density, medium density and low density viscoelastic spheres, respectively.

2. LUMPED-PARAMETER MODEL

To enable the identification of the modal frequencies and the composite loss factors of the viscoelastic sphere-filled hollow beams from the measured frequency response characteristics, a lumped-parameter mathematical model was used. The model is based on a discrete system approximation of the composite beam. Assuming hysteretic damping model the equation of motion of n lumped masses of the composite beam connected by n complex springs is given by

$$[M]\{\ddot{y}(t)\} + [k(1+j\eta)]\{y(t)\} = \{f(t)\} \quad (1)$$

where $[M]$ and $[k(1+j\eta)]$ are mass and complex stiffness matrices, $y(t)$ is displacement, $f(t)$ is the external excitation force, and $j=\sqrt{-1}$ is the imaginary unit. Applying the Fourier transform to Eq (1) gives

$$\{[k(1+j\eta)] - [M]\omega^2\}\{\bar{Y}(\omega)\} = \{\bar{F}(\omega)\} \quad (2)$$

where $\bar{Y}(\omega)$ and $\bar{F}(\omega)$ are the Fourier transforms of $y(t)$ and $f(t)$ respectively. For an excitation point q and a response point p , the transfer inertance frequency response function of the composite beam is given by

$$H(j\omega)_{pq} = \frac{-\omega^2 \bar{Y}(\omega)}{\bar{F}(\omega)} = -\omega^2 \sum_{r=1}^n \frac{X_r}{\lambda_r^2 - \omega^2} \quad (3)$$

where the modal participation factor X_r , and the complex eigenvalues λ_r are defined as

$$X_r = \phi_p^{(r)} \phi_q^{(r)}; \quad \lambda_r^2 = \omega_r^2 (1 + j\eta_r) \quad (4)$$

The parameters $\phi_p^{(r)}$ and $\phi_q^{(r)}$ are the complex mode shapes while ω_r and η_r are the modal angular frequency and modal loss factor respectively. The modal loss factor η_r is related to the real and imaginary parts, k'_r and k''_r , of the complex modal stiffness by

$$\eta_r = k''_r / k'_r \quad (5)$$

By means of a nonlinear least squares curve-fitting method, an algorithm based on Eqs (3) and (4) is used to determine the modal frequencies and the modal loss factors of the composite viscoelastic sphere-filled hollow beams from the measured transfer inertance frequency response functions (FRF).

3. EXPERIMENTAL MEASUREMENT PROCEDURE

Figure 1 shows the setup for the experimental measurement of transfer inductance frequency response characteristics of the hollow beams filled with viscoelastic spheres. Three hollow steel beams, of external dimensions 50 x 100 mm, 100 x 100 mm, and 100 x 150 mm, were tested. These beams, which were denoted as small rectangular, square and large rectangular hollow-section beams respectively, had an identical wall thickness of 5 mm and an identical length of 1.9 m. Two sets of viscoelastic spheres were used: one set consisted of three types of 15 mm diameter viscoelastic spheres made from slightly different viscoelastic materials and of different densities designated as low density, medium density and high density. The other set consisted of three sizes of viscoelastic spheres made from the same batch of the low density viscoelastic material and of diameters of 9, 15 and 18 mm.

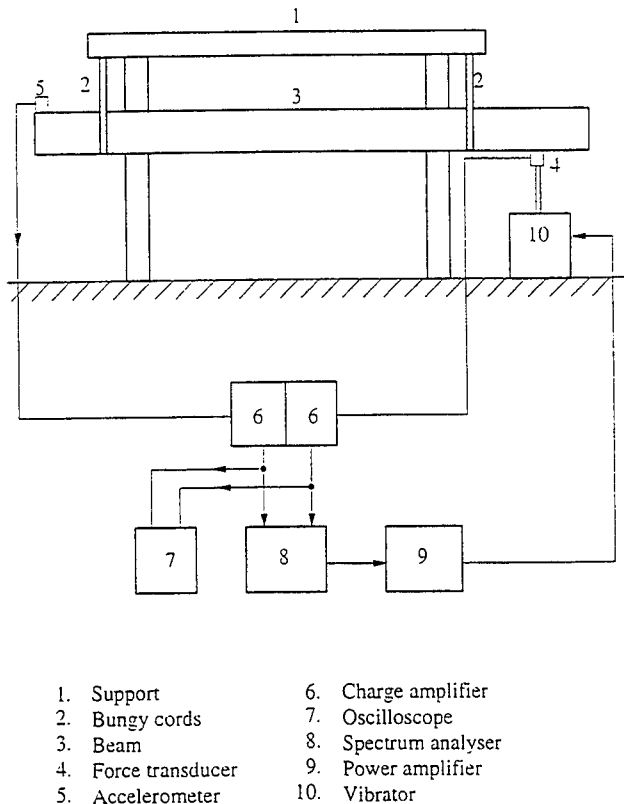


Figure 1 : Experimental Test Configuration for the Measurement of Transfer Inductance Frequency Response Functions

Each beam was filled, in turn, with each type of viscoelastic sphere. The composite beam assembly was suspended horizontally in a free-free configuration using bungy cords as shown in Figure 1. The open ends of the hollow beam were blocked with transparent perspex sheets. By means of an electromagnetic exciter, which was attached to one end of the beam via a force transducer, the beam was subjected to random force

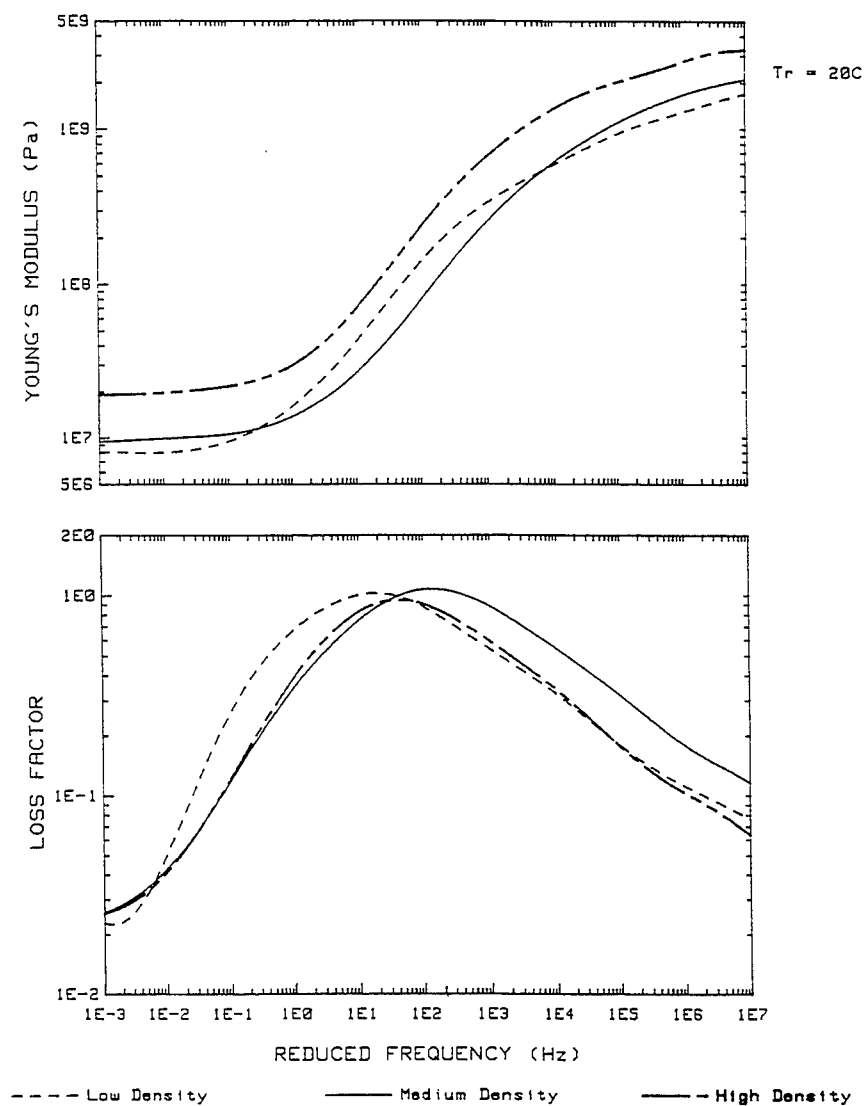


Figure 2 : Master Curves of Complex Young's Modulus of Low, Medium and High Density Viscoelastic Materials

excitation over the frequency range from 0.0 to 2.0 kHz. The random excitation signal was provided by a spectrum analyser via a power amplifier. The acceleration response of the beam was monitored at the other end of the beam using an accelerometer. The input force-versus-time signal and the output acceleration-versus-time signal were sampled by the spectrum analyser which also computed the transfer inertance frequency response function as the ratio of the acceleration to the force signals using a Fast Fourier Transform technique.

The experimental procedure outlined above was repeated for different combinations of hollow beams and viscoelastic spheres. Also, the rectangular-section hollow beams were tested in their vertical and horizontal orientations. A rectangular-section beam was considered to be in vertical orientation when the larger cross-sectional dimension was aligned vertically, while the beam was considered to be in horizontal orientation when the larger cross-sectional dimension was aligned horizontally.

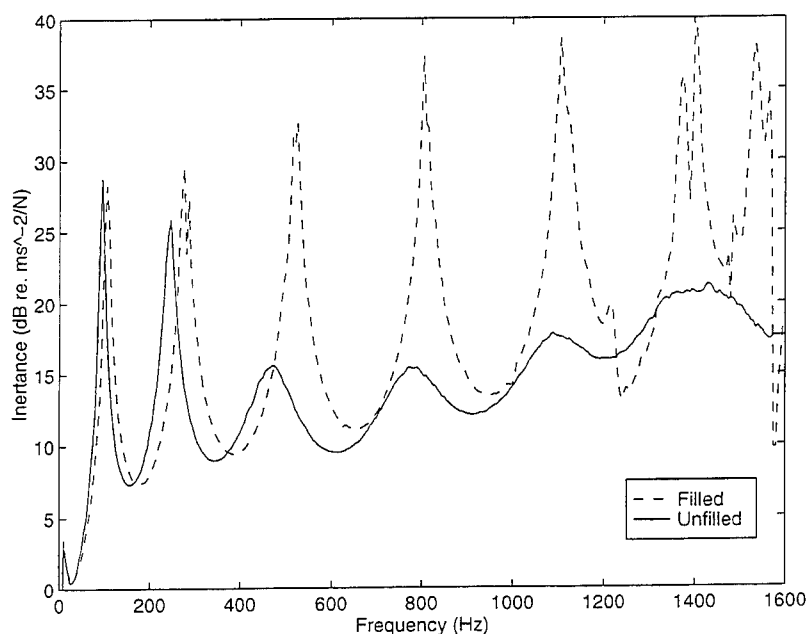


Figure 3: Transfer Inertance Characteristics of the Small Rectangular-Section Hollow Steel Beam Filled/ Unfilled with 9mm Diameter Low Density Viscoelastic Spheres

4. DISCUSSION OF RESULTS

Ordinarilly, the intrinsic loss factor of a steel beam is approximately 0.005. In the previous paper [5], the international plot of the master curves of complex Young's modulus of the low density viscoelastic material was shown. It was stated in that paper that within the frequency range from 1.0 Hz to 10 kHz of the random excitation of the viscoelastic sphere-filled hollow beams, the intrinsic loss factors of the low density viscoelastic material at room temperature were 0.6, 1.0, 0.9, 0.6 and 0.3 at frequencies of 1 Hz, 10 Hz, 100 Hz, 1 kHz and 10 kHz respectively. Thus, it was concluded that the composite loss factor of the viscoelastic sphere-filled beams cannot exceed a value of 0.9. This upper limit of 0.9 for the loss factor holds true for the medium density and high density viscoelastic materials as well. This is clearly evident from Figure 2 which shows the comparison of the complex Young's modulus properties of the three materials.

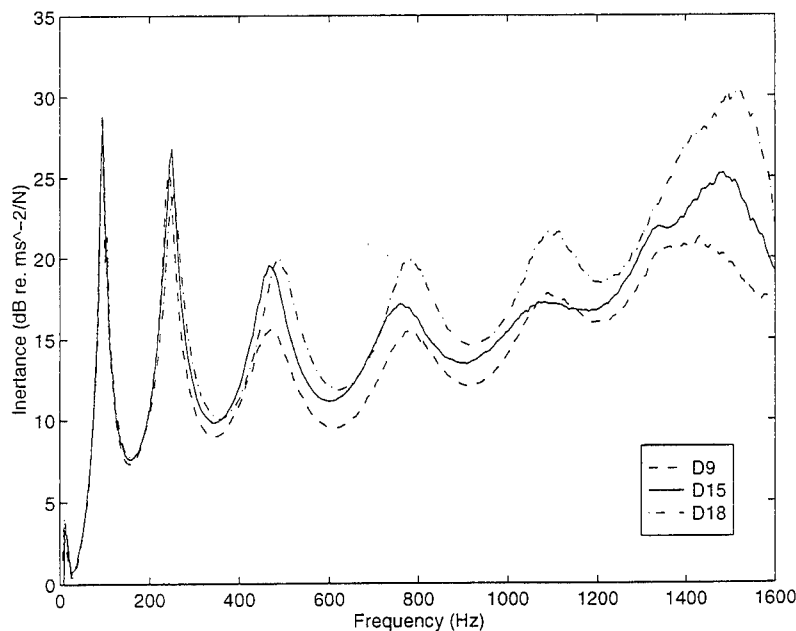


Figure 4: Transfer Inertance Characteristics of the Small Rectangular-Section Hollow Steel Beam Filled with 9mm, 15 mm and 18mm Diameter Low Density Viscoelastic Spheres

In Figure 3, the transfer inertance FRFs of the small rectangular-section hollow steel beam, in horizontal orientation, when empty and when

filled with the 9 mm diameter low density viscoelastic spheres are compared. The figure shows that the peak amplitudes of the first and second modes of flexural vibration of the empty beam are slightly reduced when the beam is filled with the viscoelastic spheres. The peak amplitudes of the subsequent modes of the empty beam are reduced by factors of between 10 and 15. However, there is a significant reduction in the modal frequencies of the beam.

Similarly, Figure 4 shows the comparison of the transfer inertance FRFs of the small rectangular-section hollow beam, in horizontal orientation, when filled with low density viscoelastic spheres of diameters of 9, 15 and 18 mm. Overall, it is seen that the level of the transfer inertance FRF of the beam when filled with the 9 mm diameter viscoelastic spheres is the least whereas the level of the transfer inertance FRF of the beam when filled with the 18 mm diameter viscoelastic spheres is the highest. This indicates that the packing density of the 9 mm diameter viscoelastic spheres is the greatest while the packing density of the 18 mm diameter viscoelastic spheres is the least. The figure also shows that the damping effectiveness of the 9 mm diameter spheres is much higher than for the other two sizes of spheres.

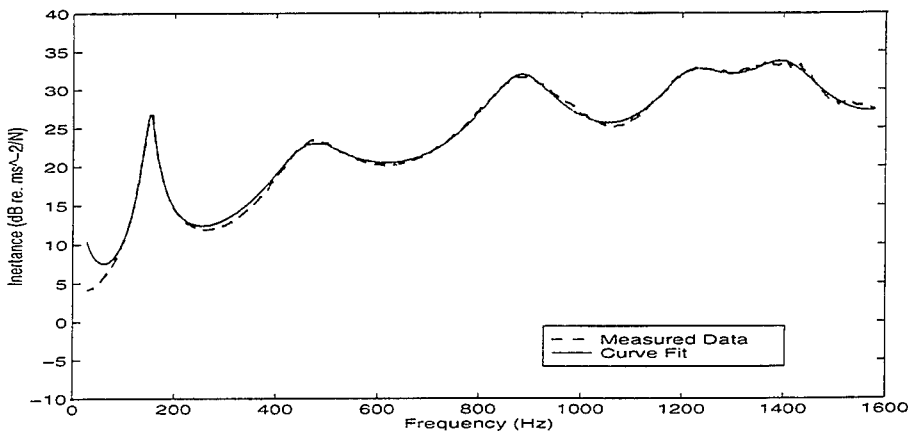


Figure 5 : Measured and Reconstructed Transfer Inertance Frequency Response Functions of the Small Rectangular-Section Hollow Steel Beam Filled with 9mm Diameter Viscoelastic Spheres

A nonlinear least squares curve-fitting algorithm based on Eqs. (3) and (4) was used to identify the modal frequencies and modal loss factors of the hollow beams, when empty and when filled with the different sizes of viscoelastic spheres, from the measured transfer inertance frequency

response functions. As a check on the accuracy of the algorithm, the transfer inertance was reconstructed from the identified modal parameters. Figure 5 shows an example of the correlation of the reconstructed FRF with the measured FRF. It is seen that the curve-fit approximates very well the measured characteristics for the five modes of vibration identified. This closeness of agreement between the curve-fitted and measured characteristics was observed to hold for all cases in which the hollow beams were filled with viscoelastic spheres. But when the hollow beams were empty, it was observed that the curve-fitted FRF did not correlate very well with the measured FRF. Thus, the nonlinear least squares curve fitting algorithm in its present form is not well suited for analysing the response of the empty hollow beams whose modal loss factors are less than 1.0 %.

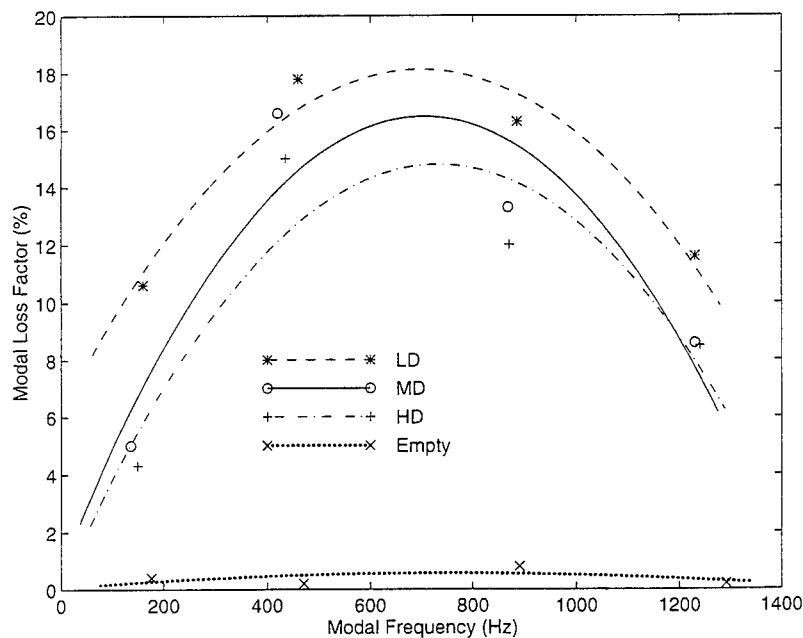


Figure 6 : Modal Loss Factor versus Modal Frequency for the Small Rectangular-Section Hollow Steel Beam Unfilled and Filled with Low, Medium and High Density Viscoelastic Spheres

Figure 6 shows the variation of the modal loss factors with modal frequencies for the small rectangular-section hollow steel beam filled with low density, medium density and high density viscoelastic spheres of 15 mm diameter. The beam was aligned in the vertical orientation. It is seen that the modal loss factors of the empty beam lie in the range of

0.2 % to 0.7 % approximately whereas the modal loss factors of the viscoelastic sphere-filled hollow beam lie within the range of 4.0 % to 18.0 %. The figure also shows that the modal loss factors of the hollow beam filled with the low density viscoelastic spheres are highest in value

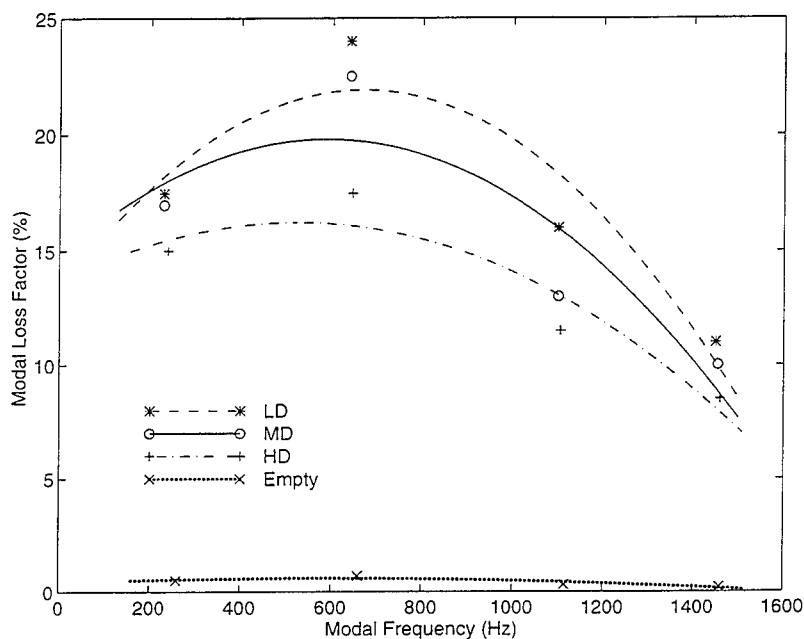


Figure 7: Modal Loss Factor versus Modal Frequency for the Square-Section Hollow Steel Beam Unfilled and Filled with Low, Medium and High Density Viscoelastic Spheres

whereas the modal loss factors of the hollow beam filled with the high density viscoelastic spheres are least in value. The modal loss factors of the hollow beam filled with the medium density viscoelastic spheres lie approximately between the other two sets of modal loss factors. Figure 7 shows that these relative magnitudes of the modal loss factors are approximately the same when the low, medium and high density spheres are used to damp the vibrations of the square-section hollow beam. Furthermore, it is seen from both Figures 6 and 7 that the loss factors of the beams are increased by factors of up to 32, 40 and 44 when they are filled with the high, medium and low density viscoelastic spheres respectively.

The variation of the modal loss factors of the large rectangular-section hollow steel beam, in horizontal orientation, when filled with the 9 mm,

15 mm and 18 mm diameter low density spheres are shown in Figure 8. It is seen that the modal loss factors of the empty beam are less than 1.0 % whereas the modal loss factors of the hollow beam filled with the viscoelastic spheres are within the range 7.0 % to 22.0 %. The figure further suggests that the 18 mm diameter viscoelastic spheres are relatively less effective at low frequencies but are relatively more effective at high frequencies in comparison to the other spheres. Overall, the modal loss factors of the hollow beam are increased by factors of between 15 and 44 as a result of filling it with the viscoelastic spheres.

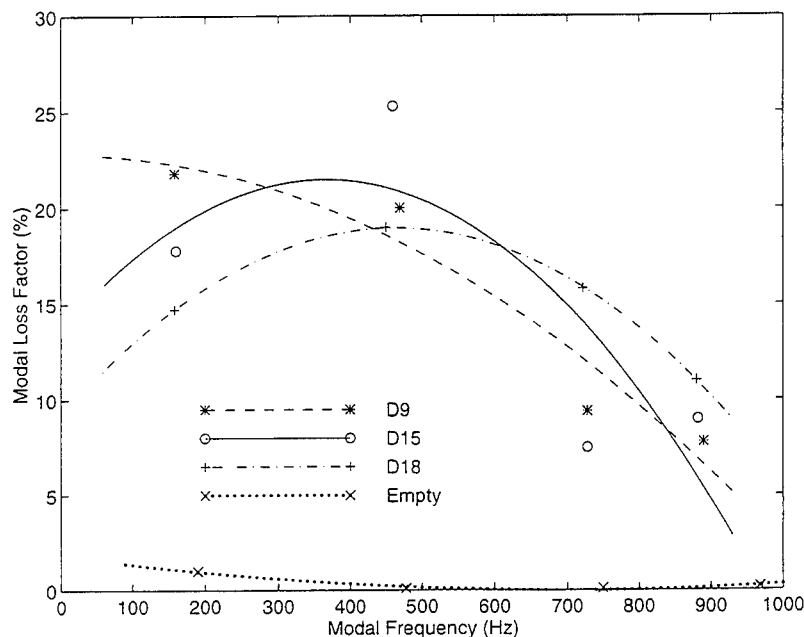


Figure 8: Modal Loss Factor versus Modal Frequency for the Large Rectangular-Section Hollow Steel Beam in Unfilled/ Filled with Low Density Viscoelastic Spheres

5. CONCLUSIONS

The modal amplitudes of the transfer inertance frequency response functions of the small rectangular-section hollow beams were reduced by factors of between 7 and 10 when the beam was filled with 9 mm, 15 mm and 18 mm diameter low density viscoelastic spheres. The modal loss factors of the three hollow beams when empty were within the range 0.2 % to 1.0 %. When the hollow beams were filled with the

viscoelastic spheres, their composite modal loss factors were in the range 4 % to 25.0 % which represent an increase in the modal loss factors of the beams by factors of between 4 and 50. Specifically, the modal loss factors of the hollow beams were increased by factors of up to 32, 40 and 44 when they were filled with the high, medium and low density viscoelastic spheres respectively. The benefits of using viscoelastic spheres for controlling vibrational response characteristics of hollow beams have been shown.

6. ACKNOWLEDGEMENTS

This is a continuation of a research programme which was originally supported by the Ministry of Defence. The assistance of the following final year undergraduate students: Messrs Qiad Rajabali (1993/94), Panagiotis Sarafianos (1994/95), Paschalis Sarafianos(1994/95) and Marios Niforos (1995/96) is gratefully acknowledged.

7. REFERENCES

1. Nashif, A.D., Jones, D.I.G. and Henderson J.P., *Vibration Damping*, John Wiley & Sons, New York, 1985.
2. Abdel-Gawad, M., "Passive Vibration Damping with Noncohesive Granular Materials", *Proceedings of Damping '91 Conference*, pp GDB1-GBD15, San Diego, February 1991.
3. Panossian, H.V., "Non-Obstructive Particle Damping Tests on Aluminium Beams", *Proceedings of Damping '91 Conference*, pp ICD1-ICD7, San Diego, February 1991.
4. Simonian, S.S., "Particle Beam Damper", in *Smart Structures and Materials 1995: Passive Damping*, C. D. Johnson, Editor, Proc. SPIE 2445, pp 149-160, 1995.
5. Oyadiji, S.O., "Damping of Vibrations of Hollow Beams using Viscoelastic Spheres", in *Smart Structures and Materials 1996: Passive Damping and Isolation*, C. D. Johnson, Editor, Proc. SPIE 2720, pp 89-98, 1996.

Measurement And Control Of Low Frequency Vibrational Power Transmission In Pipeline Structures.

P Clark (1) & R G White (2)*

- (1) Larson Davis Ltd, Redcar Station Business Centre, Redcar, UK.
- (2) Dept. of Aeronautics and Astronautics, University of Southampton, Highfield, Southampton, UK.

Abstract.

With the majority of machinery installations, it is one-dimensional structures such as pipework vibrating at low frequencies, which form the main vibration path which bypasses isolator systems. In addition to this, it is well known that the introduction of discontinuities into these types of structure can significantly affect the vibrational power transmission properties of the complete installation. One such discontinuity that may be employed as a vibration control device is the neutralizer (often referred to as a "Dynamic Vibration Absorber"). In this work, the vibrations of structures representative of pipes vibrating at low frequencies are considered both theoretically and experimentally and the effects of added neutralizers are investigated.

By considering that the dynamical behaviour of a pipe vibrating at low frequencies can be approximated by that of a simple beam it has been possible to develop theoretical models to predict the attenuation performance of vibration neutralizers attached to pipeline structures. Axial, flexural and torsional vibrations have been considered in turn and it is shown that the use of novel mounting arrangements can significantly enhance the attenuation performance of the attached device. In this paper, these theoretical models are reviewed and corresponding experimental studies using a laboratory pipeline structure are then presented. It is shown that prototype pipeline vibration control devices have been designed, built and tested successfully in a laboratory environment.

1.0 Introduction.

Vibration control in pipeline structures is of considerable interest in practical engineering since it is these types of structure which most often bridge the main machinery vibration isolation mounting system. Flexible bellows are often employed in pipeline systems to account for static misalignment and to act as vibration attenuators. However, these

* This work was carried out whilst both authors were at the ISVR, University of Southampton, U.K.

pipelines are often internally pressurised by the fluid that they convey, as a result their performance as a vibration control device is severely reduced. The internal pressure stiffens the bellows. In addition to this the steel braiding inherently used in the construction of these bellows to increase maximum allowable working pressure decreases its attenuation performance since the impedance change between the pipe and bellows is greatly reduced by the braiding. Also, in many cases, the fundamental vibration frequency of a machine often manifests itself as a vibration control problem since it is usually of a low frequency and therefore easily transmitted; it therefore follows that there is a need to develop a low frequency vibration attenuating device capable of operation at a discrete frequency or over a narrow frequency range. The basis of such a device is the vibration neutralizer.

In previous work [1,2] theoretical assessments of the effects of utilizing these types of device for controlling the vibrations of beam-like or one-dimensional structures have been carried out in terms of neutralizer design parameters and novel mounting configuration assemblies. In each example, all three structural wave-types commonly observed in these types of structure have been considered namely axial, flexural and torsional motion. In addition to these analytical studies, experimental work has also been undertaken to test three prototype flexural vibration neutralizers [3]; the "force-only" assembly, the "moment-only" assembly and the "force and moment" assembly. In this work the device was attached to a simple beam structure and comparisons between theory and experiment were made by considering the performance of the device in terms of transmitted vibrational power.

In this work, these types of devices are applied to a pipeline structure and practical vibration control devices have been designed, built and fitted to an experimental pipeline structure and their vibration attenuation performance assessed using the concept of vibrational power transmission

2.0 Theory.

The basis for the vibration control technique of prime interest in this work is the vibration neutralizer which is assumed to be a simple lumped mass attached to the pipeline by a massless hysteretically damped spring, Figure 1. The device is attached to the primary pipeline structure and the resulting theoretical assessment of its performance as a vibration attenuation device is presented. The pipeline structure is modelled as a simple beam-like system representative of a pipe vibrating at low frequencies and the neutralizer is then considered as a simple discontinuity attached at a point in the otherwise continuous collinear structure. By satisfying the conditions of beam equilibrium and continuity at the point of attachment the resulting reflected and transmitted wave amplitude coefficients can then be determined in terms of the properties of the discontinuity. The resulting proportions of reflected and transmitted vibrational power can then be readily derived from a knowledge of these wave amplitude coefficients.

In second phase of the theoretical studies, flexural vibration is considered in greater detail. The potential for enhanced performance of the flexural wave neutralizer is assessed using novel mounting configurations. Three configurations are analysed, the "force-only" device, the "moment-only" device and finally a device that induces a simultaneously acting "force and moment" onto the primary vibrating structure, see Fig. 2 below.

For full details of the modelling assumptions used in the theoretical analyses and listings of the derived wave amplitude reflection and transmission coefficients the reader's attention is drawn to previously

published work [1,2,3]. For respective wave-types, reflection and transmission coefficients are given in terms of the following non-dimensional parameters:

Axial Vibration: $\mu = 2\pi \frac{\text{Neutralizer Mass}}{\text{Mass in one wavelength of beam}}$

$$\omega_d = \sqrt{\frac{k_d}{m_d}} = \text{Natural frequency of the neutralizer}$$

where $k_d = k_d'(1 + j\eta)$ and η is the hysteretic damping loss factor of the neutralizer spring.

and $\Omega_d = \frac{\omega}{\omega_d} = \frac{\text{Excitation frequency}}{\text{Natural frequency of neutralizer}}$

Flexural Vibration: $\mu_f = 2\pi \frac{\text{Neutralizer Mass}}{\text{Mass in one wavelength of beam}}$

a = moment arm,

ω_d , k_d , and Ω_d are as previously defined.

Torsional Vibration: $\mu_\theta = 2\pi \frac{\text{Neutralizer Mass}}{\text{Mass in one wavelength of beam}}$

$$r_p = \frac{r_{g\theta}}{r_{gb}} = \frac{\text{Polar radius of gyration of neutralizer}}{\text{Polar radius of gyration of beam}}$$

ω_d , k_d , and Ω_d are as previously defined.

When the undamped neutralizer is considered in terms of axial (longitudinal) and torsional vibration, zero transmission of incident power can be seen to occur when the frequency of the incident vibration is equal to the natural frequency of the neutralizer. However, when flexural vibration is considered a more complex situation is

observed. In the first example, a "force-only" device is considered, zero transmission occurs at a frequency given by:

$$\Omega_d^2 = 1 + \frac{1}{4} \mu_f \quad (1)$$

This result is readily explained by considering the two components of power transfer along a beam vibrating in flexure; the product of shear force and transverse velocity and the product of bending moment and angular velocity. Examination of the expression describing the instantaneous values of the respective terms reveals that at this frequency the respective terms remain finite but act in exactly opposite phase thus reducing the total net or time-averaged power to zero. Equation (1) shows that the zero transmission frequency occurs at a frequency greater than the natural frequency of the device attached to the beam. In a similar study the performance of the "moment-only" device has also been analysed. In this example the frequency of zero power transmission is given by:

$$\Omega_d^2 = 1 - \frac{1}{4} \mu_f \{k_f a\}^2 \quad (2)$$

where: k_f = flexural wavenumber of the beam

This frequency occurs at a frequency below the natural frequency of the neutralizer.

Finally, a combined "force and moment" device was considered. In this example the frequency of zero power transmission is given by:

$$\Omega_d^2 = 1 + \frac{1}{4} \mu_f [1 - \{k_f a\}^2] \quad (3)$$

Examination of this expression reveals that when the condition, $k_1 a = 1$, is satisfied zero transmission occurs when the frequency of the incident wave corresponds to the natural frequency of the neutralizer. In addition to this, incorporating a moment arm into the assembly increases the resulting bandwidth of effectiveness of the device without compromise to the resulting mass of the installation.

3.0 Experimental Apparatus and Method.

The experimental structure consisted of a straight 2 inch nominal bore empty PERSPEX pipe approximately 3.5 m long¹. The pipe was mounted vertically and driven at the free end using an electrodynamic shaker. In order for the experimental properties of the structure to be "semi-infinite", the opposite end of the pipe was fitted with an anechoic termination.

To facilitate the mounting of devices on the pipe wall, the experimental structure was fitted with a flange set approximately 2 m from the anechoic termination. During the experiments the driving point input force and acceleration were measured (input torque and angular acceleration for the torsional experiments). In addition to this, the response of the pipe wall downstream of the flange set was measured using combinations of accelerometer pairs. The vibration of the pipe was determined at each measurement position by considering the response of pairs of accelerometers mounted on the pipe wall. The

¹At frequencies well below the ring frequency of the pipe only beam-like motion can occur and so the pipe can be considered to exhibit the dynamical properties of a simple beam or rod [4].

use of multiple sets of accelerometers proved advantageous in minimising the effects of extraneous wave-types in the structure [5].

First axial vibration was considered. The anechoic termination at the base of the pipe was based on a method used by Horner [5]. The principle of operation of this termination is to dissipate the incident energy in a series of plates vibrating in flexure. The termination therefore consisted of a series of flat plates such that the total flexural mechanical impedance of these plates matched, as closely as possible, the axial mechanical impedance of the pipe. Good dissipation of energy in the plates was then achieved by ensuring that the dimensions of the plates were at least one-quarter wavelength of the lowest frequency of interest. In addition to this, to allow for a gradual impedance change and to allow for energy to be dissipated over a broad frequency range, the dimensions of the plates were tapered exponentially and dry sand was placed around and under the termination.

A schematic representation of the experimental apparatus is given in Figure 3a. The same outline experimental procedure was used for all three wave types considered in this work as follows; measure the input power and the transmitted vibrational power at a point downstream of the point of attachment for the device; fit the device and determine its installed dynamic properties; then measure the input power and transmitted powers as before. In all cases the measurement of vibrational power was normalized with respect to the magnitude of the driving point force. The installed performance is then determined from the measurement of transmitted power with and without the

neutralizer fitted; this is then compared with the equivalent predicted performance.

The experimental axial neutralizer consisted of a mild steel ring fitted around the pipe attached to the mounting flange by a series of aluminium alloy cantilevers. Details of the this experimental neutralizer are given in Figure 3b.

Although simple lumped parameter models are useful for predicting the approximate frequency range of operation for these types of device, the natural frequency of the installed device is highly dependent on the actual mounting stiffness. In order to overcome these problems a simple method of determining the installed natural frequency was developed [6] by considering the relative responses of the pipe wall at the point of attachment with respect to the neutralizer mass.

For the flexural vibration experiments the free end of the pipe was driven transversely and the anechoic termination consisted of a tapered sand bag around the base of pipe. The layout of the apparatus is shown in Figure 4 which also shows the format of the flexural neutralizer which can be seen to follow the "force and moment" design.

Finally torsional vibration was considered by driving the free end of the pipe transversely using a moment arm arrangement, see Figure 5. An "anechoic" termination was designed for the base of the structure to attenuate incident torsional waves. The basis of the design of this termination was to dissipate energy by allowing the incident torsional

waves to propagate, largely unhindered, into an array of damped beams attached to the base of the pipe. The respective wavelength of the vibrations in these beams would be considerably shorter and therefore energy would be dissipated more efficiently. To provide attenuation over a range of frequencies, beams of varying thickness were attached to the base of the pipe. To increase energy dissipation in these beams, they were based on a sandwich type construction such that a strip of damping material was constrained between the two surfaces. The dimensions of the attenuator beams were determined by attempting to match, as closely as possible, the torsional impedance of the pipe to the flexural impedance of the beams excited by a torque. Four of each attenuating beam were then fixed to the pipe wall equidistantly around the circumference.

The experimental neutralizer consisted of a mild steel ring fitted around the pipe using four aluminium alloy cantilevers, see Figure 5.

4.0. Results.

First the axial attenuation device was fitted to the pipe flange and the relative response of neutralizer mass and pipe wall were measured. From this result the natural frequency was found to be 160 Hz with a damping loss factor of 0.023. The neutralizer mass was then accurately measured and found to be 1.01 kg. The predicted attenuation performance was then determined using the theoretical models developed in [1] and the resulting theoretical and experimental attenuation performances are given in Fig. 6.

In a similar exercise the dynamic properties of the flexural neutralizer were found to be as follows; natural frequency, 54 Hz; loss factor, 0.054; mass, 0.82 kg and effective moment arm length, 0.075m. The corresponding comparison between theoretical and measured performance is given in Figure 7. A reasonable agreement between theory and experiment was achieved. The narrower measured bandwidth is considered to result from a source/discontinuity interaction discussed in [6].

Finally, the results of the torsional experiments were considered. The dynamic properties of the neutralizer were found to be as follows; natural frequency, 160 Hz, loss factor, 0.01; mass 1.01 kg. Theory and experiment are compared in Figure 8. The experimental result shows that the general trend of the attenuation is observed. The inertia of the torsional device was so great that the device acted over a wide frequency range with significant effect. The overall attenuation at the natural frequency is sufficiently large to be masked by noise in the measured signals and the characteristic "notch" in the attenuation curve is not seen.

5.0 Conclusions.

In this work, measurements of the attenuation performance of vibration neutralizers have been presented. Three wave-types have been considered; axial, flexural and torsional vibration. For each wave-type in turn, experiments have been undertaken to determine the installed attenuation performances. The results of these experiments have then been compared to theoretically derived performance characteristics developed in earlier studies. Corresponding theoretical

predictions have indicated reasonable agreement with experimental behaviour, provided the dynamical properties of the device are determined "in-situ".

6.0 Acknowledgement.

The work has been carried out with the support of the Marine Technology Directorate Ltd, the Science and Engineering Research Council, and the Procurement Executive, Ministry of Defence.

7.0 References.

- [1] Clark, P. and White, R.G., *Vibration control in one-dimensional structures using discontinuities*. Proceedings of the Fifth International Conference on Recent Advances in Structural Dynamics, Southampton, U.K. (1994).
- [2] Clark, P. and White, R.G., *Vibrational power transmission in beam-like structures fitted with asymmetric discontinuities*. Proceedings of the Institute of Acoustics. Vol 16, pp 179-190. (1994).
- [3] Clark, P. and White, R.G., *Vibrational power transmission in one-dimensional structures fitted with neutralizers*. Proceedings of the Conference Vibration and Noise '95, Venice, Italy (1995)
- [4] Fahy, F J., *Sound and Structural Vibration: Radiation, Transmission and Response* Academic Press (1985)
- [5] Horner, J L, *Vibrational power transmission in beam-like structures*. PhD Thesis, University of Southampton (1990)
- [6] Clark, P, *Devices for the reduction of pipeline vibration*. PhD Thesis, University of Southampton (1995)

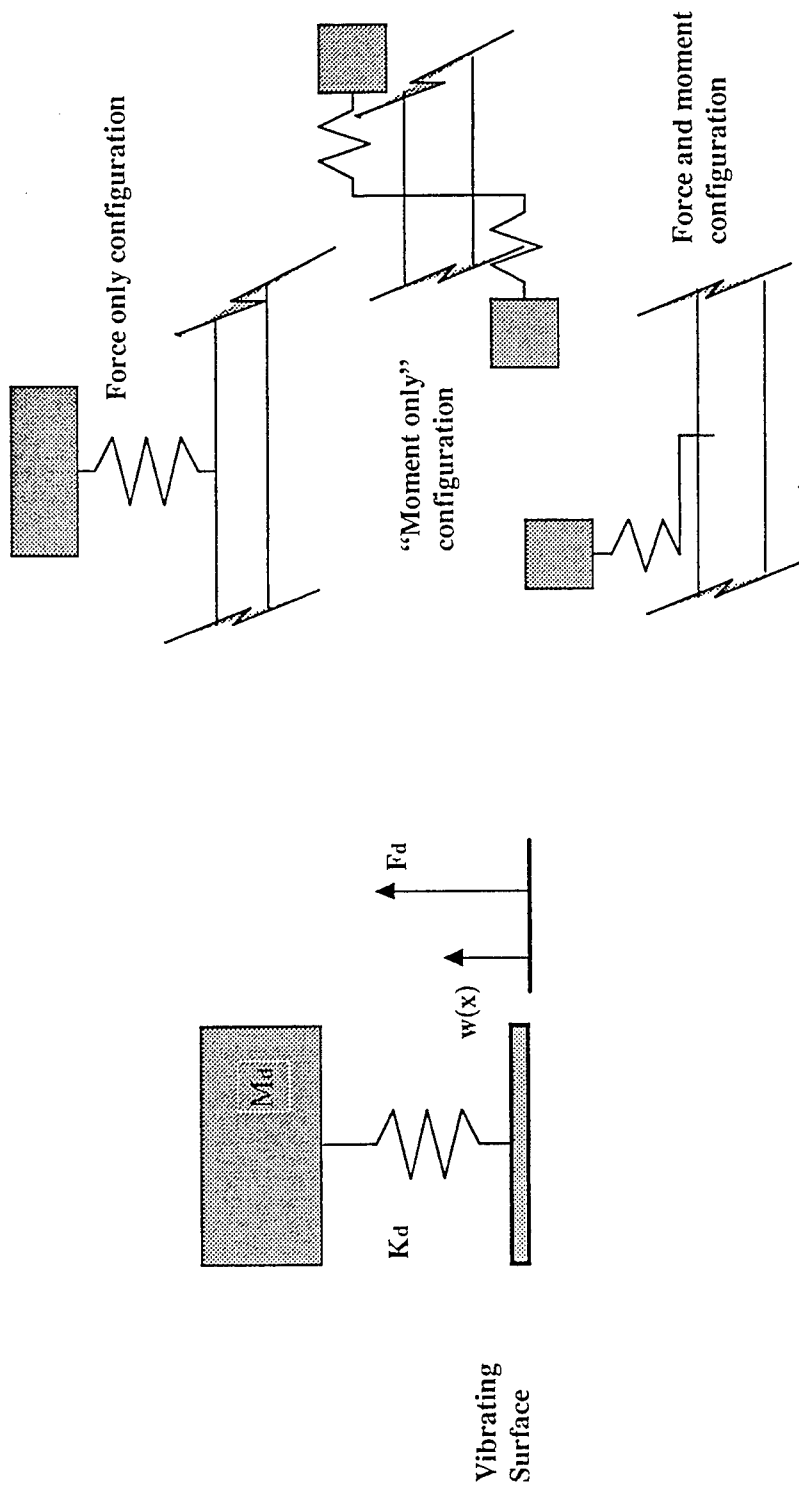


Figure 1: The simple vibration neutralizer.

Figure 2: Flexural vibration neutralizers

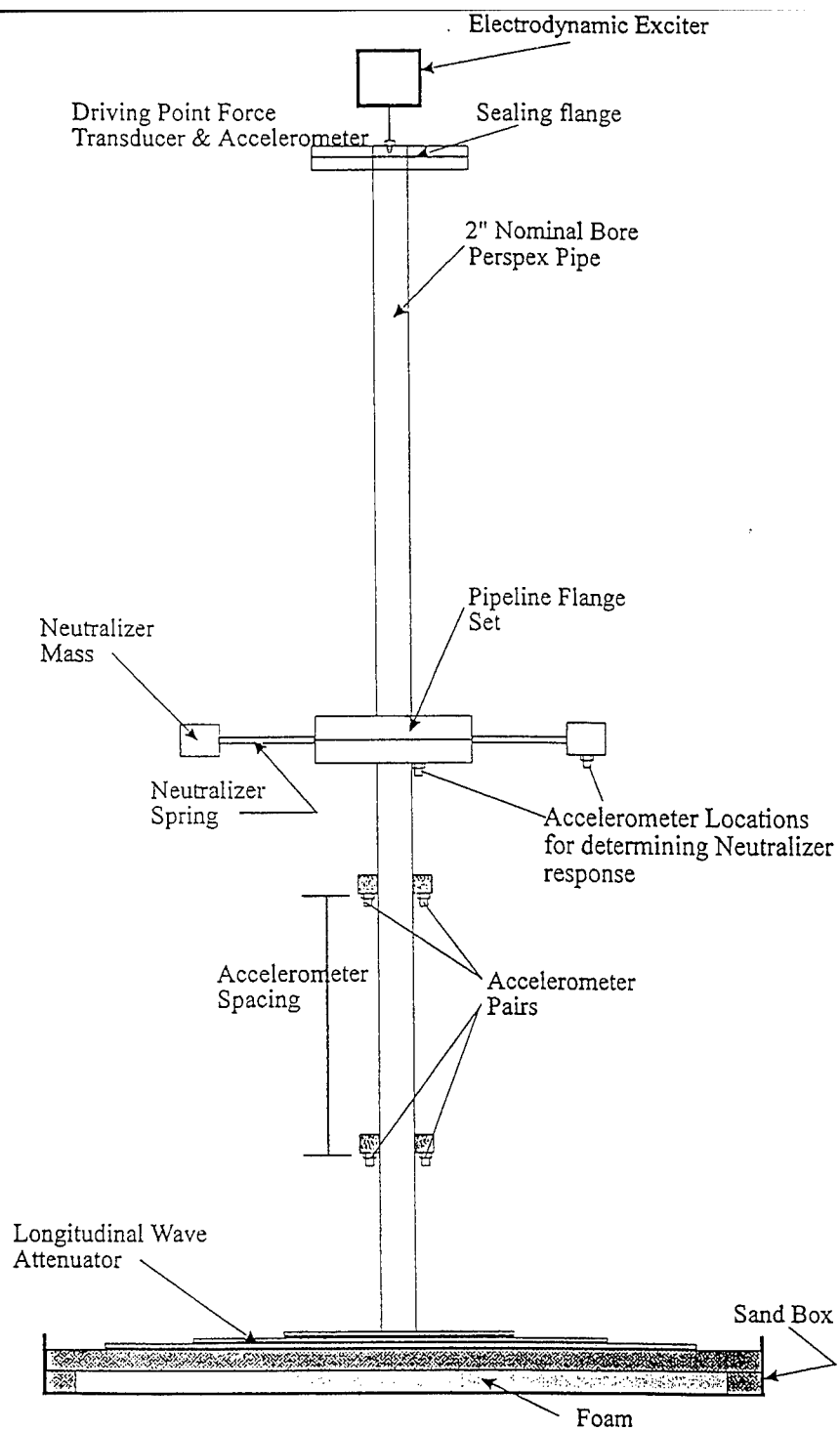


Figure 3a: Schematic representation of the experimental pipe apparatus fitted with axial pipeline neutralizer.

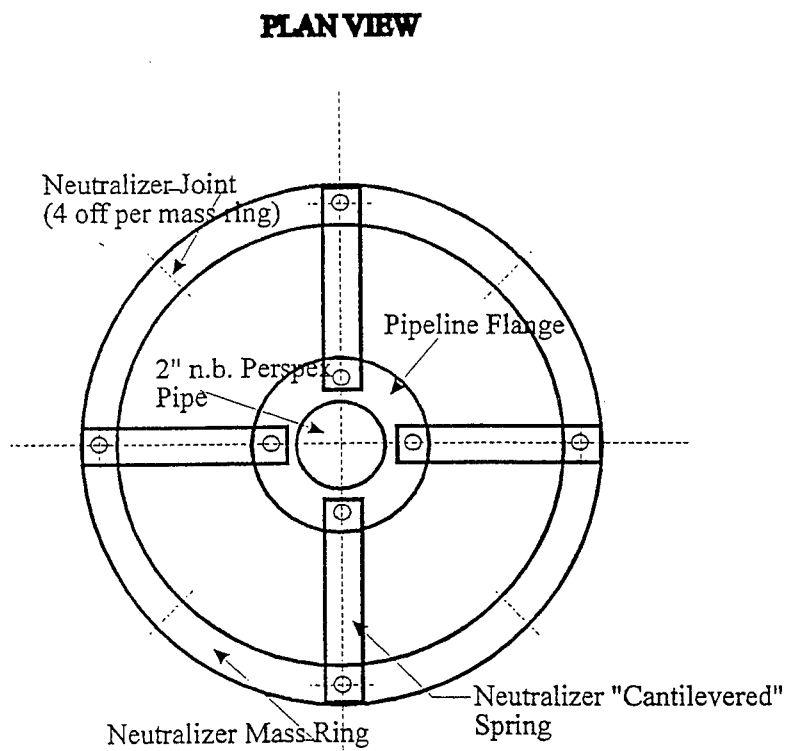


Figure 3b: Schematic representation of the pipeline neutralizer.

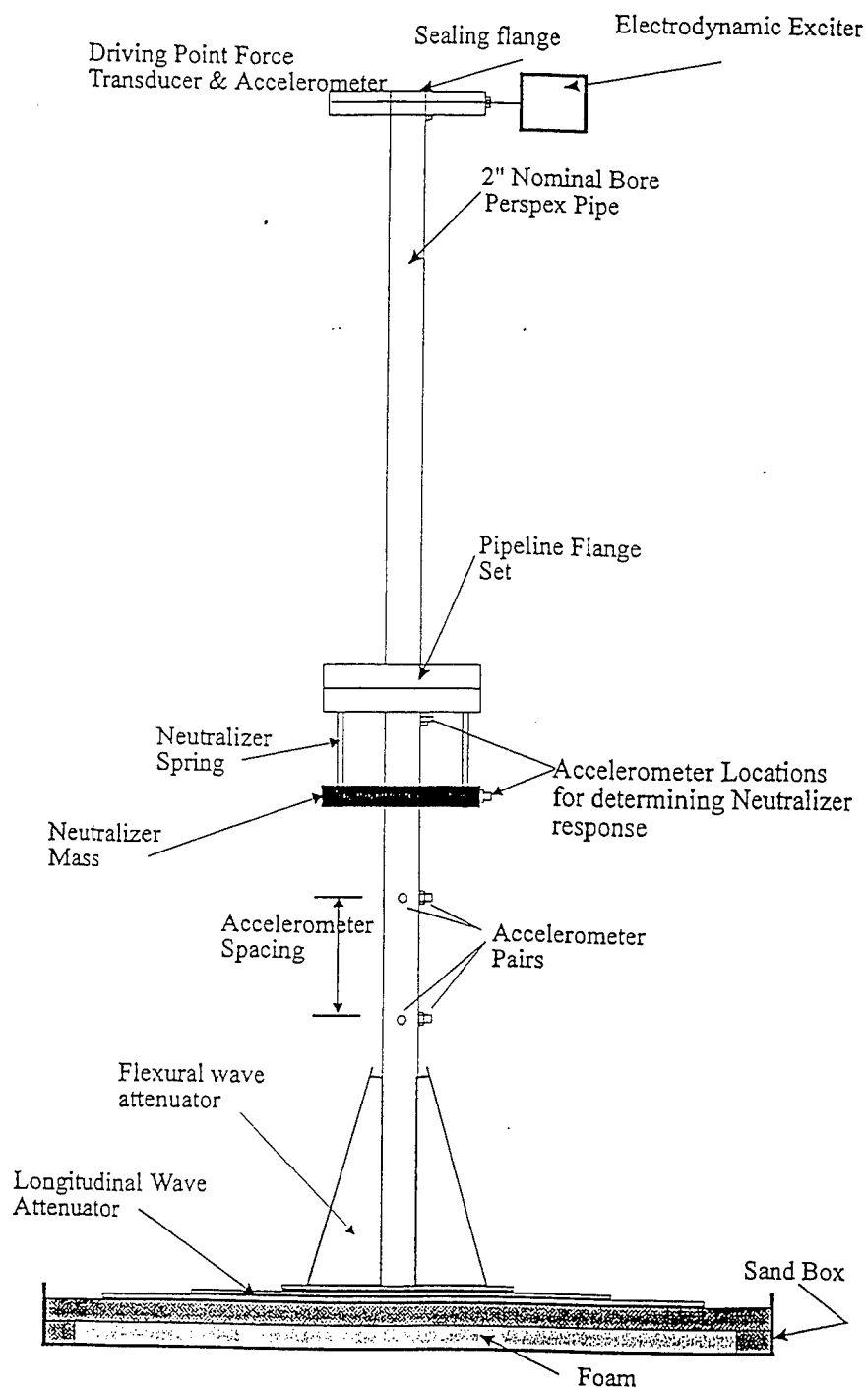


Figure 4: Schematic representation of the experimental pipe apparatus fitted with flexural pipeline neutralizer.

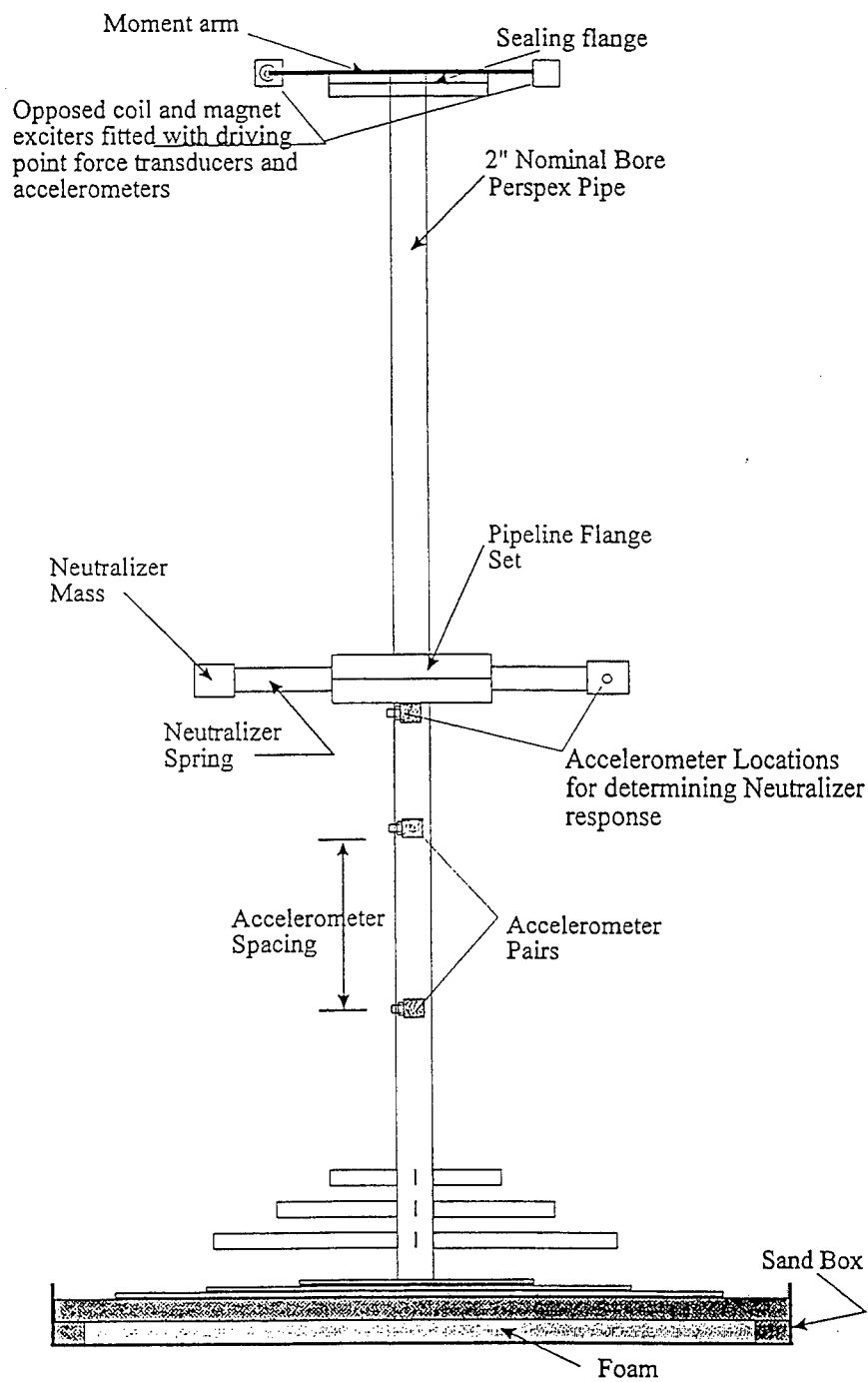


Figure 5: Schematic representation of the experimental pipe apparatus fitted with torsional pipeline neutralizer.

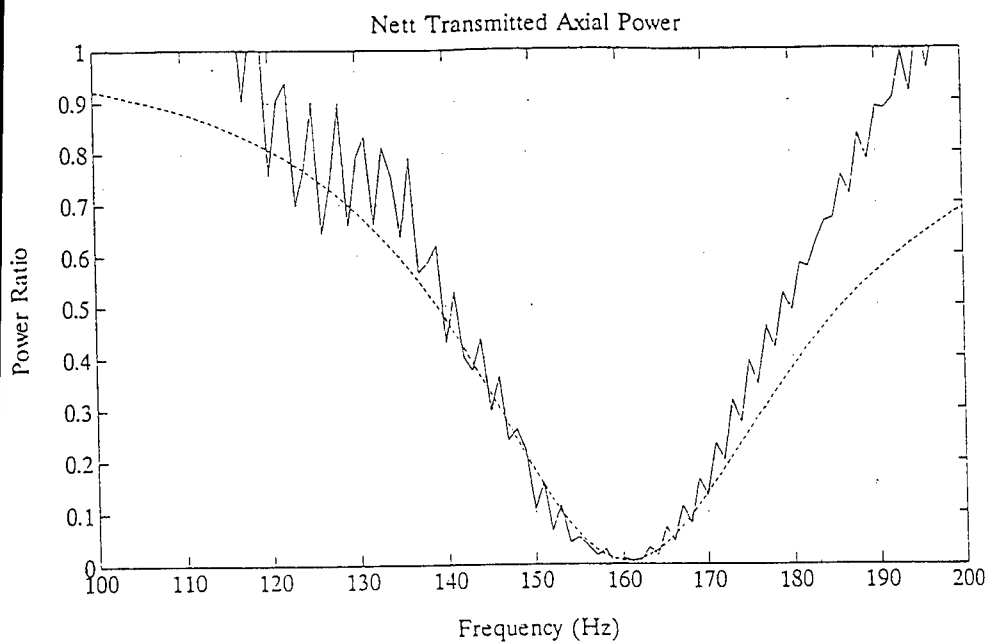


Figure 6: Measured v. predicted attenuation - axial vibration. Solid line: measured; dashed line: predicted.

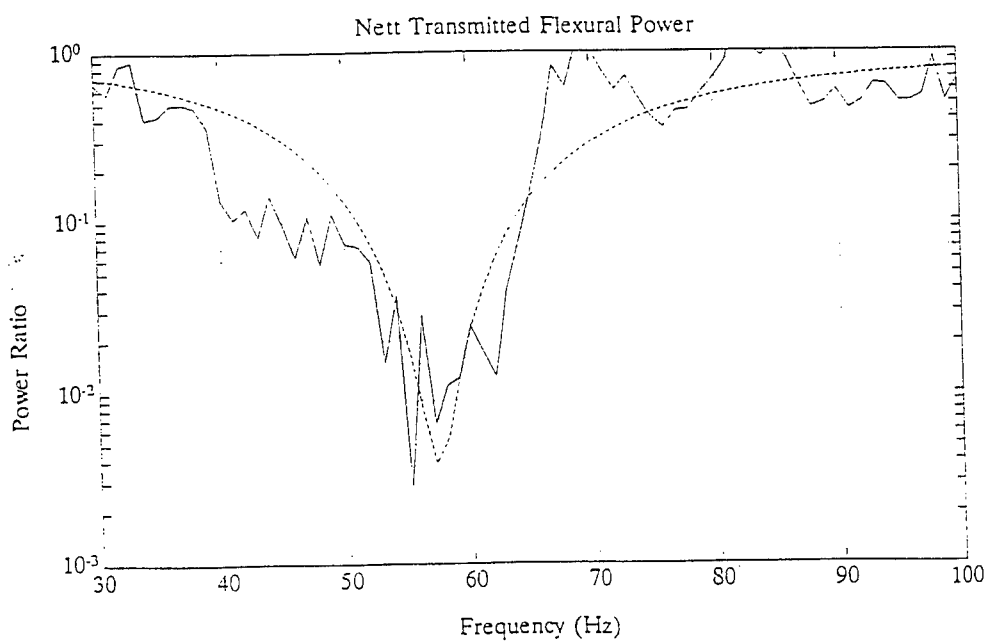


Figure 7: Measured v. predicted attenuation - flexural vibration. Solid line: measured; dashed line: predicted.

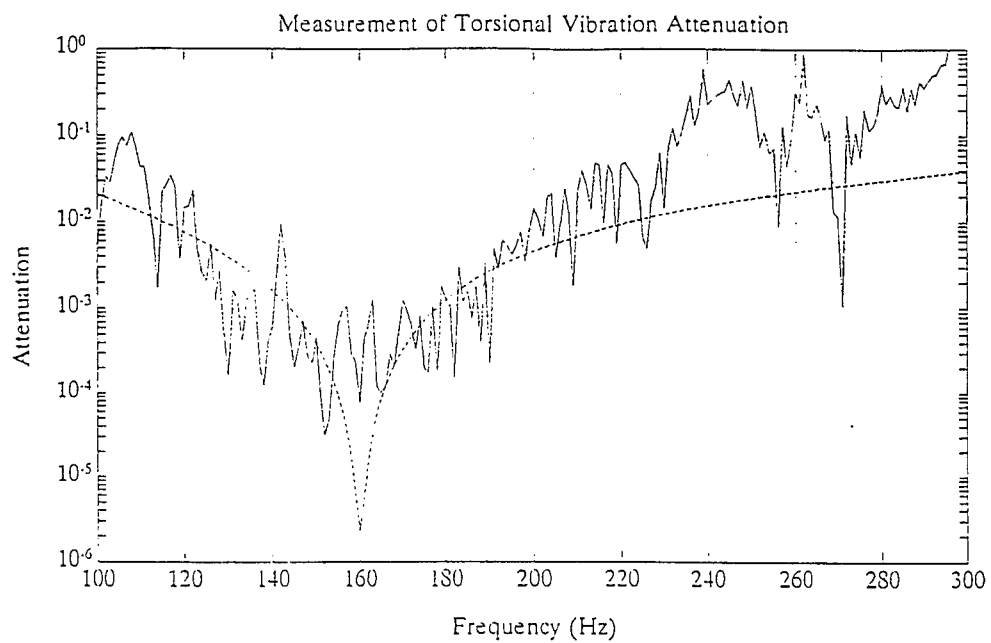


Figure 8: Measured v. predicted attenuation - torsional vibration. Solid line: measured; dashed line: predicted.

FINITE ELEMENT METHODS I

**SOME LIMITATIONS ASSOCIATED WITH THE USE OF
K-ORTHOGONAL POLYNOMIALS IN HIERARCHICAL
VERSIONS OF THE FINITE ELEMENT METHOD**

L.J. West[†], N.S. Bardell^{*}, J.M. Dunsdon^{*} and P.M. Loasby^{*}

[†] James Rennell Division for Ocean Circulation,
Southampton Oceanography Centre, University of Southampton,
Highfield, Southampton SO17 1BJ, Hampshire, ENGLAND.

^{*} Department of Aeronautics and Astronautics,
University of Southampton,
Highfield, Southampton SO17 1BJ, Hampshire, ENGLAND.

ABSTRACT

Central to the hierarchical concept of the finite element method is the ability [independently] to enrich the polynomial content of selected elements within the mesh. Like all approximate methodologies, the efficacy of such versions is critically dependent on keeping the numerical rounding errors in the actual calculation procedures to an absolute minimum. It is shown, by reference to an appropriate family of K -orthogonal polynomials, that numerical rounding errors associated with floating point arithmetic prescribe the maximum available degree of polynomial enrichment. The principal source of these errors can be traced to the wide dynamic range found in the coefficients that define a given K -orthogonal polynomial; it is, therefore, an inherent feature of the function itself. The implications of the modest levels of p -enrichment that reliably can be incorporated within a vibration analysis are discussed with reference to a free-free beam. Finally, some simple guidelines are presented that might beneficially be incorporated in an adaptive h - p algorithm.

1. INTRODUCTION

The finite element method (FEM) is essentially a numerical analysis technique which allows an approximate solution to be found to the set of differential equations that govern a particular problem [1]. This is achieved [mathematically] by dividing the domain of interest into a number of smaller sub-domains, called finite elements, and then approximating the solution by using local, piecewise-continuous, polynomial functions within each element. The accuracy of the solution may be improved in two ways. The first, and

most common, is to refine the finite element mesh, retaining the same degree of the elements used - this is known as the classical, or h -version of the FEM [1]. The second method involves fixing the mesh size and increasing the degree of the approximating polynomial functions - this is known as the p -version of the FEM [2,3]. More recently, an hybrid h - p version of the FEM has been advanced, which effectively marries the previous two concepts [4-6]. Convergence is now sought *simultaneously* by refining the mesh and increasing the degree of the elements. Both the p - and h - p methodologies are hierarchical versions of the finite element method.

The h - p version, especially in its adaptive mode, can be quite [computationally] costly to implement [6]. This is because the trade-off between h -refinement and p -enrichment usually is not known in advance, and it may prove necessary at some point in the adaptive process to add a significant number of hierarchical functions to certain elements in the mesh; the ability to carry out such localized enrichment is central to the whole h - p concept. Since any form of finite element analysis is, by definition, an approximate process, it is very important that numerical rounding errors in the actual calculation procedure itself are kept to an absolute minimum. It is shown in this paper that it is easy [unwittingly] to introduce such errors in a typical hierarchical analysis, given that to generate the additional polynomial functions, and then perform their integration as the field variable(s) over specific element domains, is a numerically intensive process.

Most modern commercial and developmental finite element codes routinely employ numerical integration schemes, such as Gauss-Legendre quadrature, using double precision floating point arithmetic hosted on a 64-bit architecture platform. This combination of software and hardware permits the energy functionals to be evaluated with great speed, accuracy, and confidence, *for an h -type analysis*. However, less is known about the numerical performance when a significant degree of p -enrichment is introduced into the problem, and the purpose of this paper is to quantify the sort of numerical

error magnitudes that might be anticipated in this type of analysis. (The "knock-on" effect caused by these errors on the solution phase of the analysis is addressed qualitatively here by means of a simple example; a quantitative assessment is more difficult to obtain since this will heavily be dependent on the nature of the problem being solved, the solution procedures employed, and the type of platform on which the calculations are being performed).

In what follows, attention is confined to the set of so-called K -orthogonal functions [7], which have been used extensively [8-10] as a means of providing local polynomial enrichment of an element field variable. One further restriction concerns the domain over which the integration of the field variable(s) is performed; only "regular" geometries characterized by a constant value of the Jacobian in the element mapping transformation are considered. This latter condition facilitates an exact benchmark solution to be obtained using symbolic computing; if any degree of element distortion is present, as is likely in practice, then the measures presented here must be regarded as the most conservative. All the computations reported here have been carried out using double precision floating point arithmetic on a Sun SPARC Centre 1000 with eight 60MHz processors (each with a floating point unit) running Solaris 2.3.

2. THEORETICAL AND NUMERICAL LIMITATIONS ASSOCIATED WITH K -ORTHOGONAL POLYNOMIALS

Most finite element models of structural dynamic processes usually require a C_0 or C_1 continuity condition to be met across the element interface. This is achieved in the h -version of the FEM by means of simple interpolation functions. In order to facilitate element-local p -enrichment, it is necessary to choose a family of polynomials which, when used in conjunction with the appropriate h -version functions, constitutes a complete set, and provides a genuine hierarchical basis. One such set, which has been used extensively for this purpose, is given [7] in Equation 1.

$$P_r(\xi) = \sum_{n=0}^{(r-1)/2} \frac{(-1)^n (2r - 2n - 6 + c)!!}{2^n n! (r - 2n - 1)!} \xi^{(r-2n-1)} \quad r > (3 - c) \quad (1a, 1b)$$

where $r!! = r(r-2)(r-4)\dots(2 \text{ or } 1)$, $0!! = (-1)!! = 1$; $(r-1)/2$ denotes its own integer part; the non-dimensional element-local co-ordinate ξ is measured from the centre of the domain R , defined here to lie along the line $-1 \leq \xi \leq +1$; and c takes the value $+1$ if the polynomials are to be used to enrich a C_0 continuity element (denoted by $g_r(\xi)$), and -1 if they are to be used to enrich a C_1 continuity element (denoted by $f_r(\xi)$). These generating formulae define two families of K -orthogonal polynomials, which are illustrated in Figures 1a and 2a; their h -version antecedents are also shown for completeness.

The first few hierarchical functions shown in Figures 1a and 2a appear to be well-behaved and easily generated. However, attempts to generate increasingly higher order functions meet with varying degrees of success, because only then does it become apparent that the coefficients of a given K -orthogonal polynomial function can vary greatly in magnitude. In fact, very large differences can occur between the various coefficients defining a particular polynomial, and it is convenient to measure this dynamic range by dividing each coefficient in the series by the least coefficient. Of particular interest is the ratio of the greatest coefficient to the least coefficient, which will provide the maximum dynamic range associated with a given polynomial. To give some idea of the way in which this maximum dynamic range evolves with increasing order of polynomial, the modulus of this quantity has been determined *exactly*, using symbolic computing [11], for each polynomial in the set $g_r(\xi)$ and $f_r(\xi)$ for values of r up to 200. This data is presented on a log-linear scale in Figures 1b and 2b. It is immediately obvious that as r increases, so the ratio of the greatest to the least coefficients for a given polynomial increases at a highly non-linear rate. By considering the envelope of these points for both families of K -orthogonal polynomials, it can be observed that the definition of even, symmetric (odd r) polynomials always yields a higher

value of Δ_r , than the definition of odd, antisymmetric (even r) polynomials, and that the value of Δ_r for the even functions follows a simple power law of the form $\log_{10}|\Delta_r| = ar + b$, where for the set $g_r(\xi)$, $a = 0.375$ and $b = -1.38$ (r odd), and for the set $f_r(\xi)$, $a = 0.378$ and $b = -0.96$ (r odd). Because the behaviour of both families of polynomials is so similar, it would be tedious to make reference to both; in what follows, discussion will be limited solely to the family of C_1 continuity functions denoted by $f_r(\xi)$.

It is interesting to note that [for both families of functions] as $r \rightarrow 45$, so the maximum dynamic range $|\Delta_r|$ exceeds 10^{16} . Since the numerical rounding errors associated with the use of double precision arithmetic are of the order 10^{-16} to 10^{-17} (although this figure may vary slightly from one computer to the next), it is clear that even if the polynomials could be defined using symbolically pre-computed arrays, numerical ill-conditioning would arise as soon as they were used in any numerical operations. Hence, for all practical purposes, the greatest number of polynomial functions that accurately could be generated and used is theoretically limited to approximately 45 for both C_0 and C_1 continuity functions; of course, the ultimate limit will be imposed by the platform. In practice however, it may not be possible to evaluate the coefficients numerically to such high orders simply because of the limited numerical accuracy with which both the [large] numerator and [large] denominator of the coefficients can be calculated.

For use in any sort of one-dimensional engineering analysis, it will usually be necessary to perform operations not on the functions alone, but on their products (e.g., to generate a stiffness or a mass matrix). With reference to Figure 2b (or Figure 1b), it can be seen that for the coefficients of the *product* to have a maximum dynamic range of 10^{16} , the sum of the maximum dynamic ranges of the two individual functions constituting the product must not exceed 10^{16} ; for equal orders, which is the most common combination, the highest number of polynomial functions that can be used is therefore limited to about 24. This limit can be determined more readily from the empirical

power laws quoted above.

Attempts to generate numerically and then multiply together some representative C_1 continuity polynomials confirm this reasoning. Figures 3-6 show the results of the following products plotted over the range $-1 \leq \xi \leq +1$: $f_{21} \times f_{21}$, $f_{23} \times f_{23}$, $f_{25} \times f_{25}$, and $f_{35} \times f_{35}$. These results graphically illustrate the onset and rapid increase in the end errors which appear at $\xi = \pm 1$ by virtue of numerical rounding errors. For $f_{21} \times f_{21}$ and $f_{23} \times f_{23}$, the end error is but a fraction of the maximum amplitude of the product, and because it is centred about the zero mean, it will therefore have little effect on the subsequent calculations. However, since one of the most important properties of the C_1 continuity family is that they maintain zero displacement and slope at each end, it is clear that this feature is completely lost when $r \geq 25$, in which case the end error completely dominates the resulting product. (This "noise" has a significant bias away from the zero mean, and therefore *will* adversely influence the subsequent calculations). It is worth being aware of this complication, since attempts [unwittingly] to introduce more than 25 K -orthogonal polynomials in an analysis is certain to be doomed to failure.

In general, use of these polynomials in two- or three-dimensional analyses will limit the maximum dynamic range between the greatest and least coefficients to 10^4 and 10^2 respectively in order to ensure the dynamic range of the resultant expression from the double and triple products does not exceed 10^{16} . The respective limits that now apply to the number of [equal order] C_1 continuity functions are approximately 14 and 8. These latter limits may be extended to the original 1-D maximum of 24 if the multiplication is separable over the area or volume of interest.

It should be emphasised that these are the theoretical limits attainable using double precision arithmetic to *manipulate* such functions; in practice, other sources of numerical error may arise and further reduce the number of shape functions that can reliably be incorporated within a particular analysis.

The formulation of a discrete solution scheme will, in general, be based on *a priori* knowledge of the structure's strain and kinetic energies, $\frac{1}{2}\mathbf{q}^T\mathbf{K}\mathbf{q}$ and $\frac{1}{2}\dot{\mathbf{q}}^T\mathbf{M}\dot{\mathbf{q}}$ respectively. This pre-supposes that the structural stiffness and mass matrices \mathbf{K} and \mathbf{M} can reliably be computed. Within the domain constraints mentioned earlier, this requirement can be met provided integrals of the type

$$I_{r,s}^{\alpha,\beta} = \int_{\mathcal{R}} P_r^{\alpha}(\xi) P_s^{\beta}(\xi) d\mathbf{R}, \quad (2)$$

can be evaluated over the domain \mathcal{R} for all possible values of r , s , α , and β . (α and β are the order of the function derivative, and normally will take the values 0, 1 and 2). The numerical computation of such integrals constitutes a major potential source of error.

To illustrate the sort of numerical problems that can arise with such a calculation, consider $I_{r,s}^{0,0}$, which represents the generic mass matrix of a simple beam. Since this set of integrals can be regarded as an inner product, it should be symmetric and positive definite. Therefore, it should possess real, positive, non-zero, eigenvalues. These eigenvalues have been calculated from this set of integrals - the integrals themselves have been evaluated using three different means: (i) exactly, using the symbolic computing package MAPLE [11], (ii) numerically, using standard Gauss-Legendre quadrature [12], and (iii) numerically, using an adaptive, ordered, oscillatory quadrature scheme [13], over the range $5 \leq r,s \leq 40$. Although standard Gauss-Legendre quadrature is designed to provide an exact solution with $(N+1)/2$ Gauss points if the highest order of the polynomial integrand is N , the highly oscillatory nature of the higher order polynomials renders the routine numerically unstable with increasing r and s . This is because the direct summation of terms is not ordered, and the differences between very large and very small numbers become lost in the rounding errors. It is for this reason that a specially ordered oscillatory scheme [13] has been used, which performs its summation in a

more robust fashion, matching terms of like order as it progresses through the calculation.

The results from these simulations, which show the progress of the lowest valued eigenvalue calculated from the integrals using techniques (i), (ii) and (iii) respectively, are shown in Figure 7. The exact results confirm the theoretical premise; however, both the numerical integration schemes deviate from the exact solution at $r = 23$, and become negative for $r \geq 24$. Even though the specially ordered oscillatory scheme is less in error than the standard Gauss-Legendre scheme for $r \geq 24$, both render the result non-positive-definite on account of the increasing amounts of the end error that are manifesting themselves at this level of polynomial definition.

Clearly, attempts to use more K -orthogonal polynomials than the limit suggested above in a dynamic analysis would result in a non-positive-definite mass matrix and hence would likely cause the solution scheme to fail. This is illustrated in the next section.

3. IMPLICATIONS FOR CONVERGENCE IN THE RAYLEIGH-RITZ METHOD

The monotonic convergence to the exact value associated with the use of increasing the number of assumed modes in a typical Rayleigh-Ritz method implicitly assumes that no significant numerical rounding errors occur in the calculation process. One qualitative example - the determination of the natural frequencies of a free-free Euler-Bernoulli beam - is used to demonstrate that this may not always happen in practice. The standard matrix-eigenvalue problem $[\mathbf{K} - \Omega^2 \mathbf{M}]\{\mathbf{q}\} = \mathbf{0}$ is set up for a simple p -version analysis (one super-element) using K -orthogonal polynomials in the usual fashion [14]. (The non dimensional frequency factor $\Omega = \omega(\rho AL^4/EI)^{1/2}$, where all the symbols have their usual meaning). The first twenty natural frequencies, calculated by each of the three methods outlined above, are plotted against increasing numbers of hierarchical shape functions r in Figure 8. (The results calculated

by the three different methods are coincident over the range $4 \leq r \leq 24$). The usual convergence behaviour is evident for the modes determined by all three methods until $r = 24$. The abrupt cessation of the plot at this level of polynomial enrichment is caused by the mass matrix becoming non positive-definite, as discussed above, and the solution scheme failing. What perhaps is of more interest is the fact that the higher order modes have not yet converged to their correct frequency value. Hence for this particular problem, the maximum amount of p -enrichment that reliably can be used is insufficient to permit study of *elastic* modes beyond the 11th.

In order to study vibration problems which involve the first few tens of modes, or perhaps even to try to explore the initial part of the medium frequency range, it is clear that with the current assumed displacement functions, resort would have to be made to an h - p type of analysis, in which the mathematical model now incorporates a number of elements using h -refinement in conjunction with local p -enrichment. In this way, it should not be necessary to boost the hierarchical functions anywhere near their [self-imposed] limit, and moreover, a more accurate result will always be obtained.

4. CONCLUSIONS

The aim of this paper was to demonstrate the limits attributable to numerical rounding errors when using two commonly-used families of K -orthogonal polynomials to hierarchically enrich a [locally selected] finite element. Its secondary purpose was to illustrate some of the pitfalls that could thwart the best endeavours of the undiscerning user of double precision floating point arithmetic.

With the aid of symbolic computing, it has been possible to obtain benchmark solutions which highlight and quantify some of the aforementioned difficulties. From the results presented here, and the implicit [although not easily-quantified] understanding of the adverse effects element distortion will have on the numerical accuracy, it would appear advantageous in h - p

applications always to restrict the degree of polynomial enrichment to (a) 24 or less in 1-D applications, (b) 14 or less in 2-D applications, (c) 8 or less in 3-D applications, *especially if a completely numerical scheme is to be used*. Clearly, some advantages may be gained by using symbolic computing and/or quadruple precision at the most appropriate stages in the computational algorithm.

Whilst these limits appear quite stringent, it must be remembered that this level of p -enrichment is still quite generous if used in combination with a suitably refined h -mesh. Such knowledge could usefully be incorporated as a decision criterion in an h - p adaptive algorithm, in order to ensure that the order of the local polynomial enrichment never exceeds a pre-set value. In this manner, the degree of error attributable to numerical rounding may more effectively be controlled, and hence greater confidence placed in the ultimate distribution of the h - and p -composition of the mesh.

Finally, if a higher level of p -enrichment is required than can be furnished by the present K -orthogonal polynomials, then resort must be made to the use of other, more suitable, hierarchical functions [15], or to alternative methods of quadrature [16].

REFERENCES

1. O.C. Zienkiewicz, *The Finite Element Method*, 3rd Edition, McGraw-Hill, London, 1979.
2. I. Babuska, B.A. Szabo and I.N. Katz, 'The p -version of the finite element method', *SIAM Journal of Numerical Analysis* **18**(3), 515-545 (1981).
3. O.C. Zienkiewicz, J.P. De S.R. Gago, and D.W. Kelly, 'The hierarchical concept in finite element analysis', *Computers and Structures* **16**(1-4), 53-65 (1983).
4. B. Guo and I. Babuska, 'The h - p version of the finite element method, Part 1: The basic approximation results', *Computational Mechanics* **1**, 21-41 (1986).

5. B. Guo and I. Babuska, 'The h - p version of the finite element method, Part 2: General results and applications', *Computational Mechanics* **1**, 203-220 (1986)
6. L. Demkowicz, J.T. Oden, W. Rachowicz and O. Hardy, 'Toward a universal h - p adaptive finite element strategy, Part 1. Constrained approximation and data structure', *Computer Methods in Applied Mechanics and Engineering*, **77**, 79-112 (1989)
7. D.C. Zhu, 'Development of hierarchical finite element methods at BIAA', *Proceedings of the International Conference on Computational Mechanics*, May 1985, Tokyo (1986)
8. D.C. Zhu, 'Hierarchical finite elements and their application to structural natural vibration problems', *AIAA Paper 82-0706*, (1982).
9. L. Meirovitch and H. Bahruh, 'On the inclusion principle for the hierarchical finite element method', *International Journal for Numerical Methods in Engineering*, **19**, 281-291 (1983)
10. N.S. Bardell, 'An engineering application of the h - p version of the finite element method to the static analysis of Euler-Bernoulli beams', *Computers and Structures*, **59**(2) 195-211, (1996).
11. B.W. Char, K.O. Geddes, G.H. Gonnet, B.L. Leong, M.B. Monagan, and S.M. Watt. *Maple V Language Reference Manual*, Springer-Verlag, Berlin, 1993.
12. NAG Fortran Library D01 BBF Mark 16, NAG Ltd, Wilkinson House, Jordan Hill Road, Oxford, UK.
13. NAG Fortran Library D01 AKF Mark 16, NAG Ltd, Wilkinson House, Jordan Hill Road, Oxford, UK.
14. N.S. Bardell, 'Free vibration analysis of a flat plate using the hierarchical finite element method', *Journal of Sound and Vibration*, **151**(2), 263-289, (1991).
15. O. Beslin and J. Nicolas, 'A hierarchical functions set for predicting very high order plate bending modes with any boundary conditions', Private Communication (1996).
16. H.E. Hinnant, 'A fast method of numerical quadrature for p-version finite element matrices', *International Journal for Numerical Methods in Engineering* **37**, 3723-3750 (1994).

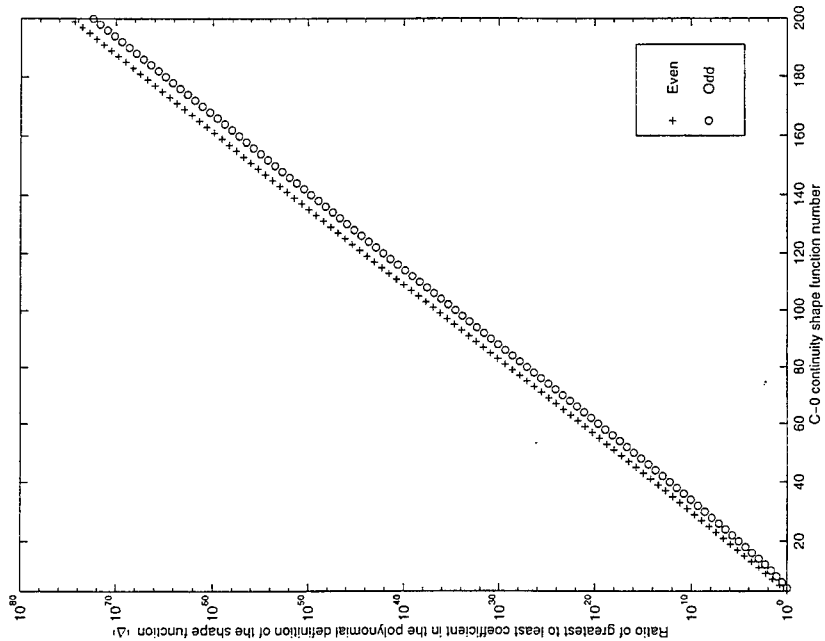


Figure 1b: $|\Delta_c|$ for the first 200 C_0 continuity polynomials.

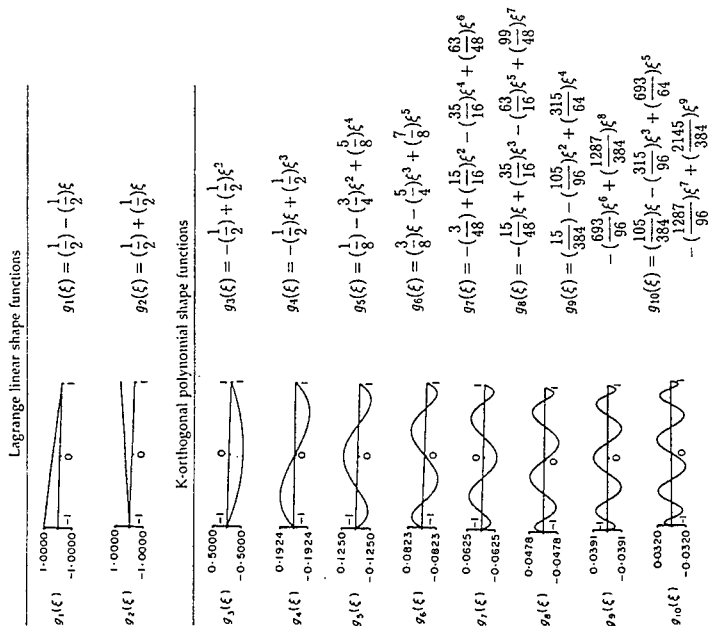


Figure 1a: The first 10 C_0 continuity polynomials.

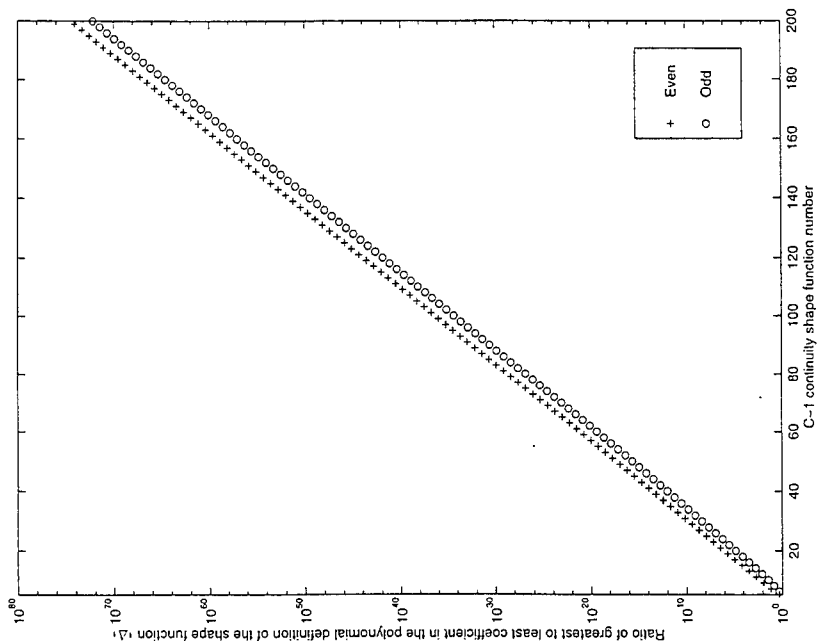


Figure 2a: The first 10 C_i continuity polynomials.

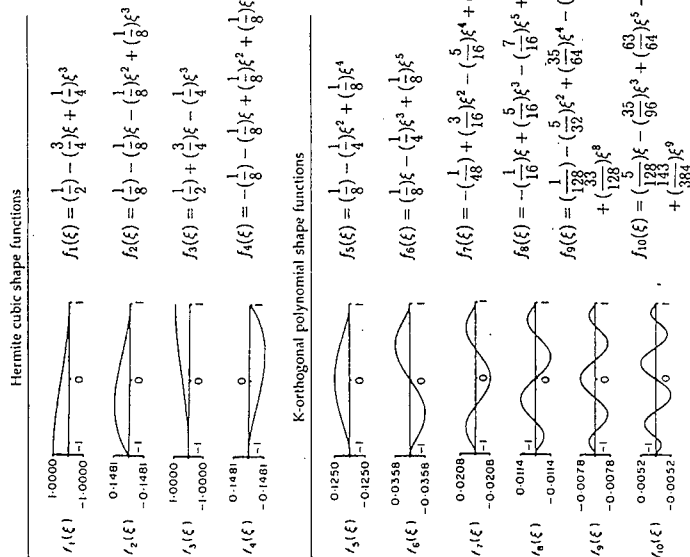


Figure 2b: $|\Delta_i|$ for the first 200 C_i continuity polynomials.

Figure 3: The product $f_{21} \times f_{21}$.

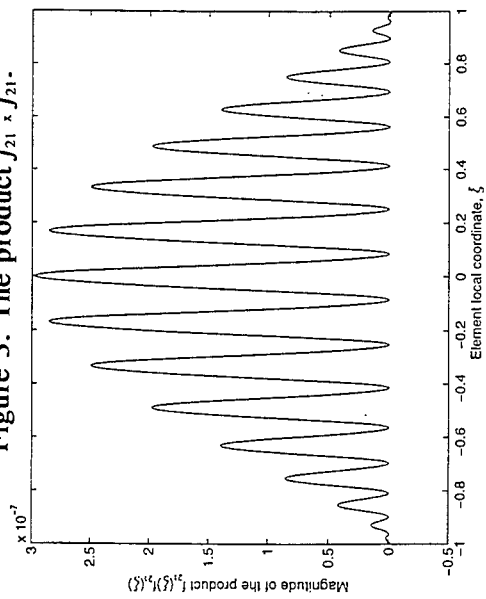


Figure 5: The product $f_{25} \times f_{25}$.

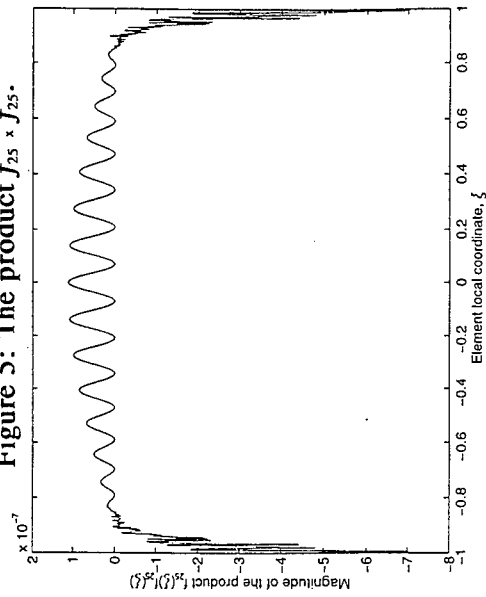


Figure 4: The product $f_{23} \times f_{23}$.

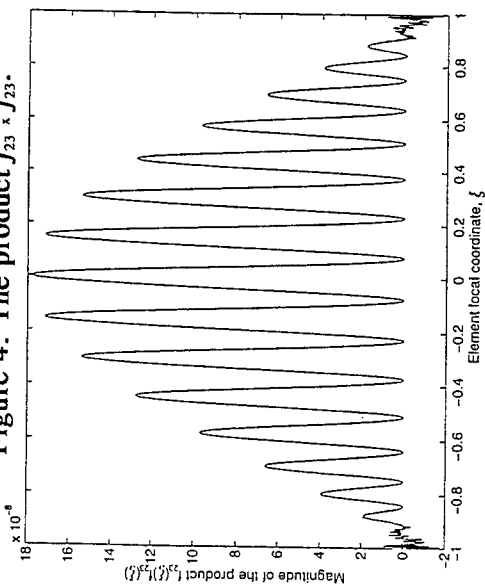
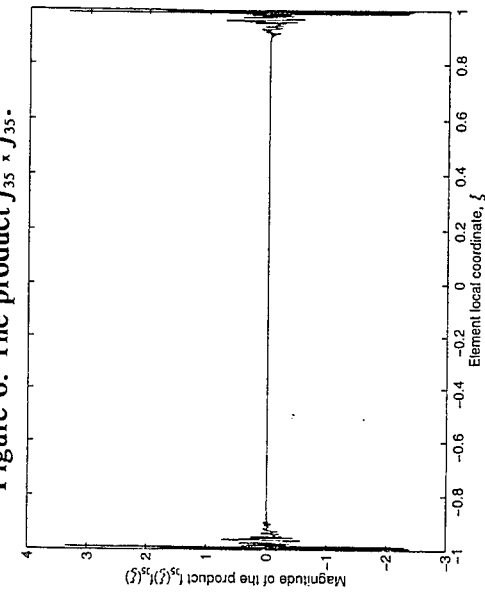


Figure 6: The product $f_{35} \times f_{35}$.



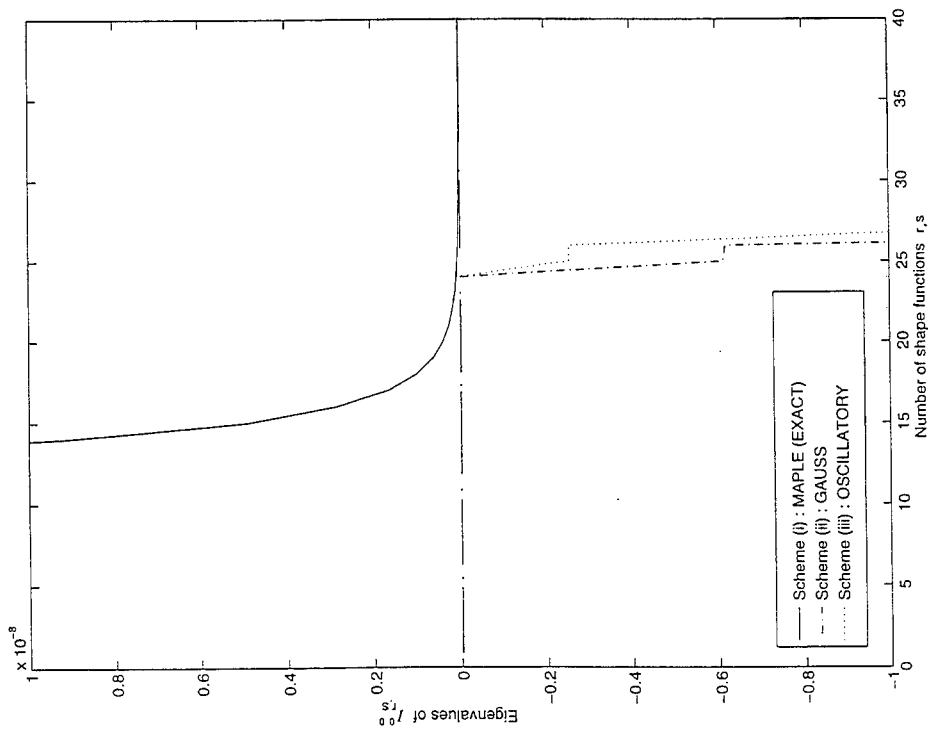


Figure 7: The progress of the numerically smallest eigenvalue $I_{r,s}^{(0)}$

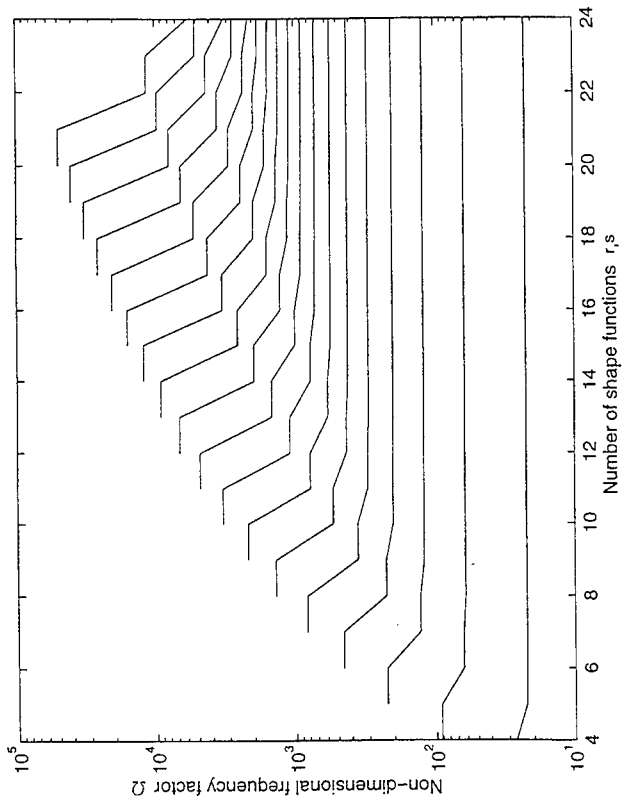


Figure 8: The convergence behaviour of the first twenty modes of a F-F beam.

ON THE FREE VIBRATION OF COMPLETELY FREE, OPEN, THIN, CONICALLY CURVED PANELS

N.S. Bardell¹, R.S. Langley, J.M. Dunsdon & K.N. Khatri²

Department of Aeronautics and Astronautics,

University of Southampton,

Highfield, Southampton SO17 1BJ, Hampshire, ENGLAND.

ABSTRACT

The h - p version of the finite element method is used to provide the first known results for the vibration characteristics of completely free, open, conically curved, isotropic shell panels. Two different conical panels have been constructed for experimental purposes, and the geometry of these panels defines the scope of the present study. Natural frequencies and modes are calculated and presented for both panels; this work is corroborated by comparing results from the present methodology with experimental data, and also from results generated by the proprietary finite element package ANSYS.

1. INTRODUCTION

Conically curved panels are commonly found in a variety of engineering applications, such as helicopter tail-rotor booms and the built-up tapering rear fuselage sections of civil aircraft. In such applications, these panels are subjected to a variety of different fluctuating loads, and it is essential that their dynamic integrity can be assured from the design stage onwards. To this end, it is important that reliable predictive techniques are available, so it may come as something of a surprise to find that as recently as 1973, a comprehensive survey conducted by Leissa [1] had to conclude that "*strangely, no references have been found which deal explicitly with the free vibrations of such [open conical] shells*". This topic has remained virtually unresearched and unreported until the present day; only

¹Westland Lecturer in Helicopter Engineering.

²Visiting Research Fellow from ARDE, Poona, India.

four relevant references can be found [2-5], and all of these address the free vibration problem of an open conical shell panel with supported edges. No work can be found referring to conical panels with *free* edges, which constitutes the most exacting test of any proposed solution scheme, and also poses the simplest set of boundary conditions for experimental work.

The purpose of this paper is twofold: (i) to obtain a solution to the title problem and hence provide some useful benchmark results for this particular category of conical shell panel; and (ii) to provide experimental validation of the theoretical results, given the absence of other numerical data.

2. METHOD OF ANALYSIS

An h - p version of the finite element method [6-7] is utilized in what follows, because it affords the user a more robust, flexible, and economic analysis tool than the conventional Rayleigh-Ritz technique. The h - p methodology adopted here is similar to that presented elsewhere by the authors [8], so only the essential details are given here.

Consider the thin conical shell element shown in Figure 1, whose middle surface is defined by the semi-vertex angle α , the radius of curvature at any point $R(x) = R_0 + x \sin \alpha$ (where R_0 is the radius of curvature of the small end), the slant length a and the total included angle ϕ . The cone is assumed to be of uniform thickness h (with $h/R(x)$ assumed to be small for all x). The components of displacement of a point on the middle surface are u , v and w in the x , θ , and z directions, respectively.

The state of strain at any point x, θ within the shell, distance z from the middle surface, is equal to the sum of the middle surface (membrane or extensional) strains and the (flexural) strains due to the changes of curvature. Denoting the middle surface extensional strains in the lengthwise and circumferential directions by ϵ_{xx}^0 , $\epsilon_{\theta\theta}^0$, the middle surface changes in curvature in the lengthwise and circumferential directions by κ_{xx}^0 , $\kappa_{\theta\theta}^0$, and the middle surface

in-plane shear strain and change in twist by $\gamma_{x\theta}^0$, $\kappa_{x\theta}^0$ respectively, then the state of strain at any point x, θ, z within the shell can be written:

$$\begin{aligned}\epsilon_{xx} &= \epsilon_{xx}^0 + z\kappa_{xx}^0 \\ \epsilon_{\theta\theta} &= \epsilon_{\theta\theta}^0 + z\kappa_{\theta\theta}^0 \\ \gamma_{x\theta} &= \gamma_{x\theta}^0 + 2z\kappa_{x\theta}^0\end{aligned}\quad (1)$$

where, for a cone [9], [10],

$$\begin{aligned}\epsilon_{xx}^0 &= \frac{\partial u}{\partial x} \\ \epsilon_{\theta\theta}^0 &= \frac{1}{R(x)} \frac{\partial v}{\partial \theta} + u \frac{\sin \alpha}{R(x)} + w \frac{\cos \alpha}{R(x)} \\ \gamma_{x\theta}^0 &= \frac{\partial v}{\partial x} + \frac{1}{R(x)} \frac{\partial u}{\partial \theta} - v \frac{\sin \alpha}{R(x)} \\ \kappa_{xx}^0 &= - \frac{\partial^2 w}{\partial x^2} \\ \kappa_{\theta\theta}^0 &= - \frac{1}{R(x)^2} \frac{\partial^2 w}{\partial \theta^2} + \frac{\cos \alpha}{R(x)^2} \frac{\partial v}{\partial \theta} - \frac{\sin \alpha}{R(x)} \frac{\partial w}{\partial x} \\ \kappa_{x\theta}^0 &= \frac{\sin \alpha}{R(x)^2} \frac{\partial w}{\partial \theta} - \frac{1}{R(x)} \frac{\partial^2 w}{\partial x \partial \theta} + \frac{\cos \alpha}{R(x)} \frac{\partial v}{\partial x} - v \frac{\cos \alpha \sin \alpha}{R(x)^2}\end{aligned}\quad (2)$$

and u, v , and w are the midplane ($z = 0$) displacements. The full kinematic relationships between the displacements at a general point x, θ, z , and the midplane displacements u, v, w are given in [9].

Substituting Equations 2 into Equations 1, and introducing the local co-ordinates ξ, η which are related to the element Cartesian co-ordinates through $\xi = 2x/a - 1$ and $\eta = 2R(x)\theta/b(x) - 1$, (see Figure 1), the form of the strain-displacement relationship becomes:

$$\begin{bmatrix} \epsilon_{xx} \\ \epsilon_{\theta\theta} \\ \gamma_{x\theta} \end{bmatrix} = \begin{bmatrix} \frac{2}{a} \frac{\partial}{\partial \xi} & 0 & -\frac{4}{a^2} \frac{\partial^2}{\partial \xi^2} \\ \phi \frac{\sin \alpha}{h(x)} & \frac{2}{h(x)} \left(1 + \phi \frac{\cos \alpha}{h(x)} \right) \frac{\partial}{\partial \eta} & \phi \frac{\cos \alpha}{h(x)} - \frac{4}{b(x)^2} \frac{\partial^2}{\partial \eta^2} - \phi \frac{2 \sin \alpha}{ab(x)} \frac{\partial}{\partial \xi} \\ \frac{2}{b(x)} \frac{\partial}{\partial \eta} & \frac{2}{a} \frac{\partial}{\partial \xi} - \phi \frac{\sin \alpha}{b(x)} - \phi^2 \frac{2 \cos \alpha \sin \alpha}{b(x)^2} + \phi \frac{4 \cos \alpha}{ab(x)} \frac{\partial}{\partial \xi} & -\frac{8}{ab(x)} \frac{\partial^2}{\partial \xi \partial \eta} + \phi \frac{4 \sin \alpha}{b(x)^2} \frac{\partial}{\partial \eta} \end{bmatrix} \begin{bmatrix} u(\xi, \eta) \\ v(\xi, \eta) \\ w(\xi, \eta) \end{bmatrix}$$

$$\text{i.e., } \{\varepsilon\} = [\Delta]\{\delta\}. \quad (3)$$

Note that every occurrence of $R(x)$ in Equation 3 has been replaced by $b(x)/\phi$ so that there is only one x -dependent term in the coefficient of each differential operator. (Note also, that the circumferential arc length of the cone, $b(x) \equiv b(\xi)$).

For an isotropic material, the constitutive relationship is given by

$$\begin{bmatrix} \sigma_{xx} \\ \sigma_{\theta\theta} \\ \tau_{x\theta} \end{bmatrix} = \frac{E}{(1 - \nu^2)} \begin{bmatrix} 1 & \nu & 0 \\ \nu & 1 & 0 \\ 0 & 0 & \frac{(1 - \nu)}{2} \end{bmatrix} \begin{bmatrix} \epsilon_{xx} \\ \epsilon_{\theta\theta} \\ \gamma_{x\theta} \end{bmatrix},$$

$$\text{i.e., } \{\sigma\} = [D]\{\varepsilon\}. \quad (4)$$

For the type of problem under consideration, it is advantageous to use the *same* set of assumed displacement functions to represent the motions in all three co-ordinate directions. To this end, an ascending hierarchy of special trigonometric functions [11], used in conjunction with Hermite cubics, will furnish a robust complete set of admissible displacement functions, $f(\xi \text{ or } \eta)$. (This set is summarized in Table 1). Hence the in-plane displacement fields u and v , and the out-of-plane displacement field w , may approximately be represented as follows:

$$\begin{aligned} u(\xi, \eta) &= \sum_{rx=1}^{p_{ux}} \sum_{sx=1}^{p_{ux}} X_{rx,sx} f_{rx}(\xi) f_{sx}(\eta) \\ v(\xi, \eta) &= \sum_{ry=1}^{p_{vx}} \sum_{sy=1}^{p_{vy}} Y_{ry,sy} f_{ry}(\xi) f_{sy}(\eta) \\ w(\xi, \eta) &= \sum_{rz=1}^{p_{wx}} \sum_{sz=1}^{p_{wy}} Z_{rz,sz} f_{rz}(\xi) f_{sz}(\eta). \end{aligned} \quad (5)$$

The nodal displacements/rotations, and the amplitudes of the hierarchical functions along the edges and in the interior of the panel element, $X_{rx,sx}$, $Y_{ry,sy}$ and $Z_{rz,sz}$ constitute the generalized co-ordinates of the problem. (Note: the in-plane degrees of freedom only require compatibility of the u - and v -displacements to effect C_0

continuity; there is no requirement to match the first derivatives of these in-plane functions). Each summation which appears in Equation 5 is taken over [any number of] p assumed modes; the first subscript on p denotes the type of displacement field and the second denotes whether it is in the x - or y -direction.

Equation 5 can be written more succinctly in matrix notation as

$$\{\delta\} = [N] \{q\}, \quad (6)$$

where $\delta = \{u(\xi, \eta), v(\xi, \eta), w(\xi, \eta)\}^T$, $q = \{X_{rx, sx}, Y_{ry, sy}, Z_{rz, sz}\}^T$, and N is a rectangular matrix containing the shape functions. Hence, the strain energy of the conical panel element, which is given by

$$U = \frac{1}{2} \int_{-1}^{+1} \int_{-1}^{+1} \int_{-\frac{h}{2}}^{+\frac{h}{2}} \{\epsilon\}^T \{\sigma\} \frac{a b(\xi)}{4} dz d\eta d\xi, \quad (7)$$

can be constructed from Equations 3, 4 and 6 thus:

$$U = \frac{1}{2} \{q\}^T \left[\frac{a}{4} \int_{-1}^{+1} \int_{-1}^{+1} \int_{-\frac{h}{2}}^{+\frac{h}{2}} [N]^T [\Delta]^T [D] [\Delta] [N] b(\xi) dz d\eta d\xi \right] \{q\}. \quad (8)$$

The term in the square brackets can be identified as the element stiffness matrix K^E of the conical panel.

Similarly, the kinetic energy of the thin conical panel element is given by

$$T = \frac{1}{2} \rho \int_{-1}^{+1} \int_{-1}^{+1} \int_{-\frac{h}{2}}^{+\frac{h}{2}} \{\dot{\delta}\}^T \{\dot{\delta}\} \frac{a b(\xi)}{4} dz d\eta d\xi. \quad (9)$$

Substituting Equation 6 into Equation 9 yields

$$T = \frac{1}{2} \{\dot{q}\}^T \left[\rho \frac{a}{4} \int_{-1}^{+1} \int_{-1}^{+1} \int_{-\frac{h}{2}}^{+\frac{h}{2}} [N]^T [N] b(\xi) dz d\eta d\xi \right] \{\dot{q}\}. \quad (10)$$

Evidently, the term in the square brackets is the element mass matrix \mathbf{M}^E of the conical panel.

The matrix multiplication and integration required to evaluate the element stiffness and mass matrices shown in Equations 8 and 10 is performed numerically using a full two-dimensional Gauss-Legendre quadrature scheme [10]. This scheme, which is implemented using commercially available software [11], dynamically allocates the number of integration points to ensure an "exact" solution is obtained. This is a particularly useful feature for the current problem where the circumferential arc length varies as a function of x .

Inter-element compatibility is achieved simply by matching the appropriate generalized co-ordinates at common element nodes and along common edges (displacement and rotation d.o.f. for the out-of-plane C_1 continuity, but only displacement d.o.f. for in-plane C_0 continuity). This procedure ensures the elements are fully conforming and, moreover, facilitates assembly of the global stiffness and mass matrices \mathbf{K}^G and \mathbf{M}^G .

Although a variety of different boundary conditions may be applied to the panel by nullifying the appropriate generalized co-ordinates, it is not necessary to do this in the current work (since the panel under consideration is unrestrained), and \mathbf{K}^G and \mathbf{M}^G remain completely intact.

By assuming simple harmonic motion and the absence of any external forcing agency, the governing equations of motion for free vibration can be obtained by combining the expressions for the strain and kinetic energy of the panel into a total potential energy expression, and then deriving Lagrange's equation. This yields a standard matrix-eigenvalue problem of the form

$$[\mathbf{K}^G - \omega^2 \mathbf{M}^G] \{\mathbf{q}\} = \mathbf{0}. \quad (11)$$

The solution to Equation 11 yields the natural frequencies in radian units, rendered here in Hz for ready comparison with the experimental results. The first six frequencies are always zero, corresponding to rigid-body modes; these will be disregarded in the "numbering" of the elastic modes. Corresponding to each eigenvalue is an eigenvector which may be used in conjunction with Equation 5 to recover the associated displacement of each element in the model, and hence the complete mode of the panel under consideration.

3. GEOMETRIC SCOPE OF THE PRESENT WORK

Two different aluminium conical panels were produced for testing, and these define the scope of the present work. The [measured] geometric properties of each cone are summarized below:

	α (deg)	a (m)	R_0 (m)	ϕ (deg)	h (mm)	E (N/mm ²)	ρ (kg/m ³)	ν
Cone #1	3.8	1.14	0.34	130	2.0	70E9	2700	0.3
Cone #2	26.5	1.12	0.16	180	2.0	70E9	2700	0.3

4. EXPERIMENTAL STUDY

In view of the limited work that has been carried out in this general subject area, it was decided that some experimental work would provide a valuable reference datum for the subsequent theoretical study. To this end, simple tap tests were performed on both conical shells. Each shell was suspended vertically, with the narrow end uppermost, using one (or two) soft elastic cords suspended from a rigid A-frame to permit both symmetric and asymmetric suspension possibilities. See Figure 2 for a full description of the rig arrangement and the measurement system used for data acquisition. A broad-band excitation was applied by tapping the shell with the hammer, and the response monitored by a wax-mounted accelerometer. A number of different tapping and monitoring positions were used to capture the *full* modal response. A short-time history of the input and response

signals was acquired and subsequently used as the basis of a FFT analysis; this was undertaken using a signal processing routine within the MATLAB environment. Natural frequencies were identified from the resonant peak and phase-shift information available from the resulting frequency response plot. Typical results are presented in Table 3, alongside the theoretically derived data. Remarkably good agreement is seen for the first ten elastic frequencies of each panel. No attempts were made experimentally to quantify the modes of vibration.

5. THEORETICAL RESULTS

A convergence study was undertaken using three different h meshes, each with different amounts of p -enrichment, for the shallow Cone #1. The frequencies of the first ten elastic modes are presented in Table 2. As would be expected, the frequency parameters are seen to converge monotonically from above, yielding upper bounds to the exact values. The various mixtures of the h - and p -parameters were chosen to reveal the effect of systematically refining the h -mesh at the expense of p -enrichment. The term *MO* refers to the final order of the matrix-eigenvalue problem solved. Such a strategy clearly reveals the greater efficiency of the single super-element, which concurs with other observations [5]. (A fully converged set of frequencies generated from a 20×20 mesh of SHELL 63 elements in ANSYS 5.3 [13] is included in the final column of Table 2 for comparison purposes). Obviously, in any given study, the number of elements, and degree of p -enrichment, required to obtain a converged solution will be *highly dependent* on the cone *geometry*. However, for Cone # 2, converged solutions arising from a variety of mesh designs revealed that the most economical solution was still forthcoming from a single super-element boosted to $p = 16$. In general, however, different mesh combinations should be considered.

Having gained confidence with the h - p formulation presented here, the natural frequencies of the first ten elastic modes were computed for both conical panels. These results are presented in Table 3. In addition, the corresponding

natural modes are illustrated for Cone # 1 and Cone # 2 in Figures 3 and 4, respectively.

Finally, use was made of the commercial finite element package ANSYS 5.3 to provide additional results and verification of the work presented here. Models of both panels were constructed using the linear elastic SHELL 63 four-noded element, which possesses both membrane and bending capabilities. A fairly dense 20×20 h -mesh of 400 elements was used in both cases to guarantee convergence of the first ten elastic modes. These results are presented in Table 3 to complete the current analysis.

Because the h - p element derived in this paper is tailored specifically to conical panels, it is not surprising that its overall performance exceeds that of its more general ANSYS counterpart. Even so, it is worth noting that by using the h - p version of the FEM in preference to the h -version, it is possible to obtain converged answers using some 50% fewer degrees of freedom.

Excellent agreement is found between all three methodologies, with the largest discrepancies of 14% arising in the comparison between the theoretical and experimental results for the 6th mode of Cone # 1, and 10% arising in the comparisons between the theoretical and experimental results for the 9th mode of Cone # 2. Considering that neither experimental sample was perfectly conical, and that the stiffness of the suspension bungies may have exerted some influence on the notionally free edge conditions, the correlation between all three sets of results is outstanding.

Referring to the shallow Cone # 1, it might initially be supposed that the modal behaviour of this particular panel will be very similar to that of an equivalent cylindrically curved panel. However, from the modes shown in Figure 3, it is evident that even a modest amount of conicity markedly alters the behaviour of a nominally cylindrically curved panel - modes 6, 9 and 10 clearly reveal how the opposite curved ends can vibrate with a different number of half waves on account of the difference in their relative bending stiffnesses. This effect

becomes more pronounced as the coning angle α is increased, as evidenced by modes 6 to 10 of Cone # 2 shown in Figure 4.

6 CONCLUSIONS

An initial study of the vibration characteristics of completely free, open, conically curved, isotropic shell panels has been undertaken using the h - p version of the finite element method. The convergence properties of this shell element have been established for particular geometries, thereby rendering it suitable for use in future parameter studies. Natural frequencies and modes have been obtained for both panels using (i) the h - p methodology reported here, (ii) ANSYS 5.3, and (iii) experimental work. Excellent agreement has been found between all three approaches, and it may therefore be concluded that further study in this subject area can be undertaken with confidence.

ACKNOWLEDGEMENTS

The assistance rendered by the following companies and individuals is gratefully acknowledged: EPSRC, under contract number GR/J 06306, for providing the financial support; the Composites Workshop of British Airways Engineering, Heathrow Airport, for producing the test specimens; and Mr J. R. Smith and Mr R.E.W. Creffield, of the Department of Aeronautics and Astronautics, for producing the ANSYS results and the illustrations, respectively.

REFERENCES

1. A.W. LEISSA 1973 *Vibration of Shells*, NASA SP 288. (Chapter 5)
2. D. TEICHMANN 1985 *AIAA Journal* **23**, 1634-1637. An approximation of the lowest eigen frequencies and buckling loads of cylindrical and conical shell panels under initial stress.
3. R.S. SRINIVASAN and P.A. KRISHNAN 1987 *Journal of Sound and Vibration* **117**(1), 153-160. Free vibration of conical shell panels.
4. Y.K. CHEUNG, W.Y. LI and L.G. THAM 1989 *Journal of Sound and Vibration* **128**(3), 411-422. Free vibration analysis of singly curved shell by spline finite strip method.

5. C.W. LIM and K.M. LIEW 1995 *Engineering Structures* **17**(1), 63-70. Vibratory behaviour of shallow conical shells by a global Ritz formulation.
6. O.C. ZIENKIEWICZ, J.P. de S. R. GAGO and D.W. KELLY 1983 *Computers and Structures* **16**(1-4), 53-65. The hierarchical concept in finite element analysis.
7. I. BABUSKA and B. GUO 1986 *Computational Mechanics* **1**, 21-41. The h - p version of the finite element method, Part 1: the basic approximation results.
8. N.S. BARDELL, R.S. LANGLEY, and J.M. DUNSDON 1997 *Journal of Sound and Vibration* (in proof). On the free vibration of completely free, open, cylindrically curved, isotropic shell panels.
9. A.E.H. LOVE, *A Treatise on the Mathematical Theory of Elasticity*, 4th Edition, Dover Publications, New York, 1944.
10. W. SOEDEL, *Vibrations of Shells and Plates*, Marcel Dekker Inc., New York, 1981.
11. O. BESLIN and J. NICOLAS, *A hierarchical functions set for predicting very high order plate bending modes with any boundary conditions*. Private Communication.
12. D01AKF. The NAG FORTRAN Workshop Library Handbook - Release 1. Oxford: NAG Ltd., 1986.
13. ANSYS, Inc., 201 Johnson Road, Houston, PA 15342-1300.

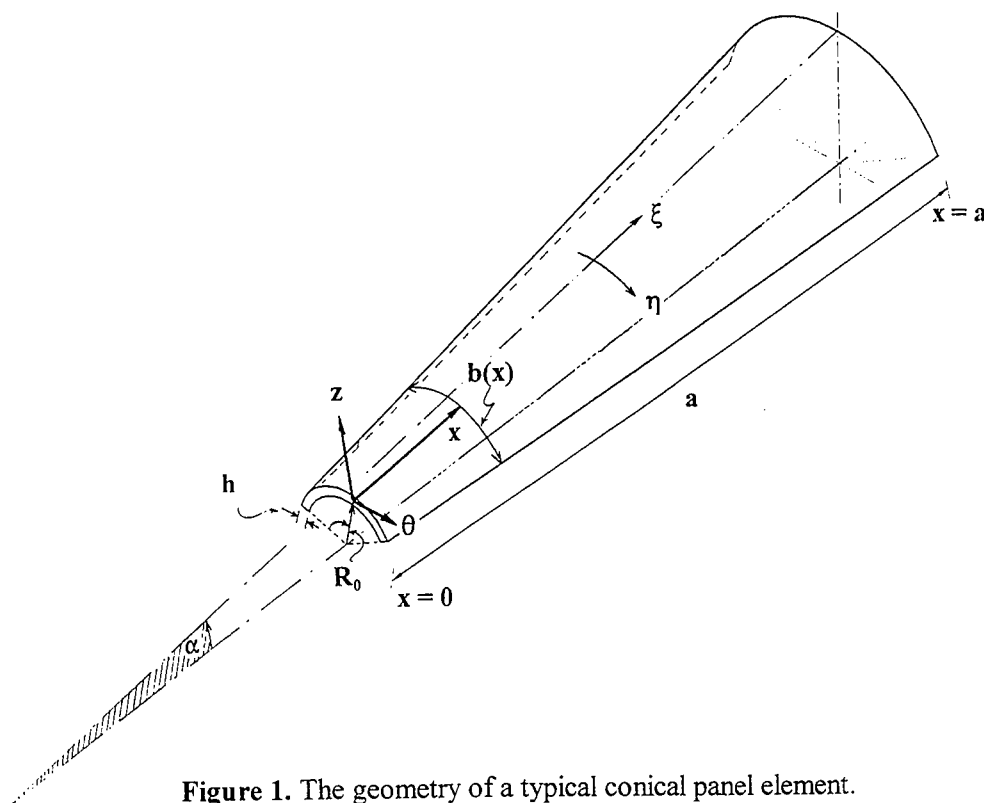
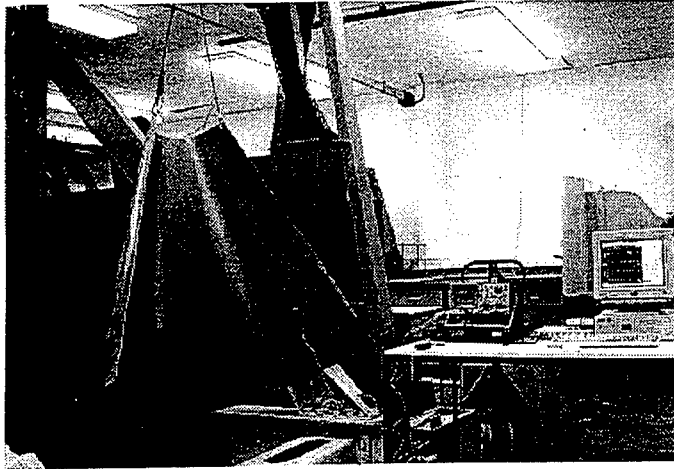


Figure 1. The geometry of a typical conical panel element.

Figure 2. The experimental arrangement.

(a) General view, illustrating the suspension of the test specimens.



(b) Block diagram of the data acquisition equipment.

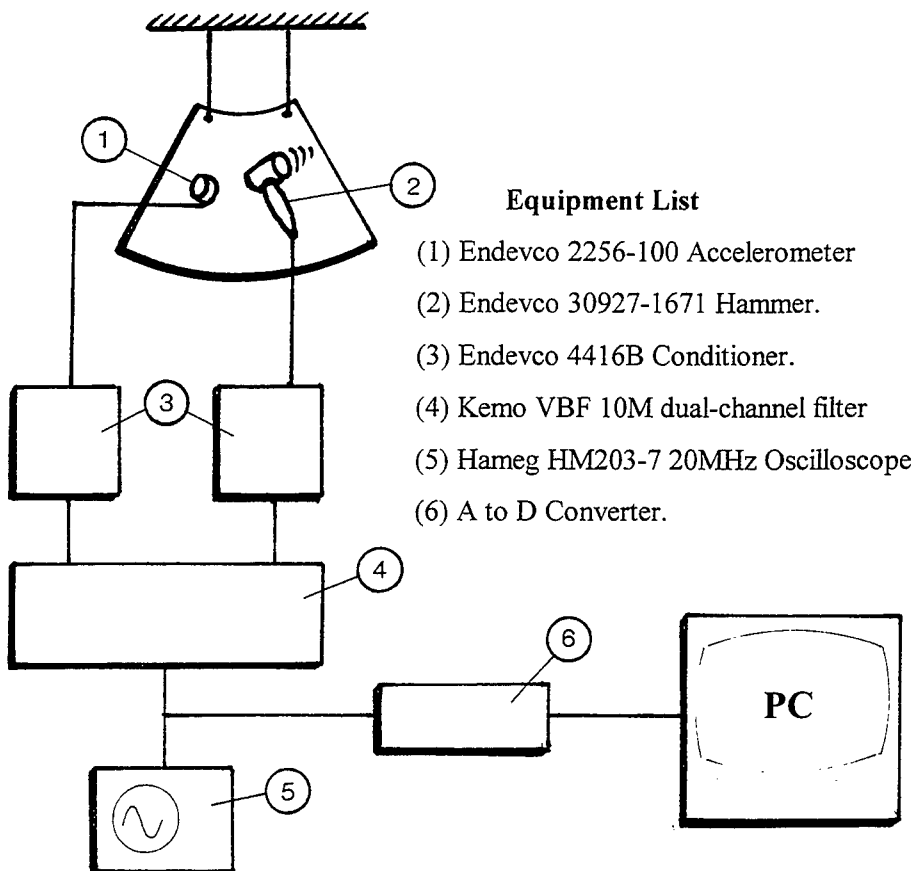
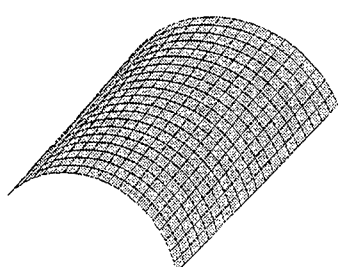
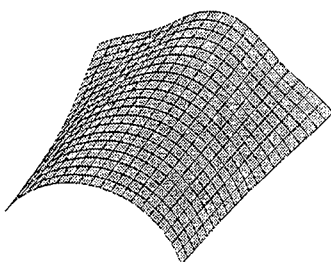


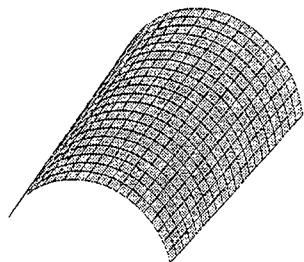
Figure 3. The first ten elastic modes of Cone # 1.



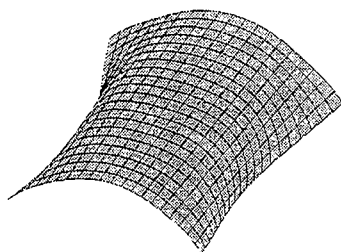
Mode 1: $f = 7.21$ Hz



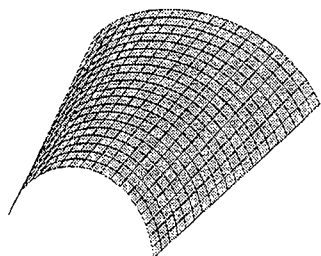
Mode 6: $f = 67.78$ Hz



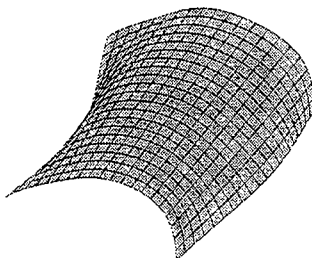
Mode 2: $f = 12.32$ Hz



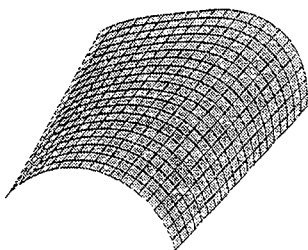
Mode 7: $f = 75.43$ Hz



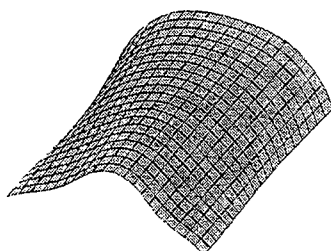
Mode 3: $f = 18.21$ Hz



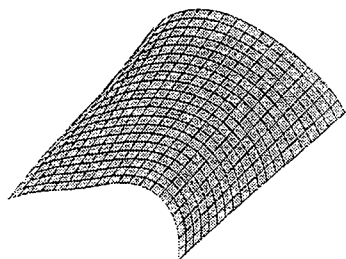
Mode 8: $f = 76.05$ Hz



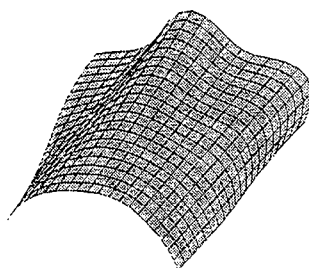
Mode 4: $f = 34.40$ Hz



Mode 9: $f = 87.80$ Hz

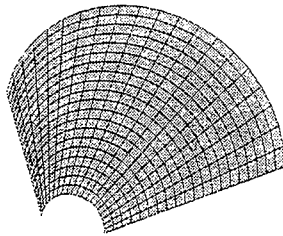


Mode 5: $f = 44.32$ Hz

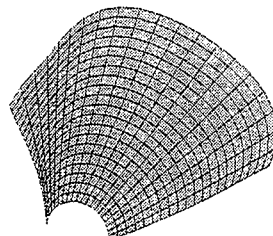


Mode 10: $f = 113.65$ Hz

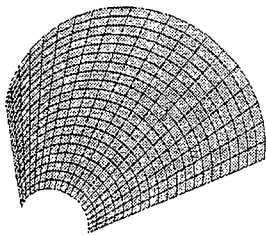
Figure 4. The first ten elastic modes of Cone # 2.



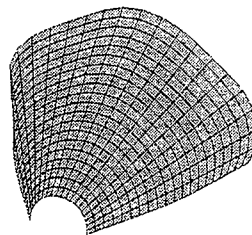
Mode 1: $f = 4.65$ Hz



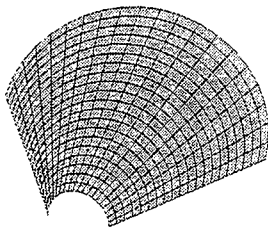
Mode 6: $f = 33.06$ Hz



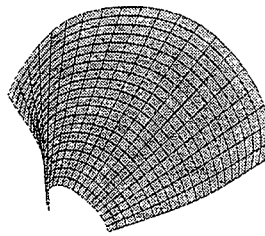
Mode 2: $f = 8.75$ Hz



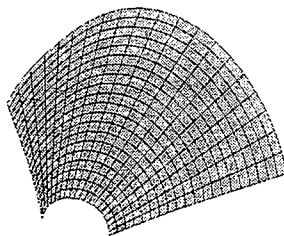
Mode 7: $f = 47.83$ Hz



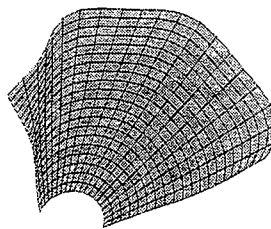
Mode 3: $f = 11.32$ Hz



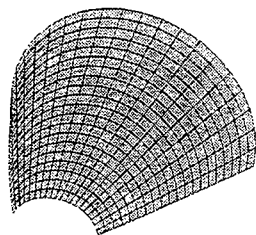
Mode 8: $f = 47.87$ Hz



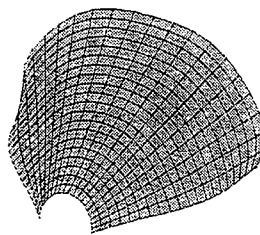
Mode 4: $f = 20.85$ Hz



Mode 9: $f = 64.51$ Hz



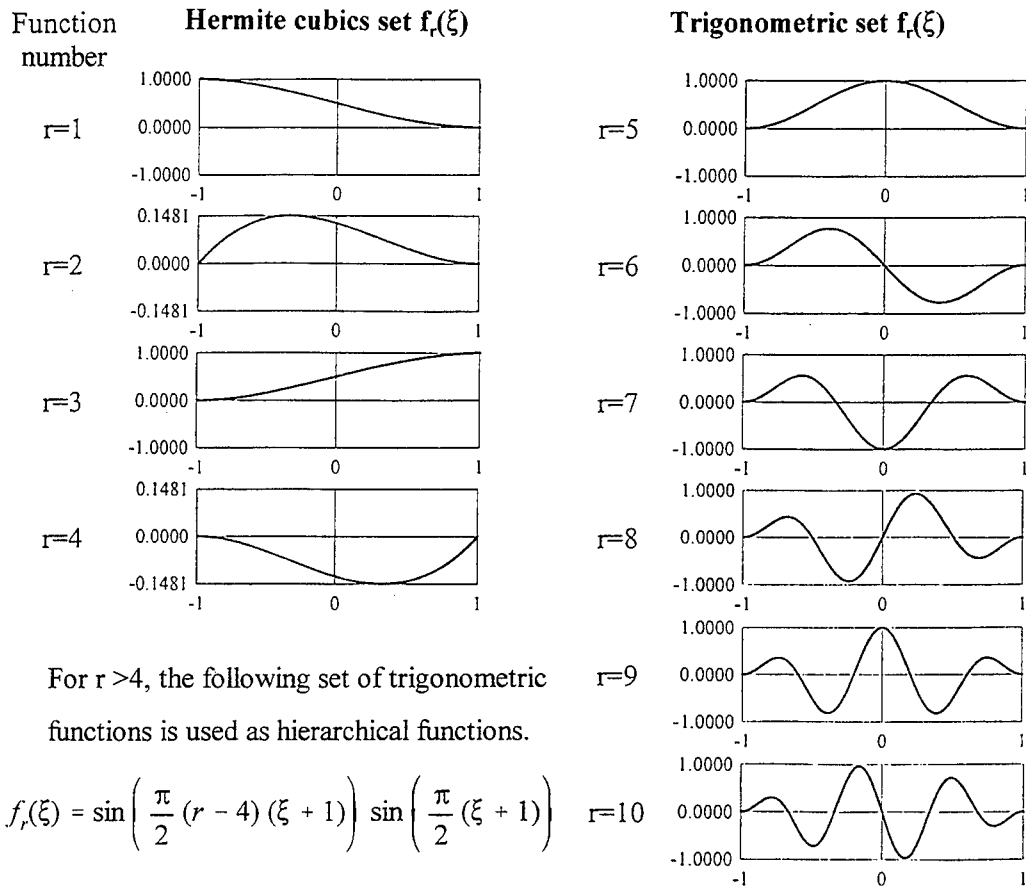
Mode 5: $f = 22.63$ Hz



Mode 10: $f = 70.95$ Hz

TABLE 1

The first ten assumed displacement functions.



For $r > 4$, the following set of trigonometric functions is used as hierarchical functions.

$$f_r(\xi) = \sin\left(\frac{\pi}{2}(r-4)(\xi+1)\right) \sin\left(\frac{\pi}{2}(\xi+1)\right)$$

TABLE 2

Convergence study based on three different mesh designs.
The first ten F-F-F-F frequencies of Cone # 1.

h	1		4		9		400
p	8	16	3	6	2	4	0
f_1 (Hz)	7.25	7.21	7.27	7.22	7.24	7.21	7.22
f_2 (Hz)	12.70	12.32	12.80	12.36	12.53	12.34	12.30
f_3 (Hz)	18.59	18.21	18.73	18.25	18.45	18.23	18.21
f_4 (Hz)	34.49	34.40	35.94	34.67	35.59	34.64	34.42
f_5 (Hz)	44.48	44.32	46.12	44.60	45.66	44.57	44.35
f_6 (Hz)	68.22	67.78	72.57	68.46	69.93	68.22	67.78
f_7 (Hz)	76.41	75.43	77.34	75.70	76.65	75.61	75.30
f_8 (Hz)	76.61	76.05	78.09	76.22	77.00	76.18	75.98
f_9 (Hz)	88.32	87.80	93.80	88.51	90.18	88.27	87.76
f_{10} (Hz)	114.13	113.65	115.70	113.97	118.62	114.58	113.53
MO	432	1200	456	1008	644	1280	2646

TABLE 3

The first ten F-F-F-F frequencies of both cones

	$h-p$		ANSYS		Experiment	
	Cone #1	Cone #2	Cone #1	Cone #2	Cone #1	Cone #2
f_1 (Hz)	7.21	4.65	7.22	4.31	7.5	4.5
f_2 (Hz)	12.32	8.75	12.30	8.58	12.7	8.9
f_3 (Hz)	18.21	11.32	18.21	11.28	18.2	11.5
f_4 (Hz)	34.40	20.85	34.44	20.63	35.6	20.9
f_5 (Hz)	44.32	22.63	44.36	21.92	46.0	21.7
f_6 (Hz)	67.78	33.06	67.81	32.71	59.5	33.2
f_7 (Hz)	75.43	47.83	75.31	46.68	70.4	46.6
f_8 (Hz)	76.05	47.87	75.98	47.20	73.1	47.4
f_9 (Hz)	87.80	64.51	87.76	63.16	90.4	58.6
f_{10} (Hz)	113.65	70.95	113.57	66.46	N/A	63.7

* For Cones # 1 and 2: $h = 1$ and $p = 16$ giving a total $MO = 1200$.

VIBRATION ANALYSIS OF CIRCUMFERENTIALLY NON-UNIFORM CYLINDRICAL SHELLS SUBJECTED TO A FLOWING FLUID

A.A. LAKIS

A. SELMANE

Department of Mechanical Eng.
École Polytechnique de Montréal
Université de Montréal
C.P. 6079, Succ. Centre-ville,
Montréal, Québec, Canada H3C 3A7

Structures, Materials and Propulsion
Laboratory
Institute for Aerospace Research
National Research Council of Canada
Ottawa, Ontario, Canada K1A 0R6

ABSTRACT

A method is presented for the determination of the effects of a flowing fluid on the vibration characteristics of non uniform cylindrical shells containing flowing fluid. The case of an empty or liquid filled shell is also investigated. The structure may be uniform or non uniform in the circumferential direction. The formulation used is a combination of finite element method and classical shell theory. The displacement functions are derived from exact solutions of Sanders' shell equations. The velocity potential and Bernoulli's equation for a liquid finite element yield an expression for fluid pressure as a function of the nodal displacements of the element and three forces (inertial, centrifugal and Coriolis) of the moving fluid. An analytical integration of the fluid pressure over the liquid element leads to three components: mass, stiffness and damping matrices. Calculations are given to illustrate the dynamic behaviour of uniform and distorted cylindrical shells subjected to a flowing fluid and shells filled with liquid.

1. INTRODUCTION

Knowledge of the vibration characteristics of fluid-filled cylindrical shells is of considerable practical interest, since cylindrical shells are commonly used to contain or convey fluids. There are many ways in which the presence of the fluid may influence the dynamics of the structure. If the structure contains a stationary gas at low pressure, then the vibration of the shell differs only slightly from that of the same shell in vacuo. If the fluid is compressible, the compressibility of the fluid alters the effective stiffness of the system. Also, if the density of the fluid is relatively high, as in the case of a liquid, then the fluid exerts considerable inertial loading on the shell, and this results in a significant lowering of the resonant frequencies. Other effects of coupled fluid-shell motions occur when the fluid is flowing. Depending upon the boundary conditions, if the flow velocities are high, buckling or oscillatory flexural instabilities are possible.

The dynamics of coupled fluid-shells were reviewed extensively by Brown [1], Au-Yang [2], Paidoussis & Li [3] and others (Mistry & Menenzes [4]; Cheng [5]; Han & Liu [6]; Brenneman & Au-Yang [7] and Goncalves & Batista [8]). There have been few analyses of closed cylindrical shells having axially or circumferentially varying thickness, subjected to an internal or external flow.

The purpose of this study is to present a method for the dynamic analysis of thin, orthotropic circumferentially non-uniform cylindrical shells containing flowing fluid (Figure 1). The case of an empty or liquid filled shell is also investigated. The structure may be uniform or non-uniform in the circumferential direction and we consider the problem of cylindrical shells simply-supported at both ends ($V=W=0$). The method is a hybrid of finite element method, classical shell theories and fluid theories. The structure is subdivided into cylindrical panel segment finite elements. The displacement functions are derived from exact solutions of Sanders' shell equations [9].

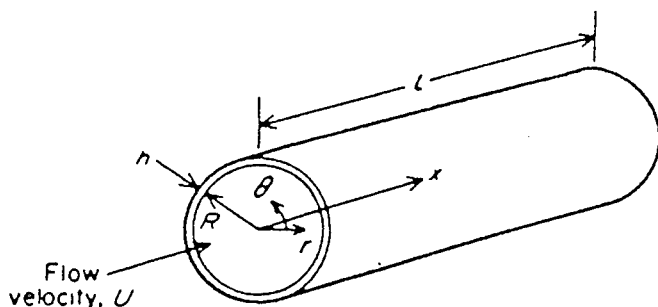


Figure 1: Cylindrical shell geometry.

In this approach, it is possible to determine the mass and stiffness matrices of the individual finite elements by exact analytical integration. Accordingly, this method is more accurate than the more usual finite element methods based on polynomial displacement functions. To account for the fluid effect on the structure, a panel finite fluid element bounded by two nodal lines was considered. By solving the equations of motion for the fluid element, an expression for fluid pressure as a function of the displacements of the element was obtained. Analytical integration for the pressure distribution along the element yielded three components: the mass, stiffness and damping matrices for a fluid element. Global matrices are, then, obtained by superimposing the individual matrices. The eigenvalue and eigenvector problem is solved by means of the equation reduction technique.

The hybrid approach (Finite element - Shell theory - Fluid theory) has been applied with satisfactory results to the dynamic linear and non-linear analysis of uniform and axially non-uniform cylindrical [10-12], conical [13] and spherical [14] shells both empty and liquid filled.

Calculations are given to illustrate the dynamic behaviour of uniform and distorted cylindrical shells subjected to a flowing fluid and shells filled with liquid. The results obtained by this method were compared with other investigations and satisfactory agreement was obtained. This method combines the advantages of finite element analysis which deals with complex shells, and the precision of formulation which the use of displacement functions derived from shell and fluid theories contributes. This method enables us to predict the vibratory characteristics of circumferentially non-uniform open or closed cylindrical shells subjected to a flowing fluid. In addition, this theory may be applied to a curved plate subjected to a flowing fluid in the case of large values of a shell's radius.

2. DETERMINATION OF THE DISPLACEMENT FUNCTIONS

Sanders' [9] equations for thin, cylindrical shells, in terms of axial, tangential and radial displacements (U , V , W) of the mean surface of the shell and in terms of element P_{ij} of the orthotropic matrix of elasticity $[P]$ are:

$$L_k (U, V, W, P_{ij}) = 0 \quad k=1 \text{ to } 3 \quad (1)$$

where L_k ($k = 1, 2, 3$) are three linear differential operators, the form of which is fully in [15].

The finite element used is shown in Figure 2. It is a cylindrical panel segment defined by two line nodes i and j . Each node has four degrees of

freedom: three displacements (axial, circumferential and radial) and one rotation. The shells are assumed to be simply-supported ($V=W=0$) at both curved ends.

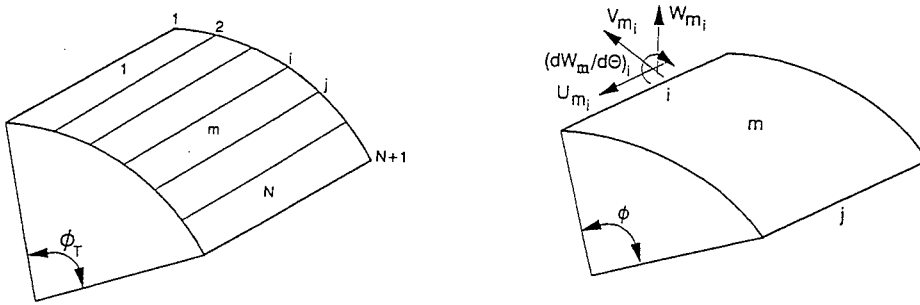


Figure 2: Nodal displacements at node i.

The displacement functions can be expressed as:

$$U(x, \theta) = A e^{\eta \theta} \cos m \pi x/L, \quad V(x, \theta) = B e^{\eta \theta} \sin m \pi x/L \quad (2)$$

and $W(x, \theta) = C e^{\eta \theta} \sin m \pi x/L$

where m is the axial mode, and η is a complex number.

Substituting (2) into equations of motion (1), a system of three homogeneous linear functions of constants A , B and C are obtained. For the solution to be non-trivial, the determinant of this system must be equal to zero. This brings us to the following characteristic equation [15]:

$$h_8 \eta^8 + h_6 \eta^6 + h_4 \eta^4 + h_2 \eta^2 + h_0 = 0 \quad (3)$$

Each root of this equation yields a solution to the linear equations of motion (1). The complete solution is obtained by adding the eight solutions independently with the constants A_p , B_p and C_p ($p = 1, \dots, 8$). The constants A_p , B_p and C_p are not independent. We can therefore express A_p and B_p as a function of C_p , for example:

$$A_p = \alpha_p C_p \quad \text{and} \quad B_p = \beta_p C_p, \quad p = 1, \dots, 8 \quad (4)$$

4. BEHAVIOUR OF THE FLUID-SHELL INTERACTION

The dynamic behaviour of shell subjected to a pressure field can be represented by the following system:

$$[[M_s] - [M_f]] \{\ddot{\delta}\} - [C_f] \{\dot{\delta}\} + [[K_s] - [K_f]] \{\delta\} = \{F\} \quad (8)$$

where $\{\delta\}$ is the displacement vector, $[M_s]$ and $[K_s]$ are, respectively, the mass and stiffness matrices of the system in vacuo; $[M_f]$ and $[C_f]$ and $[K_f]$ represent the inertial, Coriolis and centrifugal forces of the liquid flow and $\{F\}$ represents the external forces.

We assume here that the structure is subjected only to potential flow which induces inertial, Coriolis and centrifugal forces to participate in the vibration pattern. These forces are coupled with the elastic deformation of the shell. The mathematical model which is developed is based on the following hypothesis: (i) the fluid flow is potential; (ii) vibration is linear; (iii) since the flow is inviscid, there is no shear and the fluid pressure is purely normal to the shell wall; (iv) the fluid mean velocity distribution is assumed to be constant across a shell section and (v) the fluid is incompressible.

With these assumptions, the velocity potential must satisfy the Laplace equation. This relation is expressed in the cylindrical coordinate system by:

$$\nabla^2 \Phi = \frac{1}{r} \frac{\partial}{\partial r} \left(r \frac{\partial \Phi}{\partial r} \right) + \frac{1}{r^2} \frac{\partial^2 \Phi}{\partial \theta^2} + \frac{\partial^2 \Phi}{\partial x^2} = 0 \quad (9)$$

Φ is the potential function that represents the velocity potential.

Therefore:

$$V_x = U_x + \frac{\partial \Phi}{\partial x} ; \quad V_\theta = \frac{1}{R} \frac{\partial \Phi}{\partial \theta} ; \quad V_r = \frac{\partial \Phi}{\partial r} \quad (10)$$

where U_x is the mean velocity along the shell in the x-direction. The remaining components of velocity are disturbance or perturbation velocity components; V_x , V_θ and V_r are respectively the axial, tangential and radial components of the fluid velocity.

The Bernouilli equation is given by:

$$\frac{\partial \Phi}{\partial t} + \frac{1}{2} V^2 + \frac{P}{\rho_f} \Big|_{r=\xi} = 0 \quad (11)$$

Introducing equation (10) into equation (11) and taking into account only the linear terms, we find the dynamic pressure P :

$$P_u = \rho_{fu} \left\{ \frac{\partial \Phi_u}{\partial t} + U_{xu} \frac{\partial \Phi_u}{\partial x} \right\} \Big|_{r=\xi} \quad (12)$$

where u subscript represents internal or external fluid as the case may be.

A full definition of the flow requires that a condition be applied to the structure-fluid interface. The impermeability condition ensures contact between the shell and the fluid. This should be:

$$V_r \Big|_{r=R} = \frac{\partial \Phi}{\partial r} \Big|_{r=R} = \left(\frac{\partial W}{\partial t} + U_x \frac{\partial W}{\partial x} + \frac{U_x^2}{2} \frac{\partial^2 W}{\partial x^2} \right) \Big|_{r=R} \quad (13)$$

From the theory of shells (equation 6), we have:

$$W(x, \theta, t) = \sum_{j=1}^8 C_j e^{\eta_j \theta} \sin \frac{m\pi x}{L} e^{i\omega t} \quad (14)$$

Using these equations, we obtain the equation for the pressure on the wall as follows:

$$P_u = -\rho_u \sum_{j=1}^8 Z_{uj} \left(\frac{im\pi R_u}{L} \right) \left[\ddot{W}_j + 2U_{xu} \dot{W}_j + \frac{U_{xu}^2}{2} \dot{W}_j + U_{xu}^2 W_j + \frac{U_{xu}^3}{2} W_j \right] \quad (15)$$

where (\cdot) and $(\dot{})$ represent $\frac{\partial()}{\partial t}$ and $\frac{\partial()}{\partial x}$ respectively, and

$$Z_{uj} \left(\frac{im\pi R_u}{L} \right) = \frac{R_u}{in_j - \frac{im\pi R_u}{L} \frac{BES_{in_j+1}(im\pi R_u/L)}{BES_{in_j}(im\pi R_u/L)}} \quad (16)$$

where η_j ($j = 1, \dots, 8$) are the roots of the characteristic equation (3) of the empty shell; $BES_{in_j} = J_{in_j}$ for internal flow and $BES_{in_j} = Y_{in_j}$ for external flow; J_{in_j} and Y_{in_j} are, respectively, the Bessel functions of the first and second kind of order " in_j "; m is the axial mode number; R is the mean radius of the shell; L its length; the subscript " u " is equal to " i " for internal flow and is equal to " e " for external flow.

By introducing the displacement function (14), into the dynamic pressure expression (15) and performing the matrix operation required by the finite element method, the mass, damping and stiffness matrices for fluid are obtained by evaluating the following integral:

$$\int_A [N]^T \{P_u\} dA \quad (17)$$

we obtain

$$\begin{aligned} [m_f] &= [A^{-1}]^T [S_f] [A^{-1}] \\ [c_f] &= [A^{-1}]^T [D_f] [A^{-1}] \\ [k_f] &= [A^{-1}]^T [G_f] [A^{-1}] \end{aligned} \quad (18)$$

The matrix $[A]$ is determined from equation (6) and given in reference [7], the elements of $[S_f]$, $[D_f]$ and $[G_f]$ are given, as follows.

$$S_f(r, s) = -\frac{RL}{2} I_{rs} (\rho_i Z_{is} - \rho_e Z_{es}) \quad (19)$$

$$D_f(r, s) = \frac{Rm^2 \pi^2}{4L} I_{rs} (\rho_i U_{xi}^2 Z_{is} - \rho_e U_{xe}^2 Z_{es}) \quad (20)$$

$$G_f(r, s) = \frac{R m^2 \pi^2}{2L} I_{rs} (\rho_i U_{xi}^2 Z_{is} - \rho_e U_{xe}^2 Z_{es}) \quad (21)$$

where $r, s = 1, \dots, 8$; ρ is the density of the fluid; U_x is the velocity of the fluid; Z is defined by relations (16); the subscript "i" means internal flow and "e" means external flow and I_{rs} is defined by :

$$\begin{cases} I_{rs} = \frac{1}{(\eta_r + \eta_s)} [e^{(\eta_r + \eta_s)\phi} - 1] & \text{for } \eta_r + \eta_s \neq 0 \\ I_{rs} = \phi & \text{for } \eta_r + \eta_s = 0 \end{cases} \quad (22)$$

where $r, s = 1, \dots, 8$; η is the root of the characteristic equation of the empty shell and ϕ is the angle for one finite element.

Finally, the global matrices $[M_f]$, $[C_f]$ and $[K_f]$ may be obtained, respectively, by superimposing the mass $[m_f]$, damping $[c_f]$ and stiffness $[k_f]$ matrices for each individual fluid finite element.

5. CALCULATIONS AND DISCUSSION

We present here some calculations to test the method in the case of liquid-filled cylindrical shells. In the case when the shell is subjected to flowing fluid, the dynamic stability of this type of problem is analysed. The number of finite elements used to model the shells is equal to 20.

5.1 Convergence of the method

A first set of calculations was undertaken to determine the required number of finite elements for a precise determination of natural frequencies. Calculations were made for the same closed cylindrical shell completely filled with internal fluid for the number of finite elements $N = 2, 4, 6, 8, 10, 15$ and 20 . This steel shell is simply supported at both ends and has the following data:

$R = 37.7\text{mm}$, $h = 0.229\text{mm}$, $L = 234\text{mm}$, $\nu = 0.29$ and $\rho_i / \rho_s = 0.128$.

The results for $m = 1$ and for $n = 2, 3, 4, 5$ and 6 are shown in Figure 3. We observe that the convergence of the shell-fluid system is very fast and demands few elements for both the low and the high modes.

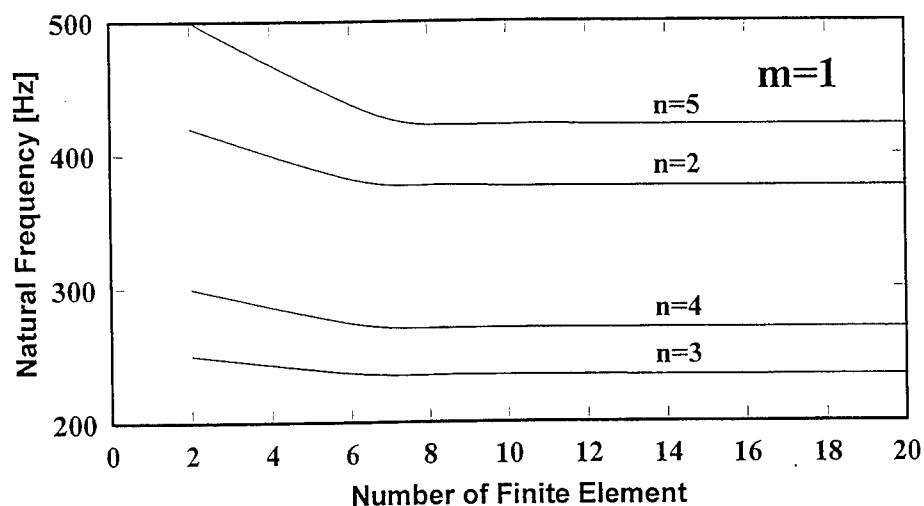


Figure 3: Linear natural frequency for a simply-supported cylindrical shell completely filled with internal fluid as a function of the number of finite elements.

5.2 Free vibration of uniform cylindrical shells filled with liquid

A calculations were made for a uniform steel cylindrical shell simply supported at both ends, empty or filled with liquid. The pertinent data are as follows: $R=37.7\text{mm}$, $h=0.229\text{mm}$, $L=234\text{mm}$, $\nu=0.29$ and $\rho_i/\rho_s = 0.128$. The effects of the inertial force were calculated by this theory assuming $U_x = 0$ in equations (19) to (21). Table 1 shows some frequencies computed by the present method and compared with experimental results [16] in the case of cylindrical shell both empty and completely filled with liquid. As may be seen the results obtained by the present method agree with experimental results. The difference between our method and the experimental results of Lindholm et al. [16] is between 0.5% and 10% for the first two axial modes.

Table 1. Natural Frequencies (Hz) of a simply-supported cylindrical shell, both when empty and when completely filled with liquid.

(m, n)	Empty		Full (inside fluid)	
	Present Method	Experimental [16]	Present Method	Experimental [16]
(1,2)	1133	1150	376	375
(1,3)	629	640	234	250
(1,4)	655	688	270	300
(1,5)	942	995	422	430
(1,6)	1353	1430	651	680
(1,7)	1853	1938	940	970
(2,3)	2067	2070	784	813
(2,4)	1368	1430	568	600
(2,5)	1248	1313	561	625
(2,6)	1489	1570	714	755
(2,7)	1927	2050	978	1000

5.3 Dynamic stability of uniform cylindrical shells subjected to a flowing fluid

When the fluid is flowing, the shell will be subjected to centrifugal, Coriolis and inertia forces. A simply-supported shell with the following characteristics ($L/R = 2$, $t/R = 0.01$, $\rho_i/\rho_s = 0.128$, $n = 5$) has been analysed, to see the influence of the speed of the flow U_{xi} on the frequencies (internal flow). The dimensionless parameters of frequency and velocity are:

$$\bar{\omega} = \omega/\omega_0 \text{ and } \bar{U} = U/U_0,$$

where:

$$\omega_0 = \frac{\pi^2}{L^2} (K/\rho_s t)^{1/2}, \quad U_0 = \frac{\pi^2}{L} (K/\rho_s t)^{1/2}, \quad K = \frac{Et^3}{12(1-\nu^2)}$$

ω and U are respectively the natural frequency and the velocity of the flowing fluid.

The results are compared to a previous analysis by Weaver & Unny [17]

in Figure 4. We observe that the natural frequencies decrease with flow velocity. At zero flow velocity, the two methods give the same results but, as the flow velocity increases the two term Galerkin method used by Weaver & Unny [17] generates significantly different results from those of the present hybrid finite element method. This is due to the limitations associated with the use of too few terms in the application of Galerkin's method.

Our results predict that the first mode frequency becomes negative imaginary at $\bar{U} = 3.1$, indicating static divergence instability in this mode. If the velocity is increased further, the first mode reappears and coalesces at $\bar{U} = 3.95$ with that of the second mode to produce coupled mode flutter.

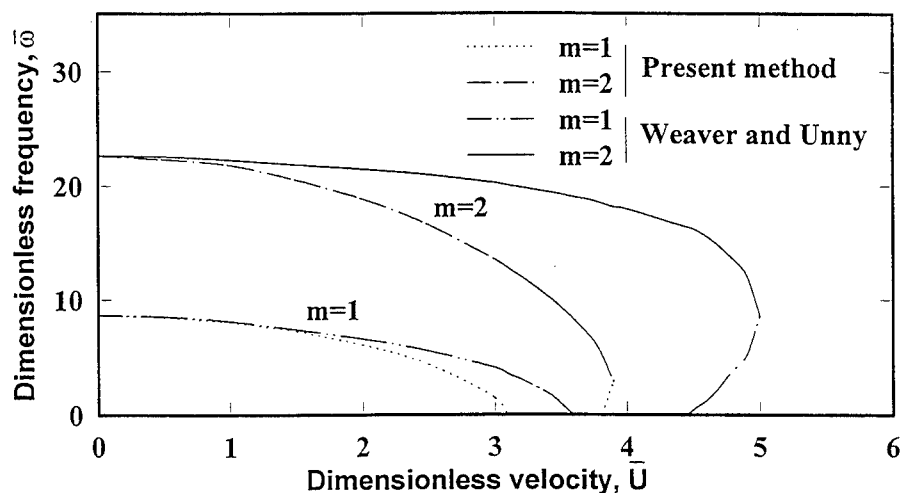


Figure 4: Stability of a simply-supported uniform cylindrical shell as a function of flow velocity (internal flow).

5.4 Calculations for shells having circumferentially varying thickness

The present method has been applied to an empty cylinder whose inner bore is circular but non-concentric with circular outer surface (Figure 5). This case was studied by Tonin & Bies [18] using the Rayleigh-Ritz method. The steel cylinder is free simply supported at both ends and the data for this analysis are as follows : $a^- = 37.83$ mm, $a^+ = 40.75$ mm, $a = 39.29$ mm, $L = 398.8$ mm, and the eccentricity e was studied for three values $e = 0, 0.5, 1$ mm. The effect of the eccentricity on the calculated natural frequencies for various modes is detailed in Table 2. Note that the effect of increasing eccentricity is to lower the frequencies of the shell.

Table 2. Variation of natural frequencies (Hz) of some modes with varying eccentricity of an empty distortion cylinder

m,n	e = 0 mm		e = 0.5 mm			e = 1 mm	
	TONIN & BIES [18]	Present method	[18]	Experimental [18]	Present method	[18]	Present method
1,2	1340	1341	1347	1330	1343	1302	1303
1,3	3553	3540	3420	3442	3410	3060	2949
1,4	6773	6758	6510	6495	6479	6177	5499
2,2	2105	2090	2071	2063	2062	1955	1954
2,3	3740	3728	3605	3627	3596	3243	3132
2,4	6905	6890	6638	6617	6607	6308	5618
3,2	3598	3568	3542	3463	3518	3302	3253
3,3	4204	4188	4083	4085	4071	3816	3743
3,4	7159	7144	6890	6861	6860	6575	5869

5.5 Dynamic stability of circumferentially non-uniform cylindrical shells subjected to a flowing fluid

A distorted cylindrical shell subjected to an internal flow has been analysed (Figure 5). The steel cylinder is free simply supported at both ends and the data for this analysis are as follows : $a^- = 37.83\text{mm}$, $a^+ = 40.75\text{mm}$, $a = 39.29\text{mm}$, $L = 398.8\text{mm}$, $\rho_f / \rho_s = 0.128$, and the eccentricity was studied for four values $e = 0, 0.5, 0.75$ and 1 mm . We present here an examination of the natural frequencies of the system as functions of the flow velocity and thereby a determination of the effect of flow on the dynamic behaviour of the system. Figure 5 shows the frequencies of the system as a function of the flow velocity for the mode ($m=1, n=2$). As the velocity increases from zero, the frequencies associated with all eccentricity decrease, they remain real (the system being conservative) until at sufficiently high velocities, they vanish, indicating the existence of buckling-type (divergence) instability. At higher flow velocity the frequencies become purely imaginary. We predict the first loss of stability for the eccentricity $e = 1\text{ mm}$, we conclude that the distortion in the cylindrical shells decrease the critical flow velocity and render the system less stable.

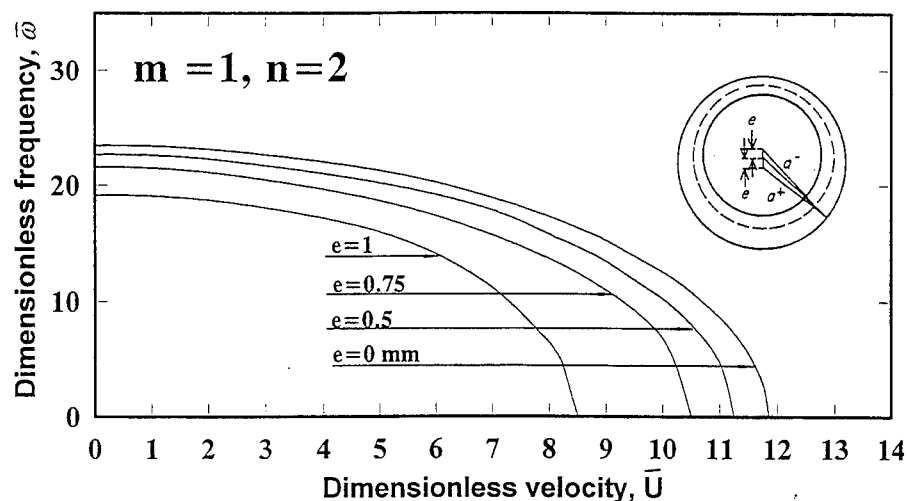


Figure 5: Stability of a simply-supported distorted cylindrical shell as a function of flow velocity (internal flow).

6. CONCLUSIONS

The method developed in this paper is used to predict the effects of inertia, Coriolis and centrifugal forces on the vibration characteristics of non-uniform cylindrical shells containing flowing fluid. The case of liquid filled shell was also investigated. A cylindrical panel finite element was developed, making possible the derivation of the displacement functions from the equations of motion of the shell. Mass and stiffness of each element were obtained by exact analytical integration. The fluid pressure was derived from the velocity potential and from the linear impermeability and dynamic conditions applied to the shell-fluid interface. The finite element method was used to obtain the mass, stiffness and damping of fluid element. The results obtained by this method were compared with other investigations and satisfactory agreement was obtained. This method combines the advantages of finite element analysis which deals with complex shells, and the precision of formulation which the use of displacement functions derived from shell and fluid theories contributes. This method enables us to predict the vibratory characteristics of circumferentially non-uniform open and closed cylindrical shells subjected to a flowing fluid. In addition, this theory may be applied to a curved plate subjected to a flowing fluid in the case of large values of a shell's radius.

7. REFERENCES

1. BROWN, S.J. (1982) "A Survey of Studies into the Hydrodynamic Response of Fluid-Coupled Circular Cylinders". J. of Pres. Vessel Tech., ASME, 104, 2-19.

2. AU-YANG, M.K. (1986) "Dynamic of Coupled Fluid-Shells". J. of Vibration, Acoustics, Stress and Reliability Design, ASME, 108, 339-347.
3. PAIDOUSSIS, M.P. & LI, G.X. (1993) "Pipes Conveying Fluid: A Model Dynamical Problem". J. of Fluids and Struc., 7, 137-204.
4. MISTRY, J. & MENENZES, J.C. (1995) "Vibration of Cylinders Partially-Filled with Liquid". J. of Vib. and Acoustics, 117, 87-93.
5. CHEN, L. (1994) "Fluid-Structural Coupling of a plate-Ended Cylindrical Shell: Vibration and Internal Sound Field". J. of S. and Vib, 174(5), 641-654.
6. HAN, R.P.S. & LIU, J.D. (1994) "Free Vibration Analysis of a Fluid-Loaded Variable Thickness Cylindrical Tank". J. of S. and Vib., 176(2), 235-253.
7. BRENNEMAN, B. & AU-YANG, M.K. (1992) "Fluid-Structure Dynamics with a Modal Hybrid Method". J. of Pres. Vessel Tech. 114, 133-138.
8. GONCALVES, P.B. & BATISTA, R.C. (1987) "Frequency Response of Cylindrical Shells Partially Submerged or Filled with liquid". J. of S. and Vib., 113(1), 59-70.
9. SANDERS, J.L. (1959). "An Improved First Approximation Theory for Thin Shells". NASA, TR-R24.
10. LAKIS, A.A. (1976). "Effects of Fluid Pressures on the Vibration Characteristics of Cylindrical Vessels". Proc. of the Int. Conf. on Pressure Surges, London, UK, J1-1,15.
11. LAKIS, A.A. & LAVEAU, A. (1991). "Non-Linear Dynamic Analysis of Anisotropic Cylindrical Shells Containing a Flowing Fluid". Int. J. Solids and Struc., 28, 1079-1094.
12. LAKIS, A.A. & SINNO, M. (1992). "Free Vibration of Axisymmetric and Beam-Like Cylindrical Shells Partially Filled with Liquid". Int. J. for Num. Methods in Eng., 33, 235-268.
13. LAKIS, A.A., VAN DYKE, P. & OURICHE, H. (1992). "Dynamic Analysis of Anisotropic Fluid-Filled Conical Shells". J. of Fluids and Struc., 6, 135-162.
14. LAKIS, A.A., TUY, N.Q. & SELMANE, A. (1989). "Analysis of Axially Non-Uniform Thin Spherical Shells". Proc. of the Int. Symposium on Structural Analysis and Optimization, Paris, France, 80-85.
15. SELMANE, A. & LAKIS, A.A. (1995). "Dynamic Analysis of Anisotropic Open Cylindrical Shell". Technical Report, No. EPM/RT-95/10, École Polytechnique de Montréal, Canada.
16. LINDHOLM, U.S., KANA, D.D. & ABRAMSON, H.N. (1962). "Breathing Vibrations of a Circular Cylindrical Shell With an Internal Liquid". J. of Aeronautical Science, 29, 1052-1059.
17. WEAVER, D.S. & UNNY, T.E. (1973). "On the Dynamic Stability of Fluid Conveying Pipes". J. of Applied Mech., ASME, 40, 48-52.
18. TONIN, R.F. & BIES, D.A. (1979). "Free Vibration of Circular Cylinders of Variable Thickness". J. of S. and Vib., 62(2), 165-180.

DYNAMIC ANALYSIS OF ONE- AND TWO-DIMENSIONAL STRUCTURES USING SPECTRAL ELEMENT METHOD

Usik Lee and Joonkeun Lee

Department of Mechanical Engineering, Inha University
253 Yonghyun-Dong, Nam-Ku, Incheon 402-751, Korea

INTRODUCTION

Structural dynamics has become an important research subject in engineering during last decades. Accordingly, many structural analysis methods exists. Finite element method (FEM) is certainly one of the most popularly used methods. However, it is well known, in FEM, that sufficiently large number of finite elements must be used so as to obtain reliable dynamic responses of a structure, especially at high frequency. Furthermore, the modal analysis, usually used in combination with FEM, is limited to the frequency regimes where relative spacing of natural frequencies remains large compared to the relative parameter uncertainty [1]. Thus, alternatives to modal analysis of linear structural dynamics, applicable to the high frequency regime, have been considered by many researchers including acousticians [2].

Since the vibration mode can be considered as a standing wave [3], the dynamic response of a structure can be derived by utilizing the wave solutions. In the literature, there have been continuing efforts to efficiently utilize the FFT and inverse FFT algorithms in solving the dynamic equations of discrete systems [4]. This spectral approach is known as the spectral analysis method (SAM). However, Doyle [5] is certainly the first to apply this SAM to the dynamic analysis of structures by summing up the spectral components of wave solutions in frequency domain. To apply this SAM to the multiply connected structures, he introduced the concept of spectrally formulated finite element (simply, spectral element). Since the spectral element of a structure is formulated directly from the wave solutions of the structure by treating the mass distribution exactly (in contrast to the finite element in FEM derived from a discretized structural model), the wave characteristics within an structural element is treated exactly as far as the structural model is valid in the frequency regime. The spectral elements can also be assembled in a completely analogous way to that used for the conventional finite elements in FEM. Thus, combining these distinctive characteristics of SAM and FEM introduces so called the spectral elem-

ent method (SEM) [6]. The applications of SEM to the structural dynamics problems can be found in recent papers by Gopalakrishnan *et al.* [7], for the multiply connected Timoshenko beam, and Horr and Schmidt [8], for the plane truss structures.

However, most of researches on the SEM applications have been confined to only one-dimensional uniform (or homogeneous) structures which are subject to *concentrated* dynamic loads. But, in many cases, a structure may be subject to *distributed* dynamic loads and, besides, it might be a two-dimensional structure rather than one-dimensional. Lee and Lee [9] is the first to modify the conventional SEM and to apply it to the problems with distributed dynamic loads. Unfortunately, this modified SEM (mSEM) was confined to the one-dimensional structures, *i.e.*, beams. Even though Danial and Doyle [10] recently considered a SAM approach to a semi-infinite plate problem, they didn't develop a SEM-like technique applicable to the plates with finite dimensions. This was probably because the wave dispersive relation for a finite plate, with two distinct wave numbers, is more complex than that for a beam, and thus this might require a special technique to extend the conventional SEM application to finite plates. Therefore, the purposes of this paper are: 1) to introduce the mSEM for a finite beam [9]; (2) to develop a new SEM algorithm for a finite plate subject to distributed dynamic loads; and 3) to verify the present mSEM through some numerical examples.

ONE-DIMENSIONAL (BEAM) STRUCTURES

In this section, a modified SEM (mSEM) for a beam will be briefly introduced. As the importance of spectral analysis technique is usually emphasized at high frequency regimes, a higher order structural beam model, which is valid at the high frequency regimes, may be recommended for the discussions in the following. However, a simple beam model (Bernoulli-Euler beam) will be considered as an example without loss of generality, because the mSEM introduced herein can be readily applied to any higher order beam models.

Spectral element matrix, which is also known as the dynamic structural stiffness matrix, can be formulated from the relation between the nodal (spectral) forces and nodal (spectral) displacements in a (finite) spectral element. The formulation begins with the equations of motion of the beam without neglecting inertia. The equation of motion for a Bernoulli-Euler beam is given as

$$EI \frac{\partial^4 w}{\partial x^4} + m \frac{\partial^2 w}{\partial t^2} = f(x, t) \quad (1)$$

where $w(x, t)$ is the transverse deflection, $f(x, t)$ the external loading, and m is the mass density per unit length of beam. The solution of Eq. (1) is assumed to have the spectral representation [6] as:

$$w(x, t) = \sum_n \bar{w}_n(x, \omega_n) e^{i\omega_n t} \quad (2)$$

where \bar{w}_n are the spatially dependent Fourier coefficients, often called the spectral displacement components. Through this paper, the overbar, as appeared in Eq.(2), will indicate the spectral components of a quantity. For shorthand, the summation and subscripts are omitted in the following since they will often be understood. Using the dispersive relation, which relates frequency (ω) to wave number (k), the spectral displacement can be shown to have the simple solution as

$$\bar{w}(x) = Ae^{-ikx} + Be^{-kx} + Ce^{ikx} + De^{kx} = [q(k; x)] \{A \ B \ C \ D\}^T \quad (3)$$

where $[q(k; x)]$ is the 1×4 matrix, and A, B, C, D are unknown coefficients to be determined so as to satisfy boundary conditions.

Using the spectral displacement of Eq. (3), the spectral nodal displacements (\bar{w}), slopes (\bar{w}'), transverse shear forces (\bar{V}), and bending moments (\bar{M}) at two end nodes ($x = 0$ and $x = l$) of a spectral beam element having length l can be represented in the forms as:

$$\{\bar{w}_0 \ \bar{w}'_0 \ \bar{w}_l \ \bar{w}'_l\}^T = [a(k)] \{A \ B \ C \ D\}^T \quad (4)$$

$$\{\bar{V}_0 \ \bar{M}_0 \ \bar{V}_l \ \bar{M}_l\}^T = [b(k)] [A \ B \ C \ D]^T \quad (5)$$

where $[a(k)]$ and $[b(k)]$ are the 4×4 matrices. Eliminating the four coefficients from Eqs. (4) and (5), the spectral nodal forces and moments can be expressed in terms of spectral nodal degrees of freedom (DOFs) (*i.e.*, displacements and slopes) in the form of

$$\{\bar{V}_0 \ \bar{M}_0 \ \bar{V}_l \ \bar{M}_l\} = [s(k)] \{\bar{w}_0 \ \bar{w}'_0 \ \bar{w}_l \ \bar{w}'_l\}^T \quad (6)$$

In Eq.(6), $[s(k)] = [b(k)][a(k)]^T$ is known as the spectral element matrix of Bernoulli-Euler beam. The spectral elements can be assembled in a completely analogous way to that used for the finite elements in FEM. Assembling all spectral elements and then applying boundary conditions, a condensed global spectral matrix equation can be derived as

$$\{\bar{W}\} = [S(k)]^{-1} \{\bar{F}\} \quad (7)$$

where $[S(k)]$ is the condensed global spectral element matrix, $\{\bar{W}\}$ the

condensed global spectral nodal DOFs vector, and $\{\bar{F}\}$ is the condensed global spectral forces vector.

Since the conventional SEM [6] can be applied only to the one-dimensional structures under concentrated dynamic loads, a modified SEM will be introduced in the following for one-dimensional (beam) structures subject to distributed dynamic loads, based on linear superposition principle. As shown in Fig. 1, a distributed dynamic load can be considered as the linear superposition of n equivalent dynamic point loads. Then, the dynamic response (measured at x) can be obtained by superposing all dynamic responses (measured at x) due to each equivalent point loads. First, the dynamic response due to an equivalent point load $p(\xi, t) = f(\xi, t)\Delta\xi$, acting at $x = \xi$ during the time interval $0 \leq \tau \leq t$, can be expressed in the form of convolution integral as :

$$\Delta w(x; \xi, t) = \int_0^t r(x; \xi, t - \tau) p(\xi, \tau) d\tau \quad (8)$$

where $r(x; \xi, t)$ is the unit impulse response function. In frequency domain, Eq. (8) can be represented as a simple multiplication of unit impulse frequency response function, $R(x; \xi, \omega)$, and the Fourier transformed concentrated load, $P(\xi, \omega)$. That is

$$\Delta \bar{w}(x; \xi, \omega) = R(x; \xi, \omega) P(\xi, \omega) \quad (9)$$

Since a concentrated dynamic load, $p(\xi, \tau)$, acting at a point $x = \xi$ always divides the beam into two separate beam elements, as shown in Fig.1(b), it can be considered as the problem with two spectral elements with a concentrated load at the connection node. By assembling two spectral elements and then by applying proper boundary conditions to the result, a spectral element matrix equation, in the form of Eq. (9), can be obtained. In this case, the condensed global spectral element matrix is 4×4 , and the condensed global spectral nodal DOFs and forces vectors are all 1×4 . The spectral displacement at x due to a concentrated dynamic load is then obtained, by eliminating four coefficients in Eq. (3) with help of Eq. (4), from

$$\Delta \bar{w}(x) = [q(x; k)][a(k)]^{-1} \{ \Delta \bar{w}_0 \quad \Delta \bar{w}'_0 \quad \Delta \bar{w}_l \quad \Delta \bar{w}'_l \}^T \quad (10)$$

The incremental spectral nodal DOFs in Eq.(10) can be expressed in terms of incremental condensed global spectral nodal DOFs, $\{\Delta \bar{W}\}$ calculated from Eq.(8), by introducing a matrix $[c]$, in the form as

$$\{ \Delta \bar{w}_0 \quad \Delta \bar{w}'_0 \quad \Delta \bar{w}_l \quad \Delta \bar{w}'_l \}^T = [c] \{ \Delta \bar{W} \} \quad (11)$$

The matrix $[c]$ is the four by four constant matrix determined depending on the location of dynamic response measurement (that is, if it is a point on the left spectral element or on the right spectral element). Combining Eqs.(7), (10) and (11) results in

$$\Delta \bar{w}(x) = [q(x; k)][a(k)]^{-1} [c][S(k)]^{-1} \{\bar{F}\} \quad (12)$$

The condensed global spectral forces vector $\{\bar{F}\}$ in Eq. (12) can be rewritten in the form of

$$\{\bar{F}\} = \{d\} F(\xi, \omega) \Delta \xi \quad (13)$$

where $\{d\}$ is the one by four vector with only one unit element which is corresponding to the concentrated dynamic load. Now, substituting Eq. (13) into Eq. (12) yields

$$\Delta \bar{w}(x) = [q][a]^{-1} [c][S]^{-1} \{d\} F(\xi, \omega) \Delta \xi \quad (14)$$

From Eqs. (9) and (14), the unit impulse frequency response function, $R(x; \xi, \omega)$, and the concentrated load, $P(\xi, \omega)$, are found to be

$$\begin{aligned} R(x; \xi, \omega) &= [q][a]^{-1} [c][S]^{-1} \{d\} \\ P(\xi, \omega) &= F(\xi, \omega) \Delta \xi \end{aligned} \quad (15)$$

Since Eq.(10), combined with Eq.(14), gives the dynamic response due to a concentrated dynamic load acting at $x = \xi$, the total dynamic response due to the load distributed over the region $a \leq \xi \leq b$, as shown in Fig. 1(a), can be obtained from

$$\bar{w}(x; \omega) = \int_a^b \Delta \bar{w}(x; \xi, \omega) d\xi \quad (16)$$

The integration in Eq.(16) can be numerically calculated by using an numerical integration algorithm, *e.g.*, the trapezoidal numerical integration [11]:

$$\begin{aligned} \bar{w}(x; \omega) &= \frac{1}{2} \Delta \xi [\Delta \bar{w}(x; a, \omega) + 2\Delta \bar{w}(x; a + \Delta \xi, \omega) \\ &\quad + 2\Delta \bar{w}(x; a + 2\Delta \xi, \omega) + \dots + \Delta \bar{w}(x; b, \omega)] \end{aligned} \quad (17)$$

Finally, the dynamic response $w(x, t)$, in time domain, can be obtained by taking the inverse Fourier transform of $\bar{w}(x; \omega)$.

Consider a simply supported Bernoulli-Euler beam subject to a uniformly distributed dynamic load of magnitude 100 *N/m*, over the whole span of beam. The load acts for 0.1 *seconds*. The beam has the

length of 2.8 m, $EI = 6 \text{ Nm}^2$, $m = 28 \text{ kg/m}$, and the loss factor $\eta = 0.03$. Figure 2(a) compares the dynamic responses at the middle of beam (non-dimensionalized with respect to beam thickness $h = 0.01 \text{ m}$), from three different solution methods. Similarly, Fig. 2(b) compares the frequency responses. The comparisons are made for the solutions sufficiently converged, within 0.03 %. It is obvious from Figs. 2(a) and 2(b) that the present mSEM gives the solutions almost identical with the analytical solutions which is considered to be exact, while this is not likely true for the FEM.

TWO-DIMENSIONAL (PLATE) STRUCTURES

Unlike beams, the two-dimensional structures (*e.g.*, plates) have much complex dispersive relations. Thus, a special technique is required to extend the modified SEM in the preceding section to such structures. Since the technique developed in this section can be applied to rectangular and circular plates, the discussion will be confined to a square plate.

Consider a simply supported thin rectangular plate, with small deflection $w(x, y, t)$. Dynamic equation of motion of a thin plate under distributed dynamic load $f(x, y, t)$ is given as follows [12]:

$$D \nabla^4 w + m \frac{\partial^2 w}{\partial t^2} = f(x, y, t) \quad (18)$$

where D is the flexural rigidity and m is the mass density per unit area of plate. The solution of Eq.(18) is assumed to have the spectral representation as

$$w(x, y, t) = \sum_n \bar{w}_n(x, y, \omega_n) e^{i\omega_n t} = \sum_n \tilde{X}_n(x, \omega_n) \tilde{w}_n(y, \omega_n) e^{i\omega_n t} \quad (19)$$

The spectral shape functions $\tilde{X}(x)$ and $\tilde{w}(y)$ in the x and y directions must satisfy relevant boundary conditions. The dispersive relation for a plate is given as

$$(k_x^2 + k_y^2)^2 = \Omega^2 \quad (\Omega^2 = \omega \sqrt{m/D}) \quad (20)$$

where k_x and k_y are the wave numbers in the x and y directions, respectively. From Eq.(20), k_y (or k_x) can be expressed in terms of k_x (or k_y) and ω . Thus the wave characteristics of a plate can be represented by using a chosen wave number (k_x or k_y) at a specified frequency ω .

It can be shown, from Eq. (20), that the wave number k_x has four values, i.e., $\pm k_x$ and $\pm i k_x$. This is also true for k_y . Thus the spectral shape functions $\tilde{X}(x)$ and $\tilde{w}(y)$ can be represented as

$$\tilde{X}(x) = A_1 e^{-i k_x x} + A_2 e^{-k_x x} + A_3 e^{i k_x x} + A_4 e^{k_x x} \quad (21)$$

$$\tilde{w}(y) = B_1 e^{-i k_y y} + B_2 e^{-k_y y} + B_3 e^{i k_y y} + B_4 e^{k_y y} \quad (22)$$

where $k_y = \sqrt{\Omega^2 - k_x^2}$ is defined. Equation (21) must satisfy the simply supported boundary conditions, at $x = 0$ and L , given by

$$\tilde{X}(0) = \tilde{X}(L) = \frac{d^2 \tilde{X}(0)}{dx^2} = \frac{d^2 \tilde{X}(L)}{dx^2} = 0 \quad (23)$$

where L is the dimension of square plate. Using boundary conditions of Eq.(23), the characteristic wave number k_x and shape function $\tilde{X}(x)$ are obtained as follows:

$$k_x = \frac{n\pi}{L} \quad (n = 1, 2, 3, \dots) \quad (24)$$

$$\tilde{X}(x) = e^{i k_x x} - e^{-i k_x x} \quad (25)$$

The spectral displacement can be rewritten, from Eqs. (19), (21), and (22) as follows :

$$\tilde{w}(x, y) = \tilde{X}(x) \tilde{w}(y) = \tilde{X}(x) [Q(y)] \{ B_1 \ B_2 \ B_3 \ B_4 \} \quad (26)$$

where

$$[Q(y)] = [e^{i k_y y} \ e^{-i k_y y} \ e^{k_y y} \ e^{-k_y y}] \quad (27)$$

To derive the spectral element matrix for a plate, the same procedure introduced for beams in the preceding section will be used. Consider a spectral plate element which has the dimensions L and l in the x and y directions, respectively. The spectral nodal DOFs on y boundary planes ($y = 0$ and $y = l$) can be expressed in the form :

$$\{ \tilde{w}_0 \ \tilde{w}'_0 \ \tilde{w}_l \ \tilde{w}'_l \}^T = [\alpha(k_x)] \{ B_1 \ B_2 \ B_3 \ B_4 \}^T \quad (28)$$

where (') indicates the partial derivative with respect to y . In Eq. (28), $\tilde{w}_0 = \tilde{w}(0)$, $\tilde{w}'_0 = \tilde{w}'(0)$, $\tilde{w}_l = \tilde{w}(l)$, and $\tilde{w}'_l = \tilde{w}'(l)$ are defined, and the (4x4) matrix $[\alpha]$ is tabulated in *Appendix*. The spectral shear force and bending moments on y plane can be obtained from

$$\begin{aligned}\bar{V} &= D \left[\frac{\partial^3 \bar{w}}{\partial y^3} + (2-\nu) \frac{\partial^3 \bar{w}}{\partial x^2 \partial y} \right] = \tilde{X}(x) \tilde{V}(y) \\ \bar{M} &= D \left[\frac{\partial^2 \bar{w}}{\partial y^2} + \nu \frac{\partial^2 \bar{w}}{\partial x^2} \right] = \tilde{X}(x) \tilde{M}(y)\end{aligned}\quad (29)$$

where ν is the Poisson's ratio.

Using Eq. (29), the spectral nodal moments and forces can be expressed in the form :

$$\{ \tilde{V}_0 \quad \tilde{M}_0 \quad \tilde{V}_l \quad \tilde{M}_l \}^T = [\beta(k_x)] \{ B_1 \quad B_2 \quad B_3 \quad B_4 \}^T \quad (30)$$

where the matrix $[\beta]$ is tabulated in *Appendix*. Combining Eqs. (28) and (30) results in

$$\{ \tilde{V}_0 \quad \tilde{M}_0 \quad \tilde{V}_l \quad \tilde{M}_l \}^T = [\sigma(k_x)] \{ \tilde{w}_0 \quad \tilde{w}'_0 \quad \tilde{w}_l \quad \tilde{w}'_l \}^T \quad (31)$$

where $[\sigma] = [\beta][\alpha]^T$ is the spectral element matrix for plates. The spectral plate elements can be assembled in the analogous way as is done in FEM. Applying relevant boundary conditions to the result of assembling may result in a condensed global spectral matrix equation in the form as:

$$\{ \tilde{W} \} = [\Xi(k_x)]^{-1} \{ \tilde{F} \} \quad (32)$$

where $[\Xi]$ is the condensed global spectral element matrix, $\{ \tilde{W} \}$ and $\{ \tilde{F} \}$ are the condensed global spectral nodal DOFs and forces vectors, respectively.

Similarly as in the preceding section, the distributed load acting on a plate also can be discretized into many line loads. Figure 3(a) shows an example of square plate subjected to a centered uniform square load $f(x, y, t)$. In this case, the distributed load can be discretized into a series of equivalent line loads parallel to the x axis or y axis depending on the choice of the direction of structural discretization. The dynamic response will be obtained by summing up all dynamic responses due to each equivalent line loads. If we discretize the plate in the y direction, as shown Fig. 3(b), then the equivalent line load is parallel to the x axis. Thus, the equivalent line load at $y = \xi$ has the magnitude of $f(x, \xi, t) \Delta \xi$ as the function of x . Taking spatial Fourier transform with respect to x , the equivalent line load can be represented as the function of wave number k_x , instead of x . By removing the x axis dependence of equivalent line load, the original two-dimensional

problem can be reduced to an equivalent one-dimensional problem, as shown in Fig. 3(c). Then, the mSEM for beams in the preceding section can be applied to this equivalent one-dimensional problem.

Since the foregoing discretization procedure represents a plate as a connection of two spectral plate elements with an equivalent line load acting along the connection line, as shown in Fig. 3(b), first two spectral plate elements should be assembled. Equation (31) or (32) shows that the spectral element matrix equation is formulated only in terms of wave number k_x , at a specified frequency ω . Unlike the one-dimensional (beam) problem, however the equivalent line load is the function of x and t . Thus, we need to convert the equivalent line load into the function of k_x and ω . That is, $f(x, \xi, t) \Delta \xi$ should be spatially Fourier transformed with respect to x , and then Fourier transformed with respect to t , to yield $\tilde{f}(\xi; k_x, \omega) \Delta \xi$. This is just the procedure which reduces a two-dimensional problem into a simple equivalent one-dimensional problem as described in the preceding.

Considering a plate discretized into two spectral plate elements, as shown in Fig. 3(b), the global spectral matrix equation, condensed using the simply supported boundary conditions at $y = 0$ and L , is derived in the form as:

$$\begin{Bmatrix} \tilde{w}_1' \\ \tilde{w}_2 \\ \tilde{w}_2' \\ \tilde{w}_3' \end{Bmatrix} = \begin{bmatrix} \sigma_{22}^1 & \sigma_{23}^1 & \sigma_{24}^1 & 0 \\ \sigma_{32}^1 & \sigma_{33}^1 + \sigma_{11}^2 & \sigma_{34}^1 + \sigma_{12}^2 & \sigma_{14}^2 \\ \sigma_{42}^1 & \sigma_{43}^1 + \sigma_{21}^2 & \sigma_{44}^1 + \sigma_{22}^2 & \sigma_{24}^2 \\ 0 & \sigma_{41}^2 & \sigma_{42}^2 & \sigma_{44}^2 \end{bmatrix}^{-1} \begin{Bmatrix} 0 \\ \tilde{f}_2(k_x, \omega) \Delta \xi \\ 0 \\ 0 \end{Bmatrix} \quad (33)$$

or, simply

$$\{\Delta \tilde{w}\} = [\Xi(k_x, \omega)]^{-1} \{\tilde{F}\} \quad (34)$$

where the superscript used for σ indicates the number of spectral element while the subscripts indicate the element number of corresponding spectral element matrix. And, the subscripts 1, 2, and 3 under \tilde{w} indicate the node lines at $y = 0$, $y = \xi$, and $y = L$, respectively.

Note that the spectral nodal DOFs, $\{\Delta \tilde{w}\}$, is the function of characteristic wave number k_x and frequency ω . Following exactly the same procedure as used in the one-dimensional problem, the dynamic response at a point (x, y) due to a line load acting at $y = \xi$, can be obtained from

$$\Delta \tilde{w}(x, y; \xi, k_x, \omega) = \bar{X}(x) [\underline{Q}] [\alpha]^{-1} [c] [\Xi]^{-1} \{d\} \tilde{f}_2 \Delta \xi \quad (35)$$

where $[Q]$, $[\alpha]$, and $[\Xi]$ are defined in Eqs. (27), (28), and (34). The matrix $[c]$ are determined from the relation between the spectral nodal DOFs and $\{\Delta\tilde{W}\}$, just like the Eq. (11) for beam problem. Similarly, the vector $\{d\}$ is determined from the vector $\{\tilde{F}\}$ itself, as explained in Eq. (23). The two-dimensional version of Eq. (9) can be written as

$$\Delta\bar{w}(x, y; \xi, k_x, \omega) = R(x, y; \xi, \omega) P(\xi, k_x, \omega) \quad (36)$$

with

$$\begin{aligned} R(x, y; \xi, \omega) &= \bar{X}(x)[Q][\alpha]^{-1}[c][\Xi]^{-1}\{d\} \\ P(\xi, k_x, \omega) &= \tilde{f}_2(\xi, k_x, \omega)\Delta\xi \end{aligned} \quad (37)$$

As Eq. (36) gives the dynamic response due to a line load, the total dynamic response can be obtained from

$$\bar{w}(x, y; k_x, \omega) = \int_{L/4}^{3L/4} \Delta\bar{w}(x, y; \xi, k_x, \omega) d\xi \quad (38)$$

A numerical integration algorithm similar to Eq. (17) may be applied to Eq. (38). One should note that \bar{w} of Eq. (38) is the value at a combination of specific values of k_x (e.g., $k_{xn} = n/L$) and ω (e.g., $\omega_n = n\Delta\omega$). Thus the dynamic response in time domain can be calculated from

$$w(x, y, t) = \sum_{n=1}^N \sum_{m=1}^M w_{mn}(x, y, k_{xn}) e^{i\omega_n t}, \quad k_{xn} = \frac{n\pi}{L} \quad (39)$$

For numerical examples, consider a simply-supported square plate having the dimension of $L = 2.8 \text{ m}$ and thickness $h = 0.01 \text{ m}$. The material properties are given as $D = 6.73 \text{ kN}$, $m = 28 \text{ kg/m}^2$, and the loss factor $\eta = 0.03$. Two types of dynamic load are considered in this study: a point load of magnitude 100 N acting at the center of plate, and a centered square load of magnitude of 100 N/m^2 , uniformly distributed over $1/4$ area of the plate. The two loads act for 0.1 seconds . The frequency responses from three different solution methods are compared in Fig.(4), for both two dynamic loads. Comparisons are made for the solutions, sufficiently converged within 0.03% . In general, the solutions by the present mSEM are found to be very close to the analytical (exact) solutions. But, for the finite element solutions, there exist large deviations from the exact solutions as the time or frequency increases.

CONCLUSIONS

In this paper, a modified spectral element method is developed

for the beams and rectangular plates subject to distributed dynamic loads. Numerical tests show that the present modified SEM (mSEM) provides very accurate solutions in comparison with the finite element solutions. Since the present mSEM is limited to only special cases of plate, the generalization of mSEM for any plate problems may need further consideration. This will be discussed in the next coming paper.

ACKNOWLEDGMENT

This study is supported by Korean Ministry of Education through the Research Fund ME95-D-14, which is gratefully appreciated.

REFERENCES

1. Plaut, R. H. and Huseyin, K., Derivatives of eigenvalues and eigenvectors in non-self-adjoint systems. *AIAA J.*, 11(2), 1973, 250-51.
2. von Flotow, A. H., The acoustic limit of control of structural dynamics. In *Large Space Structures: Dynamics and Control*, eds. Atluri, S. and Amos, T., Springer Verlag, 1987, 213-37.
3. Graff, K. F., *Wave Motion in Elastic Solids*. Dover Pub., New York, 1973, 11-3.
4. Mehl, J. D. and Miles, R. N., Finite element modeling of the transient response of viscoelastic beams. *Proc. Smart Struct. & Mat.*, San Diego, CA, 1995, 306-11.
5. Doyle, J. F., A spectrally formulated finite element for longitudinal wave propagation. *Int. J. Anal. & Exper. Modal Anal.*, 3(1), 1988, 1-5.
6. Doyle, J. F., *Wave Propagation in Structures: An FFT-Based Spectral Analysis Methodology*, Springer Verlag, New York, 1989, 32-57.
7. Gopalakrishnan, S., Martin, M. and Doyle, J. F., A matrix methodology for spectral analysis of wave propagation in multiple connected Timoshenko beams. *J. Sound & Vib.*, 158(4), 1992, 11-24.
8. Horr, A. M. and Schmidt, L. C., Dynamic response of a damped large space structures: a new fractional-spectral approach. *Int. J. Space Struc.*, 10(2), 1995, 113-19.
9. Lee, J. and Lee, U., Spectral element analysis of the structures under dynamic distributed loads. *Proc. 37th Structures, Structural Dynamics and Materials Conference*, Salt Lake, Utah, 1996, 1605-14.
10. Daniai, A. N. and Doyle, J. F., Transverse impact of a damped plate near a straight edge. *ASME J. Vib. & Acoust.*, 117(1), 1995, 103-8.

11. Chapra, S. C. and Canale, R. P., *Numerical Methods for Engineers*, McGraw-Hill, New York, 1989, 478-89.
12. Szilards, R., *Theory and Analysis of Plates*, Prentice Hall, New Jersey, 1974, 28-42.

APPENDIX : ELEMENTS OF MATRICES $[\alpha_{ij}]$ AND $[\beta_{ij}]$

$$\begin{aligned}
 \alpha_{11} = \alpha_{12} = \alpha_{13} = \alpha_{14} = 1, \quad \alpha_{21} = -\alpha_{22} = ik_y, \quad \alpha_{23} = -\alpha_{24} = k_y, \quad \alpha_{31} = \alpha_{32}^{-1} = e^{ik_y l} \\
 \alpha_{33} = \alpha_{34}^{-1} = e^{k_y l}, \quad \alpha_{41} = ik_y e^{ik_y l}, \quad \alpha_{42} = -ik_y e^{-ik_y l}, \quad \alpha_{43} = k_y e^{k_y l}, \quad \alpha_{44} = -k_y e^{-k_y l} \\
 \beta_{11} = -\beta_{12} = -iDk_y\{k_y^2 + (2-\nu)k_x^2\}, \quad \beta_{13} = -\beta_{14} = Dk_y\{k_y^2 - (2-\nu)k_x^2\} \\
 \beta_{21} = \beta_{22} = -D\{k_y^2 + \nu k_x^2\}, \quad \beta_{23} = \beta_{24} = D\{k_y^2 - \nu k_x^2\} \\
 \beta_{31} = -iDk_y\{k_y^2 + (2-\nu)k_x^2\}e^{ik_y l}, \quad \beta_{32} = iDk_y\{k_y^2 + (2-\nu)k_x^2\}e^{-ik_y l} \\
 \beta_{33} = Dk_y\{k_y^2 - (2-\nu)k_x^2\}e^{k_y l}, \quad \beta_{34} = -Dk_y\{k_y^2 - (2-\nu)k_x^2\}e^{-k_y l} \\
 \beta_{41} = -D\{k_y^2 + \nu k_x^2\}e^{ik_y l}, \quad \beta_{42} = -D\{k_y^2 + \nu k_x^2\}e^{-ik_y l} \\
 \beta_{43} = D\{k_y^2 - \nu k_x^2\}e^{k_y l}, \quad \beta_{44} = D\{k_y^2 - \nu k_x^2\}e^{-k_y l}
 \end{aligned}$$

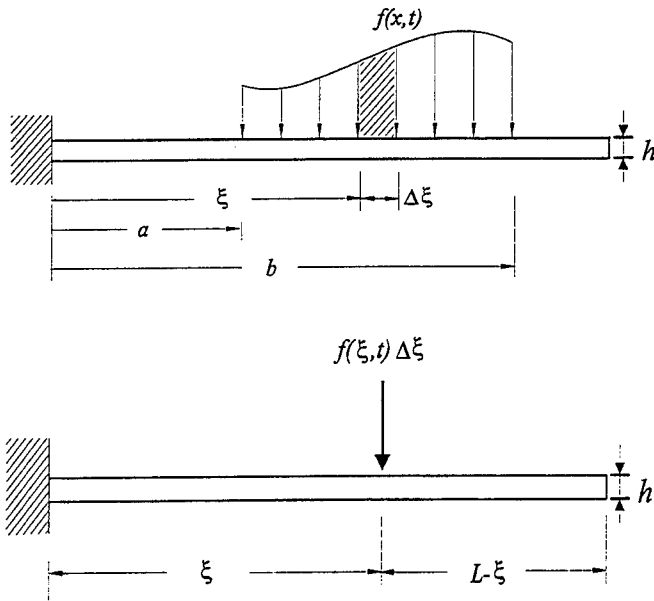


Fig. 1 Linear superposition representation of a dynamic distributed load acting on a beam

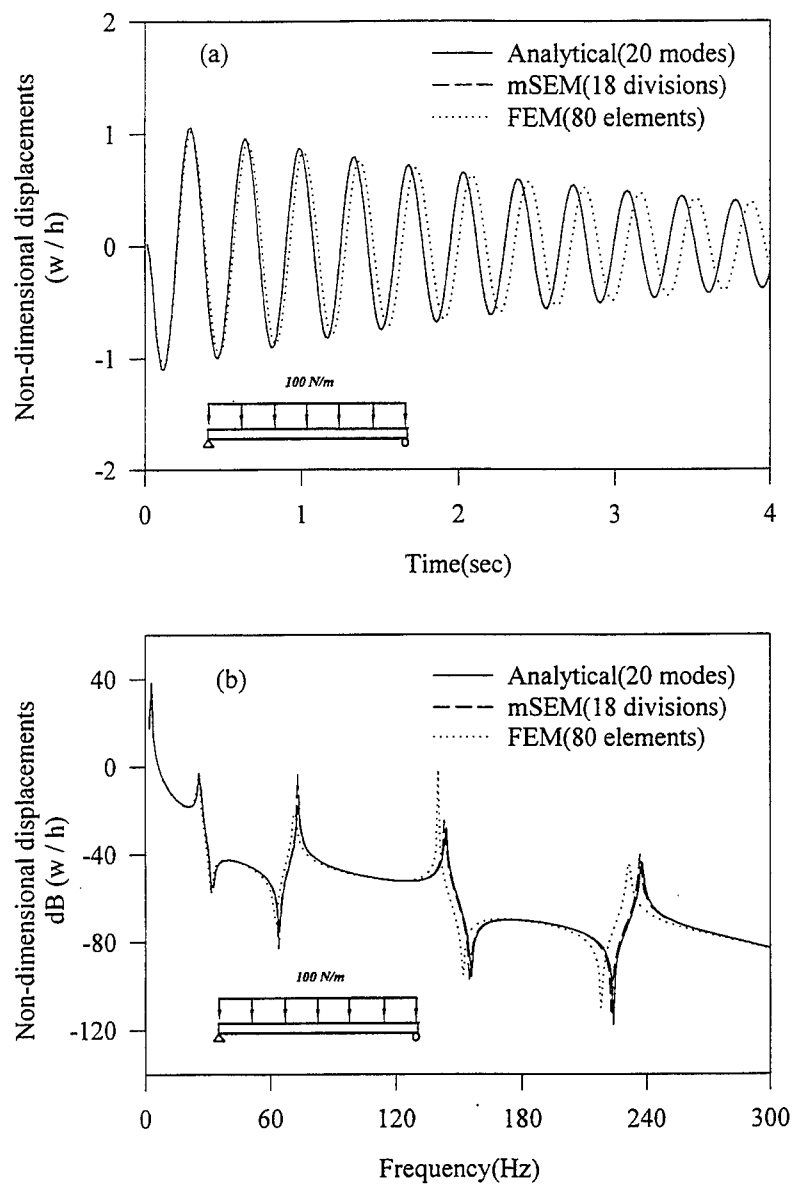


Fig. 2 Comparison of the dynamic and frequency responses at the middle of a simply supported Bernoulli-Euler beam, subject to a dynamic load of magnitude 100 N/m , uniformly distributed over the whole span of beam, and acting for 0.1 seconds : (a) dynamic responses, and (b) frequency responses

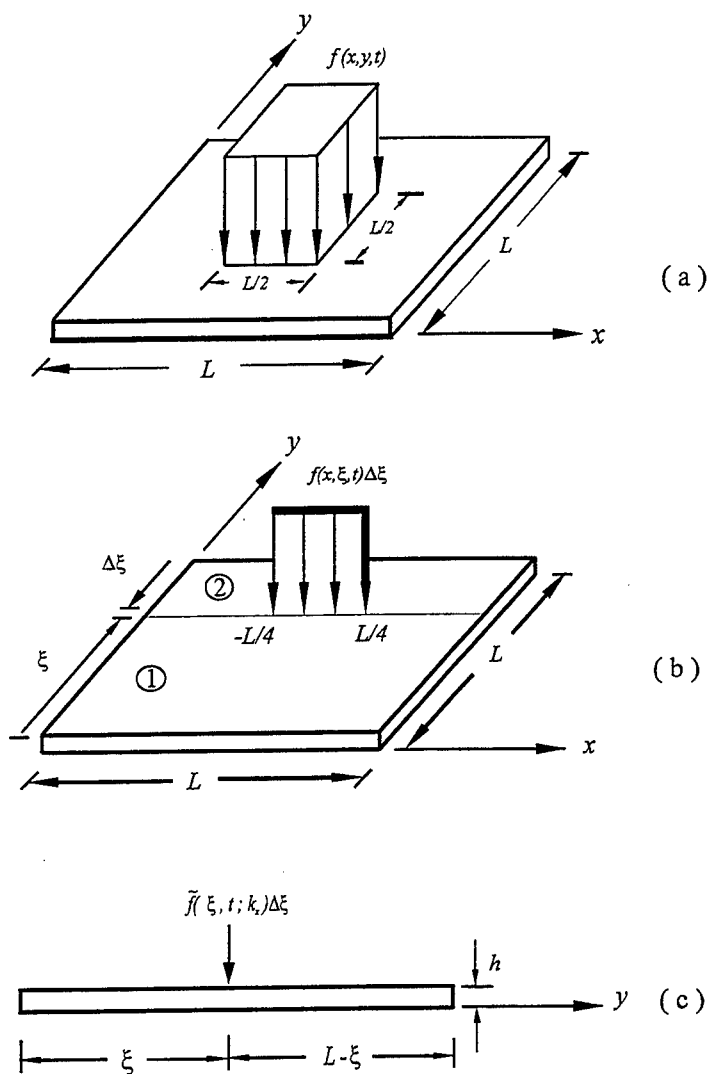


Fig. 3 Spectral element discretization procedure for plate problems: (a) a square plate subject to a centered square load, (b) discretization into two spectral plate elements with a line load, and (c) its equivalent one-dimensional problem representation

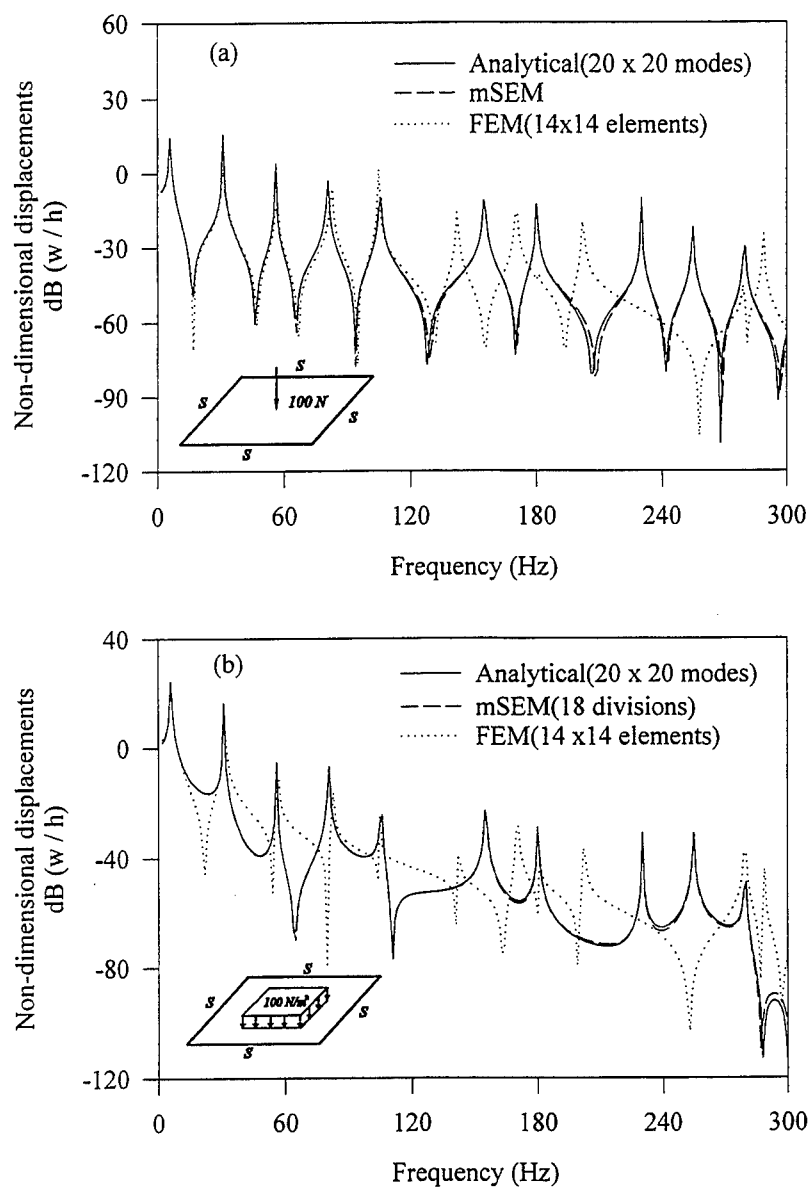


Fig. 4 Comparison of the frequency responses (at the middle of square plate) from three different solution methods : when (a) a centered point dynamic load of magnitude 100 N , and (b) a centered uniformly distributed dynamic load of magnitude 100 N/m^2 act for 0.1

Spectral Elements for Acoustic Wave Propagation through Thin-walled Complex Structures

Brian A. Bilodeau and James F. Doyle

SCHOOL OF AERONAUTICS & ASTRONAUTICS, PURDUE UNIVERSITY
WEST LAFAYETTE, INDIANA 47907

Abstract: A spectral element method is developed for analyzing acoustic wave propagation through multi-connected thin-walled structures. The flat- and curved- plate elements, which incorporate the effect of fluid loading on the structure, accurately model the responses over large domains. The elements may be conveniently joined to form complex structures composed of many segments.

1. Introduction

Noise generation is an important aspect of structural dynamics; it is computationally expensive, however, because problems require analyzing the solid/fluid interaction as well as require the modeling of extended regions. This paper reviews a method we have been developing that offers great potential in solving this class of problem for the type of thin-walled structures depicted in Figure 1.

Our approach is based on the spectral element method — References [1, 2, 3] give summaries of the approach as applied to frame structures. The method has the following characteristics. First, it is a frequency domain formulation. Consequently, frequency domain information such as transfer functions and system functions are generated automatically. This enables a duality between the time domain and frequency domain — information not readily seen in one is usually apparent in the other. Second, it is geared toward handling very large areas. It is a counterpoint to conventional elements which always model a region as a collection of many small sub-domains. Third, it is stiffness formulated. This means the process of assemblage for complex structures is easy. More fundamentally, however, it identifies the minimum essential variables (the degrees of freedom) for a dynamic description of the structure. The application to thin-walled structures begins by combining the spectral analysis for in-plane wave responses and out-of-plane flexural behavior to form a matrix method approach for folded plate structures [4, 5]. The variety of structural shapes encompassed is enhanced by adding a segmented curved shell element [6].

The solid/fluid interaction problem is tackled by incorporating the effect of fluid loading on the structure directly into the element formulation. In this way, the structural formulation is unaffected. Utilizing the shape functions for these extended elements then allow computation of the pressure response in the fluid as a post-processing operation.

The method is a work in progress and the sample results presented are chosen so as to highlight its main features and attributes.

2. Spectral Analysis of Waves in Extended Media

By way of example, we will use the flexural behavior of flat plates to introduce our approach to modeling the dynamics of structures. The governing equation of motion for a plate is described by [2]

$$D\nabla^2\nabla^2w + q = \rho h \frac{\partial^2 w}{\partial t^2} + \eta h \frac{\partial w}{\partial t}$$

where $w(x, y, t)$ is the transverse displacement, D is the plate stiffness, ρ is the mass density, h is the thickness, and η is the damping coefficient. The response is given a spectral representation in the form

$$w(x, y, t) = \sum_n^N \hat{w}(x, y, \omega_n) e^{i\omega_n t} \quad (1)$$

where ω_n is frequency and N is the total number of terms (typically 1024 to 4096). On substituting into the homogeneous form of the governing equation, we get the representation

$$\begin{aligned} \hat{w}(x, y) = \sum_m^M \tilde{w}(x, \xi_m, \omega_n) e^{i\xi_m y} = \sum_m [A_{mn} e^{-ik_1 x} + B_{mn} e^{-ik_2 x} + C_{mn} e^{-ik_1(L-x)} \\ + D_{mn} e^{-ik_2(L-x)}] \{\cos(\xi_m y), \sin(\xi_m y)\} \end{aligned}$$

where M is typically 512 to 2048. The spectrum relations are given by

$$k_1 = \sqrt{\beta_n^2 - \xi_m^2}, \quad k_2 = -i\sqrt{\beta_n^2 + \xi_m^2}, \quad \beta_n^4 = (\rho h \omega_n^2 - i\eta h \omega_n)/D$$

Note that these are both frequency and wavenumber dependent.

This discretized form of solution is an approximation to the double continuous Fourier transform; under the proper circumstances, however, this approximation can be highly accurate. In addition, the discrete representation can be implemented on a computer with great efficiency. Values for the time window T and N are chosen together to satisfy two constraints: the Nyquist frequency (given by $N/2T$) must exceed the most significant frequency components in the input force history, and the value of T must be large enough so that the response at the point of interest has diminished to zero at time T . The latter condition arises from our use of the FFT; it prevents the response at time T from wrapping around and affecting the response at time zero. Values for the space window W and M are chosen in a similar manner: the wavenumbers ξ_m must be small enough to sufficiently model the spatial distribution of the applied load in the y direction, and W must be large enough to prevent waves from neighboring space windows from propagating into the window we are monitoring.

The kinematics of a curved plate [7, 8] are described by the variables (u, v, w) which represent the hoop, lengthwise, and transverse displacements, respectively. A spectral representation of these is given the form

$$\hat{u} = \sum_m u_o e^{-iks} \cos(\xi y), \quad \hat{v} = \sum_m v_o e^{-iks} \sin(\xi y), \quad \hat{w} = \sum_m w_o e^{-iks} \cos(\xi y)$$

Substitution of these into the governing differential equations leads to the characteristic system

$$\begin{bmatrix} \alpha_1 - [k^2 + (1 - \nu)\xi^2]D/R^2 & \gamma & [\bar{E} + (k^2 + \xi^2)D]ik/R \\ \gamma & \alpha_2 & \nu\bar{E}\xi/R \\ [\bar{E} + (k^2 + \xi^2)D]ik/R & \nu\bar{E}\xi/R & \alpha_3 + \bar{E}/R^2 \end{bmatrix} \begin{Bmatrix} u_o \\ v_o \\ w_o \end{Bmatrix} = 0$$

where

$$\begin{aligned} \alpha_1 &\equiv -\bar{E}[k^2 + \xi^2 - \frac{1}{2}(1 + \nu)\xi^2] + \rho h \omega^2, & \gamma &\equiv \frac{1}{2}(1 + \nu)\bar{E}ik\xi \\ \alpha_2 &\equiv -\bar{E}[k^2 + \xi^2 - \frac{1}{2}(1 + \nu)k^2] + \rho h \omega^2, & \alpha_3 &\equiv D[k^2 + \xi^2]^2 - \rho h \omega^2 \end{aligned}$$

The α_1, α_2 and γ terms alone define the flat membrane problem, while α_3 alone defines the flat plate flexural problem. All the other terms are couplings. There are four pairs of roots for k and an idea of the variety of behaviors is shown in Figure 3 for a value of $\xi = 2\pi m/W$ with $m = 50$. Most of the complicated behavior occurs in the vicinity of low frequency where the thickness is relevant. To exaggerate its effects, the plots are for the case when $h/R = 0.1$ and $R = 250$ mm for aluminum material.

The coefficients **A**, **B**, and so on, are generally determined from boundary conditions. In our case, however, we replace them in terms of edge degrees of freedom so that the representations can be put in a convenient matrix formulation. For brevity, we demonstrate the formulation of the double noded element — the single noded element follows along similar lines. The single noded or throw-off element models boundaries which completely absorb wave energy or are very distant. A segment of a folded plate structure, which exhibits both membrane and flexural behavior, has eight degrees of freedom. A segment of a curved cylindrical shell exhibits behavior similar to that of the folded plate and therefore also has eight degrees of freedom. The curved element has all displacements coupled and hence we have to tackle the stiffness matrix directly as an $[8 \times 8]$ system. This is too cumbersome to do explicitly; consequently, we lay out a computer based method for establishing the shape functions and subsequently the stiffness matrix.

The displacement solution is written in terms of the amplitude ratios ϕ and the undetermined coefficients **A**, **B**, ... as

$$\{u(s), v(s), w(s), \psi(s)\}^T = \{u\}(s) = [\Phi_A][e(s)]\{\mathbf{A}\} + [\Phi_B][e(L - s)]\{\mathbf{B}\}$$

where $\{\phi_A\}_j$ are evaluated at k_j while $\{\phi_B\}_j$ are evaluated at $-k_j$, and we have

defined for either $[\Phi_A]$ or $[\Phi_B]$

$$[\Phi] \equiv \left[\begin{array}{c} \left\{ \begin{array}{c} 1 \\ \phi_v \\ \phi_w \\ \phi_\psi \end{array} \right\}_1 \dots \left\{ \begin{array}{c} \phi_1 \\ \phi_v \\ \phi_w \\ \phi_\psi \end{array} \right\}_4 \end{array} \right], \quad [e(s)] \equiv \begin{bmatrix} e^{-ik_1 s} & 0 \\ 0 & \dots & 0 \\ 0 & & 0 \\ 0 & & e^{-ik_4 s} \end{bmatrix}$$

We replace the vectors $\{A\}$ and $\{B\}$, which contain the undetermined coefficients, in terms of the nodal displacements at $s = 0$ and $s = L$. Let us write all eight equations as $\{u\} = [Q]\{A, B\}$. Solving for the coefficients gives

$$\{A, B\} = [Q^{-1}]\{u\} = [G]\{u\} = \begin{bmatrix} [G_{11}] & [G_{12}] \\ [G_{21}] & [G_{22}] \end{bmatrix} \begin{Bmatrix} \{u_1\} \\ \{u_2\} \end{Bmatrix}$$

where each partition of $[G]$ is of size $[4 \times 4]$. We are now in a position to write the displacements in terms of the shape functions as

$$\{u\}(s) = [g_1(s)]\{u\}_1 + [g_2(s)]\{u\}_2 \quad (2)$$

where the $[4 \times 4]$ matrix functions of s are given by

$$\begin{aligned} [g_1(s)] &= [\Phi_A][e(s)][G_{11}] + [\Phi_B][e(L-s)][G_{21}] \\ [g_2(s)] &= [\Phi_A][e(s)][G_{12}] + [\Phi_B][e(L-s)][G_{22}] \end{aligned} \quad (3)$$

It is clear that even in this general case that the second collection of shape functions are the image of the first set. These formulas can be used to recover all the shape functions already derived in the cited references.

By way of example, Figure 4 shows the $\tilde{g}_{33}(s)\cos(\xi_m y)$ shape function of a 270° shell segment; this shape function is associated with the \tilde{w}_1 degree of freedom and thus can be plotted as a radial displacement off the original shape. These play the same role as shape functions in a conventional finite element formulation but with the significant difference that they are frequency and wavenumber dependent.

The resultants associated with the boundary conditions for a curved plate are

$$\{F\} = \{N_{ss} + \frac{1}{R}M_{ss}, N_{sy}, V_{sz}, M_{ss}\}^T = [\partial]\{u\}$$

where $[\partial]$ is the matrix collection of differential operators of size $[4 \times 4]$. After substituting for $\{u\}(s)$ in terms of the shape functions and relating the member forces at $s = 0$ and $s = L$ to the nodal loads leads to the stiffness relation

$$\begin{Bmatrix} \{F_1\} \\ \{F_2\} \end{Bmatrix} = \begin{bmatrix} [-\partial g_1(0)] & [-\partial g_2(0)] \\ [+ \partial g_1(L)] & [+ \partial g_2(L)] \end{bmatrix} \begin{Bmatrix} \{u_1\} \\ \{u_2\} \end{Bmatrix}, \quad \{F\} = [\tilde{k}(\xi, \omega)]\{u\} \quad (4)$$

where $[\tilde{k}]$ is the $[8 \times 8]$ dynamic element stiffness that is frequency and wavenumber dependent. It relates applied tractions along the edges to the displacements

along the edge. Figure 5 shows the behavior of the first two diagonal terms for a flat plate in flexure; note the wide dynamic range of these stiffnesses. More details are given in References [4, 5] for flat plates, in Reference [3] for a deep curved beam, and in Reference [6] for the thin shell.

3. Folded Plate Structures

The advantage of the element approach is that many elements – either flat or curved – can be combined to form interesting complex structures. The dynamic structural stiffness matrix is assembled using techniques analogous to those used for conventional finite elements [9]. The major difference is the addition of a *Do-Loop* over all of the frequency and wavenumber components. This results in the assemblage of a different dynamic stiffness matrix at each frequency and wavenumber.

The assemblage process is illustrated in Figure 2. The nodal loads and displacements in local coordinates are arranged as

$$\begin{aligned}\{\tilde{\bar{F}}\}^T &\equiv \{\tilde{N}_{xx1}, \tilde{N}_{xy1}, \tilde{V}_{xz1}, \tilde{M}_{xx1}; \tilde{N}_{xx2}, \tilde{N}_{xy2}, \tilde{V}_{xz2}, \tilde{M}_{xx2}\}, & \{\tilde{\bar{F}}\} &= [\tilde{\bar{k}}] \{\tilde{\bar{u}}\} \\ \{\tilde{\bar{u}}\}^T &\equiv \{\tilde{u}_1, \tilde{v}_1, \tilde{w}_1, \tilde{\psi}_{x1}; \tilde{u}_2, \tilde{v}_2, \tilde{w}_2, \tilde{\psi}_{x2}\}\end{aligned}$$

Both in-plane and out-of-plane components are included. These is transformed to global form as

$$\tilde{\bar{F}} = [\tilde{\bar{k}}] \{\tilde{\bar{u}}\}, \quad [\tilde{\bar{k}}] = [T^T] [\tilde{k}] [T]$$

where the transformation matrix $[T]$ depends only on the geometry. After assemblage, we are in a position to present the structural dynamics problem in the form of a dynamic stiffness relation

$$[\tilde{K}(\omega, \xi)] \{\tilde{\bar{u}}\} = \{\tilde{\bar{P}}\} \quad (5)$$

where $\{\tilde{\bar{u}}\}$ is the set of unknown nodal responses, $\{\tilde{\bar{P}}\}$ is the applied load vector, and $[\tilde{K}(\omega, \xi)]$ is the frequency and space wavenumber dependent structural dynamic stiffness. The structural stiffness matrix has many of the attributes (such as symmetry and bandedness) of the static stiffness matrix. This equation is solved for $\{\tilde{\bar{u}}\}$ at a sufficient number of frequencies and wavenumbers to allow an inverse Fourier transform to be performed thus giving a reconstruction of the time history responses. The program SPlaDyn is a full implementation of this method. Reference [10] has more programing details and, in particular, how this was implemented on a massively parallel computer.

In the case of point loads applied proportionally (that is, each load component has the same time history) we can write

$$\{\tilde{\bar{P}}_{mn}\} = \{r\} \tilde{P}_{mn} = \{r\} \hat{P}_n \epsilon_m$$

where $\{r\}$ is the vector indicating the distribution of loads among the degrees of freedom, and \hat{P}_n is the FFT of the loading history. For single point impacts, for example, the vector $\{r\}$ has a unit value at the loaded degree of freedom, and zeros everywhere else. The real scalars ϵ_m are Fourier cosine series coefficients describing the distribution of loads in the y direction. The response at a particular degree of freedom q is related to the load at the impact site by

$$\hat{u}_n = \hat{P}_n \hat{G}_{q,n}^p, \quad \hat{G}_{q,n}^p = \sum_{m=0}^M \tilde{q}_{mn} \epsilon_m \cos(\xi_m y)$$

where \tilde{q}_{mn} refers to the m and n components of the solution vector $[\tilde{K}_{mn}]^{-1}\{r\}$ at the degree of freedom q , and the superscript p on \hat{G}_q^p refers to the impact site. We call \hat{G}_q^p the frequency domain transfer (or system response) function which relates displacement at point q to load applied at point p . Exact solutions at arbitrary locations between nodes can be obtained from the nodal values $\{\tilde{u}\}$ simply by using the shape functions as interpolating functions.

By way of example, we consider the impact of a simple structure; Reference [5] gives a full discussion of this problem. Our test structure is a thin walled cylindrical box with a square cross section having sides of length 102 mm as shown in Figure 1. We model it as a collection of folded plates with the folds located at the indicated nodal dots. The top face of the box is impacted at its center with a smoothed force history of approximately 200 μs duration. What we wish to do here is show the effect of the various folds on the reflections and in doing so illustrate some of the unique features of the spectral element method.

Figure 6 shows the sequence of models of the box beam where an additional corner is added at each step. For clarity, only the right half of the symmetric sections are shown. The first four models in this figure have the same properties as the complete 102 mm \times 102 mm structure. Throw-off elements (denoted by elements ending with a squiggle, !) absorb all waves transmitting through the last corner in each model. Each fold adds a new set of reflections. These reflections are discernible in Figure 7(a). A deeper insight is gained by looking at the system transfer functions \hat{G} for the same cases. What we see in Figure 7(b) is the formation of spectral peaks. This is essentially the vibration resonance behavior. Note that while the time domain responses have established themselves by the third fold, the frequency plots show that the spectral peaks will get sharper. This is because the spectral element method shows the system response not modified by the spectrum of the input loading \hat{P} .

This dual view of the dynamic response – time domain and frequency domain – is achieved very conveniently using spectral elements, and is one of the prime features of the approach.

The schematic for the impact of a complete cylindrical shell is shown in Figure 8. The accuracy of the curved element is confirmed in Figure 9 where a comparison is made with using many flat spectral elements. The agreement is excellent out to a significant number of reflections.

4. Waveguide Modeling with Fluid Loading

Our goal here is to formulate the acoustics problem in terms of a waveguide. The difficulty is that while the effect of the fluid loading is of a distributed pressure, it's non-local character makes it different in many respects from the pressure caused by a distributed spring, say, and hence we must invoke special procedures to handle it.

To begin our construction of a plate waveguide, we ask if it is possible for free waves to propagate in the plate immersed in a fluid. The spectral form for the equations of motion for the plate and the fluid can be written as [2]

$$D\nabla^2\nabla^2\hat{w}(x,y) - (\rho h\omega^2 - i\omega\eta h)\hat{w}(x,y) = -\hat{p}(x,y,z=0), \quad B\nabla^2\hat{p} + \rho_a\omega^2\hat{p} = 0$$

where the second equation is for the fluid pressure $\hat{p}(x,y,z)$. Assume a solution for the plate of the form $\hat{w} = \tilde{w}e^{-ik_x x}e^{i\xi y}$ which leads to the pressure response of

$$\hat{p} = \tilde{p}e^{-ik_x x}e^{i\xi y}e^{-ik_z z}, \quad k_z \equiv \sqrt{k_a^2 - k^2 - \xi_m^2}, \quad k_a^2 \equiv \frac{\omega^2}{c_a^2}$$

It must be borne in mind that as long as k_z is chosen as above then irrespective of the value of k the fluid equations are satisfied. This leads to the characteristic equation

$$(k^2 + \xi_m^2 - \beta^2)(k^2 + \xi_m^2 + \beta^2) - \frac{\rho_a\omega^2}{iDk_z} = 0, \quad \beta^2 \equiv \sqrt{\frac{(\rho h\omega^2 - i\omega\eta h)}{D}} \quad (6)$$

The third term in the first equation describes the effect of the fluid loading. The roots of this characteristic equation for $m = 0$ have been studied extensively in Reference [11].

When viewed as a contour integral [12], the response has contributions from two poles and a third contribution which arises from the branch cut associated with k_z . This latter contribution is most significant at impact points and corners. Reference [13] used a finite element model to show that this branch cut contribution can be neglected. A fluid loading of $\epsilon = 0.02$ was used which corresponds to a loading factor nearly ten times that of the cases of interest here.

Numerical solutions for the roots of the characteristic equation are shown in Figure 10 as circles along with the in vacuum roots indicated as the dashed lines. These plots, which are for 2.5 mm aluminum plates in air, show that the fluid loading primarily has the effect of altering the imaginary part of the first mode. We see that at coincidence and beyond, the effect is of increased viscous damping — this is consistent with the observation that the fluid is receiving more of the energy at these frequencies. But otherwise the behavior is very similar to the in vacuum behavior. That is, the pole contributions are associated with root k_1 which corresponds predominantly to the propagating flexural wave and root k_2 which corresponds predominantly to an evanescent flexural wave.

Making the assumption that there are only two dominant structural waves allows us to obtain approximate analytical expressions for the roots as

$$\begin{aligned} k_1 &\approx \pm \sqrt{\beta^2 - \xi_m^2 + \frac{\rho_a \omega^2}{2Dik_{z1}\beta^2}}, & k_{z1} &\equiv \sqrt{k_a^2 - \beta^2 - \xi_m^2} \\ k_2 &\approx \pm i \sqrt{\beta^2 + \xi_m^2 + \frac{\rho_a \omega^2}{2Dik_{z2}\beta^2}}, & k_{z2} &\equiv \sqrt{k_a^2 + \beta^2 - \xi_m^2} \end{aligned} \quad (7)$$

These approximations are also plotted in Figure 10. There is very good agreement with the exact numerical roots over the entire frequency range including the region near coincidence.

An enclosed structure is viewed as having two distinct regions; an interior region and an exterior region. The interior region has loadings due to both the fluid and the radiation from the vibration of other plates. However, the exterior region only experiences loadings from the fluid. Using the modified spectrum relations, the fluid loading for the exterior problem can be accounted for without considering the fluid response. In this way, the solid/fluid interaction problem is partially decoupled.

5. Radiation from Finite Plates

When investigating the interior noise of a cabin, say, the response of the fluid, in addition to that of the structure, is required. We are also interested in the fluid response because it can be the source of an excitation on a different part of the structure.

In determining the fluid response from a finite plate, we encounter a difficulty. The challenge is to match the motion of the finite plate to that of the fluid. But the domain for the fluid is (at least) the half space $z > 0$ and $-\infty < x < \infty$ which is considerably larger than the length of the plate. Therefore, to match the plate and fluid boundaries, we must extend the plate boundary in the x direction. If the finite plate is *baffled*, that is, extended on both sides with very stiff material, then the displacements can be matched by imposing $w = 0$ outside of the finite plate. We will assume that this can always be done even if the plate is not physically baffled but is attached to other plate segments.

At the surface of the plate, $z = 0$, the fluid displacement must be equal to the plate displacement. This response in the fluid has the spectral representation

$$\hat{w}(x, y, z) = \sum_m \sum_j \check{w}_{mj} e^{-ik_z z} e^{-in_j x} \cos(\xi_m y), \quad k_z \equiv \sqrt{k_a^2 - \eta_j^2 - \xi_m^2}$$

and $\check{p} = [\rho\omega^2/(-ik_z)]\check{w}_{mj}$. By extending the plate deflection over the full space window of the fluid, we can then give it the spectral representation

$$\hat{w}(x, y) = \sum_m \sum_j \check{w}_m e^{-in_j x} \cos(\xi_m y)$$

Applying this to the shape functions gives

$$\ddot{w}_m = \ddot{w}_1 \check{g}_{1mj} + L \ddot{\psi}_1 \check{g}_{2mj} + \ddot{w}_2 \check{g}_{3mj} + L \ddot{\psi}_2 \check{g}_{4mj}, \quad \check{g}_{ij} = \int_W \check{g}_i(x) e^{-i\eta_j x} dx$$

These integrals are easily evaluated and are given in Reference [2].

These equations were applied to the case of a finite aluminum plate in air. The pressure responses for the fluid can be seen in Figure 12. Similar to the plate response, these responses indicate the presence of multiple reflections occurring in the plate. This figure also indicates that the baffled finite plate not only excites the fluid directly in front of it but also at a distance along the baffle. The pressure at $x = 2L, z = 0$, for example, is non-zero even though the plate is baffled at that location — this is further indication that, in fluids, the relation between the pressure and displacement is non-local. Also shown are the resonance frequencies for a vibrating plate, it is clear that the impact has excited many of the symmetric modes of vibration.

It can be seen that the structural resonances

readily transmitted into the fluid. Intuitively, we might have thought that the response should be largest along a line normal to the plate. The responses shown in Figure 12 indicate that this is not so. Furthermore, the frequency plot shows that it is even frequency dependent. Figure 13 shows the directivity patterns at a number of frequencies; the near field behavior was computed from the full solution with $r = 2L$. It is clear that these patterns are very sensitive to direction when the frequency gets close to coincidence. Also shown are the deflected shapes of the plate at each frequency. These shapes indicate an almost sinusoidal plate deflection except at the center and edges — these are the points of significant radiation.

6. Discussion

Based on the problems we have considered, it is clear that once there is more than one connection in a structure, it is essential to have a matrix methodology to handle the many unknowns. The spectral element approach presents itself as a well founded matrix method that embodies a number of efficiencies we have long associated with the conventional finite element method. For the range of problems they are suited for, the spectral elements described here have been shown to conveniently model wave propagation in structures made of multiple panels.

Other advantages of the method are that the effect of material damping and viscoelasticity can easily be incorporated simply by changing the spectrum relation, higher order plate theories can be implemented without adding degrees of freedom to the system, and very large (semi-infinite) bodies are handled efficiently. It also has the advantage of being in a form to solve deconvolution type problems. That is, if the response is known at some location then the disturbance causing it can be determined.

The method discussed in this paper is a work in progress — there are many more developments needed (especially as it applies to the solid/fluid interaction problem) before it is considered mature. Some of the most important of them are itemized as: Verify the radiation approximation from edges, Implement radiation from curved surfaces, and, Add discontinuity in the lengthwise direction. Perhaps the biggest immediate challenge is to implement the book-keeping necessary for solving reverberation in a enclosed space.

Although, the spectral element approach to extended areas is still in relative infancy, the above has attempted to show that there are exciting challenges to be overcome in extending it to more general structural problems. The success of the waveguide spectral elements shows that such an effort is well worth undertaking.

References

- [1] Martin, M.T., Gopalakrishnan, S. and Doyle, J.F., Wave Propagation in Multiply Connected Deep Waveguides, *Journal of Sound and Vibration*, **174**(4), pp. 521-538, 1994.
- [2] Doyle, J.F., *Wave Propagation in Structures*, 2/E, Springer-Verlag, New York, 1997.
- [3] Bilodeau, B.A. and Doyle, J.F., A Spectral Element for Wave Propagation in Deep Curved Beams and Rings, *Journal of Sound and Vibration*, *submitted*, 1997.
- [4] Rizzi, S.A. and Doyle, J.F., A Spectral Element Approach to Wave Motion in Layered Solids, *Journal of Vibration and Acoustics*, **114**, pp. 569-577, 1992.
- [5] Danial, A.N., Rizzi, S.A. and Doyle, J.F., Dynamic Analysis of Folded Plate Structures, *Journal of Vibration and Acoustics*, **118**, pp. 591-598, 1996.
- [6] Bilodeau, B.A. and Doyle, J.F., Dynamic Response of Segmented Cylindrical Shell Structures, *Journal of Vibration and Acoustics*, *submitted*, 1997.
- [7] Leissa, A.W., *Vibration of Shells*, NASA SP-288, 1973.
- [8] Markus, S., *Mechanics of Vibrations of Cylindrical Shells*, Elsevier, New York, 1988.
- [9] Doyle, J.F., *Static and Dynamic Analysis of Structures*, Kluwer, The Netherlands, 1991.
- [10] Danial, A.N. and Doyle, J.F., Dynamic Response of Folded Plate Structures on a Massively Parallel Computer, *Journal of Computers and Structures*, **54**, pp. 521-529, 1995.
- [11] Crighton, D.G., The 1988 Rayleigh Medal Lecture: Fluid Loading — The Interaction between Sound and Vibration, *Journal of Sound and Vibration*, **133**(1), pp. 1-27, 1989.
- [12] Junger, M.C. and Feit, D., *Sound, Structures, and their Interaction*, MIT Press, Cambridge, 1986.
- [13] Bilodeau, B.A. and Doyle, J.F., Acoustic Radiation from Folded Plate Structures: The External Problem, *Journal of Sound and Vibration*, *submitted*, 1997.

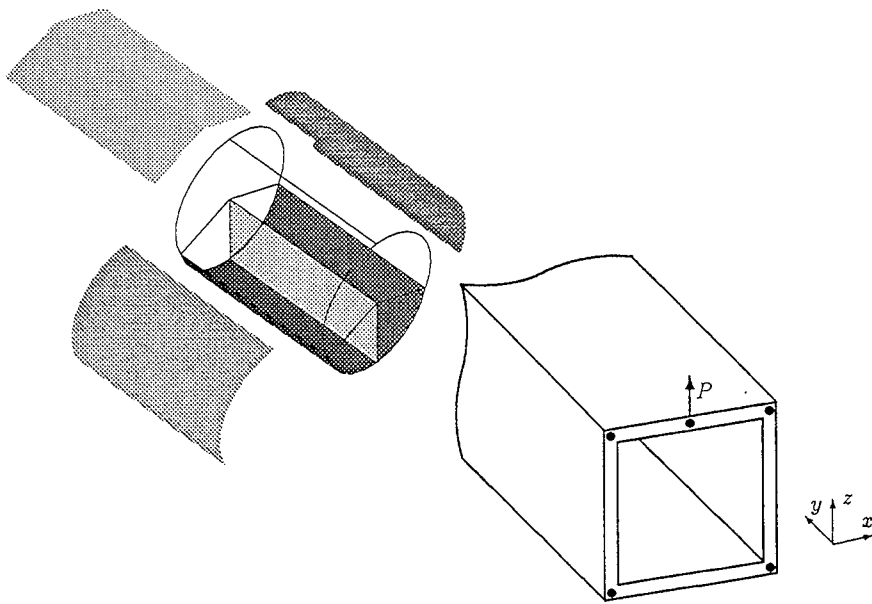


Figure 1: Complex multi-celled thin-walled structures modeled as a collection of flat and curved extended elements.

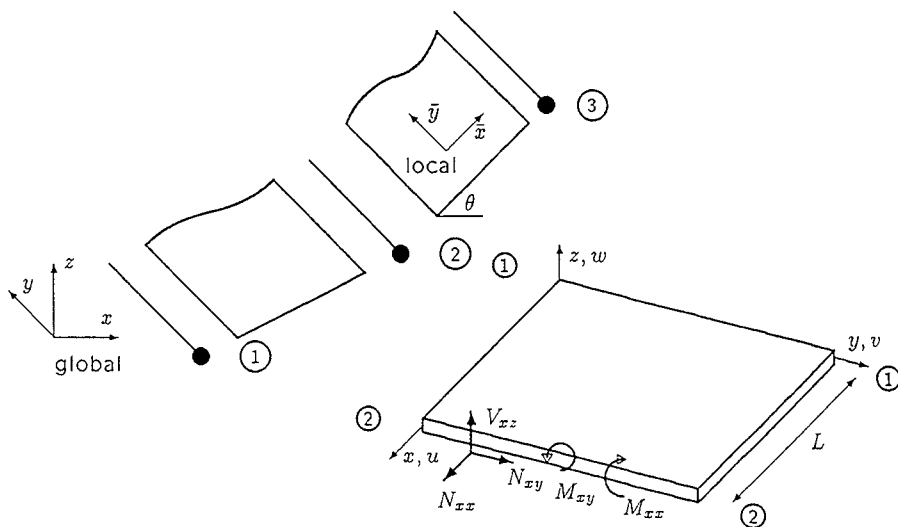


Figure 2: Assemblage procedure in global coordinates (left) for elements (right) showing the degrees of freedom in local coordinates.

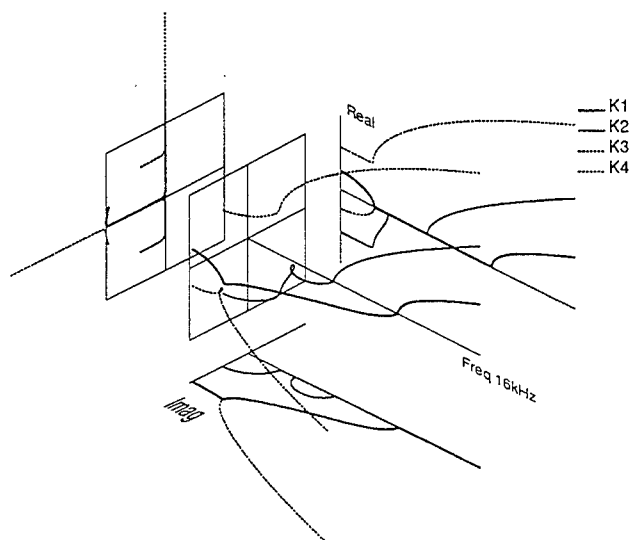


Figure 3: Spectrum relations $k_j h$ for a shell segment with $R = 254 \text{ mm}$, $h = 25.4 \text{ mm}$, and $m = 40$.

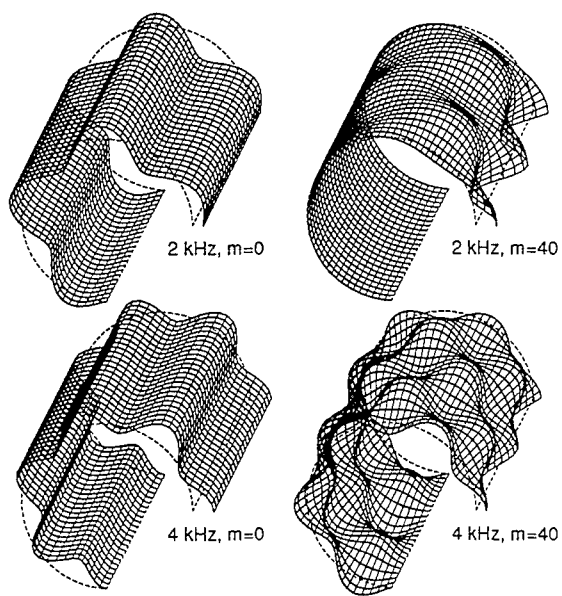


Figure 4: Sample of shape functions for a 270° shell segment.

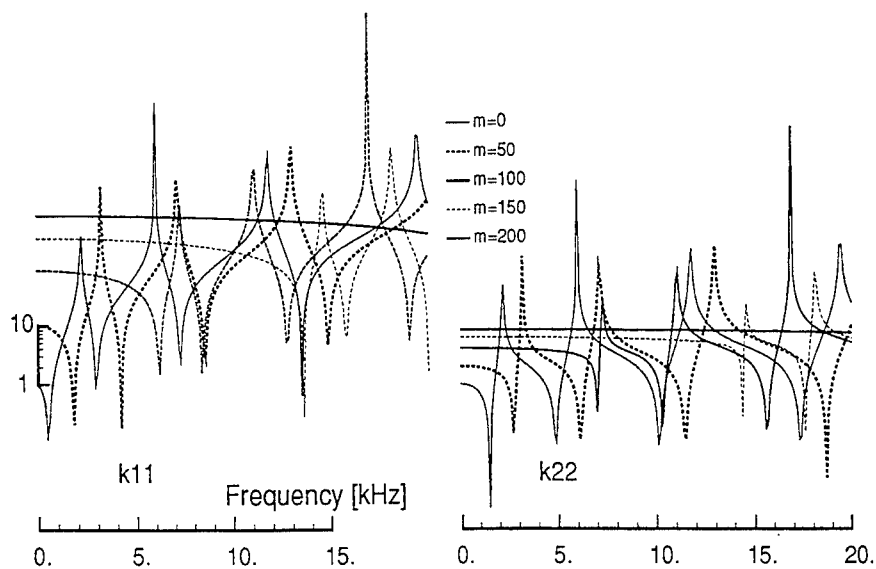


Figure 5: Dynamic stiffness for $\bar{k}_{11}/(12D/L^3)$ and $\bar{k}_{22}/(4D/L^3)$ for different values of m .

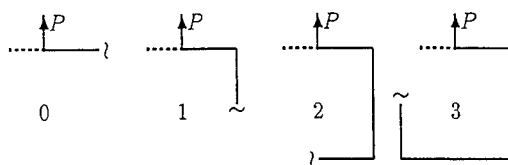


Figure 6: Folded plate sequence geometries. The structures are symmetric.

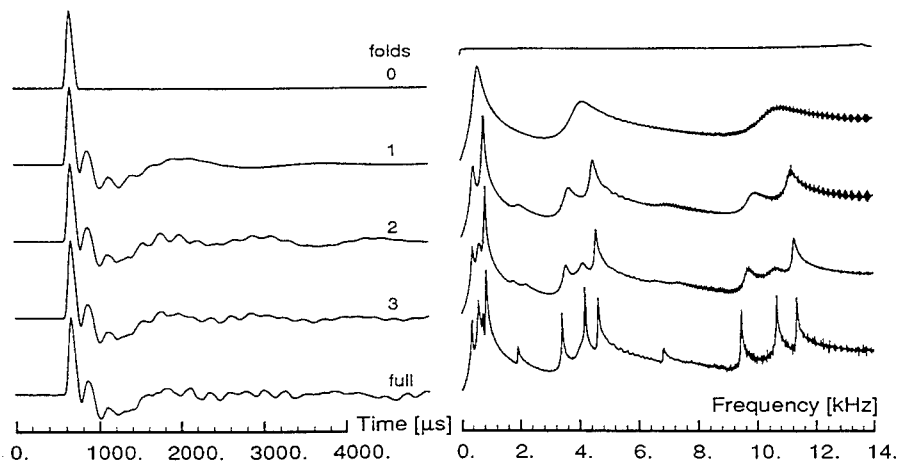


Figure 7: The evolution of structural resonances at the impact site. (a) Time responses, $\dot{w}(t)$, (b) system frequency response $|\hat{G}|$.

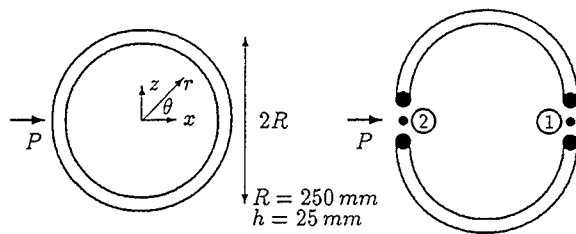


Figure 8: Geometry for impacted circular cylinder.

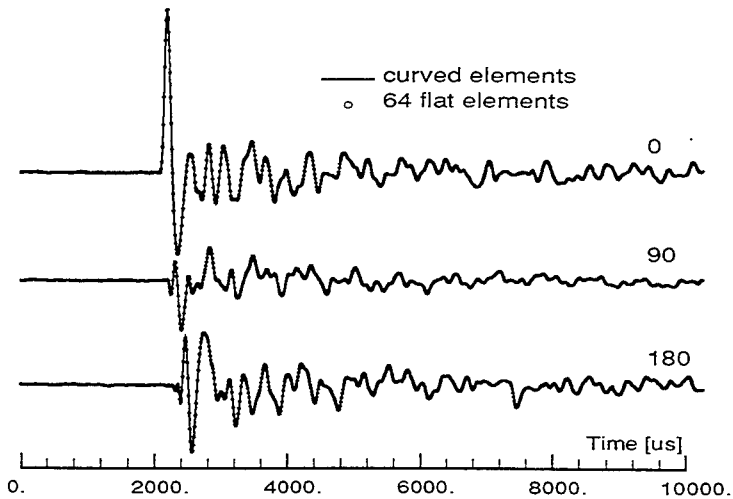


Figure 9: Velocity reconstructions for the point excitation of a closed cylinder.

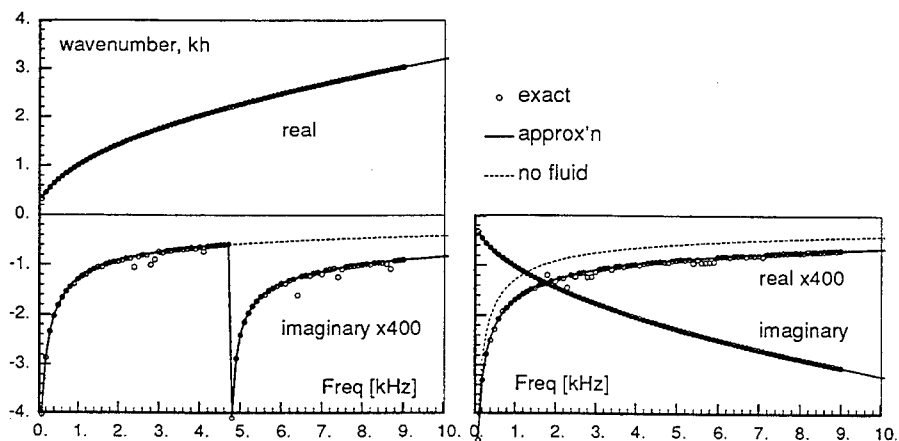


Figure 10: Wavenumber behavior for an aluminum plate in air. Left is $k_1(\omega)$, right is $k_2(\omega)$.

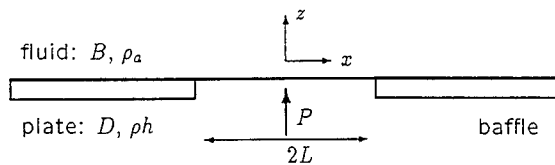


Figure 11: Geometry of the finite plate baffled to infinity.

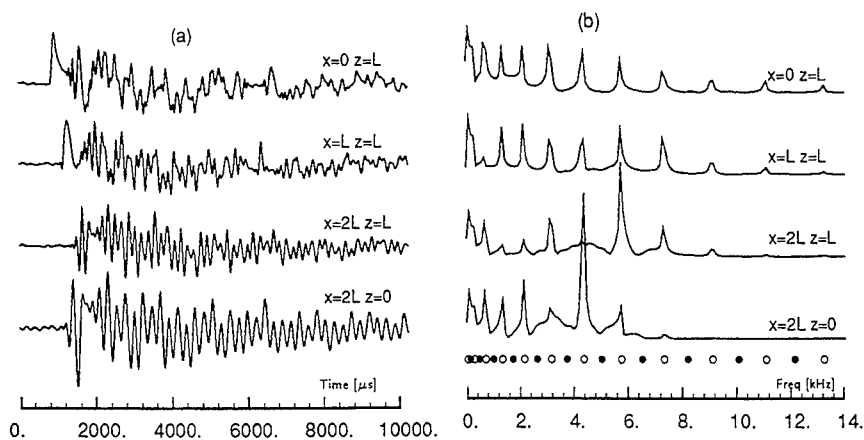


Figure 12: Time and frequency domain fluid responses for an impacted aluminum plate of length $2L$.

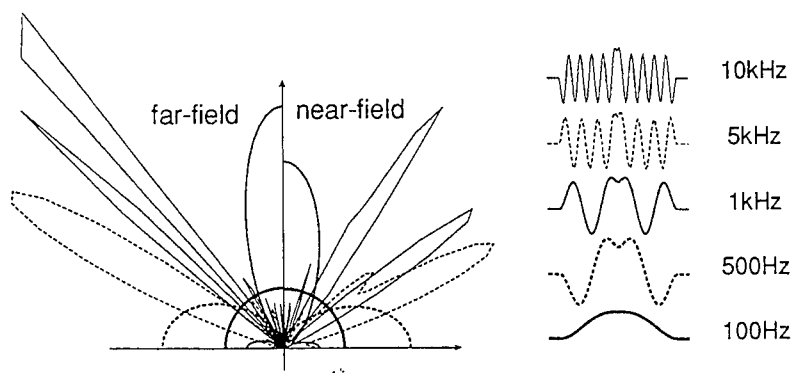


Figure 13: Directivity patterns for impacted finite plate. Also shown are the plate shapes at each frequency.

FINITE ELEMENT ANALYSIS OF ADAPTIVE LAMINATED SHELL VIBRATION

G.I.Lvov, V.V. Ovcharenko

Kharkov State Polytechnical University, The Chair of Dynamics and
Strength of Machines, Kharkov 310002, Frunze St. 21, Ukraine.

Laminated composite shells with piezoelectric layers and rigid filler are considered in this paper. For such shells the kinematic model is plotted on the basis of the model of shells with the broken normal and piezoelectric model deduced from the electromechanical model of three-dimensional piezoelectric body and variational equations of movement are received. The finite element analysis of free and forced vibration of laminated composite shells with the use of piezomaterials is conducted.

1. INTRODUCTION.

The adaptive structures, using in engineering in recent years, attract the large attention of engineers and researchers of different countries. These structures possess increased liveability, allow to reduce considerably noise affects, can realise the control of damages and have still a number of advantages in comparison with usual structures. The area of application of adaptive structures is extraordinary high: from space high precision structures to devices of noise suppression in passenger planes. Now, significant interest is manifested to the distributed sensors and actuators in the capacity of which may serve the layers from the adaptive materials built-in in the structure (laminated plate or shell). Under rather great choice of adaptive materials preference is often given to the piezoelectric materials (piezoelectric ceramics and piezopolymers) in connection with the fact that they can perform both sensitive and actuative functions relatively easy.

In 1967, Eer Nisse and Holland [3] cast the equation of motion of piezoelectric shells in variational form and introduced a Ritz approximation for piezoelectric shells. The finite element method has also been extensively used to solve the problems involving piezoelectric media, (Allik and Hughes [4], Naillon et al. [5] and Osiergaard and Pawlak [6]). Tzou [7,8] has completed several studies on piezoelectric shells and has also complied the basic elements of thin piezoelectric shell theory.

In this study, approximate theory is developed for the analysis of laminated composite shells that contain piezoelectric layers and rigid filler.

The theory developed herein explicitly represent the coupled relationship between the elastic and electrical variables as included in the linear theory of piezoelectricity.

2. THE KINEMATIC MODEL.

In this paper the gentle laminated shell, which consists of rigid filler, non-piezoelectric and piezoelectric layers is considered (see Fig. 1). Here it is given the derivation of the equations on the basis of equations for the shells with the broken normal. At construction the equations for the filler the hypothesis about incompressibility of the material in the direction of the axle x^3 and the hypothesis about noncurving of the normal at deformation, i.e. stress shears are distributed uniformly according to the thickness of the filler, are used. For the other layers the Kirchhoff-Love's hypotheses are used.

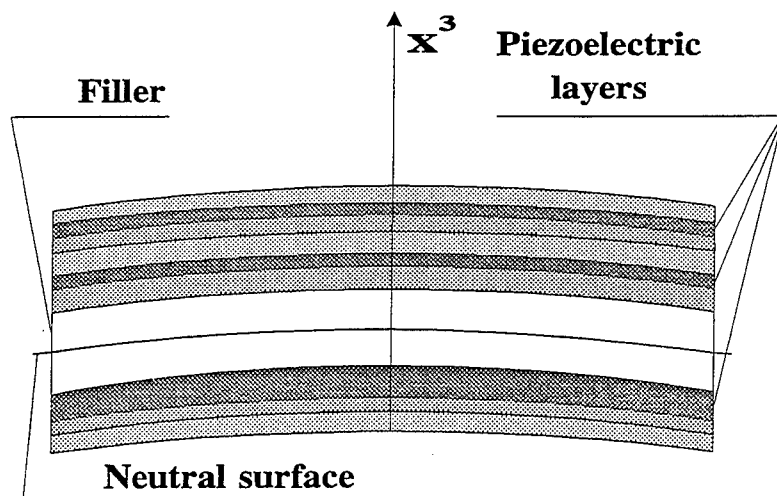


Fig. 1

Laminated composite shell, quantity of layers in which is n , is considered. The coordinate x^3 for bottom limited surface of κ -th layer is equal $z_{\kappa-1}$, and for top limited surface - z_{κ} . Neutral surface of the studied shell in the initial non-deformed state is assigned with the help of the material curvilinear coordinates x^i (here and subsequently $i, j, k, l = 1..2$) by the parametric equation $R_0 = R_0(x^1, x^2)$ and the displacements vector of the points of middle surface $U = U(x^1, x^2)$.

To determine mechanical displacements and deformations it will be necessary to represent the mechanical displacements vector in the local basis of the curvilinear coordinates system:

$$U = u_k r^k + w r^3 = u^k r_k + w r^3$$

$$r_k = \frac{\partial R_0}{\partial x^k} \quad (1)$$

where u_k , u^k are covariant and contravariant tangential components of the vector U , w is deflection, r_k , r^k are coordinate vectors of the main and mutual basis of the local curvilinear system of coordinates, m is normal unit vector of non-deformed neutral surface.

The mechanical displacements vector for the filler in accordance with the adopted kinematic model has a form of

$$U^m = U + x^3 \gamma \quad (2)$$

where the top index for mechanical displacements, deformations, potential and intensity of electrical field, and bottom index for efforts and moments here and subsequently indicates the layer number (m - for the filler) and γ is turn vector of the normal element in the filler.

The deformation of the transversal shear in filler is connected with the mechanical displacements by means of nonlinear relationship:

$$\varepsilon_{i3}^m = \frac{1}{2} (\gamma_i + w_{,i}) \quad (3)$$

To simplify the subsequent expressions vector α is introduced which covariant components $\alpha_i = 2\varepsilon_{i3}^m = \gamma_i + w_{,i}$. Expressing the turn vector of the normal element in the filler γ through the vector α and substituting it into the expression for filler mechanical displacements vector we have for tangential components of the filler mechanical displacements vector:

$$u_i^m = u_i + \alpha_i x^3 - w_{,i} x^3 \quad (4)$$

For other layers tangential components of the mechanical displacement vector will be noted by the following way:

$$\begin{aligned} u_i^{\text{hi}} &= u_i + c\alpha_i - w_{,i}x^3 \\ u_i^{\text{lo}} &= u_i - c\alpha_i - w_{,i}x^3 \end{aligned} \quad (5)$$

Where the index hi means the numbers of layers from $m + 1$ to n , and lo - numbers of layers from 1 to $m-1$.

Then the deformations will equal

$$\begin{aligned} e_{ij}^m &= e_{ij} + \alpha_{ij}x^3 + \chi_{ij}x^3 \\ e_{ij}^{\text{hi}} &= e_{ij} + c\alpha_{ij} + \chi_{ij}x^3 \\ e_{ij}^{\text{lo}} &= e_{ij} - c\alpha_{ij} + \chi_{ij}x^3 \end{aligned} \quad (6)$$

where

$$e_{ij} = \frac{1}{2}(u_{i,j} + u_{j,i}) - b_{ij}w; \quad \alpha_{ij} = \frac{1}{2}(\alpha_{i,j} + \alpha_{j,i}); \quad \chi_{ij} = -w_{,ij}. \quad (7)$$

And b_{ij} are components for the second square-law form of the initial surface.

To obtain constitutive laws connecting efforts and moments in the layers with the deformation of the middle surface it is necessary to introduce generalised efforts and moments express them by means of the efforts and moments in the shell layers. It will be required for these purposes to express the variation of the potential energy of the internal stresses in the shell both through efforts and moments in separate layers and through generalised efforts and moments.

The variation of the potential energy if the internal shell stresses with regard for the shear in the filler may be written the following way:

$$\begin{aligned} \int_V \delta W_S dV &= \iint \left[\int_{z_{m-1}}^{z_m} \sigma^{i3} \delta e_{i3} dx^3 + \sum_{\kappa=1}^n \int_{z_{\kappa-1}}^{z_{\kappa}} \sigma^{ij} \delta e_{ij} dx^3 \right] dx^1 dx^2 = \\ &= \iint (T^{ij} \delta e_{ij} + H^{ij} \delta \alpha_{ij} + M^{ij} \delta \chi_{ij} + Q^i \delta \alpha_i) dx^1 dx^2 \end{aligned} \quad (8)$$

here double integral is extended to all the initial surface.

Proceeding from the expression for the variation of potential energy of the internal stresses the generalised efforts and moments are determined by the next formulae:

$$\begin{aligned} T^{ij} &= \sum_{\kappa=1}^n T_{\kappa}^{ij}; \quad M^{ij} = \sum_{\kappa=1}^n M_{\kappa}^{ij}; \\ H^{ij} &= M_m^{ij} + c \left(\sum_{\kappa=m+1}^n T_{\kappa}^{ij} - \sum_{\kappa=1}^{m-1} T_{\kappa}^{ij} \right); \\ Q^i &= \int_{z_{m-1}}^{z_m} \sigma^{i3} dx^3 = 2C_m^{i3kl} e_{kl} + 4C_m^{i3k3} \alpha_k. \end{aligned} \quad (9)$$

where

$$T_{\kappa}^{ij} = \int_{z_{\kappa-1}}^{z_{\kappa}} \sigma^{ij} dx^3; \quad M_{\kappa}^{ij} = \int_{z_{\kappa-1}}^{z_{\kappa}} \sigma^{ij} x^3 dx^3 \quad (10)$$

Let us receive the variational equation of movement for integrated efforts and moments of the shell with accounting of mechanical boundary conditions, expressing deformations through the mechanical displacements and shear of the neutral surface:

$$\begin{aligned} \int_V \delta W_S dV &= - \iint \left\{ T^{ij}_{,j} \delta u_i + (H^{ij}_{,j} - Q^i) \delta \alpha_i + \right. \\ &\quad \left. (M^{ij}_{,ij} + T^{ij} b_{ij} + T^{ij} w_{,ij} + T^{ij}_{,j} w_{,i}) \delta w \right\} dx^1 dx^2 + \\ &+ \iint \left\{ T^{ij} \delta u_i + H^{ij} \delta \alpha_i + (M^{ij}_{,i} + T^{ij} w_{,i}) \delta w - M^{ij} \delta w_{,i} \right\}_{,j} dx^1 dx^2 \end{aligned} \quad (11)$$

Noting the variation of the work of the external forces δA_e , variation of the work of the inertia forces δA_e and substituting it into the equation:

$$\delta A_e + \delta A_i - \delta \Pi = 0 \quad (12)$$

we obtain equilibrium equation and mechanical boundary conditions.

The variation of the work of the external forces for the shell is a sum of the variation of the work of the external surface load δA_1 and the variation of the boundary forces δA_2 . Let's note the variation of the work

of the external surface load:

$$\delta A_{e1} = \iint (p^i \delta u_i + q \delta w) dx^1 dx^2 \quad (13)$$

Variation of the boundary forces δA_2 is noted in dependence on form of contour. Variation of the work of the inertia forces δA_e can be submitted as follows:

$$\delta A_i = - \iint \rho \left(\frac{\partial u^i}{\partial t} \delta u_i + \frac{\partial w}{\partial t} \delta w \right) dx^1 dx^2 \quad (14)$$

where ρ - weigh of square meter of laminated composite shell.

Then the variational equation of movement of considered shell may be written so:

$$\begin{aligned} & \iint \rho \left(\frac{\partial u^i}{\partial t} \delta u_i + \frac{\partial w}{\partial t} \delta w \right) dx^1 dx^2 - \\ & - \iint \left\{ T^{ij}_{,j} \delta u_i + (H^{ij}_{,j} - Q^i) \delta \alpha_i + \right. \\ & \left. (M^{ij}_{,ij} + T^{ij} b_{ij} + T^{ij} w_{,ij} + T^{ij}_{,j} w_{,i}) \delta w \right\} dx^1 dx^2 + \\ & + \iint \left\{ T^{ij} \delta u_i + H^{ij} \delta \alpha_i + (M^{ij}_{,i} + T^{ij} w_{,i}) \delta w - M^{ij} \delta w_{,i} \right\}_{,j} dx^1 dx^2 = \\ & = \iint (p^i \delta u_i + q \delta w) dx^1 dx^2 + \delta A_{e2} \end{aligned} \quad (15)$$

The variational equation (15) will be hereinafter used for substantiation of finite element analysis of free and forced vibration of laminated composite shell with piezolayers.

3. PIEZOELECTRIC MODEL.

Kirchoff-Love's hypotheses are used for piezoelectric layers. It is not difficult to prove that if piezoelectric layer is sufficiently thin and Kirchoff-Love's hypotheses are performed for it then the potential and intensity of the electrical field will be linearly distributed in the layer thickness:

$$E_p = \zeta_p + \xi_p x^3; \quad \phi = \varphi + \psi x^3, \quad (16)$$

here and subsequently $p, q = 1..3$.

The connection between the intensity of the electrical field and potential is noted by the following way:

$$E_p = -\phi_{,p} \Rightarrow \begin{matrix} \zeta_i = -\phi_{,i}; & \zeta_3 = -\psi; \\ \xi_i = -\psi_{,i}; & \xi_3 = 0. \end{matrix} \quad (17)$$

It is obviously that the electrical displacements will be linearly distributed in the thickness of the layer, i.e. it will be possible to change it by the electrical "efforts" and "moments" statically equivalent. It is important to underline that electrical efforts and moments should be introduced by connect the electrical displacements distributed in the thickness with the deformation of the middle surface. For these purposes lets note the variation of the potential energy of the electrical displacements of the internal electrical field in the piezoelectric layer:

$$\begin{aligned} \int_V \delta W_D dV &= \iiint D^p \delta E_p dx^1 dx^2 dx^3 = \\ &= \iiint \left(D^p dx^3 \delta \zeta_p + \int D^p x^3 dx^3 \delta \xi_p \right) dx^1 dx^2 = \\ &= \iint \left(\Xi^p \delta \zeta_p + \Theta^p \delta \xi_p \right) dx^1 dx^2 \end{aligned} \quad (18)$$

Hence electrical efforts and moments will be written in the same way as mechanical efforts and moments:

$$\Xi^p = \int D^p dx^3; \quad \Theta^p = \int D^p x^3 dx^3. \quad (19)$$

To obtain Maxwell-Gauss's variational equation for electrical efforts and moments of the piezoelectric layer, with accounting of the boundary conditions, it is necessary to transform the expression for the variation of the potential energy of the electrical displacements of the internal electrical field in the layer expressing the intensity of the electrical field by means of the potential. So, transforming the expression (18) we obtain:

$$\begin{aligned} \int_V \delta W_D dV &= \iint \left(\Xi^p \delta \zeta_p + \Theta^p \delta \xi_p \right) dx^1 dx^2 = \\ &= -\iint \left(\Xi^i \delta \phi + \Theta^i \delta \psi \right)_{,i} dx^1 dx^2 + \\ &+ \iint \left(\Xi^i_{,i} \delta \phi + \left(\Theta^i_{,i} + \Xi^3 \right) \delta \psi \right) dx^1 dx^2 \end{aligned} \quad (20)$$

We consider the case, when external electrical field is not applied to piezoelectric layers. It is also assumed that the external electrical field is not applied to the boundary of piezoelectric layers. So, the work of the external electrical field equals zero. Hence the variational equilibrium equation will be noted in the following way:

$$\begin{aligned} & \iint \left(\Xi^i \delta \varphi + \Theta^i \delta \psi \right)_{,i} dx^1 dx^2 - \\ & - \iint \left(\Xi^i_{,i} \delta \varphi + \left(\Theta^i_{,i} + \Xi^3 \right) \delta \psi \right) dx^1 dx^2 = 0 \end{aligned} \quad (21)$$

The variational equations (15) and (21) are the main equations for finite element analysis of free and forced vibration of laminated composite shell with piezolayers.

4. FINITE ELEMENT ANALYSIS.

To draw the finite element model it is necessary to note the system of variational equations, which represents the association of equations (15) and (21):

$$\left\{ \begin{aligned} & \iint \rho \left(\frac{\partial u^i}{\partial t} \delta u_i + \frac{\partial w}{\partial t} \delta w \right) dx^1 dx^2 - \\ & - \iint \left\{ T^{ij}_{,j} \delta u_i + \left(H^{ij}_{,j} - Q^i \right) \delta \alpha_i + \right. \\ & + \left(M^{ij}_{,ij} + T^{ij} b_{ij} + p^i w_{,i} \right) \delta w \left. \right\} dx^1 dx^2 + \\ & + \iint \left\{ T^{ij} \delta u_i + H^{ij} \delta \alpha_i + \right. \\ & + \left. \left(M^{ij}_{,i} + T^{ij} w_{,i} \right) \delta w - M^{ij} \delta w_{,i} \right\}_{,j} dx^1 dx^2 = \\ & = \iint \left(p^i \delta u_i + q \delta w \right) dx^1 dx^2 + \delta A_{e2} \\ & \iint \left(\Xi^i \delta \varphi + \Theta^i \delta \psi \right)_{,i} dx^1 dx^2 - \\ & - \iint \left(\Xi^i_{,i} \delta \varphi + \left(\Theta^i_{,i} + \Xi^3 \right) \delta \psi \right) dx^1 dx^2 = 0 \end{aligned} \right. \quad (22)$$

Bending deformation for chosen model of laminated composite shell is determined through the second derivative from deflection. Therefore for its approximation is necessary to use a polynom not less than second order.

Also, the finite element mechanical displacements depend on the covariant derivative from deflection, according to kinematic Kirchhoff-Love's hypothesis. Therefore for the maintenance of appropriate to physical sense of smooth of change of displacements on interelement borders, it is necessary to include in the finite element node's parameters not only the deflection, but also the covariant derivative from deflection by coordinates x^1, x^2 . Hence, Eremite's approximation has to be applied. The additional complexity is that usually to simplify determination of basic functions each finite element has own orientation of the local coordinate system. For the maintenance of cinematic connection of adjacent finite elements is necessary to include in node parameters the covariant derivative from deflection by coordinates of some uniform for all finite elements' coordinate system. In these purposes, and to simplify the ensembling of the global stiffness matrix, it is necessary to define the basic functions as follows:

We consider the finite element of the shell with n units. Let we approximate displacements within the limits of finite element by following function:

$$U = \sum_{i=1}^n a_i f_i \quad (23)$$

where a_i - are numerical coefficients, and f_i - are the linearly independent functions from coordinates in uniform for all finite elements' coordinates system.

We receive the system from n linear equations, using the substitution of node significance of coordinates and displacements in equation (23). The following significance a_i is the decision of that system:

$$a_i = \sum_{j=1}^n (-1)^{i+j} \frac{\Delta f_{ij}^*}{\Delta f^*} u_j \quad (24)$$

where u_j - node significance of mechanical displacements, Δf^* - determinant of matrix f^* , obtained from node significance of functions f_i , and Δf_{ij}^* - determinants of main minors of matrix f^* , received by deletions i -th column and j -th row.

Hence, the required basic functions may be noted as follows:

$$N_j = \sum_{i=1}^n (-1)^{i+j} \frac{\Delta f_{ij}^*}{\Delta f^*} f_i \quad (25)$$

Then, we can write the approximations of neutral surface's mechanical displacements and the approximations electrical potential in piezolayers, using founded basic functions:

$$\begin{aligned} u_1 &= \sum_{i=1}^n N_i u_{1i}^*; \quad u_2 = \sum_{i=1}^n N_i u_{2i}^*; \\ w &= \sum_{i=1}^n N_i^* w_i^* + \sum_{i=1}^n M_i^* (w_{,1})_i^* + \sum_{i=1}^n L_i^* (w_{,2})_i^*; \\ \phi &= \sum_{i=1}^n N_i \phi_i^*; \end{aligned} \quad (26)$$

where u_{1i}^* , u_{2i}^* and w_i^* - node significance of appropriate displacements, $(w_{,1})_i^*$ and $(w_{,2})_i^*$ - node significance covariant derivatives from deflection, and ϕ_i^* - node significance of the potential of electrical field.

Approximations of deformations and intensity of electrical field can be found from expressions (7), (17) and (26). Further, we receive approximations for mechanical and electrical efforts and moment from constitutive equations. Let we assume also that variations of neutral surface's displacements and variations of electrical potential can be approximated by the same basic functions, that the appropriate displacements and electrical potential and substitute approximation for mechanical and electrical efforts and moments in systems of variational equations (22). Then, we obtain the system of equations:

$$[K - \omega^2 M] \{u\} = \{Q\} \quad (27)$$

where K - stiffness matrix of finite element, M - matrix of weights, Q - vector of loads, ω - vibration frequency, and u - vector of displacements.

For the case of forced vibration of laminated composite shell the frequency ω is known. Therefore the system (27) can be resolved concerning to amplitudes of node significance of displacements and potential of electrical field.

In the case of free vibration of the shell the own frequencies can be found from condition of equality to zero of determinant of system (27):

$$\det[K - \omega^2 M] = 0 \quad (28)$$

The own forms of vibration of considered shell can be found from system of equations (27), taking into account the obtained significance of own frequencies.

5. CONCLUSION.

So, stated work conducts the most general analysis of vibration of laminated composite shells with piezolayers. The kinematic, piezoelectric and general finite element models of the considered shell are constructed. The purpose of the work consist in introduction of the rigid filler in the traditionally considered laminated adaptive shell. We assume, that the offered design of adaptive shell finds the wide application. One of such applications is the reflector of the space structures. At present, on the base of the stated finite element model, the programme pack for behaviour simulation of such reflector, which represent laminated composite shells with piezolayers and rigid filler is developing.

6. REFERENCE.

1. Burfoot, J.C., FERROELECTRICS An introduction to the physical principles, Princeton, New Jersey Toronto, 1967, 352p.
2. Jaffe, B., Cook, W.R., Jaffe, Piezoelectric ceramics, Academic Press, London & New York, 1971, 288p.
3. R. Holland and E.P. Eer Nisse, Variational evalution of admittance of multielectroded three-dimensional piezoelectric structures, IEEE Transactions on Sonics and Ultrasonics 15, 1968, pp. 119-132.
4. H. Allik and T.J. Hughes, Finite element for piezoelectric vibration, International Journal for Numerical Methods in Engineering 2, 1970, pp. 151-157.

5. M. Naillon, R.H. Coursant and F. Besnier, Analysis of piezoelectric structures by finite element method, *Acta Electronica* 25, 1983, pp. 341-362.
6. D.F. Ostergaard and T.P. Pawlak, Three-dimensional finite element for analyzing piezoelectric structures, *IEEE Ultrasonic Symposium*, 1986, pp. 639-644.
7. H.S. Tzou and M. Gadre, Theoretical analysis of a multi-layered thin shell coupled with piezoelectric shell actuators for distributed vibrations control, *Journal of Sound and Vibration* 132, 1989, pp. 433-450.
8. H.S. Tzou and C.I. Tseng, Distributed piezoelectric sensor/actuator design for dynamic measurement/control of distributed parameter systems: a piezoelectric finite element approach, *Journal of sound and Vibration* 138, 1990, pp. 17-34.
9. Lammering, R., Structural Analysis and Optimization of Adaptive Structures by use of the Finite Element Method, *Proceedings 531, AGARD, Conference on Smart Structures for Aircraft and Spacecraft*, pp. 23.1-23.11.
10. Baier, H., On Shape Control of Precision Structures: Concepts, Analysis, Technology, *Proceedings, SPIE 1995 Conference on Smart Structures and Materials, San Diego, California, Feb. 27 - March 3, Vol. 2443*, pp. 91-138.
9. Kim, S.J., Yu, J.Y., Adaptive design of laminated composite plate by using anisotropic piezo polymers, *Proceedings, SPIE 1995 Conference on Smart Structures and Materials, San Diego, California, Feb. 27 - March 3, Vol. 2443*, pp. 385-395.
10. Shieh, R.S., Multiaxial Piezoelectric Beam Sensor/Actuator Theory and Design for 3-D Structural Vibration Control, *Archives of Mechanics, Warszawa 1993, Vol. 47, Session J*, pp. 647-661.
11. Li, Z., Bainum, P.M., Vibration Control of Flexible Spacecraft Integrating a Momentum Exchange Controller and a Distributed Piezoelectric Actuator, *Archives of Mechanics, Warszawa 1993, Vol. 47, Session G*, pp. 402-415.
12. Song, O., Librescu, L., Rogers, C.A., Static Aeroelasticity Behavior of Adaptive Aircraft Wing Structures as Composite Thin-Walled Beams, *Proceedings 471, AGARD, Conference on Smart Structures for Aircraft and Spacecraft*, pp. 46-55.

-
13. Yang, J.S., Batra, R.C., Liang ,X.Q., The Vibration of a Simply Supported Rectangular Elastic Plate due to Piezoelectric Actuators, Proceedings, SPIE 1995 Conference on Smart Structures and Materials, San Diego, California, Feb. 27 - March 3, Vol. 2442, pp. 168-181.
 14. D'Cruz, J., Global Multivariable Vibration Control with Distributed Piezoceramic Actuators, Journal of Intelligent Material Systems and Structures, Vol. 6, May 1995, pp. 419-423.
 15. Yu,Y.Y., Some Recent Advances in Linear and Nonlinear Dynamical Modeling of Elastic and Piezoelectric Plates, Journal of Intelligent Material Systems and Structures, Vol. 6, March 1995, pp. 237-254.

NUMERICAL METHODS I

ANALYSIS OF INFLUENCE OF TECHNOLOGICAL AND DESIGN DISTORTIONS OF ROTATIONALLY PERIODIC SYMMETRY ON FORCED RESPONSE CHARACTERISTICS AND STRESS SCATTERING OF BLADED DISKS

E.P. Petrov

SSTC Research Fellow of the University of Liege, Belgium^{*}

1 INTRODUCTION

Small distinctions of blade characteristics in bladed disks of axial flow turbomachines arise inevitably during their manufacturing and assembling on the disks. Moreover, sometimes the designs of linkage blades by shrouds or wires are used that distort periodic symmetry of the system. These symmetry distortions provide appearance of scattering of amplitudes of stresses for different blades and, more important, they have essential influence on maximal stress levels upon forced vibration. Importance of vibration analysis of mistuned blade disks for practice of turbomachinery stipulated a great number of papers devoted to this problem. Up to now the most widely used models of blades are single-degree-of-freedom (SDOF) models (e.g. see [1]-[4]). These models are good enough for qualitative analysis of occurrences arising in disordered cyclic symmetry systems but when we try to use SDOF models in analysis of practical bladed disks and to obtain answers for questions of type: whether this or other kind of mistuning leads to increasing or decreasing of stress levels for the considered bladed disk and vibration excitation, how vibration stresses are distributed among blades, where we need to maintain transmitters for experimental testing of the bladed disk -- we are crossed with complete inadequacy SDOF models. The major difficulties that detained use more detailed models are: large number of degrees of freedom in the whole system, great calculation expenses and complexity to support accuracy and stability of computations of the systems that have very closely spaced resonance frequencies and for which vibration of blades may be coupled very slightly for some of their families.

In the paper an effective technique is proposed, which allows to overcome these difficulties and to calculate forced and natural vibrations of practical bladed disks with any mistuning and manners of blade connections by shrouds. Multi-degrees-of-freedom (MDOF) models are used. Centrifugal and Coriolis forces, elasticity of blade-disk and blade-shroud joints, peculiarities of vibration excitation and damping are accounted. The technique uses finite element method, transfer matrix method and multilevel substructuring and allows to consider models containing hundreds of thousands degrees of freedoms with preservation accuracy of computations.

^{*} On leave from Kharkov State Polytechnic University, The Ukraine

2 DISTORTIONS OF ROTATIONALLY PERIODIC SYMMETRY OF BLADED DISKS

Bladed disks are often designed to have rotationally periodic symmetry. This kind of symmetry is characterized by invariance of characteristics of a bladed disk when it rotates for the angles that are multipliers of $\alpha = 2\pi/N$ (N - total number of blades). If bladed disks are actually made to have such kind of symmetry then under rotating loading, which occurs really upon service, all blades have equal amplitudes. However even small distortions of rotationally periodic symmetry lead to appearance of distinctions between vibration amplitudes, that may be varied very much from blade to blade, and moreover, stress levels are very sensitive to such distinctions.

There are two major reasons of distortions of rotationally periodic symmetry of bladed disks:

1) Scatters of geometry shape of blades that are connected with manufacturing and assembling inaccuracies. These scatters are small and inevitable as a rule. Their magnitudes lie inside manufacturing tolerances.

2) Use of special design of a bladed disk or change of its initial design during operating service that distorts rotationally periodic symmetry or reduce its degree.

For the first case a few manners of description of scatters of blade geometry have been foreseen.

- If actual blade geometry may be measured for each blade of a bladed disk then individual geometry shape for each blade is used for analysis of a bladed disk.

- Measurement of actual shape and size for all blades is tedious. At turbomachinery plants the blade shape scattering is controlled often by measurement of frequencies for each blade from a manufactured set. The scattering is estimated by distinctions of lower natural frequencies of a single blade $f_1^{(j)}$ for j -th blade from the standard magnitude $f_1^{(0)}$. Since geometry of a pretwisted variable cross-section blade is usually described by geometry of a set of datum cross-sections the simulation of such mistuning is carried out by multiplication of sizes of all datum blade cross-sections for each j -th blade by a so-called mistuning parameter $\mu_j = f_1^{(j)} / f_1^{(0)}$. The cross-section shapes are assumed to be invariable. Owing that the cross-section characteristics used in equations for twisted beam may be recalculated using simple formulas: $A^{(j)} = \mu_j^2 A^{(0)}$; $J_x^{(j)} = \mu_j^4 J_x^{(0)}$; $J_{xr}^{(j)} = \mu_j^5 J_{xr}^{(0)}$; $J_z^{(j)} = \mu_j^6 J_z^{(0)}$; $J_t^{(j)} = \mu_j^4 J_t^{(0)}$; $e_x^{(j)} = \mu_j e_x^{(0)}$, etc., where $A(z)$ - area, $J_x(z)$, $J_y(z)$, $J_{xy}(z)$, $J_p(z)$, $J_{xr}(z)$, $J_{yr}(z)$ - inertia moments of the section, $J_t(z)$ - moment of torsional stiffness; $e_x(z), e_y(z)$ - projections of distance between inertia and shear centers of the cross-section.

- If there is not deterministic information about distribution of mistuning among impeller blades but there is statistical one then random number generator is used to simulate the distribution. In the calculations the normal

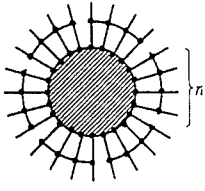
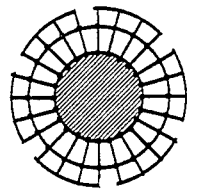
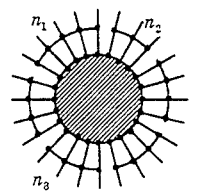
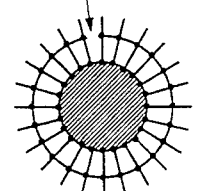
Gaussian distribution of mistuning with restrictions on range of admissible mistuning has been used. Its density of probability takes the form:

$$p(\mu) = \begin{cases} (\sigma_\mu \sqrt{2\pi})^{-1} \exp[-(\mu - 1)^2 / 2\sigma_\mu^2] & \text{for } |\mu - 1| \leq \delta\mu \\ 0 & \text{for } |\mu - 1| > \delta\mu \end{cases} \quad (1)$$

where $\delta\mu$ - maximal admissible distinction of blade frequency from standard one; σ_μ - deviation of mistuning distribution.

The second case of symmetry distortions or reduction appears: 1) due to special design when asymmetric schemes of blade connections by interblade linkage are used intentionally; 2) due to casual violation of contact between one or a few pairs of shrouded blades of a bladed disk during operating service. Some such schemes are shown in the Table 1.

Table 1. Design distortions of cyclic symmetry of a bladed disk.

equal packets of n blades in each	equal blade packets connected by circular linkage	different numbers of blades in packets	violation of interaction through shroud between a pair of blades
			
symmetry order $s = N/n$	symmetry order $s = N/n$	asymmetric system	asymmetric system

3 CALCULATION METHOD

3.1 Vibration excitation and damping

The vibration excitation is considered that is caused by nonhomogeneity of gas flow. It is accounted that loads are distributed inhomogeneously in circumferential and radial directions of the impeller. The distributed loads act on blades and they may be reduced to the resulting forces: axial forces $P_y(r, \varphi)$, tangential forces $P_x(r, \varphi)$ and torsion moment $P_\psi(r, \varphi)$ (r, φ - radial and circumferential coordinates). The vibrations are considered in the coordinate system that is coupled with the bladed disk rotating with angular velocity ω . Loading distribution along circumferential direction is expanded into Fourier series and takes the form:

$$P(r, \varphi, t) = P_0(r) + \sum_{k=1}^{\infty} P_k(r) e^{ik(\omega t + \varphi)} + \overline{P}_k(r) e^{-ik(\omega t + \varphi)}, \quad (2)$$

where $i = \sqrt{-1}$; $P_k = \{P_x^k(r), P_y^k(r), P_\psi^k(r)\}^T$ - vector-column of complex functions that describe varying of amplitudes and phases along the blade for k -th loading harmonic.

In some cases the kinematical vibration excitation of a bladed disk by rotor torsional vibration should be considered. In this case it is supposed that frequency ω_r and amplitude θ_0 of rotor vibration at the place of the attachment of the disk to the rotor are known. This kind of excitation may be considered as vibration excitation by inertia forces that arises during rotor rotation with torsional vibrations: $\theta = \theta_0 \cos \omega_r t - \omega t$. Transfer acceleration is expressed so: $\vec{a} = [\vec{\theta} \times \vec{r}] + [\vec{\theta} \times [\vec{\theta} \times \vec{r}]]$ and multiplication of the accelerations by material density allows to obtain excitation loading applied to unit volume. For a mistuned impeller such loading is inhomogeneous along impeller circumference.

The complex elasticity modulus $E = E_0(1 + i\psi_E/2\pi)$ and shear modulus $G = G_0(1 + i\psi_G/2\pi)$ are used to take into account damping in the material (ψ_E and ψ_G are damping factors for normal and shear strains accordingly). The forces of aerodynamic damping and blade interaction through flow are introduced by complex aerodynamic influence coefficients. These coefficients have been calculated in [5] upon consideration of flow through vibrating lattice of thin airfoils. The forces acting on each airfoil of j -th blade are expressed through blade vibration amplitudes:

$$R_\xi = \frac{1}{2} \rho_f V_f^2 c \sum_{j=-n_f}^{n_f} k_{j\xi}^{(\xi)} u_j(r) + k_{jy}^{(\xi)} v_j(r) + b k_{j\psi}^{(\xi)} \psi_j(r), \quad (3)$$

where u, v, ψ - airfoil displacements; $k_{j\xi}^{(\xi)}, k_{jy}^{(\xi)}, k_{j\psi}^{(\xi)}$ - aerodynamic influence coefficients, which are dependent on airfoil shape; ρ_f, V_f - density and speed of gas flow; b - characteristic size of airfoil; $\xi = x, y, \psi$ and $c=1$ (for $\xi = x, y$) or $c = b$ (for $\xi = \psi$); n_f - maximal number of blades that can interact through flow (often the interaction of neighboring blades may be accounted only).

3.2 Models and relations of major components of a bladed disk

A bladed disk consists of components of different vibration properties such as blades, disk, shrouds, blade-disk joints, etc. To calculate vibration of a bladed disk assembly precisely enough and to supply fast calculations of such complicated system as mistuned bladed disk a set of different models and methods has been developed that is aimed to obtain matrix relations as for the bladed disk components of and as for the whole assembly. Special attention has been devoted to ensure computational accuracy and stability.

3.2.1 Blade. A pretwisted variable cross-section beam model is used. Matrix relation of blade is calculated by transfer matrix method. To obtain expressions of transfer matrix components in the form of definite integrals

the blade is divided into elements and their masses are lumped. The number of elements is chosen large enough so that to supply accurate description of vibration properties for in considered wide frequency ranges.

The transfer matrix of blade element relates vibration parameters at the begin and at the end of n -th element:

$$X_{n+1} = L_n X_n + P_n, \quad (4)$$

where $X_n = \{u, v, w, \varphi, \theta, \psi; F_x, F_y, F_z, M_x, M_y, M_z\}^T = \{q, Q\}^T$ - vector column, which consists of complex amplitudes of linear u, v, w and angular φ, θ, ψ displacements; lateral F_x, F_y and longitudinal F_z forces; bending M_x, M_y and torsional M_z moments, L_n - transfer matrix; $P_n = \{p_q, p_Q\}^T$ - vector column of loading components. Recurrence of the relation (4) provides obtaining of the relation for whole blade or for any its part:

$$X_{n_e+1} = \left(\prod_{n=n_e}^1 L_n \right) X_1 + \sum_{j=1}^{n_e} \left(\prod_{n=n_e-j+1}^1 L_n \right) P_j, \quad (5)$$

where n_e - the number of elements in the blade or in a considered its part. Transfer matrices are calculated for all blades having different characteristics.

Matrix relation of a blading is obtained by using superelement approach and FEM procedure (see section 3.3). The superelements are chosen the parts of a blade that are divided by nodes of interblade linkage (see Table 1 and Fig.1). Degrees of freedom at blade-shroud and blade-disk joints are adopted as master degrees of freedom. To use finite element procedure the matrix relations for blade are transformed from the form of transfer matrix method (5) to the form that is usual in finite element method. Since size of the transfer matrix for whole blade is equal to size of matrix for single element there is not necessity to apply special procedure to exclude internal nodes. At this stage the boundary conditions at a blade top (if it is free): $Q_{j1} = 0$ and at blade-disk joints: $q_{j2} = A^{(j)} Q_{j2}$, (where $A^{(j)}$ - compliance matrix of clamping at a tail of j -th blade) allow to reduce number of master degrees of freedom in addition. The next relations are obtained:

- for blade part between two blade-shroud joints:

$$\begin{Bmatrix} Q_{j1} \\ Q_{j2} \end{Bmatrix} = \begin{bmatrix} -L_{12}^{-1} L_{11} & L_{12}^{-1} \\ -L_{21} - L_{22} L_{12}^{-1} L_{11} & L_{22} L_{12}^{-1} \end{bmatrix} \begin{Bmatrix} q_{j1} \\ q_{j2} \end{Bmatrix} + \begin{Bmatrix} -L_{12}^{-1} p_q \\ p_Q - L_{22} L_{12}^{-1} p_q \end{Bmatrix} \quad (6)$$

- for blade part containing free top:

$$Q_{j1} = L_{21} L_{11}^{-1} q_{j1} + (p_Q - L_{21} L_{11}^{-1} p_q) \quad (7)$$

- for blade part containing clamped tail:

$$Q_{j2} = (L_{12} - A^{(j)} L_{22})^{-1} (A^{(j)} L_{21} - L_{11}) q_{j2} + (L_{12} - A^{(j)} L_{22})^{-1} (A^{(j)} p_Q - p_q) \quad (8)$$

In these relations L_{ij} - are blocks of the blade transfer matrix introduced in (5).

3.2.2 Disk. A disk model is circular variable thickness plate that is subjected out-of-plane (flexural) and in-plane (longitudinal-torsional) vibrations. The following original technique has been developed to supply effective accounting of disk axial symmetry for obtaining its compliance matrix for all nodes of blades joining.

Owing to axial symmetry of the disk if loading varies in circumferential direction harmonically - $e^{im\varphi}$, then strains and stresses vary in the same form.

Disk vibrations may be described by ordinary differential equations in which the number of harmonic m is included as a parameter. Transfer matrix method is used to obtain disk matrix relations between vector-column of vibration parameters at outer r_b and at inner r_a radii of a disk:

$\tilde{X} = \{\tilde{u}, \tilde{v}, \tilde{w}, \tilde{\theta}, \tilde{T}_r, \tilde{N}_r, \tilde{V}_r, \tilde{M}_r\}^T = \{\tilde{q}, \tilde{Q}\}^T$ that vary harmonically along disk

circumference (here - \tilde{T}_r, \tilde{N}_r - tangential and radial forces, \tilde{V}_r - generalized Kirchhoff's transverse force, \tilde{M}_r - bending moment, all they are distributed along disk circumference and directed along its radius). Disk transfer matrix is calculated by multiplying transfer matrices of all elastic and inertia elements similar to relation (5). Elastic supports of the disk at a few given radii are accounted by transfer matrices of the disk supports if they are present. Since in-plane and out-plane vibrations of a single disk are disconnected they are considered separately upon calculation of a disk transfer matrix but for bladed disk assembly these kinds of disk vibration are coupled through blades and this fact is accounted in the technique.

The elasticity of attachment of the disk to rotor is accounted by the relation: $\tilde{q}_{r_a} = \tilde{A}_{r_a} \tilde{Q}_{r_a}$, where \tilde{A}_{r_a} - compliance matrix of disk attachment. This relation allows to express displacements through forces at the outer disk radius from relation of transfer matrix method:

$$\tilde{q}_{r_a} = \tilde{A}_m \tilde{Q}_{r_a} \quad (9)$$

where $\tilde{A}_m = (\tilde{l}_{12} + \tilde{l}_{11} \tilde{A}_{r_a})(\tilde{l}_{22} \tilde{A}_{r_a} + \tilde{l}_{22})^{-1}$ - wave dynamic compliance matrix for wave number m ; \tilde{l}_{ij} - blocks of disk transfer matrix.

The disk matrix relation is determined in the form that allows to express column vector $q_d = \{q_1, q_2, \dots, q_N\}^T$ of displacements at the nodes of blades joining to the disk (see Fig.1) through vector-column of forces $Q_d = \{Q_1, Q_2, \dots, Q_N\}^T$:

$$q_d = A_x(\Omega) Q_d, \quad (10)$$

where A_x - dynamic compliance matrix of the disk. To obtain matrix A_x the disk vibrations caused by forces of blade-disk interaction at blade-disk joints are considered. Distribution of these forces along circumference has the form:

$$Q(\varphi) = \sum_{j=1}^N Q_j \delta(\varphi - \alpha(j-1)), \quad (11)$$

where $\delta(\varphi)$ - Dirac's impulsive function; Q_j - vector column of forces at the place of joining of j -th blade. For displacements at any point of outer radius of the disk the following expression may be obtained by expanding distribution (11) into Fourier series and using relations (9) for each harmonic:

$$q(\varphi) = \frac{1}{2\pi r_0} \sum_{j=1}^N \left[\tilde{A}_0 + \sum_{m=1}^{\infty} e^{im(\varphi-\alpha(j-1))} \tilde{A}_m + e^{-im(\varphi-\alpha(j-1))} \tilde{A}_{-m} \right] Q_j. \quad (12)$$

From this relation the displacements at all disk-blade joints may be expressed in the required form (10) and the disk compliance matrix may be obtained:

$$A_z = \text{diag}\{A^{(1)}, A^{(2)}, \dots, A^{(N)}\} + \frac{1}{2\pi r_0} \sum_{m=-\infty}^{\infty} \lambda_m C_m^* \tilde{A}_m C_m \quad (13)$$

where $A^{(j)}$ - compliance matrix of blade-disk joints; * - symbol of Hermetian conjugation; $C = [I, Ie^{-m\alpha}, \dots, Ie^{-m(N-1)\alpha}]$; I - unit matrix; $\lambda_m = 0.5$ (for $m=0$) or 1 (for $m \neq 0$). It should be noted that although for determination A_z a set of impulsive functions is expanded in Fourier series, series in (13) converge very quickly due to sharp decreasing of wave disk compliance when m is risen.

3.2.3 Shrouds, wires and blade-disk joints. Depending on design of interblade linkage their different models are used such as curvilinear beam subjected to longitudinal-bending-torsional vibrations, plates of complex shape, three-dimensional solids. For blade-disk joints (fairtail, dovetail, etc.) finite element three-dimensional models of tens thousands of degrees of freedom and the developed in [6] technique are used to supply detailed description of intricate shapes of blade-disk and blade-shroud joints, different conditions on contact surfaces, large gradients of stresses. The proposed in [6] condensation technique allows to decrease size of matrix relations from thousands to small number without any essential simplifying assumptions and owing to that it allows to use such models even in vibration analysis of a mistuned bladed disk.

3.3 Calculation of a bladed disk assembly

Since minimization of computational expenses is vitally important requirement for analysis of mistuned bladed disks different algorithms have been developed for analysis of bladed disks of three kinds of structure. Examples of such kinds of bladed disks and nodes of superelements are shown in Fig. 1.

3.3.1 Case of stiff disk. When a disk is stiff and its natural frequencies are essentially higher than frequency range for which calculation should be fulfilled then exact enough results may be obtained by consideration of vibration of blades-interblade linkage system. Interaction of blades through interblade linkage and flow is considered but their interaction through disk is neglected. Elastic properties of blade-disk joints and elastic properties of disk itself are taken into account by matrices of compliance coefficients that are

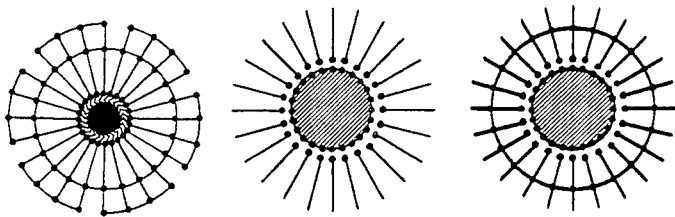


Fig.1. Different kinds of considered systems: a) blading with stiff disk, b) bladed disk without interblade linkage, c) bladed disk with any linkage

regardless on vibration frequency. The matrix relation of blading is obtained by using superelement approach. Parts of blades that are divided by interblade linkage and parts of interblade linkage between neighboring blades are superelements. Any manner of blade connections by one, two or more interblade linkages that are used in power or transport turbomachinery such as: packets, circular linkage, chess-like linkage, etc., may be considered by using usual finite element procedure to form matrix relation of blading. The manners of interblade linkage are described by incidence matrix and each of impeller blades may have its own characteristics.

The size of resulting matrix relations is determined by the number of blade-shroud joints. The sparse sky-line structure of the matrix has symmetrical form but asymmetry of its complex coefficients is taken into account.

3.3.2 Bladed disk without interblade linkage. Interaction through disk and disk vibration properties should be accounted in the most cases. For bladed disk without any interblade linkage the following effective technique may be proposed to obtain matrix relation of blades-disk system without necessity of handling of large matrices. For each j -th blade of the impeller its matrix relation from form (5) is transformed to the form:

$$q_{j2} = a_j Q_{j2} + p_j \quad (14)$$

where $a_j = L_{11} L_{21}^{-1}$; $p_j = P_q - a_j P_Q$. By combining such relations for all impeller blades we have:

$$q_d = \text{diag}(a_j) Q_d + P_d \quad (15)$$

Displacements of a disk and blades at blade-disk joints are equal and equilibrium conditions should be satisfied. Using these conditions and the relation (10) we obtain the resulting matrix equation:

$$(A_z + \text{diag}(a_j)) Q_d = P_d \quad (16)$$

This relation has solid matrix because solid matrix A_z reflects interactions of all blades through disk.

3.3.3 Blades-disk-shrouds assembly. For this case the matrix relation of blading is obtained by same technique as for case of stiff disk but the nodes at blade-disk joints is considered as superelement nodes also and

corresponding degrees of freedom are not eliminated. The relation for the blading takes the form:

$$\begin{Bmatrix} Q_b \\ Q_d \end{Bmatrix} = \begin{bmatrix} K_{11} & K_{12} \\ K_{21} & K_{22} \end{bmatrix} \begin{Bmatrix} q_b \\ q_d \end{Bmatrix} + \begin{Bmatrix} P_b \\ P_d \end{Bmatrix} \quad (17)$$

where q_b, Q_b - vector columns of displacements and forces at nodes of blade-linkage joints; q_d, Q_d - vector columns of displacements and forces at nodes of blade-disk joints. Equilibrium conditions at blade-shroud joints ($Q_b = 0$) allow to obtain from (17) the next relation:

$$Q_d = (K_{22} - K_{21}K_{11}^{-1}K_{12})q_d + (P_d - K_{21}K_{11}^{-1}P_b) \quad (18)$$

Matrix K_{11} has skyline form and the other matrices in (18) are very sparse so this transformation may be fulfilled effectively. Combining (18) and the disk relation (10) we obtain resolving equation in the form:

$$[(K_{22} - K_{21}K_{11}^{-1}K_{12})A_\Sigma - I]Q_d = K_{21}K_{11}^{-1}P_b - P_d \quad (19)$$

All relations here were deduced for case of forced vibration. For natural vibration analysis the terms corresponding to loading are omitted and damping is not accounted. When displacements at master nodes of the superelements are determined then displacements and stresses for all their rest nodes may be calculated without difficulties using transfer matrix method.

4 RESULTS

The proposed technique has been realized and used for analysis of natural and forced vibrations of practical bladed disks of power turbomachines and gas turbine engines.

For example in the paper, results of calculations of two bladed disks are given:

- the first is the bladed disk that contains 56 blades and has a flexible disk (Figs.2a,3,6,7);
- the second is the bladed disk that contains 33 long pretwisted variable cross-section blades connected by midspan shrouds and has a stiff disk (Figs.2b,4,5,8).

For the first bladed disk three cases have been examined:

- interblade linkage is absent;
- all blades are connected by continuous shroud band at their tips;
- the shroud band has been broken between one pair of the blades and there is a long packet containing all blades.

For the second bladed disk two cases were considered:

- the case of circular linkage by integrally shrouds connecting blades at 1/3 of blade length from its tip and
- the case when contact between one of pair of the blade shrouds has been violated and there is long blade packet also.

Linear along blade distribution of the loads was adopted and shift in phase caused by rotating harmonics of loads was accounted for both bladed

disks for forced vibration analysis. Material damping factor was adopted equal 0.03. Each from blades of the impellers is described about 150 degrees of freedoms and the disk model contains about 2500 degrees of freedoms. Stiffness properties of shrouds have been calculated separately from vibration analysis of the impeller by using technique described in [6]. The plate finite element model of shroud between each pair of neighboring blades contains about 900 degrees of freedom. So, for example, the total number of degrees of freedom for the first bladed disk was about 50.000. The random blade mistuning was obtained by generator supplying restricted Gaussian normal distribution with deviation $\sigma_\mu = 0.02$ and maximal admissible mistuning $\delta\mu = 0.05$.

It should be noted that for analysis of the considered bladed disks the models of their major components were used that have shown their effectiveness during long-term experience for vibration analysis of tuned bladed disks. Owing that the obtained calculation results allow to estimate of vibration characteristics of mistuned practical disks in quantity.

In Fig.2 all natural frequencies in prescribed frequency ranges for both considered bladed disks with tuned blades are presented in dependence on number of nodal diameters: a) - the first bladed disk without shroud; b) - the second one with circular linkage. The curves on the figures have been numbered on the right, in the region of high numbers of nodal diameters. For the first bladed disk blades interact through disk and for the second one - through shrouds. Horizontal parts of the curves correspond to the cases when stiffness of a disk (for the first bladed disk) or a shroud (for the second) becomes so high that its further increasing does not practically act to vibration of a tuned bladed disk. For the first bladed disk some of the curves are entire near horizontal, e.g., the curves corresponding to prevalently tangential blade vibration (the curves 1,3) or and torsional blade vibration (the curves 4,6). The sloping parts of other curves reflect the fact of essential interaction of axial, tangential, torsional blade vibration and axial, tangential, radial disk vibration in the region of small numbers of nodal diameters.

For mistuned systems all natural frequencies corresponding to frequencies presented in Fig.2 were calculated also. Natural frequencies having been dual for tuned system for all values of nodal diameters except 0 and $N/2$ are splitted under introducing of mistuning and change slightly their magnitudes. Because of that in the considered frequency ranges the number of natural frequencies becomes larger almost for two times. In Table.2 the example of natural frequencies of the mistuned second bladed disk are shown, the frequencies that corresponds to curve 1 in the Fig.2a.

In contrast to action to natural frequencies influence of mistuning on natural modes and forced response is very different for horizontal and sloping parts of curves in Fig.2. In Fig.3 axial and tangential displacements of blades and disk radii on natural modes of the first bladed disk are plotted. Here displacements of disk radii are drawn between two long horizontal lines. The first drawn mode corresponds to sloping part of the curve 2 in Fig.2a the next two corresponds to its horizontal part and the last - to sloping

part of the curve 5. Here and further indexes upon frequencies are numbers of the modes in spectrum. In Fig.4 distribution of axial displacements at blade tips among blades on natural modes corresponding to curve 1 of Fig.2b and results of their harmonic analysis are shown. For tuned system all blades have equal modes and distribution of amplitudes along disk circumference obeys to harmonic law. For the mistuned systems large distortions arise for modes corresponding to horizontal parts of the frequency curves and even harmonic analysis cannot allow to trace which mode of a tuned bladed disk has been distorted.

In Fig.5,6 examples of amplitudes of displacements among blades of the first bladed disk are shown. Vibrations were induced by 6th harmonic of loads on different frequencies far from resonances. In Fig.5 the amplitudes are plotted that are selected at blade tips of the system without shrouds. Here the amplitudes of tuned system are plotted by solid heavy line (they are equal for all blades) and for mistuned assembly they are marked by circles. Mistuning leads as to scatter of amplitudes and as to change stress levels in large extent. Amplitudes may change very much upon small variation of excitation frequency (see Figs.5a,b) in the range where there are many resonance frequencies corresponding to horizontal parts in Fig.2. In Fig.6 amplitudes at tips (rings) and middles (circles) of the blades with discontinuous shroud are shown (solid heavy line represents amplitudes for circular linkage). Fig.6a corresponds to system with equal blades and Fig.6b - with random mistuned blades. Shroud discontinuity leads to loss of cyclic symmetry even if all blades are equal (Fig.6a) and to appearance scatter of amplitudes and to enlargement of their total levels.

In Fig.7 forced response characteristics for maximal stresses that have been found among all blades of the tuned and mistuned 2nd bladed disk are shown for excitation by 4-th harmonics. Cases of circular linkage (Fig.7a,b) and violation of contact between a pair of its blades (Fig.7c,d) are presented. In contrast to tuned impeller, for which natural modes resonate only if the next relation between nodal diameter number m and excitation harmonic number k is valid: $k=\pm m+jN$ ($j=0,1,2,\dots$), for the mistuned impeller even harmonic excitation induces all resonance modes. The condition $k=\pm m+jN$ continues to determine major resonance peaks but frequency ranges having high stress levels widened and stress levels at major resonance peaks for mistuned impeller become higher essentially. Design symmetry distortion due to violence of shroud contact leads to very large change of response in all excitation range but in this case mistuning affect on amplitudes essentially also.

Contours of the ratio of maximal stresses of mistuned and tuned system are shown in Fig.8 against parameters of mistuning μ . The second bladed disk with circular linkage was considered. Maximal stresses were found among all points of the system and excitation frequencies from range 470...510 Hz. Parameters of mistuning were varied for two of blades, and the other blades were adopted equal. It is obvious that mistuning is very

sensitive to variation of mistuning, and for considered system it increases stress levels up to factor 1.8.

5 CONCLUSIONS

In contrast to preceding investigations of forced vibrations of mistuned bladed disks that were carried out mainly for SDOF blade models in the paper an effective computational technique and results of numerical investigations of practical bladed disk have been suggested that are based on MDOF models.

The technique allows to perform extensive investigations of forced and natural vibrations of bladed disks having any kind of distortions of blading symmetry and any schemes of blade linkage that include as separated and as simultaneous action of design and small manufacturing distortions of symmetry. Forced vibrations caused by rotating field of aerodynamic loads and by torsional vibrations of rotor may be considered.

REFERENCES

1. Basu P., Griffin J.H., "The effect of limiting aerodynamic and structural coupling in modes of mistuned bladed disk vibration." *Trans. ASME: J. of Vibr., Acoust., Stress and Reliability in Design*, 1986, 108 (2), pp. 132-139
2. Sanliturk K.Y., Imregun M., "Vibration analysis of mistuned bladed disk assemblies - inverse approach." *AIAA J.*, 1994, Vol. 32, No 4. pp. 857-865
3. Matveev V.V., Zinkovskiy A.P., Buslenko I.N., "Vibration of mistuned bladed disk assemblies with elastic dissipative coupling." *Proc. Int. Conf. Vibr. Engrg.*, Beijing, China, June 15-18, 1994, pp. 737-747
4. Lin C.C., Mignolet M.P., "Effects of damping and damping mistuning on the forced vibration response of bladed disks." *J. Sound and Vibration*, 1996, 193 (2), pp. 525-543
5. Gorelov D.N., Kurzin V.B., Saren V.E., "Album of unsteady aerodynamic characteristics of profile lattices." Nauka, Novosibirsk, 1974.
6. Petrov E.P., "Large-scale finite element models of blade-shroud and blade-disk joints and condensation technique for vibration analysis of turbomachine impellers." *Proc. 7-th World Congress on Finite Element Methods: "FEM: Today and The Future,"* 1993, pp. 507-513

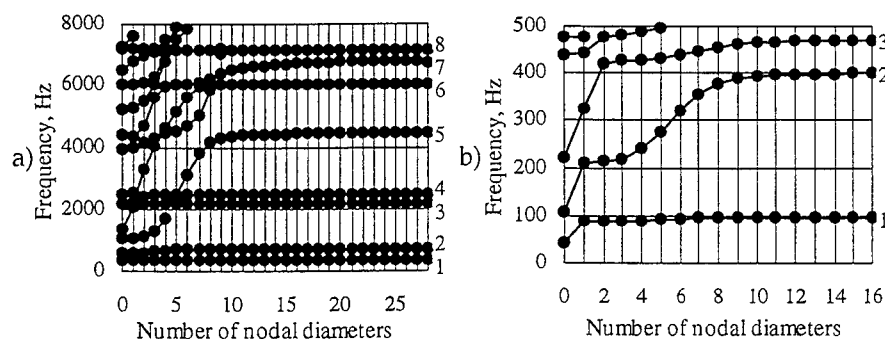


Fig.2 Natural frequencies of the tuned bladed disks: a) blades-disk assembly, b) shrouded blading with circular linkage

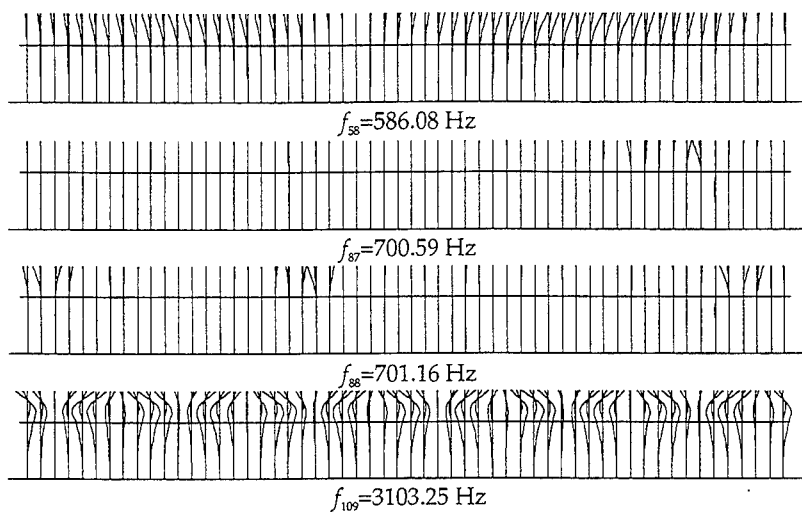


Fig.3. Some natural modes of the mistuned bladed disk

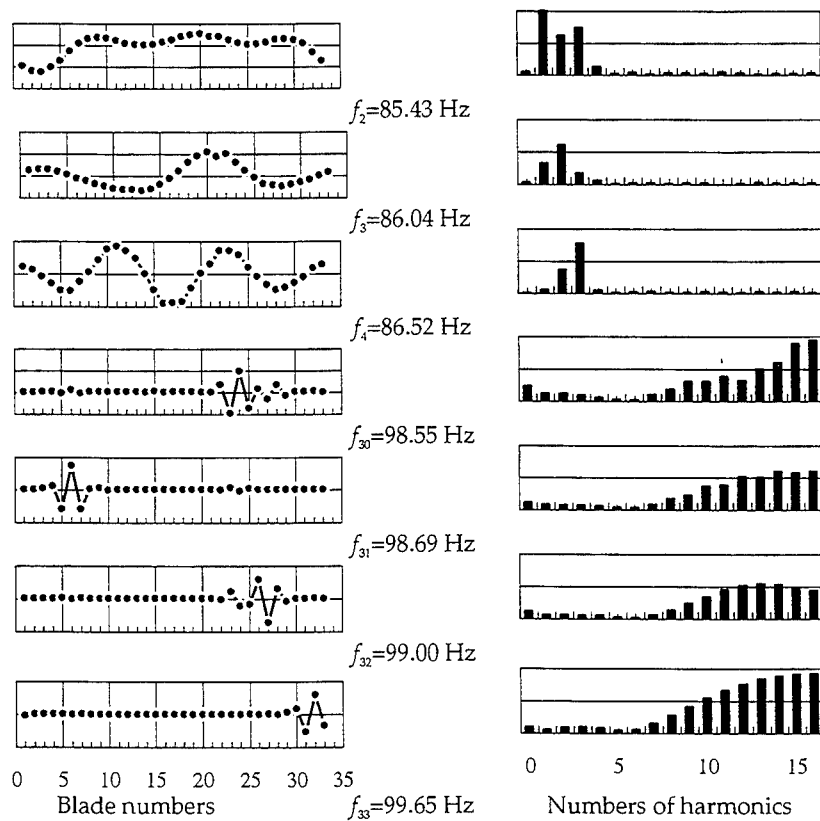


Fig.4. Natural modes of mistuned blading and results of their harmonic analysis

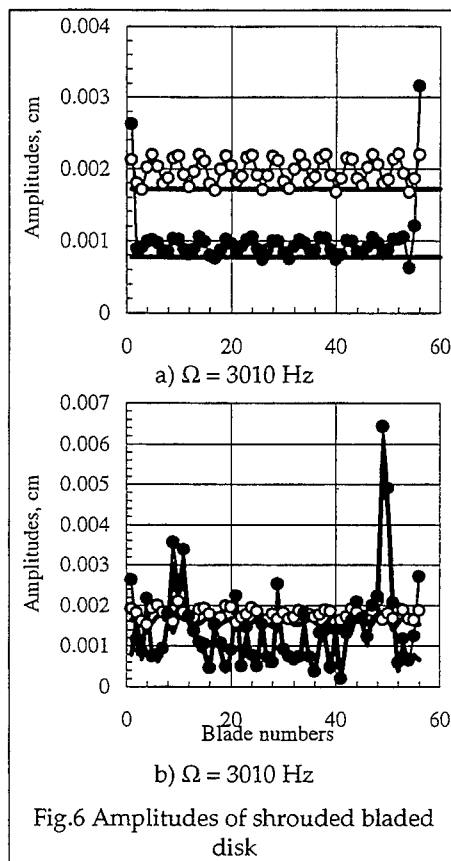
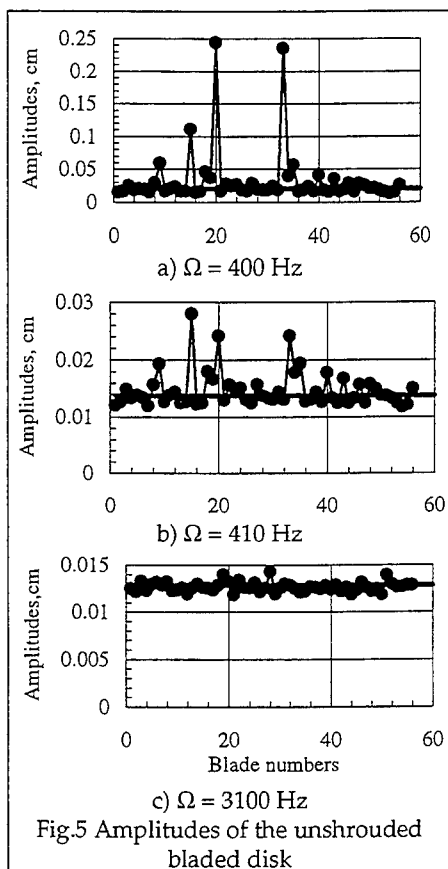


Table 2. Natural frequencies of the mistuned bladed disk

Numbers	Natural frequencies, Hz	Numbers	Natural frequencies, Hz	Numbers	Natural frequencies, Hz
1	41.47	11	90.84	21	96.48
2	85.43	12	92.85	22	96.93
3	86.04	13	93.00	23	96.95
4	86.52	14	94.05	24	97.05
5	86.69	15	94.42	25	97.21
6	86.76	16	94.74	26	97.49
7	86.97	17	95.22	27	97.72
8	87.93	18	95.73	28	98.09
9	88.51	19	95.88	29	98.13
10	90.67	20	96.11	30	98.55
				31	98.69
				32	99.00
				33	99.65

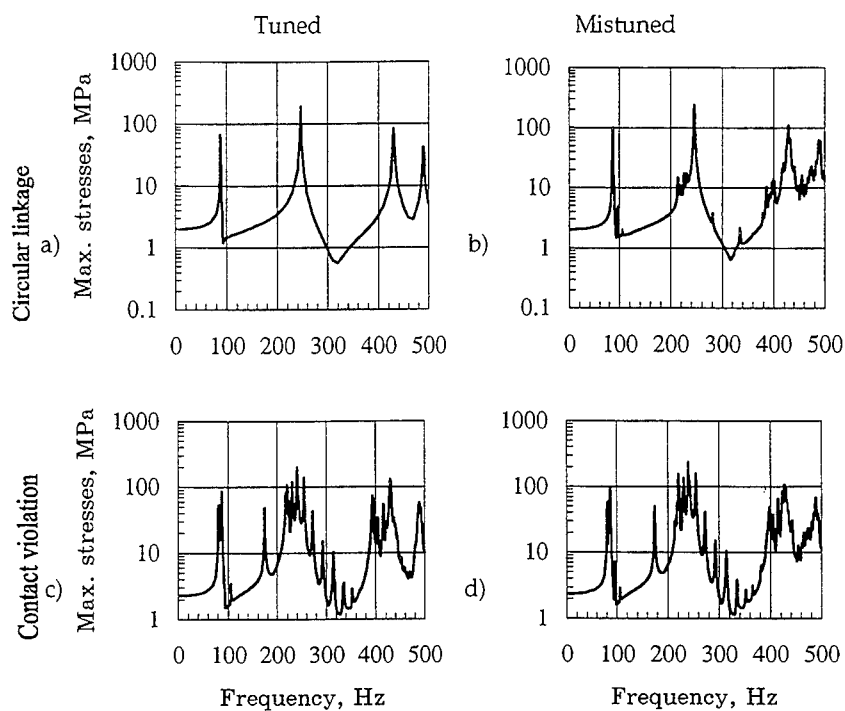


Fig.7 Forced response characteristics of tuned and mistuned bladed disks for cases of a) circular interblade linkage and b) with violation of contact between one pair of the blades

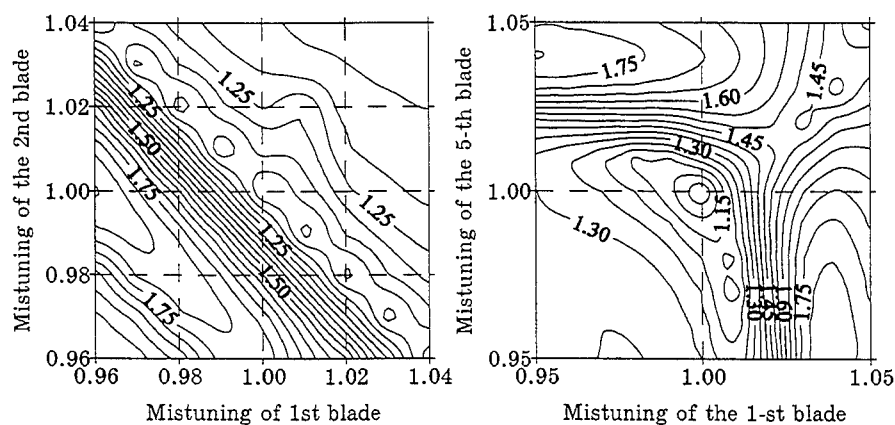


Fig.8. Contour maps of maximal stresses of the bladed disk found among all blades in the range 470...510 Hz in dependence on blade mistuning

ESSENTIALLY NONLINEAR FORCED VIBRATIONS OF MISTUNED TURBINE BLADE PACKETS

E.P. Petrov

Dynamics and Strength of Machines Department, Kharkov State Polytechnic University, Frunze St. 21, Kharkov, The Ukraine

1 INTRODUCTION

For increasing of strength and efficiency of stages of axial flow turbomachine their blades are connected by interblade linkage. One of the most widespread kinds of blade design used in gas turbine engines and power turbomachines is their manufacturing in the form of so called "integrally shrouded" blades. Parts of shrouds of such blades are interacted with neighboring ones through contact surfaces (Fig.1). Assembling of the blades on a disk is carried out as a rule to supply tight press of the shrouds at contact surfaces but for some operating regimes and blade designs interaction forces have essentially nonlinear character. The reasons of nonlinear forces are: unilateral character of interaction forces at contact surfaces, dry friction forces, impact damping forces, variation of contact conditions during period of vibration, etc.

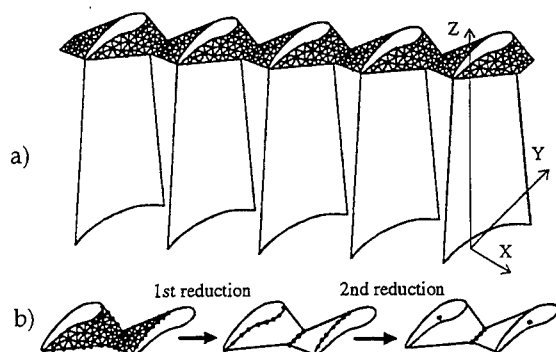


Figure 1. System of MDOF blades interacting through shrouds (a) and two stages of reduction of shroud nodes (b)

Mistuning of blades may lead to dramatically large change of stress levels for some regimes of forced vibrations even upon small magnitudes of inevitable mistuning caused by technological tolerances of blade manufacturing. Large practical and theoretical value of analysis of mistuned bladed disks determines a great number of publications devoted to this problem. However in preceding investigations analysis of system of mistuned blades was carried out for cases of linear vibrations only. Since nonlinear interaction of blades appears rather frequently it is important to develop method and fulfill analysis of essentially nonlinear vibrations of systems of mistuned blades.

There are a small number of papers devoted to analysis of nonlinear vibration of blade systems. In the papers [1],[2] the questions of development of computational models were considered for calculation of forced response. Nonlinear friction on contact surfaces upon microslip and macroslip of shrouds as well as gap between neighboring shrouds are examined. Harmonic balance method is used and an approximation by first harmonic is applied; analysis of vibration of blade system is reduced to analysis of equations describing one blade by imposing a relation between displacements of all blades in the system. In paper [3] vibration of single blade with friction damper was calculated by harmonic balance method and approximation up to three terms was used.

In these papers ideally tuned or single blades were considered. Moreover use of the methods that are based on assumptions in respect to variation of displacements during period (such as harmonic balance method, harmonic linearization method, etc.) is collided with difficulties for essential nonlinear blade systems with abrupt varied parameters during vibration. Such difficulties are increased sharply with increasing of number of degrees of freedom and retention of large number of terms in series used for approximation the displacements. Assumptions about in-time process, introduced by these methods, for badly investigated problems should be examined and based on analysis by numerical methods that guarantee preservation of all regimes that are possible for adopted computational model.

This paper is devoted to development of method and models for search and tracing of periodic regimes of forced essentially nonlinear vibration of mistuned blade systems. The method is aimed to analyze blade systems based as on single degree of freedom (SDOF) blade model and as on multi-degrees-of-freedom (MDOF) finite element models and dose not restrict search of periodic solutions by any assumption about in-time vibration process.

2 VIBRATION EQUATIONS OF BLADE PACKETS

2.1 Case of SDOF models of blades

Single degrees of freedom models of blade are widespread enough for analysis of linear vibrations, especially for very time-consuming computational problems, such as analysis of bladed disks with mistuning, optimization. Since they are quite suitable for analysis qualitative vibration characteristics of such systems they are used here for analysis the nonlinear problem.

For the group consisted from n single degree of freedom blades the simultaneous set of motion equations may be written in the form:

$$m_i \ddot{x}_i + c_i^b \dot{x}_i + \mu \dot{x}_i + R_{i-1} - R_i = P(\omega t - 2\pi(i-1)/N) \quad (1)$$

for $(i = \overline{1, n_b})$

where m_i and c_i^b - mass and stiffness of the i -th blade; $P(t)$ - arbitrary periodic excitation force that is equal for all blades but acts with shift in phase $2\pi(i-1)/N$ between neighboring ones due to rotation of the impeller; ω - rotation speed of a bladed disk; n_b - number of blades in the group; N - total number of blades on a considered bladed disk; $R_i = r_i^{shroud} + r_i^{friction} + r_i^{impact}$ - forces of blade interaction through shrouds, which consist from forces of elastic interaction r_i^{shroud} , dry friction forces $r_i^{friction}$ and impact damping forces r_i^{impact} . Elastic interaction forces are dependent on contact conditions and are expressed using different stiffness coefficients for cases of shroud compression - c_i^{s+} and extension - c_i^{s-} (for practically important case of unilateral interaction: $c_i^{s-} = 0$). The condition of occurrence of shroud compression is $x_{i+1} - x_i + g < 0$, where g - initial gap between shroud contact surfaces (if there is initial tension, then g has the corresponding negative value). Forces of elastic interaction are expressed in the form:

$$r_i^{shroud} = \begin{cases} c_i^{s-} (x_{i+1} - x_i + g), & \text{for } x_{i+1} - x_i + g \geq 0 \\ c_i^{s+} (x_{i+1} - x_i + g), & \text{for } x_{i+1} - x_i + g < 0 \end{cases} \quad (2)$$

Since the normal force at contact surface is proportional to r_i^{shroud} then the force of dry friction takes the specific form:

$$r_i^{friction} = 0.5c^f \sin 2\alpha r_i^{shroud} \text{sign}(\dot{x}_{i+1} - \dot{x}_i) \quad (3)$$

where c^f - coefficient of dry friction, α - angle between direction of vibration and slip plane. Slip at contact surfaces arises only if $c^f \leq |tg(\pi/2 - \alpha)|$.

Impact damping arises in result of transformation of part of kinetic energy to high frequency waves that are not reflected in the used computational model and as result of some local deformations at contact surfaces:

$$r_i^{impact} = S\delta(t - t^*) \quad (4)$$

where S - impact damping force impulse, which is assumed to be proportional relative velocity of impacting surfaces; $\delta(t - t^*)$ - Dirac's impulse function; t^* - moments of time when contact conditions change from contact absence to its presence (such moments may be many per a period).

2.2 Case of MDOF models of blade system

For analysis of practical problems models should allow to describe in detail geometry shape, interaction of system parts and their vibration characteristics. Most effectively it may be performed by use of finite element method (FEM). However the numbers of degrees of freedom in finite element models of blade systems are too large to use these models immediately in analysis of nonlinear vibrations. It is necessary to develop technique for

condensation FEM matrices of the blade system that would remain essential properties of the system, that were included in initial MDOF model, in analysis of nonlinear vibrations. Taking into account peculiarities of geometry shape and vibration characteristics of a blade and a shroud, we use for them different finite element models and different methods for reduction of a number of degrees of freedom. The approaches for such reduction account that the parts of system are linear deformed, and their interaction forces are nonlinear only.

2.2.1 Beam model of a blade. A blade is considered as pretwisted rod of variable along blade asymmetric cross-section. Bending vibrations in the plane of blade rotation and in the plane perpendicular to it, as well as torsion vibrations are coupled owing to initial twist and asymmetry of the cross-section. At each node of FE blade model the vector column of nodal parameter has the form: $q = \{u, v, \varphi_x, \varphi_y, \varphi_z\}^T$, where u and v displacements in rotation plane and perpendicular to it, φ_x, φ_y bending angles, φ_z - torsion angle. Matrix equation for whole blade is composed by standard FEM routine and is written in the form:

$$\begin{bmatrix} M_{mm} & M_{ms} \\ M_{sm} & M_{ss} \end{bmatrix} \begin{Bmatrix} \ddot{q}_m \\ \ddot{q}_s \end{Bmatrix} + \begin{bmatrix} C_{mm} & C_{ms} \\ C_{sm} & C_{ss} \end{bmatrix} \begin{Bmatrix} \dot{q}_m \\ \dot{q}_s \end{Bmatrix} + \begin{bmatrix} K_{mm} & K_{ms} \\ K_{sm} & K_{ss} \end{bmatrix} \begin{Bmatrix} q_m \\ q_s \end{Bmatrix} = \begin{Bmatrix} p_m(t) \\ p_s(t) \end{Bmatrix} \quad (5)$$

where q_m - so-called 'master' displacements that are retained after matrix condensation and q_s - so-called 'slave' displacements that will be removed after condensation. Mode synthesis method is used for the condensation in the from of fixed boundaries [4]. In accordance with this method all nodal displacements can be expressed through 'master' displacements and natural modes of the substructure in the following form:

$$\begin{Bmatrix} q_s \\ q_m \end{Bmatrix} = \begin{bmatrix} \Phi & -K_{ss}^{-1}K_{sm} \\ 0 & I \end{bmatrix} \begin{Bmatrix} q_\Phi \\ q_m \end{Bmatrix} \quad (6)$$

where Φ - matrix, consisted from vector column of natural modes of the blade with clamped 'master' degrees of freedom; I - unit matrix; q_Φ - introduced column of degrees of freedom, which are coefficients upon natural modes.

Writing motion equation in the basis of independent variables $\{q_\Phi, q_m\}$ and taking into account that the natural modes are orthonormal in respect to mass matrix the condensed equations for a blade take the form:

$$\begin{bmatrix} I & M_{\Phi m}^* \\ M_{m\Phi}^* & M_{mm}^* \end{bmatrix} \begin{Bmatrix} \ddot{q}_\Phi \\ \ddot{q}_m \end{Bmatrix} + \begin{bmatrix} C_{\Phi\Phi}^* & C_{\Phi m}^* \\ C_{m\Phi}^* & C_{mm}^* \end{bmatrix} \begin{Bmatrix} \dot{q}_\Phi \\ \dot{q}_m \end{Bmatrix} + \begin{bmatrix} \Omega & 0 \\ 0 & K_{mm}^* \end{bmatrix} \begin{Bmatrix} q_\Phi \\ q_m \end{Bmatrix} = \begin{Bmatrix} p_\Phi \\ p_m \end{Bmatrix} \quad (7)$$

where $\Omega = \text{diag}(\omega_i^2)$ -diagonal matrix consisted from natural frequencies corresponding to modes Φ . Matrices and vector column of loads are obtained

by projecting of matrices from relation (5) to this basis: $K^* = V^T K V$; $M^* = V^T M V$; $C^* = V^T C V$; $P^* = V^T P$. Here V - matrix of relation (6) and matrices without asterisk correspond to equation (5).

2.2.2 Plate model of a shroud. Natural frequencies of a shroud are much higher as a rule than ones of a blade and higher than considered frequency range of excitation and vibration of blade system. Accounting that the inertia forces in result of shroud deformation are neglected, but inertia forces of displacements of a shroud as a rigid body are applied to blades at place of shroud attachment. Three-nodal triangular plate finite elements accounting bending and membrane deformations are used as it is shown in [5]. The used MDOF models of the shroud allow to describe its complex geometry shape and variable along boundary contact conditions. Vector column of displacements at i -th node of finite elements has the form: $q_i = \{u, v, w, \phi_x, \phi_y\}^T$. It is assumed that contact boundary and conditions are given. The technique allows to reflect any practical case for each part of contact boundary: full contact, slip along contact boundary, fracture or relative rotation of middle planes of contacting shrouds, etc. Matrix relation for shrouds between neighboring blades is formed by FEM routine in the form:

$$\begin{Bmatrix} Q_b \\ Q_i \end{Bmatrix} = \begin{bmatrix} K_{bb} & K_{bi} \\ K_{ib} & K_{ii} \end{bmatrix} \begin{Bmatrix} q_b \\ q_i \end{Bmatrix} \quad (8)$$

where q_b and q_i - displacements at shroud nodes adjoined to blade and at internal nodes correspondingly. Size of this relation is counted by hundreds or thousands. Condensation of this relation is fulfilled in two stages (see Fig.1b). At first stage displacements at internal nodes are excluded and static condensation of stiffness matrix is realized:

$$Q_b = (K_{bb} - K_{bi} K_{ii}^{-1} K_{ib}) q_b \quad (9)$$

At second stage we take into account that a shroud is joined to rod blade model, which cross-section is not deformable. Displacements of all nodes adjoined to i -th blade q_{bi} may be expressed through displacements of blade cross-section q_{mi} and all nodal forces Q_{bi} may be reduced to vector column forces applied to shear center of the i -th blade Q_{mi} : $q_{bi} = R_{mi} q_{mi}$; $Q_{mi} = R_{mi}^T Q_{bi}$. Here reduction matrix R_i depends on coordinates of nodes adjoined to blade and coordinates of shear center of blade cross-section. Size of shroud stiffness matrix is reduced to size of rod matrix using these relations. Relation (9) for interaction forces of neighboring i -th and $(i+1)$ -th blades through shroud is transformed to the form:

$$\begin{Bmatrix} Q_{mi} \\ Q_{mi+1} \end{Bmatrix} = \begin{bmatrix} R_{mi}^T & 0 \\ 0 & R_{mi+1}^T \end{bmatrix} \begin{bmatrix} K_{i,i} & K_{i,i+1} \\ K_{i+1,i} & K_{i+1,i+1} \end{bmatrix} \begin{bmatrix} R_{mi} & 0 \\ 0 & R_{mi+1} \end{bmatrix} \begin{Bmatrix} q_{mi} \\ q_{mi+1} \end{Bmatrix} \quad (10)$$

2.2.3 Matrix relation of blade system. Differential equations of blade system are formed by combining matrices of blades and shrouds in the following form:

$$M\ddot{X} + C(X, \dot{X})\dot{X} + K(X, \dot{X})X = P(t) \quad (11)$$

If there is no contact between shrouds then their stiffness matrices are not added to system matrix. Impact damping is accounted by decreasing of translation velocities of blade nodes that are nearest to the impact surface.

3 SEARCH AND ANALYSIS OF PERIODIC REGIMES

Although there are well-developed methods for integration of equations that contain second deviations in respect of time it is more convenient for our purposes to transform the equations (1) and (11) to the form:

$$\frac{d}{dt} \begin{Bmatrix} X \\ \dot{X} \end{Bmatrix} = \begin{bmatrix} 0 & I \\ -M^{-1}K & -M^{-1}C \end{bmatrix} \begin{Bmatrix} X \\ \dot{X} \end{Bmatrix} + \begin{Bmatrix} 0 \\ -M^{-1}P(t) \end{Bmatrix} \quad (12)$$

and to use for their integration methods of Runge-Kutta's family with varied step. Since we are not going to use any assumptions about in-time variation of degrees of freedom the search of periodic regimes is carried out only from periodicity conditions:

$$Y(t_0 + T) - Y(t_0) = 0 \quad (13)$$

where $Y(t) = \{X, \dot{X}\}^T$. Periodicity condition (13) may be considered as a set of nonlinear equations in respect of vector column of displacements and velocities at initial time moment $Y_0 = Y(t_0)$:

$$F(Y_0) \equiv Y(Y_0, t_0 + T) - Y_0 = 0 \quad (14)$$

where $Y(Y_0, t_0 + T)$ is determined as result of integration of differential equations (12). To find main, sub-, superharmonic, combinative vibration regimes any rational relations between period of the found solution T and period of excitation T_p may be examined, i.e. $T = iT_p / j$, where i, j - integer numbers. Search of solution of equations (14) is based on version of globally convergent Newton's method described in [6]. Finite-difference approximation for Jacobian of the set of equations (14) is calculated by finite-difference formula at start of the iteration process:

$$J \equiv \frac{\partial F}{\partial Y_0} \approx \left[\frac{F(Y_0 + e_1 h_1) - F(Y_0)}{h_1}, \frac{F(Y_0 + e_2 h_2) - F(Y_0)}{h_2}, \dots, \frac{F(Y_0 + e_n h_n) - F(Y_0)}{h_n} \right] \quad (15)$$

where n - number of components in vector columns Y_0, F
 $e_j = \{\delta_{1j}, \delta_{2j}, \dots, \delta_{nj}\}^T$; δ_{ij} - Kronecker's symbol. Then iterations is calculated in accordance with the next formulas:

$$J^{(k)} \dot{g} = -F(Y_0^{(k)}); \quad g = \xi \dot{g}; \quad Y_0^{(k+1)} = Y_0^{(k)} + g \quad (16)$$

up to reaching of required accuracy for equations (14). Parameter ξ is chosen at each k -th iteration to be equal 1 if it supplies decreasing of Euclidean norm $\|F(Y_0)\|$ otherwise it is found in range $[0,1]$ by minimization $\|F(Y_0)\|$. Approximated Jacobian is recalculated by Broyden's formula at each iteration:

$$J^{(k+1)} = J^{(k)} + [F(Y_0^{(k+1)}) - F(Y_0^{(k)}) - J^{(k)}]g^T / (g^T g) \quad (17)$$

It should be noted that only one integration of equations (12) per an iteration is fulfilled here for updating the Jacobian instead of n times that would be necessary with utilizing finite-difference approximation (15). To supply accuracy of analysis of the solution stability and of tracing of periodic regimes it is necessary to have more precise approximation of Jacobian than Broyden's one. Because of that at last iteration the Jacobian is calculated using formula (15).

Stability of a periodic regime is reduced to analysis of stability of trivial solution for the equations that are obtained by linearization of the considered nonlinear equations in vicinity of the found periodic regime. Owing that Floquet's theory is applied for such analysis. Analysis of stability of the found periodic regime is performed by analysis of eigenvalues of a monodromy matrix. The approximation of the monodromy matrix is matrix $J(Y_0) - I$ calculated for vector column Y_0^* supplying periodic vibration. For each found periodic solution eigenvalue problem is solved:

$$[J(Y_0) - I]\tilde{Y} = \lambda \tilde{Y} \quad (18)$$

The characteristic of stability of found periodic regime is so called "spectral radius": $\rho = \max_i |\lambda_i|$ (λ_i eigenvalues of the problem given by the equation (18)). If $\rho \leq 1$ - then the found regime is stable otherwise it is unstable. Vibrations during period are calculated by integration for found vector column of initial conditions Y_0^* . Computed displacements are expanded into Fourier series to analyze spectrum, obtain dominant harmonics in vibration, determine superharmonic regimes.

4 TRACING OF PERIODIC REGIMES UPON PARAMETER VARIATION

For nonlinear systems due to rich variety of vibration regimes, existence of bifurcation points tracing of periodic regimes upon variation of system parameters is necessary. When response characteristics of blade packets are calculated such varied parameter γ is often excitation frequency but it may be the parameter of excitation level or some another design parameter also.

The tracing technique is based on the following approach. Iteration process described in Section 3 allows to obtain for given system parameters

the vector column of initial conditions Y_0^* that supplies periodic vibration regime. If one of system parameters is varied then the vector column $Z = \{Y_0^{*T}, \gamma\}^T$ consisted from Y_0^* and the varied parameter γ will describe in coordinate space Z a trajectory that corresponds to periodic regimes, i.e. $Z = Z(s)$. Here s - some formally introduced parameter of trajectory length that is counted along the trajectory. The trajectory is surrounded by the tube that restricts domain of convergence of the iteration process (16). Choice of approximation of initial conditions inside the tube allows to obtain periodic regime connected to the initially found periodic regime. The closer to solution the approximation is chosen the more quickly iteration process is converged. In accordance with this the most effective way of tracing of the periodic regimes is moving from the already obtained point in direction of tangent to the trajectory. Taking into account that the equations (14) are dependent on parameter γ as well as on initial conditions Y_0 they may be differentiated in respect to s . As a result the following equation in respect to directing cosines of the tangent to the trajectory is obtained:

$$J(Y_0^*) \frac{\partial Y}{\partial s} + \frac{\partial F(Y_0)}{\partial \gamma} \frac{\partial \gamma}{\partial s} = 0 \quad (19)$$

It should be noted that if γ is excitation frequency then dependence of vibration period on excitation frequency is taken into account $T_p = 2\pi / \gamma$ for calculation of deviations $\partial F(Y_0) / \partial \gamma$. Solution of this set of n linear homogeneous linear equations (19) with $(n+1)$ unknowns $\partial Z / \partial s$ gives the direction of the following step along the trajectory of periodic regimes. If the rank is equal n , then tangent direction is determined uniquely and the considered point on the trajectory is not branch point otherwise the considered point is a branching point of periodic solution. The approximation of the next point on the trajectory is calculated in the next form:

$$Z(s + \Delta s) = Z(s) + \Delta s T(s) \quad (20)$$

where normalised vector column of trajectory directing cosines takes the form: $T(s) = \|\partial Z(s) / \partial s\|^{-1} \partial Z(s) / \partial s$. Length Δs for the first step is determined by prescribed first step in respect of varied parameter γ but lengths of all next steps are governed by absolute value ξ of scalar product of normalised vector columns of trajectory directing cosines at considered point and at preceding points, i.e. $\xi = |(T(s + \Delta s), T(s))|$. It is obvious that if the direction is not varied at the considered step then $\xi = 1$, and the range of magnitudes of ξ should satisfy the next relation $0 < \xi^- \leq \xi \leq \xi^+ < 1$. Step changing is fulfilled when ξ leaves the range $[\xi^-, \xi^+]$ in other cases it is invariable. When $\xi < \xi^-$ then step Δs is decreased by such way $\Delta s = \Delta s / k$ ($k > 1$) and when $\xi > \xi^+$ it is increased

$\Delta s = k\Delta s$. Magnitudes of k and ξ^-, ξ^+ are dependent on specific nature of the considered system and should be chosen from experience.

Important feature of the iteration process for tracing of periodic regimes is equal status of Y_0^* and γ in equation (14). The iterations are fulfilled in respect of n selected components of vector column Z . The selection is done by analyzing of normalized tangent cosines $T(s)$ at each tracing step. One component with maximal such cosine is fixed and rest components are found from the iteration process. Such choice corresponds to searching of solution in coordinate plane that cuts the trajectory with maximal angle. This supplies that the plane drawn through point of solution approximation inside convergence tube contains the nearest solution point on the trajectory.

5 RESULTS

The proposed technique has been realized in computer codes and a number of numerical investigations of practical blade packets as well as test problems have been fulfilled.

5.1 SDOF models of blades

The blade packet consisted from 5 steel blades of length 19 cm that interacts nonlinearly through shrouds at blade tips were considered using SDOF model of blades. Stiffness coefficient $c_b = 2.807 \cdot 10^6$ N/m and mass $m_b = 0.5235$ kg of SDOF model of tuned blade were chosen to supply exact first natural frequency and static response to force applied at blade tip. The shrouds were assumed having different stiffness characteristics for compression c^{s+} and extension c^{s-} . Shroud stiffness was adopted $c^{s+} = 1.869 \cdot 10^7$ N/m for compression and a set of different shroud stiffness characteristics was adopted for extension. Harmonic excitation was applied to blades with shift in phase $38\pi/77$ between adjacent blades. Amplitude of excitation force was adopted equal 10 N and coefficient of viscous damping has been adopted equal 20 kg/sec. Amplitudes of forced vibrations were obtained for tuned and mistuned blade packets. Mistuning was considered for case when one of the blades had natural frequency increased for 5% in comparison with the other tuned blades (mass and stiffness were multiplied by 1.05^2 and 1.05^4 correspondingly). Response characteristics were obtained for different shroud stiffness characteristics by tracing of periodic regimes of nonlinear vibrations. Initial periodic regime was searched at excitation frequency 3 kHz and then excitation frequency was decreased. Among collection of possible regimes the periodic regimes were searched that have period coinciding with excitation period.

In the Table 1 major resonance frequencies for a few ratios c^{s-}/c^{s+} are shown for tuned and for mistuned blade packet.

Table 1 Resonance frequencies for different shroud nonlinearities

Nonlinearity degree	Resonance frequencies, Hz				
c^{s-}/c^{s+}	f_1	f_2	f_3	f_4	f_5
Tuned blades					
1.0	364.4	688.1	1168.4	1568.4	1830.2
0.5	364.4	613.6	998.61	1331.6	1548.6
0.1	364.4	509.1	753.8	980.2	1178.9
0.0	364.6	476.9	631.4	825.9	949.7
Mistuned blades					
1.0	368.8	682.1	1154.5	1558.6	1825.6
0.5	368.7	608.6	990.3	1323.2	1547.9
0.1	366.9	518.9	752.0	981.2	1159.4
0.0	368.8	481.4	638.5	834.0	976.9

It is obvious that the first resonance frequency is practically unchanged upon variation of c^{s-} as for tuned and as for mistuned packets but the four next are changed very much upon variation of ratio c^{s-}/c^{s+} . This fact is connected with different character of blade interaction under excitation on these frequencies. Analysis of natural modes of linear vibrations of this blade packet was fulfilled. It shows that for the first mode all blades vibrate in phase with equal amplitudes but for the next four blades vibrate out-of-phase and with different amplitudes. The first natural frequency for blade packet is close to first natural frequency of a single blade and accounting on nonlinearity of interaction conditions during vibration period acts on this resonance frequency for a little. The magnitudes of the other four frequencies are strongly dependent on interaction of blades through shroud and this fact is reflected in large variations of corresponding resonance frequencies for different magnitudes c^{s-}/c^{s+} . Comparison of forced response characteristics for the packet of tuned and mistuned blades is shown in Figs.5,6. Since the vibration process is nonharmonic, on these figures maximal displacements are shown that were calculated by integration of equations (12) over vibration period using found from iteration process (16) initial magnitudes. In addition so called 'spectral coefficient' is plotted on these figures to show distinction degree in calculated response from pure harmonic. This coefficient is equal to ratio of the largest two harmonics in the spectrum of in-time vibration process: $\chi = a_{\max-1}/a_{\max}$. Although forced response characteristics for considered blade models are similar as for tuned and as for mistuned packets but spectrums of nonlinear vibration is very different.

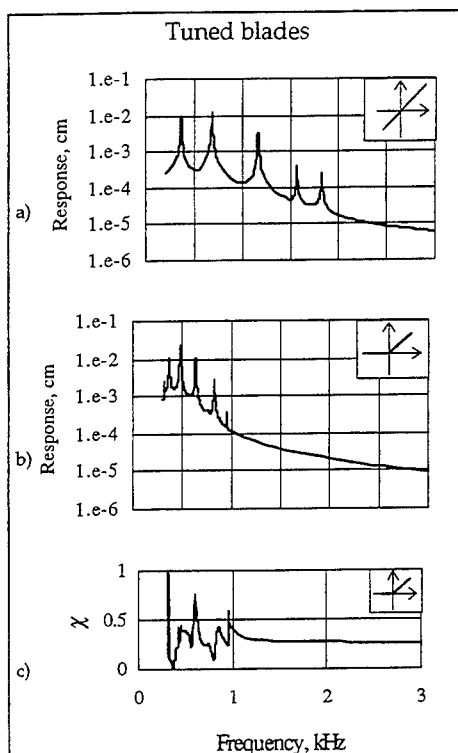


Fig.5 Forced response characteristics for linear (a), nonlinear (b) blade interaction and spectral coefficient (c) for nonlinear vibrations

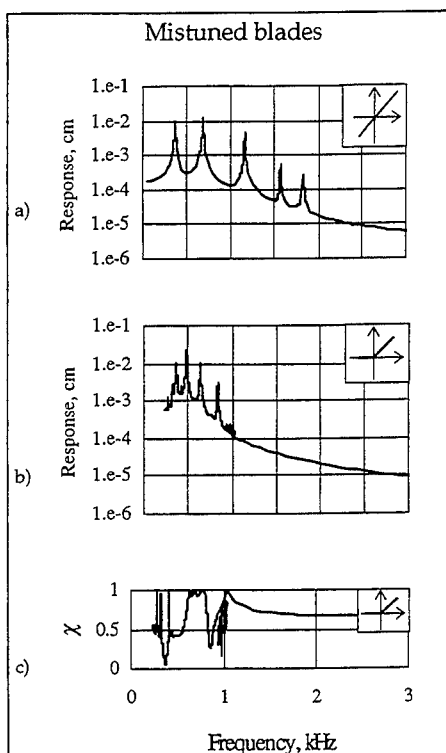


Fig.6 Forced response characteristics for linear (a), nonlinear (b) blade interaction and spectral coefficient (c) for nonlinear vibrations

5.2 MDOF models of blades

The blade packet from the same blades was analyzed with MDOF models and bending blade vibration in tangent direction was considered. Mistuning was introduced by increasing of blade cross-sections for one of the blades for 5%. Each blade of the packet was modeled by FE model having 30 degrees of freedom.

Applicability and parameters of the reduction technique, described in section 2.2 were examined. Natural frequencies, modes and forced responses of linear vibration were compared with results obtained from all-nodal models by technique developed earlier [7]. Two degrees of freedom corresponding to linear and angular bending displacements at each blade tip were retained for description of nonlinear interaction of blades. Results of calculation of natural frequencies using different numbers of component modes are shown in Table 2. Excellent convergence of results with increasing of number of component modes is obvious. For exact enough description of modal properties of a blade in wide frequency range a small number of

degrees of freedom may be used – two master degrees of freedom at blade tip and one degree corresponding to one component mode. Forced response analysis for this packet has been fulfilled in [8] and it has shown good coincidence of results for reduced and all-modal models.

Table 2 Natural frequencies (Hz) of packet of 7 blades with different number of component modes per a blade

Frequency number	Reduced blade models				All-nodal blade model
	Number of component modes per a blade				
	0	1	2	3	
1	454.6	451.3	451.1	451.1	449.1
2	2205	1650	1648	1648	1645
3	2251	1665	1663	1663	1661
4	2300	1683	1681	1681	1678
5	2319	1692	1690	1690	1685
6	2378	1714	1712	1712	1706
7	2387	1716	1714	1714	1707

Forced response characteristics and spectral radius of tuned and mistuned packets of two blades for case of MDOF models are shown in Figs.7,8. In Fig.7a resonance modes of linear system are shown too. For nonlinear cases in presence of contact of shrouds as transversal and as bending moment were supposed to be transmitted to blades but in absence of contact they were adopted 0. For both linear and nonlinear cases the damping matrix has been adopted to be proportional to stiffness matrix. To simulate frequency-independent damping in material of blades and shrouds this matrix was represented in the form $C(X) = \mu \Omega_\mu / \Omega K(X)$, where μ - damping coefficient; Ω - varied excitation frequency; Ω_μ - frequency for which μ was determined. Although from the figures it may be seen that the curves are similar in general for tuned and mistuned packets but it is necessary to note that the forced response characteristics are plotted in semilogarithmic scales. More detailed information about resonance frequencies and amplitudes is shown in Table 3. It is obvious essential influence of nonlinear blade interaction not only on frequency of out-of-phase blade vibration mode - f_2 but on frequency of in-phase mode - f_1 . This is connected with the fact that the used MDOF models take into account as variation of interaction forces and as bending moment in contrast to considered above case of SDOF blade model. Influence of mistuning to resonance amplitudes is large and for considered regimes it leads to

reduction of amplitudes. It is interesting that unilateral blade interaction leads to increasing of vibration amplitudes of mistuned packet for first resonance regime approximately of factor 1.8 and for the second one amplitudes are increased up to factor 3.3 in comparison with linear vibration. In the range of high excitation frequencies the found periodic regimes were unstable as it is obvious from Figs. 7d,8d.

Table 3. Resonance frequencies and amplitudes of linear and nonlinear vibrations (case of MDOF models)

	Tuned blades		Mistuned blades	
c^{s-}/c^{s+}	1	0	1	0
$f_1, \text{ Hz}$	427.0	376.8	434.0	386.7
$\text{ampl}_1, \text{ cm}$	0.0822	0.184	0.075	0.126
$f_2, \text{ Hz}$	1648.7	584.2	1684.0	599.3
$\text{ampl}_2, \text{ cm}$	0.0142	0.0483	0.0140	0.0460

6 CONCLUSIONS

Models and the effective method for calculation of essentially nonlinear forced vibrations of blade packets have been developed. They allow to study as tuned and as mistuned blade packet using SDOF and MDOF models as well. For the first time the numerical investigations of periodic regimes of nonlinear vibrations of mistuned blade packets have been fulfilled and comparison with different vibration characteristics of tuned packets has been shown. The results show essential influence of mistuning on amplitudes, in-time variation of displacements during vibration period and its spectrum. Importance of accounting of nonlinearity of blade interaction and essential influence of nonlinearity degree to amplitudes and resonance frequencies has been demonstrated as for tuned and as for mistuned blade packets.

REFERENCES

1. C.-H. Menq, J.H. Griffin and J. Bielak, "The forced response of shrouded fan stages." Transactions of the ASME: J. of Vibration, Acoustics, Stress, and Reliability in Design, Vol. 108, No 1, 1986, pp. 50-55
2. L.F. Wagner and J.H. Griffin, "Blade vibration with nonlinear tip constraint: Model development." Trans. of the ASME: J. of Turbomachinery, Vol. 112, No 10, 1990, pp. 778-785

3. J.H. Wang and W.K. Chen, "Investigation of the vibration of a blade with friction damper by HBM." Trans. ASME: J. of Engineering for Gas Turbines and Power, Vol. 115, No 4, 1993, pp. 294-299
4. R.R. Craig, "Structural dynamics: Introduction to computer methods," John Wiley & Sons, NY, 1981
5. E.P. Petrov, "Large-scale finite element models of blade-shroud and blade-disk joints and condensation technique for vibration analysis of turbomachine impellers," Proc. 7-th World Congress on Finite Element Methods: "FEM - Today and the Future," Monte-Carlo, 1993, pp. 507-513
6. J.E. Dennis and R.B. Schnabel, "Numerical methods for unconstrained optimization and nonlinear equations." Prentice-Hall, Englewood Cliffs, N.J., 1983
7. E.P. Petrov, "Analysis and optimal control of stress amplitudes upon forced vibration of turbomachine impellers with mistuning," Proc. IUTAM Symp. "Active Control of Vibration," Bath, 1994, pp. 189-196
8. E.P. Petrov and A.A. Tarelin, "Usage of superelements and mode synthesis method in vibration calculations of turbine blade packets." 1-st Int. Symposium of Ukrainian Mechanical Engineers in Lviv, Abstracts, Lviv, 1993, pp. 239-240, (in Ukrainian).

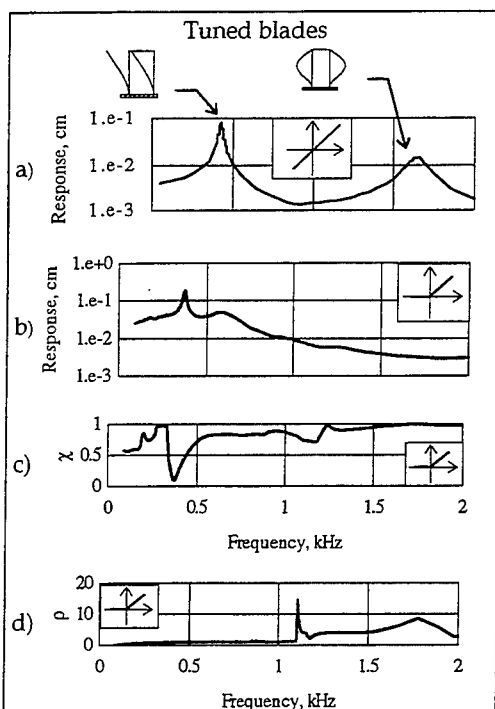


Fig.7 Vibration characteristics for linear - (a) and nonlinear vibrations - (b,c,d) of tuned packet. (a,b) - response, (c) - spectral coefficient, (d) - spectral radius

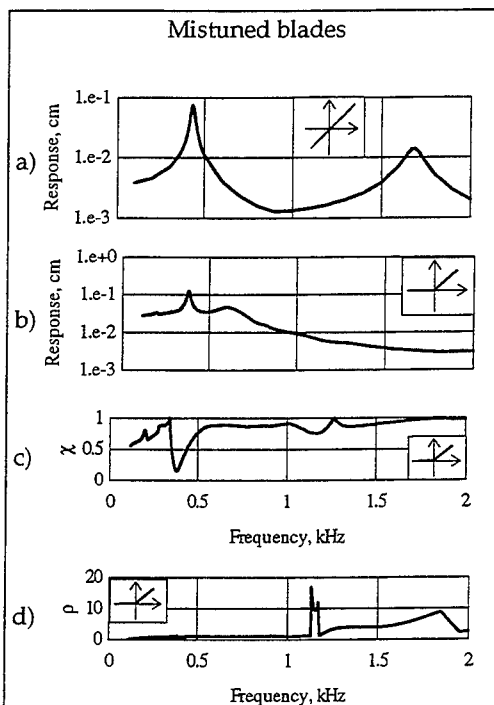


Fig.8 Vibration characteristics for linear - (a) and nonlinear vibrations - (b,c,d) of mistuned packet. (a,b) - response, (c) - spectral coefficient, (d) - spectral radius

A Component Mode Synthesis Method for Substructures Connected by Elastic Joints

Y.F. Hwang and L. Louie

Naval Surface Warfare Center, Carderock Division
West Bethesda, Maryland 20817-5700, USA

ABSTRACT

The standard component mode synthesis method expresses the modes of a large structure in terms of the component modes of its substructures, which are usually formed by artificial partitioning for the ease of numerical computation. In this paper, a modified method is developed for an assembled structure consisting of physically divided substructures joined together by elastic connections such as bolts, rivets, bars, springs or elastic mounts, etc.. The system dynamics is expressed as the Lagrangian function which includes the motions of substructures expressed in terms of component modes and the motions of the joints modeled as general beam elements. The joints are thus capable of resisting and transmitting axial forces, bending moments about the two principal axes in the plane of its cross section, and twisting moments about its centroidal axis. The constraints that the motions of substructures and that of the elastic joints be identical at interfacial points are imposed by Lagrange multipliers. Both free-interface and fixed-interface formulations are presented for component modes with free and fixed interfacial point boundary condition, respectively. Numerical examples are given for two cantilever beams connected by a spring at their end points. Results calculated from the free- and fixed-interface formulation are compared and shown in good agreement with each other and with that calculated from the finite-element method.

INTRODUCTION

Component mode synthesis method expresses the modes of a large structure in terms of the component modes of each of its substructures [1-6]. Substructures are usually formed for the ease of numerical eigenvalue analysis by artificially partitioning a large continuous structure. The methods of synthesis for calculating the original unpartitioned structural modes are usually accomplished

by expressing the system dynamics in terms of component modes with constraints that motions at any pair of interfacial points along the boundaries of partition be identical. This implies that substructures are reattached, or rigidly connected, at any pair of interfacial points. In many practical cases, however, substructures are formed not for ease of computation but rather for actual representation of a large assembled structure consisting of many physically divided substructures joined together by elastic connections such as bolts, rivets, springs, bars, beams, or elastic mounts, etc..

In principle, existing methods mentioned above can also solve this problem by either treating the elastic joints as substructures or allotting the joints to one of the two adjacent substructures. The former solution may become cumbersome when there are many joints. In the latter solution, the joints become parts of a substructure, which is inefficient for a dynamic design process that is required to optimize the elastic joint design to obtain the most desirable dynamic feature of an assembled structure. This is because the latter solutions not only lose the joint dynamic property as an independent parameter but they also require many repetitive computation of the component modes of the substructure containing the joints; i. e., each time the dynamic properties of the joint are changed during design iteration, those component modes containing the joints must be recalculated. This paper presents a more explicit and efficient method of modal synthesis for an assembled structure using component modes of substructures excluding the joints. The system dynamics is expressed as the Lagrangian function which includes the motions of substructures expressed in terms of component modes and the motions of the joints in the inertial frame of reference [7]. The joint dynamic properties are expressed as independent variables in the Lagrangian function. The constraints that motions of substructures and that of the joints at any pair of interfacial points be identical are imposed by Lagrange multipliers. This method is formulated by using the component modes with either free or fixed boundary condition. Numerical examples are given for the case of two cantilever beams connected by a spring at their end points. Results calculated from the free- and fixed-interface formulation will be compared with each other and with that calculated independently by the finite-element method.

METHODOLOGY

As shown in Fig. 1, an assembled structure system may consist of many substructures, A, B, C, and D, etc.. Any of these substructures are connected to at least one of the other

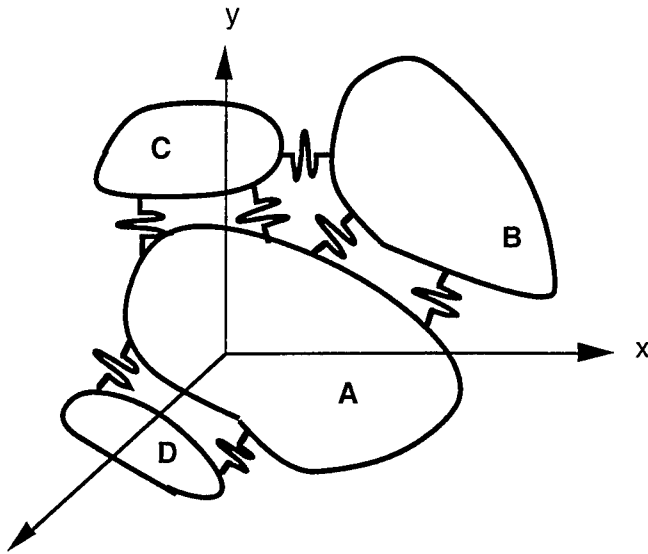


Fig. 1 A sketch of an assembled structural system.

substructures via elastic joints. In the mathematical formalism, however, we will show only the synthesis of two elastically connected substructures, say Substructure A and Substructure B. The extension to including all substructures is a rather straightforward process. The elastic joints will be modeled as general beam elements which are thus capable of resisting and transmitting axial forces, bending moments about the two principal axes in the plane of its cross section, and twisting moments about its centroidal axis. In the simplest case, the joint may be modeled as a linear spring with two lumped masses at its opposite ends. The two substructures may be joined together by any arbitrary number of elastic joints. Each of the joints, say the n^{th} joint, will be represented by a mass and a stiffness matrices, \mathbf{M}^n and \mathbf{K}^n ; both are 12×12 matrices for a general beam element (6 degrees of freedom for each of its end points). Since one of the end points is connected to Substructure A and the other to Substructure B, as will be shown later it is more convenient to partition these matrices as shown below:

$$\mathbf{M}^n = \begin{bmatrix} \mathbf{M}_{aa}^n & \mathbf{M}_{ab}^n \\ \mathbf{M}_{ba}^n & \mathbf{M}_{bb}^n \end{bmatrix} \quad \text{and} \quad \mathbf{K}^n = \begin{bmatrix} \mathbf{K}_{aa}^n & \mathbf{K}_{ab}^n \\ \mathbf{K}_{ba}^n & \mathbf{K}_{bb}^n \end{bmatrix}$$

where the diagonal matrices characterize the dynamic properties of the joint at the interfacing points while the off diagonal matrices are the coupling mass and stiffness matrices between two end points. The coupling mass matrices, \mathbf{M}_{ab}^n and \mathbf{M}_{ba}^n , will be neglected because they are usually either small or zero. The coupling stiffness matrices, \mathbf{K}_{ab}^n and \mathbf{K}_{ba}^n are crucial to transmit forces and moments across the elastic joint. As mentioned earlier, two methods of synthesis which use component modes with different boundary conditions at the interfacial points (where the joint and substructure meet) will be presented. The free-interface formulation will be first discussed and then followed by the fixed-interface formulation.

Free-Interface Method

In the free-interface method, both substructures have a free boundary condition at the joint interfacial points. Depending on the boundary condition that may be imposed elsewhere on the substructures, each substructure will be required to have zero to six rigid body (three translational and three rotational) modes in addition to the required elastic modes. A modal synthesis is by definition to seek the solution for the displacement fields, $\mathbf{w}(\mathbf{x},t)$ and $\mathbf{u}(\mathbf{x},t)$ for Structures A and B, respectively, to be expressed in terms of the following expansion:

$$\left. \begin{aligned} \mathbf{w}(\mathbf{x},t) &= \sum_{m=1}^{N_a^t} q_m(t) \boldsymbol{\varphi}_m(\mathbf{x}) \\ \mathbf{u}(\mathbf{x},t) &= \sum_{n=1}^{N_b^t} p_n(t) \boldsymbol{\psi}_n(\mathbf{x}) \end{aligned} \right\} \quad (1)$$

where N_a^t and N_b^t are the total numbers of modes (elastic and rigid body, say the elastic mode from number 1 to $N_{a,b}$, and the rigid body mode from number $N_{a,b}+1$ to $N_{a,b}^t$) to be included in Substructure A and B, respectively. The displacement vectors and eigenvectors shown in Eq. (1) will, in general, contain the translational and rotational displacements, which is common in the finite-element analysis. In classical analyses, however, solutions are often given for the translational displacement only. In such a case, the rotational displacement can be usually obtained

by simply taking the spatial derivative of the translational displacement field. Let the displacement fields for motions of the two subsystems A and B be associated with self-adjoint stiffness and mass operators, $K_{a,b}$ and $\rho_{a,b}$ in the Hilbert space. The mass operator may be, simply, the mass density, mass per unit area, or mass per unit length for a 3-dimensional, 2-dimensional, or 1-dimensional structure, respectively. Imposing the stiffness operator $K_{a,b}$ on a rigid body mode will produce no net force, i.e., $K_{a,b}\phi_{\text{rigid}}=0$. Accordingly, the kinetic energy, T , and the potential energy, U , of the joined system can be expressed as follows:

$$T = \frac{1}{2} \langle \dot{\mathbf{w}}, \rho_a \dot{\mathbf{w}} \rangle + \frac{1}{2} \langle \dot{\mathbf{u}}, \rho_b \dot{\mathbf{u}} \rangle + \frac{1}{2} \sum_{i=1}^{N_c} \left[\dot{\mathbf{w}}_i \cdot \mathbf{M}_{aa}^i \dot{\mathbf{w}}_i + \dot{\mathbf{u}}_i \cdot \mathbf{M}_{bb}^i \dot{\mathbf{u}}_i \right] \quad (2)$$

$$U = \frac{1}{2} \langle \mathbf{w}, K_a \mathbf{w} \rangle + \frac{1}{2} \langle \mathbf{u}, K_b \mathbf{u} \rangle + \frac{1}{2} \sum_{i=1}^{N_c} \begin{bmatrix} \mathbf{w}_i \\ \mathbf{u}_i \end{bmatrix} \cdot \begin{bmatrix} \mathbf{K}_{aa}^i & \mathbf{K}_{ab}^i \\ \mathbf{K}_{ba}^i & \mathbf{K}_{bb}^i \end{bmatrix} \begin{bmatrix} \mathbf{w}_i \\ \mathbf{u}_i \end{bmatrix} \quad (3)$$

where $\langle \cdot, \cdot \rangle$ is the inner product in the Hilbert Space, " \cdot " is a dot product between two vectors, upper dot is the time derivative, N_c is the number of elastic joints, $\mathbf{w} = \mathbf{w}(\mathbf{x}, t)$, $\mathbf{u} = \mathbf{u}(\mathbf{x}, t)$, $\mathbf{w}_i = \mathbf{w}(\mathbf{x}_i, t)$, $\mathbf{u}_i = \mathbf{u}(\mathbf{x}'_i, t)$, and \mathbf{x}_i and \mathbf{x}'_i are a pairs of interfacial points where the i^{th} elastic joint is connected to the substructures. Although \mathbf{x}_i and \mathbf{x}'_i are in general two separate points, we will use $\mathbf{w}_i = \mathbf{w}(\mathbf{x}_i, t)$ and $\mathbf{u}_i = \mathbf{u}(\mathbf{x}_i, t)$, because \mathbf{w}_i and \mathbf{u}_i are by definition the quantities at two separated points.

According to Eq. (1), at the elastic joint and the substructure connecting points, it is required that:

$$\left. \begin{aligned} \mathbf{w}_i &= \mathbf{w}(\mathbf{x}_i, t) = \sum_{m=1}^{N_a^i} q_m(t) \boldsymbol{\varphi}_m(\mathbf{x}_i) \\ \mathbf{u}_i &= \mathbf{u}(\mathbf{x}_i, t) = \sum_{n=1}^{N_b^i} p_n(t) \boldsymbol{\psi}_n(\mathbf{x}_i) \end{aligned} \right\}, \quad i = 1, 2, \dots, N_c \quad (4)$$

This is the required constraint among the generalized coordinates, $[q_1, q_2, \dots, p_1, p_2, \dots, \mathbf{w}_1, \mathbf{w}_2, \dots, \mathbf{u}_1, \mathbf{u}_2, \dots]^T$, at each interfacing point. Therefore, the constraint equations are given as follows:

$$\left. \begin{aligned} \mathbf{f}_i &= \mathbf{w}_i - \sum_{m=1}^{N_a^t} q_m(t) \boldsymbol{\varphi}_m(\mathbf{x}_i) = 0 \\ \tilde{\mathbf{f}}_i &= \mathbf{u}_i - \sum_{n=1}^{N_b^t} p_n(t) \boldsymbol{\psi}_n(\mathbf{x}_i) = 0 \end{aligned} \right\}, \quad i = 1, 2, \dots, N_c \quad (5)$$

It follows that the Lagrangian, L , of the constrained system is now of the form

$$L = T - U + \sum_{i=1}^{N_c} (\boldsymbol{\lambda}_i \cdot \mathbf{f}_i + \tilde{\boldsymbol{\lambda}}_i \cdot \tilde{\mathbf{f}}_i) \quad (6)$$

where $\boldsymbol{\lambda}_i$ and $\tilde{\boldsymbol{\lambda}}_i$ are the Lagrange multipliers. Substituting Eqs. (1-5) into (6) and then substituting the resulting Eq. (6) into the Lagrange equations of motion with respect to the generalized coordinates, $[q_1, q_2, \dots, p_1, p_2, \dots, \mathbf{w}_1, \mathbf{w}_2, \dots, \mathbf{u}_1, \mathbf{u}_2, \dots]^T$. This yields the constrained equation of motion given as follows:

$$\left. \begin{aligned} \mathbf{M}_q \ddot{\mathbf{q}} + \mathbf{K}_q \mathbf{q} + \sum_{i=1}^{N_c} \boldsymbol{\lambda}_i \cdot \boldsymbol{\varphi}(\mathbf{x}_i) &= 0 \\ \mathbf{M}_p \ddot{\mathbf{p}} + \mathbf{K}_p \mathbf{p} + \sum_{i=1}^{N_c} \tilde{\boldsymbol{\lambda}}_i \cdot \boldsymbol{\psi}(\mathbf{x}_i) &= 0 \\ \mathbf{M}_{aa}^i \ddot{\mathbf{w}}_i + \mathbf{K}_{aa}^i \mathbf{w}_i + \mathbf{K}_{ab}^i \mathbf{u}_i - \boldsymbol{\lambda}_i &= 0; \quad i = 1, 2, \dots, N_c \\ \mathbf{M}_{bb}^i \ddot{\mathbf{u}}_i + \mathbf{K}_{ba}^i \mathbf{w}_i + \mathbf{K}_{bb}^i \mathbf{u}_i - \tilde{\boldsymbol{\lambda}}_i &= 0; \quad i = 1, 2, \dots, N_c \end{aligned} \right\} \quad (7)$$

where \mathbf{M}_q and \mathbf{M}_p are the mass matrices (excluding the joint masses) with respect to the generalized coordinates \mathbf{q} and \mathbf{p} , respectively; \mathbf{K}_q and \mathbf{K}_p are the corresponding stiffness matrices; $\mathbf{p} = [p_1, p_2, \dots]^T$; $\mathbf{q} = [q_1, q_2, \dots]^T$; $\boldsymbol{\varphi}(\mathbf{x}_i) = [\varphi_1(\mathbf{x}_i), \varphi_2(\mathbf{x}_i), \dots]^T$; and $\boldsymbol{\psi}(\mathbf{x}_i) = [\psi_1(\mathbf{x}_i), \psi_2(\mathbf{x}_i), \dots]^T$.

The Lagrange multipliers in Eq. (7) can be eliminated by substitution within the equation itself and the generalized coordinates, \mathbf{w}_i , and \mathbf{u}_i can also be eliminated by substitution of the constraint condition, Eq. (5), into Eq. (7). If we further assume that the motion to be time-harmonic, i.e.,

$$\mathbf{q}(t) = \mathbf{a} e^{-i\omega t}; \quad \mathbf{p}(t) = \mathbf{b} e^{-i\omega t}, \quad (8)$$

by eliminating λ_i , $\tilde{\lambda}_i$, \mathbf{w}_i , and \mathbf{u}_i in Eq. (7), we have the following generalized linear eigenvalue equations:

$$\begin{bmatrix} \mathbf{K}_{AA} & \mathbf{K}_{AB} \\ \mathbf{K}_{BA} & \mathbf{K}_{BB} \end{bmatrix} \begin{bmatrix} \mathbf{a} \\ \mathbf{b} \end{bmatrix} = \omega^2 \begin{bmatrix} \mathbf{M}_{AA} & \mathbf{M}_{AB} \\ \mathbf{M}_{BA} & \mathbf{M}_{BB} \end{bmatrix} \begin{bmatrix} \mathbf{a} \\ \mathbf{b} \end{bmatrix} \quad (9)$$

where

$$\left. \begin{aligned} \mathbf{M}_{AA, mn} &= \langle \phi_m, \rho_a \phi_n \rangle + \sum_{i=1}^{N_c} \phi_m(\mathbf{x}_i) \cdot \mathbf{M}_{aa}^i \phi_n(\mathbf{x}_i) \\ \mathbf{K}_{AA, mn} &= \langle \phi_m, K_a \phi_n \rangle + \sum_{i=1}^{N_c} \phi_m(\mathbf{x}_i) \cdot \mathbf{K}_{aa}^i \phi_n(\mathbf{x}_i) \end{aligned} \right\} \quad m, n=1, 2, \dots, N_a^t$$

$$\left. \begin{aligned} \mathbf{M}_{BB, mn} &= \langle \psi_m, \rho_b \psi_n \rangle + \sum_{i=1}^{N_c} \psi_m(\mathbf{x}_i) \cdot \mathbf{M}_{bb}^i \psi_n(\mathbf{x}_i) \\ \mathbf{K}_{BB, mn} &= \langle \psi_m, K_b \psi_n \rangle + \sum_{i=1}^{N_c} \psi_m(\mathbf{x}_i) \cdot \mathbf{K}_{bb}^i \psi_n(\mathbf{x}_i) \end{aligned} \right\} \quad m, n=1, 2, \dots, N_b^t$$

$$\mathbf{K}_{AB, mn} = \sum_{i=1}^{N_c} \phi_m(\mathbf{x}_i) \cdot \mathbf{K}_{ab}^i \psi_n(\mathbf{x}_i), \quad m=1, 2, \dots, N_a^t; \quad n=1, 2, \dots, N_b^t$$

and $\mathbf{K}_{BA} = \mathbf{K}_{AB}^T$, $\mathbf{M}_{AB} = \mathbf{M}_{BA} = 0$.

Since the elastic component modes (for mode numbers up to $N_{a,b}$) are orthogonal with respect to $K_{a,b}$ and $\rho_{a,b}$, the inner products shown above may be simplified as follows:

$$\left. \begin{aligned} \langle \phi_i, \rho_a \phi_j \rangle &= M_{ai} \delta_{ij}, & \langle \psi_i, \rho_b \psi_j \rangle &= M_{bi} \delta_{ij} \\ \langle \phi_i, K_a \phi_j \rangle &= \omega_{ai}^2 M_{ai} \delta_{ij}, & \langle \psi_i, K_b \psi_j \rangle &= \omega_{bi}^2 M_{bi} \delta_{ij} \end{aligned} \right\} \quad \forall i, j \leq N_{a,b} \quad (11)$$

where M_{ai} and M_{bi} are the modal masses for Structures A and B, respectively, and ω_{ai} and ω_{bi} are the corresponding modal resonance frequencies. However, when a rigid body mode (the mode number $> N_{a,b}$) is involved, the orthogonality will, in general, not hold, e.g.,

$$\left. \begin{aligned} \langle \phi_i, \rho_a \phi_j \rangle &= \mathbf{M}_{AA,ij} \quad i \text{ or } j > N_a; \quad \langle \psi_i, \rho_b \psi_j \rangle = \mathbf{M}_{BB,ij} \quad i \text{ or } j > N_b \\ \langle \phi_i, K_a \phi_j \rangle &= 0, \quad \langle \psi_i, K_b \psi_j \rangle = 0 \quad \text{when } i \text{ or } j > N_{a,b} \end{aligned} \right\} \quad (12)$$

which shows that some of the cross modal mass terms between elastic and rigid body modes may not be zero and rigid body modes produce zero modal stiffness. The mass matrices, \mathbf{M}_{AA} and \mathbf{M}_{BB} , contain the modal masses defined above and the non-diagonal mass terms contributed by the joint masses, \mathbf{M}_{aa}^i and \mathbf{M}_{bb}^i . Because we assume that $\mathbf{M}_{ab}^i = \mathbf{M}_{ba}^i = 0$, there is no coupled mass term between A and B, i.e., $\mathbf{M}_{AB} = \mathbf{M}_{BA} = 0$. The stiffness matrices, \mathbf{K}_{AA} and \mathbf{K}_{BB} , contain the uncoupled modal stiffnesss (the diagonal terms) and the cross modal stiffness within structures A and B, respectively, contributed by the joints. The other stiffness matrices, \mathbf{K}_{AB} and \mathbf{K}_{BA} , are evidently the cross-coupling matrices between the modes in Structures A and those in Structure B.

Fixed-Interface Method

In the fixed-interface method, the component mode functions must satisfy the fixed boundary condition at the joint interfacial points. Summation over all of these modes produces no net displacement at the joint interfacing points. In this formulation, the interfacial point motions at each degree of freedom is usually described by a static influence function [6]. The ℓ^{th} - component of the static influence function for Substructure A at i^{th} joint location, \mathbf{g}_{ie}^a , is the internal displacement of the structure due to a unit ℓ^{th} - component displacement at that location while all other components at that location and all components at all other interfacing points fixed. These functions may be considered as static modes which replace the rigid body modes in Eq. (1). If we let the number of degrees of freedom at each interfacing point to be n_j , and define a mapping of (i, ℓ) into a number sequence, say $m = N_a + (i-1)n_j + \ell$ and $n = N_b + (i-1)n_j + \ell$, we may represent \mathbf{g}_{ie}^a and \mathbf{g}_{ie}^b by $\phi_m(\mathbf{x})$ and $\psi_n(\mathbf{x})$, respectively. Consequently, the expansion including static influence functions can then be represented by Eq. (1).

With the expansion described above, the equations for the free-interface formulation, Eqs. (2)-(3), are also applicable to this case. According to the definition of \mathbf{g}_{ie}^a and \mathbf{g}_{ie}^b , Eq. (4) becomes

$$\mathbf{w}_{i\ell} = \mathbf{q}_{N_a + (i-1)n_j + \ell} \quad \mathbf{u}_{i\ell} = \mathbf{p}_{N_b + (i-1)n_j + \ell}$$

where $\mathbf{w}_{i\ell}$ and $\mathbf{u}_{i\ell}$ are ℓ^{th} -component of \mathbf{w}_i and \mathbf{u}_i , respectively. With this simplified constraint condition, using Lagrange multipliers will no longer advantageous. In order to reach Eq. (9), we may substitute above relationship into Eqs. (2-3) and form the Lagrangian, L. By substituting L into the Lagrange equations, we reach Eq. (9) with the following mass and stiffness matrices:

$$\mathbf{M}_{AA,mn} = \begin{cases} M_{am} \delta_{mn}, & m, n \leq N_a \\ \langle \boldsymbol{\varphi}_m, \rho_a \boldsymbol{\varphi}_n \rangle, & m \leq N_a, n > N_a \text{ or } m > N_a, n \leq N_a \\ M_{aa,\ell}^i + \langle \boldsymbol{\varphi}_m, \rho_a \boldsymbol{\varphi}_n \rangle, & m = N_a + (i-1)n_j + \ell, n = N_a + (i-1)n_j + \ell' \end{cases}$$

$$\mathbf{M}_{BB,mn} = \begin{cases} \text{similar to } \mathbf{M}_{AA,mn}, \text{ except replacing subscript "a" and} \\ \text{symbol "}\boldsymbol{\varphi}\text{" by "}\boldsymbol{\psi}\text{"}, \text{ respectively.} \end{cases}$$

$$\mathbf{K}_{AA,mn} = \begin{cases} \omega_{am}^2 M_{am} \delta_{mn}, & m, n \leq N_a \\ \langle \boldsymbol{\varphi}_m, K_a \boldsymbol{\varphi}_n \rangle, & m \leq N_a, n > N_a \text{ or } m > N_a, n \leq N_a \\ K_{aa,\ell}^i + \langle \boldsymbol{\varphi}_m, K_a \boldsymbol{\varphi}_n \rangle, & m = N_a + (i-1)n_j + \ell, n = N_a + (i-1)n_j + \ell' \end{cases} \quad (13)$$

$$\mathbf{K}_{BB,mn} = \begin{cases} \text{similar to } \mathbf{K}_{AA,mn}, \text{ except replacing subscript "a" and} \\ \text{symbol "}\boldsymbol{\varphi}\text{" by "}\boldsymbol{\psi}\text{"}, \text{ respectively.} \end{cases}$$

$$\mathbf{K}_{AB,mn} = \begin{cases} 0, & m \leq N_a, n \leq N_b \\ K_{ab,\ell}^i, & m = N_a + (i-1)n_j + \ell, n = N_b + (i-1)n_j + \ell' \end{cases}$$

$$\text{and } \mathbf{K}_{BA} = \mathbf{K}_{AB}^T, \quad \mathbf{M}_{AB} = \mathbf{M}_{BA} = 0.$$

It is to note that, the inner product of two static influence functions does not vanish. Instead, it is equal to the external stiffness, $S_{A,ij}$ and $S_{B,ij}$ for Substructure A and B, respectively [4], i.e.,

$$\begin{aligned} \langle \phi_m, K_a \phi_n \rangle &= S_{A,mn}, \quad \langle \psi_m, K_b \psi_n \rangle = S_{B,mn}, \\ \text{when } m &= N_{a,b} + (i-1)n_j + \ell, \quad n = N_{a,b} + (i-1)n_j + \ell'. \end{aligned} \quad (14)$$

External stiffness matrices relate the forces and displacements for all degrees of freedom at the interfacing points. The eigenvalue analysis with the fixed-interface method can then be performed with the matrices defined by Eqs. (9) and (13).

The major advantage for the above modal synthesis is the possibility of determining the modal interaction between substructures via the coupling effect of elastic joints. For example, if

$\begin{bmatrix} a \\ b \end{bmatrix}_\ell$ is the eigenvector for eigenvalue, ω_ℓ^2 , we can determine the modal interaction by evaluating the coefficients $a_{\ell m}$'s and $b_{\ell n}$'s at that frequency because these coefficients represent the level of component mode participation in that mode. The deviation of assembled structural modes from those of the unassembled component modes depends on the coefficients $a_{\ell m}$'s and $b_{\ell n}$'s as well. For example, if either $a_{\ell m}$'s or $b_{\ell n}$'s are dominated by one particular term then there is a mode in Structure A or a mode in Structure B that is not affected by the coupling of elastic joints. On the other hand, if $a_{\ell m}$'s and $b_{\ell n}$'s are broadly distributed, the ℓ^{th} mode of the assembled structure are then substantially modified from the component modes of the uncoupled structures, which indicates that the two structures are strongly coupled at angular frequency, ω_ℓ .

NUMERICAL EXAMPLES AND RESULTS

Examples of using component mode synthesis methods formulated previously with free-interface and fixed-interface boundary conditions will be given in this section. The system consists of two cantilever beams connected by a linear, massless spring at their respective endpoints. This is depicted in Fig. 2. For both beams, the mass density is $0.000733 \text{ lbs-sec}^2/\text{in}^4$, Young's modulus is $30,000,000 \text{ lbs/in}^2$, spring constant is $100,000 \text{ lbs/in}$. The height and width of beam A are 5 inches and 2 inches respectively, its length is 144 inches; the height and width of beam B are 4 inches and 2 inches respectively, and its length is 72 inches.

In the free-interface method, the component modes are calculated with the fixed-free boundary condition and there is no rigid body mode. All elastic modes are orthogonal with respect to the mass and stiffness operator. The elastic joint stiffness matrix is obviously,

$$\mathbf{K}^1 = \begin{bmatrix} k & -k \\ -k & k \end{bmatrix},$$

where k is the spring constant. The formation of the matrices for eigenvalue analysis is quite straightforward according to Eqs. (9) to (12).

In the fixed-interface method, the component modes are calculated with fixed-hinged boundary condition. The static influence function is the normalized cantilever beam deflection function due to a load at the tip of the beam. The external stiffness matrices (1x1 matrices) are $3EI/(L_a^3)$ and $3EI/(L_b^3)$ for beam A and B, respectively. Again, the formation of the matrices for eigenvalue analysis is quite straightforward according to Eqs. (9) and (13).

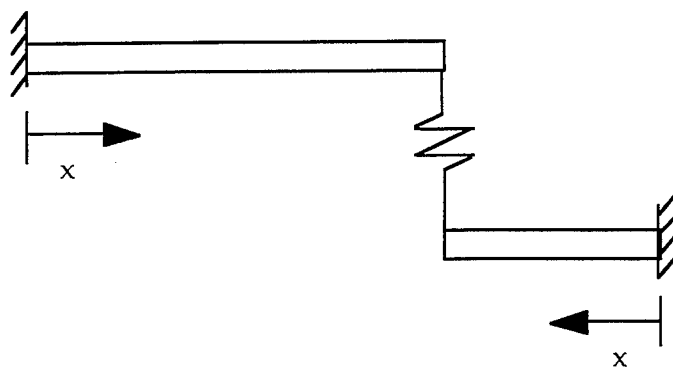


Fig. 2 The system of two cantilever beams connected by a spring.

The calculated eigen frequencies of the joined-beam with the two methods are tabulated in Table A. In order to provide a independent check, a finite-element analysis is also performed for the same system. Considering there are only 10 modes in each beam are used in the synthesis, results from all three methods converge to the solution with small errors. If we use the finite-element results as the reference, the difference between the fixed-interface and finite-element solutions are less than 1% while that between the

free-interface and finite-element methods are less than 10%. The mode shapes calculated with the free- and fixed-interface methods are compared and shown to be similar (see Fig. 3). For Mode 1, results using the two methods are identical. The differences for Mode 3 are also small.

Table A: Comparison of calculated resonance frequencies by free- and fixed -interface method and finite-element method

FINITE-ELEMENT METHOD (Hz)	FREE INTERFACE METHOD (Hz)	% ERROR *	FIXED INTERFACE METHOD (Hz)	% ERROR *
14.5	14.5	0	14.4	0
44.1	44	0	44	0
103.7	99.4	4.1	104.3	0.5
142.9	143.9	0.7	143	0.06
230.5	215	6.7	232.2	0.7
299.1	273.6	8.5	300.8	0.6

* ERROR = (Current method calculations - FEM calculations)/(FEM calculations)

SUMMARY AND CONCLUSION

In this paper, a modified component mode synthesis method has been developed for an assembled structure consisting of physically divided substructures joined together by elastic connections such as bolts, rivets, springs, beams, or elastic mounts, etc.. Both free-interface and fixed-interface methods are presented for the component modes with free and fixed interface boundary conditions, respectively. Numerical examples are given for the case of two cantilever beams connected by a spring at their end points. Results calculated from the free- and fixed-interface formulation are compared and shown in good agreement with that calculated from the finite-element method.

In the simple numerical example shown in this paper, use of component mode synthesis with fixed interface boundary conditions produce better results than those calculated using free-interface boundary conditions. This trends to confirm with Farstad and Singh's [6] conclusion that component mode synthesis

formulated with fixed interface boundary conditions converge to the lower mode solution faster than that with the free interface boundary conditions.

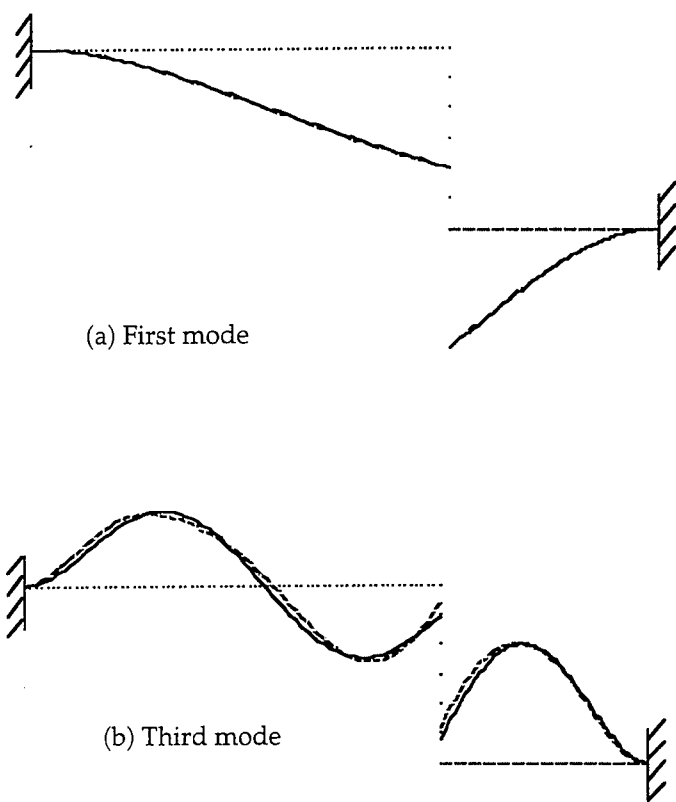


Fig. (3) Comparison of the calculated first and third mode using free (dash line) and fixed (solid line) interface methods.

ACKNOWLEDGMENTS

This work was supported by the ILIR Program of the Carderock Division, Naval Surface Warfare Center (NSWCCD). The authors are grateful for the encouragement and support from Dr. Bruce Douglas, the Research Director of NSWCCD. The finite-element

calculation provided by Dr. Raymond Cheng of NSWCCD is gratefully acknowledged.

REFERENCES

1. Hurty, W.C., "Dynamic Analysis of Structural Systems Using Component Modes," AIAA Journal, Vol. 3, 1965, pp. 678-685.
2. Craig, R. R. Jr. and Bampton, M.C.C., "Coupling of Substructures for Dynamic Analysis," AIAA Journal, Vol. 6, No. 7, 1968, pp. 1313-1319.
3. Dowell, E.H., "Free Vibration of a Linear Structure with Arbitrary Support Conditions," ASME J. Appl. Mech., Vol. 38, 1971 pp. 595-600.
4. Dowell, E.H., "Free Vibration of an Arbitrary Structure in Terms of Component Modes," ASME J. Appl. Mech., Vol. 39, 1972, pp. 727-732.
5. Meirovitch, L., *Computational Methods in Structural Dynamics*, Sijthoff & Noordhoff, Alphen aan den Rijn, The Netherlands, 1980.
6. Farstad, J.E., and Singh, R., "Structurally Transmitted Dynamic Power in Discretely Joined Damped Component Assemblies," J. Acoust. Soc. Am., Vol. 97, No. 5, 1995, pp. 2855-2865.
7. Hwang, Y.F., Louie, L.L., "Numerical Model of a Coupled Structural System Connected by Active/Passive Springs," paper presented at 1996 ASME International Mechanical Engineering Congress and Exposition, Atlanta, GA, Nov. 1996, available as ASME publication No. DE-Vol. 93, *Active Control of Vibration and Noise*, edited by C.A. Tan, H.S. Tzou, R. Shoureshi and E.W. Hendricks, 1996, pp. 389-397.

COMPLEX EIGENSOLUTIONS FOR FREQUENCY DEPENDENT SOIL-STRUCTURE INTERACTING SYSTEMS

G. Oliveto and I. Calì

Istituto di Scienza delle Costruzioni, Università di Catania
Viale A. Doria 6, 95125 Catania, Italy

A. Santini

Istituto di Ingegneria Civile ed Energetica, Università di Reggio Calabria
Via E. Cuzzocrea 48, 89128 Reggio Calabria, Italy

ABSTRACT

This paper presents a method for the calculation of eigenvalues and eigenvectors of frequency dependent soil-structure interacting systems. Two sets of orthogonality conditions are derived for subsequent application in dynamical analyses. Numerical applications, showing the performance of the method, are also reported.

INTRODUCTION

The dynamical response of structures to earthquake excitations is usually evaluated by considering the supporting soil as rigid. This is a sufficiently accurate assumption for relatively flexible structures on firm soil. As the soil becomes softer and the structure becomes stiffer and massive, the above hypothesis is no longer adequate. In this case soil-structure interaction may significantly effect the structural response. The relative importance of these effects depends on several parameters as has been pointed out in the literature [1, 2]. A review paper on the subject by J.E. Luco was published in the early eighties [3].

The subject has received considerable attention in the literature, especially in connection with the design of nuclear power plants, and is now included as a chapter in some of the best known textbooks on Structural Dynamics [4, 5]. Some specialist books have been published in recent years [6, 7] and in 1993 a NATO Advanced Study Institute was dedicated to Developments in Dynamic Soil-Structure Interaction [8].

Obviously the interaction between soil and structure occurs

through the foundation system. In the literature this has been considered either rigid or flexible. Although a truly rigid foundation system is only an idealisation, it has been shown that in many cases such an assumption is sufficiently representative of the actual behaviour of the structure-foundation system [9]. A flexible foundation would definitely be a more realistic model, but the analysis of the structural response would be much more involved.

In this paper only the case of a rigid foundation is considered. The soil is modelled as an elastic half-space with a rigid massless foundation bonded to it. The interaction between the soil and the structure is then described by the forces exchanged through this rigid interface. In order to write the equations of motion for the structure, the forces applied to it by the soil through the foundation system are needed. These are usually provided by the 'so-called impedance functions of the rigid foundation in terms of the six degrees of freedom of the foundation itself. The impedance functions were initially provided for a rigid circular massless foundation [10, 11] and extended by several authors to foundations of various shapes [12]. Originally the impedance functions were computed numerically and were provided in the form of tables as a set of values depending on the excitation frequency. Subsequently analytical expressions were fitted in order to facilitate their use in the numerical calculation of the structural response [13, 14].

The analytical expressions for the impedance functions, besides being obtained through curve-fitting procedures, have also been derived from physical models [15-18]. These present some particularly appealing features for the analysis that will be pursued in this paper. It should be recognised that the representation of the soil by the impedance functions is equivalent to a set of springs and dash-pots whose properties are, however, dependent on the frequency. Furthermore, the impedance functions are complex in the algebraic sense of the term, even if the excitation frequency is real. This implies that the natural frequencies of a soil-structure interacting system are generally complex, although sometimes a few of them may be purely imaginary. The problem of finding the natural frequencies and the corresponding modes of vibration of such systems has not so far been solved. Therefore only approximate procedures have been presented in the literature for the calculation of the dynamical response of soil-structure interacting systems in the time domain [19-21].

In this paper, after briefly describing the impedance functions for the rigid massless foundation-soil system, the equations of motion for a typical soil-structure system are formulated.

Subsequently the free vibration problem is analysed and, through some simple algebraic manipulations, is transformed into a constant coefficient eigenvalue problem. Two sets of orthogonality conditions are established for the eigenvalues and eigenvectors for subsequent use in the evaluation of the dynamical response. Numerical applications are finally reported in order to show in actual calculations the performance of the proposed method and the satisfaction of the orthogonality conditions.

IMPEDANCE FUNCTIONS

The impedance functions, Figure 1, relate the amplitude of the harmonic forces applied to the rigid massless foundation to that of the corresponding displacements in the following form

$$\begin{bmatrix} V \\ M \end{bmatrix} = \begin{bmatrix} K_{VV}(\omega) & K_{VM}(\omega) \\ K_{MV}(\omega) & K_{MM}(\omega) \end{bmatrix} \begin{bmatrix} u_o \\ \vartheta_o \end{bmatrix}$$

where

$$\begin{aligned} K_{VV}(\omega) &= K_u(k_{11} + i\alpha_o c_{11}) \\ K_{MM}(\omega) &= K_g(k_{22} + i\alpha_o c_{22}) \\ K_{VM}(\omega) &= K_{ur_o}(k_{12} + i\alpha_o c_{12}). \end{aligned}$$

In the above expressions k_{ij} and c_{ij} are dimensionless coefficients depending on Poisson's ratio ν for the soil and on the frequency parameter

$$\alpha_o = \omega r_o / c_s,$$

where r_o is the radius of the foundation plate and c_s is the shear wave velocity in the soil. This latter is given by

$$c_s = \sqrt{G/\rho},$$

where G and ρ are the shear modulus and the mass density of the soil. Furthermore

$$K_u = \frac{8Gr_o}{2-\nu} \quad \text{and} \quad K_g = \frac{8Gr_o^3}{3(1-\nu)}$$

are the translational and rotational static stiffnesses of the foundation plate respectively.

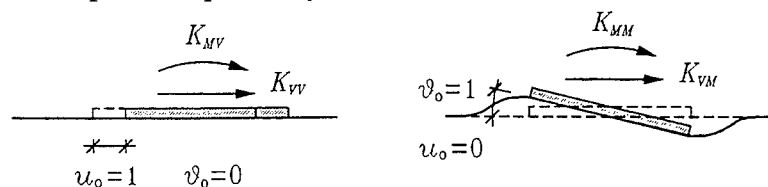


Figure 1. Definition of impedance functions for rigid massless foundations on elastic or visco-elastic soil.

The representation of the impedance functions may be found in the literature as graphs of the real and the imaginary parts in terms of the frequency [4, 10].

In the literature the coupling terms have been found to be small and have often been neglected in the applications to the evaluation of the structural response. The cone theory, that was originated by Ehlers [22] and has been subsequently developed by Meek and Veletsos [15] and by Meek and Wolf [16-18], does not account for the coupling terms. In this paper the cone model theory is used for the particularly appealing analytical expressions which prove to be extremely useful in the subsequent developments.

For the applications that follow only two particular cones are needed, i.e. the horizontal translational cone and the rotational or rocking cone. The impedance functions for such cones take the following expressions

$$K_{VV}(\omega) = K_u(1 + i a_0 c_u) \quad (1a)$$

$$K_{MM}(\omega) = K_g[k_g(a_0) + i a_0 c_g(a_0)] \quad (1b)$$

where

$$c_u = \pi(2 - \nu)/8, \quad k_g(a_0) = 1 - \frac{1}{3} d a_0^2 - \frac{1}{3} \frac{a_0^2}{b^2 + a_0^2}, \quad c_g(a_0) = \frac{1}{3b} \frac{a_0^2}{b^2 + a_0^2},$$

$$d = \frac{4\mu_g}{\pi} \frac{z_0}{r_0} \left(\frac{c_s}{c}\right)^2, \quad b = \frac{r_0}{z_0} \frac{c}{c_s}, \quad \frac{z_0}{r_0} = \frac{9\pi}{32} (1 - \nu) \left(\frac{c}{c_s}\right)^2,$$

$$\mu_g = \begin{cases} 0 & \text{for } \nu \leq 1/3 \\ 0.3 \pi (\nu - 1/3) & \text{for } \nu > 1/3 \end{cases}, \quad \frac{c}{c_s} = \begin{cases} \sqrt{2(1 - \nu)/(1 - 2\nu)} & \text{for } \nu \leq 1/3 \\ 2 & \text{for } \nu > 1/3 \end{cases}.$$

A representation of these impedance functions in terms of frequency is given in reference [18]. This representation, as are all the others presented in the literature, is based on the assumption that the frequency parameter a_0 is real. However, as has been mentioned in the introduction, the natural frequencies are usually complex and those expressions need appropriate conversion in terms of real and imaginary parts of the frequency parameter. A particularly simple expression can be found for the case when the frequency is a purely imaginary number and the eigenvalue parameter $s_0 = i a_0$ is a real number. In this case the impedance functions become real and take the following expressions

$$K_{VV}(\omega) = K_u(1 + s_0 c_u) \quad (2a)$$

$$K_{MM}(\omega) = \frac{K_g}{b + s_0} \left[b + s_0 + \frac{1 + b^2 d}{3b} s_0^2 + \frac{d}{3} s_0^3 \right] \quad (2b)$$

which have been represented in Figures 2, 3 and 4. Obviously expressions (1) and (2) are in fact equivalent and can be reconverted from one set into the other.

It should be noticed that the translational impedance has one zero corresponding to

$$\alpha_{ou} = -is_{ou} = i/c_u$$

in terms of a purely imaginary frequency. This corresponds to a free creeping motion of the soil with the bonded rigid foundation towards the static equilibrium position.

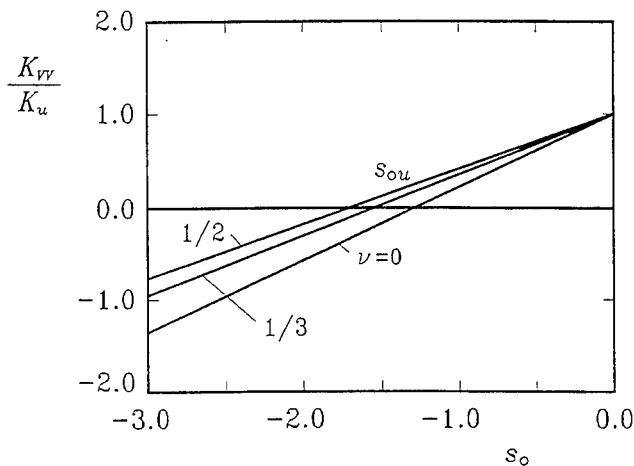


Figure 2. Translational impedance function for the real eigenvalue parameter s_o .

The rocking impedance presents, instead, two complex conjugate zeros for $\nu \leq 1/3$, namely

$$s_{o,g} = b(-3 \pm i\sqrt{3})/2 \quad \text{or} \quad \alpha_{o,g} = -is_{o,g} = b(\pm\sqrt{3} + 3i)/2,$$

which correspond to a damped free vibration motion of the soil with the bonded rigid foundation. For $1/3 < \nu \leq 1/2$ there exist two complex conjugate zeros and a real one which cannot be expressed in a simple mathematical form. They correspond, respectively, to a free vibration motion and to a creeping motion of the soil with the rigid foundation bonded to it. Furthermore the rocking impedance exhibits a pole provided by

$$\alpha_{op} = -is_{op} = ib$$

in terms of a purely imaginary frequency. This corresponds to a free creeping motion of the soil with the bonded rigid foundation and zero surface rotation and translation.

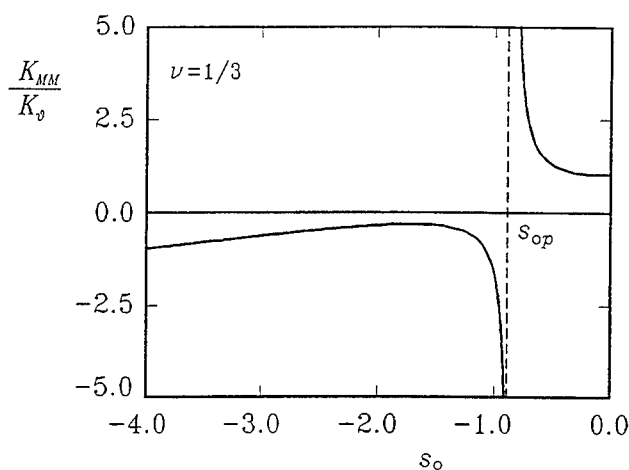


Figure 4. Rocking impedance function for the real eigenvalue parameter s_o ($\nu = 1/3$).

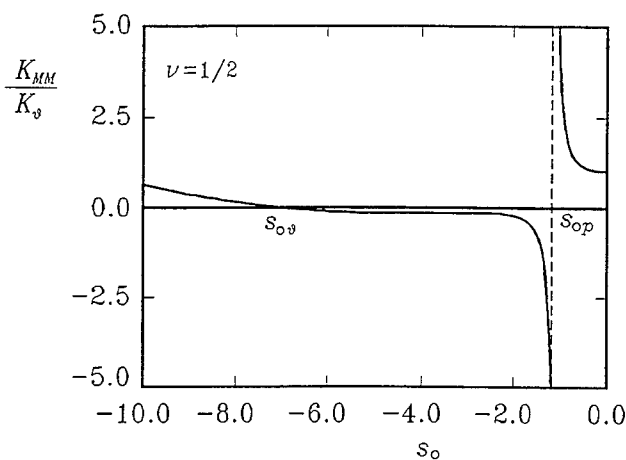


Figure 4. Rocking impedance function for the real eigenvalue parameter s_o ($\nu = 1/2$).

EQUATIONS OF MOTION

The equations of motion for the free vibrations of a soil-structure interacting system may be written as follows

$$\begin{bmatrix} \mathbf{M} & \mathbf{M}_b \\ \mathbf{M}_b^T & \mathbf{M}_{bb} \end{bmatrix} \begin{bmatrix} \ddot{\mathbf{u}} \\ \ddot{\mathbf{u}}_b \end{bmatrix} + \begin{bmatrix} \mathbf{C} & \mathbf{C}_b \\ \mathbf{C}_b^T & \mathbf{C}_{bb} \end{bmatrix} \begin{bmatrix} \dot{\mathbf{u}} \\ \dot{\mathbf{u}}_b \end{bmatrix} + \begin{bmatrix} \mathbf{K} & \mathbf{K}_b \\ \mathbf{K}_b^T & \mathbf{K}_{bb} + \mathbf{K}_f \end{bmatrix} \begin{bmatrix} \mathbf{u} \\ \mathbf{u}_b \end{bmatrix} = \begin{bmatrix} \mathbf{0} \\ \mathbf{0} \end{bmatrix}$$

where \mathbf{u} is the displacement vector of the structure and \mathbf{u}_b is the vector that contains the degrees of freedom of the rigid foundation. It should be noticed that in the case where $\mathbf{u}_b = \mathbf{0}$, i.e. when the soil

is rigid and there is no interaction, the equations of motion reduce to those for the free vibration of the structure, that is

$$\mathbf{M}\ddot{\mathbf{u}} + \mathbf{C}\dot{\mathbf{u}} + \mathbf{K}\mathbf{u} = \mathbf{0}.$$

The meaning of the matrices \mathbf{M}_{bb} , \mathbf{C}_{bb} , \mathbf{K}_{bb} , \mathbf{M}_b , \mathbf{C}_b , \mathbf{K}_b may be found in textbooks on Structural Dynamics and Earthquake Engineering [5], while \mathbf{K}_I is the matrix of the impedance functions for the rigid massless foundation.

THE EIGENVALUE PROBLEM

By taking the following expressions for the displacement vectors

$$\mathbf{u}(t) = \mathbf{u} \exp\{st\}, \quad \mathbf{u}_b(t) = \mathbf{u}_b \exp\{st\}$$

the equations of motion become

$$\left\{ s^2 \begin{bmatrix} \mathbf{M} & \mathbf{M}_b \\ \mathbf{M}_b^T & \mathbf{M}_{bb} \end{bmatrix} + s \begin{bmatrix} \mathbf{C} & \mathbf{C}_b \\ \mathbf{C}_b^T & \mathbf{C}_{bb} \end{bmatrix} + \begin{bmatrix} \mathbf{K} & \mathbf{K}_b \\ \mathbf{K}_b^T & \mathbf{K}_{bb} + \mathbf{K}_I \end{bmatrix} \right\} \begin{bmatrix} \mathbf{u} \\ \mathbf{u}_b \end{bmatrix} = \begin{bmatrix} \mathbf{0} \\ \mathbf{0} \end{bmatrix}. \quad (3)$$

It should be noted that all the matrices in the above equations are constant with the exception of the impedance matrix which is dependent on the frequency or, for that matter, on the eigenvalue parameter s . With reference to a plane problem, in which only the horizontal translational motion and the rocking motion are considered, these impedance functions take the form already specified in a previous paragraph. In terms of the eigenvalue parameter s these may conveniently be written as follows

$$\mathbf{K}_I = \frac{1}{b + as} \hat{\mathbf{K}}_I$$

where

$$\hat{\mathbf{K}}_I = \begin{bmatrix} K_u \{ b + (1 + bc_u)as + c_u a^2 s^2 \} & 0 \\ 0 & K_g \left\{ b + as + \frac{(1 + b^2 d)a^2}{3b} s^2 + \frac{da^3}{3} s^3 \right\} \end{bmatrix}$$

in which $a = r_0/c_s$. The cumbersome dependence of the impedance functions on the frequency or on the eigenvalue parameter, makes it difficult to apply standard algorithms for the solution of the eigenvalue problem. However this problem can be transformed in a standard form by some appropriate algebraic manipulations. To this aim it is convenient to write the impedance matrix in the following form

$$\mathbf{K}_I = \frac{1}{b + as} (\mathbf{K}_{I0} + s\mathbf{K}_{I1} + s^2\mathbf{K}_{I2} + s^3\mathbf{K}_{I3})$$

with

$$\mathbf{K}_{I0} = \begin{bmatrix} K_u b & 0 \\ 0 & K_g b \end{bmatrix}, \quad \mathbf{K}_{I1} = \begin{bmatrix} K_u(1+bc_u)\alpha & 0 \\ 0 & K_g \alpha \end{bmatrix},$$

$$\mathbf{K}_{I3} = \begin{bmatrix} 0 & 0 \\ 0 & K_g d \alpha^3 / 3 \end{bmatrix}, \quad \mathbf{K}_{I2} = \begin{bmatrix} K_u c_u \alpha^2 & 0 \\ 0 & K_g (1+b^2 d) \alpha^2 / (3b) \end{bmatrix}.$$

Next it is necessary to remove the pole, given by $s_p = -b/\alpha$, from the eigenvalue equations. This may be achieved by multiplying the eigenvalue equations by $b + \alpha s$. These then become

$$(b + \alpha s) \left\{ s^2 \left[\frac{\mathbf{M}}{\mathbf{M}_b^T} \middle| \frac{\mathbf{M}_b}{\mathbf{M}_{bb}} \right] + s \left[\frac{\mathbf{C}}{\mathbf{C}_b^T} \middle| \frac{\mathbf{C}_b}{\mathbf{C}_{bb}} \right] + \left[\frac{\mathbf{K}}{\mathbf{K}_b^T} \middle| \frac{\mathbf{K}_b}{\mathbf{K}_{bb} + \mathbf{K}_I} \right] \right\} \begin{bmatrix} \mathbf{u} \\ \mathbf{u}_b \end{bmatrix} = \begin{bmatrix} \mathbf{0} \\ \mathbf{0} \end{bmatrix}. \quad (4)$$

By performing the algebraic operations these equations may be simplified as follows

$$(s^3 \mathbf{A}_3 + s^2 \mathbf{A}_2 + s \mathbf{A}_1 + \mathbf{A}_0) \mathbf{y} = \mathbf{0} \quad (5)$$

where

$$\mathbf{y}^T = [\mathbf{u}^T \mid \mathbf{u}_b^T],$$

$$\mathbf{A}_3 = \begin{bmatrix} \alpha \mathbf{M} & \alpha \mathbf{M}_b \\ \alpha \mathbf{M}_b^T & \alpha \mathbf{M}_{bb} + \mathbf{K}_{I3} \end{bmatrix}, \quad \mathbf{A}_2 = \begin{bmatrix} b \mathbf{M} + \alpha \mathbf{C} & b \mathbf{M}_b + \alpha \mathbf{C}_b \\ b \mathbf{M}_b^T + \alpha \mathbf{C}_b^T & b \mathbf{M}_{bb} + \alpha \mathbf{C}_{bb} + \mathbf{K}_{I2} \end{bmatrix},$$

$$\mathbf{A}_1 = \begin{bmatrix} b \mathbf{C} + \alpha \mathbf{K} & b \mathbf{C}_b + \alpha \mathbf{K}_b \\ b \mathbf{C}_b^T + \alpha \mathbf{K}_b^T & b \mathbf{C}_{bb} + \alpha \mathbf{K}_{bb} + \mathbf{K}_{I1} \end{bmatrix}, \quad \mathbf{A}_0 = \begin{bmatrix} b \mathbf{K} & b \mathbf{K}_b \\ b \mathbf{K}_b^T & b \mathbf{K}_{bb} + \mathbf{K}_{I0} \end{bmatrix}.$$

This cubic eigenvalue problem (5) may be transformed into a linear one through simple algebraic manipulations. By noting that

$$s \mathbf{y} = \dot{\mathbf{y}}, \quad s^2 \mathbf{y} = \ddot{\mathbf{y}},$$

equation (5) may be written

$$s (\mathbf{A}_3 \ddot{\mathbf{y}} + \mathbf{A}_2 \dot{\mathbf{y}} + \mathbf{A}_1 \mathbf{y}) + \mathbf{A}_0 \mathbf{y} = \mathbf{0}. \quad (6)$$

By including the two identities

$$\mathbf{I} \ddot{\mathbf{z}} - \mathbf{I} \dot{\mathbf{z}} = \mathbf{0}, \quad \mathbf{I} \dot{\mathbf{z}} - \mathbf{I} \mathbf{z} = \mathbf{0},$$

and the supervector $\mathbf{z}^T = [\ddot{\mathbf{y}}^T \mid \dot{\mathbf{y}}^T \mid \mathbf{y}^T]$,

the following linear eigenvalue problem may be formulated

$$(\mathbf{A} + s \mathbf{B}) \mathbf{z} = \mathbf{0} \quad (7)$$

where

$$\mathbf{A} = \begin{bmatrix} -\mathbf{I} & \mathbf{0} & \mathbf{0} \\ \mathbf{0} & -\mathbf{I} & \mathbf{0} \\ \mathbf{0} & \mathbf{0} & \mathbf{A}_0 \end{bmatrix}, \quad \mathbf{B} = \begin{bmatrix} \mathbf{0} & \mathbf{I} & \mathbf{0} \\ \mathbf{0} & \mathbf{0} & \mathbf{I} \\ \mathbf{A}_3 & \mathbf{A}_2 & \mathbf{A}_1 \end{bmatrix}.$$

This may be solved through standard methods for non-symmetrical eigenvalue problems. It should be noticed that, to the knowledge of

the authors, this formulation has not been presented previously in the literature. The transformation of the cubic eigenvalue problem (5) in the linear eigenvalue problem (7) requires the amplification of the order of the problem from N to $3N$.

The technique used for the removal of the pole from the impedance matrix implies that this will appear as an eigenvalue of the transformed problem. In fact, all but one term of the eigenvalue equations (4) are multiplied by $b + as$ and therefore the pole will appear as an eigenvalue of multiplicity $N - 1$. By excluding the pole there remain $2N + 1$ eigenvalues. Therefore, for the fundamental theorem of algebra and corollaries, there exists at least one real eigenvalue. Most of the remaining eigenvalues occur in complex conjugate pairs, but a few of them may turn out to be real.

ORTHOGONALITY CONDITIONS

The orthogonality conditions will be established in a form suitable for subsequent dynamical analyses. Therefore reference is made to equation (3) which is rewritten in the following form

$$[s^2 \mathbf{M}_c + s \mathbf{C}_c + \mathbf{K}_c(s)] \mathbf{y} = \mathbf{0}. \quad (8)$$

The mass, damping and stiffness matrices, \mathbf{M}_c , \mathbf{C}_c and \mathbf{K}_c are the complete matrices reported in partitioned form in equation (3). When equation (8) is written for the n th eigenvalue s_n and the corresponding eigenvector \mathbf{y}_n , becomes

$$[s_n^2 \mathbf{M}_c + s_n \mathbf{C}_c + \mathbf{K}_c(s_n)] \mathbf{y}_n = \mathbf{0}. \quad (9)$$

Similarly for the m th eigenvalue and corresponding eigenvector the following equation is obtained

$$[s_m^2 \mathbf{M}_c + s_m \mathbf{C}_c + \mathbf{K}_c(s_m)] \mathbf{y}_m = \mathbf{0}. \quad (10)$$

Multiplying equation (9) to the left by \mathbf{y}_m^T and equation (10) by \mathbf{y}_n^T and by taking into account the symmetry of the matrices \mathbf{M}_c , \mathbf{C}_c and \mathbf{K}_c , the following two conditions are obtained

$$s_n^2 \mathbf{y}_m^T \mathbf{M}_c \mathbf{y}_n + s_n \mathbf{y}_m^T \mathbf{C}_c \mathbf{y}_n + \mathbf{y}_m^T \mathbf{K}_c(s_n) \mathbf{y}_n = 0 \quad (11)$$

$$s_m^2 \mathbf{y}_m^T \mathbf{M}_c \mathbf{y}_n + s_m \mathbf{y}_m^T \mathbf{C}_c \mathbf{y}_n + \mathbf{y}_m^T \mathbf{K}_c(s_m) \mathbf{y}_n = 0. \quad (12)$$

Subtracting equation (12) from equation (11) it follows that

$$(s_n^2 - s_m^2) \mathbf{y}_m^T \mathbf{M}_c \mathbf{y}_n + (s_n - s_m) \mathbf{y}_m^T \mathbf{C}_c \mathbf{y}_n + \mathbf{y}_m^T [\mathbf{K}_c(s_n) - \mathbf{K}_c(s_m)] \mathbf{y}_n = 0$$

or

$$(s_n + s_m) \mathbf{y}_m^T \mathbf{M}_c \mathbf{y}_n + \mathbf{y}_m^T \mathbf{C}_c \mathbf{y}_n + \frac{\mathbf{y}_m^T [\mathbf{K}_c(s_n) - \mathbf{K}_c(s_m)] \mathbf{y}_n}{s_n - s_m} = 0 \quad (13)$$

which provides the first set of orthogonality conditions. Multiplying equation (11) by s_m and equation (12) by s_n the following is obtained

$$s_n^2 s_m \mathbf{y}_m^T \mathbf{M}_c \mathbf{y}_n + s_n s_m \mathbf{y}_m^T \mathbf{C}_c \mathbf{y}_n + s_m \mathbf{y}_m^T \mathbf{K}_c(s_n) \mathbf{y}_n = 0 \quad (14)$$

$$s_n s_m^2 \mathbf{y}_m^T \mathbf{M}_c \mathbf{y}_n + s_n s_m \mathbf{y}_m^T \mathbf{C}_c \mathbf{y}_n + s_n \mathbf{y}_m^T \mathbf{K}_c(s_m) \mathbf{y}_n = 0. \quad (15)$$

Subtracting equation (15) from equation (14) it follows that

$$(s_n - s_m) s_n s_m \mathbf{y}_m^T \mathbf{M}_c \mathbf{y}_n - \mathbf{y}_m^T [s_n \mathbf{K}_c(s_m) - s_m \mathbf{K}_c(s_n)] \mathbf{y}_n = 0$$

or

$$s_n s_m \mathbf{y}_m^T \mathbf{M}_c \mathbf{y}_n - \frac{\mathbf{y}_m^T [s_n \mathbf{K}_c(s_m) - s_m \mathbf{K}_c(s_n)] \mathbf{y}_n}{s_n - s_m} = 0 \quad (16)$$

which provides the second set of orthogonality conditions. It may be interesting to notice that, when the matrix \mathbf{K}_c is frequency independent, the orthogonality conditions (13) and (16) become identical with those provided by Veletsos and Ventura [23] for frequency independent non-classically damped systems

$$(s_n + s_m) \mathbf{y}_m^T \mathbf{M}_c \mathbf{y}_n + \mathbf{y}_m^T \mathbf{C}_c \mathbf{y}_n = 0$$

$$s_n s_m \mathbf{y}_m^T \mathbf{M}_c \mathbf{y}_n - \mathbf{y}_m^T \mathbf{K}_c \mathbf{y}_n = 0$$

The two sets of orthogonality conditions (13) and (16) are only valid if the eigenvalues are distinct. It may happen, however, that an eigenvalue has a multiplicity k greater than one. In such cases it follows that $s_m = s_n$ for $m \neq n$ and the terms

$$\frac{\mathbf{K}_c(s_n) - \mathbf{K}_c(s_m)}{s_n - s_m} \quad \text{and} \quad \frac{s_n \mathbf{K}_c(s_m) - s_m \mathbf{K}_c(s_n)}{s_n - s_m}$$

in equations (13) and (16) take a finite limit. However equations (13) and (16) are no longer satisfied by an arbitrary couple of eigenvectors associated to the same eigenvalue. Nevertheless it is always possible to find in the k -dimensional eigenspace associated to the multiple eigenvalue, k eigenvectors that satisfy the orthogonality conditions.

NUMERICAL APPLICATIONS

The method for the evaluation of eigenvalues and eigenvectors of soil-structure interacting systems presented in the previous paragraphs can be applied to any plane structure and can be extended to space structures in a straightforward manner. For the sake of simplicity it will be applied here to a periodic shear-type framework. For such a structural system the mass and stiffness matrices may be written as follows

$$\mathbf{M} = m \begin{bmatrix} 1 & 0 & 0 & \cdots & 0 & 0 \\ 0 & 1 & 0 & \cdots & 0 & 0 \\ 0 & 0 & 1 & \cdots & 0 & 0 \\ \cdots & \cdots & \cdots & \cdots & \cdots & \cdots \\ 0 & 0 & 0 & \cdots & 1 & 0 \\ 0 & 0 & 0 & \cdots & 0 & 1 \end{bmatrix}, \quad \mathbf{K} = k \begin{bmatrix} 2 & -1 & 0 & \cdots & 0 & 0 \\ -1 & 2 & -1 & \cdots & 0 & 0 \\ 0 & -1 & 2 & \cdots & 0 & 0 \\ \cdots & \cdots & \cdots & \cdots & \cdots & \cdots \\ 0 & 0 & 0 & \cdots & 2 & -1 \\ 0 & 0 & 0 & \cdots & -1 & 1 \end{bmatrix},$$

where m is the floor mass and k is the interstorey stiffness. In order to define the complete mass and stiffness matrices of the interacting system the following submatrices are needed

$$\mathbf{K}_b = \mathbf{0}, \quad \mathbf{K}_{bb} = \mathbf{0},$$

$$\mathbf{M}_b = m \begin{bmatrix} 1 & h \\ 1 & 2h \\ 1 & 3h \\ \cdots & \cdots \\ 1 & (N-1)h \\ 1 & Nh \end{bmatrix}, \quad \mathbf{M}_{bb} = \begin{bmatrix} m_o + Nm & mh \sum_{i=1}^N i \\ mh \sum_{i=1}^N i & I_o + NI + mh^2 \sum_{i=1}^N i^2 \end{bmatrix},$$

where N is the number of storeys, h is the interstorey height, m_o is the mass of the foundation, I_o and I are the moments of inertia of the foundation and storey masses. The impedance matrix \mathbf{K}_f has been defined in a previous paragraph. Structural damping is neglected in this application and therefore the damping matrix \mathbf{C}_c is set equal to zero.

Dimensionless parameters

The dynamical characteristics of the system defined above may be described in terms of a few dimensionless parameters. These were identified as follows

N	number of storeys,
$\alpha = m_o/m$	mass ratio,
$\beta = I_o/I$	rotational inertia ratio,
$\gamma = \sqrt{mh^2/I}$	storey slenderness ratio,
$\lambda = Nh/r_o$	geometrical ratio,
$\varepsilon = Gr_o/k$	stiffness ratio,
$\eta = \rho c_s \pi r_o^2 / \sqrt{km}$	radiation damping ratio,
ν	Poisson's ratio for the soil.

The previously defined mass and stiffness matrices take the following expressions in terms of these dimensionless parameters.

$$\mathbf{M}_b = m \begin{bmatrix} 1 & 1 \\ 1 & 2 \\ 1 & 3 \\ \dots & \dots \\ 1 & N-1 \\ 1 & N \end{bmatrix}, \quad \mathbf{M}_{bb} = m \begin{bmatrix} \alpha + N & \sum_{i=1}^N i \\ \sum_{i=1}^N i & \frac{\beta + N}{\gamma^2} + \sum_{i=1}^N i^2 \end{bmatrix},$$

$$\mathbf{K}_I = k \begin{bmatrix} \frac{8\varepsilon}{2-\nu} + \eta \hat{s} & 0 \\ 0 & \frac{8\varepsilon N^2}{3(1-\nu)\lambda^2} \frac{b + \hat{a}\hat{s} + [(1+b^2d)/3b]\hat{a}^2\hat{s}^2 + (d\hat{a}^3/3)\hat{s}^3}{b + \hat{a}\hat{s}} \end{bmatrix},$$

where

$$\hat{a} = \sqrt{\frac{k}{m}} \frac{r_o}{c_s} = \frac{\eta}{\pi\varepsilon} \quad \text{and} \quad \hat{s} = s/\sqrt{k/m}$$

is the dimensionless eigenvalue. It should be noticed that, in order to achieve this representation, rotations have been multiplied and moments have been divided by the interstorey height h .

Eigenvalues and eigenvectors

The calculations of the eigenvalues and the eigenvectors have been carried out for the following values of the dimensionless parameters

$$\begin{aligned} N=1, \quad \alpha=1, \quad \beta=1, \quad \gamma=4, \\ \lambda=2, \quad \varepsilon=3, \quad \nu=1/3. \end{aligned}$$

The three cases reported in Tables 1, 2 and 3 have been considered.

Table 1. Eigenvalues and eigenvectors; $\eta = 4$.

n	Eigenvalues $s_n/\sqrt{k/m}$	Eigenvectors y_n		
		y_{1n}	y_{0n}	$h g_{0n}$
1	$-0.0072 + 0.8359i$	$2.7625 + 0.0585i$	$0.1917 - 0.0424i$	1.0000
2	$-0.0072 - 0.8359i$	$2.7625 - 0.0585i$	$0.1917 + 0.0424i$	1.0000
3	-2.0000 (pole)			
4	-2.0000 (pole)			
5	-2.8302	-0.8230	-0.0742	1.0000
6	$-1.9480 + 3.2710i$	$0.1727 - 0.5688i$	$-1.2015 + 0.5396i$	1.0000
7	$-1.9480 - 3.2710i$	$0.1727 + 0.5688i$	$-1.2015 - 0.5396i$	1.0000
8	$-1.6298 + 4.6323i$	$-1.1308 - 0.0003i$	$0.0942 + 0.0296i$	1.0000
9	$-1.6298 - 4.6323i$	$-1.1308 + 0.0003i$	$0.0942 - 0.0296i$	1.0000

It should be noticed that the value $\eta = 7.533145$ was chosen specifically to obtain two real eigenvalues very close to each other, as may be seen from Table 2.

Table 2. Eigenvalues and eigenvectors; $\eta = 7.533145$.

n	Eigenvalues	Eigenvectors y_n		
	$s_n/\sqrt{k/m}$	y_{1n}	y_{0n}	$h g_{0n}$
1	$-0.0204 + 0.8288i$	$2.5193 + 0.2795i$	$0.1614 - 0.0533i$	1.0000
2	$-0.0204 - 0.8288i$	$2.5193 - 0.2795i$	$0.1614 + 0.0533i$	1.0000
3	-1.0620 (pole)			
4	-1.0620 (pole)			
5	-1.8634	-0.6457	-0.1684	1.0000
6	-3.6604	-0.1807	-0.8058	1.0000
7	-3.6688	-0.1796	-0.8071	1.0000
8	$-3.4474 + 3.0744i$	$-1.1094 + 0.0297i$	$0.1167 + 0.0218i$	1.0000
9	$-3.4474 - 3.0744i$	$-1.1094 - 0.0297i$	$0.1167 - 0.0218i$	1.0000

Table 3. Eigenvalues and eigenvectors; $\eta = 8$.

n	Eigenvalues	Eigenvectors y_n		
	$s_n/\sqrt{k/m}$	y_{1n}	y_{0n}	$h g_{0n}$
1	$-0.0227 + 0.8280i$	$2.4873 + 0.3187i$	$0.1579 - 0.0533i$	1.0000
2	$-0.0227 - 0.8280i$	$2.4873 - 0.3187i$	$0.1579 + 0.0533i$	1.0000
3	-1.0000 (pole)			
4	-1.0000 (pole)			
5	-1.8289	-0.6172	-0.1982	1.0000
6	-2.4827	-0.3867	-0.5506	1.0000
7	$-3.6830 + 2.7308i$	$-1.1027 + 0.0301i$	$0.1193 + 0.0197i$	1.0000
8	$-3.6830 - 2.7308i$	$-1.1027 - 0.0301i$	$0.1193 - 0.0197i$	1.0000
9	-5.2771	-0.0299	-0.9690	1.0000

For increasing values of η these eigenvalues tend to become more distant, as may be seen from Table 3. In fact, the two complex and conjugate eigenvalues corresponding to $n = 6$ and $n = 7$ for $\eta = 4$ (Table 1) become real for $\eta = 7.533145$ (Table 2). For $\eta = 8$ they become further apart and correspond respectively to $n = 6$ and $n = 9$. It should be noticed that eigenvalues and poles have been ordered in terms of increasing amplitude.

Orthogonality conditions

Tables 4, 5 and 6 were constructed in order to verify the orthogonality conditions (13) and (16). The amplitude of the left-hand side of equations (13) and (16) is reported in part (a) and part (b) respectively of the above mentioned tables. In spite of the fact that two of the real eigenvalues corresponding to $\eta = 7.533145$ are very close, the orthogonality conditions are satisfied exactly, as is shown in Table 5.

Table 4. Orthogonality conditions; $\eta = 4$.

(a) equation (13)

m^n	1	2	3	4	5	6	7
1	27	0	0	0	0	0	0
2	0	27	0	0	0	0	0
3	0	0	3.2	0	0	0	0
4	0	0	0	12	0	0	0
5	0	0	0	0	12	0	0
6	0	0	0	0	0	1.3	0
7	0	0	0	0	0	0	1.3

(b) equation (16)

m^n	1	2	3	4	5	6	7
1	29	0	0	0	0	0	0
2	0	29	0	0	0	0	0
3	0	0	71	0	0	0	0
4	0	0	0	76	0	0	0
5	0	0	0	0	76	0	0
6	0	0	0	0	0	8.4	0
7	0	0	0	0	0	0	8.4

Table 5. Orthogonality conditions; $\eta = 7.533145$.

(a) equation (13)

m^n	1	2	3	4	5	6	7
1	23	0	0	0	0	0	0
2	0	23	0	0	0	0	0
3	0	0	1.2	0	0	0	0
4	0	0	0	0.006	0	0	0
5	0	0	0	0	0.006	0	0
6	0	0	0	0	0	0.8	0
7	0	0	0	0	0	0	0.8

(b) equation (16)

m^n	1	2	3	4	5	6	7
1	29	0	0	0	0	0	0
2	0	29	0	0	0	0	0
3	0	0	27	0	0	0	0
4	0	0	0	20	0	0	0
5	0	0	0	0	20	0	0
6	0	0	0	0	0	1.4	0
7	0	0	0	0	0	0	1.4

Table 6. Orthogonality conditions; $\eta = 8$.

(a) equation (13)

m^n	1	2	3	4	5	6	7
1	23	0	0	0	0	0	0
2	0	23	0	0	0	0	0
3	0	0	0.9	0	0	0	0
4	0	0	0	0.8	0	0	0
5	0	0	0	0	0.7	0	0
6	0	0	0	0	0	0.7	0
7	0	0	0	0	0	0	2.8

(b) equation (16)

m^n	1	2	3	4	5	6	7
1	28	0	0	0	0	0	0
2	0	28	0	0	0	0	0
3	0	0	24	0	0	0	0
4	0	0	0	20	0	0	0
5	0	0	0	0	0.5	0	0
6	0	0	0	0	0	0.5	0
7	0	0	0	0	0	0	28

The case $N = 1$ was considered only for the sake of brevity in the representation of the eigenvalues and the eigenvectors. However the method has also been applied to large values of N without any complication.

CONCLUSIONS

A method for the calculation of eigenvalues and eigenvectors of frequency dependent soil-structure interacting systems has been presented. Two sets of orthogonality conditions, to be used in subsequent dynamical analyses, have been derived. Some numerical applications showing the performance of the method have been

reported and the orthogonality conditions have been verified.

The method presented allows the exact calculation of eigenvalues and eigenvectors of soil-structure interacting systems and equivalently the calculation of frequencies and modes of vibration. The complex modal analysis can therefore be applied also to soil-structure interacting systems for the evaluation of the dynamical response. This, up to now, has not been possible because a method for the calculation of the eigenvalues and the eigenvectors of such systems was not available. Therefore only approximate solutions were presented in the literature.

ACKNOWLEDGEMENTS

This research has been carried out with grants from the Italian Ministry for Scientific and Technological Research (MURST) and from the National Research Council (CNR) within the National Group for Defence against Earthquakes (GNĐT).

REFERENCES

1. Veletsos, A.S., Dynamics of Structure-Foundation Systems. In *Structural and Geotechnical Mechanics, A Volume Honoring N.M. Newmark*, ed. W.J. Hall, Prentice-Hall, Englewood Cliffs, New Jersey, 1977, pp. 333-61.
2. Veletsos, A.S., Design Concepts for Dynamics of Soil-Structure Interaction. In *Developments in Dynamic Soil-Structure Interaction*, ed. P.G. Gulkan and R.W. Clough, NATO ASI Series, Series C: Mathematical and Physical Sciences, Vol. 390, Kluwer Academic Publishers, Dordrecht, 1993, pp. 307-26.
3. Luco, J.E., Linear Soil-Structure Interaction: A Review, In *Earthquake Ground Motion and its Effects on Structures*, ASME, AMD 53, ed. S.K. Datta, New York, 1980, pp. 41-57.
4. Warburton, G.B., *The Dynamical Behaviour of Structures (Second Edition)*, Pergamon Press, Oxford, 1976.
5. Clough, R.W. and Penzien, J., *Dynamics of Structures (Second Edition)*, McGraw-Hill, New York, 1993, chapter 27.
6. Wolf, J.P., *Dynamic Soil-Structure Interaction*, Prentice-Hall, Englewood Cliffs, New Jersey, 1985.
7. Wolf, J.P., *Soil-Structure Interaction in Time Domain*, Prentice-Hall, Englewood Cliffs, New Jersey, 1988.
8. Gulkan P. and Clough, R.W. editors, *Developments in Dynamic Soil-Structure Interaction*, NATO ASI Series, Series C: Mathematical and Physical Sciences, Vol. 390, Kluwer Academic Publishers, Dordrecht, 1993.

9. Johnson, J.J. and Asfura, A.P., Soil-Structure Interaction (SSI) : Observations, Data and Correlative Analysis. In *Developments in Dynamic Soil-Structure Interaction*, ed. P.G. Gulkan and R.W. Clough, NATO ASI Series, Series C: Mathematical and Physical Sciences, Vol. 390, Kluwer Academic Publishers, Dordrecht, 1993, pp. 219-58.
10. Veletsos, A.S. and Wei, Y.T., Lateral and Rocking Vibration of Footings, *Journal of the Soil Mechanic and Foundation Division, ASCE*, 1971, **97**, 1227-48.
11. Luco, E.J. and Westman, R.A., Dynamic Response of Circular Footings, *Journal of the Engineering Mechanics Division, ASCE*, 1971, **97**, 1381-95.
12. Pais, A. and Kausel, E., Approximate Formulas for Dynamic Stiffnesses of Rigid Foundations, *Soil Dynamics and Earthquake Engineering*, 1988, **7**, 213-27.
13. Veletsos, A.S. and Verbic, B., Vibration of Viscoelastic Foundations, *Earthquake Engineering and Structural Dynamics*, 1973, **2**, 87-102.
14. Veletsos, A.S. and Verbic, B., Basic Response Functions for Elastic Foundations, *Journal of the Engineering Mechanics Division, ASCE*, 1974, **100**, 189-202.
15. Meek, J.W. and Veletsos, A.S., Simple models for foundations in lateral and rocking motion, *Proceedings of the 5th World Conference on Earthquake Engineering*, Rome, Italy, 1974, Vol. 2, 2610-13.
16. Meek, J.W. and Wolf, J.P., Cone models for homogeneous soil, *Journal of Geotechnical Engineering, ASCE*, 1992, **118** (5), 667-85.
17. Meek, J.W. and Wolf, J.P., Cone models for soil layer on rigid soil, *Journal of Geotechnical Engineering, ASCE*, 1992, **118** (5), 686-703.
18. Wolf, J.P., *Foundation Vibration Analysis Using Simple Physical Models*, Prentice-Hall, Englewood Cliffs, New Jersey, 1994.
19. Clough, R.W. and Mojtahedi, S., Earthquake response analysis considering non-proportional damping, *Earthquake Engineering and Structural Dynamics*, 1976, **4**, 489-96.
20. Bielak, J., Modal Analysis for Building-Soil Interaction, *Journal of the Engineering Mechanics Division, ASCE*, 1976, **102**, 771-86.
21. Warburton, G.B., Soil-Structure Interaction for Tower Structures, *Earthquake Engineering and Structural Dynamics*, 1978, **6**, 535-56.
22. Ehlers, G., The Effect of Soil Flexibility on Vibrating Systems, *Beton und Eisen*, 1942, **41**, 197-203 (in German).
23. Veletsos, A.S. and Ventura, C.E., Modal analysis of non-classically damped linear systems, *Earthquake Engineering and Structural Dynamics*, 1986, **14**, 217-43.

EIGENVALUE EVALUATION FOR NONLINEAR MATRIX POLYNOMIALS IN STRUCTURAL DYNAMICS IN ORIGINAL SPACE OF DOF.

P. Ruge

Professur Dynamik der Tragwerke, Technical University Dresden,
D-01062 Dresden, Germany.

Abstract The numerical treatment of the equations of motion in structural dynamics and control is accompanied by nonlinear algebraic eigenvalue representations. High-performance eigenvalue solvers are developed for only pairs \mathbf{A} , \mathbf{B} of matrices; that means for linear eigenvalue-problems $\mathbf{Ax} = \lambda\mathbf{Bx}$. To profit from software packages it is common practice to transform the nonlinear eigenvalue problem into a formal linear one but with multiple order compared with the original number of DOFs. This paper presents a vector iteration process, which actually works in the original space of DOFs and which needs no simultaneous approach if conjugate complex eigenvalues with identical norm have to be calculated.

INTRODUCTION

Nonlinear eigenvalue-problems

$$(\mathbf{S}_0 + \lambda\mathbf{S}_1 + \lambda^2\mathbf{S}_2 + \dots + \lambda^p\mathbf{S}_p)\mathbf{q} = 0, \quad \mathbf{q}^T = [q_1 \dots q_n], \quad (1)$$

with $p=2$ are typical in structural dynamics including general viscous damping and gyroscopic effects. The standard symmetric situation,

$$\begin{aligned} \mathbf{S}_0 &= \mathbf{K}, & \mathbf{K} &= \mathbf{K}^T, \\ \mathbf{S}_1 &= \mathbf{D}, & \mathbf{D} &= \mathbf{D}^T, \\ \mathbf{S}_2 &= \mathbf{M}, & \mathbf{M} &= \mathbf{M}^T, \end{aligned} \quad (2)$$

with mass \mathbf{M} , damping \mathbf{D} and stiffness \mathbf{K} can be transformed into a corresponding hypersystem with matrices \mathbf{A} , \mathbf{B} of double order $2n$, still symmetric but not definite in general.

$$\begin{aligned} p=2: (\mathbf{K} + \lambda\mathbf{D} + \lambda^2\mathbf{M})\mathbf{q} &= 0. \\ \begin{bmatrix} \mathbf{M} & \mathbf{0} \\ \mathbf{0} & -\mathbf{K} \end{bmatrix} \begin{bmatrix} \lambda\mathbf{q} \\ \mathbf{q} \end{bmatrix} &= \lambda \begin{bmatrix} \mathbf{0} & \mathbf{M} \\ \mathbf{M} & \mathbf{D} \end{bmatrix} \begin{bmatrix} \lambda\mathbf{q} \\ \mathbf{q} \end{bmatrix}, \\ \text{short form } \mathbf{Az} &= \lambda\mathbf{Bz}. \\ \mathbf{A} &= \mathbf{A}^T, \quad \mathbf{B} = \mathbf{B}^T \text{ if } \mathbf{M} = \mathbf{M}^T, \quad \mathbf{D} = \mathbf{D}^T, \quad \mathbf{K} = \mathbf{K}^T. \end{aligned} \quad (3)$$

An alternative gyroscopic part $\Omega\lambda\mathbf{G}$ with skewsymmetric \mathbf{G} , $\mathbf{G}^T = -\mathbf{G}$, instead of damping \mathbf{D} in the eigenvalue problem (3) can be incorporated

in such a way, that hypermatrix **A** is symmetric and **B** skewsymmetric.

$$\begin{aligned}
 p = 2 : & \quad (\mathbf{K} + \lambda \Omega \mathbf{G} + \lambda^2 \mathbf{M}) \mathbf{q} = \mathbf{0}, \\
 & \quad \mathbf{G}^T = -\mathbf{G}, \quad \Omega : \text{angular velocity.} \\
 & \quad \mathbf{K} = \mathbf{K}^T, \mathbf{M} = \mathbf{M}^T. \\
 & \quad \begin{bmatrix} \mathbf{M} & \mathbf{0} \\ \mathbf{0} & \mathbf{K} \end{bmatrix} \begin{bmatrix} \lambda \mathbf{q} \\ \mathbf{q} \end{bmatrix} = \lambda \begin{bmatrix} \mathbf{0} & \mathbf{M} \\ -\mathbf{M} & -\Omega \mathbf{G} \end{bmatrix} \begin{bmatrix} \lambda \mathbf{q} \\ \mathbf{q} \end{bmatrix}, \\
 & \quad \text{short form } \mathbf{A} \mathbf{z} = \lambda \mathbf{S} \mathbf{z}, \\
 & \quad \mathbf{A} = \mathbf{A}^T, \quad \mathbf{S}^T = -\mathbf{S}.
 \end{aligned} \tag{4}$$

The special gyroscopic situation with **D** = **0** is characterized by sets $\lambda = \pm(\alpha \pm i\beta)$ of 4 complex eigenvalues with identical norm. Matrix polynomials (1) with degree $p > 2$ are common in structural control; for example if systems with time delay ([1], [2]) have to be considered.

Further nonlinear eigenvalue problems arise from algebraic representations of dynamic BEM-formulations. The natural BEM-approach allows no formulation incorporating the eigenvalue (eigenfrequency) λ directly as a parameter for itself. This disadvantage can be avoided by using methods like multiple reciprocity or power series expansion of the fundamental solution.

Whatever the mechanical background may be; the resulting eigenvalue problem (1) has to be solved and it is common practice, to introduce hypermatrices **A**, **B** of order $n \cdot p$ which are passed over to high-performance solvers.

TRANSFORMATION AND CONDENSATION

Symmetry properties of each of the matrices **S_j** involved in (1) can be saved with respect to the hypermatrices **A**, **B** if the original parts **S_j** are arranged in a very special manner; equation (5) shows the situation for $p=4$:

Original space of DOF; order n .

Degree $p=4$.

$$(\mathbf{S}_0 + \lambda \mathbf{S}_1 + \lambda^2 \mathbf{S}_2 + \lambda^3 \mathbf{S}_3 + \lambda^4 \mathbf{S}_4) \mathbf{q} = \mathbf{0}, \quad \mathbf{S}_j = \mathbf{S}_j^T.$$

Expanded linear problem; order $p \cdot n$:

$$\begin{bmatrix} \mathbf{0} & \mathbf{0} & \mathbf{S}_4 & \mathbf{0} \\ \mathbf{0} & \mathbf{S}_4 & \mathbf{S}_3 & \mathbf{0} \\ \mathbf{S}_4 & \mathbf{S}_3 & \mathbf{S}_2 & \mathbf{0} \\ \mathbf{0} & \mathbf{0} & \mathbf{0} & -\mathbf{S}_0 \end{bmatrix} \begin{bmatrix} \lambda^3 \mathbf{q} \\ \lambda^2 \mathbf{q} \\ \lambda \mathbf{q} \\ \mathbf{q} \end{bmatrix} = \lambda \begin{bmatrix} \mathbf{0} & \mathbf{0} & \mathbf{0} & \mathbf{S}_4 \\ \mathbf{0} & \mathbf{0} & \mathbf{S}_4 & \mathbf{S}_3 \\ \mathbf{0} & \mathbf{S}_4 & \mathbf{S}_3 & \mathbf{S}_2 \\ \mathbf{S}_4 & \mathbf{S}_3 & \mathbf{S}_2 & \mathbf{S}_1 \end{bmatrix} \begin{bmatrix} \lambda^3 \mathbf{q} \\ \lambda^2 \mathbf{q} \\ \lambda \mathbf{q} \\ \mathbf{q} \end{bmatrix}, \tag{5}$$

short form $\mathbf{A} \mathbf{z} = \lambda \mathbf{B} \mathbf{z}$.

$$\mathbf{A} = \mathbf{A}^T, \quad \mathbf{B} = \mathbf{B}^T \text{ if } \mathbf{S}_j = \mathbf{S}_j^T.$$

Otherwise, without total symmetry, \mathbf{A} , \mathbf{B} should be arranged as sparse as possible.

Original nonlinear problem

$$(\mathbf{S}_0 + \lambda \mathbf{S}_1 + \lambda^2 \mathbf{S}_2 + \lambda^3 \mathbf{S}_3 + \lambda^4 \mathbf{S}_4) \mathbf{z}_0 = 0.$$

Expanded linear problem

$$\begin{bmatrix} 1 & 0 & 0 & 0 \\ 0 & 1 & 0 & 0 \\ 0 & 0 & 1 & 0 \\ 0 & 0 & 0 & -\mathbf{S}_0 \end{bmatrix} \mathbf{z} = \lambda \begin{bmatrix} 0 & 1 & 0 & 0 \\ 0 & 0 & 1 & 0 \\ 0 & 0 & 0 & 1 \\ \mathbf{S}_4 & \mathbf{S}_3 & \mathbf{S}_2 & \mathbf{S}_1 \end{bmatrix} \mathbf{z}. \quad (6)$$

Some properties of the eigensolutions λ_j, \mathbf{z}_j are well known and are added for the sake of completeness. If \mathbf{A} and \mathbf{B} are pure real any complex eigenvalue $\lambda = \alpha + i\beta$ has a conjugate complex partner $\bar{\lambda} = \alpha - i\beta$. A normal pair \mathbf{A} , \mathbf{B} of symmetric matrices can be transformed into a diagonal pair by means of the modal matrix \mathbf{Z} which contains all of the $p \cdot n$ complex eigenvectors \mathbf{z}_j ;

$p = 4 :$

$$\mathbf{Z} = \begin{bmatrix} \mathbf{z}_1 & \dots & \mathbf{z}_{4n} \end{bmatrix} = \begin{bmatrix} \lambda_1^3 \mathbf{x}_1 & \dots & \lambda_{4n}^3 \mathbf{x}_{4n} \\ \lambda_1^2 \mathbf{x}_1 & \dots & \lambda_{4n}^2 \mathbf{x}_{4n} \\ \lambda_1 \mathbf{x}_1 & \dots & \lambda_{4n} \mathbf{x}_{4n} \\ \mathbf{x}_1 & \dots & \mathbf{x}_{4n} \end{bmatrix} = \begin{bmatrix} \mathbf{X} \lambda^3 \\ \mathbf{X} \lambda^2 \\ \mathbf{X} \lambda \\ \mathbf{X} \end{bmatrix}.$$

$$\begin{aligned} \mathbf{Z}^T \mathbf{A} \mathbf{Z} &= \text{diag} \{a_j\}, j = 1, \dots, pn. \\ \mathbf{Z}^T \mathbf{B} \mathbf{Z} &= \text{diag} \{b_j\}, \\ \lambda &= \text{diag} \{\lambda_j\}. \end{aligned} \quad (7)$$

$$\begin{aligned} a_j = \mathbf{z}_j^T \mathbf{A} \mathbf{z}_j &= 3 \lambda_j^4 \mathbf{x}_j^T \mathbf{S}_4 \mathbf{x}_j + 2 \lambda_j^3 \mathbf{x}_j^T \mathbf{S}_3 \mathbf{x}_j + \\ &\quad \lambda_j^2 \mathbf{x}_j^T \mathbf{S}_2 \mathbf{x}_j - \mathbf{x}_j^T \mathbf{S}_0 \mathbf{x}_j, \\ b_j = \mathbf{z}_j^T \mathbf{B} \mathbf{z}_j &= 4 \lambda_j^3 \mathbf{x}_j^T \mathbf{S}_4 \mathbf{x}_j + 3 \lambda_j^2 \mathbf{x}_j^T \mathbf{S}_3 \mathbf{x}_j + \\ &\quad 2 \lambda_j \mathbf{x}_j^T \mathbf{S}_2 \mathbf{x}_j + \mathbf{x}_j^T \mathbf{S}_1 \mathbf{x}_j. \quad \lambda_j = \frac{a_j}{b_j}. \end{aligned}$$

The scalar products a_j, b_j are complex numbers in general which can be taken to describe the eigenvalue λ_j directly.

Rather similar but real products

$$\tilde{a}_j = \bar{\mathbf{z}}_j^T \mathbf{A} \mathbf{z}_j, \quad \tilde{b}_j = \bar{\mathbf{z}}_j^T \mathbf{B} \mathbf{z}_j \quad (8)$$

using conjugate complex solutions

$$(\lambda_j, \mathbf{z}_j), \quad (\bar{\lambda}_j, \bar{\mathbf{z}}_j) \quad (9)$$

are zero. These properties present no new information; they are part of the orthogonalities hidden in $\mathbf{Z}^T \mathbf{A} \mathbf{Z} = \text{diag} \{a_j\}$ and $\mathbf{Z}^T \mathbf{B} \mathbf{Z} = \text{diag} \{b_j\}$;

if we take the 2 solutions from (9) we immediately get the result already mentioned:

$$\bar{\mathbf{z}}_j^T \mathbf{B} \mathbf{z}_j = 0; \quad \bar{\mathbf{z}}_j^T \mathbf{A} \mathbf{z}_j = 0. \quad (10)$$

A detailed evaluation of the identities (10) for a typical complex pair allows a real-valued scalar condensation of the (pn)-ordered problem:

$$\mathbf{z}_j = \begin{bmatrix} \lambda^3 \mathbf{x} \\ \lambda^2 \mathbf{x} \\ \lambda \mathbf{x} \\ \mathbf{x} \end{bmatrix}_{(j)}, \quad \bar{\mathbf{z}}_j = \begin{bmatrix} \bar{\lambda}^3 \bar{\mathbf{x}} \\ \bar{\lambda}^2 \bar{\mathbf{x}} \\ \bar{\lambda} \bar{\mathbf{x}} \\ \bar{\mathbf{x}} \end{bmatrix}, \quad \lambda_j = \alpha + i\beta, \quad \bar{\lambda}_j = \alpha - i\beta.$$

$$\begin{aligned} \tilde{a}_j &= \lambda_j[\dots] - s_0 = 0, \\ \tilde{b}_j &= [\dots] + s_4 \lambda_j^3 + s_3 \lambda_j^2 + s_2 \lambda_j + s_1 = 0, \\ [\dots] &= \{s_4(\bar{\lambda}_j^2 + \lambda_j^2 + \bar{\lambda}_j \lambda_j) + s_3(\lambda_j + \bar{\lambda}_j) + s_2\} \bar{\lambda}_j, \\ s_k &= \bar{\mathbf{x}}_j^T \mathbf{S}_k \mathbf{x}_j. \end{aligned} \quad (11)$$

Eliminating the bracket [...] in \tilde{a}_j, \tilde{b}_j (11) results in a scalar polynomial of fourth degree with real coefficients if all of the matrices \mathbf{A}_k are real symmetric.

$$\begin{aligned} p(x) &= s_0 + \lambda s_1 + \lambda^2 s_2 + \lambda^3 s_3 + \lambda^4 s_4 = 0, \\ s_k &= \bar{\mathbf{x}}_j^T \mathbf{S}_k \mathbf{x}_j \in \mathbf{R}; \quad \mathbf{S}_k = \mathbf{S}_k^T, \\ p(\lambda_{jk}) &= 0, \quad k = 1, 2, 3, 4. \end{aligned} \quad (12)$$

Eigensolution:

$$\mathbf{x}_j, \bar{\mathbf{x}}_j; \quad \lambda_{j1}, \lambda_{j2}, \lambda_{j3}, \lambda_{j4}.$$

The roots λ_{jk} of the polynomial (12) are the corresponding eigenvalues of the eigenspace $\mathbf{x}_j, \bar{\mathbf{x}}_j$, including $\lambda_j, \bar{\lambda}_j$.

A normal pair \mathbf{A}, \mathbf{B} of unsymmetric matrices can be transformed into a diagonal pair by means of the left eigenvectors $\boldsymbol{\ell}_j$ arranged in the left modal matrix \mathbf{L} and the right eigenvectors \mathbf{r}_j with \mathbf{R} .

$p = 4$:

$$\begin{aligned} \mathbf{A}^T \boldsymbol{\ell}_j &= \lambda_j \mathbf{B}^T \boldsymbol{\ell}_j, \\ \mathbf{A} \mathbf{r}_j &= \lambda_j \mathbf{B} \mathbf{r}_j, \\ \mathbf{L} &= [\boldsymbol{\ell}_1 \dots \boldsymbol{\ell}_{4n}] = \begin{bmatrix} \lambda_1^3 \mathbf{y}_1 & \dots & \lambda_{4n}^3 \mathbf{y}_{4n} \\ \lambda_1^2 \mathbf{y}_1 & \dots & \lambda_{4n}^2 \mathbf{y}_{4n} \\ \lambda_1 \mathbf{y}_1 & \dots & \lambda_{4n} \mathbf{y}_{4n} \\ \mathbf{y}_1 & \dots & \mathbf{y}_{4n} \end{bmatrix} = \begin{bmatrix} \mathbf{Y} \boldsymbol{\lambda}^3 \\ \mathbf{Y} \boldsymbol{\lambda}^2 \\ \mathbf{Y} \boldsymbol{\lambda} \\ \mathbf{Y} \end{bmatrix}; \end{aligned}$$

$$\mathbf{R} = \begin{bmatrix} \mathbf{r}_1 & \dots & \mathbf{r}_{4n} \end{bmatrix} = \begin{bmatrix} \lambda_1^3 \mathbf{x}_1 & \dots & \lambda_{4n}^3 \mathbf{x}_{4n} \\ \lambda_1^2 \mathbf{x}_1 & \dots & \lambda_{4n}^2 \mathbf{x}_{4n} \\ \lambda_1 \mathbf{x}_1 & \dots & \lambda_{4n} \mathbf{x}_{4n} \\ \mathbf{x}_1 & \dots & \mathbf{x}_{4n} \end{bmatrix} = \begin{bmatrix} \mathbf{X} \boldsymbol{\lambda}^3 \\ \mathbf{X} \boldsymbol{\lambda}^2 \\ \mathbf{X} \boldsymbol{\lambda} \\ \mathbf{X} \end{bmatrix}.$$

$$\begin{aligned} \mathbf{L}^T \mathbf{A} \mathbf{R} &= \text{diag} \{a_j\}, \quad \mathbf{L}^T \mathbf{B} \mathbf{R} = \text{diag} \{b_j\}, \\ \boldsymbol{\lambda} &= \text{diag} \{\lambda_j\}. \quad j = 1, \dots, p \cdot n. \end{aligned} \quad (13)$$

Once more, the products a_j, b_j in (13) are complex numbers.

Taking a pair

$$(\bar{\lambda}_j, \bar{\ell}_j), \quad (\lambda_j, \mathbf{r}_j); \quad \lambda \in \mathbb{C}, \quad (14)$$

of 2 different eigensolutions with complex λ results in similar products

$$\begin{aligned} \bar{\ell}_j^T \mathbf{A} \mathbf{r}_j &= \bar{a}_j \stackrel{!}{=} 0, \\ \bar{\ell}_j^T \mathbf{B} \mathbf{r}_j &= \bar{b}_j \stackrel{!}{=} 0 \end{aligned} \quad (15)$$

as in (13) but zero-valued. The exact eigenvectors $\bar{\ell}_j, \mathbf{r}_j$ restrict the original $(p \cdot n)$ -ordered eigenvalue problem to a scalar polynomial with degree p which contains the spectral information corresponding with $\bar{\ell}_j, \mathbf{r}_j$; that means at least $\lambda_j, \bar{\lambda}_j$.

The following sections present special equations and results for $p=2$. The condensed version (11), (12) for symmetric matrices $\mathbf{S}_2, \mathbf{S}_1, \mathbf{S}_0$ simplifies to a quadratic scalar equation with real coefficients:

$$\begin{aligned} \mathbf{A} &= \begin{bmatrix} \mathbf{S}_2 & \mathbf{0} \\ \mathbf{0} & -\mathbf{S}_0 \end{bmatrix}, \quad \mathbf{B} = \begin{bmatrix} \mathbf{0} & \mathbf{S}_2 \\ \mathbf{S}_2 & -\mathbf{S}_1 \end{bmatrix}. \\ \bar{a}_j &= s_2 \lambda_j \bar{\lambda}_j - s_0 = 0, \\ \bar{b}_j &= s_2 (\lambda_j + \bar{\lambda}_j) + s_1 = 0. \\ s_k &= \bar{\mathbf{x}}_j^T \mathbf{S}_k \mathbf{x}_j, \quad s_k \in \mathbb{R} \text{ if } \mathbf{S}_k = \mathbf{S}_k^T. \end{aligned} \quad (16)$$

Corresponding scalar equation

$$\begin{aligned} R^2 s_2 + R s_1 + s_0 &= 0, \\ \text{with } R_1 &= \lambda_j, \quad R_2 = \bar{\lambda}_j. \end{aligned}$$

The unsymmetric version with $\mathbf{S}_k^T \neq \mathbf{S}_k$ is described by similar formulae but with different values s_k .

$$\mathbf{S}_k^T \neq \mathbf{S}_k: \quad s_k = \bar{\mathbf{y}}_j^T \mathbf{S}_k \mathbf{x}_j. \quad (17)$$

VECTOR ITERATION. SYMMETRIC MATRICES

Vector iteration methods combine two essential properties:

- Known eigensolutions from similar problems can be taken to accelerate the iteration.
- The most interesting first greatest or first smallest eigenvalues can be calculated instead of all eigenvalues.

The algorithm presented here for $p=2$ operates within the original space of degrees of freedom of order n . Nevertheless the theoretical justification of the modified method turns back to the $2n$ -order pair \mathbf{A}, \mathbf{B} in equation (16), because the vector iteration itself and its convergence properties can be proved and explained only for a pair of matrices.

First results for symmetric matrices have been presented by the author [3]. In literature there seems to exist only one contribution by Nordmann [4] which deals with vector iteration in the original space of order n . The subject of his paper are eigenvalue problems in rotordynamics where a velocity part $\mathbf{D}\dot{\mathbf{u}}$ in the equations of motion can be caused by damping and by gyroscopic effects, as well. Special attention is paid to double roots, that means a complex pair $\lambda = \alpha \pm i\beta$ of eigenvalues with identical norm. Nordmann's method as well as the identical power iteration can not decide whether to approach $\mathbf{z}_1 = \mathbf{a}_1 + i\mathbf{b}_1$ for $\lambda_1 = \alpha + i\beta$ or $\bar{\mathbf{z}}_1 = \mathbf{a}_1 - i\mathbf{b}_1$ for $\lambda_2 = \alpha - i\beta$; in other words, a kind of simultaneous iteration has to be established.

Here, the vector iteration towards the smallest eigenvalue λ_1 starts with a trialvector \mathbf{w}_0 and generates a sequence $\mathbf{w}_1, \mathbf{w}_2 \dots$ towards the corresponding hypereigenvector \mathbf{z}_1 to λ_1 .

$$\begin{aligned} \begin{bmatrix} \mathbf{M} & \mathbf{0} \\ \mathbf{0} & -\mathbf{K} \end{bmatrix} \begin{bmatrix} \mathbf{v}_1 \\ \mathbf{u}_1 \end{bmatrix} &= R_0 \begin{bmatrix} \mathbf{0} & \mathbf{M} \\ \mathbf{M} & \mathbf{D} \end{bmatrix} \begin{bmatrix} \mathbf{v}_0 \\ \mathbf{u}_0 \end{bmatrix}, \quad \mathbf{w}_0 = \begin{bmatrix} \mathbf{v}_0 \\ \mathbf{u}_0 \end{bmatrix}. \quad (18) \\ \text{In General} \quad \mathbf{A}\mathbf{w}_{j+1} &= R_j \mathbf{B} \mathbf{w}_j. \\ \mathbf{w}_j &\rightarrow \mathbf{z}_1; \quad R_j \rightarrow \lambda_1. \end{aligned}$$

The convergence of this process depends on the magnitude $r = |\lambda| = |\alpha + i\beta| = \sqrt{\alpha^2 + \beta^2}$ of the two eigenvalues with smallest magnitudes. The decision whether to approach $\lambda = \alpha + i\beta$ or $\bar{\lambda} = \alpha - i\beta$ in situations with conjugate complex eigenvalues is made when solving the scalar condensed equation (16). The approximation R choosen, either for λ or for $\bar{\lambda}$, shows the iteration $\mathbf{A}\mathbf{w}_{j+1} = R_j \mathbf{B} \mathbf{w}_j$ where to go; either towards \mathbf{z} or towards $\bar{\mathbf{z}}$; [3].

The special internal structure of **A** and **B** allows a sequential calculation of the n-order parts \mathbf{u}_j and \mathbf{v}_j of the 2n-order vector \mathbf{w}_j .

$$\begin{aligned} \mathbf{v}_1 &= R_0 \mathbf{u}_0 \rightarrow \mathbf{v}_1. \\ -\mathbf{K} \mathbf{u}_1 &= R_0 (\mathbf{M} \mathbf{v}_0 + \mathbf{D} \mathbf{u}_0) \rightarrow \mathbf{u}_1. \end{aligned} \quad (19)$$

In general, \mathbf{u}_0 and \mathbf{v}_0 can be chosen any way. Known eigenvectors from similar problems should be taken advantage of. Otherwise total neutrality with $u_j = 1$; $j = 1, \dots, n$ would be an optimal choice. A corresponding partner \mathbf{v}_0 with \mathbf{u}_0 should reflect the relation between the parts of the exact eigenvector \mathbf{z} .

$$\mathbf{v}_0 = R_0 \mathbf{u}_0. \quad \mathbf{z} = \begin{bmatrix} \lambda \mathbf{x} \\ \mathbf{x} \end{bmatrix}. \quad (20)$$

A proper value R_0 follows from solving the scalar "condensed algebraic equation" (16) evaluated with \mathbf{u}_0 .

$$\begin{aligned} R^2 m_0 + R d_0 + k_0 &= 0. \\ \rightarrow \text{Roots } R_1, R_2. \\ R_0 &= |R_j|_{\text{Min}}. \\ m_0 = \bar{\mathbf{u}}_0^T \mathbf{M} \mathbf{u}_0, \quad d_0 = \bar{\mathbf{u}}_0^T \mathbf{D} \mathbf{u}_0, \quad k_0 &= \bar{\mathbf{u}}_0^T \mathbf{K} \mathbf{u}_0. \\ m_0, d_0, k_0 \in \mathbb{R} \text{ if } \mathbf{M} = \mathbf{M}^T, \quad \mathbf{D} = \mathbf{D}^T, \quad \mathbf{K} = \mathbf{K}^T. \end{aligned} \quad (21)$$

A typical k. iteration step from $\mathbf{u}_j, \mathbf{v}_j, R_j$ to $\mathbf{u}_k, \mathbf{v}_k, R_k$ follows from equation (19):

k. step

$$\begin{aligned} \text{Input:} \quad & \mathbf{u}_j, \mathbf{v}_j, R_j. \quad \mathbf{v}_j = R_{j-1} \mathbf{u}_{j-1}. \\ \text{Output:} \quad & -\mathbf{K} \mathbf{u}_k = R_j (\mathbf{M} \mathbf{v}_j + \mathbf{D} \mathbf{u}_j). \\ & R_k \text{ from } R^2 m_k + R d_k + k_k = 0. \\ & \mathbf{v}_k = R_j \mathbf{u}_j. \text{ Here } R_j, \text{ not } R_k! \end{aligned} \quad (22)$$

The vector iteration towards λ_2, \mathbf{z}_2 and higher eigenterms must be free from parts in direction of \mathbf{z}_1 ; otherwise the first eigenpair will be approached once more. An explicit way in order to produce clean vectors takes a provisional iterated vector $\tilde{\mathbf{w}}_{j+1}$,

$$\mathbf{A} \tilde{\mathbf{w}}_{j+1} = R \mathbf{B} \mathbf{w}_j, \quad (23)$$

and eliminates the \mathbf{z}_1 -part.

$$\mathbf{w}_{j+1} = \tilde{\mathbf{w}}_{j+1} - \frac{\mathbf{z}_1^T \mathbf{B} \tilde{\mathbf{w}}_{j+1}}{\mathbf{z}_1^T \mathbf{B} \mathbf{z}_1} \mathbf{z}_1 \quad (24)$$

This process can be extended with respect to r known eigensolutions.

$$\mathbf{w}_{j+1} = \tilde{\mathbf{w}}_{j+1} - \sum_{k=1}^r \frac{\mathbf{z}_k^T \mathbf{B} \tilde{\mathbf{w}}_{j+1}}{\mathbf{z}_k^T \mathbf{B} \mathbf{z}_k} \mathbf{z}_k. \quad (25)$$

k. step

$$\begin{aligned} \text{Input: } & \mathbf{u}_j, \mathbf{v}_j, R_j, \mathbf{x}_1, \bar{\mathbf{x}}_1, \lambda_1, \bar{\lambda}_1. \\ \text{Output: } & \tilde{\mathbf{v}}_k = R_j \mathbf{u}_j, \\ & -\mathbf{K} \tilde{\mathbf{u}}_k = R_j (\mathbf{M} \mathbf{v}_j + \mathbf{D} \mathbf{u}_j). \end{aligned}$$

Since complex eigenpairs \mathbf{x}_1, λ_1 appear together with a conjugate pair $\bar{\mathbf{x}}_1, \bar{\lambda}_1$ these parts are taken together to evaluate the sweeping process.

$$\text{Sweeping process with respect to } \mathbf{x}_1, \lambda_1; \bar{\mathbf{x}}_1, \bar{\lambda}_1 : \quad (26)$$

$$\begin{aligned} \mathbf{v}_k &= \tilde{\mathbf{v}}_k - \frac{Z}{N} \lambda_1 \mathbf{x}_1 - \frac{Z^*}{N^*} \bar{\lambda}_1 \bar{\mathbf{x}}_1, \\ \mathbf{u}_k &= \tilde{\mathbf{u}}_k - \frac{Z}{N} \mathbf{x}_1 - \frac{Z^*}{N^*} \bar{\mathbf{x}}_1, \\ N &= \mathbf{x}_1^T \mathbf{D} \mathbf{x}_1 + 2 \lambda_1 \mathbf{x}_1^T \mathbf{M} \mathbf{x}_1, \\ N^* &= \bar{\mathbf{x}}_1^T \mathbf{D} \bar{\mathbf{x}}_1 + 2 \bar{\lambda}_1 \bar{\mathbf{x}}_1^T \mathbf{M} \bar{\mathbf{x}}_1 = \bar{N}, \\ Z &= \mathbf{x}_1^T \mathbf{D} \tilde{\mathbf{u}}_k + \lambda_1 \mathbf{x}_1^T \mathbf{M} \tilde{\mathbf{u}}_k + \mathbf{x}_1^T \mathbf{M} \tilde{\mathbf{v}}_k, \\ Z^* &= \bar{\mathbf{x}}_1^T \mathbf{D} \tilde{\mathbf{u}}_k + \bar{\lambda}_1 \bar{\mathbf{x}}_1^T \mathbf{M} \tilde{\mathbf{u}}_k + \bar{\mathbf{x}}_1^T \mathbf{M} \tilde{\mathbf{v}}_k. \\ \text{Root } & R_k \text{ from } R^2 m_k + R d_k + k_k = 0. \\ & R_k = |R_{1,2}|_{\min}. \end{aligned}$$

End of k. step.

VECTOR ITERATION. UNSYMMETRIC MATRICES

The vector iteration towards the smallest eigenvalue λ_1 starts with a pair of left trial vector \mathbf{w}_{L0} and right trial vector \mathbf{w}_{R0} and generates sequences $\mathbf{w}_{L1}, \mathbf{w}_{L2}, \dots$ and $\mathbf{w}_{R1}, \mathbf{w}_{R2}, \dots$ towards the corresponding hypereigenvector ℓ_1, \mathbf{r}_1 with eigenvalue λ_1 . $\mathbf{S}_2, \mathbf{S}_1, \mathbf{S}_0$ are replaced by $\mathbf{M}, \mathbf{D}, \mathbf{K}$ in order to simplify the comparison with the equations from the former section.

$$\begin{aligned} \begin{bmatrix} \mathbf{M} & \mathbf{0} \\ \mathbf{0} & -\mathbf{K} \end{bmatrix} \begin{bmatrix} \mathbf{v}_{R1} \\ \mathbf{u}_{R1} \end{bmatrix} &= R_0 \begin{bmatrix} \mathbf{0} & \mathbf{M} \\ \mathbf{M} & \mathbf{D} \end{bmatrix} \begin{bmatrix} \mathbf{v}_{R0} \\ \mathbf{u}_{R0} \end{bmatrix}, \quad \mathbf{w}_{R0} = \begin{bmatrix} \mathbf{v}_{R0} \\ \mathbf{u}_{R0} \end{bmatrix}. \\ \text{In general } \mathbf{A} \mathbf{w}_{R,j+1} &= R_j \mathbf{B} \mathbf{w}_{Rj}. \\ \mathbf{w}_{Rj} &\rightarrow \mathbf{r}_j; \quad R_j \rightarrow \lambda_1. \end{aligned} \quad (27)$$

$$\begin{aligned} \begin{bmatrix} \mathbf{M}^T & \mathbf{0} \\ \mathbf{0} & -\mathbf{K}^T \end{bmatrix} \begin{bmatrix} \mathbf{v}_{L1} \\ \mathbf{u}_{L1} \end{bmatrix} &= R_0 \begin{bmatrix} \mathbf{0} & \mathbf{M}^T \\ \mathbf{M}^T & \mathbf{D}^T \end{bmatrix} \begin{bmatrix} \mathbf{v}_{L0} \\ \mathbf{u}_{L0} \end{bmatrix}, \quad \mathbf{w}_{L0} = \begin{bmatrix} \mathbf{v}_{L0} \\ \mathbf{u}_{L0} \end{bmatrix}. \\ \text{In general } \mathbf{A}^T \mathbf{w}_{L,j+1} &= R_j \mathbf{B}^T \mathbf{w}_{Lj}. \\ \mathbf{w}_{Lj} &\rightarrow \ell_j; \quad R_j \rightarrow \lambda_1. \end{aligned}$$

Once more, the unknowns $(\mathbf{v}_{R1}, \mathbf{u}_{R1})$, $(\mathbf{v}_{L1}, \mathbf{u}_{L1})$ can be calculated separately from n-order linear equations.

$$\begin{aligned}\mathbf{v}_{R1} &= R_0 \mathbf{u}_{R0}, \\ -\mathbf{K} \mathbf{u}_{R1} &= R_0 (\mathbf{M} \mathbf{v}_{R0} + \mathbf{D} \mathbf{u}_{R0}), \\ \mathbf{v}_{L1} &= R_0 \mathbf{u}_{L0}, \\ -\mathbf{K}^T \mathbf{u}_{L1} &= R_0 (\mathbf{M}^T \mathbf{v}_{L0} + \mathbf{D}^T \mathbf{u}_{L0}).\end{aligned}\quad (28)$$

Identical starting vectors,

$$\mathbf{u}_{R0} = \mathbf{u}_{L0} = \begin{bmatrix} 1 & \dots & 1 \end{bmatrix} \quad (29)$$

define a condensed scalar form similar to (17)

$$\begin{aligned}R^2 m_0 + R d_0 + k_0 &= 0, \\ m_0 &= \bar{\mathbf{u}}_{L0}^T \mathbf{M} \mathbf{u}_{R0}, \quad d_0 = \bar{\mathbf{u}}_{L0}^T \mathbf{D} \mathbf{u}_{R0}, \\ k_0 &= \bar{\mathbf{u}}_{L0}^T \mathbf{K} \mathbf{u}_{R0}, \\ \rightarrow \text{roots } R_1, R_2. \quad R_0 &= |R_{1,2}|_{Min},\end{aligned}\quad (30)$$

from which the smallest root R_0 is taken to approximate λ_1 and to calculate $\mathbf{v}_{R0} = R_0 \mathbf{u}_{R0}$ and $\mathbf{v}_{L0} = R_0 \mathbf{u}_{L0}$. Higher iteration steps are similar to the starting step.

k. step

$$\begin{aligned}\text{Input: } & \mathbf{u}_{Lj}, \mathbf{v}_{Lj}; \quad \mathbf{u}_{Rj}, \mathbf{v}_{Rj}. \quad R_j \\ \text{Output: } & \mathbf{v}_{Lk} = R_j \mathbf{u}_{Lj}, \quad \mathbf{v}_{Rk} = R_j \mathbf{u}_{Rj}. \\ & -\mathbf{K} \mathbf{u}_{Rk} = R_j (\mathbf{M} \mathbf{v}_{Rj} + \mathbf{D} \mathbf{u}_{Rj}), \\ & -\mathbf{K}^T \mathbf{u}_{Lk} = R_j (\mathbf{M}^T \mathbf{v}_{Lj} + \mathbf{D}^T \mathbf{u}_{Lj}). \\ & R_k \text{ from } R^2 m_k + R d_k + k_k = 0. \\ & \text{Roots } R_1, R_2. \quad R_k = |R_{1,2}|_{Min}. \\ & m_k = \bar{\mathbf{u}}_{Lk}^T \mathbf{M} \mathbf{u}_{Rk}, \quad d_k, k_k \text{ dito.}\end{aligned}\quad (31)$$

A simplified iteration process towards \mathbf{x}_1 with only right trial vectors \mathbf{u}_{Rj} instead of left/right pairs $\mathbf{u}_{Lj}, \mathbf{u}_{Rj}$ results in a scalar condensed equation,

$$\begin{aligned}R^2 \hat{s}_2 + R \hat{s}_1 + \hat{s}_0 &= 0, \\ \hat{s}_k &= \bar{\mathbf{u}}_{Rj} \mathbf{S}_k \mathbf{u}_{Rj}; \quad \mathbf{S}_2 = \mathbf{M}, \quad \mathbf{S}_1 = \mathbf{D}, \quad \mathbf{S}_0 = \mathbf{K},\end{aligned}\quad (32)$$

with complex coefficients \hat{s}_k in general. Finally, the result \mathbf{x}_1, λ_1 of an iteration process should be examined by the original eigenvalue problem $(\lambda_1^2 \mathbf{S}_2 + \lambda_1 \mathbf{S}_1 + \mathbf{S}_0) \mathbf{x}_1 \stackrel{?}{=} \mathbf{0}$.

The iteration towards $\lambda_2, \ell_2, \mathbf{r}_2$ must be free of parts in direction of $\ell_1, \bar{\ell}_1$,

$\mathbf{r}_1, \bar{\mathbf{r}}_1$. An explicit way in order to produce clean vectors takes provisional iterated vectors, $\tilde{\mathbf{w}}_{Lj}, \tilde{\mathbf{w}}_{Rj}$,

$$\begin{aligned} \mathbf{A} \tilde{\mathbf{w}}_{R,j+1} &= R_j \mathbf{B} \mathbf{w}_{Rj}, \\ \mathbf{A}^T \tilde{\mathbf{w}}_{L,j+1} &= R_j \mathbf{B}^T \mathbf{w}_{Lj}, \end{aligned} \quad (33)$$

and cleans them with respect to $\ell_1, \bar{\ell}_1; \mathbf{r}_1, \bar{\mathbf{r}}_1$.

$$\begin{aligned} \mathbf{w}_{R,j+1} &= \tilde{\mathbf{w}}_{R,j+1} - \frac{\ell_1^T \mathbf{B} \tilde{\mathbf{w}}_{R,j+1}}{\ell_1^T \mathbf{B} \mathbf{r}_1} \mathbf{r}_1 - \frac{\bar{\ell}_1^T \mathbf{B} \tilde{\mathbf{w}}_{R,j+1}}{\bar{\ell}_1^T \mathbf{B} \bar{\mathbf{r}}_1} \bar{\mathbf{r}}_1; \\ b_1 &= \ell_1^T \mathbf{B} \mathbf{r}_1, \quad \bar{b}_1 = \bar{\ell}_1^T \mathbf{B} \bar{\mathbf{r}}_1. \end{aligned} \quad (34)$$

$$\begin{aligned} \mathbf{w}_{L,j+1} &= \tilde{\mathbf{w}}_{L,j+1} - \frac{\mathbf{r}_1^T \mathbf{B}^T \tilde{\mathbf{w}}_{L,j+1}}{\mathbf{r}_1^T \mathbf{B}^T \ell_1} \ell_1 - \frac{\bar{\mathbf{r}}_1^T \mathbf{B}^T \tilde{\mathbf{w}}_{L,j+1}}{\bar{\mathbf{r}}_1^T \mathbf{B}^T \bar{\ell}_1} \bar{\ell}_1; \\ \mathbf{r}_1^T \mathbf{B}^T \ell_1 &= \ell_1^T \mathbf{B} \mathbf{r}_1 = b_1, \quad \bar{\mathbf{r}}_1^T \mathbf{B}^T \bar{\ell}_1 = \bar{b}_1. \end{aligned} \quad (35)$$

An amount of r known eigensolutions is treated in a similar manner. The numerical process itself can be evaluated within the original space of order n corresponding with the number of degrees of freedom.

$$\begin{aligned} \ell_1 &= \begin{bmatrix} \lambda_1 y_1 \\ y_1 \end{bmatrix}; \quad \mathbf{r}_1 = \begin{bmatrix} \lambda_1 x_1 \\ x_1 \end{bmatrix}. \quad \mathbf{B} = \begin{bmatrix} \mathbf{0} & \mathbf{M} \\ \mathbf{M} & \mathbf{D} \end{bmatrix}. \\ \mathbf{v}_{Rk} &= \tilde{\mathbf{v}}_{Rk} - \frac{Z_R}{b_1} \lambda_1 x_1 - \frac{Z_R^*}{\bar{b}_1} \bar{\lambda}_1 \bar{x}_1. \\ \mathbf{u}_{Rk} &= \tilde{\mathbf{u}}_{Rk} - \frac{Z_R}{b_1} x_1 - \frac{Z_R^*}{\bar{b}_1} \bar{x}_1. \\ b_1 &= \ell_1^T \mathbf{B} \mathbf{r}_1 = y_1^T \mathbf{D} x_1 + 2\lambda_1 y_1^T \mathbf{M} x_1. \\ Z_R &= \ell_1^T \mathbf{B} \tilde{\mathbf{w}}_{Rk} = \lambda_1 y_1^T \mathbf{M} \tilde{\mathbf{u}}_{Rk} + y_1^T (\mathbf{M} \tilde{\mathbf{v}}_{Rk} + \mathbf{D} \tilde{\mathbf{u}}_{Rk}), \\ Z_R^* &= \bar{\ell}_1^T \mathbf{B} \tilde{\mathbf{w}}_{Rk} = \bar{\lambda}_1 \bar{y}_1^T \mathbf{M} \tilde{\mathbf{u}}_{Rk} + \bar{y}_1^T (\mathbf{M} \tilde{\mathbf{v}}_{Rk} + \mathbf{D} \tilde{\mathbf{u}}_{Rk}). \end{aligned} \quad (36)$$

$$\begin{aligned} \mathbf{v}_{Lk} &= \tilde{\mathbf{v}}_{Lk} - \frac{Z_L}{b_1} \lambda_1 y_1 - \frac{Z_L^*}{\bar{b}_1} \bar{\lambda}_1 \bar{y}_1. \\ \mathbf{u}_{Lk} &= \tilde{\mathbf{u}}_{Lk} - \frac{Z_L}{b_1} y_1 - \frac{Z_L^*}{\bar{b}_1} \bar{y}_1. \\ b_1 &= y_1^T \mathbf{D} x_1 + 2\lambda_1 y_1^T \mathbf{M} x_1. \end{aligned} \quad (37)$$

$$\begin{aligned} Z_L &= \mathbf{r}_1^T \mathbf{B}^T \tilde{\mathbf{w}}_{Lk} = \lambda_1 x_1^T \mathbf{M}^T \tilde{\mathbf{u}}_{Lk} + x_1^T (\mathbf{M}^T \tilde{\mathbf{v}}_{Lk} + \mathbf{D}^T \tilde{\mathbf{u}}_{Lk}), \\ Z_L^* &= \bar{\mathbf{r}}_1^T \mathbf{B}^T \tilde{\mathbf{w}}_{Lk} = \bar{\lambda}_1 \bar{x}_1^T \mathbf{M}^T \tilde{\mathbf{u}}_{Lk} + \bar{x}_1^T (\mathbf{M}^T \tilde{\mathbf{v}}_{Lk} + \mathbf{D}^T \tilde{\mathbf{u}}_{Lk}). \end{aligned} \quad (38)$$

EXAMPLES

Example 1: A simple but significant example shown in fig. 1 is examined in order to demonstrate the iteration process towards the first two pairs of complex conjugate eigenvalues.

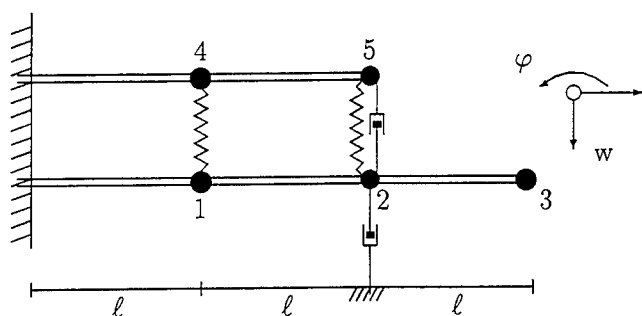


Fig.1: Vibration system with massless elastic beams, discrete elastic and viscous elements and masses.

Each of the 5 beams is approximated by cubic interpolation functions; consequently there are $n=10$ degrees of freedom.

$$\mathbf{q}^T = [w_1 \ \varphi_1 \ w_2 \ \varphi_2 \ \dots \ w_5 \ \varphi_5].$$

$$\mathbf{M} = \text{diag} \{1.5, 0.1, 2.0, 0.1, 1.0, 0.1, 1.5, 0.1, 1.0, 0.1\};$$

$$d_{ij} = 0 \text{ except } d_{33} = 0.2 + 0.2 = 0.4, \\ d_{39} = d_{93} = -0.2, \ d_{99} = 0.2;$$

$$\mathbf{K} = \begin{bmatrix} 27 & 0 & -12 & -6 & 0 & 0 & -3 & 0 & 0 & 0 \\ 0 & 8 & 6 & 2 & 0 & 0 & 0 & 0 & 0 & 0 \\ -12 & 6 & 27 & 0 & -12 & -6 & 0 & 0 & -3 & 0 \\ -6 & 2 & 0 & 8 & 6 & 2 & 0 & 0 & 0 & 0 \\ 0 & 0 & -12 & 6 & 12 & 6 & 0 & 0 & 0 & 0 \\ 0 & 0 & -6 & 2 & 6 & 4 & 0 & 0 & 0 & 0 \\ -3 & 0 & 0 & 0 & 0 & 0 & 27 & 0 & -12 & -6 \\ 0 & 0 & 0 & 0 & 0 & 0 & 0 & 8 & 6 & 2 \\ 0 & 0 & -3 & 0 & 0 & 0 & -12 & 6 & 15 & 6 \\ 0 & 0 & 0 & 0 & 0 & 0 & -6 & 2 & 6 & 4 \end{bmatrix}.$$

The iteration sequences towards $\lambda_{1,2}$ and $\lambda_{3,4}$ are shown in table 1.

step k	$R \rightarrow \lambda_{1,2}$	$R \rightarrow \lambda_{3,4}$
1	$-0.0133\,333 \pm 3.50\,235\,i$	$-0.0133\,333 \pm 3.50\,235\,i$
2	$-0.0149\,064 \pm 0.329\,075\,i$	$-0.0092\,787 \pm 1.33\,050\,i$
3	$-0.0154\,106 \pm 0.331\,581\,i$	$-0.0123\,665 \pm 1.248\,325\,i$
5	$-0.0149\,038 \pm 0.326\,985\,i$	$-0.0138\,118 \pm 1.244\,679\,i$
10	$-0.0141\,243 \pm 0.325\,045\,i$	$-0.0139\,574 \pm 1.244\,747\,i$
15	$-0.0144\,109 \pm 0.325\,188\,i$	$-0.0139\,575 \pm 1.244\,747\,i$
20	$-0.0140\,193 \pm 0.325\,127\,i$	$-0.0139\,575 \pm 1.244\,747\,i$
30	$-0.0141\,902 \pm 0.325\,110\,i$	
QZ	$-0.0141\,902 \pm 0.325\,110\,i$	$-0.0139\,575 \pm 1.244\,747\,i$

Table 1: Iteration sequences for example 1.

The results achieved by using the QZ-algorithm, described by Moler and Stewart [5] and implemented in EISPACK in an optimized version, are added in order to show the correspondence with the results coming out of the vector iteration process.

Example 2: Another example without mechanical background is characterized by an unsymmetric matrix \mathbf{K} .

$$\mathbf{M} = \begin{bmatrix} 3 & 2 & 1 & 1 \\ 2 & 3 & 2 & 1 \\ 1 & 2 & 8 & 1 \\ 1 & 1 & 1 & 2 \end{bmatrix}, \mathbf{D} = \begin{bmatrix} 16 & 14 & 12 & 2 \\ 14 & 34 & 32 & 20 \\ 12 & 32 & 32 & 20 \\ 2 & 20 & 20 & 22 \end{bmatrix}, \mathbf{K} = \begin{bmatrix} 97 & 95 & 85 & 2 \\ 95 & 295 & 285 & 200 \\ 85 & 285 & 285 & 200 \\ 40 & 200 & 200 & 202 \end{bmatrix}.$$

The iteration sequences towards $\lambda_{1,2}$ and $\lambda_{3,4}$ using the simplified iteration process are shown in table 2.

step k	$R \rightarrow \lambda_{1,2}$	$R \rightarrow \lambda_{3,4}$
1	$-4.750\,000 \pm 7.764\,100\,i$	$-4.750\,000 \pm 7.764\,100\,i$
2	$-0.139\,727 \pm 1.250\,032\,i$	$-2.328\,012 \pm 5.131\,843\,i$
3	$-0.118\,934 \pm 1.158\,852\,i$	$-0.909\,217 \pm 4.050\,397\,i$
5	$-0.128\,928 \pm 1.139\,867\,i$	$-0.791\,635 \pm 3.410\,302\,i$
10	$-0.126\,919 \pm 1.135\,577\,i$	$-0.825\,569 \pm 3.502\,506\,i$
15	$-0.128\,615 \pm 1.137\,635\,i$	$-0.830\,765 \pm 3.499\,874\,i$
20	$-0.129\,364 \pm 1.141\,156\,i$	$-0.830\,586 \pm 3.499\,624\,i$
30	$-0.126\,890 \pm 1.138\,091\,i$	$-0.830\,575 \pm 3.499\,636\,i$
40	$-0.126\,878 \pm 1.138\,085\,i$	$-0.830\,575 \pm 3.499\,636\,i$
50	$-0.126\,883 \pm 1.138\,091\,i$	
QZ	$-0.126\,883 \pm 1.138\,091\,i$	$-0.830\,575 \pm 3.499\,636\,i$

Table 2: Iteration sequences for example 2.

CONCLUSION

Vector iteration methods are optimal tools in structural dynamics and control because of the iterative character of the design process itself. The restriction of all the calculations to be done to the original n -order space of degrees of freedom is a significant property which makes the method attractive for nonlinear eigenvalue problems. Of course, well known methods like inverse iteration and spectral shifting should be incorporated in order to improve the convergence behaviour.

REFERENCES

1. Bellmann, R.; Cooke, K.L., Differential-difference equations. Academic Press Inc., New York-London, 1963.
2. Weweries, R., Zur Stabilitätsuntersuchung von gewöhnlichen mechanischen Systemen mit Totzeitrückkopplung. ZAMM 69, 1989, T414-T417.
3. Ruge, P., Eigenvalues of damped structures: Vector iteration in the original space of DOF. Computational Mechanics. To appear.
4. Nordmann, R., Ein Näherungsverfahren zur Berechnung der Eigenwerte und Eigenformen von Turborotoren mit Gleitlagern, Spalterregung, äußerer und innerer Dämpfung. Dissertation D17, Darmstadt, 1974.
5. Moler, C. B.; Stewart, G. W., An algorithm for generalized matrix eigenvalue problems. SIAM J. Numer. Anal. 10, 1973, 241-256.

SYSTEM IDENTIFICATION I

Parameter Subset Selection in Damage Location

M. I. Friswell

Department of Mechanical Engineering
University of Wales Swansea, UK

S. D. Garvey and J. E. T. Penny

Department of Mechanical and Electrical Engineering
Aston University, Birmingham, UK

ABSTRACT

Damage detection and location often produces sets of equations whose solution are ill conditioned. These equations must be regularised in some way to produce a solution. This paper considers one such method for this regularisation, by considering only a subset of the parameters to be in error. The standard method uses the sensitivity matrix based on the initial finite element model to choose the parameter subset. Many residuals used for damage location are non-linear functions of the parameters, and this paper examines the relationship between the subset selection and the iteration required for the parameter estimation. Several strategies are outlined and the methods are tested on a simulated cantilever beam, both with and without systematic errors.

1. INTRODUCTION

In damage location there are often many candidate parameters which could be used to reproduce the changes in the model. With a limited amount of measured information, one has to choose extra constraints to produce a well conditioned parameter estimation problem. One approach is to assume that only a limited number of parameters are in error. This has been successfully applied in damage detection and location using statistical performance measures and an exhaustive search of all the parameter combinations [1-4]. Subset selection is well established in the statistical literature [5], and is based on a sub-optimal choice of parameters to reduce the computational burden. In general for damage location, this is obtained by linearisation via a Taylor series, and the parameter estimation requires a non-linear optimisation, usually performed by iteration.

The selection of a suitable subset of parameters for estimation has been used in structural dynamics [6], for actuator location [7] and for damage detection [8, 9].

The problem to be addressed may be stated as follows: we have a set of n equations in the p parameters θ given by

$$\mathbf{A}\theta = \mathbf{b} \quad (1)$$

where \mathbf{A} is an $n \times p$ matrix and \mathbf{b} is a vector of length n . Typically, for damage location and error localisation in model updating, there are many more parameters than measurements ($p > n$). Although using mode shapes or frequency response functions it may be possible to produce an over-specified set of equations, in general the solution to these equations will be ill-conditioned. Physically this means that there is insufficient information in the measured data to identify all the parameters. Other methods may be used to obtain a well-conditioned solution through a regularisation approach [10-14]. Regularisation generally yields a solution where all the parameter changes are non-zero, and so the methods have limited value for damage location.

2. APPLICATION TO DAMAGE LOCATION

In recent years, there has been a considerable demand for more accurate techniques to detect and locate damage, particularly in large space structures. Damage will cause the stiffness distribution in the structure to change which may be detected by measuring its dynamic response. Two distinct philosophies have been considered to locate the damage in a structure using measured vibration data. The first group of methods use techniques of finite element model updating [15] to obtain a corrected set of physical parameters or a corrected stiffness matrix that reproduces the measured data. Mottershead and Friswell [16] gave a survey of model updating methods and Kaouk and Zimmerman [17] outlined a typical method of this type. The alternative group of methods assume a candidate set of possible damage scenarios which include both the damage mechanism and the location. The change in dynamic response due to the damage is predicted, usually in terms of the natural frequencies. The predicted change in response of the structure for all the damage scenarios is then compared to the measured change and the closest damage case is chosen. Statistical methods are often used to identify the most likely location of the damage. Cawley and Adams [2-4] used this type of method and found that damage in specimens fabricated from composite materials could be detected. Friswell *et al.* [1] used a similar method but also obtained an indication of the quality of the predictions.

In this paper we will use the techniques of model updating. We parameterise the model in such a way that all the likely damage scenarios are modelled by some combination of the parameter values. The methods detailed in this paper are then used to pick out a limited number of these parameters that produce the 'best' fit to the measured data. For example, if the location of damage in a space frame structure is required, then the complete set of parameters might consist of the stiffness of the constituent spars. It is expected that only one or two of these spars might be damaged, and hopefully the corresponding parameters would be identified by the following procedure. Of course, there might be other errors in the undamaged model, and the damage location method will identify these as well as the damage sites.

The parameters should consist of perturbations from the modelled quantities. Thus the measured data may be assembled into a vector \mathbf{z}_m and the parameters should be changed to improve the correlation between the predictions and the measurements. Fritzen [18] considered a range of residuals. Let \mathbf{z} represent the predictions from the model, in the same form as the measurements. Then the measured data may be written in terms of a first order Taylor Series in the parameters θ_j as

$$\mathbf{z}_m = \mathbf{z} + \mathbf{S} \boldsymbol{\theta} + \text{higher order terms} \quad (2)$$

where $\boldsymbol{\theta}$ is the vector of parameter values and \mathbf{S} is the sensitivity matrix, which contains first order derivatives of the measured quantities with respect to the parameters. The calculation of these derivatives for eigenvalues and eigenvectors is standard [19-21] and is relatively straight-forward for most residuals. Neglecting the higher order terms, and rearranging equation (2) gives

$$\mathbf{S} \boldsymbol{\theta} = \mathbf{z}_m - \mathbf{z} \quad (3)$$

which is an equation of the same form as equation (1). One approach to eliminate the problem of errors in the analytical model of the undamaged structure is to look at differences between the damaged and undamaged measurements. If the parameter errors not associated with the damage are unchanged between the damaged and undamaged structure, then to first order their effect will cancel. Thus, if \mathbf{z}_u represents the measurements on the undamaged structure and \mathbf{z}_d represents the measurements on the damaged structure, the equations of interest are

$$\mathbf{S} \boldsymbol{\theta} = \mathbf{z}_u - \mathbf{z}_d \quad (4)$$

which is of the same form as equation (1). Usually the equations will be weighted. For example, if natural frequencies were used directly in equation (4) then the higher frequencies will effectively be weighted more highly. Using

relative (or percentage) changes in the natural frequencies is a good solution. The relative weighting between natural frequencies and mode shapes should recognise the relative uncertainty in each measurement.

Thus far we have considered only the initial linearisation of the residual. The real quantity of interest is the residual after convergence, that is the parameter subset that minimises the penalty function

$$J = \| \mathbf{z}_m - \mathbf{z}(\theta) \|^2 \quad (5)$$

where $\mathbf{z}(\theta)$ is a non-linear function of the parameters. Equation (5) is equivalent to equation (3); a similar expression exists for equation (4).

3. PARAMETER SUBSET SELECTION

Millar [1] gave a good summary of the subset selection method for the single measurement case. The important aspects for the application to structural dynamics will be outlined briefly. Millar also considered the statistical properties of the estimators, including the bias in the parameter estimates due to the selection procedure and due to the omission of parameters (named selection bias and omission bias). Millar also discusses in depth the trade-off between reduced bias but increased variance in the parameter estimates as the number of parameters is increased. He also discusses other strategies to select parameters, such as backward selection and sequential replacement algorithms, that have limited value in damage location [8].

3.1 Forward Selection

The approach adopted in this paper is to assume that only a subset of the parameters in equation (1) are non-zero. The optimum subset is chosen that minimises the residual in equation (1). Lallement and Piranda [6] used an iterative procedure to produce a sub-optimal solution, commonly known as *forward selection*. Among the columns of \mathbf{A} , the single column is sought which best represents the vector \mathbf{b} . If the columns of \mathbf{A} are given by \mathbf{a}_j , so that $\mathbf{A} = [\mathbf{a}_1 \ \mathbf{a}_2 \ \dots \ \mathbf{a}_p]$, then the selected parameter is that which minimises the residual

$$J = \| \mathbf{b} - \mathbf{a}_j \hat{\theta}_j \|^2 \quad (6)$$

where $\hat{\theta}_j$ is the least squares estimate of the j th parameter, and is

$$\hat{\theta}_j = \mathbf{a}_j^T \mathbf{b} / \mathbf{a}_j^T \mathbf{a}_j \quad (7)$$

Expanding equation (6), using equation (7), gives

$$J = \mathbf{b}^T \mathbf{b} - (\mathbf{a}_j^T \mathbf{b})^2 / \mathbf{a}_j^T \mathbf{a}_j \quad (8)$$

and the j th parameter is selected that maximises

$$(\mathbf{a}_j^T \mathbf{b})^2 / \mathbf{a}_j^T \mathbf{a}_j$$

Equivalently, since \mathbf{b} is a constant vector,

$$\cos^2 \phi_j = (\mathbf{a}_j^T \mathbf{b})^2 / (\mathbf{a}_j^T \mathbf{a}_j)(\mathbf{b}^T \mathbf{b}) \quad (9)$$

is maximised where ϕ_j is the angle between the vectors \mathbf{b} and \mathbf{a}_j . Thus the j th parameter is selected that minimises the angle between the vectors \mathbf{b} and \mathbf{a}_j .

Next the combination of two columns of \mathbf{A} which constitutes the best sub-basis for the representation of \mathbf{b} is determined. In the forward selection procedure the second parameter is obtained in a sub-optimal way, by retaining the first parameter selected. Let j_1 represent the first parameter selected and let the corresponding column of \mathbf{A} be \mathbf{a}_{j_1} . The optimum value for the j_1 th parameter is then

$$\hat{\theta}_{j_1} = \mathbf{a}_{j_1}^T \mathbf{b} / \mathbf{a}_{j_1}^T \mathbf{a}_{j_1} \quad (10)$$

The vector $\mathbf{b} - \mathbf{a}_{j_1} \hat{\theta}_{j_1}$ is then orthogonal to \mathbf{a}_{j_1} and the subspace spanned by the columns of \mathbf{A} that is orthogonal to \mathbf{a}_{j_1} must be searched. Thus the columns of \mathbf{A} and the vector \mathbf{b} are replaced with

$$\begin{aligned} \mathbf{a}_j &\rightarrow \mathbf{a}_j - \mathbf{a}_{j_1} \hat{\alpha}_j & \text{where } \hat{\alpha}_j &= \mathbf{a}_{j_1}^T \mathbf{a}_j / \mathbf{a}_{j_1}^T \mathbf{a}_{j_1} \\ \mathbf{b} &\rightarrow \mathbf{b} - \mathbf{a}_{j_1} \hat{\theta}_{j_1} \end{aligned} \quad (11)$$

The procedure is now repeated on this reduced problem, to find the parameter θ_j , for $j \neq j_1$, that gives the smallest residual, or equivalently the smallest angle ϕ_j .

An iterative process is then produced. Let m be the number of parameters selected. First, with $m=1$ the single parameter that is best able to represent the

data is selected. Subsequent iterations retain the parameters chosen in previous steps and select the parameter from those remaining that, together with those already chosen, is best able to represent the data. At each value of m this represents a one dimensional optimisation, rather than a m dimensional optimisation in the general case, but the method is sub-optimal.

3.2 Efroymsen's Algorithm

The algorithm proposed by Efroymsen [5, 22] is a variation on the forward selection, but allows for selected parameters to be deleted. Suppose that m is the number of parameters selected, given by $[\theta_{j_1}, \theta_{j_2}, \dots, \theta_{j_m}]$. Then the residual sum of squares, J_m , is given by

$$J_m = \left\| \mathbf{b} - \sum_{i=1}^m \mathbf{a}_{j_i} \hat{\theta}_{j_i} \right\|^2 \quad (12)$$

where $\hat{\theta}_j$ is the least squares estimate of the j th parameter, using only the m selected parameters. For each parameter in the selected subset, the residual sum of squares using just the remaining $m-1$ parameters is calculated. The test ratio, R_d , based on the minimum of these sums, J_{m-1} , is calculated as

$$R_d = \frac{J_{m-1} - J_m}{J_m / (n - m - 1)} \quad (13)$$

and compared to a predetermined value. If R_d is less than this value the corresponding parameter is eliminated from the selected subset.

Efroymsen also determined a ratio to decide whether a parameter should be added to the selected subset. If J_{m+1} is the minimum residual sum of squares that may be obtained by adding the parameter $\theta_{j_{m+1}}$ to the original set $[\theta_{j_1}, \theta_{j_2}, \dots, \theta_{j_m}]$, then if the ratio

$$R_a = \frac{J_m - J_{m+1}}{J_{m+1} / (n - m - 2)} \quad (14)$$

is greater than a predetermined value the parameter $\theta_{j_{m+1}}$ is added to the selected set. The ratio R_d may also be used as a guide to determine the optimum number of parameters to use.

4. ITERATION AND SELECTION STRATEGIES

As in the linear case, an exhaustive search of all possible parameter selections to find the lowest residual in equation (5), is computational prohibitive. Sub-optimal algorithms must therefore be derived. These may be based on the selections from the linearised equations of the standard method. There are a number of possible strategies determined by the ordering of iteration and selection. All of these are based on retaining a number of the best performing subsets throughout the process, which may therefore produce subsets that are chosen more than once. These will now be outlined in order of increasing computational requirements.

4.1 The Standard Method

The standard method may be applied and a relatively small number of the best parameters retained at each stage. Suppose n_s parameters are selected at each of m stages. For example, if $n_s = 2$ then we might choose parameters 5 and 9 as the best two parameters which on their own are best able to represent the measured data. Then we retain parameter 5 and look for the parameter that combined with parameter 5, yields the best match. We retain the best 2 and then repeat the process with parameter 9, and so on. The result will be a total of n_s subsets of size 1, n_s^2 subsets of size 2, n_s^3 subsets of size 3, and so on up to n_s^m subsets of size m . The parameter subsets have been selected using the sensitivity matrix based on the initial finite element model. For each of these subsets the parameters are updated using the standard method until convergence. The size of the residuals based on the updated parameters may then be compared and the subset with the lowest residual chosen.

4.2 Optimising Already Chosen Parameters

An alternative strategy is to iterate until convergence at every stage based on the parameters selected during the previous stages. Thus at the first stage the parameters are chosen as before. The optimum value for the selected parameter is then calculated by iteration. Using the sensitivity matrix based the converged parameter a second parameter is selected. Note that this sensitivity matrix must be orthogonalised with respect to the column of the converged sensitivity matrix corresponding to the chosen parameter. The optimum values of the two parameters are then obtained by iteration. Note that both of the chosen parameters are optimised together, and in general the value of the first parameter will not be equal to its value at the first stage. This process continues with subsequent stages. As in the standard method more than one selection may be retained at each stage to produce a number of parameter subsets.

4.3 Iteration at Every Stage

The final strategy is to iterate before the best parameters are chosen. Thus, at the first stage, the optimum value for each candidate parameter is obtained by iteration. The values of the residuals based on these converged parameter estimates are compared and the best parameter is chosen. This parameter is retained and the second stage considers each remaining candidate parameter in turn. The optimum values of the parameters (the one already selected and the candidate parameter) are obtained by iteration, and the best parameter chosen based on the lowest residual. Once again, more than one selection may be retained at each stage to produce a number of parameter sets.

5. NUMERICAL EXAMPLE

The ideas contained in this paper will now be tested on a simulated cantilever beam example. Although somewhat artificial, all the important features and problems of error location and damage detection/location may be demonstrated. The beam has a cross section of 25 mm x 50 mm, a length of 1 m and is assumed to be rigidly clamped at one end. Only motion in the plane of the thinner beam dimension is considered. The beam has a Young's modulus of 210 GN/m² and a mass density of 7800 kg/m³. The set of candidate parameters is chosen to be large and consists of one global parameter, the Young's modulus, two parameters per element, the element stiffness and the element mass, and two parameters per node, namely a discrete mass and a discrete spring.

5.1 The Standard Method - No Errors

The first test of any method is its application to a simulated example with no noise or systematic errors. Any parameter changes in the model should be identified exactly. The simulated 'measurements' are assumed to be the relative changes in the first eight natural frequencies of the beam and are taken from a model with 20 elements. The undamaged natural frequencies are taken from the uniform beam, whilst the damaged frequencies are derived from a model where the stiffness of element 4 has been reduced by 30%. Table 1 gives the damaged and undamaged natural frequencies, showing that the 30% damage only results in a 2.4% change in natural frequency at most. These small frequency changes are typical in damage location and are one of the major difficulties in the identification of the location of damage [23]. Measurement noise, environmental factors and structure non-stationarity can easily lead to incorrect conclusions on damage location.

Figure 1 shows the angles between the columns of the sensitivity matrix of the initial finite element model and the vector of the changes in the first 8 natural frequencies due to the damage. Clearly the column relating to the stiffness of

element 4 has a small angle, although it is not zero. It is not zero because equation (4) is only a first order approximation and the extent of the damage (30%) is large. For the four parameters with the lowest angle, Table 2 shows the residual at the first iteration and also after convergence based on optimising the single chosen parameter. Clearly the residual relating to the stiffness of element 4 goes to zero on convergence, showing that this parameter does indeed represent the damage location. Returning to Figure 1, changing the mass of element 17 is also able to model the 'measured' changes accurately. This is a problem that relates to the symmetry of the beam, and the fact that no spatial information is incorporated into the measurements. Mode shapes could also be incorporated into the measurement vector, although the accuracy with which they could be measured may be insufficient to show a change in mode shape due to damage. This is an example of the more general problem, where damage or changes of parameters at more than one location causes the same changes in the lower natural frequencies.

What happens if we change more than one parameter? Suppose that a 0.1 kg mass is added to node 12, in addition to the 30% stiffness change to element 4. Table 3 shows the results when the best subsets of 1, 2 and 3 parameters are chosen. At each stage the 2 best parameters are chosen. The residuals under the first 2 parameters relate to the values when a subset of size 1 or 2 is selected. Also shown are the residuals after convergence based on optimising the values of the chosen parameters. From the values of the test ratio R_a and the residuals, it is clear that the two correct parameters should be selected. A number of other parameter subsets have small residuals and the addition of random noise would make the selection of the best subset more difficult.

5.2 The Standard Method - With Systematic Errors

This example demonstrates the problems associated with systematic errors, introduced in this case from three sources; discretisation errors, a discrete mass not at a node of the finite element model used for the identification and a stiffness reduction covering only half of one element. The 'measurements' are taken from a beam with 40 elements, giving a maximum discretisation error in the first 8 natural frequencies of only 0.1%. Again the changes in the first 8 natural frequencies are 'measured'. Damage is simulated by reducing the stiffness of element number 8 in the fine mesh model by 30%, which is equivalent to changing the stiffness of element 4 in the coarse mesh model. Of course, the damage only covers one half of the element in the coarse mesh model. A mass of 0.1 kg is also added to node 23 of the fine mesh model, corresponding to a point in the middle of element 12 in the coarse mesh model. Subsets of 1, 2 and 3 parameters are tested and the 2 best parameters are retained at each stage. Table 4 shows the resulting parameter selections. Clearly the method has more difficulty locating the errors, although the correct regions

of the structure are identified, together with those regions arising from the symmetry in this example.

5.3 Optimising Already Chosen Parameters

What happens if the previously chosen parameters are optimised before the sensitivity matrix is computed? Table 5 shows the selected parameter subsets using the 'measured' data described in Section 5.2. Only the residuals on convergence are shown. The effect on the choice of the second parameter is small, although significant differences in the choice of parameters at the third stage are evident. In particular sets of 3 parameters may be chosen that have considerably smaller residuals on convergence than those shown in Table 4. Even so the parameter subsets chosen all correspond to the regions of actual damage, or to those regions arising from the symmetry in this example. Thus the damage is located satisfactorily.

6. CONCLUSIONS

This paper has summarised the 'best' subspace approach to locate errors in a finite element model of a structure. Strategies to cope with non-linearities in typical damage location applications have been discussed. The simulated results are encouraging, although the lack of spatial information and the symmetry of the structure cause considerable problems for these methods. The method seems reasonably robust to systematic errors, although large errors, either random or systematic, are likely to cause the selection of incorrect parameters. Although the actual parameters were not always chosen in the example, the regions of damage were correctly identified.

ACKNOWLEDGEMENT

Dr. Friswell gratefully acknowledges the support of the Engineering and Physical Sciences Research Council through the award of an Advanced Fellowship.

REFERENCES

1. Friswell, M.I., Penny, J.E.T. and Wilson, D.A.L., Using Vibration Data and Statistical Measures to Locate Damage in Structures. *Modal Analysis: The International Journal of Analytical and Experimental Modal Analysis*, 1994, 9(4), 239-254.
2. Cawley, P. and Adams, R.D., The Location of Defects in Structures from Measurements of Natural Frequencies. *Journal of Strain Analysis*, 1979, 14(2), 49-57.
3. Cawley, P. and Adams, R.D., A Vibration Technique for Non-Destructive Testing of Fibre Composite Structures. *Journal of Composite Materials*, 1979, 13, 161-174.

4. Cawley, P., Adams, R.D., Pye, C.J. and Stone, B.J., A Vibration Technique for Non-Destructively Assessing the Integrity of Structures. *Journal of Mechanical Engineering Science*, 1978, **20**(2), 93-100.
5. Millar, A.J., *Subset Selection in Regression*. Monographs on Statistics and Applied Probability 40, Chapman and Hall, 1990.
6. Lallement, G. and Piranda, J., Localisation Methods for Parameter Updating of Finite Element Models in Elastodynamics. *8th International Modal Analysis Conference*, Orlando, Florida, 1990, 579-585.
7. Ruckman, C.E. and Fuller, C.R., Optimizing Actuator Locations in Active Noise-Control Systems using Subset-Selection. *Journal of Sound and Vibration*, 1995, **186**(3), 395-406.
8. Friswell, M.I., Garvey, S.D. and Penny, J.E.T., The Optimum Choice of Parameters for Single and Multiple Measurement Sets. *ISMA21 Noise and Vibration Engineering*, Leuven, Belgium, 1996, 1907-1919.
9. Fritzen, C.-P., Jennewein, D. and Buchen, D., Model Based Damage Detection from Vibration Data. *ISMA21 Noise and Vibration Engineering*, Leuven, Belgium, 1996, 1017-1031.
10. Mottershead, J.E., Ahmadian, H. and Friswell, M.I., Regularisation Methods for Finite Element Model Updating. submitted, *Mechanical Systems and Signal Processing*.
11. Fregolent, A., D'Ambrogio, W., Salvini, P. and Sestieri, A., Regularisation Techniques for Dynamic Model Updating Using Input Residuals. *Inverse Problems in Engineering*, 1996, **2**(3), 171-200.
12. Ojalvo, I.U., and Zhang, L.-M., Fundamentals of Ill-Conditioning. *Modal Analysis: The International Journal of Analytical and Experimental Modal Analysis*, 1993, **8**(2), 165-176.
13. Rothwell, E. and Drachman, B., A Unified Approach to Solving Ill-Conditioned Matrix Problems. *International Journal of Numerical Methods in Engineering*, 1989, **28**, 609-620.
14. Natke, H.G., On Regularisation Methods Applied to the Error Localisation of Mathematical Models. *9th International Modal Analysis Conference*, Florence, Italy, 1991, 70-73.
15. Friswell, M.I. and Mottershead, J.E., *Finite Element Model Updating in Structural Dynamics*. Kluwer Academic Publishers, 1995.
16. Mottershead, J.E. and Friswell, M.I., Model Updating in Structural Dynamics: A Survey. *Journal of Sound and Vibration*, **167**(2), 347-375, 1993.
17. Kaouk, M. and Zimmerman, D.C., Evaluation of the Minimum Rank Update in Damage Detection: An Experimental Study. *11th International Modal Analysis Conference*, Kissimmee, Florida, 1993, 1061-1068.
18. Fritzen, C.-P., Identification of Mass, Damping and Stiffness Matrices of Mechanical Systems. *Transactions of the ASME, Journal of Vibration, Acoustics, Stress and Reliability in Design*, 1986, **108**(1), 9-16.
19. Fox, R.L. and Kapoor, M.P., Rates of Change of Eigenvalues and Eigenvectors. *AIAA Journal*, 1968, **6**(12), 2426-2429.
20. Nelson, R.B., Simplified Calculation of Eigenvector Derivatives. *AIAA Journal*, 1976, **14**(9), 1201-1205.

21. Friswell, M.I., The Derivatives of Repeated Eigenvalues and their Associated Eigenvectors. *ASME Journal of Vibration and Acoustics*, 1996, 118(3), 390-397.
22. Efroymsen, M.A., Multiple Regression Analysis. In *Mathematical Methods for Digital Computers*, eds. A. Ralston and H.S. Wilf, Wiley, 1960, 191-302.
23. Banks, H.T., Inman, D.J., Léo, D.J. and Wang, Y., An Experimentally Validated Damage Detection Theory in Smart Structures. *Journal of Sound and Vibration*, 1996, 191(5), 859-880.

Mode Number	Undamaged Frequency (Hz)	Damaged Frequency (Hz)	Percentage Difference
1	20.96	20.45	2.39
2	131.3	131.1	0.15
3	367.7	366.6	0.31
4	720.6	711.3	1.29
5	1191	1172	1.61
6	1780	1762	1.02
7	2487	2479	0.32
8	3313	3303	0.30

Table 1. Natural Frequencies of the Undamaged and Damaged Beam

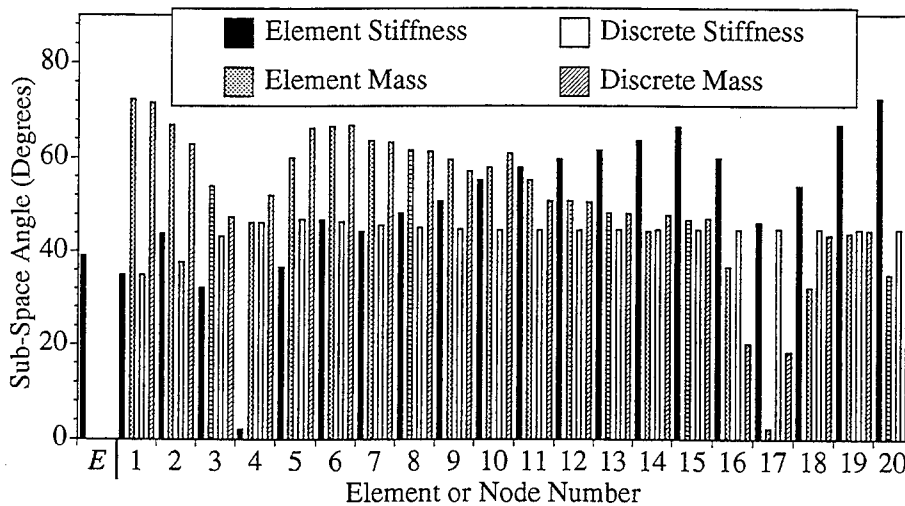


Figure 1. Sub-Space Angles for a 30% Change to the Stiffness of Element 4

Parameter	$J_m (\times 10^6)$ First Iteration	$J_m (\times 10^6)$ On Convergence	Parameter Value On Convergence
$(EI)_4$	1.460	0.000000	-30.0 %
$(\rho A)_{17}$	1.461	0.000028	42.9 %
m_{17}	112.8	94.19	0.183 kg
m_{16}	135.6	139.2	0.197 kg

Table 2. Residuals and Parameter Estimates on Convergence

Choice of Parameter									
Parameter 1			Parameter 2				Parameter 3		
	J_m ($\times 10^6$)	J_m ($\times 10^6$) Conv- erged		J_m ($\times 10^6$)	R_a	J_m ($\times 10^6$) Conv- erged		J_m ($\times 10^6$)	R_a J_m ($\times 10^6$) Conv- erged
$(\rho A)_{17}$	154.6	160.4	m_{12}	1.49	514	0.782	m_8	1.21	0.933 0.701
							$(\rho A)_{12}$	1.48	0.026 0.286
			m_8	8.70	83.9	4.76	m_{12}	1.21	24.8 0.701
							$(\rho A)_{12}$	8.68	0.008 4.75
$(EI)_4$	154.7	160.5	m_{12}	1.49	515	0.000	m_8	1.20	0.937 0.000
							$(\rho A)_{12}$	1.48	0.027 0.000
			m_8	8.70	83.9	5.40	m_{12}	1.20	24.9 0.000
							$(\rho A)_{12}$	8.69	0.007 5.35

Table 3. The Selection of Three Parameters - Beam Example with No Errors. The Parameters are Specified by Type and Element/Node number. Thus $(\rho A)_{17}$ is the Mass/Unit Length of Element 17, $(EI)_4$ is the Stiffness of Element 4, k_1 is a Discrete Spring at Node 1 and m_{12} is a Discrete Mass at Node 12.

Choice of Parameter									
Parameter 1			Parameter 2				Parameter 3		
	J_m ($\times 10^6$)	J_m ($\times 10^6$) Conv- erged		J_m ($\times 10^6$)	R_a	J_m ($\times 10^6$) Conv- erged		J_m ($\times 10^6$)	R_a J_m ($\times 10^6$) Conv- erged
k_1	140.4	145.5	$(\rho A)_{17}$	75.8	4.26	77.7	$(EI)_9$	8.27	32.7 7.29
							$(\rho A)_{12}$	8.27	32.7 7.95
			$(EI)_4$	75.8	4.26	77.5	$(EI)_9$	8.27	32.7 7.96
							$(\rho A)_{12}$	8.27	32.7 7.24
$(\rho A)_{17}$	154.2	154.6	$(EI)_9$	8.35	87.3	7.29	$(\rho A)_{12}$	8.33	0.01 -
							$(EI)_{12}$	8.30	0.03 7.19
			$(\rho A)_{12}$	8.35	87.3	7.96	$(EI)_9$	8.33	0.01 -
							$(EI)_{12}$	8.30	0.03 7.82

Table 4. The Selection of Three Parameters - Beam Example with Systematic Errors. Parameters as Specified in Table 3.

Choice of Parameter							
Parameter 1		Parameter 2			Parameter 3		
	J_m $(\times 10^6)$		J_m $(\times 10^6)$	R_a		J_m $(\times 10^6)$	R_a
k_1	145.5	$(EI)_4$	77.5	4.39	$(\rho A)_{12}$	7.24	38.8
					$(EI)_9$	7.96	34.9
		$(\rho A)_{17}$	77.7	4.36	$(EI)_9$	7.29	38.6
					$(\rho A)_{12}$	7.95	35.1
$(\rho A)_{17}$	154.6	$(EI)_9$	7.29	101	m_{17}	1.24	19.6
					m_{16}	3.19	5.15
		$(\rho A)_{12}$	7.96	92.1	m_{17}	1.81	1.81
					m_{16}	3.72	3.72

Table 5. The Selection of Three Parameters - Beam Example with Systematic Errors. Selection of Parameters 2 and 3 Based on Model with Updated Previously Selected Parameters. The Values of the Residuals are on Convergence. Parameters as Specified in Table 3.

DIAMOND: A Graphical Interface Toolbox for Comparative Modal Analysis and Damage Identification

Scott W. Doebling¹, Charles R. Farrar²

*Los Alamos National Laboratory
Los Alamos, NM, 87545
USA*

Phillip J. Cornwell³

*Rose Hulman Institute of Technology
5500 Wabash Ave.
Terre Haute, IN, 47805
USA*

Abstract

This paper introduces a new toolbox of graphical-interface software algorithms for the numerical simulation of vibration tests, analysis of modal data, finite element model correlation, and the comparison of both linear and nonlinear damage identification techniques. This toolbox is unique because it contains several different vibration-based damage identification algorithms, categorized as those which use only measured response and sensor location information ("non-model-based" techniques) and those which use finite element model correlation ("model-based" techniques). Another unique feature of this toolbox is the wide range of algorithms for experimental modal analysis. The toolbox also contains a unique capability that utilizes the measured coherence functions and Monte Carlo analysis to perform statistical uncertainty analysis on the modal parameters and damage identification results. This paper contains a detailed description of the various modal analysis, damage identification, and model correlation capabilities of toolbox, and also shows a sample application which uses the toolbox to analyze the statistical uncertainties on the results of a series of modal tests performed on a highway bridge.

¹Technical Staff Member, Engineering Sciences and Applications Division, Engineering Analysis Group (ESA-EA), M/S P946, (505) 667-6950, doebling@lanl.gov

²Materials Behavior Team Leader, Engineering Sciences and Applications Division, Engineering Analysis Group (ESA-EA)

³Associate Professor, Dept. of Mechanical Engineering

INTRODUCTION

This paper introduces a new suite of graphical-interface software algorithms to numerically simulate vibration tests and to apply various modal analysis, damage identification, and finite element model refinement techniques to measured or simulated modal vibration data. This toolbox is known as DIAMOND (Damage Identification And MOdal aNalysis for Dummies), and has been developed at Los Alamos National Laboratory over the last year. DIAMOND is written in MATLAB [1], a numerical matrix math application which is available on all major computer platforms. DIAMOND is unique in three primary ways:

1. DIAMOND contains several of the most widely used modal curve-fitting algorithms. Thus the user may analyze the data using more than one technique and compare the results directly. This modal identification capability is coupled with a numerical test-simulation capability that allows the user to directly explore the effects of various test conditions on the identified modal parameters.
2. The damage identification and finite element model refinement modules are graphically interactive, so the operation is intuitive and the results are displayed visually as well as numerically. This feature allows the user to easily interpret the results in terms of structural damage.
3. DIAMOND has statistical analysis capability built into all three major analysis modules: modal analysis, damage identification, and finite element model refinement. The statistical analysis capability allows the user to determine the magnitude of the uncertainties associated with the results. No other software package for modal analysis or damage identification has this capability.

The development of DIAMOND was motivated primarily by the lack of graphical implementation of modern damage identification and finite element model refinement algorithms. Also, the desire to have a variety of modal curve-fitting techniques available and the capability to generate numerical data with which to compare the results of each technique was a motivating factor. The authors are unaware of any commercial software package that integrates all of these features.

This paper is organized as follows: An overview of DIAMOND is provided, including an outline of each module (except for the numerical test simulator): experimental modal analysis and statistical analysis of modal data, damage identification, and finite element model updating. In each section, a flowchart of the menu structure of DIAMOND is presented. Following the overview sec-

tion is an example of the application of DIAMOND to vibration data obtained from an actual highway bridge. This section contains a description of the test-bed, data acquisition equipment, and testing procedure. It also contains a sample experimental modal analysis, complete with statistical analysis of the variability of the results with respect to the variations inherent in the data acquisition process as well as variations resulting from changes in the environmental conditions of the bridge.

OVERVIEW OF DIAMOND

DIAMOND is divided into four primary modules at the top level: numerical vibration test simulator, experimental modal curve fitting and statistical analysis, damage identification, and finite element model refinement. These four modules constitute the primary hierarchy in DIAMOND, as shown in Figure 1.

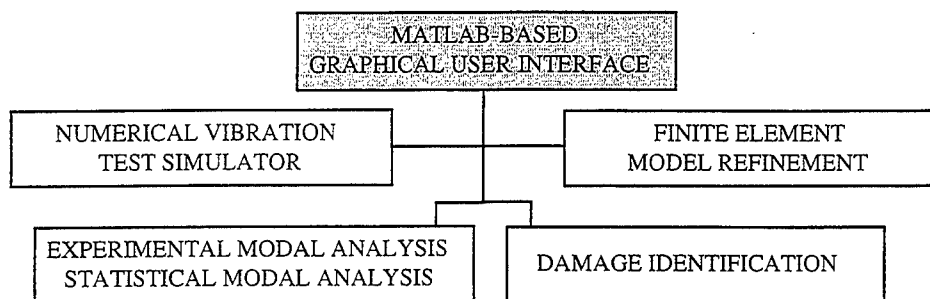


Figure 1: Flowchart of Top Level of DIAMOND

In this paper, the three analysis-oriented modules (all but the test simulator) will be discussed in further detail.

Experimental Modal Analysis / Statistical Analysis of Modal Data

The experimental modal analysis module provides a series of tools for plotting the data in various forms, plotting data indicator functions, defining sensor geometry, performing modal curve-fits, analyzing the results of modal curve fits, and analyzing the variance of identified modal parameters as a function of the noise in the measurements as defined by the measured coherence function. A flowchart of this module is shown in Figure 2.

The most important feature of the experimental modal analysis module is the variety of modal parameter identification algorithms which are available. These include:

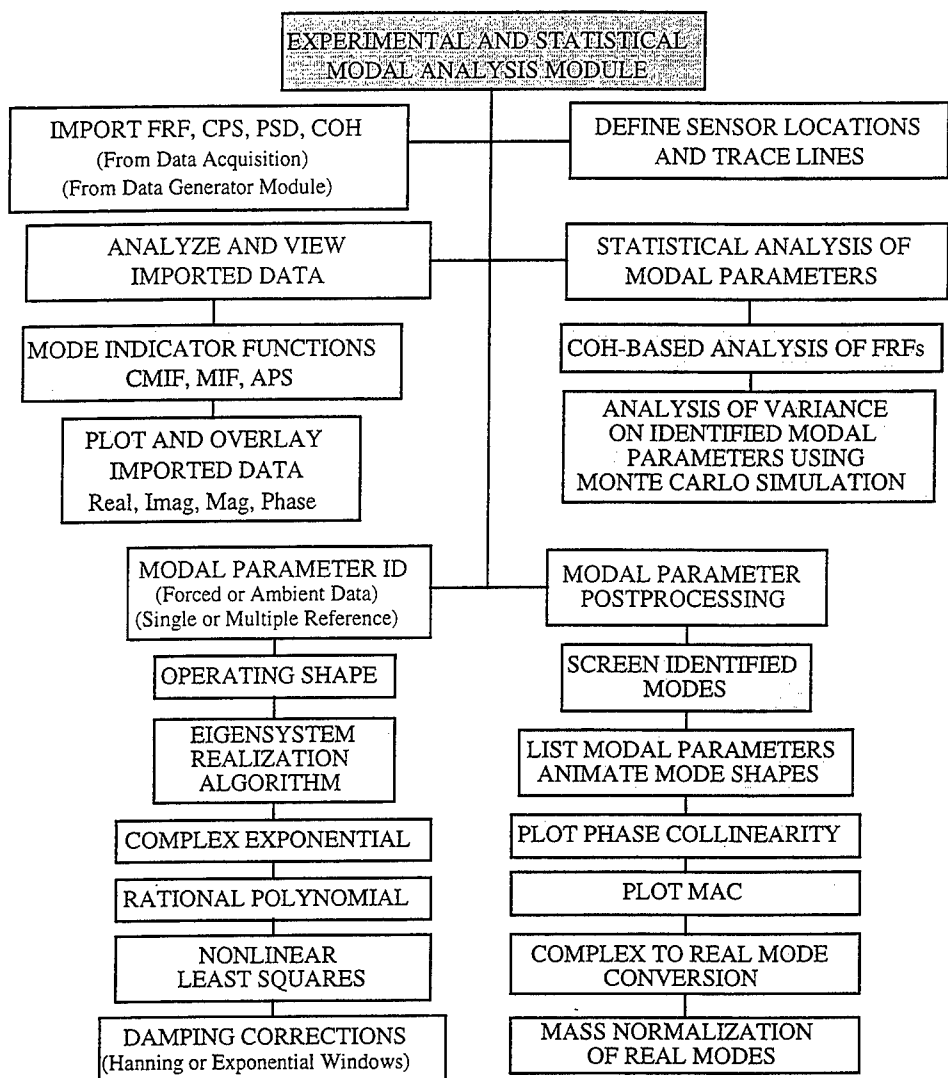


Figure 2: Flowchart of Experimental Modal Analysis / Statistical Modal Analysis Module

1. Operating shapes (which is simply “peak picking,” or “slicing” the FRF matrix at a particular frequency bin)
2. Eigensystem Realization Algorithm (ERA), [2] which is a low-order time domain modal parameter estimation algorithm.

3. Complex exponential algorithm, which is a high-order time domain modal parameter estimation algorithm. The specific algorithm implemented is the Polyreference Time Domain [3] approach.
4. Rational Polynomial Curve fit [4], which is a high-order frequency domain technique that uses orthogonal polynomials to estimate the coefficients of a rational polynomial representation of the frequency response function.
5. Nonlinear least squares fit, which uses a Levenberg-Marquardt nonlinear least-squares curve fitting routine [5] to estimate modal frequencies and modal damping ratios from the unfiltered Fourier spectral responses of a base-excited structure.

Any of these modal identification algorithms can be implemented in a statistical Monte Carlo [6] technique. In such an analysis, a series of perturbed data sets, based on the statistics of the measured FRFs as defined by the measured coherence functions, are generated and propagated through the selected algorithm. The statistics on the results are then used as uncertainty bounds on the identified modal parameters.

Damage Identification

The algorithms contained in the damage identification module of DIAMOND can be classified as modal-based, finite element refinement-based, or nonlinear. A flowchart of the damage identification module is shown in Figure 3.

The damage identification module presents a number of different algorithms:

1. Strain energy methods are based on the work of Stubbs [7], Cornwell [8], and others. The basic idea of these methods is the division of the structure into a series of beam or plate-like elements, and then the estimation of the strain energy stored in each element both before and after damage. The curvatures (second-derivatives with respect to space) of the mode shapes are used to approximate the strain energy content.
2. Flexibility methods all use some measure of the change in the modal flexibility matrix, estimated from the mass-normalized measured mode shapes, $[\Phi]$, and modal frequencies squared, $[\Lambda]$, as

$$[G] \approx [\Phi][\Lambda]^{-1}[\Phi]^T \quad (1)$$

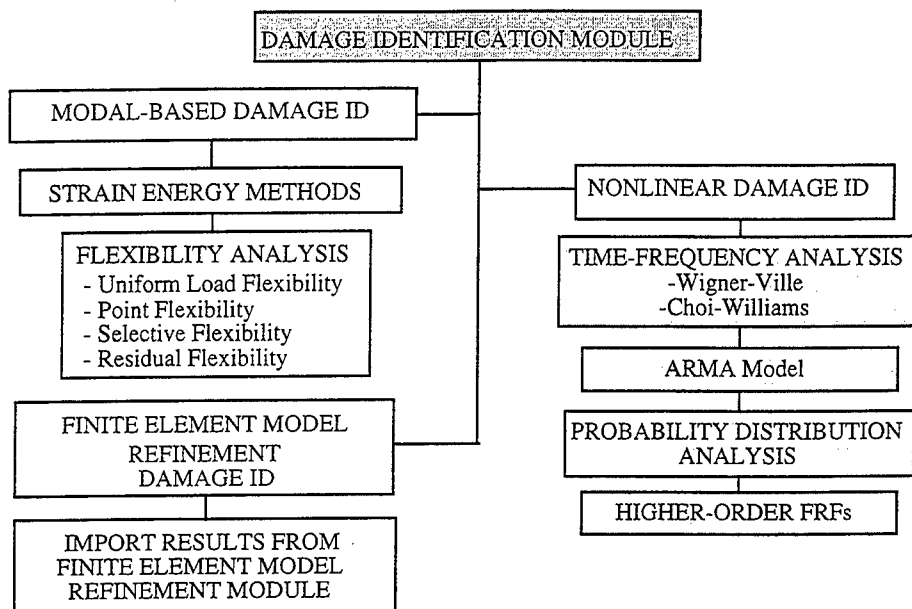


Figure 3: Flowchart of Damage Identification Module

The modal flexibility matrix is used to estimate the static displacements that the structure would undergo as a result of a specified loading pattern. The uniform load flexibility method [9] involves specifying a unit load at all measurement degrees of freedom (DOF), then comparing the change in the resulting displacement pattern before and after damage. The point flexibility method [10] specifies the application of a unit load at each measurement DOF one at a time, then looking for a change in the resulting displacements at the same point before and after damage.

The selective flexibility method, which is still under development, uses one of the above two flexibility approaches but filters the modes used to form the flexibility matrix according to their relative statistical uncertainty. The idea of this method is to exclude modes with a high uncertainty from the analysis to avoid biasing the results.

The residual flexibility method [11] also uses one of the above two flexibility approaches but includes the estimate of the residual flexibility, which is the contribution to the flexibility matrix from the modes above the bandwidth of interest. The resulting flexibility matrix is a closer approximation to the true static flexibility matrix than is the modal flexibility matrix.

eters should be updated.

The optimal matrix update methods are based on the minimization of the error in the structural eigenproblem using a closed-form, direct solution. The minimum rank perturbation technique (MRPT) [13] is one such method which produces a minimum-rank perturbation of the structural stiffness, damping, and/or mass matrices reduced to the measurement degrees of freedom. The minimum rank element update (MREU) [14] is a similar technique which produces perturbations at the elemental, rather than the matrix, level. The Baruch updating technique [15] minimizes an error function of the eigenequation using a closed-form function of the mass and stiffness matrices.

The sensitivity-based model update methods also seek to minimize the error in the structural eigenequation, but do so using a Newton-Raphson-type technique based on solving for the perturbations such that the gradient of the error function is near zero. [6] Thus these methods require the computation of the sensitivity of the structural eigenproblem to the parameters which are to be updated. The Hemez/Alvin algorithm [16],[17] computes the sensitivities at the elemental level, then assembles them to produce the global sensitivity matrices. The Ricles/Kosmatka [18] algorithm computes a "hybrid" sensitivity matrix using both analytical and experimental sensitivities.

EXAMPLE APPLICATION: THE ALAMOSA CANYON BRIDGE

The following analysis of modal data from a series of tests performed on a highway bridge is intended to demonstrate the application of the unique capabilities of DIAMOND to data from an actual field test.

The Alamosa Canyon Bridge has seven independent spans with a common pier between successive spans. An elevation view of the bridge is shown in Figure 5. The bridge is located on a seldom-used frontage road parallel to Interstate 25 about 10 miles North of the town of Truth or Consequences, New Mexico, USA. Each span consists of a concrete deck supported by six W30x116 steel girders. The roadway in each span is approximately 7.3 m (24 ft.) wide and 15.2 (50 ft.) long. Integrally attached to the concrete deck is a concrete curb and concrete guard rail. Inspection of the bridge showed that the upper flanges of the beams are imbedded in the concrete, which implies the possibility of composite action between the girders and the deck. Between adjacent beams are four sets of channel section cross braces equally spaced along the length of the span. At the pier the beams rest on rollers, and at the abutment the beams are bolted to a half-roller to approximate a pinned connection.

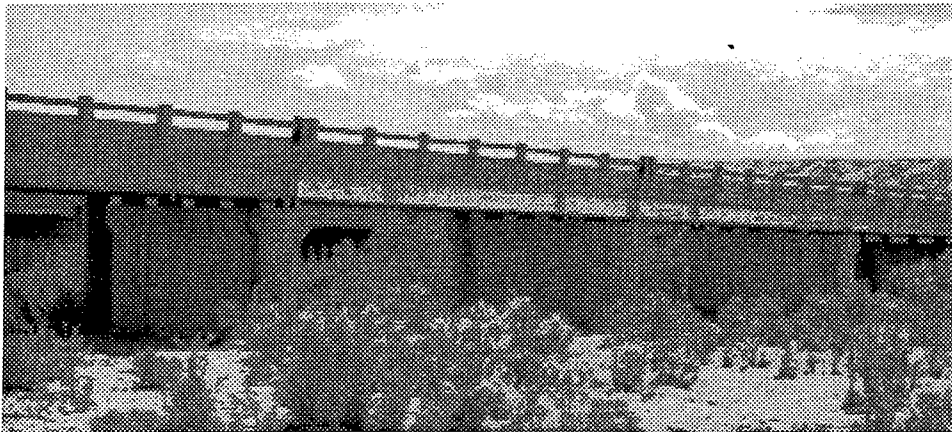


Figure 5: Elevation View of the Alamosa Canyon Bridge

The data acquisition system was set up to measure acceleration and force time histories and to calculate frequency response functions (FRFs), power spectral densities (PSDs), cross-power spectra and coherence functions. A modal sledge hammer was used as the impact excitation source. Accelerometers were used for the vibration measurements. More details regarding the instrumentation can be found in Ref. [19].

A total of 31 acceleration measurements were made on the concrete deck and on the girders below the bridge as shown in Figure 6. Five accelerometers

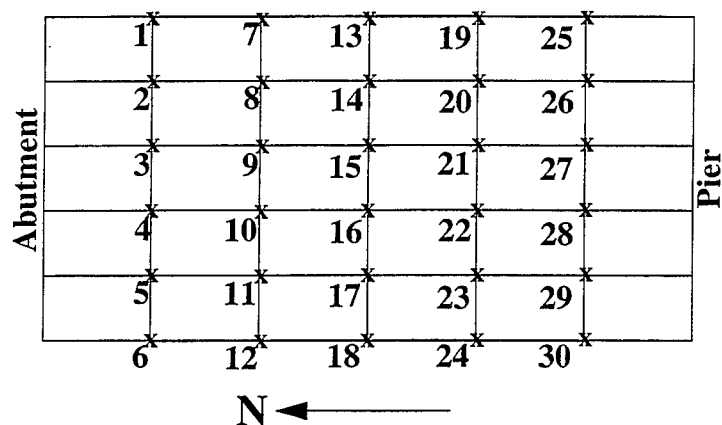


Figure 6: Accelerometer and Impact Locations

were spaced along the length of each girder. Because of the limited number of data channels, measurements were not made on the girders at the abutment or at the pier. Two excitations points were located on the top of the concrete deck.

Point 2 was used as the primary excitation location. Point 23 was used to perform a reciprocity check. The force-input and acceleration-response time histories obtained from each impact were subsequently transformed into the frequency domain so that estimates of the PSDs, FRFs, and coherence functions could be calculated. Thirty averages were typically used for these estimates. With the sampling parameters listed above and the overload reject specified, data acquisition for a specific test usually occurred over a time period of approximately 30 - 45 minutes. All of the results in this paper are from measurements made on span 1 of the bridge, which is located at the far North end.

A total of 52 data sets were collected over the course of the six days of testing. Temperature measurements were made at 9 locations around the bridge, both above and below the deck, to track the effects of ambient temperature changes on the test results. Reciprocity and linearity checks were conducted first. A series of modal tests was conducted over a 24 hour period (one test every 2 hours) to assess the change in modal properties as a result of variations in ambient environmental conditions, as discussed in Ref. [19]. A series of tests with various levels of attempted damage was also conducted, but the permitted alterations in the bridge did not cause a significant change in the measured modal properties. Specifically, the nuts on the bolted connections that hold the channel-section cross members to the girders, as shown in Figure 7 were removed.

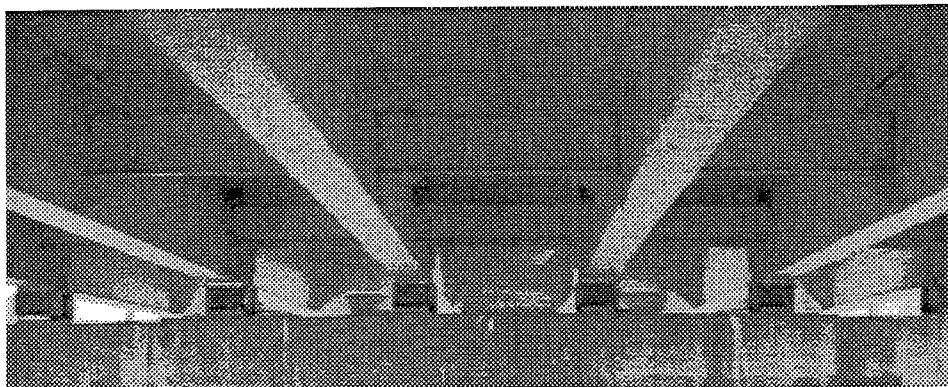


Figure 7: Bolted Connections of Cross-Members to Girders

However the bolts could not be loosened sufficiently, and no relative motion could be induced at the interface under the loading of the modal excitation. For this reason, the damage cases presented in this paper are results from simulated stiffness reduction using a correlated FEM. The identified modal frequencies and mode shapes from the modal analysis of one of these data sets are shown in Figure 8.

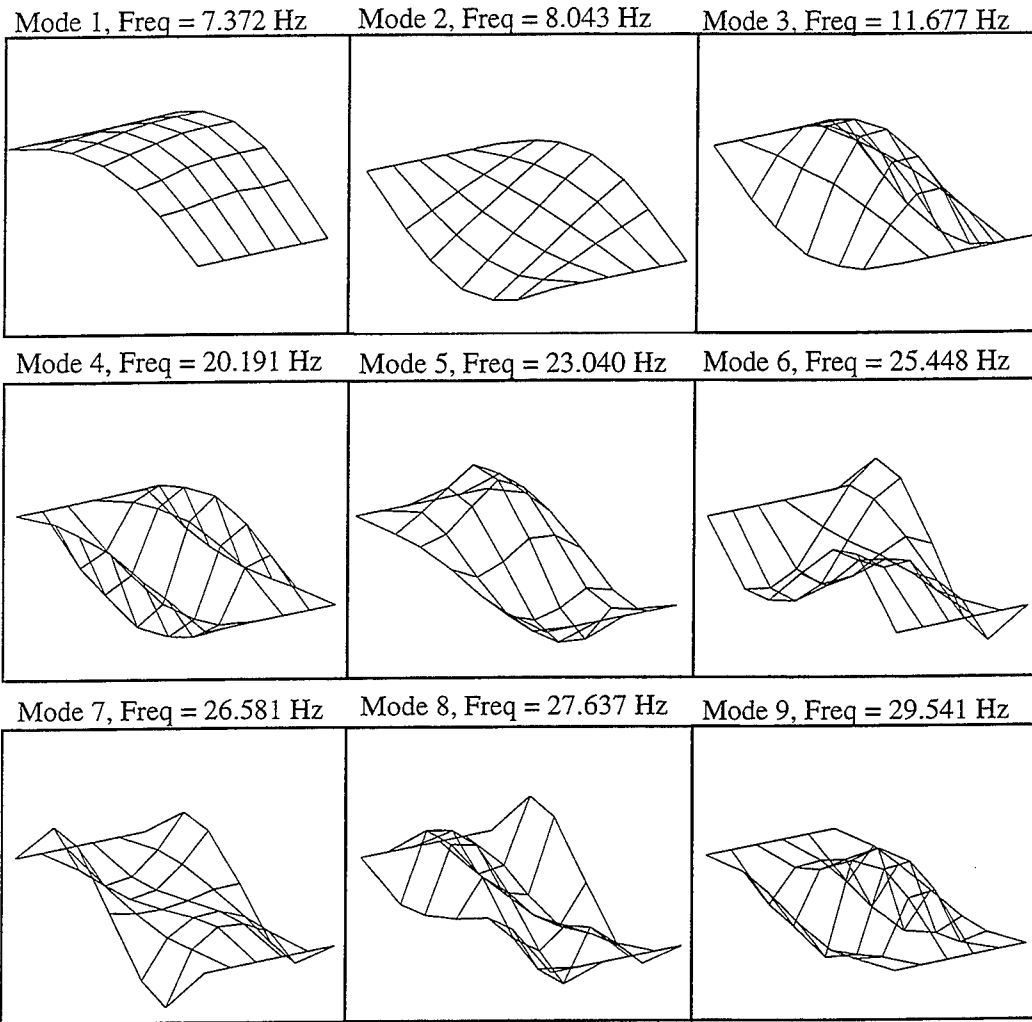


Figure 8: Identified Mode Shapes for Alamosa Canyon Bridge

Analysis of Uncertainty in Each Test

Statistical uncertainty bounds on the measured frequency response function magnitude and phase were computed from the measured coherence functions, assuming that the errors were distributed in a Gaussian manner, according to the following formulas from Bendat and Piersol [20]:

$$\begin{aligned}\sigma(|H(\omega)|) &= \frac{\sqrt{1-\gamma^2(\omega)}}{|\gamma(\omega)|\sqrt{2n_d}}|H(\omega)| \\ \sigma(\angle H(\omega)) &= \frac{\sqrt{1-\gamma^2(\omega)}}{|\gamma(\omega)|\sqrt{2n_d}}\angle H(\omega)\end{aligned}\tag{2}$$

where $|H(\omega)|$ and $\angle H(\omega)$ are the magnitude and phase angle of the measured FRF, respectively, $\gamma^2(\omega)$ is the coherence function, n_d is the number of measurement averages, and $\sigma(\bullet)$ is the value of 1 standard deviation (68% uncertainty bound). These uncertainty bounds represent a statistical distribution of the FRF based on a realistic level of random noise on the measurement. Once the 1 standard deviation (68% uncertainty) bounds were known, 2 standard deviation (95% uncertainty) bounds were computed. Statistical uncertainty bounds on the identified modal parameters (frequencies, damping ratios, and mode shapes) were estimated using the uncertainty bounds on the FRFs via a Monte Carlo analysis [6]. The details of this procedure are shown in Ref. [21].

Effects of Uncertainties on Damage Identification

The changes in the bridge as a result of damage were predicted using the finite element model. The damage case modeled was the 100% failure of a connection between a cross-member and an interior girder. A comparison of the estimated 95% confidence bounds and the predicted changes as a result of damage for the modal frequencies are shown in Figure 9. The modal frequencies of modes 3, 4, 7, 8, and 9 undergo a change that is significantly larger than the corresponding 95% confidence bounds. The relative magnitudes of the changes indicate that the frequency changes of these modes could be used with confidence in a damage identification analysis. It should be noted from the y-axis scale of Figure 9 that the overall changes in frequency as a result of damage are quite small ($< 1.2\%$), but as a consequence of the extremely low uncertainty bounds on the modal frequencies (many less than 0.2%), these small changes can be considered to be statistically significant.

The relative statistical significance of the changes in the various modes is one of the primary motivating factors for a "selective flexibility" approach. Using the selective flexibility approach, those modes where the frequency changes are statistically insignificant would be considered to be unchanged, while those modes with significant frequency change would be used in the flexibility analysis. This technique would prevent modes which are insensitive to the damage from masking the indications of damage from modes which are sensitive to the damage.

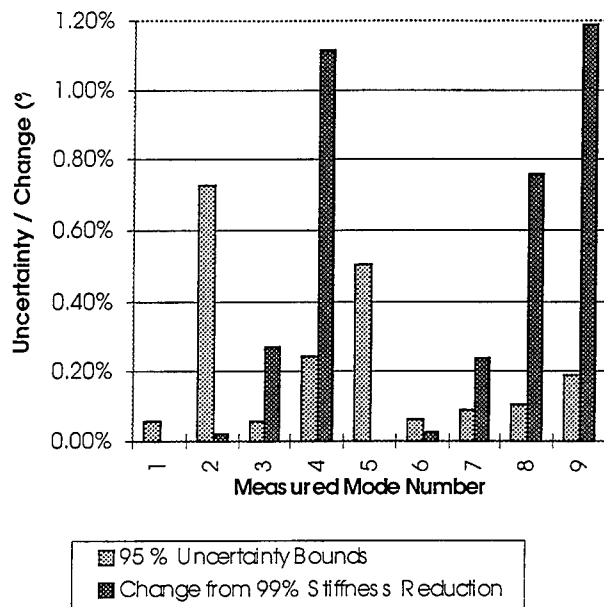


Figure 9: Comparison of Modal Frequency 95% Confidence Bounds to Changes Predicted as a Result of Damage

CONCLUSION

A new toolbox of graphical-interface software algorithms, known as DIAMOND, has been introduced and demonstrated. The toolbox provides the capability to simulate vibration tests, perform experimental modal analysis including statistical bounds, apply various damage identification techniques, and implement finite element refinement algorithms. The structure of the toolbox menus was described in detail in this paper, and a sample application to measured data from a highway bridge was presented.

ACKNOWLEDGMENTS

This work was supported by Los Alamos National Laboratory Directed Research and Development Project #95002, under the auspices of the United States Department of Energy. The authors wish to recognize the contributions of Mr. Erik G. Straser and Mr. A. Alex Barron of Stanford University.

REFERENCES

1. MATLAB, *Users Manual*, The Mathworks, Inc., 1994.

2. Juang, J.N. and Pappa, R.S., "An Eigensystem Realization Algorithm for Modal Parameter Identification and Model Reduction," *Journal of Guidance, Control and Dynamics*, Vol. 8, No. 5, pp. 620-627, 1985.
3. Vold, H., Kundrat, J., Rocklin, T., and Russell, R., "A Multi-Input Modal Estimation Algorithm for Mini-Computers," *SAE Transactions*, Vol. 91, No. 1, January 1982, pp. 815-821.
4. Richardson, M.H. and Formenti, D.L., "Parameter Estimation from Frequency Response Measurements using Rational Fraction Polynomials," *Structural Measurement Systems Technical Note 85-3*, 1985.
5. McVerry, G.H., "Structural Identification in the Frequency Domain from Earthquake Records," *Earthquake Engineering and Structural Dynamics*, Vol. 8, 1980, pp.161-180.
6. Press, W.H., Teukolsky, S.A., Vetterling, W.T., and Flannery, B.P., *Numerical Recipes in FORTRAN: The Art of Scientific Computing*, Second Edition, Cambridge Univ. Press, 1992, pp. 684-686.
7. Stubbs, N., J.-T. Kim, and C.R. Farrar, 1995, "Field Verification of a Nondestructive Damage Localization and Severity Estimation Algorithm," in *Proc. 13th International Modal Analysis Conference*, 210-218.
8. Cornwell, P., Doebling, S.W., and Farrar, C.R., "Application of the Strain Energy Damage Detection Method to Plate-Like Structures," to appear in *Proc. of the 15th International Modal Analysis Conference*, Orlando, FL, February, 1997.
9. Catbas, F.N., Lenett, M., Brown, D.L., Doebling, S.W., Farrar, C.R., and Turer, A., "Modal Analysis of Multi-Reference Impact Test Data for Steel Stringer Bridges," to appear in *Proc. of the 15th International Modal Analysis Conference*, Orlando, FL, February, 1997.
10. Robinson, N.A., L.D. Peterson, G.H. James, and S.W. Doebling, 1996, "Damage Detection in Aircraft Structures Using Dynamically Measured Static Flexibility Matrices," in *Proc. of the 14th International Modal Analysis Conference*, 857-865.
11. Doebling, S.W., Peterson, L.D., and Alvin, K.F., "Estimation of Reciprocal Residual Flexibility from Experimental Modal Data," *AIAA Journal*, Vol. 34, No. 8, pp. 1678-1685, August 1996.
12. Doebling, S.W., Farrar, C.R., Prime, M.B., and Shevitz, D.W., "Damage Identification and Health Monitoring of Structural and Mechanical Systems From Changes in Their Vibration Characteristics: A Literature Review," Los Alamos National Laboratory report LA-13070-MS.

13. Zimmerman, D.C. and M. Kaouk, 1994, "Structural Damage Detection Using a Minimum Rank Update Theory," *Journal of Vibration and Acoustics*, **116**, 222–230.
14. Doebling, S.W., "Damage Detection and Model Refinement Using Elemental Stiffness Perturbations with Constrained Connectivity," in *Proc. of the AIAA/ASME/AHS Adaptive Structures Forum*, pp. 360–370, AIAA-96-1307, 1996. Accepted and to appear in *AIAA Journal*.
15. Baruch, M., 1982, "Optimal Correction of Mass and Stiffness Matrices Using Measured Modes," *AIAA Journal*, **20**(11), 1623–1626.
16. Hemez, F.M. and C. Farhat, 1995, "Structural Damage Detection via a Finite Element Model Updating Methodology," *Modal Analysis: The International Journal of Analytical and Experimental Modal Analysis*, **10** (3), 152–166.
17. Alvin, K.F., 1996, "Finite Element Model Update via Bayesian Estimation and Minimization of Dynamic Residuals," in *Proc. of the 14th International Modal Analysis Conference*, Dearborn, MI, February 1996, 561–567.
18. Ricles, J.M. and J.B. Kosmatka, 1992, "Damage Detection in Elastic Structures Using Vibratory Residual Forces and Weighted Sensitivity," *AIAA Journal*, **30**, 2310–2316.
19. Farrar, C.R., Doebling, S.W., Cornwell, P.J., and Straser, E.G., "Variability Of Modal Parameters Measured On The Alamosa Canyon Bridge," in *Proc. of the 15th International Modal Analysis Conference*, Orlando, FL, February 1997. 257–263.
20. Bendat, J.S. and Piersol, A.G., *Engineering Applications of Correlation and Spectral Analysis*, John Wiley and Sons, New York, 1980, p. 274.
21. Doebling, S.W., Farrar, C.R., and Goodman, R.S., "Effects of Measurement Statistics on the Detection of Damage in the Alamosa Canyon Bridge," in *Proc. of the 15th International Modal Analysis Conference*, Orlando, FL, February 1997, 919–929.

FAULT DETECTION IN MACHINERY USING ORTHOGONAL WAVELET DECOMPOSITION

W.J. Staszewski

Dynamics Research Group
Department of Mechanical Engineering
University of Sheffield
Mappin Street
Sheffield S1 3JD
United Kingdom

Abstract

The paper presents a new fault detection procedure based on the time-scale decomposition of vibration data. The procedure employs the orthogonal wavelet transform. The orthogonal wavelet transform is implemented using the pyramidal Mallat algorithm. A number of statistical parameters are then applied to the decomposed vectors. The statistical parameters form a vector which represents the condition signature of the machine. The process of fault detection is based on similarity analysis. The method is validated using experimental vibration data from a spur gear.

INTRODUCTION

The most general basis for fault detection in rotating machinery is provided by vibration and acoustical signals. Many different procedures have been developed in machinery diagnostics to obtain features from vibration signals in order to detect faults. Measurements of the overall vibration level given by a peak amplitude or the *RMS* (Root Mean Square) value and employing a simple vibration meter is probably the first of several well known time-domain techniques. The frequency-domain methods include spectral analysis, cepstrum and many other Fourier transform based procedures. The increasing complexity of machinery together with demands for early detection procedures means that classical time-invariant analysis is not sufficient for fault detection.

The past twenty years have seen major developments in the area of time-variant analysis. There exist many different methods in the area of time-dependent models, time-frequency and time-scale analysis [1, 2, 3]. The 1990s has shown growing interest in wavelets for machinery diagnostics. The analysis includes applications to gearboxes [4, 5, 6, 7, 8, 9] ball-bearings [10], compressors [11] and centrifugal pumps [12]. Wavelet based methods produce very often multi-dimensional display formats and require

pattern recognition analysis. The complicated nature of these results lead to difficult diagnostic interpretation. It appears in practice that there is a great demand for condition monitoring techniques which simplify fault detection.

This paper considers a fault detection procedure based on the time-scale decomposition of vibration data. The procedure employs the orthogonal wavelet transform. In contrast to previous applications [8, 9] the method presented in the paper does not involve any multi-dimensional wavelet mapping or pattern analysis. Similarity analysis between different decomposed vectors is used instead. The paper is structured as follows.

A brief discussion of the orthogonal wavelet transform is given in Section Two. The orthogonal wavelet transform is used to decompose the data into different scale levels. The orthogonal basis is formed by Daubechies wavelets. The orthogonal wavelet transform is implemented using the pyramidal Mallat algorithm. Section Three describes briefly the concept of statistical analysis of vibration data. The application of the decomposition procedure to gearbox vibration data is presented in Section Four. The analysis employs a fully controlled spur gear experiment with relatively simple tooth damage simulations where a part of a tooth was progressively removed to simulate a broken tooth. The similarity analysis between wavelet results is used in Section Five. A number of statistical parameters are applied to decomposed gearbox vibration data. These statistical parameters form a vector which represents the condition signature of the gearbox. The Mahalanobis distance is used to classify the data representing different fault conditions.

ORTHOGONAL WAVELET TRANSFORM

For the sake of completeness a brief introduction to the relevant wavelet theory is given in this section. More detailed analysis can be found in [13].

The wavelet transform is a linear transformation that decomposes a given function $x(t)$ into a superposition of elementary functions $g_{a,b}(t)$ derived from an analysing wavelet $g(t)$ by scaling and translation i.e.,

$$g_{a,b}(t) = g^*\left(\frac{t-b}{a}\right) \quad (1)$$

where $*$ denotes complex conjugation, b is a translation parameter indicating the locality and a is a dilation or scale parameter.

The discrete wavelet transform refers to a discrete time-scale framework. Within this framework, when a binary dilation and dyadic translation is used, the orthogonal wavelet transform can be defined. A function $g(t)$ is called an orthogonal wavelet if the family

$$g_{m,k}(t) = 2^{m/2}g(2^m t - k) \quad (2)$$

forms an orthonormal basis, that is

$$\langle g_{m,k}, g_{n,l} \rangle = \delta_{m,n} \cdot \delta_{k,l} \quad (3)$$

for all integer m, n, k, l , where $\langle \cdot, \cdot \rangle$ is the usual inner product and $\delta_{m,n}$ is the Kronecker symbol. The orthogonal wavelet transform can now be defined as

$$x_k^m = \int_{-\infty}^{+\infty} x(t) g_{m,k}(t) dt \quad (4)$$

The transform can be interpreted as a filter bank decomposition. The scale (frequency) partitioning leads to a partitioning in the time domain that is finer in the higher frequency bands. The wavelet synthesis formula is given by

$$x(t) = \sum_m \sum_k x_k^m g_{m,k}(t) \quad (5)$$

This clearly shows that the analysed signal can be represented as a sum of m so called wavelet levels

$$x_m(t) = \sum_k x_k^m g_{m,k}(t) \quad (6)$$

Each of these levels represents time behaviour of the signal within different frequency bands and gives the contribution to the whole signal energy.

A number of different bases have been proposed to construct orthogonal wavelets. The simplest basis can be given by the well known Haar function $h(t)$ that is equal to 1 on $[1, 1/2)$, -1 on $[1/2, 1]$ and 0 outside the interval $[0, 1]$. Much more effective analysis and synthesis can be obtained with the wavelets $g_r(t)$ of Daubechies [13], which are of the form given by equation (2) and have the following properties:

1. the support of $g_r(t)$ is the interval $[0, 2r + 1]$;
2. $g_r(t)$ have r vanishing moments, i.e. $\int_{-\infty}^{+\infty} t^r g_r(t) dt = 0$;
3. $g_r(t)$ has γr (γ is about 0.2) continuous derivatives.

Figure 1 shows the 4th order Daubechies basis function. It can be shown that when $r = 0$ this basis reduces to the Haar wavelet analysis. The orthogonal wavelet decomposition based on the Daubechies' wavelets can

be obtained using the pyramidal Mallat algorithm. For more details about the calculation procedure the reader is referred to [14, 15].

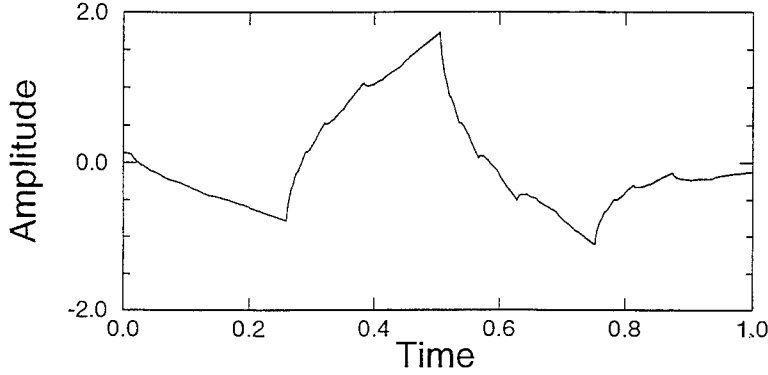


Figure 1:Daubechies' wavelet basis function.

STATISTICAL ANALYSIS OF VIBRATION DATA

The concept of statistical analysis of time-domain data is well known in the literature. There exist different measures used in machinery diagnostics which are fault oriented [16, 17]. These include the peak-to-peak value, shape factor, crest factor, impulse factor and statistical moments. The statistical moments are used to describe the shape of the probability density function of the data. The definition of the statistical moment of any type distribution is given by

$$m_i = \frac{1}{T} \int_0^T (x(t) - \bar{x})^i dt \quad (7)$$

where \bar{x} is the mean value of $x(t)$. Two parameters, namely skewness and Kurtosis, are the most widely used fault indicators based on statistical moments. The skewness coefficient, which is the normalised third moment, is used to identify lack of symmetry. Kurtosis, which is the normalised fourth moment, indicates the spikeness of the data. In general, higher moments are more sensitive to deviations in the data as a result of a fault. The advantage of the statistical characteristics is that they are independent of loading and speed of machinery and very often allow much earlier fault detection [16].

Simulation [18] and experimental [19] study shows that the results from the higher moment calculations tend to become more sensitive to

spurious spikes in the data not related to a fault. In such situations the beta distribution [18] can be used as it is less sensitive to freak maxima or minima. However low levels of load and small advancements of faults mean that fault detection is not a trivial task. This can be improved when the statistical parameters are applied to wavelet levels defined in Section 2. The wavelet is a high pass filter which can smooth out the noise at large scales. Thus any transients in the vibration data due to the impacts caused by the fault can be more efficiently detected in some arbitrary chosen wavelet levels given by equation (6). For these levels the statistical characteristics can be applied to enhance the fault detection procedure.

WAVELET DECOMPOSITION OF GEARBOX DATA

Gearbox Vibration

Gearboxes are significant contributors to damage incidents and maintenance costs. Thus gearbox vibration has been studied extensively for many years. Many vibration components can be observed in a spectrum. These include [20]: harmonics of the toothmeshing frequency, ghost components, sidebands, low frequency harmonics of the shaft speed and intermodulation components. All major faults in gearboxes can be classified into shaft (misalignment, unbalance) and tooth (wear, scuffing, cracking) related problems. Tooth related faults can produce impulses in the gearbox vibration signals [21, 22]. Damaged teeth suffer deflection due to stiffness reduction. This causes improper meshing action between teeth and produces impacts. The amplitude of the impact is a function of the velocity which in turn is proportional to the clearance between the circumferential distance between tooth contacts and the actual width of the tooth [23]. As a result of this phenomenon an impulse in the vibration signal is produced. This causes amplitude and frequency modulations of the meshing vibration. Locally, within one rotation of the damaged wheel, the vibration signal is a sum of stationary meshing vibration and a transient in a form of an impulse caused by a fault.

Experimental Results

A simple experiment which simulated the damage due to breakage at a point on the working tip was performed [24]. This type of failure is a common type of a fault in many industrial applications [25]. The damage involved 25%, 50%, 75% and 100% removal (1mm) of the facewidth at a given radius. Two load conditions were used in the experiment. These were: 70% and 40% of the maximum design load. Figure 2 shows an example of an acceleration response obtained from the experiment. Here one pinion rotation is analysed. The meshing vibration of the spur gear can be observed. An impulse in the signal at about 60° – 100° of pinion rotation

can be seen in Figure 2c where the vibration from the 100% damaged spur gear is given. This fault feature cannot be seen in the 25% damaged spur gear data.

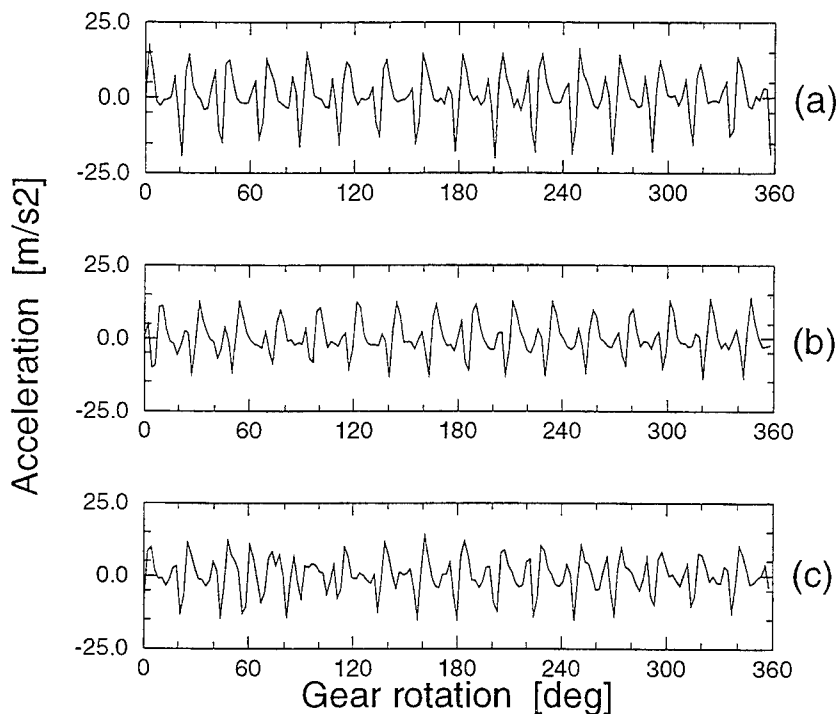


Figure 2: Spur gear vibration data: (a) no fault condition (b) damaged tooth (25% fault advancement) (c) damaged tooth (100% fault advancement).

Since the amplitude level of a gearbox vibration signal depends on the load, it is beneficial to remove the meshing vibration from the data. This can be done in the time-domain by using a bandstop filter or in the frequency-domain by suppressing the meshing harmonics. A 10th order Butterworth bandstop filter was used to remove the meshing vibration from the data. The filtered or residual signal should display any impulsive perturbations within the vibration signal better, thus improving the possibility of fault detection.

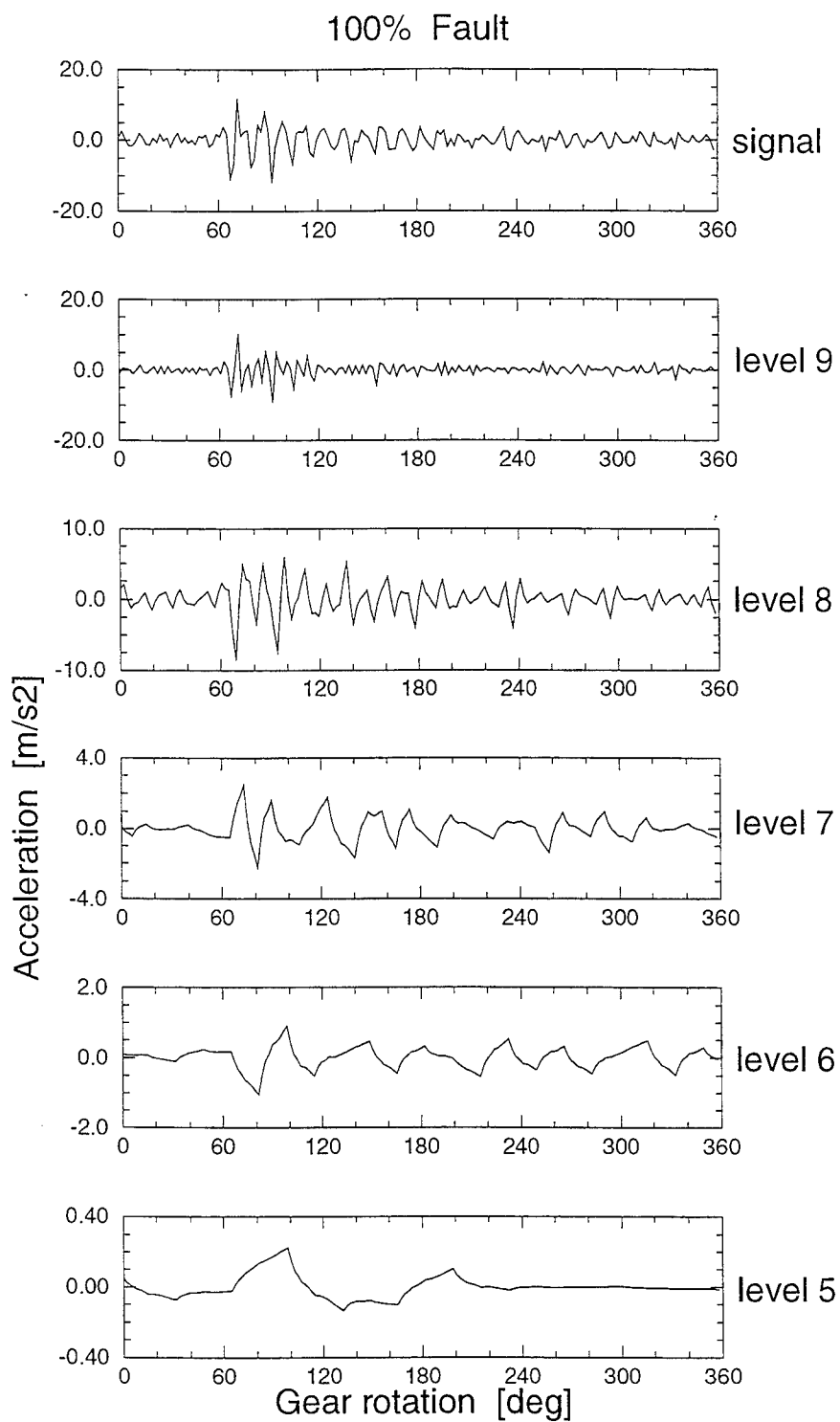


Figure 3: Orthogonal wavelet transform results for the damaged tooth with the 100% fault advancement.

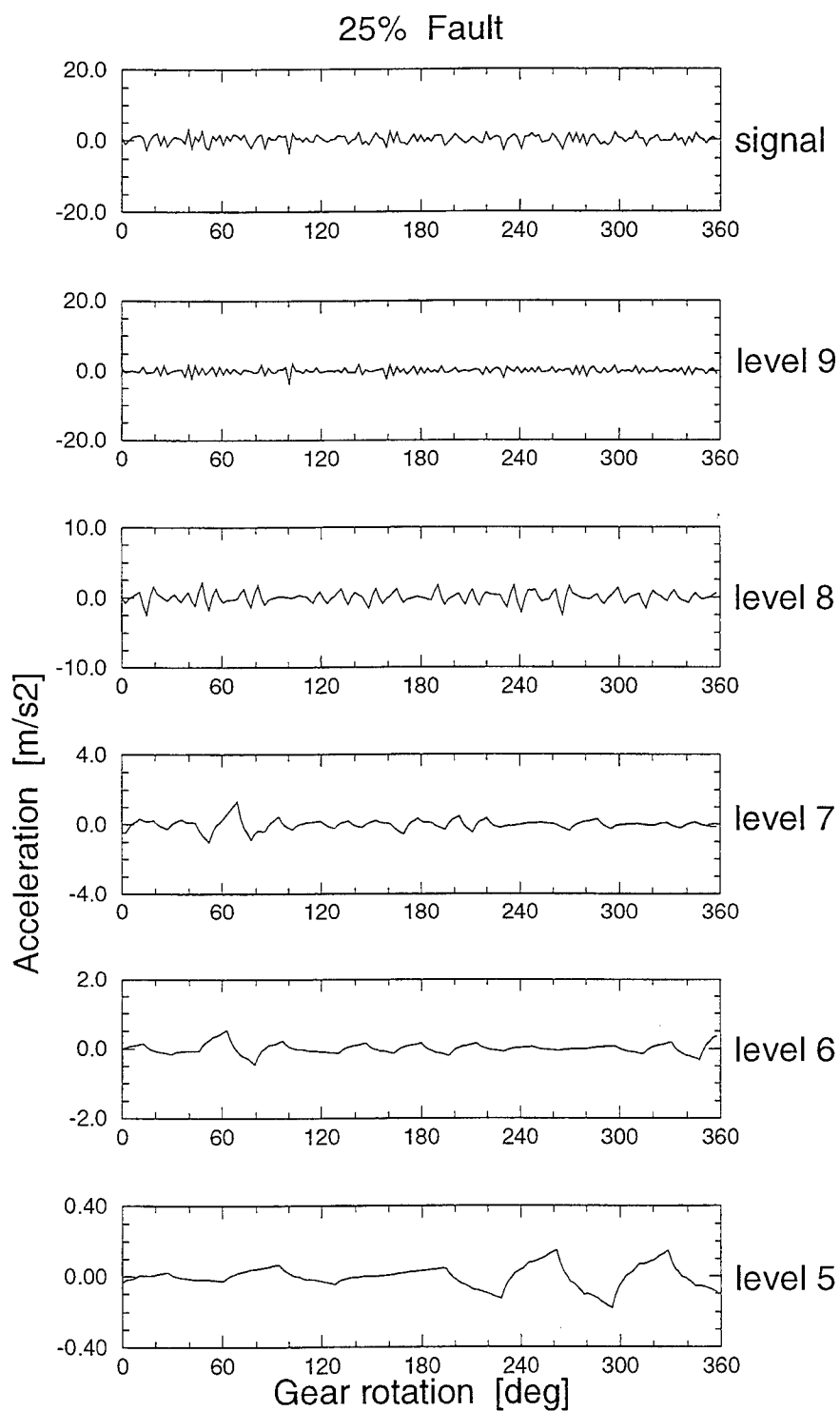


Figure 4: Orthogonal wavelet transform results for the damaged tooth with the 50% fault advancement.

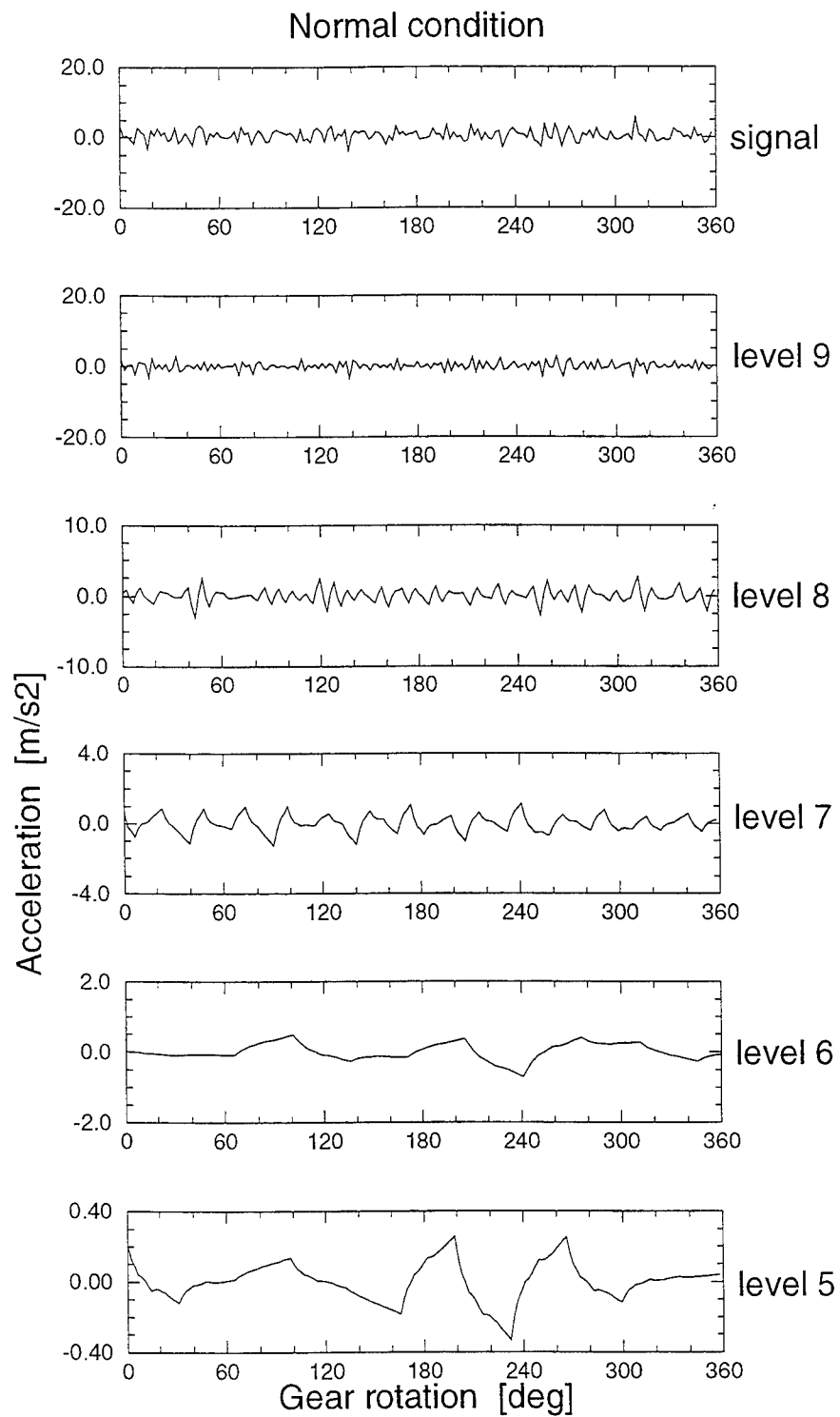


Figure 5: Orthogonal wavelet transform results for the normal (no fault) condition gearbox.

The residual signals were decomposed using the orthogonal wavelet transform. Figure 3 shows an example of the residual signal together with the highest five wavelet levels, representing 100% fault advancement. Here a clear impulse due to the fault can be observed in the levels at about $60^\circ - 100^\circ$ of the gear rotation. Each of the levels represents a different bandwidth in which the impulse is formed. Higher levels are equivalent to higher frequency bandwidths. Similar results for the 25° fault advancement are given in Figure 4. Here the impulse can be observed at about $60^\circ - 80^\circ$ in wavelet levels 6 and 7. For comparison Figure 5 shows the same results for normal condition gearbox; impulses cannot be observed in the wavelet decomposed data. One can also notice that low levels (e.g. 5 in Figure 5) display low amplitude characteristics which are features related to Daubechies' wavelets and not the the impulse caused by the fault.

SIMILARITY ANALYSIS OF DECOMPOSED DATA

Following the initial results obtained in the previous section, four wavelet levels, namely 6,7,8 and 9, were chosen for further study. The study involved statistical analysis of chosen decomposed levels. This employed the peak-to-peak value and the 4-th and 6-th statistical moments. It has been shown [16, 18] that these parameters are good impulse indicators in vibration data. Table 1 gives an example set of the statistical parameters from the wavelet level 8 used in the analysis. Here two different load conditions and fault advancements are represented. The wavelet based results are compared with the raw vibration data results. It can be seen that within the same fault condition the values of the statistical parameters are sensitive to the load. This feature could lead in practice to false fault alarms.

Load of the system	Fault condition	Wavelet level 8			Raw data		
		<i>peak</i>	m_4	m_6	<i>peak</i>	m_4	m_6
70%	no fault	8.05	4.93	45.03	5.09	2.84	13.12
	100% fault	11.44	11.71	295.04	9.71	9.26	162.48
40%	no fault	7.19	4.19	29.91	5.89	2.75	11.62
	100% fault	10.58	10.74	267.22	9.98	8.63	146.42

Table 1: Statistical parameters for wavelet decomposed data and raw vibration data

The statistical similarity analysis was performed to detect impulses in the wavelet decomposed data. The square of the Mahalanobis distance given by [26],

$$d^2(k) = ||\bar{\beta} - \bar{\mu}||_{\Sigma^{-1}}^2 = (\bar{\beta} - \bar{\mu})^T \Sigma^{-1} (\bar{\beta} - \bar{\mu}), \quad (8)$$

is used to measure the distance between vectors $\bar{\beta}$ and $\bar{\mu}$, normalised with a Σ^{-1} norm. Here $\bar{\beta}$ is a primary feature vector representing patterns, $\bar{\mu}$ is a mean vector representing the pattern template and Σ^{-1} denotes the inverse of the covariance matrix Σ_k . Given N sample feature vectors β_i ($i = 1, 2, \dots, N$) two unbiased estimators of the mean vector $\bar{\mu}$ and covariance Σ are given respectively [26] by

$$\bar{\mu} = E[\bar{\beta}] = \frac{1}{N} \sum_{i=1}^N \bar{\beta}_i, \quad (9)$$

$$\Sigma = \frac{1}{N-1} \sum_{i=1}^N (\bar{\beta}_i - \bar{\mu}) (\bar{\beta}_i - \bar{\mu})^T. \quad (10)$$

The larger the value of d^2 the more diverged $\bar{\beta}$ is from its template.

Gear pair	Fault type	Advancement of fault	Mahalanobis distance	
			Wavelet results	Raw data
1	no fault	0%	1.22	1.05
2	no fault	0%	1.38	1.35
3	no fault	0%	1.33	1.23
	damaged tooth	25%	5.07	1.10
		50%	8.82	3.38
		75%	18.22	8.41
		100%	320.75	104.32
Alarm values			1.67	1.82

Table 2: Similarity analysis results for the fault detection procedure based on the orthogonal wavelet transform.

An overall number of 12 statistical parameters from the wavelet decomposed levels were used to form feature vectors representing different fault conditions. The 150 feature vectors representing gearbox normal condition for two different load levels were used to obtain the mean vector $\bar{\mu}$ and covariance Σ^{-1} . Finally, the values of the Mahalanobis distance were calculated from equation (8). The results for different fault advancements are given in Table 2. Here the values of the Mahalanobis distances represent the averaged values from the set of ten different vibration signals

representing different load and fault conditions. The simple alarm values were established from the sets of the data representing the normal condition of the gearbox. These values are the Mahalanobis distances above which it can be considered that the condition of the gearbox is abnormal and require further investigations. The alarm value was taken as $\bar{d} + 4\sigma_d$, where \bar{d} and σ_d are the mean and the standard deviation of the Mahalanobis distance d . The same procedure was applied to statistical parameters taken from the raw vibration data. It can be seen that, for both types of the analysis, the Mahalanobis distance increases monotonically with the fault advancement. However, the comparison between the methods shows that the smallest (25%) fault advancements was detected only by the wavelet based analysis.

CONCLUSIONS

The fault detection procedure based on the orthogonal wavelet transform has been proposed. The procedure has involved the signal decomposition into wavelet levels. The statistical moments for the chosen levels were used to create fault features. The statistical concept of similarity analysis was applied to classify fault advancements. The method has been illustrated using the vibration data from a simple spur gear experiment. The method has shown the potential for fault detection in machinery diagnostics. Further analysis, involving vibration data from different machinery, is required to fully establish the procedure.

ACKNOWLEDGEMENTS

It is a pleasure to acknowledge VSEL Barrow-in-Furness, Cumbria, for the technical assistance and providing the vibration data.

References

- [1] Priestley M B. *Non-linear and Non-stationary Time Series Analysis*. Academic Press, London, 1988.
- [2] Cohen L. Time-frequency distributions - a review. *Proceedings of the IEEE*, 77(7):941-981, 1989.
- [3] Flandrin P. Some aspects of non-stationary signal processing with emphasis on time-frequency and time-scale methods. In Combes J M, Grossmann A, and Tchamitchian Ph, editors, *Wavelets. Time-Frequency Methods and Phase Space*. Springer-Verlag, Berlin, 1989.

-
- [4] Staszewski W J and Tomlinson G R. Time-variant methods in machinery diagnostics. In *International Workshop on Safety Evaluation of Time-Variant and Nonlinear Structures Using Identification Approaches.*, Lambrecht, Germany, 6-9 September, 1992.
 - [5] Staszewski W J and Worden K. Classification of faults in spur gears. In *The World Congress on Neural Networks.*, Portland, Oregon, 11-15 July, 1993.
 - [6] Wang W J and McFadden P D. Application of the wavelet transform to gearbox vibration analysis. In *The 16th Annual Energy-Sources Technology Conference and Exhibition, Structural Dynamics and Vibration. Houston, Texas, USA, 31 January - 4 February, 1993.*
 - [7] Staszewski W J and Tomlinson G R. Application of the wavelet transform to fault detection in a spur gear. *Mechanical Systems and Signal Processing*, 8(3):289-307, 1994.
 - [8] Wang W J and McFadden P D. Application of orthogonal wavelets to early gear damage detection. *Mechanical Systems and Signal Processing*, 9(5):497-507, 1995.
 - [9] Wang W J and McFadden P D. Application of wavelets to gearbox vibration signals for fault detection. *Journal of Sound and Vibration*, 192(5):927-939, 1996.
 - [10] Wang W J and McFadden P D. Early detection of gear failure by time-frequency analysis. part 1: Calculation of the time-frequency distribution. *Mechanical Systems and Signal Processing*, 7(3):193-204, 1993.
 - [11] Grivelet P. Monitoring of reciprocating compressors by vibration. In *Proc. of IMMDC Congress.*, Los Angeles, October, 1990.
 - [12] Leducq D. Hydraulic noise diagnostics using wavelet analysis. In *Proceedings of the International Conference on Noise Control Engineering.* edited by H G Jonasson, Gothenburg, Sweden, 13-15 August 1990.
 - [13] Chui Ch K. *An Introduction to Wavelets.* Wavelet Analysis and its Applications. vol 1. Academic Press, Inc., Boston, 1992.
 - [14] Mallat S. A theory for multiresolution signal decomposition: the wavelet representation. *IEEE Trans. on Pattern Anal. and Machine Intell.*, PAMI-2(7), 1989.

-
- [15] Newland D E. *Random Vibration, Spectral and Wavelet Analysis*. Longman, Harlow and John Wiley, New York, 3rd edition, 1993.
- [16] Stewart R M. Some useful data analysis techniques for gearbox diagnostics. Technical Report Paper MHM/R/10/77, Institute of Sound and Vibration Research., Southampton, 1977.
- [17] Cempel C. Diagnostically oriented measures of va processes. *Journal of Sound and Vibration*, 73:547-561, 1983.
- [18] Ismail F Martin H R and Sakuta A. Algorithms for statistical moment evaluation for machine health monitoring. *Mechanical Systems and Signal Processing*, 6(4):317-327, 1992.
- [19] Ismail F Martin H R and Sakuta A. New statistical approach for gear damage detection. In *Proceedings of the 2nd IMMDC Conference, Los Angeles*, pp. 329-334, 1990.
- [20] Randall R B. A new method of modelling gear faults. *Trans. ASME, J. Mechanical Design*, 104:259-267, 1982.
- [21] McFadden P D. Detecting fatigue cracks in gears by amplitude and phase demodulation of the meshing vibration. *Transaction of the ASME. Journal of Vib. Acoustics, Stress and Rel. in Design*, 108:165-170, 1986.
- [22] Staszewski W J and Tomlinson G R. Report on the application of the signal demodulation procedure to the detection of broken and cracked teeth utilizing the pyestock fzg spur gear test rig. Technical report, University of Manchester. Department of Engineering. Dynamics and Control Research Group., 1992.
- [23] Ognjanovic M and Subic A. Gear quality prediction using vibration analysis. *Machine Vibration.*, 2(2):92-100, 1993.
- [24] Staszewski W J. *The Application of time-variant analysis to gearbox fault detection. PhD Thesis*. Univeristy of Manchester, Department of Engineering, 1994.
- [25] Johnson N. Gearbox health monitoring - definitions of fzg spur gear seeded fault trials. Technical Report Doc. No 155/1163, Vickers Shipbuilding and Engineering Ltd., Burrow in Furness, Cumbria, 1991.
- [26] Schalkoff R. *Pattern Recognition. Statistical, Structural and Neural Approaches*. John Wiley & Sons, Inc., New York, 1992.

INFORMATION-BASED REDUCED-DIMENSIONALITY GEOMETRIC APPROACH TO FAULT IDENTIFICATION IN STOCHASTIC STRUCTURAL SYSTEMS

M.H. Sadeghi* and S.D. Fassois**

*Department of Mechanical Engineering
University of Tabriz
516 66 Tabriz, Iran

**Department of Mechanical & Aeronautical Engineering
University of Patras
GR-265 00 Patras, Greece
E-mail: fassois@mech.upatras.gr

ABSTRACT

An information-based reduced-dimensionality formulation of the recently introduced geometric approach to fault identification in stochastic structural systems is presented. The feature vector, being a key element of the general geometric approach, is transformed into a suitable coordinate system, within which information compression may be best achieved. Dimensionality selection is subsequently based upon bounding of the information loss, expressed in terms of logarithmic entropy, below a certain threshold. The information-based reduced-dimensionality formulation thus presents a formal and systematic procedure for the proper selection of a minimal dimensionality feature vector, and leads to substantial simplification and potentially improved fault identification. Its application to fault identification in a laboratory-scale beam demonstrates high effectiveness, which is roughly equivalent to that of the full-dimensionality formulation.

List of Symbols

- F_{α}^i : fault of magnitude α within the i -th fault mode
- θ : feature vector composed of the model parameters ($N \times 1$)
- μ_{θ} : feature vector mean ($N \times 1$)
- P_{θ} : feature vector covariance ($N \times N$)
- s : transformed feature vector ($N \times 1$)
- μ_s : transformed feature vector mean ($N \times 1$)
- P_s : transformed feature vector covariance ($N \times N$)

\mathbf{s}_M	: reduced transformed feature vector ($M \times 1$)
$\boldsymbol{\mu}_{\mathbf{s}_M}$: reduced transformed feature vector mean ($M \times 1$)
$\mathbf{P}_{\mathbf{s}_M}$: reduced transformed feature vector covariance ($M \times M$)
$\boldsymbol{\theta}_K$: vector of the first/second order moments of \mathbf{s}_M ($\rho \times 1$)
$H_R(\mathbf{s})$: entropy function associated with the vector \mathbf{s}
$\tilde{H}_R(\mathbf{s}_M, \mathbf{s})$: ratio of entropy functions of the vectors \mathbf{s}_M and \mathbf{s}
\mathbf{T}	: feature vector transformation matrix ($M \times N$)
$g^i(\boldsymbol{\theta}_K) = 0$: equation of the i -th fault mode hyper-plane
N	: dimension of the original feature vector
M	: dimension of \mathbf{s}_M ($M < N$)
N_F	: number of fault modes
p	: number of faults per fault mode considered during training

Superscripts:

i	: indicates the i -th fault mode
i_j	: indicates the j -th fault within the i -th fault mode
u	: indicates the unclassified current fault

Convention:

Lower-case/capital bold-face characters represent vector/matrix quantities, respectively.

1. INTRODUCTION

Fault detection and identification in structural systems, such as aerospace structures, buildings, bridges, offshore platforms, and so on, is of paramount importance for reasons associated with safety and proper maintenance. Techniques aiming at non-destructive structural fault detection and identification, based upon the study of behavioral discrepancies between the nominal (unfailed) and failed systems, have thus received considerable attention in recent years [1-5].

A large category of structural fault identification methods is based upon the evaluation of changes incurred in the system's structural stiffness matrix [6], usually under the constant mass matrix assumption. These methods may use static test data [7], dynamic test data [1,8,9], or combinations of the two [3]. The main idea is in the use of the test data to formulate an optimization problem through which the changes of the structural stiffness matrix from its nominal (unfailed) value (often determined from a Finite Element Model of the structure) are computed. The methods achieve simultaneous fault detection and identification based upon the determination of the changed stiffness matrix elements.

An alternative category of methods is based upon the evaluation of changes incurred in the structural system's modal parameters [4,10,11].

The basic idea is the comparison of the modal parameters of the nominal system to those of the failed, and the detection and identification of faults through observation of the incurred change patterns.

Both categories of methods are, nevertheless, characterized by a number of drawbacks and limitations: Static testing may be a problem with certain structures, whereas complete eigenmode information (required in the dynamic test case) is difficult to obtain and requires elaborate testing procedures. The determination of eigenmode information additionally requires cumbersome numerical procedures for the solution of non-linear equations, while "high" frequency eigenmodes are in any case difficult to obtain but their omission may seriously affect the scheme's efficiency. A complete structural model, which may be of considerably "high" dimensionality, is also necessary to estimate, and this leads to a "large" non-linear optimization problem. In addition, stochastic noise effects are not always accounted for, an omission that may lead to further difficulties [9]. The fact that the eigenmode estimates are themselves stochastic quantities with inherent variability is not taken into account either, with the result being that there can be no sufficient certainty that an observed change in any given parameter is due to a fault and not to the inherent variability of the test data [11].

In addition, the first category of methods may lead to problematic fault localization, as a stiffness matrix element may admit contributions from several structural elements sharing the same node. The second category, on the other hand, relaxes the requirement for stiffness matrix determination, but faults may not be always possible to properly identify from mode shape pattern changes.

In a recent paper (Sadeghi and Fassois [12]) a novel *geometric approach* to the non-destructive identification of faults in stochastic structural systems was introduced. This approach is distinctly different from previous schemes, making use of reduced-order and partial stochastic structural models, a proper *feature vector*, a corresponding *feature space* equipped with a proper metric, and the notion of *fault mode* as the union of faults of all possible magnitudes but of common cause.

The geometric approach is based on the fact that fault-induced changes in the structural system's properties affect the selected model parameters, and, through them, the feature vector statistical characteristics. Within the selected feature space all individual (fixed magnitude) faults assume a point-wise representation, whereas each fault mode is represented as a proper subspace. Approximate representations of these subspaces are pre-constructed in a training stage. Once a system fault is detected, an interval estimate of the current feature vector, defining its point representation in the feature space, is obtained. Fault identification is then accomplished by determining the specific fault mode subspace within which the current fault point lies.

The geometric fault identification approach overcomes many of the limitations of the previous structural fault identification schemes, as it effectively accounts for *stochastic effects* and the inherent variability of test data, requires a *minimal number* of measurement locations, is capable of operating on *any type* (acceleration, velocity, or displacement) of vibra-

tion test data, requires only *partial* (even single-input single-output) and reduced-order models, and eliminates the difficulties associated with stiffness matrix or modal parameter based procedures. In addition it is very general, and potentially capable of identifying faults within any type of linear or non-linear structural system [12].

In the present paper an *information-based reduced-dimensionality* formulation of the geometric fault identification approach is introduced. In contrast to the original formulation in which the feature vector is arbitrarily selected to consist of the estimated model parameters, the present formulation uses an information-based framework for feature vector, and thus feature space, transformation and reduction. The feature vector is, indeed, transformed into a suitable coordinate system, within which information compression, and thus feature vector reduction, may be best achieved. Feature vector dimensionality selection is then based upon bounding of the information loss, expressed in terms of logarithmic entropy, below a certain threshold.

The information-based reduced-dimensionality geometric fault identification approach therefore offers a formal and systematic procedure for the proper selection of a minimal-dimensionality feature vector, and achieves two important goals: (a) Substantial simplification of the fault identification procedure by way of reduced feature space dimensionality, and, (b) potentially improved fault identification performance over arbitrarily truncated feature vectors.

The rest of this paper is organized as follows: A brief account of the main ideas pertaining to the geometric fault identification approach is presented in Section 2. The information-based reduced-dimensionality formulation is presented in Section 3, and its application to fault identification in a laboratory-scale simply-supported beam discussed in Section 4. The conclusions of this study are summarized in Section 5.

2. OVERVIEW OF THE MAIN IDEAS

The geometric fault identification approach is based upon vibration test data, typically force excitation along with the resulting vibration displacement, velocity, or acceleration, measured at selected locations. It consists of the following elements: (a) A partial (even single excitation single response) and reduced-order mathematical system *model*; (b) a properly selected *feature vector*; (c) a *feature space* equipped with a proper metric; and (d) the notion of *fault mode* and its geometrical representation.

The mathematical system *model* is of the discrete-time stochastic dynamical type and provides a partial and reduced-order representation of the actual structure. These features are very important, not only because a complete system model may be difficult to construct, but also difficult or impractical to use. The model is typically obtained through identification techniques using vibration test data [13,14].

The *feature vector* $\theta \in \mathbb{R}^N$ consists of selected model parameters that convey system information. The *feature space* is a space spanned by the first and, perhaps, second order moments of the feature vector, collected

into the vector $\theta_K \in \mathbb{R}^p$. The feature space is also equipped with a proper metric.

The notion of *fault mode* refers to the union of faults of all possible magnitudes (severities) but common cause. Within this context a particular fault from fault mode i and of magnitude a is represented as F_a^i , with the i -th fault mode thus defined as $F^i = \{F_a^i \mid a \in A \subseteq \mathbb{R}\}$ in the one-dimensional fault magnitude case.

Within the selected feature space all individual (fixed magnitude) faults assume a point-wise representation. A fault mode, being a "continuum" of variable-magnitude faults, assumes, on the other hand, a *subspace* representation. The dimensionality of this subspace depends upon the dimensionality of the fault magnitude, which may not be always possible to accurately define.

The *operational stages* of the geometric fault identification approach are as follows:

(i) In an initial training stage, and with the aid of measurements obtained from a detailed simulation (often finite element) model of the structure, a partial and reduced-order nominal system model is obtained. Based upon this, a proper feature vector and the corresponding feature metric space are selected. Approximate geometric representations of the various fault mode subspaces are constructed by using training data (obtained by injecting faults of various magnitudes into the simulation model) and appropriate regression techniques [15].

(ii) Once the presence of a system fault is detected based upon periodically obtained system data and statistical fault detection schemes [12], an interval (mean and covariance) estimate of the current feature vector, defining a point that represents the current (unknown) fault in the feature space, is obtained. The fault identification problem is then viewed as the problem of determining the specific fault mode subspace within which the incurred fault lies.

Note that, due to estimation and modeling inaccuracies, the point representing the current fault may not strictly belong to its proper subspace, but to its immediate vicinity. To account for this, the fault identification problem is formulated as a geometric minimal "distance" one, according to which the current fault is associated with the fault mode with the subspace of which its "distance" (computed via a constrained optimization scheme) is minimal.

3. THE INFORMATION-BASED REDUCED-DIMENSIONALITY GEOMETRIC APPROACH

The reduced-dimensionality geometric fault identification approach is based upon an information-based formalism that allows for the effective treatment of two main issues: (a) Feature vector transformation into a coordinate system within which information compression, and thus feature vector reduction, may be best achieved, and, (b) feature vector dimensionality selection.

3.1 Feature Vector Transformation and Reduction

Let the feature vector $\boldsymbol{\theta} \in \mathbb{R}^N$, composed of selected model parameters, be characterized by mean $\boldsymbol{\mu}_\theta$ and covariance \mathbf{P}_θ . Also let $\mathbf{P} \in \mathbb{R}^{N \times N}$ indicate an arbitrary (symmetric and positive definite) covariance matrix. \mathbf{P} may be decomposed as:

$$\mathbf{P} = \mathbf{U} \cdot \boldsymbol{\Lambda} \cdot \mathbf{U}^T \quad (1)$$

where:

$$\boldsymbol{\Lambda} = \text{diag}(\lambda_1, \lambda_2, \dots, \lambda_N) \in \mathbb{R}^{N \times N} \quad (2)$$

$$\mathbf{U} = [\mathbf{u}_1 \mathbf{u}_2 \dots \mathbf{u}_N] \in \mathbb{R}^{N \times N} \quad (3)$$

with $\text{diag}(\cdot, \cdot, \dots, \cdot)$ designating a diagonal matrix composed of the indicated elements, $\lambda_i (> 0)$ ($i = 1, 2, \dots, N$) the i -th eigenvalue of \mathbf{P} , and \mathbf{u}_i the corresponding normalized eigenvector. The eigenvectors are thus orthonormal, satisfying the relation $\mathbf{u}_i^T \cdot \mathbf{u}_j = \delta_{ij}$, with δ_{ij} denoting the Kronecker delta. The normalized eigenvector matrix \mathbf{U} therefore satisfies the relation $\mathbf{U} \cdot \mathbf{U}^T = \mathbf{I}_N$ (\mathbf{I}_N denoting the N -dimensional identity matrix). In view of this, $\boldsymbol{\Lambda}$ may be expressed as:

$$\boldsymbol{\Lambda} = \mathbf{U}^T \cdot \mathbf{P} \cdot \mathbf{U} \quad (4)$$

The feature vector $\boldsymbol{\theta}$ may be then analyzed in terms of the orthonormal vectors $\{\mathbf{u}_1, \mathbf{u}_2, \dots, \mathbf{u}_N\}$ which constitute a basis in \mathbb{R}^N :

$$\boldsymbol{\theta} = \sum_{j=1}^N s_j \mathbf{u}_j = [\mathbf{u}_1 \dots \mathbf{u}_N] \begin{bmatrix} s_1 \\ \vdots \\ s_N \end{bmatrix} = \mathbf{U} \cdot \mathbf{s} \quad (5)$$

with $\mathbf{s} \in \mathbb{R}^N$ denoting the transformed [in the $\{\mathbf{u}_1, \mathbf{u}_2, \dots, \mathbf{u}_N\}$ coordinate system] feature vector. Premultiplying (5) by \mathbf{U}^T gives the following expression for the transformed feature vector:

$$\mathbf{s} = \mathbf{U}^T \cdot \boldsymbol{\theta} \iff s_j = \mathbf{u}_j^T \cdot \boldsymbol{\theta} \quad (j = 1, 2, \dots, N) \quad (6)$$

Hence:

$$\boldsymbol{\mu}_s = \mathbf{U}^T \cdot \boldsymbol{\mu}_\theta \quad \text{Cov}[\mathbf{s}] \triangleq \mathbf{P}_s = \mathbf{U}^T \cdot \text{Cov}[\boldsymbol{\theta}] \cdot \mathbf{U} \quad (7)$$

Feature vector reduction to dimensionality M ($< N$) may be achieved in the $\{\mathbf{u}_1, \mathbf{u}_2, \dots, \mathbf{u}_N\}$ coordinate system as follows: Let $\{\mathbf{u}_1, \mathbf{u}_2, \dots, \mathbf{u}_M\}$ denote the eigenvectors that correspond to the largest M variances $\text{Var}[s_j]$. Expression (5) may be then re-written as:

$$\boldsymbol{\theta} = \sum_{j=1}^M s_j \mathbf{u}_j + \sum_{j=M+1}^N s_j \mathbf{u}_j = [\mathbf{U}_M : \mathbf{U}_{N-M}] \cdot \begin{bmatrix} \mathbf{s}_M \\ \dots \\ \mathbf{s}_{N-M} \end{bmatrix} \quad (8)$$

with $\mathbf{U}_M \in \mathbb{R}^{N \times M}$, $\mathbf{U}_{N-M} \in \mathbb{R}^{N \times (N-M)}$ denoting the indicated submatrices of \mathbf{U} , and $\mathbf{s}_M \in \mathbb{R}^M$, $\mathbf{s}_{N-M} \in \mathbb{R}^{N-M}$ the indicated subvectors of \mathbf{s} .

Keeping only the first M coordinates $\{\mathbf{u}_1, \mathbf{u}_2, \dots, \mathbf{u}_M\}$ in expression (8) one has:

$$\boldsymbol{\theta} = \sum_{j=1}^M s_j \mathbf{u}_j + \boldsymbol{\epsilon} \quad (9)$$

with $\boldsymbol{\epsilon}$ indicating the error vector due to coordinate system reduction.

Premultiplying Eq. (8) by \mathbf{U}_M^T and using the eigenvector orthonormality property, the reduced transformed feature vector is obtained as:

$$\mathbf{s}_M = \mathbf{U}_M^T \cdot \boldsymbol{\theta} \implies \mathbf{s}_M = \mathbf{T} \cdot \boldsymbol{\theta} \quad (10)$$

with $\mathbf{T} = \mathbf{U}_M^T \in \mathbb{R}^{M \times N}$ representing the transformation matrix. Hence:

$$\boldsymbol{\mu}_{\mathbf{s}_M} = \mathbf{T} \cdot \boldsymbol{\mu}_{\boldsymbol{\theta}} \quad \text{Cov}[\mathbf{s}_M] \triangleq \mathbf{P}_{\mathbf{s}_M} = \mathbf{T} \cdot \text{Cov}[\boldsymbol{\theta}] \cdot \mathbf{T}^T \quad (11)$$

Remark: It should be noted that for \mathbf{P} equal to the covariance $\mathbf{P}_{\boldsymbol{\theta}}$ of the feature vector $\boldsymbol{\theta}$, (5) represents the vector's *Karhunen-Lòeve expansion* [16]. In that case, due to property (4), the covariance matrix (7) of the transformed feature vector \mathbf{s} becomes:

$$\text{Cov}[\mathbf{s}] = \mathbf{U}^T \cdot \text{Cov}[\boldsymbol{\theta}] \cdot \mathbf{U} = \mathbf{A} \quad (12)$$

This indicates that the Karhunen-Lòeve expansion diagonalizes the feature vector covariance matrix, or, in other words, transforms the feature vector $\boldsymbol{\theta}$ into a vector with mutually uncorrelated components. It is known [16] that the Karhunen-Lòeve expansion leads to optimal, in the sense of minimum mean square error $E\{\boldsymbol{\epsilon}^T \boldsymbol{\epsilon}\}$, information compression, and thus feature vector reduction for any selected dimensionality. Furthermore, since the variances $\text{Var}[s_j]$ are, in this case, equal to λ_j ($j = 1, 2, \dots, N$), the coordinates $\{\mathbf{u}_1, \mathbf{u}_2, \dots, \mathbf{u}_M\}$ are those associated with the M largest eigenvalues of $\mathbf{P}_{\boldsymbol{\theta}}$. \square

Within the context of the reduced-dimensionality geometric approach a transformation matrix $\mathbf{T} \in \mathbb{R}^{M \times N}$, obtained from a single covariance matrix \mathbf{P} , is used for transforming the feature vector. Two possibilities are considered:

- (a) $\mathbf{P} = \mathbf{P}_{\boldsymbol{\theta}^o}$, with $\mathbf{P}_{\boldsymbol{\theta}^o}$ representing the feature vector covariance for the nominal (unfailed) system, or,
- (b) $\mathbf{P} = \mathbf{P}_{\boldsymbol{\theta}^{ave}}$, with $\mathbf{P}_{\boldsymbol{\theta}^{ave}}$ representing an average feature covariance matrix obtained during the training stage.

Denoting as $\boldsymbol{\theta}^{ij}$ the feature vector obtained from data corresponding to the j -th fault ($j = 1, 2, \dots, p$) from within the i -th fault mode ($i =$

$1, 2, \dots, N_F$), the average feature covariance matrix may be obtained as:

$$\mathbf{P}_{\theta^{ave}} = \frac{1}{p \cdot N_F} \sum_{i=1}^{N_F} \sum_{j=1}^p \mathbf{P}_{\theta^{ij}} \quad (13)$$

3.2 Feature Vector Dimensionality Selection

The selection of the dimensionality M of the transformed feature vector \mathbf{s}_M is based upon the assessment of the information conveyed by each one of its components, that is the information conveyed along each axis of the coordinate system. Toward this end the *logarithmic entropy function* [17] of the transformed feature vector $\mathbf{s} \in \mathbb{R}^N$:

$$H_R(\mathbf{s}) \triangleq - \sum_{i=1}^N \nu_i \log_2 \nu_i \quad (14)$$

with ν_i ($\nu_i = 1, 2, \dots, N$):

$$\nu_i \triangleq \text{Var}[s_i] / \sum_{i=1}^N \text{Var}[s_i] \quad (15)$$

is used as a measure of the information conveyed by \mathbf{s} . $H_R(\mathbf{s})$ also represents a decomposition of that information into each axis of the coordinate system $\{\mathbf{u}_1, \mathbf{u}_2, \dots, \mathbf{u}_N\}$.

The loss of information caused by truncating the transformed feature vector into dimension M ($M < N$) may be then quantified by the difference between the logarithmic entropy of the original N -dimensional vector \mathbf{s} and that of its M -dimensional truncated counterpart \mathbf{s}_M . The smaller the difference, the smaller the loss of information, and thus the incurred approximation error. The truncation dimension M may be then selected by considering the quantity:

$$\tilde{H}_R(\mathbf{s}_M, \mathbf{s}) \triangleq \frac{H_R(\mathbf{s}_M)}{H_R(\mathbf{s})} = \frac{\sum_{j=1}^M \nu_j \log_2 \nu_j}{\sum_{j=1}^N \nu_j \log_2 \nu_j} \in (0, 1] \quad (16)$$

Indeed, selecting an appropriate threshold value δ (generally close to unity), M may be selected as:

$$M = \min_{\mu} \left\{ \mu \in [1, N] \mid \delta \leq \tilde{H}_R(\mathbf{s}_{\mu}, \mathbf{s}) = \frac{\sum_{j=1}^{\mu} \nu_j \log_2 \nu_j}{\sum_{j=1}^N \nu_j \log_2 \nu_j} \right\} \quad (17)$$

Since this study deals with feature vectors corresponding to the nominal (unfailed) system as well as to the system in various fault modes (with various fault magnitudes in each case), M may be selected as:

$$M = \max_l \{M_l\} = \max_l \left\{ \min_{\mu_l} \left\{ \mu_l \in [1, N] \mid \delta \leq \tilde{H}_R(\mathbf{s}_{\mu_l}, \mathbf{s}) = \frac{\sum_{j=1}^{\mu_l} \nu_j \log_2 \nu_j}{\sum_{j=1}^N \nu_j \log_2 \nu_j} \right\} \right\} \quad (18)$$

where $l \in [1, 2, \dots, p \cdot N_F]$, with p representing the number of faults per fault mode used in the training stage and N_F the number of fault modes considered.

3.3 The Fault Identification Approach

The fault identification approach consists of the following stages:

Stage A: Feature space selection and fault mode subspace construction (training stage).

Based upon data obtained from a detailed simulation model, the "structure" and interval parameter estimates of a partial and reduced-order system model are obtained through suitable identification techniques [13,14]. Let θ denote the original N -dimensional feature vector composed of selected model parameters and characterized by mean μ_θ and covariance P_θ .

Additional experiments, in which p faults of various magnitudes, are, for each one of the N_F fault modes injected into the detailed simulation model, performed, and the corresponding interval estimates of θ^{ij} obtained [i_j refers to the j -th fault ($j = 1, \dots, p$) within the i -th fault mode ($i = 1, \dots, N_F$)].

The feature vector estimates are subsequently transformed according to expressions (6), (7), to produce the vectors s^{ij} along with their associated covariances $P_{s^{ij}}$. The reduced feature vector dimensionality M is selected according to (18), following which the interval estimate of the reduced feature vector s_M^{ij} is determined by using Eq. (11).

A ρ -dimensional stochastic feature space is then defined as the space spanned by the first and, perhaps, the diagonal elements (variances) of the second order moments of the reduced feature vector s_M . Let these selected quantities compose the ρ -dimensional vector θ_K .

The fault mode subspace representations are constructed by using linear $(\rho - 1)$ -dimensional hyper-plane approximations. The mathematical form of the i -th fault mode hyper-plane thus is:

$$\begin{aligned} g^i(\theta_K) &= \theta_{K_1} + \omega_1^i \theta_{K_2} + \dots + \omega_{\rho-1}^i \theta_{K_\rho} - \omega_\rho^i = 0 \implies \\ \implies (\bar{\omega}^i)^T \theta_K - \omega_\rho^i &= \theta_{K_1} + \bar{\theta}_K^T \cdot \omega^i = 0 \end{aligned} \quad (19)$$

with ω_l^i denoting the hyper-plane's l -th coefficient, and:

$$\omega^i = [\omega_1^i \omega_2^i \dots \omega_\rho^i]^T \quad \bar{\omega}^i = [1 \ \omega_1^i \dots \omega_{\rho-1}^i]^T \quad (20)$$

$$\theta_K = [\theta_{K_1} \ \theta_{K_2} \dots \theta_{K_\rho}]^T \quad \bar{\theta}_K = [\theta_{K_2} \dots \theta_{K_\rho} \ -1]^T \quad (21)$$

Given the i -th ($i = 1, \dots, N_F$) fault mode estimates θ_K^{ij} ($j = 1, \dots, p$) with $p > \rho$, the corresponding hyper-plane representation is estimated through linear regression [15] using the model form:

$$\theta_{K_1}^{ij} + (\bar{\theta}_K^{ij})^T \cdot \omega^i = \epsilon^{ij} \quad (1 \leq j \leq p) \quad (22)$$

with ϵ^j denoting the j -th regression error. These expressions lead to the estimator:

$$\hat{\omega}^i = - \left[(\bar{\Theta}_K^i)^T \cdot \bar{\Theta}_K^i \right]^{-1} \cdot (\bar{\Theta}_K^i)^T \cdot \theta_{K_1}^i \quad (23)$$

where:

$$\bar{\Theta}_K^i \triangleq \left[\bar{\theta}_K^{i_1} \ \bar{\theta}_K^{i_2} \cdots \bar{\theta}_K^{i_p} \right]^T \in \mathbb{R}^{p \times p} \quad (24)$$

and:

$$\theta_{K_1}^i \triangleq \left[\theta_{K_1}^{i_1} \ \theta_{K_1}^{i_2} \cdots \theta_{K_1}^{i_p} \right]^T \in \mathbb{R}^{p \times 1} \quad (25)$$

Stage B: Current feature vector estimation.

Once a fault is, based upon periodically obtained system data, detected [12], an interval estimate of the current (unknown fault) feature vector θ^u is obtained and transformed, according to Eq. (11) into s_M^u , from which θ_K^u is formed.

Stage C: Distance computations.

Appropriate “distances” between the current (unknown fault) point θ_K^u and each fault mode hyper-plane are subsequently computed. The distance between θ_K^u and the i -th mode hyper-plane is obtained by optimizing the Lagrangian:

$$L(\theta_K, \gamma) = D(\theta_K, \theta_K^u) + 2\gamma \cdot g^i(\theta_K) \quad (26)$$

with respect to θ_K and γ . In this expression 2γ represents the Lagrange multiplier, $g^i(\theta_K)$ the i -th mode hyper-plane defined by Eq. (19), and $D(\cdot, \cdot)$ an appropriate distance function (metric) of the form:

$$D(\theta_K, \theta_K^u) \triangleq \|\theta_K - \theta_K^u\|^2 \triangleq (\theta_K - \theta_K^u)^T \cdot (\theta_K - \theta_K^u) \quad (27)$$

The form of θ_K depends upon the metric space used. In the *deterministic* metric space case $\theta_K = \mu_{s_M}$, implying that only the mean of the truncated feature vector is used. In the *stochastic* metric space case $\theta_K = [\mu_{s_M}^T, (\text{col diag } P_{s_M})^T]^T$, implying that both the mean and diagonal elements of the feature vector covariance are used.

4. FAULT IDENTIFICATION IN A SIMPLY SUPPORTED BEAM

The performance characteristics of the information-based reduced-dimensionality geometric approach are examined in connection with fault identification in the laboratory-scale beam of Sadeghi and Fassois [12], so that comparisons with the original formulation may be made.

The beam (Figure 1) is based on four rigid supports, dividing it into three *spans*, as well as on two additional flexible supports: One stationary, referred to as “auxiliary spring”, and one movable that is at the mid-point of the central span in the nominal (unfailed) system case and is referred

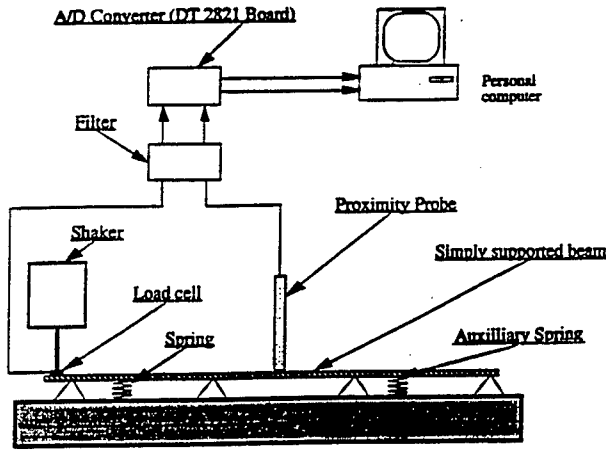


Figure 1: Schematic diagram of the experimental set-up [12].

to simply as “spring”. The considered faults correspond to deviations of the beam local stiffness characteristics (local changes in the modulus of elasticity) realized by transporting the movable support (“spring”) to any desired point in any span.

The *objective* of the experiments is fault identification, that is the determination of the span in which a particular fault occurs, based upon vibration test data obtained from a single pair of measurement points. Three fault modes ($N_F = 3$), denoted as F^1 , F^2 , and F^3 and corresponding to changes in the local stiffness characteristics at a point lying anywhere in the first, second, and third, respectively, span of the beam, are considered.

Fault identification is based upon measurements of the exerted force and resulting vibration displacement at the midpoint of the central span, as obtained by a load cell and proximity probe, respectively (Figure 1). The two signals are driven through analog anti-alias filters (cut-off frequency at 400 Hz) and are subsequently digitized at 1 kHz.

The system’s dynamics are described by a stochastic *ARMA* (6, 5, 3) (AutoRegressive Moving Average with eXogenous excitation) model of the form [12]:

$$\sum_{i=0}^6 a_i \cdot y[t-i] = \sum_{i=1}^5 b_i \cdot F[t-i] + \sum_{i=0}^3 c_i \cdot w[t-i]$$

with $a_0 \equiv c_0 \equiv 1$, $y[t]$ representing the measured vibration displacement, $F[t]$ the exerted force signal, $w[t]$ a zero-mean and uncorrelated noise-generating stochastic sequence, and a_i , b_i , c_i the i -th autoregressive (AR), exogenous (X), and moving average (MA) parameter, respectively. This model attempts to account for both the structural and noise dynamics, although only three of the four structural modes present in the 0 – 400 Hz

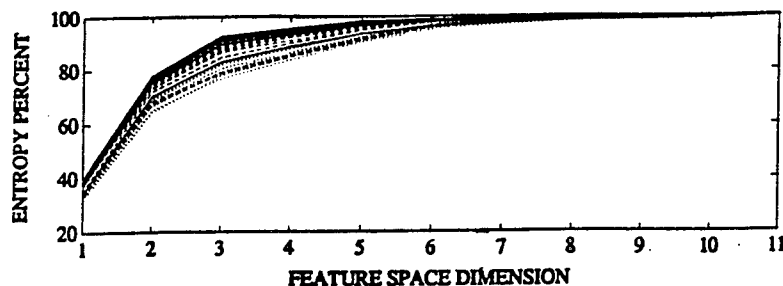


Figure 2: Normalized logarithmic entropy of the transformed feature vectors versus feature vector dimension.

frequency range are represented. The original feature vector θ consists of the model's autoregressive (AR) and exogenous (X) parameters, with its dimensionality being equal to $N = 11$.

Interval estimates of θ , obtained via identification techniques operating upon data corresponding to faults realized at various points of each span during training, are transformed according to Eqs. (6), (7), with the covariance matrix P selected as either P_{θ^o} or $P_{\theta^{ave}}$ (subsection 3.1). Transformed feature vector dimensionality selection is based upon the logarithmic entropy function, a normalized version of which is presented, for the various transformed feature vectors, in Figure 2 ($P = P_{\theta^{ave}}$). From this a measure of the information conveyed along each coordinate may be identified. Applying the criterion of expression (18) with $\delta = 0.970$ yields a reduced feature vector dimensionality of $M = 9$. Following the selection of θ_K , the F^1 , F^2 , and F^3 fault mode hyper-planes are constructed according to the procedure of subsection 3.3.

Eighteen Test Cases, the first six (1 – 6) corresponding to faults belonging to fault mode F^1 (realized by inserting the spring at the positions $L/24$, $2L/24$, $3L/24$, $5L/24$, $6L/24$, $7L/24$, with L denoting the length of the beam between the left and right rigid supports), the next six (7 – 12) to faults belonging to fault mode F^2 (spring at $9L/24$, $10L/24$, $11L/24$, $13L/24$, $14L/24$, $15L/24$), and the last six (13 – 18) to faults belonging to fault mode F^3 (spring at $17L/24$, $18L/24$, $19L/24$, $21L/24$, $22L/24$, $23L/24$), are considered. Note that none of the above fault locations were used in the hyper-plane construction (training) stage.

Fault identification results with the reduced-dimensionality geometric approach, using the transformed stochastic metric space, are presented in Table 1. In each Test Case the distances of the current (unknown fault) point to the fault mode hyper-planes are presented, with the minimal one indicated in bold face characters. Despite the difficulties of this particular set-up and the use of a *single* transfer function model, only two misclassification errors (Test Cases 14 and 17) are encountered (compared to one

Stochastic Distance				
	Test Case	Distance from Hyper-plane F^1	Distance from Hyper-plane F^2	Distance from Hyper-plane F^3
Faults F^1 (Span 1)	1	2.7733e-01	4.4287e-01	1.9341e-00
	2	1.1813e-01	1.4202e-00	1.5859e-00
	3	3.3341e-01	1.2078e-00	1.6386e-00
	4	5.5534e-01	7.6988e-01	1.9670e-00
	5	1.1079e-00	1.9402e-00	1.8091e-00
	6	2.7344e-01	3.8364e-01	2.0165e-00
Faults F^2 (Span 2)	7	3.5566e-00	3.4436e-01	1.6562e-00
	8	2.0700e-00	1.0308e-01	4.2317e-01
	9	3.8165e-00	5.6934e-02	4.1950e-01
	10	2.3498e-00	7.5420e-02	5.6329e-01
	11	4.4883e-00	8.6493e-02	4.2183e-01
	12	2.2013e-00	1.0751e-02	5.1501e-01
Faults F^3 (Span 3)	13	2.5372e-00	7.7870e-02	3.3583e-02
	14	1.5444e-00	6.8563e-02*	7.6861e-02
	15	1.2513e-00	8.0988e-02	6.5441e-02
	16	1.0696e-00	4.2530e-01	5.2299e-02
	17	4.1148e-01	4.2383e-02*	7.4034e-02
	18	2.6294e-00	4.7392e-01	1.6920e-01

Table 1: Fault identification results by the information-based reduced-dimensionality Geometric approach using the stochastic metric space. (The minimal distance in each Test Case is indicated in bold-face characters; misclassification errors are marked by an asterisk.)

in the original geometric approach [12]). Like in the original case, a deterioration is observed when the deterministic metric space is used; in that case four misclassification errors are encountered (compared to five in the original geometric approach [12]). This underscores the importance of using the stochastic space in conjunction with systems characterized by non-negligible (for instance standard deviation noise-to-signal ratios of 1% or higher) random effects.

5. CONCLUDING REMARKS

An information-based reduced-dimensionality formulation of the geometric fault identification approach was introduced. According to it, the feature vector is transformed into a suitable coordinate system, within which information compression, and thus feature vector truncation, may be best achieved. Feature vector dimensionality selection is based upon bounding of the information loss, expressed in terms of logarithmic entropy, below a certain threshold. The information-based reduced-dimensionality formulation offers a formal and systematic procedure for the proper selection of a minimal dimensionality feature vector and corresponding feature space, thus achieving two important goals: (a) Substantial simplification of the fault identification procedure, and, (b) potentially improved fault identification performance over arbitrarily truncated feature vectors.

The performance characteristics of the approach were demonstrated via fault identification in a laboratory-scale simply-supported beam, where the reduced-dimensionality ($M = 9$) formulation performed roughly equivalently to the original, full-dimensionality ($N = 11$), version.

REFERENCES

- [1] Chen, J.C. and Garba, J.A., On orbit damage assessment for large space structures. *Proceedings of the AIAA/ASME/ASCE/AHS 28th Structures, Structural Dynamics and Materials Conference*, AIAA, 1987, pp.714-721.
- [2] Yao, J.T.P., Identification of structural damage in civil engineering. In *Application of System Identification in Engineering*, ed. H.G. Natke, Springer-Verlag, 1988, pp.349-390.
- [3] Hajela, P. and Soeiro, F.J., Structural damage detection based on static and modal analysis, *AIAA Journal*, **28**, 1989, pp.110-115.
- [4] Hearn, G. and Testa, R.B., Modal analysis for damage detection in structures. *ASCE Journal of Structural Engineering*, **117**, 1991, pp.3042-3063.
- [5] Lew, J.-S., Using transfer function parameter changes for damage detection of structures. *AIAA Journal*, **33**, 1995, pp.2189-2193.
- [6] DiPasquale, E., Ju, J.W., Aksar, A. and Cakmak, A.S., Relation between global damage indices and local stiffness degradation. *Journal of Structural Engineering*, **116**, 1990, pp.1440-1456.

- [7] Sanayei, M. and Onipede, O., Damage assessment of structures using static test data. *AIAA Journal*, **29**, 1991, pp.1174-1179.
- [8] Smith, S.W. and Hendricks, S.L., Evaluation of two identification methods for damage detection in large space structures. *Proceedings of the VPI & SU/AIAA 6th Symposium on Dynamics and Control of Large Structures*, 1987.
- [9] Hemez, F.M., Practical guide to high accuracy identification of structural damage in complex structures. *Proceedings of the International Modal Analysis Conference*, Nashville, TN, USA, 1995, pp.1297-1304.
- [10] Shahriyar, F. and Bouwkamp, J.G., Damage detection in offshore platforms using vibration information. *ASME Journal of Energy Resources Technology*, **108**, 1986, pp.97-106.
- [11] Wolff, T. and Richardson, M., Fault detection in structures from changes in their modal parameters. *Proceedings of the International Modal Analysis Conference*, 1989, pp.87-94.
- [12] Sadeghi, M.H. and Fassois, S.D., Geometric approach to the non-destructive identification of faults in stochastic structural systems. *AIAA Journal*, **35**, April 1997 (in press). Also in *AIAA Journal on Disc*, **2**, No. 3, 1997. Short version in the *Proceedings of the International Conference on Identification in Engineering Systems*, Swansea, U.K., pp.28-37, 1996.
- [13] Lee, J.E. and Fassois, S.D., Suboptimum maximum likelihood estimation of structural parameters from multiple-excitation vibration data. *ASME Journal of Vibration and Acoustics*, **114**, 1992, pp.260-271.
- [14] Fassois, S.D. and Lee, J.E., On the problem of stochastic experimental modal analysis based on multiple-excitation multiple-response data. Part II: The modal analysis approach. *Journal of Sound and Vibration*, **161**, 1993, pp.57-87.
- [15] Draper, N.R. and Smith, H., *Applied Regression Analysis*, 2nd edition, John Wiley, 1981.
- [16] Fukunaga, K., *Introduction to Statistical Pattern Recognition*, Academic Press, 2nd edition, 1990.
- [17] Devijver, P.A. and Kittler, J., *Pattern Recognition: A Statistical Approach*, Prentice-Hall International, 1982.

FATIGUE BEHAVIOUR OF CARBON FIBRE REINFORCED PLATES WITH EMBEDDED OPTICAL FIBRES

by B. Benchekchou and N. S. Ferguson

Abstract

Finite element (FE) techniques are used to simulate the strain and stress concentrations in and around an optical fibre (OF) embedded in XAS/914 carbon fibre reinforced laminates. Analytical results produced show the location of high stresses and therefore the position of possible damage when specimens are subjected to tension and flexure. Also mechanical fatigue tests are carried out on specimens with optical fibres embedded within different orientation plies, in order to see the effect of the fibres on the fatigue behaviour of the specimens.

1-Introduction

There is a requirement for continuous non-destructive testing (NDT) of advanced composite structures whilst in service. Advanced analytical tools, such as the finite element method (FE) and measurement techniques, such as strain gauges, piezoelectric devices, etc... are normally used for determining high stress levels and areas prone to damage and fatigue. However, many of the measurement techniques are via surface measurements and cannot be undertaken during service. The development of fibre optic sensors, in combination with advances in composite material technology, has led to the introduction of fibre optic smart structures whose basic functions are to sense environmental conditions in or around the structure, to transfer the information back to an optical and or electronic signal processor and to react following the information sensed or measured, [1]. Technologies associated with fibre optic smart structures and their interrelationship are well stated in Udd [2]. Embedding the optical fibres into the structure is an important issue since the interface between the optical fibre (OF) and the surrounding material has to allow accurate measurements. One has to admit that optical fibres are foreign entities to the host structure and therefore will always alter the stress and strain in the vicinity of the embedded sensor, [3]. The coating is also important for embedding optical fibres successfully. It protects the optical fibre from moisture; this is due mostly to the significant strength degradation that may occur in the fibre when microcracks on the surface of the fibre are penetrated by moisture, causing the cracks to propagate.

However, the coating must form an appropriate interface between the optical fibre and the host material, allowing accurate measurement of the dynamic response or environmental effect to be monitored. Dasgupta and Sirkis [4] showed that strain concentrations near an embedded OF are highly dependent on the thickness and material properties of the coating. An optimum coating can minimise or eliminate stress concentrations in the host material immediately surrounding the embedded fibre, in the coating or in the OF itself.

Studies have been carried out in order to determine the state of strain in the optical fibre and the host material. This relationship between the host strain and the sensor strain must be determined to make accurate measurements with the fibre optic sensor. Therefore, it has been noted that:

*stress concentrations in the host and at the interfaces are sometimes tensile in nature and can therefore create fatigue damage under cyclic loading, [3].

*resin-rich pockets form when optical fibres are embedded in laminated composite hosts along any orientation other than parallel to the orientation of the reinforcing fibres. A resin pocket becomes smaller when the laminate's thickness and/or the angle between the optical fibre and the reinforcing fibres directly adjacent to the optical fibre are reduced, [3].

The purpose of this research is to integrate the use of optic fibres within composites and to study the fatigue behaviour of carbon fibre reinforced plates (CFRP) with embedded optical fibres, while subjected to flexural loading. The finite element (FE) method is being used as an analytical tool to investigate the stress concentration and the relationship between the fibre strain and the far-field host strain. Complementary experimental fatigue tests carried out on CFRP specimens with OF embedded within different plies. Acrylate coated optical fibres embedded in XAS/914 carbon fibre specimens are used in order to take strain measurement, while composite samples are being subjected to flexural loading without any damage present.

2-Finite element analyses

XAS/914 samples (140 mm x 70 mm x 2 mm) were simulated using the finite element software ANSYS. Meshes were formed using a three-dimensional (3D), layered element: STIF46. The choice of a three-dimensional element was made in order to have stress and strain details in three directions, [4]. The element is defined by eight nodal points, average layer thickness, layer material direction angles and orthotropic material properties. The element theory is based upon a formulation which includes modified extra displacement shapes as described in [5–6]. The element STIF46 cannot represent a zero transverse shear stress at the top or bottom

surfaces of the element. STIF46 elements can be stacked one over another to obtain detailed through-thickness effects. The element geometry permits modelling of a solid structure tapering to an edge using shapes like tetrahedrons and triangular prisms.

Firstly, simulations were performed in order to see whether the presence of the OF changes the stress patterns in the specimen while subjected to either tension, compression or bending. This was achieved by comparing stress patterns obtained from FE analyses carried out on specimens with and without an optical fibre in the samples along the centre, lying within two 0° orientation plies in the middle as recommended by [7]. The stacking sequence chosen for the specimens was $((\pm 45^\circ/90^\circ/0^\circ)_2)_s$. It has been proven to be a very good fatigue resistant lay-up comparatively to others, such as: $((0^\circ/\pm 45^\circ/90^\circ)_2)_s$ and $((+45^\circ)_2(-45^\circ)_2(90^\circ)_2(0^\circ)_2)_s$, [4]. The coated OF diameter was equivalent to twice the thickness of each composite ply, and therefore was embedded within the two mid- 0° orientation plies. Meshes were produced in order to have maximum detail around and along the OF. Each element had a ply thickness and definition was increased in the vicinity of the OF. Models had a total of 3080 elements, with a 998 wavefront. Meshes for specimens with or without OF were very similar. The only difference was the different material properties when acrylate coated OF were incorporated. Table 1 gives the properties of the XAS/914 material, the acrylate coating and the optical fibre. The boundary conditions were such that specimens were subjected to tension, compression, upwards bending and downwards bending. These were produced by node displacements along one specimen end whilst the other end being fixed in all directions. Thus, a tension was simulated by a displacement in the z-direction, (i.e. along the specimen), and a bending by a displacement in the y-direction, (i.e. the thickness direction), along one end of the sample.

Static analyses were carried out and results are being presented in stress/strain contour plots. Maximum and minimum stresses are also identified and saved.

***Specimens subjected to tension:**

The stacking sequence used being $((\pm 45^\circ/90^\circ/0^\circ)_2)_s$, the first layer; i.e. the first $+45^\circ$ orientation ply will be then called layer1 and the last one will be subsequently called layer 16. Comparison between both models, i.e. with and without optical fibre show that stress distributions for layers 1–7 and 10–16 are the same for both models, while stress distributions are slightly different in layers 8 and 9, layers within which the optical fibre is embedded. This is to be expected since the OF and its coating have different material properties from those of the composite material. In fact, when

considering model A, (i.e. with OF) stress ranges in the x-, y- and z-directions as well as shear stress ranges in the x-z and y-z planes in layers 8 & 9 are higher than those given from model B, (i.e. without OF).

Results from model A show that high stress concentrations are seen in the OF and the surrounding layers to the OF, where high shear stresses are also present. High stress concentrations in the OF can clearly be seen in figures 1.a-b where direct stresses S_z and S_y are presented across the optical fibre at two different positions respectively, $z=0$ and 140 mm; i.e. at both edges of the specimen. Uniform strain field occurs in the OF, coating and the surrounding layers to the OF, once far from the clamped end of the specimen. Localised concentrations of tensile and compressive stress exist in the laminate near the OF coating. Direct and shear stress distributions in layers 8 and 9 show that the laminate is in tension with similar stress patterns in both plies, obviously high stresses are present along the clamped end, see figures 2.a-b. Maximum (tensile and compressive) direct and shear stresses do occur in nodes located between the OF and its coating and between the OF and the composite, which shows that delamination and/or debonding are likely to happen in these locations. Comparison between S_z values (i.e. in the centre and at the circumference of the core of the OF) shows that S_z is higher in the centre than at the circumference of the core of the OF, see figure 3, which shows also that lower S_z stresses are presented in layers 8 & 9 than in the OF.

***Specimens subjected to an upwards bending:**

Simulation results show that stress distributions in both models A&B are the same in layers 1-7 and 10-16. Again, slight different patterns are shown in plies 8 and 9 while comparing both models. Stress range values are higher in model A while considering the OF than in model B while considering the same elements. Results from model A show some high stress concentrations in the OF, especially between the OF and its coating, as shown in figures 4.a-b where direct stress distributions S_y and S_z are shown across the OF at both edges respectively of the specimen. This shows that delamination and/or debonding are likely to happen in these locations. Uniform stress fields occur at the surrounding layers to the OF, as shown in figures 5.a-b, where direct and shear stress distributions are plotted for layers 8 & 9. Simulation results show that compressive stress exists in the laminate within the top layers while tensile stress occurs in the bottom plies. Comparison of S_z stress distributions in the OF and in layer 8 shows that stresses are higher in the OF than in layers within which the OF is embedded, see figure 6 and as for specimen in tension, very similar stress values were found in layers 8 and 9, whether the OF is embedded or not.

3-Experimental investigation

The first experimental tests were carried out to find out the fatigue strength of the optical fibre to be used. A flexural fatigue rig was used for this purpose. The objectives were to mechanically fatigue an XAS/914 sample with an embedded OF, determine the duration for which the OF is intact whilst the sample is subjected to flexural loading and, finally, compare the performance of several specimens with OF embedded in different positions.

An already existing mechanical (flexural) fatigue rig, with half-sine clamps was used for this purpose. This particular clamp has been designed by Drew [8] to induce damage in the centre of the specimen instead of having edge damage, i.e. peeling while flexural tests are carried out. The rest of the components of the rig were designed and modified earlier by Benchekchou [4]. An electronic circuit, enabling the monitoring of an OF, was assembled. Three XAS/914 samples X1, X2 and X3, with the following stacking sequence $((\pm 45^\circ/90^\circ/0^\circ)_2)_s$, $((\pm 45^\circ/90^\circ/0^\circ)_2)_{s2}$ and $((\pm 45^\circ/90^\circ/0^\circ)_2)_s$ respectively, were manufactured. X1 had an OF embedded within the two centre 0° orientation plies. The OF in X2 was situated at a quarter of the way through the thickness, i.e. between the first two 0° orientation plies, while the OF was embedded between the second $\pm 45^\circ$ orientation plies in X3. Specimens X1, X2 and X3 were then put on the rig and the flexural deflection was such that the strain value recorded by a strain gauge mounted at the top surface by the summit of the sine clamp were $7000 \mu\text{S}$ for X1, $4000 \mu\text{S}$ for X2 and X3. After 70 000 loading cycles, the optical fibre showed no sign of breakage for all three specimens. Samples though were delaminated as shown in Figure 7.a-b, where ultrasonic scans are given before any loading cycles and after 70 000 loading cycles, for X1 and X2 respectively. Note that for specimen X1, the OF was positioned in a very low strain level, the neutral bending plane, hence it would take much longer to break. It was also clear that either the strain induced for specimen X2 and X3 was not high enough to break the OF or that delamination between the OF and its coating occurs early on and creates a stress relief, leading to no strain transfer to the actual OF.

To avoid occurrence of delamination between the OF and its coating, further mechanical tests were carried out with stripped fibres, embedded in further samples. Three more specimens were made X4, X5 and X6 with the $((\pm 45^\circ/90^\circ/0^\circ)_2)_s$ lay-up. The OF was embedded between the second $\pm 45^\circ$ orientation plies in X4, in the two centre 0° orientation plies in X5 and between the first $(90^\circ/0^\circ)$ orientation plies in X6. Specimens X4, X5 and X6 were then put on the rig and the flexural

deflection was such that the strain value recorded by a strain gauge mounted at the top surface by the summit of the sine clamp was 7000me. The fatigue experiments were carried out to the following procedure:

- (a) a specimen was first ultrasonically scanned to identify any unwanted initial defects;
- (b) the specimen was then driven in flexure through a certain number of loading cycles. The number of cycles were counted by optical counter and the driving motor was switched off after the desired number of cycles was monitored and controlled through the use of a computer;
- (c) the specimen was then removed from the rig and an ultrasonic scan was made;
- (d) stages (b) and (c) were then repeated till damage had been induced in the specimen and the test judged to be complete.

The tests results are shown, in the form of ultrasonic scans, in Figures 9.a–c. For specimen X4, a slight damage starts after 2000 loading cycles and increases slowly, see scans after 5000 and 10000 loading cycles. For specimen X5, no damage was detected even after 5000 loading cycles whilst for specimen X6, the first signs of delamination started to show after 15000 loading cycles. This continued to increase slowly, as shown from scans after 25000 and 30000 loading cycles. Specimens X5 and X6 were shown to be more fatigue resistant than specimen X4, which means that embedding an OF within a 0° orientation ply leads to a better fatigue behaviour than if the OF is embedded within the $\pm 45^\circ$ orientation plies. More fatigue tests are being carried out, which will enable more comparisons to be done.

4–Conclusions

3D FE simulations have shown that the presence of an optical fibre within a carbon fibre XAS/914 specimen, while it is subjected to flexure and tension, does not change the stress distributions in plies others than those where the OF is embedded. Analytical results also showed that high stresses appears between the OF and its coating and also the coating and the specimen, which will eventually lead to delamination and/or debonding. Fatigue experiments also showed that the location of the OF in a specimen is important, and could alter the fatigue behaviour and resistance of the specimen. Future work will be involved in measuring the dynamic strain in the optical fibres, correlating it with the strain in the composite and, eventually, detect and interpret damage of the composite host structure.

5–Acknowledgments

The authors wish to thank the EPSRC for sponsorship of the programme of research

under which the work is being carried out (ROPA award) .

6-References

- 1-Udd. E., "The evolution of fiber optic smart structures", in "Fiber optic in smart structures", Edited by Udd, Wiley series in pure and applied optics, 1994, Chapter 1, 1-4.
- 2-Udd. E., "Fiber smart structure technology", in "Fiber optic in smart structures", Edited by Udd, Wiley series in pure and applied optics, Chapter 2, 1994, 5-21.
- 3-Sirkis. J.S. and Dasgupta. A., "Optical fiber/composite interaction mechanics", in "Fiber optic in smart structures", Edited by Udd, Wiley series in pure and applied optics, 1994, Chapter 4, 61-107.
- 4-Benchekchou. B., "Stresses around fasteners in composite aircraft structures and effects on fatigue life", PhD thesis, University of Southampton, 1994.
- 5-ANSYS theoretical manual, Swanson Analysis Systems Inc.
- 6-ANSYS tutorial manual for composite structures, Swanson Analysis Systems Inc.
- 7-Eaton. N.C., Drew. R.C. and Geiger. H., "Finite element stress and strain analysis in composites with embedded optical fiber sensors" Smart material structures 4, 1995, 113-117.
- 8-Drew, R.C., "An investigation into damage initiation and propagation in carbon fibre reinforced plastics", PhD thesis, University of Southampton, 1988.

Table 1: Material properties used.

	XAS/914 composite material	Acrylate coating	Optical fibre (core)
Young's Modulus in the x-direction Ex (GPa)	106.5	0.045	70.7
Young's Modulus in the y-direction Ey (GPa)	8.6		
Young's Modulus in the z-direction Ez (GPa)	8.6		
Shear Modulus in the x-y plane Gxy (GPa)	4.59	0.0167	26.185
Poisson's Ratio vxy=vyz	0.02281	0.35	0.35
Poisson's Ratio vxz	0.28		
Density g/cm ³	1360		

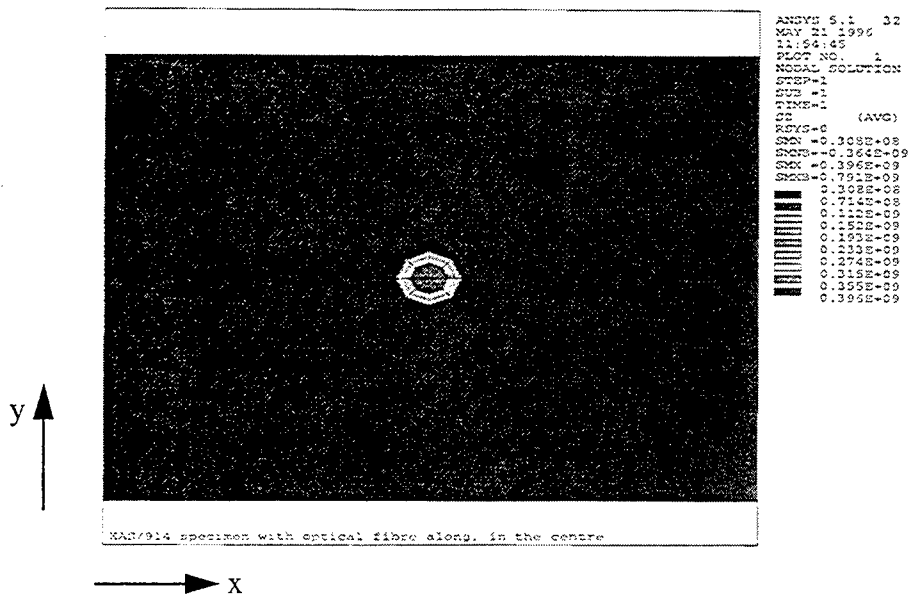


Figure1.a: Stress distribution S_z (longitudinal) across the optical fibre, at position $z=0$ mm, specimen in tension and stress values in N/m^2 .

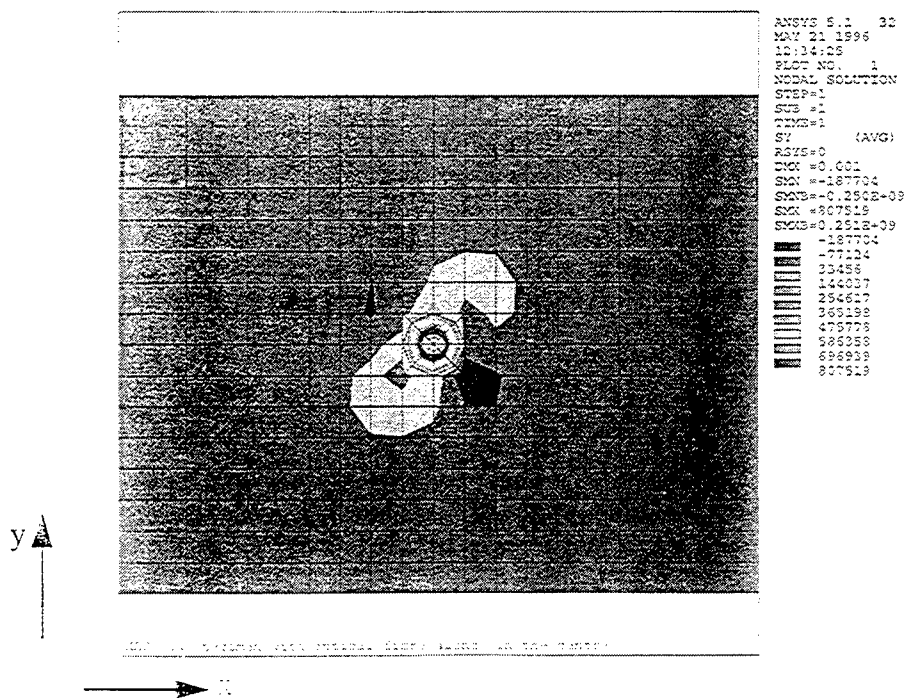


Figure1.c: Stress distribution S_y (through thickness) across the optical fibre, at position $x=-40$ mm, specimen in tension and stress values in N/m^2 .

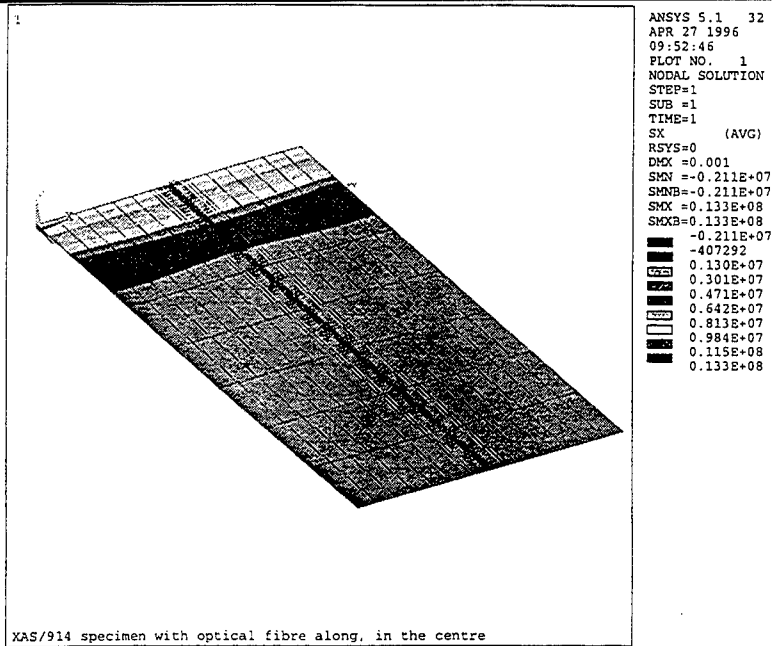


Figure2.a: Stress distribution S_x , in layer 8, a 0° orientation ply, specimen in tension and stress values in N/m^2 .

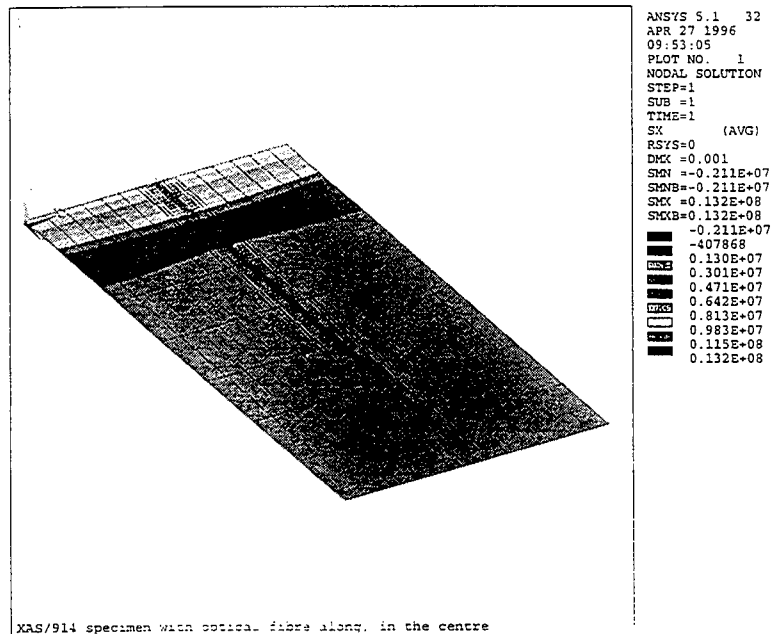


Figure2.b: Stress distribution S_x , in layer 9, a 0° orientation ply, specimen in tension and stress values in N/m^2 .

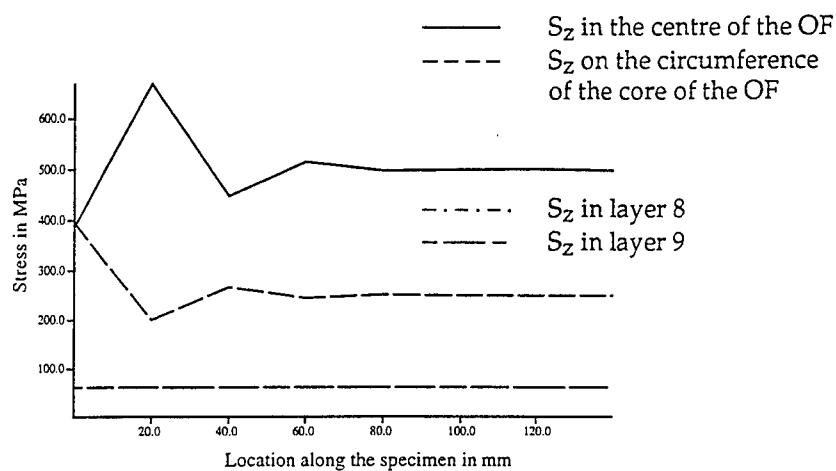


Figure 3: S_z (longitudinal) stress distributions in the centre and on the circumference of the core of the optical fibre and in layers 8 & 9, layers within which the OF is embedded; values given for specimen in tension.

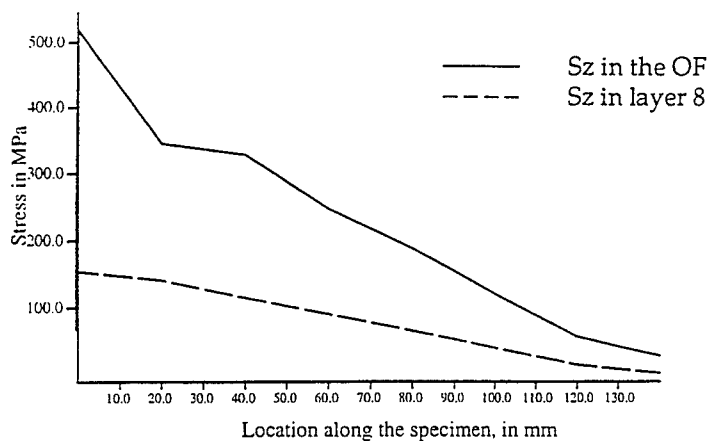


Figure 6: Comparison of S_z (longitudinal) stress distributions in the optical fibre and in layers 8 (i.e. first layer housing the OF) along the specimen; values given for specimen bent upwards.

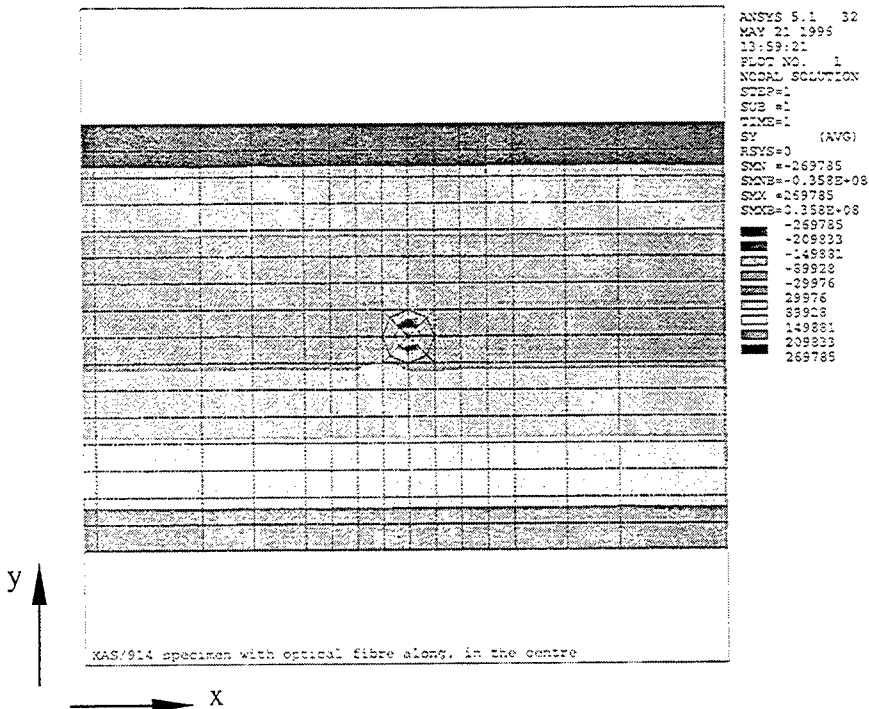


Figure 4.a: Stress distribution S_y (through thickness) across the optical fibre, at position $z=0$ mm, specimen being bent up and stress values in N/m^2 .

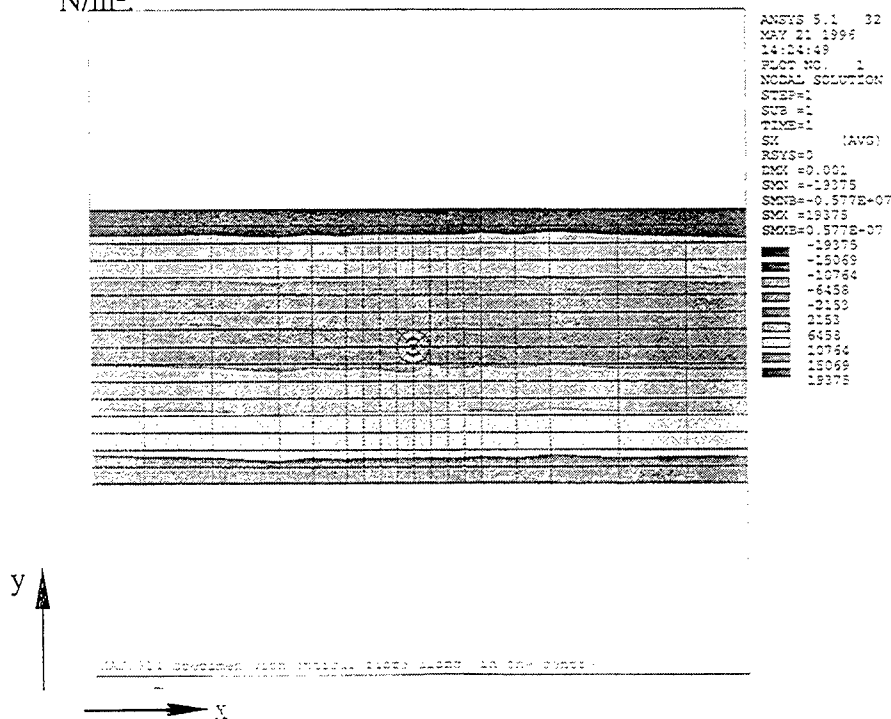


Figure 4.b: Stress distribution S_x across the optical fibre, at position $z=140$ mm, specimen being bent up and stress values in N/m^2 .

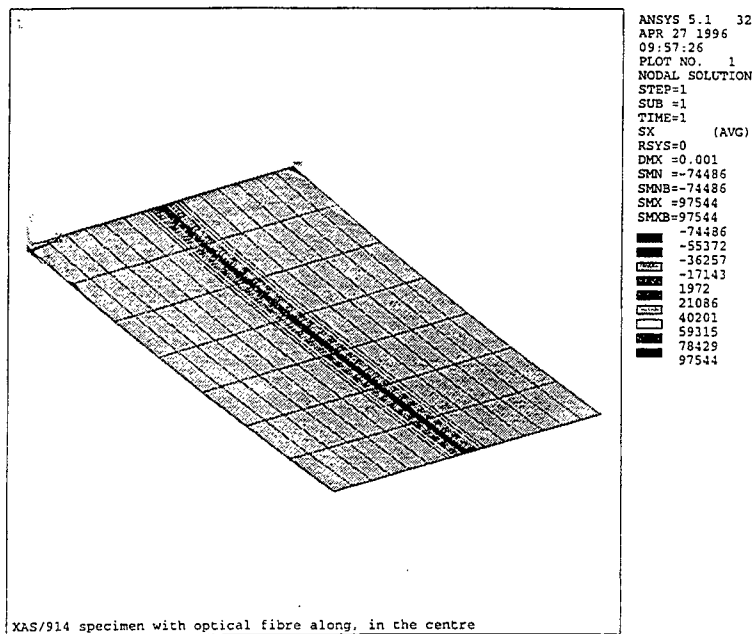


Figure5.a: Stress distribution S_x , in layer 8, a 0° orientation ply, specimen being bent up and stress values in N/m^2 .

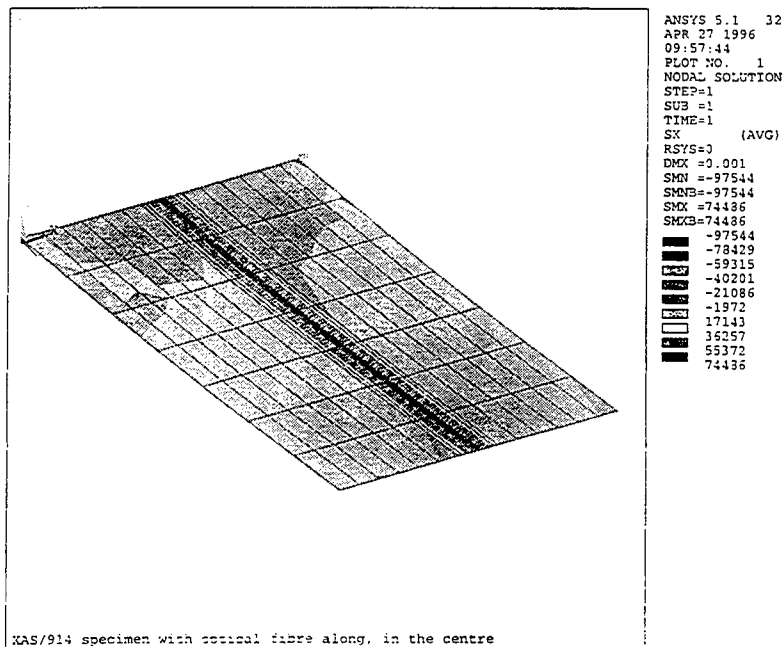
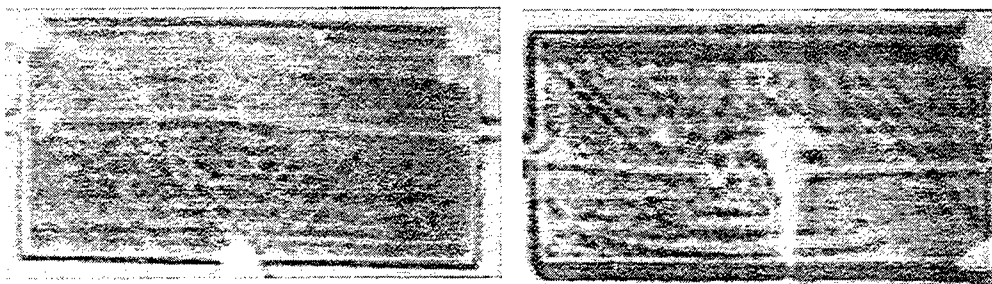


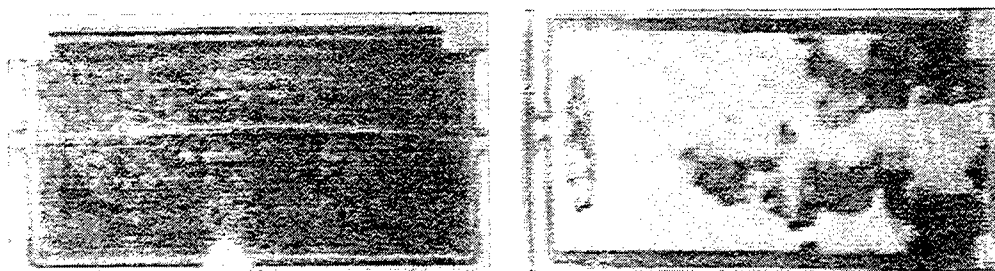
Figure5.b: Stress distribution S_x , in layer 9, a 0° orientation ply, specimen being bent up and stress values in N/m^2 .



a: before any loading cycles.

b: after 70 000 loading cycles.

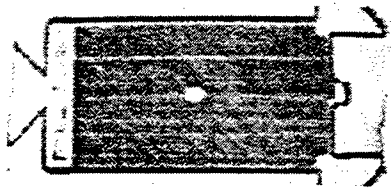
Figure 7.a: Ultrasonic scans of specimen X1.



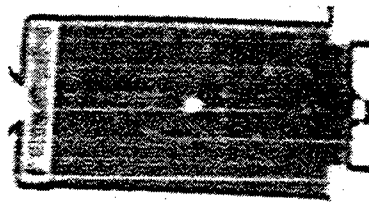
a: before any loading cycles.

b: after 70 000 loading cycles.

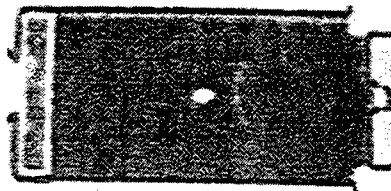
Figure 7.b: Ultrasonic scans of specimen X2.



a: before any loading cycles.

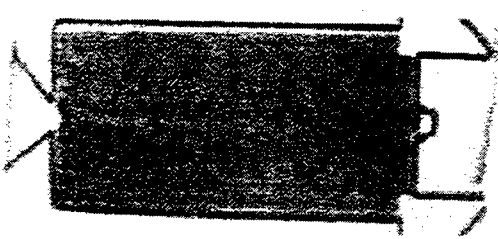


b: after 2000 loading cycles.

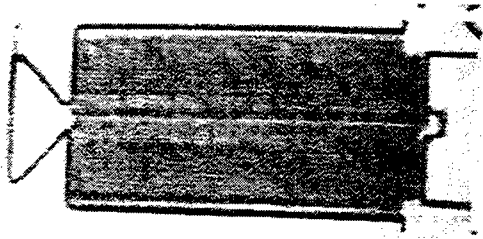


c: after 10 000 loading cycles.

Figure 8.a: Ultrasonic scans of specimen X4.

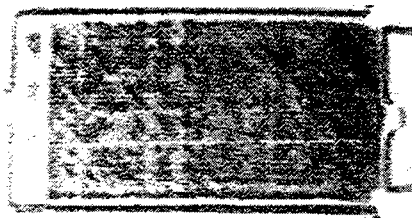


a: before any loading cycles.

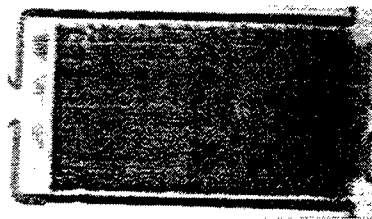


b: after 5000 loading cycles.

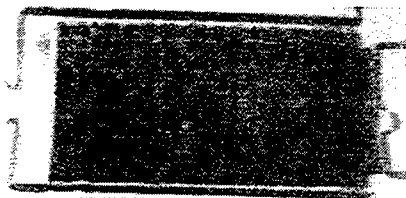
Figure 8.b: Ultrasonic scans of specimen X2.



a: before any loading cycles.



b: after 15000 loading cycles.



c: after 35000 loading cycles.

Figure 8.c: Ultrasonic scans of specimen X6.

PARAMETRIC SYSTEM IDENTIFICATION USING HIGHER-ORDER STATISTICS

Donghae Kim and Paul R. White

Institute of Sound and Vibration Research, University of Southampton, UK

1. INTRODUCTION

System identification algorithms based on output only measurements, which use second-order statistics, generally estimate only a spectrally equivalent minimum phase (SEMP) system whose poles and zeros lie inside the unit circle. However, several applications, such as the modelling of source signatures in reflection seismology, and the channel equalisation problem in communication systems, the minimum phase assumption is inappropriate. Since correlation carries no phase information, certain higher-order statistics (HOS), namely cumulants, have become increasingly popular in several areas of system identification and signal processing. During recent years, several methods using HOS have been proposed for the identification of the nonminimum phase (NMP) linear time invariant (LTI) systems.

As in ordinary spectral analysis, higher-order spectra analysis techniques can be divided into two categories: nonparametric (i.e., conventional or Fourier type) and parametric approaches, which are based on autoregressive (AR), moving average (MA) or ARMA models. The resolution of conventional estimators is limited by the "uncertainty principle" of the Fourier transform, namely, the trade-off between low resolution and high variance. Parametric methods first estimate the parameters of an underlying data-generating model and then use the model to compute the higher-order spectrum with high resolution, but require some form of model order determination.

This paper considers parametric system identification using HOS based algorithms. Further, it is concerned with the case where the input signal is unobservable. The main objectives of this paper are performance analyses and simulation studies, comparing the various algorithms. Theoretical background for HOS is briefly presented in section 2, and, in section 3, various algorithms for MA, AR and ARMA, are classified and presented. In section 4, the parameters of unknown systems are estimated for 100 Monte Carlo realisations. The estimated parameters and impulse response coefficients for the considered system are compared with the true values in terms of their mean squared error (MSE) and zero/pole positions. Discussion on the parametric identification methods is given in section 5.

2. BACKGROUND AND PRELIMINARIES

If $\{x(k)\}$, $k=0, \pm 1, \pm 2, \dots$ is a real stationary discrete-time signal and its moments up to order n exist, then

$$m_{nx}(\tau_1, \tau_2, \dots, \tau_{n-1}) \equiv E\{x(k) x(k + \tau_1) \dots x(k + \tau_{n-1})\} \quad (1)$$

represents the n th-order moment function of the stationary signal, which depends only on the time differences $\tau_1, \tau_2, \dots, \tau_{n-1}$, $\tau_i=0, \pm 1, \pm 2, \dots$ for all i . $E\{\bullet\}$ denotes statistical expectation. Similarly, the n th-order cumulants of $\{x(k)\}$ can be written as [1]:

$$c_{nx}(\tau_1, \tau_2, \dots, \tau_{n-1}) \equiv \text{Cum}[x(k), x(k + \tau_1), \dots, x(k + \tau_{n-1})] \quad (2)$$

If the process $\{x(k)\}$ is zero mean ($m_{1x}=0$), it follows that the second- and third-order cumulants are identical to the second- and third-order moments, respectively. However, the fourth-order cumulants are related to both the second- and fourth-order moments.

Consider the single-input single-output LTI model. In this model, the system $h(k)$ is assumed to be causal and stable, $v(k)$ is assumed to be independent, identically distributed and non-Gaussian, and $n(k)$ is Gaussian noise. The convolution equation describes the noise free output $x(k)$ of this system, $h(k)$ excited by input $v(k)$. The noisy signal $y(k)$, is observed.

$$x(k) = h(k) * v(k) = \sum_{i=0}^{\infty} h(i) v(k-i) \text{ and } y(k) = x(k) + n(k) \quad (3)$$

The system is assumed to be causal and all poles are inside the unit circle, $\{v(k)\}$ is assumed to be independent, identically distributed (i.i.d.) and non-Gaussian, i.e.,

$$c_{nv}(\tau_1, \dots, \tau_{n-1}) = \begin{cases} \gamma_{nv}, & \tau_1 = \tau_2 = \dots = \tau_{n-1} = 0 \\ 0, & \text{otherwise} \end{cases} \quad (4)$$

where γ_{nv} denotes the n th-order cumulant of $v(k)$.

The n th order cumulant can be expressed in function of $h(k)$ as follows [2]:

$$c_{ny}(\tau_1, \dots, \tau_{n-1}) = \gamma_{nv} \sum_{k=0}^{\infty} h(k) h(k + \tau_1) \dots h(k + \tau_{n-1}) \quad (5a)$$

$$\text{and } C_{ny}(\omega_1, \dots, \omega_{n-1}) = \gamma_{nv} H(\omega_1) H(\omega_2) \dots H(\omega_{n-1}) H(-\sum_{i=1}^{n-1} \omega_i) \quad (5b)$$

From (5b), new relationship [3], which links the n th- and $(n-i)$ th order cumulants ($i=1, \dots, n-2$) of the output sequence $x(k)$ can be derived as follows:

$$\frac{C_{nx}(\omega_1, \dots, \omega_{n-1})}{C_{(n-i)x}(\omega_1 + \dots + \omega_{i+1}, \omega_{i+2}, \dots, \omega_{n-1})} = \frac{\gamma_{nv} H(\omega_1) H(\omega_2) \dots H(\omega_{i+1})}{\gamma_{(n-i)v} H(\omega_1 + \omega_2 + \dots + \omega_{i+1})} \quad (6)$$

The time domain counterpart of (6) taking the Gaussian hypothesis for the additive measurement noise into account, can be written in terms of the measured output sequence cumulants of $y(k)$ ($n > 2, i=1, \dots, n-2$):

$$\sum_{k=0}^{\infty} h(k) c_{ny}(\tau_1 - k, \dots, \tau_{i+1} - k, \tau_{i+2}, \dots, \tau_{n-1}) = \sum_{k=s_2}^{\infty} \epsilon_n h(k) h(\tau_2 - \tau_1 + k) \dots h(\tau_{i+1} - \tau_1 + k) \\ \bullet [c_{(n-i)y}(\tau_1 - k, \tau_{i+2}, \dots, \tau_{n-1}) - c_{(n-i)v}(\tau_1 - k, \tau_{i+2}, \dots, \tau_{n-1})] \quad (7)$$

where $s_2 = \max(0, \tau_1 - \tau_2, \dots, \tau_1 - \tau_{i+1})$ and $\epsilon_n = \gamma_{nv} / \gamma_{(n-i)v}$. From this general relation, several algorithms can be obtained by setting n, i and τ_i 's, properly.

One of the most popular and useful approaches for the interpretation of time series data is the construction of white noise driven linear parametric models from the underlying physical process. Consider a real ARMA(p, q) process $\{x(k)\}$ described by

$$\sum_{i=0}^p a(i)x(k-i) = \sum_{j=0}^q b(j)v(k-j), \quad a(0)=1 \quad (8)$$

where $\{v(k)\}$ are i.i.d. random variables. The impulse response coefficients can be expressed in terms of the $a(i)$ and $b(i)$ parameters as follows:

$$\sum_{k=0}^p a(k)h(n-k) = \sum_{k=0}^p b(k)\delta(n-k) = b(n) \quad (9)$$

From (5a) and (9), the following equation can be obtained.

$$\begin{aligned} & \sum_{k=0}^p a(k)c_{ny}(\tau_1 - k, \tau_1 - \tau_2, \dots, \tau_1 - \tau_{n-1}) \\ &= \gamma_{nv} \sum_{k=0}^q b(k)h(k - \tau_1)h(k - \tau_2) \dots h(k - \tau_{n-1}) \end{aligned} \quad (10)$$

where the last equality follows from the change of variables, $k=i+\tau_l$. If $q=0$ and $b(0)=1$ in equation (10), becomes the normal equations used to estimate AR coefficients.

3. PARAMETER ESTIMATION

3.1 MA Parameter Estimation

The equation that describes a Moving Average of order q process $x(k)$ can be obtained from (8) by setting $p=0$, i.e.,

$$x(k) = \sum_{j=0}^q b(j)v(k-j) \quad (11)$$

where q is the order of the MA model. In this section, numerous methods which have been appeared in the literature for the identification of causal MA systems using higher-order statistics, are investigated through numerical simulations. These algorithms fall into three broad categories according to the method of solution: closed form solutions, linear algebraic solutions, and optimisation solutions. In closed form solutions there are the same equations as unknowns, as a result they are easy to manipulate. However they do not smooth the effect of additive noise on the estimated cumulants, consequently this paper does not consider such solutions.

So far, a large number of algorithms using linear algebraic solution have appeared in the literature. In the noisy case, putting $n=3$ and $i=1$ ($h(i)=b(i)$) in equation (7) and taking the i.i.d. hypothesis for measurement noise sequence into account, gives the relationship between correlations and third-order cumulants:

$$\sum_{k=0}^q b(k)c_{3y}(\tau_1 - k, \tau_2 - k) = \sum_{k=0}^q \epsilon_{32} b(k)b(\tau_2 - \tau_1 + k) [c_{2y}(\tau_1 - k) - \gamma_{2v}\delta(\tau_1 - k)] \quad (12)$$

where $\varepsilon_{32}=\gamma_3/\gamma_2$. Similar relationships between the different order cumulants can be derived. Many MA parameter estimation methods which use third-order cumulants and correlations, are obtained from equation (12). If one sets $\tau_1=\tau_2=\tau$ in (12), a MA identification approach based on both second and third-order statistics proposed by [4] is obtained. The so-called *GM* method is the first linear algebraic method which requires the solution of equations viewed as linear in the set of parameters. This method treats the problem as a linear system of equations in terms of $b(k)$ and $b^2(k)$ ($k=1, 2, \dots, q$). These equations are solved, using least-squares and, then $b(k)$ and $b^2(k)$ are combined to obtain the final estimates for $b(k)$. For the additive white noise case, rows of the coefficient matrix that contain the sample $c_{2x}(0)$ are removed; this eliminates $q+1$ equations, leaving only $2q$ equations in the $2q+1$ unknowns, i.e., an underdetermined system of equations. Tugnait [5] modified *GM* method appending $2q$ equations, and will be denoted as *GMT*.

Alshebeili, *et al.* [6] proposed a method that used all samples of the second- and third-order cumulants with great redundancy in the unknown vector. This method will be denoted *AVEC*. Most methods are sensitive to the true system order. Fonollosa and Vidal [7] proposed an algorithm using a linear combination of cumulants of any order to estimate the MA coefficients. This method, denoted *WS*, so-called *w*-slice method, has a good behaviour even if the order is overestimated.

Nonlinear least squares, an n th-order cumulant matching method, estimates the parameters $b(i)$ by minimising some performance criterion, e.g., the sum of the squared difference between the observed cumulants and the cumulants of the proposed model

$$\varepsilon^2 = \sum_R \left[c_{ny}(\tau_1, \dots, \tau_{n-1}) - \hat{c}_{ny}(\tau_1, \dots, \tau_{n-1}) \right]^2 \quad (13)$$

where R denotes the principal region. Firstly, Lii and Rosenblatt [8] proposed the cumulant matching method for the case of the third order diagonal cumulants. Later, Mendel [9] introduced objective functions using third-order and fourth-order cumulants in equation (13) and Nandi [10] proposed similar objective function using the third-order cumulants to avoid a numerical instability, denoted by *ND_OPT*.

Friedlander and Porat [11] developed the following MA optimisation method for estimating moving-average coefficients: (a) establish a vector, s , of second- and third-order statistics, (b) estimate s as $\hat{s} = s_N(y_N)$, y_N is a vector of N samples of the system output, (c) estimate the asymptotic covariance of s , Σ , as $\hat{\Sigma}(y_N)$, (d) obtain an initial estimate of the MA parameters $b(k)$, (e) compute the gradient of s evaluated at $b(k)$, (f) let

$$V(x) = [s(x) - \hat{s}]^T \hat{\Sigma}^{-1} [s(x) - \hat{s}], \text{ then } b(i) = \arg \min V(x) \quad (14)$$

If $\hat{\Sigma}$ is not positive definite, an eigenvalue decomposition must be performed to convert s into a lower-dimensional vector ξ . Step 5 is actually performed for ξ rather than s . Note that (13) can be obtained by assuming $\hat{\Sigma} = I$ in (14). The estimation of Σ generally imposes large computational burden.

Nonlinear optimisation may converge to a local minimum and is quite dependent on the initial vector. We propose modification to the procedures of [10], denoted by *ND_OPT* γ , for the optimisation solutions: (a) Estimate impulse responses by the robust estimation algorithms. (b) Estimate γ_{3v} by optimising the cumulant matching condition with the estimated impulse response of (a). (c) Estimate impulse response by optimising the cumulant matching condition with the initial vector including (a) and (b). (d) If necessary, repeat (b) and (c), but replace initial vector with final estimate of the impulse response and γ_{3v} . We also consider a modified version of the procedure of [11] for the optimisation solutions including the combination of second-, third- and/or fourth-order cumulant matching methods, denoted by *FP_ND23*.

3.2 AR Parameter Estimation

Assume that $x(k)$ is truly a p th-order AR(p) process, obtained from (8) by setting $q=0$, $a(0)=b(0)=1$, i. e.,

$$\sum_{i=0}^p a(i)x(k-i) = v(k) \quad (15)$$

where p is the order of the AR model. Many methods exist for determining AR coefficients of either the ARMA model or the AR model, according to the type of solutions. For identification of causal AR systems, the following correlation-based normal equations have been widely used.

$$\sum_{i=0}^p a(i) c_{2y}(\tau-i) = 0, \text{ for } \tau > 0 \text{ (or } \tau > q \text{ in the ARMA case.)} \quad (16)$$

If the AR order p is known then (16) is collected for p values of τ , from which the AR coefficients $a(1)$, $a(2)$, ..., $a(p)$ can be determined. When more equations are collected than unknowns, so that the resulting system is overdetermined, least-squares, total least-squares (TLS), or singular-value decomposition (SVD) techniques can be used to solve for the AR parameters. SVD techniques can also be used to determine the AR order p . Any 1-D cumulant slice satisfies the following AR recursion of maximum order p .

$$\sum_{i=0}^p a(i) c_{ny}(\tau-i, k_0, 0, \dots, 0) = 0, \text{ for } \tau > 0 \text{ (or } \tau > q \text{ in the ARMA case.)} \quad (17)$$

where k_0 is a parameter whose choice is discussed in the following. Concatenating (17) for $\tau=1, 2, \dots, p+M$, (or $\tau=q+1, q+2, \dots, q+p+M$ in the ARMA case) where $M \geq 0$ and k_0 is arbitrary, the cumulant based normal equations can be obtained. $C(k_0) \mathbf{a} = 0$ where the entries in Toeplitz matrix $C(k_0)$ are easily deduced, and $\mathbf{a} = [1, a(1), \dots, a(p)]^T$. If $C(k_0)$ has rank p then the corresponding 1-D slice of the n th order cumulant is a full rank slice and p AR coefficients can be solved. Equation (4.3) must be concatenated for $\tau=1, 2, \dots, p+M$ and $k_0 = -p, \dots, 0$ (or $\tau=q+1, q+2, \dots, q+p+M$ and $k_0 = q-p, \dots, q$ in the ARMA case) where $M \geq 0$.

Vidal and Fonollosa [12] addressed a different approach to the estimation of the coefficients of causal AR system. They showed that each sample of the impulse response of the AR system that generates the process may be expressed as a linear combination of cumulant slices of any order, thus providing a new framework to

combine cumulants of different orders. The AR w -slice algorithm can be summarised as the three steps: (a) Compute the minimum-norm weights that yield a causal w -slice using SVD to obtain the pseudo-inverse from this equation $S_a w = I$ where S_a is the anticausal w -slice matrix, w is the weight vector and I the anticausal impulse response. (b) Estimate the causal part of the impulse response using $\hat{h} = S_c w$ where S_c denotes the causal counterpart of S_a and \hat{h} is the estimated impulse response. (c) Solve the equation (10).

In the exhaustive search method [13], (a) a spectrally-equivalent (SE) stable causal AR(p) model is fit to the noisy measurements using only second-order statistics, (b) the resulting $A(z)$ is factored into n_r+n_c terms, where n_r is the number of real roots and n_c is the number of complex roots, (c) 2^l SE $\hat{H}(z)$'s are created, where $l = n_r+n_c/2$, by reflecting one or more of poles; let $\hat{\theta}(i)$ denote the AR parameters for the i th model, where $i=1,2, \dots, 2^l$, (d) a squared-error function is evaluated between $c_{3y}(m,n)$ and $c_{3y}(m,n|\hat{\theta}(i))$ over an admissible range of m and n values, for each $i=1,2, \dots, 2^l$, where $c_{3y}(m,n)$ is estimated from the given data and $c_{3y}(m,n|\hat{\theta}(i))$ is computed for the i th model, and, (e) the winning model is chosen as the one with the smallest mean squared error in the $c_{3y}(m,n)$.

In the optimisation method [13] the coefficients of the AR model, as well as the statistics of the non-Gaussian input and the Gaussian additive measurement noise are chosen to minimise an objective function. This objective function combines squared differences between correlations computed from the data and from an AR model, and cumulants computed from the data and from the same AR model. The respective differences are summed over correlation or cumulant ranges.

3.3 ARMA Parameter Estimation

Consider the ARMA model described by (8), which is assumed to be causal, stable, and generally nonminimum phase.

$$\sum_{i=0}^p a(i)x(k-i) = \sum_{j=0}^q b(j)v(k-j), a(0)=1 \quad (18)$$

Several methods have been reported in the literature for identifying the coefficients of an ARMA model from just noisy output measurements. Current cumulant-based parametric system identification methods falls into three broad categories: (a) methods that require computation of the residual MA (i.e., AR compensated) time series, and then estimate MA parameters from the residual time series: (b) methods that determine all of the ARMA coefficients simultaneously: and (c) methods based on nonlinear optimisation and linear programming.

Giannakis and Mendel [4] developed a method that estimates the ARMA parameters using autocorrelations and higher-order cumulants, the so-called residual time series method. The basic idea of their method is to estimate the AR coefficients first, and then form a residual MA time series from which the MA parameters can be estimated

by any of the methods described in section 3.1. The process $y(k)$ is applied as input to the p -th order filter, where $\{\hat{a}(i)\}$ are the AR coefficients previously computed. The

residual time series is given by $\hat{y}(k) = y(k) + \sum_{i=1}^p \hat{a}(i)y(k-i)$ and letting

$$\tilde{a}(k) = a(k) - \hat{a}(k), \text{ then } \tilde{y}(n) = \sum_{k=0}^q b(k)v(n-k) - \sum_{k=1}^p \tilde{a}(k)y(n-k).$$

Swami and Mendel [14] have developed the q -slice algorithm for determining MA coefficients in an ARMA model: (a) determine the AR coefficients by any one of the methods described earlier in section 3.2, (b) determine the first q IR coefficients using 1-D cumulant slices, and (c) determine the MA coefficients using (10). From (11), let $\tau = \tau_1, t = \tau_1 - \tau_2, \tau_3 = \dots = \tau_{n-1} = \tau$. Then, define the scalar function $f_n(t; \tau)$ as

$$f_n(t; \tau) = \sum_{k=0}^p a(k)c_{ny}(\tau - k, t, 0, \dots, 0) = \gamma_{ny} \sum_{k=0}^q b(k)h(k - \tau + t)h^{n-2}(k - \tau) \quad (19)$$

If AR coefficients are known, and the cumulants are computed from the data, then these functions can be computed. Since $b(k)$ is non-zero only over $0 \leq k \leq q$, $f_n(t; q)$ is $\gamma_{ny}h(t)b(q)$ and therefore from $h(t) = f_n(t; q)/f_n(0; q)$, $h(t)$ can be obtained. The MA coefficients are then obtained via (9). q -slices are required to estimate the first q coefficients of the impulse response; hence, this algorithm is called the “ q -slice” solution. The q -slice algorithm does not introduce errors due to the computation of a residual time series, and it is not recursive so that it is not prone to error propagation.

Vuattoux, *et. al.*, [15] presented an extension to the ARMA case of the w -slice algorithm for MA and AR models. They showed that each sample of the impulse response of the ARMA system may be defined as a linear combination of third-order cumulant slices. The impulse response $h(n)$ of the system that generates $y(n)$ satisfies the following recursion (where $\delta(n)$ is the Dirac pulse):

$$\sum_{i=0}^p a(i)h(n-i) = \sum_{k=0}^q b(k)\delta(n-k), \quad b(0) = a(0) = h(0) = 1, \quad b(q) \neq 0 \quad (20)$$

The impulse response $h(n)$ can be represented in a weighted sum of the third-order cumulant slices (w -slices):

$$C_w(i) = \sum_{j=-M}^N w(j)C_{3y}(i, j) \quad (21)$$

without previous knowledge of ARMA parameters if the weights $w(j)$ are appropriately chosen. If the weights $w(j)$ are chosen in such a way that: $C_w(0) = 1$ and $C_w(i) = 0$ when $K \leq i < 0$ and if the following conditions are fulfilled $M \geq p-q$, $N \geq q$ and $K-M \geq q$, then for all $i \geq -K$ $C_w(i) = h(i)$. The algorithm can be divided in 4 steps: (a) Computation with the SVD of the minimum-norm weights vector w_m : $w_m = S_a^\# I$ where $S_a^\#$ denotes the pseudo-inverse of S_a and w is the weights vector $w = (w_2 \ w_3(j) \dots w_4(j, k) \dots w_5(j, k, l) \dots)^T$ and I the anticausal impulse response $I = (0, \dots, 0, 1)^T$. (b) Estimation of the causal part of the impulse response using $\hat{h} = S_c w_m$ where $\hat{h} = (1, \hat{h}(1), \dots, \hat{h}(P))^T$ is the estimated impulse response, and S_c denotes the causal counterpart of S_a : (c) Solve (20) for $n = q+1, \dots, K$ with the least squares method to

estimate the AR parameters of the ARMA model. (d) Solve (20) for $n=1, \dots, q$ to estimate the MA parameters of the ARMA model.

Tugnait [16] extended the exhaustive search technique, first proposed by [9], to the identification of ARMA coefficients. This method uses prediction-error identification techniques to determine SEMP model and then applies procedures similar to the AR exhaustive search method. This leads to a model with p poles and $p-1$ zeros, but which is blind to all-pass factors because only correlation information is used in determining the SEMP model.

The rational transfer function $H(z)$ is the (one-sided) z -transform of $h(k)$. Assume $b_0=1$ and the signal $x(k)$ is ARMA($p, p-1$). Let $\theta=[a(1), a(2), \dots, a(p), b(1), b(2), \dots, b(p-1), \gamma_{2v}, \gamma_{2n}]^T$ and $\psi=[\theta^T, \gamma_{3v}]^T$ be vectors that contain the unknown parameters. In order to estimate the vector θ from the noisy observations $y(k)$. The following cost function is minimised with respect to ψ : $J(\psi) = J_2(\psi) + \lambda J_3(\psi)$, where $\lambda > 0$ is a scalar which determines the contribution of the third-order cumulants to the criterion.

4. SIMULATIONS

In this section, the algorithms described above are applied to an MA, AR and ARMA system and compared to each other in terms of mean square error and variance. The systems employed in the simulations are presented in Table 1.

Table 1 MA, AR and ARMA system

Index	Z-transform of systems	Zeros/Poles
NMP5 ^{*1}	$1+0.1z^{-1}-1.87z^{-2}+3.02z^{-3}-0.435z^{-4}+0.49z^{-5}$	zeros: 2, $0.7 \pm j0.7$, $0.25 \pm j0.433$
AR4 ^{*2}	$1/(1-0.3z^{-1}-0.1z^{-2}-0.39z^{-3}+0.72z^{-4})$	poles: $-0.6 \pm j0.7348$, $0.75 \pm j0.4873$
ARMA32 ^{*3}	$\frac{(1-1.3z^{-1}-1.4z^{-2})}{1/(1-1.4358z^{-1}+0.8867z^{-2}-0.1279z^{-3})}$	zeros: -0.7, 2 poles: 0.2, $0.6179 \pm j0.5077$

^{*1} NMP5 denotes the fifth-order nonminimum phase MA system

^{*2} AR4 denotes the fourth-order causal AR system

^{*3} Nonminimum phase ARMA(3,2) system

The input signal $v(k)$ is zero-mean exponentially distributed i.i.d. noise. The additive noise $n(k)$ is a zero mean and the signal to noise ratio in this paper is defined as $SNR=E\{x^2(k)\}/E\{n^2(k)\}$. Output data length was $N=2048$ in this study. The impulse response coefficients of the unknown system were computed for 100 output realisations at SNR values of ∞ (noise free case), 100, 10 and 1. Mean squared error (MSE_{av}) for the averaged impulse responses, mean (μ_{MSE}) of mean squared error for each impulse responses of Monte Carlo runs, respectively, are defined as

$$MSE_{av} = \frac{\sum_{n=0}^q (h(n) - h_{av}(n))^2}{\sum_{n=0}^q h^2(n)}, \quad \mu_{MSE} = \text{mean} \left[\frac{\sum_{n=0}^q (h(n) - h_i(n))^2}{\sum_{n=0}^q h^2(n)} \right], \quad (22)$$

where $h(n)$, $h_{av}(n)$ and $h_i(n)$ are the true, the averaged, and individual impulse responses, respectively, and $mean[\bullet]$ denotes the mean of the argument.

The following methods were used for MA parameters estimation:

GMT_23. GMT method [4,5] using 2nd- and 3rd-order diagonal cumulants.

AV_23S. AVEC method [6], but SVD is used after solving LS solution.

WS_23. W-slice method [7] using autocorrelations and all slices of 3rd-order cumulants.

ND_OPT γ . Cumulant matching method, but includes optimisation of γ_3 .

FP_ND23. Minimum variance cumulant matching method, but using autocorrelations and all information of third-order cumulants.

The following linear algebra methods were used for the causal AR parameters:

YW_2. Yule-Walker equation using the autocorrelations.

YW_3. Similar to YW_2, but using the third-order cumulants [4].

YW_20. Similar to YW_2, but rows of the coefficient matrix that contain the sample $c_{2y}(0)$ are removed.

WS_3. Vidal and Fonollosa [12] method using all slices of the third-order cumulants.

OPT. Optimisation [13] method.

The following methods were used to estimate the parameters of the ARMA systems:

QS_TLS. q -slice algorithm [14]; estimate the AR and impulse response coefficients simultaneously and use the Total Least Squares (TLS) solution.

RTS_AV. First, use YW_23 for the AR system and AV_23 for the residual time series [4] of the MA system.

ES. First, use Prediction Error Method (PEM) and then apply exhaustive search [16] method.

CM23. Cumulant matching method using the autocorrelations and third-order cumulants.

WS. w -slice algorithm [15].

Table 2 ~ Table 4 show MSE and μ_{MSE} of NMP5, AR4 and ARMA32 systems with respect to the variation of SNR. Fig. 1 displays the estimated zero positions of NMP5 system for each run. Fig. 2 displays the estimated pole positions of AR4 system for each run, and Fig. 3 displays the estimated pole/zero positions of ARMA32 system for each run. Note that the solution of some methods are not guaranteed to be stable, in which case the unstable poles have been replaced with their reciprocals.

The following conclusions are readily drawn:

- (1) For the case of MA system in Table 2 and Fig. 1, optimisation solutions give better results than linear algebraic solutions in most cases, but require longer data length and computational complexities. Among linear algebra solutions, AV_23S and WS_23 method have better performance and the latter is less bias but has a larger variance compared with the former.

- (2) For the case of causal AR system, most algorithms worked well as shown in Table 3 and Fig. 2. The algorithms using the normal equations give slightly better results than w -slice algorithms except at low SNR (eg. SNR=1). The algorithms using the autocorrelations have smaller MSE than others, but their performances are degraded at low SNR. Removing the rows of the coefficients matrix that contain the sample $c_{2y}(0)$, the algorithms using the autocorrelations can reduce the effects of additive Gaussian noise at low SNR.
- (3) For the case of ARMA system in Table 4 and Fig. 3, the MSE of AR parameters of ARMA model is smaller than that of the MA parameters of ARMA model. *RTS_AV*, *ES* and *WS* give better results than others. However, for estimating pole positions, *WS* method has greater variance than the other two methods. *QS_TLS* gives good estimates of pole positions, but poor estimates of zero positions and impulse responses. When few samples are available the *ES* shows the best performance but it is inconsistent and when a large number of samples are available the *RTS_AV* is better.

5. CONCLUSIONS

In this paper, we have discussed the parameter estimation methods using higher order cumulants and presented performance analyses and simulation studies. Cumulant-based solutions are usually computationally more expensive than corresponding correlation-based methods. However, the correlation cannot provide complete information, such as the location of the zeros and the detection of all-pass factors in an ARMA model, but cumulants provide a complete solution. In the simulations, the proposed modifications have improved the performance of the existing methods.

REFERENCES

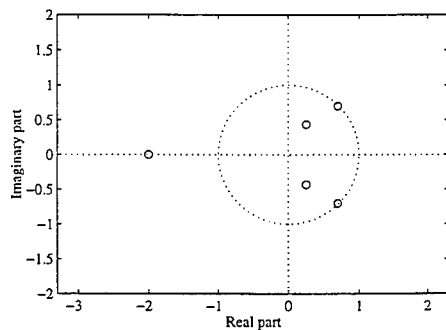
1. Nikias, C.L. and Petropulu, A.P., *Higher-Order Spectral Analysis: A Nonlinear Processing Framework*, Prentice-Hall, 1993.
2. Brillinger, D.R. and Rosenblatt, M., "Asymptotic theory of estimates of k th order spectra," *Advanced Seminar on Spectral Analysis of Time series* (ed. B. Harris), Wiley, 1967, pp. 153-188.
3. Favier, G., Dembede, D. and Peyre, J.L., "ARMA identification using high-order statistics based linear methods: An unified presentation," *Proc. Int. Conf. EUSIPCO-94*, 1994, pp. 203-207.
4. Giannakis, G. B. and Mendel, J.M., "Identification of nonminimum phase systems using higher order statistics," *IEEE Trans. on Acoustics, Speech, and Signal Processing*, Vol. 37(3), 1989, pp. 360-377.
5. Tugnait, J.K., "Approaches to FIR system identification with noisy data using higher order statistics," *IEEE Trans. on Acoustics, Speech, and Signal Processing*, Vol. 38(7), 1990, pp. 1307-1317.

6. Alshebeili, S.A., Venetsanopoulos, A.N. and Cetin, A.E., "Cumulant based identification approaches for nonminimum phase FIR systems," *IEEE Trans. on Signal Processing*, Vol. 41(4), 1993, pp. 1576-1588.
7. Fonollosa, J. A. R. and Vidal, J., "System identification using a linear combination of cumulant slices," *IEEE Trans. on Signal Processing*, Vol. 41(7), 1993, pp. 2405-2412.
8. Lii, K.S. and Rosenblatt, M., "Deconvolution and estimation of transfer function phase and coefficients for non-Gaussian linear process," *The Annals of Statistics*, Vol. 10(4), 1982, pp. 1195-1208.
9. Mendel, J.M., "Tutorial on higher-order statistics(spectra) in signal processing and system theory: theoretical results and some applications," *Proc. of the IEEE*, Vol. 79, 1991, pp. 278-305.
10. Nandi, A.K., "Blind identification of FIR systems using third order cumulants," *Signal processing*, Vol. 39, 1994, pp. 131-147.
11. Friedlander, B. and Porat, B., "Asymptotically optimal estimation of MA and ARMA parameters of non-Gaussian processes from high-order moments," *IEEE Trans. on Automatic Control*, Vol. 35(1), 1990, pp. 27-35.
12. Vidal, J. and Fonollosa, J.A.R., "Causal AR modeling using a linear combination of cumulant slices," *Signal Processing*, Vol. 36, 1994, pp. 329-340.
13. Tugnait, J.K., "Fitting noncausal AR signal plus noise models to noisy non-Gaussian linear processes," *IEEE Trans. on Automatic Control*, Vol. 32, 1987, pp. 547-552.
14. Swami, A. and Mendel, J.M., "ARMA parameter estimation using only output cumulants," *IEEE Trans. on Acoustics, Speech, and Signal Processing*, Vol. 38(7), 1990, pp. 1257-1265.
15. Vuattoux, J.L., Zazula, D. and Carpentier, E.L., "Causal ARMA parameter estimation using a linear combination of third-order cumulant slices," *IEEE Signal Processing ATHOS Workshop on Higher-Order Statistics, HOS'95*, 1995, pp. 464-468.
16. Tugnait, J.K., "Identification of nonminimum phase linear stochastic system," *Automatica*, Vol. 22, 1986, pp. 457-462.

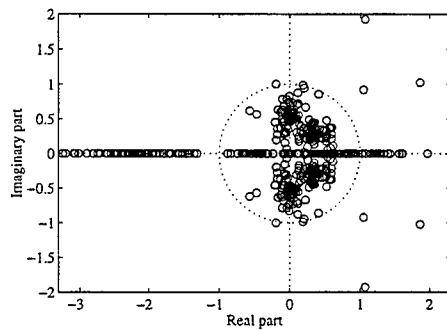
Table 2 MSE_{av} and μ_{MSE} of NMP5 MA system with respect to SNR (N=2048)

SNR	∞ (noise free)		100 (20dB)		10 (10dB)		1 (0dB)	
Methods	MSE_{av}	μ_{MSE}	MSE_{av}	μ_{MSE}	MSE_{av}	μ_{MSE}	MSE_{av}	μ_{MSE}
<i>GMTI_23</i>	0.4044	9.7577	0.4044	9.7530	0.4039	9.3144	0.4183	9.9455
<i>AV_23S</i>	0.0205	0.1140	0.0205	0.1140	0.0205	0.1142	0.0502	0.1006
<i>WS_23</i>	0.0416	0.1347	0.0416	0.1347	0.0418	0.1350	0.1577	0.3034
<i>ND_OPTγ</i>	0.0068	0.6357	0.0068	0.6369	0.0913	1.7935	0.0023	0.1237
<i>FP_ND23</i>	0.0003	0.1006	0.0003	0.1003	0.0005	0.1195	0.0021	0.0696

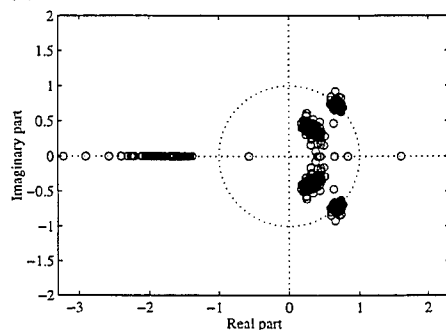
(a) True Zeros



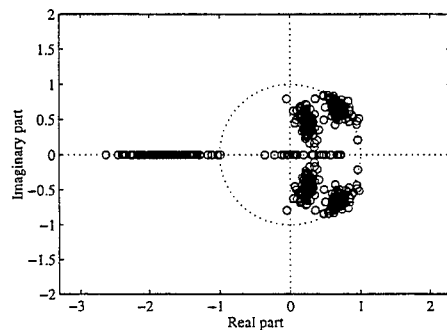
(b) *GMTI_23*



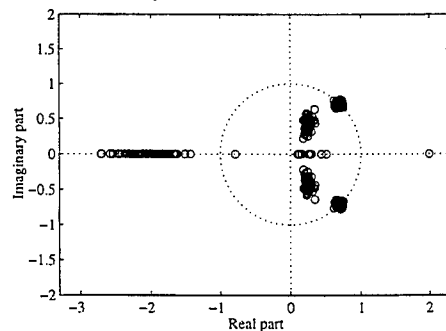
(c) *AV_23S*



(d) *WS_23*



(e) *ND_OPT γ*



(f) *FP_ND23*

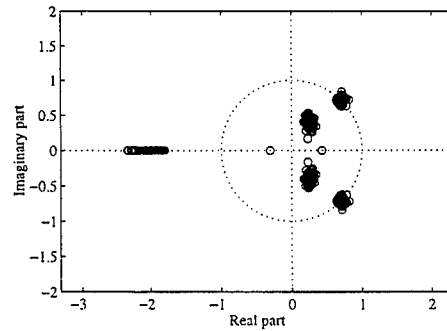
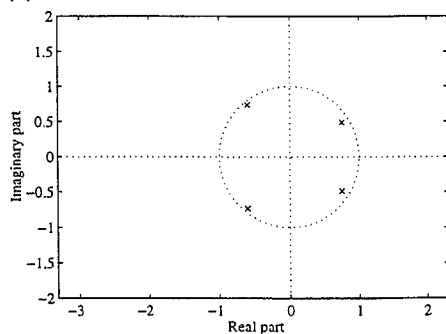


Fig.1 Estimated zero position (NMP5, N=2048, SNR=10)

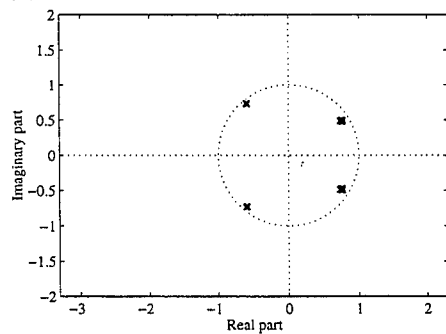
Table 3 MSE_{av} and μ_{MSE} of AR4 AR system with respect to SNR (N=2048)

SNR	∞ (noise free)		100 (20dB)		10 (10dB)		1 (0dB)	
Methods	MSE_{av}	μ_{MSE}	MSE_{av}	μ_{MSE}	MSE_{av}	μ_{MSE}	MSE_{av}	μ_{MSE}
YW_2	9.999e-6	6.336e-4	9.999e-6	6.336e-4	1.010e-5	6.337e-4	2.954e-2	3.071e-2
YW_3	1.816e-4	2.540e-3	1.816e-4	2.540e-3	1.819e-4	2.544e-3	5.904e-3	1.434e-2
YW_20	7.160e-6	1.152e-3	7.160e-6	1.152e-3	7.180e-6	1.151e-3	1.514e-5	1.940e-3
WS_3	1.051e-3	3.712e-3	1.051e-3	3.712e-3	1.052e-3	3.711e-3	4.830e-3	1.316e-2
OPT	4.504e-2	6.384e-2	8.920e-2	1.144e-1	4.518e-2	6.406e-2	4.636e-2	1.087e-1

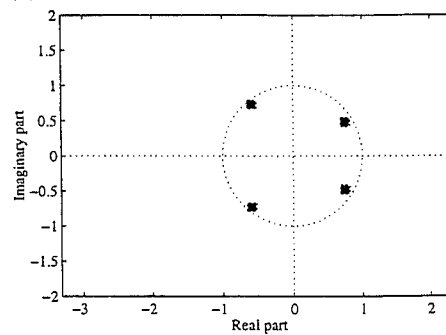
(a) True Poles



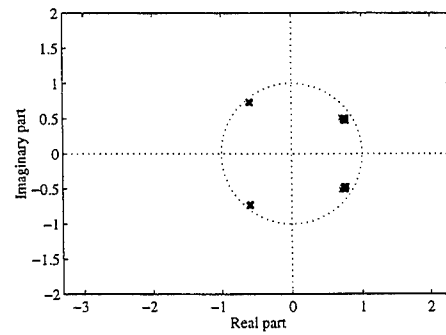
(b) YW_2



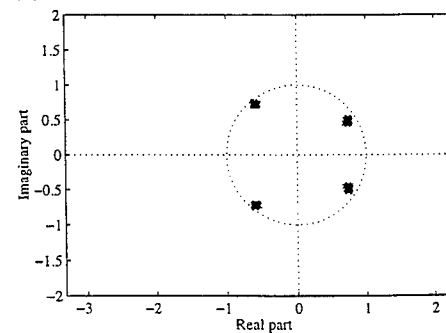
(c) YW_3



(d) YW_20



(e) WS_3



(f) OPT

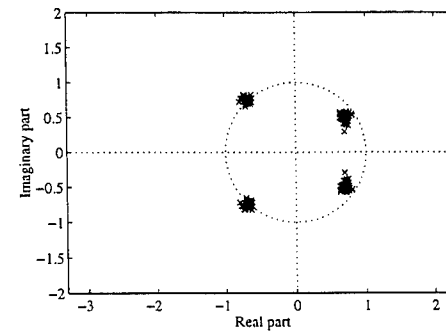
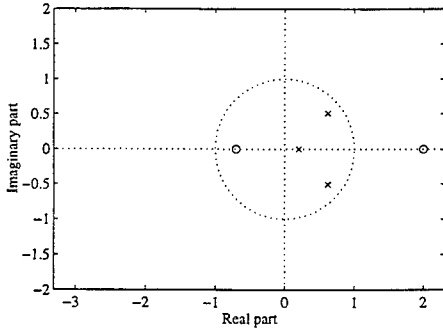


Fig.2 Estimated pole position (AR4, N=2048, SNR=10)

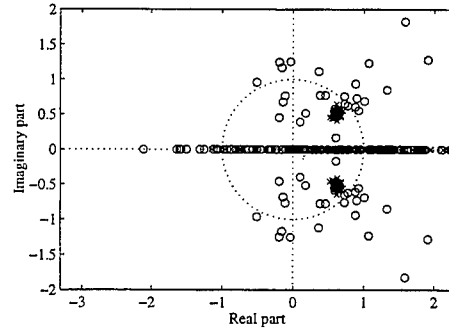
Table 4 MSE_{av} and μ_{MSE} of ARMA32 ARMA system with respect to SNR (N=2048)

SNR	∞ (noise free)		100 (20dB)		10 (10dB)		1 (0dB)	
Methods	MSE_{av}	μ_{MSE}	MSE_{av}	μ_{MSE}	MSE_{av}	μ_{MSE}	MSE_{av}	μ_{MSE}
<i>QS_TLS</i>	5.406e+0	1.342e+2	5.405e+0	1.341e+2	5.309e+0	1.262e+2	2.969e+0	1.011e+2
<i>RTS_AV</i>	3.191e-1	5.521e-1	3.191e-1	5.521e-1	3.189e-1	5.519e-1	8.387e-1	8.618e-1
<i>ES</i>	1.422e-2	1.338e+0	1.421e-2	1.337e+0	1.415e-2	1.234e+0	3.298e+1	2.127e+3
<i>CM23</i>	1.470e-1	1.560e+0	1.464e-1	1.558e+0	1.479e-1	1.573e+0	5.418e+1	2.889e+3
<i>WS</i>	2.900e-1	4.985e-1	2.900e-1	4.985e-1	2.898e-1	4.986e-1	4.717e-1	6.096e-1

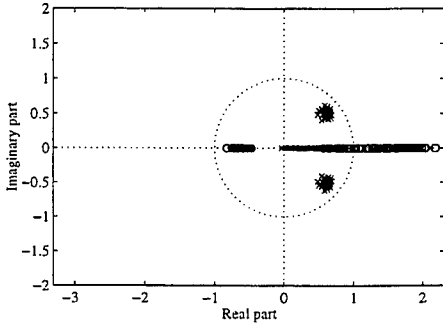
(a) True Zeros/Poles



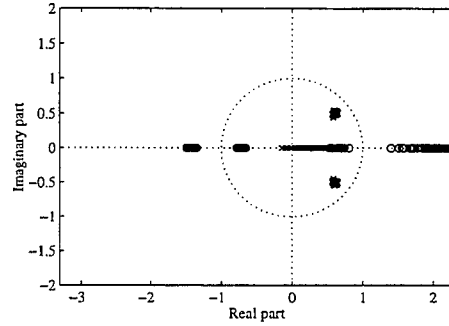
(b) *QS_TLS*



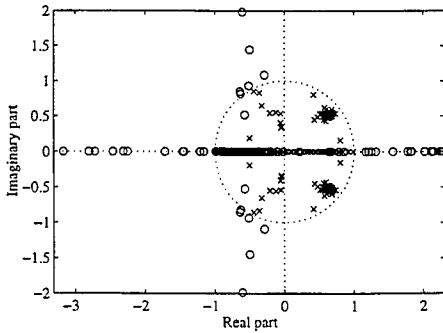
(c) *RTS_AV*



(d) *ES*



(e) *CM23*



(f) *WS*

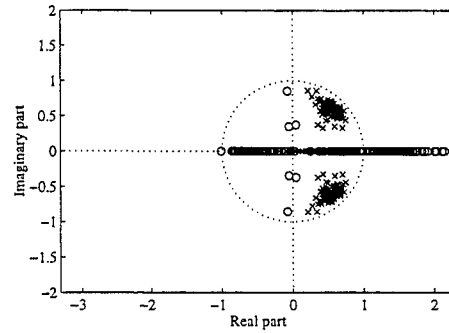


Fig.3 Estimated pole/zero position (ARMA32, N=2048, SNR=10)

PASSIVE AND ACTIVE CONTROL II

Static and Dynamic Structural Evaluation of Workpiece/Fixturing Systems for Machining Operations

Chung-Yung Wu ¹
Reha R. Haymanali ¹
Edward C. De Meter ²
Martin W. Trethewey ¹

Department of Mechanical Engineering ¹
Department of Industrial & Manufacturing Engineering ²
Penn State University
University Park, PA 16802
USA

ABSTRACT

A number of factors can affect the geometric accuracy of machined surfaces, such as machine tool positioning error, thermal errors, and variability of the workpiece datum features. One of the major factors is the cutting operation which applies a combination of static and dynamic forces on the workpiece. The static forces induce deflections which need to be considered in order to maintain acceptable part tolerances. The dynamic loads are important since they can potentially excite resonances in the workpiece creating damaging chatter situations and unacceptable geometric errors. The method in which the workpiece is held in the machining operation can have a significant impact on the structural behavior. The placement of the locators and supports affects the workpiece boundary conditions which in turn affects the system's static and dynamic structural characteristics. The paper presents a case study where the static and dynamic structural characteristics of the workpiece/fixturing system in relation to the manufacturing process are evaluated. A combination of experimental and computational structural analysis methods is used. Experimental methods are used to evaluate the workpiece compliance and structural resonances in situ. A process model is used to estimate the cutting forces during manufacturing. The results from these analyses are compiled to assess the relative errors. A Finite Element Model is developed and used to evaluate various fixturing configurations which meet the desired manufacturing specifications.

I. INTRODUCTION

A variety of factors can affect the geometric accuracy of machined surfaces. Examples include: machine tool positioning error, workpiece datum feature variability, and thermal and structural distortion of the workpiece during machining. Of these, structural distortion is one of the most difficult to control. Workpiece structural distortion manifests itself in two basic forms, one related to the static characteristics and one related to the structural dynamic behavior of the system. Both types of distortion are

dependent on the inherent structural characteristic of the workpiece and the boundary conditions imposed when the workpiece is anchored to the machine tool.

The workpiece is held in the machine tool by a machining fixture which consists of locators, clamps, supports and a base. Locators are passive elements used to define the position of the workpiece with respect to a machine tool axial reference frame. Clamps are mechanisms that are used to hold the workpiece against the locators and supports. Most clamps are actuated either hydraulically, pneumatically, or manually with a constant preload. Supports are mechanisms that are used to increase the rigidity of the workpiece. They are extended into contact with the workpiece after the workpiece has been clamped against the locators. The base is the structural interface between the machine tool table and the locators, supports, and clamps.

The structural distortion results from the complex, dynamic forces that are exerted on the workpiece by the cutting process. The dynamic distortion is caused by the time variant nature of the cutting forces which potentially may excite resonant conditions in the workpiece. The dynamic response of the workpiece affects the cutting force by altering the instantaneous chip load. These conditions can have negative consequences on the production quality and the tool life. In many applications, the dynamics are further complicated by the fact that the workpiece mass and stiffness can vary significantly with the inherent geometric changes produced by the machining process.

The placement of fixture elements greatly affects the boundary conditions imposed on the workpiece. This in turn affects the static and dynamic structural characteristics. Consequently for many applications, workpiece distortion can be controlled through proper fixture design. Typically machining fixtures are designed and implemented on a trial and error basis. This process involves creating a detailed fixture design, manufacturing the fixture, utilizing the fixture in the machining process, assessing the geometric variability of the machined workpiece, and using this knowledge to improve the design of the fixture and/or process. In general this is a very expensive and time consuming process.

To a large degree, this cycle time can be reduced through the application of structural analysis. The objective of this paper is to describe a case study in which a combination of experimental and computational structural analysis methods was employed to improve the design of a machining fixture to help control workpiece distortion.

II. BACKGROUND

A manufacturer of image processing equipment was experiencing difficulties in manufacturing the drive plate shown in Figure 1. Two critical features of the drive plate are a pair of film tracks and a set of four pads. Each pad has a clearance hole for a bolt to fasten the drive plate to the image processing machine. The pads and film tracks geometries ultimately dictate the critical film paths in the image processing machine.

Consequently both features need to be manufactured with great precision. In particular, the film tracks must be manufactured to within a bi-lateral profile tolerance of 2.54×10^{-1} mm (0.01 in) with respect to a datum plane defined by the four pads. The manufacturer was having difficulty in satisfying this tolerance on a consistent basis.

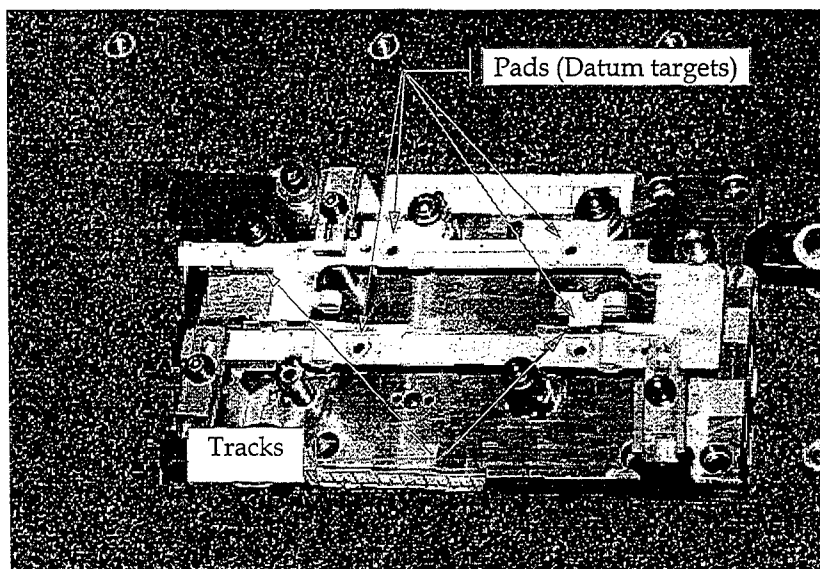


Figure 1. Drive plate workpiece mounted in original fixture system.

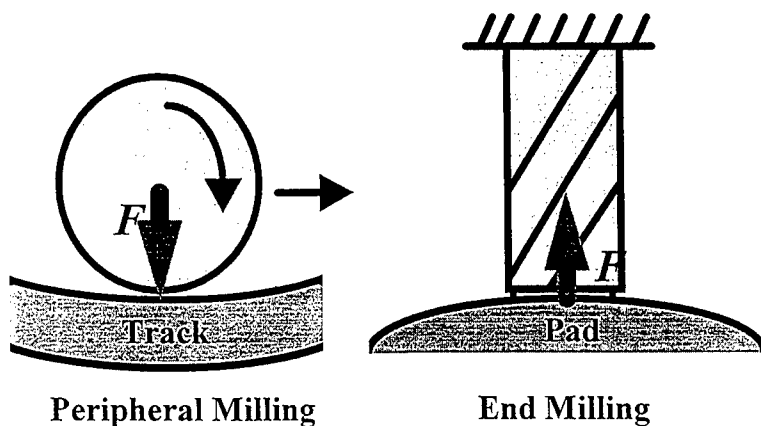


Figure 2. Illustration of cutting forces due to the milling processes.

The drive plate initiates as a casting (A356 T51 aluminum) and is subsequently machined in two setups. The film tracks and pads are machined in the fixture shown in Figure 1. The film tracks are peripherally milled with a side tooth cutter, shown in Figure 2. Due to the kinematic-

geometry of the cutter, the forces exerted on the workpiece push it away from the cutter in the radial direction. Consequently the film tracks have the tendency to be undercut. The pads are milled axially with an end mill. The forces exerted by this process pull the workpiece into the cutter. Consequently the pads have the tendency to be overcut. The manufacturer did not know to the degree which the undercutting of the film tracks and the overcutting of the pads contributed to the measured profile errors of the film track. The focus of this effort is to quantify this contribution, and if necessary determine how the boundary conditions imposed by the fixture could be changed to modify the static and dynamic structural response of the workpiece and potentially reduce production failure rates.

III. WORKPIECE/FIXTURE STRUCTURAL EVALUATION METHODOLOGY

A combination of experimental and computational methods was used to examine the static and dynamic characteristics of the workpiece/fixturing system in relation to the profile errors. The following assumptions were made in the analysis:

1. *Mode of Flexure*: Considering the drive plate geometry and fixturing design, only flexure, as illustrated in Figure 3, was considered. In other words, the drive plate was analyzed as if it were a plate subject to a sequence of normal loads.
2. *Invariant Stiffness and Dynamic Response*: The drive plate originates as a casting and consequently machining of the film tracks and pads results in very little material removal. As a result the geometry, mass, stiffness, and dynamic response of the fixture-workpiece system were considered invariant.
3. *Stick-Stick Boundary Conditions*: The drive plate is pinched against the locators and supported by manual clamps. It was assumed that no slip occurred at these joints.
4. *Chip Load Independence*: The magnitude of workpiece flexure is small relative to the nominal chip loads seen by the cutting tool. As a consequence, it was assumed that workpiece flexure is independent of the cutting force.

Experimental methods were applied to the existing system, as seen in Figure 1, to evaluate the fixture/workpiece static (compliance) and dynamic (resonant frequencies) structural characteristics. This was done in order to achieve the most accurate assessment of the in situ characteristics. An analytical milling force model was used to predict the forces (as a function of time) acting on the film tracks and pads during machining. The predicted machining forces were coupled with the static compliance data in order to assess the static flexure of the workpiece and the resultant profile error. The spectral contents of the milling forces were compared to the resonant frequencies of the fixture-workpiece system in order to evaluate the effects of forced vibration. Assessment of these results provides insight into the problem regions and an indication of the potential for fixture redesign.

A. Characterization of Fixture-Workpiece Compliance

Since the workpiece is a plate like structure, only normal loads need to be considered. Furthermore, only the important machined zones of the workpiece, such as the pads and the film tracks need to be considered. Ten nodes were identified on or near these important workpiece features and used for the static compliance evaluation, as seen in Figure 3. The static compliance was measured using a specially designed test rig similar to Figure 4. The test equipment has the capability to apply a controlled point load and measure the corresponding deflections at any desired position on the workpiece. The compliance testing procedure can be summarized as;

1. A 22.24 N (5 lb) load is applied at a test node. The deflections at all ten nodes are recorded with digital indicators each with a resolution of 1.27×10^{-3} mm (5.0×10^{-5} in). The load is released, reapplied and deflections recorded. A total of four sets of load-deflection data are obtained to improve statistical reliability.
2. To evaluate potential nonlinear effects, additional load-deflection data was recorded with 44.48 N (10 lb) and 66.72 N (15 lb) respective forces applied.
3. The load-deflection data for the twelve data was plotted and evaluated. After linear behavior was assessed, a linear regression was applied to estimate the compliance (mm/N) value for each node.
4. The ten nodal compliance values were arranged in a 10×1 column vector array.
5. Steps 1- 4 were repeated for each of the remaining nine test nodes.

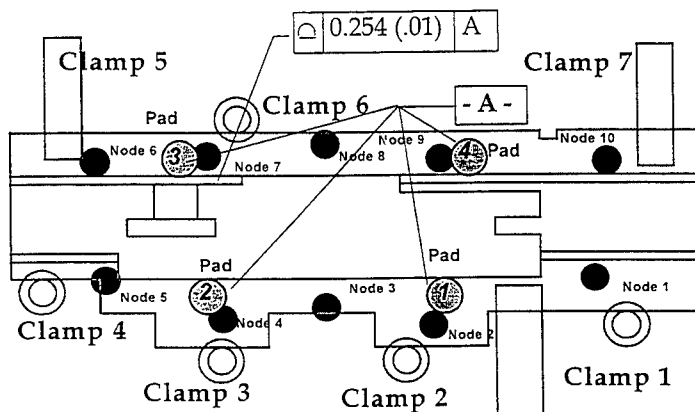


Figure 3. Experimental nodal layout on the drive plate.

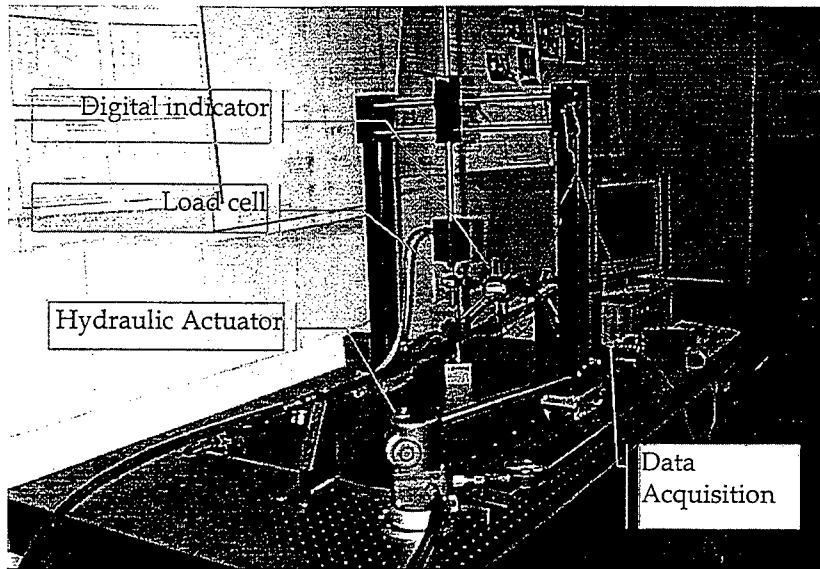


Figure 4. Static compliance tester.

The resulting ten arrays were arranged to form a square 10×10 compliance matrix, $[C]$. Each term in the compliance matrix represents the deflection of a unit load at the respective set on nodes. For example, C_{16} , represents the deflection at node 1 for a unit load applied at node 6. With the assumption of linearity, the $[C]$ matrix would be expected to be symmetric from Maxwell's Reciprocal Theorem. However, experimental and nonlinear effects combine to produce nonsymmetric compliance terms, $C_{ij} \neq C_{ji}$, which differ on the order of 10% for nodes which had appreciable deflections. Measurement difficulties are encountered when localized stiffness is large causing deflections to become very small, on the order of the digital indicator resolution (1.27×10^{-3} mm). Nonlinear effects are introduced by the inherent contact mechanics of the interface between the workpiece and fixture. Since the nonsymmetric effects were viewed as being small, the linearity assumption was imposed by forcing the compliance to be symmetric by averaging itself with its transpose.

B. Characterization of Fixture-Workpiece Dynamic Response

Next, the structural resonances of the workpiece/fixture system were evaluated experimentally. Standard experimental modal analysis procedures were used (Figure 5). An accelerometer was fixed at a node and a roving impact test was employed to estimate the frequency response functions at each of the ten nodal points. The magnitude of a typical frequency response function is shown in Figure 6. The modal characteristics were estimated with the StarModal software using a rational fraction polynomial identification routine. The first four structural natural frequencies are listed in Table 1.

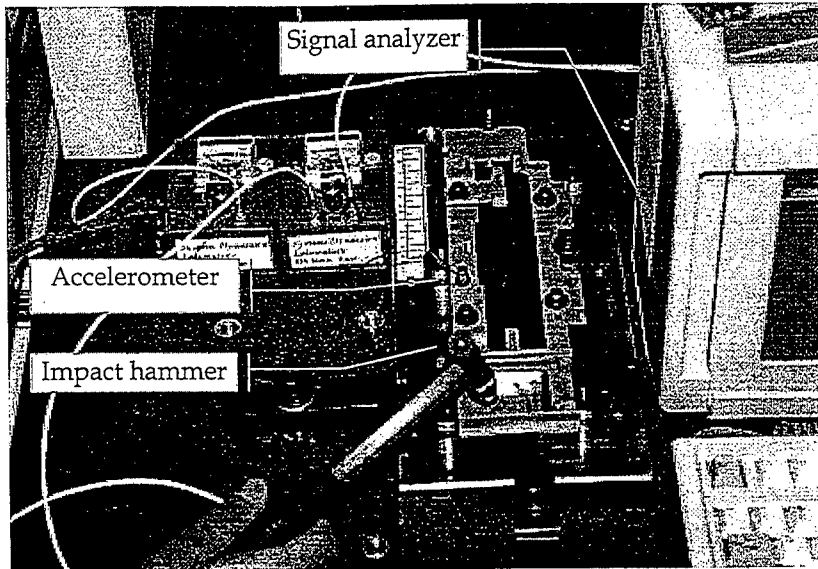


Figure 5 The experimental set up for the modal analysis testing. A roving impact was used with a fixed accelerometer.

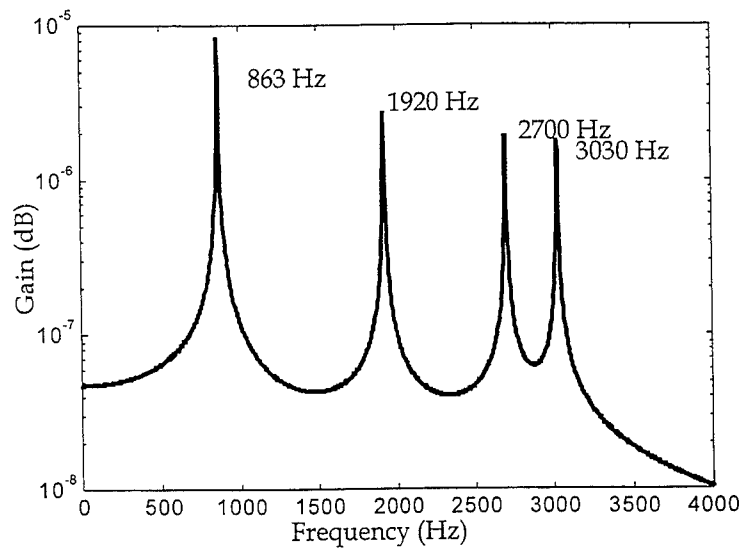


Figure 6. The magnitude of a typical Frequency Response Function from the drive plate fixture system.

Table 1. Experimental natural frequencies of the drive-plate fixture-workpiece system.

Mode	Frequency (Hz)
1	862.74
2	1920
3	2700
4	3030

C. Characterization of Milling Forces

Each track undergoes one 3.30 mm (0.13 in) rough cut and one 2.54×10^{-1} mm (0.01 in) finish cut. An 18-tooth 76.2 mm (3 in) diameter end-mill was used for peripheral cutting. The pads were end milled with a 2.54 mm (0.1 in) finish cut using a 15.88 mm (6.25×10^{-1} in) cutter.

The resultant milling force exerted on the workpiece is dependent upon the stress on the contact area between the cutter and the workpiece. The stress in this region is in turn dependent upon the workpiece material and the instantaneous chip load being swept away. The chip load is affected by the kinematic geometry of the cutter relative to the cut and by cutter-workpiece deflection. If cutter-workpiece deflection is relatively small, then the chip load is strictly affected by the cutter kinematic geometry. Since the cutter geometry is fixed, variation in the resultant milling force is due to the angular rotation. Under steady state conditions in which the swept geometry of the cut region is constant along with spindle speed, the resultant milling force is periodic with respect to both rotation and time. Under these conditions, analysis of the forces can be evaluated using the EMSIM (End Milling Simulation Interface). EMSIM was developed by the University of Illinois at Urbana-Champaign and can be accessed at "<http://mtamri.me.uiuc.edu/software.testbed.html>" [1]. EMSIM was used to characterize the various milling forces acting on the workpiece during the cutting operations. It was assumed that the milling forces were independent of workpiece deflection. Consequently the static chip load model in EMSIM was used to predict the steady state, radial force exerted on the film tracks by the side tooth cutter and the steady state, axial force exerted on the pads by the end mill. Both operations were modeled as step cuts. The tool and process parameters for these operations can be found in Table 2.

Table 2. Process parameters used in EMSIM to estimate the milling forces.

	Film track/finish	Pad
Model	static	static
Workpiece material	Cast Aluminum	Cast Aluminum
Tool material	Uncoated Carbide	Uncoated Carbide
End mill diameter mm (in.)	76.2 (3)	15.875 (0.625)
Projection length mm (in.)	97.79 (3.85)	92.075 (3.625)
Number of flutes	18	4
Helix angle (Degree)	15	30
Radial rake angle (Degree)	10	10
Milling convention	Climb Milling	Climb Milling
Axial depth of cut mm (in.)	5.1689 (0.2035)	2.54 (0.1)
Radial depth of cut mm (in.)	0.254~0.762 (0.01~0.03)	15.875 (0.625)
Feed per tooth mm/RPM (in/RPM)	0.03352 (0.00132)	0.05280 (0.00208)
Spindle speed (RPM)	250	3000

The characteristics of the vertical and end milling forces, Figures 7 and 8, show a high level of harmonic content. The milling forces are periodic with respect to the cutter rotation and hence with respect to time. The respective milling force power spectra are also illustrated in Figures 7 and 8. The radial milling has a static load (average) of 20.02 N (4.5 lb) with a fundamental frequency of 75 Hz. Most of the "power" is contained in the static (DC) component and the first six harmonics. The axial milling produces an average static load of 12.72 N (2.86 lb) with a fundamental frequency of 200 Hz. Again, the majority of the power is contributed by the static and the fundamental frequency components.

D. Profile Error Assessment

The results from the compliance and experimental modal analysis can be used in conjunction with the milling force predictions to evaluate profile errors attributed to structural deformation. The error analysis concentrates on the tracks and pads since they are the key features subject to profile tolerances problems.

Computation of the static deflection profile error in the film tracks used the maximum radial force 39.32 N (8.54 lb) computed by EMSIM in a quasi-static manner. This force was assumed to act independently at each node (node 1,5,6,7,9 and 10) near the two film tracks. The corresponding nodal displacements were computed by multiplying this force with the experimentally derived, driving point compliance coefficients. A similar procedure was used to compute the nodal displacements (node 2,4,7 and 9) at the four pads due to the application of the minimum (greatest negative) axial force.

Because the tracks were peripherally milled, they were undercut; however, the pads were overcut by the end milling operation. The track profile tolerance was specified with respect to the pads and the profile error was associated with the dimension difference between two geometries. The profile error was computed as two times the difference between the maximum track node displacement and the minimum (greatest negative) pad node displacement. The computed profile error was 8.81×10^{-2} mm (3.47×10^{-3} in). Since the profile tolerance is bilaterally allocated, this profile error consumes 70% of the allowable tolerance.

By itself, static deflection of the workpiece will not cause the film tracks to be manufactured out of tolerance. However, since static deflection is but one of many contributors to workpiece geometric error, its relatively large contribution is of concern. The static analysis also revealed that the nodes near pad 4 experienced relatively large deflections when subject to either the maximum radial load or the minimum axial load.

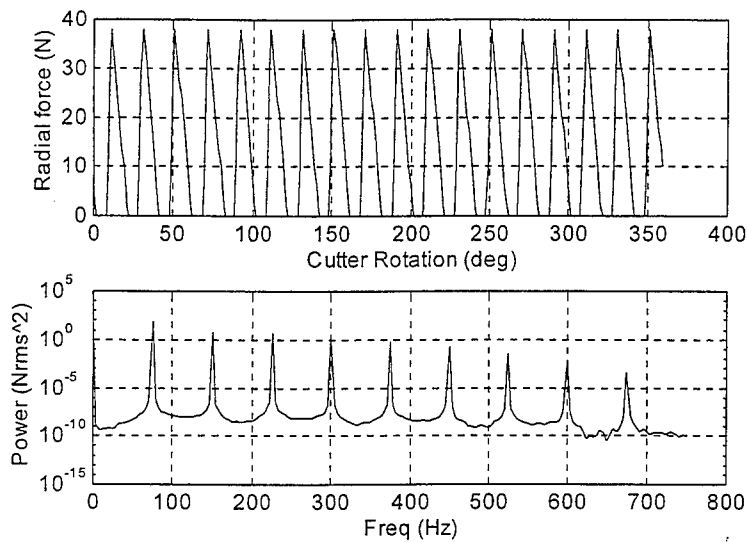


Figure 7. Time and spectral results of the radial forces predicted by EMSIM for the peripheral milling of the drive plate film tracks. The cutter tooth passing frequency is at 75 Hz.

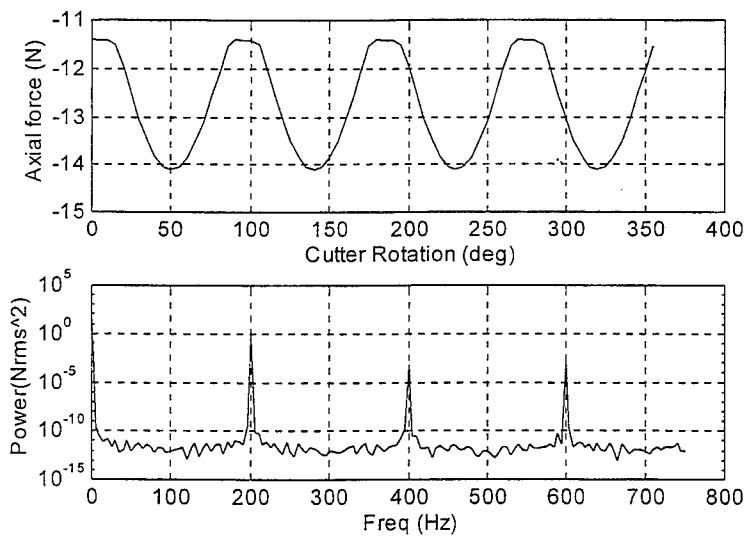


Figure 8. Time and spectral results of the axial forces predicted by EMSIM for the end milling of the drive plate pads. The cutter tooth passing frequency is at 200 Hz.

The experimental modal analysis indicates that the first resonant frequency of the workpiece-fixture is 863 Hz. The spectra of both the radial and end milling forces (Figures 7 and 8) show that nearly all the power is contained by harmonics well below this frequency. It was concluded that forced vibration was not a significant contributor to workpiece flexure and the resultant film track profile error.

IV. FIXTURE REDESIGN VIA FINITE ELEMENT ANALYSIS

The analysis revealed that static flexure contributed to 70% of the allowable profile error, and that forced vibration was not a significant factor. The analysis also revealed that pad 4 was significantly more compliant than the others. Consequently an FEA model of the workpiece was developed to evaluate alternative fixturing arrangements in an effort to increase the rigidity in this area and decrease the profile error.

The workpiece model was developed using the PATRAN FEA package. The model consisted of 1250 nodes and 488 3-D brick elements. The model attempted to capture the basic static behavior of the workpiece without an over burdensome mesh. Simplifications in the geometry were made which initially eliminated some of the fine geometric characteristics of the workpiece. A static analysis was performed which replicated the experimental compliance test. Comparison of the FEM to the experimental deflections showed an unacceptable level of difference. This result is not unexpected since finite element models have inherent modeling imperfections related to boundary conditions and geometric definition of the complex structure.

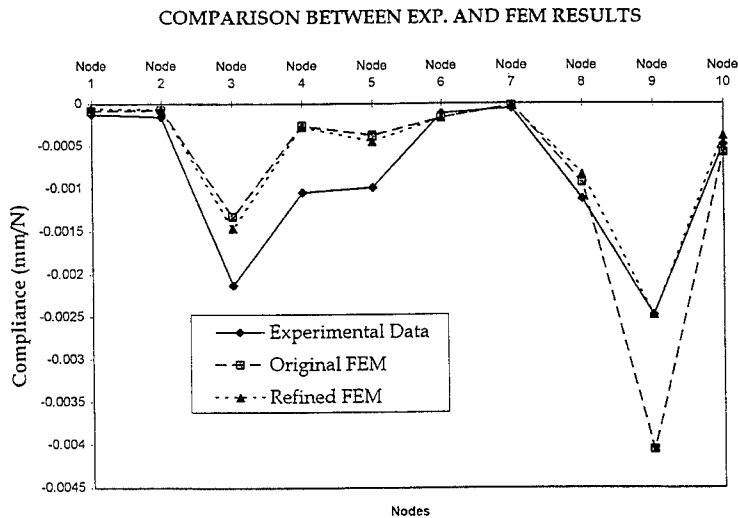


Figure 9. Comparison of FEM and experimental compliance results

The FEA model was fine tuned using the experimental compliance data. Many methods exist to localize errors in finite element models. For the sake of time and simplicity, a manual calibration of the FEM was used. Because of the complex workpiece geometry only the major characteristics were initially modeled. The manual tuning concentrated on refining the mesh to capture the more subtle geometric workpiece characteristics. The iterative process used the experimental compliance data as the target. The geometry was continually refined until the FEM nodal compliance

corresponded closely with the experimental data. Once the geometry was sufficiently defined, the FEM was further calibrated by either adding or removing stiffness where differences between data were observed. The results are summarized in Figure 9 which compares the responses for the original FEM, the refined FEM and the experimental data. The updated FEM shows compliance differences on the order of 6.85×10^{-4} mm/N (1.2×10^{-4} in/lb), which was deemed acceptable for this analysis. The updated model could now be used to evaluate changes to the fixturing configuration.

A. Analysis of Alternative Fixture Modifications

From the error analysis, the region between Clamp 6 and Clamp 7 was identified to be particularly over compliant. To avoid the cost of a total fixture redesign, the structural analysis focused only on the identified problem area. Two approaches were considered to improve the localized stiffness: 1) the addition of an extra support, and 2) a movement in the location of Clamp 6.

Adding extra supports is the most straightforward method to gain structural rigidity. Theoretically, by the increasing number of supports the workpiece-fixture system can yield any degree of stiffness. In practice, assembling a workpiece to the fixture is time consuming. Most supports are engaged through either spring action or hydraulic pressure, while hold down nuts are screwed on manually. To avoid unwanted distortion of the workpiece, operators often place a dial indicator on the workpiece surface and manually adjust the supports and hold down nuts to ensure the workpiece is in a free state. To minimize any additional manufacturing set up time the study was limited to adding only one new support.

The placement of the extra support is critical. Limited optimization work is available associated with maximizing global or local rigidity by changing the boundary conditions. Hence, the approach used here determined the best location from a predetermined candidate set. The set was selected by taking into consideration physical accessibility of the new clamp in the fixture. The clamp is about 20 mm (0.785 in) in diameter. Based on the size and the existing fixture layout, five likely candidates were selected along the workpiece between Clamp 6 and Clamp 7 (Figure 10). The workpiece compliance was then reevaluated with the FEM for each candidate support location. Note, since the cutting parameters are unchanged, the previous loads were used in the analysis. The best result was obtained with the support placed 76.2 mm (3 in) away from Clamp 6. A minimum profile error of 3.15×10^{-2} mm (1.24×10^{-3} in) was obtained compared to an original value of 8.81×10^{-2} mm (3.47×10^{-3} in).

The second approach to increase the local rigidity in the problem area was to change the current support configuration. Again to avoid a complete fixture redesign, the analysis was restricted to moving only one support. Examination of the profile errors indicated a problematic region around pad 4. Since this is close to Clamp 6 it seemed reasonable to reposition the clamp in order to improve the localized stiffness. Ten

candidate locations were selected along the edge of the workpiece between Clamp 6 and Clamp 7 (Figure 11). The compliance for each case was evaluated through the finite element analysis. Again, the same cutting forces were applied to compute the deflections, and hence assess the induced profile errors. The best performance was obtained by moving the support 25.4 mm (1 in.) away from Clamp 6. This scenario produced a profile error of 5.03×10^{-2} mm (1.98×10^{-3} in).

A summary of the profile errors for the fixture redesign is shown in Table 3. These results need to be interpreted carefully. Although the FEM has been updated correspond to the experimental data, the model tends to overestimate the stiffness (Figure 9). Obviously, this causes an underestimation of the deflections. Thus in practice, the values shown in Table 3 might not be completely representative. The results, however, do show that significant improvement can be obtained by implementing either of the proposed modifications. The final selection is left to the manufacturing engineer who also needs to consider how these changes may affect the entire set up and machining process.

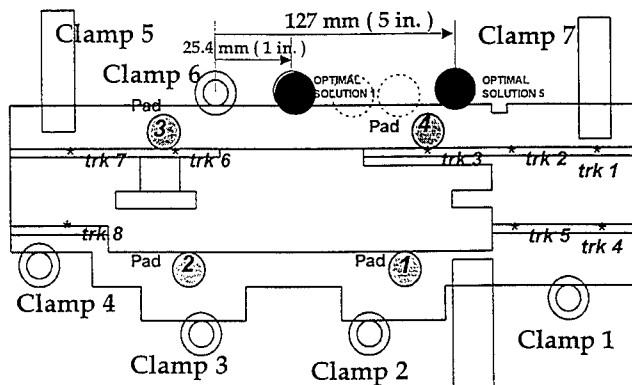


Figure 10. Candidate locations for additional support.

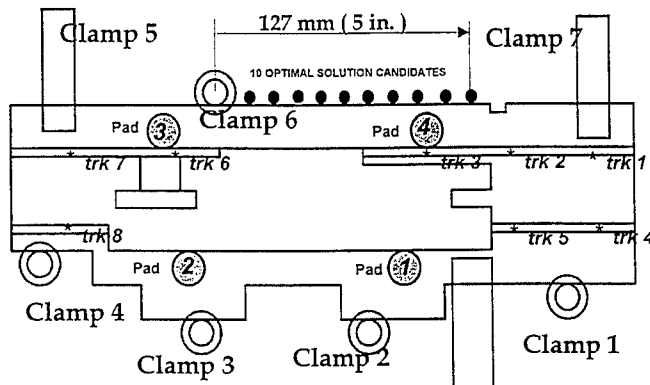


Figure 11. Candidate locations considered to move a support

Table 3. Summary of maximum profile errors of the original fixture and two redesigns.

Original design	8.81×10^{-2} mm (3.47×10^{-3} in)
Added support	3.15×10^{-2} mm (1.24×10^{-3} in)
Moved support	5.03×10^{-2} mm (1.98×10^{-3} in)

V. SUMMARY

The work presented in this paper evaluated the static and dynamic structural characteristics of a workpiece/fixtures system in relation to the manufacturing process. Initially manufacturing profile errors related to the static and dynamic structural characteristics of the workpiece/fixtures system were assessed experimentally. A milling process model was used to estimate the dynamic cutting forces and frequencies. The analysis showed the dynamic structural response was inconsequential and identified localized regions where relatively lower stiffness contributed significantly to the profile errors.

Subsequently a Finite Element Model was developed to evaluate various fixtures redesigns in an effort to decrease the static stiffness related profile error. The finite element model was first calibrated against the experimental compliance data. The model was then applied to evaluate a candidate set of support locations. In essences, this modified the workpiece boundary conditions imposed by the fixture. The analysis showed that the structurally weak zone could be strengthen by changing the support conditions. In this particular case, the addition of an extra support reduced the likely maximum profile error contributed by cutting forces by 64%.

The fixture redesign is inherently requires an accurate FEM. Since the FEM inherently contains modeling errors, it must be updated using experimental results. Recently the finite element model updating has been widely studied and a variety of updating methods proposed [2]. In this case, the finite element model was tuned manually with low effort and achieved an acceptable level of accuracy.

The analysis approach presented in this paper can generally be applied for existing workpiece-figures systems. Obviously, if these procedures are used earlier in the process-tool design cycle greater benefits could be realized. Cutting force and workpiece stiffness can be readily determined early via the computational methods described. The difficulty arises from the modeling of the boundary conditions imposed on the workpiece by the clamps and supports. The clamping of workpieces in a fixtures system is a dominant factor controlling the static and dynamic structural characteristics, and hence can greatly affect the machining process itself. The mechanics of clamping is complicated and dependent on a number of parameters. To effectively examine the structural responses of workpieces in a machining operation, effective methods of capturing the effects of the clamping on the workpiece boundary

conditions need to be developed. Hence, the accurate characterization of fixture boundary conditions remains a major area of interest.

ACKNOWLEDGMENTS

The authors wish to MachineTool-Agile Manufacturing Research Institute (MT-AMRI) and University of Illinois at Urbana-Champaign for the financial support of this work.

REFERENCES

- [1] De Meter, E. C., Sayeed, Q., DeVor, R. E., and S. G. Kapoor, (1995), An Internet-Based Model for Technology Integration and Access, Part 2: Applications to Process Modeling and Fixture Design, *Proceedings of the 1995 International Mechanical Engineering Congress & Exposition (ASME)*, November 1995, San Francisco, CA.
- [2] Mottershead, J. E., and Friswell, M. I., "Model Updating In Structural Dynamics, A Survey," *Journal of Sound and Vibration*, Vol. 167(2), 1993.

VARIABLE GAIN CONTROL FOR STRUCTURES WITH CLOSELY SPACED NATURAL FREQUENCIES

Masato Abé

Department of Civil Engineering, The University of Tokyo,
Hongo 7-3-1, Bunkyo-ku, Tokyo 113, Japan.

ABSTRACT

A variable gain direct velocity feedback law is constructed to control vibrations in structures with two closely spaced natural frequencies using a single actuator. At the first half of the paper, optimization and limitation of constant gain direct velocity feedback are discussed based on perturbation analysis of the free response of structures with two vibration modes and a single actuator. At the second half of the paper, a variable gain feedback is constructed from the physical intuitions obtained from these responses. The variable feedback gain is derived in terms of the states of the system while the feedback loop remains direct velocity feedback. Numerical studies confirm the efficiency of the proposed method. The proposed control law is also applied to dynamic vibration absorbers to improve the performance.

INTRODUCTION

Control of structures with closely spaced natural frequencies is known to be difficult owing to coupling between modes, especially when few actuators are used, i.e., number of actuators are fewer than the number of closely spaced natural frequencies [1,2,3,4]. For example, in the active control experiment of cable-structure system, spill-over was observed when natural frequencies of the cable and the supporting structure are close to each other [1]. Detailed analysis of a structure with two closely spaced modes and a single actuator has shown that state feedback can enhance the performance, but robustness of stability is reduced considerably [2,3]. One of the solutions used to overcome this difficulty is the use of direct velocity feedback which guarantees asymptotic stability of the system [5]. However, it has mathematically been proven that the control effect of direct velocity feedback has a certain upper bound, which is inversely proportional to the closeness of each natural frequency [2,3,4].

In this paper, a new control strategy to improve the control performance which preserves asymptotic stability of direct velocity feedback is studied. The fundamental idea is shown in the block diagram of Figure 1. The feedback loop itself is direct velocity feedback, while the gain for direct velocity feedback is scheduled by state information. This control strategy can also be realized by semi-active devices such as variable orifice dampers, electro/magneto rheological fluids dampers, or magnetic dampers whose damping characteristics can be varied according to command [6,7,8,9]. Although this control strategy is attractive, calculation of the appropriate gain is somewhat involved and requires extensive computation such as dynamic programming. To obtain simple interpretation of this control strategy, analysis in this paper is concentrated on control of impulse response of structures with two closely spaced natural frequencies using one actuator. This can be considered as the most fundamental situation.

The paper starts with perturbation analysis of free response solutions of two degrees of freedom structure [2,3,10], and a discussion of the optimization and the limitation of the constant gain direct velocity feedback control. Then, state varying gain of direct velocity feedback is constructed based on physical intuitions obtained from these time domain solutions. Because the time domain solutions are given in relatively simple expressions, the control algorithm is also developed in an analytical form. Thus, the proposed method is readily applicable to any structures with two closely spaced natural frequencies without recourse to numerical iterations. Control of two identical oscillators which are connected by weak spring (Figure 2) is employed to demonstrate the efficiency of the proposed control law. This structural system has been employed in Reference [11] for analysis of fundamental characteristics of dynamic vibration absorber attached to structures with closely spaced natural frequencies. Numerical simulations show that the proposed control law has higher performance than that of the constant gain direct velocity feedback.

In the last part of the paper, the control strategy is applied to the semi-active dynamic vibration absorber where the damping coefficient of the absorber is adjustable. The control law of the current paper is shown to approximate the optimal control law which has been developed specifically for semi-active dynamic vibration absorbers [12].

OPTIMAL CONSTANT GAIN DIRECT VELOCITY FEEDBACK

At the first half of this section, perturbation solutions for free response of structures with two closely spaced natural frequencies controlled by a single actuator are developed. Then, the optimal gain for the constant gain direct velocity feedback which maximizes the modal damping ratios of the system is derived using these solutions.

Equations of motion for free response of a two degrees of freedom structure controlled by a single force actuator with direct velocity feedback are,

$$\mathbf{M}\ddot{\mathbf{x}} + \mathbf{K}\mathbf{x} = \mathbf{b}u, \quad (1a)$$

$$u = -g\mathbf{b}^T\dot{\mathbf{x}}, \quad (1b)$$

where, \mathbf{M} and \mathbf{K} are 2x2 mass and stiffness matrices; \mathbf{b} is the actuator position vector; g is the gain of direct velocity feedback; and $\mathbf{x} = [x, y]^T$ is the displacement vector. The actuator position is assumed to be associated with x coordinate without loss of generality, and hence vector \mathbf{b} is expressed by $[1, 0]^T$. This installation is explained by the example of two identical oscillators which are connected by weak spring in Figure 2. If the actuator is attached to the mass 2, the same \mathbf{b} vector can be used by exchanging x and y coordinate. Although placement of actuator at the connection of masses 1 and 2 cannot be expressed by this selection of \mathbf{b} matrix, the placement is not appropriate for control purpose and is not considered here, because it makes the vibration mode with parallel motion of both masses uncontrollable.

The open loop natural frequencies and associated mode shapes are denoted by ω_{j0} and ϕ_j , where $j = 1, 2$. The mode shape matrix is defined by,

$$\Phi = [\phi_1, \phi_2] = \begin{bmatrix} \phi_{11} & \phi_{12} \\ \phi_{21} & \phi_{22} \end{bmatrix}, \quad (2)$$

which is normalized with respect to the mass matrix \mathbf{M} , i.e., $\Phi^T \mathbf{M} \Phi = \mathbf{I}$. The equation of motion can be transformed by this matrix to

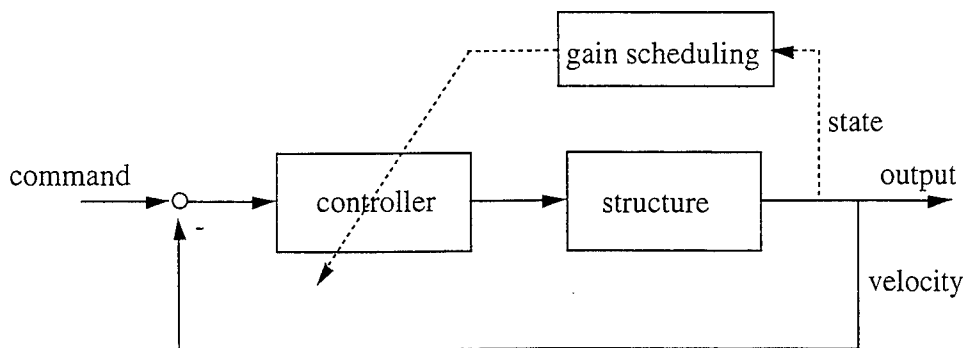


Figure 1. Block diagram for the proposed variable gain control.

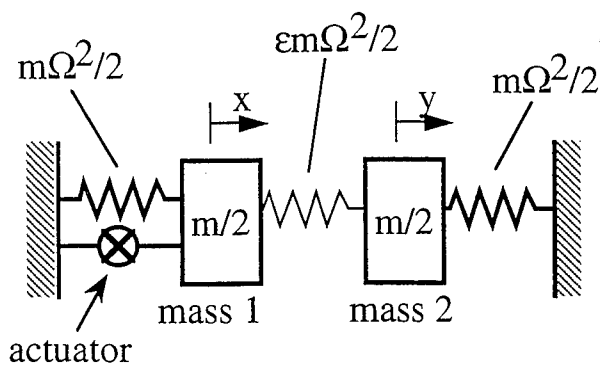


Figure 2. Example of structures with two closely spaced natural frequencies:
Two identical oscillators connected with weak spring.

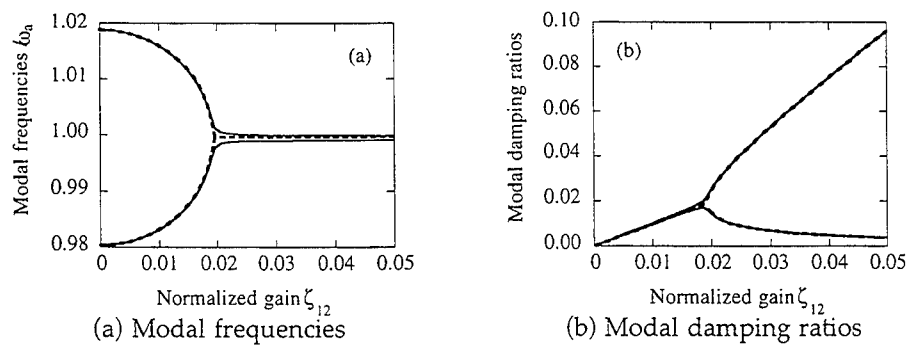


Figure 3. Modal properties of the two-oscillator system:
— Numerical solutions, - - - - - Perturbation solutions.

$$\mathbf{I}\ddot{\mathbf{q}} + \Gamma\dot{\mathbf{q}} + \Lambda\mathbf{q} = \mathbf{0}, \quad (3)$$

where $\mathbf{q}=[q_1, q_2]^T$, $\Gamma=g\Phi^T\mathbf{b}\mathbf{b}^T\Phi$ and $\Lambda=\text{diag}\{\omega_{10}^2, \omega_{20}^2\}$. The matrix Γ is generally not diagonalized and transformed to,

$$\Gamma = \begin{bmatrix} g\phi_{11}^2 & g\phi_{11}\phi_{12} \\ g\phi_{11}\phi_{12} & g\phi_{12}^2 \end{bmatrix} = \begin{bmatrix} 2\omega_{10}\zeta_{11} & 2\omega_a\zeta_{12} \\ 2\omega_a\zeta_{12} & 2\omega_{20}\zeta_{22} \end{bmatrix} \quad (4)$$

where $\omega_a=(\omega_{10}+\omega_{20})/2$, $\zeta_{11}=(g\phi_{11}^2)/(2\omega_{10})$, $\zeta_{12}=(g\phi_{11}\phi_{12})/(2\omega_a)$, and $\zeta_{22}=(g\phi_{12}^2)/(2\omega_{20})$. Laplace transform of the closed loop system is,

$$[s^2\mathbf{I}+s\Gamma+\Lambda]\mathbf{Q}(s)=\Gamma\mathbf{q}(0)+s\dot{\mathbf{q}}(0)+\ddot{\mathbf{q}}(0). \quad (5)$$

where $\mathbf{Q}(s)$ is Laplace transform of $\mathbf{q}(t)$. The characteristic equation for this system is found from the matrix determinant:

$$\det\{s^2\mathbf{I}+s\Gamma+\Lambda\}=0. \quad (6)$$

To solve this fourth order polynomial in terms of s , perturbation analysis which follows References [2,3,10] is applied here.

The following two parameters, related to the natural frequencies, are introduced for the convenience of the analysis:

$$\omega_a \equiv (\omega_{10} + \omega_{20})/2, \quad (7)$$

$$\beta \equiv (\omega_{10} - \omega_{20})/(2\omega_a). \quad (8)$$

Because the two modes are closely spaced, the parameter β is small relative to unity. Normalized gain ζ_{ij} 's are assumed to be small. Also an approximation $\zeta_{11} \approx \zeta_{22} \approx \zeta_a = (\zeta_{11} + \zeta_{22})/2$ is introduced, because it is reasonable to place the actuator where $\phi_{11} \approx \phi_{12}$ holds, to control both modes equally. Note that the signs of ϕ_{11} and ϕ_{12} can always be made the same by appropriate definition of coordinate systems.

Substituting these perturbation parameters into the characteristic equation and keeping only the lowest order terms, one obtains the perturbation solutions of eigenvalues as,

$$s_1 = \omega_a[i - (\zeta_a + \gamma)], \quad s_2 = \omega_a[i - (\zeta_a - \gamma)], \quad (9a,b)$$

$$s_3 = \omega_a[-i - (\zeta_a + \gamma)], \quad s_4 = \omega_a[-i - (\zeta_a - \gamma)]. \quad (9c,d)$$

where,

$$\gamma = \sqrt{\zeta_{12}^2 - \beta^2}. \quad (9e)$$

Details of derivation can be found in References [2,3,10].

Figure 3 shows modal frequencies and modal damping ratios calculated for the system of Figure 2. Modal frequencies and damping ratios are calculated by $|s_j|$ and $-\text{Re}[s_j]/|s_j|$, respectively, following the common practice. The mass and the spring constant of each oscillator are $m/2$ and $m\Omega^2/2$, and weak spring between the masses is $\varepsilon m\Omega^2/2$ where ε is set to 0.04. For this system, the natural frequencies are $\omega_{10} = \Omega$, and $\omega_{20} = \Omega\sqrt{1+2\varepsilon} \approx \Omega(1+\varepsilon)$, and the mode shapes are $\phi_1 = [1/\sqrt{m}, 1/\sqrt{m}]^T$ and $\phi_2 = [1/\sqrt{m}, -1/\sqrt{m}]^T$. Therefore, the parameter β is equal to $-\varepsilon/2 = -0.02$. The perturbation solutions of equation (9) are shown to give good approximation of numerically obtained eigenvalues.

In Figure 3, it is observed that both modal damping ratios increase with ζ_{12} up to $\zeta_{12} = |\beta|$ and bifurcate into high-damped and low-damped modes when ζ_{12}

$>|\beta|$, as can be expected from equation (9). Hence, the optimal gain for direct velocity feedback is

$$\zeta_{12} = |\beta|, \text{ or } g = \frac{2\omega_a|\beta|}{\phi_{11}\phi_{12}}, \quad (10)$$

which maximizes the minima of the damping ratios. This relationship substantiates the assumption of the analysis that ζ_{12} is small relative to unity.

By applying inverse Laplace transform to equation (5) using the eigenvalues of equation (9), time-domain solutions for arbitrary initial conditions are also obtained:

$$\mathbf{z}(t) = \mathbf{V} \exp(\mathbf{S}t) \mathbf{W} \mathbf{z}(0), \quad (11)$$

where

$$\mathbf{z}(t) = [q_1(t), q_2(t), \dot{q}_1(t)/\omega_a, \dot{q}_2(t)/\omega_a]^T, \quad \mathbf{S} = \text{diag}\{s_1, s_2, s_3, s_4\}, \quad (11a, b)$$

$$\mathbf{V} = \begin{bmatrix} \frac{1}{i\beta + \gamma} & \frac{1}{i\beta - \gamma} & \frac{1}{-i\beta + \gamma} & \frac{1}{-i\beta - \gamma} \\ \frac{\zeta_{12}}{s_1} & \frac{\zeta_{12}}{s_2} & \frac{\zeta_{12}}{s_3} & \frac{\zeta_{12}}{s_4} \\ \frac{\omega_a}{\omega_a} & \frac{\omega_a}{\omega_a} & \frac{\omega_a}{\omega_a} & \frac{\omega_a}{\omega_a} \\ \frac{s_1(i\beta + \gamma)}{\zeta_{12}\omega_a} & \frac{s_2(i\beta - \gamma)}{\zeta_{12}\omega_a} & \frac{s_3(-i\beta + \gamma)}{\zeta_{12}\omega_a} & \frac{s_4(-i\beta - \gamma)}{\zeta_{12}\omega_a} \end{bmatrix}, \quad (11c)$$

$$\mathbf{W} = \begin{bmatrix} -i\beta + \gamma & -i\beta - \gamma & \zeta_{12} & -i\zeta_{12} \\ i\beta + \gamma & i\beta - \gamma & -\zeta_{12} & i\zeta_{12} \\ i\beta + \gamma & -i\beta + \gamma & \zeta_{12} & i\zeta_{12} \\ -i\beta + \gamma & i\beta + \gamma & -\zeta_{12} & -i\zeta_{12} \end{bmatrix}. \quad (11d)$$

Impulse response of the two mass system of Figure 2 is shown in Figures 4 to 6. The structure is subject to the initial conditions of (a) $\dot{x}(0) = \dot{y}(0) \neq 0$, $x(0) = y(0) = 0$; and (b) $\dot{x}(0) \neq 0$, $x(0) = y(0) = \dot{y}(0) = 0$. The response is normalized so that the initial kinetic energy corresponds to the potential energy of unit displacement. Normalized time τ is given by $2\pi t/\omega_a$. The response of mass 1 (x) and mass 2 (y) are plotted in solid lines and dashed lines respectively. The responses shown here are all obtained through numerical integration. Although they are not shown here, responses calculated through equation (11) had good agreement.

Figure 4 shows the response when $\zeta_{12} = 0$. Because the initial condition of (a) is precisely in the shape of the first mode, the calculated response is just the same as that of a single oscillator. In Figure 4(b), beating between the first and second modes are observed, because of the two closely spaced natural frequencies appearing in Figure 3(a) when $\zeta_{12} = 0$. Figure 5 shows the response when ζ_{12} is set to the optimal value of equation (10), i.e., $\zeta_{12} = |\beta| = 0.02$. Responses of both masses are decaying at approximately the same rate. Figure 6 shows the response when $\zeta_{12} = 4|\beta| = 0.08$. Because of the existence of low-damped mode as observed in Figure 3(b), response of mass 2 in Figure 6(a) decays very slowly. However, the responses subject to the initial condition (b) decays very fast, because the actuator is attached to mass 1, and initial velocity is also localized in x . Hence increasing gain over the optimal value of equation (10) does not generally increase the

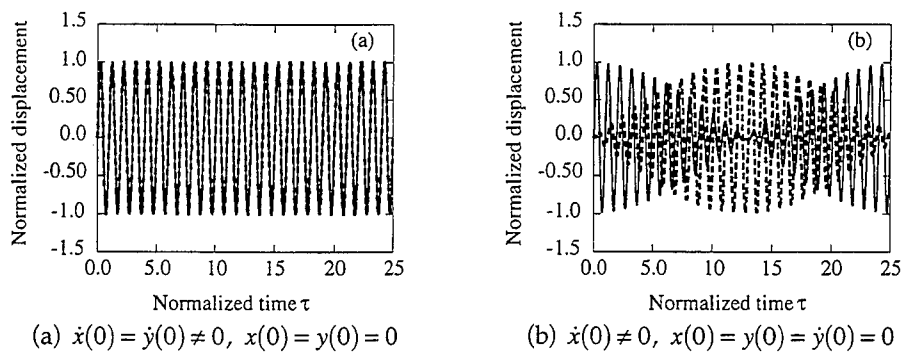


Figure 4. Impulse response of the two oscillators system with $\zeta_{12}=0$:
 ——— Mass 1 (x), - - - - - Mass 2 (y)

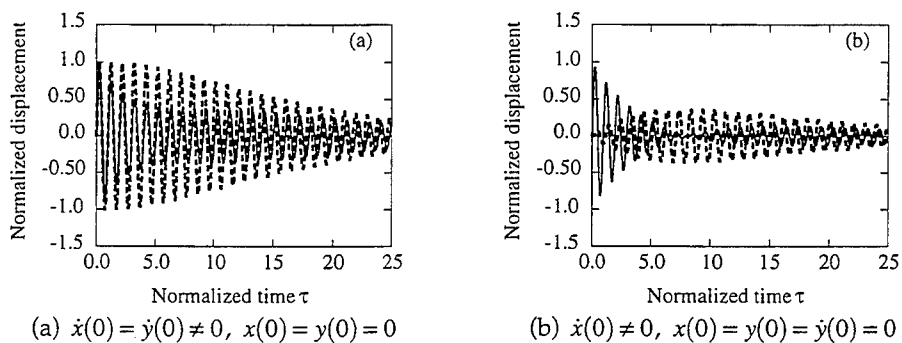


Figure 5. Impulse response of the two oscillators system with $\zeta_{12}=|\beta|$:
 ——— Mass 1 (x), - - - - - Mass 2 (y).

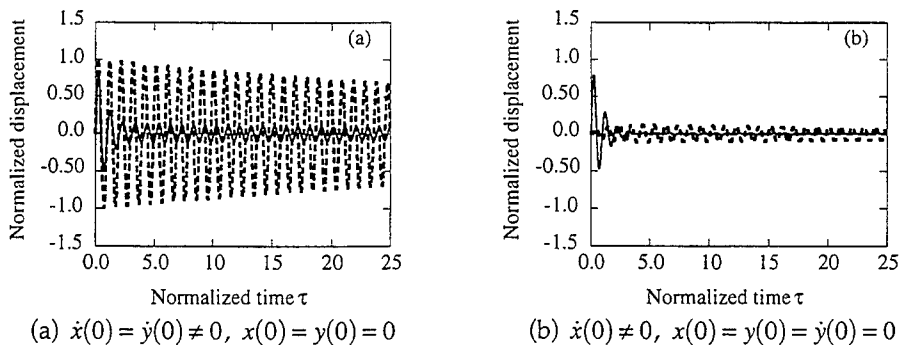


Figure 6. Impulse response of the two oscillators system with $\zeta_{12}=4|\beta|$:
 ——— Mass 1 (x), - - - - - Mass 2 (y).

damping of the system, although it may make the response faster for special kind of initial conditions.

In this section, optimization and limitation of constant gain direct velocity feedback has been discussed based on analyses of eigenvalues and time history responses. In the next section, variable gain control law is constructed based on these observations.

VARIABLE GAIN CONTROL STRATEGY

Variable feedback gain for control of transient vibration is developed in this section. Here, the normalized gain ζ_{12} , or equivalently, g is assumed to be adjustable upon command. However, sudden changes of ζ_{12} cause excessive variation in control force when \dot{x} is large, because control force is the multiplication of ζ_{12} and \dot{x} . This sudden change in damping force may cause trouble especially in semi-active devices, where the gain ζ_{12} is directly controlled by variation of dynamic properties of the elements or the materials. To avoid this difficulty, ζ_{12} is adjusted only at the zero-crossings of the velocity of the actuator \dot{x} and is kept constant between each zero-crossing. In this way, the control force in the actuator is zero when ζ_{12} is changed. Because of this adjustment policy, only the responses which correspond to the initial condition of the zero-crossing of \dot{x} , i.e.,

$$x(0) = x_0, \dot{x}(0) = 0, y(0) = y_0, \dot{y}(0) = \dot{y}_0, \quad (12)$$

needs to be considered in the following development.

The fundamental strategy is to use larger gain when the response is localized in x , where the actuator is attached, to maximize the control effect. A similar situation has been shown in Figure 6(b). When the gain is large, i.e., $\zeta_{12} \gg |\beta|$, the response of equation (11) can be simplified to:

$$x \approx X_1 \exp(-2\zeta_a \omega_a t) \sin(\omega_a t + \theta_1) + X_2 \sin(\omega_a t + \theta_2) \quad (13a)$$

$$y \approx Y_1 \exp(-2\zeta_a \omega_a t) \sin(\omega_a t + \theta_3) + Y_2 \sin(\omega_a t + \theta_4) \quad (13b)$$

where,

$$X_1 = \sqrt{\left(x_0 - \frac{\beta\phi_{11}}{2\zeta_{12}\phi_{21}} \frac{\dot{y}_0}{\omega_a}\right)^2 + \left(\frac{\beta\phi_{11}}{2\zeta_{12}\phi_{21}} y_0\right)^2} \quad (13c)$$

$$X_2 = \frac{|\beta\phi_{11}|}{2\zeta_{12}\phi_{21}} \sqrt{\left(\frac{\dot{y}_0}{\omega_a}\right)^2 + y_0^2} \quad (13d)$$

$$Y_1 = -\frac{\beta\phi_{22}}{2\zeta_{12}\phi_{12}} x_0 \quad (13e)$$

$$Y_2 = \sqrt{y_0^2 + \left(\frac{\beta\phi_{22}}{2\zeta_{12}\phi_{12}} x_0 + \frac{\dot{y}_0}{\omega_a}\right)^2} \quad (13f)$$

$$\theta_1 = \tan^{-1} \left(\frac{x_0 - \frac{\beta\phi_{11}}{2\zeta_{12}\phi_{21}} \frac{\dot{y}_0}{\omega_a}}{\frac{\beta\phi_{11}}{2\zeta_{12}\phi_{21}} y_0} \right) \quad (13g)$$

$$\theta_2 = \tan^{-1} \left(\frac{\dot{y}_0}{\omega_a y_0} \right) \quad (13h)$$

$$\theta_3 = 0 \quad (13i)$$

$$\theta_4 = \tan^{-1} \left\{ y_0 / \left(\frac{\beta \phi_{22}}{2 \zeta_{12} \phi_{12}} x_0 + \frac{\dot{y}_0}{\omega_a} \right) \right\} \quad (13j)$$

Response in x decreases by increasing ζ_{12} , because the first term of equation (13a) is highly damped with the damping ratio of $2\zeta_a$ and the second term has coefficient X_2 which is inversely proportional to ζ_{12} . This is natural since the actuator is attached in x . However, the second term of equation (13b) is undamped and its coefficient Y_2 is not inversely proportional to ζ_{12} . Nevertheless, by taking the gain of

$$\zeta_{12} = - \frac{\beta \phi_{22}}{2 \phi_{12}} \frac{\omega_a x_0}{\dot{y}_0} \quad (14)$$

the amplitude of this undamped oscillation Y_2 is minimized to $Y_2 = |y_0|$.

Now, consider the case that the structural motion in y is much larger than that in x . In this case, increasing gain will not reduce response in y , just as observed in Figure 6(a). However, when the value of ζ_{12} is small, i.e., $0 < \zeta_{12} < |\beta|$, the response becomes,

$$x \approx \frac{\phi_{11}}{\phi_{21}} \sqrt{y_0^2 + \left(\frac{\dot{y}_0}{\omega_a} \right)^2} \sin(|\beta| \omega_a t) \sin(\omega_a t + \tan^{-1}[-\dot{y}_0/(\omega_a y_0)]) \quad (15a)$$

$$y \approx \sqrt{y_0^2 + \left(\frac{\dot{y}_0}{\omega_a} \right)^2} \cos(|\beta| \omega_a t) \sin(\omega_a t + \tan^{-1}[(\omega_a y_0)/\dot{y}_0]) \quad (15b)$$

These equations describe the beating between two closely spaced modes with the frequency of $|\beta| \omega_a$ which has been observed in Figure 4(b). Introduction of beating is advantageous when vibration is localized in y , because it can transfer energy from y to x where the actuator is attached. By looking at equation (14), one can observe that the gain ζ_{12} becomes small when vibration energy in y is much greater than that in x . Hence, the relation of (14) is expected to induce beating and introduce desirable effect on the response of the structure in this situation too.

Based on the above observation, the following variable gain control law is proposed:

$$\zeta_{12} = \left| \frac{\beta \phi_{22}}{2 \phi_{12}} \cdot \frac{\omega_a x_0}{\dot{y}_0} \right|, \text{ or } g = \left| \frac{\beta \omega_a^2 \phi_{22} x_0}{\phi_{11} \phi_{12}^2 \dot{y}_0} \right| \quad (16)$$

Here, the absolute value of equation (14) is taken to prevent negative velocity feedback and to guarantee asymptotic stability of the system.

The advantage of the proposed analytical method over numerical optimization is that the control law of equation (16) can easily be applied to any structures with two closely spaced natural frequencies for any initial conditions without recourse to numerical iteration.

The control law of equation (16) is applied to the structure of Figure 2. All the structural parameters are kept same as the previous analyses of Figures 4 to 6, and the initial condition of $\dot{x}(0) = \dot{y}(0) \neq 0$, $x(0) = y(0) = 0$ is employed here.

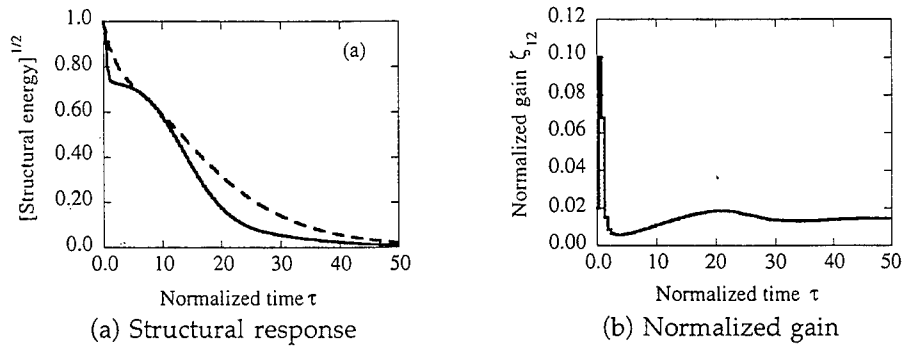


Figure 7. Impulse response of the two oscillators system with control
 — Proposed control law, - - - - - Optimal constant gain feedback.

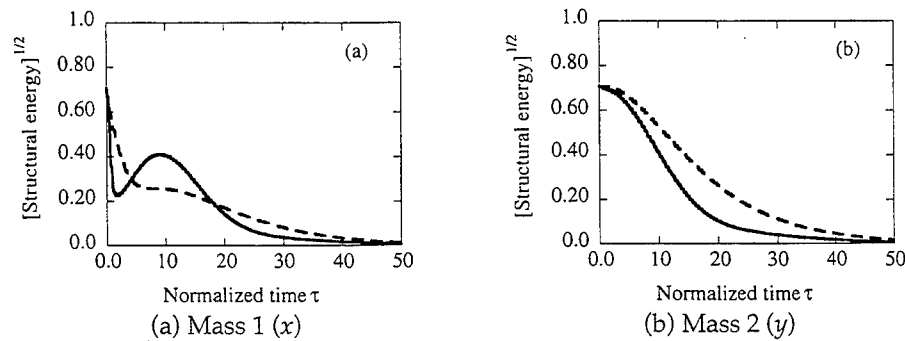


Figure 8. Impulse response of the two oscillators system with control
 — Proposed control law, - - - - - Optimal constant gain feedback.

The calculated structural energy are shown in Figures 7 and 8. Square root of structural energy normalized by initial structural energy is plotted as the indicator of the amplitude, which shows the envelop process of the response. For variable gain control, the upper bound for gain is set to $\zeta_{12}=5|\beta|=0.1$. Based on the previously listed natural frequencies and mode shapes, the control law of equation (16) becomes,

$$\zeta_{12} = \left| \frac{\varepsilon \omega_a x_0}{4 \dot{y}_0} \right|, \text{ or } g = \left| \frac{m \varepsilon \omega_a^2 x_0}{2 \dot{y}_0} \right|. \quad (17)$$

Look at the properties of the proposed variable gain control which are shown by solid lines in more details. Figure 7(a) shows that the proposed variable gain control gives faster decay of structural response than optimal constant gain feedback with $\zeta_{12}=|\beta|=0.02$, especially after $\tau > 10$. Figure 7(b) gives the time history of ζ_{12} . The highest value of gain is observed at the beginning, which is immediately followed by the minimum value of gain. Afterwards, the gain ζ_{12} increases again and remains almost constant around $\zeta_{12}=0.02=|\beta|$. The response

of each mass is given in Figure 8. The response of mass 1 increases around $\tau = 10$ as shown in Figure 8(a), whereas the response of mass 2 given in Figure 8(b) decays monotonically with time. The timing of this increase in response of mass 1 coincides with the lower gain region in Figure 7(b). This behavior is actually expected from the construction of the varying gain control rule in the preceding section. As energy in mass 1 is dissipated, the gain becomes lower to allow energy of mass 2 to flow into mass 1 around $\tau = 10$ by the beating effect. Because of this energy transfer, the response of mass 2 decays much faster than that of constant gain feedback. Then the gain increases up to approximately $|\beta| = 0.02$ to dissipate the energy stored in mass 1.

APPLICATION TO DYNAMIC VIBRATION ABSORBER

Dynamic vibration absorbers are commonly used to control vibrations in mechanical systems. Because the absorber is tuned to a natural frequency of the structure, the resulting absorber/structure system has closely spaced natural frequencies. In usual practice of dynamic absorbers, passive viscous damper, which can be interpreted as actuator with constant gain direct velocity feedback, is attached to broaden bandwidth of vibration suppression [13]. Here, the damper is replaced by actuator with variable gain control. To make the notation consistent, the x coordinate is assigned to the displacement of the absorber relative to the main mass, while the displacement of the main mass is denoted by y (see Figure 9). The main structure is modeled as a single degree of freedom structure with mass m_s and natural frequency Ω_s , and the vibration absorber has mass m_v and natural frequency Ω_v . The absorber frequency is given by the well-known optimal tuning ratio, i.e., $\Omega_v = \Omega_s / (1 + \mu)$. Simple approximate solutions of modes are available when mass ratio $\mu = m_v / m_s$ is much smaller than unity [14], in which the natural frequencies and mode shapes are given by $\omega_{10} = \Omega_s (1 - \sqrt{\mu}/2)$, $\omega_{20} = \Omega_s (1 + \sqrt{\mu}/2)$, $\phi_1 = [1/\sqrt{2m_v}, \sqrt{\mu}/\sqrt{2m_v}]^T$, and $\phi_2 = [1/\sqrt{2m_v}, -\sqrt{\mu}/\sqrt{2m_v}]^T$, where $\Omega_a = (\Omega_s + \Omega_v)/2$. The parameter β can be calculated as $-\mu^{1/2}/2$. Then, control law of equation (16) yields,

$$\zeta_{12} = \left| \frac{\mu \omega_a x_0}{4 \dot{y}_0} \right|, \text{ or } g = \left| \frac{\mu m_v \omega_a^2 x_0}{2 \dot{y}_0} \right|. \quad (18)$$

Response of the main structure with $\mu = 0.01$ and initial condition of $\dot{y}_0 \neq 0$, $x_0 = \dot{x}_0 = y_0 = 0$ is shown in Figure 10. The energy transferred to the absorber is not included here because the response reduction of structure by attachment of absorber is of interest but not the absorber response itself. Hence, the response is smoothly decreasing. This response characteristic is similar to what was observed in the response of the mass 2 in Figure 8(b).

The optimal variable gain, which gives the fastest decay of impulse response of structure excluding the energy of absorber, has been derived analytically [12]:

$$\zeta_{12}(t) = \begin{cases} 0, & \text{if } y_{\text{limit}} \leq y_0 \leq 0; \\ -\frac{1}{4} \left[\frac{\dot{x}_0}{\omega_a y_0} + \frac{\mu \omega_a y_0}{\dot{x}_0} \right], & \text{if } y_0 < y_{\text{limit}}; \end{cases} \quad (19)$$

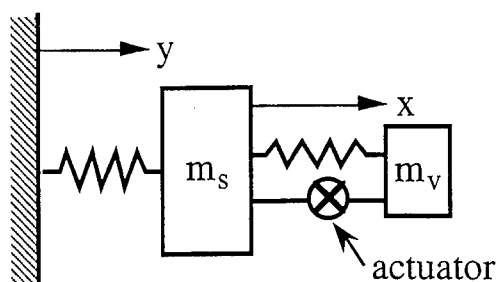


Figure 9. Dynamic vibration absorber/ structure system.

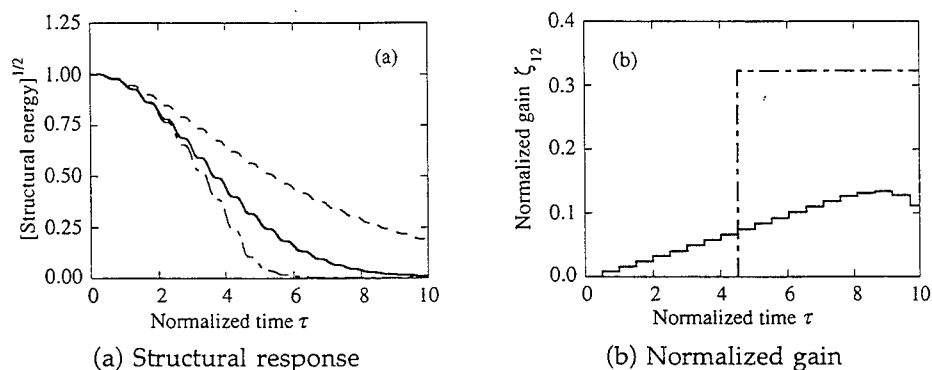


Figure 10. Impulse response of structure with dynamic vibration absorber:
 ——— Proposed control law, - - - - - Optimal constant gain feedback,
 - . - . - Optimal variable gain feedback.

where,

$$y_{\text{limit}} \equiv -\cot(\sqrt{\mu}\pi/2) \frac{\dot{x}_0}{\sqrt{\mu}\omega_a} \quad (19a)$$

Response due to this optimal variable gain is also plotted in the same figure. The proposed control law is shown to give slightly worse response than the optimal solution, but faster decay than the optimal passive absorber. Variation of gain is shown in Figure 10(b). The optimal gain variable gives more drastic variation of gain than the proposed control law.

5. CONCLUSIONS

A variable gain control strategy for direct velocity feedback to suppress transient response of structures with two closely spaced natural frequencies is constructed based on analytical perturbation solutions of the initial value problem. The design method is applied to the examples of two identical oscillators connected by a weak spring and dynamic vibration absorber. Validity

of the method is confirmed in each numerical example. The main conclusions are as follows:

1. Analytical expressions are developed for structures which consist of two closely spaced natural frequencies and an actuator with direct velocity feedback. The results provide useful insights on optimization and limitation of constant gain direct velocity feedback.
2. Variable gain direct velocity feedback control is constructed using physical intuitions obtained from analytical solutions. Numerical studies confirm that the efficiency of the proposed method is higher than that of conventional constant gain direct velocity feedback.
3. The proposed control law is applied to dynamic vibration absorbers, and is shown to qualitatively approximate the optimal variable gain developed in previous study [12].

ACKNOWLEDGMENT

The research work in this paper was partially supported by the U.S. National Science Foundation under Grant No. BCS-8858549 and by the Izumi Research Institute of Shimizu Corporation. This support is gratefully acknowledged. The author wishes to thank Professor T. Igusa of Northwestern University for his invaluable advice in the course of the study, and anonymous reviewers for thorough and critical review of the manuscript.

REFERENCES

1. Warnitchai, P., Nonlinear vibrations and active control of cable-stayed bridges, Ph.D. Thesis, Department of Civil Engineering, University of Tokyo, Tokyo, Japan. 1990.
2. Xu, K., Warnitchai, P., and Igusa, T., Active control of a structure with two closely spaced natural frequencies, *Proceedings of the 33rd AIAA/ASME/ASCE/AHS/ASC Structures, Structural Dynamics, and Materials Conference*, Washington D. C., 1992, pp.1285-1295.
3. Xu, K., Warnitchai, P., and Igusa, T., Control of a structure with two closely spaced natural frequencies, *AIAA Journal of Guidance, Control, and Dynamics*, 1993, **16**, pp.1177-1178.
4. Abé, M., and Igusa, T., Tuned mass dampers for structures with closely spaced natural frequencies, *Earthquake Engineering and Structural Dynamics*, 1995, **24**, pp.247-261.
5. Balas, M. J., Direct velocity feedback control of large space structures, *AIAA Journal of Guidance and Control*, 1979, **2**, pp.252-253.
6. Hovorat, D., Barak, P. and Rabins, M., Semi-active versus passive or active tuned mass dampers for structural control, *ASCE Journal of Engineering Mechanics*, 1983, **109**, pp.691-705.
7. Coulter, J. P., and Duclos, T. G., Applications of electrorheological materials in vibration control, *Proceedings of the Second International Conference on ER fluids*, Raleigh, North Carolina, ed. J. Carlson et al., 1989, pp.300-325.
8. Carlson, J.D and Spencer, B.F., Jr., Magneto-rheological fluid dampers for semi-active seismic control, *Proceedings of the 3rd International Conference on Motion and Vibration Control*, Chiba, Japan, 1996, pp. 35-40..

-
9. Seto, K., and Yamanouchi, M., On the effect of a variable stiffness-type dynamic absorber with eddy-current damping, *Bulletin of the JSME*, 1978, 21, pp.1482-1489.
 10. Abé, M., Vibration control of structures with closely spaced frequencies by a single actuator, *ASME Journal of Vibration and Acoustics*, (accepted for publication).
 11. Warburton, G. B., Optimum absorber parameters for minimizing vibration response, *Earthquake Engineering and Structural Dynamics*, 1981, 9, pp.251-262.
 12. Abé, M., and Igusa, T., Semi-active dynamic vibration absorbers for controlling transient vibration, *Journal of Sound and Vibration*, (in press).
 13. Den Hartog, J. P., *Mechanical Vibrations*, McGraw-Hill, 4th Ed., New York, 1956.
 14. Fujino, Y. and Abé, M., Design formulas for tuned mass dampers based on a perturbation technique," *Earthquake Engineering and Structural Dynamics*, 1993, 22, pp. 833-854.

MOBILITY MODEL FOR ACTIVE ISOLATORS

P. GARDONIO S. J. ELLIOTT and R. J. PINNINGTON
Institute of Sound and Vibration Research, University of Southampton, U.K.

1. INTRODUCTION

This paper presents a theoretical study of the active isolation of structural vibration transmission. The content of this paper can be divided into two parts: first the formulation of a mathematical model which allows the analysis of active isolator systems and second a simulation of different control strategies.

Recent studies of active isolation have suggested the need for mathematical models which give a detailed analysis of the coupled wave transmission mechanism when control sources are acting and, at the same time, to provide a summary of the overall phenomenon and thus allow a global interpretation of the dynamics of the system.

With reference to these requirements, a matrix model has been used which assumes that the system is divided into three elements: the source, the receiver and the active mounts. The dynamics of each of these elements is evaluated using point and transfer mobility terms. The elements are modelled either as lumped systems or distributed systems on which structural waves can propagate. Vibration transmission within the system has been expressed in terms of power. This parameter is useful for both local and global analysis of the vibration. There are two major advantages in using power: first, an examination of the power related with specific degrees-of-freedom allows a direct comparison of different types of motion (for example it is possible to compare the effects of angular and linear vibration); second, the total power transmitted to an element gives an indication of the energy available either for noise emission or for vibration transmission to a substructure.

The second part of the paper presents a review of the different strategies for the active isolation. In principle the minimisation of total power transmitted to the receiver is the optimal control strategy but this turns out not to be a practical solution. Therefore it has been used as a "benchmark" for gauging other approaches which can be implemented in practice. Four alternative control strategies have been considered with reference to the receiver junctions: first, the cancellation of out-of-plane velocities below the mounts; second, the cancellation of out-of-plane forces at the bottom of the mounts; third, the minimisation of power due only to the out-of-plane velocities and forces and fourth, the minimisation of the weighted sum of squared out-of-plane velocity and squared out-of-plane forces.

2. MATRIX MODEL FOR AN ACTIVE ISOLATING SYSTEM

Many of the studies of isolators are concerned with systems having only a single mount vibrating in one direction [1]. A more detailed study is needed for a system with many mounts (usually 3 or 4), each of which is a distributed flexible component. The Finite Element Method can be used to study this problem but the model can then be complicated and physical insight limited. Good results have been obtained by using an approach where the system is divided into individual components and each component is studied in terms of input and transfer mobilities or impedances [2, 3].

In reference [2] a matrix model is introduced where the dynamics of the source and the receiver are expressed in terms of input mobility matrices and the dynamics of the mounting system connecting these two members is given in terms of the transfer

mobility matrices. This formulation is valid for linear systems and can describe the dissipative effects of all three members, but was limited to axial motion only. In the following section this approach will be generalised for multi-axis vibration.

The complete isolating system is divided into three flexible parts as shown in figure 1: the source, the mounting system, composed by n elements, and the receiver. These parts are connected at a finite number of junctions. At each junction, the motion and the forces transmitted are characterised by six complex parameters at a single frequency of excitation. These velocity and force parameters are grouped in a velocity junction vector and a force junction vector which, for the j -th junction can be written as

$$\mathbf{v}_j \equiv \{\dot{u}_j, \dot{v}_j, \dot{w}_j, \dot{\theta}_{xj}, \dot{\theta}_{yj}, \dot{\theta}_{zj}\}^T \quad \mathbf{f}_j \equiv \{N_{xj}, N_{yj}, N_{zj}, M_{xj}, M_{yj}, M_{zj}\}^T \quad (1,2)$$

where $\dot{u}_j, \dot{v}_j, \dot{w}_j$ are the linear velocities respectively along the x, y and z directions, $\dot{\theta}_{xj}, \dot{\theta}_{yj}, \dot{\theta}_{zj}$ are the angular velocities referred respectively to the x, y and z axis, N_{xj}, N_{yj}, N_{zj} are the forces in the x, y and z directions and finally M_{xj}, M_{yj}, M_{zj} are the moments referred respectively to the $\dot{\theta}_{xj}, \dot{\theta}_{yj}$ and $\dot{\theta}_{zj}$ rotations.

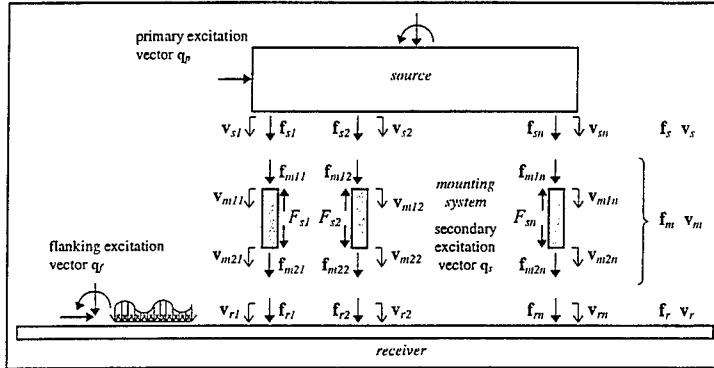


Fig. 1: Scheme of a general complete isolating system.

With reference to the notation shown in figure 1, combinations of these junction vectors are then grouped together to form three combined pairs of vectors: the source velocity vector (\mathbf{v}_s) and force vector (\mathbf{f}_s), the receiver velocity vector (\mathbf{v}_r) and force vector (\mathbf{f}_r), and the mounting system velocity vector (\mathbf{v}_m) and force vector (\mathbf{f}_m). The source and receiver velocity vector and force vector are given by:

$$\mathbf{v}_s \equiv \begin{Bmatrix} \mathbf{v}_{s1} \\ \mathbf{v}_{s2} \\ \vdots \\ \mathbf{v}_{sn} \end{Bmatrix} \quad \mathbf{f}_s \equiv \begin{Bmatrix} \mathbf{f}_{s1} \\ \mathbf{f}_{s2} \\ \vdots \\ \mathbf{f}_{sn} \end{Bmatrix} \quad \mathbf{v}_r \equiv \begin{Bmatrix} \mathbf{v}_{r1} \\ \mathbf{v}_{r2} \\ \vdots \\ \mathbf{v}_{rn} \end{Bmatrix} \quad \mathbf{f}_r \equiv \begin{Bmatrix} \mathbf{f}_{r1} \\ \mathbf{f}_{r2} \\ \vdots \\ \mathbf{f}_{rn} \end{Bmatrix} \quad (3-6)$$

where $\mathbf{v}_{sj}, \mathbf{f}_{sj}$ represent the velocity junction vector and the force junction vector at the source junction for the j^{th} mount, while $\mathbf{v}_{rj}, \mathbf{f}_{rj}$ represent the velocity junction vector and the force junction vector at the receiver junction for the j^{th} mount. The vectors of velocities and forces of the mounting system are given by:

$$\mathbf{v}_m \equiv \{\mathbf{v}_{m11} \quad \mathbf{v}_{m12} \quad \cdots \quad \mathbf{v}_{m1n} \quad \mathbf{v}_{m21} \quad \mathbf{v}_{m22} \quad \cdots \quad \mathbf{v}_{m2n}\}^T \quad (7)$$

$$\mathbf{f}_m \equiv \{\mathbf{f}_{m11} \quad \mathbf{f}_{m12} \quad \dots \quad \mathbf{f}_{m1n} \quad \mathbf{f}_{m21} \quad \mathbf{f}_{m22} \quad \dots \quad \mathbf{f}_{m2n}\}^T \quad (8)$$

where \mathbf{v}_{m1j} , \mathbf{f}_{m1j} represent the velocity junction vector and the force junction vector at the source junction for the j^{th} mount and \mathbf{v}_{m2j} , \mathbf{f}_{m2j} represent the velocity junction vector and the force junction vector at the receiver junction for the j^{th} mount. The dynamics of the source and the receiver are studied using a mobility matrix approach so that their velocity and force vectors can be written in the form:

$$\mathbf{v}_s = \mathbf{M}_{s1}\mathbf{f}_s + \mathbf{M}_{s2}\mathbf{q}_p \quad \mathbf{v}_r = \mathbf{M}_{r1}\mathbf{f}_r + \mathbf{M}_{r2}\mathbf{q}_f \quad (9,10)$$

where \mathbf{M}_{s1} , \mathbf{M}_{s2} and \mathbf{M}_{r1} , \mathbf{M}_{r2} are mobility matrices respectively of the source and the receiver [4] and \mathbf{q}_p , \mathbf{q}_f are the primary excitation vector and the flanking excitation vector. The flanking excitation acting on the receiver \mathbf{q}_f could be due to a subsystem connected with it or to a flanking path connecting the source with the receiver. A detailed description of the source and receiver mobility matrices for a rigid body (source) and a flat plate (receiver) is given in appendices A and C. The dynamics of the mounting system are expressed using an impedance matrix approach:

$$\mathbf{f}_m = \mathbf{Z}_{m1}\mathbf{v}_m + \mathbf{Z}_{m2}\mathbf{q}_s \quad (11)$$

where \mathbf{Z}_{m1} and \mathbf{Z}_{m2} are impedance matrices of the mounting system [4] and \mathbf{q}_s is the excitation vector of the control forces acting on the mounts. Appendix B gives the details of these impedance matrices when evaluated for a flexible one-dimensional mount. The source and receiver equations (9), (10) can be grouped together in one equation:

$$\mathbf{v}_{sr} = \mathbf{M}_{sr1}\mathbf{f}_{sr} + \mathbf{M}_{sr2}\mathbf{q}_{pf} \quad (12)$$

where the mobility matrices and the excitation vector have the form:

$$\mathbf{M}_{sr1} = \begin{bmatrix} \mathbf{M}_{s1} & \mathbf{0} \\ \mathbf{0} & \mathbf{M}_{r1} \end{bmatrix} \quad \mathbf{M}_{sr2} = \begin{bmatrix} \mathbf{M}_{s2} & \mathbf{0} \\ \mathbf{0} & \mathbf{M}_{r2} \end{bmatrix} \quad \mathbf{q}_{pf} = \begin{Bmatrix} \mathbf{q}_p \\ \mathbf{q}_f \end{Bmatrix} \quad (13-15)$$

and the junctions *velocity* and *force vectors* are given by:

$$\mathbf{v}_{sr} \equiv \begin{Bmatrix} \mathbf{v}_s \\ \mathbf{v}_r \end{Bmatrix} \quad \mathbf{f}_{sr} \equiv \begin{Bmatrix} \mathbf{f}_s \\ \mathbf{f}_r \end{Bmatrix} \quad (16,17)$$

where \mathbf{v}_{sr} and \mathbf{f}_{sr} are called respectively source-receiver *velocity vector* and source-receiver *force vector*. The source receiver vectors are related with the analogous mounting system vectors by a *transformation matrix* \mathbf{T} [4] in such a way as to satisfy the continuity principle (for the velocity vectors) and the equilibrium principle (for the force vectors) at each junction:

$$\mathbf{f}_m = -\mathbf{T}\mathbf{f}_{sr} \quad \mathbf{v}_m = \mathbf{T}\mathbf{v}_{sr} \quad (18,19)$$

Using these two relations, equations (11) and (12) can be related in such a way as to find the source-receiver velocity vector or the source-receiver force vector as a function of the primary-flanking and secondary sources:

$$\mathbf{v}_{sr} = \mathbf{Q}_{pv}\mathbf{q}_{pf} + \mathbf{Q}_{sv}\mathbf{q}_s \quad \mathbf{f}_{sr} = \mathbf{Q}_{pf}\mathbf{q}_{pf} + \mathbf{Q}_{sf}\mathbf{q}_s \quad (20,21)$$

where: $\mathbf{Q}_{pv} = (\mathbf{I} + \mathbf{M}_{sr1}\mathbf{T}^{-1}\mathbf{Z}_{m1}\mathbf{T})^{-1}\mathbf{M}_{sr2}$ (22)

$$\mathbf{Q}_{sv} = -(\mathbf{I} + \mathbf{M}_{sr1}\mathbf{T}^{-1}\mathbf{Z}_{m1}\mathbf{T})^{-1}\mathbf{M}_{sr1}\mathbf{T}^{-1}\mathbf{Z}_{m2} \quad (23)$$

$$\mathbf{Q}_{pf} = -\mathbf{T}^{-1}\mathbf{Z}_{m1}\mathbf{T}(\mathbf{I} + \mathbf{M}_{sr1}\mathbf{T}^{-1}\mathbf{Z}_{m1}\mathbf{T})^{-1}\mathbf{M}_{sr2} \quad (24)$$

$$\mathbf{Q}_{sf} = \mathbf{T}^{-1}\mathbf{Z}_{m1}\mathbf{T}(\mathbf{I} + \mathbf{M}_{sr1}\mathbf{T}^{-1}\mathbf{Z}_{m1}\mathbf{T})^{-1}\mathbf{M}_{sr1}\mathbf{T}^{-1}\mathbf{Z}_{m2} - \mathbf{T}^{-1}\mathbf{Z}_{m2} \quad (25)$$

The vibration transmission to the receiver will be quantified by using power and for the specific model investigated five types of power parameters can be defined:

- (i) the power input by the primary excitation $\mathbf{q}_p, \{P_p\}$;
- (ii) the power input by the flanking excitation $\mathbf{q}_f, \{P_f\}$;
- (iii) the power input by the secondary excitation $\mathbf{q}_s, \{P_s\}$;
- (iv) the power input by both primary and secondary excitations, $\{P_i\}$ (which is the minimised power cost function);
- (v) the total power input into the receiver, $\{P_r\}$.

Because the source is considered as a flexible distributed system with dissipation the power input by the primary source into the complete isolating system is given by:

$$P_p = \frac{1}{2} \text{Re}(\mathbf{q}_p^H \mathbf{v}_p) \quad (26)$$

where \mathbf{v}_p is a vector containing the velocity parameters at the source points where the primary excitations act [4] and H denotes the Hermitian transpose. The power input into the complete isolating system by the flanking excitation is given by:

$$P_f = \frac{1}{2} \text{Re}(\mathbf{q}_f^H \mathbf{v}_f) \quad (27)$$

where \mathbf{q}_f is the flanking excitation vector and \mathbf{v}_f is a vector containing the velocity parameters at the receiver points where the flanking excitations act [4]. The power input into the complete isolating system by the secondary source is given by:

$$P_s = \frac{1}{2} \text{Re}(\mathbf{q}_s^H \bar{\mathbf{v}}_m) \quad (28)$$

where $\bar{\mathbf{v}}_m$ is a vector containing only the axial velocity at the mounts junctions. The power transmitted to the receiver by the primary and secondary sources is given by:

$$P_r = \frac{1}{2} \text{Re}(\mathbf{f}_r^H \mathbf{v}_r) \quad (29)$$

and the total power input to the receiver is obtained by summing the power transmitted to the receiver by the source and the power input to the receiver by the flanking excitation $P_i = P_f + P_r$.

3. CONTROL STRATEGIES

The strategies considered here for active control can all be expressed in terms of a quadratic cost function which is minimised and this can always be written in the form [5,6]:

$$J = \mathbf{q}_s^H \mathbf{A} \mathbf{q}_s + \mathbf{q}_s^H \mathbf{b} + \mathbf{b}^H \mathbf{q}_s + c \quad (30)$$

The control source that minimises this quadratic equation is given by [5,6]:

$$\mathbf{q}_{s0} = -\mathbf{A}^{-1} \mathbf{b} \quad (31)$$

The control strategy of -a- minimising total power transmitted by the source to the receiver was assumed as a reference for assessing the efficacy of four alternative control strategies that are the -b- cancellation of out-of-plane input velocities to the receiver or the -c- cancellation of out-of-plane input forces to the receiver, the -d- minimisation of an estimate of power transmitted by the source to the receiver and finally the -e- minimisation of the weighted sum of squared values of out-of-plane input velocities and forces to the receiver. The estimate of the power quantity is the power associated with the out-of-plane velocities and forces at the receiver junctions. In this paper these four control strategies will be referred to as: -a- total power minimisation (J_p), -b- velocity cancellation (J_v), -c- force cancellation (J_f), -d- axial power minimisation (J_{pa}) and finally (e) velocity and force minimisation (J_{vf}). When the total power is minimised the cost function is:

$$J_p = \frac{1}{2} \text{Re}(\mathbf{f}_r^H \mathbf{v}_r) = \frac{1}{4} (\mathbf{f}_r^H \mathbf{v}_r + \mathbf{v}_r^H \mathbf{f}_r) \quad (32)$$

where the receiver velocities and forces parameters at the receiver junctions are given by the two following equations $\mathbf{v}_r = \mathbf{R}_{r1} \mathbf{v}_{sr}$ and $\mathbf{f}_r = \mathbf{R}_{r1} \mathbf{f}_{sr}$ where $\mathbf{R}_{r1} = [\mathbf{0}_{t \times t} \quad \mathbf{I}_{t \times t}]$ and $\mathbf{0}_{t \times t}$, $\mathbf{I}_{t \times t}$ are respectively a zero matrix and a unit matrix, t is the dimension of the source and receiver vectors. The two matrices in the quadratic form of equation (30) are then needed

$$\mathbf{A}_p = \frac{1}{4} (\mathbf{Q}_{sf}^H \mathbf{R}_{r1}^T \mathbf{R}_{r1} \mathbf{Q}_{sv} + \mathbf{Q}_{sv}^H \mathbf{R}_{r1}^T \mathbf{R}_{r1} \mathbf{Q}_{sf}) \quad \mathbf{b}_p = \frac{1}{4} (\mathbf{Q}_{sf}^H \mathbf{R}_{r1}^T \mathbf{R}_{r1} \mathbf{Q}_{pv} \mathbf{q}_{pf} + \mathbf{Q}_{sv}^H \mathbf{R}_{r1}^T \mathbf{R}_{r1} \mathbf{Q}_{pf} \mathbf{q}_{pf}) \quad (33,34)$$

When velocity cancellation is implemented then the cost function has the form:

$$J_v = \mathbf{v}_r^H \mathbf{v}_r \quad (35)$$

and the velocity vector \mathbf{v}_r is obtained with the following equation $\mathbf{v}_r = \mathbf{R}_{r2} \mathbf{v}_{sr}$ [6]. The two matrices in equation (30) are then given by:

$$\mathbf{A}_v = \mathbf{Q}_{sv}^H \mathbf{R}_{r2}^T \mathbf{R}_{r2} \mathbf{Q}_{sv} \quad \mathbf{b}_v = \mathbf{Q}_{sv}^H \mathbf{R}_{r2}^T \mathbf{R}_{r2} \mathbf{Q}_{pv} \mathbf{q}_{pf} \quad (36, 37)$$

When force cancellation is implemented then the cost function has the form:

$$J_f = \mathbf{f}_r^H \mathbf{f}_r \quad (38)$$

and the force vector \mathbf{f}_r is obtained with the following equation $\mathbf{f}_r = \mathbf{R}_{r2} \mathbf{f}_{sr}$ [6]. The two matrices in equation (30) are then given by:

$$\mathbf{A}_f = \mathbf{Q}_{sf}^H \mathbf{R}_{r2}^T \mathbf{R}_{r2} \mathbf{Q}_{sf} \quad \mathbf{b}_f = \mathbf{Q}_{sf}^H \mathbf{R}_{r2}^T \mathbf{R}_{r2} \mathbf{Q}_{pf} \mathbf{q}_{pf} \quad (39, 40)$$

If the axial power is minimised the cost function J_{pa} assumes the same form as equation (32) and the velocity \mathbf{v}_r and force \mathbf{f}_r vectors are given by the two equations $\mathbf{v}_r = \mathbf{R}_{r2} \mathbf{v}_{sr}$, $\mathbf{f}_r = \mathbf{R}_{r2} \mathbf{f}_{sr}$ [6]. Finally when velocity and force minimisation are implemented then the cost function has the form:

$$J_{vf} = \mathbf{v}_r^H \mathbf{v}_r + \mu \mathbf{f}_r^H \mathbf{f}_r \quad (41)$$

and the velocity and force vectors are the same as those considered above respectively for velocity or force cancellation. Thus the two matrices in equation (30) are given by:

$$\mathbf{A}_{v,f} = \mathbf{Q}_{sv}^H \mathbf{R}_{r2}^T \mathbf{R}_{r2} \mathbf{Q}_{sv} + \mu \mathbf{Q}_{sf}^H \mathbf{R}_{r2}^T \mathbf{R}_{r2} \mathbf{Q}_{sf} \quad \mathbf{b}_{v,f} = (\mathbf{Q}_{sv}^H \mathbf{R}_{r2}^T \mathbf{R}_{r2} \mathbf{Q}_{pv} + \mu \mathbf{Q}_{sf}^H \mathbf{R}_{r2}^T \mathbf{R}_{r2} \mathbf{Q}_{pf}) \mathbf{q}_{pf} \quad (42, 43)$$

The coefficient μ is a weighting factor used to make homogeneous the two parameters minimised and have the dimensions of a mobility squared (s/Kg). The coefficient μ can, for example, be assumed to be equal to the square of the point mobility of an infinite plate when out-of-plane velocity and force are considered [4].

4. ACTIVE CONTROL WHEN THE RECEIVER IS AN INFINITE PLATE

Figure 2 shows the geometry of the system considered. The source is an aluminium mass whose dimensions are $0.52 \times 0.3 \times 0.25$ m. The two mounts are modelled as rings of rubber with two reactive control forces acting at the ends. The external and internal diameters and the height of the suspensions are respectively 6 cm, 3 cm and 10 cm. Two types of receiver structure are analysed: first an infinite plate; second, a simply supported finite plate. In both cases the aluminium plate is 0.5 cm thick. The source is

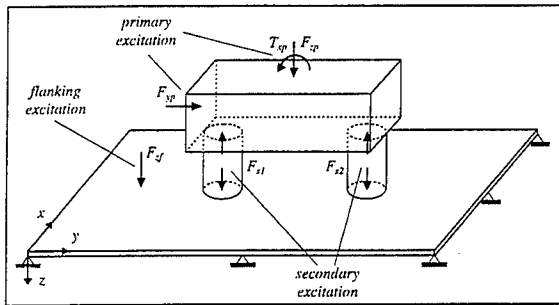


Fig. 2: Complete isolating system.

modelled as a rigid body since the first natural frequency due to the structural waves which propagate on it is well above the frequency range considered in the simulations. The receiver thin plate is assumed to be distributed and the model considers the propagation of longitudinal and shear in-plane waves and the propagation of flexural out-of-plane waves. The mounts are also modelled as distributed systems on which longitudinal and flexural waves can propagate. It has been assumed that the rigid mass vibrates in a plane (y - z plane) and in this way both the effects due to multi-degree-of-freedom vibration and the effects due to multi-mounts are taken into account in the simulations. Appendices A, B and C contain the mobility or impedance formulation for the three elements of the system. The primary excitation considered in the simulation was composed by unitary axial and transverse harmonic forces and by a unitary harmonic moment in the y - z plane whose time dependence was $\exp(j\omega t)$.

Considering the total power minimisation strategy, figure 3 shows the frequency distribution of the power transmitted to the infinite receiver plate while figure 4 shows the contribution to the power transmission due to each degree-of-freedom. The dynamics of the system without control are characterised by three rigid body modes (transverse, axial and pitching modes) at low frequency (at around 7 Hz) [4] and by natural modes of the distributed mounts at around 500 Hz [4]. The control action produces an average reduction in the power transmitted to the receiver of about 30 dB and the maximum and minimum reductions are about 45 dB and 6 dB respectively. When active control is implemented the dynamics of the system change a bit at low frequency; in fact now only two rigid body modes characterise the system vibration [4,6,7].

As shown in figure 4 the main contribution to the power transmission when the active control is implemented is due to the axial or transverse power at low frequency and

to the angular power at high frequency. When the two rigid modes of the controlled system are excited the power transmission is due to all of the components. The axial power is, however, larger than the total power transmitted to the receiver at these frequencies. The reason for this is that axial power is not transmitted to the receiver but is absorbed from the receiver. Power thus circulates in the system with part of the transverse and angular power transmitted to the receiver being absorbed by the control sources as axial power. So, when the active control of total power transmission is implemented the transverse displacements and the rotations become as important as the axial displacements and a new phenomenon of "power circulation" characterises the power transmission to the receiver.

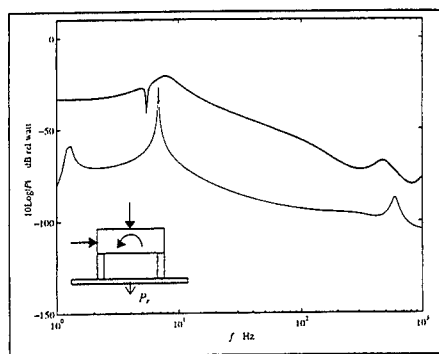


Fig. 3: Power transmitted to an infinite 0.5 cm thick plate when a combined excitation acts on the source, thick line uncontrolled system, thin line total power minimisation.

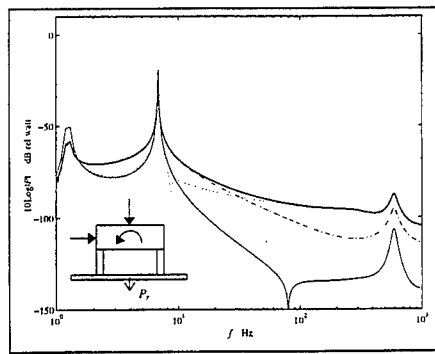


Fig. 4: Power transmitted to an infinite 0.5 cm thick plate when a combined excitation acts on the source and the total power control strategy is implemented, thick line total power, dash-dotted line transverse power, thin line axial power, dotted line angular power.

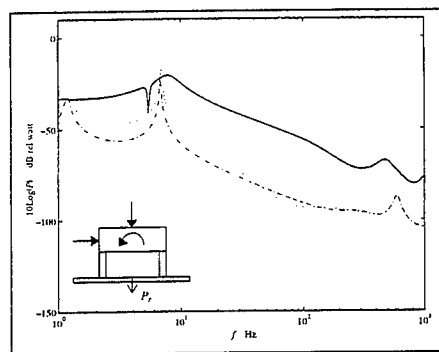


Fig. 5: Power transmitted to an infinite 0.5 cm thick plate when a combined excitation acts on the source, thick line uncontrolled system, dash-dotted line velocity cancellation, dotted line force cancellation.

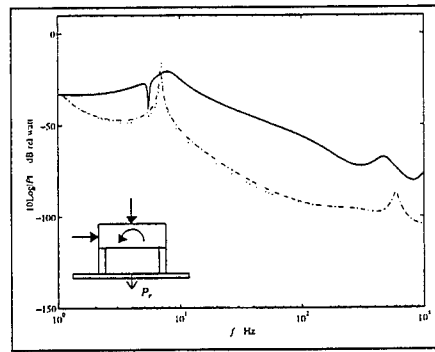


Fig. 6: Power transmitted to an infinite 0.5 cm thick plate when a combined excitation acts on the source, thick line uncontrolled system, dash-dotted line velocity and force minimisation, dotted line axial power minimisation.

The efficacy of the four active control strategies which use only axial velocity and force signals is shown in figures 5 and 6. The global effects of these four control strategies are quite similar to each other in this case and the average reduction of the power transmitted to the receiver is about 20 dB while the maximum value is about 40 dB. However, when active control is implemented and the transverse or pitching rigid body modes of the isolator are excited the performance is very poor since the power transmitted to the receiver is even larger than before control.

Jenkins *et al* [8] and Pan *et al* [9] used the efficiency ratio [4] to represent the effectiveness of the passive and active isolation. This parameter can be defined as the

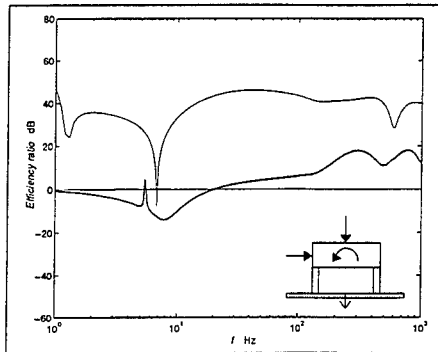


Fig. 7: Efficiency of the passive isolation (thick line) and active isolation minimising total power (thin line) when an infinite 5 mm thick plate is considered.

ratio of the power transmitted to the receiver by an isolator with rigid mounts and the power transmitted to the receiver by an isolator with flexible mounts,

$$E = \frac{P_i \text{ (rigid mounts)}}{P_i \text{ (passive or active mounts)}} \quad (44)$$

Figure 7 shows the frequency distribution of the efficiency ratio when passive isolation and active control isolation based on total power minimisation are used. This figure shows that the active isolator system on average increases the efficiency of the

isolation by about 20 dB. The problems of passive isolation at low frequency are overcome since, apart from the frequency at which the pitching rigid body mode is excited, the efficiency after active control is always larger than one.

5. ACTIVE CONTROL WHEN THE RECEIVER IS A FINITE PLATE

In this section the effects of active control are examined when the receiver is a finite plate of dimensions 1 m × 1.5 m × 5 mm. Figure 8 shows the frequency distribution of the power transmitted to the receiver without control and by controlling the total power transmission. The dynamics of the system is quite similar to that having an infinite plate: now the resonances of the rigid body modes (transverse mode 3 Hz, axial mode 4.2 Hz and pitching mode 9 Hz) and the distributed mounts (500 Hz) are mixed with a relatively large number of resonances due to the finite receiver plate dynamics. Total power control produces an average reduction of the power transmission of about 20 dB. From 20 Hz to 200 Hz large attenuations are achieved, of the order of 30 dB, but for frequencies greater than 200 Hz the reduction is diminished to 20 dB. The reason for this lessening of the active control efficacy is related to the dynamics of the receiver. At around 80 Hz the flexural waves propagating in the receiver plate have wavelengths which are comparable to the distance between the two mounts and so the coupling between the motion under the two mounts becomes weaker and therefore the power injected by them becomes more independent [10]. At frequencies where the flexural wavelength is long compared to the distance between the mounts, the axial secondary force generated by one mount can influence the moment introduced at the other mount [11] and thus the active mounts have a greater capability for controlling the total motion of the receiving structure.

The frequency distribution of the efficiency ratio is shown in figure 9 for total power minimisation which shows that an average efficiency improvement of about 20 dB is achieved. The active isolation is also effective at frequencies below 100 Hz where the passive isolation can produce negative efficiencies at the receiver resonances [4].

The efficacy of the velocity and force cancellation control strategies is shown in figure 10. At low frequencies the active isolator produces poor results. The reason for this low capability of controlling the rigid modes is due to the power circulation phenomenon described in the previous section. At frequencies above the two

resonances of the rigid modes and below 200 Hz the control effectiveness of these two strategies is poorer than that of controlling total power. The velocity and force control are characterised by an average power reduction of about 18 dB which becomes smaller when the modes of the distributed mounts and receiver plate are excited.

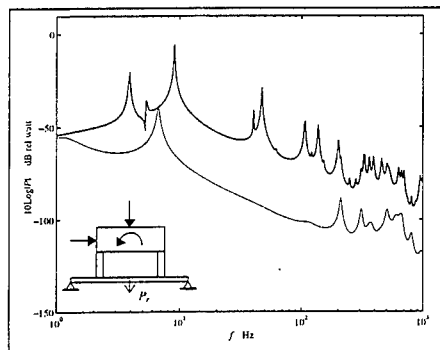


Fig. 8: Power transmitted to a finite 0.5 cm thick plate when a combined excitation acts on the source, thick line uncontrolled system, thin line total power minimisation.

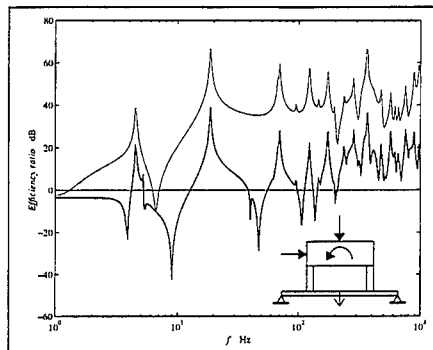


Fig. 9: Efficiency of the passive isolation (thick line) and active isolation minimising total power (thin line) when a finite 5 mm thick plate is considered.

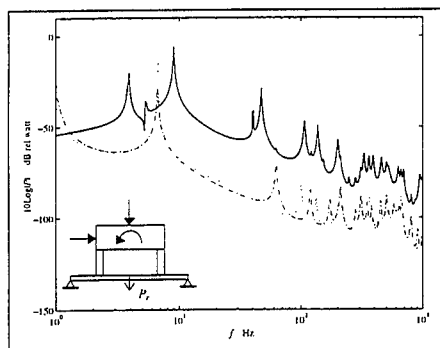


Fig. 10: Power transmitted to a finite 0.5 cm thick plate when a combined excitation acts on the source, thick line uncontrolled system, dash-dotted line velocity cancellation, dotted line force cancellation.

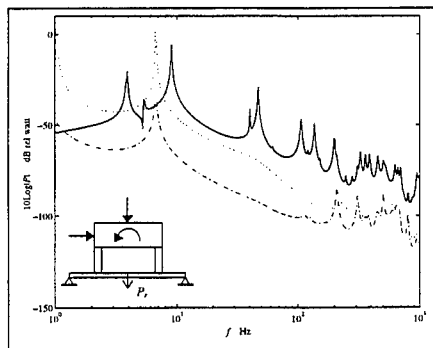


Fig. 11: Power transmitted to a finite 0.5 cm thick plate when a combined excitation acts on the source, thick line uncontrolled system, dash-dotted line velocity and force minimisation, dotted line axial power minimisation.

It should be noted that the resonances due to the receiver modes occur at different frequencies in the two control cases and this can be explained in terms of the modal behaviour of the receiving plate. The velocity cancellation control strategy constrains the out-of-plane vibration at the two junctions where the mounts are connected to the plate. Thus, for the velocity cancellation control strategy, the plate can be assumed to be simply supported at the four edges and pinned at the two junction points. This new configuration of the boundary conditions increases the stiffness of the plate and therefore the natural frequencies occur at higher frequencies than in the reference case. On the other hand the force cancellation control strategy does not produce any change in the boundary conditions of the plate and therefore the natural frequencies remain those of the simply supported plate. At frequencies above 200 Hz the results obtained by the velocity, and force, control strategies are similar to the one produced by the total power control strategy. It must be emphasised that the efficacy of these two control strategies comes closer to that of total power control because the total

power control strategy performance is reduced above 200 Hz, as described above, and not because the velocity or force control strategy have improved their effectiveness.

As figure 11 shows, the control of axial power produces even worse results than force or velocity cancellation giving average reductions of only about 10 dB. Power circulation is found to be very strong in this case, which causes a lot of problems particularly when the rigid body modes are excited after control. In fact, when active control is implemented, there is greater power transmission after control when the rigid body modes are excited. For frequencies above 200 Hz the control performance is similar to velocity or force cancellation.

The control of out-of-plane velocity or force produces poor results when the modes of the receiver are excited. The fact that these modes occur at different frequencies, as described above, suggest that using a cost function which minimises a combination of both out-of-plane velocities and out-of-plane forces at the receiver junctions should give better control.

Figure 11 shows results of minimising the cost function given by the weighted sum of the squared velocity and squared force, as described in section 3. This performs very well when compared with conventional velocity or force cancellation: the rigid body modes after control are quite successfully controlled. In the frequency range between 20 and 200 Hz most of the peaks due to either velocity or force cancellation are suppressed and even at higher frequencies the isolation is increased. The value of this control strategy becomes even more evident when compared with the total power minimisation control strategy (figure 8). In general we observe that the minimisation of the weighted sum of squared values of velocities and forces gives almost as good a performance as minimising total power except that the control of forces and velocities give slightly higher peak values (by a few decibels) at the controlled resonance frequencies.

6. CONCLUSIONS

The first part of this paper is concerned with the description of the matrix model used to describe the vibration transmission from a source to a receiver through active mounts. A detailed formulation for the mobility or impedance terms for the source, for the mounts and for the receiver is reported in the appendices. Particular attention has been devoted to the consistent derivation of the individual terms required in this formulation, since even though many of the individual terms have previously been derived, it is still difficult to find references in which a complete and consistent set of mobility or impedance terms is given.

The vibration transmission to the receiver has been quantified by using structural power since this single parameter can be used to describe the dynamics of the system in a consistent manner. The power transmitted to the receiver does not only give a measure of the vibration in the receiving structure but also gives the estimate of noise radiation that in many applications is the real target of the vibration isolation.

The second part of the paper considers the efficacy of four different control strategies with reference to the optimal approach which is the minimisation of total power input to the receiver. The strategies of cancelling the velocities or forces under the mounts are generally less effective than minimising total power while the minimisation of axial power perform very poorly [12]. Minimisation of weighted sum of squared velocities and forces, however, gives similar results to the control of total power.

It has also been shown in references [6,7,12] that for more realistic cases, characterised by measurement errors and flanking paths, the cancellation of velocity or force is more effective than the active control of measured power. The minimisation of the

sum of squared velocities and weighted square forces gives a particularly interesting result since the efficacy of the isolation is almost equal to the total power minimisation control strategy and this performance is not sensitive to measurement errors or flanking paths.

ACKNOWLEDGEMENTS

The content of this paper is part of a Brite-Euram project supported by the EEC Commission under the contract BREU 7228 ASPEN.

7. REFERENCES

1. C. M. Harris, *Shock and Vibration Handbook*, McGraw-Hill New York 1961.
2. J. I. Soliman and M. G. Hallam, Vibration isolation between non-rigid machines and non-rigid foundations, *Journal of Sound and Vibration* 1968, 8(2), 329-351.
3. J. H. Gordis, R. L. Bielawa and W. G. Flannelly, A general theory for frequency domain structural synthesis, *Journal of Sound and Vibration* 1990, 150(1), 139-158.
4. P. Gardonio, S. J. Elliott and R. J. Pinnington, Active isolation of structural vibration on multiple degree of freedom system. Part I: dynamic of the system, *Submitted to Journal of Sound and Vibration* 1996.
5. P. A. Nelson and S. J. Elliott, *Active control of sound* Academic Press London 1991.
6. P. Gardonio, S. J. Elliott and R. J. Pinnington, Active isolation of structural vibration on multiple degree of freedom system. Part II: active control strategies effectiveness, *Submitted to Journal of Sound and Vibration* 1996.
7. P. Gardonio, S. J. Elliott and R. J. Pinnington, Active control of structural vibration transmission from a vibrating rigid body to a flexible panel using two active mounts, *Proceedings of ISMA 21, 18-20 Sept. 1996 Katholieke Univ., Leuven Belgium*
8. M. D. Jenkins, P. A. Nelson, R. J. Pinnington and S. J. Elliott, Active isolation of periodic machinery vibration, *Journal of Sound and Vibration* 1991, 166(1), 117-140.
9. J. Pan, J. Pan and C. H. Hansen, Total power flow from a vibrating rigid body to a thin panel through multiple elastic mounts, *Journal Acoustical Society of America* 1992, 92(2), pp 895-907, 1992.
10. R. J. Pinnington, Vibrational Power Transmission to a Seating of a Vibration Isolated Motor, *Journal of Sound and Vibration* 1987, 118(3), 515-530.
11. O. Bardou, P. Gardonio, S. J. Elliott and R. J. Pinnington, Active power minimisation and power absorption in a plate with force and moment excitation, *Submitted to Journal of Sound and Vibration* 1996.
12. P. Gardonio, S. J. Elliott and R. J. Pinnington, Flanking path effects in the active control of structural power transmission, *Proceedings of INTER NOISE 96, 30 July - 2 August 1996, Liverpool UK*.
13. L. Cremer, M. Heckl and E. E. Ungar, *Structure-Borne Sound*, Springer-Verlag Berlin Heidelberg New York 1988, 2nd ed.
14. R. J. Pinnington, Approximate mobilities of built up structures, *ISVR Technical Report No 162, University of Southampton* 1988.
15. I. Dyer, Moment Impedance of Plates, *The Journal of the Acoustical Society of America* 1960, 32(10), pp 1290-1297.
16. H. G. D. Goyder and R. G. White, Vibrational power flow from machines into built-up structures, part I: introduction and approximate analyses of beam and plate-like foundations, *Journal of Sound and Vibration* 1980, 68(1), pp 59-75.
17. S. Ljunggren, Generation of waves in an elastic plate by a torsional moment and a horizontal force, *Journal of Sound and Vibration* 1984, 93(2), pp 161-187.

18. S. Ljunggren, Generation of waves in an elastic plate by a vertical force and by a moment in the vertical plane, *Journal of Sound and Vibration* 1983, 90(4), pp 559-584.
 19. W. Soedel, *Vibrations of Shells and Plates*, Marcel Dekker Inc, New York 1993, 2nd ed.

APPENDIX A: SOURCE DYNAMICS

Practical applications of complete isolating systems often involve systems having a source of vibration that can be modelled as a rigid mass on which act external forces and moments that represent the source excitation. When more than one mount is

attached to the source then the mobility and load matrices of such sub-systems become quite involved. In this appendix, the matrix formulation is derived for a source modelled as a rigid mass free to vibrate in the y - z plane and excited by forces and a moment acting in the same plane. Two mounts, reacting to axial (z -direction), and transverse (y -direction) displacements and to rotation (θ_x -direction), are connected to the source. As shown in figure 12 the primary excitation is divided into three components acting on the centre of gravity of the mass (N_{yG} , N_{zG} , M_{xG});

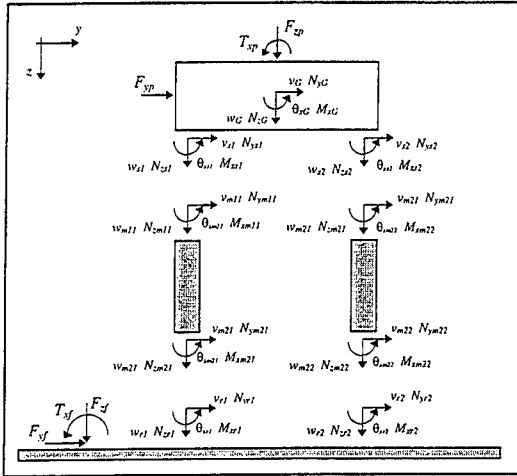


Fig. 12: Scheme with the junctions parameters of the complete isolating system.

figure 12 also shows the displacement and force parameters for the two junctions where the source is connected to the mounts. With reference to the source vectors notation introduced in section 2 for this particular case the source velocity and force vectors are given by the following set of parameters:

$$\mathbf{v}_s = \left\{ \dot{v}_{s1} \quad \dot{w}_{s1} \quad \dot{\theta}_{sx1} \quad \dot{v}_{s2} \quad \dot{w}_{s2} \quad \dot{\theta}_{sx2} \right\}^T \quad (\text{A.1})$$

$$\mathbf{f}_s = \left\{ N_{ys1} \quad N_{zs1} \quad M_{xs1} \quad N_{ys2} \quad N_{zs2} \quad M_{xs2} \right\}^T \quad (\text{A.2})$$

To describe the block mass dynamics with a matrix approach it is convenient to use two new vectors giving the linear-angular velocities and the force-moment parameters at the block mass centre of gravity as shown in figure 12:

$$\mathbf{v}_G = \left\{ \dot{v}_G \quad \dot{w}_G \quad \dot{\theta}_{xG} \right\}^T \quad \mathbf{f}_G = \left\{ N_{yG} \quad N_{zG} \quad M_{xG} \right\}^T \quad (\text{A.3, A.4})$$

Considering the block mass as a rigid body, for small oscillations these two vectors are related with the source vectors in the following way:

$$\mathbf{v}_s = \mathbf{V}_s \mathbf{v}_G \quad \mathbf{f}_G = \mathbf{F}_s \mathbf{f}_s \quad (\text{A.5, A.6})$$

where:

$$\mathbf{V}_s = \begin{bmatrix} 1 & 0 & 0 \\ 0 & 1 & (l_1 - \phi_c)/2 \\ 0 & 0 & 1 \\ 1 & 0 & 0 \\ 0 & 1 & -(l_1 - \phi_c)/2 \\ 0 & 0 & 1 \end{bmatrix} \quad \mathbf{F}_s = \begin{bmatrix} 1 & 0 & 0 & 1 & 0 & 0 \\ 0 & 1 & 0 & 0 & 1 & 0 \\ l_2/2 & (l_1 - \phi_c)/2 & 1 & l_2/2 & -(l_1 - \phi_c)/2 & 1 \end{bmatrix} \quad (\text{A.7, A.8})$$

l_1, l_2 are the dimensions of the block mass and ϕ_c is the diameter of the suspension cross section. With reference to the centre of gravity parameters and, considering a motion with time dependence of the form $\exp(j\omega t)$, the dynamic equilibrium principle can be used to obtain the following equations:

$$\begin{cases} N_{xG} + F_{xp} = m\ddot{v}_G = j\omega m\dot{v}_G \\ N_{yG} + F_{yp} = m\ddot{w}_G = j\omega m\dot{w}_G \\ M_{xG} + T_{xp} = I_G\ddot{\theta}_{xG} = j\omega I_G\dot{\theta}_{xG} \end{cases} \quad (\text{A.9-A.11})$$

where F_{xp}, F_{yp}, T_{xp} are the three components of the primary source of vibration and m, I_G represent respectively the source mass and the source moment of inertia with respect to the x axis. These three equations can be summarised in matrix form:

$$\mathbf{f}_G = \mathbf{L}_G \mathbf{q}_p + \mathbf{H}_G \mathbf{v}_G \quad (\text{A.12})$$

so that:

$$\mathbf{v}_G = \mathbf{H}_G^{-1} \mathbf{f}_G - \mathbf{H}_G^{-1} \mathbf{L}_G \mathbf{q}_p \quad (\text{A.13})$$

where:

$$\mathbf{q}_p = \{F_{xp} \quad F_{yp} \quad T_{xp}\}^T \quad (\text{A.14})$$

is the primary excitation vector and the two matrices $\mathbf{L}_G, \mathbf{H}_G$ have the form:

$$\mathbf{L}_G = \begin{bmatrix} -1 & 0 & 0 \\ 0 & -1 & 0 \\ 0 & 0 & -1 \end{bmatrix} \quad \mathbf{H}_G = \begin{bmatrix} j\omega m & 0 & 0 \\ 0 & j\omega m & 0 \\ 0 & 0 & j\omega I_G \end{bmatrix} \quad (\text{A.15, A.16})$$

Then using equations (A.5) and (A.6) it is possible to express the dynamics of the system in terms of the junction parameters and the primary excitation vector as shown by equation (9) where in this case \mathbf{M}_{s1} and \mathbf{M}_{s2} are given by:

$$\mathbf{M}_{s1} = \mathbf{V}_s \mathbf{H}_G^{-1} \mathbf{F}_s \quad \mathbf{M}_{s2} = -\mathbf{V}_s \mathbf{H}_G^{-1} \mathbf{L}_G \quad (\text{A.17, A.18})$$

This result can be extended to a rigid mass free to oscillate into the space and connected with several mounts by using the same approach presented above.

APPENDIX B: MOUNTING SYSTEM DYNAMICS

The mounts of an isolator system can be studied as a one dimensional system composed of several elements. A general *multi-degree-of-freedom mount* reacts to normal and transverse (in two cross directions) forces and also reacts to bending moments (in two cross directions) and to a torsional moment. In this paper a system is studied that can vibrate in a plane and then excite the mounts with normal and

transverse forces and a bending moment; these excitations produce longitudinal and flexural waves propagating in the one-dimensional mount.

In this appendix the impedance matrices of a pair of mounts reacting to an axial force (N_{xm}), to a transverse force (N_{ym}) and to a bending moment (M_{xm}) are given. The mounts have an actuator which is able to act only in the axial direction. The mounts are considered as a flexible continuous system, having a passive behaviour given by a ring of rubber. The control actuator action is modelled as a couple of opposite forces (F_z) applied to the ends of the mounts, and all the passive effects of the actuating device are neglected.

With reference to the matrix formulation introduced in section 2, the dynamics of the mounting system is given by equation (11). Considering the notation of figure 12, the velocity and force vectors of the mounts are given by:

$$\mathbf{v}_m = \{\mathbf{v}_{m11} \quad \mathbf{v}_{m12} \quad \mathbf{v}_{m21} \quad \mathbf{v}_{m22}\}^T \quad \mathbf{f}_s = \{\mathbf{f}_{m11} \quad \mathbf{f}_{m12} \quad \mathbf{f}_{m21} \quad \mathbf{f}_{m22}\}^T \quad (\text{B.1, B.2})$$

where for example $\mathbf{v}_{m11} = \{\dot{v}_{m11} \quad \dot{w}_{m11} \quad \dot{\theta}_{xm11}\}$ and $\mathbf{f}_{m11} = \{N_{ym11} \quad N_{zm11} \quad M_{xm11}\}$. The impedance matrix \mathbf{Z}_{m1} of equation (11) is given by:

$$\mathbf{Z}_{m1} = \frac{E}{j\omega} \begin{bmatrix} \mathbf{Z}_{11} & \mathbf{0} & \mathbf{Z}_{12} & \mathbf{0} \\ \mathbf{0} & \mathbf{Z}_{11} & \mathbf{0} & \mathbf{Z}_{12} \\ \mathbf{Z}_{21} & \mathbf{0} & \mathbf{Z}_{22} & \mathbf{0} \\ \mathbf{0} & \mathbf{Z}_{21} & \mathbf{0} & \mathbf{Z}_{22} \end{bmatrix} \quad (\text{B.3})$$

where [13]:

$$\mathbf{Z}_{11} = \begin{bmatrix} \frac{I_x k_f^2 (\varphi_4 \varphi_2 - \varphi_1 \varphi_3)}{\varphi_4 \varphi_2 - \varphi_1^2} & 0 & \frac{I_x k_f^2 (\varphi_3 \varphi_1 - \varphi_2^2)}{\varphi_4 \varphi_2 - \varphi_1^2} \\ 0 & \frac{A k_f \lambda_1}{\lambda_2} & 0 \\ \frac{I_x k_f^2 (\varphi_4^2 - \varphi_1 \varphi_3)}{\varphi_4 \varphi_2 - \varphi_1^2} & 0 & \frac{I_x k_f (\varphi_4 \varphi_1 - \varphi_2 \varphi_3)}{\varphi_4 \varphi_2 - \varphi_1^2} \end{bmatrix} \quad \mathbf{Z}_{12} = \begin{bmatrix} \frac{I_x k_f^2 \varphi_2}{\varphi_4 \varphi_2 - \varphi_1^2} & 0 & -\frac{I_x k_f^2 \varphi_3}{\varphi_4 \varphi_2 - \varphi_1^2} \\ 0 & -\frac{A k_f}{\lambda_2} & 0 \\ \frac{I_x k_f^2 \varphi_1}{\varphi_4 \varphi_2 - \varphi_1^2} & 0 & -\frac{I_x k_f \varphi_4}{\varphi_4 \varphi_2 - \varphi_1^2} \end{bmatrix} \quad (\text{B.4, B.5})$$

$$\mathbf{Z}_{21} = \begin{bmatrix} \frac{I_x k_f^2 \varphi_2}{\varphi_4 \varphi_2 - \varphi_1^2} & 0 & \frac{I_x k_f^2 \varphi_3}{\varphi_4 \varphi_2 - \varphi_1^2} \\ 0 & \frac{A k_f}{\lambda_2} & 0 \\ -\frac{I_x k_f^2 \varphi_1}{\varphi_4 \varphi_2 - \varphi_1^2} & 0 & -\frac{I_x k_f \varphi_4}{\varphi_4 \varphi_2 - \varphi_1^2} \end{bmatrix} \quad \mathbf{Z}_{22} = \begin{bmatrix} \frac{I_x k_f^2 (\varphi_4 \varphi_2 - \varphi_1 \varphi_3)}{\varphi_4 \varphi_2 - \varphi_1^2} & 0 & -\frac{I_x k_f^2 (\varphi_3 \varphi_1 - \varphi_2^2)}{\varphi_4 \varphi_2 - \varphi_1^2} \\ 0 & \frac{A k_f \lambda_1}{\lambda_2} & 0 \\ -\frac{I_x k_f^2 (\varphi_4^2 - \varphi_1 \varphi_3)}{\varphi_4 \varphi_2 - \varphi_1^2} & 0 & \frac{I_x k_f (\varphi_4 \varphi_1 - \varphi_2 \varphi_3)}{\varphi_4 \varphi_2 - \varphi_1^2} \end{bmatrix} \quad (\text{B.6, B.7})$$

where E is the Young's modulus of elasticity, A and I_x are respectively the area and the moment of inertia for the cross section of the mount (with reference to the x axis), k_f and k_f are respectively the wave number of the quasi longitudinal and flexural waves in a beam. The damping effect can be introduced by considering the complex wave number. The other terms are given by the following expressions:

$$\lambda_1 = \cos k_f h \quad \lambda_2 = \sin k_f h \quad (\text{B.8, B.19})$$

$$\varphi_1 = \frac{1}{2} [\cosh k_f h + \cos k_f h] \quad \varphi_3 = \frac{1}{2} [\cosh k_f h - \cos k_f h] \quad (\text{B.10, B.11})$$

$$\varphi_2 = \frac{1}{2} [\sinh k_f h + \sin k_f h] \quad \varphi_4 = \frac{1}{2} [\sinh k_f h - \sin k_f h] \quad (\text{B.12, B.13})$$

and h is the height of the actuator for a single mount. The impedance matrix \mathbf{Z}_{m2} and the control excitation vector in equation (11) have the form:

$$\mathbf{Z}_{m2} = [-\mathbf{T}_1^T \quad -\mathbf{T}_2^T \quad +\mathbf{T}_1^T \quad +\mathbf{T}_2^T] \quad \mathbf{q}_s = \{F_{s1} \quad F_{s2}\}^T \quad (\text{B.14, B.15})$$

where:

$$\mathbf{T}_1 = \begin{bmatrix} 1 & 0 & 0 \\ 0 & 0 & 0 \end{bmatrix}^T \quad \mathbf{T}_2 = \begin{bmatrix} 0 & 0 & 0 \\ 1 & 0 & 0 \end{bmatrix}^T \quad (\text{B.16, B.17})$$

The procedure to determine the impedance matrices presented above can be extended to a system having several mounts vibrating in all directions.

APPENDIX C: RECEIVER DYNAMICS

In this appendix the dynamics of a flat infinite or finite plate are studied, when excited by out-of-plane and in-plane forces and by bending moments. The in-plane force are assumed to act in the middle of the plate cross section and then generating only in-plane longitudinal waves and in-plane shear (transverse) waves while the out-of-plane force and the flexural moment generate only out-of-plane flexural waves. Longitudinal and shear (transverse) waves are characterised by in-plane displacements $u(x,y)$ and $v(x,y)$ while the flexural wave is characterised by out-of-plane displacements $w(x,y)$ and plate cross section rotations $\theta_x(x,y)$ and $\theta_y(x,y)$. The formulation reported in this appendix does not consider the action of a torsional moment which generates shear (transverse) waves.

The dynamics of the receiver system is given by equation (10). As shown in figure 2 the complete isolating system studied in this paper is characterised by a rigid mass connected to the receiver plate through two mounts. The junctions connecting the mounts to the plate and the flanking excitation forces and moment are placed along the y axis. As shown in figure 12, the two mounts excite the plate with a pair of out-of-plane forces N_{x1} and N_{x2} , with a pair of in-plane forces N_{y1} and N_{y2} and with a pair of moments M_{x1} and M_{x2} . The flanking excitation consists of an out-of-plane force F_{yf} , a in-plane force F_{yf} and a torque in the y,z plane T_{yf} . So, the formulation of the two mobility matrices are simplified since only some of the degrees-of-freedom at a fixed position of the receiver plate are considered. In fact, with reference to the notation of figure 12, the receiver velocity, force vector and flanking excitation vector used in equation (10) are given respectively by:

$$\mathbf{v}_r = \{\dot{v}_{r1} \quad \dot{w}_{r1} \quad \dot{\theta}_{x1} \quad \dot{v}_{r2} \quad \dot{w}_{r2} \quad \dot{\theta}_{x2}\}^T \quad \mathbf{f}_r = \{N_{y1} \quad N_{x1} \quad M_{x1} \quad N_{y2} \quad N_{x2} \quad M_{x2}\}^T$$

$$\mathbf{q}_f = \{F_{yf} \quad F_{yf} \quad T_{yf}\}^T \quad (\text{C.1-C.3})$$

Because only the in-plane force (N_{y1}) produces in-plane vibration (v_r) while only the out-of-plane force (N_{x1}) and the moment (M_{x1}) produce out-of-plane (w_r) and angular (θ_{x1}) vibration the two mobility matrices \mathbf{M}_{r1} and \mathbf{M}_{r2} of equation (10) are given by:

$$\mathbf{M}_{r1} = \begin{bmatrix} m_{vN_1}^{11} & 0 & 0 & m_{vN_1}^{12} & 0 & 0 \\ 0 & m_{wN_1}^{11} & m_{wM_1}^{11} & 0 & m_{wN_1}^{12} & m_{wM_1}^{12} \\ 0 & m_{\theta N_1}^{11} & m_{\theta M_1}^{11} & 0 & m_{\theta N_1}^{12} & m_{\theta M_1}^{12} \\ m_{vN_1}^{21} & 0 & 0 & m_{vN_1}^{22} & 0 & 0 \\ 0 & m_{wN_1}^{21} & m_{wM_1}^{21} & 0 & m_{wN_1}^{22} & m_{wM_1}^{22} \\ 0 & m_{\theta N_1}^{21} & m_{\theta M_1}^{21} & 0 & m_{\theta N_1}^{22} & m_{\theta M_1}^{22} \end{bmatrix} \quad \mathbf{M}_{r2} = \begin{bmatrix} m_{vN_2}^{1p} & 0 & 0 \\ 0 & m_{wN_2}^{1p} & m_{wM_2}^{1p} \\ 0 & m_{\theta N_2}^{1p} & m_{\theta M_2}^{1p} \\ m_{vN_2}^{2p} & 0 & 0 \\ 0 & m_{wN_2}^{2p} & m_{wM_2}^{2p} \\ 0 & m_{\theta N_2}^{2p} & m_{\theta M_2}^{2p} \end{bmatrix} \quad (\text{C.4,C.5})$$

where m^{ij} indicates a point mobility term at the j -th junction while the term m^k indicates a transfer mobility term between junction j (where the velocity is evaluated)

and junction k (where the excitation is acting). It should be said that equation (C.4) refers to any case of plate element and when the infinite plate case is considered the point mobility terms m_{θ_d, N_i}^j and m_{w, M_i}^j are zero.

The next two subsections give general mobility equations considering either an infinite or a finite plate. With these formulae it is then possible to derive the mobilities of the two matrices \mathbf{M}_{r1} and \mathbf{M}_{r2} . The notation used in these subsections is shown in figures 13 and 14. Figure 13 shows the notation used for the in-plane displacements (u and v) and the in-plane forces (N_x and N_y) at two generic points of a plate while figure 14 shows the notation at two generic points of a plate used for the out-of-plane displacement (w), for the rotation in a general direction in the x - y plane (θ_d), for the out-of-plane force (N_z) and for the moment in a

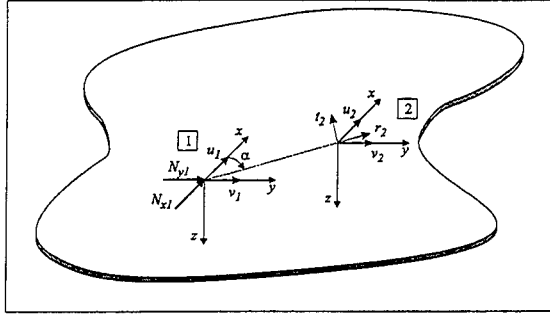


Fig. 13: Notation for in-plane velocity and force parameters.

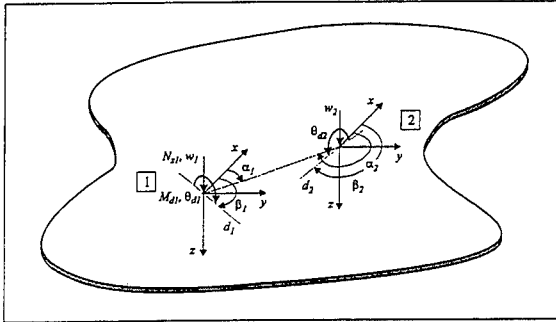


Fig. 14: Notation for out-of-plane velocity and force parameters.

general direction in the x - y plane (M_d). At each of these two points a local system of reference composed of a right-handed triple of vectors (x , y , z) is defined. The formulation of the transfer mobility terms in an infinite plate require the knowledge of the angle α which is defined as the angle between the x axis and the segment r joining the two points examined. This angle is defined as positive with reference to the right-handed screw rule. For the mobilities involving angular velocities or flexural moments a second angle β is used and this is defined as the angle between the x axis and the segment d as shown in figure 14.

C.1. INFINITE PLATE

In the formulation below the point mobility for in-plane or out-of-plane forces and for the moments contains the local indenter effect, which is the cause of the imaginary parts in the mobility; when the transfer mobilities are considered, however, these local effects can be ignored, and the imaginary parts of the mobilities are due only to the wave propagating effects. The input mobility terms m^j are considered first with reference to position 1. The in-plane velocities \dot{u}_1 and \dot{v}_1 relate respectively to the in-plane forces N_{x1} and N_{y1} by two mobility terms, one for the longitudinal wave and one for the shear (transverse) wave [14]:

$$m_{ux}^{11} = \frac{\dot{u}_{x1}}{N_{x1}} = m_{vy}^{11} = \frac{\dot{v}_{y1}}{N_{y1}} = \frac{\omega}{8D} \left[1 + \frac{j}{\pi} \ln \left(\frac{\omega_l}{\omega} \right)^2 \right] + \frac{\omega}{8S} \left[1 + \frac{j}{\pi} \ln \left(\frac{\omega_s}{\omega} \right)^2 \right] \quad (C.6)$$

where $D = sE/(1-\nu^2)$ and $S = sG$ are respectively the longitudinal and shear stiffness, s is the plate thickness, E is the Young's modulus of elasticity, G is the shear Young's modulus of elasticity and ν is the Poisson's ratio. $\omega_l = \pi\sqrt{D/4\rho s\phi_c^2}$, $\omega_s = \pi\sqrt{S/4\rho s\phi_c^2}$, ρ is the density and ϕ_c is the diameter of the indenter. The out of plane force N_{z1} generates a flexural wave that at position 1 is characterised only by transverse \dot{w}_1 velocity. So the point mobility associated with this excitation is [13]:

$$m_{wz}^{11} = \frac{\dot{w}_1}{N_{z1}} = \frac{\omega}{8Bk_f^2} \quad (C.7)$$

where $B = Es^3/12(1-\nu^2)$ is the flexural stiffness for a plate and k_f is the wave number of flexural waves in a plate. Also the torques M_{x1} and M_{y1} generate a flexural wave that at position 1 is characterised only by plate angular velocities that are respectively $\dot{\theta}_{x1}$ and $\dot{\theta}_{y1}$. The two mobilities are then given by [15]:

$$m_{ux}^{11} = \frac{\dot{\theta}_{x1}}{M_{x1}} = m_{vy}^{11} = \frac{\dot{\theta}_{y1}}{M_{y1}} = \frac{\omega}{8B(1+L)} \left[1 + j \frac{4}{\pi} \ln k_f \phi_c - \frac{j8L}{\pi(1-\nu^2)} \left(\frac{s}{\pi\phi_c} \right)^2 \right] \quad (C.8)$$

where L is a parameter which tends to unity for large ϕ_c/s [16]. The transfer mobilities are now examined for the particular case where the velocities are evaluated at position 2 while the forces or moments are applied at position 1. With reference to the notation introduced in figure 13 the in-plane forces N_{x2} or N_{y2} produce axial and shear waves that propagate with a typical dipole velocity distribution. The transfer mobilities in polar co-ordinates (r, θ) considering the in-plane N_{y2} excitation are given by the following two equations [17]:

$$M_{ny}^{21} = \frac{\dot{r}_2}{N_{y1}} = \frac{\omega}{4D} \left[H_0^{(2)}(k_l r) - \frac{1}{k_l r} H_1^{(2)}(k_l r) \right] \cos \alpha + \frac{\omega}{4S} \left[\frac{1}{k_l r} H_1^{(2)}(k_l r) \right] \cos \alpha \quad (C.9)$$

$$M_{ny}^{21} = \frac{\dot{r}_2}{N_{y1}} = \frac{\omega}{4D} \left[\frac{1}{k_l r} H_1^{(2)}(k_l r) \right] \sin \alpha + \frac{\omega}{4S} \left[H_0^{(2)}(k_s r) + \frac{1}{k_s r} H_1^{(2)}(k_s r) \right] \sin \alpha \quad (C.10)$$

where k_l and k_s are respectively the wave numbers of quasi-longitudinal waves and shear waves in a plate. $H_i^{(2)}$ is the second kind of Hankel function of the i -th order. With these two equations it is then possible to derive the two mobility terms m_{ny}^{21} and m_{vx}^{21} relating the N_{y1} in-plane force with the in-plane \dot{u}_2 and \dot{v}_2 velocities. As similar procedure can be used to derive the two mobility terms m_{ux}^{21} and m_{vx}^{21} relating the N_{x1} in-plane force with the in-plane \dot{u}_1 and \dot{v}_1 velocities respectively. If a bending moment $M_{\theta 1}$ and an angular velocity $\dot{\theta}_{\theta 2}$ with general orientation defined respectively by the angles β_1 and β_2 are considered, the following four transfer mobility terms can be derived [11,18]:

$$M_{wz}^{21} = \frac{\dot{w}_2}{N_{z1}} = \frac{\omega}{8Bk_f^2} \left[H_0^{(2)}(k_f r) - j \frac{2}{\pi} K_0(k_f r) \right] \quad (C.11)$$

$$M_{wMl}^{21} = \frac{\dot{w}_2}{M_{d1}} = \frac{\omega}{8Bk_f} \left[H_1^{(2)}(k_f r) - j \frac{2}{\pi} K_1(k_f r) \right] \cos \varepsilon_1 \quad (C.12)$$

$$M_{\theta dMl}^{21} = \frac{\dot{\theta}_{d2}}{N_{z1}} = \frac{\omega}{8Bk_f} \left[H_1^{(2)}(k_f r) - j \frac{2}{\pi} K_1(k_f r) \right] \cos \varepsilon_2 \quad (C.13)$$

$$M_{\theta dMl}^{21} = \frac{\dot{\theta}_{d2}}{M_{d1}} = \frac{\omega}{8B} \left\{ \left[H_0^{(2)}(k_f r) - \frac{1}{k_f r} H_1^{(2)}(k_f r) + j \frac{2}{\pi} \left(K_0(k_f r) + \frac{1}{k_f r} K_1(k_f r) \right) \right] \cos(\varepsilon_1 - \delta_2) \cos \varepsilon_1 - \frac{1}{k_f r} \left[H_1^{(2)}(k_f r) - j \frac{2}{\pi} K_1(k_f r) \right] \sin(\varepsilon_1 - \delta_2) \sin \varepsilon_1 \right\} \quad (C.14)$$

where the following parameters are defined: $\delta_1 = \beta_2 - \beta_1$, $\delta_2 = \beta_1 - \beta_2$, $\varepsilon_1 = \alpha_1 - \beta_1$, $\varepsilon_2 = \alpha_2 - \beta_2$. $H_i^{(2)}$ is the second kind of Hankel function of the i -th order and K_i is the second kind modified Bessel function of the i -th order. If the moment and the angular velocity parameters are aligned then $\beta_1 = \alpha_1$ or $\beta_1 = \alpha_1 + \pi$ and $\beta_2 = \alpha_2$ or $\beta_2 = \alpha_2 + \pi$. Therefore $\varepsilon_1 = 0$ and $\varepsilon_2 = 0$ and equation (C.14) assumes the following simplified form:

$$Y_{\theta dMl}^{21} = \frac{\dot{\theta}_{d2}}{M_{d1}} = \frac{\omega}{8B} \left[H_0^{(2)}(k_f r) - \frac{1}{k_f r} H_1^{(2)}(k_f r) + j \frac{2}{\pi} \left(K_0(k_f r) + \frac{1}{k_f r} K_1(k_f r) \right) \right] \quad (C.15)$$

Using equation (C.12) it is possible to derive the expressions of the mobility terms m_{wMl}^{21} and m_{wMf}^{21} while from equation (C.13) the mobility terms $m_{\theta wNz}^{21}$ and $m_{\theta yNz}^{21}$ can be derived. Finally, using equation (C.14) the four mobility terms $m_{\theta zMx}^{21}$, $m_{\theta yMx}^{21}$, $m_{\theta zMy}^{21}$, and $m_{\theta yMy}^{21}$ can be evaluated.

C.2. FINITE PLATE

The notation used is the same as shown in figures 13 and 14 and a main system of reference is considered at the left bottom corner of the plate as shown in figure 2. The simply supported boundary condition imposes the following restraints at the edges of the plate:

$$\begin{array}{lll} x=0 \text{ and } x=l_x & v=w=0 & \frac{\partial^2 v}{\partial x^2} = \frac{\partial^2 w}{\partial x^2} = 0 \quad \frac{\partial u}{\partial x} = 0 \\ y=0 \text{ and } y=l_y & u=w=0 & \frac{\partial^2 u}{\partial x^2} = \frac{\partial^2 w}{\partial x^2} = 0 \quad \frac{\partial v}{\partial x} = 0 \end{array}$$

When a finite structure is considered the formulae of point and transfer mobilities have the same form. So, the following equations are given for transfer mobilities but can equally be applied for point mobilities. The in-plane velocities \dot{u}_2 and \dot{v}_2 relate respectively to the in-plane forces N_{x1} and N_{y1} by two mobility terms, one for the longitudinal wave and one for the shear (transverse) wave [19]:

$$m_{uNz}^{21} = \frac{\dot{u}_2}{N_{x1}} = j\omega \sum_{m=0}^{\infty} \sum_{n=0}^{\infty} \frac{\lambda_{m,n}^{(x)}(x_2, y_2) \lambda_{m,n}^{(x)}(x_1, y_1)}{\Lambda[\omega_{lm,n}^2(1+j\eta) - \omega^2]} + j\omega \sum_{m=0}^{\infty} \sum_{n=0}^{\infty} \frac{\lambda_{m,n}^{(x)}(x_2, y_2) \lambda_{m,n}^{(x)}(x_1, y_1)}{\Lambda[\omega_{\theta m,n}^2(1+j\eta) - \omega^2]} \quad (C.16)$$

$$m_{wNy}^{21} = \frac{\dot{u}_2}{N_{y1}} = j\omega \sum_{m=0}^{\infty} \sum_{n=0}^{\infty} \frac{\lambda_{m,n}^{(x)}(x_2, y_2) \lambda_{m,n}^{(y)}(x_1, y_1)}{\Lambda[\omega_{lm,n}^2(1+j\eta) - \omega^2]} + j\omega \sum_{m=0}^{\infty} \sum_{n=0}^{\infty} \frac{\lambda_{m,n}^{(x)}(x_2, y_2) \lambda_{m,n}^{(y)}(x_1, y_1)}{\Lambda[\omega_{sm,n}^2(1+j\eta) - \omega^2]} \quad (C.17)$$

$$m_{wNx}^{21} = \frac{\dot{v}_2}{N_{x1}} = j\omega \sum_{m=0}^{\infty} \sum_{n=0}^{\infty} \frac{\lambda_{m,n}^{(y)}(x_2, y_2) \lambda_{m,n}^{(x)}(x_1, y_1)}{\Lambda[\omega_{lm,n}^2(1+j\eta) - \omega^2]} + j\omega \sum_{m=0}^{\infty} \sum_{n=0}^{\infty} \frac{\lambda_{m,n}^{(y)}(x_2, y_2) \lambda_{m,n}^{(x)}(x_1, y_1)}{\Lambda[\omega_{sm,n}^2(1+j\eta) - \omega^2]} \quad (C.18)$$

$$m_{wNy}^{21} = \frac{\dot{v}_2}{N_{y1}} = j\omega \sum_{m=1}^{\infty} \sum_{n=1}^{\infty} \frac{\lambda_{m,n}^{(y)}(x_2, y_2) \lambda_{m,n}^{(y)}(x_1, y_1)}{\Lambda[\omega_{lm,n}^2(1+j\eta) - \omega^2]} + j\omega \sum_{m=1}^{\infty} \sum_{n=0}^{\infty} \frac{\lambda_{m,n}^{(y)}(x_2, y_2) \lambda_{m,n}^{(y)}(x_1, y_1)}{\Lambda[\omega_{sm,n}^2(1+j\eta) - \omega^2]} \quad (C.19)$$

where $\Lambda = \rho s l_x l_y / 4$ is the modal mass, $\omega_{lm,n}$ and $\omega_{sm,n}$ are the m, n -th natural frequencies associated respectively with the longitudinal and shear waves propagating on the plate η is the loss factor and $\lambda_{m,n}^{(x)}, \lambda_{m,n}^{(y)}$ are the m, n -th eigenfunctions:

$$\omega_{lm,n} = \sqrt{\frac{E}{\rho(1-\nu^2)}} \left[\left(\frac{m\pi}{l_x} \right)^2 + \left(\frac{n\pi}{l_y} \right)^2 \right] \quad \omega_{sm,n} = \sqrt{\frac{G}{\rho}} \left[\left(\frac{m\pi}{l_x} \right)^2 + \left(\frac{n\pi}{l_y} \right)^2 \right] \quad (C.20, C.21)$$

$$\lambda_{m,n}^{(x)}(x, y) = \cos \frac{m\pi x}{l_x} \sin \frac{n\pi y}{l_y} \quad \lambda_{m,n}^{(y)}(x, y) = \sin \frac{m\pi x}{l_x} \cos \frac{n\pi y}{l_y} \quad (C.22, C.23)$$

with $m = 0, 1, 2, \dots$ and $n = 0, 1, 2, \dots$. The out of plane force N_{z1} and the flexural moments M_{x1} and M_{y1} at position 1 generate flexural waves that at position 2 are characterised by both transverse \dot{w}_2 velocity and angular $\dot{\theta}_{x2}$ and $\dot{\theta}_{y2}$ velocities. So the point mobility associated with this excitation are [19]:

$$\begin{aligned} m_{wNx}^{21} &= \frac{\dot{w}_2}{M_{x1}} = j\omega \sum_{m=1}^{\infty} \sum_{n=1}^{\infty} \frac{\Phi_{m,n}(x_2, y_2) \Psi_{m,n}^{(x)}(x_1, y_1)}{\Lambda[\omega_{fm,n}^2(1+j\eta) - \omega^2]} & m_{wNy}^{21} &= \frac{\dot{w}_2}{M_{y1}} = j\omega \sum_{m=1}^{\infty} \sum_{n=1}^{\infty} \frac{\Phi_{m,n}(x_2, y_2) \Psi_{m,n}^{(y)}(x_1, y_1)}{\Lambda[\omega_{fm,n}^2(1+j\eta) - \omega^2]} \\ m_{\theta Nx}^{21} &= \frac{\dot{\theta}_{x2}}{M_{x1}} = j\omega \sum_{m=1}^{\infty} \sum_{n=1}^{\infty} \frac{\Psi_{m,n}^{(x)}(x_2, y_2) \Psi_{m,n}^{(x)}(x_1, y_1)}{\Lambda[\omega_{fm,n}^2(1+j\eta) - \omega^2]} & m_{\theta Ny}^{21} &= \frac{\dot{\theta}_{y2}}{M_{y1}} = j\omega \sum_{m=1}^{\infty} \sum_{n=1}^{\infty} \frac{\Psi_{m,n}^{(y)}(x_2, y_2) \Psi_{m,n}^{(y)}(x_1, y_1)}{\Lambda[\omega_{fm,n}^2(1+j\eta) - \omega^2]} \\ m_{\theta Nx}^{21} &= \frac{\dot{\theta}_{x2}}{N_{z1}} = j\omega \sum_{m=1}^{\infty} \sum_{n=1}^{\infty} \frac{\Psi_{m,n}^{(x)}(x_2, y_2) \Phi_{m,n}(x_1, y_1)}{\Lambda[\omega_{fm,n}^2(1+j\eta) - \omega^2]} & m_{\theta Ny}^{21} &= \frac{\dot{\theta}_{y2}}{N_{z1}} = j\omega \sum_{m=1}^{\infty} \sum_{n=1}^{\infty} \frac{\Psi_{m,n}^{(y)}(x_2, y_2) \Phi_{m,n}(x_1, y_1)}{\Lambda[\omega_{fm,n}^2(1+j\eta) - \omega^2]} \\ m_{wNz}^{21} &= \frac{\dot{w}_2}{N_{z1}} = j\omega \sum_{m=1}^{\infty} \sum_{n=1}^{\infty} \frac{\Phi_{m,n}(x_2, y_2) \Phi_{m,n}(x_1, y_1)}{\Lambda[\omega_{fm,n}^2(1+j\eta) - \omega^2]} \end{aligned} \quad (C.24-C.30)$$

where $\Lambda = \rho s l_x l_y / 4$ is the modal mass, $\omega_{fm,n}$ is the m, n -th natural frequency due to the flexural wave propagating on the plate, η is the loss factor and $\Phi_{m,n}, \Psi_{m,n}^{(x)}, \Psi_{m,n}^{(y)}$ are the m, n -th eigenfunctions:

$$\omega_{fm,n} = \sqrt{\frac{Es^2}{12\rho(1-\nu^2)}} \left[\left(\frac{m\pi}{l_x} \right)^2 + \left(\frac{n\pi}{l_y} \right)^2 \right] \quad \Phi_{m,n}(x, y) = \sin \frac{m\pi x}{l_x} \sin \frac{n\pi y}{l_y} \quad (C.31, C.32)$$

$$\Psi_{m,n}^{(x)}(x, y) = \frac{m\pi}{l_x} \cos \frac{m\pi x}{l_x} \sin \frac{n\pi y}{l_y} \quad \Psi_{m,n}^{(y)}(x, y) = \frac{n\pi}{l_y} \sin \frac{m\pi x}{l_x} \cos \frac{n\pi y}{l_y} \quad (C.33, C.34)$$

An Application of An Artificial Neural Network Method to Nonlinear Vibration Control Systems

Meiling Zhu Chunsheng Zhao

Institute of Vibration Engineering Research
Nanjing University of Aeronautics & Astronautics
Nanjing, 210016, People's Republic of China

Abstract: An artificial Neural Network Method (ANNM) used for nonlinear vibration control systems is investigated. The fundamental descriptions of the network structure and its learning rules are briefly given. A back propagation neural network control scheme is presented in combination with the theory of a state feedback control. The scheme provides a very efficient method for investigating the nonlinear vibration control systems in the case that their analysis models are difficult to build. Two examples are cited to illustrate its effectiveness. Furthermore, how to select some values of the important parameters of the ANN structure is discussed.

Introduction

Various control methods of vibration systems have been researched and widely used in the past few decades. The methods may be categorized into two major classes in terms of the approaches of building model. The first, being the most often used, uses known, fixed and lined system models, such as optimum control, suboptimal control and eigenstructure assignment. These methods have been successfully applied to some linear vibration systems (Matsumura and Yoshimoto, 1986; Lee and Kim, 1992; Nonamic *et. al.*, 1990). The second is to utilize an adaptive control method that is a kind of advance control technique, because it does not require a complete knowledge of controlled systems before designing the controllers and the controller parameters can be turned on real time according to the changes in the systems. It has been applied for controlling some nonlinear systems (Ulsoy and Koren, 1989; Butler *et. al.*, 1989). However, the adaptive control technique can be only used in such a case that the forms of models of the systems are known and based on a linear system theory (Liu, 1993). Moreover, these put heavy computational burdens for the control systems, because a large number of parameters of the models have to be estimated on-line. Thus, this limits the scope of its application.

Therefore, the control system must possess some performances of intelligence to learn and control a practical complex system (Shoureshi, 1991). Expert systems have been proven to be

In ANN1, the output u of ANN2 and measurement signal $Y(k)$ are used as the input layer signals of ANN1 and its output layer signal is $Y(k+1)$. Hence the learning signal can be expressed as

$$E = \frac{1}{2} [Y(k+1) - \hat{Y}(k+1)] \quad (3)$$

where $\hat{Y}(k+1)$ is a calculated output value of the network ANN1.

The model built by means of the neural network is following form

$$\hat{Y}(k+1) = \hat{f}(X(k), u(k), \theta(k), W(k), k) \quad (4)$$

where $\hat{f}(\cdot)$ is an estimated function of the vectors expressed by weights of the network.

In ANN2, its input layer signals are measurement signals $Y(k)$, its output signals are control signals. So learning signals can be expressed as

$$E = \frac{1}{2} [Y_d(k+1) - \hat{Y}(k+1)] \quad (5)$$

where Y_d is the target vector of desired output.

The output of ANN2 is

$$U(k+1) = G(Y(k), u(k), \theta(k), k) \quad (6)$$

where $G(\cdot)$ is expressed by the weights of the network. In the condition of a current state given, the neural network control scheme above presented can generate the correct control signals and drive the system to reach the desired state. It is necessary to monitor the output errors $[Y(k+1) - Y(k+1)]$ between the practical process and ANN1 model. If the errors are more than the boundary line, the connection weights of the neural network system must be updated at once.

Artificial Neural Network Model

Artificial neural networks, ANN1 and ANN2, consist of a large number of simple neurons. The typical artificial neuron model is shown in Fig. 2 (Kohonen, 1986). It is a nonlinear model having n inputs (x_1, x_2, \dots, x_n) , single output Y and some threshold θ . The neuron can receive the signals from other neurons by connecting weights ω_i , and/or from the external world, and/or from itself signal feedback. The connection strength between them can be adjusted by the weights ω_i . The relationship between the inputs and the output of the neurons can be expressed as follows

$$\begin{aligned} u &= \sum_{i=1}^n \omega_i x_i \\ Y &= f\left(\sum_{i=1}^n \omega_i x_i - \theta\right) \end{aligned} \quad (7)$$

where f is a sigmoid function. For symmetrical case

$$f_{\theta} = \frac{1 - e^{-(u - \theta)}}{1 + e^{-(u - \theta)}} \quad (8)$$

For unsymmetrical case

$$f_{\theta} = \frac{1}{1 + e^{-(u - \theta)}} \quad (9)$$

The multilayered feedforward neural network structure presented by Rumalhart and so on (1986) and employed in this paper is shown in Fig. 3. It is composed of three layers: input layer, hidden layer and output layer. Each neuron is represented by a circle, and each interconnection with its associated weight by an arrow. The neurons labeled b are bias neurons. These bias neurons always have an output of 1. They serve as threshold units for the layers.

For given an input vector $X = (x_1, x_2, \dots, x_n)$, the network can produce an output vector $Y = (y_1, y_2, \dots, y_m)$, and

$$Y = f(X) \quad (10)$$

where f is a nonlinear vector function between the inputs and outputs. It has been shown that this network is able to approximate arbitrary nonlinear functions with the arbitrary desired accuracy (Funahashi, 1989).

Learning algorithm

A learning algorithm is the role of adjusting mechanism of the weights ω_i . How to adjust the weights is a very important problem which influences upon the adaptability and anti-disturbance ability of control systems. Therefore, it is a nucleus in designing a neuron controller. Among the most current algorithms, the method of error Back-Propagation is one of the successful algorithms, often shortened to BP network algorithm. The gradient descent method and the error back-propagation are employed to adjust the weights between layers so as to minimize average sum-squared errors between the goals of learning and practical outputs of the network. The learning equations can be divided into two categories: feed-forward calculation from the input to the output, and error back-propagation from the output to the input. The calculation is made layer by layer, and parallelly in the same of layers in the learning algorithm. The relation between the input space and the output space of the nonlinear function is obtained. In the view of network structure shown in Fig. 2, a concrete algorithm is described as follows.

For given pairs of some inputs and outputs of the network, their errors between the goals of learning and practical outputs of the network are defined as

$$E_p = \frac{1}{2} \sum_{j=1}^J (t_{pj} - O_{pj})^2 \quad (11)$$

where E_p is the summation of the errors squared ; J is the total number of the output nodes; t_{pj} and O_{pj} are the goals of the learning and practical outputs of the network belonging to the p th training mode and the j th output node, respectively.

For the feed-forward calculation, the output O_i of the input layer node i is equal to its input , and the input of the hidden node j is expressed as follows

$$net_j = \sum_i^I \omega_{ji} \cdot x_i + \theta_j \quad (12)$$

Therefore, we obtain its output O_j

$$O_j = f(net_j) = \frac{1 - e^{(-net_j)}}{1 + e^{(-net_j)}} \quad j = 1, 2, \dots, J \quad (13)$$

The input of the output layer node l is expressed as follows

$$net_l = \sum_j^J \omega_{lj} \cdot O_j + \theta_l \quad (14)$$

Then, its output is

$$O_l = f(net_l) = \frac{1 - e^{(-net_l)}}{1 + e^{(-net_l)}} \quad l = 1, 2, \dots, L \quad (15)$$

where ω_{ji} and ω_{lj} are the weights of the network from the i th input neuron to the j th hidden neuron, and from the j th hidden neuron to the l th output neuron, respectively. θ_j and θ_l are thresholds of the j th hidden and the l th output neurons, respectively. I , J and L are the total number of its input, hidden and output nodes, respectively.

For the error back-propagation from the output toward the input, the equations used to update the ω_{lj} between the output layer and the hidden layer, and the ω_{ji} between the hidden layer and the input layer are respectively

$$\begin{aligned} \omega_{lj}(k+1) &= \omega_{lj}(k) + \eta \cdot \delta_l \cdot O_j + \alpha [\omega_{lj}(k) - \omega_{lj}(k-1)] \\ \omega_{ji}(k+1) &= \omega_{ji}(k) + \eta \cdot \delta_j \cdot O_i + \alpha [\omega_{ji}(k) - \omega_{ji}(k-1)] \end{aligned} \quad (16)$$

in which

$$\begin{aligned} \delta_l &= f'(net_l) \cdot (t_l - O_l) \\ \delta_j &= f'(net_j) \cdot \sum_l \delta_l \omega_{lj} \end{aligned} \quad (17)$$

k the number of learning;

η learning rate coefficient;

α defined as momentum coefficient.

η and α can be assigned an arbitrary value from 0 to 1.

When E_p is less than a given training error ε of the network, the learning process will be stopped.

Numerical Examples and Results

To demonstrate the ability of the scheme for identifying and controlling nonlinear vibration systems, computer simulations are performed for the systems with Van Del Pol equation and Duffing equation. The numerical solutions of the differential equations are sought through the applications of the fourth order Runge-Kuta method. The C language is chosen for the implementation of the numerical examples.

Example 1. Identification for the system with Van Del Pol equation

$$\ddot{x} + \varepsilon(cx^2 - 1)\dot{x} + x = 0$$

with $\varepsilon=0.1$. Introducing the state variables into Van Del Pol equation, that is, $x_1 = x$ and

$x_2 = \dot{x}$, we have

$$\dot{x}_1 = x_2$$

$$\dot{x}_2 = -\varepsilon(x_1^2 - 1)x_2 - x_1$$

Supposing that some measurement values about x_1 and x_2 are obtained, 250 group datum of the input and corresponding output are used for the training samples. In addition, the different number of hidden nodes, learning rate η and momentum coefficient α are chosen in the process of training. The network training error chosen is equal to 0.005.

The phase plane chart identified by the scheme is shown in Fig. 4. in which $\alpha=0.3$, $\eta=0.5$; $x_1(0)=2.22$, $x_2(0)=0.45$; $I=2$, $J=10$, $L=2$.

Example 2. Control for the system with Duffing equation

$$\ddot{x} + \mu C \dot{x} + x + \varepsilon dx^3 = \varepsilon B \cos \omega t + u(t)$$

with $\mu=0.1$, $C=0.2$, $\varepsilon=0.3$, $d=0.2$, $B=10$, $\omega=3.0$. In this equation, $u(t)$ is a control force. For the sake of comparison, the response curves of system verse time are also shown in Fig. 5(a) and in Fig. 5(b), respectively, without control and with the neural network control.

To select some values of important parameters of ANN structure, the relationships between the output mean square errors and the number of learning steps with different the number of hidden nodes, learning rates and momentum parameters are shown in Fig. 6, 7 and

8, respectively. In Fig. 6, $\alpha=0.3$, $\eta=0.45$. In Fig. 7, the number of hidden nodes is equal to 15. In Fig. 8, the number of hidden nodes is equal to 15, α is equal to 0.6 and 0.9.

Discussions and Conclusions

An artificial Neural Network Method (ANNM) used for nonlinear vibration control systems is investigated in combination with the theory of a state feedback control. The conclusion is drawn on the follows:

It can be used for a controller by learning the practical system, without the requirement for the a mathematical model and control algorithm of the controlled system.

It has some kind of abilities of adaptation and parallel dealing for nonlinear vibration control systems which models are complex and difficult established.

Further work is to analyze the stability and convergence of the neural network control system and solve its acceleration of the calculation so as to obtain real time control.

References

1. Matsumura, F, and Yoshimoto, T., system Modeling and Control Design of a Horizontal- Shaft Magnetic-Bearing System, IEEE Transactions on Magnetics, 1986, Vol. MAG-22, No.3, pp.196-203.
2. Lee, C.W. and Kim, J. S., Modal Testing and Suboptimal Vibration Control of Flexible Rotor Bearing System by Using a Magnetic Bearing, ASME Journal of Dynamic Systems, Measurement, and Control, 1992 Vol.114, pp.244-251.
3. Nonamic, *et al*, Vibration and Control of Flexible Rotor Supported by Magnetic Bearings, JSME Inter. J., Series III, 1990, Vol.33, No.4, pp.475-482.
4. Ulsoy, A. and Koren, Y., Application of Adaptive Control to Machine Tool Process Control, IEEE Control Systems Magazine, 1989, Vol. 9, No. 4, pp.33-36.
5. Butler, H. *et al*, Modal Reference Adaptive Control of a Direct-Drive DcMotor, IEEE Control Systems magazine, 1989, Vol. 9, No. 1, pp.80-84.
6. Shoureshi, R., The Mystique of Intelligent Control, IEEE Control Systems Magazine, 1991, Vol. 11, No. 1, pp.33-45.
7. Wiley. J. and sons, Neural and Concurrent Real-Time Systems, America,U.S., New York Press, 1989, pp.43-139.
8. Liu, T.I. *et al*, Intelligent Monitoring of tapping tools, ASME J. Mater. Shaping Technol., 1990, Vol.8, No.4, pp.249-254.
9. Liu, T. I. *et al*, Diagnosis of tapping Operation Using A.I. Approach, ASME J. Mater. Shaping Technol., 1991, Vol.9, No.1, pp. 49-54.

10. Kung, S.Y. and Hwang, J. H., Neural Network Architectures for Robotic Applications, IEEE Trans. Robotics Automation, 1989, Vol.5, No.5, pp.641-656.
11. Psaltis, D. et al, A Multilayered Neural Network Controller, IEEE Control Systems Magazine, 1988, Vol.8, No.2 pp.17-21..
12. Shoureshi, R. and Chu, R., Neural Space Representation of Dynamical Systems, Proc. ASME Winter Annual Meeting Symp. on Intelligent Control Systems, San Francisco, CA., 1989, pp.63-68.
13. Narendra, K.S. and Parthasarathy, K., Neural Networks in Dynamical Systems, SPIE, Intelligent Control and Adaptive Systems, 1989, Vol.1196, pp.230-241.
14. Kohonen, T., An Introduction to Neural Computing, Neural Network, 1986, Vol.1, pp.3-16.
15. Rumelhart, D.E, and McClelland, J.L, 1986, "Parallel Distributed Processing," Vol.1, MIT Press, Cambridge, MA.
16. Funahashi, K.I., 1989, On the Approximate Realization of Continuous Mapping by Neural Network, Neural Network, pp.183-192.

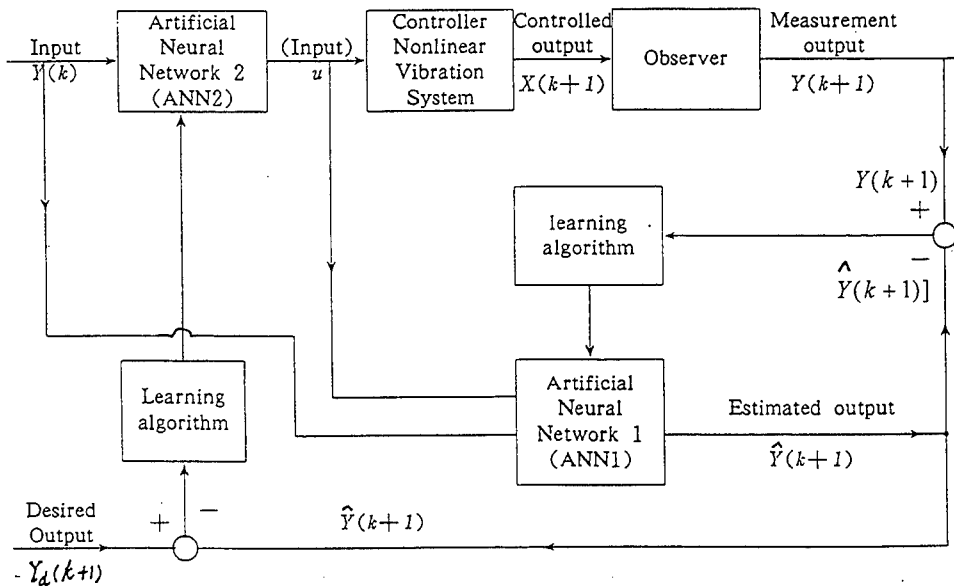


Fig. 1 A Neural Network Control Scheme

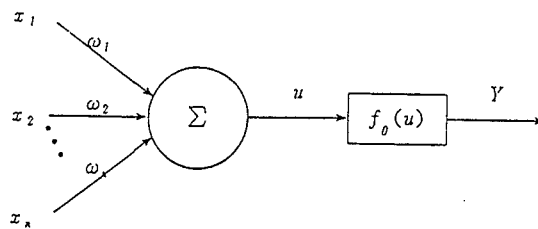


Fig. 2 Typical artificial neuron model

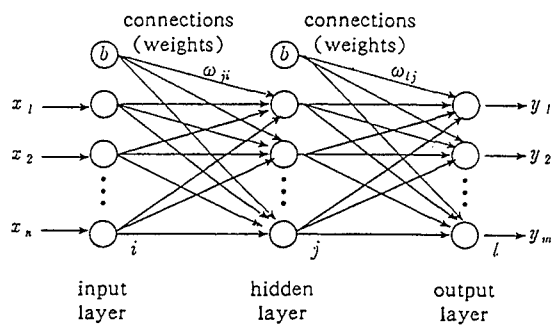


Fig. 3 A Neural network model

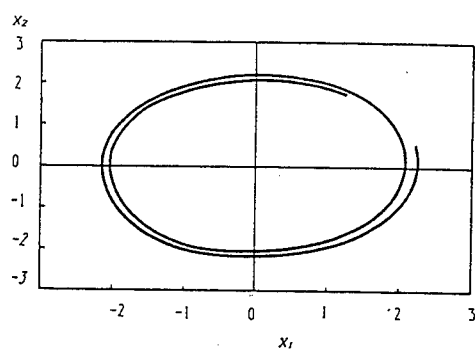


Fig. 4 Phase plane chart of Van Del Pol
identified by the neural network

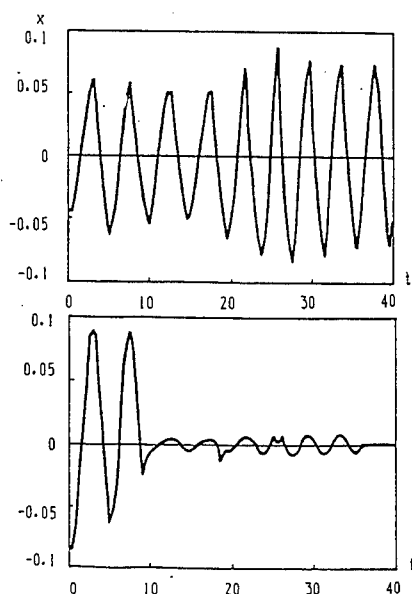


Fig. 5 Response curve of the system without control and with neutral network method

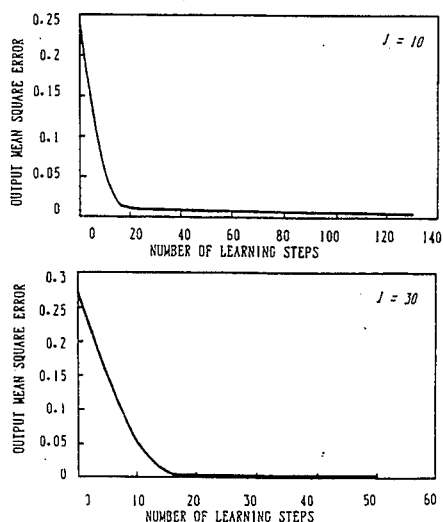


Fig. 7 Relationship between the output mean square error and the number of learning steps

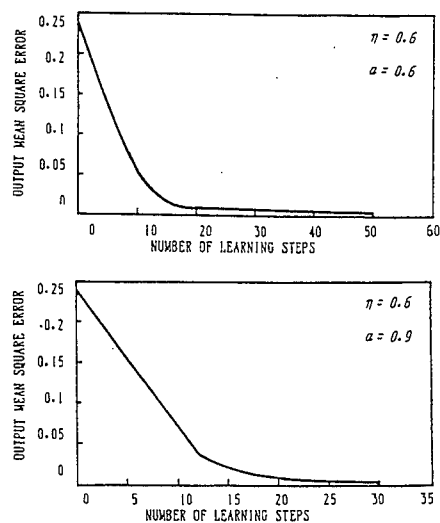


Fig. 6 Relationship between the output mean square error and the number of learning steps with different learning rates

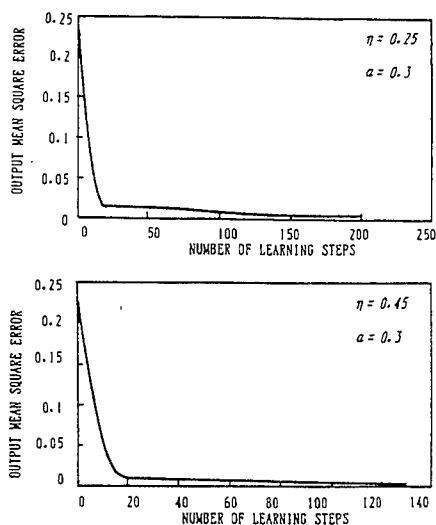


Fig. 8 Relationship between the output mean square error and the number of learning steps with different momentum parameters

A Stability Analysis of a Rotor System with Electromagnetic Control Forces

Meiling Zhu Chunsheng Zhao

Institute of Vibration Engineering Research
Nanjing University of Aeronautics & Astronautics
Nanjing, 210016, People's Republic of China

Fengquan Wang

Department of Mathematics and Mechanics
Southeast University
Nanjing, 210018, People's Republic of China

Abstract: The stability analysis of a rotor system with electromagnetic control forces is investigated. The formulas for the electromagnetic forces between the stator and rotor of the electromagnetic actuator are derived with respect to the displacements of the journal center and coil currents. The minimum setting values of the controller, and the relationship between mode shapes at the positions of sensors and actuators of the system, are given by using a perturbation method and Routh-Hurwitz theory.

INTRODUCTION

Many modern rotational machines, such as high speed and high precision machine tools, and turbines, are usually designed such that the systems run at supercritical rotor speeds. The vibrations induced by various perturbations, for example, mass distribution unbalance, support perturbation, unstable self-excited vibration, have drawn considerable investigators' attention. These issues may cause large displacements with respect to the support structures, and/or may also lead to some instabilities, even to the point of severe accidents of the systems. These rotor machines would benefit from additional control forces at the proper locations of the systems (Stanway and Burrow, 1981).

In recent years, the development of electromagnetic bearing technology (Schweitzer, 1990) enables active vibration control of the rotor system with bearings to be practical, because this kind of device can effectively suppress the vibration of the system. Many studies concerning electromagnetic bearings can be found in the literature. Gondhalekar and Holms (1984) reported on the design of magnetic bearings for long flexible shafts. Salm and Schweitzer (1984), Matsumura and Yoshimoto (1986), and Youcef-Toumi and Reddy (1992) discussed the modeling and controlling of flexible rotor systems with

electromagnetic bearings. Bradfield *et al.* (1987) investigated the performance of an electromagnetic bearing used for rotor vibration control operating in the supercritical rotor speed condition. Ulbrich and Anton (1984) studied some details about magnetic bearing applications. Hebble (1985, 1986) carried out a nonlinear theoretical analysis of magnetic bearings. Stanway and Reilly (1984) presented a state space control method and a pole assignment method for the system. Lee and Kim (1992) discussed modal test and sub-optimal vibration control. Tong *et al.* (1992) calculated the electric current of optimal output feedback control. Humphris *et al.* (1986), and Williams *et al.* (1991) studied the effect of control algorithms on properties of magnetic journal bearings and made a comparison of analog and digital controls. Nonami and Yamanaka (1990), Kasarda *et al.* (1990) did some important experiments.

However, many of the investigators mentioned above have not accounted for dynamic characteristics of electromagnetic bearings and the stability of a flexible rotor system with electromagnetic control forces. The stability analysis of the system with these forces is investigated in this paper. The formulas of magnetic forces between the stator and rotor of an electromagnetic actuator are derived with respect to displacements of the journal center and coil currents. The minimum setting values of the controller, and the relationship between modal shapes at the positions of the sensors and actuators of the system, are given by using a perturbation method and Routh-Hurwitz theory.

Equation of Motion of the Rotor System

The equation of motion for n degrees of freedom of the system with electromagnetic control forces can be written as

$$[M]\{\ddot{x}\} + [C]\{\dot{x}\} + [K]\{x\} = \{F(t)\} + \{u(t)\} \quad (1)$$

where

$[M]$, $[C]$ and $[K]$ are the $n \times n$ inertia matrix, damping matrix and stiffness matrix, respectively.

$\{F(t)\}$ and $\{u(t)\}$ are the $n \times 1$ external perturbation force vector and control force vector.

Electromagnetic Force

The control forces $\{u(t)\}$ in Eq.1 are the electromagnetic forces induced by the electromagnetic actuator as shown in Fig.1. The actuator consists of a stator and rotor. There are eight control coils and four static ones on the stator. The control currents are i , and static currents are I_0 . According to electromagnetic theory, the attractive forces between electromagnets of the stator and rotor can be generally written

$$f = \frac{\mu_0 S N^2 I^2}{4 \delta^2} \cos \varphi \quad (2)$$

where

f is the attractive force between electromagnets of the stator and rotor.

μ_0 is the permeability in the air gaps between the stator and rotor.

S is the effective area of the cross section of one electromagnet.

N is the number of windings around the core.

I is the coil current that is equal to a control current and static current.

δ is the radial clearance between the stator and rotor of the actuator.

φ is the corresponding half angle of a radial magnetic circuit as shown in Fig. 1.

Eq.(2) is derived upon the following assumptions:

(1) The magnetic fields in the air gap and core are uniformly distributed.

(2) The ferromagnetic material has the property of non-saturation.

(3) The effects of the leakage and overflow of the magnetic flux are ignored.

For our purpose, we assume that all of the electromagnets have the same cross section area, all coils have the same number of windings, that is, $S_1 = S_2 = \dots = S_8$, $N_1 = N_2 = \dots = N_8$. When the rotor deviation from the journal center is x and y , the radial clearance for the angle α_i can be written as:

$$\delta_i = \delta_0 - x \cos \alpha_i + y \sin \alpha_i, i = 1, 2, \dots, 8 \quad (3)$$

where α_i as shown in Fig. 1. The corresponding radial clearances for α_i are

$$\begin{aligned} \delta_1 &= \delta_0 - x \cos \alpha + y \sin \alpha \\ \delta_2 &= \delta_0 - x \sin \alpha + y \cos \alpha \\ \delta_3 &= \delta_0 + x \sin \alpha + y \cos \alpha \\ \delta_4 &= \delta_0 + x \cos \alpha + y \sin \alpha \\ \delta_5 &= \delta_0 + x \cos \alpha - y \sin \alpha \\ \delta_6 &= \delta_0 + x \sin \alpha - y \cos \alpha \\ \delta_7 &= \delta_0 - x \sin \alpha - y \cos \alpha \\ \delta_8 &= \delta_0 - x \cos \alpha - y \sin \alpha \end{aligned} \quad (4)$$

The corresponding coil currents are

$$\begin{aligned} I_1 &= I_8 = I_0 - i_x \\ I_2 &= I_3 = I_0 - i_y \\ I_4 &= I_5 = I_0 + i_x \\ I_6 &= I_7 = I_0 + i_y \end{aligned} \quad (5)$$

The electromagnetic forces induced by every pair of electromagnets can be represented as follows

$$f_i = \frac{\mu_0 S N^2 I_i^2}{4 \delta_i^2} \cos \varphi \quad i = 1, 2, \dots, 8 \quad (6)$$

So the resultants of the electromagnetic forces between the stator and rotor of the actuator in the horizontal and vertical directions are, respectively, of the forms

$$\begin{aligned} f_x &= (f_1 - f_4 - f_5 + f_8) \cos \varphi \cos \alpha + (f_2 - f_3 - f_6 + f_7) \cos \varphi \sin \alpha \\ f_y &= (f_2 + f_3 - f_6 - f_7) \cos \varphi \cos \alpha + (f_1 + f_4 - f_5 - f_8) \cos \varphi \sin \alpha \end{aligned} \quad (7)$$

The four variables are x, y, i_x , and i_y , while all other variables in Eq.(4)~(7) are dependent. Therefore, f_x and f_y are nonlinear functions with respect to the journal displacements x and y , and coil currents i_x and i_y , that is,

$$\begin{aligned} f_x &= f_x(x, y, i_x, i_y) \\ f_y &= f_y(x, y, i_x, i_y) \end{aligned} \quad (8)$$

Stability Analysis

According to the literature (Saito, 1985; Jean, 1990; and Shiau, 1993), the steady state solution of Eq.(1) can be approximately described

$$\{x_s\} = \{x_0\} + \sum_{i=1}^{N_W} \{u_{ci}\} \cos \omega_i t + \sum_{i=1}^{N_W} \{u_{si}\} \sin \omega_i t \quad (9)$$

where N_W is an integer. To examine the stability of the steady state solution, the dynamics are perturbed and the resulting motion is expressed as

$$\{x\} = \{x_s\} + \{\delta x\} \quad (10)$$

Assuming that the electromagnetic actuators are assigned at the points $\{x_c\}$ of the system, and the sensors at $\{x_m\}$, we can express the electromagnetic forces as

$$\{f_x\} = \{f\}_s + \frac{\partial f_x}{\partial x} \{\delta x_c\} + \frac{\partial f_x}{\partial x} \{\delta i_c\} \quad (11)$$

where the subscript s denotes the steady state solution.

Consider a general feedback control with the following equation

$$\{\delta \ddot{x}_x\} = -k \{\delta \dot{x}_m\} - c \{\delta \dot{x}_m\} \quad (12)$$

where k is the proportional gain and c is the rate gain of a controller.

The corresponding electromagnetic control force is

$$\{f_x\} = \{f\}_s + \frac{\partial f_x}{\partial x} \{\delta x_c\} - k \frac{\partial f_x}{\partial x} \{\delta x_m\} - c \frac{\partial f_x}{\partial x} \{\delta \dot{x}_m\} \quad (13)$$

Substituting Eqs.(9), (10) and (13) into Eq.(1), the perturbed equation of the system is of the form.

$$[M] \{\delta \ddot{x}\} + [C + c \frac{\partial f_x}{\partial x} E_{cm}] \{\delta \dot{x}\} + [K - \frac{\partial f_x}{\partial x} E_{mm} + k \frac{\partial f_x}{\partial x} E_{cm}] \{\delta x_m\} = \{0\} \quad (14)$$

where the element of the c th row and the m th column in the E_{cm} matrix, and the m th row and the m th column in the E_{mm} matrix are equal to one. The other elements are equal to zero.

The corresponding eigenequation belonging to Eq.(16) is

$$\{\lambda^2[M] + \lambda[C + c \frac{\partial_x}{\partial_x} E_{cm}] + [K - \frac{\partial_x}{\partial_x} E_{mm} + k \frac{\partial_x}{\partial_x} E_{cm}]\} \{\delta x\} = \{0\} \quad (15)$$

The eigenvector are normalized as follows

$$\begin{aligned} \Phi^T [M] \Phi &= I \\ \Phi^T [K] \Phi &= [\omega_i^2] = \Lambda \end{aligned} \quad (16)$$

where

$$\Phi = [\Phi_1 \Phi_2 \dots \Phi_n] \quad (17)$$

and

$$\{x\} = \Phi \{q\} \quad (18)$$

where $\{q\}$ is the modal coordinate, and $\{q\} = \{q_1 q_2 \dots q_n\}^T$.

Substituting Eq.(18) into Eq.(15), and premultiplying Φ^T , Eq.(15) becomes

$$[\lambda^2 I + \lambda \bar{C} + \bar{K}] q = \{0\} \quad (19)$$

where

$$\begin{aligned} \bar{C} &= \Phi^T [C] \Phi + c \frac{\partial_x}{\partial_x} E \\ \bar{K} &= \Lambda - \frac{\partial_x}{\partial_x} E_m + k \frac{\partial_x}{\partial_x} E \end{aligned} \quad (20)$$

and

$$\begin{aligned} E &= \Phi^T E_{cm} \Phi = \begin{bmatrix} e_{ij} \end{bmatrix} \\ E_m &= \Phi^T E_{mm} \Phi = \begin{bmatrix} e'_{ij} \end{bmatrix} \\ e_{ij} &= \Phi_i^T(x_c) \Phi_j(x_m) \\ e'_{ij} &= \Phi_i^T(x_m) \Phi_j(x_m) \end{aligned} \quad (21)$$

If the eigenvalues satisfy

$$\lambda^2 I + \lambda \bar{C} + \bar{K} = 0 \quad (22)$$

and all of the real parts of eigenvalues in Eq.(22) are negative, the rotor system is stable.

EXAMPLE

For one example, consider the range of the first critical rotational speed. Taking the first mode in Eq.(18), Eq.(22) can be simplified

$$\lambda^2 + (C_1 + c \frac{\partial_x}{\partial_x} e_{11}) \lambda + (\omega_1^2 - \frac{\partial_x}{\partial_x} e'_{11} + k \frac{\partial_x}{\partial_x} e_{11}) = 0 \quad (23)$$

where

$$\begin{aligned}
C_1 &= \Phi_1^T [C] \Phi_1 > 0 \\
e_{11} &= \Phi_1^T(x_c) \Phi_1(x_m) \\
e'_{11} &= \Phi_1^T(x_m) \Phi_1(x_m)
\end{aligned} \tag{24}$$

According to Routh-Hurwitz theory, the stability conditions of the system can be obtained as follows

$$\begin{aligned}
e_{11} &= \max \left[-\frac{C_1}{\frac{\partial x}{\partial x}}, (-\omega_1^2 + \frac{\partial x}{\partial x} e'_{11}) / k \frac{\partial x}{\partial x} e_{11} \right] \\
k &> (-\omega_1^2 + \frac{\partial x}{\partial x} e'_{11}) / \frac{\partial x}{\partial x} e_{11} = k_0 \\
c &> 0
\end{aligned} \tag{25}$$

Because the proportional gain k and rate c are both larger than zero, the sufficient conditions for a stable system are

$$\begin{aligned}
e_{11} &= \Phi_1^T(x_c) \Phi_1(x_m) \\
k &> (-\omega_1^2 + \frac{\partial x}{\partial x} e'_{11}) / \frac{\partial x}{\partial x} e_{11} = k_0 \\
c &> 0
\end{aligned} \tag{26}$$

For another example, consider the range of the first two modes. Eq.(22) can be simplified into Eq.(27) by the same way as above

$$a_0 \lambda^4 + a_1 \lambda^3 + a_2 \lambda^2 + a_3 \lambda + a_4 = 0 \tag{27}$$

where

$$\begin{aligned}
a_0 &= 1 \\
a_1 &= c \frac{\partial x}{\partial x} (e_{11} + e_{22}) \\
a_2 &= \omega_1^2 + \omega_2^2 + k \frac{\partial x}{\partial x} (e'_{11} + e'_{22}) - \frac{\partial x}{\partial x} (e'_{11} + e'_{22}) \\
a_3 &= c \frac{\partial x}{\partial x} (e_{11} \omega_2^2 + e_{11} \omega_1^2) \\
a_4 &= k \frac{\partial x}{\partial x} (e_{11} \omega_2^2 + e_{22} \omega_1^2) + \omega_2^2 \omega_1^2 - \frac{\partial x}{\partial x} (e'_{11} \omega_2^2 + e'_{22} \omega_1^2)
\end{aligned} \tag{28}$$

in which

$$\begin{aligned}
e_{11} &= \Phi_1^T(x_c) \Phi_1(x_m) \\
e_{22} &= \Phi_1^T(x_c) \Phi_1(x_m) \\
e'_{11} &= \Phi_2^T(x_m) \Phi_2(x_m) \\
e'_{22} &= \Phi_2^T(x_m) \Phi_2(x_m)
\end{aligned} \tag{29}$$

According to Routh-Hurwitz theory again, the stable conditions of the system are

$$\begin{aligned}
e_{11} &= \Phi_1^T(x_c) \Phi_1(x_m) > 0 \\
e_{22} &= \Phi_1^T(x_c) \Phi_1(x_m) > 0 \\
k &> \frac{\frac{\partial x}{\partial x} \cdot \frac{e_{11}}{\omega_1^2} + \frac{e_{22}}{\omega_2^2}}{\frac{\partial x}{\partial x} \cdot \frac{e_{11}}{\omega_1^2} + \frac{e_{22}}{\omega_2^2}} - \frac{1}{\frac{\partial x}{\partial x} \cdot \frac{e_{11}}{\omega_1^2} + \frac{e_{22}}{\omega_2^2}} \\
c &> 0
\end{aligned} \tag{30}$$

CONCLUSIONS

The stability analysis of a rotor system with electromagnetic control forces is investigated. The formulas of the magnetic forces between the stator and rotor of an electromagnetic actuator are derived with respect to the displacements of the journal center and coil currents. The minimum setting values of the controller and the relationship between mode shapes at the positions of sensors and actuators of the system are given by using a perturbation method and Routh-Hurwitz theory.

Reference

1. Stanway, R., and Burrows, C., Active vibration control of a flexible rotor mounted journal bearings, *ASME, J. Dynamic Systems, Measurement and Control*, Vol.103, 383-388.
2. Burrows, C. R., Sahikaya, M. N., and Turkey, O. S., An adaptive squeeze film bearing, *ASME, J. Tribology*, 1984, Vol. 106, 145-151.
3. Schweitzer, G., Magnetic bearings-applications, concept and theory, *JSME International Journal Series III* 1990, Vol.33, No.1, 13-18.
4. Gondhalekar, V., and Holms, R., Design of electromagnetic bearing for the vibration control of a supercritical shafts, *Proc. Instn. Mech, Engrs.*, 1984, Vol.198.C, No. 16, 235-242.
5. Salm, J., and Schweitzer, G., Modeling and control of a flexible rotor with magnetic bearing, *Third International conference on vibrations in rotating machinery*, 1984, 553-561.
6. Matsumura, F., Yoshimoto, T., System modeling and control design of a horizontal-shaft magnetic-bearing system, *IEEE, on Magnetic, Vol. MAG.22*, 1986, No.3, 196-203.
7. Youcef-Toumi, K., and Reddy, S., Dynamic analysis and control of high speed and High precision active magnetic bearings, *ASME, J. Dynamic Systems, Measurement and Control*, 1992, Vol.144, 623-633.

8. Bradfield, C. D., Rorberts, J. B., and Karunendiran, R., Performance of an electromagnetic bearing for the vibration control of a supercritical shafts, *Proc. INSTN. Mech. Engrs.*, 1987, Vol.201c, No.3, 201-211.
9. Ulbrich, H., and Anton, E., Theory and application of magnetic bearing with integrated displacement and velocity sensor, *Third International Conference on Vibration in Rotating Machinery*, 1984, 543-552.
10. Hebbale, K. V., A theoretical model for the study of nonlinear dynamics of magnetic bearings, *Ph. D. Thesis, Cornell University*, 1985.
11. Hebbale, K. V., and Taylor, D. L., Nonlinear dynamics of attractive magnetic bearings, Rotor dynamic Instability Problems in High Performance Turbo machinery, *NASA Conference*, 1986, 397-418.
12. Stanway, R., Reilly, J. O., State-variable feedback control of rotor bearing suspension system, *Third International Conference on Vibration in Rotating Machinery*, 1984, 515-524.
13. Lee, C. W., and Kim, J. S., Modal testing and suboptimal vibration control of flexible rotor bearing system by using a magnetic bearing, *ASME, J. Dynamic Systems, Measurement and Control*, 1992, Vol.114, 244-252.
14. Tong, S. G., Wang, X. X., Theoretical research on electromagnetic damper in the rotor bearing system, *J. Vibration Engineering*, 1992, Vol.5, No.1, 17-24.
15. Humphris, R. R., Kelm, R. D., Lewis, D. W., and ALLAIRE, P. E., Effect of Control Algorithms of magnetic journal bearing properties, *ASME, J. Engineering for Gas Turbines and Power*, 1986, Vol. 108, 624-632.
16. Williams, R. D., Keith, F. I., and Allaire, P. E., A comparison of analog and digital control for rotor dynamic vibration reduction through active magnetic bearings, *ASME, J. Engineering for Gas Turbines and Power*, 1991, Vol.113, 535-543.
17. Nonami, K., and Yamanaka, T., Vibration and control of a flexible rotor supported by magnetic bearing, *JSME, International Journal Series III*, 1990, Vol.33, No.4, 475-482.
18. Kasarda, M. E. F., Allaire, P. E., Humphris, R. R., and Barrett, L. E., A magnetic damper for first mode vibration reduction in the multimass flexible rotor, *ASME, J. Engineering for Gas Turbines and Power*, 1990, Vol.112, 463-469.
19. Saito, S., Calculation of nonlinear unbalance response of horizontal rotor supported by ball bearing with radial clearances, *ASME, Journal of Vibration, Acoustics, Stress, and Reliability in Design*, 1985, Vol. 107, 416-420.

20. Jean, A. N., and Nelson, H. D., Periodic response investigation of large order nonlinear rotor dynamic systems using collocation, *Journal of Sound and Vibration*, 1990, Vol.143, No. 3, 473-490.
21. Shiau, T. N., Huang, J. L., and Chang, Y. B., A study on stability and response analysis of a nonlinear rotor system with mass unbalance and side load, *ASME, J. Engineering for Gas Turbines and Power*, 1993, VOL.115, 218-226.

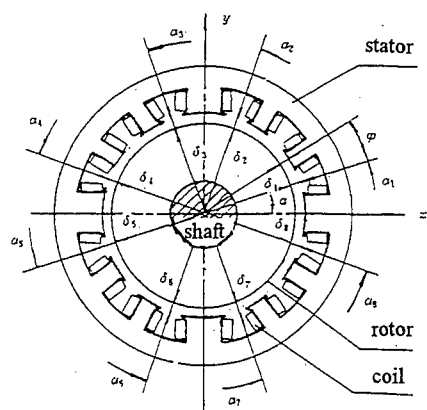


Fig. 1 Electromagnetic actuator geometry

Effect of System Delays on Semiactive Suspension Performance

Mehdi Ahmadian, Assistant Professor
Xubin Song, Graduate Research Assistant
Department of Mechanical Engineering
Virginia Tech
Blacksburg VA 24061-0238 USA
(540) 231-4920/Fax 9100
ahmadian@vt.edu

Abstract

For semiactive primary suspensions, the potential sources of time delay in the system are evaluated. The model for a single suspension is used to evaluate the effect of system delays in suspension performance. The time-domain results indicate that body acceleration, wheelhop, and rattle spaces are not much affected by time delays expected in a practice. The frequency-domain results show that time delays influence suspension performance more strongly near the body resonance frequency. At the axle resonance frequency, system delays had no appreciable influence on suspension performance.

Introduction

The advent of electronics and microprocessors in recent years have enabled suspension manufacturers to use more advanced, electronically-controlled suspension systems that can provide a more favorable compromise between ride and handling. The idea of electronically-controlled dampers dates back to early 70's, when the concept of skyhook dampers was invented [1- 2]*. The skyhook dampers attempt to adjust damping such that the damper nearly behaves the same as a hypothetical damper connected between the vehicle body and the ground. The original skyhook concept was introduced by Karnopp and Crosby, and since then many other variations of this concept have been introduced in the open literature [3 - 10]. These schemes require changing damping between a "high" and "low" level, in single or multiple steps, based on a switching policy that is generally a combination of the body vertical velocity and the relative velocity across the suspension. Since only a minimal amount of control energy is needed to generate the desired damping levels, these systems are referred to as "semiactive."

* Numbers in parentheses indicate references cited at the end of the text.

Semiactive dampers benefit from several advantages. First, they require a minimal amount of control energy (commonly 10-20 watts). This makes them suitable for most vehicle applications without concerns for the energy overhead to the vehicle. Second, they are fail safe, because they cannot generate any force beyond a passive damper. If a semiactive damper fails, it reverts back to a passive damper. Lastly, they are simple to design and implement in vehicles, in the sense that they don't require the complex hydraulic system needed for a fully active system. Fully active suspension systems are those that use hydraulic actuators to aid as well as to resist motion. Active suspensions require a hydraulic system that is heavier, more complicated, more costly, and consume considerably more energy (as much as 3-5 hp) than semiactive suspensions. Although active suspensions perform better than semiactive suspension in certain conditions, their necessity and benefit-to-cost ratio has been questioned in some studies.

In this study we examine the effect of system delays on the performance of semiactive dampers. System delays are defined as the time lag that exists between the sensor signal and damper response. This lag is affected by the electronic and mechanical delays that exist in any practical system. Although theoretically it is not possible to completely eliminate system delays, it is possible to reduce them to as little as 1-2 milliseconds (m-sec). In some cases system delays can be as much as 40-50 m-sec. Reducing system delays increases the system cost. In this study we will examine if the benefits of reducing system delays justify the added cost to the system.

A model for a single suspension is used to represent the vehicle body, axle, and suspension dynamics. The results of our study shows that system delays affect the body dynamics far more than the suspension or axle dynamics. For small system delays (less than 10 milliseconds) the effects are nearly negligible. For larger delays, however, the body acceleration at the natural frequency of the body approaches the levels for a passive suspension; therefore reducing the benefits of the semiactive system.

Semiactive Damper Implementation

Semiactive suspensions are implemented on a vehicle, using a switchable damper that can be switched between two or more damping levels to obtain varying damping rates needed for a semiactive suspension. The switching between different damping states is achieved using a driver such as solenoids or stepper motors. The driver adjusts a valve internal to the damper, therefore adjusting the fluid resistance and damping rate. Commonly, a dedicated or a central controller is used to command the driver. The controller receives information from the sensors, analyzes them according to a specified control policy, and commands the damper drivers to their proper position. A typical schematic of a semiactive suspension system is shown in Figure 1.

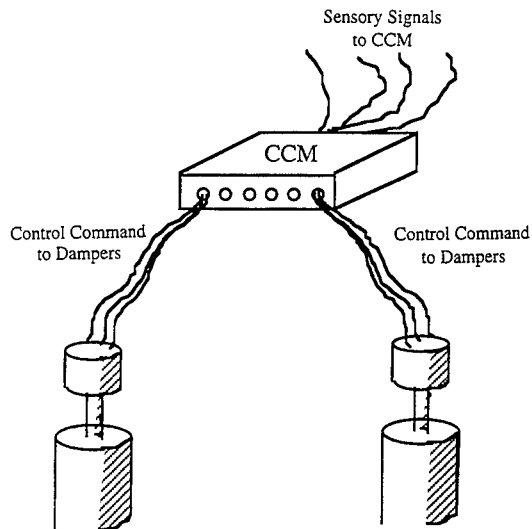


Figure 1. System Concept for the Adaptive Suspension System

Although in most analytical studies, semiactive suspensions are modeled as perfect systems without any delay, in practice it has been proven that the real-time implementation of semiactive suspensions can involve as much as 50 m-sec of time delay. The time delay is defined as the elapsed time between the sensor measurement and the damper response. The delay is due to a number of electrical and mechanical factors, including

- Circuit Delays: The circuits connecting the sensors to the controller and the controller to the damper will include some delay. Commonly, the capacitance, inductance, and resistance of the circuit determines time delays due to the circuit. Therefore, the circuit should be selected such that it has a small time constant (i.e., $t = 1/RC$ or L/R is small, where R , C , and L are the circuit resistance, capacitance, and inductance, respectively).
- Processor Delays: Depending on the clock speed of the microprocessor or micro-controller and the number of computations in each step (or tick), there exists a certain amount of time delays associated with the controller. For most applications it is possible to select the micro-controller such that the controller delays are minimized.
- Driver Delays: The drivers that are used for driving the damper valve often include considerable amount of time delays, due to their electromechanical nature. The speed of the driver is often weighted

against the system costs. Although it is possible to select drivers that are relatively fast, their high costs often prevent their use for most vehicle applications. The driver delays are often a major source of system delays, second only to the valve delays that are discussed next.

- **Valve Delays:** The valve that is implemented inside the damper to adjust the fluid resistance and the damping level is often the largest source of time delays in a semiactive system. The delays are caused by the mechanical effects of the valve, such as its inertia, friction, and interaction with the damper fluid. Although not well-understood, the fluid turbulence inside the damper and its interaction with the valve appear to significantly increase time delay. Proper design of the valve and the means of connecting it to the driver can somewhat reduce valve delays. Alternatively switchable magneto-rheological dampers, can be used to lower valve delays, when cost and other practical issue allow their use.

Other elements that can contribute to time delays include temperature, damper fluid viscosity, and stiffness of damper bushings. The combination of different time delays is referred to as the “system delays”. Any loss of performance due to system delays is discussed next.

Mathematical Formulation

The system considered for this study represents the dynamics of a single suspension, as shown in Figure 2.

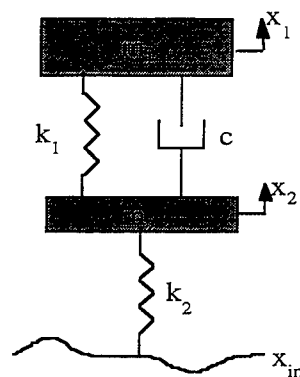


Figure 2. Primary Suspension Model

This model has been used widely in the past for analyzing automobile suspensions, due to its effectiveness in demonstrating fundamental issues relating to suspension performance. Although this model does not include

many dynamic aspects of an actual vehicle, it still can serve as an effective first step in comparing different suspension systems. Additional full-size vehicle modeling and actual field testing is necessary to more accurately assess the suspension effects. The dynamic equations for the model in Figure 2 are:

$$m_1 \ddot{x}_1 + c(\dot{x}_1 - \dot{x}_2) + k_1(x_1 - x_2) = 0 \quad (1a)$$

$$m_2 \ddot{x}_2 - c(\dot{x}_1 - \dot{x}_2) - k_1(x_1 - x_2) + k_2 x_2 = k_2 x_{in} \quad (1b)$$

Variables x_1 and x_2 represent the body and axle vertical displacement, respectively. The variable x_{in} indicates road input, that is assumed to be random with a low-pass (0-25 Hz) filter. Such a function has proven to sufficiently represent actual road input to the tires.

Table 1 indicates the model parameters that are selected to represent a typical automobile. The suspension is assumed to be linear in its operating range. Again, for most automobile applications this is a good approximation of the actual damper.

Table 1 Single Suspension Model Parameters

Description	Symbol	Value
Body mass ¹	m_1	240 Kg
Axle mass ²	m_2	45.7 Kg
Suspension stiffness	k_1	14720 N/m
Tire stiffness	k_2	135680 N/m
Suspension damping--rebound (damper extension)	c	1089, 440 N-s/m
Suspension damping--jounce (damper compression)	c	658, 440 N-s/m

¹ Represents the appropriate portion of automobile sprung mass for a single suspension

² Represents 1/2 of axle (unsprung) mass

Time-delay Modeling

Re-writing Eq. (1) in a discrete-time form with damper time delay, we obtain:

$$m_1 \ddot{x}_1(t_k) + c_{k-n} [\dot{x}_1(t_k) - \dot{x}_2(t_k)] + k_1 [x_1(t_k) - x_2(t_k)] = 0 \quad (2a)$$

$$m_2 \ddot{x}_2(t_k) - c_{k-n} [\dot{x}_1(t_k) - \dot{x}_2(t_k)] - k_1 [x_1(t_k) - x_2(t_k)] + k_2 [x_2(t_k)] = k_2 x_{in}(t_k) \quad (2b)$$

for $k = 1, 2, \dots, m$

$k-n > 0$

The damper force shown in the above equations is a function of the relative velocity across the damper at time k and the damper constant that is evaluated based on measurements made at time $k-n$, i.e.,

$$c_{k-n} [\dot{x}_1(t_k) - \dot{x}_2(t_k)] \quad (3)$$

The integer indices k and n represent the discrete time step and time delay. The time delay is defined in terms of the number of time steps the damper is lagging behind, i.e.,

$$n = TD/\Delta t$$

$$TD = \text{time delay (sec)}$$

$$\Delta t = \text{computation step size (sec)}$$

Therefore, from the above equation, the damper force is lagging behind the inertial and stiffness force by TD seconds.

Numerical Results

The dynamic system in Figure 1 is modeled in Matlab and used to evaluate the effect of different time delays on the suspension performance. The measures that were used for this purpose include:

- vehicle body (sprung mass) acceleration
- axle (unsprung mass) displacement
- rattle space (relative displacement across the suspension)

The selection of the above measures are based on their importance in vehicle ride comfort and handling, and suspension design. Vehicle body (or sprung mass) acceleration is often used as a measure of ride comfort, particularly in automobiles. Axle displacement (or wheelhop) is directly related to the vehicle stability and ride handling. The lower the wheelhop, the more stable the system is. Finally, rattle space (or relative displacement across the damper) is an important parameter in suspension design. This is particularly true for automobiles where commonly there is a limited amount of space between the axle and the vehicle body. A suspension that requires a large rattle space may prove unfeasible in practice.

For each of the above measures, the data is evaluated in both time and frequency domain. In time domain, the root mean square (RMS) and maximum of the data for a five-second simulation are compared. In frequency domain, the transfer function between each of the measures and road displacement input is plotted vs. frequency for different amounts of time delay. The frequency plots highlight the effect of each damper on body and axle resonance frequencies.

Figures 3 and 4 show the RMS and maximum time data for the three measures selected to evaluate the performance of the suspension system. The RMS and maximum values are calculated from the results for a five-second simulation run. Both figures indicate that time delays of up to 50 m-sec does not have an appreciable effect on the body acceleration, wheelhop, or rattle space. Although in each case there is an increase in the measures as time delay increases, the increase is less than 2 percent of the case with no time delay (i.e., the perfect case). A look at the frequency results, shown in Figures 5 and 6, reveals that there is some increase in body acceleration and rattle space transfer functions at the sprung mass resonance frequency (i.e., 1.2 Hz). These figures show no change at the wheelhop frequency. Further, Fig. 7 shows that the wheelhop transfer function is not affected by the time delay.

To further highlight the effect of time delay at the vehicle body (sprung mass) and axle (unsprung mass) resonance frequencies, the suspension performance was evaluated with pure-tone input. Two sinusoidal inputs at 1.2 and 9.3 Hz are selected since they match the resonance frequencies of the system. The results shown in Figs. 8 and 9 further support the results in Figs. 5-7. There is a significant increase in all three measures when the system is excited at 1.2 Hz as time delay increases. There is no appreciable change in measures at the input frequency associated with wheelhop.

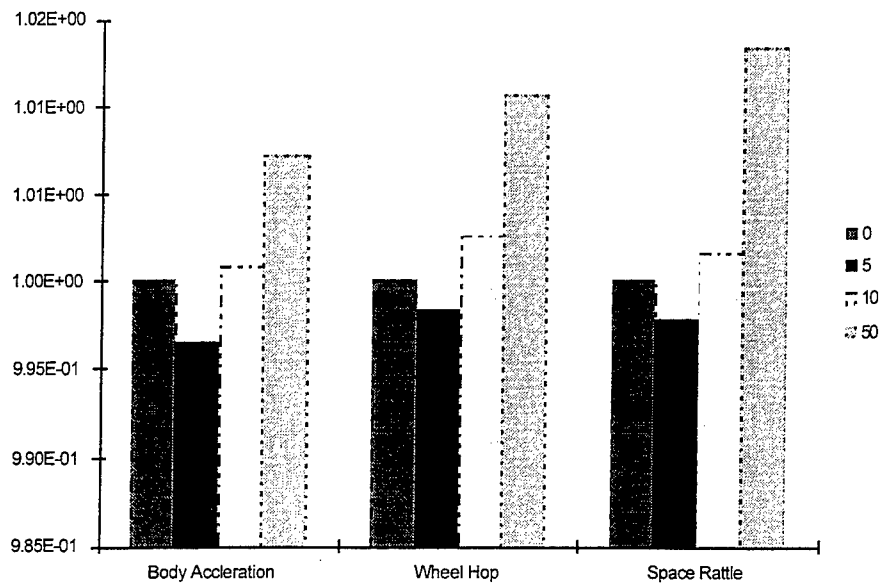


Figure 3. Maximum data Normalized w.r.t. Results for Time Delay = 0

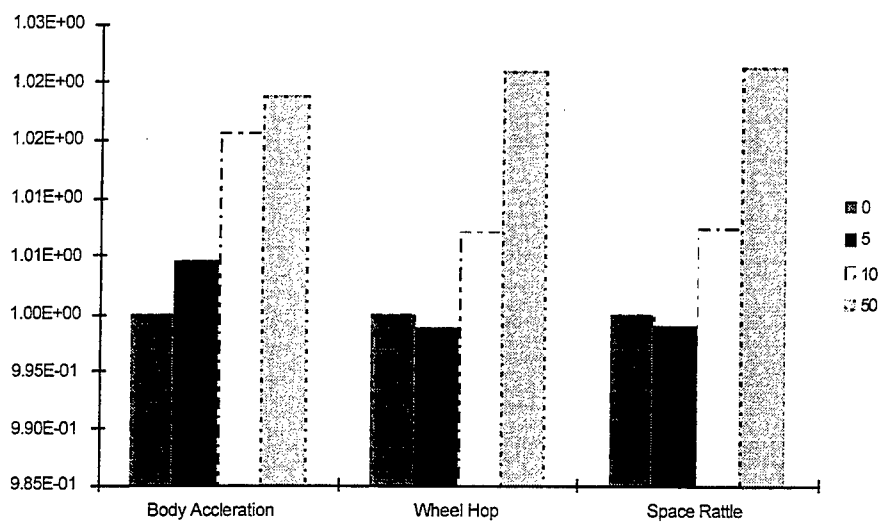


Figure 4. RMS data Normalized w.r.t. Results for Time Delay = 0

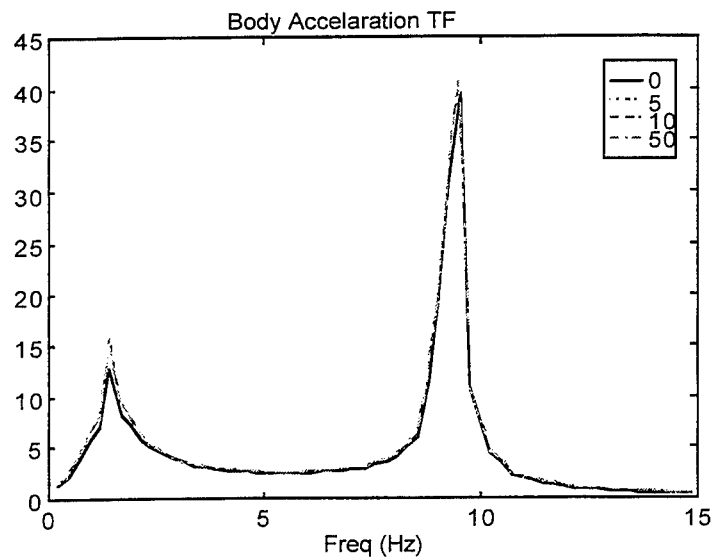


Figure 5. Body Acceleration Transfer Function w.r.t Input Velocity for Different System Delays

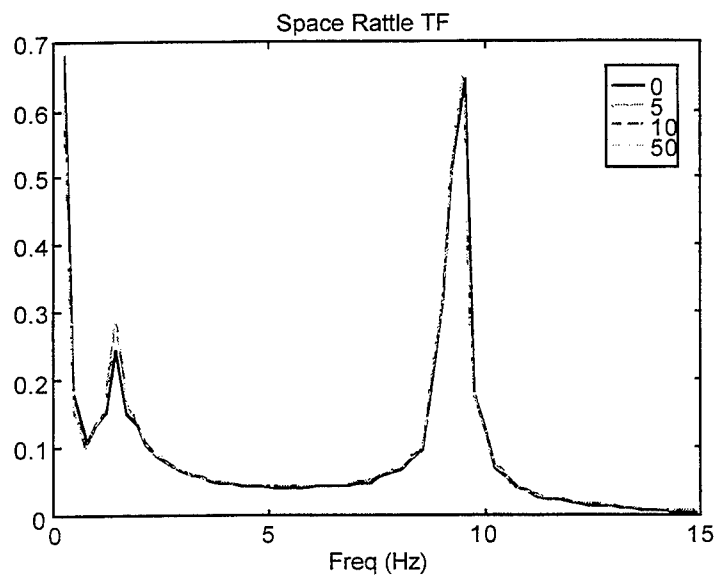


Figure 6. Rattle Space Transfer Function w.r.t Input Velocity for Different System Delays

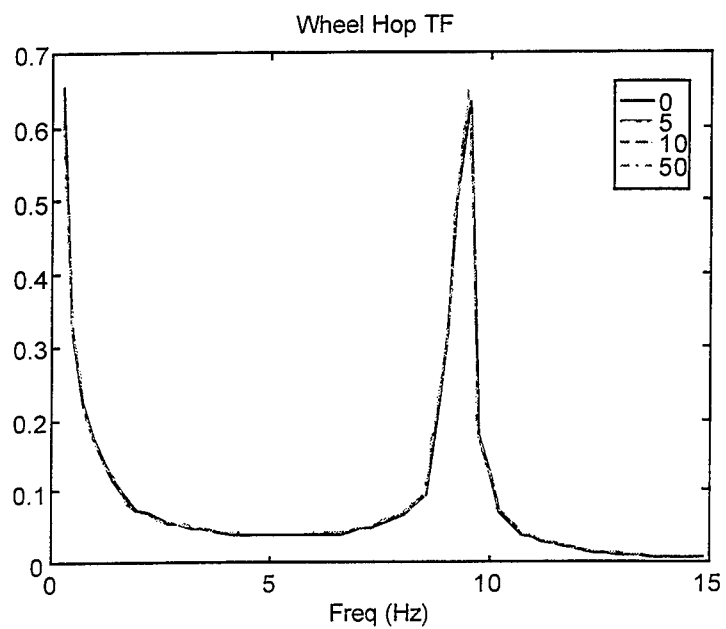


Figure 7. Wheel Hop Transfer Function w.r.t Input Velocity for Different System Delays

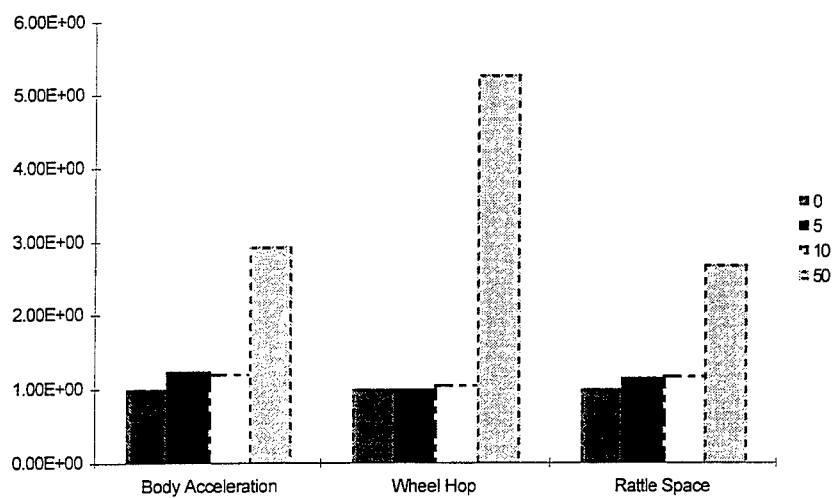


Figure 8. RMS data Normalized w.r.t. Results for Time Delay = 0 with input of 1.3 Hz

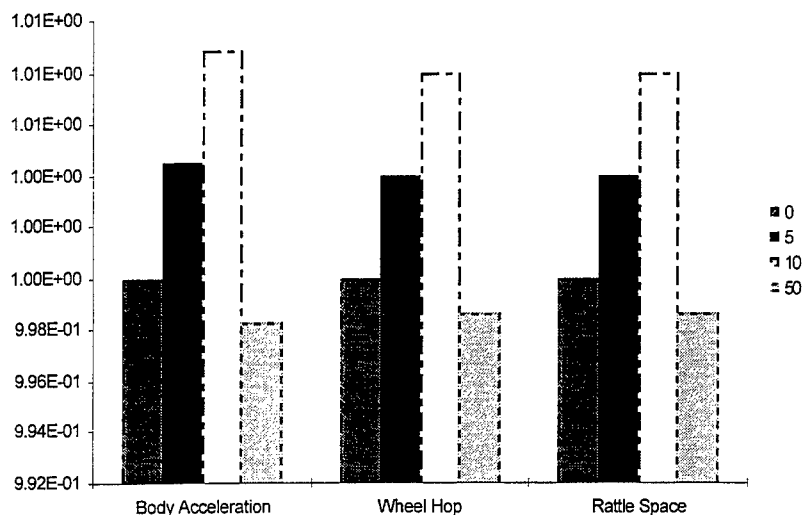


Figure 9. RMS data Normalized w.r.t. Results for Time Delay = 0 with input of 9.2 Hz

CONCLUSIONS

Various sources of time delay in a semiactive primary suspension were discussed. A simulation model for a single suspension was used to evaluate the suspension performance in terms of body acceleration, wheelhop, and rattle space. The results show that overall time delays have an insignificant effect on the suspension performance, as compared with a perfect suspension with no time delay. In the range of time delays considered (0-50 m-sec), the suspension performance is more sensitive to time delays at body frequencies than wheelhop frequencies. Further simulation of the suspensions, using full-vehicle models, and vehicle testing is needed to validate these initial results.

REFERENCES

1. Crosby, M. J. and Karnopp, D. C., "The Active Damper," *The Shock and Vibrations Bulletin* 43, Naval Research Laboratory, Washington DC, 1973.
2. Karnopp, D. C. and Crosby, M. J., "System for Controlling the Transmission of Energy Between Spaced Members," US Patent, 3,807,678, April 1974.
3. Ahmadian, M. and Marjoram, R. H., "Effects of Passive and Semi-active Suspensions on Body and Wheelhop Control," *Journal of Commercial Vehicles*, Vol. 98, 1989, pp. 496-604.
4. Ahmadian, M. and Marjoram, R. H., "On the Development of a Simulation Model for Tractor Semitrailer Systems with Semiactive Suspensions," *Proceedings of the Special Joint Symposium on Advanced Technologies*, 1989 ASME Winter Annual Meeting, San Francisco CA, Dec 1989 (DSC-Vol 13).
5. Hedrick, J. K., "Some Optimal Control Techniques Applicable to Suspension System Design," American Society of Mechanical Engineers, Publication No. 73-ICT-55, 1973.
6. Hac, A., "Suspension Optimization of a 2-DOF Vehicle Model Using Stochastic Optimal Control Technique," *Journal of Sound and Vibration*, 1985.
7. Thompson, A. G., "Optimal and Suboptimal Linear Active Suspensions for Road Vehicles," *Vehicle System Dynamics*, Vol. 13, 1984.
8. Karnopp, D., Crosby, M. J., and Harwood, R. A., "Vibration Control Using Semiactive Force Generators," *ASME Journal for Engineering for Industry*, May 1974, pp. 619-626.
9. Krasnicki, E. J., "Comparison of Analytical and Experimental Results for a Semiactive Vibration Isolator," *Shock and Vibration Bulletin*, Vol. 50, September 1980.
10. Chalasani, R. M., "Ride Performance Potential of Active Suspension Systems--Part 1: Simplified Analysis Based on a Quarter-Car Model," *Proceedings of the 1986 ASME Winter Annual Meeting*, Los Angeles, CA, Dec 1986.

POWER FLOW TECHNIQUES I

Insertion Loss of Stiffened Enclosures

Raymond Y. Y. Lee

Department of Aerospace Engineering
Old Dominion University, Norfolk, VA 23529-0247

C. F. Ng

Department of Civil and Structural Engineering,
The Hong Kong Polytechnic University,
Hung Hom, Kowloon, Hong Kong

Abstract

The paper reports a theoretical study of the insertion loss of close-fitting enclosures made of stiffened plates in low frequencies. The theoretical analysis is based on, the Finite Element Method for the structural part, and the classical solutions suggested in [1] for the acoustic part. The effects of, boundary conditions, acoustic resonances and structural resonances on the insertion loss, are studied. The theory shows two important points; 1) the contribution of the non-fundamental mode of the source plate is important for insertion loss as the enclosure; and 2) Stiffeners can be used to enhance the insertion loss ability of an enclosure plate at the frequencies below the fundamental resonance. However, in other frequencies, the enclosure plate could give worse insertion loss performance.

Descriptions of The Theoretical Model

An enclosure system is similar to that of [2] shown in fig. 1. The boundaries at $z=0$, $z=c$ are flexible that they can vibrate in typical mode shapes while the other walls are acoustically rigid.

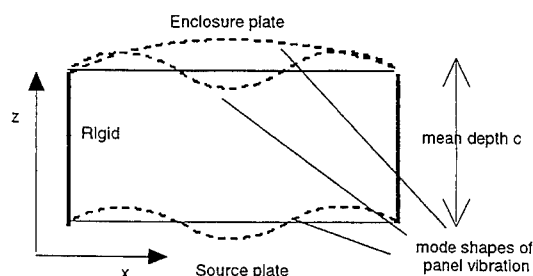


Fig. 1 Side view of rectangular enclosure model

The acoustic velocity potential within the rectangular cavity is given by the following homogeneous wave equation [3],

$$\nabla^2 \phi - \frac{1}{C_a^2} \frac{\partial^2 \phi}{\partial t^2} = 0 \quad eq.(1)$$

where

$\phi = f(x)g(y)h(z)e^{i(\omega t - \delta)}$. velocity potential function

C_a = the speed of sound.

and the vibration velocities in x, y and z directions and pressures within the air cavity can be derived from the following equations [9],

$$\dot{X} = \frac{\partial \phi}{\partial x}, \quad \dot{Y} = \frac{\partial \phi}{\partial y}, \quad \dot{Z} = \frac{\partial \phi}{\partial z}, \quad P = -\rho \frac{\partial \phi}{\partial t}. \quad eq.(2)$$

The phase lag δ is inserted for a reason which will be explained later. The boundary conditions of the rectangular cavity to be satisfied are

$$\begin{aligned} \text{B.C. (i) at } x=0 \text{ and } x=a, \quad \dot{X} = \frac{\partial \phi}{\partial x} = 0; \quad \text{B.C. (ii) at } y=0 \text{ and } y=b, \quad \dot{Y} = \frac{\partial \phi}{\partial y} = 0; \\ \text{B.C. (iii) at } z=0, \quad \dot{Z} = \frac{\partial \phi}{\partial z} = \dot{w}_s(x, y, t); \quad \text{B.C. (iv) at } z=c, \quad \dot{Z} = \frac{\partial \phi}{\partial z} = \dot{w}_p(x, y, t). \end{aligned}$$

Here $w_s(x, y, t)$, $w_p(x, y, t)$ are the displacements of the source plate and the enclosure plate, so their velocities are marked with dot sign. Because of B.C.s (i) and (ii), the solution of eq.(1) takes the modal form as [4],

$$\phi = \sum_{U=0}^{\infty} \sum_{W=0}^{\infty} \cos\left(\frac{U\pi x}{a}\right) \cos\left(\frac{W\pi y}{b}\right) [L_{UW} \cosh(\mu_{UW} z) + N_{UW} \sinh(\mu_{UW} z)] e^{i(\omega t - \delta)} \quad eq.(3)$$

where

L_{UW} , N_{UW} = coefficients which depend on the boundary conditions at $z=0$ and $z=c$

Acoustic-Structural Boundary Conditions

In this subsection, the two variables, L_{UW} and N_{UW} in eq.(3) will be rewritten in term of w_s^{ST} and w_p^{PQ} , the modal amplitudes of the source plate and the enclosure plate. Then, the velocity potential and the pressure within the air cavity can also be in terms of them.

It is assumed that (P,Q) is the dominant mode shape of the enclosure plate and the source plate is forced to vibrate in the (S,T) mode shape with constant velocity; and the effect of the fluid loading within the cavity on the enclosure plate is negligible. Thus, the profiles of the displacements of the source plate and the enclosure plate are given by

$$w_s^{ST}(x, y, t) = \mathcal{W}_s^{ST} \psi^{ST}(x, y) e^{i\omega t} \quad eq.(4)$$

$$w_p^{PQ}(x, y, t) = \mathcal{W}_p^{PQ} \phi^{PQ}(x, y) e^{i(\omega t - \delta_{PQ})} \quad eq.(5)$$

where

$\psi^{ST}(x, y)$ = the (S,T) mode shape of the source plate

$\phi^{PQ}(x, y)$ = the (P,Q) mode shape of the enclosure plate

\mathcal{W}_s^{ST} = the modal amplitude of the (S,T) mode of the source plate

\mathcal{W}_p^{PQ} = the modal amplitude of the (P,Q) mode of the enclosure plate

The in-vacuo mode shapes of the source plate and the enclosure plate are found by using the isoparametric stiffness plate element [5]. In other words, $\psi^{ST}(x, y)$ and $\phi^{PQ}(x, y)$ are not analytical.

The phase lag δ_{PQ} is now seen to be the lag between the modal motions of the enclosure plate and the motion of the source plate. By substituting eq.(3), eq.(4) and eq.(5) into B.C.(iii) and B.C.(iv), then the two variables, L_{UW} & N_{UW} can be rewritten in term of w_s^{ST} & w_p^{PQ} . The velocity potential in eq.(2) within the rectangular air cavity can be expressed in term of the modal displacement amplitudes of the source plate and the enclosure plate, w_s^{ST} & w_p^{PQ} .

$$\phi = i\omega e^{i(\omega t - \delta_{PQ})} \sum_{U=0}^{\infty} \sum_{W=0}^{\infty} \cos\left(\frac{U\pi x}{a}\right) \cos\left(\frac{W\pi y}{b}\right) \times$$

$$\left[\frac{(\beta_{UW}^{PQ} \mathcal{W}_P'^{PQ} - \alpha_{UW}^{ST} \mathcal{W}_s'^{ST} e^{i\delta_{PQ}} \cosh(\mu_{UW} c))}{\mu_{UW} \sinh(\mu_{UW} c)} \cosh(\mu_{UW} z) + \frac{\alpha_{UW}^{ST} \mathcal{W}_s'^{ST} e^{i\delta_{PQ}}}{\mu_{UW}} \sinh(\mu_{UW} z) \right]$$

eq.(6)

where

$$\alpha_{UW}^{ST} = \frac{\int_0^a \int_0^b \psi^{ST}(x, y) \cos\left(\frac{U\pi x}{a}\right) \cos\left(\frac{W\pi y}{b}\right) dx dy}{\int_0^a \int_0^b \cos\left(\frac{U\pi x}{a}\right)^2 \cos\left(\frac{W\pi y}{b}\right)^2 dx dy}, \quad \beta_{UW}^{PQ} = \frac{\int_0^a \int_0^b \varphi^{PQ}(x, y) \cos\left(\frac{U\pi x}{a}\right) \cos\left(\frac{W\pi y}{b}\right) dx dy}{\int_0^a \int_0^b \cos\left(\frac{U\pi x}{a}\right)^2 \cos\left(\frac{W\pi y}{b}\right)^2 dx dy}$$

From eq.(2) and eq.(6), pressure at the $z=c$ is

$$p_c = \rho_0 \omega^2 e^{i(\omega t - \delta_{PQ})} \sum_{U=0}^{\infty} \sum_{W=0}^{\infty} \left[\frac{\beta_{UW}^{PQ} \mathcal{W}_P'^{PQ} \cosh(\mu_{UW} c) - \alpha_{UW}^{ST} \mathcal{W}_s'^{ST} e^{i\delta_{PQ}}}{\mu_{UW} \sinh(\mu_{UW} c)} \right] \cos\left(\frac{U\pi x}{a}\right) \cos\left(\frac{W\pi y}{b}\right)$$

eq.(7)

Response of Structural Vibration solved by the FEM

Consider the air pressure at the face $z=c$, which is induced by the constant vibration motion of the source plate. The parameters of the enclosure plate such as stiffness and mass etc., are used for evaluating the vibration displacement amplitudes of the source plate and the enclosure plate, \mathcal{W}_s^{ST} & \mathcal{W}_p^{PQ} . Then, considering the FEM equation of the forced motion of the enclosure plate due to the acoustical pressure at $z=c$

$$([K] - \omega^2 [M]) \{V_{PQ}\} \mathcal{W}_p'^{PQ} = \{f\}$$

eq.(8)

where

$[M]$ = mass matrix of the enclosure plate

$[K]$ = stiffness matrix of the enclosure plate

$\{V_{PQ}\}$ = the eigenvector of the (P,Q) in-vacuo mode of the enclosure plate

$$\{f\} = - \sum_{i=1}^{NE} \int_A [N]_i p_c dA = \text{force vector}$$

$[N_i]$ =weight function of the isoparametric stiffness plate element
 NE = No. of element

In the above formulation, \mathcal{W}_p^{PQ} can be seen as the modal degree of freedom of the FEM system. To perform modal reduction, the ratio of \mathcal{W}_p^{PQ} to \mathcal{W}_s^{ST} can be found by substituting eq. (7) into eq.(8) and multiplying $\{V_{PQ}\}^T$ on both sides. The sound insertion loss can be obtained by

$$IL = 10 \log \left(\frac{S.E.UENC}{S.E.ENC} \right) = -10 \log \left\{ \sum_{P=1}^{\bar{P}} \sum_{Q=1}^{\bar{Q}} \left(\left| \frac{\mathcal{W}_p^{PQ}}{\mathcal{W}_s^{ST}} \right|^2 \frac{A_p \sigma_{PQ}}{A_s \sigma_{ST}} \right) \right\} \quad eq.(9)$$

where

A_p = area of the enclosure plate

A_s = area of the source plate

$S.E.UENC$ = acoustic energy radiated by the unenclosed source plate [6]

$S.E.ENC$ = acoustic energy radiated by the enclosure plate [6]

σ_{PQ} = radiation efficiency of (P,Q) mode [6]

Theoretical Results

The insertion losses of an enclosure plate with different cavity depths are shown in fig. 2. The predictions are based on the source plate vibrating in a (1,1) mode shape and enclosure plate vibrating in symmetric mode shapes. Smaller cavity depth can also make the structural resonance frequency higher. On the other hand, cavity depth is an important factor which can largely affect insertion loss at low frequencies. It can be seen that at the frequencies below the structural resonance, it is noted that greater cavity depth results in higher insertion loss. In the frequencies ranged from 800Hz to 900Hz, the structural resonance of the (1,3) mode of the enclosure plate in the dash line is close to the acoustical resonance. This makes the two resonances form a "wider and deeper" dip. In each case, the acoustical resonance parallel to the source plate has no change. It is independent of the cavity depth and the stiffness of the enclosure plate. The acoustic resonance perpendicular to the source plate is changed because of different cavity depths.

In fig. 3, the predictions are based on the source plate vibrating in a (2,1) mode shape and enclosure plate vibrating anti-symmetry mode shapes. Unlike

the acoustic (2,0) mode in the fig.2, the (0,1) acoustic mode in the fig. 3 imposes greater effect on insertion loss than the structural mode.

In fig. 4a, the effect of the boundary conditions of the enclosure plate on the insertion loss is presented. The insertion loss above the fundamental resonant frequency of the clamped case is slightly lower than that of the simply supported case. Below this frequency, boundary conditions appear to have a considerable effect on the insertion loss, with the insertion loss for the clamped plate being higher than that for the simply supported plate. The enclosure plate with a stiffener has a higher fundamental resonant frequency, when compared the plates without any stiffener (the location of the stiffener is showed in fig. 4b). At the frequencies below the fundamental resonance, the stiffener of the enclosure plate makes the insertion loss much higher than those of the other two enclosure plates. Above this frequency however, the coupling effect between the structural and acoustic modes has a significant effect, resulting in lower insertion loss.

Experimental Results

The general theoretical predicted insertion losses of the 1mm steel panel and the 3mm aluminum plate with a stiffener in fig. 5 are confirmed experimentally over the frequency range. The resonance frequencies of the enclosure panels are different from the predicted values because the boundary conditions were not truly simple supports. This would not make large difference between the predicted and measured insertion loss. It is because the experimental data were measured with one-third octave filter white noise (i.e. average insertion loss over each frequency band is given). Since the theoretical models cannot give the predictions of the effects of the structural and acoustical damping, the main uncertainty remains in the structural and acoustical damping loss factor. It can be seen in the both cases that the coupling effect between (1,0) acoustical mode and (2,1) structural mode is an important factor which can decrease the insertion loss of an enclosure plate.

The result obtained for the 3 mm aluminum plate is compared with that obtained for the 3 mm aluminum plate with a stiffener in fig. 6. Given higher insertion loss in the frequencies below the fundamental resonance resulting from the application of the stiffener, that is not surprising according to the result in fig. 4a. In other frequencies, the stiffener cannot act as an efficient method to enhance the insertion loss ability of the enclosure plate.

Conclusion

A model for predicting the insertion loss of an enclosure panel has been presented. The results of the measurements made to test the validity of the model suggest it can give a reasonable prediction. From the both theoretical and experimental data, it can be concluded that, 1) the coupling effect between (1,0) acoustical mode and (2,1) structural mode is an important factor which can decrease the insertion loss of an enclosure plate; 2) Stiffeners can be used to enhance the insertion loss ability of an enclosure plate at the frequencies below the fundamental resonance. However, in other frequencies, the enclosure plate could give worse insertion loss performance.

References

1. Lee, Y. Y., "STRUCTURAL-ACOUSTIC ANALYSIS OF CLOSE-FITTING ENCLOSURES", *MPhil thesis*, The Hong Kong Polytechnic University (1995)
2. Oldham, D. J. and Hillarby, S. N., "THE ACOUSTICAL PERFORMANCE OF SMALL CLOSE FITTING ENCLOSURES, PART 1: THEORETICAL MODELS", *Journal of Sound and Vibration*, vol. 150, p.261-281 (1991)
3. Carrier, George F., "PARTIAL DIFFERENTIAL EQUATIONS, THEORY AND TECHNIQUE", *Academic press, Inc. Second Edition*, Chapter 3
4. Zauderer, Erich, "PARTIAL DIFFERENTIAL EQUATIONS OF APPLIED MATHEMATICS", *John Wiley & Sons Inc.*, Chapter 4 (1989)
5. Mukherjee, A. & Mukhopadhyay, M., "FINITE ELEMENT FREE VIBRATION OF ECCENTRICALLY STIFFENED PLATES", *Computers & Structures*, vol. 30, No.6, p.1303-1317 (1988)
6. Wallace, C. E., "RADIATION RESISTANCE OF A RECTANGULAR PANEL", *Journal of the Acoustical Society of America*, vol. 51, p.946-952 (1972)

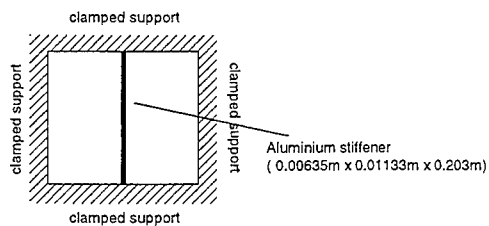
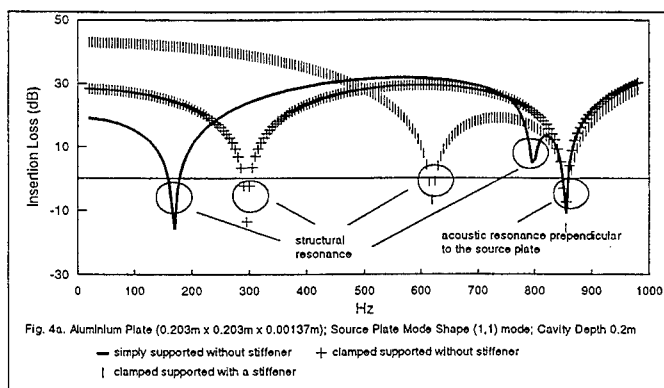
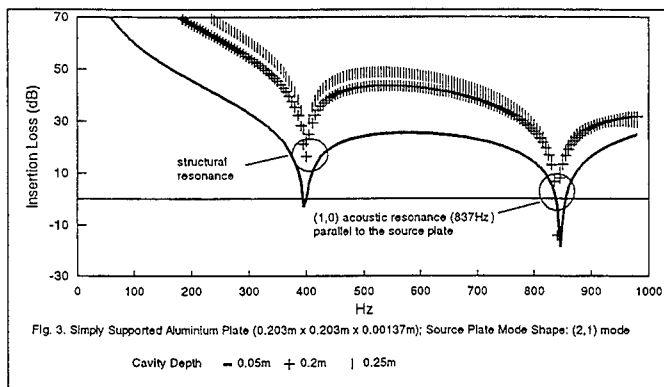
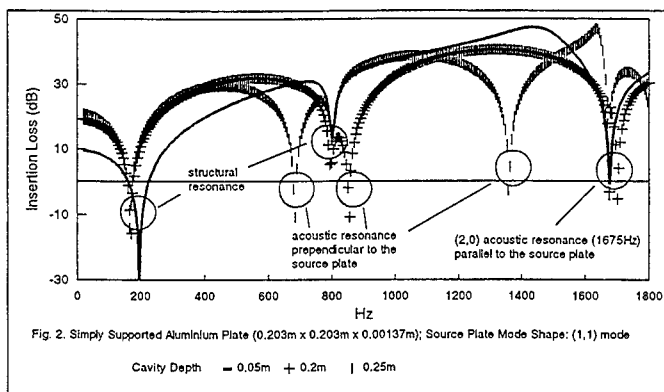
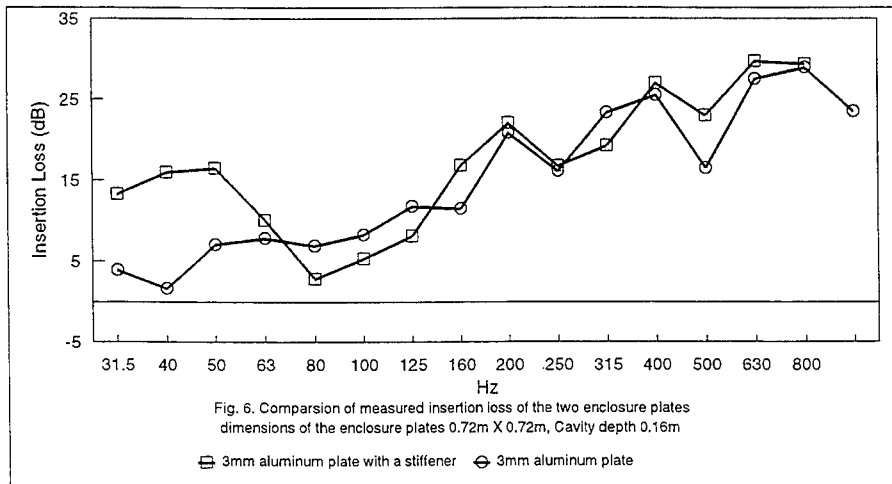
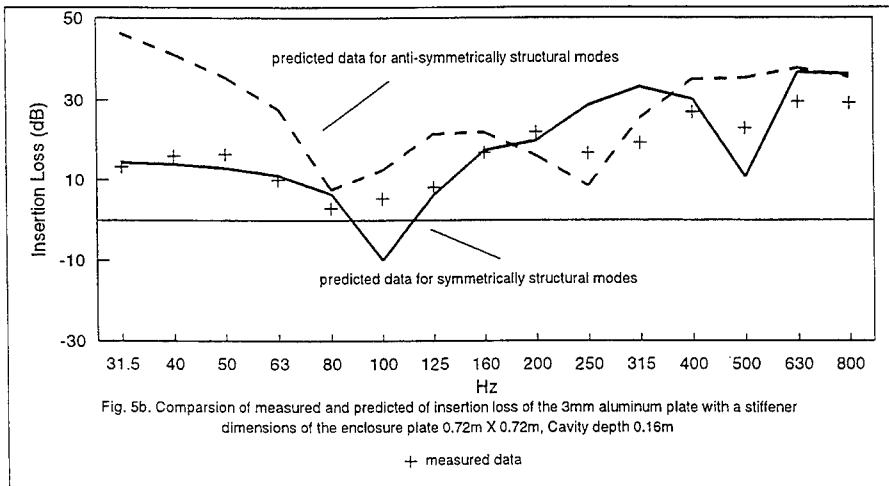
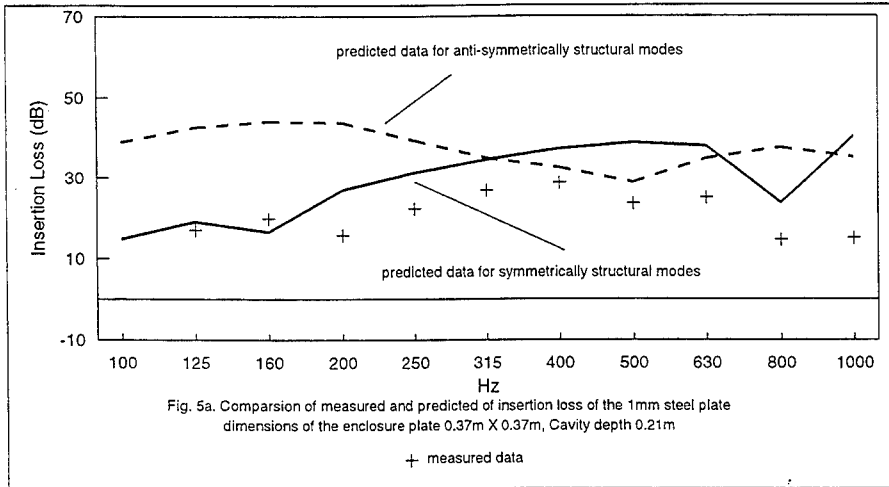


Fig. 4b. Clamped support aluminium Plate with a stiffener



Free Response and Wave Propagation in Constrained Strings and Beams on Partial Elastic Foundations

C. H. Riedel¹ and C. A. Tan²
Department of Mechanical Engineering
Wayne State University
Detroit, Michigan 48202, U. S. A.

ABSTRACT

The free vibration response of a string and a Euler-Bernoulli beam partially supported by an elastic foundation is studied. The transfer function method is used in the analysis of the system which consists of three subsystems coupled by constraints imposed at the subsystem interfaces. Reflection and transmission coefficients are formulated to show the effect of the foundation on the system as well as the coupling of the subsystems. For both the string and beam systems, curve veering and mode localization are observed in the lower modes when the foundation length is varied. As the mode number increases, the modes of the system become extended indicating that the foundation as well as the coupling springs have little affect on the system at higher frequencies. The addition of a rotational spring to the beam system produces an interesting phenomena where a particular mode becomes delocalized while other modes are localized. The *delocalization frequency*, defined as the frequency at which the delocalization occurs, is obtained by solving for the frequency which renders the reflection coefficient of the propagating waves to be zero. The results compare very well with what the localization factor predicts.

¹ Graduate Research Assistant, Tel: +1-313-577-6823, Fax: +1-313-577-8789, E-mail: criedel@hu.eng.wayne.edu

² Associate Professor (Corresponding Author), Tel: +1-313-577-3888, Fax: +1-313-577-8789, E-mail: tan@tan.eng.wayne.edu
Submitted to: *Sixth International Conference on Recent Advances in Structural Dynamics*, Institute of Sound and Vibration, Southampton, England, July 1997

2 Problem Formulation

A schematic of the system to be studied is shown in Figure 1. This system represents a string or a beam between two fixed supports. The string or beam is constrained by pointwise linear translational and/or rotational springs (for beams) at x_1 and x_2 , and a uniform linear foundation that extends from x_1 to x_2 . The translational and rotational spring constants are denoted by k_{ti} and k_{ri} at x_i , $i = 1, 2$, respectively. Assumptions for both models include: (i) the mass per unit length is uniform and constant; (ii) the equilibrium position is straight; (iii) damping is neglected. The beam is modeled as an Euler-Bernoulli beam with the effects of rotary inertia, transverse shear deformation, and axial deformation being neglected. Tension is also neglected in the beam model but the analysis procedure is the same if tension had been included.

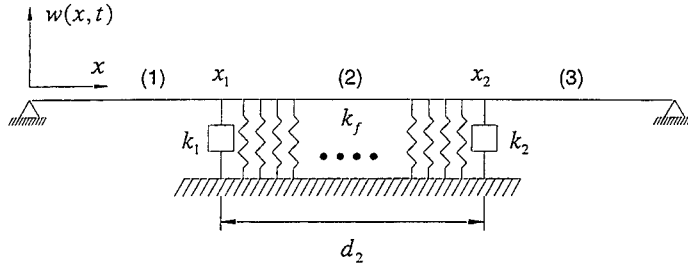


Figure 1. A string or beam partially constrained by an elastic foundation.

The system is partitioned into three subsystems as shown in Figure 1. Under the assumptions above, the non-dimensional equation of motion governing the transverse displacement $w(x, t)$ of each subsystem is

$$\left(\frac{\partial^2}{\partial t^2} + K \right) w(x, t) = f_e(x, t), \quad x \in (0, x_1), \quad x \in (x_2, l) \quad (1a)$$

$$\left(\frac{\partial^2}{\partial t^2} + K + k_f \right) w(x, t) = f_e(x, t), \quad x \in (x_1, x_2) \quad (1b)$$

with boundary conditions expressed in the general form

$$M_j w(x, t) \Big|_{x=0} + N_j w(x, t) \Big|_{x=l} = \gamma_{Bj}(t), \quad t \geq 0, \quad j = 1, \dots, n \quad (2)$$

where n is the highest order of derivatives in x . M_j and N_j are spatial, linear differential operators of the proper order and $\gamma_{Bj}(x, t)$ are functions describing the inhomogeneous boundary

conditions. For fixed supports, $\gamma_{B_i}(x, t) = 0$. In Eqn. (1a,b), k_f is the dimensionless foundation stiffness, $f_e(x, t)$ is the transverse force, and K is the stiffness spatial differential operator

$$\text{string model:} \quad K = -\frac{\partial^2}{\partial x^2} \quad (3a)$$

$$\text{beam model:} \quad K = \frac{\partial^4}{\partial x^4} \quad (3b)$$

The constraint conditions at x_1, x_2 are the continuity of generalized displacements and balance of generalized forces which are determined as

$$\text{string model:} \quad w_x(x_i^+, t) - w_x(x_i^-, t) = k_{ri} w(x_i, t), \quad i = 1, 2 \quad (4)$$

$$\text{beam model:} \quad w_{xx}(x_i^-, t) - w_{xx}(x_i^+, t) = -k_{ri} w_x(x_i, t), \quad (5a)$$

$$w_{xxx}(x_i^-, t) - w_{xxx}(x_i^+, t) = k_{ri} w(x_i, t), \quad i = 1, 2 \quad (5b)$$

3 Free Response Analysis

The response of the system is determined by the distributed transfer function method and the generalized displacement method (GDM) [15]. The procedure is summarized as follows. First transform the global coordinate x into a local coordinate $z \in (0, 1)$ for each subsystem, and represent the Laplace transformed equations (1a,b) and (2) in the state space form. Define $\eta^{(i)}(z, s)$ as the state vector where, for the string

$$\eta^{(i)}(z, s) = \left\{ \bar{w}^{(i)}(z, s) \quad \bar{w}_z^{(i)}(z, s) \right\}^T, \quad (6)$$

and for the beam

$$\eta^{(i)}(z, s) = \left\{ \bar{w}^{(i)}(z, s) \quad \bar{w}_z^{(i)}(z, s) \quad \bar{w}_{zz}^{(i)}(z, s) \quad \bar{w}_{zzz}^{(i)}(z, s) \right\}^T, \quad (7)$$

and $\bar{w}^{(i)}(z, s)$ is the Laplace transform form of $w(z, t)$ for the i -th subsystem. The response solution for each subsystem is [14]

$$\eta^{(i)}(z, s) = \int_0^1 G^{(i)}(z, \xi, s) q^{(i)}(\xi, s) d\xi + H^{(i)}(z, s) \gamma^{(i)}(s), \quad z \in (0, 1), \quad (8)$$

where the matrix transfer functions $G^{(i)}(z, \xi, s)$ and $H^{(i)}(z, s)$ are given by

$$G^{(i)}(z, \xi, s) = \begin{cases} H^{(i)}(z, s) M^{(i)}(s) e^{-F^{(i)}(s)\xi}, & \xi < z \\ -H^{(i)}(z, s) N^{(i)}(s) e^{F^{(i)}(s)(1-\xi)}, & \xi > z \end{cases} \quad (9a)$$

$$H^{(i)}(z, s) = e^{F^{(i)}(s)z} \left(M^{(i)}(s) + N^{(i)}(s) e^{F^{(i)}(s)} \right)^{-1} \quad (9b)$$

The state matrices $F^{(i)}(s)$ and boundary operators $M^{(i)}(s)$, $N^{(i)}(s)$ are listed in Appendix A. In Equation (8), $q^{(i)}(\xi, s)$ and $\gamma^{(i)}(s)$ are the state vectors for excitations and inhomogeneous boundary conditions, respectively.

Equations (8) and (9a,b) give the formal, closed-form solution of the response for each subsystem. For free vibration analysis, $q^{(i)}(\xi, s) = 0$ and the boundary conditions at $x = 0$ and 1 are homogeneous, the response of each subsystem is obtained from Eqn. (8)

$$\eta^{(i)}(z, s) = H^{(i)}(z, s) \gamma^{(i)}(s), \quad z \in (0, 1) \quad (10)$$

where,

$$\gamma^{(1)}(s) = \begin{Bmatrix} 0 \\ \bar{w}(x_1, s) \end{Bmatrix}, \quad \gamma^{(2)}(s) = \begin{Bmatrix} \bar{w}(x_1, s) \\ \bar{w}(x_2, s) \end{Bmatrix}, \quad \gamma^{(3)}(s) = \begin{Bmatrix} \bar{w}(x_2, s) \\ 0 \end{Bmatrix} \quad (11)$$

for the string, and

$$\gamma^{(1)}(s) = \begin{Bmatrix} 0 \\ 0 \\ \bar{w}(x_1, s) \\ \bar{w}_x(x_1, s) \end{Bmatrix}, \quad \gamma^{(2)}(s) = \begin{Bmatrix} \bar{w}(x_1, s) \\ \bar{w}_x(x_1, s) \\ \bar{w}(x_2, s) \\ \bar{w}_x(x_2, s) \end{Bmatrix}, \quad \gamma^{(3)}(s) = \begin{Bmatrix} \bar{w}(x_2, s) \\ \bar{w}_x(x_2, s) \\ 0 \\ 0 \end{Bmatrix} \quad (12)$$

for the beam. Combining Eqns. (11) and (12) with the displacement continuity and force balance conditions (4)-(5a,b) leads to the following eigenvalue problem

$$[T_c(s)] \bar{w}_d(s) = 0 \quad (13)$$

where, for the string

$$\bar{w}_d(s) = \{ \bar{w}(x_1, s) \quad \bar{w}(x_2, s) \} \quad (14a)$$

$$T_s(s) = \begin{bmatrix} -k_{t1} - \frac{1}{d_1} H_{22}^{(11)} + \frac{1}{d_2} H_{21}^{(20)} & \frac{1}{d_2} H_{22}^{(20)} \\ -\frac{1}{d_2} H_{21}^{(21)} & -k_{t2} - \frac{1}{d_2} H_{22}^{(21)} + \frac{1}{d_3} H_{21}^{(30)} \end{bmatrix} \quad (14b)$$

and for the beam

$$\bar{w}_d(s) = \{ \bar{w}(x_1, s) \quad \bar{w}_x(x_1, s) \quad \bar{w}(x_2, s) \quad \bar{w}_x(x_2, s) \} \quad (15a)$$

$$T_c(s) = \begin{bmatrix} \frac{1}{d_2^2} H_{31}^{(20)} - \frac{1}{d_1^2} H_{33}^{(11)} & \frac{1}{d_2^2} H_{32}^{(20)} - \frac{1}{d_1^2} H_{34}^{(11)} - k_{r1} & \frac{1}{d_2^2} H_{33}^{(20)} & \frac{1}{d_2^2} H_{34}^{(20)} \\ \frac{1}{d_2^3} H_{41}^{(20)} - \frac{1}{d_1^3} H_{43}^{(11)} + k_{r1} & \frac{1}{d_2^3} H_{42}^{(20)} - \frac{1}{d_1^3} H_{44}^{(11)} & \frac{1}{d_2^3} H_{43}^{(20)} & \frac{1}{d_2^3} H_{44}^{(20)} \\ -\frac{1}{d_2^2} H_{31}^{(21)} & -\frac{1}{d_2^2} H_{32}^{(21)} & \frac{1}{d_2^3} H_{31}^{(30)} - \frac{1}{d_2^2} H_{33}^{(21)} & \frac{1}{d_2^3} H_{32}^{(30)} - \frac{1}{d_2^2} H_{34}^{(21)} - k_{r2} \\ -\frac{1}{d_2^3} H_{41}^{(21)} & -\frac{1}{d_2^3} H_{42}^{(21)} & \frac{1}{d_2^3} H_{41}^{(30)} - \frac{1}{d_2^2} H_{43}^{(21)} + k_{r2} & \frac{1}{d_2^3} H_{42}^{(30)} - \frac{1}{d_2^2} H_{44}^{(21)} \end{bmatrix} \quad (15b)$$

$H_{mn}^{(iz)}$ denotes the (m,n) element of $H^{(i)}(z,s)$ and $d_1 = x_1$, $d_2 = x_2 - x_1$, and $d_3 = 1 - x_2$. The eigenvalues of the system are the roots of the transcendental characteristic equation

$$\text{Det}[T_c(s)] = 0 \quad (16)$$

Note that classical methods would require the evaluation of the determinant of a 6×6 and a 12×12 matrix for the characteristic equation of the string and the beam system, respectively. The eigenfunctions of the distributed parameter system are obtained by first determining the eigenvalues s_j of the system from (16). The corresponding eigenvector $\bar{w}_d(s_j)$ from (13) is then back substituted into (10) to give the j -th eigenfunction

$$w(x, s_j) = h_1^{(i)}(x, s_j) \gamma^{(i)}(s_j), \quad i = 1, 2, 3, \quad x \in [x_{i-1}, x_i]. \quad (17)$$

Consider an elastic foundation located *symmetrically* along the span of the string or the beam, i.e., $d_1 = d_3$. Figure 2 shows the locus of the natural frequency as a function of the foundation length d_2 for the string model with $k_{r1} = k_{r2} = k_f = 50$. For comparison, the natural frequencies of the uncoupled subsystems ($k_{r1}, k_{r2} \rightarrow \infty$) are also plotted as dashed lines. From Figure 2, it is seen that eigenvalue veering occurs in the first few modes and loci of the coupled system appear to closely follow the loci of the uncoupled systems. However, as the mode number increases, the "fluctuating amplitudes" of the loci decrease, becoming much flatter over the entire range of the foundation length. This results in the loci of the coupled system moving away from the loci of the uncoupled systems. Chung and Tan [4] showed that the coupling of the subsystems increases with $1/k_{ri}$, and for weakly coupled subsystems, mode localization occurs when the frequency loci of a particular mode is close to some frequency loci of the uncoupled subsystem. Thus, as the mode number increases, with the loci of the coupled system becoming increasingly flatter and moving away from the loci of the uncoupled system, the theory of [4] predicts that mode localization will become less prominent and eventually will not occur regardless of the length of the foundation. This prediction agrees with simulation results. To reduce the number of figures in this paper, only mode shapes of the higher modes of the beam system are presented (see Fig. 4). It should be noted that the loci for higher modes are not flat, that is, a straight line. The overall shapes of the loci only appear to be flat relative to the loci of the lower modes because the "fluctuating amplitudes" of the loci decrease as the mode number increases.

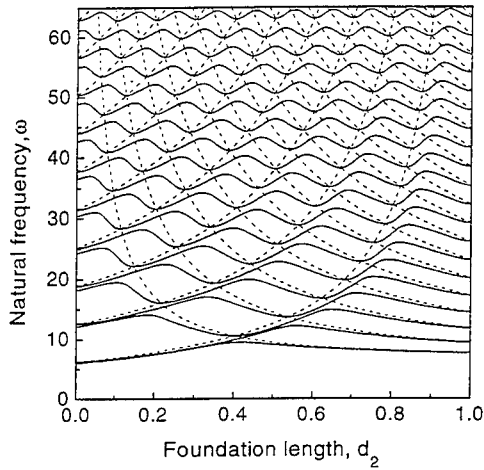


Figure 2. Loci of the natural frequencies of the string model versus the foundation length d_2 for $k_{t1} = k_{t2} = k_f = 50$.

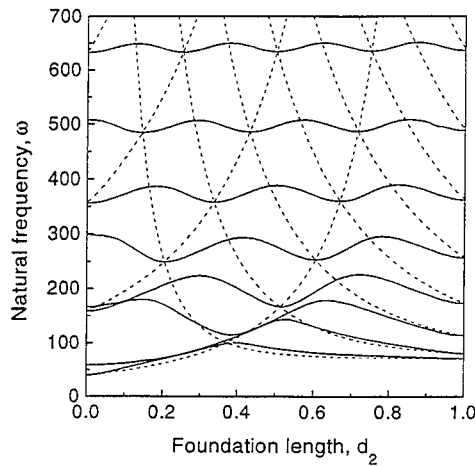


Figure 3. Loci of the natural frequencies of the beam model versus the foundation length d_2 for $k_{t1} = k_{t2} = k_f = 5000$, $k_{r1} = k_{r2} = 0$.

Figure 3 shows the results for the beam model with $k_{t1} = k_{t2} = k_f = 5000$, $k_{r1} = k_{r2} = 0$. The results for $k_{t1} = k_{t2} \rightarrow \infty$ (dashed curves) are also shown to explain the loci veering and mode localization. Note that, for a beam model, each subsystem is *bi-coupled* through translational and rotational constraints. Thus the dashed curves are not the eigenvalue loci of the uncoupled subsystems ($k_t, k_r \rightarrow \infty$). Nevertheless, similar loci veering phenomenon for the first few modes are also observed in the beam model, and the loci of the higher modes deviate away from the loci of the dashed curves significantly. Again the degree of mode localization diminishes for higher modes. This is clearly shown in Fig. 4, where the mode shapes of the eighth mode are plotted for several values of the foundation length. It is noted that in the study of mode localization in a two-span, mono-coupled beam [10], the authors hypothesized that the localized behavior of the first few modes are representative of the behavior of higher modes. However, Langley [16] showed that it was not the case. The results for the beam/foundation system considered here agree with the general findings of Langley. The effects of rotational constraints in the mode localization of the beam model will be examined in Section 5.

Figure 5 shows the first mode of the string model; the modes are localized. Similar results can also be shown for the lower modes of the beam model. Chung and Tan [4] showed that mode localization occurs in weakly coupled systems and the amount of coupling is a function of $1/k_t$ and not k_f . It thus suggests that the partial foundation does not contribute to the occurrence of the mode localization. From Fig. 5, it is obvious that k_f affects the amount of localization. To further understand the influence of k_f and to further show that localization diminishes at high frequencies for the systems studied here, a wave analysis is performed.

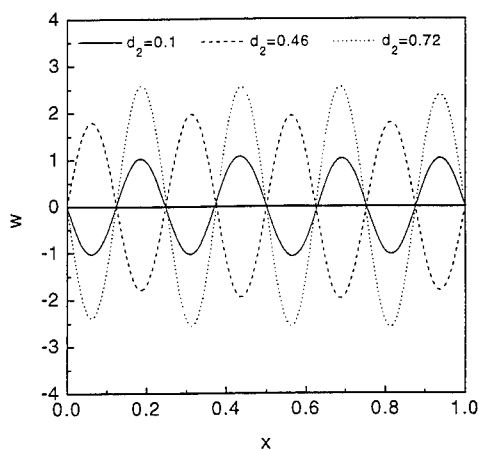


Figure 4. Eighth mode of the beam model, for $k_{t1} = k_{t2} = k_f = 5000$, $k_{r1} = k_{r2} = 0$.

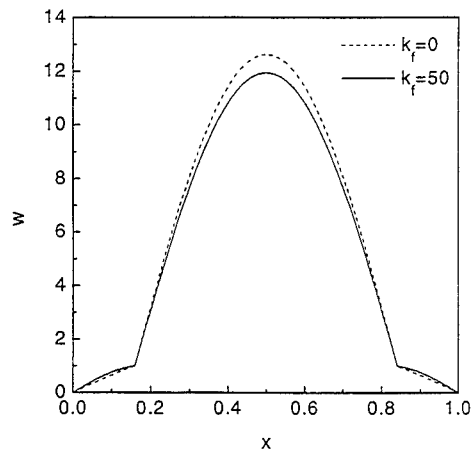


Figure 5. First mode of the string model, for $d_2 = 0.68$, $k_{t1} = k_{t2} = 50$.

4 Wave Reflection and Transmission

Consider a local wave analysis of a wave incident at the subsystem interface. It is well known that when a propagating wave in an elastic medium is incident upon some discontinuity in the medium, a reflected and a transmitted wave are generated [12]. Denote the coupling point as $x = 0$, and because the wave propagates from one medium to another, two different cases need to be considered, as shown in Figure 6.

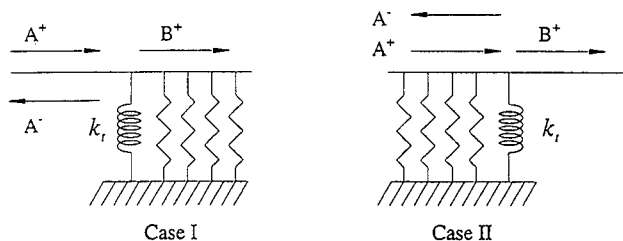


Figure 6. Two cases for an incident wave at the coupling point of the string system.

4.1 String Model

Considering a wave propagating in the positive direction in the subsystem without the foundation, subsystem (1), the dispersion relation is

$$-\omega^2 + \gamma_{s1}^2 = 0 \quad (18)$$

which gives the wavenumbers

$$\gamma_{s1} = \pm\omega = \gamma_1, -\gamma_1 \quad (19)$$

where $\gamma_1 = \omega$. For subsystem (2), the string/foundation medium, the dispersion relation is

$$-\omega^2 + \gamma_{s2}^2 + k_f = 0 \quad (20)$$

which gives

$$\gamma_{s2} = \pm\sqrt{\omega^2 - k_f} = \gamma_2, -\gamma_2 \quad (21)$$

where $\gamma_2 = \sqrt{\omega^2 - k_f}$. The string/foundation subsystem is dispersive with a cutoff frequency $\omega_c = \sqrt{k_f}$, above which all waves propagate and below which all waves attenuate.

4.1.1 Case I: Propagation from string to string/foundation

For this case, the positive traveling incident wave is in the subsystem without the foundation. The wave motions at the subsystem interface are expressed as

$$w(x, t) = \begin{cases} A^+ e^{i(\omega t - \gamma_1 x)} + A^- e^{i(\omega t + \gamma_1 x)} & ; x < 0^- \\ B^+ e^{i(\omega t - \gamma_2 x)} & ; x > 0^+ \end{cases} ; \omega > \omega_c \quad (22)$$

$$w(x, t) = \begin{cases} A^+ e^{i(\omega t - \gamma_1 x)} + A^- e^{i(\omega t + \gamma_1 x)} & ; x < 0^- \\ B^+ e^{i(\omega t - \bar{\gamma}_2 x)} & ; x > 0^+ \end{cases} ; \omega < \omega_c \quad (23)$$

where $\bar{\gamma}_2 = \sqrt{k_f - \omega^2}$. The constraint conditions at the subsystem interface are the continuity in the displacement and the force balance (4). Substituting (22), (23) into the constraint conditions gives the reflection and transmission coefficients, r and t , for $\omega > \omega_c$ and $\omega < \omega_c$

$$r = \frac{A^-}{A^+} = \frac{k_f + i\sqrt{\omega^2 - k_f} - i\omega}{-k_f - i\sqrt{\omega^2 - k_f} - i\omega}, \quad t = \frac{B^+}{A^+} = \frac{2i\omega}{k_f + i\sqrt{\omega^2 - k_f} + i\omega} \quad ; \omega > \omega_c \quad (24a)$$

$$r = \frac{A^-}{A^+} = \frac{k_f + \sqrt{k_f - \omega^2} - i\omega}{-k_f - \sqrt{k_f - \omega^2} - i\omega}, \quad t = \frac{B^+}{A^+} = \frac{2i\omega}{k_f + \sqrt{k_f - \omega^2} + i\omega} \quad ; \omega < \omega_c \quad (24b)$$

Figure 7(a) shows the magnitude (modulus) of the above coefficients for several values of k_f . When $\omega < \omega_c$, $|r| = 1$ since no wave can propagate in the string/foundation medium; i.e.,

the transmitted wave is attenuating. When $\omega > \omega_c$, all waves propagate and $|r|$ decreases as ω increases, while the transmission modulus $|t|$ increases with ω and approaches the value of 1. As ω increases, it is seen that the curves for both r and t converge to the case of $k_f = 0$ implying that the foundation appears to have almost no effect on r or t as ω becomes large. In fact, it can be shown from (24a) that, as $\omega \rightarrow \infty$, $|r| \rightarrow 0$ and $|t| \rightarrow 1$ independent of k_f . In other words, at high frequencies there are no reflected waves; all waves are transmitted. Therefore at high frequencies, both the foundation and point springs are transparent to the system and the system behaves as if $k_f = k_{r1} = k_{r2} = 0$. This means that for $\omega > \omega_c$, and for increasing ω , the coupling between the subsystems becomes stronger. As the coupling becomes stronger, the effect of mode localization will decrease. Therefore, as ω increases, the degree of mode localization decreases regardless of the length of the foundation. This is exactly what Figure 2 predicts based on [4].

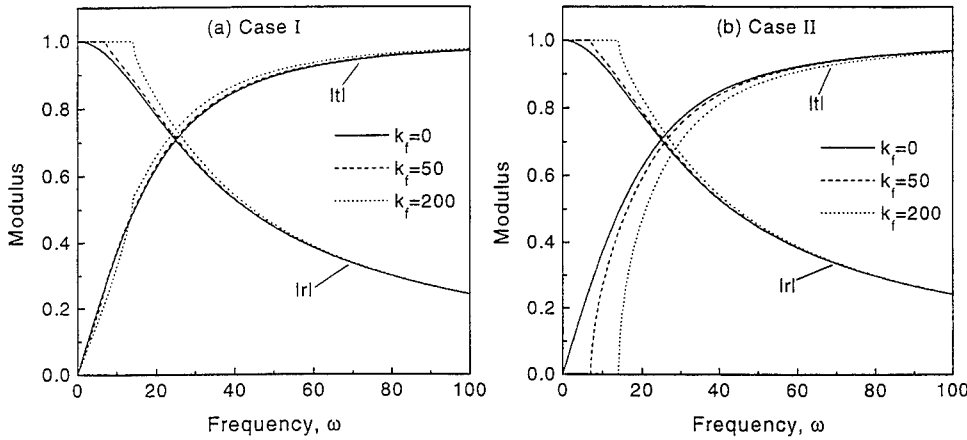


Figure 7. Reflection and transmission coefficients for the string/foundation system for $k_{r1} = k_{r2} = 50$, (a) Case I, (b) Case II.

4.1.2 Case II: Propagation from string/foundation to string

In this case, the positive traveling incident wave is in the string/foundation medium. The wave motions at the subsystem interface for $\omega > \omega_c$ and $\omega < \omega_c$ are

$$w(x, t) = \begin{cases} A^+ e^{i(\omega t - \gamma_2 x)} + A^- e^{i(\omega t + \gamma_2 x)} & ; x < 0^- \\ B^+ e^{i(\omega t - \gamma_1 x)} & ; x > 0^+ \end{cases}, \quad \omega > \omega_c \quad (25a)$$

$$w(x, t) = \begin{cases} A^+ e^{(i\omega t - \bar{\gamma}_2 x)} + A^- e^{(i\omega t + \bar{\gamma}_2 x)} ; & x < 0^- \\ B^+ e^{i(\omega t - \gamma_1 x)} ; & x > 0^+ \end{cases}, \quad \omega < \omega_c \quad (25b)$$

where γ_1, γ_2 , and $\bar{\gamma}_2$ are as previously defined. The transmission and reflection coefficients can be determined as before, and are

$$r = \frac{A^-}{A^+} = \frac{-k_t + i\sqrt{\omega^2 - k_f} - i\omega}{k_t + i\sqrt{\omega^2 - k_f} + i\omega}, \quad t = \frac{B^+}{A^+} = \frac{2i\sqrt{\omega^2 - k_f}}{k_t + i\sqrt{\omega^2 - k_f} + i\omega} ; \quad \omega \geq \omega_c \quad (26a)$$

$$r = \frac{A^-}{A^+} = -1, \quad t = \frac{B^+}{A^+} = 0 ; \quad \omega < \omega_c \quad (26b)$$

Figure 7b shows $|r|$ and $|t|$ for the same values of k_f that were used in Case I. Note that, for $\omega < \omega_c$, $|r| = 1$ for both cases, as shown in Figs. 7(a, b) and by Eqns. (24a), (26a). However, $t = 0$ for $\omega < \omega_c$. This is due to the fact that all waves are attenuating in the string/foundation medium and therefore no propagating wave can be transmitted. When $\omega > \omega_c$, t increases with ω . Again, it is seen that as ω becomes large, $|r|$ and $|t|$ approach 0 and 1, respectively, meaning that the subsystems behave as if they are completely coupled and the degree of mode localization diminishes. Thus, the results of Figs. 7 (a, b) confirm the findings in Section 3 for large ω .

5.2 Beam Model

The reflection and transmission coefficients for the beam model can also be determined for the same two cases as the string. The dispersion relation for the subsystem without the foundation is

$$-\omega^2 + \gamma_{b1}^4 = 0 \quad (27)$$

which results in the following wavenumbers

$$\gamma_{b1} = \pm\sqrt{\omega}, \quad \pm i\sqrt{\omega} = \pm\gamma_1, \quad \pm i\gamma_1 \quad (28)$$

where $\gamma_1 = \sqrt{\omega}$. For the beam/foundation subsystem, the dispersion relation is

$$-\omega^2 + \gamma_{b2}^4 + k_f = 0 \quad (29)$$

which gives the wavenumbers

$$\gamma_{b2} = \pm(\omega^2 - k_f)^{1/4}, \quad \pm i(\omega^2 - k_f)^{1/4} = \pm\gamma_2, \quad \pm i\gamma_2 \quad (30)$$

where $\gamma_2 = (\omega^2 - k_f)^{1/4}$. As with the case of the string, Eqn. (30) shows that the beam has a cutoff frequency $\omega_c = \sqrt{k_f}$.

5.2.1 Case I: Propagation from beam to beam/foundation

From Eqns. (28) and (30), the beam has four wave components; two of which are propagating and two are attenuating. At the subsystem interface, the wave solutions are

$$w(x, t) = \begin{cases} A^+ e^{i(\omega t - \gamma_1 x)} + A_a^+ e^{i(\omega t - \gamma_1 x)} + A^- e^{i(\omega t + \gamma_1 x)} + A_a^- e^{i(\omega t + \gamma_1 x)}; & x < 0^- \\ B^+ e^{i(\omega t - \gamma_2 x)} + B_a^+ e^{i(\omega t - \gamma_2 x)} & ; x > 0^+ \end{cases} \quad \omega > \omega_c \quad (31a)$$

$$w(x, t) = \begin{cases} A^+ e^{i(\omega t - \gamma_1 x)} + A_a^+ e^{i(\omega t - \gamma_1 x)} + A^- e^{i(\omega t + \gamma_1 x)} + A_a^- e^{i(\omega t + \gamma_1 x)}; & x < 0^- \\ B_1^+ e^{i(\omega t - (m_1 - m)x)} + B_2^+ e^{i(\omega t - (m_1 + m)x)} & ; x > 0^+ \end{cases} \quad \omega < \omega_c \quad (31b)$$

where A^+ and A_a^+ are the positive propagating and attenuating waves, A^- and A_a^- are the negative propagating and attenuating waves, respectively, B_1^+ and B_2^+ are propagating/spatially varying waves, and

$$m = \frac{(k_f - \omega^2)^{1/4}}{\sqrt{2}} \quad (32)$$

The 2×2 reflection and transmission matrices \mathbf{r} and \mathbf{t} are expressed as [17]

$$\mathbf{A}^- = \mathbf{r} \mathbf{A}^+, \quad \mathbf{B}^+ = \mathbf{t} \mathbf{A}^+, \quad (33a, b)$$

where,

$$\mathbf{A}^+ = \begin{Bmatrix} A^+ \\ A_a^+ \end{Bmatrix}, \quad \mathbf{A}^- = \begin{Bmatrix} A^- \\ A_a^- \end{Bmatrix}, \quad \mathbf{B}^+ = \begin{Bmatrix} B^+ \\ B_a^+ \end{Bmatrix}. \quad (34)$$

At the coupling point and for $\omega > \omega_c$, applying the continuity of generalized displacements and force balance conditions based on Eqns. (5a, b) leads to the following set of equations

$$\begin{bmatrix} 1 & 1 \\ -i\gamma_1 & -\gamma_1 \end{bmatrix} \mathbf{A}^+ + \begin{bmatrix} 1 & 1 \\ i\gamma_1 & \gamma_1 \end{bmatrix} \mathbf{A}^- = \begin{bmatrix} 1 & 1 \\ -i\gamma_2 & \gamma_2 \end{bmatrix} \mathbf{B}^+ \quad (35)$$

$$\begin{bmatrix} -\gamma_1^2 & \gamma_1^2 \\ i\gamma_1^3 & -\gamma_1^3 \end{bmatrix} \mathbf{A}^+ + \begin{bmatrix} -\gamma_1^2 & \gamma_1^2 \\ -i\gamma_1^3 & \gamma_1^3 \end{bmatrix} \mathbf{A}^- = \begin{bmatrix} -\gamma_2^2 & \gamma_2^2 \\ i\gamma_2^3 & -\gamma_2^3 \end{bmatrix} \mathbf{B}^+ + \begin{bmatrix} i\gamma_2 k_r & \gamma_2 k_r \\ k_t & k_t \end{bmatrix} \mathbf{B}^+ \quad (36)$$

Resolving (35), (36) in the forms of (33a, b) yields the reflection and transmission matrices \mathbf{r} and \mathbf{t} for $\omega > \omega_c$. The same procedure can be used to determine \mathbf{r} and \mathbf{t} for $\omega < \omega_c$.

Figures 8-11 plot various reflection and transmission coefficients as a function of frequency, with $k_f = 5000$ and $k_r = 0$. As seen in all figures, for sufficiently large $\omega > \omega_c$, the curves for $k_f \neq 0$ approach the corresponding ones for $k_f = 0$, as in the case of the string. This means that the foundation appears to be transparent at high frequencies. Comparing Fig. 3 with Figs. 8-11, it can be concluded that, for this particular case, the foundation has negligible effect on the wave motions for mode number greater than 6. Figure 10 shows that $|t_{11}| \rightarrow 1$ as ω increases (i.e., most of the propagating waves are transmitted), regardless of the value of k_f . The subsystems

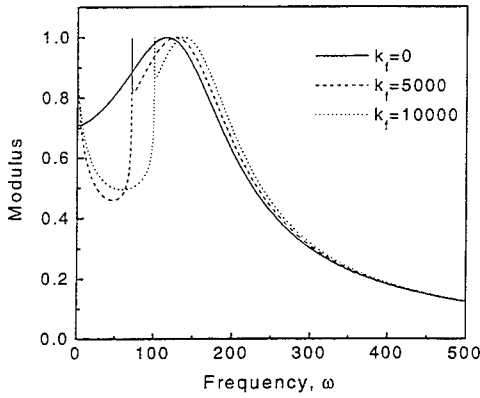


Figure 8. Reflection coefficient r_{11} for Case I of the beam model with $k_f = 5000$, $k_r = 0$.

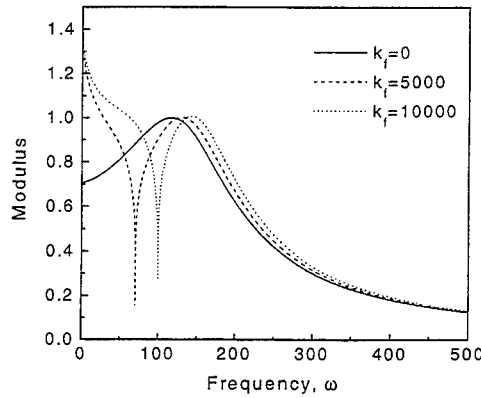


Figure 9. Reflection coefficient r_{12} for Case I of the beam model with $k_f = 5000$, $k_r = 0$.

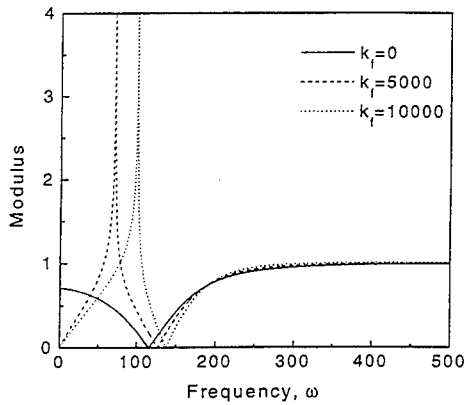


Figure 10. Transmission coefficient t_{11} for Case I of the beam model with $k_f = 5000$, $k_r = 0$.

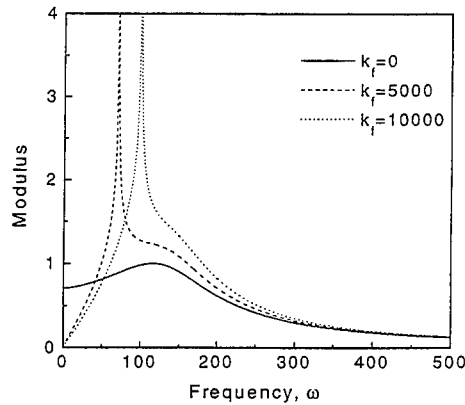


Figure 11. Transmission coefficient t_{12} for Case I of the beam model with $k_f = 5000$, $k_r = 0$.

are thus strongly coupled and the degree of mode localization diminishes, agreeing with the results implied by Fig. 3. Now since the effect of k_f is negligible at high frequencies, the diminishing of the mode localization is thus independent of the presence of the foundation.

In Figs. 8-11, it is seen that the reflection and transmission coefficients change drastically at $\omega \approx \omega_c$, and are significantly affected by k_f . In particular, the wave transmission coefficients go to infinity at $\omega = \omega_c$, for both the transmitted propagating (Fig. 10) and attenuating waves (Fig. 11). To explain this, it is noted that γ is complex for $\omega < \omega_c$, and is either real or purely imaginary for $\omega > \omega_c$. Thus the characteristics of wave motions are different as the cutoff frequency is passed. Also, why does this phenomenon occur only in the beam model and not the string model (Fig. 7)? At this point, it is suspected that this could be due to a deficiency in the modeling of the Winkler foundation which constrains only the transverse displacement and has no effect on the rotational motion of the beam. The foundation represents a series of point springs, assuming that the beam interacts with it only at discrete points and deformation at a material point of the beam is not affected by motions of neighboring material points. The effects of rotational constraints on the wave reflection and transmission will be explored in Section 5 to explain the phenomenon seen in Figs. 8-11. Similar observations in the deficiency of the Winkler foundation model have also been made in civil engineering applications, and a more realistic model of a Pasternak foundation was suggested [18, 19].

5.2.2 Case II: Propagation from beam/foundation to beam

With the incident wave in the beam/foundation medium, the wave solution becomes

$$w(x, t) = \begin{cases} A_1^+ e^{i(\omega t - \gamma_1 x)} + A_2^+ e^{i(\omega t - \gamma_2 x)} + A_3^- e^{i(\omega t + \gamma_2 x)} + A_4^- e^{i(\omega t + \gamma_1 x)}; & x < 0 \\ B_1^+ e^{i(\omega t - \gamma_1 x)} + B_2^+ e^{i(\omega t - \gamma_2 x)}; & x > 0 \end{cases} \quad \omega > \omega_c \quad (37a)$$

$$w(x, t) = \begin{cases} A_1^+ e^{i(\omega t - (mi - m)x)} + A_2^+ e^{i(\omega t - (mi - m)x)} + A_3^- e^{i(\omega t + (mi - m)x)} + A_4^- e^{i(\omega t + (mi - m)x)}; & x < 0 \\ B_1^+ e^{i(\omega t - \gamma_1 x)} + B_2^+ e^{i(\omega t - \gamma_2 x)}; & x > 0 \end{cases} \quad \omega < \omega_c \quad (37b)$$

where the notations used are the same as in Case I with A_1^+, A_2^+, A_3^- , and A_4^- being propagating/spatially varying waves. A similar procedure can be applied to obtain the wave reflection and transmission matrices. Again, the simulation results show that k_f has no effect on the wave propagation at high frequencies.

5 Role of the Rotational Constraint in the Beam Model

Due to the suspected deficiency in the modelling of a Winkler foundation for a beam structure which has rotational stiffness, the effects of having both translational and rotational springs at the subsystem interfaces are studied. To simplify the problem, only a two-span beam is considered, i.e., $x_2 = 1$ and $d_3 = 0$. Figure 12 shows the frequency loci versus the foundation

length d_2 for the two-span beam with $k_t = k_r = k_f = 5000$. The loci exhibit veering for the first three modes while the loci of the fourth mode becomes almost flat relative to the other loci over the range of $d_2 = 0.05 \sim 0.95$. Veering then occurs for the fifth mode and continues for higher modes. This “flattening” of the fourth mode loci is similar to the beam model at high frequencies shown in Fig. 3. This suggests that the fourth mode is extended (global mode), while the other modes above or below the fourth mode are localized. In other words, the modes are first localized, delocalized at the fourth mode, and then localized again. Results for the mode shapes of the first seven modes show exactly this behavior.

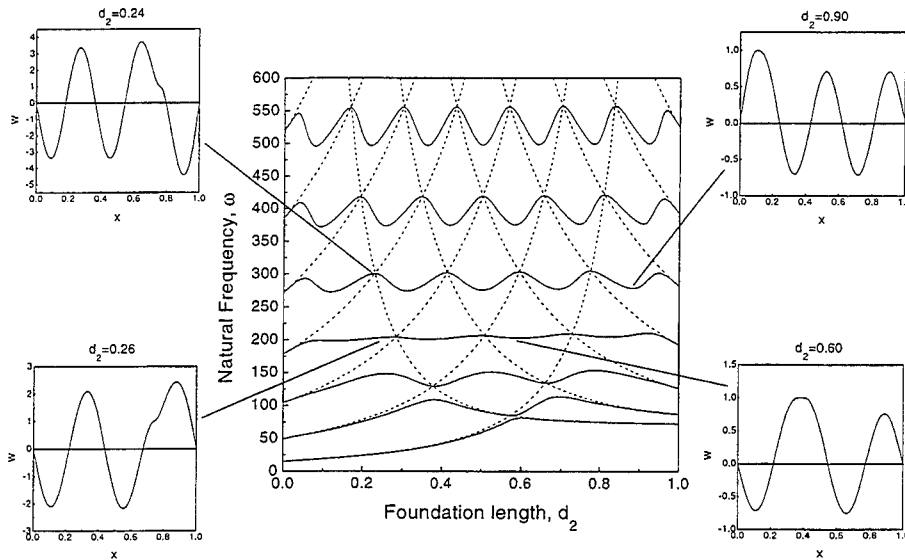


Figure 12. Loci of natural frequencies versus foundation length for a two-span beam on partial foundation with $k_t = k_r = k_f = 5000$. Mode shapes for the fourth and fifth modes are also shown.

To help explain this phenomenon, the reflection and transmission matrices at the coupling point are determined in a similar manner as before. For Case I, with the incident propagating wave in the subsystem without the foundation, the modulus of r_{11} , r_{12} , t_{11} , and t_{12} are shown in Figures 13 and 14 for different values of k_f with $k_t = k_r = 5000$. The figures show that, for $k_f = 0$, there is a frequency where $r_{11} = 0$ and $t_{11} = 1$, implying that at this frequency all incident propagating waves are completely transmitted, and therefore if the natural frequency of the system coincides with that particular frequency, mode localization will not occur. This frequency, hereby termed the *delocalization frequency*, can be found by equating the numerator of r_{11} to 0 and then solving for ω . For the case shown in Figure 13, the delocalization frequency is 184.87. The figures also show that the addition of the foundation shifts the reflection coefficient up and to the right so that now there is no frequency at which r_{11} becomes 0.

However, for the current case where $k_f = 5000$, its minimum value $r_{11} \approx 0.05$ occurs at $\omega \approx 192$. This minimum value is still very low and will cause the modes near that frequency to become extended. This explains why the eigenvalue loci of the fourth mode in Figure 12 is nearly flat. Note that the delocalization is basically independent of the foundation. The addition of the rotational pointwise constraint also removes the singularity phenomenon seen in Figs. 8-11 except at ω_c . Thus a rotational constraint and a foundation model which includes rotational constraints are needed to properly formulate the wave propagation problem in a constrained beam model.

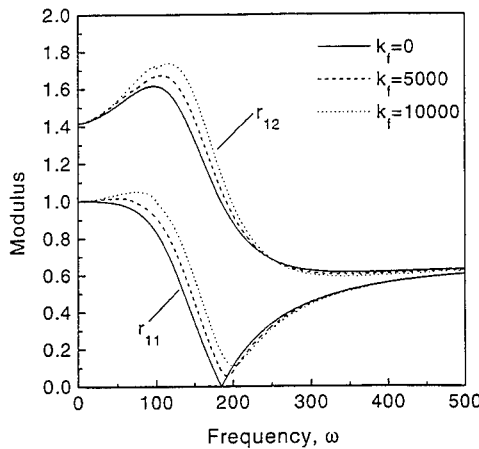


Figure 13. Reflection coefficients for Case I of the beam model with $k_t = k_r = 5000$.

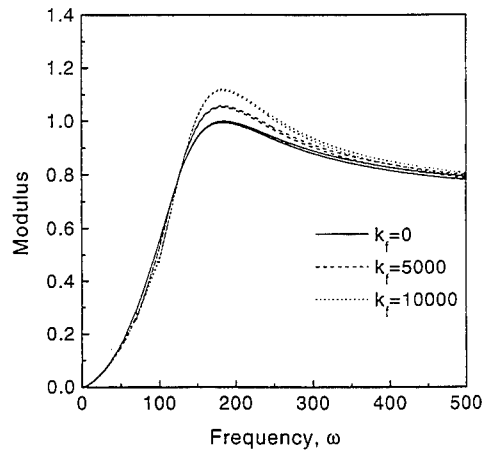


Figure 14. Transmission coefficients for Case I of the beam model with $k_t = k_r = 5000$. For given k_f , lower curve is t_{12} , upper curve is t_{11} .

A similar delocalization phenomenon for a two-span Timoshenko beam joined by a pin joint with a translational and rotational spring at the pin joint was reported by Lust et al. [20]. Their finite elements results show that there is first mode localization, then followed by delocalization as the transverse spring is increased. It was suggested that the delocalization is due to interactions of the bending and shear modes and the disorder of the beam span lengths. It is interesting that the fact that delocalization does not occur in the string model may suggest that this phenomenon has to do with the interactions of transverse and bending motions in a beam (bi-coupled system).

Consider the case of $k_f = 0$ and neglect attenuating wave components, the degree of mode localization of the two subsystems due to the coupling can be quantified by the localization factor $|\delta|$ which is expressed as [16]

$$|\delta| = \frac{(1 + |r|^2 - 2|r|\cos\psi_1)^{\frac{1}{2}}}{|t|}, \quad \psi_1 = \phi_{s1} + \phi_r + \phi_t + \phi - 2\gamma_1 L_1 \quad (38)$$

where r and t are the reflection and transmission coefficients, respectively, at the coupling point, ϕ_{s1} is the phase angle of the reflection coefficient at boundary associated with subsystem 1, ϕ_r and ϕ_t are the phase angles of r and t respectively, γ_1 is the wavenumber of subsystem 1, and L_1 is the length of subsystem 1. The values of ϕ can be $\pm\frac{1}{2}\pi$ and for our case is taken to be $\frac{1}{2}\pi$. When $|\delta|$ is evaluated at a particular natural frequency, it determines the degree of localization for the corresponding mode. When $|\delta|=1$ the modes are completely extended (not localized). In Fig. 15, the localization factor is plotted against frequency for several locations of the coupling point x_1 of the two-span beam. The line $|\delta|=1$ is also shown for reference. The points on each curve (*, o, +) represent the second to sixth natural frequencies of the system. At low frequencies, the amplitude of the curves are very large indicating that the modes are strongly localized. As the frequency increases, the amplitude of the curves decrease and eventually all the curves coalesce at the delocalization frequency of 184.87 where $r=0$. At this point the localization factor is 1. The fourth modes of all three cases are very close to the delocalization frequency indicating that the localization factor is near unity and hence mode localization does not occur in the fourth mode. As the frequency increases beyond this point, the localization curves begin to increase thus showing that localization can occur in the modes above the fourth mode. It can be seen directly from (38) that when $|r|=0$ and $|t|=1$ the localization factor is 1. Note that Fig. 15 agrees with the hypothesis that mode localization is strongest at the lower modes [10].

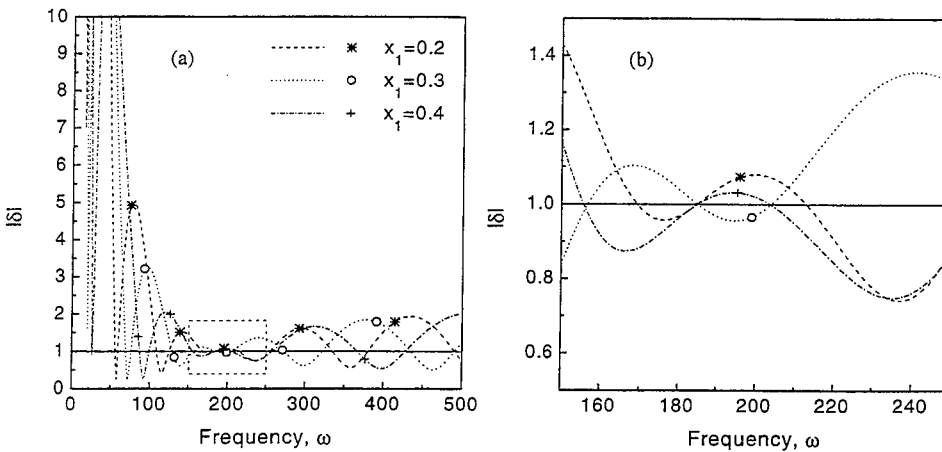


Figure 15. Localization factor versus frequency for a two-span beam with $k_t = k_r = 5000$, $k_f = 0$.

The implication of the delocalization is that, with the parameters of the system, E, I, L, k_r , and k_t , the system can be tuned such that a particular mode coincides with the delocalization frequency and becomes delocalized. Moreover, the delocalization is virtually unaffected by the location of the translational and rotational springs; that is its mode shape is practically independent of the position of the coupling point. Of course modes which are not exactly at this frequency but are sufficiently close to it will also exhibit delocalization. The delocalization phenomenon poses an important design criterion, and must be avoided if particular mode localization is desired.

6 Summary and Conclusions

The free response and wave propagation of a constrained string and beam on a partial elastic foundation is studied in this paper. Plots of eigenvalues show that at high frequencies loci veering diminishes and hence the degree of mode localization decreases. The wave analysis confirms this and further shows that the spring constraints become transparent to the system at high frequencies and thus the subsystems are strongly coupled. The effect of the foundation on the free response is also examined. It is shown that the foundation has negligible effect on the wave propagation at high frequencies and does not seem to affect the fundamental characteristics of the free response of the system. With the inclusion of a rotational constraint, a *mode delocalization* phenomenon occurs in which the lower modes are localized, delocalized (extended) at a particular mode, and localized at higher modes again. The frequency at which delocalization occurs is the frequency which makes the reflection coefficient of the propagating waves become zero. This delocalization frequency matches well with the prediction obtained from a plot of the localization factor [16] even though the attenuating wave components were neglected in the analysis.

Acknowledgment

The authors gratefully acknowledge the support of the National Science Foundation and the Institute of Manufacturing Research of Wayne State University for this research work.

REFERENCES

1. Doyle, P. F., and Pavlovic, M. N., 1982, "Vibration of Beams on Partial Elastic Foundations," *Earthquake Engineering and Structural Dynamics*, Vol. 10, pp. 663-674.
2. Eisenberger, M., Yankelevsky, D. Z., and Adin, M. A., 1985, "Vibrations of Beams Fully or Partially Supported on Elastic Foundations," *Earthquake Engineering and Structural Dynamics*, Vol. 13, pp. 651-650.
3. Burke, S. E., and Hubbard, J. E., 1987, "Active Vibration of a Simply Supported Beam Using a Spatially Distributed Actuator," *IEEE Control systems Magazine*, August, pp. 25-30.

4. Chung, C. H., and Tan, C. A., 1993, "Transfer Function Formulation of Constrained Distributed Parameter Systems, Part II: Applications," *ASME Journal of Applied Mechanics*, Vol. 60, December, pp. 1012-1019.
5. Tan, C. A., and Zhang, L., 1994, "Dynamic Characteristics of a Constrained String Translating Across an Elastic Foundation," *ASME Journal of Vibration and Acoustics*, Vol. 116, July, pp. 318-325.
6. Hodges, C. H., 1982, "Confinement of Vibration by Structural Irregularity," *Journal of Sound and Vibration*, Vol. 82, No. 3, pp. 411-424.
7. Hodges, C. H., and Woodhouse, J., 1983, "Vibration Isolation from Irregularity in a Nearly Periodic Structure: Theory and Measurements," *Journal of the Acoustical Society of America*, Vol. 74, September, pp. 894-905.
8. Bendiksen, O. O., 1987, "Mode Localization Phenomena in Large Space Structures," *AIAA Journal*, Vol. 25, No. 9, September, pp. 1241-1248.
9. Pierre, C., and Dowell, E. H., 1987, "Localization of Vibrations by Structure Irregularity," *Journal of Sound and Vibration*, Vol. 114, No. 3, pp. 549-564.
10. Pierre, C., Tang, D. M., and Dowell, E. H., 1987, "Localized Vibrations of Disordered Multispan Beams: Theory and Experiment," *AIAA Journal*, Vol. 25, No. 9, September, pp. 1249-1257.
11. Pierre, C., 1988, "Mode Localization and Eigenvalue Loci Veering Phenomena in Disordered Structures," *Journal of Sound and Vibration*, Vol. 126, No. 3, pp. 485-502.
12. Graff, K. F., 1975, *Wave Motion in Elastic Solids*, Ohio State University Press.
13. Perkins, N. C., 1990, "Linear Dynamics of a Translating String on an Elastic Foundation," *ASME Journal of Vibration and Acoustics*, Vol. 112, Vol. 1, pp. 2-7.
14. Yang, B., and Tan, C. A., 1992, "Transfer Functions of One-Dimensional Distributed Parameter Systems," *ASME Journal of Applied Mechanics*, Vol. 59, December, pp. 1009-1014.
15. Tan, C. A., and Chung, C. H., 1993, "Transfer Function Formulation of Constrained Distributed Parameter Systems, Part I: Theory," *ASME Journal of Applied Mechanics*, Vol. 60, December, pp. 1004-1011.
16. Langley, R. S., 1995, "Mode Localization Up to High Frequencies in Coupled One-Dimensional Subsystems," *Journal of Sound and Vibration*, Vol. 185, No. 1, pp. 79-91.
17. Mace, B. R., 1984, "Wave Reflection and Transmission in Beams," *Journal of Sound and Vibration*, Vol. 97, No. 2, pp. 237-246.
18. Rades, M., 1970, "Steady-State Response of a Finite Beam on a Pasternak-Type Foundation," *International Journal of Solids and Structures*, Vol. 6, pp. 739-756.
19. Wang, T. M., and Stephens, J. E., 1977, "Natural Frequencies of Timoshenko Beams on Pasternak Foundation," *Journal of Sound and Vibration*, Vol. 51, No. 2, pp. 149-155.

20. Lust, S. D., Friedmann, P. P., and Bendiksen, O. O., 1993, "Mode Localization in Multispan Beams," *AIAA Journal*, Vol. 31, No. 2, February, pp. 348-355.

Appendix A

The state matrices and the boundary operators in local coordinates for the string are

$$F^{(1)}(s) = \begin{bmatrix} 0 & 1 \\ s^2 d_1^2 & 0 \end{bmatrix}, \quad F^{(2)}(s) = \begin{bmatrix} 0 & 1 \\ (s^2 + k_f) d_2^2 & 0 \end{bmatrix}, \quad F^{(3)}(s) = \begin{bmatrix} 0 & 1 \\ s^2 d_3^2 & 0 \end{bmatrix}$$

$$M^{(i)}(s) = \begin{bmatrix} 1 & 0 \\ 0 & 0 \end{bmatrix}, \quad N^{(i)}(s) = \begin{bmatrix} 0 & 0 \\ 1 & 0 \end{bmatrix}, \quad i = 1, 2, 3.$$

The state matrices and the boundary operators in local coordinates for the beam are

$$F^{(1)}(s) = \begin{bmatrix} 0 & 1 & 0 & 0 \\ 0 & 0 & 1 & 0 \\ 0 & 0 & 0 & 1 \\ -s^2 d_1^3 & 0 & 0 & 0 \end{bmatrix}, \quad F^{(2)}(s) = \begin{bmatrix} 0 & 1 & 0 & 0 \\ 0 & 0 & 1 & 0 \\ 0 & 0 & 0 & 1 \\ -(s^2 + k_f) d_2^3 & 0 & 0 & 0 \end{bmatrix}, \quad F^{(3)}(s) = \begin{bmatrix} 0 & 1 & 0 & 0 \\ 0 & 0 & 1 & 0 \\ 0 & 0 & 0 & 1 \\ -s^2 d_3^3 & 0 & 0 & 0 \end{bmatrix}$$

$$M^{(1)}(s) = \begin{bmatrix} 1 & 0 & 0 & 0 \\ 0 & 0 & \frac{1}{d_1^2} & 0 \\ 0 & 0 & 0 & 0 \\ 0 & 0 & 0 & 0 \end{bmatrix}, \quad N^{(1)}(s) = \begin{bmatrix} 0 & 0 & 0 & 0 \\ 0 & 0 & 0 & 0 \\ 1 & 0 & 0 & 0 \\ 0 & \frac{1}{d_1} & 0 & 0 \end{bmatrix}$$

$$M^{(2)}(s) = \begin{bmatrix} 1 & 0 & 0 & 0 \\ 0 & \frac{1}{d_2} & 0 & 0 \\ 0 & 0 & 0 & 0 \\ 0 & 0 & 0 & 0 \end{bmatrix}, \quad N^{(2)}(s) = \begin{bmatrix} 0 & 0 & 0 & 0 \\ 0 & 0 & 0 & 0 \\ 1 & 0 & 0 & 0 \\ 0 & \frac{1}{d_2} & 0 & 0 \end{bmatrix}$$

$$M^{(3)}(s) = \begin{bmatrix} 1 & 0 & 0 & 0 \\ 0 & \frac{1}{d_3} & 0 & 0 \\ 0 & 0 & 0 & 0 \\ 0 & 0 & 0 & 0 \end{bmatrix}, \quad N^{(3)}(s) = \begin{bmatrix} 0 & 0 & 0 & 0 \\ 0 & 0 & 0 & 0 \\ 1 & 0 & 0 & 0 \\ 0 & 0 & \frac{1}{d_3^2} & 0 \end{bmatrix}$$

THE MEASUREMENT OF IN-PLANE WAVE POWER FLOW IN PLATES

S.H. Liu* and R.J. Pinnington

Institute of Sound and Vibration Research, University of Southampton,
Southampton SO17 1BJ, England

1. INTRODUCTION

The measurement of power flow in beams and plates was first introduced by Noiseux [1], who described flexural wave power in terms of surface vibrations so that power transmission under far field condition could be measured by two accelerometers - one measuring the transverse acceleration and the other measuring rotational acceleration. Fahy [2] and Verheij [3] introduced a measurement method by using cross spectral density in the frequency domain that provided a convenient method for practical measurements with FFT analysers.

Most of the structural intensity measurements have been focused on the flexural wave by using various accelerometer arrays and finite difference approximations [4-7]. One reason for this is that the local accelerations and strains associated with flexural wave motion are larger and more noticeable than those of in-plane wave motion and therefore easier to measure. For in-plane measurements, the accelerometers have to be positioned parallel to the

* Present address : Department of Mechanical Engineering, National Taipei Institute of Technology, Taipei, Taiwan 10643, Republic of China

structure, usually via an attached to a mounting block. The introduction of the mounting block, together with the problem of the transverse sensitivity of accelerometers, can cause the measurement to be less accurate. Though strain gauges can instead be used for measurement, problems however occur in practice because their sensitivity is low at high frequencies. Another drawback with strain gauges is that rather than the use of charge amplifiers (as used with piezo-type sensors such as load cells and accelerometers) they require special conditioning amplifiers. Phase is crucial in power measurements and the simultaneous introduction of different types of amplifier when using strain gauges alongside piezo-type sensors can cause severe phase mismatch errors.

Piezo film gauges have been used to measure the flexural wave and longitudinal wave power transmission in beams [8]. Piezo gauges are lightweight, with negligible mass effect on structures, and low cost. Unlike strain gauges, piezo gauges are very sensitive to strain and can be used in the high frequency range. Piezo gauges like other piezo-type sensors such as accelerometers and load cells use charge amplifiers converting an output charge signal to a voltage signal, therefore piezo gauges can be used together with accelerometers and load cells in power measurements without causing any phase mismatch problem.

This paper discusses the use of the piezo film gauge in measuring in-plane wave structural intensity in plates. Also experimental investigations were carried out to verify the new measurement method.

2. MEASUREMENT OF IN-PLANE STRUCTURAL INTENSITY

2.1 Theory of measurement

The x and y component of in-plane structural intensity, power transmission per unit cross-section area (W/m^2), can be obtained from in-plane stresses and motions as [9]

$$I_x = -\sigma_{xx} \dot{u} - \tau_{xy} \dot{v} , \quad (1)$$

$$I_y = -\sigma_{yy} \dot{v} - \tau_{yx} \dot{u} , \quad (2)$$

where \dot{u} and \dot{v} are velocity in the x and y direction respectively, σ_{xx} and σ_{yy} are normal stress in the x and y direction, τ_{xy} and τ_{yx} are shear stresses.

Equations (1) and (2) represent instantaneous intensity, but only time-averaged intensity is referred to in this paper. In practice acceleration rather than velocity was monitored and broadband forces rather than harmonic forces were often occur. In this case the spectral density of time-averaged intensity ($\text{W/m}^2/\text{Hz}$) in the x and y directions are given by [3]

$$\frac{I_x}{\text{Hz}} = \frac{1}{\omega} \text{Im} \left\{ \sigma_{xx} a_x^* + \tau_{xy} a_y^* \right\} , \quad (3)$$

$$\frac{I_y}{\text{Hz}} = \frac{1}{\omega} \text{Im} \left\{ \sigma_{yy} a_y^* + \tau_{yx} a_x^* \right\} , \quad (4)$$

where a_x^* and a_y^* denote conjugate of acceleration $a_x = \partial^2 u / \partial t^2$ and $a_y = \partial^2 v / \partial t^2$.

In equations (3) and (4) all the stresses σ_{xx} , σ_{yy} , τ_{xy} and accelerations a_x , a_y are the Fourier transform functions of the responses in the time domain.

By substituting in-plane stress-strain relations from elasticity theory [10], the x and y component of the time-averaged in-plane intensity therefore can be expressed in terms of strains and accelerations as

$$\frac{I_x}{Hz} = \frac{E}{\omega} \text{Im} \left\{ \left(\frac{\varepsilon_x + \nu \varepsilon_y}{1 - \nu^2} \right) a_x^* + \left(\frac{\gamma_{xy}}{2(1 + \nu)} \right) a_y^* \right\}, \quad (5)$$

$$\frac{I_y}{Hz} = \frac{E}{\omega} \text{Im} \left\{ \left(\frac{\varepsilon_y + \nu \varepsilon_x}{1 - \nu^2} \right) a_y^* + \left(\frac{\gamma_{xy}}{2(1 + \nu)} \right) a_x^* \right\}. \quad (6)$$

If a three-element rectangular rosette which employs uni-axial piezo gauges placed at the 0° , 45° and 90° position (see Figure 1) is applied to measure in-plane strains ε_x , ε_y and γ_{xy} , it would give [11]

$$\varepsilon_x = \varepsilon_1, \quad (7)$$

$$\varepsilon_y = \varepsilon_2, \quad (8)$$

$$\gamma_{xy} = 2\varepsilon_3 - \varepsilon_1 - \varepsilon_2. \quad (9)$$

By substituting equations (7)-(9) into equations (5) and (6), the x and y component of time-averaged in-plane intensity can be measured by using three uni-axial piezo gauges and two accelerometers as

$$\frac{I_x}{Hz} = G_{FF} \frac{E}{\omega} \text{Im} \left\{ \left(\frac{H_{F\varepsilon_1} + \nu H_{F\varepsilon_2}}{1 - \nu^2} \right) H_{Fa_x}^* + \left(\frac{2H_{F\varepsilon_3} - H_{F\varepsilon_1} - H_{F\varepsilon_2}}{2(1 + \nu)} \right) H_{Fa_y}^* \right\}, \quad (10)$$

$$\frac{I_y}{Hz} = G_{FF} \frac{E}{\omega} \text{Im} \left\{ \left(\frac{H_{F\varepsilon_2} + \nu H_{F\varepsilon_1}}{1 - \nu^2} \right) H_{Fa_y}^* + \left(\frac{2H_{F\varepsilon_3} - H_{F\varepsilon_1} - H_{F\varepsilon_2}}{2(1 + \nu)} \right) H_{Fa_x}^* \right\}, \quad (11)$$

where G_{FF} is autospectrum of input force signal, $H_{F\varepsilon}$ and H_{Fa} are transfer functions.

2.2. Uni-axial piezo gauge

The uni-axial piezo gauge (see Figure 2) has been used successfully in measuring the flexural and longitudinal power transmission in beams [8]. The piezo gauges were made from 52 μm thick piezo film (PVDF) with Cu/Ni electrode layers. The size of piezo gauge was 20mm \times 15mm (length \times width) and the active area was 20mm \times 5mm in the middle of the gauge. The sensitivity coefficient (output charge per strain) of uni-axial piezo gauge is 6.5 pC/ μ .

2.3. Flexural wave effect

In practice flexural waves usually occur when measuring in-plane structural intensity. As accelerometers have a low transverse sensitivity (smaller than 3%) the errors caused by flexural waves in measuring in-plane acceleration can be ignored. But for the signal from piezo gauge the surface strains caused by flexural waves and in-plane waves may have the same order, so the flexural wave effect cannot be ignored for piezo gauges. An averaging method can be applied to cancel out the flexural wave effect by gluing the piezo gauges on both sides of a plate. The output signals from the piezo gauges on both sides caused by flexural waves are out-of-phase, because surface strains of the plate are opposite on the opposite sides. On the other hand surface strains caused by in-plane waves are the same for both sides. The surface strain at a certain position purely caused by in-plane waves therefore can be obtained by averaging the output signals of piezo gauges on both sides of the plate and the flexural wave effect can be cancelled out.

3. EXPERIMENT

The application of in-plane structural intensity measurement was carried out to investigate the power input and transmission in a semi-infinite plate from an in-plane point force excitation.

Consider an in-plane force applied at the edge of a semi-infinite plate (see Figure 3) the total power transmitted through the cross-section at radius r should equal to the input power from the force if r is far smaller than an in-plane wavelength. The energy dissipated by the material damping can be neglected.

To simulate a semi-infinite plate, where only outgoing waves from an excitation on the edge exist and no reflection occurs, a large Perspex plate with the dimensions 2026mm× 1520mm×11.7mm (width×height×thickness) was mounted on a laminated absorber and clamped on the left and right sides (see Figure 4). Perspex was chosen because it has a high loss factor $\eta=0.02$. Other material properties from the manufacturer data sheet are Poisson's ratio $\nu=0.4$, Young's modulus $E=3.2\times10^9$ N/m² and density $\rho=1189$ kg/m³. The laminated absorber was made by laminating strips of steel and rubber to match plate impedance, so waves created by an exciting force would be absorbed at the junction and wave reflection could be reduced. Also rubber strips were glued along the vertical edges to reduce wave reflection on the edges.

The plate was excited at the top edge by a hammer in two conditions : vertically and horizontally.

Input power was measured directly and used for the comparison with the transmitted power measured by in-plane structural intensity technique. The

active input power is proportional to the imaginary part of the accelerance according to [7] :

$$\frac{P_{in}}{Hz} = G_{FF} \frac{1}{\omega} \text{Im} \{ H_{Fu} \} , \quad (12)$$

where H_{Fu} is the input accelerance.

The total transmitted in-plane power was obtained by integrating the radial component of in-plane structural intensity (I_R) over the surface at radius r , where the radial component of structural intensity was calculated from the intensities measured in the x and y directions (see Figure 5) as

$$I_R = I_x \cos\theta + I_y \sin\theta. \quad (13)$$

In this experimental investigation the structural intensity was measured at three positions, $\theta = 30^\circ, 60^\circ$ and 90° on the radius $r=200\text{mm}$, because of symmetry measurements are required only on the half-plane. The surface at radius r was divided into five regions, $0^\circ-45^\circ, 45^\circ-75^\circ, 75^\circ-105^\circ, 105^\circ-135^\circ, 135^\circ-180^\circ$ (see Figure 6), and the radial intensity was assumed to be uniformly distributed over each region. An approximate transmitted power was obtained by summing up the product of the radial intensity and cross-section area over each region, where the radial intensity was calculated from the x and y components of intensity measured with accelerometers and piezo gauges.

At each position two accelerometers were mounted on an aluminium block together with three uni-axial piezo film gauges to measure structural intensity in the x and y direction by using equations (10) and (11). To cancel out

flexural waves three other piezo gauges were also glued on the opposite side of the plate and the averaged signals were used in the calculation.

The plate was excited by an impact hammer. Signals from the hammer, accelerometers and piezo gauges were fed into a FFT analyser via charge amplifiers.

Figure 7 and Figure 8 show the comparison between input power and transmitted power measured from a vertical and horizontal point force excitation. Input power was measured directly by using equation (12). Transmitted power was estimated from the measured in-plane intensity. Averaged piezo gauge signals were used to cancel out flexural wave effect. Experimental results show that the transmitted power agreed with input power satisfactorily. It demonstrates that the new measurement technique is capable of measuring in-plane wave power in plates.

4. CONCLUSIONS

A new measurement method for in-plane structural intensity by using piezo film gauges and accelerometers has been developed. Experimental result shows that flexural wave effect is important in measuring in-plane structural intensity and it can be cancelled out by averaging signals from piezo gauges on both sides of the plate.

With the new in-plane structural intensity measurement method and the existing methods for flexural wave, power transmission through a range of structural components by a variety of wave types can be investigated in order to determine the dominant propagation mechanisms.

REFERENCES

1. Noiseux, D.U., Measurement of power flow in uniform beams and plates. *Journal of the Acoustical Society of America*, 1970, **47**, 238-247.
2. Fahy, F.J. and Pierry, R., Application of the cross-spectral density to a measurement of vibration power flow between connected plates. *Journal of the Acoustical Society of America*, 1977, **62**, 1297-1298.
3. Verheij, J.W., Cross spectral density methods for measuring structure borne power flow on beams and pipes. *Journal of Sound and Vibration*, 1980, **70**, 133-138.
4. Redman-White, W. The experimental measurement of flexural wave power flow in structures. *Proceedings of the Second International Conference on Recent Advances in Structural Dynamics, Southampton, England*, 1984, 467-474.
5. Meyer, B., Balannec, T., Sans, P. and Thomasson, D., Structural intensity in plates : formulation and experimental results. *CETIM International Congress on Intensity Techniques, Senlis, France*, 1990, 299-306.
6. Linjama, J. and Lahti, T., Estimation of bending wave intensity in beams using the frequency response technique. *Journal of Sound and Vibration*, 1992, **153**, 21-36.
7. Bauman, P.D., Measurement of structural intensity : analytic and experimental evaluation of various techniques for the case of flexural waves in one-dimensional structures. *Journal of Sound and Vibration*, 1994, **174**, 677-694.
8. Liu, S.H. and Pinnington, R.J., Measurement of flexural and longitudinal wave power flow in beams with piezoelectric films. *Proceedings INTER-NOISE 96, Liverpool, UK*, 1996, 2773-2776.

9. Heckl, M., Waves, intensities, and powers in structures. CETIM - *International Congress on Intensity Techniques, Senlis, France, 1990*, 13-20.
10. Timoshenko, S.P. and Goodier, J.N., *Theory of Elasticity*, McGraw-Hill, New York, 1970, third edition.
11. Dally, J.W. and Riley, W.F., *Experimental Stress Analysis*, McGraw-Hill, New York, 1991, third edition.

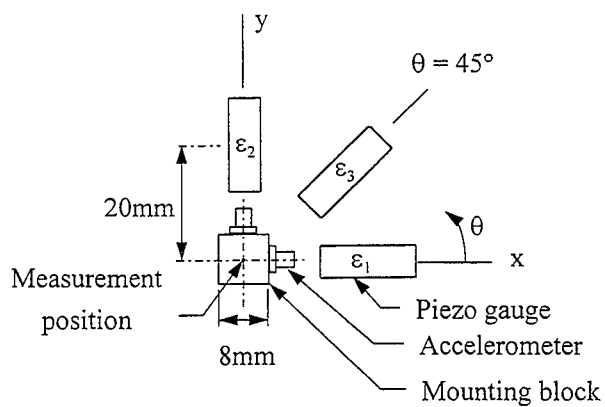


Figure 1. Transducer arrangement for in-plane structural intensity measurement.

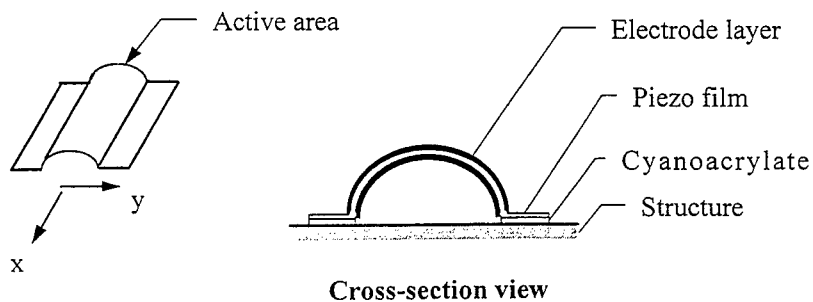


Figure 2. Sketch of a uni-axial piezo film gauge.

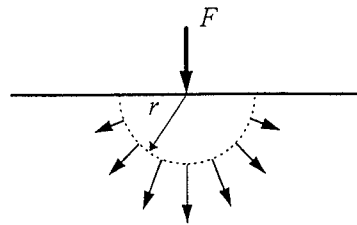


Figure 3. Power transmission from a point excitation.

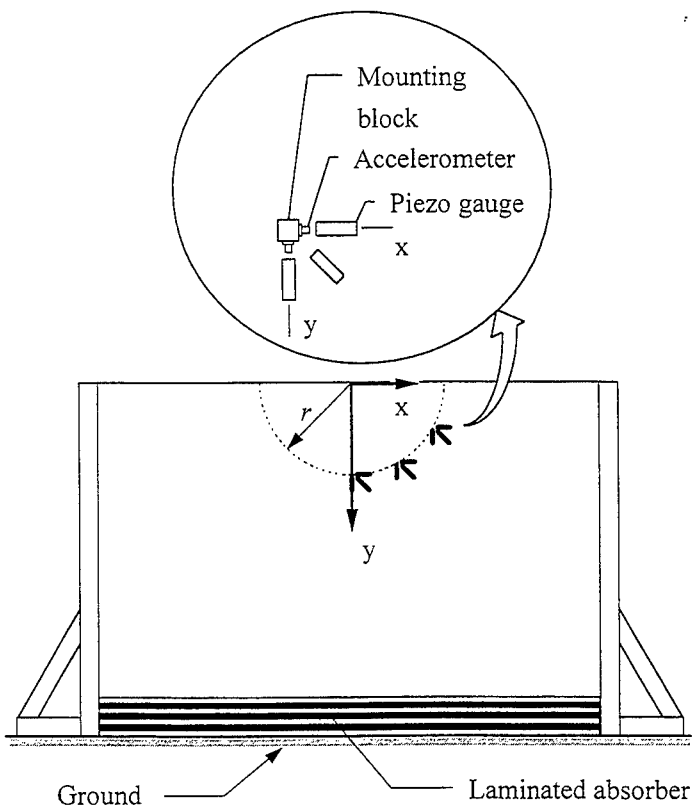
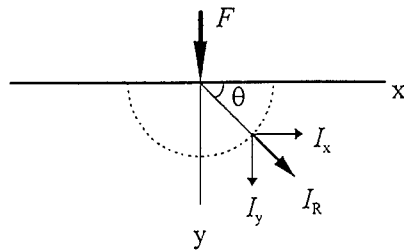
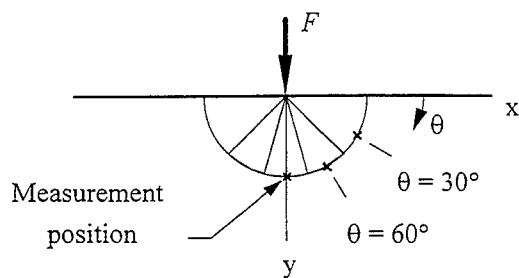


Figure 4. Experiment set-up for the measurement of in-plane structural intensity.



I_R : structural intensity in the radial direction
 I_x : structural intensity in the x direction
 I_y : structural intensity in the y direction

Figure 5. Definition of intensity in the different direction.



- * Measurement position at $\theta = 30^\circ$, 60° and 90°
- * Five uniform radial intensity region :
 0° - 45° , 45° - 75° , 75° - 105° , 105° - 135° and 135° - 180°

Figure 6. Approximation for estimating transmitted power.

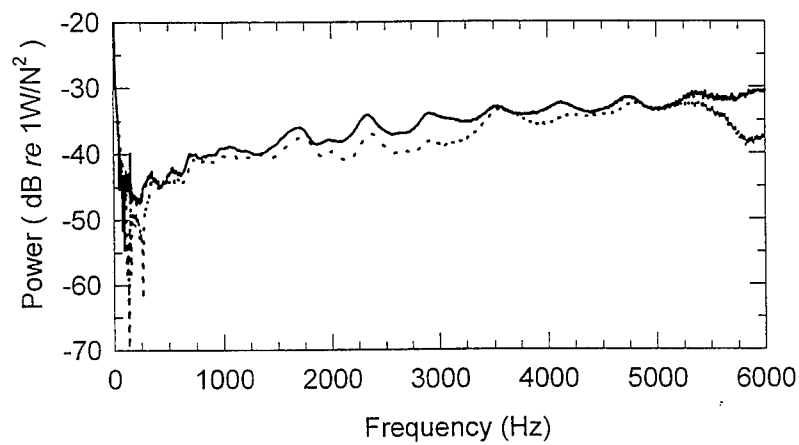


Figure 7. Comparison of input power and transmitted power from a vertical point force excitation : —, input power; ····, transmitted power.

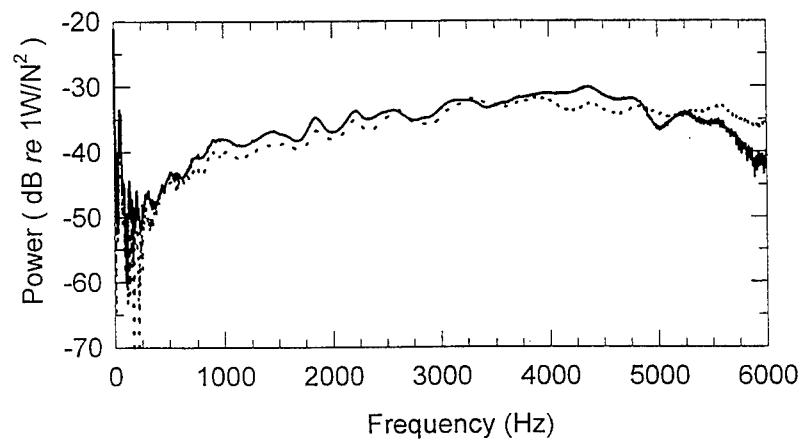


Figure 8. Comparison of input power and transmitted power from a horizontal point force excitation : —, input power ; ····, transmitted power.

VIBRATION TRANSMISSION AT LARGE INTERFACES

B.A.T. Petersson

Dept. of Aeronautical and Automotive Engineering
Loughborough University, LE 11 3TU, UK.

ABSTRACT

The influence on the vibrational energy transmission of the shape of the interface between a superstructure and a recipient is analysed. The real parts of the zero and first order interface mobilities are derived for a basic rectangular shape. Numerical results are presented for various aspect ratios but comparisons are also made with the corresponding results for an annular shape. It is concluded that the primary parameter is the perimeter of the interface and the condition that the wavelength is larger than the perimeter constitutes the transition from point to distributed contact. Also it is demonstrated that for closed-contour, strip-like interfaces, the real parts are independent of the strip width in a large and practically relevant range. With respect to the zero order interface mobility, the aspect ratio is of subordinate importance for the overall trend whereas the details of the signature are influenced. In contrast, the first order interface mobility includes two orthogonal cases, which are affected differently by the aspect ratio. Straight-forward estimation procedures are proposed for both interface mobilities.

1. INTRODUCTION

In the analysis of structure-borne sound and vibration transmission between structural elements, use is often made of the assumption that subsystems are attached to each other over a finite number of contact areas of dimensions smaller than the governing wavelength. For many kinds of built-up structures like machine casings, seating structures and ventilation systems, plate elements are folded or welded together to partially or fully form a hollow section which, in turn, joins some recipient acting as a radiator or dissipator for vibrational energy. The interface between the superstructure and the recipient in those cases is generally far from point-like but becomes a closed or partially closed contour which can have dimensions larger than the wavelength in the, from a practical viewpoint, interesting frequency range.

In a recent study [1], the dynamic interaction between an annular superstructure and the recipient for the vibrational energy has been considered and the important conclusion was drawn that for a large class of structural configurations, the zero and first order stress

distributions suffice for the modelling. It was argued, moreover, that for not too extreme geometrical shapes of the interface, the annular interface constitutes the generic case. In this contribution that argument is considered in more detail.

Interface mobilities of plate-like structures have been derived [2] for the generic case which show that for both the zero (transverse force) and first order (lateral force or moment) excitation distributions, the real parts equal those found for ordinary point excitation when the governing wavelength of the recipient is larger than the circumference of the interface but decrease markedly at high frequencies. The imaginary part of the zero order interface mobility is small and negative and can be termed a negative spring while that of the first order interface mobility is stiffness controlled in the region of point-like behaviour. Although the quantitative details may vary with the shape of the interface the overall character will remain the same.

In order to investigate the shape dependence, the transmission of vibrational power at a rectangular interface is addressed. The theoretical analysis is carried out for both a primary transverse force excitation and a primary lateral force or moment excitation. As in the case of an annular interface, a plate-like recipient is assumed.

2. ANALYSIS

2.1 Zero order excitation distribution. Consider a thin homogeneous, linearly elastic plate subject to an excitation distributed over a strip with an overall rectangular form as depicted in Figure 1. Since the primary objective of the present study is to clarify the influence of the shape of the interface on the power transmission, the real part of the mobility constitutes the appropriate quantity. Owing to the fact that the dimensions of the interface can be larger than the wavelength of the free flexural wave, however, the mobility concept must be extended. This is achieved by considering the so-called effective interface mobility, suggested in [1]. As discussed in e.g. [3], a suitable analytical model in conjunction with power transmission, is realized by a recipient plate of infinite extent.

For the sake of rigour, the strip is assumed to be of finite width and the stress to be uniformly distributed both along and across the strip-like interface. Therefore, let the zero order stress be given by,

$$\sigma = \frac{F_0}{4\Delta(a+b)} \quad (1)$$

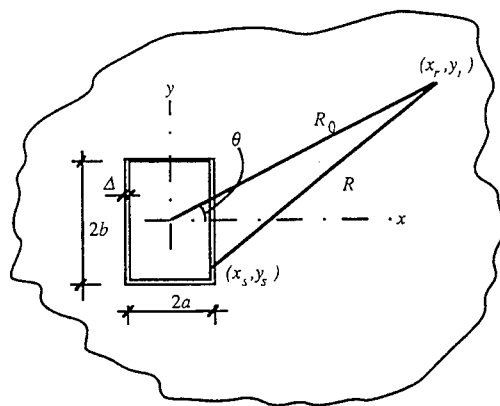


Figure 1. A thin plate excited over a rectangularly shaped strip.

For a thin infinite plate, the velocity due to a distributed excitation can be written [4]

$$v(x_r, y_r) = Y^\infty \iint_S \sigma(x_s, y_s) E(k_B R) dS \quad , \quad (2)$$

where $Y^\infty = \omega/8B'k_B^2$ is the ordinary point force mobility of an infinite plate and $E(kR) = H_0^{(2)}(kR) - H_0^{(2)}(-ikR)$. Following [1], the real part of the interface mobility can be established by considering the far-field. For large distances between the excitation and an arbitrary response position, the propagation function above simplifies into $E(kR) \approx \sqrt{2/\pi k R} e^{-i(kR - \pi/4)}$. Moreover, under such conditions, $R^2 = x_r^2 - 2x_r x_s + x_s^2 + y_r^2 - 2y_r y_s + y_s^2$, which can be approximated by $R \approx R_0 - x_s \cos \theta - y_s \sin \theta$. This means that since essentially the phase is sensitive to the small geometrical perturbations,

$$v(R_0, \theta) \approx Y^\infty \frac{F_0 e^{i\pi/4}}{4\Delta(a+b)} \sqrt{\frac{2}{\pi k R_0}} \left\{ \int_{-a-b}^a \int_{-b}^b e^{-ik(R_0 - x_s \cos \theta - y_s \sin \theta)} dx_s dy_s \right. \\ \left. - \int_{-a+\Delta}^{a-\Delta} \int_{-b+\Delta}^{b-\Delta} e^{-ik(R_0 - x_s \cos \theta - y_s \sin \theta)} dx_s dy_s \right\} \quad (3)$$

The integrations are readily obtained as,

$$v(R_0, \theta) = Y^\infty \frac{F_0 e^{-i(kR_0 - \pi/4)}}{4\Delta(a+b)} \sqrt{\frac{2}{\pi k R_0}} \left\{ \left[\frac{2 \sin(ka \cos \theta)}{k \cos \theta} \right] \left[\frac{2 \sin(kb \sin \theta)}{k \sin \theta} \right] \right. \\ \left. - \left[\frac{2 \sin(k(a-\Delta) \cos \theta)}{k \cos \theta} \right] \left[\frac{2 \sin(k(b-\Delta) \sin \theta)}{k \sin \theta} \right] \right\} \quad (4)$$

where, for small Δ ,

$$v(R_0, \theta) = Y^\infty \frac{F_0 e^{-i(kR_0 - \pi/4)}}{(a+b)} \sqrt{\frac{2}{\pi k R_0}} \left[a \cos(kb \sin \theta) \frac{\sin(ka \cos \theta)}{ka \cos \theta} \right. \\ \left. + b \cos(ka \cos \theta) \frac{\sin(kb \sin \theta)}{kb \sin \theta} \right] \quad (4a)$$

Hence, for $k\Delta$ less than, say, 0.1, the farfield is independent of the width of the strip interface.

A power balance can now be employed to determine the real part of the interface mobility which, with the perimeter $p = 4(a+b)$, yields

$$\text{Re}[Y_0] = \frac{8}{\pi} Y^\infty \int_0^{2\pi} \left[\frac{a}{p} \cos\left(kp \frac{b}{p} \sin \theta\right) \frac{\sin\left(kp \frac{a}{p} \cos \theta\right)}{kp \frac{a}{p} \cos \theta} \right. \\ \left. + \frac{b}{p} \cos\left(kp \frac{a}{p} \cos \theta\right) \frac{\sin\left(kp \frac{b}{p} \sin \theta\right)}{kp \frac{b}{p} \sin \theta} \right]^2 d\theta \quad (5)$$

To get an analytical overview, the integrands can be expanded in terms of $\sin \theta$ and $\cos \theta$ which for $ka < 1$ and $kb < 1$ leads to,

$$\text{Re}[Y_0] \approx \frac{Y^\infty}{2\pi(a+b)^2} \int_0^{2\pi} \left\{ (a+b)^2 \right. \\ \left. - 2(a+b)k^2 \left[\frac{a^2}{6}(3b+a)\cos^2 \theta + \frac{b^2}{6}(3a+b)\sin^2 \theta \right] \right\} d\theta \quad (6)$$

and in the limit one finds,

$$\text{Re}[Y_0] \rightarrow Y^\infty \left[1 - \frac{k^2}{6}(a+b)^2 \right] = Y^\infty \left[1 - \frac{k^2}{96}(4(a+b))^2 \right] \quad (6a)$$

This is to be compared with that of the annular case [2] i.e.,

$$\text{Re}[Y_0] = Y^\infty (J_0(kr_0))^2 \rightarrow Y^\infty \left[1 - \frac{k^2}{8\pi^2}(2\pi r_0)^2 \right] \approx Y^\infty \left[1 - \frac{k^2}{80}(2\pi r_0)^2 \right] \quad (7)$$

and it is seen that the decrease of the interface mobility compared with the ordinary point force mobility is slightly larger in the annular case than in the case of a rectangular strip for the same perimeter as illustrated in Figure 2.

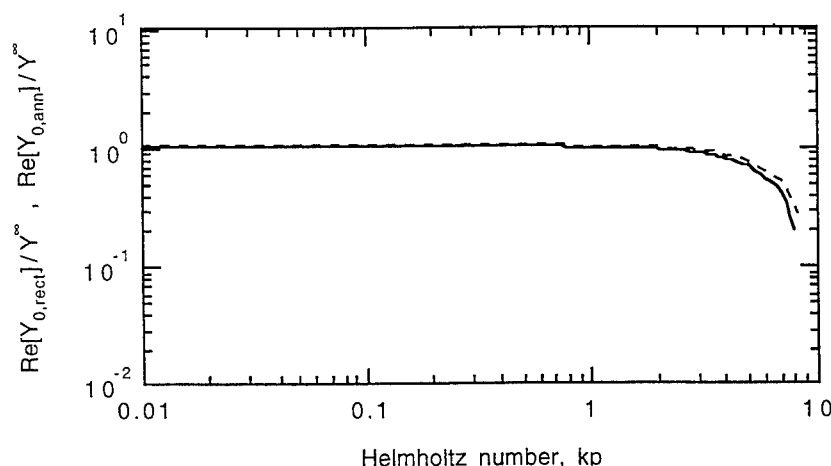


Figure 2. Schematic comparison of asymptotic behaviour of annular [1] (—) and rectangular (----) interface mobility for the same perimeter p .

In Figure 3 is displayed the interface mobility versus Helmholtz number for various aspect ratios b/a . It is clearly seen that the onset of the reduction is controlled by the aspect ratio and that an order of magnitude increase in the aspect ratio means a shift of a decade downwards in Helmholtz number of the onset.

A perhaps more adapted way of displaying the variation in interface mobility with aspect ratio is as function of Helmholtz number based on the perimeter, used in Figure 4. Here, as indicated in Figure 2, it is evident that, when the perimeter equals a wavelength of the governing wave, the spatial matching of the free wave and the excitation distribution starts to deteriorate and the real part of the interface mobility diminishes irrespective of the aspect ratio. Hence, the

tentative conclusion drawn in [2] is strongly corroborated for this excitation distribution and accordingly the perimeter-wavelength criterion appears applicable for the onset of the influence of the distributed excitation.

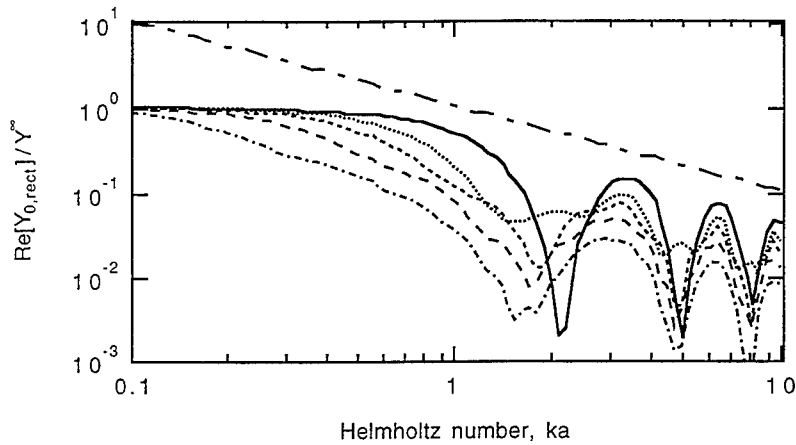


Figure 3. Interface mobility versus Helmholtz number based on side length for some aspects ratios: $b/a = 1$ (—), $b/a = 2$ (.....), $b/a = 3$ (-----), $b/a = 5$ (— —) and $b/a = 10$ (-·-·-·-). Slope of characteristic beam mobility (---)

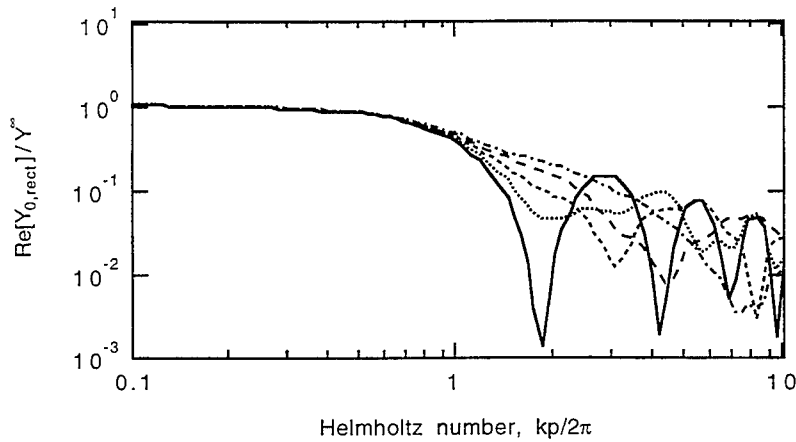


Figure 4. Interface mobility versus Helmholtz number based on perimeter for some aspects ratios: $b/a = 1$ (—), $b/a = 2$ (.....), $b/a = 3$ (-----), $b/a = 5$ (— —) and $b/a = 10$ (-·-·-·-).

The more or less deep troughs stem, of course, from the fact that power circulation occurs between the sides of the rectangular interface. Only in the case of a square-shaped strip interface is the pattern regular.

Since, as illustrated in Figure 3, the envelope for the upper range of Helmholtz numbers follows a square root law it is possible to establish a simple estimation procedure as depicted in Figure 5. For the upper range, the estimates will be conservative. By shifting the onset of the inverse square root dependence to $kp/2\pi = 1/2$, the estimation in the upper range is somewhat improved.

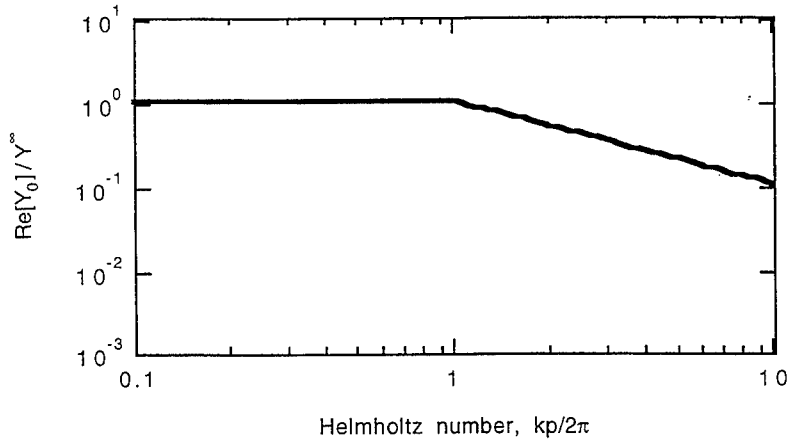


Figure 5. Estimation procedure for the zero order real part of interface mobility of closed contour strip interfaces.

2.2 First order excitation distribution. For this case as well, the strip is assumed to be of finite width but the stress to be linearly distributed in either x - or y -directions and to have a uniform distribution along the perpendicular strips. Hence, the stress can be written on the form,

$$\sigma(x, y) = -\frac{M_0}{4a(a/3 + b)\Delta} \begin{cases} \text{sign}(a); & -b \leq y \leq b, |x| = a \\ \frac{x}{a}; & -a \leq x \leq a, |y| = b \end{cases} \quad (8)$$

As in the previous sub-section, a power balance can be employed which leads to.

$$\text{Re}[Y_1] = \frac{4c_B m''}{\pi k |M_0|^2} (Y^\infty)^2 \int_0^{2\pi} \left| \int_{-a-b}^a \int_{-a-b}^b \sigma(x_s, y_s) e^{-ik(R_0 - x_s \cos \theta - y_s \sin \theta)} dx_s dy_s \right|^2 d\theta. \quad (9)$$

The real part of the first order interface mobility thus becomes,

$$\begin{aligned} \text{Re}[Y_1] = \frac{Y^\infty}{2\pi(a/3+b)^2} \int_0^{2\pi} \left[\frac{b}{a} \sin(ka \cos \theta) \left[\frac{\sin(kb \sin \theta)}{kb \sin \theta} \right] \right. \\ \left. + \cos(kb \sin \theta) \left[\frac{\sin(ka \cos \theta)}{(ka \cos \theta)^2} - \frac{\cos(ka \cos \theta)}{ka \cos \theta} \right] \right]^2 d\theta \end{aligned} \quad (10)$$

which also is independent of the width of the strip interface for small enough $k\Delta$.

As for the uniform stress, the integrand can be expanded to get an analytical overview which for $ka < 1$ and $kb < 1$ asymptotically leads to,

$$\text{Re}[Y_1] \rightarrow Y^\infty \frac{k^2}{2} \left\{ 1 - \frac{k^2 ba}{180(a/3+b)^2} [3a^2(8+a/b) + 5b^2(4+3b/a) + 50ba] \right\}. \quad (11)$$

As expected, the real part of the first order interface mobility converges towards that of the ordinary point moment mobility as the wavenumber and the dimensions decrease. It is clear from Eq. (11) however, that the dependence on the aspect ratio is more involved than in the case of a uniform stress. Indeed, the asymptote demonstrates an area dependence. The real part of the first-order interface mobility for the rectangular case can be compared with that of the annular case [2], i.e.,

$$\text{Re}[Y_1] = 2Y^\infty \left(\frac{J_1(kr_0)}{r_0} \right)^2 \rightarrow \frac{k^2}{2} Y^\infty \left[1 - \frac{(kr_0)^2}{4} \right] \approx \frac{k^2}{2} Y^\infty \left[1 - \frac{(kp)^2}{158} \right] \quad (12)$$

and so by rewriting Eq. (11) as,

$$\begin{aligned} \text{Re}[Y_1] \rightarrow Y^\infty \frac{k^2}{2} \left\{ 1 - \frac{(ka)^2 b/a}{180(1/3+b/a)^2} [3(8+a/b) \right. \\ \left. + 5(b/a)^2(4+3b/a) + 50b/a] \right\}, \end{aligned} \quad (11a)$$

it is seen that for $a=b$ and letting a correspond to the radius r_0 , the square interface implies a smaller mobility;

$$\text{Re}[Y_1] \rightarrow \frac{k^2}{2} Y^\infty \left\{ 1 - \frac{7}{20} (ka)^2 \right\} \approx \frac{k^2}{2} Y^\infty \left\{ 1 - \frac{(kp)^2}{183} \right\}.$$

This is illustrated in Figure 6 where also two rectangular cases are included. As in the case of a uniform stress excitation, it is seen that compared with the annular case, a decrease or increase of the present interface mobility, normalised with respect to the ordinary point moment mobility, is dependent on the aspect ratio although the perimeter is the same.

In Figure 7 is displayed the interface mobility versus Helmholtz number, based on the short side length, for various aspect ratios b/a . It is seen that the onset of the reduction is controlled by the aspect ratio and that an order of magnitude increase of the aspect ratio means a shift of a decade downwards in Helmholtz number of the onset. One can note, however, that the signature in the upper range is more regular than that of the zero order stress distribution.

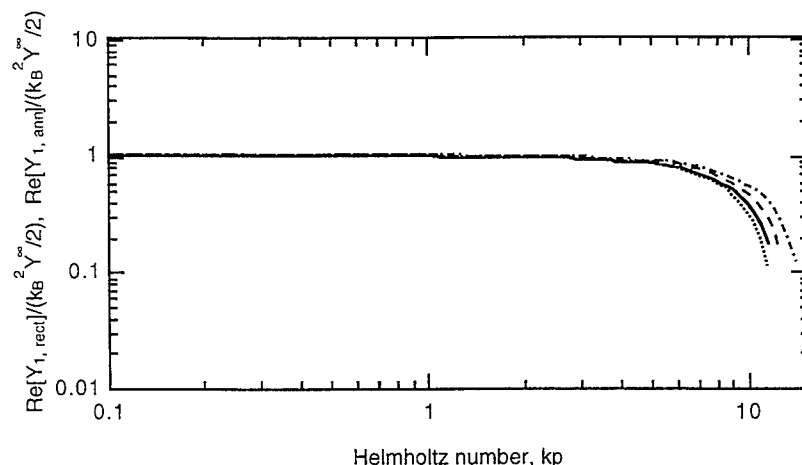


Figure 6. Schematic comparison of asymptotic behaviour of annular (—) and square-shaped (---), $b/a=2$ (-.-.-) and $b/a=1/2$ (.....) first order interface mobility for the same perimeter p .

The adapted presentation of the first order interface mobility as a function of Helmholtz number based on the perimeter, is given in Figure 8. It is again observed that the onset of the reduction in real part occurs when the perimeter equals the wavelength of the governing wave.

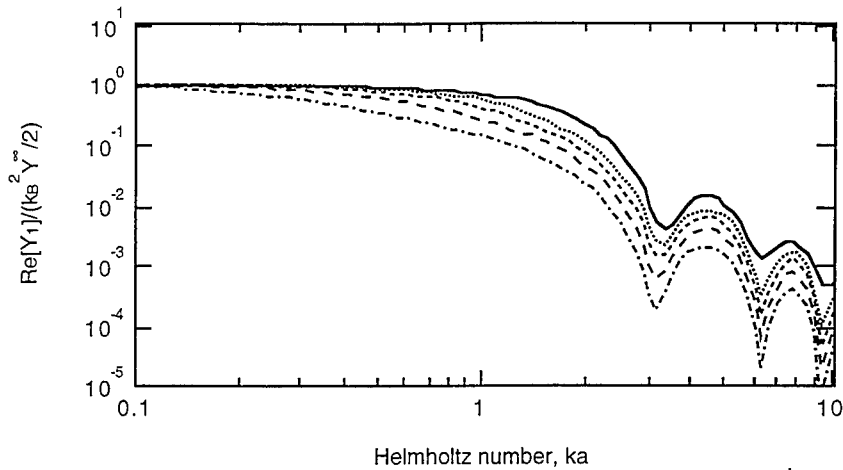


Figure 7. Interface mobility versus Helmholtz number based on the side length for some aspects ratios: $b/a=1$ (—), $b/a=2$ (.....), $b/a=3$ (- - - -), $b/a=5$ (— —) and $b/a=10$ (-·-·-·).

Owing to the fact that the first order excitation distribution is only single symmetric, it is necessary to numerically analyse also the influence of the shape of the interface for aspect ratios smaller than unity. In Figure 9 are shown the real parts of the moment interface mobilities for some aspect ratios smaller than unity.

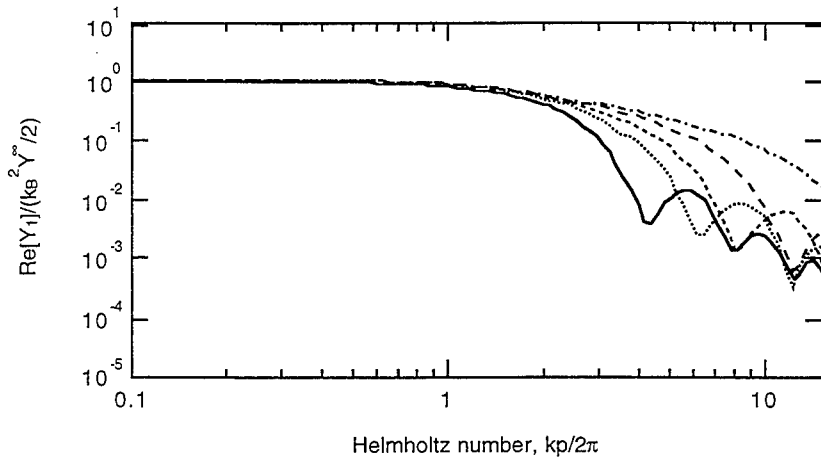


Figure 8. Interface mobility versus Helmholtz number based on perimeter for some aspects ratios: $b/a=1$ (—), $b/a=2$ (.....), $b/a=3$ (- - - -), $b/a=5$ (— —) and $b/a=10$ (-·-·-·).

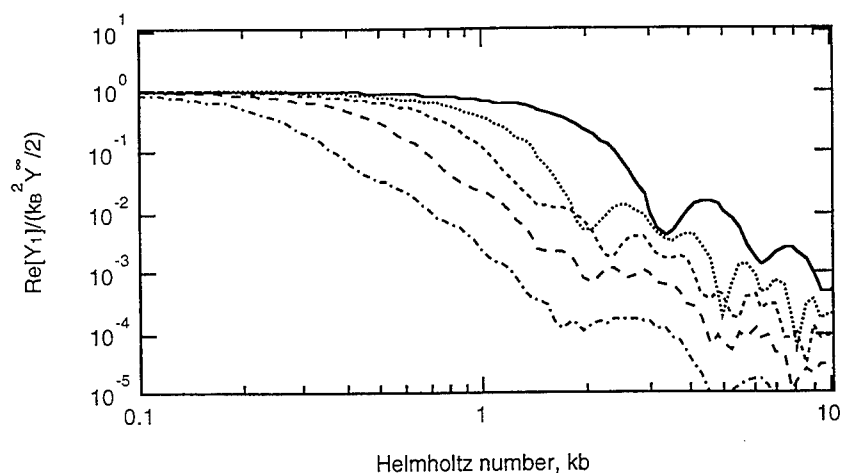


Figure 9. Interface mobility versus Helmholtz number based on perimeter for some aspects ratios: $b/a=1$ (—), $b/a=1/2$ (.....), $b/a=1/3$ (- - - -), $b/a=1/5$ (— —) and $b/a=1/10$ (- · - ·).

It is seen that when the aspect ratio becomes smaller than unity, i.e. the interface becomes long in the direction perpendicular to the moment, the pattern of constructive and destructive interference is irregular, cf. Figure 7. Although such a trend is indicated also for the zero order distribution it is more pronounced for the first order distribution owing to the basically elliptical field in the plate. The irregularity thus stems from the fact that here, sections of the interface stress can interfere when the long direction of the interface is perpendicular to the major axis of the elliptical field.

For the sake of completeness, the interface mobility is displayed also as a function of Helmholtz number based on the perimeter, see Figure 10. Accordingly, when the aspect ratio falls below unity, the normalised interface mobilities versus Helmholtz number based on the perimeter cluster and the aspect ratio i.e. the shape becomes more or less irrelevant provided the interface is long in the direction perpendicular to the moment vector.

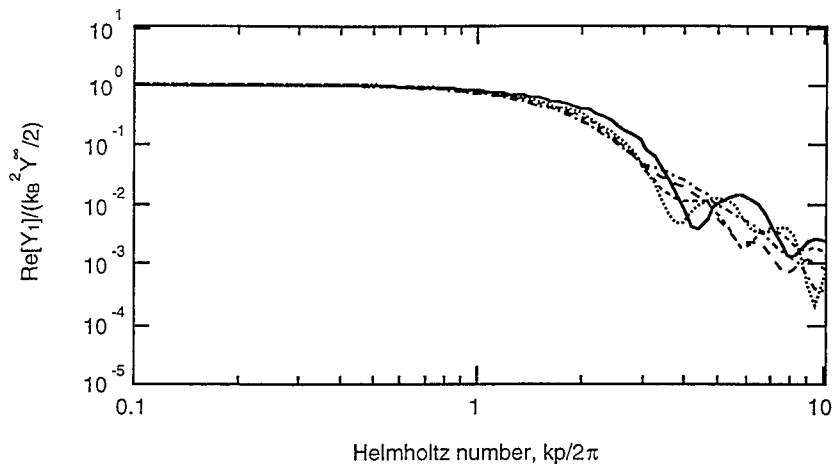


Figure 10. Interface mobility versus Helmholtz number based on perimeter for some aspect ratios: $b/a = 1$ (—), $b/a = 1/2$ (.....), $b/a = 1/3$ (----), $b/a = 1/5$ (— —) and $b/a = 1/10$ (-·-·-).

As for the zero order interface mobility, one may rather easily identify the overall trends of the first order interface mobility. If one lets the length of the rectangular interface become very large in the direction of the moment, then the problem approaches a two-dimensional counterpart i.e., a line moment on a plate. In such a case the slope is proportional to the square root of frequency.

As the wavelength approaches the length of the short side of the rectangular interface, the spatial mismatch between the excitation and the wave field increases markedly and a reduction in the power transmission is obtained. In this region therefore the slope becomes inversely proportional to the square root of frequency, as demonstrated in [2]. The complication with an estimation procedure for the first order interface mobility hence, is the transition point between the two upper regions. As discussed in conjunction with Eq. (11), a direct relationship does not exist between the mobility and the aspect ratio nor the perimeter but a combined dependence on aspect ratio and the area enclosed is found. By focusing on the range of the aspect ratio $b/a < 5$, however, a reasonably straight-forward procedure can be established from the critical point where the length of the short side of the rectangular interface equals a wavelength. This means that the estimation procedure can be summarised as,

$$\operatorname{Re}[Y_1] \approx \begin{cases} Y^\infty \frac{(kp)^2}{2p^2}; & kp/2\pi \leq 1; \quad b/a \leq 5 \\ Y^\infty \frac{\pi}{p^2} kp; & 1 \leq kp/2\pi \leq \pi b/a; \quad 1 \leq b/a \leq 5 \\ 4Y^\infty \frac{\pi^3}{p^2} \frac{1}{kp}; & \pi b/a \leq kp/2\pi; \quad b/a \leq 5 \end{cases} \quad (13)$$

In Figure 11, the results using the estimation procedure are compared with the calculated results for the limiting case $b/a = 5$. It is seen that the overall signature of the first order interface mobility is captured by the simple procedure although minor under- and over-estimations are obtained in limited regions.

This means that when the aspect ratio is in the range of $1 \leq b/a \leq 5$, the first order interface mobility has three distinct regions, a first in which the ordinary point moment mobility gives an adequate description, an intermediate in which the principal behaviour is that of a moment excited beam and finally, an upper region in which the interface mobility is markedly reduced compared with plate moment mobility owing to the distribution of the moment. As the aspect ratio falls below unity, the intermediate region vanishes and the first, constant region joins the third, steep region. For aspect ratios larger than five the uppermost, steep region can be omitted if the range of interest is below the upper transition point, approximately given by $kp \approx 2\sqrt{\pi^3 b/a}$.

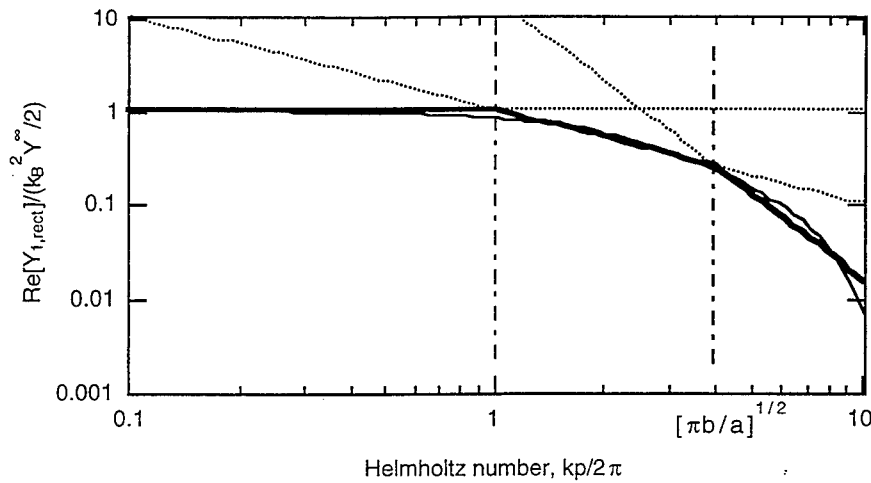


Figure 11. Estimation procedure for the real part of first order interface mobility of closed contour strip interfaces, displayed for $b/a = 5$ (—) $\text{Re}[Y_1(b/a=5)]$, (.....) generating curves.

3. DISCUSSION AND CONCLUDING REMARKS

The limited effect of interface geometry on the transmission of vibrational power from a superstructure to a recipient, previously heuristically inferred, is theoretically confirmed. It can thus be concluded that as long as the perimeter is less than the wavelength of the governing wave in the recipient, the ordinary point quantities are valid. For larger Helmholtz numbers where the perimeter is larger than the wavelength, the real part of the interface mobility exhibits more or less pronounced, rounded maxima and sharp minima set by the constructive and destructive interferences at the enclosed area of the plate. In the case of a hollow rectangular interface, the envelopes of the zero and first order interface mobilities, are those obtained for an annular one [2].

In this study, focusing on the vibration transmission, the imaginary part of the interface mobility is not treated explicitly. so, Foremost, this is because at large Helmholtz numbers, it is sensitive to the details of the interface geometry as well as the stress distribution cf. [5] and thus any result is valid merely for a specific configuration. Qualitatively, however, the behaviour for large Helmholtz numbers is that of the annular case when the aspect ratio of the rectangular interface is not

extreme, typically less than 3. For large aspect ratios the behaviour tends to that of the strip mobility [6].

The zero order interface mobility is, qualitatively as well as quantitatively, practically independent of shape provided the perimeter is retained. As the aspect ratio grows large, the interface mobility approaches that of a point excited beam, again largely irrespective of shape. Accordingly, these two tendencies constitute a conservative basis for an estimation procedure.

In contrast, the first order mobility for a rectangular interface must be treated differently for aspect ratios larger and smaller than unity respectively. In the former case, the interface mobility, at large Helmholtz numbers, tends to the corresponding beam mobility (moment excitation) whereas in the latter, the 'moment' interface mobility decreases like the force interface mobility, cf. [2]. This means that two different bases are required for an estimation procedure with respect to the first order interface mobility.

For a first order excitation it is not necessarily beneficial to design the interface long in the direction of the moment vector whereas it is always advantageous to increase the length in the direction across the moment vector.

5. REFERENCES

- [1] B.A.T. Petersson, 1994. Journal of Sound and Vibration 176, 625-639. Efficiency of annularly distributed moment and force excitation regarding structural acoustic power transmission to plate-like structures.
- [2] B.A.T. Petersson, 1997. Journal of Sound and Vibration (Scheduled for March). Geometrical and spatial effects on effective mobilities of interfaces.
- [3] B.A.T. Petersson, 1993. Proc. of International conference on Noise and Vibration control, St. Petersburg, vol. 2, 31-36. System definition for structure-borne sound and vibration transmission analysis.
- [4] L. Cremer and M. Heckl, 1995. Springer Verlag, Berlin. Körperschall (2nd ed.).
- [5] B.A.T. Petersson and M. Heckl, 1996. Journal of Sound and Vibration, 196, 295-321. Concentrated excitation of structures.
- [6] P. Hammer and B. Petersson, 1988. Journal of Sound and Vibration, 129, 119-132. Strip excitation; Part I: Strip mobility.

VIBRATION ENERGY TRANSMISSION IN FLUID-FILLED PIPES CONNECTED WITH FLANGES

S. Finnveden †
I.S.V.R, The University of Southampton,
Highfield, Southampton SO17 1BJ, UK.

ABSTRACT

The vibration energy transmission between two semi-infinite pipes connected by a flange is investigated using a frequency dependant Finite Element formulation. In this formulation, the shape functions are the solutions to the equations of harmonic motion in straight fluid-filled pipes. The flange is described as a thin-walled plate using a standard FE formulation. The object is to provide input data to SEA calculations. The scheme presented for doing this is highly efficient and should apply to many other prismatic structures.

1. INTRODUCTION

Predictions of vibration in pipe-systems are essential for the assessment of noise radiation and of vibration fatigue. For economic reasons, the latter is of great interest today as there is a general demand for 'life-extension'. However, analysis of high frequency vibration in complete pipe-systems is not possible. Even though FE - models possibly may be used the cost, in man-time and in computer capacity, renders such models impractical. Hence, simpler methods are needed for screening pipe-works so that accurate calculations and/or measurements could be directed towards critical systems and components.

One such, convenient and efficient, method is Statistical Energy Analysis [1]. Using this method models are readily made, a minimum of calculations are needed and only general information of the investigated structure is required. The purpose of the present project is to develop SEA so that its application to pipe structures eventually will become possible.

When applying SEA, the required data are the input powers from the sources of vibration, the loss factors, describing dissipation of vibration energy and the modal densities, specifying the expected numbers of resonances per unit frequency in the elements. Also needed are the coupling factors relating averaged vibration energy in connected elements to the energy flow between them. Expressions for the modal density in fluid-filled pipes and for the input power from fluid and mechanical point sources are derived in [2]. Here, the energy flow between straight pipe sections joined with flanges are considered.

† Now also at Dept. of Vehicle Engineering, KTH, S-100 44 Stockholm, Sweden

Today there is a general trend to save cost and weight. Thus, higher quality steels are used making a reduction of pipe-wall thickness possible. This, in turn, makes the vibration problem more 'interesting'. With thinner walls, in general the vibration amplitudes increase. Perhaps more important, the vibration field becomes more complex as the cut-on frequencies of higher order radial-axial modes largely decrease. In addition, the coupling between contained fluid and pipe become more important. Considering this general trend, the explicit calculations are made for a thin-walled pipe [3, Schedule 10s].

The dynamic behaviour of pipes is quite different for frequencies above and below the ring-frequency (the frequency for which the dilatational wavelength is equal to the pipe circumferential). While the methods used also applies for frequencies above the ring-frequency, the more important low frequency region is focused. Thus for the considered 10 inch-pipe the results apply up to 6 kHz.

The calculations are made with an efficient finite element method [4]. The application of this method is outlined in Section 2. In Section 3, first the application of standard Timoshenko beam theory at low frequencies is discussed. Then, for frequencies up to the ring-frequency, calculation results for water-filled pipes joined with flanges, according to standard [5], are presented

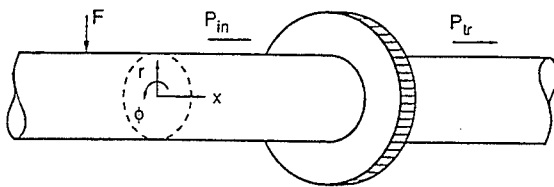


Figure 1. Pipe-flange structure and coordinate directions.

2. METHODOLOGY

The transmission factors are calculated considering a structure comprising of two semi-infinite pipes and a flange, see Figure 1. The motion of the structure is investigated assuming a time dependence of the form $e^{-i\omega t}$. Dissipative losses in the cylinder and flange are described with a complex Young's modulus, $E = E_0(1 - i\eta_e)$, and with a viscous loss factor η_v . The equations of motion are solved by the spectral (frequency dependent) finite element formulation presented in [4]. The used FE-mesh is shown in Figure 2. Below, the assumptions made are accounted for and the mode of calculation is outlined. While the details are found in [4], it is beneficial with a general description as the technique is thought to apply to many other prismatic structures.

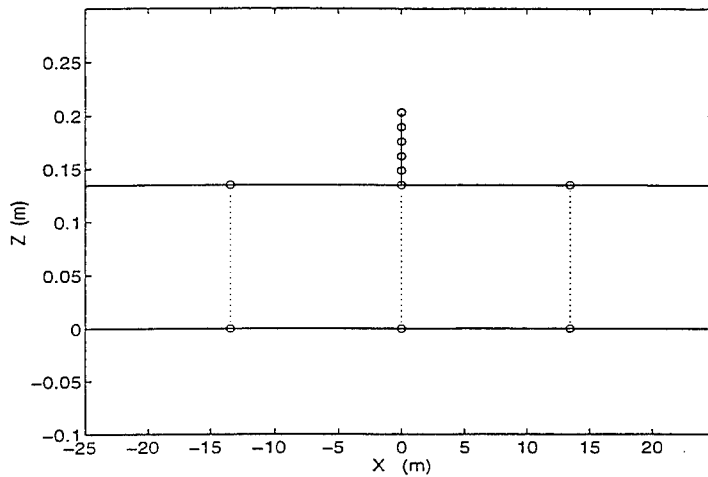


Figure 2. FE mesh used in the calculations; o, node. Nodes joined by dotted lines belong to the same pipe-elements. The nodes at $\pm 100 \text{ km}$ are not shown.

GOVERNING EQUATIONS FOR FLUID-FILLED PIPES

In thin-walled cylinder theory the equations of motion are formulated using a Fourier decomposition of the circumferential dependence of the displacements and assuming plane stress in the cross-section according to the Kirchhoff hypothesis. The displacements are

$$\begin{aligned} u_x &= (u - z \partial w / \partial x) \cos n\phi, \quad u_\phi = (v + z(v + n w) / R) \sin n\phi \\ u_z &= w \cos n\phi \end{aligned} \quad (1)$$

where $z = r - R$, where R is the cylinder radius and where u , v and w are the displacements on the cross sectional mid-plane in the x , ϕ and r directions, see Figure 1. The Arnold and Warburton cylinder theory is used and the equations of motion are found, e.g., in [6, equations (1)-(10)].

The fluid motion is described by the Helmholtz equation

$$\nabla^2 \psi + \omega^2 (1 + i\eta_f) / c_f^2 \psi = 0, \quad p = \rho_f \omega \cos(n\phi) \psi, \quad (2)$$

while the coupling condition between fluid and cylinder is

$$w = \frac{1}{\omega (1 + i\eta_f)} \frac{\partial \psi}{\partial r}. \quad (3)$$

Above, p is the sound pressure, ψ is an analogue to the fluid velocity potential, ρ_f is fluid density, c_f is fluid sound velocity and η_f is the viscous loss factor.

A functional L , being similar to the Lagrangian, and which is stationary for the solutions to the non-conservative equations of motion for the cylinder and fluid is presented in [4]. This functional is the basis for the FE calculation as discussed below.

FLANGES

The flange's motion is described with thin-walled plate theory. The assumed displacements are

$$u_r = \left(w - x \frac{\partial u}{\partial r} \right) \cos(n\phi), \quad u_\phi = \left(v + x \frac{n u}{r} \right) \sin(n\phi), \quad u_x = u \cos(n\phi), \quad (4)$$

where u , v and w are the displacements on the flanges mid-plane in the x , ϕ and r directions as in Figure 1.

A finite element formulation for the flange is made [4]. In this formulation the radial dependence of the motion is described within cylindrical segments with standard FE-polynomial shapefunctions - cubic polynomials for the out-of-plane motion and linear polynomials for the in-plane motion. Upon this the local dynamic stiffness matrices are calculated and are assembled using standard methods. But for the Fourier decomposition of the circumferential dependence, the flange's motion is thus described with a standard FE-formulation.

FINITE ELEMENT FORMULATION FOR FLUID-FILLED PIPES

The FE formulation for pipes is made in three steps. In the first step the dispersion relations are formulated and solved using a method originally proposed by Gavric [7]. Using this method the cross-sectional motion of a prismatic structure is approximated by FE shape functions. In [4], the method is developed by the inclusion of dissipative losses and by the use of the p-version of the FE method [8]. Thus, the radial dependence of the fluid motion is approximated with a polynomial

$$\psi(r, x) = g(r) * \mathbf{B}_r * \mathbf{f}(x), \quad g(r) = \left[(r/R)^{n_1} \quad (r/R)^{n_2} \quad \dots \quad (r/R)^{n_N} \right], \quad (5)$$

where n_i is a set of N non-negative integers and where the N by N matrix \mathbf{B}_r is chosen so that the polynomials in r form a convenient set. Equation (5) is inserted into the functional L and the integral over r is performed. The resulting functional depends on the cylinder displacements u , v , and w and the elements of the vector \mathbf{f} , all these being functions of only x . The corresponding Euler-

Lagrange equations are therefor a set of ordinary differential equations with constant coefficients and their solutions may be expressed with exponential functions, $\exp(\alpha x)$. Assuming this, the equations of motion are transformed to a linear eigenvalue problem which is solve by standard methods.

In the second step of the FE-formulation, the set of solutions found above are used to express the solution to the equations of motion with arbitrarily prescribed values of the cylinder displacements and the fluid velocity potential at the ends of the pipe. Thus, considering a pipe of length $2L$, its motion is given by

$$\begin{bmatrix} u \\ v \\ w \end{bmatrix} = \begin{bmatrix} \mathbf{B}_u \\ \mathbf{B}_v \\ \mathbf{B}_w \end{bmatrix} * \text{diag}(\exp(\alpha x - \alpha_p L)) * \mathbf{A} * [\mathbf{V}_1^T \quad \mathbf{V}_2^T]^T, \quad (6a)$$

$$\psi(x, r) = \mathbf{g}(r) * \mathbf{B}_r * \mathbf{B}_r * \text{diag}(\exp(\alpha x - \alpha_p L)) * \mathbf{A} * [\mathbf{V}_1^T \quad \mathbf{V}_2^T]^T, \quad (6b)$$

where the columns of the matrix \mathbf{B}_r and the elements of the row-vectors \mathbf{B}_u , \mathbf{B}_v and \mathbf{B}_w are given by the eigenvectors found in step one whereas the vector α contains the corresponding eigenvalues. The vectors \mathbf{V}_i contains the nodal displacements at the pipe ends, at $x = -L$ and $x = L$,

$$\begin{aligned} \mathbf{V}_1 &= [u(-L) \quad v(-L) \quad w(-L) \quad \partial w(-L)/\partial x \quad \Psi_1^T]^T, \\ \mathbf{V}_2 &= [u(L) \quad v(L) \quad w(L) \quad \partial w(L)/\partial x \quad \Psi_2^T]^T, \end{aligned} \quad (7)$$

where the $2*N$ fluid nodal d.o.f. Ψ_1 and Ψ_2 are given by

$$\psi(-L, r) = \mathbf{g}(r) * \Psi_1; \quad \psi(L, r) = \mathbf{g}(r) * \Psi_2. \quad (8)$$

The matrix \mathbf{A} in equations (6) is calculated by the linear equation system resulting when these two equations are inserted into the boundary conditions (7) and (8).

In equations (6), the vector α_p is given by

$$\alpha_p[m] = \begin{cases} \alpha[m], & \text{Re}(\alpha[m]) \geq 0 \\ -\alpha[m], & \text{Re}(\alpha[m]) < 0 \end{cases}. \quad (9)$$

Thus, in equations (6), the m 'th base function is multiplied by $\exp(-\alpha_p[m]L)$.

This scales the exponential base functions so that they have magnitudes that are unity at one end of the pipe and that decrease exponentially towards the other end. It is introduced to ensure numerical stability when the matrix **A** and when the local dynamic stiffness matrix are calculated. With this scaling the spectral finite element formulation is applicable to arbitrary long elements. Without it, severe numerical problems may result, as found by de Jong [9] and recently by Gry [10].

In the final, third, step of the FE formulation, the trial function (6) is inserted into the functional L and the local dynamic stiffness matrix is calculated. This calculation requires the x -derivatives of the trial functions and the calculation of an integral over x . These calculations are greatly facilitated by algorithms presented in [4].

SOLVING THE EQUATION OF MOTION

The finite elements described above are assembled using standard methods. The structure is excited by a point force, or a fluid monopole source, at a distance $100 * R$ away from the flange. Because of the geometry, the equations of motion for the different trigonometric orders are uncoupled and may be solved separately. The total computational time for this - including solving the dispersion relations, calculating the local dynamic stiffness matrices, assembling these and solving the equations for the nodal displacements - on a PC is approximately 0.6 s per trigonometric order and frequency.

3. ANALYSIS

TRANSMISSION FACTOR

The transmission factor, τ , of a joint is defined by the relation

$$P_{tr} = \tau P_{in}. \quad (10)$$

P_{in} is the power coming in to the joint and P_{tr} is the power transmitted.

The axial energy flow in a cylinder, described by the Arnold and Warburton cylinder theory, is derived by Langley [6, equations (21)-(29)]. These expressions and the standard expression for the acoustic energy flow in a fluid are easily evaluated when the motion is as in equations (6), once the nodal displacements are known. However, such a calculation yields the total energy flow, comprising of the difference between the incoming and the reflected powers. In this context, one of the major advantages with the spectral FE formulation is that one may distinguish between these two energy-flows.

The dispersion relations are such that if a propagation constant α is a solution so is also $-\alpha$ and one of them corresponds to an incoming 'wave'.

Without losses, the 'waves' fall into one of three categories. Either α is purely imaginary or purely real or complex in which cases it corresponds to a propagating wave or a decaying nearfield or a "standing decaying wave". Traditionally, the incoming power is calculated as the power in only the incoming propagating waves [11]. However, if losses are present, all wavenumbers are complex and the distinction between categories becomes (especially around the cut-on frequencies) a matter of consideration. To avoid this, in the present work all incoming 'waves' are included in the incoming power, these 'waves' being selected by energy considerations. If there are losses, the amplitude of a wave must decrease as it propagates. Thus a propagating constant α corresponds to a 'wave' propagating in the positive x -direction if its real part is negative.

When there are only sinusoidal waves the concept of energy flow in individual waves is justified as they are energetically independent, when averaged over x . However, this is not the case when also exponentially decaying terms are present. In such a case the definitions of incoming and reflected power must be made in an ad hoc manner. In the present analysis the excitation is at a distance of 100 radius from the junction. For this structure spurious results have resulted (mainly at lower frequencies and around cut-on) when energy flows in nearfield and in standing decaying terms are neglected.

To sum up, the incoming and the transmitted powers are calculated including only positive waves. These waves are those solutions to the dispersion relations that has a negative real part. Thus, the displacements inserted into the expressions for energy flow are as in equations (6), but, those elements of α that have a positive real part and the corresponding elements of α_p , B_u , B_v and B_w and the corresponding columns of B_F have all been removed.

TABLE 1

Geometrical and material parameters

Material	Poisson's ratio ν	Density ρ (kg/m^3)	Free wave speed $\sqrt{E/\rho}$, c_f (m/s)	Loss factors η_e, η_v, η_f
Steel	0.3	7800	4961	0.001
Water	-	1000	1500	0.01
Air	-	1.3	340	0.01

	Outer diameter (mm)	Wall thickness (mm)
Pipe	273	4.19
Flange	406	2*38

TRANSMISSION FACTORS FOR THE $n = 1$ BEAM-MODE IN EMPTY PIPES

At lower non-dimensional frequencies the only propagating radial-axial mode in a cylinder is the $n = 1$ mode. For obvious reasons this mode may be described by beam theory. The resonance frequencies for the bending vibrations of annular plates are found in [13, Table 11-2]. The lowest $n = 1$ resonance is for simply supported boundary conditions towards the pipe, which is found to be a reasonable approximation for thin walled pipes. For frequencies below this resonance the flange may be considered as a rigid mass.

For the $n = 1$ mode, using the data in Table 1, the transmission factor is calculated with the Arnold and Warburton theory for the cylinder and the FE model for the flange. It is also calculated using Timoshenko beam theory while considering the flange rigid. The results are shown in Figure 3 as functions of non-dimensional frequency, Ω

$$\Omega = \omega R / \sqrt{E' / \rho}, \quad E' = E / (1 - \nu^2) \quad (11)$$

where ρ is the cylinder density, E is Young's modulus and ν is Poisson's ratio.

At lower frequencies the transmission factor is close to unity, then, at $\Omega \approx 0.2$, there is a complete breakthrough after which energy transmission drops. Then near the ring frequency transmission increases. The result from the cylinder theory becomes somewhat 'shaky' at frequencies above $\Omega \approx 0.6$. This corresponds to the cut-on frequency for the $n = 1$ torsional mode. Above this frequency there are two waves that can carry energy and since they originate

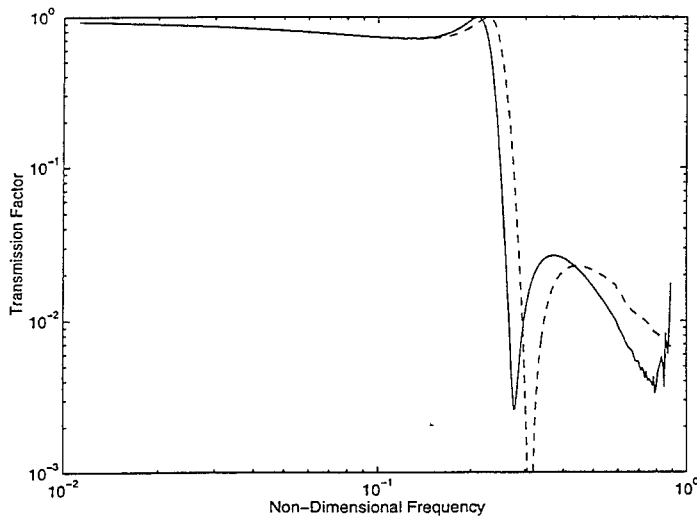


Figure 3. Transmission factor for cylinders joined by flange; —, Cylinder theory; - - -, Timoshenko beam theory.

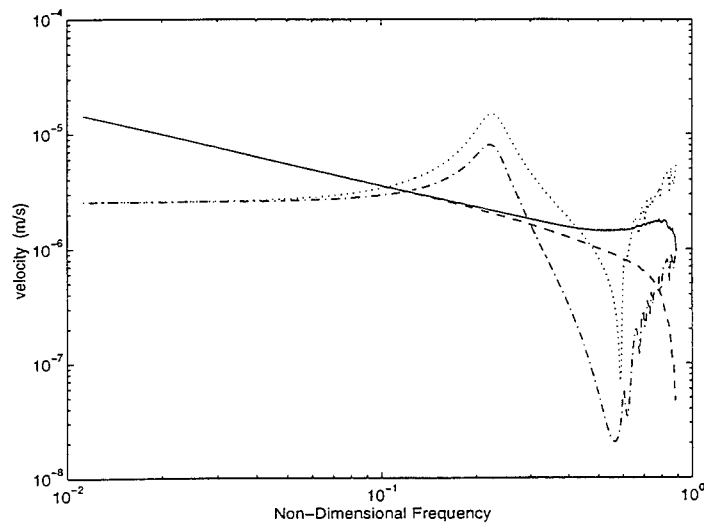


Figure 4. Velocity at attachment of flange; —, w ; --, v ; -·-, u ; ···, $R^*\phi_y$.

from the same source they are correlated. These waves are coupled at the flange and when their relative phase varies with frequency so does the transmission coefficient. The relative amplitudes of incoming waves depend on the excitation and therefore forced response calculations, or measurements, of transmission coefficients become non-unique if there are several waves that can carry energy.

The results in Figure 3 are in qualitative agreement with those for an Euler beam and a rigid mass [11, Section 5.4b]. Measurements presented in [11] indicates that such models often over estimates the total-transmission frequency since there may be a local rotational flexibility of the attachment between mass and beam. As in Figure 3, this also applies for pipes connected with a flange.

The beam theory accounts for cross sectional motion in the vertical and rotational directions. The cylinder theory, besides this, also accounts for flexural motion of the pipe-wall and for that the amplitudes of tangential and radial displacements may be different, which implies non-vanishing cross-sectional in-plane strain [12].

Figure 4 shows the displacements, predicted by the cylinder theory, at the attachment line of the flange. The beam theory is based on the assumption of in-extensional in-plane motion, that is $v = -w$. It is seen this criterion is fulfilled up until approximately $\Omega = 0.2$. It is also noted, the total-transmission frequency is associated with large flexural motion of the pipe-wall. Above this frequency the rotation of the pipe-wall is no longer governed by the cross sectional rotation.

Figures 5a and 5b show the displacement of the cylinder at the total-transmission frequency. It is seen that this frequency is associated with a resonance phenomena. For the propagating waves, the flexural displacements

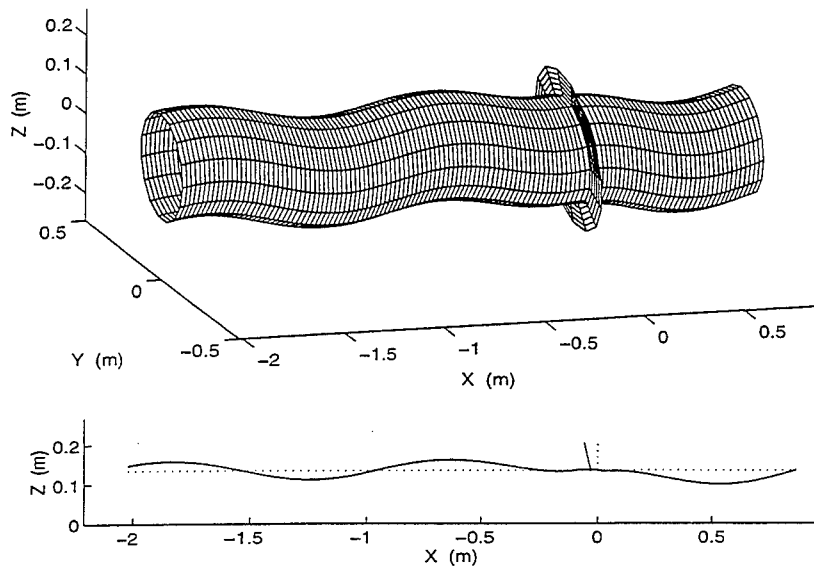


Figure 5a. Displacements of pipe-flange structure at $\Omega \approx 0.2$. Lower graph shows the displacements along the upper of the lines $y = 0$.

of the cylinder wall are quite small at low frequencies. The purely flexural modes are not cut-on until above the ring-frequency. Thus the large flexural motion seen in Figures 5b is predominantly restricted by evanescent modes. This means the flexibility of the attachment of the flange is of stiffness character, this confirming the explanation for the decrease of total-transmission frequency when compared to the beam model.

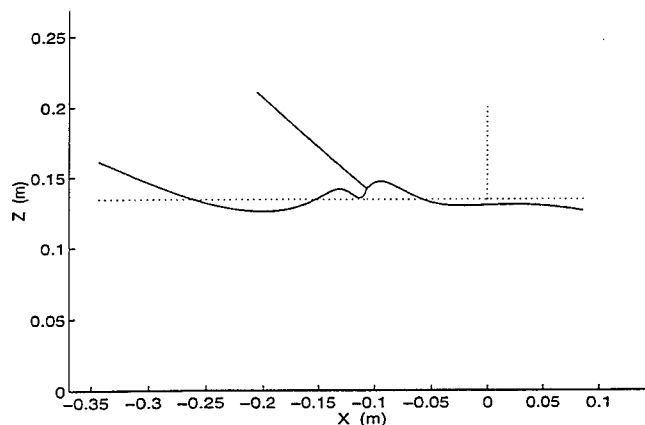


Figure 5b. As Figure 5a but amplified close-up.

BEAM-THEORY FOR MODELLING FLUID-FILLED PIPES

In reference [12] the application of equivalent Timoshenko beam theory for describing the propagating radial-axial waves in fluid-filled pipes is investigated. If the fluid inertia is added to that of the cylinder, such a simplified description, for each $n \geq 1$, is valid up to approximately half the cut-on frequency for higher order internal fluid modes.

Numerical experiments have been made using the beam theory for describing the fluid-filled pipe while considering the flange a rigid mass. The transmission factors are calculated and compared to those found using the accurate approach outlined in Section 2. For the higher order radial-axial modes, $n \geq 2$, it is found: the simplified beam theory gives inaccurate results. Most probably so as the description of the flange as a rigid mass is not correct.

For the $n = 1$ mode, the pipe is excited either by a mechanical point force or a fluid monopole source. Using beam theory, the fluid source may be treated as an equivalent mechanical force [2]. The results, in Figures 6 and 7 shows that the transmission factors are independent of excitation as long as there is only one propagating wave-type. For the water-filled pipe, the coupling between fluid and structure is strong, this amplifying the 'shakiness' of the calculation results above cut-on of the fluid mode. For the air-filled pipe coupling is not so strong. Thus, with mechanical excitation the transmission factor is not much different from the one for an empty pipe whereas with fluid excitation the flange does not influence transmission very much. In summary, for the $n = 1$ mode, the equivalent Timoshenko beam theory applies for calculations of transmission factors for

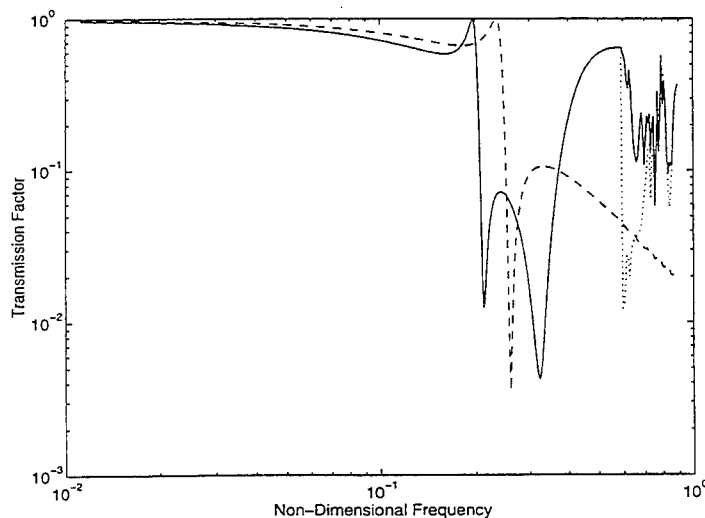


Figure 6. Transmission factor for water-filled pipe. —, cylinder theory mechanical excitation; --, Timoshenko beam theory; ···, cylinder theory fluid excitation.

frequencies below the first resonance in the flange and below the cut-on frequencies of the higher order fluid modes in the pipe.

TRANSMISSION FACTORS FOR AXI-SYMMETRIC MOTION

Transmission factors for the $n = 0$ axi-symmetric motion are shown in Figures 8. For this mode, the rotational motion is uncoupled from the radial-axial motion and is not excited by the point force or the monopole source. The other two types of wave motion, almost plane acoustic motion and longitudinal cylinder motion, are strongly coupled for the water-filled pipe. This results in very shaky curves for the transmission factors that are close to unity as the fluid motion is not restricted by the flange. For the air-filled pipe the fluid and structure motion are more independent. With fluid excitation the transmission factor is close to unity for all frequencies but close to the ring frequency. With mechanical excitation there is a minimum in the transmission at $\Omega \approx 0.04$. This minimum corresponds to a resonance, similar to the one for the $n = 1$ mode, in which the flanges and the cylinders axial motions become 180° out of phase. It is anticipated that large stresses may occur at this relatively low frequency.

HIGHER ORDER RADIAL-AXIAL MODES

Transmission factors for the $n = 2$ and the $n = 4$ modes are shown in Figures 9 and 10. For the $n = 2$ mode, in a water-filled steel pipe, only the radial-axial mode is propagating below the ring-frequency, hence the transmission factors are equal for fluid and mechanical excitations. For the air-filled pipe the first acoustic mode is cut- at $\Omega \approx 0.2$. Because of the higher fluid inertia, the radial-axial mode is cut-on at a somewhat lower frequency for the water-filled pipe.

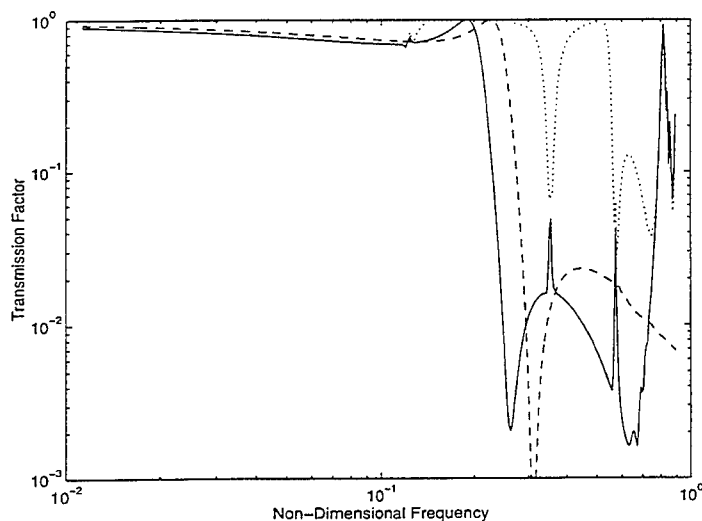


Figure 7. As Figure 6 but air-filled pipe.

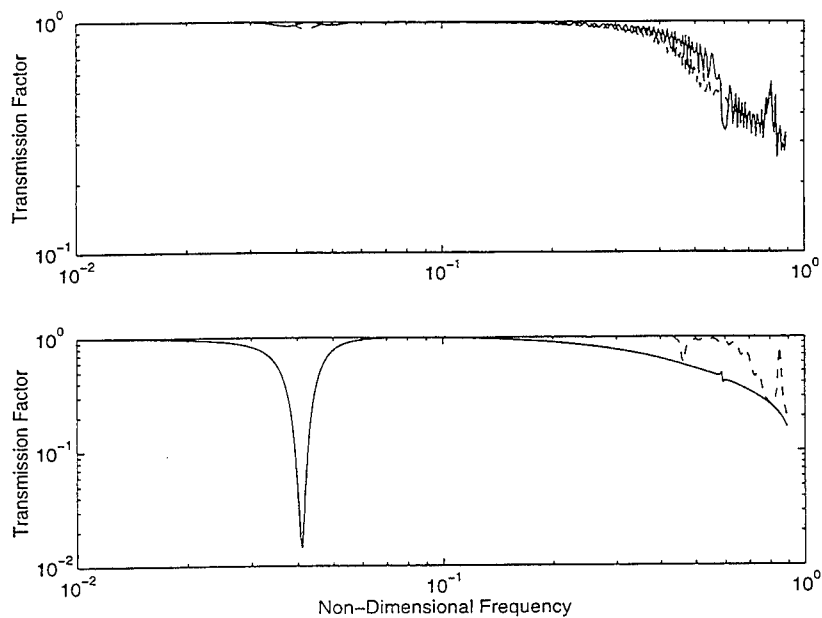


Figure 8. Transmission factor for fluid-filled pipe, $n = 0$; upper water-filled pipe; lower air-filled pipe; —, mechanical excitation; --, fluid excitation.

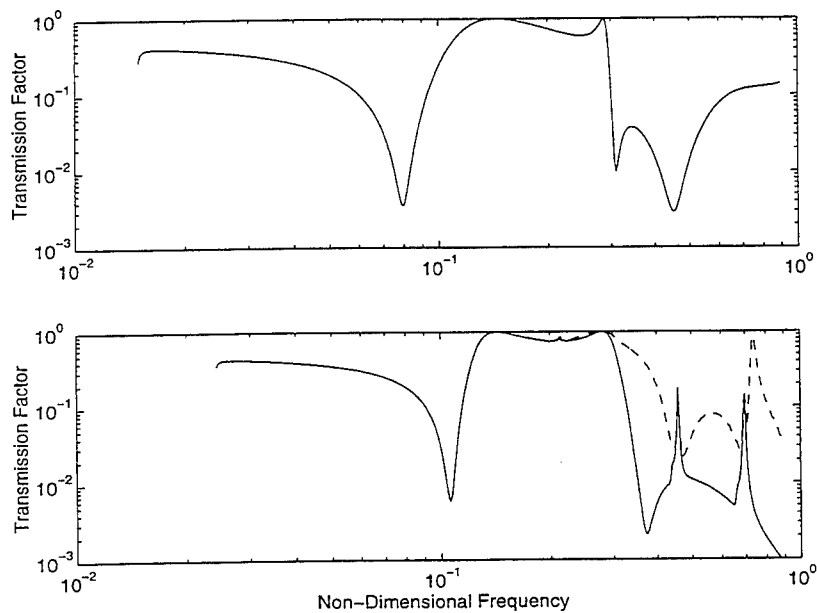


Figure 9. As Figure 8 but $n = 2$.

For both fluids, just above cut-on transmission is good, $\tau \approx 0.5$. Then there is a decrease, a region with almost perfect transmission and yet another decrease.

For the $n = 4$ mode, the first acoustic mode in the air-filled pipe is not cut-on until $\Omega \approx 0.36$. For all frequencies, the difference between fluid and mechanical excitation is only minor, hence results only for the latter are shown. The transmission factors for the $n = 4$ mode are similar to those for the $n = 2$ mode. Above cut-on transmission is fairly good, $\tau \approx 0.25$; then, for the water-filled pipe, it decreases; there is a region with good transmission and finally, near the ring-frequency transmission is poor.

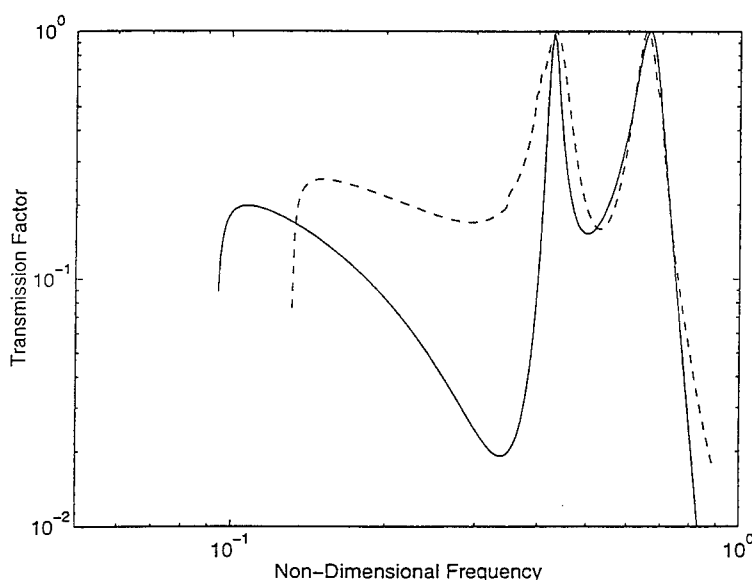


Figure 10. Transmission factor for fluid-filled pipe, $n = 4$; —, water-filled pipe; — —, air-filled pipe.

CONCLUSIONS

A finite element method for the calculation of the transmission factors for flange-coupled fluid-filled pipes is presented. Applying this method, first the dispersion relations for fluid-filled pipes are solved using a FE-discretization of the cross-sectional motion. Then, the solutions are used to express the displacements within an element as functions of arbitrarily prescribed displacements at the ends. Finally, these displacements are used as shape functions in a frequency dependent finite element formulation. The presented scheme is possibly applicable to any prismatic structure and is therefore thought

to provide a versatile tool for a large class of problems in structure-borne-sound analysis.

Calculation results for one, water- or air-filled, pipe-flange structure are presented. The calculation times are moderate; the results for 5 trigonometric orders and 200 frequency points require approximately 10 minutes cpu-time on a PC. If compiled code is used and if the future increase in computer efficiency is accounted for, these routines could be incorporated into SEA-programs and be used on-line without too much waiting time. Alternatively, since the piping standards only include a limited number of pipes and pipe fittings, it should be possible to tabulate transmission factors, e.g., in third-octave bands.

ACKNOWLEDGEMENT

The financial supports from TFR, Sweden and EPSRC, UK are gratefully acknowledged.

REFERENCES

1. R. H. Lyon and R. G. DeJong 1995 *Theory and application of SEA*. Butterworth-Heinemann
2. S. Finnveden *Journal of Sound and Vibration* (Submitted September 1996) Formulas for modal density and for input power from mechanical and fluid point-sources in fluid-filled pipes.
3. British Standard *BS 1600:91*. Dimensions for steel pipes for the petroleum industry.
4. S. Finnveden 1996 *Journal of Sound and Vibration* **199**, 125-254. Spectral finite element analysis of the vibration of straight fluid-filled pipes with flanges.
5. British Standard *BS 1560:89*. Circular flanges for pipes (Class designated).
6. R. S. Langley 1994 *Journal of Sound and Vibration* **169**, 29-42. Wave motion and energy flow in cylindrical shells.
7. L. Gavric 1994 *Journal of Sound and Vibration* **173**, 113-124. Finite element computation of dispersion properties of thin-walled waveguides.
8. L. Meirovitch 1986 *Elements of Vibration Analysis*. McGraw-Hill.
9. C. de Jong 1994 *Ph. D. Thesis Technische Universiteit Eindhoven*. Analysis of pulsations and vibrations in fluid-filled pipe systems.
10. L. Gry 1998 *Journal of Sound and Vibration* **195**, 477-505. Dynamic modelling of railway track based on wave-propagation.
11. Cremer L. Heckl M. and Ungar E. E. 1988 *Structure-borne sound*. Springer-Verlag, Second edition.
12. S. Finnveden *Journal of Sound and Vibration* (Submitted May 1996). Simplified equations of motion for the radial-axial vibrations of fluid-filled pipes.
13. R. D. Blevins 1979 *Formulas for natural frequencies and mode shapes*. Van Nostrand Reinhold.

STATISTICAL ENERGY ANALYSIS OF PERIODICALLY STIFFENED DAMPED PLATE STRUCTURES

R.S. Langley^{*}, J.R.D. Smith^{*}, F.J. Fahy^{*}

^{*}Department of Aeronautics and Astronautics

^{*}Institute of Sound and Vibration Research

University of Southampton, UK.

1. INTRODUCTION

Many types of engineering structures are subjected to high frequency excitation, in the sense that the induced response has a vibrational wavelength which is small in comparison to the overall system dimensions. The short wavelength of the structural response leads to severe analytical difficulties in attempting to predict the system vibration levels at the design stage.

Much research effort has been devoted to the development of analysis techniques which are capable of predicting high frequency vibration levels, and the most well known approach is perhaps Statistical Energy Analysis (SEA) [1]. In SEA no attempt is made to recover the detailed displacement pattern of the structure, but rather the structure is modelled as an assembly of "subsystems" and the aim is to predict the vibrational energy level of each subsystem. This is done by establishing a set of power balance equations which are based on the key assumption that the energy flow between two connected subsystems is proportional to the difference in the subsystem modal energies. Whilst SEA has been applied with considerable success to a wide range of structures, there is a continuing debate over the theoretical validity of the method (for example [2-4]), and it is true to say that the method yields very poor results for certain types of structure. One practical difficulty associated with the application of the method to aerospace and marine vehicles arises from the widespread use of stiffened plating in these structures; as yet there is no clear guideline as to how such plating is best incorporated within an SEA model, and this issue is discussed in what follows.

The present study is concerned with vibration transmission through a plate which is stiffened by a series of parallel stiffeners which are (nominally) evenly spaced. This situation can be likened to vibration transmission along an aircraft fuselage or a section of a ship hull, with the present stiffeners taking on the role of the structural frames. It is often argued that a stiffened plate can be modelled to a reasonable degree of accuracy by "smearing" the stiffener properties to produce an equivalent orthotropic plate. However, such an approach can only be expected to be successful if (i) the half wavelength of the

panel vibration exceeds the stiffener spacing, and (ii) the stiffeners are sufficiently weak in bending relative to the plate bending stiffness. Condition (ii) depends to some extent on the boundary conditions which are imposed on the panel edges - a stiffened panel which is simply supported on the edges parallel to the stiffeners and free on the other two edges will tend to have lower modes of vibration which are reasonably well predicted by a smeared model. If however the panel is simply supported on all four sides then "rigid body" motion of the stiffeners will be restrained, and the stiffener bending stiffness will have a crucial influence on the nature of the lower modes of vibration. For aerospace and marine vehicles the frames are relatively stiff, and certainly at higher frequencies the conditions required for the successful application of the smearing approach will not be met.

In SEA terms, the other extreme to a "smeared" model of a stiffened plate would be to model each inter-stiffener plate element as a subsystem (or more generally as three subsystems to allow for the three types of wave motion which can occur in a flat plate). With this approach the stiffeners act as coupling elements between the SEA subsystems, and the associated coupling loss factors can be found by considering wave transmission across a stiffener [5]. This general modelling approach has been applied with great success to box-type structures by Heron [6], although in that case the structure did not contain stiffened plates - rather the stiffeners were used to assemble a set of relatively large panels. When applied to a stiffened plate this type of approach could face three potential difficulties: (i) the mode count in each plate element may be insufficient to justify inclusion as a separate SEA subsystem, (ii) the method could lead to a very large SEA model for a complete vehicle, and (iii) the method cannot capture any "periodic structure" type behaviour of the stiffened panel. Point (iii) is related to the fact that a periodically stiffened structure has very distinctive vibration characteristics, as outlined in what follows.

A periodic structure is defined as a structure which is composed of a number of identical units which are connected in a regular pattern. The stiffened plate structure considered in the present work forms a one-dimensional periodic structure, in which the basic unit consists of an inter-stiffener plate element with an attached stiffener. It is well known that wave motion through a structure of this type can only occur within certain frequency intervals known as pass bands; the pass bands are separated by stop bands in which propagating wave motion cannot occur. The incorporation of this type of behaviour within an SEA model has received little attention other than in the work of Keane and Price [7] who considered two coupled periodic rod structures.

Each rod structure was modelled as an SEA subsystem in which the modal density was calculated on the basis of periodic structure theory, it being noted that the natural frequencies of a periodic structure tend to lie within the pass bands. Whilst this approach led to excellent results for the structure considered, it would appear to be difficult to extend the methodology to more general situations - not in terms of the validity of the method, but rather in terms of the practical calculation of the coefficients which appear in the SEA equations. For this reason a quite different approach is used here to model the stiffened plate: the plate is modelled as a *non-conservative coupling element* between different parts of the structure. Specifically, a three plate structure is considered in which the middle plate is stiffened. The two outer plates are modelled as conventional SEA subsystems, while the middle plate is considered to act as a coupling element. The properties of this coupling element are calculated on the basis of periodic structure theory, and in this regard use is made of recent results concerning the band-averaged transmission coefficient of a periodic structure [8]. There has been much debate as to how the energy loss associated with a non-conservative coupling should be modelled within the context of SEA [9-12], and this issue is dealt with in the present work simply by using the absorption coefficient of the coupling element to make an appropriate addition to the loss factors of the adjoining elements.

2. SEA MODELLING OF NON-CONSERVATIVELY COUPLED SUBSYSTEMS

A schematic of two two-dimensional subsystems which are coupled along an edge is shown in Figure 1. In the present context, the two subsystems represent unstiffened plates while the coupling represents a stiffened plate which both transmits and dissipates energy. For the purposes of the present argument, the stiffened plate is assumed to have symmetric stiffeners so that only the bending motion of each plate need be considered.

An SEA model of the system shown in Figure 1 can be derived by considering energy flow across the coupling, and this is most easily done by considering the transmission of elastic wave motion. If the time averaged vibrational energy in subsystem 1 is represented by E_1 , then the energy density can be written as E_1/A_1 , where A_1 is the area of the subsystem.

If it is assumed that the wave motion in the subsystem is "diffuse" so that the energy flow is evenly spread among all directions, then the energy flow associated with the angular range θ to $\theta+d\theta$ can be written as $c_{g1}(E_1/A_1)(d\theta/2\pi)$, where c_{g1} is the wave group velocity. This is strictly the energy flow per unit length measured along the wave crest, so that the power incident on the coupling is $c_{g1}(E_1/A_1)(d\theta/2\pi)L\cos\theta$, where L is the length of the coupled edge. Now part of this power is transmitted to subsystem 2 and part is dissipated within the coupling, with the remainder being reflected back into subsystem 1. The fraction of power which is transmitted is given by the *transmission coefficient* $\tau_{12}(\theta)$, while the fraction absorbed is given by the *absorption coefficient* $\alpha_{12}(\theta)$. The total power lost through the coupling can thus be written as

$$P_{\text{loss}} = \int_{-\pi/2}^{\pi/2} [\tau_{12}(\theta) + \alpha_{12}(\theta)] (E_1 c_{g1} L / 2\pi A_1) \cos\theta d\theta = [\langle \tau_{12} \rangle + \langle \alpha_{12} \rangle] (E_1 c_{g1} L / \pi A_1), \quad (1)$$

where the diffuse field transmission and absorption coefficients $\langle \tau_{12} \rangle$ and $\langle \alpha_{12} \rangle$ are defined as

$$\langle \tau_{12} \rangle = \frac{1}{2} \int_{-\pi/2}^{\pi/2} \tau_{12}(\theta) \cos\theta d\theta, \quad \langle \alpha_{12} \rangle = \frac{1}{2} \int_{-\pi/2}^{\pi/2} \alpha_{12}(\theta) \cos\theta d\theta. \quad (2,3)$$

Now subsystem 1 will also gain power through the junction from subsystem 2. By analogy with the above equation, this power can be written in the form

$$P_{\text{gain}} = \langle \tau_{21} \rangle (E_2 c_{g2} L / \pi A_2). \quad (4)$$

The total power balance equation for subsystem 1 then takes the form

$$\omega \eta_1 E_1 + P_{\text{loss}} - P_{\text{gain}} = P_1, \quad (5)$$

where the first term on the left is the power dissipated internally (η_1 being the loss factor), and the term on the right is the power input from external sources. Equations (1)-(5) can be combined to yield the power balance equation in the standard SEA format [1].

$$\omega \eta_{1\text{eff}} E_1 + \omega \eta_{12} v_1 (E_1 / v_1 - E_2 / v_2) = P_1, \quad (6)$$

where

$$v_i = \omega A_i / (2\pi c_i c_{gi}), \quad (7)$$

$$\eta_{12} = c_{g1} L \langle \tau_{12} \rangle / (\pi \omega A_1), \quad (8)$$

$$\eta_{1\text{eff}} = \eta_1 + \eta_{12} \langle \alpha_{12} \rangle / \langle \tau_{12} \rangle. \quad (9)$$

Here v_i is the modal density of subsystem i (c_i is the phase speed), and η_{12} is the coupling loss factor. It should be noted that in deriving equation (6) the reciprocity relation $\langle \tau_{12} \rangle / c_1 = \langle \tau_{21} \rangle / c_2$ has been employed. The power balance equation for subsystem 2 has precisely the form of equation (6) with the subscripts 1 and 2 interchanged.

It has been shown in this section that under the normal "diffuse wave" set of assumptions, the basic form of the SEA equation is unchanged by the presence of dissipation in a coupling element. The only detailed changes are that: (i) the transmission coefficient used in the coupling loss factor is that which arises in the presence of dissipation, and (ii) an appropriate addition must be made to the subsystem loss factors to account for absorption by the junction.

3. TRANSMISSION AND ABSORPTION COEFFICIENTS

As mentioned in the introduction, the present concern is with vibration transmission through a stiffened panel, and a schematic of the system under investigation is shown in Figure 1. In order to apply the analysis of Section 2 to this structure it is necessary to compute the transmission and absorption coefficients $\langle \tau_{12} \rangle$ and $\langle \alpha_{12} \rangle$ of the stiffened panel, and two methods of doing this are outlined in the present section. The first approach is an exact calculation in which the transmission through an M-bay stiffened panel is analysed by using a variant of the dynamic stiffness method [13]. In order to facilitate this calculation it is assumed that the stiffened panel is simply supported along the two longitudinal edges, and the stiffeners are taken to be symmetric, so that there is no coupling between the in-plane and out-of-plane motion of the plate. The second method of calculating $\langle \tau_{12} \rangle$ and $\langle \alpha_{12} \rangle$ is an approximate and computationally efficient technique which is based on the one-dimensional waveguide theory developed in reference [8]; with this approach it is only necessary to calculate the wave transmission coefficient of a single plate/stiffener junction.

3.1 EXACT CALCULATION

The structure is assumed to be simply supported along each of the longitudinal edges. This implies that the out-of-plane displacement may be expressed as a Fourier series involving terms proportional to $\sin(n\pi x/b)$ where n is an integer and b is the panel width. For each value of n , bending wave transmission through the system can be analysed by using a variant of the dynamic stiffness method (DSM) presented in reference [13]: essentially the DSM is used to derive the dynamic stiffness matrix of the stiffened panel, and this is then

coupled to two semi-infinite plate elements which carry the incident, reflected and transmitted waves. Applying the dynamic stiffness approach to a semi-infinite plate, the edge displacement w_e and rotation θ_e may be expressed as

$$\begin{bmatrix} w_e \\ \theta_e \end{bmatrix} = \begin{bmatrix} 1 & 1 \\ \mu_{B1} & \mu_{B2} \end{bmatrix} \begin{bmatrix} \alpha_{B1} \\ \alpha_{B2} \end{bmatrix} \sin\left(\frac{n\pi x}{b}\right) e^{i\alpha x}, \quad (10)$$

and the edge tractions (shear S_e and moment M_e) as

$$\begin{bmatrix} S_e \\ M_e \end{bmatrix} = \frac{D}{\mu_{B1} - \mu_{B2}} \begin{bmatrix} \mu_{B2}\mu_{B1}^3 - \mu_{B1}\mu_{B2}^3 & \mu_{B2}^3 - \mu_{B1}^3 + (2-\nu)(\mu_{B1} - \mu_{B2})\left(\frac{n\pi}{b}\right)^2 \\ \mu_{B2}^3 - \mu_{B1}^3 + (2-\nu)(\mu_{B1} - \mu_{B2})\left(\frac{n\pi}{b}\right)^2 & \mu_{B1}^2 - \mu_{B2}^2 \end{bmatrix} \begin{bmatrix} w_e \\ \theta_e \end{bmatrix} \quad (11)$$

where D is the plate flexural rigidity, μ_{B1} and μ_{B2} are the valid wavenumbers and α_1 and α_2 are the corresponding complex wave amplitudes.

The matrix which appears in equation (11) is the dynamic stiffness matrix of the semi-infinite plate. The dynamic stiffness matrix of the stiffened panel may be found by employing the analysis presented in reference [13]. With this approach the panel is modelled as an assembly of plate elements, and to this end a node is introduced at each plate/stiffener junction. The stiffeners may either be modelled by using beam theory, or a fully dynamic model may be developed by using plate elements to model the behaviour of the flanges and webs. Following assembly, the dynamic stiffness equations for the complete structure (for a specified number of lateral half-wavelengths n) then have the form

$$\begin{bmatrix} D_{\infty L11} + D_{E11} & D_{\infty L12} + D_{E12} & \dots & 0 & 0 \\ D_{\infty L21} + D_{E21} & D_{\infty L22} + D_{E22} & \dots & 0 & 0 \\ 0 & 0 & D_E & 0 & 0 \\ 0 & 0 & \dots & D_{\infty R11} + D_{E(Q-1)(Q-1)} & D_{\infty R12} + D_{E(Q-1)Q} \\ 0 & 0 & \dots & D_{\infty R21} + D_{EQ(Q-1)} & D_{\infty R22} + D_{EQQ} \end{bmatrix} \begin{bmatrix} w_{Lr} \\ \theta_{Lr} \\ \vdots \\ w_{Re} \\ \theta_{Re} \end{bmatrix} = \begin{bmatrix} S_{Lr} \\ M_{Lr} \\ \vdots \\ S_{Re} \\ M_{Re} \end{bmatrix}, \quad (12)$$

where the 'L' and 'R' subscripts represent the left and right semi-infinite plates and the 'E' subscript represents the embedded stiffened panel, which is taken to have Q degrees of freedom.

By introducing an incident wave of amplitude α_{inc} into one of the semi-infinite plates (say the left), equation (12) can be solved to yield the degrees of freedom w_e and θ_e for each semi-infinite plate. These can then be substituted into equation (10) to provide the

complex amplitudes of the transmitted and reflected waves (α_t and α_r , say) for the specified number of transverse half-waves, n . The transmission and reflection coefficients are defined as $\tau = |\alpha_t/\alpha_{inc}|^2$ and $\rho = |\alpha_r/\alpha_{inc}|^2$.

3.2 APPROXIMATE CALCULATION

The calculation procedure described in the previous section leads to exact results for the transmission and absorption coefficients of the M-bay stiffened panel which is shown in Figure 1. A more approximate approach which requires significantly less computational effort is described in the present section; this approach is based on the general analysis of a one-dimensional waveguide which is presented in reference [8], and it leads to closed form approximate results for the transmission and absorption coefficients associated with a particular Fourier component n .

For each Fourier component n the system shown in Figure 1 forms a one-dimensional waveguide. As described in reference [8], the transmission coefficient for the one-dimensional waveguide may be written in the form

$$\tau_M = \left| \frac{a_M}{a_0} \right|^2 = |\lambda^{2M}|^2 \left(\frac{|1 - \alpha_1 \alpha_2|^2}{|1 - \alpha_1 \alpha_2 \lambda^{2M}|^2} \right). \quad (13)$$

The reflection coefficient may similarly be expressed as

$$\rho_M = \left| \frac{b_0}{a_0} \right|^2 = |\alpha_1|^2 \left(\frac{|1 - \lambda^{2M}|^2}{|1 - \alpha_1 \alpha_2 \lambda^{2M}|^2} \right). \quad (14)$$

Here, λ is the propagation factor of the periodic system, defined such that $\lambda = \exp(-i\varepsilon - \delta)$ where ε is the phase constant and δ is the attenuation constant. Furthermore, α_1 and α_2 are related to the waveforms of right and left travelling periodic waves: $b_m/a_m = \alpha_1$ for right travelling waves and $a_m/b_m = \alpha_2$ for a left travelling wave.

As discussed in reference [8], τ_M and ρ_M can be locally 'smoothed' by averaging over a cycle of $e^{-2i\varepsilon M}$ on the assumption that α_1 and $\alpha_1 \alpha_2$ remain approximately constant. This approach yields

$$\bar{\tau}_M = \frac{e^{-2\delta} |1 - \alpha_1 \alpha_2|^2}{1 - |\alpha_1 \alpha_2|^2 e^{-4\delta M}}, \quad (15)$$

$$\bar{\rho}_M = |\alpha_1|^2 \left(\frac{1 - \alpha_1 \alpha_2 (1 + e^{-4M\delta}) + Z^2 - (Z^4 - 4Z^2 + 1)^{\frac{1}{2}}}{\alpha_1 \alpha_2 (Z^4 - 4Z^2 + 1)^{\frac{1}{2}}} \right), \quad (16)$$

where $Z = \alpha_1 \alpha_2 e^{-2M\delta}$. Equation (15) was first derived in reference [8].

To facilitate the evaluation of equations (15) and (16) it can be shown that

$$\alpha_1 \alpha_2 = 1 + (2/r^2) \left(t^2 \sin^2(\varepsilon - i\delta) - t \sin(\varepsilon - i\delta) \sqrt{1 - t^2 \cos^2(\varepsilon - i\delta)} \right), \quad (17)$$

and

$$|\alpha_1|^2 = \frac{1}{r^2} \left(1 + t^2 e^{-2\delta} - 2t e^{-\delta} \cos(kL - \phi_t - \varepsilon) \right), \quad (18)$$

where r and t are the reflection and transmission coefficients of a single stiffener and ϕ_t is the phase of the transmission coefficient.

In principle the band-averaged transmission and reflection coefficients can be obtained by integrating τ_m and ρ_m over the appropriate wave number range. A more approximate approach is to assume that within a stop-band $\tau_m = 0$ and $\rho_m = 1$, while within a pass-band τ_m and ρ_m are constant and equal to the *mid-band* value (i.e. the value at $\varepsilon = \pi/2$). It can be noted that the value of the mid-band attenuation constant, δ_{mid} , is given by [8]

$$\delta_{mid} = \sinh^{-1}[(1/t) \sinh(\pi m_f / 2)] \quad (19)$$

where $m_f = \omega \eta v$, the *modal overlap factor* for a single bay of the system with loss factor η at angular frequency ω . The modal density, v , for a one-dimensional waveguide is given by $(L/\pi c_g)$, where L is the length of each bay and $c_g = \partial\omega/\partial k$ the group velocity.

3.3 DIFFUSE COEFFICIENTS

In both the exact and approximate cases, the diffuse transmission and reflection coefficients, at frequency ω , may be evaluated by integrating the contributions of all propagating values of n . The diffuse absorption coefficient can then be calculated using equation (20).

$$\alpha = 1.0 - \tau - \rho \quad (20)$$

4. EXAMPLE APPLICATION

The foregoing theory has been applied to an example aluminium structure consisting of an eight bay stiffened panel which forms a coupling between two rectangular unstiffened plates. The geometry of the stiffened panel is shown in Figure 5; the whole structure is of width 1m, and the two unstiffened plates are of length 2.4m and 3.6m, and each has thickness 2mm.

Example propagation constants ε and δ for the periodically stiffened panel are shown in Figure 3(a) for the case of zero damping ($\eta=0$); these results concern only the first Fourier component of the motion ($n=1$) and the upper frequency is limited to 190 Hz. Three pass bands (in which $\delta=0$) are discernible in Figure 3(a), and it can be expected that vibration transmission through a finite stiffened panel will be concentrated within these bands. This is confirmed by Figure 3(b) which shows the transmission coefficient of the 8-bay panel for the case $\eta=0.01$. The "exact" results yielded by the analysis presented in section 3.2 display 8 peaks per pass band; were the panel undamped then the transmission coefficient would achieve a value of unity at each of these peaks [8]. The approximate results yielded by the analysis presented in section 3.3 provide a good estimate of the average transmission coefficient in each pass band, and a similar level of agreement is shown in Figure 3(c) for the absorption coefficient.

The results shown in Figure 3 relate only to the $n=1$ Fourier component. Results for all relevant values of n over an extended frequency range are shown in Figure 4, where it can be seen that a complex system of overlapping pass bands occurs. The agreement between the exact and approximate values of the transmission and absorption coefficients is generally good for the transmission coefficient and reasonably good for the absorption coefficient. It has been found that response predictions are not sensitive to the value of the absorption coefficient for the present structure, since the absorption tends to make a less than 20% difference to the internal loss factors via equation (9).

Results for the response of the structure to rain-on-the-roof forcing of the left hand plate are shown in Figure 6. The results are presented in terms of a dB energy level difference between the two plates i.e. $10\text{Log}(E_2/E_1)$, and five sets of results are shown as follows: (i) benchmark exact results computed by applying the dynamic stiffness method [13] to the complete system; (ii) standard SEA results obtained by treating each bay of the stiffened panel as a separate subsystem; (iii) wave intensity analysis results (WIA) [14] in which the SEA diffuse wave assumption is relaxed; (iv) results yielded by the present two subsystem model with

exact transmission and absorption coefficients; (v) results yielded by the present two subsystem model with approximate transmission and absorption coefficients.

In considering the standard SEA results which are shown in Figure 6, it can be recalled that the method assumes that: (a) the wavefield in each subsystem is diffuse, and (b) all wave components are uncorrelated. Assumption (a) is in error for the present structure, since the stiffeners act as spatial filters which favour waves near to normal incidence. This assumption is relaxed in WIA, where the angular distribution of the wavefield in each subsystem is expanded in terms of a Fourier series - this leads to much improved results, as shown in Figure 6, although for the present example 50 Fourier components were required to ensure converged results at the higher frequencies. Assumption (b) regarding the phase of the various wave components is also adopted in WIA, and this means that neither SEA nor WIA are able to model pass band/stop band behaviour. For the present structure this leads to significant differences between WIA and the exact results at frequencies above 750Hz.

The present approach to modelling the system as two SEA subsystems incorporates a detailed model of the stiffened panel behaviour, and thus wave filtering and phase effects are captured, as evidenced by the good agreement with the exact results shown in Figure 6. For the present example, the use of the approximate formulae for the transmission and absorption coefficients does not lead to a significant loss in accuracy.

5. CONCLUSIONS

The present work has considered how a stiffened panel might be modelled within the context of SEA. It has been suggested that such a panel might be represented as a damped coupling element whose transmission and absorption coefficients are calculated on the basis of periodic structure theory. This approach has lead to good results for the example structure considered here, and further studies will consider the effects of disorder and fluid loading.

REFERENCES

1. LYON, R.H. and DeJONG, R.G., *Theory and Application of Statistical Energy Analysis, Second Edition*. Boston: Butterworth-Heinemann, 1995
2. FAHY, F.J., Statistical energy analysis: a critical overview. *Philosophical Transactions of the Royal Society* 1994, **346**, 431-447.
3. LANGLEY, R.S.. A general derivation of the statistical energy analysis equations for coupled dynamic systems. *Journal of Sound and Vibration*, 1989, **135**, 499-508.
4. WESTER, E.C.N. and MACE, B.R., Statistical energy analysis of two edge-coupled rectangular plates: ensemble averages. 1996, *Journal of Sound and Vibration* **193**, 793-822.
5. LANGLEY, R.S. and HERON, K.H., Elastic wave transmission through plate/beam junctions. *Journal of Sound and Vibration*, 1990 **143**, 241-253.
6. HERON, K.H., Predictive Statistical Energy Analysis using the wave approach. *Personal communication* 1996.
7. KEANE, A.J. and PRICE, W.G., Statistical energy analysis of periodic structures. *Proceedings of the Royal Society of London Series A* 1989, **A423**, 331-360.
8. LANGLEY, R.S. The frequency band-averaged wave transmission coefficient of a periodic structure. *Journal of the Acoustical Society of America* 1996, **100**(1), 304-311.
9. SUN, J.C., LALOR, N. and RICHARDS, E.J. Power flow and energy balance of non-conservatively coupled structures, I: Theory. *Journal of Sound and Vibration*, 1987, **112**, 321-330.
10. FAHY, F.J. and De-YUAN, Y. Power flow between non-conservatively coupled oscillators. *Journal of Sound and Vibration* 1987, **114**, 1-11.
11. YAPP, F.F. and WOODHOUSE, J., Investigation of the damping effects on Statistical Energy Analysis of coupled structures. *Journal of Sound and Vibration*, 1996, **197**, 351-372.
12. BESHARA, M. and KEANE, A.J., Statistical Energy Analysis of multiple, non-conservative coupled systems, *Journal of Sound and Vibration*, 1996, **198**(1), 95-122.
13. LANGLEY, R.S. A dynamic stiffness technique for the vibration analysis of stiffened shell structures. *Journal of Sound and Vibration*, 1992, **156**, 521-540.
14. LANGLEY, R.S. A wave intensity analysis technique for the analysis of high frequency vibrations. *Journal of Sound and Vibration*, 1992, **159**, 483-502.

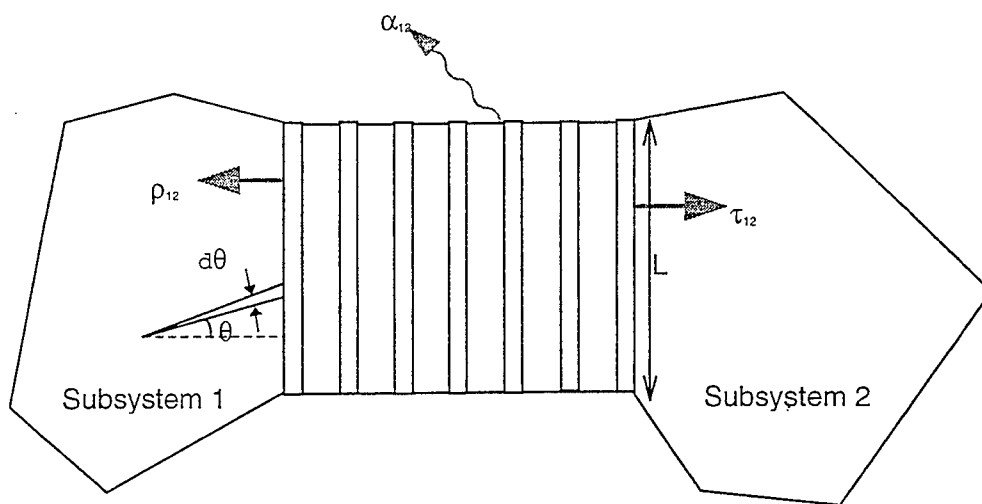


Figure 1 : Schematic of Two-subsystem SEA model

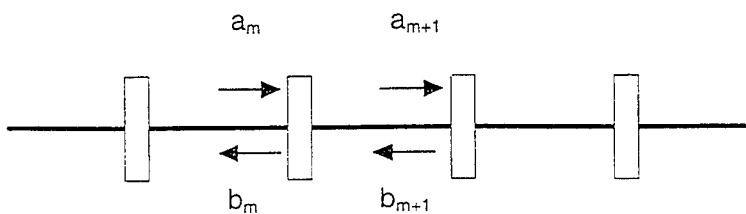


Figure 2 : Schematic of One-dimensional Waveguide

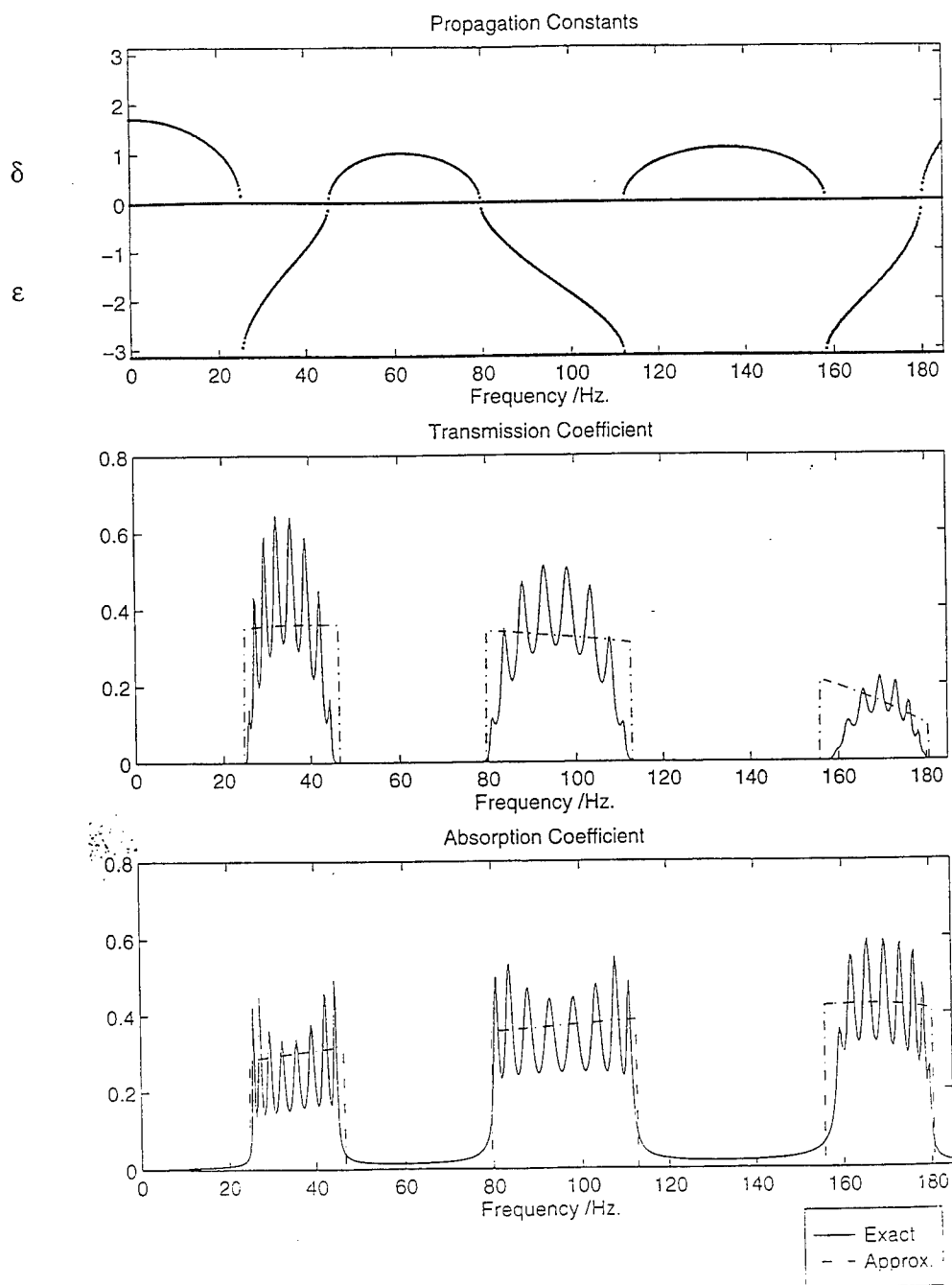


Figure 3 : Propagation Constants, Transmission Coefficients and Absorption Coefficients for $n=1$

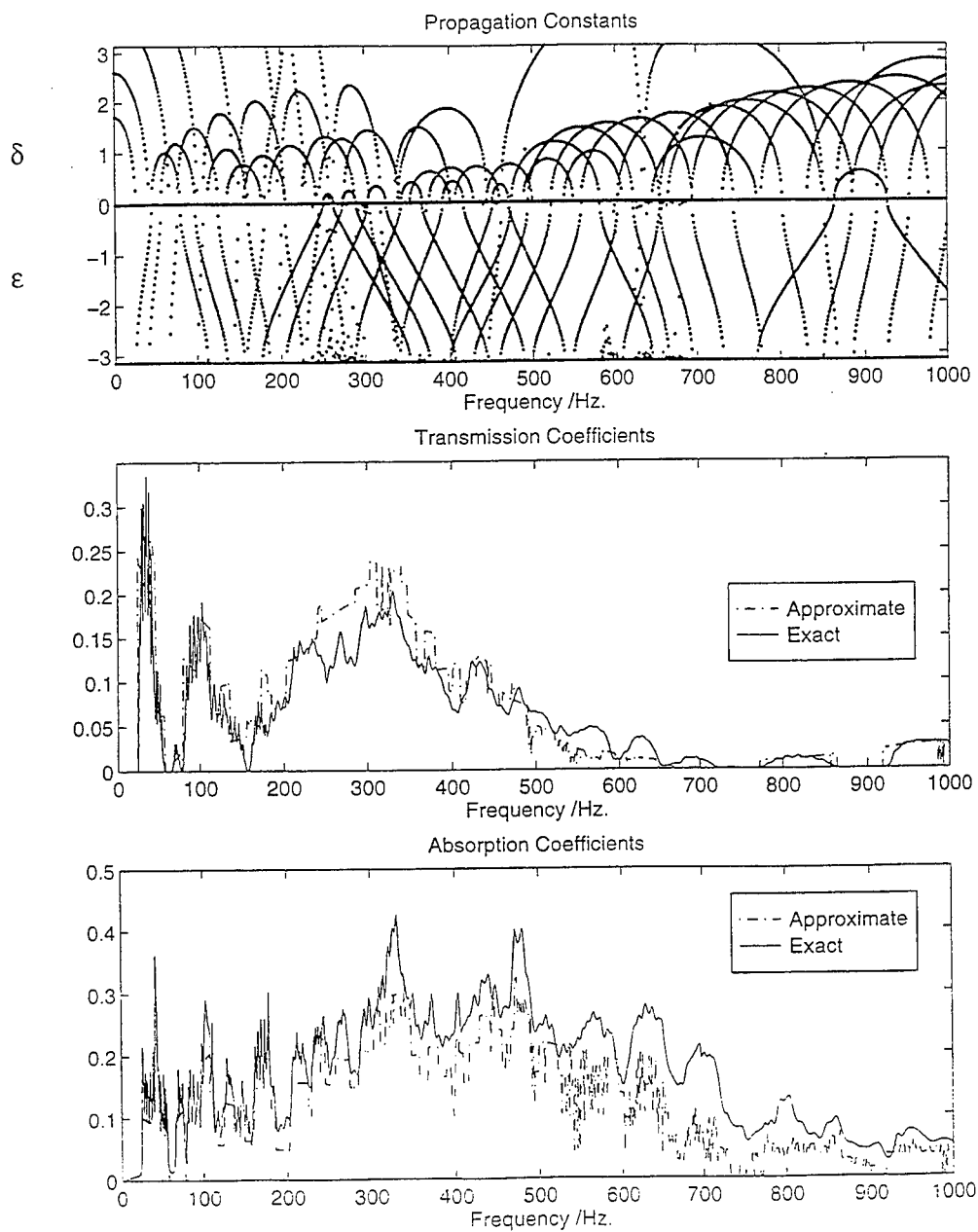


Figure 4 : Propagation Constants, Transmission Coefficients and Absorption Coefficients for valid n.

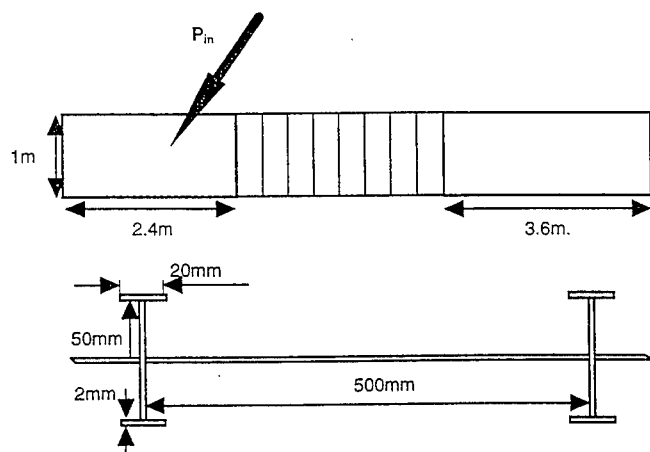


Figure 5 : Geometry of Example Application

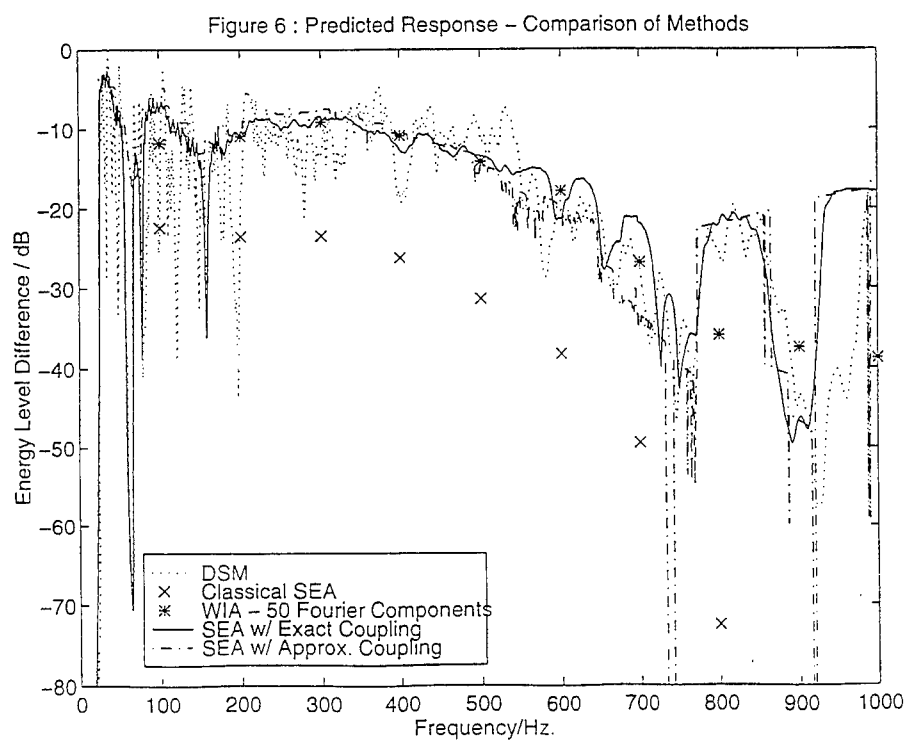


Figure 6 : Example Application - Comparison of Methods

EXPERIMENTAL METHODS I

BOUNDARY INFLUENCES IN DYNAMIC TESTING

Malcolm A. Cutchins, Professor
Aerospace Engineering Department
Auburn University, AL 36849 USA

Michael L. Tinker Aerospace Technologist
NASA/Marshall Space Flight Center
Structural Dynamics and Loads Branch/ED 23
Huntsville, AL 35812 USA

ABSTRACT

The role of boundaries in testing and some of the appropriate literature is briefly discussed. A very large NASA modal test fixture located on the Marshall Space Flight Center in Huntsville, Alabama is described. Its purpose, to conduct modal tests of large Space Station elements and other Shuttle payloads, has led to a number of tests, calibrations, refinements, and better delineation of boundary influences, some of which are described herein.

INTRODUCTION

The contrast in realistic structural supports is no more apparent than in the ease of making textbook/chalkboard sketches of fixed ends, and the much more difficult reality of attempting to duplicate such idealistic boundary conditions in the laboratory or in the real world. Only with great attention to detail can such idealistic supports be built.

Qu and Cutchins [1] were successful in a hammer test by mounting a small, light aluminum scaled model of a joined-wing in a special tapered, clamped base support which was mounted on a massive steel beam loading frame. In this manner, a wing root fixed end finite element model worked well with only tip-beam modeling iterations needed to successfully correlate experiment and theory with no significant boundary modeling problems.

Despite careful attention to detail, even attempts such as this one with a small scale model often yield contrasting experiment/theoretical results which require many man-hours of analysis or re-testing in order to reconcile the almost inevitable discrepancies.

Most realistic boundary influence problems are virtually ignored in the textbook literature with a few notable exceptions such as Ewins' classic [14]. One of the best to address this problem in relation to this paper is Rao [2], in which the author briefly but carefully describes testing and analysis techniques, suspension with elastic cords, various ways of exciting the system, and other related material. Junkins and Kim [3] and Donaldson [4] address boundary influences in very significant and unique ways, the former developing equations (related to Hamilton's Principle and the Lagrange Equation technique) from which boundary conditions can be derived. The latter centers on beam boundary conditions, but includes Winkler's elastic foundation approach and some other oft-neglected boundary considerations.

In contrast with the dearth of material in textbooks, there are numerous archival papers and conference proceedings which address various aspects of the problems, and the solutions, associated with boundary influences. Representative of these are conference papers such as [5], [6], and [7], internal reports [8], [9] and [10], and trade journal papers such as Stroud [11].

In [10], a number of NASTRAN runs were made with variations in the 3-dimensional spring stiffnesses which modeled the supports at eight different locations for a multiple-litter, 3-D frame stanchion proposed to collectively transport a high density of litter patients in numerous civil aircraft. (In this manner, seat support tracks could be used for structural restraint of the litter stanchions for emergency use of the civilian fleet of airliners in large scale disaster evacuations.) Using a 9-g longitudinal load case, a comparison of rigidly supported stanchions vs elastically supported stanchions (with 3-D linear springs only at each support; no torsional springs) revealed several constraint forces that varied within a range of several thousand pounds, with no changes other than the support-spring stiffnesses. Some constraint forces even changed their sense for this statically indeterminate structure with eight support points. No dynamic influences (other than the FAA specification 9-g loading level) were measured in this static loads study.

Tinker [12] shows the interdependence of static tests and dynamic tests for the large test facility described later.

A number of generic and fundamental dynamic cases appear in the literature, illustrated well by the 12 foot flexibly-supported beam in [5]. In this elastic cord supported dynamic case, good agreement between

theory and experiment was obtained. Elastic cord suspension is not always feasible, however.

Most published results are of necessity structure-specific. But it is readily apparent that boundary influences are quite significant, their idealization often oversimplified, and their better definition highly sought. One answer may be a better use for flexures, like the typical wind tunnel balance systems have used for years, in dynamic testing. A NASA test facility to be described below provides for making inroads into improved understanding of boundary effects for complicated dynamic tests.

INITIAL DESIGN AND TESTING

Built in 1990, the NASA Universal Test Fixture (UTF) still is probably the largest of its kind. The concrete and steel, bedrock-anchored facility is quite impressive. It has a floor stiffness of 60 million pounds/inch. Figure 1 is an isometric view; note that the two massive sides are about 15 feet (almost 4.6 meters) apart. Figure 2 shows a Space Station Common Module Prototype mounted in the UTF, viewed from one end of the fixture.

In the initial design, a combination of bearings and flexures was used to simulate typical Shuttle payload bay constraints. Several test/analysis sequences have occurred since then in moving toward more accurate testing of Space Station elements. It has been the focus of several tests to uncover and identify significant nonlinearities, assess desired interface conditions, evaluate different techniques, and complete a fixed base modal survey. Fixture design requirements included:

- ◆ No natural frequencies below 40 Hz, 60 Hz if possible.
- ◆ Horizontal mounting of all Space Station module elements.
- ◆ Trunnion and keel pins (the Orbiter interfaces) restrained in all seven Orbiter-constrained degrees of freedom
- ◆ Fixture 10 times as stiff as test article.

Design of the fixture-to-test-article interfaces to achieve these requirements has pushed the ingenuity of the engineers involved. Use has been made of spherical bearings to allow rotational motion, a pendulum system to allow swinging motion in the X direction, and bearings to allow for sliding in the lateral or Y coordinate and rotational motion. Figure 3 illustrates the most novel of these interfaces. The airbag system shown at the top of each figure (one atop each of the four interface mechanisms) has the capability to offload the trunnions and free the interfac-

es and test article to slide and rotate in appropriate directions.

A cross sectional view of the UTF (Figure 4) shows the relationship of the two other types of interface elements tested and a typical Space Station module. One of the concepts explored is a flexure interface concept as shown in Figure 5. These have been tested in the four trunnion positions at the fore and aft ends of the test module. Geometry details of the flexures are given in [13]. Basically, they have been sized to get axial stiffnesses greater than 4×10^6 lb/inch in order to prevent coupling of flexure modes with test article modes. Table 1 shows a comparison of the rectangular and round flexure geometries; rectangular blade flexures were chosen because they gave a softer lateral stiffness while maintaining more adequate axial stiffness.

Table 1. Comparison of Stiffnesses for Blade and Rod Flexure Geometries

<u>Direction</u>	<u>Stiffness (Lb/in, In-lb/rad)</u>	
	0.6 Inch Width*	1.5 Inch Round*
Axial	4,500,000	3,900,000
Lateral	1,330	2,300
Torsional	474,000	745,000
Bending	704,000	994,000
Axial/Lateral Ratio	3,400	1,708

* 2 flexures, 2.75 inches in length

Also shown in Figure 4 is a keel interface located at the bottom of the module. This interface, of much different geometry and principle, is shown in more detail in Figure 6. Much higher y-stiffness and low x- and z- stiffnesses are required for it.

A frequency comparison is shown, see Table 2, in which analytically determined frequencies are compared with ideal 7-DOF orbiter-constrained modes of the model with the flexures removed. Based on these data, it is obvious that this concept works well.

Table 2. Comparison of Analytical Constrained Frequencies in Hz for Space Station Resource Node with and without Flexures

Mode Nr.	w/o Flexures	w/Flexures	Percent Difference
1	8.21	8.53	3.9
4	10.71	11.76	9.8
5	13.37	14.11	5.5

Others of these modes (26 through 31) at frequencies without flex-

ures of 18.94, 21.35, 22.52, 22.92, 23.68, and 23.79 all varied only slightly, between 0.2 and 1.0 percent, in comparison to the with-flexure frequencies.

Two views of the keel rectangular flexure design of the type conceptualized in Figure 5 are shown in Figure 7.

INTERNATIONAL SPACE STATION ALPHA (ISSA) CALIBRATION BEAM

The modal survey [9] and other studies have used the International Space Station Alpha (ISSA) Calibration Beam (often referred to as "the Boeing Beam" since Boeing is the prime support contractor for NASA in Huntsville). See Figure 8. A near-planar structure, the beam-like truss-trunnion arrangement has been useful for "proof of concept" tests, especially as they relate to the flexure designs and verification of finite element models. The boundary conditions for the beam have been primarily

- A. Free-Free
- B. Fixed Base with various flexure combinations

Test frequencies have usually been 0-64 Hz, but have also ranged upward to 200 Hz, a range which includes 14 modes.

Other tests involving the UTF relate especially to particular techniques. As a couple of examples, with the advent of more sophisticated test equipment, the residual flexibility method has become increasingly attractive [5, 7]. The concept of flexures used solely to simulate the desired interface conditions has been the emphasis of several calibration test efforts at NASA.

Accounting for undesired test stand flexibility and the analytical removal of such test stand influences from measured modes is the subject of Lin & Cole [6]. A similar approach, now dealing with the Figure 8 structure and flexures intentionally incorporated in the test stand, is being utilized by the authors of this paper to attempt to remove the influence of flexures from measured modal data [7]. Further evaluation of the residual flexibility method is also made in the latter reference.

A new, much more three-dimensional test structure, Pathfinder, has recently begun to be used in further NASA tests.

CONSTRAINED-BOUNDARY OR FIXED-BASE TESTING

Constrained-boundary or fixed-base testing has historically been the most common approach for verifying finite element mathematical models for structures constrained in service. At best, the boundary conditions of the test article are designed to match the actual in-use constraints. However, there are difficulties involved with fixed-base testing, in some cases making the approach impractical. As stated in a number of references, it is not possible to conduct a truly fixed-base test due to coupling between the test article and the fixture. In addition, it is often difficult to accurately simulate the actual boundary constraints, and the cost of designing and constructing even the fixture itself may be prohibitive.

Examples of these difficulties as they relate to the NASA modal test fixture include the following:

- ◆ Shuttle Payload Models and Orbiter Interface Constraints
 - Contamination of test data due to coupling between the test article and the fixture,
 - Difficulties in actual simulation of the boundary conditions existing in flight,
 - Cost of design, construction and checkout of the fixture.
- ◆ International Space Station Flight Hardware - Common Module Prototype
 - Nonlinear effects of varying shaker force amplitude and airbag pressure level,
 - Softening spring effects,
 - Disappearance of modes due to changing boundary conditions with higher force levels.

Solutions to these difficulties involve redesigned fixture interfaces as shown in this paper, and continuing evaluation of various methods as described in [5, 7, 12, 13, 15].

Figures 9 - 12 illustrate several of the test observations as described in the brief summary above. For example, Figures 9 and 10 show the nonlinear effects observed during sine sweep testing. Observe in Figure 9 that the fundamental yaw mode about the Z axis near 7.5 Hz experiences a "bending over" of the response peak. This appears to be the classical softening spring seen in many nonlinear structures [14]. A second phenomenon seen in Figure 9 is that for a given airbag pressure

(which controls the trunnion preload), the resonance peak (near 23 Hz) corresponding to the first ovaling mode collapsed for increased shaker excitation force (i.e. the mode disappears).

Figure 10 shows the gradual changes in the phenomenon previously described as a function of varying shaker force amplitude. Ref. [12] shows the actual modes which were observed during the tests described above.

Figure 11 is indicative of the drastic shift of the first X-translational resonance peak. Driving with increasing force brought joint clearance into play, leading to trunnion back and forth movement within the fixture constraints, thereby creating a softer boundary condition and shifting the mode (near 13 Hz) to a much lower frequency (near 5 Hz). Figure 12 is for a similar vertical response. The contrast in the shape of the response for 30 pound (solid) versus 5 pound (dashed) shaker force suggests a free-floating condition and excessive clearance in the aft trunnion-bearing interface.

ALTERNATIVE FREE-BOUNDARY TEST METHODS

For use when fixed-base testing proves impractical or undesirable, alternative free-boundary test methods have been investigated, including the residual flexibility method (RFM) and the mass-additive technique. The residual flexibility approach has been treated analytically in considerable detail by several researchers, but has had limited application as a test method. Current efforts [7] are underway to further evaluate the approach's accuracy in test applications. By way of illustration, Figure 13 shows a residual function for a SSM Prototype [15]. In this case, while showing good agreement using the RFM between theory and test, the curves are averages obtained with modal testing software. They are not indicative of the typical very noisy residual functions. Tinker [15] has shown that the frequency response functions for this approach should have a well defined stiffness line (a general upward sloping trend) if acceptable accuracy is to result.

The mass-additive technique has been an alternative of interest as well. In the approach, masses are added to the boundaries - experimentally; analytically, masses are added as rigid bodies attached to the interface degrees of freedom. Figure 14 shows one of the orbiter interfaces of the SSM Prototype, with an added mass.

CONCLUSIONS

Current interpretations are that the mass-additive approach is simpler than the RFM and is in general easier to perform experimentally, although more free-boundary modes need to be measured. The RFM is more accurate and is, with the advent of better instrumentation, judged to have greater potential for testing space station hardware.

The attempt to adequately account for either expected-in-use or deliberately designed boundaries in dynamic tests is a continuing challenge. There are needs to explore these phenomena more at the fundamental level, as well as with more advanced real-world structures. Some of the latter, their inherent problems, and current solution techniques have been identified and discussed in this paper.

REFERENCES

1. Qu, B. and Cutchins, M. A., "Joined-Wing Model Vibrations Using PC-Based Modal Testing and Finite Element Analysis, *Journal of Aircraft*, Vol. 31, No. 2, March-April 1994, pps 449-452.
2. Rao, S. S., Mechanical Vibrations (3rd Edition), Addison-Wesley, 1995, pps. 661-665.
3. Junkins, J. L. and Kim, Y., Introduction to Dynamics and Control of Flexible Structures, AIAA, Reston, Virginia, 1993, p. 153 and others.
4. Donaldson, B. K., Analysis of Aircraft Structures, McGraw-Hill, 1993, pps. 287-310.
5. Tinker, M. L., and Bookout, P. S., "Measurement of Residual Flexibility for Substructures Having Prominent Flexible Interfaces," AIAA-94-1566-CP, 35th AIAA/ASME/ASCE/AHS/ASC Structures, Structural Dynamics, and Materials Conference, Hilton Head, South Carolina, April 18-20, 1994, pps. 1944-1958.
6. Lin, C. S. and Cole, T. R., "Development of GPS IIR Space Vehicle Dynamic Model," AIAA-96-1587-CP, 37th AIAA/ASME/ASCE/AHS/ASC Structures, Structural Dynamics, and Materials Conference Proceedings, Salt Lake City, Utah, April 15-17, 1996, pps. 2374-2383.
7. Cutchins, M. A., Tinker, M. L., and Bookout, P. S., "Comparison of Methods for Modal Testing of a Space Station Element Simulator," AIAA-97-1270, Proceedings of the 38th AIAA/ASME/ASCE/AHS/ASC Structures, Structural Dynamics, and Materials Conference, Kissimmee, Florida, April 7-10, 1997 (page numbers not yet available).

8. Phillips, E. B. and Britt, H., Internal Letter Boeing Report No. 2-8F1A- HAB-015/96R1 relating to Structural Math Models, February 21, 1996.
9. Anderson, J. B., Chandler, K. O., and Driskill, T. C., "ISSA Modal Test Bed Calibration Beam Fixed Base Modal Survey Test Report," SS-DEV- ED95 -077, Experimental Dynamics Test Branch, Structural Test Division, Structures and Dynamics Laboratory, NASA/MSFC, Huntsville, Alabama, September 22, 1995.
10. Cutchins, M. A., Foster, W. A., Jr., and Hamner, B. A., "Analysis and Design of an Aeromedical Evacuation Litter Stanchion," USAFSAM-TR-86-14, prepared for the USAF School of Aerospace Medicine, San Antonio, TX, AE Department, Auburn University, August 1986 (and related MS thesis by Hamner).
11. Stroud, R. S., "The Modal Survey of the Galileo Spececraft," Sound and Vibration, April 1984.
12. Tinker, M. L., "Nonlinearities Due To Joint Friction and Clearance in a Structural Dynamic Test Fixture," ASME DE-Vol. 90, *Elasto-Impact and Friction in Dynamic Systems* (Ferri, Flowers & Sinha, Editors), Nov. 1996, pps. 35-46.
13. Tinker, M. L., "Stiffness-Additive Technique for Assessment of Modal Test-Article to Fixture Interface Flexures," 38th AIAA/ASME/ASCE/AHS/ASC Structures, Structural Dynamics, and Materials Conference, Kissimmee, Florida, April 7-10, 1997 (page numbers not yet available).
14. Ewins, D. J., Modal Testing: Theory and Practice, Research Studies Press, Letchworth, Hertfordshire, England, UK, 1986.
15. Tinker, M. L., "Modal Vibration Test Facilities and Methods for Space Station Modules., AIAA-95-1295, 36th AIAA/ASME/ASCE/AHS/ASC Structures, Structural Dynamics, and Materials Conference, New Orleans, LA, April 10-13, 1995, pps. 1190-1197.

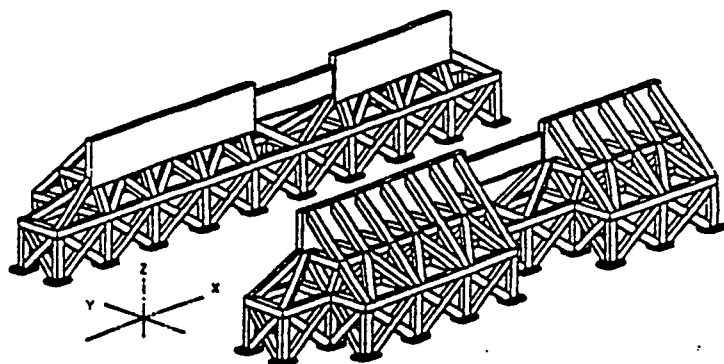


Figure 1. Universal Test Fixture for Modal Tests of Space Station Modules

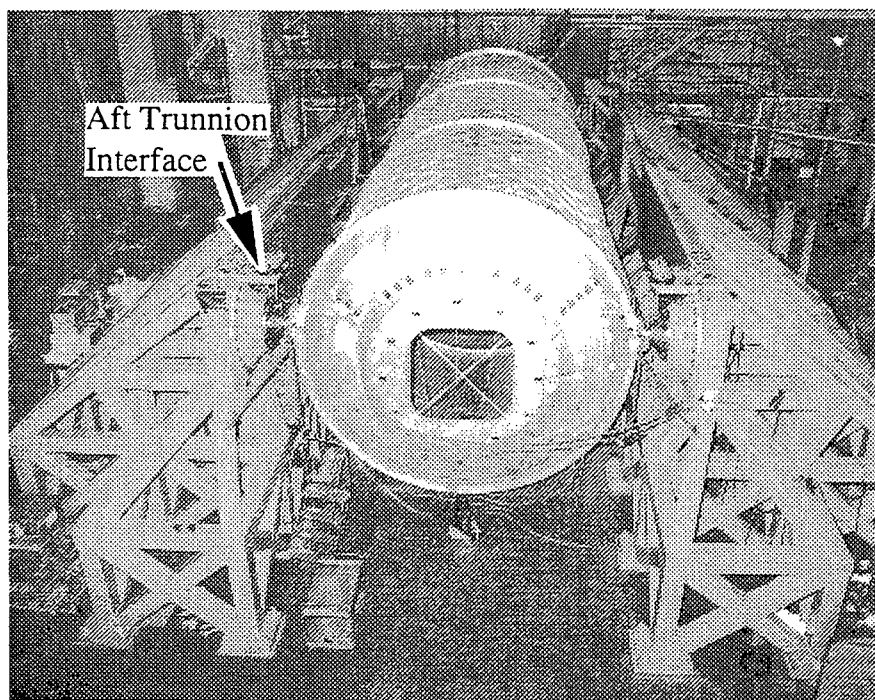
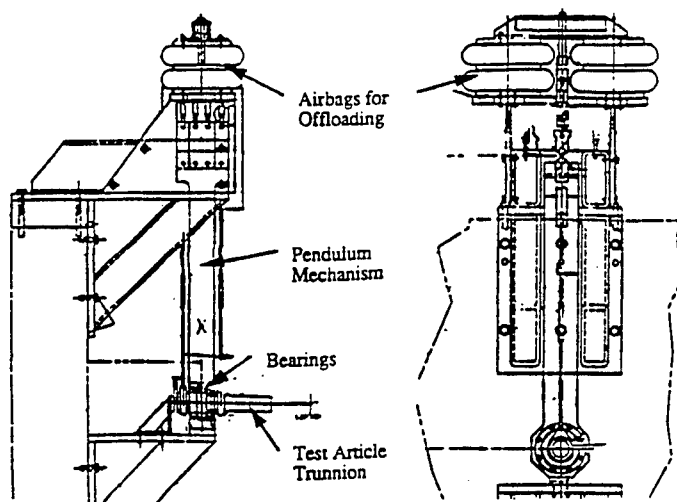
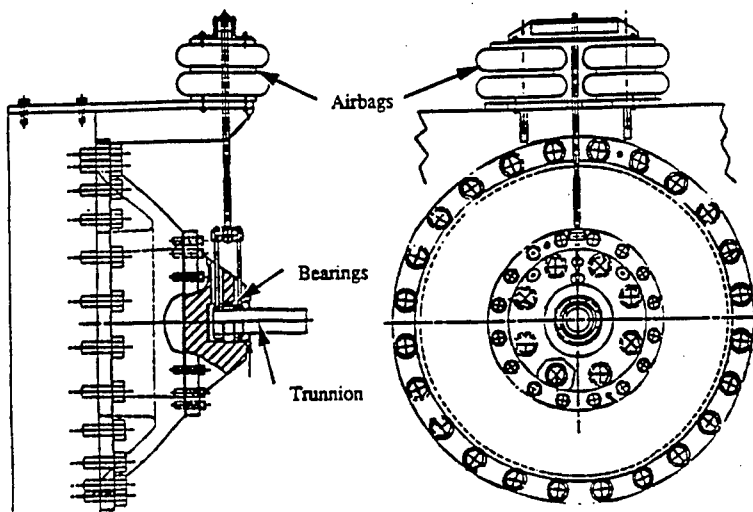


Figure 2. Space Station Module (SSM) Prototype in Universal Test Fixture



(a) X- and Y-Views of Forward Trunnion Interface



(b) X- and Y-Views of Aft Trunnion Interface

Figure 3. Details of Forward and Aft Test Article Interfaces for Universal Test Fixture

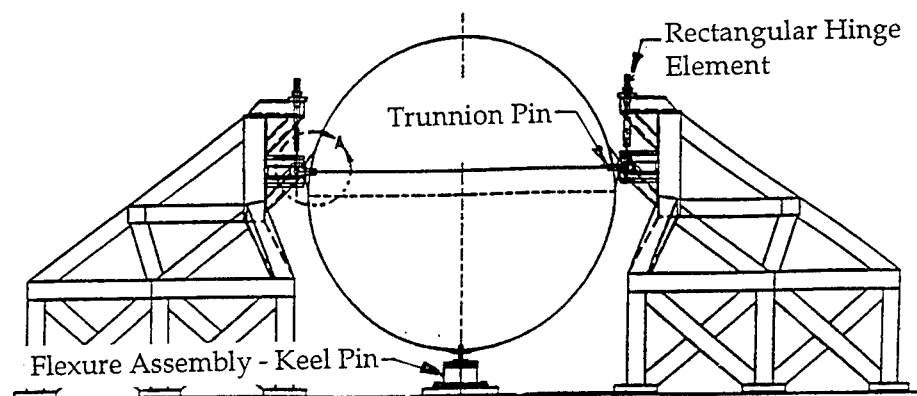


Figure 4. X-Direction View of Cross-Section of Universal Test Fixture with Redesigned Interfaces

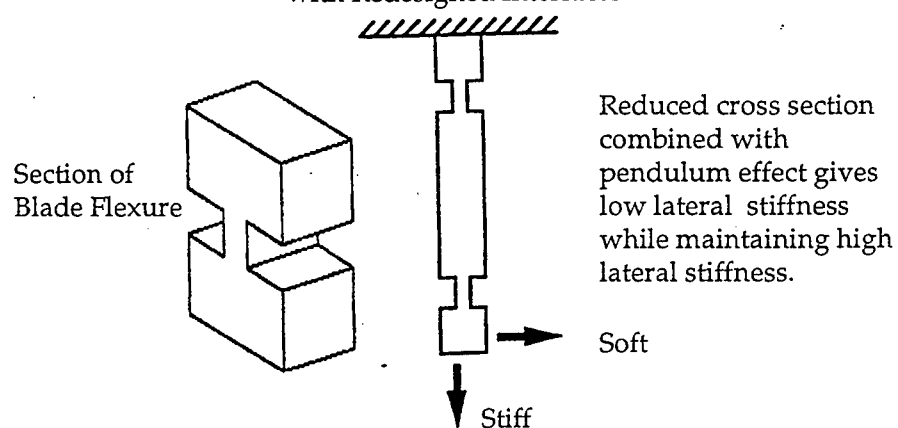
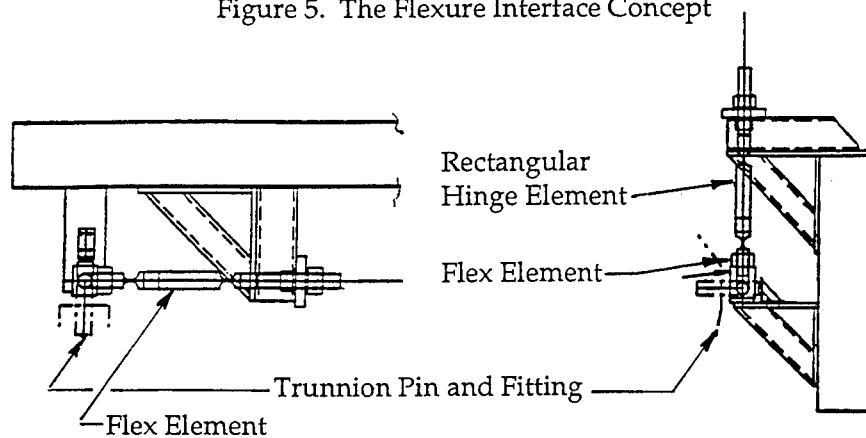


Figure 5. The Flexure Interface Concept



(a) X-Direction Flexure

(b) Z-Direction Flexure

Figure 6. Flexures in Test Fixture

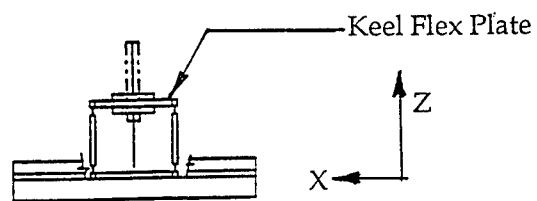
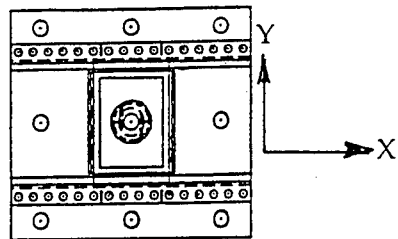


Figure 7. Keel Flexure Design

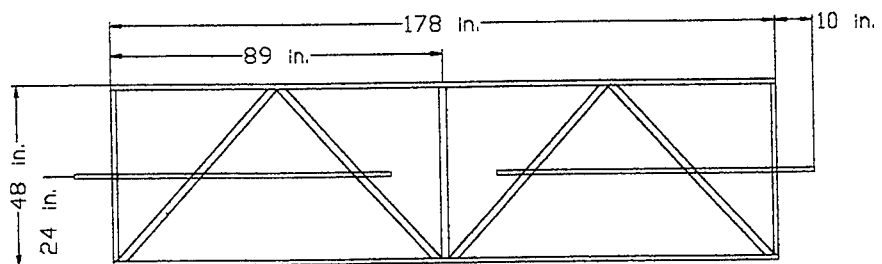


Figure 8. The Boeing Beam

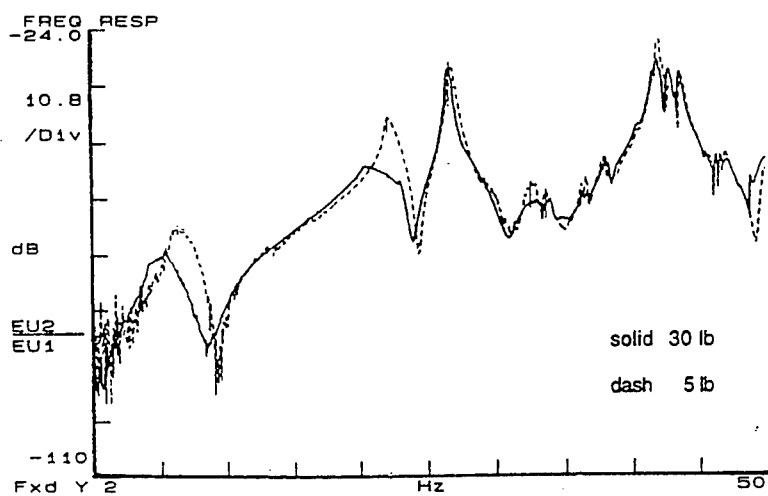


Figure 9. Y-Direction Acceleration/Force Frequency Response for 5 lb. and 30 lb. Sine Sweep Excitation and Airbag System Offload 100 lb. Below Balanced Condition

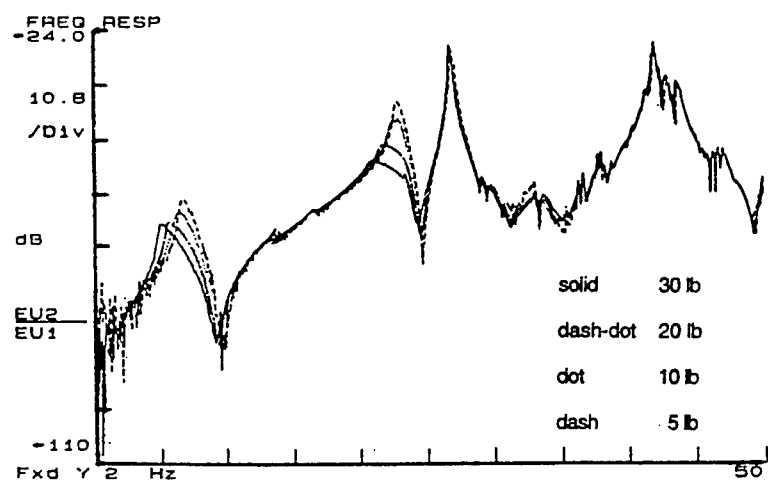


Figure 10. Y-Direction Frequency Response for Various Excitation Amplitudes, Offload 250 lb. Below Balanced

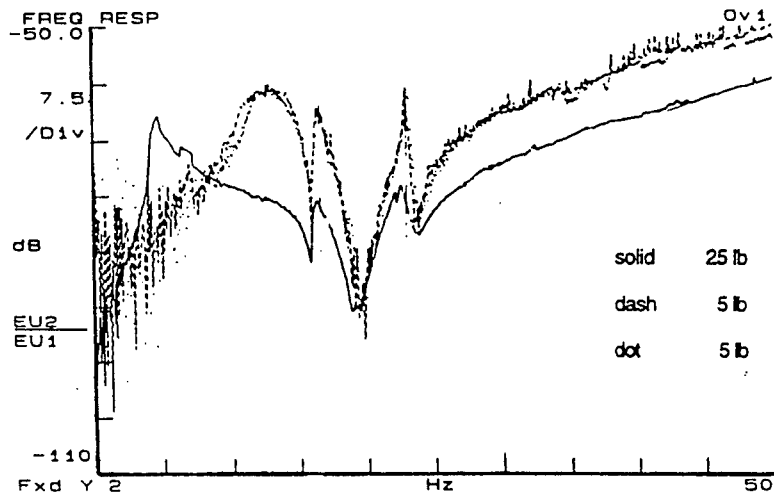


Figure 11. X-Direction Acceleration/Force Frequency Response with Varying Shaker Amplitude and Offload 100 lb. Below Balanced Condition

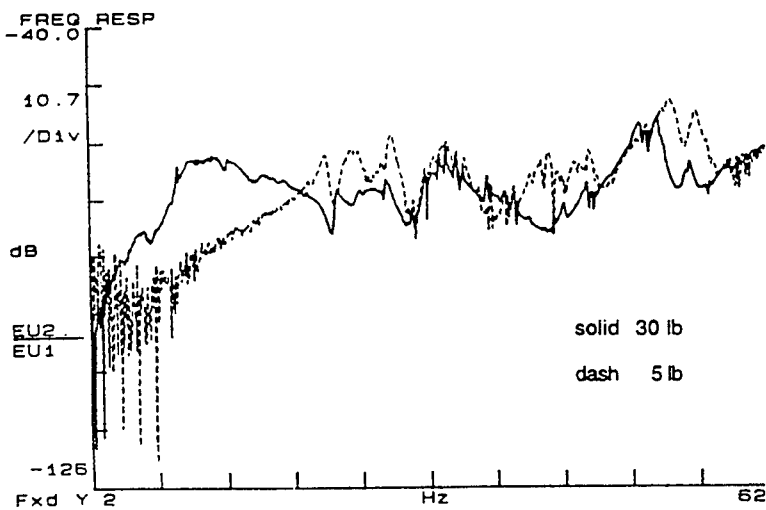


Figure 12. Response in Z Direction for 5 lb. and 30 lb. Shaker Force and Below Balanced Condition

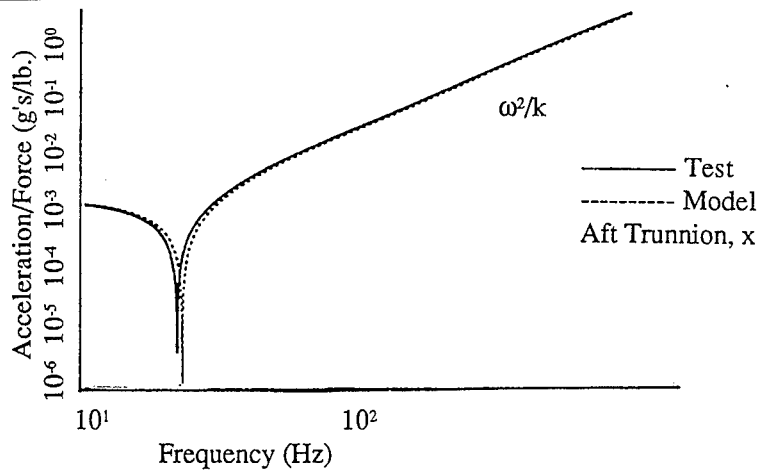


Figure 13. An Interface Residual Function for the SSM Prototype

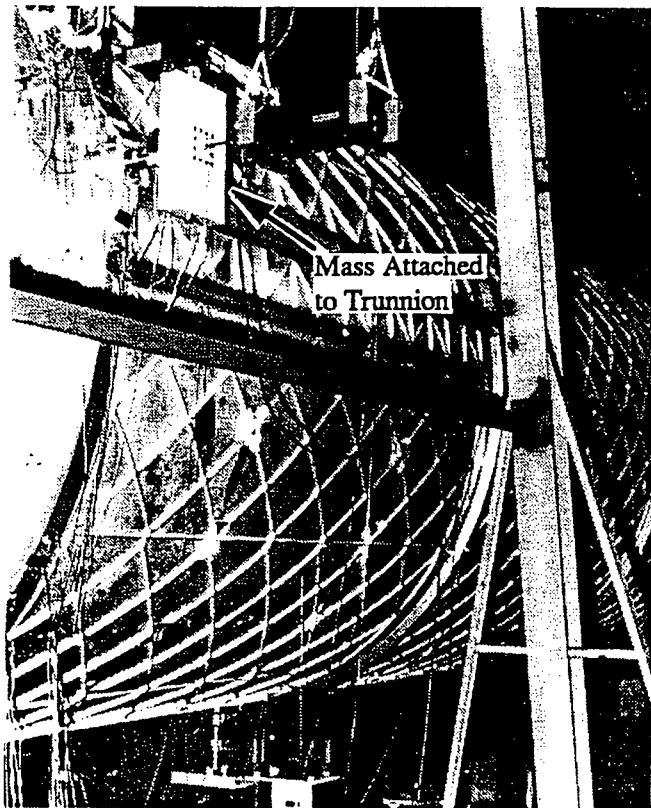


Figure 14. Mass-Additive Test Configuration for the SSM Prototype

EFFECT OF ELASTIC CONSTRAINTS INTRODUCED BY MICROCRACKS ON MODE SHAPES IN ALUMINUM 6061 SHEET

D. Ravi and K.M. Liew
School of Mechanical and Production Engineering
Nanyang Technological University
Nanyang Avenue
Singapore 639798

Abstract:

This paper presents the detection of microcrack initiation, arrest and growth in Aluminum 6061 using acoustic emission (AE) technique. Rate of AE energy released is correlated to the damage process and initiation of microcrack when aluminum 6061, is subjected to compression loading. The presence of damage and microcracks were verified using a metallographic technique and electron microscopy. The damage for initiation of microcrack was introduced in a aluminum 6061 sheet (500x1000x1 mm). Modal analysis was conducted on the sheet under free-free boundary condition, using a frequency response analyser 1250 and ICATS. The mode shapes were mapped using velocity pattern imager (VPI) sensor when the sheet was vibrated at the modal frequency. The modal frequencies and the mode shape were compared to the results of a finite element analysis. The overall mode shape did not provide any information regarding the elastic constraints introduced due to the presence of microcracks. Scans were made at distances of 5mm intervals on either side of the plastically deformed region on the plate in the horizontal and the vertical directions. It was found that the only by making line scans around the area of deformation the effect of microcracks on modal constraint could be detected. The elastic constraints introduced on the modes due to the presence of microcracks were directional depending on the mode position. Frequency response analysis was performed around the deformed region. The second modal frequency measured at the edge of the sheet was very close to that of the first response frequency at the region near the deformed region. Micrograph analysis and plastic material flow studies were made on the deformed region. The direction of material flow was correlated to the elastic constrained area.

1 Introduction

When a structure is subjected to damage, it is obvious that the modal parameters will change because the damage reduces the structures stiffness. Considerable effort has been taken in the last few years in the investigation of damage location and damage size. Recently, finding relationship between the extent and location of damage in a structure has received considerable attention. Many of the proposed damage detection methods exploiting changes in the modal parameters adopt sensitivity approach and utilize only natural frequency changes. A major disadvantage of sensitivity based methods is the significant amount of computations required especially for large and complex structures. In addition frequency changes alone may not be sufficient to locate the damage position since similar defects at different positions may cause the same change in frequency. In contrast vibration mode shapes can be heavily influenced by local damage. The greatest change occurs around the defect, thus offering the possibility of locating the damage. In most cases, the damage of a structure is due to the

presence of cracks in the structure or the extension of the cracks; therefore, monitoring of damage region and identifying the size of damage is very important. Vibration monitoring has proven to be a very feasible way to detect damage in structures. This kind of monitoring is based on a better understanding of relationship between the crack location, the crack size the corresponding change in modal parameters, such as natural frequencies, displacement, modes and elastic constraints [1-2]. Most vibration analysis experiments, until this date has been performed on macrocracks or damages which are not quantified for microcrack initiation. Hence it is essential to evaluate the microcrack damage using a very sensitive technique to evaluate microcrack initiation during the damage process. Many techniques have emerged in recent year to detect the initiation of cracks. Acoustic emission is a very sensitive technique capable of detecting microcrack initiation and propagation [3]. Acoustic emission is the term used to describe the spontaneous release of transient elastic waves in solids caused by sudden localized changes in stress. Major damage processes in engineering materials, such as crack advance and plastic deformation, are accompanied by local changes in the stress and strain states of the body, and thus radiate elastic waves away to external surfaces of the body. Provided that the elastic waves are of sufficient amplitude to be detected by receivers attached to the body, they can be used to give an indication of defect growth.

The first clearly documented and serious investigation of acoustic emission was made Kaiser in 1950 [4], at the Technical University of Munich. Taturo in 1959 [5], explored the possibility of detecting slip in metals with sonic techniques. An extensive investigation of acoustic emission phenomenon was initiated by Schofield in 1961 [6]. He reported that acoustic emission did not originate entirely from boundaries, as single crystals also emitted the stress waves. Numerous mechanisms have been proposed and confirmed as the sources of acoustic emission. A partial listing of reported sources include movement of dislocations and grain boundaries (Gills, 1972 [7]), formation and growth of twins (Wadley, 1981 [8]), Peak amplitude correlation with microcrack initiation and propagation (Pollock, 1981 [9]), microcrack formation (Teleman and Chow, 1972 [10]), generation and propagation of cracks (Masov and Gradov, 1986 [11]). Fatigue failures normally originate at places where there is stress concentration. Crack growth begins under conditions of local plasticity. The dependence of crack propagation rate, da/dN , on stress intensity range, ΔK , does not apply if the crack is less than a critical length. These cracks which shows anomalous behavior are called short cracks (David Taylor, 1995 [12]). Study of short crack is useful to estimate the life of a component.

Any damage in the structure will be reflected in the dynamic response spectrum as a shift in natural frequencies. This phenomenon has been exploited by Yang [13] and Zhang [14] to detect damage in practical structures. Yuen [15] has used a finite element modeling technique to establish the relationship between damage and the changes of modal parameters when a uniform cross-sectioned cantilever was subjected to damage. The damage in the cantilever beam was represented by the reduction of the modulus of elasticity. It has been proved that the first mode eigen parameters can well reflect both the location and the size of the crack in the cantilever beam. N. Stubb's [16,17] work on damage-detecting theory was evaluated by a formulation that expressed the change of modal stiffness in terms of modal masses, modal damping, eigen frequencies, eigen vector and their respective changes. Adams and Cawley [18] have developed a method of sensitivity analysis to deduce the location of damage based on the application of a finite element method with assumption that the modulus of elasticity in the damage area was equal to zero. In the case on system identification and modal updating schemes are limited by the accuracy of the system identification algorithm

used [19]. In addition, modal updating tends to spread the effect of change around the structure [20], making damage location difficult.

Since strain modal analysis is now a particular interest Song [21] and Feng [22] have used the strain modal parameters to detect a slot in the cantilever beam. In their papers, the strain modal analysis in the time domain was applied. The strain modal testing which a strain gage was used as a transducer proves to be more convenient method than displacement modal tests.

Non-contacting vibration measurement is a convenient tool to employ during the evolution of mechanical designs. A variety of optical techniques have been developed in recent years to study the vibrational displacement of a surface or structure with high spatial resolution while avoiding the loading effects of attached transducers. The Vibration Pattern Imager (VPI) offers a particularly versatile solution to many industrial vibration measurement requirements. The system offers an alternative to using contacting accelerometers for mobility measurements, not only during sinewave testing but also under broadband or service loading conditions.

In the present work microcracks initiation arrest and propagation was evaluated using the acoustic emission technique. The VPI was used to extract the frequency response and modal shapes of a rectangular sheet of aluminum after it was deformed at its center at microcrack initiation load. Analysis was made to understand the plastic flow influencing the directional elastic constraint during vibration.

2 Experimental Procedures

Aluminum 6061 was selected for microcrack initiation and growth study for modal analysis. Micrograph and EDAX composition analysis was made on the specimens to study the presence of defects and the composition of the material. Samples were compressed using a 24mm diameter, mild steel rod in an Instron machine (4206). The cross head speed was fixed at 0.1 mm/min. The load applied for a range of 0 to 80 kN. A Spatran 8000 (Physical Acoustics Corp.) acoustic emission measurement equipment, was used to detect acoustic emission by placing a piezoelectric transducer (DUNEGAN CORP., S9204-AB71) 10 cm away from the point of loading. The load data were fed into the acoustic emission system as an analog signal. Experiment was repeated for duration's of 120 seconds keeping the load rate constant. After each test the samples were electropolished and prepared for microscopic analysis. The electrolyte used for electropolishing had a chemical composition of 14 % Distilled water, 80 % Ethanol and 6 % Perchloric acid. The initiation of microcracks were identified after 240 seconds by noting the sudden change in acoustic emission energy rate emitted. Their presence was verified by using electron microscope. The experiments were repeated by loading for a duration of 240 seconds, and the results were consistent.

A rectangular sheet of dimension 500x1000x1 mm of aluminum 6061 was loaded for a duration of 240 seconds at its center over a diameter of 24mm. The sheet was supported for free boundary condition type of vibration analysis, by suspending the sheet using thread. The frequency response for the structure was measured by vibrating it for a white noise range of 0 to 25 Hz. The frequency response was obtained by comparing the force sensor output and that of the VPI output. The response frequencies at the 4 corners of the sheet were plotted. By vibrating the aluminum sheet at its modal frequencies the mode shape

corresponding to each mode was mapped using the VPI. Thereafter the experiment was repeated by vibrating the sheet at the modal frequency and data was extracted by line scans. Scans were performed at 5mm intervals starting from the center to either side of the deformed region. Using the data from the line scans extracted for mode two of 6.9Hz, an elastic constraint curve was plotted. The experiment was repeated twice and similar trends of elastic constraint was seen. The frequency response data was extracted at a distance of 12mm from the center and at point of angle 45 degrees intervals around the deformed region.

A finite element analysis was performed using Ansys5.2. The finite element analysis results did not indicate any effect of damage on mode shapes, in contrast to the experimental results. The aluminum sheet was analysed for plastic flow direction at its center, by metallurgical analysis.

3 Results and Discussion

Data analysis for AE was made on the basis of information obtained with regard to energy release rate in each 120 seconds interval to 480 seconds. Figure 1 shows the complete acoustic emission, energy release rate history for the compression test for a loading duration of 0 to 480 seconds. Figure 2 shows that after 240 second of loading the microcracks had initiated.

The plot for events by energy release rate for a loading duration of 120 seconds shows that the elastoplastic process is initiated, hence the surface deformation is expected to start. The AE energy release rate was very high, confirming the onset of surface deformation. There after had decreased, indicating the arrest mechanisms were predominant.

In the 240 seconds duration of loading range, the AE energy release rate had decreased. At very close to 240 second duration of loading, there was a sudden increase in emission rate, indicating the initiation of microcrack growth.

The AE energy release rate for the loading duration from 240 upto 360 seconds was high AE energy release rate remained significant for a duration from 240 to 300 seconds. After 300 seconds of loading, AE energy release rate decreased. The decrease in AE energy release rate is probably because material is utilizing the strain energy for crack growth in random directions. The situation of low AE release rate, continued for the load duration from 360 upto 480 seconds. The micrograph analysis of the initiation arrest and growth of microcracks revealed the validity of the prediction based on AE.

The experiments were repeated 10 times for loading duration's of 120 seconds interval upto 480 seconds. The AE energy release rate followed the same trend in each set of 10 experiments. The aluminum sheet which was deformed at its center at the microcrack initiation load was used to do modal analysis. Frequency response data acquired at the edge of the sheet is shown in figure 3. Mode shape analysis was done using the frequency response data extracted at the edges of the sheet. The overall mode shape does not provide any information regarding the elastic constraints introduced due to the presence of microcracks. The experiment repeated by using line scans had significant results for the second modal frequency. The amplitude response data in the direction along the length is shown in figure 4. The boundary of constrained area is identified by noting the sudden change in data along the scanning line. The results of the response from the data collected at the edge of the deformed region had its first response very close to 17.9 Hz (the second modal frequency at the edge).

Figure 5 shows the frequency response evaluated at point at the edge of the plastic zone. The elastic constraint map showed, directional influence on the mode two. The micrograph analysis performed to verify the presence of microcracks at the center of the sheet provided positive results.

4 Concluding Remarks

Acoustic emission is a very sensitive technique for in microcrack evaluation. The FEM analysis depends on overall modal response frequencies and was insensitive to local responses at damage sites. The VPI is found to be a effective tool to study the elastic constraints introduced by a deformed region on the elastic surrounding. The VPI is very sensitive to deformation provided the response frequency at the deformed region is very close to the any one of the overall modal frequency. The elastic constrain direction depended directly on the direction of flow of the material. VPI has proved to be a effect tool to study plastic flow, at microcrack initiation loads.

Reference

1. C.Dong, P.Q.Zhang, W.Q.Feng, T.C.Huang, "The sensitivity studies of the modal parameters of a cracks beam", IMAC 12th, pp. 98-104, 1994.
2. William T. Springer and Antony Reznick, "The prediction of the natural frequencies shifts for a cantilever L-section beam due to the presence of a crack", IMAC 12th, pp. 889 - 897, 1994.
3. Doraiswami Ravi and Sethuramiah, A., 1995, "Acoustic emission in dynamic compression and its relevance to tribology", Tribology international, Vol. 28, 301 - 306.
4. Kaiser, J., 1950, "Untersuchungen uber das Auftreten Geräuschen beim Zugversuch", Ph.D Thesis Techn Hochschule, Munchen.
5. Tatro, C. A., and Liptai, G.R., 1962, "Acoustic emission from crystalline substances", Proc. Symp. Physics and NDT SWRI, San Antonio, Texas, USA.
6. Schofield, B. H., 1961, "Acoustic emission under applied stress", Aeronautical Research Laboratory, Report ARL 150, US Air Force.
7. Gillis, P.P., 1972, "Dislocation motions and acoustic emissions" Acoustic Emission, ASTM STP 505, 20 - 29.
8. Wadley, H.N.G., Scruby, C. B and Shrimpton, G., 1981, "Quantitative acoustic emission source characterisation during low temperature cleavage and intergranular fracture", Acta Metallurgica, vol. 29, 399 - 414.
9. Adrin A. Pollock, 1981, "Acoustic emission amplitude distribution", International advances in Nondestructive Testing, Vol. 7, 215 - 239.
10. Tetelman, A. S., and Chow, R., 1972, "Acoustic emission testing and microcracking process", Acoustic Emission, ASTM STP 505, 30 - 40.
11. Maslov, I. I., and Gradov, O.M., 1986, "Fracture energy analysis via acoustic emission", Int. J. Fatigue, Vol. 8, 67 - 71.
12. David Taylor, 1989, "Fatigue thresholds", Butterworth and Co. Ltd., pp 132-133.
13. J.C.S.Yang, N.Dagalakis and M.Hirt, "Computational method for offshore structure", ASME publication AMP 37, pp. 55-68, 1980.
14. P.Q.Zhang, T.X.Song and T.C.Huang, "Modal analysis of a cantilever with changing stiffness and with added concentrated mass," IMAC 4th, pp. 787-794, 1986.
15. M.M.F.Yuen, "A numerical study of the eigen parameters of a damaged cantilever," Journal of sound and vibration, 103 (3), pp. 301-331, 1995.
16. N.Stubbs, "Global non-destructive damage evaluation in solids," The international journal of analytical and experimental modal analysis, 5 (2), pp. 67-79, 1990.
17. N.Stubbs, "global damage detection in solids experimental verification," The international journal of analytical and experimental modal analysis, 5 920, pp. 81-97, 1990.
18. R.D.Adams and P.Cawley, "Location of defects in structures from measurement of natural frequencies," Journal of strain Analysis, 14, pp. 49-55, 1979.
19. Salawn, O.S.and Williams.C., "Structural damage detection using experimental modal analysis- A comparison of some methods", proceedings, 11th International Modal analysis conference, Kissimmee, Florida, Vol. 1, pp. 254-260, 1993.

20. Penny, J.E.T., Wilson, D.A. and Freswell, M.I., "Damage detection in structures using vibration data", Proceedings, 11th International Modal analysis conference, Kissimmee, Florida, Vol. 2, pp. 861-867, 1993.
21. T.X.Song, P.Q.Jhang, W.Q.Feng, T.C.Heang, "Experimental strain modal analysis by space-time regression method in the time domain, "The International journal of analytical and experimental modal analysis", vol. 4, No.1, pp 15-18, 1989.
22. W.Q.Feng,K.Y.Zhang and X.Y.We, " Research on the change of modal parameters of a beam resulted from a slot, "IMAC, pp . 1000-1110, 1989.

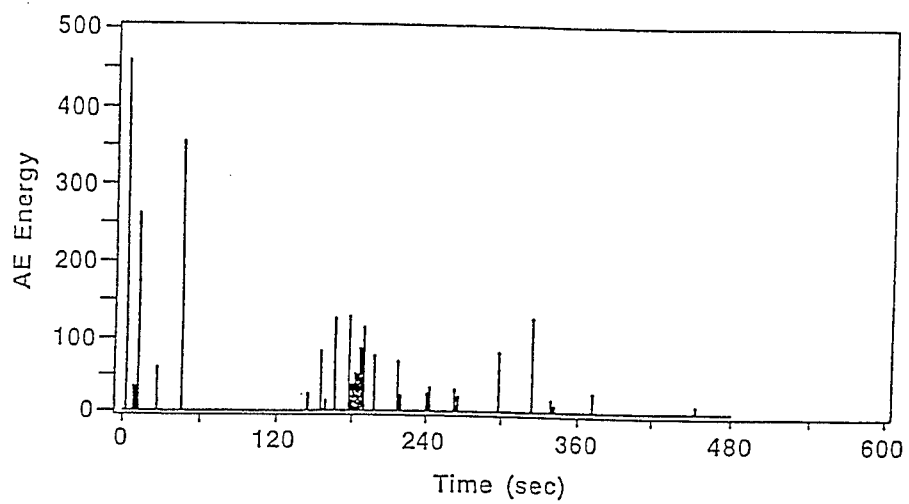


Figure 1 Acoustic Emission energy release vs Time



Figure 2 Micrograph of specimen loaded for 240 sec.

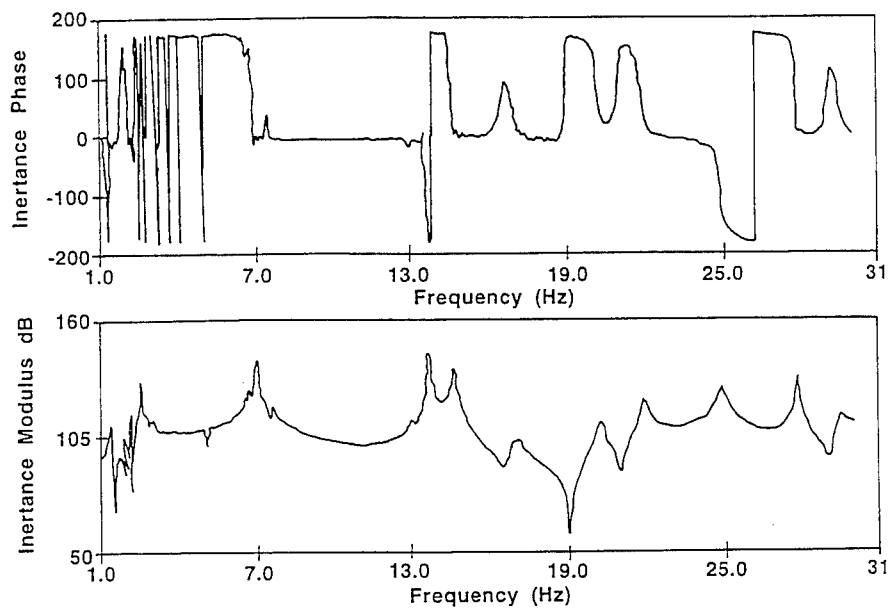
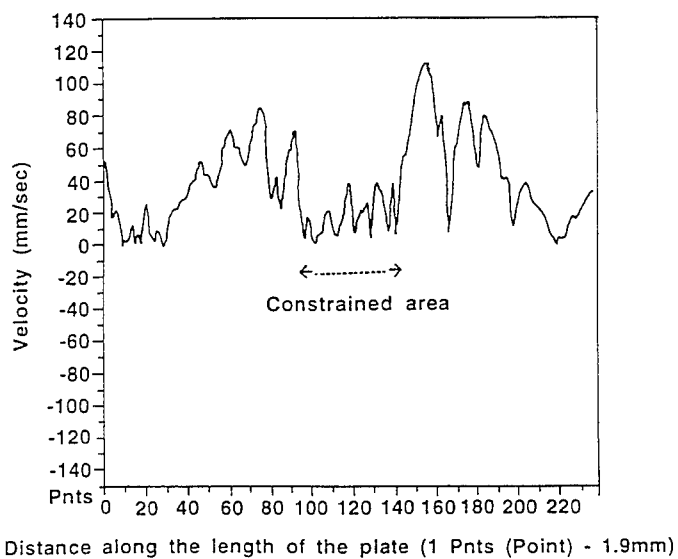


Figure 3 Amplitude and phase response for the outer edge of the plate.



Distance along the length of the plate (1 Pnts (Point) - 1.9mm)

Figure 4 Amplitude response along the length of the plate.

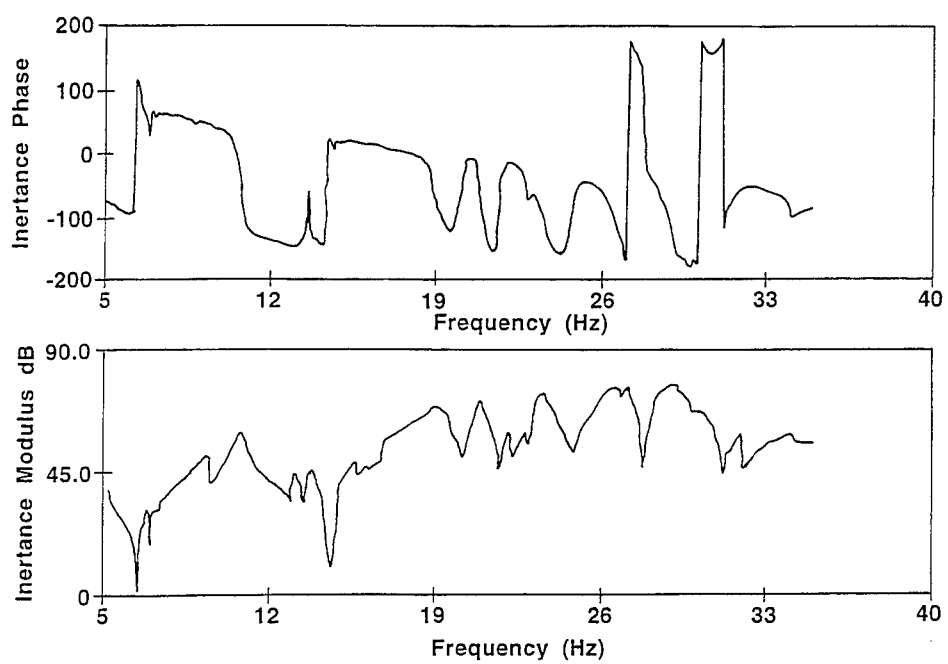


Figure 5 Amplitude and phase response at the edge of the deformed area.

ASSESSING THE TRANSVERSE CRACK LOCATION IN FLEXURAL VIBRATIONS OF STRAIGHT UNIFORM BEAMS

M. Boltežar, B. Štrancar and A. Kuhelj

University of Ljubljana, Faculty of Mechanical Engineering, Aškerčeva 6,
1000 Ljubljana, Slovenia

ABSTRACT

This paper deals with the crack identification procedure for free-free uniform beams in flexural vibrations. The model of a transverse crack includes an equivalent linear spring, connecting two segments of a beam. By measuring the changes of natural frequencies in flexural vibrations it is possible to study the inverse problem - the crack site identification. The method is based on the assumption that the crack stiffness does not depend on the frequency of vibration. It requires at least two natural frequencies to be measured which are changed due to the crack existence. The comparison to the crack sites, identified by measuring the axial vibrations, showed even some better results for flexural vibrations.

1. INTRODUCTION

In recent years, the dynamics of cracked structural members, especially beams, has been the subject of much research. A crack in a structural member can be thought of as a local flexibility, and as such, depends on crack depth. The existence of a crack further reduces the natural frequencies of the structure, so consequently, by measuring changes in natural frequencies the location of crack can be identified.

The problem of dynamic behavior of cracked beams has been studied by many authors. Adams *et al.* [1] were among the first to use the equivalent spring to model a damaged section. They used axial vibrations of one-dimensional beams to locate the damaged region in inverse problem. Rizos *et al.* [2] proposed measurements of amplitudes at two distinct points for a cantilever beam at flexural vibrations in order to locate the depth and magnitude of a crack. Pandey *et al.* [3] found that absolute changes in curvature mode shapes are localized in the region of damage and they increase with increased size of damage. Chondros and Dimarogonas [4] studied the relation between the change in the natural frequency of vibration of a cantilever beam and the crack depth that appears at the built-in edge which is clamped by way of a weld.

Christides and Barr [5] investigated the natural modes of simply supported beams with symmetric cracks using two-term Rayleigh-Ritz solution to obtain the variation in the fundamental frequency of beams with a mid-span crack. Shen and Pierre [6] suggested another series solution, using an approximate Galerkin procedure. Narkis [7] studied the dynamics of a cracked, simply supported beam for either bending or axial vibrations. He showed that the only information

required for accurate crack identification is the variation of the first two natural frequencies due to a crack.

For rotating shafts, Papadopoulos and Dimarogonas [8,9] found coupling of vibration modes of bending and longitudinal vibration of a cracked shaft. They modeled the crack with a 2x2 local flexibility matrix with coupling terms. Gudmundson [10] generalized this idea to a 6x6 flexibility matrix relating all six generalized forces and corresponding displacements.

The approach in this paper, developed by Adams *et al.* [1] is extended from axial to flexural vibrations. The crack is modeled as a torsional spring, following Rizos *et al.* [2]. The solution is then applied to the inverse problem in order to locate the damage site from measuring natural frequencies of flexural vibrations of a cracked beam.

2. THEORY

The method of damage location, developed by Adams *et al.* [1] for axial vibrations of one-dimensional bars is based on the calculation of direct receptance. A linear spring of stiffness K_x was used to model damage. Based on the assumption that K_x does not vary with frequency, authors have shown that the value of damage location required is that which will yield the same value of K_x from the measured change in natural frequency of each vibrating mode. So a graph superimposing values of $1/K_x$ for different vibrating modes plotted against the length of the bar will give the possible damage site at the intersection of the curves. This theory was developed neglecting damping since just the changes in natural frequencies were considered.

2.1. EXTENSION OF THE THEORY TO IDENTIFY DAMAGE LOCATION FROM AXIAL TO FLEXURAL VIBRATIONS

The physical model being investigated in this work is uniform Euler-Bernoulli beam, supported free-free as shown in Figure 1. The length of a beam is L , and R_0 denotes the true position of a transverse surface crack extending uniformly along the width of the beam, starting at the left end. The beam has constant cross section A and area moment of inertia I . Young's modulus E and mass density ρ are also constant. The effect of material damping on natural frequencies is assumed to be negligible. We started with Euler-Bernoulli equation of motion governing the flexural free vibration of a uniform beam

$$EI \frac{\partial^4 y}{\partial^4 x} + \rho A \frac{\partial^2 y}{\partial^2 t} = 0. \quad (1)$$

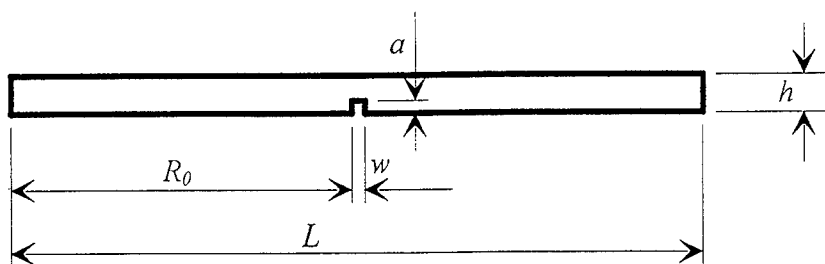


Figure 1. Schematic model of the cracked free-free beam

In the vicinity of the crack, this equation does not hold due to the abrupt change of the cross section. Since only flexural vibrations are considered, the rotational crack compliance is assumed to be dominant in the local flexibility matrix. This is the base of the decision to model a crack with torsional spring.

In order to avoid some unreliability of the material data from the literature such as Young's modulus, what is found not accurate enough for our purpose, the idea of determination of the effective Young's modulus has been adopted, following Adams *et al.* [1]. To solve eq. 1 for the undamaged beam, standard method of separation of variables can be applied

$$y(x, t) = V(x) \cdot \sin(\omega t + \alpha). \quad (2)$$

Mode of harmonic vibration can be written as

$$V(x) = A_1 \cdot \sin \lambda x + A_2 \cdot \cos \lambda x + A_3 \cdot \sinh \lambda x + A_4 \cdot \cosh \lambda x, \quad (3)$$

where A_i are constants to be determined from the boundary conditions and

$$\lambda^4 = \frac{\rho A \omega^2}{EI}. \quad (4)$$

By substituting solution after eq. 3 into the boundary conditions for free-free beam, the following determinant must be zero in order to find natural frequencies

$$Det(\lambda, L) = \begin{vmatrix} 0 & -1 & 0 & 1 \\ -1 & 0 & 1 & 0 \\ -\sin \lambda L & -\cos \lambda L & \sinh \lambda L & \cosh \lambda L \\ -\cos \lambda L & \sin \lambda L & \cosh \lambda L & \sinh \lambda L \end{vmatrix} = 0. \quad (5)$$

The problem of overcoming the published values of the material properties is solved by calculating the effective value of Young's modulus. It can be found using eq. 4 as

$$E_{eff} = \frac{\rho A \omega^2}{\lambda^4 I} \quad (6)$$

where dimensions of the beam are measured, the value of mass density is taken from the literature, value for λ_i are computed after eq. 5 and ω are measured natural frequencies. Effective values for Young's modulus must be found for each natural vibrating mode of the uncracked beam separately.

Now consider the cracked beam from Figure 1. It is modeled by two uniform segments of beams on both sides of the crack and the torsional spring between which model the crack itself and is shown in Figure 2. [2,10].

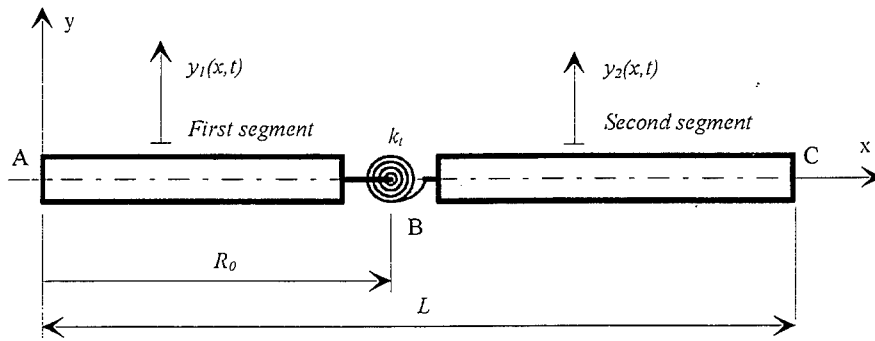


Figure 2. Model of the cracked beam with linear spring

The left segment is denoted by subscript 1 and the right segment by subscript 2. A and C denote the left and right end of the beam and B denotes an arbitrary position of the crack. Mode shapes can be written for both segments after eq. 3

1. segment ($0 \leq x \leq R$):

$$V_1(x) = B_1 \cdot \sin \lambda x + B_2 \cdot \cos \lambda x + B_3 \cdot \sinh \lambda x + B_4 \cdot \cosh \lambda x \quad (7a)$$

2. segment ($R \leq x \leq L$):

$$V_2(x) = C_1 \cdot \sin \lambda x + C_2 \cdot \cos \lambda x + C_3 \cdot \sinh \lambda x + C_4 \cdot \cosh \lambda x \quad (7b)$$

Boundary conditions include zero moments and shear forces at both ends A and C

$$y_A'' = y_C'' = 0, \quad y_A''' = y_C''' = 0 \quad (8)$$

The continuity condition at the crack position B requires

$$y_{1B} = y_{2B}, \quad y_{1B}'' = y_{2B}'', \quad y_{1B}''' = y_{2B}''' \quad (9)$$

lengths and the relative crack positions for both beams, denoted by I and II respectively, are shown in Table 1.

Table 1. Details of lengths and relative crack positions for both beams of experimentation

Beam	Length [mm]	R_0/L
I	498.5	0.38
II	498	0.5

The damage was being artificially introduced by a saw, so consequently the width of a cut was 1 mm and remained open during the testing. The depth of the crack has been varied. The boundary conditions were free-free; the beam was supported by a thin nylon rope the length of which was 1.5m. Simple scheme of the test rig is shown in Figure 3. The excitation was impulsive using both the impact hammer and impacts of a steel ball, attached to a cord.

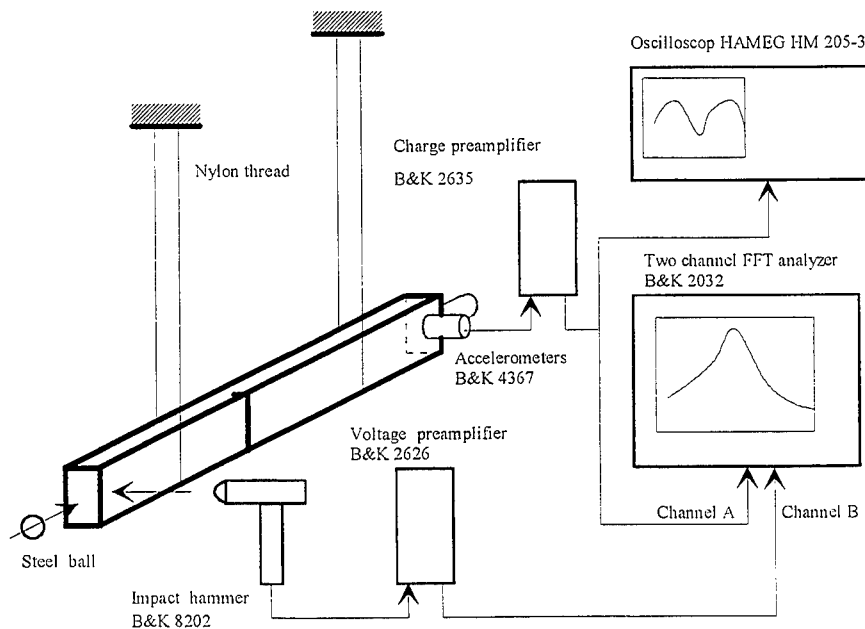


Figure 3. Scheme of experimental set-up

4. RESULTS

The positions of resonance peaks were estimated for first 6 natural frequencies of flexural vibrations for both undamaged beams and are shown in Table 2. Relative frequency resolution was about 0.01% according to the used zoom technique.

Table 2. First 6 natural frequencies, measured on undamaged beams

Beam	f_{01} [Hz]	f_{02} [Hz]	f_{03} [Hz]	f_{04} [Hz]	f_{05} [Hz]	f_{06} [Hz]
I	306.781	841.187	1635.25	2627.0	3933.0	5397.5
II	307.062	842.062	1637.00	2676.0	3938,0	5405.0

The changes in first 6 natural frequencies were then successively measured for each increasing depth of a saw cut. The relative changes of natural frequencies as a function of a relative crack depth is shown in Figure 4. The changes of the first, third and fifth natural frequency are much bigger than those of the second, fourth and sixth. This phenomenon is in accordance with theoretical expectations, while the stresses at the mid point of the beam II, where the crack lies, are zero for the even modes of the natural flexural vibrations.

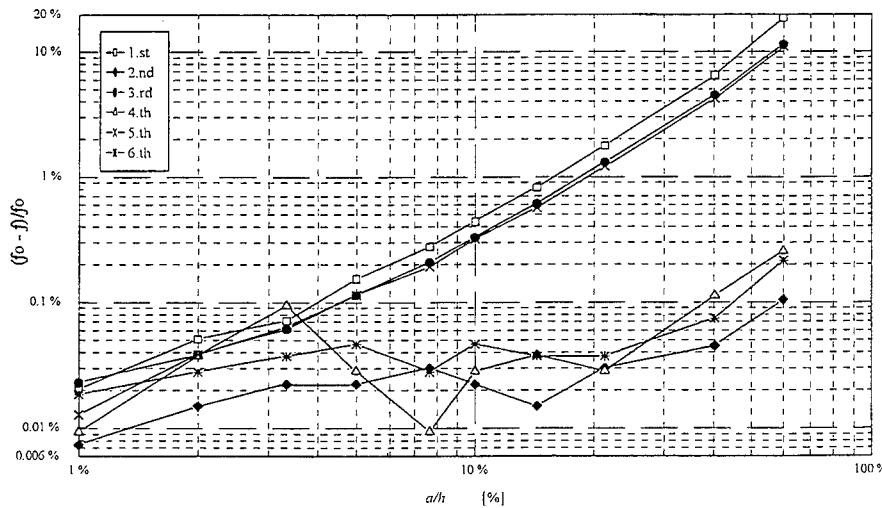


Figure 4. Changes of first 6 natural frequencies of flexural vibrations as a function of the crack depth for beam II in log-log plot

From the measured changes of natural frequencies first the effective values of the Young's modulus were calculated after eq. 6, see Table 3. The relative crack stiffness was computed next using eq. 11 for 10 different values of relative crack

for beam I are plotted against the relative crack position R/L and are shown in Figure 5.

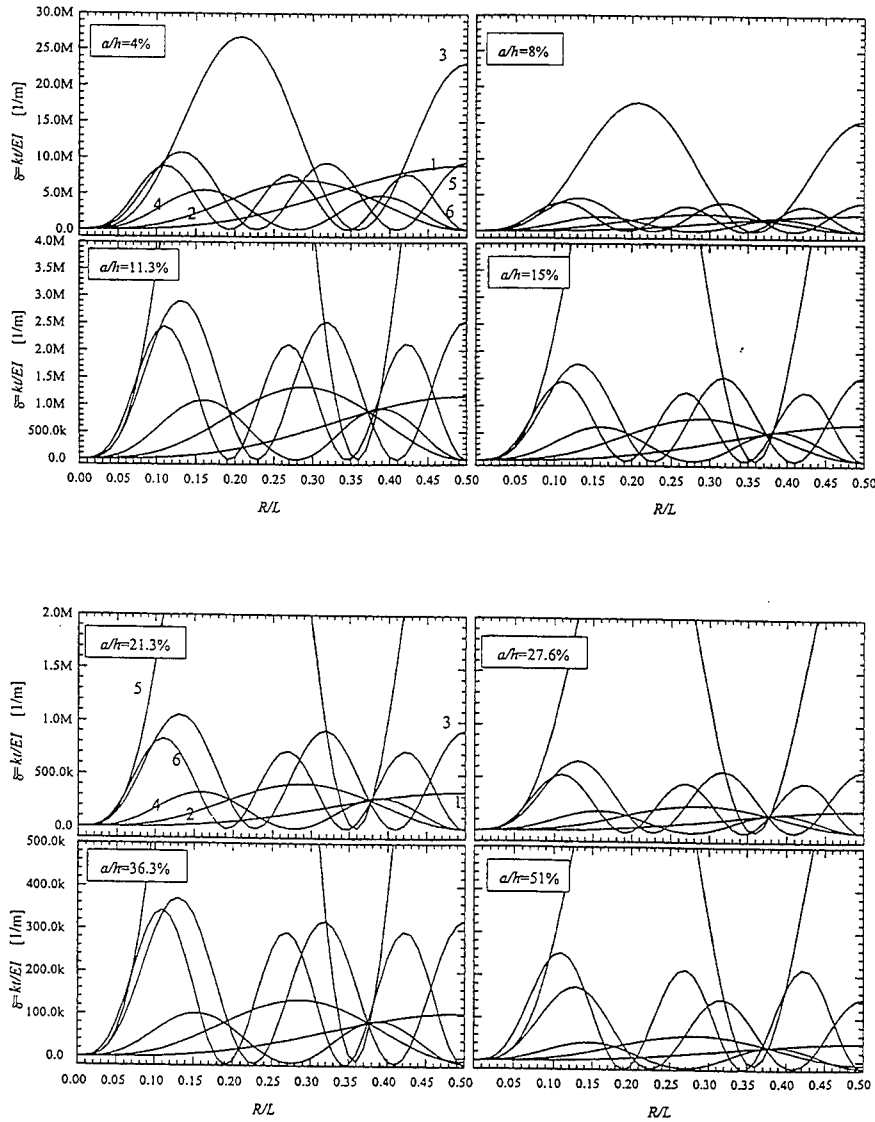


Figure 5. Relative crack stiffness versus crack position for first 6 natural frequencies and for 8 different relative crack depths, beam I

Table 3. Estimated values of effective values of the Young's modulus for the first natural frequencies after eq.6

Beam	Effective values of the Young's modulus $E_f [10^{11} Pa]$	
	AXIAL VIBRATIONS	FLEXURAL VIBRATIONS
I	2.03	1.92
II	2.04	1.93

For the relative crack depth of 4% one could hardly speak of a perfect intersection of all curves that represents the relative crack stiffness. Upward from 8% of the relative crack depth the intersection of curves is clearly seen. The true crack position was at $R/L=0.38$. In order to compare the adopted approach the natural frequencies of axial vibrations were also measured and the crack location identified, directly following the procedure of Adams *et al.* [1]. In Table 4 the differences of the identified crack location versus true values are shown both for axial and for flexural vibrations for beam I.

Table 4. Identification of the crack location for axial and flexural vibrations, difference to true crack site, for beam I

Relative crack depth [%]	AXIAL VIBRATIONS		FLEXURAL VIBRATIONS	
	R/L	difference [%]	R/L	difference [%]
4	0.37	-1.1	0.38	-0.1
8	0.29	-9.1	0.379	-0.2
11.3	0.34	-4.1	0.38	-0.1
15	0.33	-5.1	0.38	-0.1
21.3	0.35	-3.1	0.376	-0.5
27.7	0.36	-2.1	0.377	-0.4
36.6	0.368	-1.3	0.376	-0.5
51	0.37	-1.1	0.374	-0.7

As it can be seen from Table 4, the error of the damage site location at flexural vibrations is less than 1% in the range from 4 - 51% of the relative crack depth for the beam I. For the beam II in Table 5, the results are somewhat worse and the error lies in the range of about 1-3%. For both beams under consideration, we found in our case of free-free support the use of flexural vibrations superior over axial, which is also good enough for engineering purpose.

REFERENCES

1. R. D. ADAMS, P. CAWLEY, C. J. PYE and B. J. STONE 1978 *Journal of Mechanical Engineering Science* **20**(2), 93-100. A vibration technique for non-destructively assessing the integrity of structures.
2. P. F. RIZOS, N. ASPRAGATHOS and A. D. DIMAROGONAS 1990 *Journal of Sound and Vibration* **138**(3), 381-388. Identification of crack location and magnitude in a cantilever beam from the vibration modes.
3. A. K. PANDEY, M. BISWAS and M. M. SAMMAN 1991 *Journal of Sound and Vibration* **145**(2), 321-2. Damage detection from changes in curvature mode shapes.
4. T. G. CHONDROS and A. D. DIMAROGONAS 1980 *Journal of Sound and Vibration* **69**, 531-8. Identification of cracks in welded joints of complex structures.
5. S. CHRISTIDES and A. D. S. BARR 1984 *International Journal of Mechanical Sciences* **26**(11), 639-648. One-dimensional theory of cracked Bernoulli-Euler beams.
6. M.-H. H. SHEN and C. PIERRE 1990 *Journal of Sound and Vibration* **138**, 115-134. Natural modes of Bernoulli-Euler beams with symmetric cracks.
7. Y. NARKIS 1994 *Journal of Sound and Vibration* **172**(4), 549-558. Identification of crack location in vibrating simply supported beams.
8. A. D. DIMAROGONAS and C. A. PAPADOPOULOS 1983 *Journal of Sound and Vibration* **91**(4), 583-593. Vibration of cracked shafts in bending.
9. C. A. PAPADOPOULOS and A. D. DIMAROGONAS 1992 *Journal of Vibration and Acoustics* **114**, 461-467. Coupled vibration of cracked shafts.
10. P. GUDMUNDSON 1982 *Journal of the Mechanics and Physics of Solids* **30**(5), 339-353. Eigenfrequency changes of structures due to cracks, notches or other geometrical changes.

USE OF PVDF FOR DISTRIBUTED SENSING OF VIBRATIONS OF A BEAM

S. O. Oyadiji and M Solook
Dynamics & Control Research Group
Division of Mechanical Engineering
Manchester School of Engineering
University of Manchester
Manchester, M13 9PL, UK

ABSTRACT

The analytical and experimental response characteristics of a distributed piezoelectric sensor film bonded to a vibrating beam are presented. Distributed sensors are designed on the basis of the principle of orthogonality of the mode shapes of vibrating structures and are used to monitor specific modes of vibration of the structure. In this paper a shaped distributed sensor is designed to monitor the first mode of a simply-supported beam. It is shown that by subdividing this mode one sensor into two halves, the sensor can be developed to monitor the second mode as well. A mathematical model is developed to predict the response of the sensor. It is shown that the theoretical response match well the experimental response for the first mode and that the theoretical response of the second mode almost match as well the experimental response. Furthermore, it is shown that the output charge generated by the distributed piezoelectric sensor is maximum for the desired mode whereas it is about zero for all other modes.

INTRODUCTION

Much research effort is being currently directed to active vibration control using piezoelectric sensors and actuators. Passive techniques are sometimes insufficient to control the vibrations of some structures. Also, passive techniques may not work very well for the fundamental modes of vibrations of structures especially at low frequencies. Furthermore, for structures for which weight minimisation is an important consideration, passive vibration technique may not be acceptable because it involves fixing additional damping materials to

the structure which leads to an increase in weight. In all these cases, active vibration control techniques need to be applied.

Active vibration control using discrete point sensors such as accelerometers often has spill over and instability problems since these types of vibration sensors detect the vibrations due to all of the modes of vibration of a structure at the same time. Applying the output signal from such discrete sensor to actuators located at specific points on the structure in order to actively damp some modes might also excite other modes and/or cause the response of these other modes to become worse.

In this paper, a new category of sensors known as distributed sensors is presented. These sensors are able to identify a specific mode of vibration of a structure clearly without the need for extensive signal processing. Distributed sensors are bonded to the surface of the structure and collect data from all points of the surface to generate a total output signal. By changing the local effective area of the sensor and by using the directional properties of the sensor film, maximum total output charge is obtained for a desired mode of vibration whereas a zero or a minimum output charge is obtained for all other modes. A distributed sensor can be designed when the vibration characteristics, especially mode shapes of a structure are fully known. However, the identification of the mode shapes of the structure usually requires the use of discrete sensors. Distributed sensors are made from piezoelectric films, such as polyvinylidene fluoride (PVDF) films, that are very thin and light.

Bailey and Hubbard [1] used PVDF films as a spatially distributed actuator to control the vibration modes of a cantilevered beam. Lee and Moon [2] designed a distributed sensor for a cantilevered beam to detect the modes of vibration. Clark, Burdisso and Fuller [3] designed two distributed sensors for detecting the modes of vibration of a simply-supported beam and a simply-supported plate. Claus and Nohr Larsen [4] made a modal sensor for a simply-supported plate in which some parts of the sensor film were removed so that the sensitivity of the film varied along the X and Y directions. Gu, Clark and Fuller [5] designed and then proved experimentally a two dimensional sensor for a simply-supported plate. They used two separate one dimensional sensors in X and Y directions to monitor a two dimensional mode. Baz, Poh and Gilheany [6] designed a distributed sensor consisting of a set of shape memory alloy (SMA) wires which were embedded off the neutral axes of vibrating

composites beam to monitor continuously not only the modal displacements but also the physical displacement at a point.

Although most of these distributed sensors are different in their shapes, their designs are based on the same theory of the orthogonality of mode shapes. Since each distributed sensor is usually designed for only a specific mode of vibration and, on the other hand, it may not be possible to bond more than one or two of these sensors on one side of a beam or plate, only few modes of vibration can be measured selectively using the classical design of distributed sensors. Solook and Oyadiji [7] have shown experimentally that a distributed sensor which is designed for monitoring the first mode of vibration of a simply-supported beam can be used to detect the second mode as well. This involves subdividing the sensor into two halves.

To some extent, distributed sensors are almost more reliable and sometimes easier to use than a series of point sensors to identify a vibration mode. Since point sensors detect vibrations due to all of the modes, they are sometimes ineffective in identifying very close natural modes, such as bending and torsional modes which, have very close natural frequencies and their frequency response characteristics merge with each other. However, most of the distributed sensors which have been reported in the literature can only be used for monitoring one mode of vibration.

In this paper, a distributed sensor which has the capability of monitoring more than one mode of vibration of a simply-supported beam is presented analytically and experimentally. The shaped sensor considered here is the classical semi-sinusoidal shape which is designed for sensing the first mode of vibration of a simply-supported beam. It is shown that by dividing this shaped sensor into two halves, the first mode of vibration of the beam can be monitored simply by adding the output charge from each half while the second mode of vibration of the beam is monitored by subtracting the output charge of one half from that of the other half.

THEORY

The design of distributed sensors is based on the orthogonality principle. Application of this principle results in an output response for only a desired mode and no response for the other modes of vibration of a structure. The charge generated in a piezoelectric film

can be determined by integrating the induced strain over the surface on which the film is bonded as [8]:

$$q = -z \int_s F(x, y) P_0 \left(e_{31} \frac{\partial^2 w}{\partial x^2} + e_{32} \frac{\partial^2 w}{\partial y^2} + 2e_{36} \frac{\partial^2 w}{\partial x \partial y} \right) dx dy \quad (1)$$

where z is the distance of the piezo electric film from the neutral axis, e_{ij} are piezoelectric constants in different directions, w is displacement, s refers to the surface, P_0 is polarity which can be positive or negative depending on the direction of polarisation, and $F(x,y)$ has a value of one on the sensor electrode and zero for points on the structure which are outside the boundaries of the sensor.

For a one dimensional structure such as a beam, in which the longitudinal axis of the piezo film coincides with the beam axis, Eq. (1) is simplified to,

$$q = -z \int_0^L F(x) \cdot P_0 \cdot \left(e_{31} \frac{\partial^2 w}{\partial x^2} \right) \cdot dx \quad (2)$$

The transverse displacement of a beam can be written as the sum of its modes as,

$$w(x, t) = \sum_i A_i(t) \varphi_i(x) \quad (3)$$

where $A_i(t)$ is generalised co-ordinate, $\varphi_i(x)$ is mode shape of the i -th mode. The transverse displacement of a simply-supported beam is [7],

$$w(x, t) = \sum_i A_i(t) \sin\left(\frac{i\pi x}{L}\right) \quad (4)$$

Strain distribution over the beam surface is proportional to the second derivative of the mode shapes ($\epsilon \propto \frac{\partial^2 w}{\partial x^2}$). If the shape of a distributed piezoelectric film is defined by a function that is proportional to the second derivative of a specific mode (e.g. $F(x) \propto \frac{\partial^2 w_n}{\partial x^2}$ for n -th mode), then the total output charge from the

another shaped sensor which is designed specifically to detect mode 2 and is bonded to the beam. A different approach is proposed in this paper and has been illustrated experimentally in a previous paper [6]. This approach involves the use of the mode 1 sensor which is divided into two halves as shown in Figure 1. In order to monitor mode 1 of the vibration of the simply-supported beam, the charge output from each half are summed to give

$$q_{total} = q_{Left} + q_{Right} \quad (7)$$

while mode 2 of vibration of the beam is given by the difference of the charge outputs as

$$q_{total} = q_{Left} - q_{Right} \quad (8)$$

The results show that this single sensor is very effective in detecting mode 1 and quite effective in detecting mode 2 of a simply-supported beam as well.

MATHEMATICAL MODELLING

An analytical model is derived to predict the response of the distributed sensor bonded to the surface of a simply-supported beam. The model is derived using the Rayleigh-Ritz method where the kinetic and potential energies are, respectively, given by

$$\text{Kinetic Energy: } T = \frac{1}{2} \int_0^l \rho A \dot{w}^2 dx \quad (9)$$

$$\text{Potential Energy: } U = \frac{1}{2} \int_0^l EI w''^2 dx \quad (10)$$

ρ , A and \dot{w} refer to density, cross-sectional area of the beam and transverse velocity, respectively, and E , I and w'' refer to Young's modulus, moment of inertia and second derivative of displacement in x direction (longitudinal beam direction) respectively.

If the first two modes of vibration are considered, then the displacement can be written as,

$$w(x,t) = A_1(t)\phi_1(x) + A_2(t)\phi_2(x) \quad (11)$$

where $A(t)$ and $\phi(x)$ are generalised co-ordinates and shape functions, respectively, and subscript 1 and 2 refer to the first and second modes.

Applying Lagrange's method gives the the equation of motion, in matrix form , as

$$[M]\{\ddot{\eta}\} + [K]\{\eta\} = \{Q\} \quad ; \quad \eta_i(t) = A_i(t) \quad (12)$$

where $\eta_i(t)$ denotes generalised displacement and $Q(t)$ refers to generalised force. By using the solutions of Eq. (12) in conjunction with Eq. (11), the output charge of the shaped sensor can be determined for modes 1 and 2 using Eqs (2), (7) and (8).

EXPERIMENTAL SET-UP

Two pieces of PVDF film of dimensions 260×50 mm each were bonded to an aluminium beam of dimensions 540×51×3.2 mm thick using a double-sided tape. By means of a sharp blade, the PVDF films were cut into the mode 1 sensor shape shown in Figure 1. The beam, which was simply-supported on a knife-edge support, was subjected to a random excitation using a Gearing and Watson electronic shaker type GWV4/II. The shaker was attached to the beam via a stinger and a force transducer of type PCB 208B. In order to compare the response of the beam monitored by the distributed PVDF film with that of a discrete sensor, an accelerometer was fixed to the beam at point $x=0.28L$ where L is the length of the beam. By means of an Onosokki CF-350 spectrum analyser, frequency response functions between the PVDF sensor output and the amplified input force excitation, and between the accelerometer output response and the input force were obtained

DISCUSSION OF THE RESULTS

In Figure 2 is shown the comparison between the theoretical and experimental frequency response functions (FRF) obtained using the discrete (accelerometer) sensor. The figure shows that the beam has four natural frequencies and mode shapes within the frequency band of 0→500 Hz of the external excitation. The differences between the

theoretical and experimental FRF in terms of natural frequencies and peak amplitudes are caused by three main reasons. These are firstly, effect of boundary conditions, secondly, effect of damping characteristic of the double-sided tape and PVDF and thirdly, effect of additional masses.

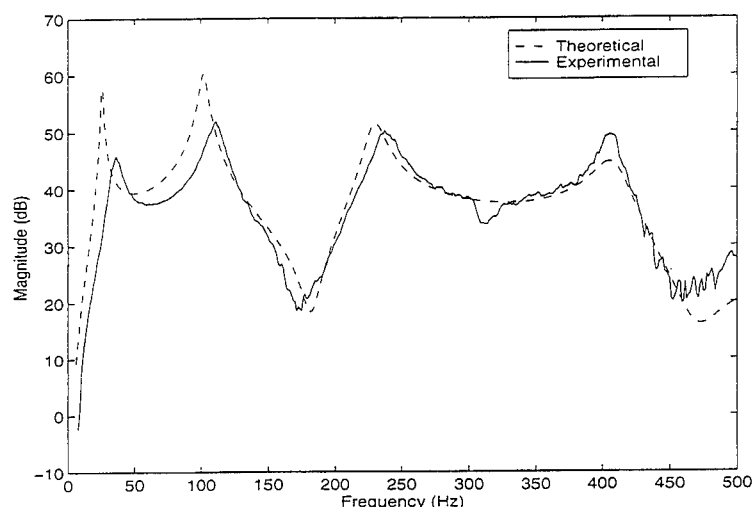


Figure 2 : Theoretical and Experimental Frequency Response Ratio of Accelerometer Response to Input Force for a Simply-Supported Beam.

The two pairs of knife edges used to support the ends of the beam are expected to make line contacts with the surfaces of the beam. However if the knife edges are not pressed sufficiently to make complete line contacts with the beam surfaces, or if the beam ends are twisted, then there will be gaps between the beam surfaces and the knife edges. This will result in point or partial contacts between the beam and knife edges instead of line contacts. On the other hand, if the knife edges are pressed too much into the beam surfaces at the two ends of the beam, then they dig into the beam surfaces and create resistant moments at the boundary. Thus there is a change in the boundary conditions from simply-supported conditions to a partially-clamped condition with depends on the level of the clamping force.

The double-sided tape and the PVDF film have passive damping effects. The damping characteristics of the tape and PVDF film were

not determined, but a total composite damping was considered in predicting the frequency response functions of the beam. A value of 12% was used for the composite loss factor of the beam, double-sided tape and PVDF assembly in the predictions. This value of composite loss factor was found to give the best overall correlation between the predicted and measured frequency response characteristics of the beam. The effects of the additional masses of the force transducer and its connector, accelerometer, double-sided tape and PVDF film should also be considered for a more accurate model. In spite of these factors, it is seen that the predicted FRF for the discrete (accelerometer) sensor correlates quite reasonably with the measured FRF.

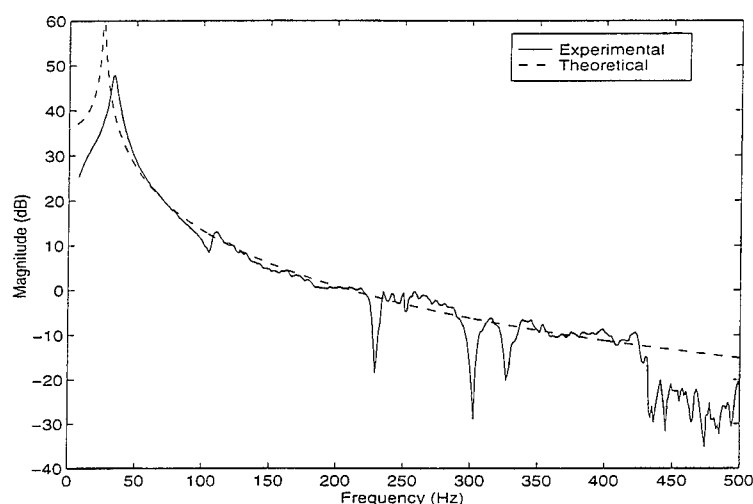


Figure 3: Theoretical and Experimental Frequency Response Functions of PVDF Response for Mode 1 with reference to Input Force.

Figure 3 shows the theoretical and experimental frequency response functions obtained from the shaped PVDF sensor film when the output charge from the two halves of the modified PVDF sensor, shown in Figure 1, are summed to produce the charge output for mode 1 of a simply-supported beam. In the theoretical predictions, the composite damping ratio of the beam, double-sided tape and PVDF assembly was also assumed as 12%. It is seen from Figure 3 that there is a discrepancy between the theoretical and experimental modal frequencies and modal amplitudes. This discrepancy is due to the three

factors enumerated earlier. However, beyond the modal frequency, there is close agreement between theoretical and experimental characteristics.

Comparing Figures 2 and 3, and overlapping the theoretical FRFs from both figures as shown in Figure 4, it is obvious that the PVDF sensor detects only the first mode of vibration of the simply-supported beam when its two output charges are added. Thus the addition of the output charges from the two halves of the PVDF sensor produces an identical response to that of a classical mode 1 sensor design for a simply-supported beam which does not involve the division of the semi-sinusoidal shape into two halves.

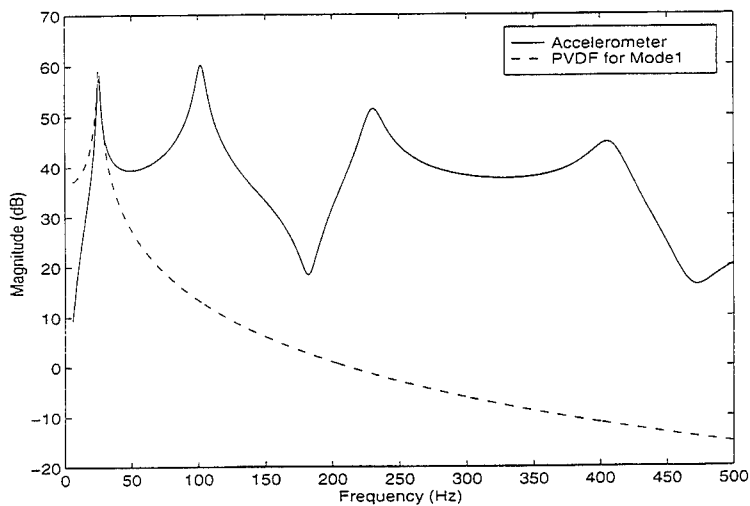


Figure 4: Theoretical Frequency Response Functions of PVDF Mode 1 and Accelerometer Response Signals with reference to Input Force.

The theoretical and experimental frequency response functions obtained from the difference of the output charges from the two halves of the shaped PVDF sensor are shown in Figure 5. In calculating the theoretical FRF, the same value of 12% was assumed for the composite damping ratio of the beam, double-sided tape and PVDF assembly. Figure 5 shows that the correlation between the theoretical and experimental FRFs is quite close. Comparing Figure 5 with Figure 2, and comparing the theoretical FRFs of the PVDF sensor output with

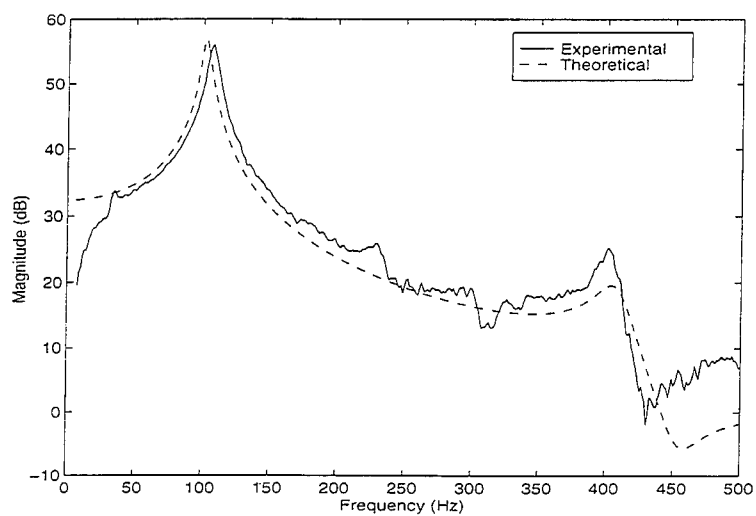


Figure 5: Theoretical and Experimental Frequency Response Functions of PVDF Response for Mode 2 with reference to Input Force

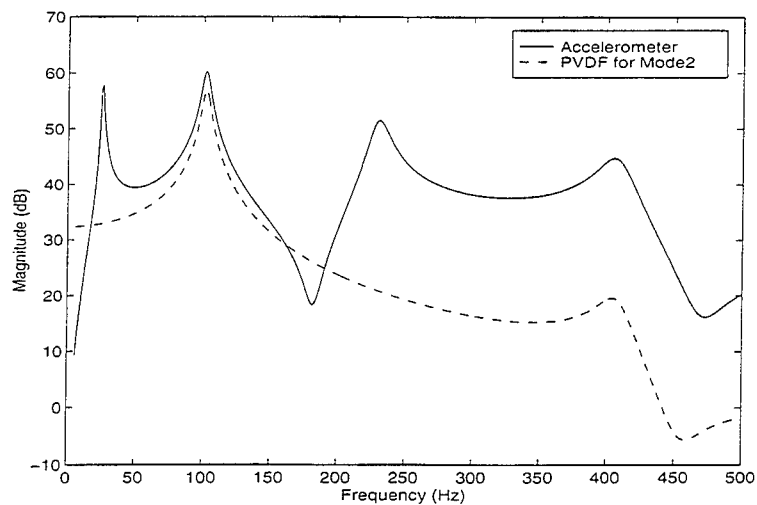


Figure 6: Theoretical Frequency Response Functions of PVDF Mode 2 and Accelerometer Responses with reference to Input Force.

the discrete sensor output as shown in Figure 6, it is obvious that the PVDF sensor now only indicates the second mode of vibration of the simply-supported beam.

Figures 5 and 6 further show that the PVDF sensor, in this case, also generates a small but significant response for the fourth mode of vibration of the beam as well. Although the level of the PVDF response for this fourth mode is considerably less than the level of the mode 4 response indicated by the accelerometer, this mode 4 response of the PVDF sensor indicates that it is not acting as a pure mode 2 sensor. This slight discrepancy is the main disadvantage of the use of a mode 1 shaped sensor as a mode 2 sensor. Nevertheless, the main and overriding advantage is that by dividing the classical semi-sinusoidal shape of the mode 1 shape sensor for a simply-supported beam into two halves, the sensor can be used to sense both modes 1 and 2 of vibration of the simply-supported beam with a reasonable degree of accuracy.

CONCLUSIONS

The theoretical basis for the design of shaped sensors for selective sensing of the modes of vibration of a structure, and of a simply-supported beam in particular, has been outlined. It has been shown that by dividing the classical semi-sinusoidal shape of the mode 1 distributed sensor of a simply-supported beam into two halves, the sensor can be used for selective sensing of the first and the second modes of vibration of the beam. The theoretical model and the experimental results show that when the sum of the output charges are used, the PVDF sensor only detects the first mode of vibration of the beam, whereas when the difference of the output charges are used, the PVDF sensor mainly detects the second mode of vibration.

REFERENCES

1. Bailey, T. and Hubbard, J.E., Distributed Piezoelectric Polymer Active Vibration Control of a Cantilever Beam. *J. of Guidance, Control and Dynamics*, 1985, Vol. 8, 605-611.
2. Lee, C.K. and Moon, F.C, Modal Sensors/Actuators", *ASME J. of Applied Mechanics*, June 1990, 57, pp. 434-441.

-
3. Clark, R.L., Burdisso, R.A. and Fuller, C.R., Design Approaches for Shaping Polyvinylidene Fluoride Sensors in Active Structural Acoustic Control (ASAC), *J. of Intelligent Material Systems and Structures*, July 1993, 4, pp. 354-365.
 4. Larsen, C. and Larsen, P.N., A New Modal Sensor for Active Vibration Control of Plates, *17th International Seminar on Modal Analysis, KULeuven*, 1992, pp. 1717-1729.
 5. Gu, Y., Clark, R.L., Fuller, C.R. and Zander, A.C., Experiments on Active Control of Plate Vibration Using Piezoelectric Actuators and Polyvinylidene Fluoride (PVDF) Modal Sensors, *ASME J. of Vibration and Acoustics*, July 1994, 116, pp. 303-309.
 6. Baz, A., Poh, S. and Gilheany, J., A Multi-Mode Distributed Sensor for Vibrating Beam. *J. of Sound and Vibration*, 1993, 165(3), pp. 481-495.
 7. Solook, M. and Oyadiji, S. O., Distributed PVDF Sensor for a Vibrating Beam, *Proceedings of Sensors and Actuators Conference, Manchester*, July 1996.
 8. Blevins, R.D., *Formulas for Natural Frequency and Mode Shape*, Van Nostrand Reinhold, NY 1979.

NONLINEAR VIBRATION I

EFFECTS OF DAMPING ON SECONDARY RESONANCES IN TORSIONAL VIBRATIONS OF A TWO-DEGREE-OF-FREEDOM SYSTEM - A VARIABLE INERTIA ASPECT IN RECIPROCATING ENGINES

M.S. Pasricha and A.Y. Hassan

School of Mechanical Engineering, Universiti Sains Malaysia,
Perak Branch Campus, Seri Iskandar, 31750 Tronoh, Perak, Malaysia

The torsional vibration problem in reciprocating engines is described by representing the reciprocating mechanism by a constant inertia and the damping forces in the system as proportional to velocity. However in reality, a slider crank mechanism is a vibrating system with varying inertia because the effective inertia of the total oscillating mass of each crank assembly varies twice per revolution of the crankshaft. This variation in inertia of the reciprocating parts causes vibratory phenomenon which cannot be explained by conventional theory incorporating only the mean values of the varying inertias. When inertia variations are small, this type of approximate analysis usually leads to satisfactory designs. But a number of engines are now in service whose pistons are so massive that large variations in inertia torques can be serious for torsional vibration causing secondary resonance effects and even instability. In the past the effects of ignoring the variable inertia characteristics of reciprocating engines on the accuracy of torsional vibration calculations were considered to be negligible but the situation changed in recent years since there was evidence of the existence of the secondary resonance effects which could have contributed to a number of otherwise inexplicable crankshaft failures in practice. It is obviously necessary to abandon the assumption of constant inertia and the analysis should take some account of variable inertia effects.

The cyclic variation of the polar moment of inertia of the reciprocating parts during each revolution causes a periodic variation of frequency and corresponding amplitude of vibration of reciprocating engine systems. It also causes an increase in the speed range over which resonance effects are experienced. In the present paper a study of the effects of damping on the motion of a two-

cylinder-in-line reciprocating engine treating it as a system with position dependent inertias, has been carried out. Taking into consideration these facts, the equations of motion are non-linear. For small displacements the equations can be linearized to predict important characteristics of the motion.

Computer methods making use of numerical analysis process, namely the Runge-Kutta equations have been applied in the investigations. The waveform responses are studied at different speeds of engine rotation. The effects of damping and of variations in the ratio of the average reciprocating inertia to average total inertia on the boundaries between resonant and non-resonant frequencies have been investigated.

INTRODUCTION

For many years the effects of the variable inertia characteristics of reciprocating engines on the accuracy of torsional vibration calculations were considered to be negligible. But in recent years several cases of crankshaft failures in large slow speed marine engines could not be explained by neglecting the variation in inertia torques of the system arising from the motion of the reciprocating parts. After repairs, measurements taken in some cases indicated torsional vibration stresses at service speed up to five times greater than expected.

In the afore-mentioned cases of crankshaft failures in practice, the conventional stress analysis carried out to predict the vibration characteristics of the engine systems showed that all the stresses were within the safe limits of the material used. Therefore, it is of considerable interest to examine in greater detail the effect of the reciprocating parts in producing or modifying the vibrations. The simplified theory neglecting the effect of variable inertia is also not adequate to explain the existence of the secondary resonance phenomenon in torsional vibrations of modern marine diesel engines - that is to say, the possibility of an n th order critical of small equilibrium amplitude occurring at or near resonance with the service speed being excited by large resultant engine excitations of order $(n - 2)$ and $(n + 2)$.

Draminsky [1] explained the phenomenon of secondary resonance in multi-cylinder engines by use of a non-linear theory and showed that this phenomenon occurred due to the variation in inertia

torques of the system arising from the motion of the reciprocating parts. Meanwhile Archer [2] added further information by citing examples of crankshaft failures in large ten-cylinder and twelve-cylinder marine engines and the Draminsky calculation in such cases clearly demonstrated the existence of a phenomenon whereby an otherwise innocuous critical in the region of the service speed could be considerably modified by interaction with a powerful, but non-resonant excitation of the $(n - 2)$ harmonic type. Pasricha and Carnegie [3,4] carried out further investigations to explain the secondary resonance phenomenon and an effort was made to understand and present the effects of variable inertia on the vibratory motion of the crank-connecting rod system more clearly than in the past.

Failures have not occurred in all cases of engines in service which were considered to be susceptible to secondary resonance and it was found that Draminsky's work based on reducing a multi-cylinder engine to an equivalent single cylinder system served only to indicate, in very broad terms, the circumstances in which adverse secondary effects could be anticipated. In view of this Pasricha [5] carried out a case study on two stroke cycle engine with suspected secondary resonance which turned out to be a case in which the predicted Draminsky resonance magnification failed to appear when measurements were taken.

It is against this background that the authors studied work done by the researchers [6, 7] to construct a non-linear theory allowing for variable inertia effects and more recently the work on the parametrically excited systems [8-10]. These methods tend to be specialized and the amount of information thus gained is inadequate for a design situation. Further these methods do not provide waveform solutions at different speeds of the crankshaft. It is important for the designer to obtain these solutions as the harmonic analysis of the waveform responses can predict the order number of external excitations that have significant effect on the vibratory motion [11]. Most mathematical formulations of the problem to date have omitted some important aspects while trying to resolve this situation and thus the aim of obtaining a full understanding of the phenomenon of secondary resonance in multi-cylinder engines, without simplifying the system into an equivalent single-cylinder system as suggested by Draminsky is yet to be realized. Also the stability of such systems is the subject of a great deal of current interest to the design engineers.

The results of the present paper predict the characteristics of motion, regions of instability and the shapes of the complex waveforms at different speeds of the two cylinder engine system, the

engine being considered as a variable inertia system including the effect of damping.

EQUATIONS OF MOTION

Figure 1 shows diagrammatically a two-cylinder-in-line reciprocating engine driving a heavy flywheel A of moment of inertia I_A (a list of symbols is given in the Appendix). The radius of each crank is 'a' and the connecting-rod to crank ratio is assumed to be large such that the reciprocating masses move with simple harmonic motion. With the mass of the connecting-rod divided into two lumped masses, one at the crank pin and the other at the piston cross-head assembly, the total mass of the reciprocating parts per cylinder is denoted by M and the total moment of inertia of the rotating parts by I. Since the inertia of the flywheel A is very large, its angular velocity, ω , can be assumed to be constant.

It is convenient to measure the rotations of the cranks relative to the unstrained equilibrium configuration of the system which exists when the crank in the cylinder line nearest to the flywheel is in its top dead centre position. At any time t when the system is rotating and vibrating, the rotations of the cranks from their datum positions will be denoted by θ_1 and θ_2 and torsional stiffnesses are represented by C_1 and C_2 .

The equations of Lagrange for the coordinates θ_i are

$$d(\partial T / \partial \dot{\theta}_i) / dt - \partial T / \partial \theta_i = Q_{\theta i} ; \quad i = 1, 2 \quad (1)$$

where T is the kinetic energy of the system and $Q_{\theta i}$ includes both conservative and non-conservative forces. The conservative force $(Q_{\theta i})_c$ can be derived from the potential energy expression U and the non-conservative force $(Q_{\theta i})_{nc}$ is the dissipative function. Hence

$$Q_{\theta i} = (Q_{\theta i})_c + (Q_{\theta i})_{nc} \quad (2)$$

where

$$(Q_{\theta i})_c = -\frac{\partial U}{\partial \theta_i}, \quad (Q_{\theta i})_{nc} = -\rho \dot{\theta}_i \quad (3)$$

The kinetic energy, T , and potential energy, U , for the system are given by

$$T = \frac{1}{2} I_A \omega^2 + \frac{1}{2} \left[I + \frac{1}{2} Ma^2 (1 - \cos 2\theta_1) \right] \dot{\theta}_1^2 + \frac{1}{2} \left[I + \frac{1}{2} Ma^2 \{1 - \cos 2(\pi + \theta_2)\} \right] \dot{\theta}_2^2 \quad (4)$$

$$U = \frac{1}{2} C_1 (\theta_1 - \omega t)^2 + \frac{1}{2} C_2 (\theta_2 - \theta_1)^2 \quad (5)$$

If piston gas forces are neglected and torsional stiffness $C_1 = C_2 = C$, substitution of the relations (3), (4) and (5) in equation (1) shows that the equations of motion of the system are

$$\left(I + \frac{1}{2} Ma^2 - \frac{1}{2} Ma^2 \cos 2\theta_1 \right) \ddot{\theta}_1 + \frac{1}{2} Ma^2 \dot{\theta}_1^2 \sin 2\theta_1 + C(2\theta_1 - \theta - \theta_2) = -\rho \dot{\theta}_1 \quad (6a)$$

$$\left(I + \frac{1}{2} Ma^2 - \frac{1}{2} Ma^2 \cos 2\theta_2 \right) \ddot{\theta}_2 + \frac{1}{2} Ma^2 \dot{\theta}_2^2 \sin 2\theta_2 + C(\theta_2 - \theta_1) = -\rho \dot{\theta}_2 \quad (6b)$$

Since

$$\theta = \omega t, \quad \theta_1 = \omega t + \gamma_1, \quad \theta_2 = \omega t + \gamma_2$$

and when the second and higher order terms are neglected equations (6) can be linearized into the form

$$\begin{aligned} & \left(I + \frac{1}{2} Ma^2 - \frac{1}{2} Ma^2 \cos 2\omega t \right) \ddot{\gamma}_1 + \left(Ma^2 \omega \sin 2\omega t \right) \dot{\gamma}_1 \\ & + \rho(\omega + \dot{\gamma}_1) + \left(Ma^2 \omega^2 \cos 2\omega t + 2C \right) \gamma_1 - C \gamma_2 \\ & = \frac{1}{2} Ma^2 \omega^2 \sin 2\omega t \end{aligned} \quad (7a)$$

$$\begin{aligned}
& \left(I + \frac{1}{2} Ma^2 - \frac{1}{2} Ma^2 \cos 2\omega t \right) \ddot{\gamma}_2 + \left(Ma^2 \omega \sin 2\omega t \right) \dot{\gamma}_2 \\
& + \rho \left(\omega + \dot{\gamma}_2 \right) + \left(Ma^2 \omega^2 \cos 2\omega t + C \right) \gamma_2 - C \gamma_1 \\
& = -\frac{1}{2} Ma^2 \omega^2 \sin 2\omega t
\end{aligned} \tag{7b}$$

If one makes use of the equations

$$\varepsilon = \frac{1}{2} Ma^2 / \left(I + \frac{1}{2} Ma^2 \right), \quad 1/v^2 = C / \omega^2 \left(I + \frac{1}{2} Ma^2 \right)$$

and changing the independent variable to $\tau = \omega t$ and letting dashes represent differentiation with respect to τ , equations (7) become

$$\begin{aligned}
& (1 - \varepsilon \cos 2\tau) \gamma_1'' + \left[2\varepsilon \sin 2\tau + \left\{ \rho / \omega \left(I + \frac{1}{2} Ma^2 \right) \right\} \right] \gamma_1' \\
& + \left\{ 2\varepsilon \cos 2\tau + \left(2/v^2 \right) \right\} \gamma_1 - \left(\gamma_2 / v^2 \right) \\
& = -\left\{ \rho / \omega \left(I + \frac{1}{2} Ma^2 \right) \right\} - \varepsilon \sin 2\tau
\end{aligned} \tag{8a}$$

$$\begin{aligned}
& (1 - \varepsilon \cos 2\tau) \gamma_2'' + \left[2\varepsilon \sin 2\tau + \left\{ \rho / \omega \left(I + \frac{1}{2} Ma^2 \right) \right\} \right] \gamma_2' \\
& + \left\{ 2\varepsilon \cos 2\tau + \left(1/v^2 \right) \right\} \gamma_2 - \left(\gamma_1 / v^2 \right) = \\
& -\left\{ \rho / \omega \left(I + \frac{1}{2} Ma^2 \right) \right\} - \varepsilon \sin 2\tau
\end{aligned} \tag{8b}$$

Upon making use of an additional parameter defined by

$$2\xi \sqrt{C / \left(I + \frac{1}{2} Ma^2 \right)} = \rho / \left(I + \frac{1}{2} Ma^2 \right), \tag{9}$$

where ξ is the damping ratio associated with each cylinder, equations (8) reduce to

$$\begin{aligned}
& (1 - \varepsilon \cos 2\tau) \gamma_1'' + \{2 \varepsilon \sin 2\tau + (2\xi / v)\} \gamma_1' \\
& + \{2 \varepsilon \cos 2\tau + (2 / v^2)\} \gamma_1 - (\gamma_2 / v^2) = -(2\xi / v) - \varepsilon \sin 2\tau
\end{aligned}
\tag{10a}$$

$$\begin{aligned}
& (1 - \varepsilon \cos 2\tau) \gamma_2'' + \{2 \varepsilon \sin 2\tau + (2\xi / v)\} \gamma_2' \\
& + \{2 \varepsilon \cos 2\tau + (1 / v^2)\} \gamma_2 - (\gamma_1 / v^2) = -(2\xi / v) - \varepsilon \sin 2\tau
\end{aligned}
\tag{10b}$$

With the effect of damping neglected, $\xi = 0$, equations (10) become

$$\begin{aligned}
& (1 - \varepsilon \cos 2\tau) \gamma_1'' + (2 \varepsilon \sin 2\tau) \gamma_1' + \{2 \varepsilon \cos 2\tau + (2 / v^2)\} \gamma_1 \\
& - (\gamma_2 / v^2) = -\varepsilon \sin 2\tau
\end{aligned}
\tag{11a}$$

$$\begin{aligned}
& (1 - \varepsilon \cos 2\tau) \gamma_2'' + (2 \varepsilon \sin 2\tau) \gamma_2' + \{2 \varepsilon \cos 2\tau + (1 / v^2)\} \gamma_2 \\
& - (\gamma_1 / v^2) = -\varepsilon \sin 2\tau
\end{aligned}
\tag{11b}$$

APPLICATION TO A TYPICAL MARINE ENGINE

The following data for a typical two cylinder engine was used to determine the response of the system at different speeds of rotation: equivalent inertia of rotating and reciprocating parts

$(I_m = I + \frac{1}{2} Ma^2)$ per cylinder, (kg-m ²).....	9,584
bore diameter (mm)	900
stroke (mm)	1,550
mip, (psi)	169.5
bhp	5,800
ε	0.3
one node frequency, (rad/s)	27.27
two node frequency, (rad/s)	71.4

With use being made of 100 steps over one cycle of the two node natural frequency of the system and the fourth order form of the Runge-Kutta relations of reference [11], equations (10) were programmed in C language for solution by a digital computer with the initial conditions $\gamma_1=1$ and $\gamma_1'=0$ at $\tau=0$, $\gamma_2=0$ and $\gamma_2'=0$ at $\tau=0$.

In Figures 2 to 5 are presented four regions of instability in the neighbourhood of $\nu = 0.309$ and $\nu = 0.618$ and also corresponding to $\nu = 0.809$ and $\nu = 1.618$ as determined from equations (11), the effects of damping being neglected. It was shown [12] that the frequency of vibration in the unstable regions in the vicinity of $\nu = 0.618$ and $\nu = 1.618$ is 1 cycle/rev of the crankshaft and in the regions of instability for $\nu \simeq 0.309$ and $\nu \simeq 0.809$ the frequency of vibration is 2 cycles/rev of the crankshaft. Outside these regions of instability the responses showed a modulation of amplitude and instantaneous frequency and that responses ($\gamma_2 \sim t$) are only slightly modified compared to corresponding ($\gamma_1 \sim t$) solutions.

The authors have further determined the boundaries between stable and unstable regions from equations (10) which include the effect of damping. The regions of instability are investigated for different values of the damping ratio ξ and for ϵ ranging from 0 to 0.8. The results of the investigations are incorporated in Figure 2 to 5 for comparison. The time responses at two specific speeds of crankshaft rotation corresponding to $\nu = 0.3$ and 0.4 for $\epsilon = 0.3$ when $\xi = 0.02$ are presented in Figures 6 and 7, respectively.

DISCUSSION OF RESULTS

In a system with constant inertia there are a series of well defined critical speeds corresponding to each mode and each order of vibration, but a perusal of Figures 2 to 5 shows that in a system with variable inertia these critical speeds are replaced by a number of regions of instability within which the amplitude of vibration may be limited by the amount of positive damping in the system. The two of the regions of instability occur when the values of parameter ν are approximately $\nu \simeq 0.618$ and $\nu \simeq 1.618$ and these values of ν correspond to the undamped torsional natural frequencies found from an equivalent linear time invariant system model. The other two

regions of instability occur at $\nu \simeq 0.309$ and $\nu \simeq 0.809$ which correspond to one half of the undamped natural frequencies found above. Engines having substantially heavy reciprocating parts are particularly unsatisfactory from the point of view of minimizing the effects of the reciprocating parts in exciting regions of instability.

In view of the practical importance of the subject and for the results obtained from numerical analysis to be more convincing, a comparison with the investigations based on the WKBJ approximation and the method of variation of parameters in a limited range of the shaft speeds for the linear motion of a single cylinder engine was discussed in another paper [13] and the results showed close agreement.

On comparison of Figures 2 and 4 with Figures 3 and 5 it becomes evident that the stabilizing effect of damping turns out to be much more pronounced when $\nu \simeq 0.309$ and $\nu \simeq 0.809$ than when $\nu \simeq 0.618$ and $\nu \simeq 1.618$. These investigations also show that if the value of the damping ratio is increased the ranges of instability become narrower and for every value of damping ratio ξ there is a certain threshold value of ε below which the motion is always stable. Figures 3 to 5 show that critical speed range at $\nu \simeq 0.618$ for first mode would coalesce with those at $\nu \simeq 0.809$ for $\varepsilon > 0.5$ and at $\nu \simeq 1.618$ for $\varepsilon > 0.7$.

Although there are no externally applied excitations, Figures 6 and 7 show, after the starting transient, a motion with sustained amplitude at two specific crankshaft speeds corresponding to $\nu = 0.3$ and $\nu = 0.4$ for $\varepsilon = 0.3$ and $\xi = 0.02$. Further analysis of such theoretical records at different speeds of the engine for $\varepsilon = 0.3$ shows that there are two vibration cycles in one revolution of the crankshaft for all values of ν below the unstable region $\nu \simeq 1.618$ and outside the instability region associated with first mode at $\nu \simeq 0.618$. The time responses at higher values of ν , namely, $\nu = 2, 4, 6$ etc., are repetitive complex waveforms. One such complex waveform is shown in Figure 8 for $\nu = 2, \varepsilon = 0.3$ and $\xi = 0.02$.

The complex waveform motions at higher values of ν , beyond the upper bound of the region of instability for $\nu \simeq 1.618$, are not of great practical interest. The secondary resonance evoked by variable inertia is considered to be detrimental only in cases of diesel engines which have their service speeds in the range of $\nu < 0.2$. These investigations are a step towards having a clear understanding of the behaviour of a variable inertia system.

Thus it can be seen that, for $\nu = 0.618; \xi = 0.02$ and $\nu = 1.618; \xi = 0.05$ and when ε is greater than 0.1, the motion is unstable, which means that the vibration amplitude can become large. Further investigations are required to study the effect of forcing terms on the

system within these unstable regions where the order number is unity and also with $\nu \leq 0.2$ where the higher order components of the forcing impulse become predominant.

CONCLUSIONS

The results presented in this paper give the analysis of the response of the variable inertia system representing a two-cylinder-in-line reciprocating engine with the effect of damping included. Due to the effect of the cyclic variation of engine inertia of the reciprocating parts, there are four principal regions in which unstable conditions can occur over an appreciable range of engine r.p.m without any externally applied excitation such as harmonic torque components arising from the cylinder gas pressure. These effects are particularly likely to occur in cases where the moment of inertia of the reciprocating parts is a large proportion of the total moment of inertia.

After the starting transient a motion with sustained amplitude is obtained at specific speeds of the engine outside the instability regions. At higher speeds beyond the upper bound of the instability region for $\nu \simeq 1.618$ the time responses become complex in form. For $\epsilon = 0.3$, the frequency of vibration is two cycles per revolution of the crankshaft for all speeds below the lower bound of the unstable region of $\nu \simeq 1.618$ and outside the critical speed range at $\nu \simeq 0.618$. In the regions of instability for $\nu \simeq 0.618$ and $\nu \simeq 1.618$, the frequency of vibration is one cycle per revolution of the crankshaft.

The effect of limiting the amplitudes by the positive damping torques which might be present in the system is more pronounced when $\nu \simeq 0.309$ and $\nu \simeq 0.809$ than when $\nu \simeq 0.618$ and $\nu \simeq 1.618$ and also if the value of the damping ratio ξ is increased the ranges of instability become narrower and the range of ϵ increases for which the motion is always stable. Thus the results of this paper are useful as a design guideline to select preferred operating speed ranges.

REFERENCES

1. Draminsky, P., Secondary resonance and subharmonics in torsional vibration. *Acta Polytechnica, Scandinavica*, Me 10, Copenhagen, 1961.

2. Archer, S., Some factors influencing the life of marine crankshafts. *Transactions of the Institute of Marine Engineers*, 1964, 76, 73 - 134.
3. Pasricha, M. S. and Carnegie, W.D., Effect of variable inertia on the damped torsional vibrations of diesel engine systems. *Journal of Sound and Vibration*, 1976, 46 (3), 339 - 345.
4. Pasricha, M. S. and Carnegie, W.D., Diesel crankshaft failures in marine industry- a variable inertia aspect. *Journal of Sound and Vibration*, 1981, 78 (3), 347 - 354.
5. Pasricha, M. S., A case study of secondary resonance in a diesel engine installation. *Journal of Institution of Engineers, Singapore*, 1985, 25, 27 - 31.
6. Brook, D. L., Shock-excited non-linear oscillation of a system having variable inertia. *Ph.D. Thesis, University of Cambridge*, 1958.
7. Porter, B., Non-linear torsional vibration of a two-degree-of-freedom system having variable inertia. *Journal of Mechanical Engineering Science*, 1965, 7, 101 - 113.
8. Zevin, A. A., Qualitative investigation of stability of periodic oscillations and rotations in parametrically excited nonlinear second-order systems. *Mechanics of Solids*, 1983, 18, No.2, 34 - 40.
9. Zadoks, R. I. and Midha, A., Parametric stability of a two degree-of-freedom machine system, Part I: Equations of motion and stability. *Transactions of ASME Journal of Mechanisms, Transmissions, and Automation in Design*, 1987, 109, 210 - 215.
10. Zadoks, R. I. and Midha, A., Parametric stability of a two degree-of-freedom machine system, Part II: Equations of motion and stability. *Transactions of ASME Journal of Mechanisms, Transmissions, and Automation in Design*, 1987, 109, 216 - 223.
11. Carnegie, W. and Pasricha, M. S., Effects of forcing terms and general characteristics of torsional vibrations of marine engine systems with variable inertia. *Journal of Ship Research*, 1974, 18, 131 - 138.
12. Pasricha, M. S., Secondary resonance in reciprocating engines - an examination of torsional vibration of a two-degree-of-freedom system having variable inertia. *Proceedings of the 5th International Conference on Recent Advances in Structural Dynamics*. Ed. N. S. Ferguson, H. F. Wolfe and C. Mei, The Institute of Sound and Vibration Research, University of Southampton, U.K., 1994.
13. Pasricha, M. S. and Carnegie, W.D., Application of the WKBJ approximation processes for the analysis of the torsional vibrations of diesel engine systems. *Stress, Vibration and Noise Analysis in Vehicles*, ed. H.G. Gibbs and T.H. Richards, Applied Science Publishers, London, 1987, 439-49.

APPENDIX : NOTATION

a	crank radius
I_A	moment of inertia of flywheel A
I	moment of inertia of rotating parts per cylinder
M	mass of reciprocating parts per cylinder
v	ratio of angular velocity ω of crankshaft to ω_n
γ_i	displacement of torsional motion ($i = 1$ or 2) in rad
θ_1, θ_2	crank rotations
ε	$\frac{1}{2} Ma^2 / \left(I + \frac{1}{2} Ma^2 \right)$
t	time in seconds
ω	steady angular velocity of crankshaft
ω_n	$\left[C / \left(I + \frac{1}{2} Ma^2 \right) \right]^{\frac{1}{2}}$
ρ	viscous damping coefficient

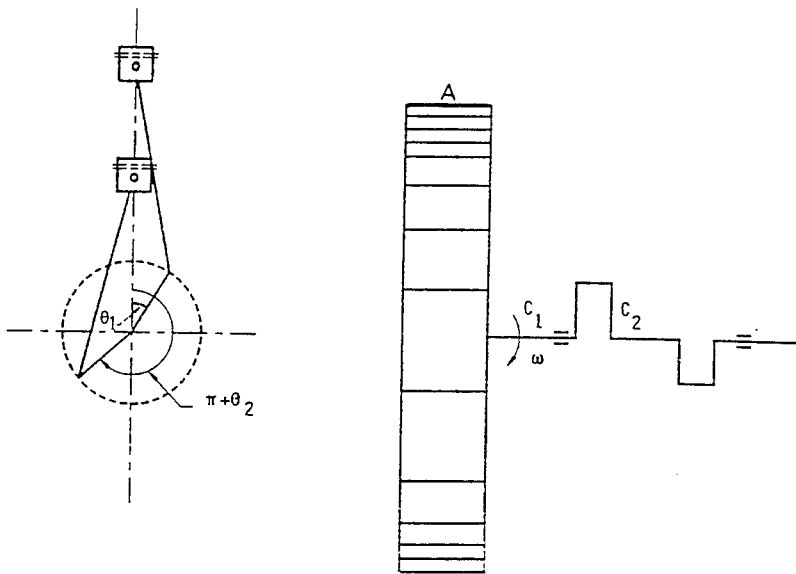


Figure 1. Diagram of the crankshaft

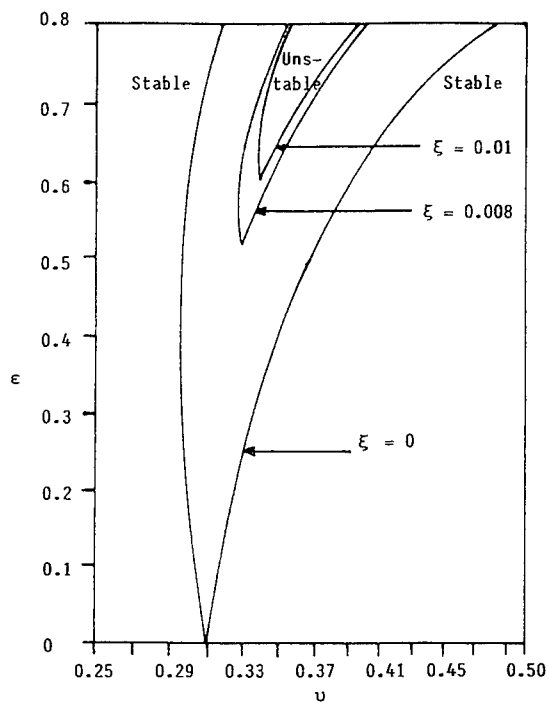


Figure 2. Stability diagram ($\epsilon \sim \nu$) for the region $\nu \approx 0.309$

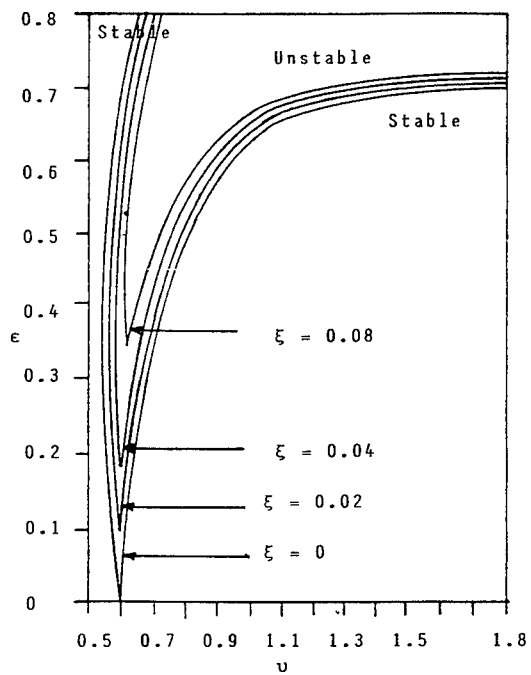


Figure 3. Stability diagram ($\epsilon \sim \nu$) for the region $\nu \approx 0.618$

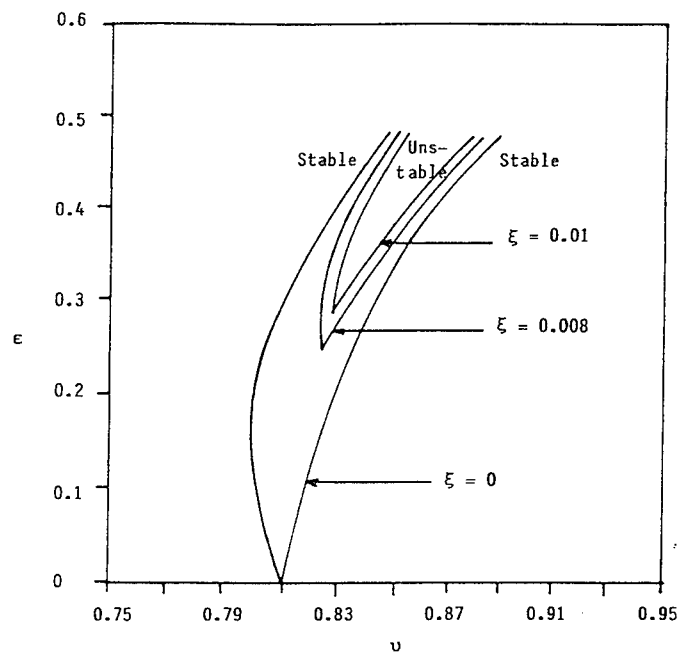


Figure 4. Stability diagram ($\epsilon \sim \nu$) for the region $\nu \approx 0.809$

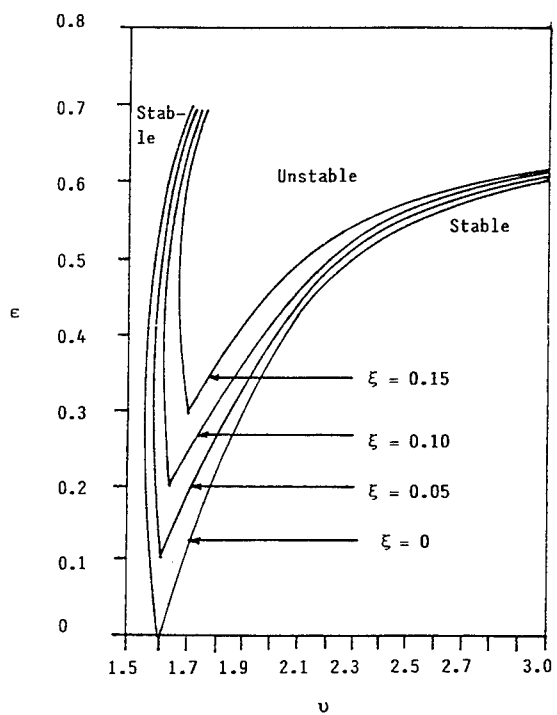


Figure 5. Stability diagram ($\epsilon \sim \nu$) for the region $\nu \approx 1.618$

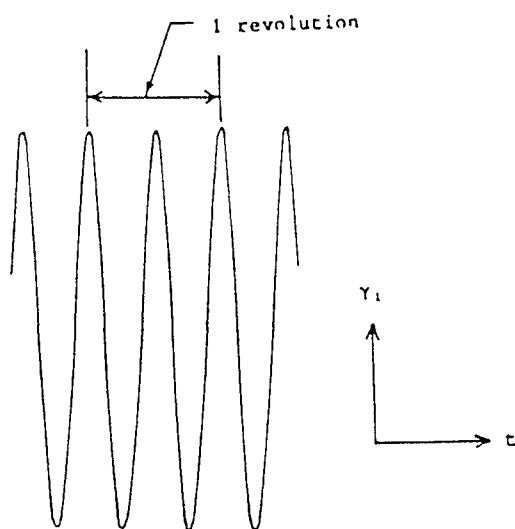


Figure 6. Waveform relationship of $\gamma_1 \sim t$ for $\nu = 0.3$, $\epsilon = 0.3$ and $\xi = 0.02$

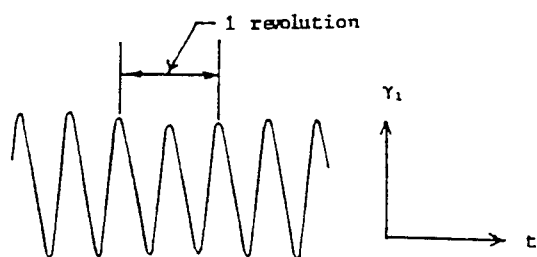


Figure 7. Waveform relationship of $\gamma_1 \sim t$ for $\nu = 0.4$, $\epsilon = 0.3$ and $\xi = 0.02$

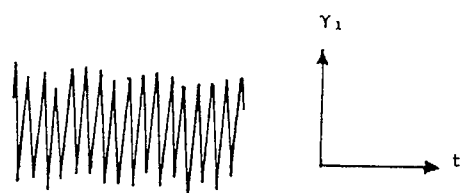


Figure 8. Waveform relationship of $\gamma_1 \sim t$ for $\nu = 2$, $\epsilon = 0.3$ and $\xi = 0.02$

SIMPLE NONLINEAR MODELS FOR AUTOMOTIVE SHOCK ABSORBERS¹

S.Cafferty, J.Giacomin and K.Worden

Dynamics Research Group

Department of Mechanical Engineering

University of Sheffield

Mappin Street

Sheffield S1 3JD

United Kingdom

Abstract

Two simple nonlinear models of an automotive shock absorber are presented. The first type assumes a polynomial form for the damping of the absorber, the second is motivated by neural network theory. In the latter case, the damping characteristics of the absorber are modelled by a hyperbolic tangent function. Simple parameter estimation schemes are presented and validated on data from numerical simulation. Models are obtained from experimental data.

INTRODUCTION

It is well-known that the characteristics of a vehicle main suspension system strongly influence the handling properties and ride comfort characteristics of the vehicle [6]. The shock absorber therefore merits careful study as a fundamental part of the suspension system. Previous research e.g. [3] [14], has shown that shock absorbers are significantly nonlinear, and this should be reflected in any absorber model used in simulating the behaviour of the suspension system [9]. Models based on the detailed physical construction of absorbers have been obtained but are prohibitively complex [7]; they are also, by their very nature, specific to each absorber. Recent research has concentrated on obtaining simple, general models, either assuming polynomial restoring forces [14], or motivated by basic physics [3] [11] [12].

A nonparametric approach to modelling was taken in [4], in which a neural network was used to predict the value of the force transmitted by the absorber as a function of lagged displacement and velocity measurements. In the course of this work it was observed that the neural network transfer

¹A preliminary version of this paper was presented at the IUTAM symposium on *Identification of Mechanical Systems* in Wuppertal, Germany in 1993.

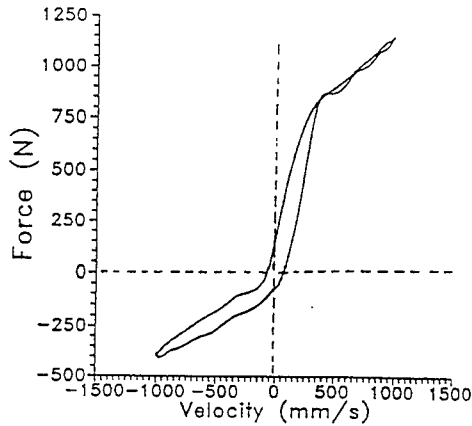


Figure 1. Force-velocity curve of typical production shock absorber.

function - the hyperbolic tangent - bears more than a passing resemblance to the force-velocity characteristics of many shock absorbers (Figure 1, - obtained from a sine test). Many shock absorber force-velocity curves show near-linear behaviour at the higher velocities in the operating range (i.e. the blow-off region), with a smooth transition to high damping centred around zero velocity (i.e. the bleed region). Such functions can be obtained by scaling, translating and rotating a hyperbolic tangent function. The proposed form of the damping force is,

$$f_d(\dot{y}) = c\dot{y} + \alpha[\tanh(\beta\dot{y} + \gamma) - \tanh(\gamma)] \quad (1)$$

For the purposes of testing the absorber, an experimental facility was designed which allowed the possibility of adding mass and a parallel stiffness to the shock absorber (as described in Section 3). This means that (1) should be extended to,

$$m\ddot{y} + c\dot{y} + ky + \alpha[\tanh(\beta\dot{y} + \gamma) - \tanh(\gamma)] = x(t) \quad (2)$$

which is a simple SDOF nonlinear oscillator (Figure 2). The usual physical characteristics of the oscillator are represented by m, c, k while α, β, γ characterise the nonlinear damping (Figure 2). Apart from the additional nonlinear damping, this equation agrees with the minimal model of the suspension system proposed by De Carbon [2], in which case m would be one quarter the car body mass. This minimal model captures much of the essential behaviour of more complex models of the suspension. Note that this model has the structure of a very simple neural network with a linear output neuron (Figure 3) [10].

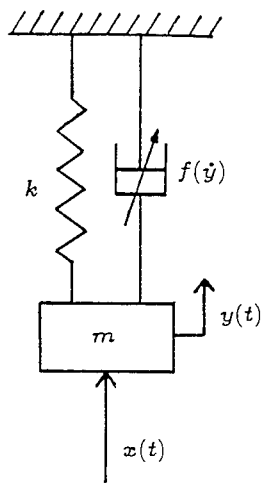


Figure 2. Nonlinear SDOF oscillator.

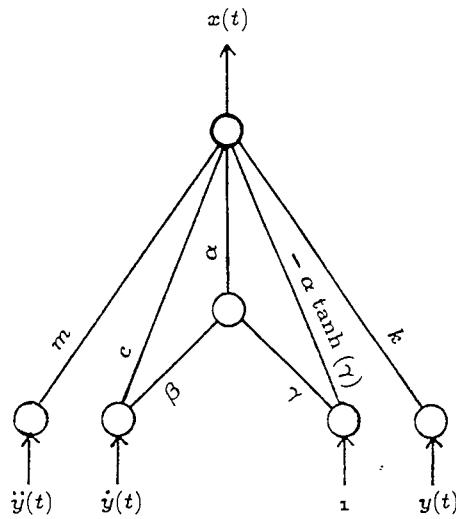


Figure 3. Neural network structure of model.

There is no physical basis for the new model. The parameters are not related to the structure of the absorber but rather to its behaviour as quantified in the force-velocity curve. This is also the case for polynomial models, where,

$$f_d(\dot{y}) = \sum_{i=1}^{N_p} c_i \dot{y}^i \quad (3)$$

so it is natural to make a comparison. The De Carbon model corresponding to (3) is of course,

$$m\ddot{y} + \sum_{i=1}^{N_p} c_i \dot{y}^i + ky = x(t) \quad (4)$$

The advantage of such models is that, with a small number of parameters, the representation of the suspension system can be improved considerably.

The remainder of the paper is structured as follows. Section Two gives the parameter estimation scheme for the polynomial models and Three presents a parameter estimation algorithm for the hyperbolic tangent model. In the latter case the procedure is validated using data from numerical simulation. In Section Four, the models are applied to experimental data. The paper concludes with a discussion of the results in Section Five.

PARAMETER ESTIMATION FOR POLYNOMIAL MODELS

The polynomial models (4) are linear in their parameters, so the estimation problem is straightforward and can be solved using linear least-squares regression. For completeness, the algorithm used in this paper will be described. For simplicity, a linear model will be used for illustration, the approach for a general polynomial model is a straightforward extension. The relation,

$$m\ddot{y} + c\dot{y} + ky = x(t) \quad (5)$$

is imposed on a set of measured input and output data $\{x_i, y_i; i = 1, \dots, N\}$. For each sampling instant,

$$\hat{m}\ddot{y}_i + \hat{c}\dot{y}_i + \hat{k}y_i = x_i + \zeta_i \quad (6)$$

where the carets denote parameter estimates and ζ_i is the residual signal. The residual signal is essentially composed of measurement noise and errors resulting from imperfect parameters. The least-squares approach seeks to remove the latter source of error.

The object is to minimise the sum of squared errors,

$$J(\hat{m}, \hat{c}, \hat{k}) = \sum_{i=1}^N \zeta_i^2 \quad (7)$$

The problem can be expressed concisely in terms of matrices. Assembling each equation of the form (6) for $i = 1, \dots, N$ into a matrix equation gives,

$$\begin{pmatrix} \ddot{y}_1 & \dot{y}_1 & y_1 \\ \ddot{y}_2 & \dot{y}_2 & y_2 \\ \vdots & \vdots & \vdots \\ \ddot{y}_{N_p} & \dot{y}_{N_p} & y_{N_p} \end{pmatrix} \begin{pmatrix} \hat{m} \\ \hat{c} \\ \hat{k} \end{pmatrix} = \begin{pmatrix} x_1 \\ x_2 \\ \vdots \\ x_{N_p} \end{pmatrix} + \begin{pmatrix} \zeta_1 \\ \zeta_2 \\ \vdots \\ \zeta_{N_p} \end{pmatrix} \quad (8)$$

or

$$[A]\{\beta\} = \{x\} + \{\zeta\} \quad (9)$$

in matrix notation, with objective function,

$$J(\hat{m}, \hat{c}, \hat{k}) = \{\zeta\}^T \{\zeta\} \quad (10)$$

The minimum of J is most simply obtained by using the normal equations,

$$\{\beta\} = ([A]^T[A])^{-1}[A]^T\{x\} \quad (11)$$

It is also possible to estimate the significance of individual terms in the model [14]. The approach described above is standard, the software has already been applied in many situations e.g. [14] and therefore requires no verification.

PARAMETER ESTIMATION FOR HYPERBOLIC TANGENT MODEL

The parameter estimation problem for the model structure (2) is a little more complicated as the expression is not linear in the parameters. This means, amongst other things, that it will not always be possible to obtain a global optimum. However, bearing this in mind, numerous methods are available for attacking this type of problem [5]. Given that the model has the structure of a neural network, it seemed appropriate to use a gradient descent or *back-propagation* scheme [10].

Like (10), the parameter estimate obtained in this case is also optimal in the least-squared error sense i.e. it minimises $J = \sum_{i=1}^N \zeta_i^2$, where,

$$\zeta_i = \hat{m}\ddot{y}_i + \hat{c}\dot{y}_i + \hat{k}y_i + \hat{\alpha}[\tanh(\hat{\beta}\dot{y}_i + \hat{\gamma}) - \tanh(\hat{\gamma})] - x_i \quad (12)$$

where y_i , \dot{y}_i and \ddot{y}_i are the sampled displacement, velocity and acceleration, and \hat{m} etc. are estimates of the parameters. The procedure is iterative; given a current estimate of the parameters, the next estimate is formed by stepping down along the gradient of the error function J ; i.e. at step k ,

$$\underline{\theta}_{k+1} = \underline{\theta}_k + \Delta \underline{\theta}_k = \underline{\theta}_k - \eta \nabla_{\underline{\theta}_k} J(\underline{\theta}_k) \quad (13)$$

where the parameters have been ordered in the vector $\underline{\theta} = (\hat{m}, \hat{c}, \hat{k}, \hat{\alpha}, \hat{\beta}, \hat{\gamma})^T$. The *learning coefficient* η determines the size of the descent step. In order to obtain the parameter update rule, it only remains to obtain the components of the gradient term in (12),

$$\nabla_{\underline{\theta}_k} J(\underline{\theta}_k) = \left(\frac{\partial J}{\partial \hat{m}}, \frac{\partial J}{\partial \hat{c}}, \frac{\partial J}{\partial \hat{k}}, \frac{\partial J}{\partial \hat{\alpha}}, \frac{\partial J}{\partial \hat{\beta}}, \frac{\partial J}{\partial \hat{\gamma}} \right) \quad (14)$$

(As confusion is unlikely to result, the carets denoting estimated quantities will be suppressed in the following discussion.) The update rules are obtained using the definition of J , (11) and (12). In forming the error-sum J it is not necessary to sum over the residuals for all N points; J can be obtained from a subset of the errors or even the single error which arises from considering one set of measurements $\{x_i, y_i, \dot{y}_i, \ddot{y}_i\}$, i.e.,

$$J_i(\theta_i) = \zeta_i^2 \quad (15)$$

The latter course is adopted here and the resulting update rules for the parameters are,

$$\begin{aligned}
\Delta m_i &= -\eta \zeta_i \ddot{y}_i \\
\Delta c_i &= -\eta \zeta_i \dot{y}_i \\
\Delta k_i &= -\eta \zeta_i y_i \\
\Delta \alpha_i &= -\eta \zeta_i [\tanh(\beta_i \dot{y}_i + \gamma_i) - \tanh(\gamma_i)] \\
\Delta \beta_i &= -\eta \zeta_i \alpha_i \dot{y}_i \operatorname{sech}^2(\beta_i \dot{y}_i + \gamma_i) \\
\Delta \gamma_i &= -\eta \zeta_i \alpha_i [\operatorname{sech}^2(\beta_i \dot{y}_i + \gamma_i) - \operatorname{sech}^2(\gamma_i)]
\end{aligned} \tag{16}$$

with ϵ the resulting error on using the measurements labelled by i at *this iteration*, this will clearly be different at the next presentation of the values labelled by i . In keeping with normal practice in back-propagation, the value of i is chosen randomly between 1 and N at each iteration. Also, a momentum term was added to the iteration to help damp out high-frequency oscillations over the error surface [10]. The final update scheme was therefore

$$\Delta \underline{\theta}_k = -\eta \nabla_{\underline{\theta}_k} J_k(\underline{\theta}_k) + \mu \Delta \underline{\theta}_{k-1} \tag{17}$$

where μ is the momentum coefficient.

It is well-known that nonlinear estimation schemes can be sensitive to the initial estimates; in order to obtain favourable starting values for the iteration, a linear model of the form,

$$m_l \ddot{y} + c_l \dot{y} + k_l y = x(t) \tag{18}$$

was fitted first, the estimates m_l and k_l were used as starting values for the coefficients m and k in the nonlinear model; the estimate c_l was divided evenly between c and α in the absence of any obvious prescription. The initial values of β and γ were set at 1.0 and 0.0 respectively.

In order to validate the algorithm, data were generated by numerical integration for the system,

$$6.3\ddot{y} + 75\dot{y} + 6300y + 2000[\tanh(\dot{y} - 0.25) - \tanh(-0.25)] = x(t) \tag{19}$$

The coefficient values were motivated by a desire to expose the parameter estimator to the same conditions as might be expected for a real absorber sub-assembly. At low levels of excitation, the effective damping coefficient is $c + \alpha\beta$, in this case 5.2 times critical; at high levels, the effective coefficient is c , giving 0.18 times critical. Data was obtained by taking $x(t)$ to be a Gaussian white noise sequence, initially of RMS 6000, band-limited into

the interval 0 to 20 Hz. The equation of motion (8) was stepped forward in time using a standard fourth-order Runge-Kutta procedure with a time step of 0.01 seconds; 10000 sets of data $\{x_i, y_i, \dot{y}_i, \ddot{y}_i\}$ were obtained.

The algorithm was applied to the simulation data, using learning and momentum coefficients of 0.2 and 0.3 respectively. As the data were noise-free the iteration was required to terminate once the estimates had stabilised to within a fractional tolerance of 10^{-8} . This level of convergence was reached after 15006 iterations (essentially covering the whole data set twice); the resulting estimates were,

$$\begin{aligned} m &= 6.3000001 \\ c &= 74.999723 \\ k &= 6300.0005 \\ \alpha &= 2000.0012 \\ \beta &= 0.99999935 \\ \gamma &= -0.24999984 \end{aligned}$$

This gives confidence in the estimator. In practice, the true values will not be known and some other objective measure of confidence will be required for the estimates. The measure used here is the normalised mean-square error or *MSE*, defined by,

$$MSE(\hat{x}) = \frac{100}{N_p \sigma_x^2} \sum_{i=1}^{N_p} (\zeta_i)^2 \quad (20)$$

this is normalised such that: if the mean of the input signal \bar{x} is used as the model i.e. $\zeta_i = x_i - \bar{x} \forall i$, the *MSE* is 100. Experience shows that an *MSE* of 5.0 shows a good fit, while an *MSE* of less than 1.0 indicates excellence. For the simulated data, the *MSE* value was found to be 8.4×10^{-13} .

RESULTS USING EXPERIMENTAL DATA

The shock absorber test facility consists of a substantial steel structure with a hydraulic actuator and controller secured to the base plate as in Figure 4. The main body of the absorber under test is connected to the actuator head, while its piston is attached via a piezoelectric force transducer to the main structure. This allows a direct measurement of the force transmitted by the absorber. Facilities were provided to add a parallel stiffness in the form of a spring of known characteristics and to load the system with an additional mass. This option was not used for the particular test described below. As the shock absorber is essentially a SDOF system under vertical excitation in this configuration, the simple model of Figure 2 applies. The excitation for the system is provided by the random signal generator of a spectrum analyser, amplified and filtered into

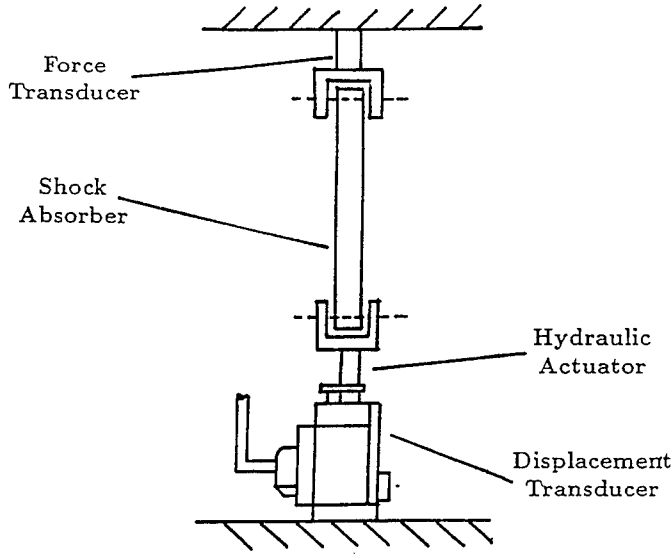


Figure 4. Shock absorber test geometry.

the interval 2 to 30 Hz. The band-limited signal facilitates post-processing of measured data, i.e. numerical differentiation or integration [13].

For the modelling of the absorber, previous tests showed that the inertia of the absorber could be neglected [11]. This means that the reduced models,

$$\sum_{i=1}^{N_p} c_i \dot{y}^i + ky = x(t) \quad (21)$$

and,

$$c\dot{y} + ky + \alpha[\tanh(\beta\dot{y} + \gamma) - \tanh(\gamma)] = x(t) \quad (22)$$

applied to the dynamics so that the piezoelectric load cell actually provided a measurement of $x(t)$. The other signal measured was displacement, the required velocity being arrived at by numerical differentiation. This decision was made because the actuator actually incorporates an LVDT displacement transducer which produces a high quality signal. A detailed account of the test structure and instrumentation can be found in [1].

For the particular test considered here, a displacement of 3.0mm RMS was applied at the base of the absorber and 7000 samples of x_i and y_i were obtained at a frequency of 500 Hz. A three-point centred difference was used to obtain the \dot{y} data. The characteristic force-velocity curve (the solid curve in Figure 5), was obtained using the sectioning method

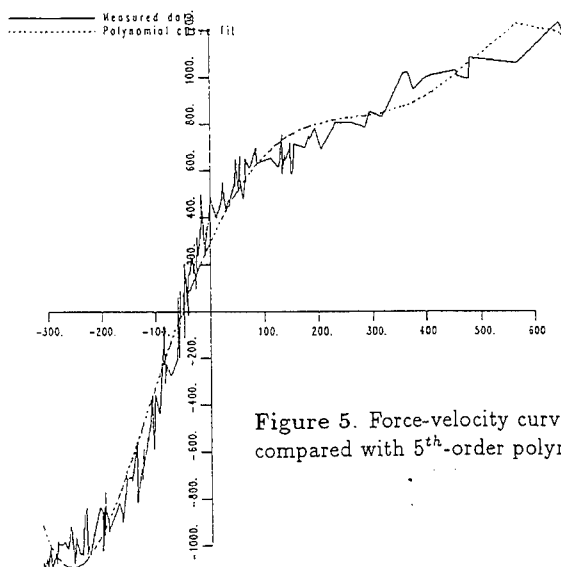


Figure 5. Force-velocity curve from experiment compared with 5th-order polynomial model.

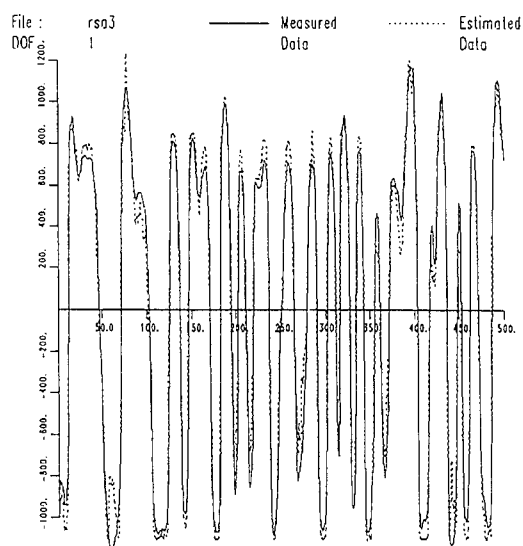


Figure 6. Force data from experiment compared with 5th-order polynomial model.

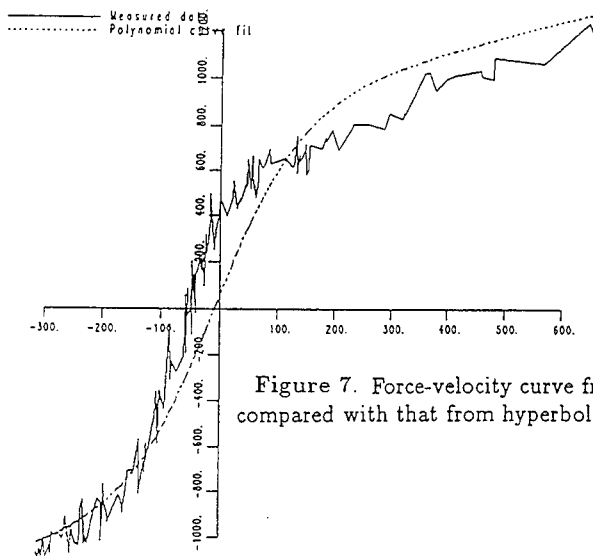


Figure 7. Force-velocity curve from experiment compared with that from hyperbolic tangent model.

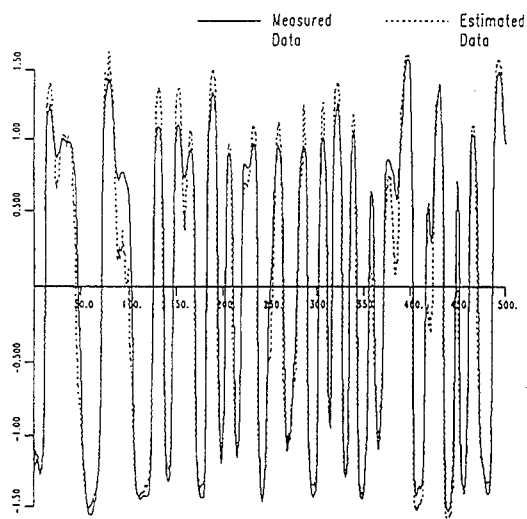


Figure 8. Force data from experiment compared with that from hyperbolic tangent model.

described in [11]. An explanation for the scatter in the curve can be found in [1].

Polynomial models were fitted to the data for various model orders, the masses (as expected) could be disregarded as insignificant. In fact, the stiffnesses could also be discarded as their contribution to the total variance of the RHS vector $\{x\}$ was small. The resulting models for the damping force f_d gave MSE values,

Model order	MSE
1	15.5
3	5.8
5	1.9
7	1.1
9	0.9

The curve-fit for the 5th-order polynomial model is given in Figure 5. The corresponding model-predicted force (before the mass of -0.0007 was deleted), is given in Figure 6.

The parameter estimation routine of the last section (mass term m suppressed) was applied to 1000 points of data, using a learning coefficient of 1.0 and no momentum. Convergence of the parameters to within a fractional tolerance of 0.00005 was obtained after 1051 iterations, the resulting parameters being,

$$\begin{aligned}
 c &= 0.63 \\
 k &= -15.0 \\
 \alpha &= 856.9 \\
 \beta &= 0.0067 \\
 \gamma &= 0.058
 \end{aligned}$$

The stiffness can be disregarded as insignificant as before, the negative sign can be regarded as a statistical fluctuation. The MSE value, was 6.9 which shows quite good agreement. Figure 8 shows a comparison between the measured force time-series and that predicted by the model (2). Figure 5 shows a comparison between the measured force-velocity curve and that of the model. Agreement is quite good.

DISCUSSION

The results of the last section show that a better representation of the force-velocity curve could be obtained using high-order polynomials, however, it could be argued that the model (2) is preferable for two reasons:

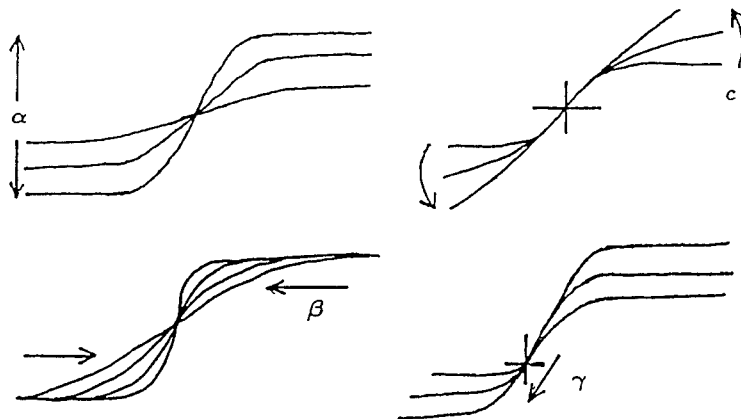


Figure 9. Behaviour of the hyperbolic tangent function under variation of the parameters.

1. Polynomial models are restricted to the excitation levels at or below the level used for parameter estimation. The reason for this is that a polynomial, on leaving the interval on which the model is defined, will tend to $\pm\infty$ as $O(x^n)$ depending on the sign and order of the leading term. In many cases this leads to instability, as a negative leading term will tend to reinforce rather than oppose the motion at high velocities (see Figure 5). Alternatively, (2) leads asymptotically to linear damping.
2. The polynomial coefficients will not usually admit a physical interpretation. In the case of the model (1) or (2), the coefficients have a direct interpretation in terms of the force-velocity characteristics; c generates rotations (shear really) and fixes the asymptotic value of the damping; α governs the overall scale of the central high damping region and β the gradient; variations in γ translate the high damping region along the velocity scale while maintaining a zero force condition at zero velocity. (Figure 7). These characteristics are the main features of interest to designers and have a direct bearing on subjective ride comfort evaluation. The model developed in this paper will also facilitate comparisons between real absorbers.

CONCLUSIONS

The new model structure proposed here has been shown to give good agreement with experimental force-velocity data. Despite the fact that polynomial models give better agreement, there are reasons to suggest that the new model will be more useful to vehicle engineers.

ACKNOWLEDGEMENTS

The authors would like to acknowledge many useful conversations with Ing. Pasquale Campanile and Professor Geoff Tomlinson.

References

- [1] Cafferty (S.) 1992 *Ph.D Transfer Report, Department of Engineering, University of Manchester*. Investigation into the use of random and transient (chirp) excitation for characterising shock absorbers.
- [2] Bourcier De Carbon C. 1950 *Atti Congresso SIA, Parigi*. Theorie matématique et réalisation pratique de la suspension amortie des véhicules terrestres.
- [3] Genta (G.) & Campanile (P.) 1989 *Meccanica* **24** pp.47-57. An approximated approach to the study of motor vehicle suspensions with nonlinear shock absorbers.
- [4] Giacomini (J.) 1991 *Engineering Applications of Artificial Intelligence* **4** pp.59-64. Neural network simulation of an automotive shock absorber.
- [5] Gill (P.E.), Murray (W.) & Wright (M.H.) 1981 *Practical Optimisation*. Academic Press, London.
- [6] Hall (B.B.) & Gill (K.F.) 1987 *Proceedings of the I.Mech.E* **201** pp.135-148. Performance evaluation of motor vehicle active suspension systems.
- [7] Lang (H.H.) 1977 *Ph.D Dissertation, Department of Mechanical Engineering, University of Michigan*. A study of the characteristics of automotive hydraulic dampers at high stroking frequencies.
- [8] Olatunbosun (O.A.) & Dunn (J.W.) 1992 in *Proceedings of the 2nd International Conference on Ride Comfort*. An evaluation of the effect of suspension nonlinearities on vehicle ride.
- [9] Pisino (E.), Giacomini (J.) & Campanile (P.) 1993 *NATO ASI Conference on Computer Aided Analysis of Rigid and Flexible Mechanical Systems, Troia, Portugal*. Numerical investigation of the influence of the shock absorber on the vertical force transmissibility of a McPherson suspension.

- [10] Rumelhart (D.E.) & McClelland (J.L.) 1988 *Parallel Distributed Processing: Explorations in the Microstructure of Cognition (Two Volumes)*. MIT press.
- [11] Surace (C.), Worden (K.) & Tomlinson (G.R.) 1992 *Proceedings of the I.Mech.E: Part D* **206** pp.3-16. On the non-linear characteristics of automotive shock absorbers.
- [12] Wallaschek (J.) 1990 *International Journal of Non-Linear Mechanics* **25** pp.299-308. Dynamics of nonlinear automotive shock absorbers.
- [13] Worden (K.) 1990 *Mechanical Systems and Signal Processing* **4** pp.295-319. Data processing and experiment design for the restoring force surface method. Part I: Integration and differentiation of measured time data.
- [14] Worden (K.) & Tomlinson (G.R.) 1992 *Proceedings of the 10th International Modal Analysis Conference, San Diego* pp.764-771. Parametric and nonparametric identification of automotive shock absorbers.

ENERGY TRANSMISSION THROUGH NONLINEAR SUSPENSION SYSTEMS

K. Worden

Dynamics Research Group
Department of Mechanical Engineering
University of Sheffield
Mappin Street
Sheffield S1 3JD
United Kingdom

Abstract

The transmission of a signal through three simple nonlinear suspension models is computed analytically (up to third order in the excitation amplitude) using the Volterra series. The results are used to define discomfort factors for the suspensions.

INTRODUCTION

The fundamental objective in designing a vehicle suspension for ride comfort is to reduce the transmission of vibrational energy to the occupants. Various standards have been proposed for quantifying the perceived discomfort caused by mechanical vibration; those outlined in ISO 2631 [13] and BS 6841 [4] being the most often used. The standards define the vibrational discomfort (labelled here as D_1) as,

$$D_1 = \left\{ \int d\omega W(\omega)^2 |A(\omega)|^2 \right\}^{\frac{1}{2}} \quad (1)$$

where $A(\omega)$ is the acceleration spectrum at the man/vehicle interface and $W(\omega)$ is the weighting function which describes human sensitivity to whole body vibration.

As the shock absorber sub-assembly is highly nonlinear, the question of energy transfer between frequency bands arises to complicate matters. Useful studies have been carried out using numerical simulation [14] [15]; however, the discussion below is intended to indicate how the analytical component of such a calculation can be increased using simple nonlinear models of the type described above.

Essentially, the problem is to determine the output spectrum given the transmission of a random or deterministic vibration signal through a nonlinear suspension. The models may vary considerably in complexity. For the sake of simplicity of exposition here, the simplest input-output

system, the De Carbon model, will be considered first. Having established the basic ideas a more complicated two degree-of-freedom model will be evaluated. The approach outlined here is based on the Volterra series. The calculations presented are fairly routine, this paper should properly be regarded as a case study.

THE DE CARBON MODEL

This, the earliest model of a vehicle suspension [5], considers the system as a Single Degree-of-Freedom (SDOF) oscillator. The classical model represents the shock absorber component as a simple linear spring-damper element. This is extended here to a nonlinear spring-damper (Figure 1).

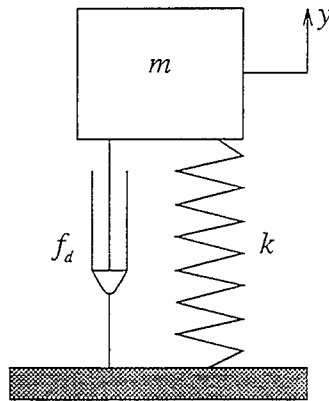


Figure 1. De Carbon Model.

The equation of motion takes the form,

$$m\ddot{y} + f_d(\dot{y}) + ky = x(t) \quad (2)$$

where m is a quarter of the car body mass, and $f_d(\dot{y})$ is the force-velocity characteristic of the nonlinear damper. Linear stiffness is assumed. It will further be assumed that a Taylor expansion of order 3 in \dot{y} is sufficient to represent the damping force i.e.

$$f_d(\dot{y}) = c_1\dot{y} + c_2\dot{y}^2 + c_3\dot{y}^3 \quad (3)$$

and that the coefficients c_1 , c_2 and c_3 are available. This is necessary as the Volterra series method described later requires a polynomial form for the nonlinearity. If a more complex form is specified the coefficients can be computed. For example consider the hyperbolic tangent model of the damper [7],

$$f_d(\dot{y}) = c\dot{y} + \alpha[\tanh(\beta\dot{y} + \gamma) - \tanh(\gamma)] \quad (4)$$

The problematic term is $\tanh(\beta\dot{y} + \gamma)$. The first step is to apply the addition theorem for the tanh function [10],

$$\tanh(\beta\dot{y} + \gamma) = \frac{\tanh(\beta\dot{y}) + \tanh(\gamma)}{1 + \tanh(\beta\dot{y})\tanh(\gamma)} \quad (5)$$

followed by the series expansion,

$$\tanh(\beta\dot{y}) = \beta\dot{y} - \frac{1}{3}(\beta\dot{y})^3 + \frac{2}{15}(\beta\dot{y})^5 - \frac{17}{315}(\beta\dot{y})^7 + \dots \quad |\beta\dot{y}| \leq \frac{\pi}{\sqrt{2}} \quad (6)$$

A little tedious algebra results in the coefficients,

$$\begin{aligned} c_1 &= c + \alpha \tanh(\gamma) \\ c_2 &= -\alpha \beta^2 \tanh(\gamma) [1 - \tanh^2(\gamma)] \\ c_3 &= -\alpha \beta^3 [1 - 3 \tanh^2(\gamma)] [1 - \tanh^2(\gamma)] \end{aligned} \quad (7)$$

It is possible to assume a polynomial model, and to obtain the coefficients directly from experiment [6].

The next section is concerned with the calculation of the discomfort factor for this model.

ENERGY TRANSMISSION THROUGH THE SDOF SYSTEM

It is well-known that any linear system or input-output process $x(t) \rightarrow y(t)$ can be realised as a mapping

$$y(t) = \int_{-\infty}^{+\infty} d\tau h(\tau) x(t - \tau) \quad (8)$$

where $h(\tau)$ uniquely characterises the system. Also well-known, is the dual frequency-domain representation,

$$Y(\omega) = H(\omega)X(\omega) \quad (9)$$

where $Y(\omega)$ (resp. $X(\omega)$) is the Fourier transform of $y(t)$ (resp. $x(t)$). $H(\omega)$ is the linear system Frequency Response Function (FRF). These equations are manifestly linear and therefore cannot hold for arbitrary nonlinear systems. However an appropriate generalisation of (8) exists as obtained in the early part of this century by Volterra [19]. It takes the form of an infinite series,

$$y(t) = y_1(t) + y_2(t) + y_3(t) + \dots + y_n(t) + \dots \quad (10)$$

where

$$y_n(t) = \int_{-\infty}^{+\infty} \dots \int_{-\infty}^{+\infty} d\tau_1 \dots d\tau_n h_n(\tau_1, \dots, \tau_n) x(t - \tau_1) \dots x(t - \tau_n) \quad (11)$$

The functions h_n are referred to as the *Volterra kernels*.

As in the linear case, there exists a dual frequency-domain representation for nonlinear systems based on the *higher-order FRFs* (HFRFs) or *Volterra kernel transforms*, $H_n(\omega_1, \dots, \omega_n)$, $n = 1, \dots, \infty$ which are defined as the multi-dimensional Fourier transforms of the kernels.

$$H_n(\omega_1, \dots, \omega_n) = \int_{-\infty}^{+\infty} \dots \int_{-\infty}^{+\infty} d\tau_1 \dots d\tau_n h_n(\tau_1, \dots, \tau_n) e^{-i(\omega_1 \tau_1 + \dots + \omega_n \tau_n)} \quad (12)$$

In the general nonlinear case, it can be shown [2], that the output spectrum of the process $x(t) \longrightarrow y(t)$ is given by,

$$\begin{aligned} Y(\omega) = & H_1(\omega)X(\omega) + \frac{1}{(2\pi)} \int_{-\infty}^{\infty} d\omega_1 H_2(\omega_1, \omega - \omega_1) X(\omega_1) X(\omega - \omega_1) + \\ & \frac{1}{(2\pi)^2} \int_{-\infty}^{\infty} \int_{-\infty}^{\infty} d\omega_1 d\omega_2 H_3(\omega_1, \omega_2, \omega - \omega_1 - \omega_2) X(\omega_1) X(\omega_2) X(\omega - \omega_1 - \omega_2) + \dots \end{aligned} \quad (13)$$

again an infinite series.

Once the displacement spectrum $Y(\omega)$ has been obtained for the system (3), the acceleration spectrum is specified by,

$$A(\omega) = -\omega^2 Y(\omega) \quad (14)$$

Given the equations above it is possible to go from a given excitation $x(t)$, to the corresponding discomfort factor. The only thing which remains to be specified are the kernel transforms H_n . There are a number of methods for determining the kernel transforms for a given system; if the equations of motion are available, the method of harmonic probing [3] is both simple and effective and will be the method applied here.

The basis of the harmonic probing method is to examine the response of the system to certain very simple inputs. In order to identify $H_1(\omega)$, for example, the system is 'probed' with the single harmonic,

$$x_i^p = e^{i\Omega t} \quad (15)$$

Substituting this expression into the Volterra series (10) the corresponding generic response is found to be,

$$y_i^p = H_1(\Omega) e^{i\Omega t} + H_2(\Omega, \Omega) e^{2i\Omega t} + H_3(\Omega, \Omega, \Omega) e^{3i\Omega t} + \dots \quad (16)$$

If the expressions (15) and (16) are now substituted into the specific equation of motion (3), equating the coefficients of $e^{i\Omega t}$ on the right-hand and left-hand sides gives,

$$(-m\Omega^2 + ic\Omega + k)H(\Omega) = 1 \quad (17)$$

and the form of H_1 follows trivially,

$$H_1(\omega) = \frac{1}{-m\omega^2 + ic_1\omega + k} \quad (18)$$

The extraction of H_2 is a little more complicated, this requires probing with two independent harmonics, so,

$$x_i^p = e^{i\Omega_1 t} + e^{i\Omega_2 t} \quad (19)$$

A straightforward computation using Equations (10), (11) and (13) shows that the corresponding response is,

$$y_i^p = H_1(\Omega_1)e^{i\Omega_1 t} + H_1(\Omega_2)e^{i\Omega_2 t} + 2H_2(\Omega_1, \Omega_2)e^{i(\Omega_1 + \Omega_2)t} + \dots \quad (20)$$

The argument proceeds as for H_1 ; if these expressions are substituted into the equation of motion (3), the only HFRFs to appear in the coefficient of the sum harmonic $e^{i(\Omega_1 + \Omega_2)t}$, are H_1 and H_2 , where H_1 is already known from Equation (16). So as before, the coefficient can be rearranged to give an expression for H_2 in terms of the second order coefficient c_2 and H_1 . In fact,

$$H_2(\omega_1, \omega_2) = c_2\omega_1\omega_2 H_1(\omega_1)H_1(\omega_2)H_1(\omega_1 + \omega_2) \quad (21)$$

H_3 is obtained by probing with a three-tone signal, the argument is a trivial modification of the above and the result is,

$$\begin{aligned} H_3(\omega_1, \omega_2, \omega_3) = & \frac{1}{6}H_1(\omega_1 + \omega_2 + \omega_3) \times \\ & [-2c_2 \{(\omega_1 + \omega_2)\omega_3 H_2(\omega_1, \omega_2)H_1(\omega_3) + (\omega_2 + \omega_3)\omega_1 H_2(\omega_2, \omega_3)H_1(\omega_1) \\ & + (\omega_3 + \omega_1)\omega_2 H_2(\omega_3, \omega_1)H_1(\omega_2)\} + \\ & -ic_3\omega_1\omega_2\omega_3 H_1(\omega_1)H_1(\omega_2)H_1(\omega_3)] \end{aligned} \quad (22)$$

In the case of the hyperbolic tangent model, although the HFRFs have been obtained for the approximation (3), if the expansion is valid, they are not only exact for (3), but also for (4). This is because H_n in general only depends on the coefficients of terms of product order n or less.

Now, the discomfort factor can be computed in principle, by substituting the expressions for the H_n into (13), converting to acceleration response via (14) and finally substituting into the expression (1).

Suppose the input $x(t)$ is a cosinusoid, $x(t) = X \cos(\Omega t)$. It can be shown that the response (up to $O(X^3)$) is [18],

$$y(t) = \frac{X^2}{2} H_2(\Omega, -\Omega) + X |H_1(\Omega)| \cos(\Omega t + \angle H_1(\Omega)) + \frac{3X^3}{4} |H_3(\Omega, \Omega, -\Omega)| \cos(\Omega t + \angle H_3(\Omega, \Omega, -\Omega)) + \frac{X^2}{2} |H_2(\Omega, \Omega)| \cos(2\Omega t + \angle H_2(\Omega, \Omega)) + \frac{X^3}{4} |H_3(\Omega, \Omega, \Omega)| \cos(3\Omega t + \angle H_3(\Omega, \Omega, \Omega)) + O(X^4) \quad (23)$$

where, from (21) and (22) it follows that,

$$H_2(\Omega, \Omega) = c_2 \Omega^2 H_1(\Omega)^2 H_1(2\Omega) \quad (24)$$

$$H_3(\Omega, \Omega, \Omega) = \Omega^3 H_1(\Omega)^3 H_1(3\Omega) \left(-2c_2^2 \Omega H_1(2\Omega) - \frac{1}{6} i c_3 \right) \quad (25)$$

and

$$H_3(\Omega, \Omega, -\Omega) = \Omega^3 H_1(\Omega)^2 |H_1(\Omega)|^2 \left(-\frac{2}{3} c_2^2 \Omega H_1(2\Omega) + \frac{1}{6} c_3 \right) \quad (26)$$

on using the reflection property of the kernel transforms $H_n(-\omega_1, \dots, -\omega_n) = H_n(\omega_1, \dots, \omega_n)^*$ where $*$ denotes the complex conjugate [17].

Equation (23) can be simplified,

$$y(t) = y_0 + \sum_{n=0}^3 Y_n \cos(n\Omega t + \phi_n) \quad (27)$$

where y_0 , Y_2 , Y_3 , ϕ_2 and ϕ_3 can be read-off directly from (20), and,

$$Y_1 = \left(|H_1(\Omega)|^2 X^2 + \frac{9}{16} |H_3(\Omega, \Omega, -\Omega)|^2 X^6 + \frac{3}{2} |H_1(\Omega) H_3(\Omega, \Omega, -\Omega)| X^4 \cos(\angle H_1(\Omega) - \angle H_3(\Omega, \Omega, -\Omega)) \right)^{\frac{1}{2}} \quad (28)$$

$$\phi_1 = \tan^{-1} \left(\frac{|H_1(\Omega)| X \sin \angle H_1(\Omega) + \frac{3}{4} |H_3(\Omega, \Omega, -\Omega)| X^3 \sin \angle H_3(\Omega, \Omega, -\Omega)}{|H_1(\Omega)| X \cos \angle H_1(\Omega) + \frac{3}{4} |H_3(\Omega, \Omega, -\Omega)| X^3 \cos \angle H_3(\Omega, \Omega, -\Omega)} \right) \quad (29)$$

Now the response in (27) can not be directly used in forming the discomfort factor D_1 in (1) because the displacement spectrum $Y(\Omega)$ and hence the acceleration spectrum $A(\Omega)$ contains δ -functions. These are not strictly functions but distributions [8], and multiplication is not defined for distributions. Specifically, they can not be squared. In order to avoid this problem, a new discomfort factor is proposed specifically for harmonic responses. In general,

$$D_2(\Omega) = \left\{ \sum_{n=1}^{\infty} n^4 \Omega^4 Y_n^2 W(n\Omega)^2 \right\}^{\frac{1}{2}} \quad (30)$$

For the present study, the summation is truncated at third order. Note that this differs from D_1 as it is a function of frequency. The weighting factor used (1), depends on the axis of vibration. The concern here is with the z-axis vibration at the seat. The appropriate weighting is W_g [11], defined according to BS 6841 by (Figure 2),

$0.5 < f < 2.0$	$W_g(f) = 0.4$
$2.0 < f < 5.0$	$W_g(f) = f/5$
$5.0 < f < 16.0$	$W_g(f) = 1.00$
$16.0 < f < 80.0$	$W_g(f) = 16.0/f$
Elsewhere	$W_g(f) = 0.00$

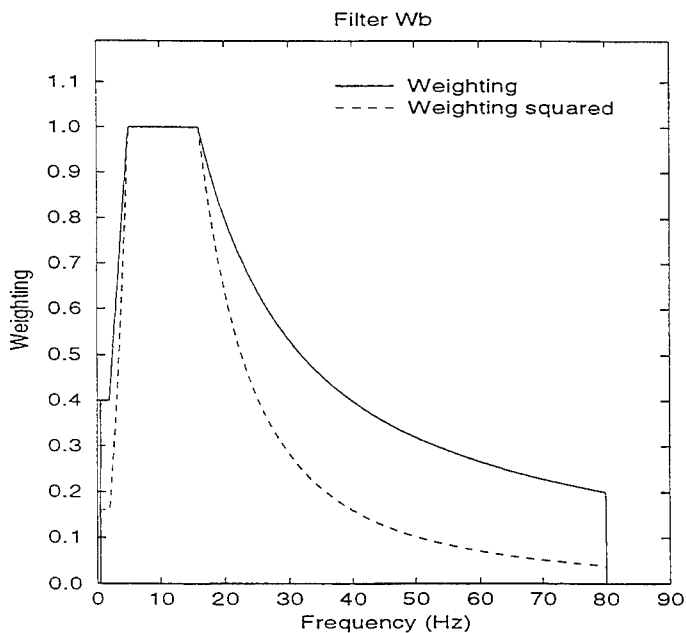


Figure 2. Comfort weighting factor.

TWO DEGREE-OF-FREEDOM MODEL

Having established the techniques needed, the study can now proceed to a more realistic model of the suspension (Figure 3) [1].

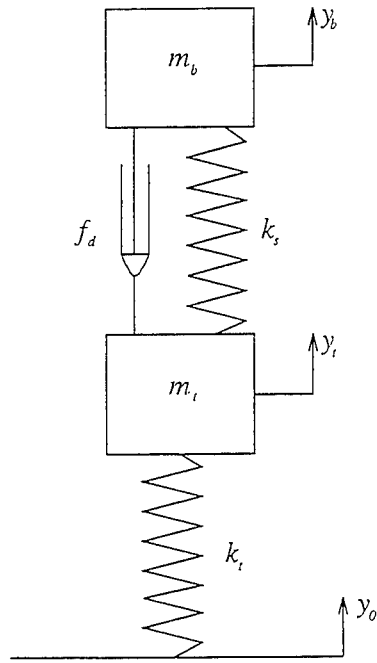


Figure 3. Two degree-of-freedom model.

The equations of motion of the system are,

$$\begin{aligned} m_t \ddot{y}_t + f_d(\dot{y}_t - \dot{y}_b) + (k_t + k_s)y_t - k_s y_b &= k_t y_0 \\ m_b \ddot{y}_b - f_d(\dot{y}_t - \dot{y}_b) + k_s(y_b - y_t) &= 0 \end{aligned} \quad (31)$$

where m_t , k_t and y_t are the mass, stiffness and displacement of the tyre - the *unsprung mass*. m_b and y_b are the mass and displacement of the body or the *sprung mass* (This is usually taken as one quarter of the total car body mass). f_d is the characteristic of the nonlinear damper and k_s is the (linear) stiffness of the suspension. A cubic characteristic will again be assumed for the damper i.e. $f_d(z) = c_1 z + c_2 z^2 + c_3 z^3$. y_0 is the displacement at the road surface and acts here as the excitation.

The discomfort factor will be computed in terms of the acceleration at the car body. It is therefore necessary to calculate the relevant response spectrum. Each of the processes $y_0 \rightarrow y_t$ and $y_0 \rightarrow y_b$ has its own Volterra series and it will be shown below that the responses will depend on the kernel transforms from both series. The notation is defined by,

$$Y_t(\omega) = H_1^t(\omega)Y_0(\omega) + \frac{1}{(2\pi)} \int_{-\infty}^{\infty} d\omega_1 H_2^t(\omega_1, \omega - \omega_1)Y_0(\omega_1)Y_0(\omega - \omega_1) +$$

$$\frac{1}{(2\pi)^2} \int_{-\infty}^{\infty} \int_{-\infty}^{\infty} d\omega_1 d\omega_2 H_3^t(\omega_1, \omega_2, \omega - \omega_1 - \omega_2)Y_0(\omega_1)Y_0(\omega_2)Y_0(\omega - \omega_1 - \omega_2) + \dots$$
(32)

$$Y_b(\omega) = H_1^b(\omega)Y_0(\omega) + \frac{1}{(2\pi)} \int_{-\infty}^{\infty} d\omega_1 H_2^b(\omega_1, \omega - \omega_1)Y_0(\omega_1)Y_0(\omega - \omega_1) +$$

$$\frac{1}{(2\pi)^2} \int_{-\infty}^{\infty} \int_{-\infty}^{\infty} d\omega_1 d\omega_2 H_3^b(\omega_1, \omega_2, \omega - \omega_1 - \omega_2)Y_0(\omega_1)Y_0(\omega_2)Y_0(\omega - \omega_1 - \omega_2) + \dots$$
(33)

The harmonic probing procedure for Multi-Degree-of-Freedom (MDOF) systems is a straightforward extension of that for SDOF systems. In order to obtain the first-order (linear) kernel transforms, the probing expressions,

$$y_0^p = e^{i\Omega t} \quad (34)$$

$$y_t^p = H_1^t(\Omega)e^{i\Omega t} + \dots \quad (35)$$

and,

$$y_b^p = H_1^b(\Omega)e^{i\Omega t} + \dots \quad (36)$$

are used. These expressions are substituted into the equations of motion (31), and the coefficients of $e^{i\Omega t}$ are extracted. The resulting equations are, in matrix form,

$$\begin{pmatrix} -m_t\Omega^2 + ic_1\Omega + k_t + k_s & -ic_1\Omega - k_s \\ -ic_1\Omega - k_s & -m_b\Omega^2 + ic_1\Omega + k_s \end{pmatrix} \begin{pmatrix} H_1^t(\Omega) \\ H_1^b(\Omega) \end{pmatrix} = \begin{pmatrix} k_t \\ 0 \end{pmatrix}$$
(37)

This 2×2 system has a straightforward solution,

$$H_1^t(\omega) = \frac{k_t(-m_b\omega^2 + ic_1\omega + k_s)}{(-m_t\omega^2 + ic_1\omega + k_t + k_s)(-m_b\omega^2 + ic_1\omega + k_s) - (ic_1\omega + k_s)^2}$$
(38)

$$H_1^b(\omega) = \frac{k_t(ic_1\omega + k_s)}{(-m_t\omega^2 + ic_1\omega + k_t + k_s)(-m_b\omega^2 + ic_1\omega + k_s) - (ic_1\omega + k_s)^2}$$
(39)

It will prove useful later to establish a little notation,

$$\Phi(\omega) = \begin{pmatrix} -m_t\omega^2 + ic_1\omega + k_t + k_s & -ic_1\omega - k_s \\ -ic_1\omega - k_s & -m_b\omega^2 + ic_1\omega + k_s \end{pmatrix}^{-1} \begin{pmatrix} 1 \\ -1 \end{pmatrix} \quad (40)$$

The second-order kernel transforms are obtained using the probing expressions,

$$y_0^p = e^{i\Omega_1 t} + e^{i\Omega_2 t} \quad (41)$$

$$y_t^p = H_1^t(\Omega_1)e^{i\Omega_1 t} + H_1^t(\Omega_2)e^{i\Omega_2 t} + 2H_2^t(\Omega_1, \Omega_2)e^{i(\Omega_1 + \Omega_2)t} + \dots \quad (42)$$

and,

$$y_b^p = H_1^b(\Omega_1)e^{i\Omega_1 t} + H_1^b(\Omega_2)e^{i\Omega_2 t} + 2H_2^b(\Omega_1, \Omega_2)e^{i(\Omega_1 + \Omega_2)t} + \dots \quad (43)$$

These expressions are substituted into the equations of motion (31) and the coefficients of $e^{i(\Omega_1 + \Omega_2)t}$ are extracted. The resulting equations are, in matrix form,

$$\begin{pmatrix} -m_t(\Omega_1 + \Omega_2)^2 + ic_1(\Omega_1 + \Omega_2) + k_t + k_s & -ic_1(\Omega_1 + \Omega_2) - k_s \\ -ic_1(\Omega_1 + \Omega_2) - k_s & -m_b(\Omega_1 + \Omega_2)^2 + ic_1(\Omega_1 + \Omega_2) + k_s \end{pmatrix} \times \\ \begin{pmatrix} H_2^t(\Omega_1, \Omega_2) \\ H_1^b(\Omega_1, \Omega_2) \end{pmatrix} = \begin{pmatrix} 1 \\ -1 \end{pmatrix} c_2 \Omega_1 \Omega_2 [H_1^t(\Omega_1) - H_1^b(\Omega_1)][H_1^t(\Omega_2) - H_1^b(\Omega_2)] \quad (44)$$

so

$$\begin{pmatrix} H_2^t(\omega_1, \omega_2) \\ H_1^b(\omega_1, \omega_2) \end{pmatrix} = \Phi(\omega_1 + \omega_2) c_2 \omega_1 \omega_2 [H_1^t(\omega_1) - H_1^b(\omega_1)][H_1^t(\omega_2) - H_1^b(\omega_2)] \quad (45)$$

The calculation of the third-order kernel transforms proceeds as above, except a three-tone probing expression is used,

$$y_0^p = e^{i\Omega_1 t} + e^{i\Omega_2 t} + e^{i\Omega_3 t} \quad (46)$$

The result of the computation is,

$$\begin{pmatrix} H_3^t(\omega_1, \omega_2, \omega_3) \\ H_3^b(\omega_1, \omega_2, \omega_3) \end{pmatrix} = \Phi(\omega_1 + \omega_2 + \omega_3) (F(\omega_1, \omega_2, \omega_3) + G(\omega_1, \omega_2, \omega_3)) \quad (47)$$

where,

$$F(\omega_1, \omega_2, \omega_3) = \frac{2}{3} c_2 \sum_c \omega_1 (\omega_2 + \omega_3) [H_1^t(\omega_1) - H_1^b(\omega_1)][H_2^t(\omega_2, \omega_3) - H_2^b(\omega_2, \omega_3)] \quad (48)$$

where \sum_c denotes a sum over cyclic permutations of ω_1, ω_2 and ω_3 . Also,

$$G(\omega_1, \omega_2, \omega_3) = -6ic_3 \prod_{n=1}^3 \omega_n [H_1^t(\omega_n) - H_1^b(\omega_n)] \quad (49)$$

The displacement spectra can now be calculated from equations (32) and (33). Note that to obtain $Y_t(\omega)$ (resp. $Y_b(\omega)$) requires a specification of H_3^t (resp. H_3^b) and H_1^t, H_1^b, H_2^t and H_2^b . The quantity of interest is actually $Y_b(\omega)$ as this is the vibration at the car body.

In the restricted case where y_0 is a cosinusoid $y_0(t) = Y_0 \cos(\Omega t)$. The displacement response at the car body is given by,

$$\begin{aligned} y^b(t) = & \frac{Y_0^2}{2} H_2^b(\Omega, -\Omega) + \\ & Y_0 |H_1^b(\Omega)| \cos(\Omega t + \angle H_1(\Omega)) + \frac{3Y_0^3}{4} |H_3^b(\Omega, \Omega, -\Omega)| \cos(\Omega t + \angle H_3^b(\Omega, \Omega, -\Omega)) + \\ & \frac{Y_0^2}{2} |H_2^b(\Omega, \Omega)| \cos(2\Omega t + \angle H_2^b(\Omega, \Omega)) + \\ & \frac{Y_0^3}{4} |H_3^b(\Omega, \Omega, \Omega)| \cos(3\Omega t + \angle H_3^b(\Omega, \Omega, \Omega)) + O(Y_0^4) \end{aligned} \quad (50)$$

which is essentially identical to (23). The subsequent definitions (24)-(30) require only notational changes in order to establish a discomfort function $D_2(\Omega)$ for the two degree-of-freedom model.

The theory above is easily adapted to the case of the 'sky-hook' suspension model (Figure 4) [12]. The equations of motion are,

$$\begin{aligned} m_t \ddot{y}_t + (k_t + k_s) y_t - k_s y_b &= k_t y_0 \\ m_b \ddot{y}_b + f_d(\dot{y}_b) + k_s(y_b - y_t) &= 0 \end{aligned} \quad (51)$$

The H_1 functions for this system are given by,

$$H_1^t(\omega) = \frac{k_t(-m_b \omega^2 + ic_1 \omega + k_s)}{(-m_t \omega^2 + k_t + k_s)(-m_b \omega^2 + ic_1 \omega + k_s) - k_s^2} \quad (52)$$

$$H_1^b(\omega) = \frac{k_t + k_s}{(-m_t \omega^2 + k_t + k_s)(-m_b \omega^2 + ic_1 \omega + k_s) - k_s^2} \quad (53)$$

The H_2 functions are given by,

$$\begin{pmatrix} H_2^t(\omega_1, \omega_2) \\ H_1^b(\omega_1, \omega_2) \end{pmatrix} = \Psi(\omega_1 + \omega_2) c_2 \omega_1 \omega_2 H_1^b(\omega_1) H_1^b(\omega_2) \quad (54)$$

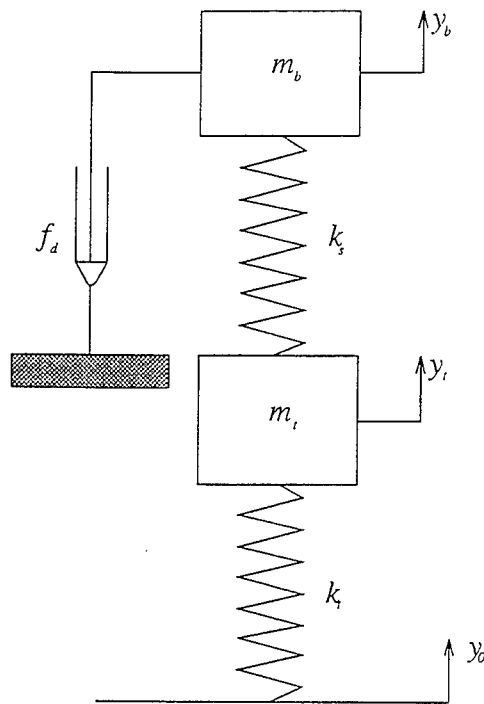


Figure 4. Two degree-of-freedom model.

where,

$$\Psi(\omega) = \begin{pmatrix} -m_t\omega^2 + k_t + k_s & -k_s \\ -k_s & -m_b\omega^2 + ic_1\omega + k_s \end{pmatrix}^{-1} \begin{pmatrix} 0 \\ 1 \end{pmatrix} \quad (55)$$

Finally, the H_3 s are given by,

$$\begin{pmatrix} H_3^t(\omega_1, \omega_2, \omega_3) \\ H_3^b(\omega_1, \omega_2, \omega_3) \end{pmatrix} = \Psi(\omega_1 + \omega_2 + \omega_3)(J(\omega_1, \omega_2, \omega_3) + K(\omega_1, \omega_2, \omega_3)) \quad (56)$$

where,

$$J(\omega_1, \omega_2, \omega_3) = \frac{2}{3}c_2 \sum_c \omega_1(\omega_2 + \omega_3)H_1^b(\omega_1)H_2^b(\omega_2, \omega_3) \quad (57)$$

and,

$$K(\omega_1, \omega_2, \omega_3) = -6ic_3 \prod_{n=1}^3 \omega_n H_1^b(\omega_n) \quad (58)$$

The output spectrum for the skyhook is given by equation (50) and the discomfort function is computed exactly as before.

AN EXAMPLE

The discomfort function for the De Carbon model is computed here. The mass m and stiffness k are taken from page 163 of [9], $m = 240$ kg and $k = 16000$ N/m. The coefficients of the damper are taken from a least-squares curve-fit to the force-velocity characteristic of a McPherson strut [6],

$$f_d(\dot{y}) = 2960\dot{y} + 9650\dot{y}^2 + -13200\dot{y}^3 \quad (59)$$

The velocity range over which the curve-fit was valid was -0.2 m/s to 0.2 m/s and this corresponds to an amplitude of excitation X of approximately 600 N. The corresponding discomfort function D_2 computed from (30) is shown in Figure 5 for frequencies from 0 Hz to 100 Hz. Also shown is the discomfort which results when f_d is taken as linear with,

$$f_d(\dot{y}) = 2960\dot{y} \quad (60)$$

(Note that this specification is not conservative. The linear damping should strictly be increased to dissipate the same amount of energy per cycle as the nonlinear model.)

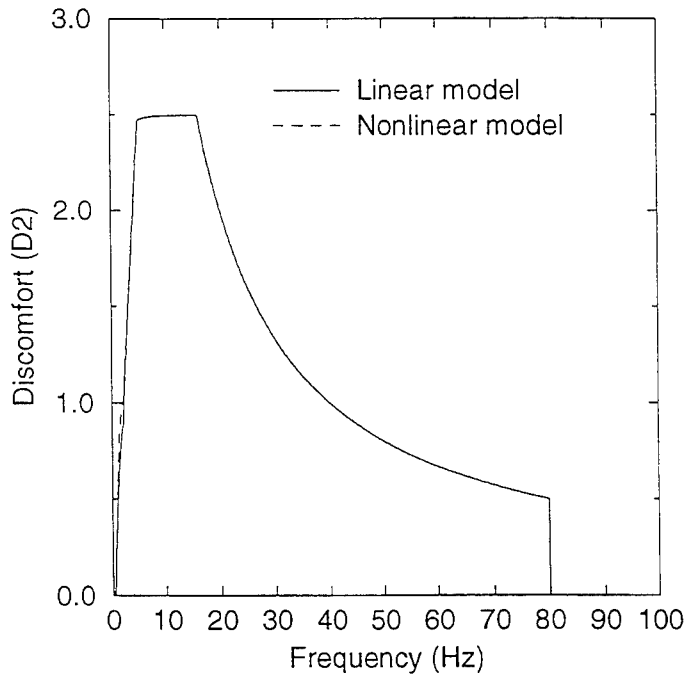


Figure 5. Discomfort functions for linear and nonlinear suspensions.

The two traces almost overlay, which seems to indicate that energy transfer from the fundamental to the third harmonic is not a substantial source of discomfort. Note that the linear resonance of the system is at 1.3 Hz, well down on the discomfort weighting factor. The region of the discomfort curve which does show a difference between linear and nonlinear dampers is between 0 Hz and 5 Hz (Figure 6). The reason for this is that as the fundamental frequency runs from 1.66 Hz to 5.33 Hz, the corresponding harmonics are in the unity weighted region of the weighting curve and contributes to the discomfort. Note that the increase in discomfort at 2.0 Hz on the graph say, is *not* due to the response component at 2.0 Hz but due to components at 4.0 and 6.0 Hz, the harmonics. Energy is transferred from frequencies where little discomfort is experienced to frequencies in the human-body resonance region at about 5.0 Hz. This mechanism can also produce discomfort when the fundamental is below 0.5 Hz even though the weighting curve is zero there. The harmonics increase the discomfort only around the resonant frequency, this is in broad agreement with the conclusions of [16], which were obtained using a multi-body simulation code.

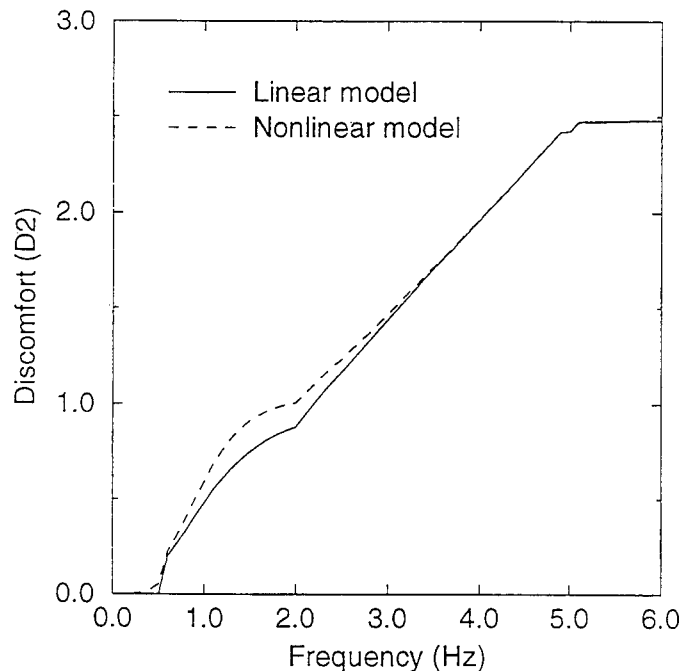


Figure 6. Discomfort functions for linear and nonlinear suspensions (zoomed).

Note that the ultimate quantity of interest is a global measure of the discomfort as local (in frequency) increases in $D_2(\omega)$ could be compensated

by local decreases elsewhere in the frequency range. A global measure can be obtained by integrating D_2 i.e.,

$$D_3 = \int_0^{\omega_{max}} d\omega D_2(\omega) \quad (61)$$

It is clear from Figures 5 and 6 that the low frequency increases in D_2 for the nonlinear system are not compensated. Thus D_3 for the nonlinear system is greater than D_3 for the linear system. In fact, if ω_{max} is taken as 10π (corresponding to 5 Hz), the D_3 index increases from 5.94 to 6.22 in going from the linear to nonlinear case; an increase of 4.7%.

CONCLUSIONS

It is shown how to compute the transmission of energy through a number of simple but often used suspension models. This allows an assessment of the ride comfort properties of the models. It is shown for the De Carbon model - the simplest suspension - that the nonlinearity of the damper does not appear to contribute substantially to discomfort except at frequencies near the linear resonance of the system. There the energy transfer mechanism from fundamental to harmonics contributes significantly to discomfort. Work is currently in progress to assess the effects of nonlinearity in the two degree-of-freedom suspension models. The ultimate aim of the research is to express the discomfort of the damper as a function of the damper parameters, thereby establishing design guidelines.

ACKNOWLEDGEMENTS

The author would like to acknowledge many useful conversations with Drs Steve Cafferty and Graeme Manson, and particularly with Mr. J. Giacomini for his advice on practical matters.

References

- [1] Ali (M.M.) & Storey (C.) 1996 *Proceedings of Conference on Adaptive Computing in Engineering Design and Control, Plymouth* pp.167-173.
The optimal control of vehicle suspension systems.
- [2] Barrett (J.F.) 1963 *Journal of Electronics and Control* **15** pp.567-615.
The use of functionals in the analysis of nonlinear systems.
- [3] Bedrosian (E.) & Rice (S.O.) 1971 *Proceedings IEEE* **59** pp.1688-1707.
The output properties of Volterra systems driven by harmonic and Gaussian inputs.

-
- [4] British Standards Institution 1987 *Measurement and Evaluation of Human Exposure to Whole-Body Mechanical Vibration and Repeated Shock*. BS 6841.
- [5] Bourcier De Carbon C. 1950 *Atti Congresso SIA, Parigi*. Theorie matématique et réalisation pratique de la suspension amortie des véhicules terrestres.
- [6] Cafferty (S.) 1996 *Ph.D Thesis, School of Engineering, Victoria University of Manchester*. Characterisation of automotive shock absorbers using time and frequency domain techniques.
- [7] Cafferty (S.), Giacomini (J.) & Worden (K.) 1997 *This Proceedings*. Simple nonlinear models for automotive shock absorbers.
- [8] Friedlander (F.G.) 1982 *Introduction to the Theory of Distributions*. Cambridge University Press.
- [9] Gillespie (T.D.) 1992 *Fundamentals of Vehicle Dynamics*. Society of Automotive Engineers, Inc.
- [10] Gradshteyn (I.S.) & Ryzhik (I.M.) 1980 *Tables of Integrals, Series and Products* Academic Press.
- [11] Griffin (M.J.) 1990 *Handbook of Human Vibration*. Academic Press.
- [12] Hall (B.B.) & Gill (K.F.) 1987 *Proceedings of IMechE part D: Journal of Automobile Engineering* **201** pp.135-148. Performance evaluation of motor vehicle active suspension systems.
- [13] I.S.O. 2631/1 1985 *Evaluation of Human Exposure to Whole-Body Vibration - Part I: General Requirements*.
- [14] Jolly (A.) 1983 *International Journal of Vehicle Design* **4** pp.233-244. Study of ride comfort using a mathematical model of a vehicle suspension.
- [15] Olatunbosun (O.A.) & Dunn (J.W.) 1992 in *Proceedings of the 2nd International Conference on Ride Comfort*. An evaluation of the effect of suspension nonlinearities on vehicle ride.
- [16] Pisino (E.), Giacomini (J.) & Campanile (P.) 1993 *NATO ASI Conference on Computer Aided Analysis of Rigid and Flexible Mechanical Systems, Troia, Portugal*. Numerical investigation of the influence of the shock absorber on the vertical force transmissibility of a McPherson suspension.

- [17] Schetzen (M.) 1980 *The Volterra and Wiener Theories of Nonlinear Systems*. John Wiley Interscience Publication. New York.
- [18] Storer (D.M.) 1991 *Ph.D. Thesis, Department of Engineering, Victoria University of Manchester*. Dynamic analysis of non-linear structures using higher order frequency response functions.
- [19] Volterra (V.) 1959 *Theory of Functionals and Integral Equations*. Dover Publications, New York.

NON-LINEAR VIBRATIONS AND INSTABILITIES OF STRUCTURAL SYSTEMS LIABLE TO ASYMMETRIC BIFURCATION

Donald M. Santee
Paulo B. Gonçalves
Pontifícia Universidade Católica - PUC-Rio
Civil Engineering Department
Rio de Janeiro - CEP 22453-900 - Brazil

ABSTRACT

The investigation of the non-linear dynamic behavior and stability of structural systems liable to asymmetric bifurcation is undertaken. Computer simulations obtained by numerical integration of the equations of motion, analytical solutions and approximate solutions obtained by perturbation procedures are used to determine the equilibrium configurations, while Floquet analysis is used to study their stability and identify the bifurcation points along the equilibrium paths. Attention is focused on the determination of stability boundaries in control space and the bifurcation events connected with these boundaries. Finally, different criteria for escape are presented and the results are compared with those obtained by numerical simulations.

INTRODUCTION

This work examines the dynamics and instabilities of a structural system that exhibits an asymmetric point of bifurcation along its fundamental equilibrium path.

A large number of structural systems such as frames, arches and shells under certain boundary and static loading conditions may display an asymmetric post-buckling equilibrium path near the bifurcation point [1,2]. This post-buckling path usually exhibits a sharp initial slope, which leads to a high imperfection sensitivity and, as a result, a large scatter of buckling loads [3]. This has a unpleasant influence on the load carrying capacity of the structure and, for a structural element under dynamic conditions (impulses, impacts, periodic loads, etc.), there is always a risk of loss of stability even for small levels of static pre-loading and dynamic disturbances. In these

circumstances refined non-linear analyses of a particular structure are of little help in accessing the safety of a real system.

Hence, because of the above-raised uncertainties, it becomes clear that what is needed for design is to understand the ways in which stability is lost and to derive theoretically well founded predictive criteria of the stability bounds of dynamic loads in the control space.

Recently, due mainly to the discovery of chaotic motions in physical systems, the field of non-linear dynamics has experienced considerable development and a large collection of theoretical and numerical algorithms were derived for the analysis of such systems [4,5,6]. These tools can be used to study the non-linear dynamics of autonomous and non-autonomous systems with any number of degrees of freedom, although most of them are particularly suited to the analysis of SDOF models. The study of basins of attraction, bifurcation diagrams, Floquet multipliers, phase portraits, energy distributions, among other tools, enables one to study the mechanics of escape and derive predictive criteria for the stability analysis of such systems. Among various loading cases, the study of harmonically excited systems is important since, in many circumstances, the external excitation can be described as an harmonic force.

Here in this paper, using a SDOF model, a detailed analysis of the non-linear dynamic behavior of pre-loaded structural systems susceptible to asymmetric bifurcation under harmonic loads is presented. Numerical and analytical tools are used to obtain stability boundaries in control space and to identify the various bifurcation events associated with these boundaries. The knowledge of these mechanisms enables one to develop predictive criteria for the dynamic instability loads. They can also be used to evaluate the safety and reliability of a given system and thus may serve as a guide-line for the design of these elements. Here, various predictive criteria are presented and critically compared with the actual escape loads. Although the analysis is concentrated on SDOF models, the phenomenological characteristics may be applicable to any structural system exhibiting asymmetric bifurcation.

STATIC ANALYSIS AND BASIC DEFINITIONS

The simplest potential energy expression for a structural system, liable to asymmetric bifurcation, under static pre-loading, is given by [1-3]

$$V(x) = \varepsilon x + \frac{1}{2}(P_{cr} - P)x^2 + \frac{1}{3}\beta x^3 \quad (1)$$

where x is a generalized coordinate, $P_{cr} - P$ is the effective stiffness of the structural system, β represents the system non-linearity and ε is a small imperfection parameter. Here P_{cr} is a critical load parameter which depends only on the physical and geometrical characteristics of the structure and P is a load parameter associated with the applied static loading.

The static equilibrium configurations, obtained from the principle of the stationary value of the total potential energy, are given by

$$x_{eq1,2} = -\frac{(P_{cr} - P)}{2\beta} \pm \frac{\sqrt{(P_{cr} - P)^2 - 4\beta\varepsilon}}{2\beta} \quad (2)$$

The stability of the equilibrium configurations are analyzed by evaluating the second derivative of (1)

$$\left. \frac{d^2V}{dx^2} \right|_{x=x_{eq}} = (P_{cr} - P) + 2\beta x_{eq} \quad (3)$$

at each equilibrium point. If (3) is positive, x_{eq} represents a local minimum and the equilibrium is stable, while if (3) is negative, x_{eq} is a local maximum of V and the equilibrium is unstable. When $\varepsilon = 0$ the structure is said to be perfect. A family of equilibrium paths for perfect and imperfect systems are shown schematically in Figure 1, where the load parameter P is plotted as a function of the incremental co-ordinate x . Here, a solid curve indicates a stable equilibrium path and a dashed curve indicates an unstable equilibrium path. The trivial fundamental path of the perfect system intersects the post-buckling path at $P = P_{cr}$, where a change of stability occurs. The asymmetric aspect caused by the non-zero slope at this bifurcation point is the reason why the structure is said to be liable to asymmetric bifurcation. The ever present imperfections break down the equilibrium path and its bifurcation. When the imperfection parameter ε has the same sign as the non-linearity parameter β , there is a load level $P_{lim} < P_{cr}$ above which there are no equilibrium positions. When $P = P_{lim}$ the stable and unstable equilibrium points meet in a saddle-node like bifurcation. In terms of the system's parameters the limit load is given by

$$P_{lim} = P_{cr} - \sqrt{4\beta\varepsilon} \quad (4)$$

Similar result was obtained by Koiter [1,3] and is shown graphically in Figure 2. At the point $\varepsilon = 0$ the slope is infinite

indicating a sharp drop in the load carrying capacity even for negligible imperfection levels. For this reason this type of structure is said to be sensitive to initial imperfection. When ε and β have the same sign there are no limit points and the stable equilibrium path increases indefinitely as the load increases. One can observe that, for either perfect or imperfect systems, at any load level, the potential energy exhibits a minimum and a maximum that coalesce at the bifurcation or limit point.

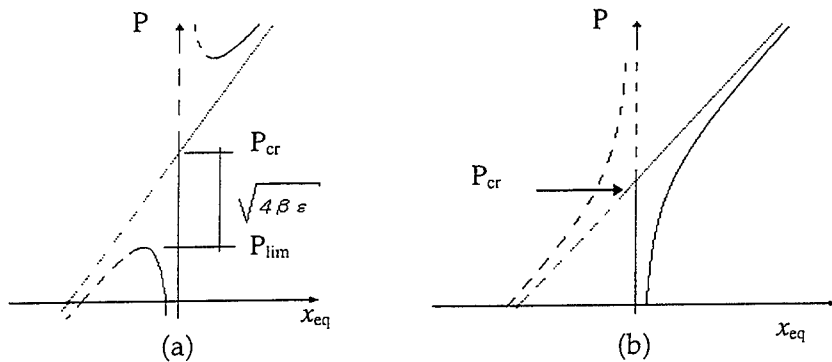


Figure 1 - Equilibrium paths for a perfect and imperfect structure: a) ε and β have the same sign; b) ε and β have opposite signs.

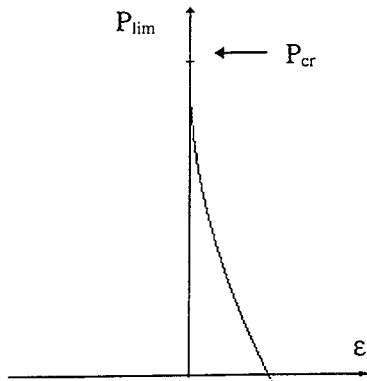


Figure 2 - The drop in loading capacity of the structure due to imperfections.

NON-LINEAR VIBRATIONS AND INSTABILITIES

In this section the mathematical model for the dynamic analysis of the system is presented and some general properties are discussed.

Conservative system.

For static load levels smaller than the critical value, the fundamental solution is stable. In many engineering problems this is

the equilibrium configuration whose stability must be preserved. Static stable solutions are only possible, according to Lyapunov, if any dynamical disturbance leads to motions in phase space which remain in the vicinity of the static equilibrium point for all time. Here the degree of safety of these stable equilibrium configurations is analyzed.

The differential equation that describes the dynamic behavior of the unforced and undamped system is given by

$$m\ddot{x} + \varepsilon + (P_{cr} - P)x + \beta x^2 = 0 \quad (5.a)$$

$$x(0) = x_0 \quad (5.b)$$

$$\dot{x}(0) = v_0$$

where m is the generalized mass and (\cdot) denotes differentiation with respect to time.

The associated total energy of the system is.

$$E(x, \dot{x}) = \frac{1}{2} m \dot{x}^2 + \varepsilon x + \frac{1}{2} (P_{cr} - P) x^2 + \frac{1}{3} \beta x^3 = E(x_0, v_0) \quad (6)$$

For static load levels below the critical load value the system displays at least two equilibrium points: one stable equilibrium point associated with pre-buckling configurations and an unstable equilibrium point related to the unstable branch of the post-buckling response. The level curves of $E(x, \dot{x}) = \text{constant}$ are the solution curves of (6). For the present case the phase portraits for different energy levels are drawn in Figure 3 for a perfect system and $P < P_{cr}$. As observed, there are mainly two types of solution: a) a type of solution that oscillates around the stable equilibrium point and remains bounded; and b) a type of solution that escapes to infinity. The type of response depends only on the initial conditions. The homoclinic orbit that connects the saddle, associated with the unstable equilibrium point, to itself and encloses the stable equilibrium point in the phase space is the frontier between the two types of solution. The area enclosed by the homoclinic orbit is given by

$$A = 2 \int_{-\frac{\sqrt{(P_{cr}-P)^2 - 4\beta\varepsilon + P_{cr}-P}}{2\beta}}^{\frac{\sqrt{(P_{cr}-P)^2 - 4\beta\varepsilon + P_{cr}-P}}{2\beta}} \sqrt{\frac{2}{m} (E_0 - \varepsilon x - 2\alpha x^2 - 3\beta x^3)} dx \quad (7)$$

For small imperfection levels ($\varepsilon \ll 1$) the safe basin area can be approximated, after expanding equation (7) in a Taylor series, by

$$\text{Area} \cong A = \frac{6(P_{cr} - P)^{5/2}}{5\beta^2} - \frac{6\varepsilon\sqrt{P_{cr} - P}}{\beta} \quad (8)$$

The set of points inside this closed curve is called here the conservative basin of attraction. This defines the region where unavoidable dynamic perturbations leads to stable motions around the fundamental configuration. So, for initial conditions inside this region of the phase plane, the pre-buckling configuration is Lyapunov stable. Any perturbation whose initial conditions lie outside this region generates a diverging motion to infinity or to a stable post-buckling configuration far away from the original equilibrium configuration, leading as a rule to a failure of the system. The region occupied by this stable basin of attraction depends greatly on the distance between the stable and unstable points and consequently on the slope of the post-buckling path of the structural system. As the static load level increases the area of this basin of attraction decreases rapidly and disappears at the bifurcation or limit point (saddle-node bifurcation), as shown in Figure 4, where the safe basin area of a perfect system is plotted as a function of the static pre-loading. This explains the high sensitivity of these systems not only to initial geometric and loading imperfections, as shown by Koiter [3], but to any class of dynamic disturbances which may arise accidentally during the construction or service life of the structure. This area can be taken as a measure of the stability of the structure. If the basin is small, then small disturbances on the initial conditions can lead to escape and, consequently, to a failure of the system. The safe basin area is only slightly affected by small damping ratios such as those usually encountered in slender structural systems and the present conclusions remain unaltered if damping is included in the analysis.

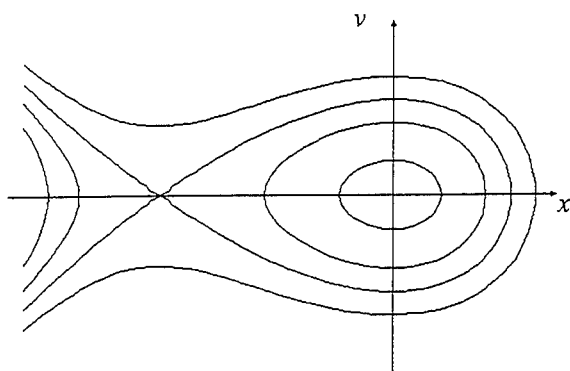


Figure 3 - Trajectories of the solution on the phase space for different initial conditions. Perfect system.

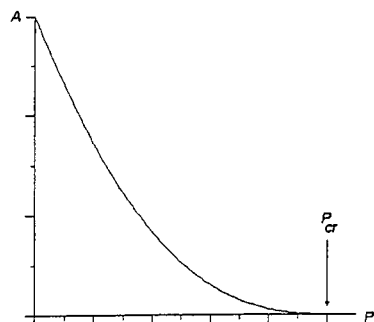


Figure 4 - Variation of the safe basin area with the static load level.

Dynamic behavior under harmonic loading.

When the structure is subjected to an external harmonic loading in a viscous damping environment, equation (5.a) becomes

$$m\ddot{x} + c\dot{x} + \varepsilon + (P_{cr} - P)x + \beta x^2 = F \cos(\Omega t) \quad (9)$$

where Ω is the frequency of the harmonic loading, F is the maximum intensity of the force, and $c > 0$ is the viscous damping coefficient.

Under these new circumstances the system is no longer autonomous and conservative, but the set of solutions can still be classified in the same sense as before, that is, bounded solutions and unbounded (escape) solutions.

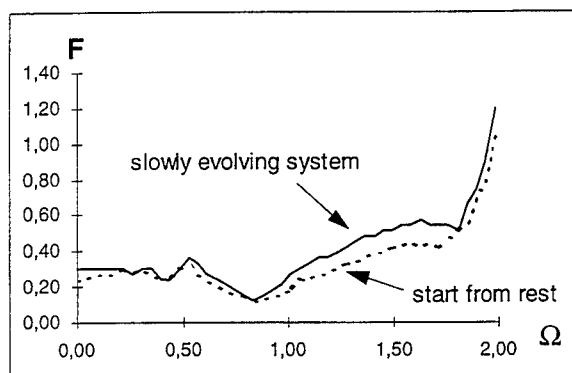


Figure 5 - Escape boundary curves: a) Gradually increased load; b) Suddenly applied load (system initially at rest).

For a system under dynamic loads, escape from the potential well associated with the stable static fundamental solution is more difficult to determine and a detailed numerical analysis of the dynamic buckling must be carried out as a function of the control variables [7-11]. For a harmonically excited system, the variation of the escape load as a function of the forcing parameters F and Ω is shown in Figure 5 (the parameter values used in these examples are: $m=1$, $c=0.1$, $\varepsilon=0$, $P_{cr}=1$ and $\beta=-1$). The slowly evolving system escape boundary was generated by the following method: for each fixed value of Ω a small initial value of F was used to integrate the differential equation over a fixed period of time. If the solution did not escape after this time a small increment ΔF was given to F and the last position and velocity values were used as the new initial conditions. This process was repeated until the solution escaped within the fixed time interval and the value of F was plotted. The start from rest escape boundary was obtained in a similar manner. The difference is that at each increment of F the initial conditions were set to zero, assuming that the system is initially at rest. As one can observe, the stability boundary is composed of various "curves", each one associated with a particular bifurcation event. The deepest well is associated with the primary non-linear resonance zone, while the other wells to the left are connected with the super-harmonic resonances of various orders. A detailed parametric analysis indicates that the descending branches are the locus of saddle-node bifurcations, whereas the ascending branches are associated with sub- and super-critical flip bifurcations. Figure 7 shows bifurcation diagrams, due to the variation of load parameter F , for different values of Ω . The stability of the periodic solutions is determined by the calculation of its Floquet or characteristic multipliers. For low values of Ω , the harmonic and static escape loads are practically the same, as expected, while in other regions the magnitude of the escape load can be much lower or higher than the static value. The lowest critical load occurs around $\Omega=0.85$, just to the left of $\Omega=1.00$, which is the natural frequency, due to the softening characteristics of the system.

Although the ascending branches appear to be smooth, they are in fact discontinuous. Figure 6 shows a region in the parameter plane $F \times \Omega$ in which the structure initially at rest escapes (white points) or not (black points) within a period of 32 times the forcing period. The fractal nature of the escape regions corroborate the assumption of a discontinuous boundary. It has been also shown in literature that the basin boundary in this region is also fractal [12,13]. In this region there is a high degree of unpredictability and a safe lower bound is necessary for design.

ESCAPE CRITERIA

One of the aims in engineering design is to predict the maximum load capacity of a structure. Thus for an imperfection sensitive structure liable to asymmetric bifurcation under a harmonic loading it is important to have a criterion that enables one to predict under which circumstances the structure may lose its stability and escape. Recently a number of papers were published on this subject [7-13]. A summary of various predictive criteria proposed in recent years are presented by Szemplinka-Stupnicka [9]. Here, based on geometric characteristics of the basin of attraction and potential energy or on approximate periodic solutions of equation (9), some criteria have been implemented for this particular problem and tested. These criteria are described below and compared with the stability boundary obtained numerically.

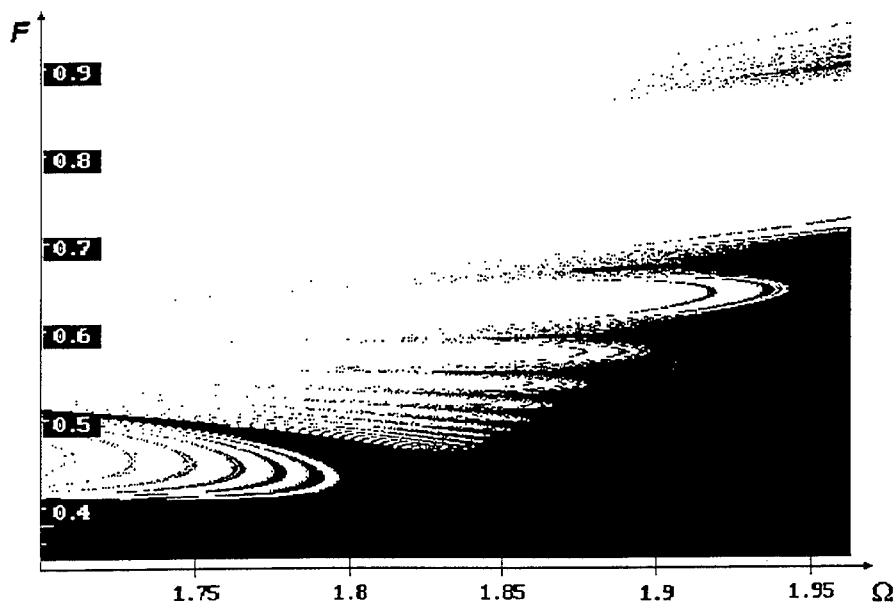
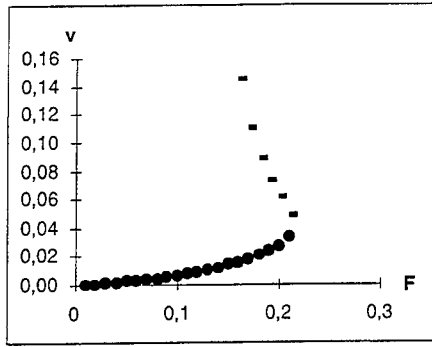
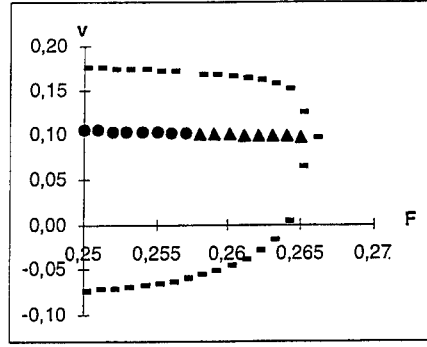


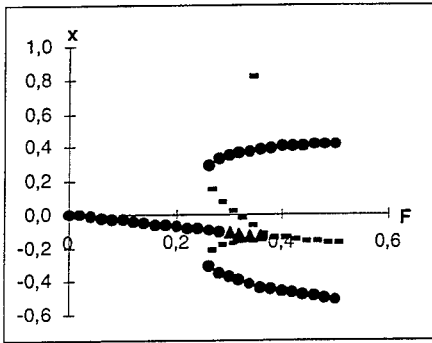
Figure 6 - Regions of escape in the $F \times \Omega$ plane of the structure under suddenly applied harmonic external loading.



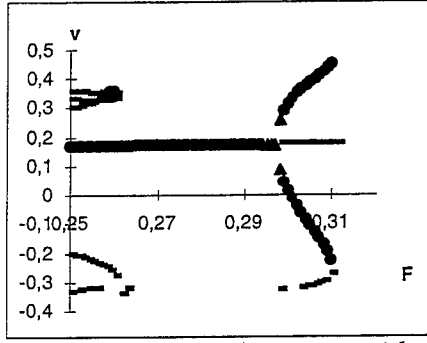
a) saddle-node bifurcation
($\Omega=0.36$)



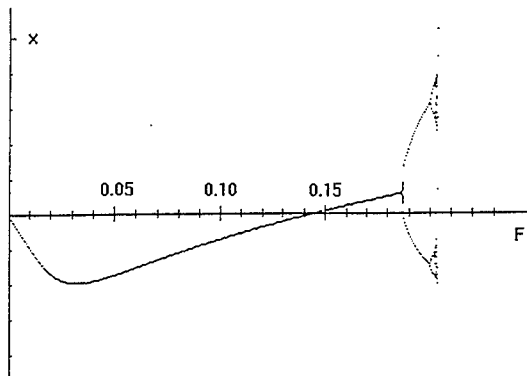
b) sub-critical bifurcation ($\Omega=0.51$)



c) sub-critical bifurcation with a
post-critical minimum ($\Omega=1.87$)



d) super-critical bifurcation with a
post-critical maximum ($\Omega=1.20$)



e) period doubling cascade of bifurcations leading to
chaos/escape ($\Omega=1.00$)

Figure 7 - Different escape mechanisms. The symbols mean: \bullet Stable Focus, \blacktriangle - Stable node and \square - Saddle.

The maximum displacement criterion.

This criterion states that escape will occur when the maximum displacement of the solution is greater than the maximum displacement of the conservative basin of attraction.

The maximum impulse criterion.

This criterion states that escape will occur when the maximum velocity of the solution is greater than the maximum velocity of the conservative basin of attraction.

The maximum energy criterion.

This criterion states that escape will occur when the instantaneous energy of the solution becomes greater than the potential energy associated with the saddle equilibrium position, called potential barrier.

The loss of stability criterion.

This criterion states that escape will occur when the fundamental period one solution loses its stability, either through saddle-node bifurcation or period doubling.

The criterion of maximum energy is similar to the criteria of maximum displacement and velocity since it is equivalent as stating that escape will happen when the solution leaves the conservative basin of attraction. None of the first three criteria uses information about the real mechanisms of escape.

On the other hand, the loss of stability criterion does take into account the actual mechanisms of escape and can be easily implemented. It must be pointed out that these criteria are extremely dependent on the quality of the approximate analytical solution of the non-linear equation of motion.

The approximate solution.

The approximate analytical solution used here was obtained by the Lindstedt-Poincaré method [6] and is given by

$$x(t) = -\frac{\varepsilon}{P_{cr} - P} - \frac{a^2 \beta}{2(P_{cr} - P)} + a \cos(\Omega t - \phi) + \frac{a^2 \beta}{3(P_{cr} - P)} \cos(2\Omega t - 2\phi) \quad (10)$$

The amplitude, a , and phase angle, ϕ , of the response can be determined by solving the non-linear system

$$\begin{aligned} \sin(\phi) &= \frac{a c \Omega}{F} \\ \frac{(P_{cr} - P)}{m} &= \Omega^2 + \frac{F \cos(\phi)}{m a} + \frac{5 a^2 \beta}{6(P_{cr} - P)} + \frac{2 \beta \varepsilon}{m(P_{cr} - P)} \end{aligned} \quad (11)$$

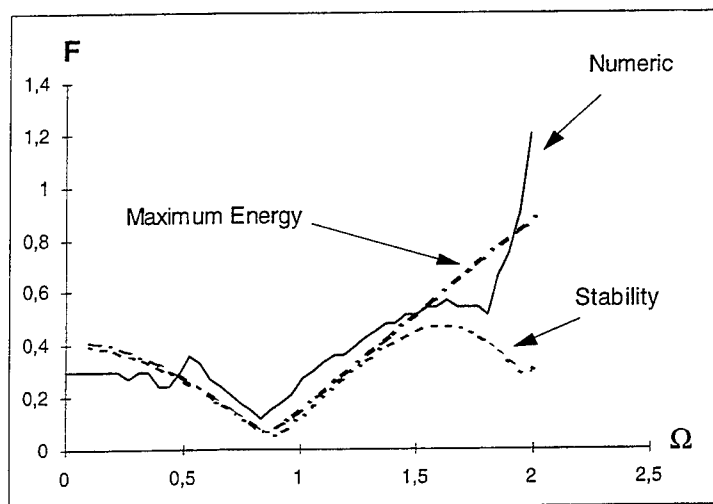


Figure 8 - Escape boundary by numerical and approximate methods.

In Figure 8 the escape boundary obtained by numerical integration is compared with the results obtained by the maximum energy and loss of stability criteria. Close to the main resonance zone both criteria are in good agreement, being a lower bound of the actual escape load. For forcing frequencies greater than the natural frequency ($1.4 < \Omega < 1.8$), the loss of stability criterion gives better results because it captures the real mechanism of escape in this frequency region. For large ($\Omega > 1.8$) or small ($\Omega < 0.5$) forcing frequencies the escape load can't be predicted by these criteria. For small forcing frequencies ($\Omega < 0.5$), the static buckling load can be used as escape load. For large forcing frequencies ($\Omega > 1.8$) the stability criterion is incapable of predicting the escape load because the load at which the period one solution loses its stability - the event predicted by this criterion - (see Figure 7.c) can be much lower than the escape load since the period two solution may remain stable for values of F much greater than this critical load. It should be pointed out that in this region the dynamic response is very sensitive to small disturbances and a safer lower bound should be derived to be used in design.

CONCLUSIONS

Structural systems liable to asymmetric bifurcation, when subjected to dynamic disturbances may exhibit dynamic buckling loads much lower than the static critical loads. In the dangerous zones, there are

different escape mechanisms whose identification is essential in deducing reliable predictive criteria for buckling loads and evaluating the integrity of a given system. The present results confirm, from a dynamical point of view, the high imperfection-sensitivity and the difficulties in accessing the load carrying capacity of these structures.

REFERENCES

- 1 - Z. BAZANT and L. CEDOLIN 1991 *Stability of Structures*. Oxford: Oxford University Press.
- 2 - J. M. T. THOMPSON and G. W. HUNT, 1973 *A General Theory of Elastic Stability*. London: Wiley
- 3 - J. W. HUTCHINSON and W. T. KOITER 1970 *Applied Mechanics Reviews* **13**, 1353-1366. Post-Buckling Theory
- 4 - M. S. EL NASCHIE 1990. *Stress, Stability and Chaos in Structural Engineering: An Energy Approach*. London: McGraw-Hill
- 5 - T. S. PARKER and L. O. CHUA 1989 *Practical Numerical Algorithms for Chaotic Systems*. Berlin: Springer-Verlag.
- 6 - E. J. HINCH 1992 *Perturbation Methods*. Cambridge: Cambridge University Press.
- 7 - J. M. T. THOMPSON 1989 Proc. R. Soc. London A421, 195-225. Chaotic phenomena triggering the escape from a potential well.
- 8 - L. N. VIRGIN, R. H. PLAUT and C. C. CHENG 1992 *Int. J. Non-Linear Mechanics* **27**(3), 357-365. Prediction of escape from a potential well under harmonic excitation.
- 9 - M. S. SOLIMAN 1993 *ASME J. of Applied Mechanics* **60**, 669-676. Jumps to resonance: long chaotic transients, unpredictable outcome, and the probability of restabilization.
- 10 - M. S. SOLIMAN 1994 *Nonlinear Dynamics* **6**, 317-329. Global transient dynamics of nonlinear parametrically excited systems.
- 11 - W. SZEMPLINSKA-STUPNICKA 1995 *Nonlinear Dynamics* **7**, 129-147. The analytical predictive criteria for chaos and escape in nonlinear oscillators: a survey
- 12 - M. S. SOLIMAN and J. M. T. THOMPSON 1989 *Journal of Sound and Vibration* **135**, 453-475. Integrity measures quantifying the erosion of smooth and fractal basins of attraction.
- 13 - F. C. MOON 1992 *Chaotic and Fractal Dynamics*. John Wiley & Sons, New York, USA.

Galloping of Twin-Bundled Conductors

N. Popplewell, M. Liao and A. Shah

Faculty of Engineering, University of Manitoba
Winnipeg, Canada R3T 5V6

ABSTRACT: A nonlinear model has been developed to investigate the full-span oscillations of an iced twin-bundled transmission line, the type of oscillations often observed in the field. Numerical solutions involve a finite element analysis in conjunction with a perturbation scheme to account for a line's geometric nonlinearity, prestress forces and nonlinear aerodynamic loads. By eliminating the sub-span motions between the two conductors, the twin bundle is modelled as an equivalent single conductor so that the total number of degrees-of-freedom is reduced by half and computational efficiency is improved greatly. The aerodynamic forces acting on the conductors are obtained from experimental wind tunnel simulations by applying a quasi-steady theory. The initiation of galloping is investigated numerically by using a conventional stability analysis. Limit cycle amplitudes, if oscillations occur, are obtained from a computationally efficient, Krylov-Bogoliubov averaging method and their stability is also studied. In addition, a computationally expedient time marching algorithm is used to compute the response for those instances where averaging procedures cannot be employed. Examples are presented to illustrate typical oscillations of iced, twin conductors.

INTRODUCTION

Overhead electrical transmission lines consist of single or bundled conductors, insulator strings, support hardware, spacers and tower components. (See Figure 1.) They are often subjected to wind-induced vibrations caused by a steady normal wind. There are three types of oscillations which bundled conductors may experience, viz. galloping, wake-induced oscillations or aeolian vibrations. Galloping is characterized by low (0.1 to 3Hz) frequency, large amplitude, self excited oscillations. It is produced by aerodynamic instabilities, which stem from asymmetry in a conductor's cross section due to ice accretion or, more rarely, the stranding of the conductor itself. Galloping instabilities of bundled conductors involve mainly the bulk motion of the bundle. Wake-induced oscillation, on the other hand, is produced by the aerodynamic forces arising from the shielding effects of the windward conductors, and has a frequency range from 0.75 to 6Hz. The resulting instabilities may involve both subspan and full span motions when the conductors are connected by spacers. Moreover, aeolian vibration is a high frequency, low amplitude oscillation compared to galloping. It is caused by an alternating wind force induced by a pressure difference due to a regular formation of air vortices behind a conductor.

It is often observed in the field that twin conductors move in phase when vibrating in a bundle. The sub-span motion, conversely, is imperceptible. Therefore, the full span motion alone, or bulk motion of the twin bundle is often studied for practical purposes. Researchers have considered an equivalent single conductor model for the bundle to study the full span motion [1] and the galloping of a single conductor transmission line has been investigated successfully [2, 3]. Moreover, an oscillator analysis based on a damped spring and mass model for twin bundles [4] and a finite element analysis using tensioned beam elements for triple bundles [5] have been performed. Based on scarcity of the available research, it can be concluded that further analytical work on full span oscillation of ice coated twin-bundle conductors needs to be performed.

In this paper, the full span bulk motion of an iced twin bundle is investigated, whereas the sub-span motion is neglected. Hence, the twin bundle is modelled as an equivalent single conductor, the motion of which can be represented by the displacement and rotation of a reference line located midway between the two conductors. A finite element technique is coupled with a perturbation scheme and the nonlinear, algebraic equations of motion are derived and solved. Cable elements are used to represent the conductors and rigid spacers are assumed to restrict the motion between two corresponding nodal points on the two conductors. Consequently, both the flexibility of the conductors and the rigidity of the spacers are considered. Compared with the case when both full span and sub-span motions are employed, the computer program is much less time consuming and needs less memory because the number of variables representing the bulk motion is the same as that for a single conductor. Again, the initiation of galloping, the limiting amplitude if galloping occurs, as well as the history of the twin-bundled transmission line's motion are investigated.

FORMULATION

Mathematical model

The bulk motion of a twin bundle can be represented by the displacement and rotation of a reference line between the two conductors that is designated the center of rotation, as shown in Figure 2. It is assumed that the rotation about this center is small and that the longitudinal motions of both conductors are negligible. The overhead conductors are modelled by using computationally efficient, three-node isoparametric cable elements. Relative movements between two corresponding nodal points on the conductors are constrained by spacers. Rigid spacers link the conductors along the lines at nodal points, e.g., a massless, fictitious spacer joins corresponding conductor nodes not defining a physical spacer. The equivalent single conductor model can take advantage of the results from previous research on single conductors [2].

Modelling the two individual conductors

By considering two separate conductors lying side by side, the equations of

motion for the windward and leeward conductors are written, respectively, as

$$[M_w]\{\ddot{q}_w\} + [C_w]\{\dot{q}_w\} + [K_w]\{q_w\} = \{F_w\} + \{F_{sw}\} \quad (1)$$

and

$$[M_l]\{\ddot{q}_l\} + [C_l]\{\dot{q}_l\} + [K_l]\{q_l\} = \{F_l\} + \{F_{sl}\}. \quad (2)$$

The $[M_i]$, $[C_i]$ and $[K_i]$, $i = w$ and l , are the $N \times N$ mass, damping and stiffness matrices and subscripts w and l denote the windward and leeward conductors, respectively. Vectors $\{q_w\}$, $\{F_w\}$ and $\{F_{sw}\}$ are the displacements, external aerodynamic loads and the forces simulating the effects of the spacers on the windward conductor, respectively. The $\{q_l\}$, $\{F_l\}$ and $\{F_{sl}\}$ are analogous vectors for the leeward conductor. The effects of the ice formation on the conductors are taken into account when forming the mass and stiffness matrices. The procedure for constructing $[M_w]$ and $[M_l]$, $[C_w]$ and $[C_l]$, as well as $[K_w]$ and $[K_l]$ is similar to that used in reference [2].

Forces on the spacers, $\{F_{sw}\}$ and $\{F_{sl}\}$

Equations of motion for the twin conductor bundle are derived from equations (1) and (2) in the following section. The forces given by spacers at each nodal point, j , are noted as $\{F_{swj}\}$ and $\{F_{slj}\}$ for the windward and leeward conductors, ie.

$$\{F_{sij}\} = \{F_{uij}, F_{vij}, F_{wij}, M_{ij}\}, \quad i = w, l. \quad (3)$$

Here, the F_{uwj} , F_{vwj} , F_{wwj} and M_{wj} are the forces in the x , y and z directions and the moment about the x -axis on the windward conductor whilst the F_{ulj} , F_{vlj} , F_{wlj} and M_{lj} are those on the leeward conductor. By using Newton's second law, the relations between the forces on the spacers and the movements at the center of rotation can be determined. The expressions for the massless fictitious spacers and the physical spacers are

$$\begin{aligned} -\delta_{sj} m_{sj} \ddot{u}_j &= F_{ulj} + F_{uwj} \\ -\delta_{sj} m_{sj} \ddot{v}_j &= F_{vlj} + F_{vwj} \\ -\delta_{sj} m_{sj} \ddot{w}_j &= F_{wlj} + F_{wwj} \\ -\delta_{sj} I_{sj} \ddot{\theta}_j &= M_{wj} + M_{lj} \\ &\quad + F_{vwj} l_w \cos \theta_{0j} + F_{wwj} l_w \sin \theta_{0j} \\ &\quad - F_{vlj} l_l \cos \theta_{0j} - F_{wlj} l_l \sin \theta_{0j}, \end{aligned} \quad (4)$$

where

$$\delta_{sj} = \begin{cases} 0 & \text{for a fictitious spacer at node } j \\ 1 & \text{for a physical spacer at node } j. \end{cases} \quad (5)$$

The I_{sj} and m_{sj} are the inertial moment and mass of the physical spacer at node j . The l_w and l_l are distances between the center of rotation and the windward and leeward conductors, respectively, for both the physical and fictitious spacers. The θ_{0j} is the angle between the spacer and horizontal

plane at node j whilst \ddot{u}_j , \ddot{v}_j , \ddot{w}_j and $\ddot{\theta}_j$ are the accelerations in the x , y and z directions and the angular acceleration of the twin bundle about the x -axis, respectively.

Constrained motions

The movements of both conductors can be expressed in terms of the motion at the center of rotation when the sub-span motion is neglected. Thus, the displacements and rotations have the matrix form

$$\{q_{ij}\} = [T_{ij}]\{q_j\}, \quad i = w, l, \quad (6)$$

for the windward and leeward conductors. The $\{q_{ij}\} = \{u_{ij}, v_{ij}, w_{ij}, \theta_{ij}\}^T$, $i = w, l$, and $\{q_j\} = \{u_j, v_j, w_j, \theta_j\}^T$ represent displacements in the x , y and z directions and rotations about the x -axis at the windward and leeward conductors and at the center of rotation of the twin bundle at nodal point j , respectively. The transformation matrices $[T_{wj}]$ and $[T_{lj}]$ are defined as

$$[T_{ij}] = \begin{bmatrix} 1 & 0 & 0 & 0 \\ 0 & 1 & 0 & l_i \cos \theta_{0j} \\ 0 & 0 & 1 & l_i \sin \theta_{0j} \\ 0 & 0 & 0 & 1 \end{bmatrix}, \quad l_i = \begin{cases} l_w \\ -l_l \end{cases} \quad (7)$$

where $i = w, l$. The l_w and l_l are the distances from the center of rotation to the centers of the windward and leeward conductors, respectively. The θ_{0j} is the initial rotation coordinate at node j at the center of rotation. There are two assumptions made in deriving equations (6) and (7). The first assumption is that the rotation, θ , is small; the second is that the longitudinal movements of both conductors are identical.

The velocities and accelerations can be obtained in a similar manner except that there are two terms involved in the expressions for accelerations due to the conductors' tangential and normal components with respect to the center of rotation. The expressions for the velocities and accelerations are

$$\{\dot{q}_{ij}\} = [T_{ij}]\{\dot{q}_j\} \quad i = w, l, \quad (8)$$

and

$$\{\ddot{q}_{ij}\} = [T_{ij}]\{\ddot{q}_j\} + [T_{ij0}]\{\dot{q}_j^2\} \quad i = w, l, \quad (9)$$

where

$$\{\dot{q}_j^2\} = \{\dot{u}_j^2, \dot{v}_j^2, \dot{w}_j^2, \dot{\theta}_j^2\}^T,$$

$$[T_{ij0}] = \begin{bmatrix} 0 & 0 & 0 & 0 \\ 0 & 0 & 0 & -l_i \sin \theta_{0j} \\ 0 & 0 & 0 & l_i \cos \theta_{0j} \\ 0 & 0 & 0 & 0 \end{bmatrix}, \quad l_i = \begin{cases} l_w \\ -l_l \end{cases} \quad (10)$$

$i = w, l.$

Equations of motion for the twin bundle

It can be shown straightforwardly from equations (3), (4) and (7), by using Newton's second law, that

$$[T_{wj}]^T \{F_{swj}\} + [T_{lj}]^T \{F_{slj}\} = -\delta_{sj} [M_{sj}] \{\ddot{q}_j\} \quad (11)$$

for the fictitious massless spacer as well as physical spacer, where

$$[M_{sj}] = \begin{bmatrix} m_{sj} & 0 & 0 & 0 \\ 0 & m_{sj} & 0 & 0 \\ 0 & 0 & m_{sj} & 0 \\ 0 & 0 & 0 & I_{sj} \end{bmatrix}. \quad (12)$$

Finally, by letting

$$\{q_i\} = [T_i] \{q\}, \quad i = w, l, \quad (13)$$

$$\{\dot{q}_i\} = [T_i] \{\dot{q}\}, \quad i = w, l, \quad (14)$$

as well as

$$\{\ddot{q}_i\} = [T_i] \{\ddot{q}\} + [T_{i0}] \{\dot{q}^2\}, \quad i = w, l, \quad (15)$$

the equations of motion becomes

$$[M] \{\ddot{q}\} + [C] \{\dot{q}\} + [K] \{q\} = \{F\}, \quad (16)$$

where $\{q\}$ is the global displacement vector of the bundle at the center of rotation and $\{q_w\}$ and $\{q_l\}$ are the displacement vectors on the windward and leeward conductors, respectively. They are defined as

$$\begin{aligned} \{q\} &= \{\{q_1\}^T, \{q_2\}^T, \dots, \{q_{n_p}\}^T\}^T, \\ \{q^2\} &= \{\{q_1^2\}^T, \{q_2^2\}^T, \dots, \{q_{n_p}^2\}^T\}^T, \end{aligned}$$

and

$$\{q_i\} = \{\{q_{i1}\}^T, \{q_{i2}\}^T, \dots, \{q_{in_p}\}^T\}^T, \quad i = w, l,$$

where n_p is the number of nodal points. The matrices in equation (16) are defined as

$$\begin{aligned} [M] &= [T_w]^T [M_w] [T_w] + [T_l]^T [M_l] [T_l] + [M_s] \\ [C] &= [T_w]^T [C_w] [T_w] + [T_l]^T [C_l] [T_l] \\ [K] &= [T_w]^T [K_w] [T_w] + [T_l]^T [K_l] [T_l] \end{aligned} \quad (17)$$

and the resultant force vector is given by

$$\{F\} = [T_w]^T \{F_w\} + [T_l]^T \{F_l\}. \quad (18)$$

Similarly, the aerodynamic vectors $\{F_w\}$ and $\{F_l\}$ are assembled from the force vectors $\{F_{wj}\}$ and $\{F_{lj}\}$ whilst the transformation matrices $[T_w]$ and $[T_l]$ are obtained similarly from matrices $[T_{wj}]$ and $[T_{lj}]$ at nodal point j ,

$j = 1, \dots, n_p$. The mass matrix $[M_s]$ is the contribution from the physical spacers' inertias. More specifically,

$$\{F_i\} = \{\{F_{i1}\}^T, \dots, \{F_{in_p}\}^T\}^T, i = w, l, \quad (19)$$

$$[T_i] = \begin{bmatrix} T_{i1} & 0 & \dots & 0 \\ 0 & T_{i2} & \dots & 0 \\ \vdots & \ddots & \ddots & \vdots \\ 0 & \dots & 0 & T_{in_p} \end{bmatrix}, i = w, l, \quad (20)$$

and

$$[M_s] = \begin{bmatrix} \delta_{s1} M_{s1} & 0 & \dots & 0 \\ 0 & \delta_{s2} M_{s2} & \dots & 0 \\ \vdots & \ddots & \ddots & \vdots \\ 0 & \dots & 0 & \delta_{sn_p} M_{sn_p} \end{bmatrix}. \quad (21)$$

The $[T_{w0}]$ and $[T_{l0}]$ have similar definitions to those for $[T_w]$ and $[T_l]$ when T_{wj} and T_{lj} are substituted by T_{wj0} and T_{lj0} , $j = 1, 2, \dots, n_p$, respectively.

Aerodynamic forces

The aerodynamic forces, $\{F\}$, in equation (16) are obtained directly from experimentally measured static forces and moments at the center of rotation of the twin bundle under a steady wind by applying a quasi-steady theory. These forces, which cause the conductors to vibrate, depend non-linearly upon the geometry of the iced conductors and the relative wind speed to the conductors. The general form of the aerodynamic forces per unit length can be written at each nodal point as

$$\begin{aligned} F_i &= \frac{1}{2} \rho_{air} U_{rel}^2 d C_i, \quad i = y, z, \\ M_\theta &= \frac{1}{2} \rho_{air} U_{rel}^2 d^2 C_\theta, \end{aligned} \quad (22)$$

where ρ_{air} , U_{rel} , d and C_i , $i = y, z, \theta$, are the density of air, relative wind speed with respect to a conductor, a reference structural dimension and the load coefficients, respectively. In this analysis, the coefficients C_y , C_z and C_θ are approximated by cubic polynomials of the fixed angle of attack, α , to simulate the experimental data. The polynomials take the general form

$$C_i = \sum_{j=0}^3 a_{ij} \alpha^j, \quad i = y, z, \theta. \quad (23)$$

The constants a_{ij} , $i = y, z, \theta$, $j = 0, 1, 2, 3$, are obtained from a least square curve fit of experimentally measured lift, drag and moment coefficients [2]. These coefficients are calculated as a function of the free stream speed as well as the relative wind speed for the moving twin conductors, and the instantaneous wind's angle of attack. They are measured along the line at

the center of rotation of the bundle.

Initiation of Galloping

Equations of motion (16) define the stability and motion of the conductors' bulk motion. The static configuration of a transmission line, subjected to ice and a mean steady wind load, is computed from the nonlinear, static equilibrium equations obtained by letting $\{\dot{q}\} = \{\ddot{q}\} = 0$ in equation (16). The resulting nonlinear static equations,

$$[K]\{q\} = \{F\}, \quad (24)$$

are solved by using the Newton-Raphson (N-R) iteration method [6].

The initiation of galloping is determined by the stability of the static equilibrium configuration of the transmission line. An unstable static configuration is generally called the initiation phase of galloping. The stability analysis is performed by linearizing the equations of motion near the static equilibrium configuration. Therefore, the N linearized equations are given by

$$[M]\{\ddot{q}\} + [C_L]\{\dot{q}\} + [K_L]\{q\} = \{0\}, \quad (25)$$

where

$$\begin{aligned} [C_L] &= [C] - [C_U] \\ [K_L] &= [K] - [K_U] \end{aligned} \quad (26)$$

The $[C_U]$ and $[K_U]$ stem from the linearization of the aerodynamic loads. They are formed by assembling the linearized element load vector, $\{F_L^e\}$, where

$$\{F_L^e\} = [C_U^e]\{\dot{q}^e\} + [K_U^e]\{q^e\} \quad (27)$$

Superscript e denotes elemental quantities and elements of $[C_U^e]$ and $[K_U^e]$ can be found in reference [2]. Eigenvalues of the resulting characteristic matrix, $[S_c]$, are computed from

$$[S_c] = \begin{bmatrix} [0] & [I] \\ -[M]^{-1}[K_L] & -[M]^{-1}[C_L] \end{bmatrix} \quad (28)$$

Here $[0]$ and $[I]$ are the $N \times N$ null and identity matrices, respectively. The static configuration is stable if all the eigenvalues of $[S_c]$ have a negative real part. If the static configuration is unstable, the limiting motion and history of motion are found by employing two independent methods, the Krylov-Bogoliubov(KB) [2] averaging scheme and direct time integration.

Limit cycles

By considering the equation of motion to be weakly nonlinear, time averaging schemes can be used to approximate the periodic solutions. The

equation of motion (16) is transformed first to the principal coordinate system, η_i , as [2]

$$\ddot{\eta}_i + \omega_i^2 \eta_i = F_{\eta_i} - \sum_{k=1}^{N_p} c_{i,k}^* \dot{\eta}_k, \quad i = 1, 2, \dots, N_p, \quad (29)$$

where

$$F_{\eta_i} = \sum_{j=1}^{n_p} (\phi_{4j-2,i} F_{y_j} + \phi_{4j-1,i} F_{z_j} + \phi_{4j,i} M_{\theta_j}).$$

Here n_p and N_p are the number of nodal points and principal coordinates, respectively. The ω_i^2 , $\phi_{i,j}$, F_{η_i} and $c_{i,k}^*$, on the other hand, are the squared natural frequencies, elements of the eigen function matrix $[\phi]$, forcing vector $\{F^*\}$ and the damping matrix $[C^*]$ in the principal coordinate system, respectively. Then the Krylov-Bogoliubov(KB) technique is applied to the modified equations

$$\ddot{\eta}_i + \omega_i^{*2} \eta_i = F_{\eta_i} - \sum_{k=1}^{N_p} c_{i,k}^* \dot{\eta}_k + (\omega_i^{*2} - \omega_i^2) \eta_i, \quad i = 1, 2, \dots, N_p, \quad (30)$$

where $\omega_j^* \equiv \omega_j$, $j = 1, \dots, k$, for the non-resonant modes and $\omega_j^* = \omega_j + O(\varepsilon)$, $j = 1, \dots, m$, for the resonant modes. The k and m are the number of the non-resonant and internally resonant modes, respectively, and $k + m = N_p$. Furthermore, the ω_i^* are expressed in terms of a common, but *unknown* frequency ω^* for the resonant modes. Periodic and quasi-periodic solutions of equation (30) are assumed to take the form

$$\eta_i(t) = A_i(t) \cos \Psi_i(t), \quad (31)$$

$$\Psi_i(t) = \omega_i^* t + \psi_i(t),$$

where $A_i(t)$ and $\Psi_i(t)$ are defined such that

$$\dot{\eta}_i = -A_i \omega_i^* \sin \Psi_i, \quad (32)$$

$$\dot{A}_i \cos \Psi_i = A_i \dot{\Psi} \sin \Psi.$$

Substituting equations (31) and (32) into equation (30) results in two decoupled equation sets in \dot{A}_i and $\dot{\psi}_i$, which are given by

$$\dot{A}_i \omega_i^* = F_{A_i} = [A_i(\omega_i^2 - \omega_i^{*2}) \cos \Psi_i - F_{\eta_i} - F_{c_i}] \sin \Psi_i, \quad (33)$$

$$A_i \dot{\psi}_i \omega_i^* = F_{\psi_i} = [A_i(\omega_i^2 - \omega_i^{*2}) \cos \Psi_i - F_{\eta_i} - F_{c_i}] \cos \Psi_i, \quad i = 1, \dots, N_p, \quad (34)$$

after manipulation, where

$$F_{c_i} = \sum_{k=1}^{N_p} c_{i,k}^* A_k \omega_k^* \sin \Psi_k. \quad (35)$$

Equations (33) and (34) are averaged by integrating them with respect to time, t , and treating the slowly varying functions $A_i(t)$ and $\Psi_i(t)$ effectively as constants \bar{A}_i and $\bar{\psi}_i$. The resulting $2N_p$ averaged equations are

$$\bar{F}_{A_i} = \lim_{T \rightarrow \infty} \frac{1}{T} \int_0^T [A_i(\omega_i^2 - \omega_i^{*2}) \cos \Psi_i - F_{\eta_i} - F_{c_i}] \sin \Psi_i dt \quad (36)$$

$$\bar{F}_{\psi_i} = \lim_{T \rightarrow \infty} \frac{1}{T} \int_0^T [A_i(\omega_i^2 - \omega_i^{*2}) \cos \Psi_i - F_{\eta_i} - F_{c_i}] \cos \Psi_i dt. \quad (37)$$

The constants \bar{A}_i and $\bar{\psi}_j$ and frequencies ω_i^* , $i = 1, 2, \dots, N_p$, $j = 1, 2, \dots, m$, are found by letting $\dot{\bar{A}}_i(t) = \dot{\bar{\psi}}_j = 0$ in equations (36) and (37) and solving the resulting nonlinear algebraic equations. Therefore the approximation of the limit cycle, given by equation (31), can be found.

The stability of a limit cycle is determined by performing the stability analysis on the following equations

$$\begin{aligned} \dot{\bar{A}}_i(t) &= \sum_{k=1}^{N_p} \frac{\partial \dot{\bar{A}}_i}{\partial A_k} A_k(t) + \sum_{k=1}^m \frac{\partial \dot{\bar{A}}_i}{\partial \psi_k} \psi_k(t), \\ i &= 1, 2, \dots, N_p, \end{aligned} \quad (38)$$

and

$$\begin{aligned} \dot{\bar{\psi}}_j(t) &= \sum_{k=1}^{N_p} \frac{\partial \dot{\bar{\psi}}_j}{\partial A_k} A_k(t) + \sum_{k=1}^m \frac{\partial \dot{\bar{\psi}}_j}{\partial \psi_k} \psi_k(t), \\ j &= 1, 2, \dots, m. \end{aligned} \quad (39)$$

Approximations for the partial derivatives $\partial \dot{\bar{A}}_i / \partial A_j$, $\partial \dot{\bar{A}}_i / \partial \psi_k$, $\partial \dot{\bar{\psi}}_l / \partial A_j$ and $\partial \dot{\bar{\psi}}_l / \partial \psi_k$, $i, j = 1, 2, \dots, N_p$, $k, l = 1, 2, \dots, m$, are obtained from equations (36) and (37). A $(N_p + m) \times (N_p + m)$ characteristic matrix $[S_c]$ is constructed from equations (38) and (39) such that

$$\begin{aligned} S_{c_{i,j}} &= \frac{\partial \dot{\bar{A}}_i}{\partial A_j}, & S_{c_{i,(N_p+k)}} &= \frac{\partial \dot{\bar{A}}_i}{\partial \psi_k}, \\ S_{c_{(N_p+l),j}} &= \frac{\partial \dot{\bar{\psi}}_l}{\partial A_j}, & S_{c_{(N_p+l),(N_p+k)}} &= \frac{\partial \dot{\bar{\psi}}_l}{\partial \psi_k}, \\ i, j &= 1, 2, \dots, N_p, & k, l &= 1, 2, \dots, m. \end{aligned} \quad (40)$$

The signs of the real parts of the eigenvalues of $[S_c]$ determine the stability of the limit cycle. When $m \neq 0$, one eigenvalue is always zero because all the ψ_i are measured with respect to a reference mode. If all other eigenvalues have negative real parts, the limit cycle is stable.

Time integration

A direct time integration of the equations of motion is performed separately in the principal coordinate system (29) as an alternative method. This algorithm may be employed to validate the results obtained from the time averaging technique. It may also be performed on the sub-space equations in order to reduce computational effort. The algorithm is summarized in reference [2].

NUMERICAL RESULTS

A single span, iced twin-conductor bundle, whose overall form is slightly simpler than that shown in Figure 1, is used to illustrate a typical full-span motion when galloping is initiated. The ice accumulations on conductors, which cause the conductors' instability, are obtained from a simulated freezing rain [2]. Sample C11, whose cross-section is illustrated in Figure 3, resembles severe icing formed naturally on a single conductor just below 0°C [3]. The icing on the windward and leeward conductors is considered identical in order to use available but limited experimental aerodynamic data. However, about 20% more ice can be accreted in a strong sideways wind on the windward conductor. It is also assumed that each line has a uniform coating of ice and that the wind speed does not change along the span.

The finite element model has 21 nodes at the center of rotation (with node numbers 1 and 21 representing the left and right supports, respectively) so that twenty elements, ten on the windward and ten on the leeward conductor, are used to discretize the two single span conductors. The physical parameters of the conductors are obtained from field measurements and they are listed in Table 1. Quasi-static aerodynamic forces are measured in a wind tunnel where the separation between the two C11 rigid models is constant. The separation used here is 0.471 m and, initially, $\alpha_w = \alpha_l = 40^\circ$ when the centers of the two conductors lie in a horizontal plane (i.e. $\alpha = 0^\circ$). By employing a least square curve fit, the experimental data are found to give the aerodynamic coefficients listed in Table 2.

The horizontal distance between two adjacent nodal points is 12.588 m and the horizontal static tension is 30 kN for both simply support or fixed ends. The only difference between these end conditions is that the longitudinal degree of freedom is retained in the former case. However, apart from dead-end spans, a simple support allows a more realistic interaction between adjacent spans so that it is studied in greater detail. The wind speed and tension are chosen so that a 1:1 resonance occurs for both end conditions.

The stability of the static profile of the conductor bundle under the aerodynamic loads is investigated to determine the initiation of galloping. The static profile is found to be unstable for both end conditions at the assumed 4 m/s wind speed.

A modal analysis is performed for the $[K]$ and $[M]$ matrices formulated in equation (16). The resulting two lowest frequency modes are one loop symmetrical modes for both end conditions. The mode shapes are similar in both cases, the first is a predominantly horizontal mode and the second is essentially a vertical mode. However, as expected, the second natural frequency is slightly higher for the fixed-end supports than for the simple supports. Because the initial stability analysis predicts an instability, limit cycles are investigated for a combination of these two modes.

An analysis for an internally resonant system when ω_2/ω_1 is close to one ($\omega_2/\omega_1 = 1^+$) is performed when the KB time averaging method is applied because the frequency ratio is considered to be closely spaced. On the other hand, step by step time integration is used in the same manner regardless of a resonant or non-resonant situation. The overall rotation of the conductor bundle is found to be very small so that the limiting motions for the windward and leeward conductors are indistinguishable from that at the center of rotation. Therefore, only the limit cycle at the center of rotation is given at the mid-span in Figure 4. This figure shows that the results of step by step time integration and the KB time averaging algorithm agree well. However, the slightly different natural frequency ratios produced by the two end conditions surprisingly lead to noticeably different horizontal movements in the limit cycles. The smaller limiting motion amplitude at the fixed ends stems from a higher longitudinal strain (or tension) because the length of the cable changes when one loop galloping happens. However, this change cannot be fed into the adjacent span when the ends are fixed.

The change in the peak limit cycle amplitude at the mid-span is investigated for the simply supported span at various steady side wind speeds. The initial stability analysis predicts that the static profile becomes unstable when this wind speed exceeds about 2 m/s. Then, Figure 5 shows that the limiting amplitude's growth rate is almost linear and about 10% that of the wind speed. However, the formulation presumes that the aerodynamic loads are weakly-nonlinear so that wind speeds in excess of 6 m/s are not considered.

Different horizontal static tensions in the conductors cause the change in the limit cycle amplitudes indicated in Figure 6. The tensions considered at the 4 m/s wind speed of the example are beyond the usual practical range of 15 kN to 30 kN determined from 20% of a conductor's ultimate tensile strength. However, Figure 6 shows that, as the tension increases, the limiting motion decreases substantially initially, attains a minimum around 60 kN before unexpectedly rising. This interesting behavior can be explained by considering the dynamic changes in the aerodynamic coefficients over a period of a limiting motion. The aerodynamic coefficients are comparable at 30 kN and 60 kN so that a larger tension in this range merely increases the bundle's stiffness and thereby reduces the midspan motion. This trend, however, is counteracted from 60 kN to 90 kN by larger coefficients (i.e. wind load) and the limit cycle's amplitude increases.

CONCLUSIONS

A simple model that is computationally efficient has been developed to analyze the galloping of a twin bundle transmission line in terms of an equivalent single conductor. Larger wind speeds and smaller tensions, in the range traditionally used, are shown to enlarge the limit cycle amplitude. On the other hand, the limit cycles found beyond this range reflect an interesting counterplay between changes in the tension and aerodynamic load.

ACKNOWLEDGMENTS

The writers gratefully acknowledge the financial support of Manitoba Hydro. Helpful discussions with Dr. P. Yu and the computer programs provided by Dr. Y.M. Desai for a single conductor are also appreciated greatly.

References

- [1] K.E. GAWRONSKI 1977. Non-linear galloping on bundle-conductor transmission lines. Ph.D Thesis, Clarkson College of Technology.
- [2] Manitoba Hydro 1992. *Modelling of Conductor Galloping : Vol I & II*. Canadian Electrical Association Report, Project No. 321 T 672, Montreal, Canada.
- [3] Manitoba Hydro 1995. *Modelling of Conductor Galloping : Phase II*. Canadian Electrical Association Report, Project No. 321 T 672A, Montreal, Canada.
- [4] Y. NAKAMURA 1980. Galloping of bundled power line conductors. *Journal of Sound and Vibration*, Vol.73, No.3, p.363-377.
- [5] G. DIANA, F. CHELI, A. MANENTI, P. NICOLINI and F. TAVANO 1990. Oscillation of bundle conductors in overhead lines due to turbulent wind. *IEEE Transaction on Power Delivery*, Vol.5, No.4, p.1910-1919.
- [6] Y. M. DESAI, N. POPPLEWELL, A. H. SHAH and D. N. BURAGOHAIN 1988. *International Journal of Computers and Structures* **29(6)**, 1001 - 1009. Geometric nonlinear static analysis of cable supported structures.
- [7] K. G. McCONNELL and C. N. CHANG 1986. *Experimental Mechanics*, 324 - 329. A study of the axial - torsional coupling effect on a sagged transmission line.
- [8] A. S. VELETSOS and G. R. DARBRE 1983. *International Journal of Earthquake Engineering and Structural Dynamics* **11**, 367 - 401. Dynamic stiffness of parabolic cables.

- [9] R. K. MATHUR, A. H. SHAH, P. G. S. TRAINOR and N. POPPLEWELL 1987. *Transactions of IEEE: Power Delivery* **PWRD - 2 (3)**, 908 – 916. Dynamics of a guyed transmission tower system.
- [10] R. W. CLOUGH and J. PENZIEN 1975. *Dynamics of structures*. New York: McGraw – Hill.
- [11] M.LIAO 1996. Galloping of bundle transmission lines. Ph.D Thesis, University of Manitoba.

Table 1. Properties of Field Lines [11]

Parameters	Data
d (m)	0.0286
E (N/m ²)	$4.78033 * 10^{10}$
GJ (N m ² /rad)	101
I (kg m)	$0.3334 * 10^{-3}$
H (N)	21733
E_y (mm)	2.05
E_z (mm)	-0.63
Area (mm ²)	594.48
Area(ice) (mm ²)	423.24
m (kg/m)	2.379
ξ_y, ξ_z	$0.743 * 10^{-2}$
ξ_θ	$0.138 * 10^{-2}$
l_w, l_l (m)	0.2355
L (m)	125.88
ρ_{air} (kg/m ³)	1.2929
U (m/s)	1.5 – 6.0

Table 2. Aerodynamic Coefficients [2]

Coefficients	C11 conductor at $\alpha = 0^\circ$ and $\alpha_w = \alpha_l = 40^\circ$
a_{yj}	2.7151, -0.3335, -8.1094, 16.7162
a_{zj}	1.7440, 1.7210, 1.6650, 3.56309
$a_{\theta j}$	0.3206, -1.4543, 0.5869, 11.9408
$j = 0, 1, 2, 3$	

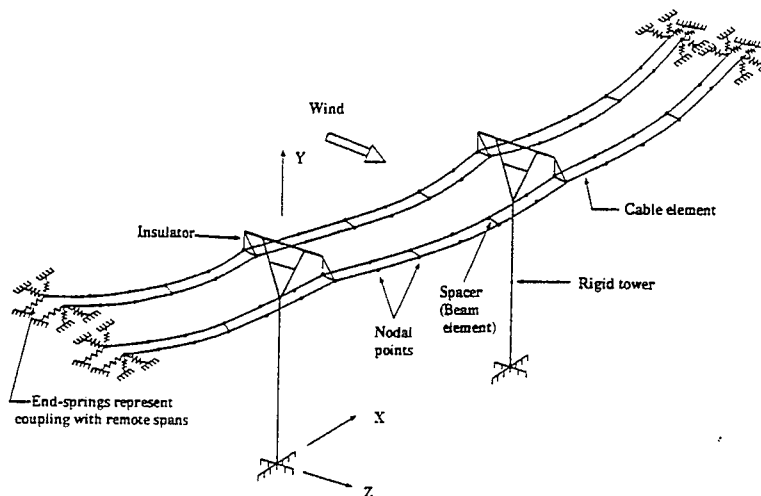


Figure 1. Model of a multi-span transmission line

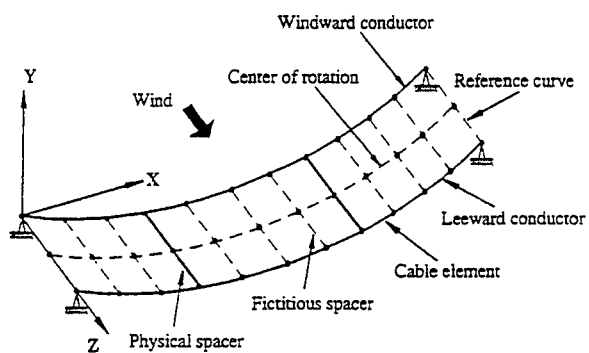


Figure 2. Bulk modelling of a twin bundle conductor

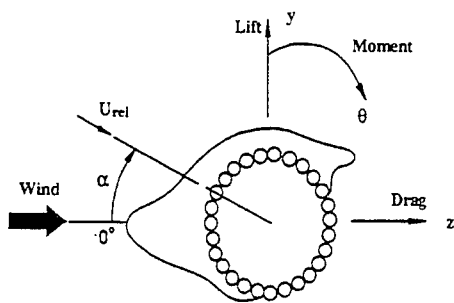


Figure 3. Cross-section of an iced, C11 conductor [2]

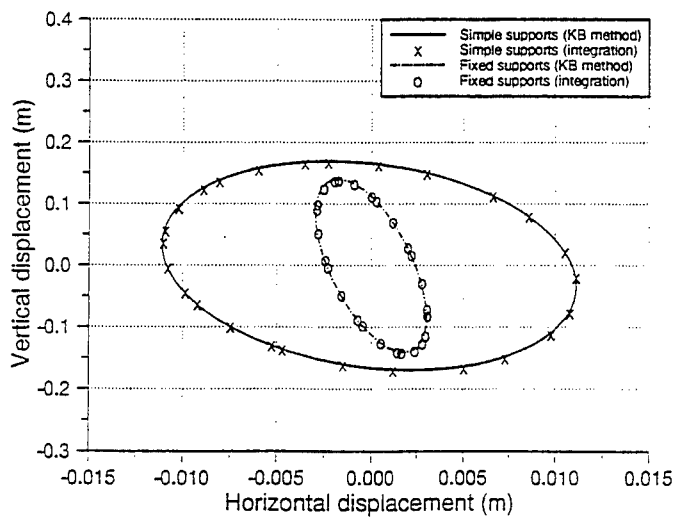


Figure 4. Limit cycle loci obtained at the mid-span by using the KB method and direct numerical integration

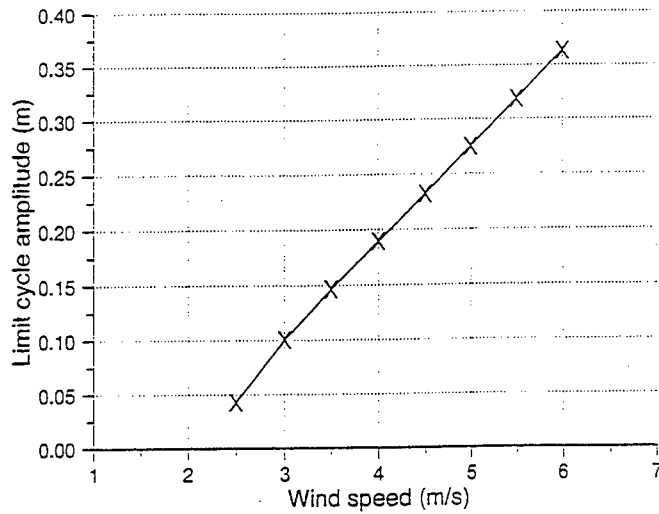


Figure 5. Amplitude of midspan's limiting motion with increasing wind speed

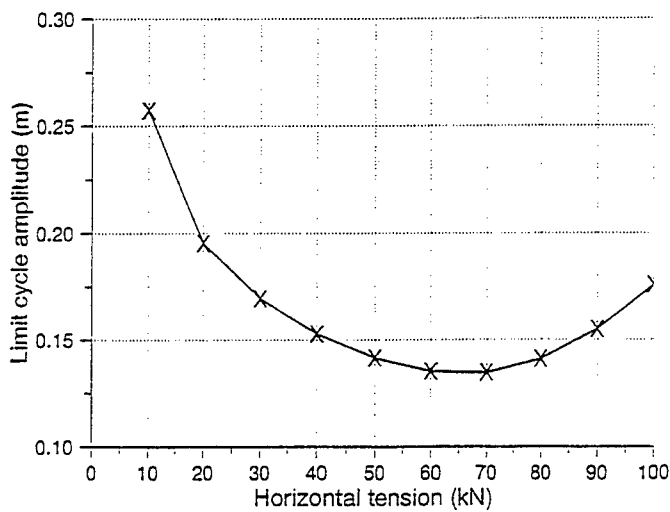


Figure 6. Amplitude of midspan's limiting motion with changing horizontal tension

SAFE DESIGN OF IMPACTING SYSTEMS

JUNE-YULE LEE and J.K. HAMMOND

Institute of Sound and Vibration Research,
Southampton University, Southampton SO17 1BJ, U.K.

Abstract Linear and nonlinear oscillators undergoing impacting are studied using analytic and numerical methods. Two strategies for chattering suppression are investigated: parametric control and isolation control. The system behavior is monitored using bifurcation diagrams as one or more of the parameters change. An experimental cantilever impacting beam is demonstrated for the validation of theoretical and numerical results.

1. INTRODUCTION

Many mechanical systems are designed to have clearances at support points to allow for thermal expansion, and in cutting processes machinery instability is due to the impacting between the workpiece and cutting tool. As a machine speeds up, damage may be caused by impact resonance. In the last ten years, impact dynamics has been researched in detail using simple mass-spring linear oscillator models with an endstop [1-9]. Researchers were interested in the fundamentals of impact dynamics, particularly in the ensuing chaotic motion. Bifurcation theory was applied to investigate the stability of system's behaviour as parameters changed. For periodic impact motion, analytic methods have explicit solutions and the bifurcation points can be predicted. However, for those ranges of driving frequency with low velocity impact response the motion is nonperiodic (unstable) and so far there is no explicit solution, so numerical simulation is applied leading to bifurcation diagrams.

The organization of this paper are as follows. In section 2, a basic mass-spring linear oscillator impact system is studied using analytic methods. In section 3, linear and nonlinear impact oscillators are introduced using numerical methods. The effect of parameter control using bifurcation diagrams are investigated. In section 4, an isolation subsystem is introduced where the concept of de-tuning of impact resonance is applied. In section 5, a cantilever impacting beam is modelled to validate the theoretical and numerical results.

2. BASIC MODEL OF IMPACTING SYSTEMS

2.1 Single-impact period- n motions

The model considered here is a single degree of freedom system shown in figure 1 where the mass is under a harmonic excitation and the motion is limited by an endstop on one side. For simplicity, we assume the deformation during impact is negligible, the contact force resulting from impact is impulsive and the duration of the contact is

much shorter than the period of the external excitation; in fact we idealise the impact as instantaneous. The non-dimensional equation of motion when not impacting is

$$\ddot{x} + 2\zeta\dot{x} + x = \cos\omega\tau; \quad x < g \quad (1)$$

where $\ddot{x} = d^2x/d\tau^2$, $\dot{x} = dx/d\tau$, ζ is damping ratio and g is gap size. The impact will occur at $x(\tau) = g$ and the velocity change is modelled as $\dot{x}(\tau+) = -r\dot{x}(\tau-)$ where r is a restitution coefficient, $(\tau+)$ is time before impact and $(\tau-)$ is time after impact. In order to analyse the impacting system in more detail we rewrite equation (1) and let $\zeta = 0$. In this case the only mechanism for energy loss is due to the coefficient of restitution at each impact, i.e.

$$\ddot{x} + x = \cos\omega\tau, \quad x < g \quad (2)$$

With initial conditions $(x, \dot{x}, \tau) = (g, v_0, \tau_0)$ and considering the trajectory starting from impact time τ_0 with velocity v_0 (before impact) and velocity $-rv_0$ (after impact), the solution of equation (2) given by Shaw (1985) is

$$\begin{aligned} x(\tau; g, -rv_0, \tau_0) &= (g - \beta \cos\omega\tau_0) \cos(\tau - \tau_0) \\ &+ (\beta \omega \sin\omega\tau_0 - rv_0) \sin(\tau - \tau_0) + \beta \cos\omega\tau \end{aligned} \quad (3)$$

Differentiating (3) with respect to τ gives velocity

$$\begin{aligned} v(\tau; g, -rv_0, \tau_0) &= -(g - \beta \cos\omega\tau_0) \sin(\tau - \tau_0) \\ &+ (\beta \omega \sin\omega\tau_0 - rv_0) \cos(\tau - \tau_0) - \beta \omega \sin\omega\tau \end{aligned} \quad (4)$$

where $\beta = 1/(1 - \omega^2)$. For the case when identical impacts occur periodically at times $\tau_0 + 2n\pi/\omega$ (i.e. single-impact period- n motion or $(1, n)$ -orbit), then we have the following conditions:

$$\begin{aligned} v_0 &= v_1 = v_2 = \dots = v_n \\ \tau_1 &= \tau_0 + \frac{2n\pi}{\omega} = \phi_n \\ x(\tau) &> g, \quad \forall \tau \in (\tau_0, \tau_1) \end{aligned} \quad (5)$$

writing $c_n = \cos(2n\pi/\omega)$, $s_n = \sin(2n\pi/\omega)$ and substituting into equation (3&4) gives

$$\begin{bmatrix} \cos(\omega\phi_n) \\ \sin(\omega\phi_n) \end{bmatrix} = \frac{1}{2\beta\omega(1 - c_n)} \begin{bmatrix} 2\omega(1 - c_n) & \omega(1 + r)s_n \\ 0 & -(1 - r)(1 - c_n) \end{bmatrix} \begin{bmatrix} g \\ v_n \end{bmatrix} \quad (6)$$

and leads to

$$\begin{aligned}\cos(\omega\phi_n) &= \frac{g}{\beta} + \frac{s_n(1+r)}{2\beta(1-c_n)}v_n \\ \sin(\omega\phi_n) &= -\frac{(1-r)}{2\beta\omega}v_n\end{aligned}\quad (7)$$

Squaring and adding the terms in equation (7) gives a quadratic equation for v_n .

$$\left(\frac{s_n^2(1+r)^2}{(1-c_n)^2} + \frac{(1-r)^2}{\omega^2}\right)v_n^2 + 4\frac{s_n(1+r)}{(1-c_n)}gv_n + 4(g^2 - \beta^2) = 0 \quad (8)$$

This was derived by Shaw (1985) Whiston (1987) and Budd (1995). The quadratic equation (8) provides a visualisation of the information of $(1,n)$ -orbit solutions; it is useful to see how v_n varies as the function of ω with a fixed g . For $g=0$, $r=0.8$, figure 2 shows single impact solutions of equation (8). The results give a resonance response curve of impact velocity against driving frequency ω . This diagram is plotted for a series of single impact period- n solutions where n from 1 to 5. As the previous study [9] $n=1$ means a harmonic solution with single point in the Poincare section; $n=2$ is a sub-harmonic solution which has two points in the Poincare section. Therefore, the first negative peak occurs at $\omega=2$ and is the fundamental solution of resonance with period-1 impact oscillation, sub-resonance impacting with period-2 occurs at $\omega=4$, period-3 at $\omega=6$ and so on. Thus, the result of this kind of behaviour can be referred to as single-impact period- n solutions having the property that impact resonance occurs at driving frequency $\omega=2n$. We call this is an incomplete bifurcation diagram. The complete bifurcation diagram will be demonstrated in the next section using numerical techniques.

2.2 Two-impact period- n motion

In the last subsection we obtained a stable single impact periodic solution, but for some parameter combinations the impact response may lose stability, i.e. the solution may bifurcate to high order impact or chaotic motions. In figure 2, it is intuitive that impact resonance occurs near the region of driving frequency $\omega=2n$. However, when ω is away from the resonant range impact velocity reduces and may transit to rattling vibration due to low impact velocities. We can say the energy is dispersed by the high impact rate with a series of low impact velocities instead of low impact rate with a series of high periodic impact velocities. This is the chattering problem and difficult to analyse because the solution may lead to singularity, i.e. zero velocity. Thus careful numerical calculation is need to be applied (see the next section). The boundary of the control parameter where the systems lose their stability can be predicted using analytic methods; i.e. bifurcation theory.

In the present studies we are interested in the impact velocity (impact map) as the parameters change. Following [8], the Jacobian matrix DP_i for differential equation between impacts is

$$DP_I = \begin{bmatrix} \frac{\partial \tau_1}{\partial \tau_0} & \frac{\partial \tau_1}{\partial v_0} \\ \frac{\partial v_1}{\partial \tau_0} & \frac{\partial v_1}{\partial v_0} \end{bmatrix} \quad (9)$$

where

$$\tau_1 = \frac{x}{v_1}, \quad v_1 = v + \ddot{x}\tau_1 \quad (10)$$

$$x(\tau_1; g, -rv_0, \tau_0) = g, \quad \tau = \tau_1 > \tau_0$$

Substituting the displacement and velocity (equation (3&4)) and periodic impact conditions (equation (5)) into equation (9), the determinant and trace of matrix DP_I are given by

$$\det(DP_I) = r^2$$

$$\text{tr}(DP_I) = -2rc_n - \frac{(1+r)s_n}{\beta} \left[\frac{\beta\omega^2 g}{v_n} - \frac{s_n(1+r)}{2(1-c_n)} \right] \quad (11)$$

The nature of the solution depends on the eigenvalues of the matrix DP_I . The eigenvalues satisfy

$$\lambda^2 - \text{tr}(DP_I)\lambda + \det(DP_I) = 0 \quad (12)$$

Therefore, as the eigenvalues λ_1 and λ_2 satisfy $\lambda_1 + \lambda_2 = \text{tr}(DP_I)$ and $\lambda_1\lambda_2 = \det(DP_I) = r^2$, a smooth bifurcation occurs. A period-doubling bifurcation occurs when a single eigenvalue passed through -1 on the unit circle. Equation (12) leads to

$$\text{tr}(DP_I) = -(1+r^2), \quad (13)$$

and this equation represents the bifurcation point. Thus one can obtain a bifurcation boundary curve with varying the parameters. When one of the control parameter value changes the eigenvalues will approach the unit circle and the single impact motion will transit to two-impact motion. Using equation (11& 13), one can obtain a period doubling bifurcation formula which is a function of v_n and g :

$$-2rc_n - \frac{(1+r)s_n}{\beta} \left[\frac{\beta\omega^2 g}{v_n} - \frac{s_n(1+r)}{2(1-c_n)} \right] = -(1+r^2) \quad (14)$$

For the special case $g=0$, this gives

$$r^2 + 2 \left(\frac{s_n^2(1-\omega^2) - 2c_n(1-c_n)}{s_n^2(1-\omega^2) + 2(1-c_n)} \right) r + 1 = 0 \quad (15)$$

The parameters in equation (15) are driving frequency ω , period- n orbit and coefficient of restitution r . For each n and ω then the roots r of the quadratic equation which fall between 0 and 1 can be obtained, therefore one can construct the boundary curve for the period-doubling bifurcation in the (ω, r) -domain. A bifurcation occurs when the quadratic equation for r and ω is satisfied. This boundary curve is shown in figure 3. One can predict a stable single-impact period- n motion occurs in the region inside the boundary curves and two-impact period- n motion appears just outside both edges of stable region.

If we calculate the eigenvalues of equation (12) for gradually changing the driving frequency from $\omega=2$ to 2.7 with $r=0.8$, $g=0$, then the eigenvalue trajectory shown in figure 4 is an example of period doubling bifurcation. Eigenvalue λ_1 (+) remains in the unit circle while λ_2 (o) pass as through unit circle via -1 direction.

3. ACTIVE PARAMETER CONTROL

3.1 Effect of restitution coefficient

The restitution coefficient depends on the material of the colliding bodies. In figure 5, we show the effect of a series of different coefficients for the bifurcation diagrams. These diagrams are obtained by numerical methods (Runge-Kutta integration algorithm) from equation (1). As discussed previously periodic impacts will loss their stability and transit to two-impact motion as the driving frequency changes. The impact resonance at $\omega=2$ (figure 5 (e)) is in good agreement with theoretical results (figure 2). A complete bifurcation diagrams is plotted for the full bandwidth of driving frequency. The details of local dynamics in different driving frequency can refer to previous studies [9-10].

The effect of the restitution coefficient is discussed as follows. When $r=0$ shown in figure 5(a) all of the mechanical energy is dissipated during the impacts, thus the mass essentially sticks to the endstop. There is no elastic rebound until the positive force drives the mass off again. This shows that the impact resonant response at $\omega=1$ is the same as vibration without impacting. After each positive excitation forcing, the motion sticks to the wall. Period doubling bifurcation is very clearly demonstrated at $\omega=2.6$. For increased coefficient r the impact resonance shifts to $\omega=2n$, $n=1,2,3...$ and the period doubling is contaminated by a small impact restoring force see figure 5(d). At parameter values with $r<0.6$ there coexist stable (1,1) (2,1) and (3,1)-orbits. Note that as $\omega=1$ this is approached from the right, the period one impact orbit is stable shown in (a-c). However, a region for $r>0.6$ and just to the right of $\omega=1$ in which the period one signal impact orbit becomes unstable shown in (d-f). From these series of diagrams we conclude that low restitution can absorb the chatter vibration and leave only stable impact responses. The high restitution coefficients produce high unstable chatter impact rates as well as relative high stable impact resonance.

3.2 Effect of the endstop

In previous cases the impact system is a linear oscillator. We concluded that a linear oscillation becomes a complex chaotic system due to the endstop. In this subsection we study a nonlinear oscillator. A classic nonlinear model (Duffing equation) is

$$\ddot{x} + 2\zeta\dot{x} + \alpha x + \rho x^3 = \gamma \cos \omega \tau \quad (16)$$

The impact oscillator is now governed by equation (16) and when impact occurs the system undergoes a nonlinear impact force which depends on impact velocity. No exact solution exists and we rely on numerical methods. Following the algorithms we developed in the previous section, results shown in figure 6(a&b) are bifurcation diagrams. The system is excited by a harmonic excitation. As expected when varying the driving frequency the motion loses stability in the range [0.9, 1.3]. For motion in this region the system vibrates over a large range. Therefore, from an engineering point of view this unstable motion must be suppressed.

The energy due to impacting can be dissipated via small impact velocities with high a impact rate for certain control parameters (e.g. chaotic chatter). This is similar to the impact damper producing energy absorption. We now apply a single side endstop to the nonlinear (Duffing equation) oscillator. The numerical results are shown in figure 6(c&d) for the bifurcation diagrams of a nonlinear oscillator with impacting. It is obvious that the unstable region is suppressed and the motion of the oscillator is simplified due to the endstop. In other words, one may find an optimum gap size to suppress the unstable force. Figure 6(e&f) demonstrates an optimal gap size $g=-0.5$, the system becomes stable throughout the whole driving frequency.

4. ISOLATION CONTROL

In classic mechanical vibration problems when a system operates 'wear' occurs and damage may result. However, passive control may be achieved using masses, stiffnesses and dampers, see figure 7. In this section we apply this concept to an appropriate impacting system.

Figure 8 (solid line) shows the response of the system in figure 7 (without endstop). The parameters are designed with a force ratio -0.1 (p_1/p_2), mass ratio 0.2 (m_1/m_2), spring ratio 1 (k_2/k_3) and damping ratio 1 and 10 (c_2/c_3). The result shows that an anti-resonance is created at frequency 2 (i.e. the first impact resonance peak). We try to suppress the impact resonance using an anti-resonance. The secondary subsystem creates a switch at driving frequency $\omega=2$. Therefore when the machine speeds up and the driving frequency passes through the impact resonance region, this control subsystem will automatically turn on. The results for the bifurcation diagram for this special design are shown in figure 9(a&b). They illustrate good attenuation where the first impact resonance peak reduces 75% and subsequent peaks compress 50% when compared to figure 5(e).

5. EXPERIMENTAL VALIDATION

The experimental model follows the previous study [10] in which an impacting cantilever beam can model a mass-spring impacting system. We chose the nodal point as an impact point to simplify the system. The n th mode will not be excited due to the impact point being at n th node. From a control point of view this is called *nodalizing* which means locating the oscillating forces (e.g. impact forces) at the predicted nodal points of the troublesome vibration modes (e.g. in the nuclear industry the steam generator tubes support points, i.e. impact points, are designed to be at nodal points along the fluid flow pipes). This way the effects due to the modal coupling will be greatly reduced. In the last section we discussed the isolation system using the concept of *de-tuning*. From the results of numerical simulation impact resonance can be suppressed by adding an isolation subsystem.

Therefore, the aim of this section is to validate the results we discussed in the last section. Passive control of the impacting system is addressed via simple addition of an isolation subsystem to impact point. In order to test the mass control of present system we attached a weight to the end of the thin beam ($120\text{mm} \times 13\text{mm} \times 0.2\text{mm}$). The beam is placed symmetrically across the main cantilever beam ($500\text{mm} \times 18\text{mm} \times 3\text{mm}$), see figure 10. When an excitation is applied to the complex structure then an anti-resonance is generated at a certain frequency. This is due to the subsystem (suspension cross beam) added to the main cantilever beam. By changing the location of the weight along the suspension beam (stiffness) or the size of weight (mass) one can create an anti-resonance curve in a particular frequency region as we do in section 4.

Therefore the structure can work safely in a specific frequency range. The results shown in figure 11(a) for a vibrating cantilever beam with (solid line) and without impacting (dashed line) have different properties. The results are measured from the tip of the beam due to impacting at the second mode node. The results show the response at the first natural frequency region as being relatively small in comparison to the system without impacting. However, due to the endstop the system generates an impact resonance at 20, 40 and 60Hz, respectively (i.e. in nondimension 2, 4, 6). As we mentioned in section 4 the impact resonance can be suppressed by adding an isolation subsystem.

Figure 11(b) dashed line shows that an anti-resonance curve appears at 20Hz which is due to the suspension beam with one mass at the tip. The solid line shows the responses of this complex impact structure with subsystem attached at the second mode node of the main beam. The results illustrate good attenuation except at 60Hz. If we increase the weight on both sides of the suspension beam then the anti-resonance curve is more efficient at 20Hz (see figure 11(c) dashed line). The suppression of impact resonance shows in figure 11(c) solid line is an improvement on figure 11(b) solid line.

REFERENCES

1. J.M.T. Thompson and R. Ghaffari 1982 *Phys. Lett.* A91, 5-8. Chaos after period-doubling bifurcation in the resonance of an impact oscillator.
2. S.W. Shaw and P.J. Holmes 1983 *Journal of sound and vibration*, 90(1), 129-155. A periodically forced piecewise linear oscillator.
3. S.W. Shaw 1985 *Journal of sound and vibration* 99(2), 199-212. Forced vibrations of a beam with one-sided amplitude constraint: Theory and experiment.
4. G.S. Whiston 1987 *Journal of sound and vibration* 118(3), 395-429. Global dynamics of a vibro-impacting linear oscillator.
5. G.S. Whiston 1992 *Journal of sound and vibration* 152(3), 427-460. Singularities in vibro-impact dynamics.
6. C. Budd and F. Dux 1994 *Phil. Trans. R. Soc. Lond.* A347, 365-389. Chattering and related behaviour in impact oscillators.
7. C. Budd and F. Dux 1994 *Nonlinearity* 7(4), 1191-1224. Intermittency in impact oscillators close to resonance.
8. C. Budd and F. Dux 1995 *Journal of sound and vibration*, 184(3), 475-502. The effect of frequency and clearance variations on single-degree-of-freedom impact oscillators.
9. J.Y. Lee and J.K. Hammond 1995 *Proceeding of 2nd International Conference on Acoustical and Vibratory Surveillance Methods and Diagnostic Techniques*, 495-505. Characterisation of mechanical vibrating systems with internal impacts.
10. J.Y. Lee and J.K. Hammond 1996 *Proceeding of 4th International Conference on Mathematics in Signal Processing*, Oxford University Press (preparing). Chattering in impacting beams: Numerical simulation and experimental validation.

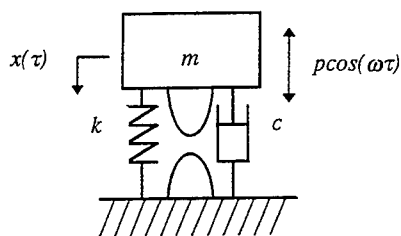


Figure 1 Single mode impact system.

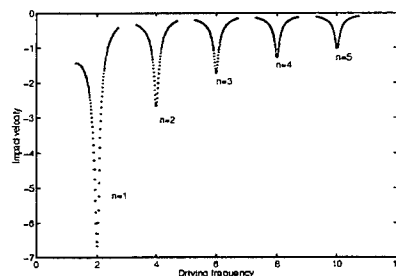


Figure 2 Impact velocity vs. driving frequency ω . The results show $(1, n)$ -orbit solutions where $r=0.8$ and $g=0$.

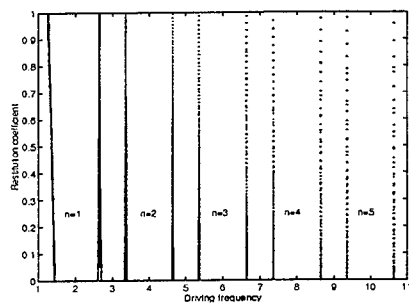


Figure 3 Period-doubling bifurcation boundary curves in restitution coefficient and driving frequency domains where $\lambda=-1$ and $g=0$.

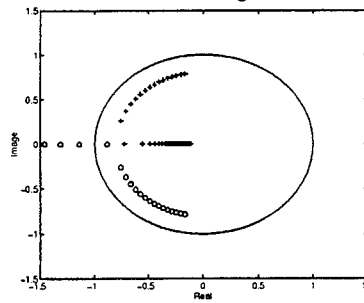


Figure 4 Eigenvalue trajectory shows period doubling bifurcation: λ_1 (+) remain in the unit circle and λ_2 (o) pass through unit circle via -1 direction.

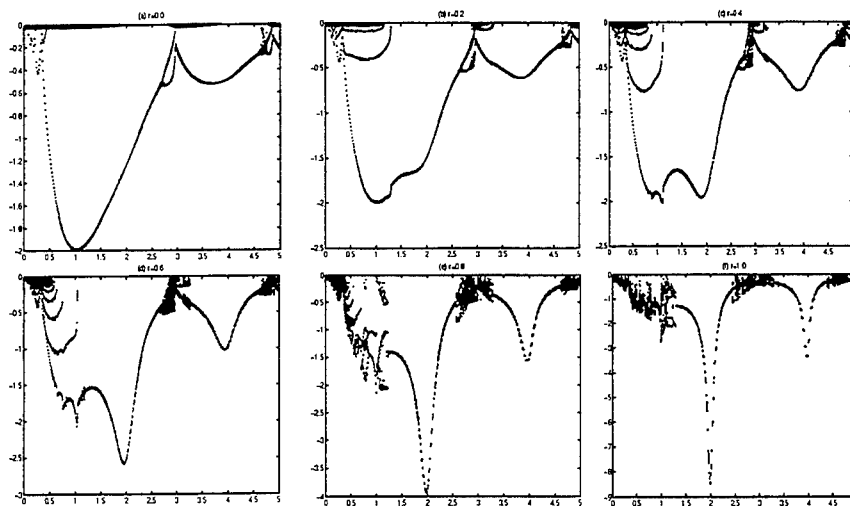


Figure 5 Bifurcation diagram with different restitution coefficient r (a-f), velocity just before impact (Y-axis) vs. varying driving frequency (X-axis).

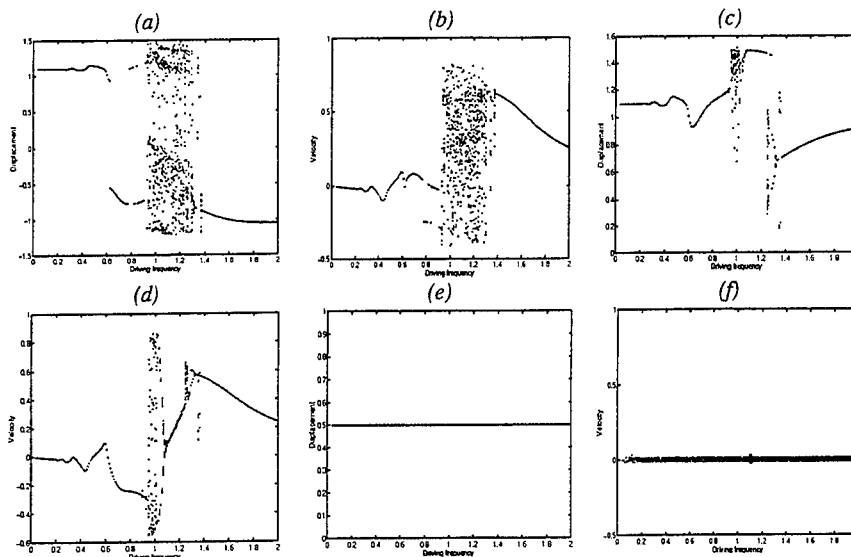


Figure 6 Bifurcation diagram of nonlinear oscillator (Duffing equation with $\zeta=0.125$, $\alpha=-1$, $\rho=1$ and $\gamma=0.3$) via Poincare section (a&b) without impact (c&d) with single side impact $g=0.01$ (e&f) with single side impact $g=-0.5$.

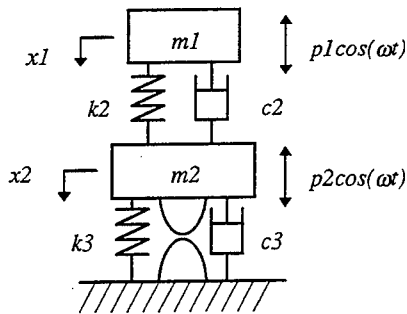


Figure 7 Isolation system with impact.

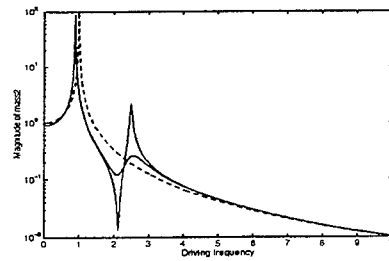


Figure 8 Motion response without impacting. System parameters are $p1=-0.1$, $p2=1$, $m1=0.2$, $m2=1$, $k2=1$, $k3=1$, $c2=0.1$, $c3=0.01$.

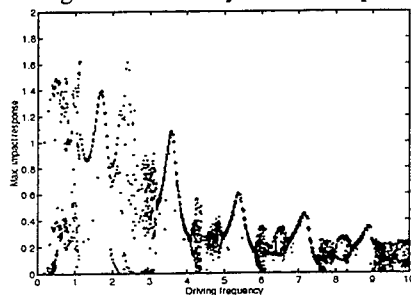


Figure 9(a) Maximum impact response in bifurcation diagram with two degree of freedom system.

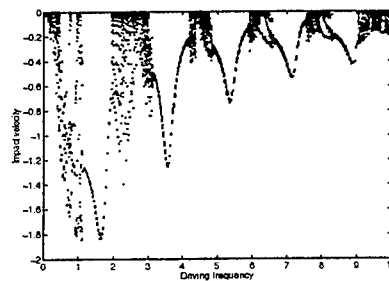


Figure 9(b) Impact velocity in bifurcation diagram with two degree of freedom system.

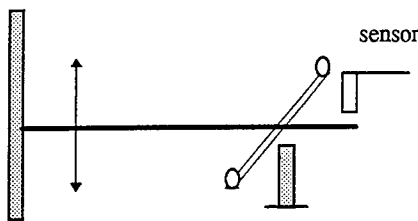


Figure 10 Cantilever impact beam with isolation subsystem (cross beam) is attached by weight at each side.

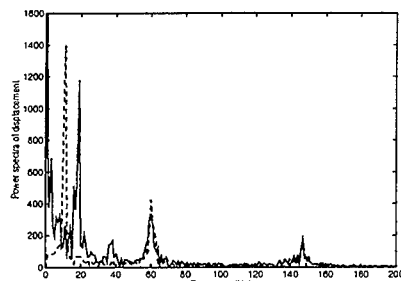


Figure 11(a) Spectra response at tip beam without isolation subsystem, impacting (solid line) and nonimpacting (dashed line)

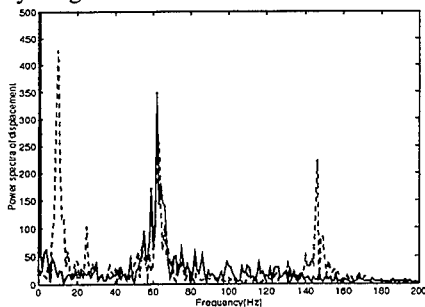


Figure 11(b) Spectra response at tip beam with impact point at 0.771 (second mode node) and isolation subsystem (one weight attached at each side of the cross beam) at 0.771

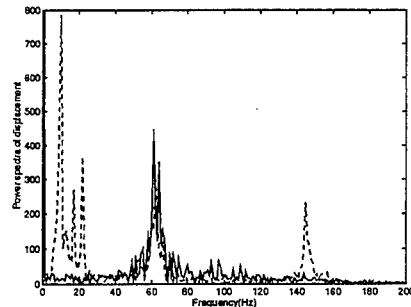


Figure 11(c) Spectra response at tip beam with impact point at 0.771 (second mode node) and isolation subsystem (two weights attached at each side of the cross beam) at 0.771.

Chaotic Stochastic Vibration On Duffing System With Friction

Feng Qi

Department of Mechanics
Tong Ji University
Shanghai, 200092, P.R.China

Abstract

In the present paper, a Duffing oscillator with combined Coulomb friction and viscous damping subjected to combined harmonic and random excitation has been considered and its chaotic stochastic behaviour has also been investigated. Instead of performing the very tedious numerical calculation, analytical solutions are elaborated. By those solutions, the chaotic stochastic behaviour may be revealed.

Introduction

Friction is a desirable damping mechanism in many vibrating systems. The effects of friction in dynamics are of great importance in our technological world. For example, friction is the principal source of damping of turbine blades ^[1] and in flexible pin - jointed space structures ^[2]. It is also exploited in robot grippers and walkers ^[3]. The above mentioned problems have been dealt with by various authors, where in those instances special problems of friction and stick - slip are considered. Those problems have been investigated for years, but only recently it has become of interest due to revelation of a connection between a dry friction force and chaotic vibrations ^[4-6].

The classical approach was originated from Den Hartog who gave an exact solution of the non - sticking periodic response when kinetic friction factor is equal to one ^[7]. Since then an extension of Den Hartog's work was

carried out in many references, in which it is quite clear that the exact solutions for stick - slip processes can be expected ^[8].

The analysis of chaotic behaviour in nonlinear systems with Coulomb damping has not been treated extensively in the literature, with the possible exception of few works. One of them, Awrejcewicz ^[9] showed the existence of a strange attractor behaviour in a single degree of freedom nonlinear system with Coulomb damping. Narayanon et al. has been concerned with the chaotic behaviour of a nonlinear oscillator with dry friction damping, by numerical simulation in a detailed manner. The existence of a strange attractor is also demonstrated ^[10]. Much of the work is concentrated upon the numerical method to solve the problem of nonlinear dynamics, but few attention has been paid to the analytical method.

In the present paper, a Duffing oscillator with combined Coulomb friction and viscous damping subjected to combined harmonic and random excitation has been considered and its chaotic stochastic behaviour has also been investigated. The concept of chaotic stochastic vibration was proposed by Kapitaniak in 1988 ^[11]. The Kapitaniak's work was based on average results of finite performances of the numerical simulation. It must take a lot of time on computer. In this paper, instead of performing of the very tedious numerical calculation, analytical solutions are elaborated. By means of approach with piecewise linear skeletoncurve to the real nonlinear restoring force ^[12] and adopting the piecewise integration method^[13], the analytical solutions of the probability densities and the mean values are derived. Those solutions are quasi - periodic. When the piece number N tends to infinite the approximated skeletoncurve approaches to be real one. In that extreme case, the solutions tend to chaotic via quasi - periodic route. By those solutions, the chaotic stochastic behaviour on a Duffing system with friction may be revealed.

Mathematical Model

In this paper the response of a simple hard spring dashpot system with

dry friction on a driving belt subjected to harmonic excitation is investigated. (see Fig.1) The equation of motion of the system can be written as

$$\ddot{x} + D(\dot{x} - v) + g(x) + q(\dot{x} - v) = f \sin \Omega t \quad (1)$$

In eq.(1), the mass is equal to unit, x is the displacement of the mass, D is a damping factor, f is exciting amplitude and Ω is exciting frequency, the nonlinear restoring force of hard spring is represented

$$g(x) = \omega^2(1 + \beta x^2)x$$

and the dry friction term $q(\dot{x} - v)$ is taken to be

$$q(\dot{x} - v) = \begin{cases} \mu' & \dot{x} - v > 0 \\ \mu & \dot{x} = v + \epsilon \\ \leq \mu & \dot{x} = v \\ \mu & \dot{x} = v - \epsilon \\ \mu' & \dot{x} - v < 0 \end{cases}$$

In which μ' and μ denote kinetic and static friction factors respectively, ϵ is a very small number. Obviously, the equation (1) is nonlinear and forced one. It is very difficult to obtain its exact solution. In this paper we try to solve it using random perturbation technique. For non-sticking motion, the sticking area tends to null and the slipping area is continuous. For random case, at $\dot{x} = v$, the probability density of the displacement do not appear to spring. On that assumption, analytical solutions can be obtained by random perturbation technique. In the following section we will discuss that motion.

The Solution For Non - Sticking Motion

Assuming that the system (1) is perturbed by white noise because a finite level of noise is present everywhere in reality. A stochastic motion equation has the form of

$$\ddot{x} + D(\dot{x} - v) + g(x) + q(\dot{x} - v) = f \sin \Omega t + \sigma \eta(t) \quad (2)$$

Where σ is noise intensity and $\eta(t)$ is standard white noise that satisfies the following conditions

$$E[\eta(t)] = 0$$

and

$$E[\eta(t)\eta(\tau)] = \delta(t - \tau)$$

It is very difficult to solve exactly the random nonlinear differential equation (2). But the closed form of response statistics of a piecewise linear system can be obtained using piecewise integration method [13]. the reliability of that method can be justified for stationary case. The solution of bilinear system in [13] coincides with [14]. Here we develop that method to solve the equation (2). First according to [12], the real nonlinear restoring force is approached with piecewise linear skeletoncurve in the following way.

$$g(x) = \begin{cases} \frac{dg(x)}{dx}|_{x=x_0} x & 0 \leq |x| \leq x_0 \\ \sum_{i=0}^{n-1} \frac{dg(x)}{dx}|_{x=x_i} (x_i - x_{i-1}) \operatorname{sgn}(x) & \\ + \frac{dg(x)}{dx}|_{x=x_i} [x - x_{i-1} \operatorname{sgn}(x)] & x_{i-1} \leq |x| \leq x_i \\ i = 1, 2, \dots, n \end{cases}$$

Based on above expression, $g(x)$ can be rewritten as

$$g^*(x) = \begin{cases} \omega_0^2 x_0 + \sum_{i=1}^{n-1} \omega_i^2 (x_i - x_{i-1}) & x \geq x_n \\ + \omega_n^2 (x - x_{n-1}) & \\ \dots\dots\dots & \dots\dots\dots \\ \omega_0^2 x_0 + \omega_1^2 (x - x_0) & x_0 \leq x \leq x_1 \\ \omega_0^2 x & -x_0 \leq x \leq x_0 \\ -\omega_0^2 x_0 + \omega_1^2 (x + x_0) & -x_1 \leq x \leq -x_0 \\ \dots\dots\dots & \dots\dots\dots \\ -\omega_0^2 x_0 - \sum_{i=1}^{n-1} \omega_i^2 (x_i + x_{i-1}) & \\ + \omega_0^2 (x + x_{n-1}) & x \leq -x_{n-1} \end{cases}$$

in which

$$\omega_i^2 = \frac{dg(x)}{dx} \Big|_{x=x_{i-1}} \quad (3)$$

Then substituting $g^*(x)$ into equation (2), the state equations in the each piecemeal region can be given out

$$\begin{cases} \dot{x} = y \\ \dot{y} = -2d\omega_0 y - \omega_0^2(1 + \gamma_G)x + (2d\omega_0 v - \mu') + S_G \\ \quad + f \sin \Omega t + \sigma \eta(t) \end{cases} \quad \dot{x} > v$$

and

$$\begin{cases} \dot{x} = y \\ \dot{y} = -2d\omega_0 y - \omega_0^2(1 + \gamma_G)x + (2d\omega_0 v + \mu') - S_G \\ \quad + f \sin \Omega t + \sigma \eta(t) \end{cases} \quad \dot{x} < v \quad (4)$$

The subscript G means the piecemeal region of function $g^*(x)$; parameters d , s_G and γ_G are calculated through the following equations

$$2d\omega_0 = D;$$

$$s_G = \omega_0^2 x_0 + \sum_1^{G-1} \omega_i^2 (x_i - x_{i-1}) - \omega_G^2 x_{G-1};$$

$$\gamma_G = (\omega_G^2 - \omega_0^2) / \omega_0^2;$$

Equations (4) are linear in each region, so their statistics of response may be solved using the piecewise integration method. The mean values m_{jG} ($j=1,2$) and variances k_G of random variables in each region can be obtained with *Ito - kaküler* equations [18], i.e.,

$$\begin{cases} m_{1G}^\pm = A_0 e^{-d\omega_0 t} \sin(\omega_d^G t - \alpha_0) + B_G \sin(\Omega t - \alpha^G) \\ \quad + \frac{(s_G + 2d\omega_0 v \pm \mu' s)}{\omega_0^2(1 + \gamma_G)} \\ m_{2G} = A_0 e^{-d\omega_0 t} [-d \sin(\omega_d^G t - \alpha_0) + \frac{\omega_d^G}{\omega_0} \cos(\omega_d^G t - \alpha_0)] \\ \quad + B_G z \cos(\Omega t - \alpha^G) \\ G = 1, 2, \dots, N = 2n - 1 \end{cases} \quad (5)$$

and

$$\begin{cases} k_0 = \frac{\sigma^2}{4d\omega_0^2} \\ k_G = \frac{k_0}{1+\gamma_G} \end{cases} \quad (6)$$

In the above relations, the parameters B_G , α^G , ω_d^G and z are represented as

$$B_G = \frac{f/\omega_0^2}{\sqrt{(1+\gamma_G-z^2)^2+4d^2z^2}}; z = \Omega/\omega_0;$$

$$tg\alpha_G = \frac{2dz}{1+\gamma_G-z^2}; \omega_d^G = \omega_0\sqrt{1+\gamma_G-d^2}$$

Because the piecewise state equations are linear in each region we can assume that the state variables in each region satisfy the Gaussian distribution, i.e.

$$W_G(y_1, y_2) = \begin{cases} W_G^+(y_1, y_2) & y_2 > v \\ W_G^0(y_1, y_2) & y_2 = v \\ W_G^-(y_1, y_2) & y_2 < v \\ G = 1, 2, \dots, N = 2n - 1 \end{cases} \quad (7)$$

where y_1 and y_2 are probability variables and $W_G(y_1, y_2)$ is two - dimensional distribution in each region. When $|y_2| > v$, that distribution is normal one as

$$W_G^\pm(y_1, y_2) = \frac{G_G^\pm}{2\pi\sqrt{k_0k_G}} \exp\left[-\frac{(y_1 - m_{1G}^\pm)^2}{2k_G}\right] \exp\left[-\frac{(y_2 - m_{2G}^\pm)^2}{2k_0}\right]$$

Here we consider only the non - sticking motion and assume that at null relative velocity the probability density of displacement is continuous, it satisfies the following condition,

$$\int_{v-\epsilon}^{v+\epsilon} W_G^0(y_1, y_2) dy_2 = W_G^0(y_1) = 0 \quad \epsilon \rightarrow 0.$$

If $\epsilon \rightarrow 0$, the probability densities as follows

$$\begin{aligned}
W_G(y_1) &= \int_{-\infty}^{+\infty} W_G(y_1, y_2) dy_2 \\
&= \int_{-\infty}^{v-\epsilon} W_G^-(y_1, y_2) dy_2 + \int_{v+\epsilon}^{+\infty} W_G^+(y_1, y_2) dy_2 \\
&\quad + \int_{v-\epsilon}^{v+\epsilon} W_G^0(y_1, y_2) dy_2 \\
&= W_G^-(y_1) + W_G^+(y_1) \\
G &= 1, 2, \dots, N = 2n - 1
\end{aligned} \tag{8}$$

and

$$W(y_2) = \frac{1}{\sqrt{2\pi k_0}} \begin{cases} W^-(y_2) & y_2 < v \\ W^0(y_2) & y_2 = v \\ W^+(y_2) & y_2 > v \end{cases} \tag{9}$$

where

$$\begin{aligned}
W_G^\pm(y_1) &= \frac{C_G^\pm}{\sqrt{2\pi k_G}} \exp\left[-\frac{(y_1 - m_{1G}^\pm)^2}{2k_G}\right] \beta_G^\pm \\
W^\pm(y_2) &= \sum_{G=1}^{2n-1} C_G^\pm \exp\left[-\frac{(y_2 - m_{2G})^2}{2k_0}\right] v_G^\pm
\end{aligned}$$

As the mean value of velocity must fluctuate around the velocity v of driving belt we assume that in case of $y_2 = v$, $W^0(y_2)$ satisfies the following condition

$$\lim_{\epsilon \rightarrow 0} \int_{v-\epsilon}^{v+\epsilon} y_2 W^0(y_2) dy_2 = v$$

Integrating the above probability densities, the mean values $E[x_1]$ and $E[x_2]$ are obtained as follows

$$\begin{aligned}
E[x_1] &= \int_{-\infty}^{+\infty} y_1 W(y_1) dy_1 \\
&= \sum_{G=1}^{2n-1} \{ C_G^- \beta_G^- [\varphi(a_G^-) + m_{1G}^- v_G^-] \\
&\quad + C_G^+ \beta_G^+ [\varphi(a_G^+) + m_{1G}^+ v_G^+] \} \\
E[x_2] &= \int_{-\infty}^{+\infty} y_2 W(y_2) dy_2 \\
&= v + \sum_{G=1}^{2n-1} \{ C_G^- v_G^- [\varphi(b_G^-) + m_{2G} \beta_G^-] \\
&\quad + C_G^+ v_G^+ [\varphi(b_G^+) + m_{2G} \beta_G^+] \}
\end{aligned} \tag{10}$$

in which the factors β_G^\pm , v_G^\pm , function $\varphi(x)$ and variables a_G , b_G are determined in the following way

$$v_G^\pm = \frac{1}{\sqrt{2\pi}} \int_{a_G^\pm}^{a_{G+1}^\pm} \exp\left(-\frac{u^2}{2}\right) du;$$

$$\beta_G^\pm = \pm \int_{b_G^\pm}^{\infty} \exp\left(\frac{u^2}{2}\right) du;$$

$$\varphi_G(x) = \sqrt{\frac{k_G}{2\pi}} \left[\exp\left(-\frac{x_G^2}{2}\right) - \exp\left(-\frac{x_{G+1}^2}{2}\right) \right];$$

$$a_G^\pm = \frac{x_G - m_{1G}^\pm}{\sqrt{k_G}}; b_G^\pm = \frac{v - m_{2G}}{\sqrt{k_G}};$$

The factors C_G^\pm must satisfy the continuous conditions

$$W_G^\pm(y_1 = x_i) = W_{G-1}^\pm(y_1 = x_i)$$

and normalized condition

$$\int_{-\infty}^{+\infty} W(y_1) dy_1 = 1$$

In expression (10), the solutions consist of two parts: stationary and non-stationary. The first part has only excitation frequency, but second part includes N frequencies, so that the solutions are quasi-periodic in a long interval. For small damping, that interval will be enough long. During that long interval, when $N=2n-1$ tends to infinite the solutions appear to be chaotic. While time t tends to infinite the solutions tend to periodic. Those solutions are not exact ones but the analytical form of solutions can be easily used to predict vibration of a nonlinear oscillator and to study its nonlinear behaviour in practice.

Example

In the above section, the analytical solution are derived. The reliability of that method can be justified for stationary case on a bilinear system,

but for non - stationary case it has not be studied. There is no existing example for equation (2), so that the accuracy of the above solutions cannot compare. As comparison, we will make some numerical experiment in the near future. In this paper, we report only results in the present.

Considering a hard spring oscillator, assuming its spring parameters to be $\beta = 0.5$ and $\omega = 1$. Taking $N=5$ piecewise linear skeletoncurve instead of the stiffness curve of the hard spring, from Eq.(3) the following parameters can be obtained: $\omega_0^2 = 1.5$; $\omega_1^2 = 29.5$; and $\omega_2^2 = 110.5$; and the coordinate of the turnaround points in the skeletoncurve $x_0 = 0$, $x_1 = 1.0$ and $x_2 = 7.0$. When the damping factor $d=0.01$; the amplitude of periodic excitation $f=12$ and white noise intensity $\sigma = \sqrt{f}$ and the initial conditions $A_0 = 2$ and $\alpha_0 = -\pi/4$ the response statistics of that oscillator are investigated in detail by using Eq.(8) - Eq.(10). The discussions proceed from the following three cases: (1) changing the time difference Δt , (2) changing the frequency Ω of excitation and (3) taking different time. The results display very interesting behaviour for some parameters.

In case (1), letting velocity of the driving belt $v=5$; frequency of periodic excitation $\Omega = 100$ and kinetic friction $\mu' = 0.1$, the probability density of displacement can be calculated from Eq.(9) and the probability time delay maps can be plotted seeing Fig.2, in which the horizontal coordinate denotes the probability density of displacement at the time $t = (3000 + k)T$, $k = 1, 2, \dots, 200$ and $T = 2\pi/\Omega$; and the vertical coordinate represents the probability density of displacement at $t + \Delta t$. The time differences are selected with $\Delta t = 6/\pi$, $\Delta t = 7/\pi$, $\Delta t = 11/\pi$ and $\Delta t = 13/\pi$. Fig.2 shows that all maps are possessed of different structures. That phenomenon means the probability density of displacement depends on the time difference and the responses are non - steady process.

In case (2), letting velocity of driving belt $v=0$, kinetic friction $\mu' = 0.05$ and time difference $\Delta t = 4/\pi$, the probability time delay maps after 3000 T are plotted in Fig.3 using the above mentioned method. Figures 3(a)-3(d) exhibit attractors that seem to be strange one. With increase of

exciting frequency Ω , it has been found that the frequency of excitation influences the structures of solutions. In Fig.3(d), the probability time delay map displays structure to be analogous to Cantor set. It predicts that the system may possess chaotic behaviour.

In case (3), when $v=0$, $\mu' = 0.05$, $\Delta t = 6/\pi$ and $\Omega = 100$, we observe the power spectrum of the mean velocity shown in Fig.4 and the time history of mean velocity shown in Fig.5. In Fig.4, there are several peaks of power spectrum of mean velocity and frequencies are not commensurate. It is proved that the closed solutions of Eq.(10) are quasi - periodic and chaotic motion becomes possible. In enough long interval, while N tends to infinite, the power spectrum will appear behaviour of broad band and the solutions will be chaotic. With the increase in time, energy in the high frequency region decreases and after $10000T$, there is only one peak of power spectrum in lower frequency region. That means the response will be steady while time tends to infinite. That phenomenon has also been observed in time history maps of mean velocity in Fig.5. Fig.5 (d) exhibits a periodic motion. In Fig.5 (b) and (c), some non - regular motion can be detected but this is not chaotic motion, but quasi - periodic one, because the power spectra do not possess broad band behaviour and just only four peaks. Fig.4 and Fig.5 show that the solutions are quasi - periodic, but when N tends to infinite, the solutions can tend to chaotic via quasi - periodic route.

Conculusion

Through above investigation, some conclusions can be drawn.

- (1) For non - sticking motion on a forced Duffing's system, solutions in analytical form derived by using random perturbation technique have been elaborated.
- (2) When piece number N is large enough and damping factor D is very small, those solutions may be used to predicate chaotic motion on the nonlinear systems.

- (3) That method is only effective for nonlinear systems with hard spring behaviour. Because those systems can be represented by using piecewise state equations that are linear in each region.
- (4) That method can be extended to multi - degrees of freedom nonlinear systems.

References

1. Goodman, L.E. and Klumpp, J.H., Analysis of slip damping with reference to turbine - blade vibration. *Journal of Applied Mechanics*, 1956, 23, 421 - 429.
2. Srinivasan, A.V., Dynamic friction, in *Large Space Structures: Dynamics and Control*, ed. Atluri, S.N. and Amos, K.A., 1987.
3. Kumar, V.R. and Waldrom, K.J., Force distribution in closed kinematic chains. *IEEE Journal of Robotics and Automation*, 1988, 4, 657 - 664.
4. Shaw, S.W., On the dynamic response of a system with dry friction. *J. Sound Vib.*, 1986, 108(2), 305 - 325.
5. Popp, K., Chaotische Bewegungen beim Reibschwinger mit simultaner Selbst - und Fremderregung. *ZAMM*, 1991, 71, 4, T71 - T73.
6. Feeny, B. and Moon, F.C., Chaos in a forced dry - friction oscillator: experiments and numerical modelling. *J. Sound Vib.*, 1994, 170(3), 303 - 323.
7. Den Hartog, J.P., Forced vibrations with combined Coulomb and viscous damping. *Transactions of the American Society of Mechanical Engineers*, 1930, 53, 107 - 115.
8. Pfeiffer, F., Dynamical systems with time - varying or unsteady structure. *ZAMM*, 1991, T6-T22.

-
9. Semplinska - Stupnicka, W., Secondary resonances and approximate models of route to chaotic motion in non - linear oscillators. J. Sound Vib., 1987, 113, 155 - 172.
 10. Narayanan, S. and Jayaraman, K., Chaotic vibration in a non - linear oscillator with Coulomb damping. J. Sound Vib., 1991, 146(1), 17 - 31.
 11. Kapitaniak, T., Chaos in system with noise, World Scientific, Singapore, etc., 1988.
 12. Mahfouz. I. A. and Badrakham. F., Chaotic behaviour of some piecewise - linear systems, Part 2: Systems with clearance, J. Sound Vib. 143 (2), 289 - 328, 1990.
 13. Wedig, W., Zur Integration stochastischer System mit stueckweise linearen Kennlinien. Ing - Archiv, 1980, 49, 201 - 215.
 14. Caughey, T. K. Random excitation of a system with bilinear hysteresis, J. Appl. Mech 27, 649 - 652, 1960.

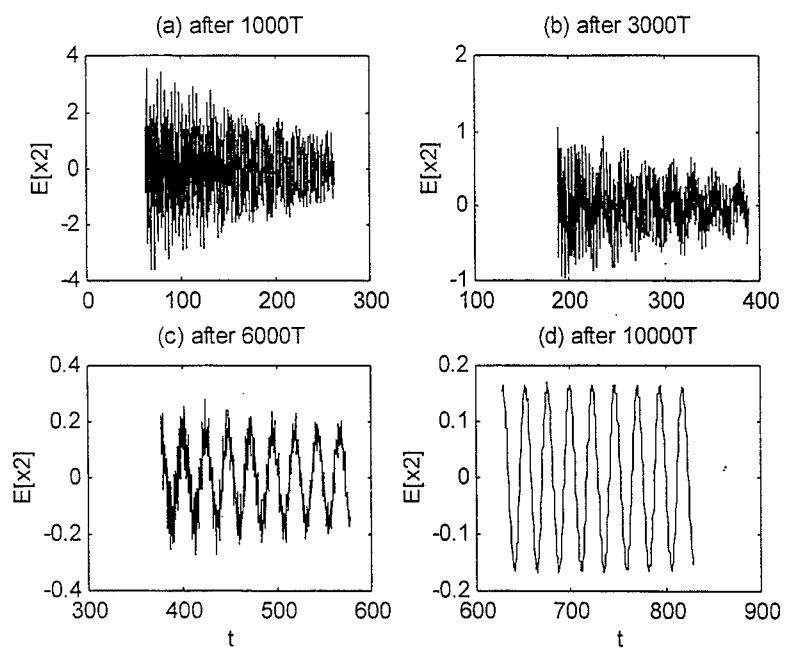


Fig. 5 Time history maps of mean velocity

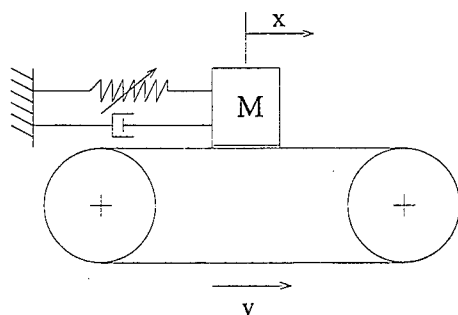


Fig. 1 Mechanical model

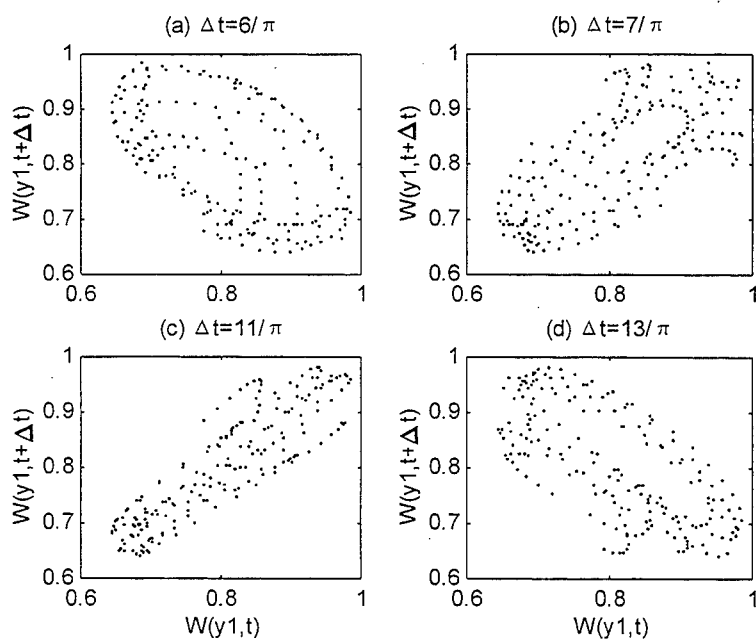


Fig. 2 Probability time delay maps of displacement changing the time difference Δt

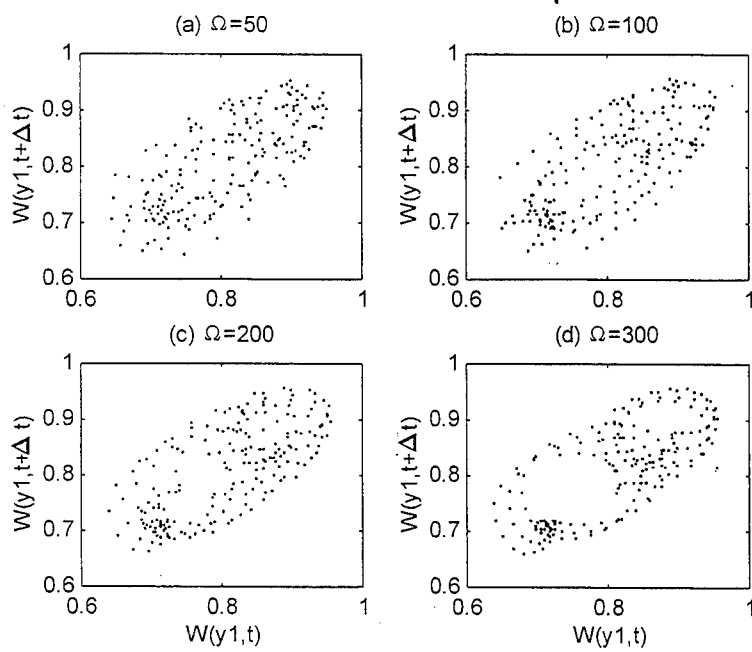


Fig. 3 Probability time delay maps of displacement changing the exciting frequency Ω

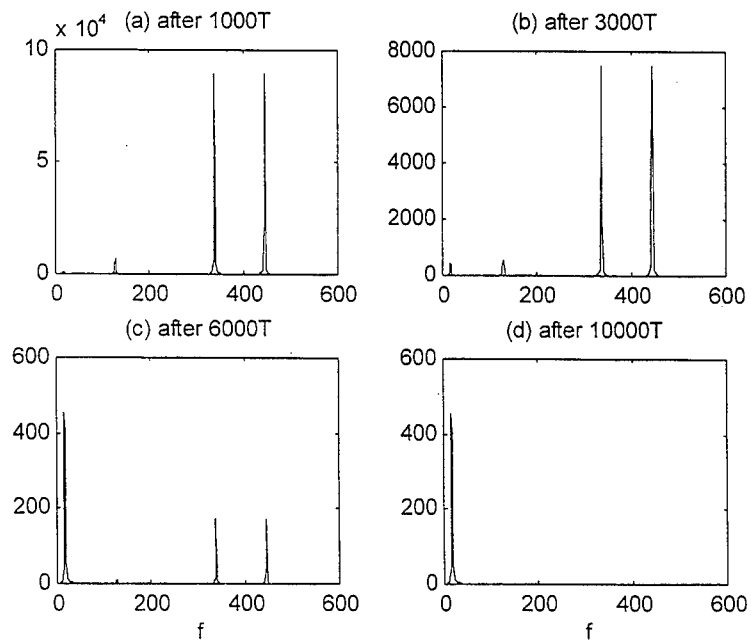


Fig. 4 Power spectra of mean velocity

NONLINEAR VIBRATION II

THE DYNAMICS OF A MODALLY COMPLEX STRUCTURE WITH A CLEARANCE NONLINEARITY

J A Brandon†, E Benoit ‡ and L Jezequel*

‡ Ecole Centrale de Paris

† Cardiff School of Engineering, University of Wales, Cardiff, CF2 1XH

* Ecole Central de Lyon

ABSTRACT

In contrast to the majority of studies reported in the literature, which concentrate on low order systems, the authors have investigated systems which could well be encountered in practical design, i.e. with substantial modal complexity. Previous studies in the group have used a cracked cantilever beam both for theoretical modelling and experimental study. The clearance nonlinearity used in the present study was expected to be easier to control than the cracked cantilever, and the results more straightforward to interpret. The experimental results vindicate this approach and show a wide range of nonlinear phenomena.

INTRODUCTION

The overwhelming majority of reported research into the dynamics of forced vibration of systems with bilinear characteristics has concentrated on low order systems, often with only one significant degree of freedom. Such systems have been shown to exhibit rich response behaviour. In contrast, the authors have investigated the response behaviour of systems of realistic engineering complexity which are characterized by multiply coupled modes.

Prior to this study, the authors' research group has been concerned with the dynamics of cracked cantilever beams [1-4]. This paper reports an experimental study on a more complex structure but with a simpler nonlinearity. As with the cracked beam, the system is subject to autonomous impulsive loading in the interface but the stiffness bilinearity at the discontinuity is primarily due to axial compression rather than the combination of bending and axial effects for the cracked beam. In particular, it was hoped that strongly nonlinear response behaviour would be observed at amplitude levels similar to those encountered in modal testing. In the earlier experimental tests on cracked beams it proved necessary to use much higher amplitude levels with the experimental specimen

yoked to a *control specimen* so that the same excitation was applied to both specimens.

As has been discussed elsewhere [5], there is a broad gap in approach between engineering practitioners and theoreticians in nonlinear structural dynamics. To the practitioner the theorist's problems are both simplistic and abstract; to the specialist in nonlinear dynamics the problems encountered in practice are simultaneously both too diffuse and too complex to respond to a rigorous approach. For example, many of the most powerful results in nonlinear dynamics rely on an assumption of a single dimension map. Such a restriction will be untenable for large classes of interesting and realisable engineering systems. The authors, and co-workers, have chosen to apply a heuristic approach - seeking analogies with systems which the analyst finds tractable - to the modelling of systems with the complexity of practical realisable systems.

This approach requires interaction between analysis, simulation and experiment. Each of these three approaches has stimulated investigation in the other two. The previous research in Cardiff had revealed a number of interesting results:

- Restriction of strongly nonlinear effects to (apparently rather small) zones of the parameter space [2,5];
- Counter-intuitive periodicities [3];
- Twin well oscillator (again counter-intuitive) [4];
- Stable period-three oscillations: observed but not yet reported [2];
- Intermittent chaos: observed but not yet reported.

Although, to the practitioner, a simple cantilever beam under sinusoidal excitation may appear a trivial system, it poses substantial theoretical challenges when the beam is cracked. The bilinear stiffness (crack open or closed) is combined with impulsive closure effects in a compliant interface and friction loading between the crack faces. Each of these phenomena poses a significant theoretical challenge (see, for example, three works on the impulsive problem [6-8]); together, their combined effects are extremely difficult to resolve.

Rightly or wrongly, it was believed that a clearance nonlinearity through the whole section would simplify the boundary conditions in comparison to the cracked beam, reducing the effect of the bilinear stiffness, possibly at a cost of increasing any contributions from friction. As will be seen, the experimental findings support this belief.

The paper will illustrate phenomena familiar from analytical studies of more simple systems. A sequence of spectra showing the descent to chaos will be presented.

EXPERIMENTAL CONFIGURATION

The current study was intended as a simplification of the earlier experimental conditions. A rectangular frame was fabricated with a cut through one side, as shown in figure 1. By adjusting the pre-loading of the discontinuity, using a tensioned piano wire stretched across the intact sides, the discontinuity could be set as a clearance, a tightly compressed joint or in a breathing state. The line of the side was maintained using a light binding of office tape which was believed to disturb the experiment only minimally. Friction effects were minimized by using a standard automotive "cold-start" aerosol lubricant.

ALUMINIUM FRAME

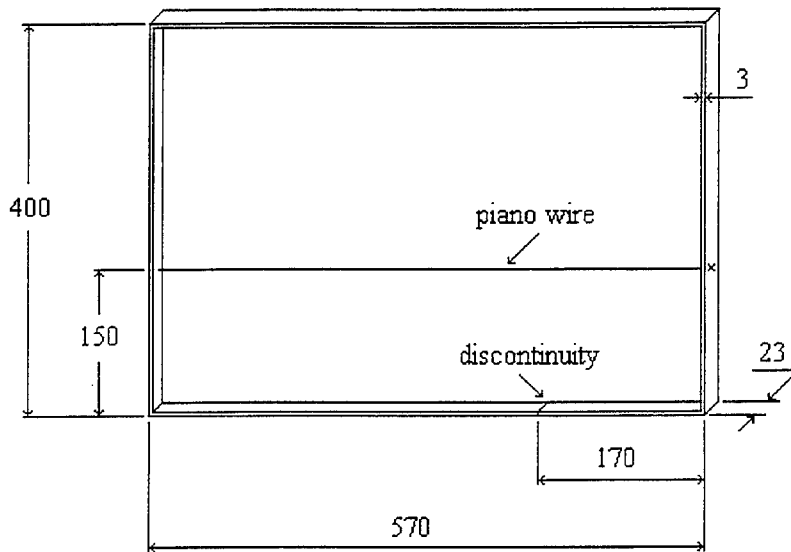
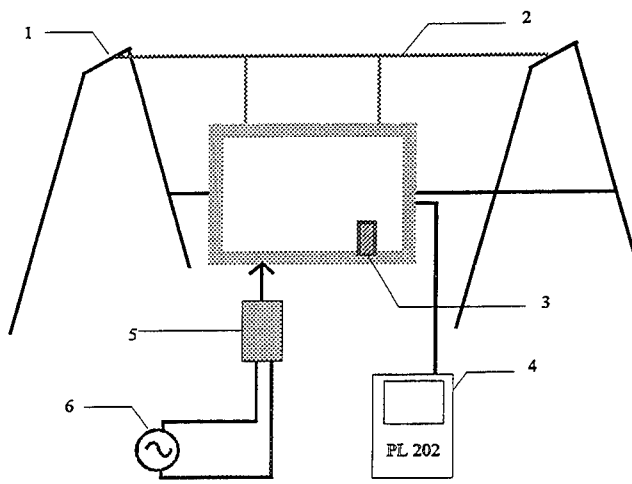


Figure 1: Experimental test frame

The frame was suspended from a steel frame using lightweight rubber links, assuring - so far as was practicable - that free-free boundary conditions applied. For the test series reported here sinusoidal excitation was provided through a standard proprietary exciter-power amplifier set. (Some representative modal tests of the states of the system were carried out under random excitation [9] but these are not reported here). A general purpose accelerometer with integral amplification was attached, using adhesive putty, close to the site of the defect. Although the added inertia effects due to this transducer were undoubtedly considerable, the position of the transducer was not varied during the test, so

that any errors were considered to be systematic. Although figure 2 is schematic, the relative scale of the components is consistent with the experimental set-up.



- 1 Frame
- 2 elastic suspension
- 3 accelerometer
- 4 frequency analyser
- 5 vibrator
- 6 signal generator

Figure 2 schematic of experimental configuration

FINDINGS

The process of searching for an excitation frequency to generate interesting response behaviour has yet to yield any systematic protocol. As was reported in an earlier study [2], regions of the parameter space where period doubling (for example) can be reliably induced are sparse and the amplitudes required are large. Indeed, it was only possible to attribute the period doubling to the interface conditions, rather than to an amplitude nonlinearity, by yoking the damaged specimen to an intact but otherwise identical *control* specimen so that both specimens had equally large deformations [2].

What can be asserted is that no useful indicators were found in the modal analysis. In particular, the linearised resonance frequencies seemed unconnected to the frequencies at which strongly nonlinear response behaviour was observed.

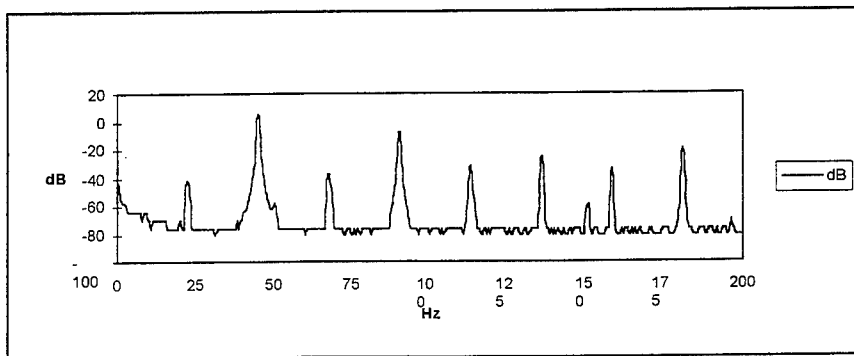
Period doubling

Much of the literature concerning period doubling relates to *pitchfork bifurcations*. As described by Geisel and Nierwetberg [10]:

"Generally, when a parameter μ is varied a period 2^{k-1} becomes unstable and a period 2^k occurs at critical values μ_k which accumulate at μ_∞ "

The essential feature of this description is that the **unstable frequency is superceded by the next sub-harmonic in the sequence**. In the experimental dynamics of discontinuous systems such simple phenomena are, in the authors' experience, never observed. On the contrary, the response frequency corresponding to the originating excitation is sustained - usually together with its own super-harmonics, whilst the subharmonic enters the response - again with its own super-harmonics.

In figure 3 a typical spectrum is illustrated. In this case, the excitation frequency is 44Hz. A clear order-two subharmonic is evident at a frequency of half the forcing frequency; the superharmonics of this subharmonic are represented in the spectrum.



Although this spectrum clearly indicates the possibility of an essentially periodic response, it is instructive to view the time response for this excitation condition.

Figure 4 is the time response corresponding to the spectrum of figure 3. It appears clear - **at first sight** - that the response is synchronous with the excitation.

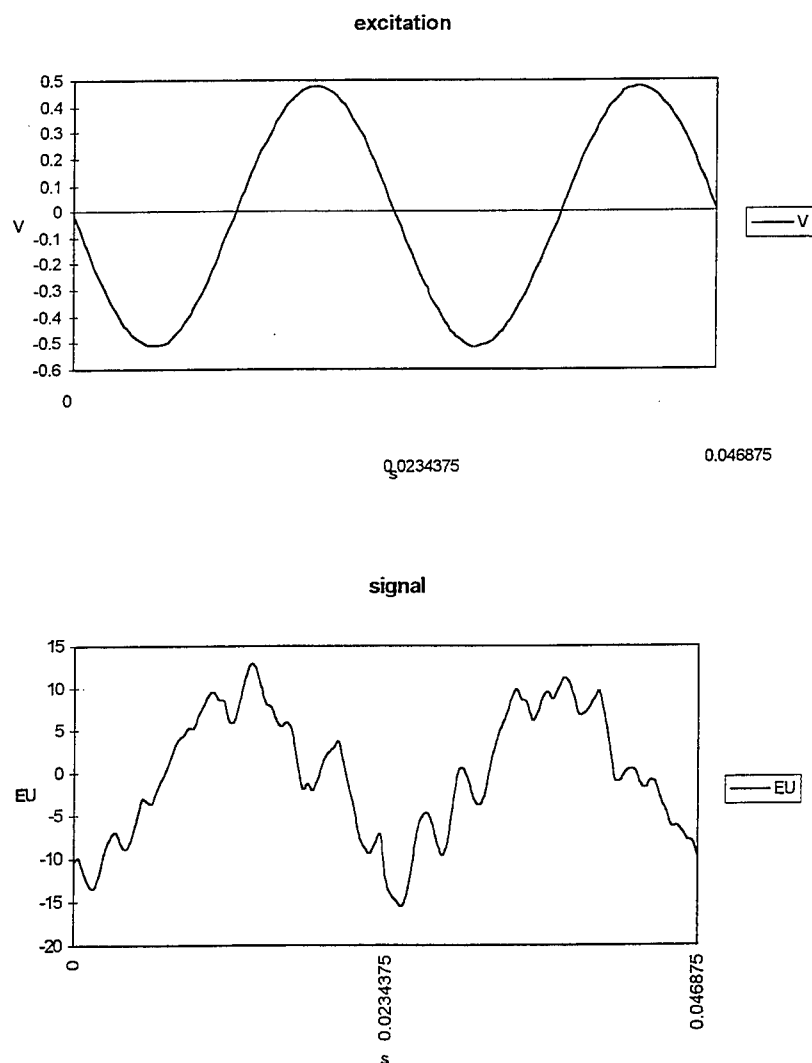


Figure 4: Excitation and response signals

Even when the traces of successive cycles of response are overlaid, as in figure 5, there is some support - in terms of the correspondence of successive peaks, for the belief that the harmonics are driven by the forcing frequency.

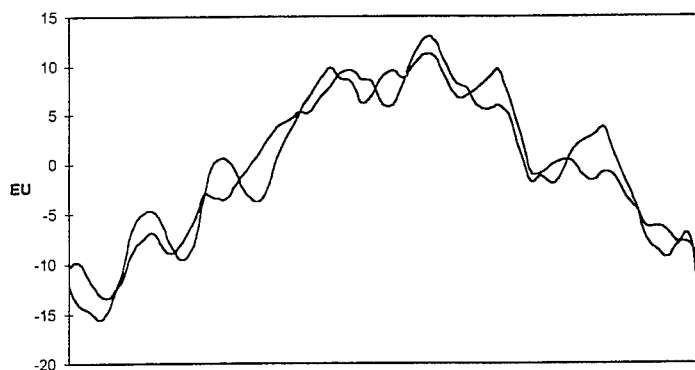


Figure 5: Overlay of two successive cycles

In figure 6, however, double cycles are overlaid. It can now be seen that the harmonics are synchronous. This suggests that, although the driving frequency dominates the energy of the spectrum, the harmonics are driven by the period doubling.

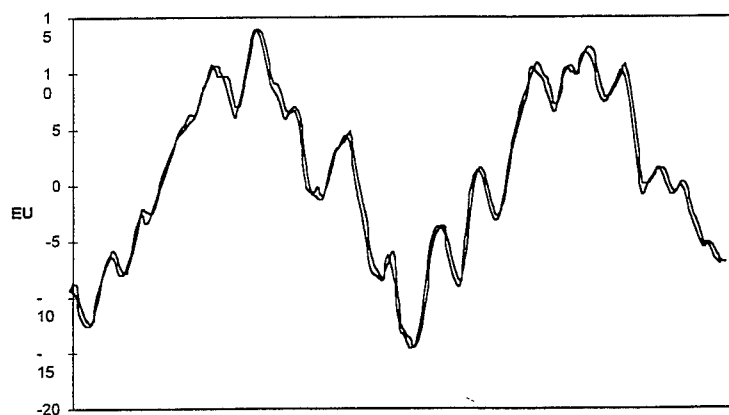


Figure 6: Overlay of two successive double cycles

More complex periodic phenomena

The authors were conditioned in their expectation of more complex periodicities by two observations: firstly, Stoker [10] suggests that complex harmonic behaviour predicted analytically may not be observed experimentally because of the effects of material damping; secondly, the authors expected - based on a syllogistic view of the topology of periodicities [11] - to see sequences of periodicities consistent with the Sarkowski series [12]:

$$\begin{aligned}
 &1 \Rightarrow 2 \Rightarrow 2^2 \Rightarrow 2^3 \Rightarrow \\
 &\quad \Rightarrow \\
 &\Rightarrow \dots \Rightarrow 2^3.7 \Rightarrow 2^3.5 \Rightarrow 2^3.3 \Rightarrow \\
 &\Rightarrow \Rightarrow 2^2.7 \Rightarrow 2^2.5 \Rightarrow 2^2.3 \Rightarrow \\
 &\Rightarrow 2.7 \Rightarrow 2.5 \Rightarrow 2.3 \\
 &\Rightarrow 7 \Rightarrow 5 \Rightarrow 3 \Rightarrow 1
 \end{aligned}$$

In the experimental studies no recognisable sequence was observed. Far from the expected pattern of occurrence of routes to chaos, periodic behaviour was identified at unexpected, and apparently unrelated, frequencies. Furthermore, the expected sequences of periodicities were rarely observed. For example, a period ten (unexpected) oscillation (figure 7) was significantly more stable than period five (expected with some optimism).

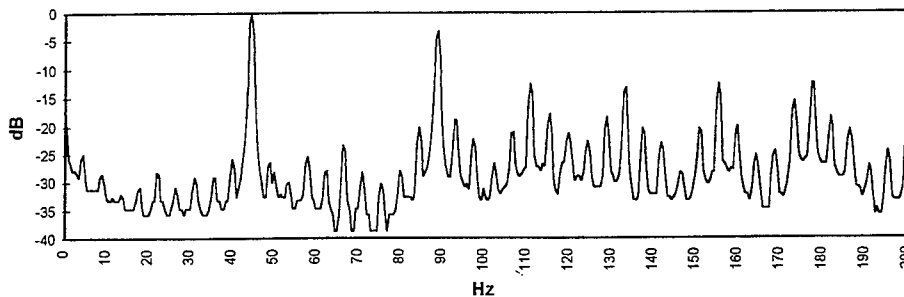


Figure 7: Stable period 10 oscillation

The transition from period two to period three was common. Figure 8 (apparently) shows a co-existence of a stable period two and stable period three. However, there is harmonic content at $\frac{5}{6}$ of the driving frequency - suggesting the existence (not apparent in the spectrum) of a period six oscillation which is simultaneously driving the periods two and three.

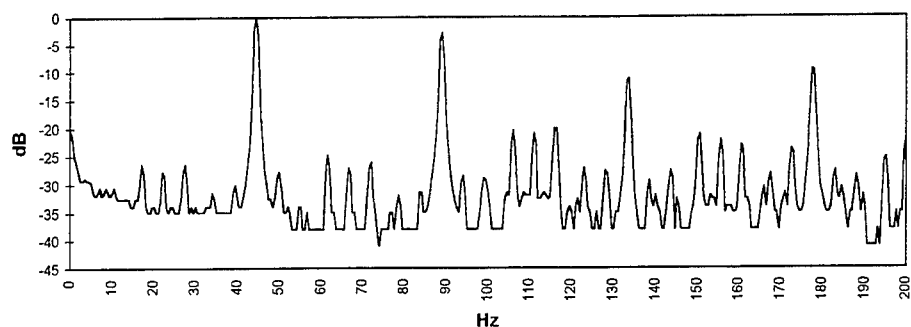


Figure 8: Co-existing period two and period three; strong suspicion of period six

Chaotic episodes were common between any of the stable periodic trajectories. A typical spectrum is shown in figure 9.

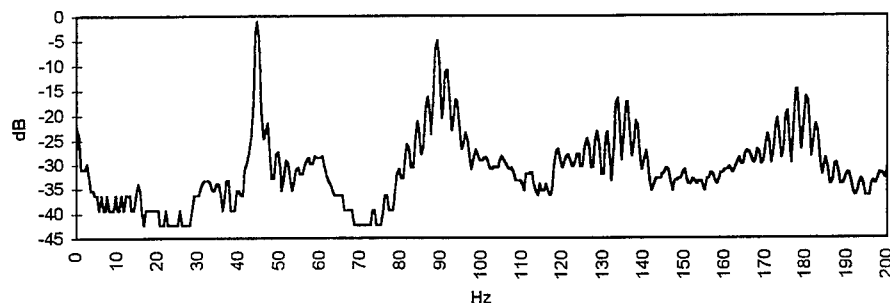


Figure 9: Stable chaotic response

(The correct interpretation of sequences of periodicities can be found in Kahrahman [6]: that the periodicities are determined by contiguities of basins of attraction in the parameter space.[11])

CONCLUDING REMARKS

This study has revealed a rich range of nonlinear response characteristics in a simple - though modally rich - system with a clearance nonlinearity. As had been hoped and anticipated, the amplitudes required to drive this nonlinearity were much smaller than those which proved necessary in previous studies of cracked beams. In particular, they were consistent in magnitude with amplitude levels used in modal testing.

As with the cracked beam, however, the frequencies at which the rich nonlinear responses were observed were sparse and largely unrelated to the frequencies expected to be sensitive from the modal survey.

REFERENCES

1. Abraham, O N L and Brandon, J A, The modelling of the opening and closing of a crack, *Transactions of the American Society of Mechanical Engineers: Journal of Vibration and Acoustics*, 1995, **117**, 370-377.
2. Brandon, J A Sudraud, C and Holford, K M, An experimental study of the dynamics of a cracked beam, *Fifth International Conference: Recent Advances in Structural Dynamics*, Institute of Sound and Vibration Research, Southampton, 1994, Volume 1, 234-242.
3. Brandon, J A and Abraham, O N L, Counter-intuitive quasi-periodic motion in the autonomous vibration of cracked Timoshenko beams, *Journal of Sound and Vibration*, 1995, **185**(3), 415-430.
4. Brandon, J A and Mathias, M H, Complex oscillatory behaviour in a cracked beam under sinusoidal excitation, *Journal of Sound and Vibration*, 1995, **186**(2), 350-354.
5. Brandon, J A, Modal Modelling of Structures with Isolated Non-linearities, *Proceedings of the International Congress MV2, New Advances in Modal Synthesis of Large Structures Nonlinear, Damped and Non-deterministic Cases*, Ecole Centrale de Lyon, October 1995, Volume 2, 385-397.
6. Kahrahan, A, On the response of a preloaded mechanical oscillator with a clearance: period doubling and chaos, *Nonlinear Dynamics*, 1992, **3** 183-192.
7. Chu, C. and Shen, M.-H. H, Analysis of forced bilinear oscillators and the application to cracked beam dynamics, *AIAA Journal*, 1992 **30**(10) 2512-2519.
8. Foale, S and Bishop, S R, Dynamical complexities of forced impacting systems, *Philosophical Transactions of the Royal Society*, 1992, **A338**, 547-556.
9. Benoit, E, Experimental study of a structure with a clearance nonlinearity, *Rapport du stage de DEA d'acoustique*, Ecole Centrale de Lyon, September 1996. (In French).
10. J Stoker, *Nonlinear vibrations in mechanical and electrical systems*, John Wiley, New York, 1950 (Wiley Classic reprint 1992).
11. J A Brandon and E Benoit, Misunderstanding Sarkovskii's theorem, *International Journal of Chaos, Fractals and Solitons*, *In press*
12. A N Sarkovskii, , Coexistence of the cycles of a continuous mapping of the line onto itself *Ukrainian Mathematical Zeitschrift*, 1964, **16**(1) 61-71.

A NOTE ON THE SCALING OF EXPERIMENTAL RESPONSES

The authors may be criticised for the absence of scaling in the figures presented. The rationale for this decision was the arbitrariness of the positioning of the response transducer, as close as practicable to the discontinuity but with no other significance. It certainly did not record the response at the discontinuity and the authors would not wish any such inference to be drawn. Similarly, the response spectra were simply referred to the frequency with maximum energy content. This study was intended to yield qualitative results, so a decision was taken - rightly or wrongly - to disregard the scaling of amplitude in the response records.

A NUMERICAL STUDY OF THE DYNAMICS OF A CRACKED BEAM

M Kisa and J A Brandon

**Cardiff School of Engineering
University Of Wales, Cardiff**

ABSTRACT

The overall aims of the authors are to develop versatile nonlinear finite elements for analysis of cracked structures which exhibit a high degree of faithfulness to the physics of the problem, i.e. are capable of inclusion of effects from fracture mechanics, impulse mechanics and frictional effects in the interface. Before embarking on the development of specialised nonlinear finite elements for research use, it is necessary to validate the approach by benchmarking specific instances of the physics of the system against analytical results (where possible) and tried-and-tested proprietary software. An adaptable research user-defined finite element was compared with the standard element of a proprietary package. It was found that the proprietary element consistently acted very slightly more stiffly than the user-defined element, leading to confidence in the integrity of the analytical model.

INTRODUCTION

For a number of years the authors' research group have used macroscopic approximations for the numerical simulation of defective structures. For example, Brandon and Abraham [1] used component mode assumptions for the linear regions of the structure coupled using constraint matrices developed originally by Dimarogonas et al. [2]. Despite these apparently rather crude macroscopic modelling assumptions a rich set of response characteristics were observed [3].

In contrast, the work of Mottershead et al. [4,5] implicitly pre-supposes a uniformity of scale at (much finer) finite element degrees of resolution. This degree of resolution would be prohibitively expensive for numerical simulation of vibration of cracked structures. In

the current study a hybrid approach is used. The locally non-linear region is analysed using fine resolution finite elements with the singularity properties necessary for realistic estimation of the response behaviour.

Whilst proprietary software packages now contain elements which provide a capability for the modelling of cracked structures in typical design problems, their applicability is less justifiable in research environments where control and adaptability of the form of element is of primary importance. The authors have access to a number of proprietary finite element packages, in each of which the user has a facility to create a *user-defined* element which incorporates a more sophisticated representation of the internal mechanics of the defective region. Some difficulties have been encountered in this approach, particularly where an element formulation appears to satisfy the conditions of the technical specification of the package but unexplainable computational failures have occurred.

The authors have, wherever possible, used the general purpose proprietary elements to provide reference benchmarks to validate the specialised user-defined elements. However it is not always reasonable to assume that the proprietary element is simply a special case of the user-defined element. For example, Abraham and Brandon initially assumed that an intact beam was comparable with a beam with a crack of zero depth [3]; it was rapidly recognised that this is not so. Some typical results of the benchmarking process are reported here.

Where the proprietary formulation and the user-defined element share the same modelling assumptions they should give identical results. However, experience shows that this is not always so. The uncertainty is, at least in part, due to the order of the approximating functions used. Once again, the user-defined element gives the necessary control.

THEORETICAL BACKGROUND

The presence of a crack in a structural member induces a local modification of its stiffness, which can be expressed as local stiffness matrix, the dimension of which depends on the number of **degrees of freedom** considered. Consequently such a crack in any structural member will affect its overall static and dynamic behaviour. Using the fracture parameters which were originally introduced to predict fracture instability, the local flexibility of cracked structures can be calculated. Thus, on the basis of the energy release rate and by application of Castigliano's theorem, the Paris integral yields the displacement of elastic bodies at any desired point. This of course, requires a knowledge of the energy release rate values or the corresponding stress intensity factors in the region of the crack [6]. In this way, the local flexibility may be considered as a single spring relating only one force to the deflection in the same direction [2]. The local flexibility method for the dynamic analysis of cracked structures is restricted only to simple structural elements, because it requires knowledge of expressions giving the stress intensity factor as a function of the crack depth [7].

While a large number of solutions exist for various crack geometries, these tend to be restricted to simple geometries and elementary loading patterns. Thus if cracks are encountered in complex stress fields or in complex geometries a numerical solution technique becomes essential. Over the last three decades the finite element method has proved to be the most effective means of solving engineering structural problems that defy solution by classical methods. The use of finite element method to analyse cracked structure problems is complicated by the stress field singularity which exists at the crack tip. To model the stress field singularity the most successful methods are based on an energy technique and the singularity function formulation. In this paper the stiffness matrix of a cracked element will be calculated based on the analytic solution. A similar type of formulation has been used by Rao et al.[8] and Apostol [9]. By using this element in an embeddable subroutine, the vibration analysis of the structures will be analysed.

CRACKED ELEMENT STIFFNESS MATRIX

If the stress and/or displacement fields within an element can be written in a matrix form of unknown parameters, then the element stiffness may be derived using either or both the internal stress and displacement fields. If only the internal displacement field is used then the resulting formulation is a minimum potential energy form, resulting in a lower bound solution. If only the stress fields are used then the formulation is a minimum complementary energy form, resulting in an upper bound solution. Using both stress and displacement fields is called as mixed formulation. These results would be expected to lie between the two bounds and produce accurate results. Sneddon [10] was the first to derive the stress field expansions for the two cases of a Griffiths' crack and a circular crack. Irwin [11] extended the work of Sneddon to represent the stress field in terms of stress intensity factors. Sih and Rice [12] further extended this work using complex function approach to Muskhelishvili [13]. The equilibrium equations of plane elasticity given by

$$\frac{\partial \sigma_x}{\partial x} + \frac{\partial \sigma_{xy}}{\partial y} = 0 \quad (1)$$

$$\frac{\partial \sigma_y}{\partial y} + \frac{\partial \sigma_{xy}}{\partial x} = 0 \quad (2)$$

are identically satisfied if the stress components are expressed in terms of an Airy stress function, $A(x,y)$, as follows

$$\sigma_x = \frac{\partial^2 A}{\partial y^2}, \quad \sigma_y = \frac{\partial^2 A}{\partial x^2}, \quad \sigma_{xy} = -\frac{\partial^2 A}{\partial x \partial y} \quad (3)$$

For a stress formulation, the compatibility equation must also be satisfied

$$\nabla^2(\sigma_x + \sigma_y) = 0 \quad (4)$$

in which ∇^2 is the usual Laplace or harmonic operator. Substituting from (3) in (4) results in the biharmonic equation

$$\nabla^4 A = \nabla^2(\nabla^2 A) = 0 \quad (5)$$

Thus the problem reduces to that of determining a stress function A which satisfies (5) and also provides stresses and displacements which satisfy the boundary condition.

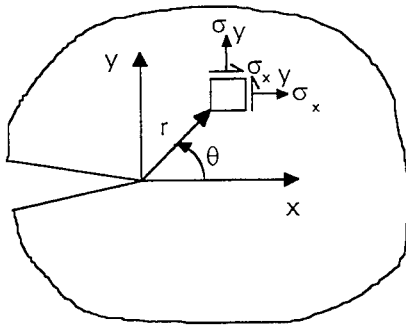


Figure 1 Coordinate axes used in the stress analysis of a plane crack.

Considering Figure 1, the boundary condition can be written as

$$\sigma_y = \sigma_{xy} = 0 \text{ for } \theta = \pm\pi \quad (6)$$

Choosing a suitable Airy function with complex variables and using boundary conditions with an infinite series solution the stresses and the displacements in the structure can be written, following Fawkes [14], as:

$$\sigma_x = \sum_{n=1}^{\infty} \frac{n}{2} r^{(n/2-1)} \left\{ \alpha_n^1 \left[\left(2 + \frac{n}{2} + (-1)^n \right) \cos\left(\frac{n}{2} - 1\right)\theta - \left(\frac{n}{2} - 1\right) \cos\left(\frac{n}{2} - 3\right)\theta \right] \right. \\ \left. - \alpha_n^2 \left[\left(2 + \frac{n}{2} + (-1)^n \right) \sin\left(\frac{n}{2} - 1\right)\theta - \left(\frac{n}{2} - 1\right) \sin\left(\frac{n}{2} - 3\right)\theta \right] \right\} \quad (7)$$

$$\sigma_y = \sum_{n=1}^{\infty} \frac{n}{2} r^{(n/2-1)} \left\{ \alpha_n^1 \left[\left(2 - \frac{n}{2} - (-1)^n \right) \cos\left(\frac{n}{2} - 1\right) \theta + \left(\frac{n}{2} - 1 \right) \cos\left(\frac{n}{2} - 3\right) \theta \right] \right. \\ \left. - \alpha_n^2 \left[\left(2 - \frac{n}{2} + (-1)^n \right) \sin\left(\frac{n}{2} - 1\right) \theta - \left(\frac{n}{2} - 1 \right) \sin\left(\frac{n}{2} - 3\right) \theta \right] \right\} \quad (8)$$

$$\sigma_{xy} = \sum_{n=1}^{\infty} \frac{n}{2} r^{(n/2-1)} \left\{ \alpha_n^1 \left[\left(\frac{n}{2} - 1 \right) \sin\left(\frac{n}{2} - 1\right) \theta - \left(\frac{n}{2} + (-1)^n \right) \sin\left(\frac{n}{2} - 1\right) \theta \right] \right. \\ \left. - \alpha_n^2 \left[\left(\frac{n}{2} - 1 \right) \cos\left(\frac{n}{2} - 3\right) \theta - \left(\frac{n}{2} - (-1)^n \right) \cos\left(\frac{n}{2} - 1\right) \theta \right] \right\} \quad (9)$$

$$u = \sum_{n=1}^{\infty} \frac{r^{n/2}}{2\mu} \left\{ \alpha_n^1 \left[\left(\kappa + \frac{n}{2} + (-1)^n \right) \cos\left(\frac{n}{2}\right) \theta - \frac{n}{2} \cos\left(\frac{n}{2} - 2\right) \theta \right] \right. \\ \left. - \alpha_n^2 \left[\left(\kappa + \frac{n}{2} - (-1)^n \right) \sin\left(\frac{n}{2}\right) \theta - \frac{n}{2} \sin\left(\frac{n}{2} - 2\right) \theta \right] \right\} \quad (10)$$

$$v = \sum_{n=1}^{\infty} \frac{r^{n/2}}{2\mu} \left\{ \alpha_n^1 \left[\left(\kappa - \frac{n}{2} - (-1)^n \right) \sin\left(\frac{n}{2}\right) \theta + \frac{n}{2} \sin\left(\frac{n}{2} - 2\right) \theta \right] \right. \\ \left. + \alpha_n^2 \left[\left(\kappa - \frac{n}{2} + (-1)^n \right) \cos\left(\frac{n}{2}\right) \theta - \frac{n}{2} \cos\left(\frac{n}{2} - 2\right) \theta \right] \right\} \quad (11)$$

where

α_n^i are unknown coefficients,

$\kappa = 3 - 4\nu$ for plane strain and $\kappa = \frac{3 - \nu}{1 + \nu}$ for plane stress,

$\mu = E/2(1 + \nu)$ is the shear modulus,

ν is the Poisson's ratio.

Applying the condition $\theta=0$ to (7), (8) and (9) (with taking $n=1$) gives stress fields as follows

$$\sigma_x = \frac{\alpha_1^1}{\sqrt{x}}, \quad \sigma_y = \frac{\alpha_1^1}{\sqrt{x}}, \quad \sigma_{xy} = \frac{\alpha_1^2}{\sqrt{x}} \quad (12)$$

Now comparing with Irwin's expression which is as follows

$$\sigma_y = \frac{K_I}{\sqrt{2\pi r}}, \quad \sigma_{xy} = \frac{K_{II}}{\sqrt{2\pi r}}, \quad \sigma_{yz} = \frac{K_{III}}{\sqrt{2\pi r}} \quad (13)$$

now, it can be written as

$$\alpha_1^1 = \frac{K_I}{\sqrt{2\pi}}, \quad \alpha_1^2 = \frac{K_{II}}{\sqrt{2\pi}} \quad (14)$$

Applying the well known energy functional in matrix form at element level

$$\pi = U - W = \frac{1}{2} \int_V \sigma^T E \sigma dV - \int_S u^T T dS \quad (15)$$

where

U=internal strain energy,
W=external work done by surface traction,
 σ = Stresses at a point,
u=displacements at a point,
T=surface traction,
V=element area,
S=section of boundary over which T is applied.

The stress and displacement fields given by expressions (7-11) can written in matrix form as follows

$$\sigma = P\alpha, \quad u = A\alpha \quad (16)$$

in which the components of α are related to the stress intensity factors according to (14).

The unknown coefficients can be related to the nodal displacements δ by evaluating equation (16) at every nodal position, thus giving

$$\delta = \bar{A}\alpha \quad (17)$$

Substituting from (16) in (15), taking the variation of (15) with respect to the components of the unknown vector α and applying (17), the following equation can be written

$$K\delta = F \quad (18)$$

where the stiffness matrix is given by

$$K = [\bar{A}^{-1}]^T \int_V P^T E P dV [\bar{A}]^{-1} \quad (19)$$

It is seen from equations (7-11), used in forming the \bar{A} matrix, that there are no rigid body terms in the formulation. It is therefore necessary to include the three modes of rigid body motion. This can be done by allocating the last three α_i terms to be the rigid body displacements θ , x , y and modifying the \bar{A} matrix accordingly, as follows:

$$u = \begin{bmatrix} \bar{A} & y & 1 & 0 \\ & x & 0 & 1 \end{bmatrix} \begin{Bmatrix} \alpha_1 \\ \vdots \\ \alpha_n \\ \theta \\ x \\ y \end{Bmatrix} \quad (20)$$

As rigid body terms do not induce any stress in the element the corresponding terms in the P matrix are as follows

$$\sigma = \begin{bmatrix} \bar{P} & 0 & 0 & 0 \\ & 0 & 0 & 0 \\ & 0 & 0 & 0 \end{bmatrix} \begin{Bmatrix} \alpha_1 \\ \vdots \\ \alpha_n \\ \theta \\ x \\ y \end{Bmatrix} \quad (21)$$

By using equations (7-11) the \bar{A} and P matrices can be found easily. After establishing these matrices element stiffness matrix can be calculated by equation (19).

MODELLING WITH FINITE ELEMENT METHOD

The equation of motion can be written as

$$[M]\{\ddot{x}\} + [C]\{\dot{x}\} + [K]\{x\} = \{F\} \quad (22)$$

where $[M]$, $[C]$ and $[K]$ are the global mass, damping and stiffness matrices respectively, $\{x\}$ and $\{F\}$ are the displacement and external force respectively. For undamped free vibration analysis equation (22) becomes

$$[M]\{\ddot{x}\} + [K]\{x\} = 0 \quad (23)$$

During the assembly of the global stiffness matrix $[K]$ of the system, if there is a crack on any of the elements then the local stiffness matrix can be calculated from equation (19), or else from standard stiffness matrix equations. After forming the global mass matrix $[M]$ the eigenvalue problem can be solved. Assuming that

$$\{x\} = \{\phi\} \sin(\omega t + \beta), \quad \ddot{\{x\}} = -\omega^2 \{\phi\} \sin(\omega t + \beta) \quad (24)$$

and substituting them into equation (23), one ends up with the standard free vibration equation,

$$\omega^2 [M] \{\phi\} = [K] \{\phi\} \quad (25)$$

this is standard eigenvalue problem and now the natural frequencies ω_i and natural modes $\{\phi_i\}$ can be solved for different crack depths by a suitable method.

BENCHMARKING A SIMPLE PLANE PROBLEM

The method has been applied to a plane problem (Figure 2). The geometrical configuration is similar to that analysed by Abraham and Brandon [3]. The crack is assumed to be open during analysis and plane strain conditions is considered. Physical properties of steel were used for the analysis.

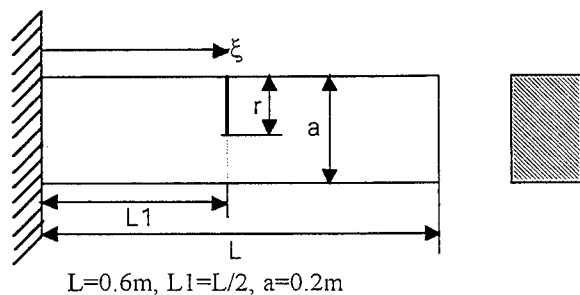


Figure 2. Geometry of the cracked structure.

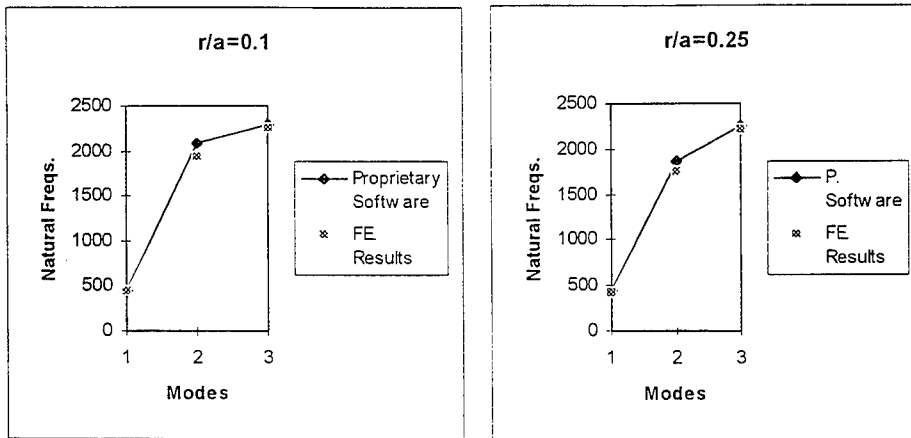


Figure 3. Frequencies for cracked structure for $\xi/L=0.5$, $r/a=0.1$ and $r/a=0.25$

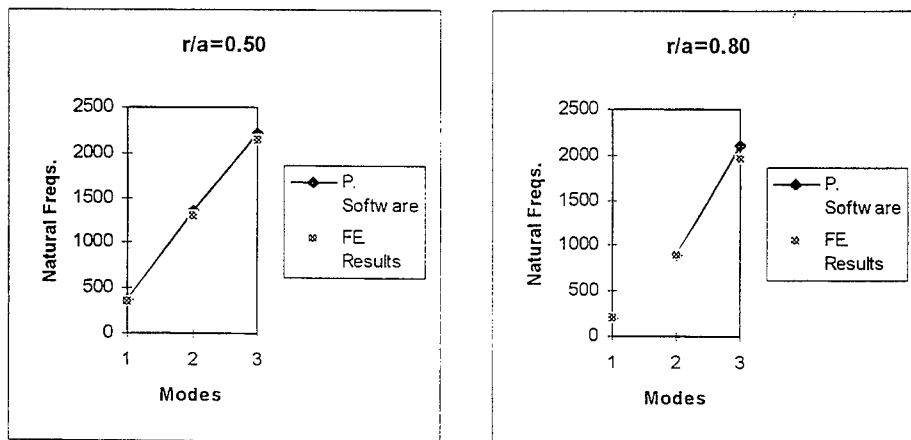


Figure 4. Frequencies for cracked structure for $\xi/L=0.5$, $r/a=0.5$ and $r/a=0.8$

DISCUSSION

The results illustrated in figures 3 and 4 are typical cases which compare the authors' computed natural frequencies with those provided from the proprietary software. As can be seen, there is a close correspondence between the two sets of results. This provides the necessary confidence to undertake broader parametric studies where the formulation of the crack element is varied under controlled conditions. Fuller results from the authors' own studies for this crack element are included in table 1.

rad/s	ξ/L	r/a ratio 0.25	r/a ratio 0.50	r/a ratio 0.80	Intact
1st mode	0.17	370.21	244.56	110.61	453.6
2nd mode	0.17	1954.69	1789.20	1290.90	1971.03
3rd mode	0.17	2141.37	1906.84	1687.51	2282.74
4th mode	0.17	4125.37	3965.11	3663.95	4146.92
1st mode	0.50	421.933	353.621	197.024	
2nd mode	0.50	1750.74	1310.12	904.512	
3rd mode	0.50	2222.28	2143.49	1964.68	
4th mode	0.50	4002.11	3843.56	3146.11	
1st mode	0.83	443.99	436.932	383.463	
2nd mode	0.83	1708.84	1337.44	705.36	
3rd mode	0.83	2235.56	2128.60	1960.16	
4th mode	0.83	3323.34	2724.64	2579.95	

Table 1. Natural frequencies of the cracked structure for various ξ/L and r/a ratios.

CONCLUSIONS

The natural frequencies and mode shapes derived from the user-defined element are extremely close to those derived using proprietary software. The extremely small systematic deviations suggest that the user-defined element is very slightly more flexible than in the proprietary formulation. The results give considerable confidence in extending the capability of the element to cases where the proprietary system cannot be used.

IMPLEMENTATIONAL DETAIL

The proprietary software used as a benchmark was LUSAS™.

The element used for the linear elements in this analysis was #10.2 from the text by Smith and Griffiths ([15] pp308-312).

Because of the assumption of a sharp crack - and consequently no loss of material - the inertia matrix for the crack element is identical to that of the standard element. The components of α are calculated repeatedly - case by case - from the stress intensity factors, as defined in equation 14..

REFERENCES

1. J A Brandon and O N L Abraham, 1995, Counter-intuitive quasi-periodic motion in the autonomous vibration of cracked Timoshenko beams, *Journal of Sound and Vibration*, **185**(3), 415-430.
2. A. D. Dimarogonas and S. A. Paipetis, 1983 *Analytical Methods in Rotor Dynamics*, Applied Science Publishers, London.
3. O N L Abraham and J A Brandon, 1995, The modelling of the opening and closing of a crack, *Transactions of the American Society of Mechanical Engineers: Journal of Vibration and Acoustics*, **117**, 370-377.
4. J E Mottershead, M I Friswell, G H T Ng and J A Brandon, 1994, Experience in mechanical joint model updating, *Sixth International Conference on Numerical Analysis and Experimental Tools for Noise and Vibration Analysis*, University of Leuven, 481-496.
5. J E Mottershead, M I Friswell, G H T Ng and J A Brandon, Geometric parameters for Finite Element Model Updating of Joints and Constraints, *Mechanical Systems and Signal Processing*, **10**(2), 1996, 171-182.
6. N. K. Anifantis, R. L. Actis and A. D. Dimarogonas, 1994, Vibration of cracked annular plates, *Engineering Fracture Mechanics*, **49**(3), 371-379.
7. C. Papadopoulos and A. D. Dimarogonas, 1987, Coupled longitudinal and bending vibration of a rotating shaft with an open crack, *Journal of Sound and Vibration*, **117**, 81-93.
8. A. K. Rao, I. Raju and A. K. Murty, 1971, A powerful hybrid method in finite element analysis, *International Journal for Numerical Methods in Engineering*, **3**, 389-403.
9. M. Apostol, 1974, Development of an Anisotropic Singularity Finite Element Utilizing the Hybrid Displacement Method, *PhD Thesis*, State University of New York
10. I. N. Sneddon, 1946, The distribution of stress in the neighbourhood of a crack in an elastic solid, *Proc. Roy. Soc. London*, **A**, 187.
11. G. R. Irwin, 1957, Analysis of stresses and strains near the end of a crack traversing a plate, *Transactions of the American Society of Mechanical Engineers: Journal of Applied Mechanics*, **24**, 361-364.
12. J. R. Rice and G. C. Sih, Plane problems of cracks in dissimilar media, *Transactions of the American Society of Mechanical Engineers: Journal of Applied Mechanics*, **32**, 418-423.
13. N. I. Muskhelishvili, 1975, *Some Basic Problems of Mathematical Theory of Elasticity*, Holland.
14. A. J. Fawkes, 1976, Finite Elements Applied to Crack-Tip Singularities, *PhD Thesis*, University of Wales, Swansea.
15. I.M. Smith and D. V. Griffiths, 1988, *Programming the Finite Element Method*, 2nd Edition, John Wiley, Chichester.

The Stability Study of Cracked Rotor Systems

By Virtual Oil-Film Bearings

G. T. Zheng

Department of Aerospace Engineering, Harbin Institute of Technology, Harbin, China

A. Y. T. Leung

Division of Mechanical Engineering, University of Manchester, Manchester, UK

Abstract: In the present paper, the stability of cracked rotor systems is discussed from the aspect of input-output stability and inner stability. The inner stability describes the influence of only the fatigue crack size on the stability. The input-output stability represents the influence of rotating speeds together with other system parameters on the stability. By introducing the concept of virtual oil-film bearing produced by a fatigue crack, the inner stability of the system is discussed. It is suggested that fatigue crack is an important reason for the existence of lower frequency vibration components in some turbo-machines and a small fatigue crack may drive a system into instability in a very short time. One numerical example and one experiment example are presented at the end of the paper.

Introduction

Recently, catastrophic accidents in power plants are reported over the world. In these accidents, rotors of turbo-machines broke into several pieces shortly after the systems came into instability states with very high vibration levels. Impacts between a rotor and bearings and finally the rotor being dead locked is a major reason for the breakdown. Nevertheless, reason of the instability is still a puzzle as there are many causes which can produce very serious vibrations, such as self-excited vibration arising from fluid film forces (i.e. oil whip) and fatigue cracks (Schöllhorn, et al, 1993).

According to some investigations, before the breakdown of steam turbines, there exist lower frequency components in vibration signals for quite a long time, where frequencies of these components are lower than a half of the rotating speed. Therefore, damages and abnormal conditions which can bring about lower frequency vibration components might be responsible for such instabilities. In this paper, from the aspect of stability, the possibility of fatigue cracks in a rotor system being one of these causes will be investigated. The crack discussed is confined to "breathing" crack, that is the crack opens and closes once per revolution under the rotor weight (Gasch, 1993).

Studies on fatigue cracks in a rotor system include mathematical models of cracked rotor systems (Gasch, 1976, Gasch, 1993, Lee, et al, 1992, Wauer, 1990), dynamics behaviours of cracked rotor systems (Davies and Mayes, 1984, Dimarogonas and Papadopoulos, 1983, Mayes and Davies, 1984, Nelson and Nataraj, 1986, Plaut, et al, 1994), detection of cracks (Collins, et al, 1991, Imam, et al, 1989, Söffker, et al, 1993) and stability of cracked rotor systems (Gasch, 1993, Huang, et al, 1993, Zheng, 1996). Since the equation of motion of a cracked rotor is periodically time-varying, Floquet's Method is widely used in studying the stability. Research is mainly on the aspect of system responses due to unbalance forces, i.e. regions of instability with respect to rotating speed. Subharmonic resonance due to the rotating speed near $1/k$ or $2/k$ of a natural frequency of the system has been

considered as a major reason for the instability of a cracked rotor system, where k is a positive integer (Gasch, 1993, Huang, et al, 1993, Tamura, et al, 1988, Wen and Wang, 1988, Zheng, 1996).

The Jeffcot- (or Laval-) rotor model is widely used for the studies on the stability of cracked rotor systems (Gasch, 1988, Gasch, 1993, Zheng, 1996). This model has two degrees-of-freedom and hence is suitable for the purpose of studying some basic properties of a rotor system having two competing effects. From the aspect of rotor -foundation (bearings) vibration, the Jeffcot-rotor can also be considered as a model constructed by a rigid rotor mounted on two identical oil-film bearings. Thus, the study on the cracked rotor vibration with the Jeffcot-rotor model may have its own limitation in exploring the stability of cracked rotor systems. In a Jeffcot-rotor model, there is no difference in elastic body vibration mode and rigid body vibration mode, thus this model is not good for the study of lower frequency vibration components of a cracked rotor system.

In the present paper, a general oil-film bearing-elastic rotor model, which is an alternative to the Jeffcot-rotor model, will be used to study the stability and the lower frequency components in the vibration of cracked rotor systems. This approach is based on a proposed concept of "Virtual Oil-Film Bearing" for the analysis of cracked rotor system vibrations.

Vibration of Cracked Rotor System

The fatigue crack studied in this section is a transverse and "breathing" crack. Let the maximum variation in the stiffness produced by the crack is ΔK , then the equation of motion of a cracked rotor system can be expressed as

$$M\ddot{X}(t) + C\dot{X}(t) + KX(t) + \alpha(t)H\Delta K \begin{bmatrix} \cos 2\Omega t & \sin 2\Omega t \\ \sin 2\Omega t & -\cos 2\Omega t \end{bmatrix} X(t) = A \cos(\Omega t + \theta) + f(\dot{X}, X) + G \quad (1)$$

where M , C and K are mass, damping and stiffness matrices, respectively; $\alpha(t)$ determines the amount of stiffness variation contributed by the crack, for the hinged crack model (Gasch, 1976)

$$\alpha(t) = \begin{cases} 1 & \text{crack open} \\ 0 & \text{crack close} \end{cases};$$

H is a matrix defining the position of the crack in the rotor; Ω is the rotating speed of the rotor; A and θ are amplitude and phase of unbalance forces, respectively; $f(\dot{X}, X)$ is the oil film force, which usually is a non-linear function; G is the vector of gravity forces.

There are several approaches available for the solution of equation (1), one of them is harmonic balance method. When $\alpha(t)$ is a periodic function of the rotation and when both the structure damping and oil film damping are ignored, a Fourier series can be used to approximate the solution. If the damping of the system can not be ignored, the opening and closing of the crack from cycle to cycle produces transient vibration to the system, the vibration may not be periodic. Therefore, the method of Fourier expansion may not be suitable. For a linear model with unbalance forces, when the crack closes and the system is in a steady state, the vibration should only contain the first harmonic component of the rotating speed and transient components about the natural frequencies. The method of Fourier expansion might not be a proper choice in such cases.

Another approach is the method of multiple scales (Nayfeh and Balachandran, 1995), which is an established method for a general solution of a dynamic system. In the case of linear oil film forces, it is supposed that the crack will either fully open or fully close (Gasch, 1976). When the crack is in the state of opening ($\alpha(t)=1$), the solution of equation (1) can be expressed as

$$X(t) = \sum_{i=1} U_i e^{\lambda_i t} + \sum_{k=1} \sum_{l=1} V_{ik} / (\lambda_i - jk\Omega) e^{jk\Omega t} + \sum_{\substack{m=1, n=1 \\ m \neq n}} \sum_{k=1} W_{mnk} / (\lambda_m + \lambda_n - jk\Omega) e^{jk\Omega t} + E \quad (2)$$

where λ_i are the eigenvalues of the system, E represents complex conjugate part of the solution, U_i , V_{ik} and W_{mnk} are coefficients determined by the system parameters and the initial conditions at the instant that the crack opens. The eigenvalue λ_i has the form of $\zeta_i + j\omega_i$, where ζ_i and ω_i are damping coefficient and natural frequency of the system, respectively; $i, k, m, n = 1, 2, 3, \dots$

It is known from equation (2) that when the rotating speed is equal to ω_i/k or $2\omega_i/k$, the system can be in a state of resonance. The vibration contains some high order harmonics of the rotating speed.

For a linear system, when the crack closes, the response of the system to the unbalance forces is

$$X(t) = \sum_{i=1} U_i e^{\lambda_i t} + \sum_{i=1} V_i / (\lambda_i - j\Omega) e^{j\Omega t} + E \quad (3)$$

If equation (1) is transformed into a state equation

$$\dot{Y}(t) = AY(t) + F(t) \quad (4)$$

by letting

$$Y(t) = \{\dot{X}^T(t), X^T(t)\}^T, A(t) = \begin{bmatrix} -M^{-1}C & -M^{-1}(K + \alpha(t)H\Delta K) \begin{bmatrix} \cos 2\Omega t & \sin 2\Omega t \\ \sin 2\Omega t & -\cos 2\Omega t \end{bmatrix} \\ I & 0 \end{bmatrix} \text{ and} \\ F(t) = \begin{Bmatrix} M^{-1}A \cos(\Omega t + \theta) \\ 0 \end{Bmatrix} + \begin{Bmatrix} M^{-1}f(Y(t)) \\ 0 \end{Bmatrix} + \begin{Bmatrix} M^{-1}G \\ 0 \end{Bmatrix}.$$

for a linear system, the response of the system can be expressed as

$$Y(t) = \Phi(t, t_0)Y(t_0) + \int_{t_0}^t \Phi(t, \tau)F(\tau)d\tau \quad (5)$$

where $\Phi(t, t_0)$ is fundamental matrix (or state transition matrix) and $f(Y(t))$ is the non-linear part of the oil-film forces. Since matrix $A(t)$ is time-varying, in general, there is no explicit solution to equation (5).

For a constant system matrix A , the fundamental matrix can be written as

$$\Phi(t, t_0) = Ue^{\Lambda(t-t_0)}V^T \quad (6)$$

where $A = U\Lambda V^T$ and Λ is the Jordan matrix, which usually is a diagonal matrix and whose diagonal elements are the eigenvalues of matrix A . With the rule of composition, by dividing the time interval $(t_0, t]$ into a series of small time interval $t_0 < t_1 < t_2 \dots < t_n = t$, and letting matrix $A(t)$ be constant in each such small time interval, the fundamental matrix can be approximately expressed as

$$\Phi(t, t_0) = \prod_{k=1}^n \Phi(t_k, t_{k-1}) = \prod_{k=1}^n U_k e^{\Lambda_k(t_k - t_{k-1})} V_k^T \quad (7)$$

where $A(t) = A_k = U_k \Lambda_k V_k^T$, $t \in (t_{k-1}, t_k]$. Substituting equation (7) into equation (5), one has

$$Y(t) = \prod_{k=1}^n U_k e^{\Lambda_k(t_k - t_{k-1})} V_k^T Y(t_0) + Q(\Omega, \theta) + Q(-\Omega, -\theta) + R(\Omega) + R(-\Omega) \quad (8)$$

$$Q(\Omega, \theta) = 0.5 \sum_{k=1}^n e^{j\Omega_k + j\theta} \Phi(t, t_k) U_k (\Lambda_k - j\Omega)^{-1} (1 - e^{(-j\Omega + \Lambda_k)(t_k - t_{k-1})}) V_k^T \{(M^{-1}A)^T, 0^T\}^T$$

$$R(\Omega) = \sum_{k=1}^n \Phi(t, t_k) U_k (\Lambda_k - j\Omega)^{-1} (1 - e^{\Lambda_k(t_k - t_{k-1})}) V_k^T \{(M^{-1}G)^T, 0^T\}^T$$

It can be seen from equation (8) that the dynamic properties are entirely determined by the eigenvalues and eigenvectors of matrix $A(t)$.

Obviously, another important feature of the cracked rotor vibration is that the vibration contains some transient components.

Input-Output stability

Equation (2) and equation (8) give different descriptions to the stability of a cracked rotor system. Equation (2) sets up a relationship between the natural frequencies of the system and the rotating speed of the rotor to the system stability. On the other hand, equation (8) describes a relationship of the system parameters to the system stability.

In equation (2), since the stability is dependent on rotating speed, that is the input of the system, such stability can be called input-output stability. The condition for a system in input-output stability is that the rotating speed is not equal to $1/k$ or $2/k$ of a natural frequency, for small positive integer k .

Since a rotor system, especially with oil-film bearings, has damping, in the state of resonance, or subharmonic resonance, the amplitude of the system response may be bounded. However, if the amplitude exceeds a certain level, the rotor will impact with oil-film bearings or other static parts of the system, such that the vibration can increase greatly. Therefore, the amplitude should be lower than a specified value. From this aspect, the stability is Langrange stability (Nayfeh and Balachandran, 1995).

In equation (2), the eigenvalues λ_i corresponds to the uncracked rotor system, thus stable and unstable regions are decided by the system itself and are irrelevant to the size of a small crack initially. When the crack develops further, the unstable regions will expand. In other words, the input-output stability is also determined by the crack size afterwards.

Inner Stability

In equation (8), if the rotor has a constant speed and the rotating speed is outside the instability regions, and if at the end of each cycle, the vibration amplitude is higher than that at the beginning of the cycle, the vibration can iteratively go to a very high level. In the sense of Langrange stability, the system is unstable. In such cases, the physical parameters and the size as well as the position of the crack play a key role in the stability of a cracked rotor system. The stability will not be decided by the rotating speed alone. When the stability is entirely decided by the parameters of the system, the stability is called inner stability.

The Floquet's theory (Harris and Miles, 1980) can be used to study the inner stability by calculating the characteristic exponents and characteristic multipliers of the fundamental matrix of the system. A difficulty exists in that there are no general methods available for the exact determination of either the characteristic exponents or characteristic multipliers. It has to rely on numerical calculations.

Like an oil-film bearing, a transverse crack can produce off diagonal terms in the stiffness matrix as shown in equation (1), the crack changes the coupling of vibrations in two orthogonal directions. Since a rotor with oil-film bearings can become unstable due to the presence of cross coupling stiffness (Krämer, 1993), the cross coupling stiffness associated with the crack can also produce instability. Thus, the study of the inner stability can also be from the aspect of cross coupling stiffness produced by the fatigue crack. If the extra stiffness matrix produced by the crack is moved to the right side of equation (1), it can be seen that the crack behaves like a oil-film bearing, which changes the support of the system. From this point of view, the crack can mathematically be considered as a "virtual oil-film bearing" to the rotor system. In the equation of motion, the only difference is that this virtual bearing has time-varying dynamic coefficients.

A rotor-bearing system is constructed by an elastic rotor mounted on an elastic foundation provided by the oil-film forces. The dynamic properties of the system contain rigid body vibration modes, which mainly caused by the elastic foundation, and elastic body vibration modes, which refer to the vibration of the rotor itself. As a virtual bearing, the crack has a great influence on the rigid body vibration modes. To examine the inner stability of a cracked rotor system, the rigid body vibration modes should be calculated. If the real parts of some eigenvalues are positive in some time intervals, the system could be in a state of instability. Because the degree of the influence to the system is determined by the size of the crack, besides the physical parameters and the dynamic coefficients of the oil-film bearings, the crack size is an important factor on the inner stability.

It is known from equations (2) and (8) that a fatigue crack can produce transient components to the system vibration. For a heavy rotor, the rigid body vibration modes usually have lower natural frequencies. Hence the appearance of lower frequency vibration components is a result of fatigue cracks. Being a virtual bearing to the system, in the equation of motion of the system, the crack changes the support condition of the system. Observed from the outside of the system, the cracked rotor system can look like suffering changes in support conditions. As a cracked rotor system is a self-excited system, the system may behave like fluid-induced self-excited vibration , such as oil whip.

Because coefficients of the extra stiffness matrix are period functions of two times of the rotating speed, it looks like that the crack provides foundation excitation to the system. As a result, the cracked rotor vibration contains the second harmonic component of the rotating speed. If unbalance forces are small, the vibration may be dominated by such second harmonic component.

Examples

The first example is a numerical example showing the influence of a fatigue crack on the inner stability of a rotor-bearing system. This is a uniform shaft with diameter 280mm and length 2100mm. The shaft is divided into 7 elements with equal length and a transverse crack is located at the 4th node from the left. For the sake of convenience, a lumped model is used. The shaft is supported by two identical oil-film bearings on two ends. The dynamic coefficients of the bearings are listed in table 1. The natural frequencies of the rigid body vibration modes are 2.40Hz and 6.35Hz, respectively. The damping matrix is defined as $10M+0.00001K$. M and K are defined in the Appendix. The crack model is hinge model (Gasch, 1976).

Table 1: Dynamic Coefficients of Oil-Film Bearing

$k_{xx}=0.17658 \times 10^7 \text{kg/mm}$	$c_{xx}=240 \text{kg-s/mm}$
$k_{yy}=0.26 \times 10^6 \text{kg/mm}$	$c_{yy}=140 \text{kg-s/mm}$
$k_{xy}=0.26 \times 10^5 \text{kg/mm}$	$c_{xy}=420 \text{kg-s/mm}$
$k_{yx}=0.68 \times 10^4 \text{kg/mm}$	$c_{yx}=120 \text{kg-s/mm}$

When the variation in the stiffness produced by the crack is increased from 2% to 5%, the system comes into a state of instability shortly after the crack occurred. The only influence of the rotating speed on the stability is that for a higher speed, the vibration amplitude will increase speedily. The shaft end orbit at the left bearing is shown in figure 1a. The spectrum of the displacement vibration in the vertical direction is shown in figure 1b. In figure 1, the rotating speed is 27Hz. It can be seen that the vibration signal contains lower frequency components with high amplitudes and the signal is dominated by the second harmonic vibration component. The variation of the real part of the eigenvalue for the lowest vibration mode (rigid body vibration mode) along with the shaft rotation is in figure 2. For a 5% stiffness variation, it can be found in figure 2 a, that in some part of the cycle, the real part is positive with large value. Figure 2b is the case of 2% stiffness variation, where the real part is almost always negative.

It can be seen from this example that for a certain rotor system, even a small fatigue crack can put the system into a state of instability.

The second example is an experimental example made on a rotor-bearing system test rig. The diameter of the rotor is 80mm. A transverse fatigue crack was produced on a fatigue test machine after about 50 hour of continuous operation. The depth of the crack is about 0.25 of the diameter. The position of the crack is shown in figure 3. Figure 4 shows the shaft end orbit at the far right bearing and the spectrum of the displacement vibration at the far right bearing in the vertical direction. The rotating speed is 30 Hz. Obviously, besides a high second harmonic vibration component, the vibration contains lower frequency components with high amplitudes.

Conclusion

Mathematically, a fatigue crack can be viewed as a oil-film bearing with time-varying dynamic coefficients. Like an oil-film bearing, in the equation of motion of a cracked rotor system, the crack adds cross coupling terms to the stiffness matrix. Considering this fact, the concept of virtual oil-film bearing is proposed for describing the influence of a fatigue crack on the dynamic properties of a cracked rotor system.

The stability of cracked rotor system are studied from two aspects, input-output stability and inner stability. The inner stability has been discussed mainly from the aspect of virtual oil-film bearing. As in the equation of motion of a cracked rotor system, both the virtual oil-film bearing and the real oil-film bearings share a common feature, cross coupling stiffness terms, the study on the stability of cracked rotor systems is similar to that of oil-film bearing-rotor systems.

A fatigue crack produces lower frequency components to the rotor system vibration. As a cracked rotor system can be a self-excited vibration system, fatigue crack induced vibration may appear like a fluid-induced vibration.

The input-output stabilisation can be realised by control the rotating speed. On the other hand, the inner instability can be avoided by carefully choosing dynamic coefficients of oil-film bearings. To avoid inner instability produced by a fatigue crack, for a given rotor system, sensitivity to fatigue cracks should be a factor in choosing oil-film bearings.

Reference

Collins K. R., Plaut R. H. and Wauer J., 1991, "Detection of Cracks in Rotating Timoshenko Shafts Using Axial Impulses", Transactions of the ASME, Journal of Vibration and Acoustics, Vol. 113, pp. 74-78

- Davies W. G. R. and Mayes I. W., 1984, "The Vibrational Behaviour of a Multi-Shaft Multi-Bearing system in the Presence of a Propagating Transverse Crack", Transactions of the ASME, Journal of Vibration, Acoustics, Stress, and Reliability in Design, Vol. 106, pp. 146-153
- Dimarogonas A. D. and Papadopoulos C. A., 1983, "Vibration of Cracked Shafts in Bending", Journal of Sound and Vibration, Vol. 91, No. 4, pp. 583-593
- Gasch R., 1993, "A Survey of the Dynamic Behaviour of a Simple Rotating Shaft with a Transverse Crack", Journal of Sound and Vibration, Vol. 160, No. 2, pp. 313-332
- Gasch R., 1988, "Dynamics Behaviour of the Laval Rotor with a Cracked Hollow shaft - a Comparison of Crack Models", Vibration in Rotating Machinery, Institution of Mechanical Engineers, Edinburgh, pp. 463-472
- Gasch R., 1976, "Dynamic Behaviour of a Simple Rotor with a cross-sectional Crack", Vibration in Rotating Machinery, Institution of Mechanical Engineers, London, pp. 123-128
- Harris C. J. and Miles J. F., 1980, "stability of Linear Systems: Some Aspects of Kinematic Similarity", Academic Press
- Huang S. C., Huang Y. M. and Shie S. M., 1993, "Vibration and Stability of a Rotating Shaft Containing a Transverse Crack", Journal of Sound and Vibration, Vol. 162, No. 3, pp. 387-401
- Imam I., Azzaro S. H., Bankert R. J. and Scheibel J., 1989, "Development of an On-Line rotor Crack Detection and Monitoring System", Transactions of the ASME, Journal of Vibration, Acoustics, Stress, and Reliability in Design, Vol. 111, pp. 241-250
- Krämer E., 1993, "Dynamics of Rotors and Foundations", Springer-Verlag.
- Lee C. W., Yun J. S. and Jun O. S., 1992, "Modelling of a Simple Rotor with a Switching Crack and Its Experimental Verification", Transactions of the ASME, Journal of Vibration and Acoustics, Vol. 114, pp. 217-225
- Mayes I. W. and Davies W. G. R., 1984, "Analysis of the Response of a Multi-Rotor-Bearing System Containing a Transverse Crack in a Rotor", Transactions of the ASME, Journal of Vibration, Acoustics, Stress, and Reliability in Design, Vol. 106, pp. 139-145
- Nayfeh A. H. and Balachandran B., 1995, "Applied Non-linear Dynamics", John Wiley & Sons, Inc.
- Nelson H. D. and Nataraj C., 1986, "The Dynamics of A Rotor system with a Cracked Shaft", Transactions of the ASME, Journal of Vibration, Acoustics, Stress, and Reliability in Design, Vol. 108, pp. 189-196
- Plaut R. H., Andruet R. H. and Suherman S., 1994, "Behaviour of a Cracked Rotating Shaft during Passage through a Critical Speed", Journal of Sound and Vibration, Vol. 173, No.5, pp. 577-589
- Schöllhorn V. K., Ebi G. and Steigleder K., 1993 "Frettinganrisse in einem 936-MW-Turbogeneratorrotor", VGB Kraftwerkstechnik, Vol. 73, No. 4, pp. 340-344
- Söffker D., Bajkowski J. and Müller P. C., 1993, "Detection of Cracks in Turborotors — A New Observer Based Method", Transactions of the ASME, Journal of Dynamic Systems, Measurement, and Control, Vol. 115, pp. 518-524
- Tamura A., Iwata Y. and Sato H., 1988, "Unstable Vibration of a Rotor with a transverse Crack", Vibration in Rotating Machinery, Institution of Mechanical Engineers, Edinburgh, pp. 647-653

Wausser J., 1990, "On the Dynamics of Cracked Rotors: A Literature Survey", Applied Mechanics Reviews, Vol. 43, No. 1, pp. 13-17

Wen B. C. and Wang Y. B., 1988, "Theoretical Research, Calculation and Experiments of Cracked Shaft Dynamic Response", Vibration in Rotating Machinery, Institution of Mechanical Engineers, Edinburgh, pp. 473-478

Zheng J. B., 1996, "Dynamic Response, Stability, bifurcation and Chaos of Cracked Rotor", PhD. Dissertation, Northwest Polytechnic University, Dec. 1996

Appendix

$M = \text{diag}\{0.5m, m, \dots, m, 0.5m\}$, $m=145.1944\text{kg}$

$$K = \begin{bmatrix} k_0 & 0 & -k_0 & & & \\ 0 & 2k_0 & 0 & -k_0 & & \\ -k_0 & 0 & 2k_0 & 0 & -k_0 & \\ \dots & \dots & \dots & \dots & \dots & \dots \\ & & -k_0 & 0 & 2k_0 & 0 \\ & & & -k_0 & 0 & k_0 \end{bmatrix}, \quad k_0=2.816 \times 10^7 \text{kg/mm}$$

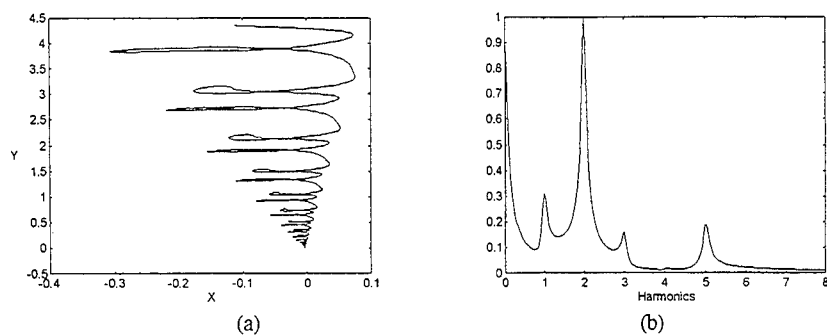


Figure 1: (a) Shaft end orbit at the left bearing (b): Spectrum of the displacement vibration in the vertical direction at the left bearing (5% stiffness variation)

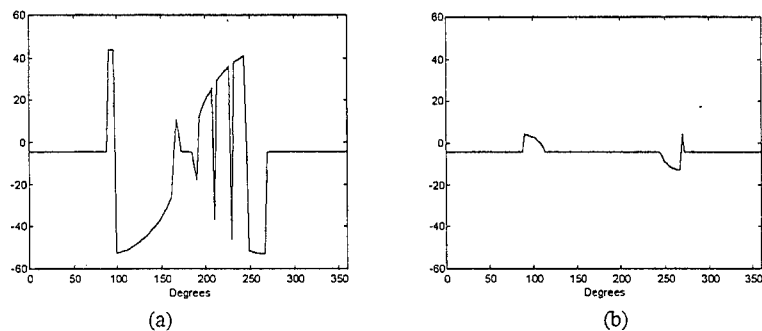


Figure 2: Variation of the real part of the eigenvalue for the lowest vibration mode (a: 5% stiffness variation; b: 2% stiffness variation)

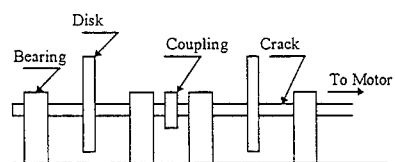


Figure 3: Test rig for cracked rotor-bearing system vibration

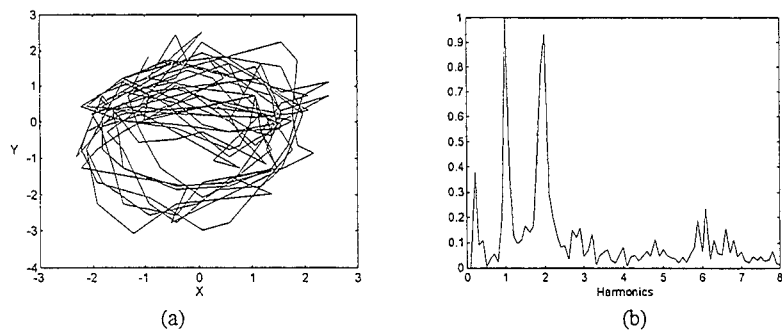


Figure 4: (a) Shaft orbit at the measure point (b): Spectrum of the displacement vibration in the vertical direction.

STABILITY OF UNCLASSICALLY DAMPED GYROSCOPIC SYSTEMS WITH PARAMETRIC EXCITATION

Zhaochang Zheng

Zhichao Hou

Engineering Mechanics, Tsinghua University, Beijing 100084, P.R. CHINA

A.Y.T.Leung

Mechanical Engineering, Manchester University, Manchester M13 9PL, UK

Abstract In this paper, by means of the complex mode theory in state space, an orthogonal condition of avoiding resonance is developed for damped linear gyroscopic systems excited by forces with the driving frequency equal to one of the eigenvalues of the system. Based on the condition, the stability of the system is analyzed and the unstable regions of the solution are given by employing the multiple scale method. Examples show that there do exist zero real part eigenvalues in some damped linear system and the approach described in this paper is correct and efficient.

Key Words damped gyroscopic system instability analysis complex mode analysis multiple scale method parametric excitation

1 INTRODUCTION

There are many systems subjected to parameter excitation in engineering, among which those dynamic systems with parameters varying periodically are of the most interest. The investigation of the system stability has been attracting many researchers' attention. Review of the early works was made by Nayfeh and Mook (1979). The usually employed methods according to Friedmann(1977) were the Hill's infinite determinants, the stability theory of Floquet-Liapunov and perturbation methods. The last two methods are still used wildly in the field and have been extended to deal with both nonlinear systems and parametrically excited systems. The method of multiple scales is popular in perturbation methods. Through the method of multiple scales Nayfeh (1987) investigated the parametric excitation of two internally resonant oscillators, while Zavodney and Nayfeh (1989) determined an approximate response of a slender beam carrying a lumped mass to a principal parametric excitation. The other contributions include Wang and Zhang (1988), Neal and Nayfeh (1990), Plaut (1990), Plaut et al (1990) and Natsiavas (1995). The work using Floquet theorem include those of Hague and Lieh (1988), Shen and Mote (1992), Sankaranarayanan et al (1994) and Kumar and Tuckerman (1994). Biryuk et al (1991) analyzed the stability of the high-power transistor switchable oscillators by means of the direct Lyapunov's methods. Some other approaches are also employed, such as the method of harmonic balance in Yuan et al (1990), McLachlan's method in Tanaka et al (1989) and numerical methods in Sorokin (1992).

Unfortunately, most of existing work are dealing with systems with one degree or two degrees of freedom, or continuous systems with single variable, there are very few papers dealing with the parametric excitation of multiple degrees of freedom systems. Hsu (1963) put forward an approach which can be used to analyze multiple degrees of freedom systems without gyroscopic effects. By application of the method of multiple

scales, Plaut and Limam (1991) considered a class of self-excited mechanical or structural systems with multiple degrees of freedom and subjected to parametric excitation. Shen and Mote (1992) developed a perturbation method, which is based on the Floquet theorem, Fourier transform and a successive approximation.

A simple example of parametric excitation is a disk mounted on a shaft with variable elasticity which was simplified by Den Hartog (1956) as a system with single degree of freedom. For a shaft carrying an unsymmetrical rotor, Yamamoto (1964) gave the unstable regions of the system by solving iteratively an 8-order eigenvalue equation. After combining a preparatory principle and the method of multiple scales, He Yanzong (1992) analyzed the stability of undamped gyroscopic systems with multiple degrees of freedom and small parametric excitation, and computed the unstable regions of the shaft of Yamamoto (1964). He's work will be extended to damped systems with or without gyroscopic effects in this paper.

Applying the complex mode theory in state space to a damped linear system, this paper develops an orthogonal condition for the system to avoid resonance when excited by forces with the driving frequency equal to one of the eigenvalues. This is an extension of the preparatory theorem in He's work (1992) through another procedure. By combining this new orthogonal condition and the multiple scale method, the analysis is carried out on the vibration and parametric excitation of a damped linear system as (He 1992):

$$M\ddot{x} + C\dot{x} + Kx + \varepsilon(M_1\ddot{x} + C_1\dot{x} + K_1x)e^{j\omega t} = 0 \quad (1)$$

where, ε is a small dimensionless parameter and ω , the driving frequency. M, C, K are real matrices with the order of $n \times n$, and are the mass, damping and stiffness matrices of the system, respectively. M_1, C_1, K_1 are corresponding real excitation matrices with the order of $n \times n$. $j = \sqrt{-1}$ is the unit of complex number. It is supposed that there exist some purely imaginary eigenvalues in the system.

2 FORCED VIBRATION AND NEW ORTHOGONAL CONDITIONS

The displacement responses of a general dynamic system

$$M\ddot{x} + C\dot{x} + Kx = f(t) \quad (2)$$

will be investigated in this section when it is excited by an external force $f(t) = f_0 e^{j\omega t}$ with zero initial conditions. Where $f(t)$ is the external force vector, f_0 is the force amplitude vector. Because of the diversity of matrix C , the equation is usually solved by employing complex theory in state space. A set of equations which are equivalent to Eq.(2) can be formed as

$$A\dot{y} - By = F(t) \quad (3)$$

where,

$$A = \begin{bmatrix} -C & -M \\ M & 0 \end{bmatrix} \quad B = \begin{bmatrix} K & 0 \\ 0 & M \end{bmatrix} \quad y = \begin{Bmatrix} x \\ \dot{x} \end{Bmatrix} \quad F(t) = \begin{Bmatrix} -f(t) \\ 0 \end{Bmatrix}$$

Supposing that U, V, Λ are the right mode matrix, the left mode matrix and the spectrum diagonal matrix of the homogenous equation

$$A\dot{y} - By = 0 \quad (4)$$

respectively, we have,

$$\begin{cases} (\lambda_i A - B)U_i = 0 \\ V_i^T(\lambda_i A - B) = 0 \end{cases} \quad (5)$$

Where U, V, Λ can be expressed as following forms separately

$$\Lambda = \begin{bmatrix} \lambda & 0 \\ 0 & \bar{\lambda} \end{bmatrix} \quad V = \begin{bmatrix} -L \\ L\Lambda \end{bmatrix} \quad U = \begin{bmatrix} R \\ R\Lambda \end{bmatrix} \quad (6)$$

and

$$\tilde{M} = V^T A U = \begin{bmatrix} a & 0 \\ 0 & \bar{a} \end{bmatrix} \quad \tilde{K} = V^T B U = \begin{bmatrix} b & 0 \\ 0 & \bar{b} \end{bmatrix} \quad \tilde{M}^{-1} \tilde{K} = \Lambda$$

in which $L = [v \quad \bar{v}]$, $R = [u \quad \bar{u}]$, $\lambda = \text{diag}\{\lambda_i\}$, $a = \text{diag}\{a_i\}$, $b = \text{diag}\{b_i\}$, $i = 1, 2, \dots, n$. λ, u, v are the eigenvalue diagonal matrix, the right mode matrix and the left mode matrix, respectively, of the homogenous equation corresponding to equations (2). Assuming that $y = Uz$ and substituting it to equation (3), after pre-multiplying two sides of the resulted equation by V^T , we have

$$\dot{z} - \Lambda z = \tilde{M}^{-1} V^T F(t) \quad (7)$$

where the equation $\tilde{M}^{-1} \tilde{K} = \Lambda$ has been utilized. With zero initial conditions, and taking $f(t) = f_0 e^{j\omega t}$ in consideration, we can get the solution to equation (7) as

$$z = \tilde{M}^{-1} \text{col} \left\{ \frac{1}{\lambda_r - j\omega} (e^{\lambda_r t} - e^{j\omega t}) V_r^T F_0 \right\} \quad F_0 = \begin{Bmatrix} -f_0 \\ 0 \end{Bmatrix} \quad (8)$$

Where, col means a column vector, and V_r ($r = 1, 2, \dots, 2n$) is the r -th column vector of V , that is to say

$$V = [V_1 \quad V_2 \quad \dots \quad V_{2n}] \quad r = 1, 2, \dots, 2n$$

Considering $y = Uz = \begin{Bmatrix} x \\ \dot{x} \end{Bmatrix}$, we have

$$y = U \tilde{M}^{-1} \text{col} \left\{ \frac{1}{\lambda_r - j\omega} (e^{\lambda_r t} - e^{j\omega t}) V_r^T F_0 \right\} \quad (9a)$$

$$x = R \tilde{M}^{-1} \text{col} \left\{ \frac{1}{\lambda_r - j\omega} (e^{\lambda_r t} - e^{j\omega t}) V_r^T F_0 \right\} \quad (9b)$$

From equation (9) we make two conclusions:

(1) When all eigenvalues λ_r ($r = 1, 2, \dots, 2n$) of a system have negative real parts, the steady responses of the system excited by $f(t) = f_0 e^{j\omega t}$ can be expressed as

$$x = -R \tilde{M}^{-1} \text{col} \left\{ \frac{V_r^T F_0}{\lambda_r - j\omega} \right\} e^{j\omega t} = q_0 e^{j\omega t} \quad y(t) = Q_0 e^{j\omega t} \quad (10)$$

where q_0 is a constant vector of order of n . Eq. (10) is the steady case, because for each r the term with factor $e^{\lambda_r t}$ becomes zero when time lasts long enough.

(2) Some eigenvalues are purely imaginary and equal to the driving frequency. Examples in the fourth part of this paper will show that the purely imaginary eigenvalues do exist in some damped linear system. Supposing that $\lambda_k = j\omega$, the k -th

component of vector $(R\tilde{M}^{-1})^{-1}x$ has a form of $V_k^T F_0 t e^{j\omega t}$. This implies that resonance

takes place although the rest components still have the form of $\frac{V_r^T F_0}{\lambda_r - j\omega} e^{j\omega t}$.

However, if $V_k^T F_0 = 0$ (11)

the responses of the system are bounded and also take the form of Eq.(10) when excited by the external force. Eq.(11) is a necessary and sufficient condition, which the amplitude vector of the excitation must satisfy for a damped linear system to have bounded responses, when the exciting frequency is equal to some imaginary eigenvalue with pure imaginary part of the system. This condition can be called an orthogonal condition and developed directly through Eq.(3), (5) and (10). Recalling the expressions of V_k, F_0 , we can rewrite Eq.(11) as

$$v_k^T f_0 = 0 \quad (12)$$

This is a universal condition in the configuration space for linear systems to avoid resonance when excited by external force $f(t) = f_0 e^{j\omega t}$ with the driving frequency equal to some eigenvalue of the system.

3 PERIODIC PARAMETER EXCITATION

The system, Eq.(1) is to be analyzed by combining the method of multiple scale and Eq.(12). Introducing new independent variables $T_s = \varepsilon^s t$ ($s = 0, 1$), the response $x(t)$ can be considered as a function of various new scales instead of t , and can be represented by an expansion as

$$x(t) = x_0(T_0, T_1) + \varepsilon x_1(T_0, T_1) \quad (13)$$

Substituting Eq.(13) into Eq.(1), and equating coefficients of like powers of ε in both sides, we obtain the set of equations

$$\varepsilon_0 \quad M \frac{\partial^2 x_0}{\partial T_0^2} + C \frac{\partial x_0}{\partial T_0} + K x_0 = 0 \quad (14a)$$

$$\varepsilon_1 \quad M \frac{\partial^2 x_1}{\partial T_0^2} + C \frac{\partial x_1}{\partial T_0} + K x_1 = -2M \frac{\partial^2 x_0}{\partial T_0 \partial T_1} - C \frac{\partial x_0}{\partial T_1} - (M_1 \frac{\partial^2 x_0}{\partial T_0^2} + C_1 \frac{\partial x_0}{\partial T_0} + K_1 x_0) e^{j\omega t} \quad (14b)$$

According to Zheng (1992), under zero initial conditions, the solution of Eq.(14a) is as follows,

$$x_0(t) = \sum_{i=1}^n [u_i e^{\lambda_i T_0} z_i(T_1) + cc] = \sum_{r=1}^{2n} u_r e^{\lambda_r T_0} z_r(T_1)$$

where cc means the complex conjugates of the first term in square bracket. It is a steady solution including only the vibration modes corresponding to purely imaginary eigenvalues because modes with negative eigenvalues tend to zero when time lasts long enough. Assume that there are $2k$ imaginary eigenvalues. Renumbering these eigenvalues in an ascending order, we rewrite the above expression as

$$x_0(t) = \sum_{l=1}^{2k} u_l e^{\lambda_l T_0} z_l(T_1) = \sum_{l=1}^{2k} u_l e^{j\omega_l T_0} z_l(T_1) \quad (15)$$

Introducing Eq.(15) into the second of Eq. (14), we obtain

$$M \frac{\partial^2 x_1}{\partial T_0^2} + C \frac{\partial x_1}{\partial T_0} + Kx_1 = - \sum_{l=1}^{2k} (2M\lambda_l + C) e^{\lambda_l T_0} z'_l u_l - \sum_{l=1}^{2k} (M_1 \lambda_l^2 + C_1 \lambda_l + K_1) e^{(\lambda_l + j\omega) T_0} z_l u_l \quad (16)$$

Here and in further discussions, primes denote differentiation with respect to T_1 , unless otherwise stated.

In the following sections, three cases are to be dealt with.

3.1 $\lambda_l + j\omega$ is not near any eigenvalue of the system

In view of Eq.(12), we know that the necessary condition for Eq.(16) to have bounded solutions is

$$v_l^T (2M\lambda_l + C) u_l z'_l = 0 \quad l = 1, 2, \dots, 2k \quad (17)$$

It can be proved that

$$v_r^T (2M\lambda_r + C) u_r \neq 0 \quad r = 1, 2, \dots, 2n$$

So, in view of Eq.(17), we get to know that all $z'_l = 0$, i.e. all z_l are not functions of T_1 , but are complex constants. Supposing that $z_l = A_l$, Eq.(15) can be rewritten correspondingly as

$$x_0(t) = \sum_{l=1}^{2k} A_l u_l e^{\lambda_l T_0} \quad (18)$$

Then x_1 can be obtained by solving the following equation

$$M \frac{\partial^2 x_1}{\partial T_0^2} + C \frac{\partial x_1}{\partial T_0} + Kx_0 = - \sum_{l=1}^{2k} (M_1 \lambda_l^2 + C_1 \lambda_l + K_1) e^{(\lambda_l + j\omega) T_0} z_l u_l \quad (19)$$

To solve Eq.(19), we can employ the superposition principle and the complex mode theory in state space. The steady solutions to system can be expressed as

$$x(t) = x_0(t) + x_1(t) \quad (20)$$

3.2 $j\omega$ is near to the difference of two eigenvalues of the system

Assuming that $j\omega = \lambda_k - \lambda_s + \varepsilon \sigma$, (σ is a complex), we get

$$j\omega + \lambda_s = \lambda_k + \varepsilon \sigma \quad j\omega + \bar{\lambda}_k = \bar{\lambda}_s - \varepsilon \bar{\sigma}$$

Recalling Eq. (12) and (16), we obtain

$$\begin{cases} v_k^T [(2M\lambda_k + C) u_k z'_k + (M_1 \lambda_s^2 + C_1 \lambda_s + K_1) u_s z_s e^{\sigma T_1}] = 0 \\ v_s^T [(2M\lambda_s + C) u_s z'_s + (M_1 \lambda_k^2 + C_1 \lambda_k + K_1) u_k z_k e^{-\sigma T_1}] = 0 \end{cases} \quad (21)$$

Here the second equation has been taken as the conjugate of the first one.

As stated before, $v_r^T (2M\lambda_r + C) u_r \neq 0$ ($r = 1, 2, \dots, 2n$), so we can let

$$H_1 = \frac{v_k^T (M_1 \lambda_s^2 + C_1 \lambda_s + K_1) u_s}{v_k^T (2M \lambda_k + C) u_k} \quad H_2 = \frac{v_s^T (M_1 \lambda_k^2 + C_1 \lambda_k + K_1) u_k}{v_s^T (2M \lambda_s + C) u_s}$$

and rewrite Eq.(21) as

$$\begin{cases} z'_k + H_1 z_s e^{\sigma T_1} = 0 \\ z'_s + H_2 z_k e^{-\sigma T_1} = 0 \end{cases} \quad (22)$$

Suppose that

$$\begin{aligned} H &= d_1 + j d_2 & H &= e_1 + j e_2 & \sigma &= \sigma_1 + j \sigma_2 \\ z_k &= (f_1 + j f_2) e^{(\zeta + \sigma) T_1} & z_s &= (g_1 + j g_2) e^{\zeta T_1} & \zeta &= \zeta_1 + j \zeta_2 \end{aligned}$$

where, $d_i, e_i, f_i, g_i, \sigma_i, \zeta_i$ ($i = 1, 2$) are all real constants. Inserting these expressions into Eq.(22), and separating the real part from the imaginary part, we obtain

$$\begin{cases} (\zeta_1 + \sigma_1) f_1 - (\zeta_2 + \sigma_2) f_2 + d_1 g_1 - d_2 g_2 = 0 \\ (\zeta_2 + \sigma_2) f_1 + (\zeta_1 + \sigma_1) f_2 + d_2 g_1 + d_1 g_2 = 0 \\ e_1 f_1 - e_2 f_2 + \zeta_1 g_1 - \zeta_2 g_2 = 0 \\ e_2 f_1 + e_1 f_2 + \zeta_2 g_1 + \zeta_1 g_2 = 0 \end{cases} \quad (23)$$

For a non trivial solution, the coefficient determinant must equal to zero, i.e.

$$\begin{vmatrix} \zeta_1 + \sigma_1 & -(\zeta_2 + \sigma_2) & d_1 & -d_2 \\ \zeta_2 + \sigma_2 & \zeta_1 + \sigma_1 & d_2 & d_1 \\ e_1 & -e_2 & \zeta_1 & -\zeta_2 \\ e_2 & e_1 & \zeta_2 & \zeta_1 \end{vmatrix} = 0 \quad (24)$$

In order to make z_k, z_s bounded, it must be satisfied that $\zeta_1 \leq 0, \zeta_1 + \sigma_1 \leq 0$. For the sake of convenience, we can let $\zeta_2 = 0, \sigma_1 = 0$, and still take the notations $\zeta = \zeta_1, \sigma = \sigma_2$ and simplify Eq.(24) as

$$\begin{vmatrix} \zeta & -\sigma & d_1 & -d_2 \\ \sigma & \zeta & d_2 & d_1 \\ e_1 & -e_2 & \zeta & 0 \\ e_2 & e_1 & 0 & \zeta \end{vmatrix} = 0 \quad (25)$$

Letting $\text{Re} = e_1 d_1 - e_2 d_2, \text{Im} = e_2 d_1 + e_1 d_2$, we can find that Re, Im are the real and imaginary part of $H_1 \cdot H_2$ respectively, i.e.,

$$\text{Re} = \text{Re}(H_1 \cdot H_2) \quad \text{Im} = \text{Im}(H_1 \cdot H_2)$$

$$\text{and rewrite Eq.(25) as} \quad (\zeta^2 - \text{Re})^2 + (\sigma \zeta - \text{Im})^2 = 0 \quad (26)$$

There are two possibilities to be discussed.

Firstly, ζ is real. In this situation Eq.(26) is identical to

$$\begin{cases} \zeta^2 - \text{Re} = 0 \\ \sigma \zeta - \text{Im} = 0 \end{cases} \quad (27)$$

If $\text{Re} > 0$ and the sign of Im is not the same as that of $\sigma, \zeta < 0$, the system comes out to be static as time lasts long enough. The solution is asymptotically stable.

Secondly, $\zeta = a + j b$. Under this situation, Eq.(26) is the same as

$$(\zeta^2 - \text{Re}) = \pm j(\sigma\zeta - \text{Im}) \quad (28)$$

and can be written as

$$\begin{cases} a^2 - b^2 - \text{Re} = -\sigma b \\ 2ab = \sigma a - \text{Im} \end{cases} \quad \text{or} \quad \begin{cases} a^2 - b^2 - \text{Re} = \sigma b \\ 2ab = -\sigma a + \text{Im} \end{cases} \quad (29)$$

When a stable but not an asymptotically stable solution is desirable, we can let $a=0$, and simplify Eq.(29) as

$$\begin{cases} -b^2 - \text{Re} = -\sigma b \\ \text{Im} = 0 \end{cases} \quad \text{or} \quad \begin{cases} -b^2 - \text{Re} = \sigma b \\ \text{Im} = 0 \end{cases} \quad (30)$$

It can be verified that the two sets expressions of Eqs.(30) give real number to b when $\sigma^2 \geq 4\text{Re}$ ($\text{Re} > 0$ and $\text{Im}=0$), with the implication that the solution to Eq.(22) is stable. The unstable region is as follows

$$\omega_k - \omega_s - 2\varepsilon\sqrt{\text{Re}} < \omega < \omega_k - \omega_s + 2\varepsilon\sqrt{\text{Re}} \quad (31)$$

For $\text{Re} < 0$, the solution is definitely stable.

3.3 $j\omega$ is in a nearby region of the sum of two eigenvalues

This can be regarded as a special case of section 3.2. In fact, taking

$$j\omega = \lambda_k - \lambda_s + \varepsilon\sigma$$

into considering, we get a result as (λ_q is another imaginary eigenvalue)

$$j\omega = \lambda_k + \bar{\lambda}_s + \varepsilon\sigma = \lambda_k + \lambda_q + \varepsilon\sigma$$

Here the assumption has also been made that there are imaginary eigenvalues. So as for the case that the driving frequency is near the sum of two pure imaginary eigenvalues, we can deal with it through the process mentioned in section 3.2. Let us consider a special case in detail.

Supposing that, $\bar{\lambda}_s = \lambda_k$, i.e., $j\omega = 2\lambda_k + \varepsilon\sigma$, $\sigma = j\sigma_2$, σ_2 is a real constant, we have

$$v_k^T [(2M\lambda_k + C)u_k z_k' + (M_1 \bar{\lambda}_k^2 + C_1 \bar{\lambda}_k + K_1) \bar{u}_k \bar{z}_k e^{\sigma T_1}] = 0 \quad (32)$$

After letting

$$H = \frac{v_k^T (M_1 \bar{\lambda}_k^2 + C_1 \bar{\lambda}_k + K_1) \bar{u}_k}{v_k^T (2M\lambda_k + C) u_k} \quad (33)$$

we rewrite Eq.(32) as, in this case, $\text{Im} = \text{Im}(H_1 \cdot \bar{H}_2) = 0$,

$$z_k' + H \bar{z}_k e^{j\sigma_2 T_1} = 0 \quad (34)$$

and then assume that $z_k = (f_1 + jf_2)e^{(\zeta + j\sigma_2)T_1}$, $H = (d_1 + jd_2)$, ζ_i, d_i ($i=1,2$) are all real, and have no relation with T_1 . Through the aforementioned procedure, we obtain

$$\begin{cases} \zeta_2 = \sigma_2 \\ \zeta_1^2 = d_1^2 + d_2^2 - \zeta_2^2 \end{cases} \quad (35)$$

The stability requires that ζ_1 must be smaller than zero or be an imaginary number. So from Eq.(35), it is required that

$$\sigma_2^2 \geq 4(d_1^2 + d_2^2) \text{ i.e., } \sigma_2^2 \geq 4\|H\|^2 \quad (36)$$

where $\|H\|$ is the length of complex number H . The unstable region is as follows

$$2\omega_k - 2\varepsilon\|H\| < \omega < 2\omega_k + 2\varepsilon\|H\| \quad (37)$$

4 EXAMPLES

4.1 Model and equations

A mono-rotor system suffers from parametric excitation when the rotor has unsymmetric diameter moments of inertia (Yamamoto and He). Suppose that the two diameter moments of inertia of the rotor are J_η, J_ζ , respectively, and $J_\eta > J_\zeta$. Letting

$$J = (J_\zeta + J_\eta) / 2 \quad \Delta J = (J_\eta - J_\zeta) / 2$$

then in an inertial coordinate system, the differential motion equations of the rotor can be expressed in complex variables ($z = x + jy$, $\theta = \theta_y - j\theta_x$) as

$$\begin{cases} m\ddot{z} + \alpha z + \gamma\theta = 0 \\ J\ddot{\theta} - jJ_p\Omega\dot{\theta} + \Delta J(\ddot{\theta} + j2\Omega\dot{\theta})e^{j2\Omega t} + \gamma z + \delta\theta = 0 \end{cases} \quad (38)$$

where, J_p, Ω are the polar moment of inertia and the rotating speed, respectively. $\bar{\theta}$ is the conjugate to θ . α, γ, δ are the stiffness coefficients of the shaft. 2Ω is the driving frequency ω in Eq.(1). This is a parametric excitation system with the driving frequency two times of the critical velocity. Now we introduce transformations

$$\begin{aligned} \sqrt{\frac{m}{J}} / \alpha &= \gamma', & \frac{m\delta}{\alpha J} &= \delta', & \sqrt{\frac{\alpha}{m}} t &= t', & \frac{J_p}{J} &= i_p \\ \frac{\Delta J}{J} &= \varepsilon, & \frac{\Omega}{\sqrt{\frac{\alpha}{m}}} &= \Omega', & \frac{z}{\sqrt{\frac{J}{m}}} &= z' \end{aligned}$$

and assign

$$\begin{aligned} q &= \begin{Bmatrix} z' \\ \theta \end{Bmatrix}, & M &= \begin{bmatrix} 1 & 0 \\ 0 & 1 \end{bmatrix}, & G &= \begin{bmatrix} 0 & 0 \\ 0 & i_p\Omega' \end{bmatrix} \\ K &= \begin{bmatrix} 1 & \gamma' \\ \gamma' & \delta' \end{bmatrix}, & M_1 &= \begin{bmatrix} 0 & 0 \\ 0 & 1 \end{bmatrix}, & G_1 &= \begin{bmatrix} 0 & 0 \\ 0 & 2\Omega' \end{bmatrix} \end{aligned}$$

then rewrite Eq.(38) as a set of dimensionless equations

$$M\ddot{q} - jG\dot{q} + Kq + \varepsilon(M_1\ddot{q} + jG_1\dot{q})e^{j2\Omega' t} = 0 \quad (39)$$

Supposing that $z' = x' + jy'$, then after extending Eq.(39) and separating the real and imaginary parts, we get

$$\begin{cases} M\ddot{p}_1 + G\dot{p}_2 + Kp_1 + \varepsilon(M_1\ddot{p}_1 + G_1\dot{p}_2)e^{j2\Omega' t} = 0 \\ M\ddot{p}_2 + G\dot{p}_1 + Kp_2 + \varepsilon(-M_1\ddot{p}_2 + G_1\dot{p}_1)e^{j2\Omega' t} = 0 \end{cases} \quad (40)$$

We can combine the two equations in Eqs. (40) into a compact form as

$$\tilde{M}\ddot{p} + \tilde{C}\dot{p} + \tilde{K}p + \varepsilon(\tilde{M}_1\ddot{p} + \tilde{C}_1\dot{p})e^{j2\Omega t} = 0 \quad p = \begin{Bmatrix} p_1 \\ p_2 \end{Bmatrix} \quad (41)$$

where

$$\tilde{M} = \begin{bmatrix} M & 0 \\ 0 & M \end{bmatrix} \quad \tilde{K} = \begin{bmatrix} K & 0 \\ 0 & K \end{bmatrix} \quad \tilde{C} = \begin{bmatrix} 0 & G \\ -G & 0 \end{bmatrix}$$

$$\tilde{M}_1 = \begin{bmatrix} M_1 & 0 \\ 0 & -M_1 \end{bmatrix} \quad \tilde{C}_1 = \begin{bmatrix} 0 & G_1 \\ G_1 & 0 \end{bmatrix}$$

Introducing damping matrix C into the Eq.(39) and demonstrating through the same procedure, we get another set of equations

$$\tilde{M}\ddot{p} + \tilde{C}'\dot{p} + \tilde{K}p + \varepsilon(\tilde{M}_1\ddot{p} + \tilde{C}_1\dot{p})e^{j2\Omega t} = 0 \quad (42)$$

where \tilde{C}' is expressed as follows

$$\tilde{C}' = \begin{bmatrix} C & G \\ -G & C \end{bmatrix} \quad C = \begin{bmatrix} c_1 & c_3 \\ c_4 & c_2 \end{bmatrix}$$

while other matrices are the same as stated in Eq.(41).

In the following section, we will give the unstable regions for three examples with different damping by means of the approach described above.

4.2 Numerical results

For the sake of validation of the aforementioned approach, the parameters except those in damping matrix C in this paper, are assigned the same values to those in the examples of Yamamoto and He, i.e.,

$$i_p = 1 \quad \delta' = 1.06 \quad \gamma'^2 = 0.731$$

In all the examples, we take the note of Ω for simplicity, to replace the non dimensional speed Ω' .

Example 1 $C=0$

That means that no damping is introduced to the system. The motion equation takes the form of Eq.(41), and the critical rotating speed is $\Omega = 0.5571$. This is the very problem dealt with by Yamamoto and He. After constituting the characteristic equation in state space according to Eq.(3), we get, by employing QR method, the eigenvalues with zero real parts $j\omega = \pm 0.5571j$ and the corresponding left- and right modes. Inserting the eigenvalues and modes into Eq.(33) results in

$$H = 0.121 - 0.06374j \quad \|H\| = 0.13676$$

Recalling Eq.(37), we get the unstable region is as follows

$$2 \times 0.5571 - 2 \times \varepsilon \times 0.13676 < 2\Omega < 2 \times 0.5571 + 2 \times \varepsilon \times 0.13676$$

$$\text{or} \quad 0.5571 - 0.13676\varepsilon < \Omega < 0.5571 + 0.13676\varepsilon$$

see Fig.1. This result agrees well with that of He(1992). The following are two new examples.

Example 2 $C = \begin{bmatrix} 1 & 1.2398 \\ 1.2398 & 1.5371 \end{bmatrix}$

It can be proved that the critical rotating speed is 0.5571, also. The pure imaginary eigenvalues and other variables are as follows

$$j\omega = \pm 0.5571j \quad H = 0.1275 + 0.05382j \quad \|H\| = 0.13675$$

So, the unstable region is (see Fig. 2)

$$0.5571 - 0.13675\varepsilon < \Omega < 0.5571 + 0.13675\varepsilon$$

It is clear that the influence of damping on the system is very small and it is due to the fact that the damping matrix is singular.

Example 3 $C = \begin{bmatrix} 1 & 3.933 \\ 3.933 & 14.9385 \end{bmatrix}$

The critical rotating speed and the corresponding variables are as follows

$$\Omega = 0.7879 \quad j\omega = \pm 0.7879j \quad H = 0.01405 + 0.02422j \quad \|H\| = 0.028$$

with the unstable region as (see Fig. 3)

$$0.7879 - 0.028\varepsilon < \Omega < 0.7879 + 0.028\varepsilon$$

The results show that damping increases the critical rotating speed of the system and condenses the unstable region greatly.

CONCLUSIONS

From the above examples, we can find out that there do exist purely imaginary eigenvalues and that the influence of damping on the parameter excitation and vibration of a linear system is very complicated. Considering the need of the reality, we think that parametric excitation and vibration of a linear system deserves further investigation. To which the works in this paper supplies with an efficient approach, because the procedure turns a parametric excitation problem with multiple degrees of freedom into some algebraic equations of low orders by employing the complex modes of corresponding linear systems without time-varying parameters.

ACKNOWLEDGEMENT

Financial support from the National Natural Science Foundation of China and from the Doctoral Training Foundation of National Education Committee of China are gratefully acknowledged.

REFERENCES

- Biryuk, N.D., Epifantsev, and Y.F., Savvinov, A.M., 1991, Parametric Excitation Analysis of Power Transistor Switchable Oscillators, *Izvestiya VUZ: Radioelektronika*, Vol.34, No.8, pp. 87-89.
- Den Hartog, J.P., 1956, *Mechanical Vibration*, McGraw-Hill Book Company, Inc.
- Friedmann P., Hammond, C.E., and Woo, Tze-Hsin, 1977, Efficient Numerical Treatment of Periodic Systems with Application to Stability Problems, *International Journal for Numerical Methods in Engineering*, Vol.11, pp. 1117-1136.
- Hague, I., and Lieh, J., 1988, Parametric Excitation of Passenger and Freight Vehicles, AMD (Symposia Series) (American Society of Mechanical Engineers, Applied Mechanics Division), Vol. 96, Published by ASME, New York, NY, USA, pp. 69-75.

- He Yanzong, 1992, Analysis on the Stability of a Flexible Rotor under the Excitation of Periodic Parameter, *Proceedings of the Third National Conference on Rotor Dynamics*, Qingdao, Shandong Province, China, pp. 60-67, (in Chinese).
- Hou Zhichao, 1995, Numerical Methods for Dynamic Analysis of Large Scale Structures, *Ph.D. dissertation*, Tsinghua University, Beijing, (in Chinese).
- Hsu C.S., 1963, On the Parametric Excitation of a Dynamic System Having Multiple Degrees of Freedom, *Journal of Applied Mechanics*, Vol.31, No.3, pp. 515-522.
- Kumar, K., and Tuckerman, L.S., 1994, Parametric Instability of the Interface between Two Fluids, *Journal of Fluid Mechanics*, Vol. 279, pp. 49-68.
- Natsiava, S., 1995, On the Dynamics of Rings Rotating with Variable Spin Speed, *Nonlinear Dynamics*, Vol. 7, Iss.3, pp. 345-363.
- Nayfeh, A.H., and Mook D.T., 1979, *Nonlinear Oscillations*, John Wiley & Sons, New York.
- Nayfeh, A.H., 1987, Parametric Excitation of Two Internally Resonant Oscillators, *Journal of Sound and Vibration*, Vol. 119, No.1, pp. 95-109.
- Neal, H.L., and Nayfeh, A.H., 1990, Response of a Single Degree of Freedom System to a Non-stationary Principal Parametric Excitation, *International Journal of Non-Linear Mechanics*, Vol. 25, No. 2-3, pp. 275-284.
- Plaut, R.H., 1990, Parametric Excitation of an Inextensible Air-Inflated Cylindrical Membrane, *International Journal of Non-Linear Mechanics*, Vol. 25, No. 2-3, pp. 253-262.
- Plaut, R.H., Gentry, J.J., and Mook, D.T., 1990, Non-Linear Oscillations under multifrequency Parametric Excitation, *International Journal of Non-Linear Mechanics*, Vol. 25, No. 2-3, pp. 187-198.
- Plaut, R.H., and Limam, W., 1991, Oscillations of Weakly Non-Linear Self-Excited Systems under Multi-Frequency Parametric Excitation, *Journal of Sound and Vibration*, Vol. 144, No.2-3, pp. 197-214.
- Sankaranarayanan, H.K., Streit, D.A., and Kim, H.Y., 1994, Parametric Excitation of Robotic Manipulators, *Journal of Mechanical Design, Transactions of the ASME*, Vol. 116, No.2, pp. 467-473.
- Shen, I.Y., and Mote, C.D.Jr., 1992, Parametric Excitation under Multiple Excitation Parameters: Asymmetric Plates under a Rotating Spring, *International Journal of Solids and Structures*, Vol. 29, No. 8, pp. 1019-1032.
- Sorokin, S.V., 1992, Finite-Difference Version of Analysis of Parametric Vibration of Elastic Systems, *Mechanics and Solids*, Vol. 27, Iss. 6, pp. 34-37.
- Tanaka, T., and Sato, C., 1989, Stability Domain of the Second-Order Discrete Oscillatory System with Parametric Excitation, *Electronic and Communications in Japan, Part III: Fundamental Electronic Science*, Vol. 72, No. 2, pp. 109-116.
- Wang, S.R., and Zhang, T.X., 1988, Parametric Excitation of The Torsional Vibration of Crank Shafts of Diesel Engines with the Effect of Variable Inertia Taken into Account, *Neiranji Xuebao*, Transaction of CSICE (Chinese Society for Internal Combustion Engines), Vol. 6, No.4, pp. 335-342.
- Yamamoto T., 1964, On the Unstable Vibrations of a Shaft Carrying an Unsymmetrical Rotor, *Journal of Applied Mechanics*, Vol.31, No.3, pp. 515-522.

Yuan, S., Tani, J., and Aso, K., 1990, Response of a Long Marine Pipe String under Parametric Excitation, *Flow-Structure Vibration and Sloshing - 1990 American Society of Mechanical Engineers, Pressure Vessels and Piping Division (Publication) PVP*, Published by ASME, New York, NY, USA, Vol. 191, pp. 119-125.

Zavodney, L. D., Nayfeh, A.H., 1989, Non-linear Response of a Slender Beam Carrying a Lumped Mass to a Principal Parametric Excitation: Theory and Experiment, *International Journal of Non-linear Mechanics*, Vol. 24, No.2, pp. 105-125.

Zheng Zhaochang, 1992, The Complex Theory for Linear Unconservative Unsymmetric System, *The Teaching Material on Modern Problem of Solid Mechanics*, edited by Huang Kezhi, et al. pp. 65-76, (in Chinese).

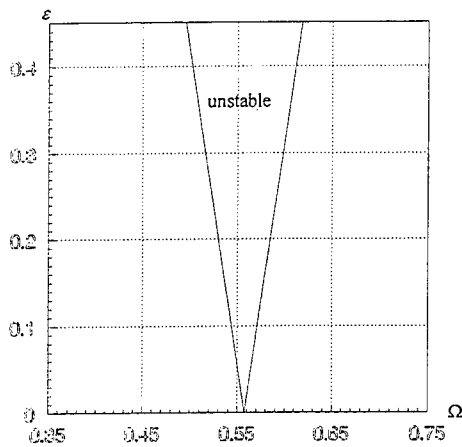


Fig.1 Unstable regions of Example 1

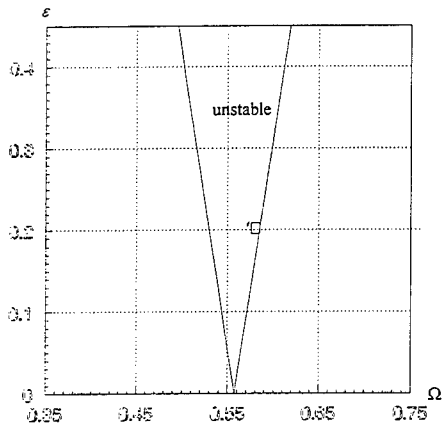


Fig. 2 Unstable regions of Example 2

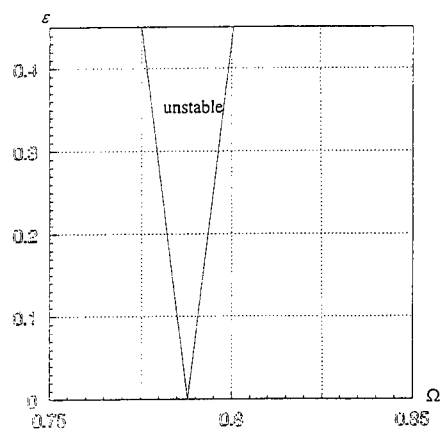


Fig. 3 Unstable regions of Example 3

FORCED VIBRATION ANALYSIS OF A BEAM WITH A NONLINEAR SUPPORT

*1 *2

Shigeru AOKI and Takeshi WATANABE

*1 Department of Mechanical Engineering
Tokyo Metropolitan College of Technology
1-10-40 Higashi-Ohi, Shinagawa-ku, Tokyo 140, Japan

*2 Faculty of Education
Yamanashi University
4-4-37 Takeda, Kofu-City 400, Japan

ABSTRACT

This paper deals with steady-state response of a continuous system with a nonlinear support having hysteresis damping characteristics. Considering the energy loss for hysteresis of spring constant of support, an analytical method of approximate solution for the nonlinear response of the beam with quadrilateral hysteresis loop characteristics is presented. Some numerical results of the approximate solution for the response of the system and the mode shapes are shown. The objectives of this paper are to determine the approximate steady-state solution of the continuous system with nonlinear support under harmonic excitation and to illustrate the numerical results of the approximate solution.

INTRODUCTION

Many mechanical equipment-piping systems in industrial facilities have many continuous elements with nonlinear supports[1]-[4]. There are nonlinear characteristics in these systems, such as hysteresis characteristics, clearance and friction. Those nonlinear characteristics affect the response of continuous systems[5],[6]. The steady forced response of a continuous system with a nonlinear support is of great importance for several engineering applications. There have been many papers on this problem in which the system has usually been considered as a single- or a multiple-degree-of-freedom system[7],[8] rather than as a continuous system, since it is difficult to find an analytical solution of the equation of motion for given nonlinear boundary conditions. In order to analyze the response of a nonlinear continuous system, however, it is necessary to consider the system as a continuous system. Moreover, in the analysis of such systems, the support has been modelled as rigid body or linear spring[9],[10]. In the actual phenomena, energy is dissipated at the supports and it is appropriate to use hysteresis damping rather than linear damping[11]. Modelling of energy loss at a support can be done

by assuming hysteresis loop characteristics in the relation between restoring force and penetration of the support.

In this paper, an elastic beam with one end simply supported and the other end supported by a piecewise-linear spring with hysteresis damping, considering the energy loss at support, is used as a model of a continuous system. An analytical method of approximate solution for the response of the beam with nonlinear support is presented. Some numerical results, such as the resonance curves and the mode shapes are shown.

ANALYTICAL METHOD

A simplified dynamical model of a continuous system with a nonlinear support is shown in Fig.1. Namely, this model consists of a beam with one end simply supported, and the other end having supports with quadrilateral hysteresis loop characteristics as shown in Fig.2.

Let ρ be the mass density, A the cross-sectional area, and EI the modulus of flexural rigidity. The equation of motion for transverse free vibration of a beam can be given as follows:

$$\frac{\partial^2 y}{\partial t^2} + \frac{EI}{\rho A} \frac{\partial^4 y}{\partial x^4} = 0 \quad (1)$$

The beam is subjected to a harmonic excitation of amplitude y_0 and frequency ω . The relations between y and z as shown in Fig.1 are given by

$$y = z + y_0 \cos \omega t \quad (2)$$

Hence we have

$$\frac{\partial^2 z}{\partial t^2} + \frac{EI}{\rho A} \frac{\partial^4 z}{\partial x^4} = y_0 \omega^2 \cos \omega t \quad (3)$$

Assuming the solution for Eq.(1) as

$$y = \sum_{n=1}^{\infty} X_n(x) \cos n \omega t \quad (4)$$

A formal solution of Eq.(3) can be expressed as follows:

$$z = -y_0 \cos \omega t + \sum_{n=1}^{\infty} (A_n \cosh \lambda_n x + B_n \sinh \lambda_n x + C_n \cos \lambda_n x + D_n \sin \lambda_n x) \cos n \omega t \quad (5)$$

where A_n , B_n , C_n , D_n are constants to be determined in each particular case from the

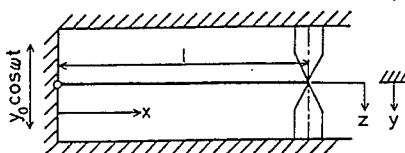


Fig.1 Analytical model of nonlinear continuous system

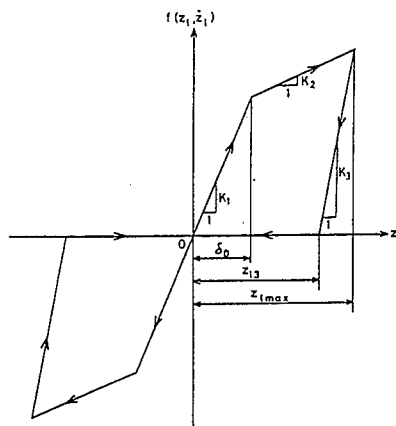


Fig.2 Hysteresis loop characteristics of restoring force of supports

boundary conditions of the beam, where

$$\lambda_n^4 l^4 = Z_1^4 n^2 \Omega_1^2, \quad \Omega_1 = \omega / \omega_1 \quad (6)$$

and

$$\omega_1 = \frac{Z_1^2}{l^2} \sqrt{\frac{EI}{\rho A}}, \quad Z_1 = 3.927 \quad (7)$$

The boundary conditions for this case are as follows:

$$1) x=0, z=0 \quad (8)$$

$$2) x=0, \frac{d^2 z}{dx^2} = 0 \quad (9)$$

$$3) x=l, \frac{d^2 z}{dx^2} = 0 \quad (10)$$

$$4) x=l, EI \frac{d^3 z}{dx^3} = f(z_l, \dot{z}_l) \quad (11)$$

where z_l is the transverse displacement at the end ($x=l$) and the nonlinear restoring force of supports $f(z_l, \dot{z}_l)$ is defined by the following piecewise-linear characteristics as shown in Fig.2:

$$f(z_l, \dot{z}_l) = \begin{cases} =K_1 z_l & ; 0 \leq z_l \leq \delta_0, \dot{z}_l > 0 & (I) \\ =K_1 \delta_0 + K_2 (z_l - \delta_0) & ; \delta_0 \leq z_l \leq z_{l \max}, \dot{z}_l \geq 0 & (II) \\ =K_3 (z_l - z_{l3}) & ; z_{l3} \leq z_l \leq z_{l \max}, \dot{z}_l \leq 0 & (III) \\ =0 & ; 0 \leq z_l \leq z_{l3}, \dot{z}_l < 0 & (IV) \\ =K_1 z_l & ; -\delta_0 \leq z_l \leq 0, \dot{z}_l < 0 & (V) \\ =-K_1 \delta_0 + K_2 (z_l + \delta_0) & ; -z_{l \max} \leq z_l \leq -\delta_0, \dot{z}_l \leq 0 & (VI) \\ =K_3 (z_l + z_{l3}) & ; -z_{l \max} \leq z_l \leq -z_{l3}, \dot{z}_l \geq 0 & (VII) \\ =0 & ; -z_{l3} \leq z_l \leq 0, \dot{z}_l > 0 & (VIII) \end{cases} \quad (12)$$

where $z_{l \max}$ denotes the maximum displacement at the end ($x=l$) and K_1 , K_2 and K_3 are the spring constants of nonlinear support as shown in Fig.2 and δ_0 is the maximum deformation by the spring constant K_1 . And then, z_{l3} is written as follows:

$$z_{l3} = (1 - \frac{K_2}{K_3}) z_{l \max} - (\frac{K_1}{K_3} - \frac{K_2}{K_3}) \delta_0 \quad (13)$$

In this paper, the steady-state vibration is dealt with. Once the vibration of the beam becomes steady and periodic, the nonlinear restoring force of supports $f(z_l, \dot{z}_l)$ becomes also periodic and can be represented as a periodic function $g(\theta)$ of θ with the period 2π . And θ is defined by the following equation:

$$\theta = \omega t - \alpha \quad (14)$$

where α is the phase lag angle.

This periodic function $g(\theta)$ must satisfy the conditions of the given characteristics of the nonlinear restoring force equation (12), which is, in this case, to be written as the following equations:

$$f(z, \dot{z}) \begin{cases} \equiv g(\theta) = K_1 z & ; -(\theta_1 + \theta_2) \leq \theta \leq -\theta_2 & (I) \\ \equiv g(\theta) = K_1 \delta_0 + K_2 (z - \delta_0) & ; -\theta_2 \leq \theta \leq 0 & (II) \\ \equiv g(\theta) = K_3 (z - z_{\lambda 3}) & ; 0 \leq \theta \leq \theta_3 & (III) \\ \equiv g(\theta) = 0 & ; \theta_3 \leq \theta \leq \pi - (\theta_1 + \theta_2) & (IV) \\ \equiv g(\theta) = K_1 z & ; \pi - (\theta_1 + \theta_2) \leq \theta \leq \pi - \theta_2 & (V) \\ \equiv g(\theta) = -K_1 \delta_0 + K_2 (z + \delta_0) & ; \pi - \theta_2 \leq \theta \leq \pi & (VI) \\ \equiv g(\theta) = K_3 (z + z_{\lambda 3}) & ; \pi \leq \theta \leq \pi + \theta_3 & (VII) \\ \equiv g(\theta) = 0 & ; \pi + \theta_3 \leq \theta \leq 2\pi - (\theta_1 + \theta_2) & (VIII) \end{cases} \quad (15)$$

where θ_1 , θ_2 and θ_3 denote the range of the phase angle θ as shown in Fig.3. In the foregoing, one period 2π of the resulting vibration is divided into eight intervals. During the first, the second and the third intervals and fifth, sixth and seventh intervals of length θ_1 , θ_2 and θ_3 , respectively, the beam end moves with nonlinear restoring force of supports. And during the fourth and eighth intervals of length $\pi - (\theta_1 + \theta_2 + \theta_3)$, the beam end moves without nonlinear restoring force.

Employing the boundary conditions Eqs.(8) and (9), Eq.(5) is reduced as:
for Eq.(8),

$$-y_0 \cos(\theta + \alpha) + \sum_{n=1}^{\infty} (A_n + C_n) \cos n(\theta + \alpha) = 0 \quad (16)$$

and for Eq.(9),

$$A_n - C_n = 0 \quad (17)$$

From Eqs.(16) and (17),

$$C_1 = A_1 = y_0/2 \quad (n=1), \quad C_n = A_n = 0 \quad (n=2, 3, 4, \dots) \quad (18)$$

Substituting Eq.(18) into Eq.(5),

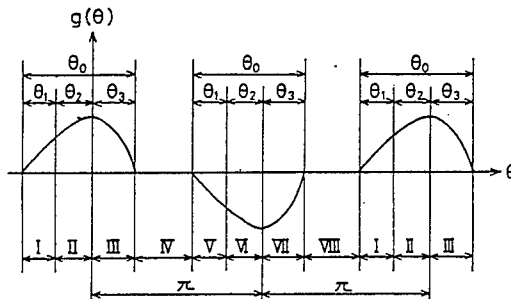


Fig.3 Waveforms of nonlinear restoring force $g(\theta)$

$$z = y_0 \left(\frac{1}{2} \cosh \lambda_1 x + \frac{1}{2} \cos \lambda_1 x - 1 \right) \cos(\theta + \alpha) + \sum_{n=1}^{\infty} (B_n \sinh \lambda_n x + D_n \sin \lambda_n x) \cos n(\theta + \alpha) \quad (19)$$

From Eq.(19) and the boundary condition Eq.(10),

$$B_1 \sinh \lambda_1 l - D_1 \sin \lambda_1 l = y_0 \left(\frac{1}{2} \cosh \lambda_1 l - \frac{1}{2} \cos \lambda_1 l \right) \quad (n=1) \quad (20)$$

$$B_n \sinh \lambda_n l - D_n \sin \lambda_n l = 0 \quad (n=2, 3, 4, \dots) \quad (21)$$

Introducing a Fourier series expansion for the periodic function $g(\theta)$ as

$$g(\theta) = \sum_{n=1, 3, \dots}^{\infty} (a_n \cos n\theta + b_n \sin n\theta) \quad (22)$$

Using Eqs.(11) and (19),

$$\frac{d^2 z}{dx^2} = y_0 \lambda_1^3 \left(\frac{1}{2} \sinh \lambda_1 x + \frac{1}{2} \sin \lambda_1 x \right) \cos(\theta + \alpha) + \sum_{n=1}^{\infty} \lambda_n^3 (B_n \cosh \lambda_n x - D_n \cos \lambda_n x) \cos n(\theta + \alpha) \quad (23)$$

and

$$B_1 \cosh \lambda_1 l - D_1 \cos \lambda_1 l = \frac{a_1 \cos \theta + b_1 \sin \theta}{EI \lambda_1^3 \cos(\theta + \alpha)} - \frac{1}{2} y_0 (\sinh \lambda_1 l + \sin \lambda_1 l) \quad (n=1) \quad (24)$$

$$B_n \cosh \lambda_n l - D_n \cos \lambda_n l = \frac{a_n \cos n\theta + b_n \sin n\theta}{EI \lambda_n^3 \cos(\theta + \alpha)} \quad (n=3, 5, \dots) \quad (25)$$

From Eqs.(20), (21), (24) and (25), for $n=1$,

$$B_1 = \frac{a_1 \cos \theta + b_1 \sin \theta}{EI \lambda_1^3 \Delta_1 \cos(\theta + \alpha)} \sin \lambda_1 l - \frac{1}{2 \Delta_1} y_0 (1 + \sinh \lambda_1 l \sin \lambda_1 l - \cosh \lambda_1 l \cos \lambda_1 l) \quad (26)$$

$$D_1 = \frac{a_1 \cos \theta + b_1 \sin \theta}{EI \lambda_1^3 \Delta_1 \cos(\theta + \alpha)} \sinh \lambda_1 l - \frac{1}{2 \Delta_1} y_0 (\sinh \lambda_1 l \sin \lambda_1 l + \cosh \lambda_1 l \cos \lambda_1 l - 1) \quad (27)$$

And for $n=3, 5, \dots$,

$$B_n = \frac{a_n \cos n\theta + b_n \sin n\theta}{EI\lambda_n^3 \Delta_n \cos(\theta + \alpha)} \sin \lambda_n l \quad (28)$$

$$D_n = - \frac{a_n \cos n\theta + b_n \sin n\theta}{EI\lambda_n^3 \Delta_n \cos(\theta + \alpha)} \sinh \lambda_n l \quad (29)$$

where

$$\Delta_n = \cosh \lambda_n l \sin \lambda_n l - \sinh \lambda_n l \cos \lambda_n l \quad (30)$$

Then,

$$\begin{aligned} z = & y_0 N_x \cos(\theta + \alpha) \\ & + \sum_{n=1,3,\dots}^{\infty} \frac{1}{EI\lambda_n^3 \Delta_n} (\sin \lambda_n l \sinh \lambda_n x \\ & + \sinh \lambda_n l \sin \lambda_n x) (a_n \cos n\theta + b_n \sin n\theta) \end{aligned} \quad (31)$$

where

$$\begin{aligned} N_x = & \frac{[(\cosh \lambda_1 x + \cos \lambda_1 x - 2)(\cosh \lambda_1 l \sin \lambda_1 l - \sinh \lambda_1 l \cos \lambda_1 l) \\ & - (1 - \cosh \lambda_1 l \cos \lambda_1 l + \sinh \lambda_1 l \sin \lambda_1 l) \sinh \lambda_1 x \\ & - (\sinh \lambda_1 l \sin \lambda_1 l + \cosh \lambda_1 l \cos \lambda_1 l - 1) \sin \lambda_1 x]}{2 \cosh \lambda_1 l \sin \lambda_1 l - \sinh \lambda_1 l \cos \lambda_1 l} \end{aligned} \quad (32)$$

Displacement at the end ($x=l$), z_k is given as

$$z_k = y_0 N_k \cos(\theta + \alpha) + \sum_{n=1,3,\dots}^{\infty} \frac{M_n}{k} (a_n \cos n\theta + b_n \sin n\theta) \quad (33)$$

where

$$k = \frac{3EI}{l^3} \quad (34)$$

$$N_k = \frac{\sin \lambda_1 l (1 - \cosh \lambda_1 l) + \sinh \lambda_1 l (\cos \lambda_1 l - 1)}{\cosh \lambda_1 l \sin \lambda_1 l - \sinh \lambda_1 l \cos \lambda_1 l} \quad (35)$$

$$M_n = \frac{6\lambda_n l (\sinh \lambda_n l \sin \lambda_n l)}{Z_1^4 n^2 \Omega_1^2 (\cosh \lambda_n l \sin \lambda_n l - \sinh \lambda_n l \cos \lambda_n l)} \quad (n=1,3,5,\dots) \quad (36)$$

Meanwhile, the switching-over conditions from one to another of the eight intervals are expressed by

$$\theta = -(\theta_1 + \theta_2), \quad z_k = 0 \quad (\text{VIII} \rightarrow \text{I}) \quad (37)$$

$$\theta = -\theta_2, \quad z_k = \delta_0 \quad (\text{I} \rightarrow \text{II}) \quad (38)$$

$$\theta = 0, \quad \dot{z}_k = 0, \quad z_k = z_{k \max} \quad (\text{II} \rightarrow \text{III}) \quad (39)$$

$$\theta = \theta_3, \quad z_k = z_{k3} \quad (\text{III} \rightarrow \text{IV}) \quad (40)$$

$$\theta = \pi - (\theta_1 + \theta_2), \quad z_k = 0 \quad (\text{IV} \rightarrow \text{V}) \quad (41)$$

$$\theta = \pi - \theta_2, \quad z_k = -\delta_0 \quad (\text{V} \rightarrow \text{VI}) \quad (42)$$

$$\theta = \pi, \quad \dot{z}_k = 0, \quad z_k = -z_{k \max} \quad (\text{VI} \rightarrow \text{VII}) \quad (43)$$

$$\theta = \pi + \theta_3, \quad z_k = -z_{k3} \quad (\text{VII} \rightarrow \text{VIII}) \quad (44)$$

Using Eqs.(38) and (39), the amplitude of the cosine part of the fundamental harmonic, Γ is given as

$$\Gamma = [\delta_0 - \sum_{n=3,5,\dots} \frac{M_n}{k} \{a_n \cos n\theta_2 - b_n (\sin n\theta_2 - n \sin \theta_2)\}] \frac{1}{\cos \theta_2} \quad (45)$$

From Eq.(33),

$$\sin \alpha = \frac{1}{y_0 N_k} \sum_{n=1,3,\dots} \frac{n b_n}{k} M_n \quad (46)$$

$$\cos \alpha = \frac{1}{y_0 N_k} (\Gamma - \frac{M_1}{k} a_1) \quad (47)$$

And the nondimensional Fourier coefficients are defined as follows:

$$x_n = \frac{a_n}{k\Gamma}, \quad y_n = \frac{b_n}{k\Gamma} \quad (n=1,3,5,\dots) \quad (48)$$

Then,

$$z_k = \Gamma [\cos \theta + \sum_{n=3,5,\dots} M_n x_n \cos n\theta + \sum_{n=3,5,\dots} M_n y_n (\sin n\theta - n \sin \theta)] \quad (49)$$

From Eq.(46),

$$y_0 N_k \sin \alpha = \Gamma \sum_{n=1,3,\dots} n M_n y_n \quad (50)$$

From Eq.(47),

$$y_0 N_k \cos \alpha = \Gamma (1 - M_1 x_1) \quad (51)$$

Thus, the phase lag angle α is expressed as:

$$\alpha = \tan^{-1} \left(\frac{\sum_{n=1,3,\dots} n M_n y_n}{1 - M_1 x_1} \right) \quad (52)$$

From Eqs.(45),(48),(49) and (37)-(44), the amplitude of the fundamntal term of cosine component at the end ($x=l$), Γ and that of sinusoidal excitaiton y_0 are determined as

$$\frac{\Gamma}{\delta_0} = \frac{y_0 N_k}{\delta_0 \sqrt{(1 - M_1 x_1)^2 + (\sum_{n=1,3,\dots} n M_n y_n)^2}} \quad (53)$$

$$\frac{y_0}{\delta_0} = \frac{\sqrt{(1 - M_1 x_1)^2 + (\sum_{n=1,3,\dots} n M_n y_n)^2}}{N_k [\cos \theta_2 + \sum_{n=3,5,\dots} M_n \{x_n \cos n\theta_2 - y_n (\sin n\theta_2 - n \sin \theta_2)\}]} \quad (54)$$

Displacement at x from simply supported end is given as:

$$Z_x = \Gamma \{ N_x \sqrt{(1 - M_1 x_1)^2 + \left(\sum_{n=1,3,\dots}^{\infty} n M_n y_n \right)^2} \cos(\theta + \alpha) / N_x + \sum_{n=1,3,\dots}^{\infty} \frac{3\lambda_n \ell}{Z_1^4 n^2 \Omega_1^2} \frac{I_x}{\Delta_n} (x_n \cos n\theta + y_n \sin n\theta) \} \quad (55)$$

where

$$I_x = \sin \lambda_n \ell \sinh \lambda_n x + \sinh \lambda_n \ell \sin \lambda_n x \quad (56)$$

From Eqs. (37) and (40),

$$\begin{aligned} \cos(\theta_1 + \theta_2) &= \sum_{n=3,5,\dots}^{\infty} M_n y_n \{ \sin n(\theta_1 + \theta_2) - n \sin(\theta_1 + \theta_2) \} \\ &\quad - \sum_{n=3,5,\dots}^{\infty} M_n x_n \cos n(\theta_1 + \theta_2) \end{aligned} \quad (57)$$

$$\begin{aligned} 1 - \cos \theta_3 &+ \sum_{n=3,5,\dots}^{\infty} M_n x_n (1 - \cos n\theta_3) - \sum_{n=3,5,\dots}^{\infty} M_n y_n (\sin n\theta_3 - n \sin \theta_3) \\ &= \frac{K_2}{K_3} \{ 1 - \cos \theta_2 + \sum_{n=3,5,\dots}^{\infty} M_n x_n (1 - \cos n\theta_2) \\ &\quad + \sum_{n=3,5,\dots}^{\infty} M_n y_n (\sin n\theta_2 - n \sin \theta_2) \} \\ &+ \frac{K_1}{K_3} \{ \cos \theta_2 + \sum_{n=3,5,\dots}^{\infty} M_n x_n \cos n\theta_2 - \sum_{n=3,5,\dots}^{\infty} M_n y_n (\sin n\theta_2 - n \sin \theta_2) \} \end{aligned} \quad (58)$$

Since $g(\theta)$ given by Eq. (15) is symmetrical characteristics, using Eqs. (37), (40) and (49), nondimensional $g(\theta)$ is expressed as follows:

$$\begin{aligned} \frac{g(\theta)}{k\Gamma} &= \sum_{n=1,3,\dots}^{\infty} (x_n \cos n\theta + y_n \sin n\theta) \\ &= \frac{K_1}{k} \left[\cos \theta + \sum_{n=3,5,\dots}^{\infty} M_n x_n \cos n\theta + \sum_{n=3,5,\dots}^{\infty} M_n y_n (\sin n\theta - n \sin \theta) \right] \quad ; -(\theta_1 + \theta_2) \leq \theta \leq -\theta_2 \\ \frac{g(\theta)}{k\Gamma} &= \sum_{n=1,3,\dots}^{\infty} (x_n \cos n\theta + y_n \sin n\theta) \\ &= \frac{K_1}{k} \left[\cos \theta_2 + \sum_{n=3,5,\dots}^{\infty} M_n x_n \cos n\theta_2 - \sum_{n=3,5,\dots}^{\infty} M_n y_n (\sin n\theta_2 - n \sin \theta_2) \right. \\ &\quad + \frac{K_2}{k} \left[\cos \theta - \cos \theta_2 + \sum_{n=3,5,\dots}^{\infty} M_n x_n (\cos n\theta - \cos n\theta_2) \right. \\ &\quad \left. \left. + \sum_{n=3,5,\dots}^{\infty} M_n y_n \{ \sin n\theta + \sin n\theta_2 \} \right] \right] \end{aligned} \quad (59)$$

$$-n(\sin\theta + \sin\theta_2)) \quad ; -\theta_2 \leq \theta \leq 0$$

$$\begin{aligned} \frac{g(\theta)}{k\Gamma} &= \sum_{n=1,3,\dots}^{\infty} (x_n \cos n\theta + y_n \sin n\theta) \\ &= \frac{K_3}{k} [\cos\theta - \cos\theta_3 + \sum_{n=3,5,\dots}^{\infty} M_n x_n (\cos n\theta - \cos n\theta_3) \\ &\quad + \sum_{n=3,5,\dots}^{\infty} M_n y_n \{\sin n\theta - \sin n\theta_3 \\ &\quad - n(\sin\theta - \sin\theta_3)\}] \quad ; 0 \leq \theta \leq \theta_3 \end{aligned}$$

$$\frac{g(\theta)}{k\Gamma} = \sum_{n=1,3,\dots}^{\infty} (x_n \cos n\theta + y_n \sin n\theta) = 0 \quad ; \theta_3 \leq \theta \leq \pi - (\theta_1 + \theta_2)$$

$g(\theta)$ given by Eq.(22) can be approximately written as:

$$g(\theta) = a_1 \cos\theta + b_1 \sin\theta \quad (60)$$

Since Eq.(49) is expressed as:

$$z_k = \Gamma \cos\theta \quad (61)$$

The phase lag angle, the amplitude at the end ($x=l$) and that of sinusoidal excitation which are given as Eqs.(52), (53) and (54) are determined as:

$$\alpha = \tan^{-1} \left(\frac{M_1 y_1}{1 - M_1 x_1} \right) \quad (62)$$

$$\frac{\Gamma}{\delta_0} = \frac{y_0}{\delta_0} \frac{N_k}{\sqrt{(1 - M_1 x_1)^2 + (M_1 y_1)^2}} \quad (63)$$

$$\frac{y_0}{\delta_0} = \frac{\sqrt{(1 - M_1 x_1)^2 + (M_1 y_1)^2}}{N_k \cos\theta_2} \quad (64)$$

where

$$M_1 = \frac{6\lambda_1 l \sin\lambda_1 l \sinh\lambda_1 l}{Z_1^4 \Omega_1^2 (\cosh\lambda_1 l \sin\lambda_1 l - \sinh\lambda_1 l \cos\lambda_1 l)} \quad (65)$$

From Eqs. (63) and (64),

$$\frac{\Gamma}{\delta_0} = \frac{1}{\cos\theta_2} \quad (66)$$

Substituting $n=1$ into Eq.(59) and applying a technique similar to that for determining Fourier coefficients, namely, multiplying both sides of Eq.(59) by $\cos\theta$ and $\sin\theta$ and integrating through the whole period of 2π , the nondimensional coefficients x_1 and y_1 are obtained as follows:

$$x_1 = -\frac{2}{\pi} \left[\frac{K_1}{k} \left\{ \frac{\theta_1 + \sin \theta_2 \cos \theta_2}{2} + \frac{\sin(\theta_1 + \theta_2) \cos(\theta_1 + \theta_2)}{2} \right\} + \frac{K_2}{k} \left(\frac{\theta_2 - \sin \theta_2 \cos \theta_2}{2} \right) + \frac{K_3}{k} \left(\frac{\theta_3 - \sin \theta_3 \cos \theta_3}{2} \right) \right] \quad (67)$$

$$y_1 = -\frac{2}{\pi} \left[\frac{K_1}{k} \left\{ \frac{\cos 2(\theta_1 + \theta_2)}{4} + \frac{1}{4} \frac{\cos^2 \theta_2}{2} - \cos \theta_2 \right\} + \frac{K_2}{k} \left(\frac{1}{2} \sin^2 \theta_2 - 1 + \cos \theta_2 \right) - \frac{K_3}{k} \left(\frac{1}{2} \sin^2 \theta_3 - 1 + \cos \theta_3 \right) \right] \quad (68)$$

From Eqs. (57) and (58),

$$\theta_1 + \theta_2 = \frac{\pi}{2}, \quad \cos(\theta_1 + \theta_2) = 0 \quad (69)$$

$$\cos \theta_3 = 1 - \frac{K_2}{K_3} - \left(\frac{K_1}{K_3} - \frac{K_2}{K_3} \right) \cos \theta_2 \quad (70)$$

From Eqs. (67) and (68),

$$x_1 = -\frac{2}{\pi} \left[\frac{K_1}{k} \left(\frac{\theta_1 + \sin \theta_2 \cos \theta_2}{2} \right) + \frac{K_2}{k} \left(\frac{\theta_2 - \sin \theta_2 \cos \theta_2}{2} \right) + \frac{K_3}{k} \left(\frac{\theta_3 - \sin \theta_3 \cos \theta_3}{2} \right) \right] \quad (71)$$

$$y_1 = -\frac{2}{\pi} \left[\frac{K_1}{k} \left(\frac{1}{2} \cos^2 \theta_2 - \cos \theta_2 \right) + \frac{K_2}{k} \left(\frac{1}{2} \sin^2 \theta_2 - 1 + \cos \theta_2 \right) - \frac{K_3}{k} \left(\frac{1}{2} \sin^2 \theta_3 - 1 + \cos \theta_3 \right) \right] \quad (72)$$

Fixing θ_2 , θ_1 and θ_3 are obtained by Eqs. (69) and (70). Then, y_0/δ_0 is obtained by Eq. (64) using x_1 and y_1 given by Eqs. (71) and (72). Γ/δ_0 is determined by Eq. (66). Thus, the resonance curve is obtained using Γ/δ_0 for fixed y_0/δ_0 .

The mode shape Z_x is obtained using Eq. (55). Substituting $n=1$ and $\theta=0$ into Eq. (55),

$$Z_x = \Gamma \left\{ \frac{N_x \sqrt{(1 - M_1 x_1)^2 + (M_1 y_1)^2}}{N_0} \cos \alpha + \frac{3\lambda_1 l}{Z_1^4 \Omega_1^2} \frac{I_x}{\Delta_1} x_1 \right\} \quad (73)$$

From Eq. (6),

$$\lambda_1^4 x^4 = Z_1^4 \Omega_1^2 x^4 / l^4 \quad (74)$$

Using Eqs. (51) and (63), Eq. (73) is written as:

$$Z_x = \Gamma \left\{ \frac{N_x}{N_0} (1 - M_1 x_1) + \frac{3\lambda_1 l}{Z_1^4 \Omega_1^2} \frac{I_x}{\Delta_1} x_1 \right\} \quad (75)$$

When $\Gamma/\delta_0 < 1$, intervals (II) and (VI) do not exist, that is, $\theta_2 = 0$, $K_2 = 0$. From Eqs. (69) and (70),

$$\theta_1 = \frac{\pi}{2}, \quad \cos \theta_1 = 0 \quad (76)$$

$$\cos \theta_3 = 1 - \frac{K_1}{K_3} \quad (77)$$

From Eqs. (71) and (72),

$$x_1 = - \left\{ \frac{2}{\pi} \frac{K_1}{k} \frac{\pi}{4} + \frac{K_3}{k} \left(\frac{\theta_3 - \sin \theta_3 \cos \theta_3}{2} \right) \right\} \quad (78)$$

$$y_1 = - \left\{ - \frac{2}{\pi} \frac{1}{2} \frac{K_1}{k} - \frac{K_3}{k} \frac{1}{2} (-\sin^2 \theta_3 - 1 + \cos \theta_3) \right\} \quad (79)$$

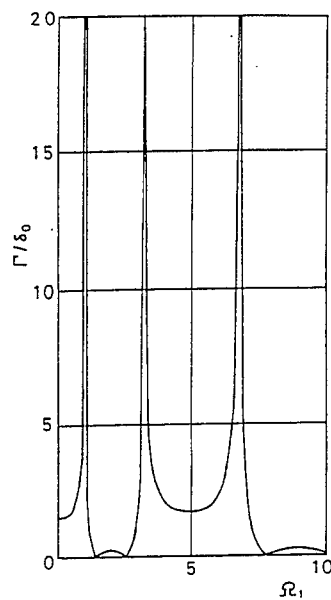
Hence, θ_1 and θ_3 are determined by Eqs. (76) and (77). x_1 and y_1 are obtained by Eqs. (78) and (79). Substituting these values into Eq. (63), Γ/δ_0 is obtained.

NUMERICAL EXAMPLES

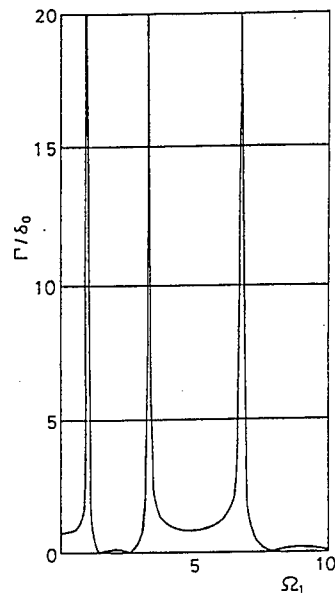
Figures 4, 5, 6 and 7 show resonance curves with the amplitude Γ/δ_0 of the beam at the end ($x=l$) versus the frequency ratio Ω_1 obtained by the method of approximate solution utilizing a digital computer in which several exciting ratios y_0/δ_0 are taken to be constant. Figures 4(a) and 4(b) show resonance curves for linear system. Figures 5(a) and 5(b) show resonance curves for $y_0/\delta_0 = 1.0$ and 0.5 of a system with low ratios of nonlinear parameters $K_1/k = 0.4$, $K_2/k = 0.2$ and $K_3/k = 1.0$, respectively. Figures 6(a) and 6(b) show resonance curves for $y_0/\delta_0 = 1.0$ and 0.5 of a system with nonlinear parameters $K_1/k = 4$, $K_2/k = 2$ and $K_3/k = 10$, respectively. Figures 7(a) and 7(b) show resonance curves for $y_0/\delta_0 = 1.0$ and 0.5 of a system with high ratios of nonlinear parameters $K_1/k = 40$, $K_2/k = 20$ and $K_3/k = 100$, respectively. Table 1 shows resonant frequencies.

From these figures and table, there is a peak in the region $\Omega_1 < 1$ for the response of nonlinear system. This peak is not obtained for linear system. It may be higher-harmonic resonance that occurs in nonlinear system. Γ/δ_0 decreases as y_0/δ_0 decreases. Γ/δ_0 at the peaks decreases as nonlinear parameters K_1/k , K_2/k and K_3/k become high ratios except for peaks at $\Omega_1 < 1$. Resonant frequencies become higher as nonlinear parameters become high ratios.

Figures 8(a) and 8(b) show the mode shapes for Ω_1 with marks ● on Fig. 6(a) and Fig. 7(a), respectively. These figures show from the first to the fourth vibrational mode. In the frequency ranges near the resonant frequencies, the

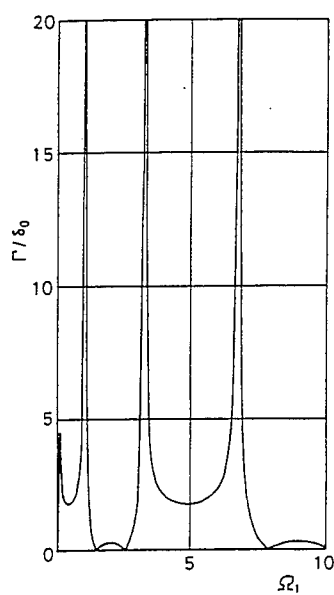


(a) $y_0/\delta_0=1.0$

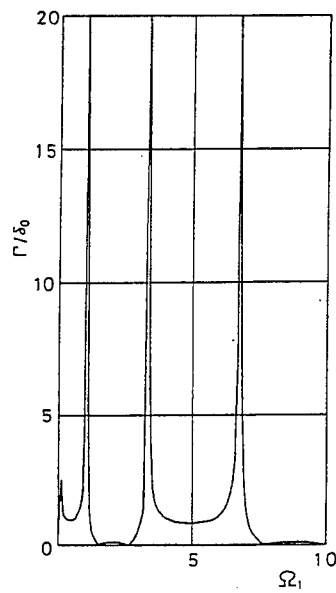


(b) $y_0/\delta_0=0.5$

Fig.4 Resonsnce curve of linear continuous system



(a) $y_0/\delta_0=1.0$



(b) $y_0/\delta_0=0.5$

Fig.5 Resonsnce curve of nonlinear continuous system
($K_1/k=0.4$, $K_2/k=0.2$ and $K_3/k=1.0$)

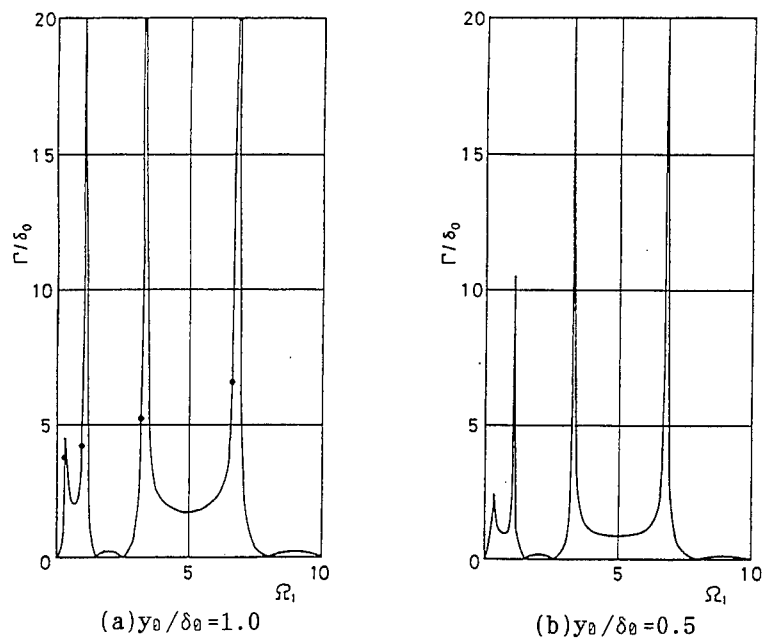


Fig.6 Resonance curve of nonlinear continuous system
($K_1/k=4$, $K_2/k=2$ and $K_3/k=10$)

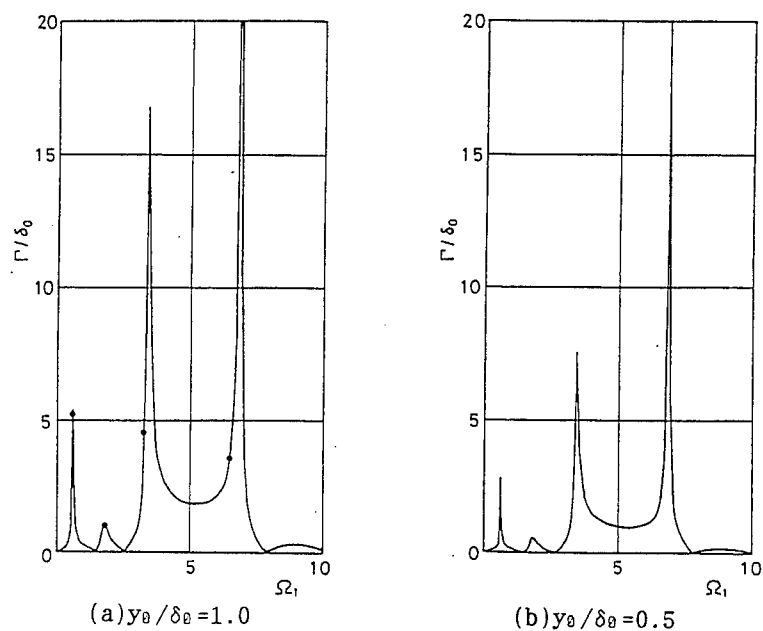
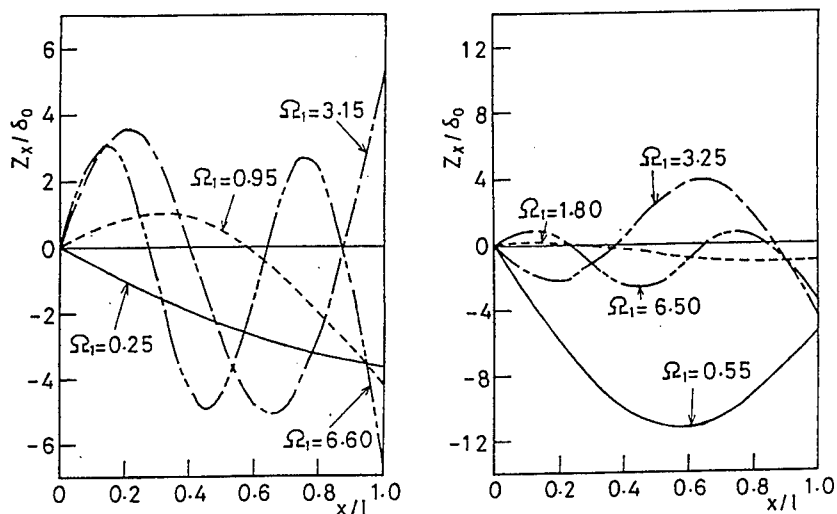


Fig.7 Resonance curve of nonlinear continuous system
($K_1/k=40$, $K_2/k=20$ and $K_3/k=100$)

Table 1 Resonat frequency ($\omega/\omega_1 = \Omega_1$)

K_1/k	K_2/k	K_3/k	y_0/e_0				
Linear				-	1.00	3.24	6.76
0.4	0.2	1.0	1.0	0.09	1.00	3.24	6.76
			0.5	0.10	1.00	3.24	6.76
4	2	10	1.0	0.27	1.04	3.25	6.77
			0.5	0.29	1.04	3.25	6.77
40	20	100	1.0	0.55	1.76	3.38	6.82
			0.5	0.56	1.77	3.40	6.82



(a) $K_1/k=4$, $K_2/k=2$, $K_3/k=10$ (b) $K_1/k=40$, $K_2/k=20$, $K_3/k=100$

Fig.8 Mode shapes of nonlinear continuous system($y_0/\delta_0=1.0$)

vibrational modes for each resonant frequency predominate. When nonlinear parameters are high ratios, displacement at the end of nonlinear support is suppressed.

CONCLUSIONS

An approximate solution for the steady-state response of the beam with nonlinear support having hysteresis damping characteristics has been proposed. A beam in which one end is simply supported and the other end is a nonlinear support, is dealt with. Resonance curves are obtained for several exciting ratios y_0/δ_0 of the systems with low and high ratios of nonlinear parameters K_1/k , K_2/k and K_3/k by applying the approximate solution. The results are summarized as follows.

1) There is a peak in the region $\Omega_1 < 1$ for the nonlinear case. This peak is not obtained for a linear system.

- 2) The amplitude of the beam end for steady-state response decreases as the amplitude of sinusoidal excitation decreases.
- 3) The peaks of the resonance curves decrease as the nonlinear parameters K_1/k , K_2/k and K_3/k become high ratios except for peaks at $\Omega_1 < 1$.
- 4) Resonant frequencies become higher as the nonlinear parameters become high ratios.
- 5) In the frequency ranges near the resonant frequencies, the vibrational modes for each resonant frequency predominate. When nonlinear parameters are high ratios, the displacement at the end of nonlinear support is suppressed.

REFERENCES

1. Watanabe, T., Forced vibration of continuous system with nonlinear boundary conditions. Trans. ASME Journal of Mechanical Design, 1978, **100**, pp.487-491.
2. Aoki, S. and Watanabe, T., Forced vibration of continuous system with hysteresis loop characteristics (System with quadrilateral hysteresis loop characteristics). Proc. of Asia-Pacific Vibration Conference '95, 1995, **1**, pp.252-7.
3. Shaw, S.W., Forced vibrations of a beam with one-sided amplitude constraint. Journal of Sound and Vibration, 1985, **99**-(2), pp.199-212.
4. Moon, F.C. and Shaw, S.W., Chaotic vibrations of a beam with nonlinear boundary conditions. International Journal of Non-Linear Mechanics, 1983, **18**-(6), pp.465-77.
5. Igusa, T. and Sinha, R., Response analysis of secondary systems with nonlinear supports. Trans. ASME Journal of Pressure Vessel Technology, 1991, **113**-(4), pp.524-31.
6. Goldman, P. and Muszynska, A., Dynamic effects in mechanical structures with gaps and impacting: Order and chaos. Trans. ASME Journal of Vibration and Acoustics, 1994, **116**-(4), pp.541-7.
7. Aidanpaa, J.O. and Gupta, R.B., Periodic and chaotic behaviour of a threshold-limited two-degree-of-freedom system. Journal of Sound and Vibration, 1993, **165**-(2), pp.305-27.
8. Lau, S.L. and Zhang, W.-S., Nonlinear vibrations of piecewise-linear systems by incremental harmonic balance method. Trans. ASME Journal of Applied Mechanics, 1992, **59**-(1), pp.153-60.
9. Lin, S.Q. and Bapat, C.N., Extension of clearance and impact force estimation approaches to a beam-stop system. Journal of Sound and Vibration, 1993, **163**-(3), pp.199-212.
10. Lin, Y.-T. and Sun, T.C., Mode superposition of viscously damped nonlinear structural systems using an incremental algorithm. Trans. ASME Journal of vibration and Acoustics, 1993, **115**-(4), pp.397-402.
11. Watanabe, T. and Shibata, H., On nonlinear vibration of a beam - Response of a beam with a gap at one end - . Report of the Institute of Industrial Science, The University of Tokyo, 1991, **36**-1, pp.1-25.

FREE NONLINEAR VIBRATIONS OF AN AXIALLY MOVING BEAM

Francesco Pellicano(*) and Fabrizio Vestroni(**)

(*) Dip. Scienze dell'Ingegneria, Università di Modena, Modena, Italy

(**) Dip. di Ingegneria Strutturale e Geotecnica, Università di Roma "La Sapienza", Rome, Italy

ABSTRACT

In the present paper the dynamic behaviour of a beam subjected to an axial transport of mass is analyzed. The Galérkin method has been used to discretize the problem; a system of ordinary differential equations with linear gyroscopic part and cubic nonlinearities is obtained. The system is studied in the sub and supercritical speed range with emphasis on the global dynamics that exhibits special features after the first bifurcation. A test case on a physical beam is developed and numerical results are presented concerning: linear sub critical behaviour, static bifurcation analysis including linear stability, direct simulation of global postcritical dynamics.

INTRODUCTION

Axially moving continua represent a wide class of mechanical systems, such as: power transmission belts, high-speed magnetic tapes, etc. The problem has been extensively studied in the past. The first studies on the subject date back to the previous century. In the fifties a growth of interest was determined by the increasing use of oil pipelines [1]: theoretical and experimental aspects of the forced problem were considered in [2]. In 1969 Thurman and Mote [3] studied the free nonlinear oscillations of an axially moving string. In 1990 Wickert and Mote [4] studied free and forced linear oscillations of moving continua using an eigenfunction method developed by Meirovich [5] for discrete systems and D'Eulerio and Huges [6] for continuous systems. In particular in 1992 Wickert [7] presented a study on the nonlinear vibrations and bifurcations of axially moving beams. He examined the sub and supercritical speed range by a one degree of freedom model able to describe a local analysis involving weak nonlinear oscillations close to the stable equilibrium positions.

In the present paper the dynamic behaviour of an axially moving beam is dealt with by means of a high dimension discrete model obtained by a Galérkin procedure. The resulting finite dimensional dynamical system presents a linear part with a skew-symmetric damping matrix called "gyroscopic matrix". The spectral analysis of this linear system provides

imaginary eigenvalues and complex eigenvectors, accordingly with the theoretical analyses [4]-[7]. The equilibrium position of the system presents pitchfork bifurcations at relative high speeds, called critical speeds. The attention is mainly focused on the postbifurcation region by extending the local analysis presented in [7] to the global dynamics, in particular the existence and stability of homoclinic orbits are numerically evaluated.

GOVERNING EQUATIONS

In this paper the nonlinear oscillations of an axially moving beam are studied, see Figure 1. When large amplitudes of oscillation are considered,

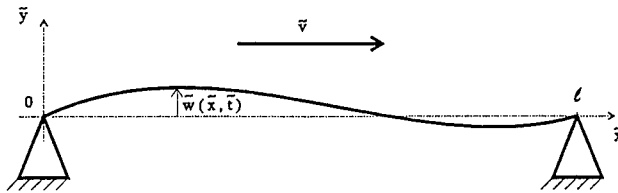


Figure 1: The travelling beam

a nonlinear coupling between longitudinal and transversal dynamics must be accounted for. Considering also the effect of the axial transport of mass, the following equations of motion of a travelling beam are obtained [7]:

$$\frac{\partial^2 u}{\partial t^2} + 2v \frac{\partial^2 u}{\partial x \partial t} + v^2 \frac{\partial^2 u}{\partial x^2} - v_T^2 \frac{\partial}{\partial x} \left[\frac{\partial u}{\partial x} + \frac{1}{2} \left(\frac{\partial w}{\partial x} \right)^2 \right] = 0, \quad (1)$$

$$\frac{\partial^2 w}{\partial t^2} + 2v \frac{\partial^2 w}{\partial x \partial t} + v^2 \frac{\partial^2 w}{\partial x^2} - \frac{\partial}{\partial x} \left\{ \frac{\partial w}{\partial x} + v_T^2 \frac{\partial w}{\partial x} \left[\frac{\partial u}{\partial x} + \frac{1}{2} \left(\frac{\partial w}{\partial x} \right)^2 \right] \right\} + v_f^2 \frac{\partial^4 w}{\partial x^4} = 0, \quad (2)$$

where $x \in (0, 1)$, $t > 0$, the following hinged boundary conditions are introduced:

$$u(0, t) = u(1, t) = 0, \quad t > 0 \quad (3)$$

$$w(0, t) = w(1, t) = 0, \quad \frac{\partial^2 w}{\partial x^2}(0, t) = \frac{\partial^2 w}{\partial x^2}(1, t) = 0, \quad t > 0 \quad (4)$$

and suitable initial conditions must be given to define the Cauchy problem.

It is worthwhile to underline that the mixed term $2v \frac{\partial^2 u}{\partial x \partial t}$ represents the Coriolis acceleration and play a role in transforming the differential operator from symmetric into skew-symmetric; the term $v^2 \frac{\partial^2 u}{\partial x^2}$ represents the centrifugal acceleration and causes the bifurcation.

The previous equations are presented in a nondimensional form, by introducing the following dimensionless quantities:

$$\begin{aligned} w &= \tilde{w}/\ell & u &= \tilde{u}/\ell & x &= \tilde{x}/\ell & t &= \tilde{t}\sqrt{P/\rho A\ell^2} \\ v &= \tilde{v}/\sqrt{P/\rho A} & v_T &= \sqrt{EA/P} & v_f &= \sqrt{EI/P\ell^2} \end{aligned}$$

where \tilde{w} and \tilde{u} are the transversal and the longitudinal displacement fields, \tilde{x} is the spatial coordinate along the axis of the beam, \tilde{t} the time, \tilde{v} is the axial speed, ℓ the beam length, P the axial tension, A the cross section area, ρ the mass density, I the inertia moment and E the Young modulus.

Neglecting the fast dynamics in the longitudinal direction, the axial displacement can be condensed. So that the transversal oscillations are governed by an integro-differential equation in terms of the transversal displacement $w(x, t)$ only:

$$\frac{\partial^2 w}{\partial t^2} + 2v \frac{\partial^2 w}{\partial x \partial t} + (v^2 - 1) \frac{\partial^2 w}{\partial x^2} + v_f^2 \frac{\partial^4 w}{\partial x^4} = \frac{v_T^2}{2} \frac{\partial^2 w}{\partial x^2} \int_0^1 \left(\frac{\partial w(\xi, t)}{\partial \xi} \right)^2 d\xi, \quad x \in (0, 1), \quad t > 0 \quad (5)$$

with the boundary conditions (4).

DISCRETIZATION APPROACH

The equation of motion (5) is discretized using the Galérkin procedure by expanding the displacement field $w(x, t)$ as series of suitable functions: $w = \sum_{n=0}^{\infty} q_n(t) \phi_n(x)$. The functional basis $\phi_n(x)$ must be a complete set of functions and respect the boundary conditions. For the present problem it is sufficient to use the sine series. In the Galérkin method the series is truncated to the N -th term and, after projection, a finite dimensional dynamical system is obtained. Applying the procedure to equation (5) one obtains:

$$\begin{aligned} \ddot{q}_n - 2v \sum_{k=1, k \neq n}^N k \left[\frac{(-1)^{n+k} - 1}{n+k} + \frac{(-1)^{n-k} - 1}{n-k} \right] \dot{q}_k + \\ + \left[v_f^2 n^4 \pi^4 - (v^2 - 1) n^2 \pi^2 \right] q_n = -\frac{v_T^2 n^2 \pi^4}{4} q_n \sum_{k=1}^N k^2 q_k^2, \quad n = 1, \dots, N \quad (6) \end{aligned}$$

The previous system of equations can be rewritten in compact form as:

$$\ddot{\mathbf{q}} + \mathbf{C}\dot{\mathbf{q}} + \mathbf{K}\mathbf{q} = \mathbf{f}(\mathbf{q}) \quad (7)$$

and in the state space

$$\dot{\mathbf{p}} = \mathbf{A}\mathbf{p} + \mathbf{F}(\mathbf{p}) \quad (8)$$

where $\mathbf{p} = [\dot{\mathbf{q}}^T, \mathbf{q}^T]^T$, $\mathbf{A} = \begin{bmatrix} \mathbf{C} & \mathbf{K} \\ \mathbf{I} & \mathbf{0} \end{bmatrix}$, \mathbf{I} is the identity matrix and $\mathbf{F}(\mathbf{p}) = -[\mathbf{f}(\mathbf{q})^T, \mathbf{0}^T]^T$ collect the nonlinear terms. Analyzing the spectra of \mathbf{A} one can study the linear stability of the trivial position and rewrite (8) into the diagonal form:

$$\dot{\xi} = \Lambda \xi + \mathbf{r}(\xi) \quad (9)$$

where Λ is the eigenvalue matrix, $\xi = Q^{-1}p$, Q is the eigenvector matrix and $r = Q^{-1}F(Q\xi)$. The transformation that leads to equation (9) is the first step for the applications of suitable perturbation procedures, that are useful to analyze local motions.

BIFURCATION ANALYSIS

When the axial speed of the beam is large enough, the inertia forces ($v^2 \partial^2 w / \partial x^2$) could exceed the elastic forces and the trivial equilibrium position $w = 0$ could become unstable. Wickert [7] studied theoretically the fixed points of equation (5) obtaining the bifurcated configurations:

$$w^{(k)} = \pm \frac{2}{k\pi v_1} \sqrt{v^2 - v^{(k)2}} \sin k\pi x, \quad k = 1, 2, \dots \quad (10)$$

Each $w^{(k)}$ exists only when v exceeds the critical speed $v^{(k)}$, where $v^{(k)} = \sqrt{1 + (k\pi v_f)^2}$, $k = 1, 2, \dots$

Even if equation (8) is able to describe any motion of the system represented by equation (5), a linear stability analysis of the bifurcated positions needs a suitable change of coordinates that moves the axes origin from the trivial equilibrium position to the bifurcated one:

$$p = p_0 + y \quad (11)$$

where p_0 indicates the new equilibrium position. The system equations written in terms of the variable y become:

$$\dot{y} = Dy + F_2(y) + F_3(y) \quad (12)$$

where:

$$\begin{aligned} d_{i,k} &= a_{i,k}, & i, k &= 1, \dots, N \\ d_{i,k+N} &= a_{i,k+N} + 2p_{0,i+N} \bar{b}_{i,k} p_{0,k+N}, & i, k &= 1, \dots, N, \quad k \neq i \\ d_{i,i+N} &= a_{i,i+N} + 2p_{0,i+N}^2 \bar{b}_{i,i} + \sum_{h=1}^N \bar{b}_{i,h} p_{0,h+N}^2, & i &= 1, \dots, N \\ d_{i+N,k} &= a_{i+N,k}, & i, k &= 1, \dots, N \\ F_{2,i} &= p_{0,i+N} \sum_{k=1}^N \bar{b}_{i,k} y_{k+N}^2 + y_{i+N} \sum_{k=1}^N 2\bar{b}_{i,k} p_{0,k+N} y_{k+N}, & i &= 1, \dots, N \\ F_{3,i} &= y_{i+N} \sum_{k=1}^N \bar{b}_{i,k} y_{k+N}^2, \quad \bar{b}_{i,k} = -\frac{v_1^2 \pi^4 i^2 k^2}{4}, & i, k &= 1, \dots, N \\ F_{2,i} &= F_{3,i} = 0, & i &= N+1, \dots, 2N \end{aligned} \quad (13)$$

The linearized system is represented by the matrix D that is quite different from the original matrix A . The spectral analysis of the operator D

enables to study the stability of the nontrivial fixed points. As far as the nonlinear portion of the vector field is concerned, the change of coordinates gives rise to quadratic terms due to the initial curvature of the bifurcated configurations.

NUMERICAL RESULTS

In the previous studies [4, 7] the linear modal characteristics, stability and bifurcations of equilibrium positions have been studied by applying suitable techniques to obtain eigenvalues and eigenfunctions of the system. Here similar results are presented for linear analysis, bifurcation and stability, confirming the validity of the discretized model. Moreover, some new results regarding the global motion are presented. In this section a test case with the following data is studied: $\ell = 0.2m$, $A = 10^{-5}m^2$, $I = 2.08 \cdot 10^{-13}$, $E = 2.1 \cdot 10^{11}$, $P = 100N$, that give: $v_f = 0.105$ and $v^{(1)} = 1.05$.

In Figure 2 the imaginary parts of the first four eigenvalues of \mathbf{A} are evaluated with $N = 8$ in the series expansion of the solution. For $v = v^{(1)}$ the first bifurcation occurs: in this condition the first natural frequency becomes zero. Up to the critical speed, the real part of all the eigenvalues is zero, while after the bifurcation the first pair of eigenvalues becomes real. This means that the trivial position becomes unstable after the bifurcation, this phenomenon is due to the centrifugal forces that exceed the elastic forces after the bifurcation.

In Figure 3 the absolute value of the component of the first four modes on the sine basis is presented when the series is truncated up to the eighth degree of freedom and $v = 1$. At high speeds the even coordinates become less important. For example the second mode shape, that for $v = 0$ is $\sin 2\pi x$, is mainly represented by $\sin \pi x$ and $\sin 3\pi x$, and less significantly by the others. In Figure 4 the real and the imaginary part of the first four modes are plotted showing clearly the shape of the modes at high subcritical velocity. In accordance to what previously discussed, the imaginary part becomes vanishing with the increasing of the mode number. This provides two effects: the linear dynamics at high frequency is described by real modes, as if the gyroscopic effects were not present; conversely the effect of the gyroscopic matrix makes the even modes almost symmetric.

In Figure 5 the bifurcation diagram is presented. The Lagrangian coordinates are represented in function of the parameter v . As expected, at the first critical speed the first bifurcation involves the coordinate q_1 only, then at the second bifurcation velocity the bifurcation of q_2 is present; the curves numerically obtained coincide analytical results.

At $v > v^{(1)}$, for example at $v = 1.1$, the trivial equilibrium position is unstable. Therefore, under a small perturbation the system evolves indefinitely far from the initial position. Moreover, if one observes that the system is linearly and nonlinearly coupled in the lagrangian coordinates

q_n , then a global motion governed by slow as well as fast dynamic components could be expected. Conversely, Figure 6 shows that a very regular homoclinic orbits exists. In fact, under an infinitesimal perturbation ($q_1(0) = 10^{-6}$, $q_i(0) = 0$, $i = 2, \dots, N$) the system slowly goes far from the unstable position and slowly comes back. Not large coupling between the degrees of freedom is present, only a small contribution of q_i , $i = 2, \dots, N$ is found. The motion is periodic; due to different time histories of the Lagrangian coordinates, the dynamic configuration change slightly during the period with respect to the fundamental $\sin \pi x$ shape. However Figures 7-10 show that, perturbing more and more strongly the unstable position or giving an initial condition far from $w = 0$ ($q_1(0) = 0.01, 0.05, 0.27, 0.28$ respectively for Figures 7-10 and $q_i(0) = 0$, $i = 2, \dots, N$), but close to the homoclinic orbit, a motion exhibiting fast as well as slow dynamics arises. The fundamental period becomes notably shorter as the homoclinic orbit more strongly perturbed. These "perturbed" trajectories confirm that the homoclinic orbit crosses a portion of the phase space where the nonlinearities as well as the coupling are strong. Moreover, the homoclinic orbit is embedded in a tangle of phase trajectories.

Figure 11-a shows the Fast Fourier Transform of the time histories of $q_1(t)$ in the following three cases: the homoclinic orbit presented in Figure 6, the strong perturbed orbit presented in Figure 9, the weak perturbation of the stable fixed point.

Finally, Figure 10 shows that, after the second bifurcation, perturbing the trivial equilibrium position ($q_1(0) = 10^{-6}$, $q_i(0) = 0$, $i = 2, \dots, N$) the homoclinic orbit breaks down and the response is characterized by a complex fast dynamics.

CONCLUSIONS

In this paper the dynamics of an axially moving beam is studied. The Galérkin method is used to discretize the spatial differential operator. Preliminary results for the linear model and the static bifurcations are fully in agreement with the literature. An interesting behaviour of the system has been observed in a suitable supercritical speed range, in between the first and the second critical velocities, where a structurally stable homoclinic trajectory exists. This orbit crosses a region of the phase space where the nonlinearities as well as the coupling between the degrees of freedom is not weak, but it seems that, close to this special orbit, the dynamics is governed by slow time scales only. After the second critical velocity the response exhibits slow as well as fast dynamics. The N degrees of freedom analysis here presented allows to solve the initial condition problem without any restriction concerning the dynamic configuration shape, thus extending the results developed in the past on the subject. Moreover, the model can be enhanced in order to develop suitable N -degrees of freedom

perturbation procedures useful to perform parametric analyses in the case of external harmonic forcing.

REFERENCES

- [1] Ashley H. and Haviland G., "Bending Vibrations of a Pipe Line Containing Flowing Fluid," *J. of Appl. Mech.*, **17**, 1950, 229-232.
- [2] Ames W. F., Lee S. Y. and Zaiser J. N., "Non-Linear Vibration of a Travelling Threadline", *Int. J. Non-Lin. Mech.*, **3**, 1968, 449-469.
- [3] Thurman A.L. and Mote C.D. Jr., "Free, Periodic, Nonlinear Oscillation of an Axially Moving Strip", *J. of Appl. Mech.*, **36**, 1969, 83-91.
- [4] Wickert J.A. and Mote C.D. Jr, "Classical Vibration Analysis of Axially Moving Continua", *J. of Appl. Mech.*, **57**, 1990, 738-744.
- [5] Meirovich L., "A Modal Analysis for the Response of Linear Gyroscopic Systems", *J. of Appl. Mech.*, **42**, 1975, 446-450.
- [6] D'Eulerio G.M.T. and Hughes P.C., "Dynamics of Gyroelastic Continua", *J. of Appl. Mech.*, **51**, 1984, 415-422,.
- [7] Wickert J.A., "Non-linear vibration of a travelling tensioned beam", *Int. J. Non-Lin. Mech.*, **27**, 1992, 503-517.
- [8] Guckenheimer J. and Holmes P., *Nonlinear Oscillations, Dynamical Systems, and Bifurcations of Vector Fields*, Springer Verlag, New York, 1983.

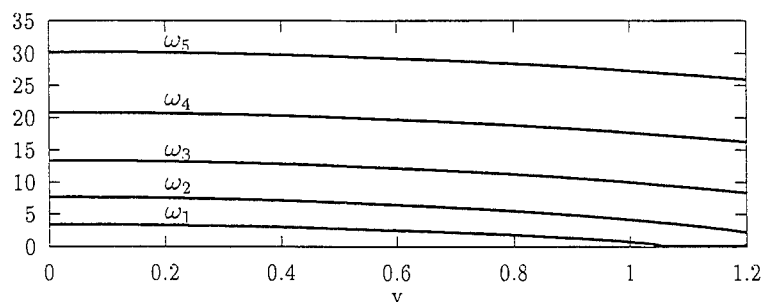


Figure 2: Behaviour of the linear natural frequencies

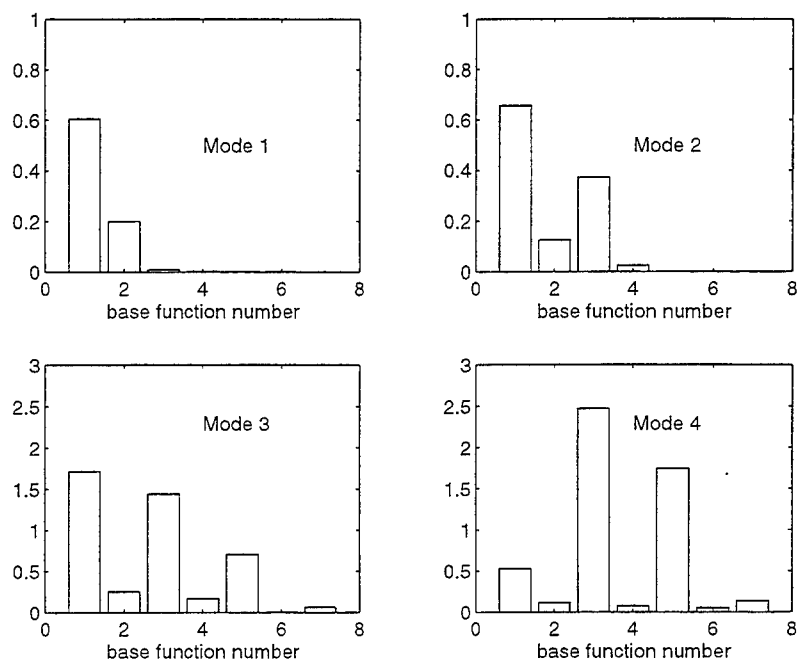


Figure 3: Representation of linear modes in terms of the lagrangian coordinates q_i , $i = 1, \dots, 8$

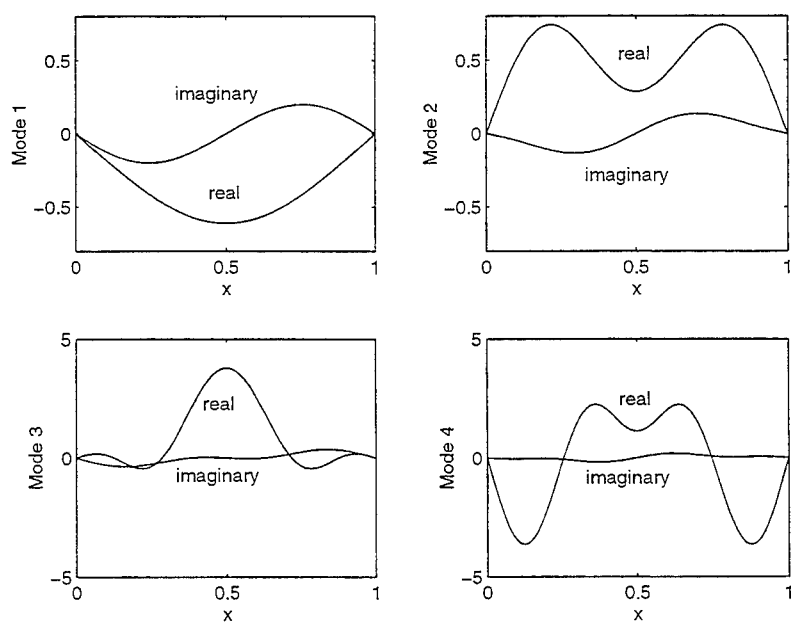


Figure 4: Spatial form of the complex eigenfunctions

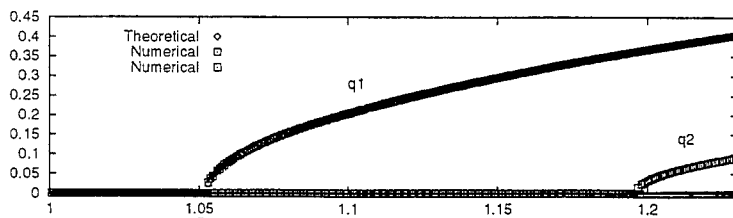


Figure 5: Bifurcation diagram

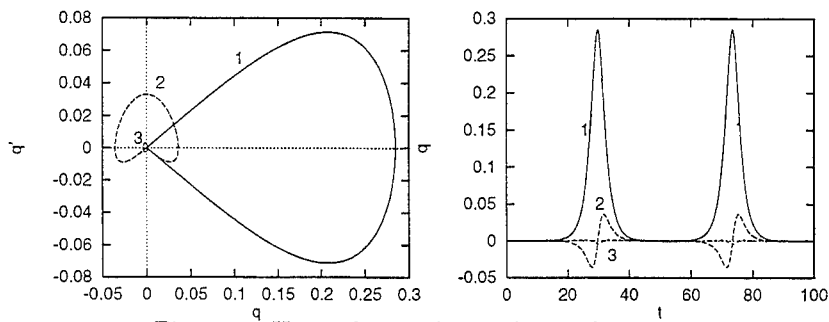


Figure 6: Homoclinic orbit and time histories

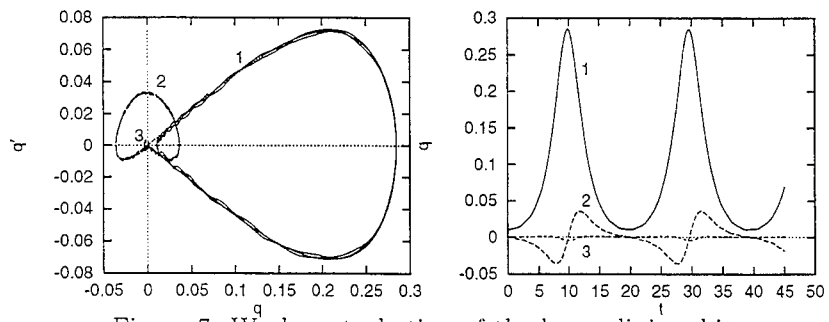


Figure 7: Weak perturbation of the homoclinic orbit

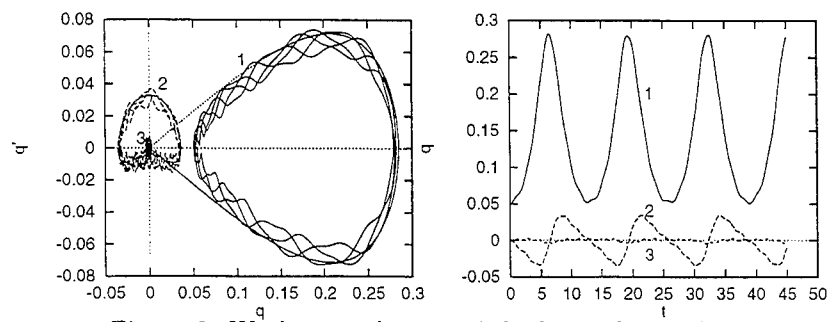


Figure 8: Weak perturbation of the homoclinic orbit

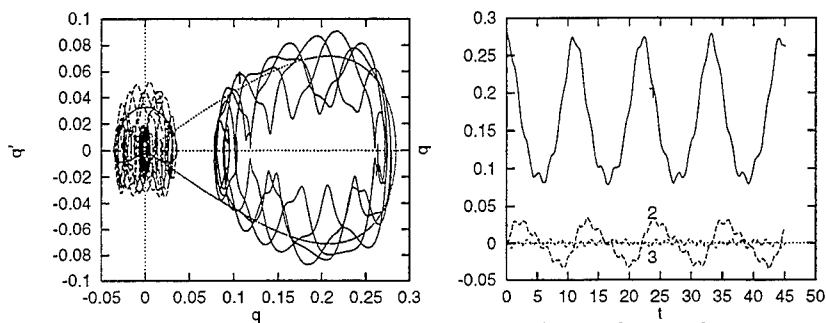


Figure 9: Strong perturbation of the homoclinic orbit

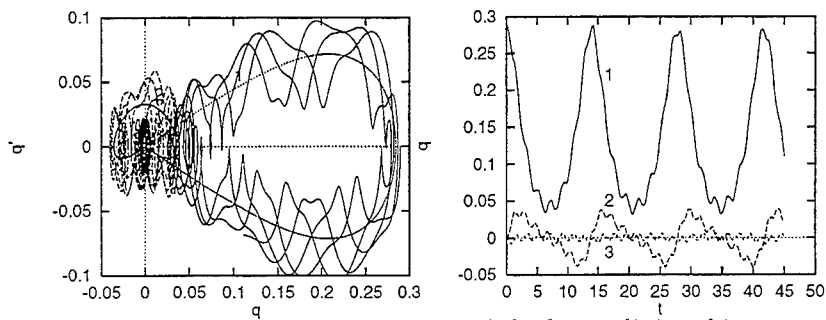


Figure 10: Strong perturbation of the homoclinic orbit

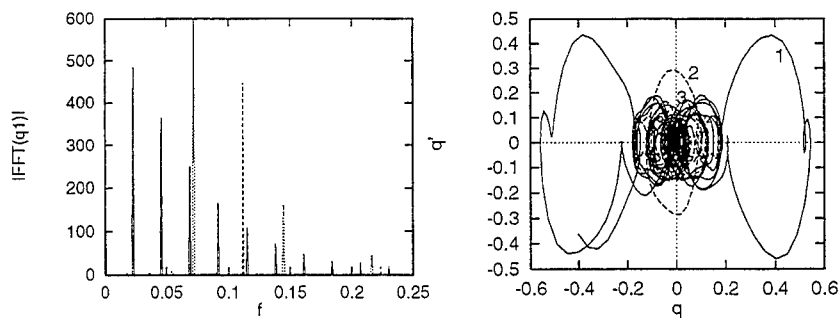


Figure 11: a) Frequency contents of the time histories of: the homoclinic orbit (—), the strongly perturbed homoclinic orbit (···), and weakly perturbed stable non-trivial equilibrium position (— —). b) Unstable trajectory after the second bifurcation, collapse of the homoclinic orbit

Transient Contact Response of a Hermetic Reciprocating Compressor Valve

İ. Yıldırım⁽¹⁾, M.Ö. Akbal⁽¹⁾, H.T. Belek⁽²⁾

(1) Research Engineers, Arçelik R & D Center 81719 Tuzla, İstanbul, Turkey

(2) Professor, Faculty of Mechanical Engineering, Istanbul Technical University, 80191 Gümüşsuyu, İstanbul, Turkey

ABSTRACT

Valve leaves in reciprocating compressors are used to open and close the inlet and discharge ports. The fatigue failure of these leaves due to bending stresses, impact and the influence of the valve behaviour on efficiency, makes the valve leaves extremely important components of the compressors. The leaf can be modelled as one edge clamped plate. One difficulty of the problem that makes it interesting is the requirement to model the contact of the valve with the stopper. In the present study Newmark-Beta direct integration method is used to solve the equation of motion. External forces are measured experimentally in the cylinder and inlet chamber of the hermetic compressor. The force distribution on the structure is calculated using a Computational Fluid Dynamics Code. The normalised pressure distribution obtained through the measurements is used to calculate the time dependant distributed forces on the leaf.

INTRODUCTION

In small refrigerator compressors, the refrigerant gas enters and leaves the compression chamber through the holes where the opening and closing mechanism is controlled by the pressure activated reed valves. In the ideal case, valves should be massless and should suddenly open and close. However in real operation, it takes some time to open and close completely due the inertia and damping of the refrigerant. Dynamic behaviour of the valve leaf has an important influence on the performance parameters. The parameters such as the noise level, volumetric efficiency, reliability is directly related to the behaviour of the valve leaf. The main components of a compressor and the suction valve are shown in Figures I and II.

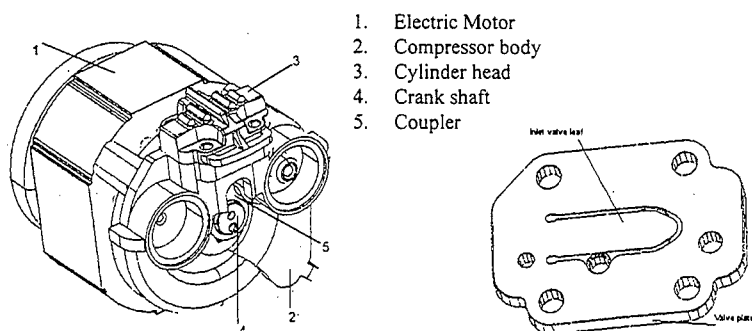


Figure I. Main components of a compressor

Figure II. Close look at the suction compressor valve.

It is possible to find extensive literature on the design of valve leaves. A general layout of the design and the mechanics of the compressor valves together with the suggestions and the rules of thumb gained from past experience are summarised by Soedel, [1].

If the Principle of Virtual Work is applied to the valve leaf problem, it can be expressed in the form of an equality of the work done by the internal forces to that of the external forces including the inertia forces applied, hence the following variational equation is obtained:

$$\int_{\Omega} \delta \varepsilon^T \sigma d\Omega - \int_{\Omega} \delta u^T b d\Omega - \int_{\Gamma_F} \delta u^T \bar{q} dS - \int_{\Gamma_c} \delta u^T \bar{q} dS + \int_{\Omega} \delta u^T \rho \ddot{u} d\Omega = 0 \quad (1)$$

This equation can be explained verbally as follows:

Given the traction vector \bar{q} on the boundary Γ_F and the body forces b in the domain Ω , for $t \in [0, T]$; find the displacement of all points in the domain, $u(x, t)$ for all $t \in [0, T]$ such that the equation of motion, constitutive equation, initial conditions, boundary conditions and the contact conditions are all satisfied. In this variational form it is suitable to apply the Finite Element Method. The leaf is modelled as one edge clamped plate, Figure III.

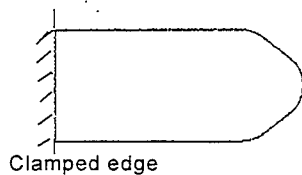


Figure III. The selected geometry of the modelled valve.

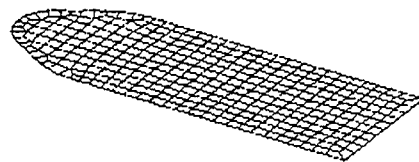


Figure IV. Selected mesh for the geometry.

To solve the virtual work equation using the Finite Element Method, the domain Ω is subdivided into elements V^e as shown in Figure IV and the displacement field is approximated by the shape functions $N_i(x)$ which are expressed in terms of the spatial parameters and the nodal displacements $u_i(t)$ incorporating the time.

$$u(x, t) = N_i(x) u_i(t) \quad (2)$$

Notice that the shape functions do not depend on time. Due to the separation of the time and space dependent part, the discretization of velocities and acceleration can easily be obtained.

With appropriate manipulations the following system of equations can be obtained:

$$M \ddot{u} + \tilde{F}_{int} = \tilde{F}_{ext} \quad (3)$$

In this equation, $M = \int \rho N^T N d\Omega$. One more term may be added into equation (3), namely, the damping force vector \tilde{F}_{damp} .

Newmark - Beta method is used for the solution of equation (3). In order to select the appropriate time interval, the natural frequencies of the system are calculated and the results are given in Table I, the valve material properties are given in Table II.

Table I. Natural frequencies of the valve.

Frequency no	1	2	3
Frequency (Hz)	365	2085	2145

Table II. The material properties of the valve.

Modulus of Elasticity (GPa)	Poisson's ratio	Density (kg/m ³)
210	0.3	7850

The time step used in the analysis should be selected in a suitable way to allow the actual response to be modelled with reasonable accuracy. If a phase error of 10% for the highest relevant frequency is selected then one can calculate the time step as follows, [2]:

$$\Delta t = \frac{1}{\omega_{max}} \quad (4)$$

For the lower frequencies the error will even be smaller. Therefore time step relating the phase error will be:

$$\Delta t = \frac{1}{4911} = 4.66e-4$$

For the contact analysis, in order to make the displacement increments small enough to detect the contact, a time step of, 0.25 e-4, is taken. This time step corresponds to 400 steps within a 0.01 second period during the transient behaviour solution.

For the contact treatment, the solver constraint equations are used. Once the contact is detected, the contact constraint equations are defined and the convergence of the solution is checked. If a separation is detected after the solution of the system equations, the contact constraints are changed and a new iteration is started. If a penetration is observed then the time increment is divided into smaller intervals.

The pressure inside the cylinder and in the cylinder inlet plenum is measured using the pressure transducers. This pressure difference, multiplied by the normalised pressure distribution for the open position of the valve is applied

on the model. The stopper in the system is modelled as a rigid body. Figure V shows the normalised pressure difference distribution on the valve surface as computed by using a Computational Fluid Dynamics code, [4].

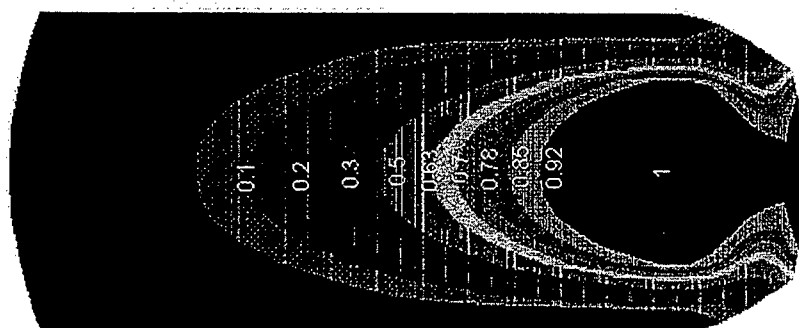


Figure V. The pressure distribution at the open position.

RESULTS AND PARAMETRIC STUDIES

In the present study, the affects of valve thickness, stopper height and using no stopper are investigated. Deflection of the valve; as an indicator of the valve opening, velocity; as for the impact criteria, bending stress; as for the bending fatigue criteria are compared. The results are obtained for the points along the mid-length of the valve. The locations are indicated in Figure VI. Temporal variation of lateral displacement and velocity at the tip are shown in Figure VII and VIII. Bending stresses are plotted as function of time at the mid-point of the valve. Four different cases, namely, (A, B, C, D) are taken into consideration as specified in Table III.

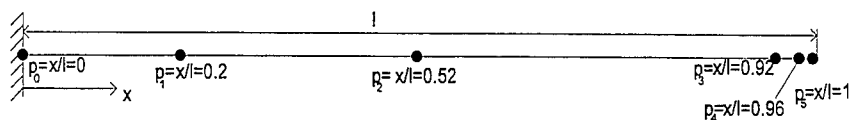


Figure VI. Representative points

The lateral displacements of four case studies are shown in Figure VII. The contact time to the stopper is shorter as the valve thickness gets thinner. The valve thickness has also an important influence on the displacements after 0.005 second due to the inertia effects.

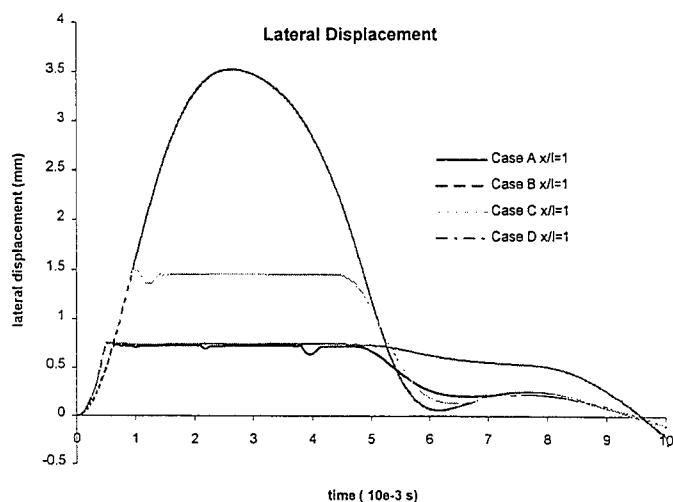


Figure VII. Lateral displacement of the tip point for different cases.

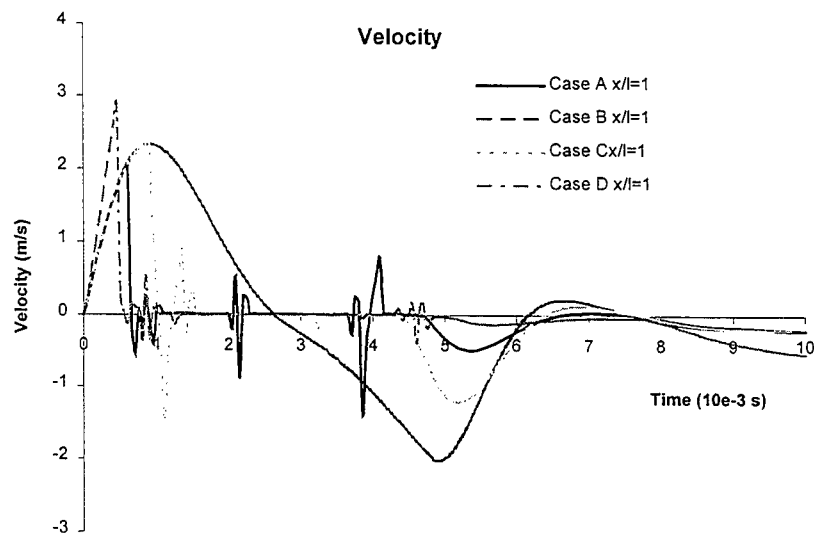


Figure VIII. Velocity of the tip point for different cases.

The velocities of the tip points for the four cases are shown in Figure VIII. Quite a smooth velocity variation is observed for the case without a stopper. For cases, which include stoppers, due to loss of contact sudden velocity changes are observed. Maximum velocity which is used as an impact fatigue criteria among the compressor manufacturers exceed the allowable limits.

The bending stresses at approximately mid-span of the valve are plotted in Figure IX. It should be noted that at the start, the stress at the lower side of the valve is compressive as expected. However, as the middle of the valve continue to deform while the tip is resting on the stopper; the sign of the bending reverses from compressive to tension due to the curving of the valve.

Table III. Results

	Case A	Case B	Case C	Case D
Valve thickness (mm)	0.2	0.2	0.2	0.15
Stopper Height (mm)	0.72	-	1.44	0.72
Max. Displacement (mm)				
P ₀	0	0	0	0
P ₁	0.09	0.26	0.13	0.14
P ₂	0.40	1.33	0.64	0.56
P ₃	0.68	3.15	1.34	0.74
P ₄	0.71	3.34	1.41	0.74
P ₅	0.73	3.52	1.48	0.75
Max. Velocity (m/s)				
P ₀	0	0	0	0
P ₁	0.16	0.17	0.19	0.30
P ₂	0.77	0.88	0.87	1.28
P ₃	1.83	2.08	2.08	2.58
P ₄	1.94	2.21	2.21	2.74
P ₅	2.05	2.33	2.33	2.88
Max. Bending Stress (Mpa)	218	596	316	265
Contact Time (ms)	0.65	-	0.9	0.5
Max. Reaction Force (N)	2.2	-	3.47	4.34

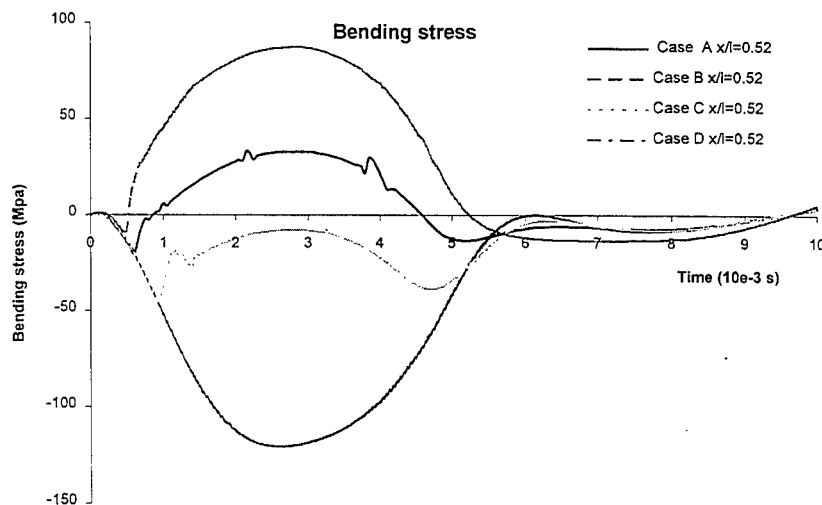


Figure IX. The bending stress of the mid-point for different cases.

CONCLUSIONS

Different parameters are changed to see their effects on the valve response. Position of the valve in time, velocities, stresses and reaction forces are obtained. Some quantitative values are obtained which may be of some importance for the design engineers.

It is seen that by making the valve softer, faster opening times may result. A valve that will completely stay open even by the slightest pressure difference, acting at the open position seems to be a suitable one. This can be achieved by making the valve softer. On the other hand for such a valve, fatigue life should also be considered. Life tests in well-defined loading conditions are recommended for the future study. Measurement of the valve motion in real operating conditions by adjusting the magnitude of the pressure loading acting on the valve should be realised to predict the behaviour of the valve. Such an experimental verification of the response of the valve will help researchers to modify the mathematical models. Thus the design of softer valves with longer fatigue life should be possible.

REFERENCES

- [1] SOEDEL, W., **Design and Mechanics of Compressor valves**, Ray. W. Herrick Laboratories, School of Mechanical Engineering, Purdue University, 1984.
- [2] GRAAF, IR. A. P. DE., KONTER, IR. A. W. A., **Dynamic analysis with Marc**, Marc Analysis Research Corporation, Munich, December, 11-12 1992.
- [3] YILDIRIM, I. **Transient contact analysis of a hermetic reciprocating compressor valve**, MSc. Thesis, Faculty of Mechanical Engineering, Istanbul Technical University, 1996.
- [4] STAR-CD 2.3 Tutorials Volume, February 1996. Computational Dynamics Limited.